





16th INTERNATIONAL COMBUSTION SYMPOSIUM

September 08-11, 2022 Aydın - TÜRKİYE

SYMPOSIUM PROCEEDINGS

Editor in Chief
Prof. Dr. Nafiz KAHRAMAN

https://www.yanmasempozyumu.com/

INCOS2022

The Proceedings of 16th International Combustion Symposium (INCOS2022)

September 08-11, 2022

Aydın Adnan Menderes University, Aydın, Türkiye

Edited by

Prof. Dr. Nafiz KAHRAMAN (Co-Chair of Symposium)

Copyright

ISBN 978-625-00-9337-5

© 2022, INCOS2022, Aydın Adnan Menderes University

Aydın, Türkiye

https://www.yanmasempozyumu.com/

The proceedings include the original papers submitted to INCOS2022. It is accessed in free of charge. All scientific and linguistic responsibilities of the published articles belong to their authors.

16th International Combustion Symposium (INCOS2022)
08-11 September 2022

Aydın Adnan Menderes University, Aydın, Türkiye

HONORARY BOARD

Prof. Dr. Hakan S. SOYHAN / (Head of Combustion Institute's Turkish Section, Sakarya University)

Prof. Dr. Osman Selçuk ALDEMİR / (Rector, Aydin Adnan Menderes University)

Prof. Dr. Oğuz BORAT /(Chairman of the Board of TAI , Founder of Combustion Institute's Turkish Section)

Prof. Dr. T. Nejat VEZİROĞLU / (Founding Editor-in-Chief, International Journal of Hydrogen Energy)

Organization Committee

Assoc. Prof. Dr. Erdinç VURAL (Aydin Adnan Menderes University) Chair

Prof. Dr. Nafiz KAHRAMAN / (Erciyes University) Co-Chair

Prof. Dr. Mustafa İLBAŞ / (Gazi University)

Prof. Dr. S. Orhan AKANSU / (Erciyes University)

Prof. Dr. Bilge A. ÇEPER / (Erciyes University)

Advisory Committee

Assoc. Prof. Dr. Serhat KARYEYEN / (Gazi University)

Prof. Dr. Ahmet ERDİL / (Kocaeli University)

Prof. Dr. Ali SÜRMEN / (Uludağ University)

Prof. Dr. Bahattin ÇELİK / (Karabük University)

Prof. Dr. Mustafa ÇANAKÇI / (Kocaeli University)

Prof. Dr. Mustafa İLBAŞ / (Gazi University)

Prof. Dr. Orhan AKANSU / (Erciyes University)

Prof. Dr. Sebahattin ÜNALAN / (Erciyes University)

Prof. Dr. Veli ÇELİK / (Yıldırım Beyazıt University)

Scientific Committee

A. Korhan BINARK / (Sabahattin Zaim University)

A. Necati ÖZSEZEN / (Kocaeli University)

A. Nilgün AKIN / (Kocaeli University)

A. S. RAMADHAS / (Indian Oil Corporation Ltd. R&D Center)

A.K. AGARWAL / (Indian Institute of Technology)

Abdülkadir BEKTAŞ / (The Ministry of Energy and Natural Resources)

Adnan SÖZEN / (Gazi University)

Ahmet YOZGATLIGİL / (Middle East Technical University)

Ali ATA / (Gebze Technical University)

Ali KESKİN / (Çukurova University)

Ali KILIÇARSLAN / (Hitit University)

Ali KOÇ / (Iskenderun Technical University)

Ali KODAL / (Istanbul Technical University)

Ali TÜRKCAN / (Kocaeli University)

Amin Paykani / (University of Hertfordshire)

Aramugam RAMADHAS / (National Institue of Technology Calicut)

Arif HEPBAŞLI / (Yaşar University)

Bart SOMERS / (Tu Eindhoven)

Battal DOĞAN / (Gazi University)

Bilge ALBAYRAK ÇEPER / (Erciyes University)

Bülent KESKİNLER / (Gebze Technical University)

C. D. RAKOPOULOS / (National Technical University of Athens)

Can ÇINAR / (Gazi University)

Can HAŞİMOĞLU / (Sakarya University)

Cem SORUSBAY / (Istanbul Technical University)

Cengiz ONER / (Fırat University)

Cenk SAYIN / (Marmara University)

Cevahir TARHAN / (Erciyes University)

Salih ÖZER / (Mus Alparslan University)

Duran ALTIPARMAK / (Gazi University)

E. G. GIAKOUMIS / (National Technical University of Athens)

Emrah Berat BİRSEN / (The Ministry of Energy and Natural Resources)

Emrah DENİZ / (Karabük University)

Erdinç VURAL / (Aydin Adnan Menderes University)

Erol ARCAKLIOĞLU / (Yıldırım Beyazıt University)

Ertan ALPTEKİN / (Kocaeli Univeristy)

Ertuğrul ARSLAN / (Istanbul Technical University)

Essam Abo-Serie / (Coventry University)

Filiz KARAOSMANOĞLU / (Istanbul Technical University)

Gautam KALGHATGI / (Shell Global Solutions)

George SKEVIS / (CPERI/CRERTH)

Gudrat I. ISAKOV / (Institute of Physics of ANAS)

Güven TUNÇ / (Gazi University)

H. İbrahim SARAÇ / (Kocaeli University)

H. Serdar YUCESU / (Gazi University)
Hafiz ALİYEV / (Khazar University)
Hakan BAYRAKTAR / (Karadeniz Technical University)
Hakan Fehmi ÖZTOP / (Fırat University)
Hakan Serhad SOYHAN / (Sakarya University)
Halim Hamid REDHWI / (King Fahd University of Petroleum)
Halit KARABULUT / (Gazi University)
Halit YAŞAR / (Sakarya University)
Hanbey HAZAR / (Fırat University)
Hasan Rıza GÜVEN / (İstanbul University)
Hendry Y. Nanlohy / (Jayapura University of Science and Technology)
Hüseyin BAYRAKÇEKEN / (Afyon Kocatepe University)
Hüseyin GÜNERHAN / (Ege University)
Hüseyin ŞANLI / (Kocaeli University)
İbrahim DİNÇER / (QUIT Canada)
İbrahim KILIÇASLAN / (Kocaeli University)
İbrahim MUTLU / (Afyon Kocatepe University)
İhsan KARAMANGİL / (Uludağ University)
İlker ÖRS / (Selçuk University)
İlker YILMAZ / (Gazi University)
İskender GÖKALP / (Middle East Technical University)
İsmail ALTUN / (Karadeniz Technical University)
İsmail ATA / (Erciyes University)
İsmail BÖĞREKÇİ / (Aydin Adnan Menderes University)
İsmail ÇELİKTEN / (Gazi University)
İsmail EKMEKÇİ / (Marmara University)
İsmail TEKE / (Yıldız Technical University)
İsmet ÇEVİK / (Sakarya University)
Joseph SWAN / (Institute for Energy Research)
Julian DIZY / (CMCL)
Kadir AYDIN / (Çukurova University)
Kadri Süleyman YİĞİT / (Kocaeli University)
Kamil ARSLAN / (Karabük University)
Kemal ERSAN / (Gazi University)
L.M.T. Bart SOMERS / (Technische Universiteit Eindhoven)
M. Bahadır ÖZDEMİR / (Gazi University)
M. Bahattin ÇELİK / (Karabük University)
M. Kemal BALKI / (Sinop University)
M. Sahir SALMAN / (Gazi University)

Malgotzata WOJTYNIAK / (Technical University of Radom)

Mario COSTA / (Instituto Superior Technico)

Mehmet AKÇAY / (Mus Alparslan University)

Melih YILDIZ / (Iğdır University)

Metin ERGENEMAN / (İstanbul Technical University)

Metin GÜMÜŞ / (Marmara University)

Mohy MANSOUR / (Cairo University)

Muammer ÖZKAN / (Yıldız Technical University)

Muhammed İbrahim AL-HASAN / (Al-Balqa' Applied University)

Murat HOSOZ / (Kocaeli University)

Murat KARABEKTAŞ / (Sakarya University)

Murat ŞAHİN / (Milli Savunma University)

Murat TAŞTAN / (Erciyes University)

Mustafa ACAROĞLU / (Selçuk University)

Mustafa BALCI / (EU Turkey Delegation)

Mustafa ÇANAKÇI / (Kocaeli University)

Mustafa İLBAŞ / (Gazi University)

Mustafa KARAGÖZ / (Karabük University)

Mustafa KAYA / (Siirt University)

Nafiz KAHRAMAN / (Erciyes University)

Nazım USTA / (Pamukkale University)

Nezahat BOZ / (Gazi University)

Nurettin DİNLER / (Gazi University)

Nuri YUCEL / (Gazi University)

Osman IŞIKAN / (Marmara University)

Philippe DAGAUTT / (CNRS)

Ramazan KÖSE / (Dumlupınar University)

Recai KUS / (Selçuk University)

Rıdvan ARSLAN / (Uludağ University)

Roger CRACKNELL / (Shell Global Solutions)

S. Orhan AKANSU / (Erciyes University)

Selami SAĞIROĞLU / (Karabük University)

Selçuk SARIKOÇ / (Amasya University)

Selim TANGÖZ / (Erciyes University)

Şeref SOYLU / (Bilecik Şeyh Edebali University)

Serhat KARYEYEN / (Gazi University)

Serkan ÖZEL / (Bitlis Eren University)

Suat SARIDEMİR / (Düzce University)

Süleyman USTUN / (Celal Bayar University)

Tamer YILMAZ / (Yıldız Technical University)

Xibin WANG / (Xi'an Jiatong University)

Yakup İÇİNGÜR / (Gazi University)

Yasin VAROL / (Fırat University)

Zafer DULGER / (Kocaeli University)

Zehra ŞAHİN / (Karadeniz Technical University)

Zuohua HUANG / (Jiatong University)

Symposium Secretariat

Esenay ARSLAN / (Kayseri University)

Caner ŞİMŞEK / (Erciyes University)

Fethi Mustafa ÇİMEN / (Gazi University)

Hüseyin Enes Fil (Erciyes University)

16th International Combustion Symposium (INCOS2022)

PREFACE

Combustion Symposium that is one of the longest running and most prestigious engineering symposium series of the periodic activities of Turkey Branch of The Combustion Institute. This series of symposiums, which have been held since 1983 and as online in 2020, and hybrid in 2022 for the 16th time, were planned to be held biyearly and were mostly held two years apart, although not every time. After the first 5 symposiums were organized in Bursa, it was open to the organization requests of other universities in order to increase the area of activity and 15 symposiums (Uludağ University (6 times), İstanbul Technical University (1 times), Gazi University (1 times), Marmara University (1 times), Kırıkkale University (1 times) and Sakarya University (1 times), International Sarajevo University (IUS) (1 times), Kocaeli University (1 times), Karabük University (1 times) and Erciyes University (1 times) have been organized so far.

Combustion and combustion technologies, which are almost the only way to obtain mechanical energy from fossil fuels, have gained much more importance today, when we are experiencing the effects of global warming and climate changes frequently.

Since combustion is the conversion of fuels into heat energy or mechanical energy, it finds a place in countless applications from the kitchens of our homes to motor vehicles, from heat boilers to iron and steel furnaces and power plants. Therefore, the techniques and efficiency of this transformation are of vital importance. Especially in today's world, where energy has become a global strategic weapon, besides energy resources, how to use these resources more effectively, so fuels and combustion issues have become one of the most prominent topics of study for researchers.

At the 16th International Combustion Symposium held as a hybrid, three invited speakers made presentations with participation from abroad.

A total of 27 sessions were held at the symposium, 9 of which were face-to-face and 18 were online. A total of 101 papers were presented orally, 34 in face-to-face sessions and 67 in online sessions, on alternative fuels, combustors, combustion technologies, fuel injection, numerical modelling and simulation on combustion, fire and carbon emissions.

The symposium was successfully held with the participation of over 250 participants from 13 different countries, both face-to-face and online.

I would like to thank the symposium honour, organization, management and advisory board members, reviewers, invited speakers, session chairs, participants and especially the symposium secretariat who contributed to the successful implementation of the symposium.

Best regards,

Prof. Dr. Nafiz KAHRAMAN

Co-Chair of the Symposium

16th International Combustion Symposium (INCOS2022)

08-11 September 2022

Keynote Speaker: PROF. DR. ALİ CEMAL BENİM

Speech Title: Challenges In Computational Modelling Of Gas Turbine Combustion

Duesseldorf University of Applied Sciences



CV: Prof. Dr. Ali Cemal Benim received his B.Sc. and M.Sc. degrees at the Bogazici University, and his Ph.D. degree at the University of Stuttgart.The topic of his PhD Thesis was Finite Element Modeling of Turbulent Flames, which was awarded by Degree of Distinction. Subsequently, he joined ABB Turbo Systems in Switzerland.
He was the manager of the group Computational Flow and Combustion Modeling. Currently, he is a Professor for Energy Technology at the Düsseldorf University of Applied Sciences, leading the Center of Flow Simulation (CFS).
He authored and co-authored over 250 publications in various fields of application including the finite element, finite analytic, lattice Boltzmann methods, Navier-Stokes solution techniques, turbulence, combustion/gasification, two-phase flows, heat transfer, erosion, turbomachinery, aerodynamics, biofluid dynamics.
He is the Executive Editor of Progress in Computational Fluid Dynamics and has editorial positions in a number of further journals along with his organizational activities in many conferences.

CHALLENGES IN COMPUTATIONAL MODELLING OF GAS TURBINE COMBUSTION

A.C. Benim

Center of Flow Simulation (CFS), Department of Mechanical and Process Engineering, Düsseldorf University of Applied Sciences, Düsseldorf, Germany; email: alicemal@prof-benim.com

Abstract

Challenges in modelling turbulent combustion in land-based gas turbine combustors are discussed in an overview, in a historical perspective. Since several decades, one of the main goals in gas turbine combustion has been to reduce Nitrogen Oxide (NO_x) emissions, while retaining high combustion efficiency. This has led to the development of lean premixed technology, which is the state-of-the-art in modern land-based gas turbine combustors. This technology, however, puts special demands on the design, and, consequently, on the associated modelling of the momentum, heat and mass transport processes in the combustor.

As one of the challenges, associated with the lean combustion, the thermoacoustic problem is shortly discussed based on the Rayleigh criterion, and modelling approaches based on the Flame Transfer Function (FTF) approach are outlined.

In the stabilization of lean flames in gas turbine combustors, swirl plays a central role, which creates special challenges for the turbulence modelling. The predominant effect of swirl on the turbulence structure is to create a strong non-isotropy, which can strongly overburden the state-of-the-art RANS (Reynolds Averaged Numerical Solutions) based turbulence models that assume an isotropic turbulence structure as implied by a scalar turbulent viscosity. A further feature of swirling flows is that an increase of the swirl number beyond a critical value leads to the so called sub-critical flow state, which is characterized by a quasi-deterministic low frequency unsteadiness, leading quite often to the so-called “precessing vortex core” (PVC), and exhibiting a strong sensitivity to the downstream conditions. These features put additional demands on the computational modelling. In the modern lean premixed combustion technology, the applied swirl numbers are quite high, for being able to stabilize the flame under lean conditions, which especially necessitates an adequate modelling strategy for the swirling flow, as far as the turbulence modelling is concerned. To this purpose, a series of investigations are discussed, where different turbulence models such as RANS, URANS (Unsteady RANS), DES (Detached Eddy Simulations) and different versions of LES (Large Eddy Simulations) are applied to different experimental configurations. It is demonstrated that for an accurate prediction of strongly swirling turbulent flows, approaches are needed that can account at least for the three-dimensional low-frequency unsteadiness of the coherent structures and the non-isotropic structure of turbulence.

For modelling the turbulence-chemistry interaction, two modelling strategies, namely the EDC (Eddy Dissipation Concept) and the LFM (Laminar Flamelet Method) are followed. In LFM, limitations of the standard non-premixed approach, based on the mixture fraction and the scalar dissipation rate, is overcome by adding the progress variable as an additional dimension to the flamelet libraries that allows the prediction of premixed and partially premixed flames within a unified approach. By comparisons with experiments, it is demonstrated that LFM and

EDC approaches lead to quite accurate and comparable results, when applied within the LES framework for turbulence modelling.

As a further challenge, the demands on fuel flexibility are addressed, with respect to the usage of syngas, biogas and natural gas-hydrogen fuel blends. As the main challenge, the increased flashback propensity of hydrogen and hydrogen containing fuels is underlined. It is demonstrated that accurate results can be obtained for a premixed turbulent swirling syngas and the flashback behaviour can be predicted, based on the LES and LFM approach. Special forms of flashback for swirling flames, such as the so-called Flashback Caused by Combustion Induced Vortex Breakdown are discussed. As one of the measures for guarding against flashback, the role of the quenching mesh is discussed and the predictability of important parameters in this respect, such as the quenching distance, by different reaction mechanisms is discussed.

The counterpart of flashback is blow-off, the precursor of which is the lifted flame. This mode has an indirect relevance to the flashback problem, as it impedes an attachment of the flame to fuel injector. A lifted hydrogen flame is computationally investigated and it is shown that quite accurate results are obtained for the field distributions of the variables and for the lift-off height for the considered operation conditions.

16th International Combustion Symposium (INCOS2022)

08-11 September 2022

Keynote Speaker: PROF. DR. NADİR YILMAZ



Speech Title: Computational Analysis And Experimental Validation Of Upward And Downward Aluminum Rocket Propellant Combustion

Department of Mechanical Engineering, Howard University

CV: Nadir Yilmaz is a professor and the department chair of Mechanical Engineering at Howard University, as well as, a licensed professional engineer (P.E.) and consultant. He received B.S., M.S., and Ph.D. degrees in Mechanical Engineering from Istanbul Technical University, Bradley University and New Mexico State University, respectively. He is a Fellow of ASME (American Society of Mechanical Engineers), a Fellow of NSPE (National Society of Professional Engineers) and a Fellow of SAE International (Society of Automotive Engineers). He has been a noted author of many publications in the fields of combustion, CFD, rocket propulsion and automotive engineering. He was a U.S. Department of Energy Visiting Faculty Fellow at Sandia National Laboratories in 2012 and 2013. He has educated and mentored many underrepresented minority and female students via various STEM programs including the NSF-funded AMP (Alliance for Minority Participation) program.

Dr. Yilmaz serves as the Editor-In-Chief for the SAE International Journal of Fuels and Lubricants and as a member of the editorial board of numerous international journals. In addition, he serves on SAE Foundation Board of Trustees, NSPE Education Foundation Board of Trustees, New Mexico AMP Advisory Board and the Board of Directors of Society of Automotive Engineers of Turkey. Dr. Yilmaz has also served as the Past Chair of SAE Education Board, NSPE Higher Education Executive Board, SAE Washington DC Section and ASME New Mexico Section.

COMPUTATIONAL ANALYSIS AND EXPERIMENTAL VALIDATION OF UPWARD AND DOWNWARD ALUMINUM ROCKET PROPELLANT COMBUSTION

Nadir Yilmaz

Department of Mechanical Engineering, Howard University, 20059 Washington D.C, USA; email: nadir.yilmaz@howard.edu

Abstract

Aluminum alloys exhibit multi-faceted complex behaviors that require further research and understanding, such as aluminum particle combustion, oxide skin formation affecting combustion dynamics and creep behavior, due to the role of the aluminum oxide layer on the deformation and the strength of the alloy above melting temperature. The study of aluminum particle behavior in an open atmosphere propellant burn is of particular interest when considering accident scenarios for rockets carrying high-value payloads. One of the major difficulties in analyzing the thermal environment that a payload will see is the behavior of aluminum particles, which are a component in the propellant formulation. In this study, aluminum particle burn was modelled in upward and downward directions, via a computational fluid dynamics code, with comparison to experimental data. Several correlations were used to formulate the evaporation rates for aluminum particles. Uncertainty quantification was determined based on a series of parameters including propellant surface velocity, propellant surface temperature, propellant surface radiation temperature, parcel count, particle diameter, turbulent Prandtl number and turbulent Schmidt number. For the downward burn, a gap was created between a downward facing combusting propellant surface and an upward facing inert surface. Perturbation of the velocity of the propellant surface and propellant surface temperature showed greater sensitivity on the plume temperature. For the upward burn configuration, as the propellant surface velocity increased, the maximum temperature would decrease, but it was shown to increase the gas temperature closer to the propellant surface. Conversely, reducing the propellant surface velocity was shown to increase the maximum temperature, but overshoot the experimental results. Variation of parcel count, particle diameter, turbulent Prandtl number and turbulent Schmidt number had insignificant effect on the outcomes. Overall, the baseline simulation data demonstrated reasonable agreement with the experimental data.

Keywords: Aluminum combustion, particle ignition, rocket propellant, validation an verification

16th International Combustion Symposium (INCOS2022)

08-11 September 2022



Keynote Speaker : Prof. Dr. SHOUYIN (IAN) YANG

Speech Title: Numerical Simulation of Biomass Fast Pyrolysis under Modified Comprehensive Multistep Kinetic Scheme

Chair of The Combustion Institute of ROC / Department of Power Mechanical Engineering, National Formosa University

CV:

Disciplines

- Bioengineering
- Environmental Engineering
- Chemical Engineering

Skills and expertise

- Biomass Energy
- Pyrolysis
- Renewable Energy
- Biofuels
- Biomass
- Biomass Conversion
- Renewable Energy Technologies
- Gasification
- Energy Engineering
- Energy Conversion
- Biomass Burning
- Biomass Torrefaction
- Lignocellulosic Conversion

NUMERICAL SIMULATION OF BIOMASS FAST PYROLYSIS UNDER MODIFIED COMPREHENSIVE MULTISTEP KINETIC SCHEME

Shouyin (Ian) Yang

Department of Power Mechanical Engineering, National Formosa University, Yunlin County 63202, Taiwan

Abstract

About 86% of world energy is supplied by fossil fuels triggering adverse environmental problems. Lignocellulosic biomass is abundantly available on a large scale. Fast pyrolysis is one of the promising technologies for converting biomass into valuable products such as bio-oil, non-condensable gas (NCG), and biochar (solid residue). A fluidized bed reactor is a mature and widely used reactor offering excellent solid mixing and heat transfer allowing the high biomass conversion and short bioparticles and pyrolytic vapor residence time beneficially for maximizing the bio-oil product yield.

Computational Fluid Dynamics (CFD) is a powerful tool in elucidating the internal behaviour of reacting flows including hydrodynamics and chemical reactions with high efficiency and cost-effectiveness. Through a formula developed by Channiwala and Parikh based on the elemental composition of species, the energy content of the species can be predicted. Thus, the energy and exergy dynamics of the pyrolysis process can be evaluated numerically using this mechanism. Most pyrolysis simulations focused on the biomass conversion, product yield, and hydrodynamics performance. None of that investigate deeply the energy and exergy dynamics. Since it has been proposed in 2008, the comprehensive kinetic scheme has undergone many improvements. However, the pyrolysis product compositions have not accorded with experimental results; specifically, the simulated bio-oil products were dominated by sugars and water and phenolic products presented in low fractions. The comprehensive kinetic scheme have more than 20 reaction steps which is the longest pyrolysis kinetic scheme.

The specific purposes of this research are:

- To modify the comprehensive multistep kinetic reaction by changing the bio-oil species based on the large species found in the experimental bio-oil product. The modified mechanism is implemented for simulating the fast pyrolysis in a tubular furnace.
- To simplify the comprehensive multistep kinetic reaction by combining the reactions and removing the negligible reaction steps. This approach compresses the reaction step from 25 into 16 steps including moisture evaporation.
- To integrate the primary simplified mechanism with the advanced secondary reaction and homogeneous gaseous reactions applied in fluidized bed pyrolysis. This approach enriches the main biomass thermal decomposition reaction with the tar cracking and gas reactions for accommodating high-temperature pyrolysis

Energy and exergy contents were strongly correlated with the pyrolysis product compositions; meanwhile, energy and exergy yields were reflected in the pyrolysis product yields. Cellulose was superior for energy and exergy of the bio-oil product; meanwhile, lignin species tended to have high energy and exergy to a solid product. Moreover, lignin species generally had superior energy and exergy efficiency. Both biomass feeding rate and fluidizing velocity significantly affected the heat for pyrolysis, energy consumption ratio (ECR), and energy efficiency. A reactor capacity rate was proposed for reactor scale-up from laboratory scale to pilot and commercial scales.

INTERNATIONAL COMBUSTION SYMPOSIUM

SCHEDULE

08 SEPT. 2022 THURSDAY-1st DAY / FIRST SESSION

Registration (08:30-09:30)

TULIP HALL

OPENING CEREMONY AND WELCOME SPEECH - (09.30-10.00)
PROF. DR. NAFİZ KAHRAMAN, CONFERENCE CO-CHAIR
ASSOC. PROF. DR. ERDİNÇ VURAL, CONFERENCE CHAIR
PROF. DR. HAKAN SERHAD SOYHAN, CHAIR OF THE TURKISH SECTION

https://meeting.mkcelikbas.com/b/inc-j2v-ul4-yb2

PLENARY SPEECH (10.00-10.30)
PROF. DR. ALİ CEMAL BENİM, Duesseldorf University of Applied Sciences
https://meeting.mkcelikbas.com/b/inc-t2r-qxj-rby

Coffee Break (10:30-10:45)

TULIP HALL / FACE TO FACE			**LILY HALL / HYBRID**			**DAISY HALL / ONLINE**		
1. Session: COMBUSTION (10:45-12:00) **Session Chair: Prof. Dr. HAKAN SERHAD SOYHAN**			**2. Session: ALTERNATIVE FUELS (10:45-12:00)** **Session Chair: Prof. Dr. MUSTAFA İLBAŞ**			**3. Session: SPRAY-INJECTION (10:45-12:00)** **Session Chair: Prof. Dr. NAFİZ KAHRAMAN**		
https://meeting.mkcelikbas.com/b/inc-356-0gx-4fx			**https://meeting.mkcelikbas.com/b/inc-h3v-uxz-fi4**			**https://meeting.mkcelikbas.com/b/inc-v8r-ole-cel**		
10:45-11:00	OP-2022-xMPSWEIN Investigation of Early Intake Valve Closing Strategy and Exhaust Gas Recirculation (EGR) on PCCI Engine Operation	Cengizhan Cengiz Salih Özen Ünverdi	**10:45-11:00**	OP-2022-D6vJS9EX Experimental investigation of the effects of gasoline, methanol and natural gas fuel on engine performance and emissions in a gasoline engine	Talip Akbiyik, Nafiz Kahraman, Tolga Taner	**10:45-11:00**	OP-2022-V3ICIN Investigation Of The Effect Of Diesel Injector Nozzle Geometry On Coking Phenemona	O. Özener, A.Ergenç A.Kaya, V. Gazi
11:00-11:15	OP-2022-COTWIN Influence Of Air-Fuel Ratio On The Combustion And Performance Characteristics Of A Wankel Engine For Unmanned Aerial Vehicle (Uav) Applications	Merve Küçük, Ali Sürmen, Ramazan Şener	**11:00-11:15**	OP-2022-XHDMSY Systematic Study Of Friction Modifiers For Motor Gasoline, Their Structure, Mechanism Of Action, Efficiency Evaluation And Role In The Production Of Modern Fuel	Vsevolod D. Savelenko, Mikhail A. Ershov, Nikita A. Klimov, Nikita O. Burov, David R. Aleksanyan, Alisa E. Makhmudova1, Tamer M.M. Abdellatief, Andrey A. Pimenov, Kirill A. Ovchinniko, Ekaterina V. Podlesnova, Alexey V. Nizovtsev	**11:00-11:15**	OP-2022-pmZlthCO Combined Effects Of Hydrogen Fuel Addition And Egr Application In A CRDI Compression Ignition Engine Fueled With Dme Under Homogeneous Charge Compression Ignition (HCCI) Mode: A Pathway To Achieve Ultra-Low Emissions Along With Energy Efficiency Improvement With Controlled Auto-Ignition	Anilkumar Shere, K. A. Subramanian
11:15-11:30	OP-2022-0DYSa2DY Dynamic Flame Behavior Of 30%H2 30%CO 20%CO2 20%CNG Synthetic Gas Mixture During Acoustic Forcing	Ömer Çam Harun Yilmaz Ilker Yilmaz	**11:15-11:30**	OP-2022-o0n3SAEX Experimental Analysis Of A Hydrogen/Diesel Dual Fuel Test Case Via Ir Imaging	C. Allouis, E. Mancaruso, R De Robbio, B.M. Vaglieco	**11:15-11:30**	OP-2022-8R3cL0TH The Effect of Multiple Injection on CI Engine Pollutant Emissions and Green House Gases	Arda Albayrak, Onur Gezer, Orkun Özener, Cihan Büyük, Muammer Özkan
11:30-11:45	OP-2022-UdaCPHAN An Experimental Investigation Of Oxygenated Fuels Blending Effect On Gasoline Engine Performance And Emissions	Mehrez Gassoumi, Zouhair Boutar, Ridha Ennetta, Hakan Serhad Soyhan	**11:30-11:45**	OP-2022-Y9QKTH The effect of addition H, H+OH and H+OH+O2 from the intake manifold on combustion parameters in a CI engine using diesel/di ethyl ether as pilot fuel	Salih Özer, Erdinç Vural	**11:30-11:45**		

11:45-12:00	OP-2022-PWCBTH The Comparison Of Quasi-Steady Evaporation Models In A Swirl Stabilized Combustion Chamber	Deniz İmamoğlu, Özgür Ertunç, Altuğ M. Başol, M.Pınar Mengüç	**11:45-12:00**	OP-2022-vEflicEX Experimental And Computational Premixed Laminar Flame Propagation Studies For Hydrogen Containing Fuels	T.B. Kıymaz, D. Güleryüz, C. Allouis, İ. Gökalp, E. Saday, M. Karaca, B. Yılmaz, O. Kaya, O.C.Kocaman, S. Gümrük, B. Yazıcı, B. Sümer, F. Coşkun	**11:45-12:00**		
LUNCH								

08 SEPT. 2022 THURSDAY-1st DAY / SECOND SESSION

TULIP HALL / FACE TO FACE			**LILY HALL / HYBRID**			**DAISY HALL / ONLINE**		
4. Session: HYDROGEN AND FUEL CELL (13:15-14:30) **Session Chair: Prof. Dr. ALİ SÜRMEN**			**5. Session: MODELLING AND SIMULATION (13:15-14:30)** **Session Chair: Prof. Dr. İSKENDER GÖKALP**			**6. Session: GENERAL (13:15-14:30)** **Session Chair: Prof. Dr. ALİ CEMAL BENİM**		
https://meeting.mkcelikbas.com/b/inc-50y-lns-mas			**https://meeting.mkcelikbas.com/b/inc-3pd-rts-lqn**			**https://meeting.mkcelikbas.com/b/inc-rle-hch-nb8**		
13:15-13:30	OP-2022-07SnzMNU Numerical Study On The Performance Of A Flat-Tubular Solid Oxide Fuel Cell: Describing The Best Furnace/Combustion Chamber Geometry And Combustion Technique	Fethi Mustafa Çimen, Serhat Karyeyen, Mustafa İlbaş	**13:15-13:30**	OP-2022-jxKhsVNU Numerical Study On Impact Of Combustor Metrics Of Turboprop Engine Used In Air Freighter	Mehmet Kirmizi, Hakan Aygun, Onder Turan	**13:15-13:30**	OP-2022-WA6BIN Investigation of the effects of different rates of hexane blended fuel utilized in a ceramic coated diesel engine on HC, NOx and Smoke Opacity by Taguchi method	Erdinç Vural, Salih Özer, Serkan Özel, Murat Binici
13:30-13:45	OP-2022-WlIU8uA A Parametric Study To Optimize The Temperature Of Hazelnut And Walnut Shell Gasification For Hydrogen And Methane Production	H. Öztan, İ. Koçyiğit Çapoğlu, D. Uysal, Ö. M. Doğan	**13:30-13:45**	OP-2022-ON3imRTH Three Dimensional Numerical Investigation Of Flow And Combustion Characteristics In An Ammonia Fueled Multi-Inlet Cyclone Combustor	Mustafa Ilbas, Assem Yerzhan, Mustafa Demirci	**13:30-13:45**	OP-2022-X2B1S4SY Synthesis of Pt/rGO Cathode Catalysts for PEM Fuel Cells through Polyol and Colloidal Methods	Tolga Kaan Kanatli, Nezihe Ayas
13:45-14:00	OP-2022-6B3FTH The Effect Of Different Charging Concepts On Hydrogen Fueled Internal Combustion Engines	İlker Güler, Onur Barış, Anıl Yaşgül, Abdullah Kılıçaslan	**13:45-14:00**	OP-2022-YemFALTH The Numerical Study On Co-Firing Of Biomass-Coal Blends In 100 Kw Lab-Scale Swirl Flame	Cansu Deniz Canal, Yakup Erhan Boke, Ali Cemal Benim	**13:45-14:00**	OP-2022-dj8UZ2FR Fragmentation of droplets of coal-water slurries containing petrochemicals under different heating methods	D.V. Antonov, O.V. Vysokomornaya, K.Y. Vershinina, G.V. Kuznetsov, P.A. Strizhak
14:00-14:15	OP-2022-NAHAEF Effects Of Hydrogen Enrichment Strategy On Combustion And Emissions In A Gasoline Fuelled Rotary Engine	Merve Küçük, Ali Sürmen, Ramazan Şener	**14:00-14:15**	OP-2022-PRFJCH Characterization Of A Partially Premixed Swirl Burner Using Openfoam Simulations With A Global Chemical Kinetics Mechanism	Emre Böncü, Dilay Güleryüz, Tahsin Berk Kiymaz, İskender Gökalp	**14:00-14:15**	OP-2022-ZJQTIN Investigations of Flame Characteristics of LPG Used in Three Different Size Household Cookers	Berkay Şahin, Nimeti Doner, Mustafa Ilbas
14:15-14:30			**14:15-14:30**	OP-2022-ILOIAN An Analysis of a Heavy-Duty Diesel Truck Powertrain System Hybridization	Yücel Karaca, Hasan Kubilay Yiğit, Caner Bayburtlu, Orkun Özener	**14:15-14:30**		
Coffee Break (14:30-14:45)								

08 SEPT. 2022 THURSDAY - 1st DAY / THIRD SESSION

TULIP HALL / FACE TO FACE			LILY HALL / HYBRID			DAISY HALL / ONLINE		
7. Session: COMBUSTION-SPRAY-INJECTION (14:45-16:00) Session Chair: Dr. RIDHA ENNETTA			**8. Session: TUBULENCE-SWIRL (14:45-16:00) Session Chair: Prof. Dr. MOHAMMAD RAFIQ KHAN**			**9. Session: GENERAL (14:45-16:00) Session Chair: Prof. Dr. NEZIHE AYAS**		
https://meeting.mkcelikbas.com/b/inc-xrs-gw6-h4o			**https://meeting.mkcelikbas.com/b/inc-6ln-dia-iqh**			**https://meeting.mkcelikbas.com/b/inc-zc5-te5-pdc**		
14:45-15:00	OP-2022-Y0PXA A Study On Capturing Acoustic Behaviour In Confined Tube Combustion Using Optical Technique	S.P. Choudhury, S. Sasidharan, R. Joarder	**14:45-15:00**	OP-2022-VaiVyqST Study On OH* Chemiluminescence Of NH3/Air Swirl Flame	Danan Chen, Jun Li, Xing Li, Yijun Guo, Hongyu Huang, Noriyuki Kobayashi	**14:45-15:00**	OP-2022-TkbyLYQU Qualitative Visualization of Butane and Helium Tracers in Air using a Digital Background-Based Schlieren Method	Frank Ulrich Rückert, Dirk Hübner, Daniel Lehser-Pfeffermann, Alexander Hamman
15:00-15:15	OP-2022-AVPH4wIN Investigation Of Soot Formation Of Swirl-Stabilized Jet A-1 Spray Flame With Rank Correlated Slw Including Ethylene And Acetylene Radiation	Berkay Halvaşi, Altuğ M. Başol, Özgür Ertunç, M. Pınar Mengüç	**15:00-15:15**	OP-2022-TPOPOP Three-Dimensional Modelling Of Ammonia_Methane_Air Turbulent Flames In A Generated Perforated Burner And Furnace	Murat Şahin, Mustafa İlbaş	**15:00-15:15**	OP-2022-HXJQSY Synthesis of Bentonite Supported Ni and Ni-La Catalysts for the Steam Reforming of Acetic Acid	Damla Dumlu, Ecem Ceylan, Merve Bayrakdar, Serkan Karadeniz, Tolga Kaan Kanatlı, Nezihe Ayas
15:15-15:30	OP-2022-uSvAAOCH Char reactivity assessment of high ash coal in packed bed environments - Experimental investigations	Shirish Kumar Sharma, Anand M Shivapuji, S. Dasappa	**15:15-15:30**	OP-2022-KBfRlTCO Combustion Characteristics And Kinetics Of Blends Of Lignite With Eggshell	Sena Erkent, Sema Yurdakul, Barış Gürel, Karani Kurtuluş, Savaş Özün	**15:15-15:30**	OP-2022-G5nYE8PY Pyrolysis And Combustion Characteristics Of Tea Stalk Lignin: Effect Of Organosolv And Sequential Hydrothermal-Organosolv Pretreatments	S. Başakçilardan Kabakci, B. Karakurt Çevik, G.S. Baş Berkem
15:30-15:45	OP-2022-WXQ7EN Energy Recovery From Spent Coffee Ground And Brewery Spent Grains: A Circular Economy Approach To Waste Valorization	I. Idowu, L.J.R. Nunes, K.S Hashim, A. Shaw	**15:30-15:45**	OP-2022-DT9nYVSW Swirler Effects On Colorless Distributed Combustion Using Methane Flame	A. İlbaş, M. B. Özdemir, S. Karyeyen	**15:30-15:45**	OP-2022-NwqoymNE New Approach To Evaluating The Functional Properties Of Detergent Additives For Motor Gasoline	Vsevolod D. Savelenko, Mikhail A. Ershov, Nikita A. Klimov, Nikita O. Burov, David R. Aleksanyan, Ulyana A. Makhova, Tamer M.M. Abdellatief, Andrey A. Pimenov, Kirill A. Ovchinnikov, Ekaterina V. Podlesnova, Alexey V. Nizovtsev
15:45-16:00			**15:45-16:00**	OP-2022-RDZDtORA RANS studies of minimum ignition energy of stoichiometric laminar methane/air fuel mixtures	Vasudevan Sooraj PM, Muppala Siva PR, Vendra C. Madhav Rao, Heidari Ali, Dembele Siaka	**15:45-16:00**	OP-2022-DSBYAN Analysis Of Cross-Flow Tube Bank Economizer-Assisted For H2S	Murat Şahin
END OF FIRST DAY – FREE TIME								

09 SEPT. 2022 FRIDAY-2nd DAY / FIRST SESSION

TULIP HALL

PLENARY SPEECH (09.15-09.45)
PROF.DR. HAKAN SERHAD SOYHAN
https://meeting.mkcelikbas.com/b/inc-nip-dqs-qkg

Coffee Break (09:45-10:00)

	TULIP HALL / FACE TO FACE			LILY HALL / HYBRID			DAISY HALL / ONLINE		
	10. Session: GENERAL (10:00-11:00) **Session Chair: Dr. ALIYA FAZAL**			**11. Session: ALTERNATIVE FUELS (10:00-11:00)** **Session Chair: Dr. ORKUN ÖZENER**			**12. Session: COMBUSTION (YANMA) (10:00-11:00)** **Session Chair: Dr. ERDİNÇ VURAL**		
	https://meeting.mkcelikbas.com/b/inc-upt-gwn-3w7			**https://meeting.mkcelikbas.com/b/inc-wk6-pzh-om2**			**https://meeting.mkcelikbas.com/b/inc-b4i-rta-lev**		
10:00-10:15	OP-2022-cpgFfNAN An Application Of The Low-Great Heat Of Recycling Water Of Food Industry Enterprieses For Electric Generation	Viktoriia Karnaukh, Hakan Serhad Soyhan, A.B. Buryukov, V.V.Varakuta	**10:00-10:15**	OP-2022-BSux0SCO Comparison Of Different Origin Biodiesel Fuels' Some Critical Fuel Properties And Fatty Acid Compositions	F. Yasar, H. Sanli	**10:00-10:15**	OP-2022-J9oeEGDİ Dizel-Bor Türevi Karişimlarinin Damlacik Yanma Davranişlarinin Incelenmesi	Ahmet Alper Yontar, Mert Şevket Biçer
10:15-10:30-	OP-2022-DCJEGE Geochemical Analysis and Desulfurization of Black Gold for Sustainable Use in Thermal Energy Sector	Aliya Fazal	**10:15-10:30-**	OP-2022-7G1SMİ Microwave Assisted Biomass-Based Electrode Material Production for Supercapacitor Applications	Musa Altınışık, Tülin Avci Hansu, Murat Akdemir	**10:15-10:30-**	OP-2022-959vHMHİ Hidrojen Kullanilan Bir Dizel Motorda Çevrimsel Yanma Değişimlerinin Incelenmesi	A. Şanlı, I.T. Yılmaz
10:30-10:45-	OP-2022-yylsZpDİ Disposal of Rice Straw and Its Conversion Into Fermentable Sugar and Ethanol by Acid, Alkali, Enzymatic and Biological Treatments	Mohammad Rafiq Khan, Rabia Batool	**10:30-10:45-**			**10:30-10:45-**	OP-2022-q0jy92HO Homojen Dolgulu Sikiştirma Ateşlemeli Bir Motorda Hafif Nafta-Benzin Karişimi Kullaniminin Motor Performansi Ve Emisyonlarina Etkisi	S. Çelebi, U. Demir, C. Haşimoğlu
10:45-11:00			**10:45-11:00**			**10:45-11:00**	OP-2022-xSvnFxFA Düşük Girdap Üreteçli Brülörün Kullanildiği Bir Doğalgaz Kazaninda Yanma Ve Emisyonlarin Numerik İncelenmesi	M.S. Cellek, A. Pınarbaşı, G. Coskun
11:00-11:15			**11:00-11:15**			**11:00-11:15**	OP-2022-LZAYEX Ağir Hizmet Tipi Bir Dizel Motorda Dizel Ve Doğalgaz Karişimlarinin Motor Performansi Ve Egzoz Emisyonlari Üzerine Etkilerinin Deneysel İncelenmesi	Volkan Sabri Kül, Selahaddin Orhan Akansu

Coffee Break (11:00-11:15)

09 SEPT. 2022 FRIDAY-2nd DAY / SECOND SESSION

TULIP HALL / FACE TO FACE			LILY HALL / HYBRID			DAISY HALL / ONLINE		
13. Session: ALTERNATIVE FUELS (11:15-12:30) **Session Chair: Prof. Dr. S. ORHAN AKANSU**			**14. Session: COMBUSTION-INJECTION (11:15-12:30)** **Session Chair: Dr. MURAT ŞAHİN**			**15. Session: HYDROGEN FUEL AND FUEL CELL (11:15-12:30)** **Session Chair: Dr. TOLGA TANER**		
https://meeting.mkcelikbas.com/b/inc-mkx-r99-xqo			**https://meeting.mkcelikbas.com/b/inc-rox-rab-lko**			**https://meeting.mkcelikbas.com/b/inc-43l-vl1-3xo**		
11:15-11:30	OP-2022-N04UEX Experimental Investigation Of Diesel-Biodiesel-Ethanol Blends On A Compression Ignition Engine Performance	F. Hamdi, I. Yahya, Z. Bouttar, R. Ennetta, H.S. Soyhan	**11:15-11:30**	OP-2022-CUYy0CDE Designing A New Bell-Type Primary Air Nozzle For A Large-Scale Circulating Fluidized Bed Boilers	Mustafa Metin Çam, Cenk Çelik, Mansour Al Qubeissi, Hakan Serhad Soyhan	**11:15-11:30**	OP-2022-MM5İMİ Microwave-assisted synthesis of Pt/C catalyst at high temperatures for PEM fuel cells	Serkan Karadeniz, Nezihe Ayas
11:30-11:45	OP-2022-4WCVIN Influence of Two-Stage Fuel Injection Timing for Combustion and Emissions under Different Engine Loads in a Direct Injection Diesel Engine	H. Enes Fil, S. Orhan Akansu	**11:30-11:45**			**11:30-11:45**	OP-2022-0HyCyyEV Evaluation Of the Effect of System Parameters on Hydrogen Production İn Steam-Methane Reformers	Kubilay Bayramoglu, Can Coskun, Zuhal Oktay
11:45-12:00	OP-2022-3cc7kzTY Tyre Pyrolytic Oil Blends In A State Of The Art Compression Ignition Engine: Towards Fuel-Optimized Combustion	J. Hunicz, M. Mikulski	**11:45-12:00**			**11:45-12:00**	OP-2022-7QvQQ2DU Dunaliella Salina Microalgae Obtained as an Effective Material for Double Applications Supercapacitor and Hydrogen Production	Rıdvan Çetin, Mustafa Kaya, Murat Akdemir, Muhammet Ali Arserim
12:00-12:15	OP-2022-lWfcmxOP Optimization Of Hydrogen Production With Aluminium-Water Reactions	R. N. Mutlu, E. Eroğlu, J. Kandasamy, H. Ü. Toffoli, İ. Gökalp	**12:00-12:15**			**12:00-12:15**	OP-2022-xM5jbDUS Use Of Hydrogen-Biogas Mixture As Fuel In Common-Rail Diesel Engine With Thermal Barrier Coating	A. Şanlı, İ.T. Yılmaz, M. Akçay, M. Gümüş
12:15-12:30	OP-2022-pGoMkcA A Thermodynamic Approach To Calculate The Mean Turbulence Intencity Of CNG And Gasoline Fuels In A Research Engine	H.E. Doğan, A.Demirci, O.A.Kutlar, Ö.Cihan, H. Arslan	**12:15-12:30**			**12:15-12:30**	OP-2022-BHLMEX Experimental Investigation On Exploiting The Biofuels Blend And Improving Its Usability By Adding TİO2 Nanoparticles	Abdülvahap Çakmak

LUNCH

09 SEPT. 2022 FRIDAY-2nd DAY / THIRD SESSION

TULIP HALL

PLENARY SPEECH (14:30-15.00)
PROF.DR. NADİR YILMAZ

Coffee Break (15:00-15:15)

TULIP HALL / FACE TO FACE			LILY HALL / HYBRID			DAISY HALL / ONLINE		
16. Session: COMBUSTION (YANMA) (15:15-16:15) **Session Chair: Dr. ERDİNÇ VURAL**			**17. Session: MODELLING AND SIMULATION (15:15-16:15)** **Session Chair: Dr. NUREDDİN DİNLER**			**18. Session: FIRE (YANGIN) (15:15-16:15)** **Session Chair: Prof. Dr. BİLGE A. ÇEPER**		
https://meeting.mkcelikbas.com/b/inc-x3o-rp1-4el			**https://meeting.mkcelikbas.com/b/inc-ifb-hcz-y9q**			**https://meeting.mkcelikbas.com/b/inc-hek-rcg-lee**		
15:15-15:30	OP-2022-kVwhFtDE Detonasyon Motoruna Sahip Roketlerde Ön-Detonatorde Farkli Hidrojen-Karbon Oranina Sahip Yakitlarin Şok Dalgasi Üzerindeki Etkisinin Incelenmesi	Ahmet Alper Yontar, Mehmet Ali Adıgüzel	**15:15-15:30**	OP-2022-FSQ5NU Numerical Investigation of Power Generation Performance of Planar Solid Oxide Fuel Cell at Different Operating Temperatures	Süleyman Altindal, Eren Gürkan Erol, Barış Gürel, Sema Yurdakul	**15:15-15:30**	OP-2022-WdGL0lTE Termik Santrallerde Yangin Güvenliğinin Bir Örnek Üzerinden İncelenmesi	Elif Çataklı, Ekrem Büyükkaya, Gökhan Coşkun

15:30-15:45	OP-2022-KMXGÇİ Çift Yakitli Doğalgaz-Dizel Bir Motorda Enjeksiyon Stratejisinin Performans Ve Emisyonlara Etkisinin Incelenmesi	Mustafa Deniz Altinkurt, Menno Merts, Martin Tunér, Ali Türkcan	**15:30-15:45**	OP-2022-GmSqAZNU Numerical Investigation of Combustion and Flame Characteristics in a Swirl Burner/Furnace for a Model Thermoelectrical Generator(TEG) Performance	Mustafa Ilbas, Sumeyye Akyildiz, Serhat Karyeyen, Ahmet Aktas	**15:30-15:45**	OP-2022-c2suo9AL Alişveriş Merkezlerinde Insanlarin Acil Durum Tahliye Davranişlarinin Deneysel Ve Simülasyon Yöntemleriyle Incelenmesi	Koray Uluç, Gökhan Coşkun, Ekrem Büyükkaya
15:45-16:00	PP-2022-EQZHRE Reaktif Kontrollü Sikiştirma İle Ateşlemeli Bir Motorun Performans Ve Emisyon Parametrelerinin İncelenmesi	Ahmet Kaya, B. Albayrak Çeper, Nafiz Kahraman, S.Orhan Akansu	**15:45-16:00**	OP-2022-2nGmnaCH Characteristics of the gas hydrates ignition process	O.S. Gaidukova, P.A. Strizhak	**15:45-16:00**	OP-2022-7VNOHA Hastane Binalarinda Yangin Aninda Kullanicilarin Tahliyesinin Simülasyon Destekli Incelenmesi	Furkan Kadı, Gökhan Coşkun, Ekrem Büyükkaya
16:00-16:15			**16:00-16:15**	OP-2022-LHLDEV Evaluation of Binary Nanoparticles to Oxygenated Fuel with Ethanol and n- Butanol on Combustion Behavior	Raşit Atelge Esenay Arslan, Nafiz Kahraman, Sebahattin Ünalan	**16:00-16:15**	OP-2022-bLyIHQEL Elektrikli Taşitlarda Batarya Yanginlarina Genel Bakiş	M.I. Karamangil, A. Sürmen, M. Tekin
16:15-16:30			**16:15-16:30**			**16:15-16:30**		

END OF SECOND DAY – FREE TIME

10 SEPT. 2022 SATURDAY-3rd DAY / FIRST SESSION

TULIP HALL

PLENARY SPEECH (09.15-09.45)
PROF.DR. SHOUYIN (IAN) YANG, Chair of The Combustion Institute of ROC
https://meeting.mkcelikbas.com/b/inc-r3o-ezb-wx8

Coffee Break (09:45-10:00)

TULIP HALL / FACE TO FACE			**LILY HALL / HYBRID**			**DAISY HALL / ONLINE**		
19. Session: FIRE (YANGIN) (10:00-11:00) **Session Chair: Dr. SALIH ÖZER**			**20. Session: ALTERNATIVE FUELS (10:00-11:00)** **Session Chair: Dr. JACEK HUNICZ**			**21. Session: COMBUSTORS-FUELS (10:00-11:00)** **Session Chair: Dr. DUYGU UYSAL**		
https://meeting.mkcelikbas.com/b/inc-cis-tgl-u0j			**https://meeting.mkcelikbas.com/b/inc-b3n-9ux-auc**			**https://meeting.mkcelikbas.com/b/inc-sak-kqf-snn**		
10:00-10:15	OP-2022-EMSKÖZ Özgün Tasarimli Bir Endüstriyel Konveksiyonlu Firinda Baca Gazi Atik Isi Geri Kazanimi	Z. Kahraman, M. Hacı, K. İçibal, H.S. Soyhan	**10:00-10:15**	OP-2022-ENS2EV Evaluation Of Natural Gas Consumption In Turkey	S.Y. Kandemir, E. Güler, M.H. Ahmadi	**10:00-10:15**	OP-2022-SLL2ON One-pot Hydrodeoxygenation Route of Microalgae Oil To Bio-jet Fuel Over NiDolomite Catalyst	B. Er, A. Cakan, B. Kiren, N. Ayas
10:15-10:30-	OP-2022-BkB9nZHA Havacılık Sektöründe Yangın Algılama ve Söndürme Sistemlerinin Projelendirme, Kurulum ve İşletim Süreçlerinin Yönetilmesi	Onur Mammacioğlu, Cemil Özkalay, Gökhan Coşkun, Hakan Serhad Soyhan	**10:15-10:30-**	OP-2022-x3sqklEX Experimental And Computational Premixed Turbulent Flame Propagation Studies for Hydrogen Containing Fuels	Dilay Güleryüz, Emre Böncü, Tahsin Berk Kiymaz, Christophe Allouis, Iskender Gökalp	**10:15-10:30-**		
10:30-10:45-	OP-2022-ACIJzNEL Elektrik Kaynaklı Yangınlar	Cemil Özkalay, Onur Mammacioğlu, Hakan Serhad Soyhan, Gökhan Coşkun	**10:30-10:45-**	OP-2022-aYCY88IN In-situ fluid dynamic characterization of a gas turbine combustor for operation with low-BTU gas from biomass	Sagar Ranjan Panda, Anand M Shivapujia, Dasappa Srinivasaiah	**10:30-10:45-**		
10:45-11:00	OP-2022-d7dUsVHİ Hidrojen Yangınlarının Önlenmesi ve Söndürme Metodları	Muhammet Mert Canca, Aliye Kaşarcı Hakan, Hakan Serhad Soyhan	**10:45-11:00**			**10:45-11:00**		

Coffee Break (11:00-11:15)

10 SEPT. 2022 SATURDAY-3rd DAY / SECOND SESSION

TULIP HALL / FACE TO FACE			LILY HALL / HYBRID			DAISY HALL / ONLINE		
22.Session: HYDROGEN AND COMBUSTION (11:15-12:15) **Session Chair: Dr. MACIEJ MIKULSKI**			**23. Session: CARBON (11:15-12:15)** **Session Chair: Dr. FRANK ULRICH RÜCKERT**			**24. Session: COMBUSTION (YANMA) (11:15-12:15)** **Session Chair: Dr. ERDİNÇ VURAL**		
https://meeting.mkcelikbas.com/b/inc-nwo-p3n-5r8			**https://meeting.mkcelikbas.com/b/inc-0vz-jmn-hkz**			**https://meeting.mkcelikbas.com/b/inc-yte-vls-d4q**		
11:15-11:30	OP-2022-5GUggQIN Investigation Of Carbon Dioxide Absorption Capacity And Dissolution Rate With Glycerol And Glycerol + Sodium Hydroxide Hybrid Solution For Post-Combustion Systems	İ. Koçyiğit Çapoğlu, H. Öztan, D. Uysal, Ö. M. Doğan	**11:15-11:30**	OP-2022-aLQ7RFCA Carbonization Of Waste Elastomer (Ethylene Propylene Diene Monomer-Epdm) To Produce Porous Carbonaceous Materials	Muhammet Ramazan Eren, Işıl Güneş, Esin Apaydın Varol	**11:15-11:30**	OP-2022-3QqD04EX Experimental Investigation On Performance Evaluation Of Pem Electrolysis Cell By Using A Taguchi Method	Safiye Nur Özdemir
11:30-11:45	OP-2022-9G21EaEX Experimental studies on the combustion behavior of different plastic content refuse derived fuel under different furnace conditions	Priyanka Tripathi, Lakshminarayana Rao	**11:30-11:45**	OP-2022-0bZvlPGL Global Warming Impact Assessment Due To Carbon Capture And Storage Technologies In Electricity Power Plants	Okan Kon, Ismail Caner	**11:30-11:45**	OP-2022-DyZc5ZTH Thermal Runaway Mechanism at Lithium Ion Batteries of Electric Vehicles and Keeping the Heat Under Control	Ümit Şenyürek
11:45-12:00	OP-2022-C1CJNU Numerical Investigations on Thermal Performance and Flame Stability of Hydrogen Diluted Ammonia Fueled Swirl Burner and Furnace	Ozan Kekul, Mustafa Ilbas, Serhat Karyeyen	**11:45-12:00**	OP-2022-TLdRpACA Carbonization, Activation and Investigation of Different Uses of Wastewater Treatment Sludge	Serhat Bilgin, S. Orhan Akansu, M. İlhan İlhak	**11:45-12:00**	OP-2022-n34rFSRO Roketlerde Tahrik İlkesi ve Nükleer İtkili Roketlerin Kavramsal Değerlendirilmesi	Hayri Yaman, Murat Kadir Yesilyurt
12:00-12:15	OP-2022-lhNn9wCH Characterization Of Hydrochar Production From Orange Peel And Sewage Sludge By Hydrothermal Processes	R. N. Mutlu, İ. Gökalp, H. Ece, G. Çelik, A. T. Koçer, D. Özçimen	**12:00-12:15**	OP-2022-YZgtDPTH The activity of zeolite-supported nickel catalyst in CO2 hydrogenation to produce CH4	Tuğba Yarbaş, Nezihe Ayas	**12:00-12:15**	OP-2022-vIToKqNU Numerical Simulation Of A RCCI Engine Performance Using Natural Gas (NG) / Diesel Fuel Under Low Load Conditions	Müjdat Fırat, Mutlu Okcu, Şehmus Altun, Yasin Varol
LUNCH								

10 SEPT. 2022 SATURDAY-3rd DAY / THIRD SESSION

TULIP HALL / FACE TO FACE			LILY HALL / HYBRID			DAISY HALL / ONLINE		
ALTERNATIVE FUEL (13:30-14:45) **Session Chair: Prof. Dr. S. ORHAN AKANSU**			**25. Session: FUEL AND COMBUSTION SESSION (13:30-14:45)** **Session Chair: Dr. ZAFER KAHRAMAN**			**26. Session: MODELLING AND SIMULATION (13:30-14:45)** **Session Chair: Dr. MEHMET SALIH CELLEK**		
https://meeting.mkcelikbas.com/b/inc-wrm-dlm-bpj			**https://meeting.mkcelikbas.com/b/inc-tjv-ivh-0nr**			**https://meeting.mkcelikbas.com/b/inc-bbw-r02-hy7**		
13:30-13:45	OP-2022-bEZRTsNU Numerical Comparison of premixed turbulent combustion models for ethylene/air mixtures up to 1 MPa	Siva Muppala	**13:30-13:45**	OP-2022-2h9tGy3D 3D Simulation Of Ammonia/Hydrogen Fuel Blends Combustion Under High Swirl Gas Turbine Conditions	O. Kumuk, M. Ilbas	**13:30-13:45**	OP-2022-AuOMKARA RANS Simulation of Bluff-Body Turbulent Swirling Flame	Orhan Veli Kazanci, Yakup Erhan Böke
13:45-14:00	OP-2022-QZLCA A Study On The Nanoparticle Contribution In A Dual Fuel Diesel Engine	Esenay Arslan, M. Raşit Atelge, Nafiz Kahraman, Sebahattin Ünalan, Bilge A. Çeper	**13:45-14:00**	OP-2022-0XKPEX Explosions Occured In A Urban Terrain According To Explosive Type	M. Şahin, S. Tulumcu, M. Yıldız	**13:45-14:00**	OP-2022-lnWYqMEF Effects Of Excess Air And Oxygen Enrichment On Sooting Flames Of Biogas	M. S. Cellek, U. Demir

14:00-14:15	OP-2022-TRdt0TYA Yaşlı Bakım Tesislerinde Yangın Sırasında Bakıma Muhtaç Kişilerin Tahliye Olanaklarının Bilgisayar Destekli Simülasyon Programı İle İncelenmesi	Kerem Ilbay, Gökhan Coşkun, Ekrem Büyükkaya	**14:00-14:15**			**14:00-14:15**	OP-2022-7ruanWNU Numerical Investigation Of Hcci Engine For Two Different Combustion Chamber Geometries	Oğuz Bostancıoğlu, Nureddin Dinler
Coffee Break (14:45-15:00)								

10 SEPT. 2022 SATURDAY-3rd DAY

CLOSING SESSION (15:00-16:00)

TULIP HALL

https://meeting.mkcelikbas.com/b/inc-erl-x7a-xtq

CLOSING SPEECH

WISHES AND REQUESTS

11 SEPT. 2022 SUNDAY-4th DAY

EPHESUS CULTURE TRIP (09:00-15:30) - EXTRA

Index

Article Title **Page Number**

Investigation of Early Intake Valve Closing Strategy and Exhaust Gas Recirculation on PCCI Engine Operation 1

Experimental Investigation of the Effects of Gasoline, Methanol and Natural Gas Fuel on Engine Performance and Emissions in a Gasoline Engine 9

Influence of Fuel-Air Equivalence Ratio on the Combustion and Performance Characteristics of a Wankel Engine for Unmanned Aerial Vehicle (UAV) Applications 14

Systematic Study of Friction Modifiers for Motor Gasoline, Their Structure, Mechanism of Action, Efficiency Evaluation and Role in the Production of Modern Fuel 21

Investigation of the Effect of Diesel Injector Nozzle Geometry on Coking Phenemona 22

Dynamic Flame Behavior of 30%H_2 30%Co 20%Co_2 20%CNG Synthetic Gas Mixture during Acoustic Forcing 28

Experimental Analysis of a Hydrogen/Diesel Dual Fuel Test Case via IR Imaging 38

Effects of Hydrogen and EGR on Energy Efficiency Improvement with Ultra-Low Emissions in a CRDI CI Engine Fueled with Dimethyl Ether (DME) Under HCCI Mode 46

An Experimental Investigation of Oxygenated Fuels Blending Effect on Gasoline Engine Performance and Emissions 51

The Effect of The Addition of H, H+OH and H+OH+O_2 from the Intake Manifold on Exhaust Emission Parameters in a CI Engine Using Diesel/Di Ethyl Ether as Pilot Fuel 52

The Effect of Multiple Injection on CI Engine Pollutant Emissions and Green House Gases 56

The Comparison of Quasi-Steady Evaporation Models in A Swirl Stabilized Combustion Chamber . 62

Experimental and Computational Premixed Laminar Flame Propagation Studies for Hydrogen Containing Fuels 70

Numerical Study on the Performance of a Flat-Tubular Solid Oxide Fuel Cell: The Effect of Burner Thermal Power and Furnace Geometry 77

Numerical Study on Impact of Combustor Metrics of Turboprop Engine Used in Air Freighter 82

Investigation of the Effects of Different Rates of Hexane Blended Fuels Utilized in A Ceramic-Coated Diesel Engine on HC, NOX, and Smoke Opacity by Taguchi Method 87

A Parametric Study to Optimize the Temperature of Hazelnut and Walnut Shell Gasification for Hydrogen and Methane Production 95

Three Dimensional Numerical Investigation of Flow and Combustion Characteristics in an Ammonia Fueled Multi-Inlet Cyclone Combustor 101

Synthesis of Pt/rGO Cathode Catalysts for PEM Fuel Cells through Polyol and Colloidal Methods 106

The Effect of Different Charging Concepts on Hydrogen Fuelled Internal Combustion Engines 110

A Numerical Study on Co-Firing of Biomass-Coal Blends in 100 kW Lab-Scale Swirl Burner 118

Fragmentation of Droplets of Coal-Water Slurries Containing Petrochemicals under Different Heating Methods 125

Effects of Hydrogen Enrichment Strategy on Combustion and Emissions in a Gasoline Fuelled Rotary Engine 133

Characterization of a Partially Premixed Swirl Burner Using Openfoam Simulations with a Global Chemical Kinetics Mechanism 138

Investigations of Flame Characteristics of LPG Used in Three Different Size Household Cookers .. 143

Evaluation on Hybridization of Heavy-Duty Long-Haul Diesel Truck Powertrains 151

A Study on Capturing Acoustic Behaviour in Confined Tube Combustion Using Optical Technique.....154

Study on OH* Chemiluminescence of NH_3/Air Swirl Flame 161

Qualitative Visualization of Butane and Helium Tracers in Air Using a Digital Background-Based Schlieren Method 169

Investigation of Soot Formation of Swirl-Stabilized Jet A-1 Spray Flame with Rank Correlated SLW Including Ethylene and Acetylene Radiation 178

Three-Dimensional Modelling of Ammonia/Methane/Air Turbulent Flames in a Generated Perforated Burner and Furnace 187

Synthesis of Bentonite Supported Ni and Ni-La Catalysts for the Steam Reforming of Acetic Acid 192

Char Reactivity Assessment of High Ash Coal in Packed Bed Environments - Experimental Investigations..... 196

Combustion Characteristics and Kinetics of Blends of Lignite with Eggshell 202

Pyrolysis and Combustion Characteristics of Tea Stalk Lignin: Effect of Organosolv and Sequential Hydrothermal-Organosolv Pretreatments..... 205

Energy Recovery from Spent Coffee Ground and Brewery Spent Grains: A Circular Economy Approach to Waste Valorization 214

Swirler Effects on Colorless Distributed Combustion Using Methane Flame 225

New Approach to Evaluating the Functional Properties of Detergent Additives for Motor Gasolines.....229

Rans Studies of Minimum Ignition Energy of Stoichiometric Laminar Methane/Air Fuel Mixtures. 230

Analysis of Cross-Flow Tube Bank Economizer-Assisted for H_2S 237

An Application of the Low-Great Heat of Recycling Water of Food Industry Enterprieses for Electric Generation 242

Dizel ve Trietil Borat ile Karışımlarının Damlacık Yanma Davranışlarının İncelenmesi 252

Geochemical Analysis and Desulfurization of Black Gold for Sustainable Use in Thermal Energy Sector..... 261

Hidrojen Kullanılan Bir Dizel Motorda Çevrimsel Yanma Değişimlerinin İncelenmesi 262

Disposal of Rice Straw and Its Conversion into Fermentable Sugar and Ethanol by Acid, Alkali, Enzymatic and Biological Treatments..... 273

An Investigation on Some Critical Fuel Properties of Biodiesel Fuels of Different Generations..... 283

Homojen Dolgulu Sıkıştırma Ateşlemeli Bir Motorda Hafif Nafta-Benzin Karışımı Kullanımının Motor Performansı ve Emisyonlarına Etkisi 287

Microwave Assisted Biomass-Based Electrode Material Production for Supercapacitor Applications..... 293

Düşük Girdap Üreteçli Brülörün Kullanıldığı Bir Doğalgaz Kazanında Yanma ve Emisyonların Nümerik İncelenmesi 297

Ağır Hizmet Tipi Bir Dizel Motorda Dizel ve Doğalgaz Karışımlarının Motor Performansı ve Egzoz Emisyonları Üzerine Etkilerinin Deneysel İncelenmesi..... 309

Experimental Investigation of Diesel-Biodiesel-Ethanol Blends on a Compression Ignition Engine Performance..... 313

Microwave-Assisted Synthesis of Pt/C Catalyst at High Temperatures for PEM Fuel Cells 314

Influence of Two-Stage Fuel Injection Timing for Combustion and Emissions under Different Engine Loads in a Direct Injection Diesel Engine..... 318

Designing a New Bell-Type Primary Air Nozzle for a Large-Scale Circulating Fluidized Bed Boilers..... 319

Evaluation of the Effect of System Parameters on Hydrogen Production in Steam-Methane Reformers..... 325

Tyre Pyrolytic Oil Blends in A State-of-The-Art Compression Ignition Engine: Toward Fuel-Optimized Combustion..... 333

Dunaliella Salina Microalgae Obtained as an Effective Material for Double Applications: Supercapacitor and Hydrogen Production..... 338

Optimization of Hydrogen Production with the Aluminium-Water Reaction..... 344

Use of Hydrogen-Biogas Mixture as Fuel in Common-Rail Diesel Engine with Thermal Barrier Coating 345

A Thermodynamic Approach to Calculate the Mean Turbulence Intensity of CNG and Gasoline Fuels in a Research Engine 349

Experimental Investigation on Exploiting the Biofuels Blend and Improving its Usability by Adding TiO_2 Nanoparticles 355

Detonasyon Motoruna Sahip Roketlerde Ön-Detonatorde Farklı Hidrojen-Karbon Oranlarına Sahip Yakıtların Şok Dalgası Üzerindeki Etkisinin İncelenmesi 363

Termik Santrallerde Yangın Güvenliğinin Bir Örnek Üzerinden İncelenmesi 369

Çift Yakıtlı Doğalgaz-Dizel Bir Motorda Enjeksiyon Stratejisinin Performans ve Emisyonlara Etkisinin İncelenmesi 374

Numerical Investigation of the Effect of Operating Temperatures on a Planar Solid Oxide Fuel Cell..... 381

Alışveriş Merkezlerinde İnsanların Acil Durum Tahliye Davranışlarının Deneysel ve Simülasyon Yöntemleriyle İncelenmesi..... 388

Reaktif Kontrollü Sıkıştırma ile Ateşlemeli Bir Motorun Performans ve Emisyon Parametrelerinin İncelenmesi..... 396

Numerical Investigation of Combustion and Flame Characteristics in a Swirl Burner/Furnace for a Model Thermoelectrical Generator (TEG) Performance..... 402

Characteristics of the Gas Hydrates Ignition Process 407
Hastane Binalarında Yangın Anında Kullanıcıların Tahliyesinin Simülasyon Destekli İncelenmesi. 411
Evaluation of Binary Nanoparticles to Oxygenated Fuel with Ethanol and N- Butanol on Combustion Behavior 421
Elektrikli Araçlarda Batarya Yangınlarına Genel Bakış 426
Waste Heat Recovery in an Original Design Commercial Convection Oven 436
Evaluation of Natural Gas Consumption in Turkey 443
Havacılık Sektöründeki Yangın Algılama ve Söndürme Sistemlerinin Projelendirme, Kurulum ve İşletim Süreçlerinin Yönetilmesi 451
Experimental and Computational Premixed Turbulent Flame Propagation Studies for Hydrogen Containing Fuels 457
Elektrik Kaynaklı Yangınlar 463
One-Pot Hydrodeoxygenation Route ıf Microalgae Oil to Bio-Jet Fuel over Ni/Dolomite Catalyst.. 475
Hidrojen Yangınlarının Önlenmesi Ve Söndürme Metodları 479
In-Situ Fluid Dynamic Characterization of a Gas Turbine Combustor for Operation with Low-Btu Gas from Biomass 481
Investigation of Carbon Dioxide Absorption Capacity and Dissolution Rate with Glycerol and Glycerol + Sodium Hydroxide Hybrid Solution for Post-Combustion Systems 485
Carbonization of Waste Elastomer (Ethylene Propylene Diene Monomer-EPDM) to Produce Carbonaceous Materials 492
Experimental Investigation on Performance Evaluation of PEM Electrolysis Cell by Using a Taguchi Method 497
Experimental Studies on the Combustion Behavior of Different Plastic Content Refuse Derived Fuel under Different Furnace Conditions 508
Global Warming Impact Assessment Due to Carbon Capture and Storage Technologies in Electricity Generating Power Plants 515
Elektrikli Araçların Lityum İyon Bataryalarında Termal Kaçak Mekanizması ve Isının Kontrol Altında Tutulması 521
Numerical Investigations on Thermal Performance and Flame Stability of Hydrogen Diluted Ammonia Fueled Swirl Burner and Furnace 534
Carbonization, Activation and Investigation of Different Uses of Wastewater Treatment Sludge..... 541
Roketlerde Tahrik İlkesi ve Nükleer Roketlerin Kavramsal Değerlendirilmesi 542
Characterization of Hydrochar Production from Orange Peel and Sewage Sludge by Hydrothermal Processes 544
The Activity of Zeolite-Supported Nickel Catalyst in CO_2 Hydrogenation to Produce CH_4 545
Numerical Investigation of a RCCI Engine Performance Using Natural Gas (NG) / Diesel Fuel under Low Load Conditions 550
Numerical Comparison of Premixed Turbulent Combustion Models for Ethylene/Air Mixtures Up to 1 MPa 560

3D Simulation of Ammonia/Hydrogen Fuel Blends Combustion under High Swirl Gas Turbine Conditions 567
Rans Simulation of Bluff-Body Turbulent Swirling Flame 572
Effects of Excess Air and Oxygen Enrichment on Sooting Flames of Biogas 579
A Study on the Nanoparticle Contribution in a Dual Fuel Diesel Engine 586
Explosions Occurred in a Urban Terrain According to Explosive Type 587
Numerical Investigation of HCCI Combustion for Two Different Combustion Chamber Geometries……591
Yaşlı Bakım Tesislerinde Yangın Sırasında Bakıma Muhtaç Kişilerin Tahliye Olanaklarının Bilgisayar Destekli Simülasyon Programı ile İncelenmesi ……...602

INVESTIGATION OF EARLY INTAKE VALVE CLOSING STRATEGY AND EXHAUST GAS RECIRCULATION ON PCCI ENGINE OPERATION

Cengizhan Cengiz[1] and Salih Özen Ünverdi[2]

1. Ford Otosan, Eskişehir Ar-Ge Test Merkezi, Eskişehir, Turkiye; email: ccengiz@ford.com.tr
2. Gebze Technical University, Engineering Faculty, Mechanical Engineering Department, Gebze-Kocaeli 41400, Turkiye; email sunverdi@gtu.edu.tr

Abstract

Premixed Charged Combustion Ignition (PCCI) is an alternative combustion concept for nitrous oxides (NO_x) and soot emissions reduction compared to conventional diffusion-controlled combustion. However, there are drawbacks to achieve the control centre of combustion near top dead centre (TDC) to minimize brake specific fuel consumption. In this study, simulations have been performed to investigate engine performance values on two Early Intake Valve Closing (EIVC) profiles. Combustion efficiency, indicated specific fuel consumption (ISFC), NO_x, soot and carbon monoxide (CO) emissions are evaluated in 40 ˚CA and 80˚CA EIVC timings compared to base diesel case in 0, 30, 50, 70% exhaust gas recirculation (EGR) rates at 3 bar brake mean effective pressure (BMEP) engine operation conditions.

The results show that, up to 5˚-10 CA reduction in centre of combustion is possible for closer TDC operation depending on EGR rate. Moreover, up to 30% NO_x reduction can be achieved in EIVC cases. In 70% EGR case, better ISFC values and near zero NO_x emissions can be obtained compared to conventional diesel combustion due to closer centre of combustion. There is also an increase in CO emissions due to reduction of air fuel ratio and in-complete combustion of EIVC profiles with EGR.

Keywords: Diesel engine, combustion, PCCI, EIVC, EGR, NOx, soot, CO

1 INTRODUCTION

Diesel engines are widely used in the automotive and energy sectors for transportation and energy generation because of their high efficiency, durability, and reliability. However, due to diffusion-controlled combustion of conventional diesel engines, they emit lots of NO_x and soot emissions [1]. Therefore, after-treatment devices are used to remove the NO_x and soot emission significantly. However, during the engine start-up, heat-up and in very part load conditions, aftertreatment devices are insufficient to eliminate these emissions due to low temperature of the catalysts and engine-out gas temperature.

For this reason, low temperature combustion (LTC) strategies are proposed to prevent NO_x and soot emission in these conditions and further to eliminate high costs of aftertreatment technologies. Homogenous Charge Compression Ignition (HCCI), Reactivity Controlled Compression Ignition (RCCI) and PCCI combustion techniques are proposed as LTC strategy. In HCCI combustion method, fuel properties, engine intake temperature and air to fuel ratio are the critical control parameters to operate the engine [2]. Otherwise, pre-ignition and knock events can easily damage the engine. RCCI strategy needs two different fuel and injection system which requires major changes on engine hardware, and it is not a cost-effective solution.

One of the most favour method is PCCI combustion strategy. PCCI strategey uses a single fuel and can be applied to conventional diesel engine without any modification on hardware, with minor changes on engine calibration.

In PCCI strategy, controlling start of combustion (SOI) and centre of combustion (CoC) is critical to control the duration for air to fuel mixing before combustion event, reduction of soot and NO_x emissions, to have a better thermal efficiency and wide load operation range [3].

Several methods are applied to control combustion event, avoid excessive pressure gradient and diesel engine knock of PCCI

operation. Split fuel injection strategy, EGR, rail pressure, fuel injector flow rate, injector angle, geometric compression ratio, piston bowl shape, intake pressure and temperature control, fuel chemistry modifications are the most promising methods to control the PCCI combustion to optimize the engine in terms of fuel efficiency and emissions [4], [5], [6].

The effective compression ratio can be reduced by using a EIVC strategy to retard the combustion with EGR. This method can improve thermal efficiency and NO_x emissions [7], [8], [9].

In this paper, combustion simulation has been performed in 3D CFD reactive flow environment to evaluate EIVC strategy of PCCI combustion to understand the impacts on combustion efficiency, ISFC, centre of combustion and NOx, soot, and CO emissions.

2 TEST ENGINE

The engine used in the simulation is a single cylinder research engine (SCRE) which is based on Ford Otosan Ecotorq 13L heavy duty truck engine. The specification of the engine is summarized in Table 1. The study is focused on the part load operating condition of BMEP=3 bar and engine speed of 1100rpm where PCCI combustion is most suitable to prevent excessive diesel noise and required to reduce NOx emissions considering the benefit of emissions and customer expectations. The operating conditions used for simulation activity of the engine is shown in Table 2.

The engine used in the validation activity is equipped with 2500 bar common-rail fuel injection system, an external air boosting system. The temperature of the boosting, cooling and lubrication of the engine is controlled by auxiliary systems.

Table 1. Engine Specification

Bore x Stroke [mm]	130 x 160
Compression ratio	17.0:1
Swept volume [L]	2.1
Nozzle hole diameter [mm]	0.18
Number of injector nozzles	8
Spray inclusion angle [°]	146
Maximum Injection pressure [bar]	2500
Intake Valve Opening [°CA BTDC]	4
Intake Valve Closing [°CA ABDC]	13
Exhaust Valve Opening [°CA BBDC]	40
Exhaust Valve Closing [°CA ATDC]	4

Table 2. Operating Conditions

Engine Speed [rpm]	1100
Injected fuel mass [mg/cycle]	39
Injection Pressure [bar]	800
Absolute Intake Pressure [bar]	1.27
Fuel (Diesel surrogate)	N-heptane
Inlet Gas Temperature [K]	298
Air to Fuel Ratio [-]	71:1
Total Residual Gas Rate [%] (no-EGR)	3.4%
Swirl ratio [Tippelmann]	1.2

3 NUMERICAL MODEL

The reactive computational fluid dynamics code, Converge CFD is used in the computational activity [10]. The code consists of RNG k-epsilon turbulence model with rapid distortion model, wall heat tansfer model, droplet brake-up model, droplet collision model, spray/wall interaction and vaporization model [11], [12]. [13], [14], [15].

Adaptive mesh refinement (AMR) algorithm is also used in the simulations to reduce the computational cost. AMR enables automatically embeds finer cells where temperature and velocity gradients are above a threshold value. [16]. Cell size is varied between 0.25-4mm depending on the criteria of AMR algorithm within a limit of 3 million cells. N-heptane (C7H16) fuel is selected as surrogate fuel to model chemical reactions due to similar characteristics of cetane number and auto-ignition temperature to diesel fuel [17]. In this study, a reduced reaction mechanism with 42

species and 168 elementary reactions is used to simulate the combustion kinetics [18]. SAGE chemical solver is used to solve the ignition, premixed and diffusion combustion-controlled regimes assuming the homogenous mixture in a cell without considering the sub-grid scale turbulence-chemistry interaction [19]. Moreover, an extended Zel'dovich NOx mechanism is used to model NO_x emissions and Hiroyasu soot model is implemented to predict soot emissions [20], [21].

In this study, a full three-dimensional single cylinder research engine geometry with a moving piston and valves including intake and exhaust ports, part of the intake manifolds is used in the simulations. Simulations are started before exhaust valve opening and run a full cycle to complete the four stroke to enable an accurate simulation. The engine geometry is shown in Figure 1

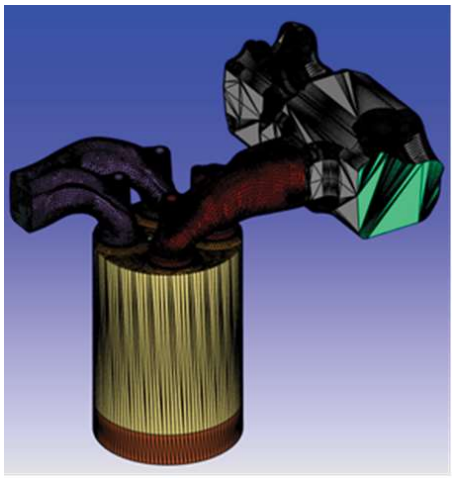


Figure 1. 3D model of the engine

4 RESULTS

4.1 Validation of simulations

The computational results are validated with the test engine of conventional diesel and PCCI engine operation conditions. Figure 2 & 3 shows the in-cylinder pressure and apparent heat release rate histories for two operating conditions with a start of injection (SOI) -10˚ crank angle (CA) and -50˚CA after top dead centre (ATDC) respectively. Results show that, the predicted in-cylinder pressure and AHRR histories of the conventional diesel are satisfactorily agreed with measurements. On the other hand, the initial peak in AHRR in the PCCI case, calculated during the premixed phase of combustion is not observed in the experimental result because of the smoothing effect of the software processing of the test data.

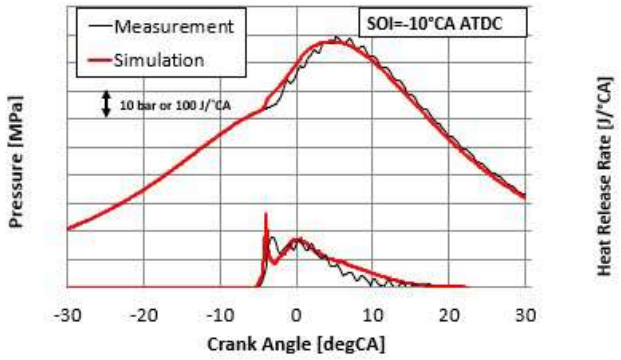


Figure 2. Experimental and simulation results of in-cylinder pressure and AHRR history for SOI of -10°CA ATDC.

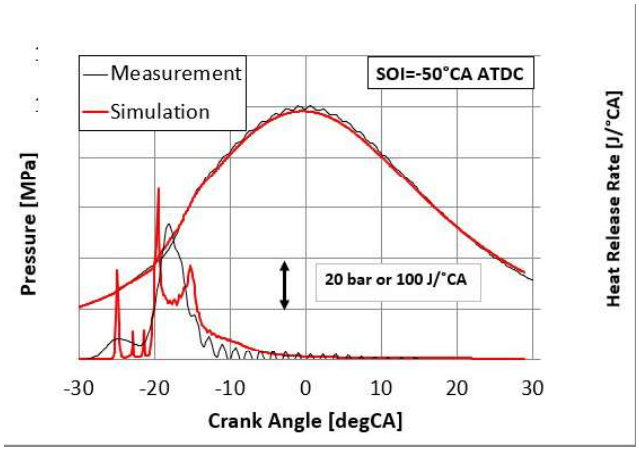


Figure 3. Experimental and simulation results of in-cylinder pressure and AHRR history for SOI of -50°CA ATDC.

Engine out NO_x and soot emissions are for SOI= -50˚CA and -10˚CA are shown in Figure 4 & 5, respectively. There is good agreement with simulation and measurements of NO_x and CO emissions on conventional diesel and PCCI operating conditions. On the other hand, soot emission prediction of Hiroyasu-NSC model is twice as big as measurement results. Soot formation and oxidation rate of the model pre-exponent factors should be calibrated according to temperature so that a unified formulation can be used for both diffusion-controlled and low temperature combustion.

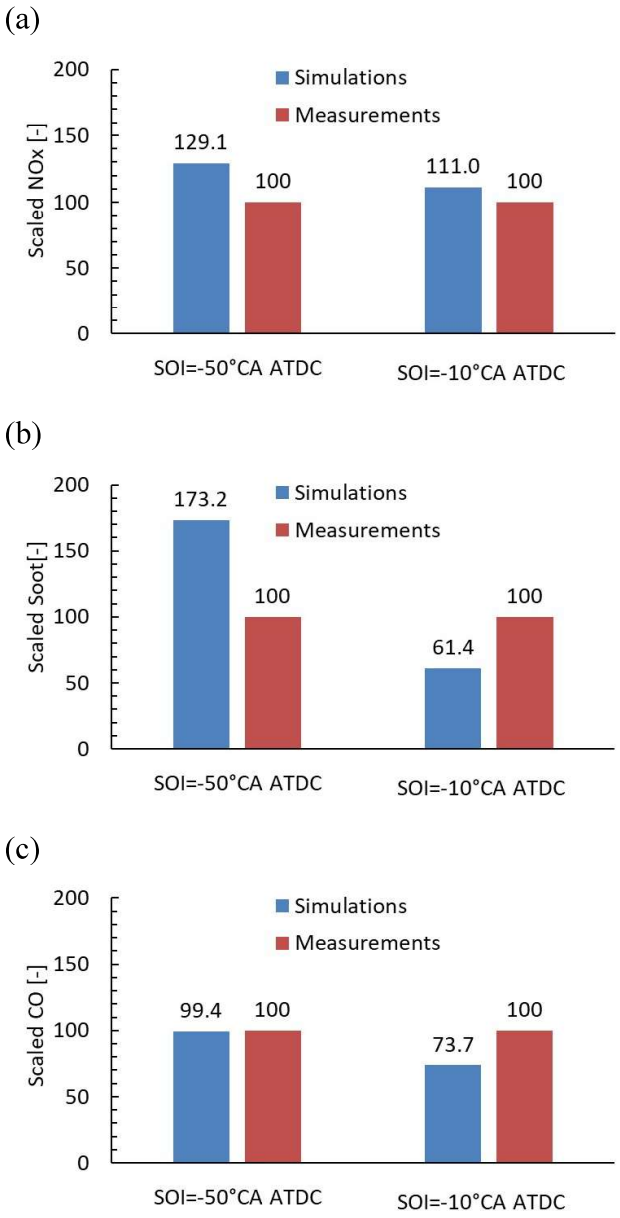


Figure 4. Calculated and measured (a) NOx, (b) Soot, (c) CO engine-out emissions.

4.2 Early Intake Valve Closing (EIVC) Cycle Investigation

Early-intake valve closing (Miller) cycle proposals are evaluating to control the start and centre of combustion. In EIVC strategy, effective compression ratio can be reduced by early intake valve closing. The effective compression ratio is reduced from the base condition of 17.0:1 to 15.65:1 and 13.73 in 40˚CA and 80˚CA EIVC profiles, respectively. The valve lift profiles used in this study is shown in Figure 5.

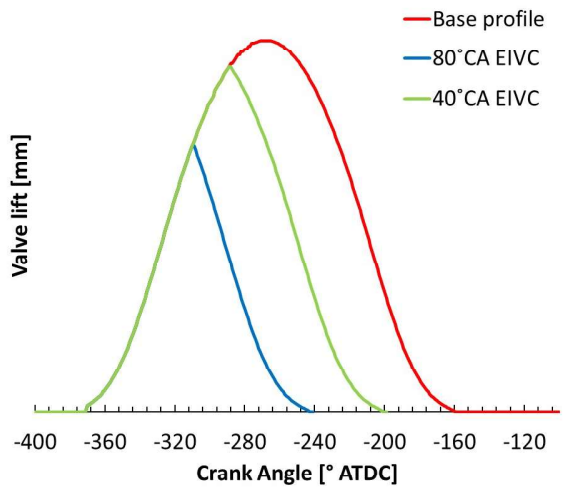


Figure 5. Valve profiles of base, 40˚CA and 80˚CA EIVC.

In the EIVC investigation, due to reduction of temperature and pressure in the combustion chamber can affects the fuel atomisation, break-up, and evaporation. Therefore, split injection strategy is chosen to prevent the risk of spray wall impingement. For this purpose, 1/3 of the fuel is injected in SOI=-60˚CA ATDC and rest of the fuel is injected SOI=-40˚CA to increase the air fuel air vapor mixture homogeneity and reduce the risk of any wall impingement.

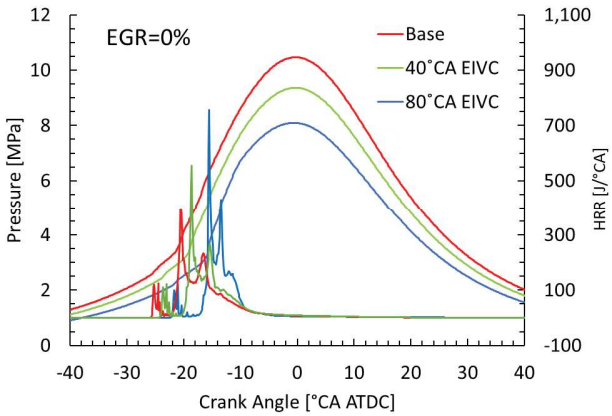
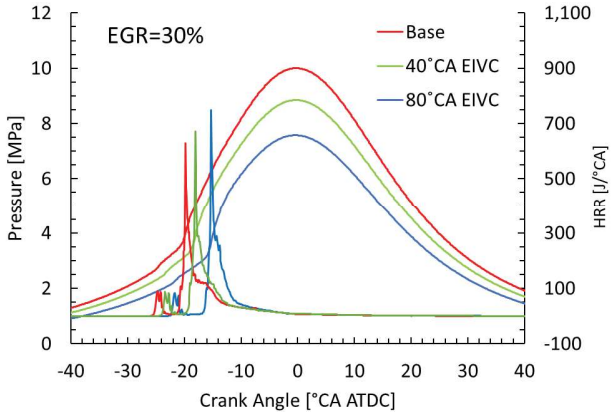


Figure 6. In-cylinder Pressure and Apparent Heat Release Rate Histories of Base and EIVC Profiles on non-EGR conditions.

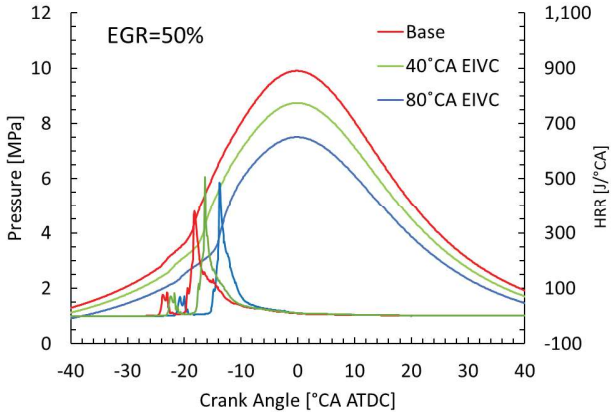
Figure 6 shows the in-cylinder pressure and AHRR histories of base and EIVC cam profiles on non-EGR operating conditions. In EIVC cases, peak in-cylinder pressure drops 11 and 24 bars in 40˚CA and 80˚CA EIVC profiles, respectively. Start of combustion is delayed on 2 to 4˚CA on EIVC profiles for first and main

combustion events. Moreover, peak apparent heat release rate of the main combustion event due to premixed combustion is increased from ~400J/˚CA to 550J/˚CA and 770J/˚CA in EIVC cases. On the other hand, centre of combustion approaches to TDC up to 4˚CA. End of combustion is similar in all cases.

(a)



(b)



(c)

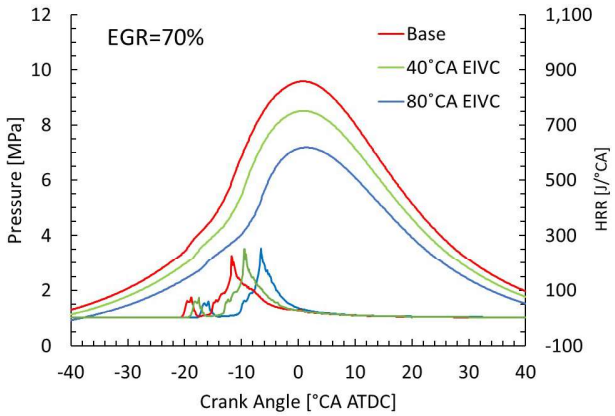


Figure 7. In-cylinder Pressure and Apparent Heat Release Rate Histories of Base and EIVC Profiles on 30% (a), 50% (b), 70% (c) EGR rates.

Figure 7 shows in-cylinder pressure and apparent heat release rates of base and EIVC profiles on 30%, 50%, 70% EGR rates, respectively. Results shows that, start of ignition is not significantly affected on 30%, and 50% EGR rates comparing the non-EGR conditions. On the other hand, heavy EGR rate (70%) conditions the start of ignition of first premixed combustion retards about 5˚CA. Peak AHHR of the main combustion event significantly affected by EGR. While increasing the EGR rate, the peak AHRR reduced to below 300J/˚CA. Moreover, heavy EGR usage conditions, there is a minor difference on peak value of the AHRR between base and EIVC profiles.

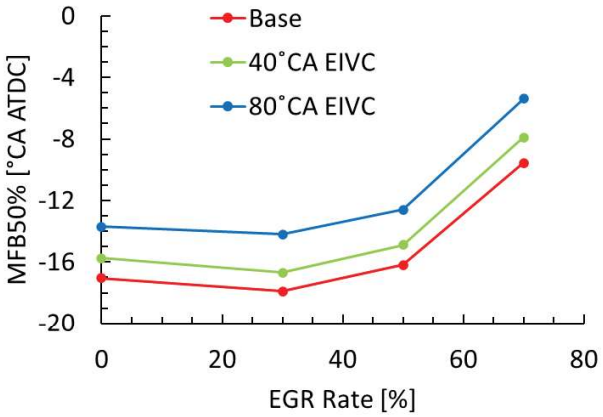


Figure 8. Centre of combustion (MFB50%) & EGR Rate Comparison with Base and EIVC Profiles

EIVC event has a major effect to reduce in-cylinder charge pressure and temperature significantly by changing the effective compression ratio. The lower temperature and pressure due to lower effective compression ratio during the spray injection, delays the start of first ignition and main combustion events. Figure 8 shows the influence of EIVC profiles on the centre of combustion on the variation of EGR rates. Use of EIVC profiles retard the combustion up to 4˚CA which enables a closer centre of combustion to TDC. EGR rate also affects the centre of combustion by delaying the SOC and slowing the down the heat release accumulation.

Combustion efficiency of base and EIVC profiles with the effect of EGR rate is shown in Figure 9. The maximum combustion efficiency values are obtained in non-EGR conditions for all valve profiles. While increasing the EGR rate, combustion efficiency drops up to 4% for base profile and 5 to 8% for EIVC profiles. EGR dilutes the O_2 concentration and affects the heat

release rate and chemical kinetics significantly in advanced injection of PCCI combustion. Moreover, on the EIVC cases, engine air charge capacity decreases significantly and reduction of O_2 concentration acts as the path of EGR. Therefore, combustion efficiency significantly reduces within the usage of EGR and EIVC strategy. On the other hand, the trend of ISFC & EGR rate behaviour is different than combustion efficiency. The combination of combustion efficiency and location of the centre of combustion develops the actual ISFC values. In 30% EGR case, there is decrease in the combustion efficiency and similar in the centre of combustion. This causes ISFC increase shown in Figure 10. However, in 70% EGR rate, 10˚CA increase in the centre of combustion outcomes the best ISFC values even if the combustion efficiency is worsened. Figure 11 compares the NO_x emission of valve profiles on EGR variation. There is tremendous change in NO_x emissions while increasing the EGR rate. 70% EGR results extremely very low NO_x emissions in both base and EIVC cases. Up to 30% EGR rate, EIVC of 40˚CA event results up to 20% NOx reduction. For 50% ad 70% EGR rates, there is no significant change in the NO_x emissions.

Soot emissions behaves a linear increase up to 50% EGR rate. Increasing EGR rate from 50% to 70% increase the soot emissions significantly. EIVC of 80˚CA result highest soot emissions while increasing the EGR rate. Because lowest air to fuel ratio due to EIVC event causes significant soot emission increase.

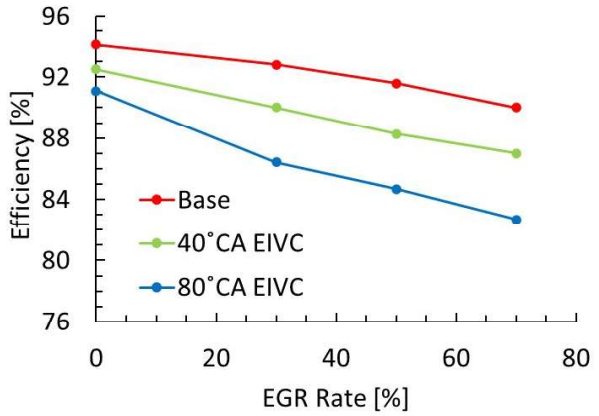


Figure 9. In-cylinder Pressure and Apparent Heat Release Rate Histories of Base and EIVC Profiles

Figure 10,11,12,13 compares the ISFC and, NO_x, soot, CO emissions of the base and EIVC profiles at 0% ,30%, 50%, 70% EGR rates.

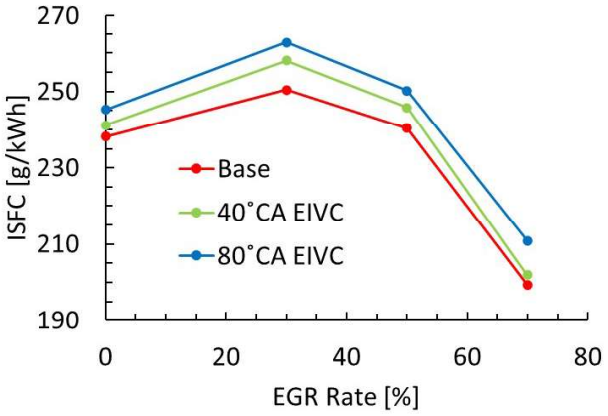


Figure 10. Indicated Specific Fuel Consumption & EGR Rate Comparison with Base and EIVC Profiles

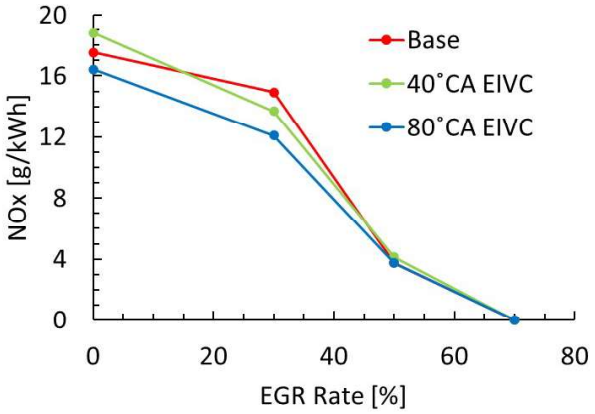


Figure 11. NOx emissions & EGR Rate Comparison with Base and EIVC Profiles

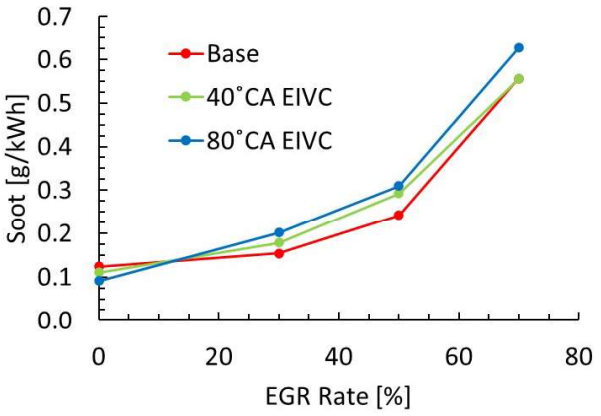


Figure 12. Soot emissions & EGR Rate Comparison with Base and EIVC Profiles

It is noted that, highest carbon monoxide emissions are obtained in EIVC of 80˚CA where the combustion efficiency values are lowest where in-complete combustion occurs. In addition, CO emissions increases with EGR rate where lower O_2 concentration can also boost the in-complete combustion.

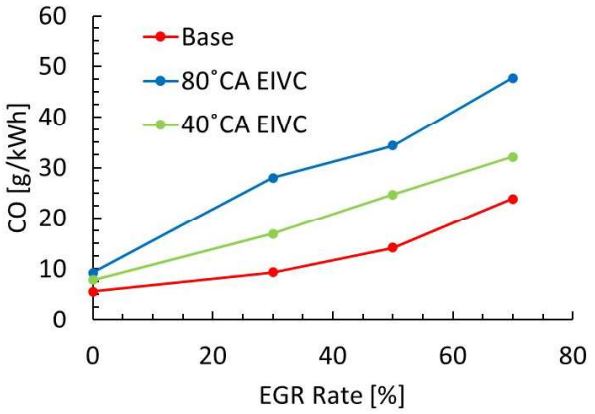


Figure 13. CO emissions & EGR Rate Comparison with Base and EIVC Profiles

5 CONCLUSION

In this study, affect of EIVC strategy is investigated in part load engine operation conditions with very advanced split injection strategy (PCCI) on various EGR rate conditions.

Start of combustion is delayed up to 5˚CA and for first premixed and main combustion events by using a 40 to 80˚CA delayed EIVC profile. Centre of combustion is also retarded up to 4˚CA by EIVC strategy on both non-EGR to up to 70% EGR rate operating conditions.

Combustion efficiency is dropped up to 4% in non-EGR conditions and decreased up to 8% with heavy (70%) EGR usage with EIVC strategy.

ISFC values in EIVC strategy is high compared to base engine operation in all EGR rates.

There is an advance to use EIVC of 80˚ CA profiles on NOx emissions on no-EGR, and 30% EGR rate.

There is a significant change in soot emissions while increasing the EGR rate. The affect of EIVC profiles results with minor change in soot increase compared to EGR rate increase.

CO emissions shows a linear increase trend while increasing the EGR rate. However, using EIVC strategy has major affect the CO emissions due to in-complete combustion and insufficient air-to fuel mixing.

6 REFERENCES

[1] J. Heywood, Internal Combustion Engine Fundamentals, Second Edition, 2018.

[2] J. Dec, “A computational study of the effects of low fuel loading and EGR on heat release rates and combustion limits in HCCI engines,” SAE Technical Paper, 2002.

[3] S. P. C. L. H.J. Kim, “Influence of the fuel spray angle and the injection strategy on the emissions reduction characteristics in a diesel engine,” *Proc. Inst. Mech. Eng. Part D J. Automob. Eng.,* Vol. 229, 2015.

[4] B. G. B. Walter, “Near zero NOx emissions and high fuel efficiency diesel engine: The NADITM concept using dual mode combustion,” *Oil Gas Sci. Technol,* Vol. 58, 2003.

[5] T. H. T. U. J. H. N. K. H. S. T. Kanda, “PCCI operation with early injection of conventional diesel fuel,” *SAE Technical Paper,* 2005.

[6] R. Z. K. N. B. J. D. A. H. P. M. Korkmaz, “Assessment of Different Included Spray Cone Angles and Injection Strategies for PCCI Diesel Engine Combustion,” *SAE Tech. Paper,* 2017.

[7] T. O. Y. I. H. S. T. e. a. Li, “Dependence of Ultra-High EGR Low Temperature Diesel Combustion on Fuel Properties,” *SAE Technical Paper,* 2006.

[8] Y. S. M. A. G. R. D. R. R. M. Nevin, “PCCI Investigation Using Variable Intake Valve Closing in a Heavy Duty Diesel Engine,” *SAE Paper,* 2007.

[9] S. M. R. N. E. B. J. Benajes, “Evaluation of massive exhaust gas recirculation and Miller cycle strategies for mixing-controlled low temperature combustion in a heavy duty diesel engine,” *Energy,* Vol. 71, pp. 355-366, 2014.

[10] P.K.S. and E.P. K. J. Richards, Converge Theory Manual, Middleton, WI, 2012.

[11] R. R. Z. Han, "Turbulence Modeling of Internal Combustion Engines Using RNG k-ε Models," *Combust. Sci. Technol.,* Vol. 106, 1995.

[12] R. R. Z. Han, "A temperature wall function formulation for variable-density turbulent flows with application to engine convective heat transfer modeling," *Int. J. Heat Mass Transf,* Vol. 40, 1997.

[13] R. R. J.C. Beale, "Modeling spray atomization with the Kelvin-Helmholtz/Rayleigh-Taylor hybrid model," *Sprays,* Vol. 9, 1999.

[14] R. R. J.D. Naber, "Modeling engine spray/wall impingement," *SAE Tech. Paper,* 1988.

[15] G.M. Faeth, "Current status of droplet and liquid combustion," *Prog. Energy Combust. Sci.,* Vol. 3, 1977.

[16] E. P. J. A. M. W. C. G. C. P. C. M. P.K. Senecal, "Predictions of transient flame lift-off length with comparison to single-cylinder optical engine experiments," *J. Eng. Gas Turbines Power,* Vol. 136, 2014.

[17] H. W. N. P. J. Weber, "Experimental validation of a surrogate fuel for diesel," *SAE Tech. Paper,* 2007.

[18] N. Nordin, Numerical Simulations of Non-Steady Spray Combustion Using Detailed Chemistry Approach, Chalmers Univ. Technol., 1998.

[19] E. P. K. R. T. B. C. C. R. M. M. P. P.K. Senecal, "Multi-dimensional modeling of direct-injection diesel spray liquid length and flame lift-off length using cfd and parallel detailed chemistry," *SAE Techical Paper,* 2003.

[20] R. Miller, G. Davis, G. Lavoie, C. Newman, and T. Gardner. "A Super-Extended Zel'dovich Mechanism for NOx Modeling and Engine Calibration." *SAE Transactions,* Vol. 107, 1998.

[21] T. K. H. Hiroyasu, "Models for combustion and formation of nitric oxide and soot in direct injection diesel engines." *SAE Tecnical Papers,* 1976.

EXPERIMENTAL INVESTIGATION OF THE EFFECTS OF GASOLINE, METHANOL AND NATURAL GAS FUEL ON ENGINE PERFORMANCE AND EMISSIONS IN A GASOLINE ENGINE

T. Akbiyik[1], N. Kahraman[2] and T. Taner*[1]

1. Department of Motor Vehicles and Transportation Technology, Aksaray Technical Sciences Vocational School, Aksaray University, Aksaray, Turkey
2. Department of Aerospace Engineering, Erciyes University, Kayseri 38280, Turkey
*email: tolgataner@aksaray.edu.tr

Abstract

In the experimental study, the effect of adding 50 g/h natural gas at 1500 rpm fixed speed to the intake air of the engine using gasoline and M20 fuel on the engine performance at different torque values as well as the emissions were investigated. A Lombardini LGW 523 MPI gasoline two-cylinder engine was used in the study. In the study, there was no significant change in power due to the addition of 50 g/h natural gas to gasoline fuel and M20 fuel. In terms of thermal efficiency, although the addition of natural gas to gasoline fuel increased the thermal efficiency, the addition of natural gas to M20 fuel caused a decrease. While the addition of natural gas to gasoline fuel caused a decrease in fuel consumption, it caused a decrease in M20 fuel with an increase in torque. The addition of natural gas to gasoline fuel caused an increase in CO emissions and a decrease in HC, NO and CO_2 emissions. In M20 fuel, while CO and NO emissions decreased, HC and CO_2 emissions increased. These results show that the addition of natural gas to different fuels not only affects engine performance, but also causes changes in emissions.

Keywords: Natural Gas, Engine Performance, Emission, Fuel Consumption

1 INTRODUCTION

Fuels constitute one of the most fundamental problems of automobile technology. Studies have been carried out on fuels that can be used as alternative fuels or in combination with liquid fuels and all gaseous fuels other than gasoline and diesel. In the use of these alternative fuels, it should be used with little or no modification on the engine. Gaseous fuels are used in internal combustion engines as they provide environmental and economic benefits as an alternative to existing fuels. Due to this feature, natural gas has started to become widespread in the transportation sector. Therefore, various studies have been carried out on the use of natural gas fuel. This study investigated power change, effective pressure, thermal efficiency, exergy efficiency of the addition of liquefied hydrogen, methane, butane, and propane to gasoline, iso-octane, benzene, toluene, hexane, ethanol and methanol fuels in a spark ignition engine. Fuel additive ratios range from 10% to 50% by mass. In the result of the study, hydrogen, methane, butane and propane ratios significantly affect the performance of the engine [1]. The effects of boron additive addition to the lubricating oil on engine performance and emissions were investigated in the case of using gasoline and natural gas as fuel in a spark-ignition engine. In the experimental results, it was revealed that when gasoline and natural gas are used as fuel in the engine, the addition of boron in the lubricating oil causes an average of 2.4-8% reduction in the specific fuel consumption. They found that the use of boron additives in lubricating oil caused a significant reduction of 11.4-12.9% in NO_X emissions and there was no significant change in other emissions [2].

The combustion characteristics and performance characteristics of a dual-fuel engine operating with natural gas/methanol and natural gas/gasoline were compared. All experiments were performed at an engine speed of 1600 rpm. The addition of both methanol and gasoline accelerated the combustion rate of natural gas, the brake thermal efficiency (BTE) for natural gas/methanol mixture increased from 27.3% to 28.1%, but the BTE of the natural gas-petrol mixture decreased from 27.3 to 25.5%. The total hydrocarbon and carbon monoxide emissions of natural gas engines went down by adding methanol and increased in gasoline [3-6].

In this study, the effects of ethanol and methanol addition on engine performance, combustion and

emissions in SI engine were investigated. The experiments were carried out on a single-cylinder, four-stroke SI engine at full engine load at different engine speeds. Although methanol addition reduced CO_2, CO, HC and NO_X emissions by 6.48%, 26.6%, 4.75% and 9.16%, respectively, compared to ethanol addition, they reported that it had 15.3% higher oxygen emission values because its oxygen content was higher than ethanol [7]. In addition, many similar studies have revealed the connection of fuels with the performance of spark ignition engine and emissions [8-11].

In this study, in addition to gasoline and M20 fuel in the engine, the use of 50 g/h natural gas at a constant speed of 1500 rpm in the intake air affects engine performance and emissions at different torque values. These results present the addition of natural gas to different fuels influenced the performance of the engine as well as causes an emission issue.

2 MATERIAL AND METHOD

The experimental setup was arranged according to the fuels and engines. Eddy Current dynamometer, which enables the change of engine load and speed in the experimental setup, BOSCH BEA 060 exhaust emission device to determine the emission amounts in the exhaust gas and Alicat mass flow-controlled gas flowmeter to determine the amount of gaseous fuel to be added into the combustion air.

In this study, in which the effects of gasoline, methanol and natural gas fuel use in a gasoline engine on engine performance and emissions are researched, Lombardini LGW 523 MPI engine was used as the engine. Technical specifications of the engine are given in Table 1.

Table 1. Engine with technical values (Lombardini LGW 523) [2]

Engine Type	Unit	Value
Number of cylinders	pcs.	2
Diameter of the cylinder	mm	72
Stroke	mm	62
Cylinder volume	cc	505
Stroke ratio	-	10, 7:1
Revolution maximum	rpm	5500
Maximum of the power, 5000 rpm	kW/HP	15/20.4
Maximum of the torque, 2150 rpm	Nm	34
Engine curb weight	kg	52

As the method of the experimental study, the performance and emission rates were arranged and calculated separately according to the fuels.

In this study, the performance and emissions of gasoline and M20 (80% Gasoline, 20% Methanol) fuel and 4 different fuels created by adding 50 g/h natural gas at different torque values to the combustion air of these fuels were investigated. Before the experiments, the test engine was run at idle until it reached the regime temperature. After obtaining the engine regime temperature, the load was gradually increased with an Eddy Current dynamometer until the maximum load value and tested at the specified torques. The amount of gasoline and M20 fuel consumed in the experiments was measured with a Krohne brand Optimass 3300C S03 type liquid flow meter. The amount of natural gas sent to the intake air to mix with the combustion air was determined by the Alicat gas mass flow meter.

Experiments were carried out at constant engine speed and torque for 4 different fuels, and the engine was kept constant at 3000 rpm. It was tested at 4 different torque values by adding 50 g/h natural gas to the combustion air. The engine was tested at torques of 5, 10, 15 and 20 Nm for each fuel. In the experiments, 90.8% of the natural gas fuel used was methane and the fuel content is presented in Table 2.

Table 2. Natural gas with chemical component and rate [2]

Chemical component	Chemical Formula	Rate (%)
Methane	CH_4	90.8
Ethane	C_2H_6	3.6
Propane	C_2H_8	1.1
Butane	C_4H_{10}	0.4
Pentane	C_5H_{12}	0.1
Nitrogen	N_2	3.5
Carbon Dioxide	CO_2	0.4

3 RESULTS AND DISCUSSION

Experimental study was organized according to power, thermal energy, fuel consumption and emissions. By creating graphs with these data, the effects of natural gas addition in fuels on performance and emissions were revealed.

3.1 Power of the Engine

One of the most important parameters in determining engine performance is power. In the

experiments carried out with four different torques with four different fuels at constant speed, the lowest power value was measured as 1.572 kW at 4 Nm torque in gasoline + 50 g/h natural gas and the highest torque value was measured as 6,294 kW at 20 Nm torque in gasoline fuel. When the power values are compared with the values in the experiments with gasoline fuel, the average of all torque values is 0.49% less in gasoline + 50 g/h natural gas, 0.59% in M20 and 1.46% in M20+ 50 g/h natural gas. The power variation depending on the torque is given in Fig.1.

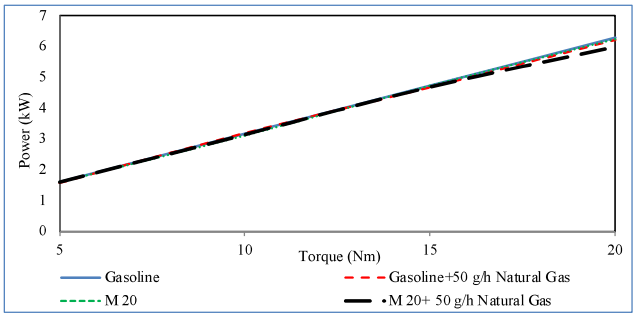


Figure 1. Power variation due to torque

3.2 Thermal Efficiency of the Engine

When the thermal efficiency values were examined, the thermal efficiency values increased with the increase in the torque value. The addition of natural gas to gasoline fuel increased the thermal efficiency values. The addition of natural gas to M20 fuel caused a decrease in thermal efficiency values. When the thermal efficiency values of gasoline fuel are compared with the average of all thermal efficiency values, there is an increase of 20.9% in gasoline + 50 g/h natural gas, 8.9% in M20 and 3.5% in M20+ 50 g/h natural gas. When the test results with M20 fuel are compared with the results for M20+ 50 g/h natural gas, there is a decrease of 4.7%. The thermal efficiency change depending on the torque is given in Fig. 2.

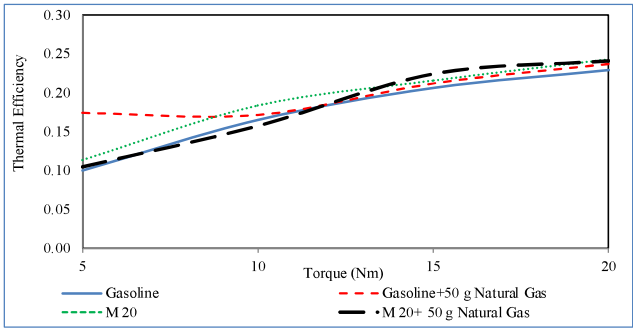


Figure 2. Variation of thermal efficiency due to torque

3.3 Fuel Consumption of the Engine

Specific fuel consumption curves for four different fuels are given in Fig. 3. The highest specific fuel consumption values were obtained at 5 Nm torque values, and the lowest values were obtained at 20 Nm torque values. As the torque values increased, the specific fuel consumption decreased. The lowest specific fuel consumption values were obtained with gasoline fuel and the highest specific fuel consumption values were obtained with M20 + 50 g/h natural gas fuel.

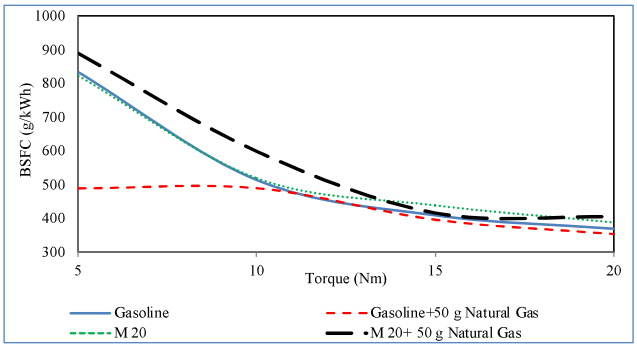


Figure 3. Variation of specific fuel consumption due to torque

Fuel consumption curves are given in Fig. 4. Fuel consumption decreased with the addition of natural gas. The lowest fuel consumption was obtained in gasoline + 50 g/h natural gas fuel and the highest fuel consumption was obtained in M20 fuel. Fuel consumption values increased with increasing torque amounts.

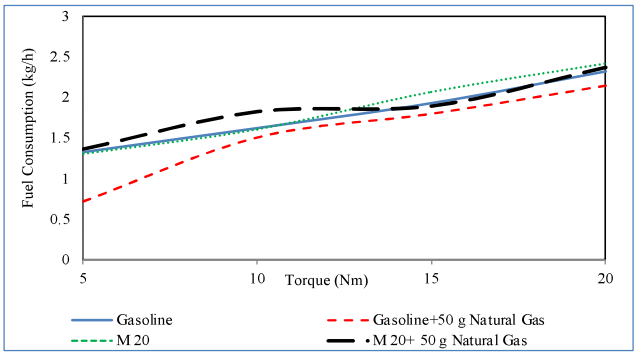


Figure 4. Fuel consumption variation depending on torque

3.4 Emissions of the Engine

The emissions of HC and NO are given in Fig. 5, and the change in CO and CO_2 emissions in Fig. 6.

In Fig. 5, when the HC emissions are examined, in the experiments performed with gasoline,

M20 and M20+50 g/h natural gas, there was an increase in torque of 5,10 and 15 Nm and a decrease in torque of 20 Nm. There was an increase in all torque values for gasoline + 50 g/h natural gas. The addition of natural gas caused a decrease in HC emissions. When NO emissions are examined, there has been an increase in the 10 Nm torque and remained constant at the next torque values. The addition of natural gas to gasoline caused a decrease in NO emissions. With the addition of natural gas to M20, there was a decrease in torques of 15 and 20 Nm.

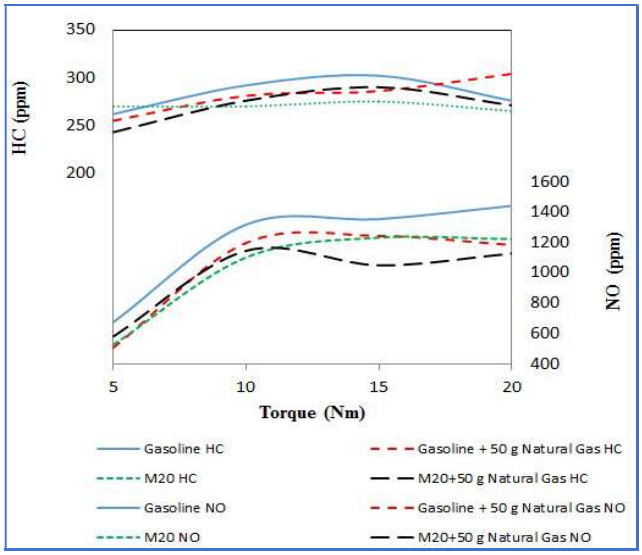


Figure 5. Variation of HC and NO emissions with torque

In Fig. 6, when CO and CO_2 emissions are examined, CO emissions decreased at 10 Nm torque and then remained constant.

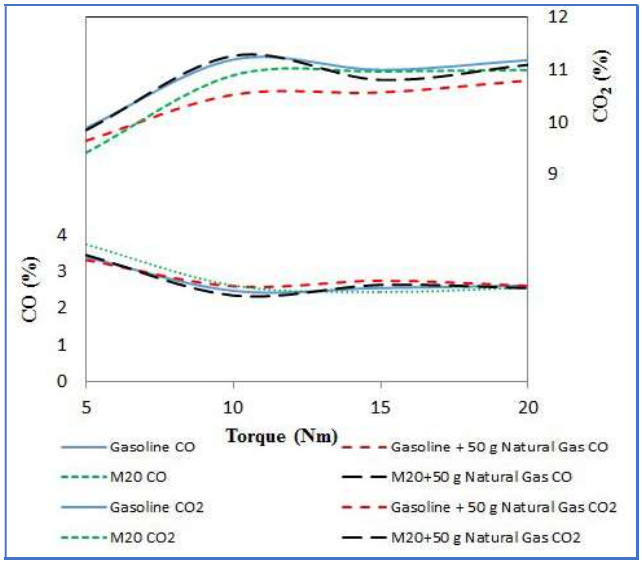


Figure 6. Torque-dependent variation of CO and CO_2 emissions

CO_2 emissions increased at 10 Nm of torque and then remained stable. The addition of natural gas to gasoline increased CO emissions, while the addition of natural gas to M20 fuel decreased it. In CO_2 emissions, the addition of natural gas to gasoline decreased, and the addition of natural gas to M20 fuel increased it.

4 CONCLUSIONS

As a result of the experiments, it was observed that engine performance improved and emission rates decreased at different torque values, thanks to the addition of 50 g/h natural gas at a constant speed of 1500 rpm to the inlet air of the engine using gasoline and M20 fuel. In the study, it was revealed that the addition of 50 g/h natural gas to the Lombardini LGW 523 MPI gasoline two-cylinder engine and 50 g/h natural gas to the M20 fuel did not cause any change in power loss. In thermal efficiency, although the addition of natural gas to gasoline fuel increased the thermal efficiency, a decrease was observed with the addition of natural gas to M20 fuel. The addition of natural gas to gasoline fuel reduced fuel consumption, resulting in a decrease in M20 fuel with an increase in torque.

In fuel consumption, while the addition of natural gas to gasoline fuel reduces fuel consumption, a decrease has occurred with the increase in torque in M20 fuel.

The addition of natural gas to gasoline fuel caused an increase in CO emissions and a decrease in HC, NO and CO_2 emissions. The addition of natural gas to M20 fuel caused a decrease in CO and NO emissions, and an increase in HC and CO_2 emissions.

This study revealed that methanol ratios (M10, M30, M40) can be changed as well as natural gas can be added to fuels at different rates (100, 150 and 200 g/h).

ACKNOWLEDGEMENTS

This work was supported was carried out at Erciyes University Engineering Faculty engine laboratory).

REFERENCES

[1] G. Gonca, B. Sahin, M. F. Hocaoglu, Influences of hydrogen and various gas fuel addition to different liquid fuels on the performance characteristics of a spark ignition engine, *International Journal of Hydrogen Energy*, Vol. 47, pp. 12421-12431, 2021.

[2] T. Akbiyik, N. Kahraman, T. Taner, Investigation of the effect of boron additive to lubricating oil on engine performance, exhaust, and emissions, *Fuel*, Vol. 312, pp. 122931, 2022.

[3] Z. Chen, T. Zhang, X. Wang, H. Chen, L. Geng, T. A. Zhang, Comparative study of combustion performance and emissions of dual-fuel engines fueled with natural gas/methanol and natural gas/gasoline, *Energy*, Vol. 237, pp. 121586, 2021.

[4] Z. Chen, L. Wang, Q. Zhang, X. Zhang, B. Yang, K. Zeng, Effect of spark timing and methanol addition on combustion characteristics and emissions of dual-fuel engine fueled with natural gas and methanol under lean burn condition, *Energy Conversion and Management*, Vol. 181, pp. 519-527, 2019.

[5] Z. Chen, L. Wang, K. Zeng, A comparative study on the combustion and emissions of dual fuel engine fueled with natural gas/methanol, natural gas/ethanol, and natural gas/n-butanol, *Energy Conversion and Management*, Vol. 192, pp. 11-19, 2019.

[6] L. Wang, Z. Chen, T. Zhang, K. Zeng, Effect of excess air/fuel ratio and methanol addition on the performance, emissions, and combustion characteristics of a natural gas/methanol dual-fuel engine, *Fuel*, Vol. 255, pp. 115799, 2019.

[7] I. Ors, B. Sayin, M. Ciniviz, A comparative study of ethanol and methanol addition effects on engine performance, combustion and emissions in the SI engine, International *Journal of Automotive Science and Technology*, Vol. 4 (2), pp. 59 – 69, 2020.

[8] N. Sharma, C. Patel, N. Tiwari, A. K. Agarwal, Experimental investigations of noise and vibration characteristics of gasoline-methanol blend fuelled gasoline direct injection engine and their relationship with combustion characteristics, *Applied Thermal Engineering*, Vol. 158, pp. 113754, 2019.

[9] Y. Qian, G. Liu, J. Guo, Y. Zhang, L. Zhu, X. Lu, Engine performance and octane on demand studies of a dual fuel spark ignition engine with ethanol/gasoline surrogates as fuel, *Energy Conversion and Management*, Vol. 183, pp. 296-306, 2019.

[10] M. S. M. Zaharin, N. R. Abdullah, H. H. Masjuki, O. M. Ali, G. Najafi, T. Yusaf, Evaluation on physicochemical properties of iso-butanol additives in ethanol-gasoline blend on performance and emission characteristics of a spark-ignition engine, *Applied Thermal Engineering*, Vol. 144, pp. 960-971, 2018.

[11] P. Chansauria, R. K. Mandloi, Effects of ethanol blends on performance of spark ignition engine-a review, *Materials Today: Proceedings*, Vol. 5 (2), pp. 4066-4077, 2018.

INFLUENCE OF FUEL-AIR EQUIVALENCE RATIO ON THE COMBUSTION AND PERFORMANCE CHARACTERISTICS OF A WANKEL ENGINE FOR UNMANNED AERIAL VEHICLE (UAV) APPLICATIONS

Merve Küçük [1], Ali Sürmen[2] and Ramazan Şener[3]

1. Department of Mechanical Engineering, Bursa Technical University, Bursa, Turkey; email: merve.altay@btu.edu.tr
2. Department of Automotive Engineering, Bursa Uludag University, Bursa, Turkey; email: surmen@uludag.edu.tr
3. Department of Automotive Engineering, Batman University, Batman, Turkey; email: Ramazan.Sener@batman.edu.tr

Abstract

Recently, there has been a great interest in the Wankel engine as the most suitable power source for UAV applications due to its high power-to-size and power-to-weight ratios. However, Wankel engine has some disadvantages in terms of fuel economy and hydrocarbon emissions at the exhaust. In the present study a computational fluid dynamics model has been established and the effects of fuel air equivalence ration on the combustion and emissions of an iso-octane fuelled Wankel engine have been investigated numerically. The main motivation behind this research is to contribute to Wankel engine designs, especially used in UAV's, in terms of fuel-air equivalence ratio influence on a Wankel engine performance, thereby reducing the existing disadvantages of the Wankel engine. The simulations were conducted at rich, stoichiometric, and lean mixture conditions with the engine speed of 6000 rev/min. The results show that the peak cylinder pressure in the stoichiometric mixture condition is the higher than other mixture conditions. Moreover, results reveal that CO HC emissions decrease with the increase of equivalence ratio.

Keywords: Combustion, CFD simulation, Fuel-air equivalence ratio, Lean mixture, Unmanned Aerial Vehicle, Wankel engine.

1 INTRODUCTION

Wankel engine has a compact design with fewer components compared to the classical piston engines [1-3]. In addition, the reciprocating motion obtained from the piston-cylinder mechanism does not need to be converted into rotational motion as in conventional reciprocating engines. Due to these features, Wankel engines can provide higher power-to-size and power-to-weight ratios and higher operating speeds. These characteristic features of the Wankel engine have a wide range of applications.

Despite all their advantages, Wankel engines have not become as common as conventional piston engines due to fuel consumption, emissions and sealing problems. However, it has become increasingly popular in recent years due to its usage advantages in UAV power systems where high power / weight ratio is very important.

In the early years of Wankel engine research, the 0-dimensional model of the system was built using only one of the combustion chambers, and the numerical analysis results of this chamber were assumed to be valid for the other two combustion chambers [4-8].

Paulos and Heywood [9] investigated the effect of chamber geometry of a spark-ignition engine combustion using one dimensional model.

Today, three-dimensional CFD analysis of reciprocating engines is a very common method for investigating engine performance or emissions, and there is various software that specialize in 3D simulation of reciprocating engines only. However, there is a limited amount of software developed for Wankel engine simulations [10].

Finkelberg et al. [11] studied on combustion of spark-ignited aviation Wankel engine. They presented a novel design of the rotor to increase the engine performance.

Boughou et al. [12] reviewed the combustion chamber design effect on the rotary engine performance.

Although there are a lot of studies examining Wankel engine performance in many aspects in the literature, there is no study investigating the effect of fuel-air equivalence ratio on combustion characteristics and emissions of a Wankel engine. However, many performance improvement strategies of Wankel engines aim to extend the lean operating limits (LOL) of fuel-air flames

[13]. According to Badr [14] the LOL is defined as the fuel-air equivalence ratio, at which first misfire occurs. Exceeding lean operating limits may lead to such challenges on Wankel engines as instability and misfire, consequently, ignition cannot be occurred. Furthermore, these challenges are more critical especially for Wankel engines used in UAV's, since ambient air temperature, pressure and density decrease with altitude. The most important step in overcoming these challenges is to keep combustion in stoichiometric mixture despite air density decreasing at high altitudes. Therefore, it is vital to know the relationship between fuel air equivalence and combustion characteristics in the designs of Wankel engines for UAVs. The main motivation behind this research is to contribute to Wankel engine designs, especially used in UAV's, in terms of the effect of fuel-air equivalence ratio on Wankel engine performance. In this context, firstly, a full Wankel engine model, with three chambers was simulated using Converge CFD software and validated with the experimental data, then CFD simulations were performed for Wankel engine cases using rich (phi=1.2), stoichiometric (phi=1.0) and lean (phi=0.8) mixture conditions.

2. MATERIALS AND METHODS

2.1. Model Description

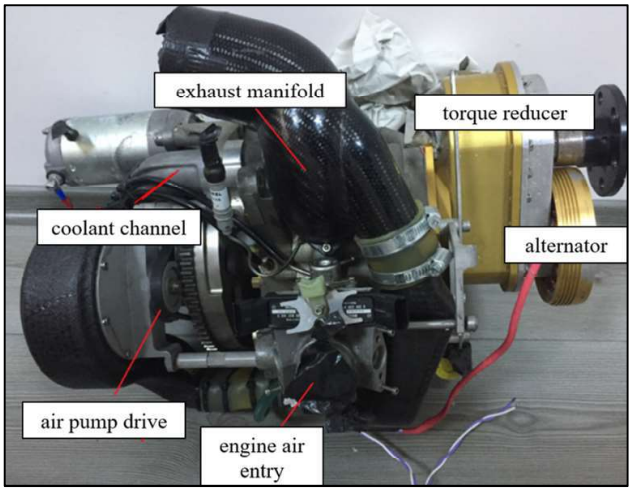
CFD model represents the test Wankel engine that was supplied by Vestel Defence Industry. A summary of the test engine specifications is presented in Table 1.

Table 1. Test engine specifications.

Engine Type	Four-stroke Wankel engine
Radius, (R) [mm]	71.89
Amount of parallel transfer of trochoid, (a) [mm]	1.05
Generating Radius, (R_g)	72.94
Eccentricity, (e) [mm]	11.5
Width [mm]	7.44
k-factor	6.34

Demonstrations of Wankel test engine are shown in Fig. 1a and Fig. 1b.

a.



b.



Figure 1. Demonstration of the test Wankel engine; a) some parts definitions b. dissembled engine.

In this study, three cases using rich, stoichiometric and lean mixtures were investigated. The equivalence ratio (ϕ) of the fuel/air mixtures is adjusted as 1.2, 1.0 and 0.8 to simulate rich, stoichiometric and lean mixtures, respectively. Housing and rotor wall temperatures are adjusted to 488 K and 443 K, respectively. Ambient temperature and pressure of this simulation is set to be sea level conditions. Characteristic dimensions of the main components of the reference Wankel engine are presented on CAD model in Fig. 2.

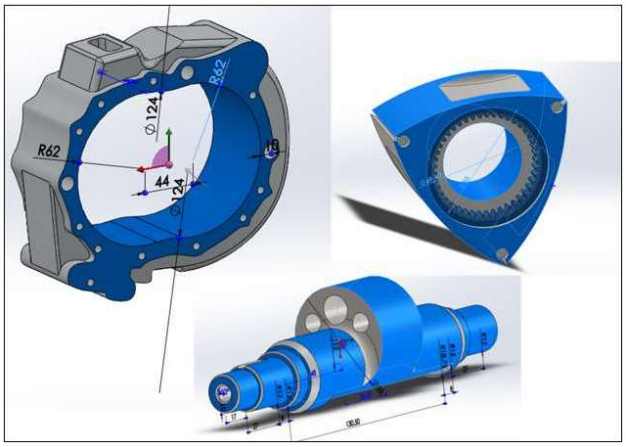


Figure 2. Demonstration of characteristic dimensions of the main components of the reference Wankel engine.

In the presented study, the numerical simulations have been conducted using Converge CFD software [15].

RNG k-ε model is more suitable for rotary engines as a turbulence model regarding the rotational flow and velocity [16,17]. Therefore, RNG k-ε turbulence model has been chosen in the simulations of the present study.

A chemical reaction mechanism for primary reference fuel (PRF) with 48 species and 152 reactions has been utilized [18].

SAGE combustion model has been preferred as a detailed chemical kinetics solver. CHEMKIN format has been utilized for the definition of chemical reaction equations. Isooctane (IC_8H_{18}) is selected as a fuel for the simulations.

Extended Zeldovich model has been used to obtain NOx formation. Hiroyasu model has been used as soot model [9].

2.2. Experimental validation of the CFD model.

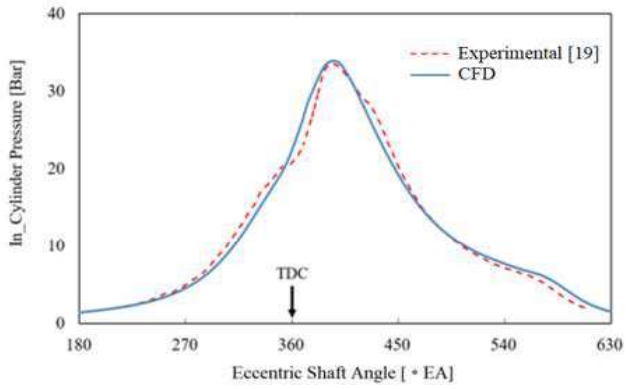
Cartesian grid method has been preferred for the grid generation in the CFD model of the reference Wankel engine.

Mesh independence test has been performed for the base test engine. Four grid construction named coarse, medium, fine, and finer are tested as shown in Fig. 3a and Fig. 3b. These mesh structures are established with a base size of 4 mm, 3 mm, 2 mm, and 1 mm, respectively. Besides, fixed embedding and adaptive mesh refinement (AMR) techniques have been also applied to all the mesh structures.

Taking into account the simulation accuracy and computational cost, the mesh structure of "fine" is chosen.

As shown in Fig. 4a and Fig. 4b, pressure and HRR results, conducted at 6000 rpm are compatible with those of the experimental results [19]. So, the CFD model is assumed to be well-calibrated.

a.



b.

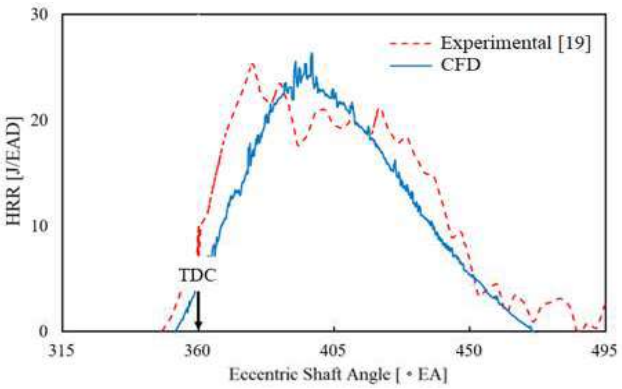


Figure 4. Validation of the CFD model with the experimental results. a. Pressure, b. HRR results versus eccentric shaft angle

3. RESULTS AND DISCUSSION

The fuel air equivalence ratio is a significant indicator and very important measure for a spark ignition piston engine performance controlling and tuning, and exhaust emissions. In this study, three mixture conditions of a Wankel engine, which are rich (phi=1.2), stoichiometric (phi=1.0) and lean (phi=0.8) mixtures, have been simulated to investigate the effect of fuel air equivalence ratio on performance of a Wankel engine. Simulations have been performed for full engine model, with three chambers.

Table 2. Parameters based on fuel mass burning rate for rich, stoichiometric, and lean mixtures.

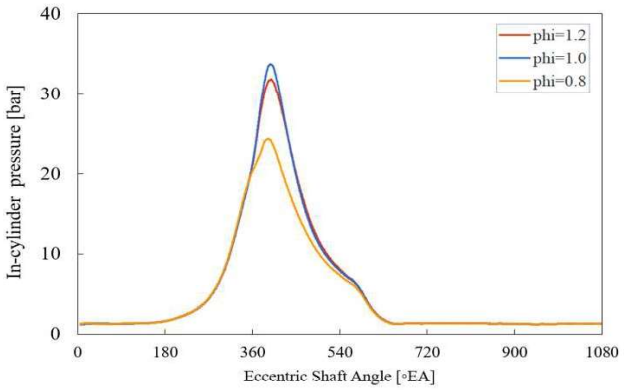
	Phi= 1.2	*Phi= 1.0*	*Phi= 0.8*
CA10 (°EA)	365.56	367.23	376.39
CA50 (°EA)	396.19	400.33	423.56
CA90 (°EA)	460.59	470.36	494.28

Combustion Duration (°EA)	95.03	102.77	117.89
Gross Work (Nm)	298.92	308.99	207.65

The case with stoichiometric mixture is assumed to be the reference and it is determined from the Table 2 that the start of combustion (CA10) is advanced by 1.67 °EA in the rich mixture condition and delayed by 9.16 °EA in the lean mixture condition. Similarly, the end of combustion (CA90) is advanced by 9.77 °EA in the rich mixture and delayed by 23.92 °EA in the lean mixture. Therefore, ignition timing is advanced in rich mixture and delayed in lean mixture condition, which is quite compatible with the literature [20,21]. Combustion duration is shortened by 7.74 °EA in rich mixture case. CA50 and CA90 increase in lean mixture, this means the gravity centre of the entire combustion process is prolonged and the combustion duration is lengthened in this case.

It is also seen from the Table 2 that gross work decreases by 3.36 % and 32.79 %. Because working with non-stoichiometric mixtures leads a worse combustion effect and a poorer working ability.

a.



b.

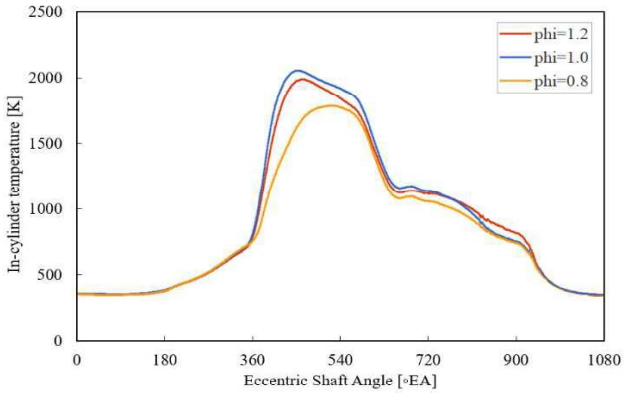


Fig 5. Comparison of a) in-cyllinder pressure, b) in-cylinder temperature for different mixture conditions.

As shown in Fig. 5, which depicts the rich, stoichiometric, and lean mixture conditions, the highest in-cylinder pressure, and mean in-cylinder temperature is obtained from stoichiometric mixture condition. When equivalence ratio is 1.2, Wankel engine has less air than the required quantity of air for the complete combustion of the fuel, so combustion gets worsened. When equivalence ratio is 0.8 Wankel engine has insufficient fuel for complete combustion therefore the lowest in-cylinder pressure and mean in-cylinder temperature occur in this condition.

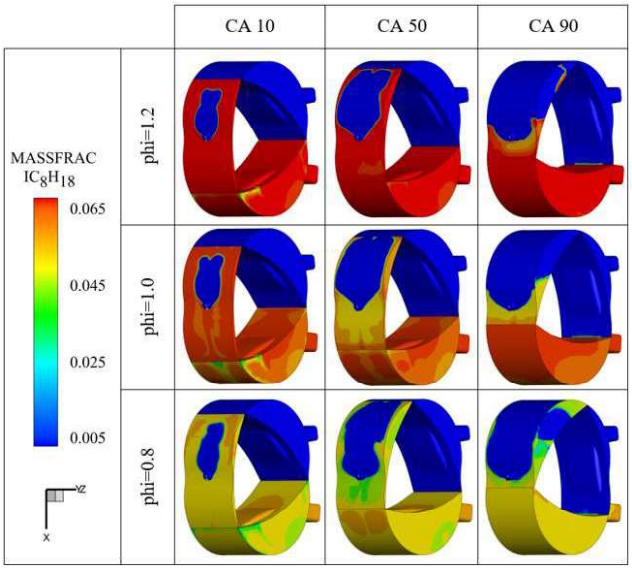


Figure 6. C_8H_{18} mass fraction distribution for different mixture conditions at CA 10, CA50, and CA90.

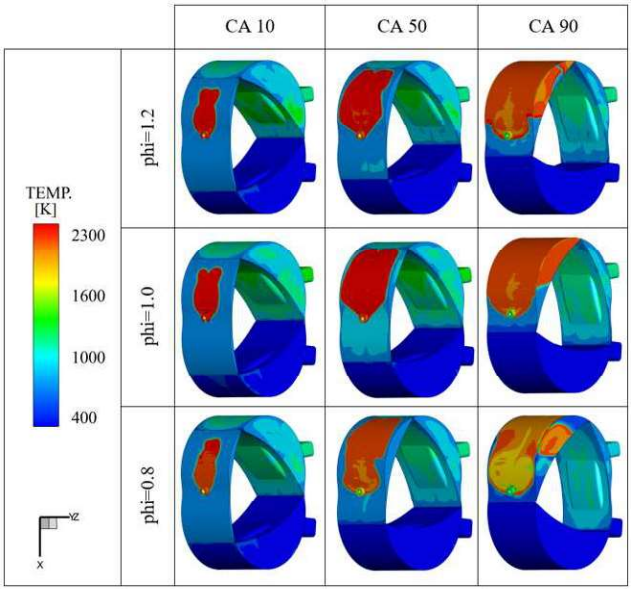
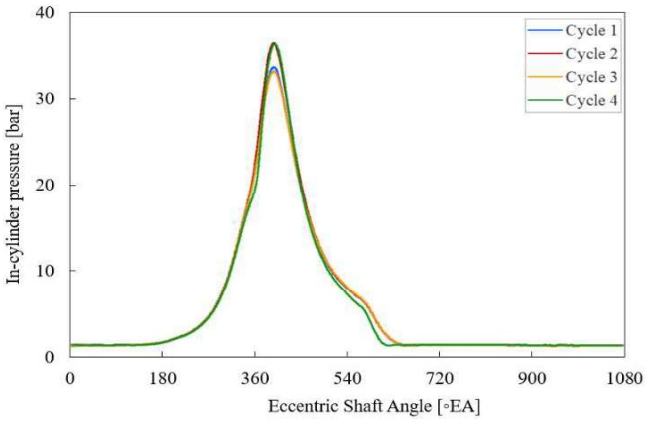


Figure 7. Temperature distribution for different mixture conditions at CA 10, CA50, and CA90.

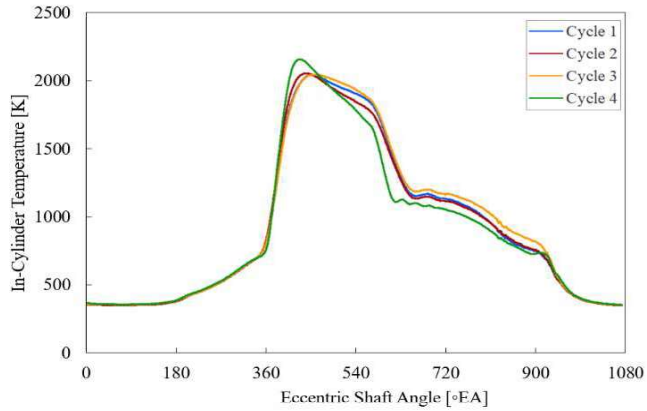
As seen in Fig. 6 C_8H_{18} mass fraction is the lowest when equivalence ratio is 0.8. As the equivalence increases mass fraction of C_8H_{18} inside the combustion chamber increases as well.

It can be observed from Fig. 7 that Wankel engine operating with lean mixture condition has the lowest temperature.

a.



b.



c.

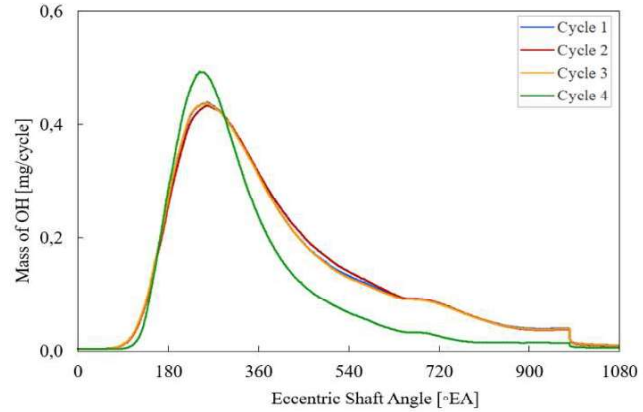
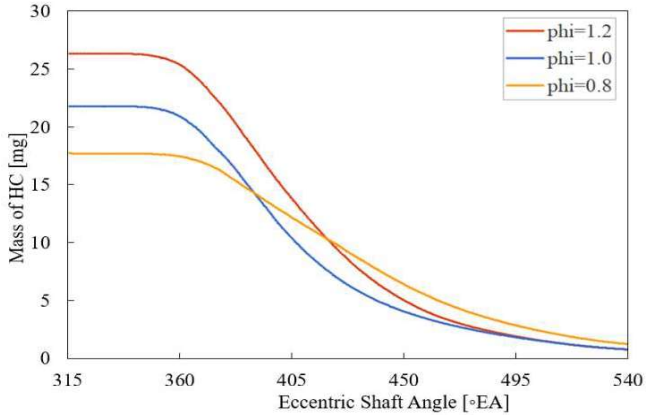


Figure 8. Cycle to cycle variations of a) in-cylinder pressure, b) in-cylinder temperature, c) OH mass of stoichiometric mixture case.

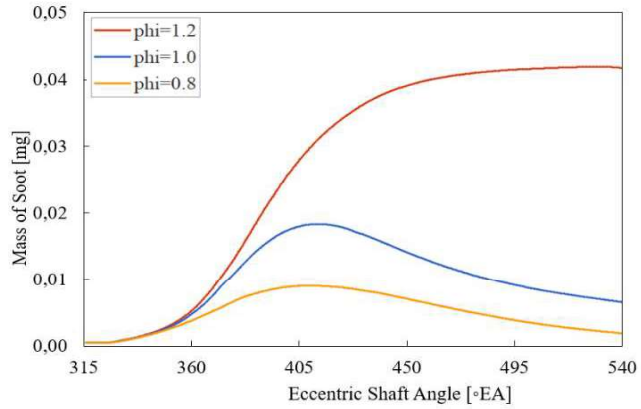
Cycle to cycle variations of some parameters of the Wankel test engine with stoichiometric mixtures is illustrated in Fig. 8. If cyclic variations are large during engine operation, combustion may not occur, causing misfires and increased hydrocarbon emissions. Minimization of cycle-to-cycle variations is a key factor in adjustments of lean operation limits.

Figure 8 a, b, c shows that all cycles' results are very close to each other except cycle 4.

a.



b.



c.

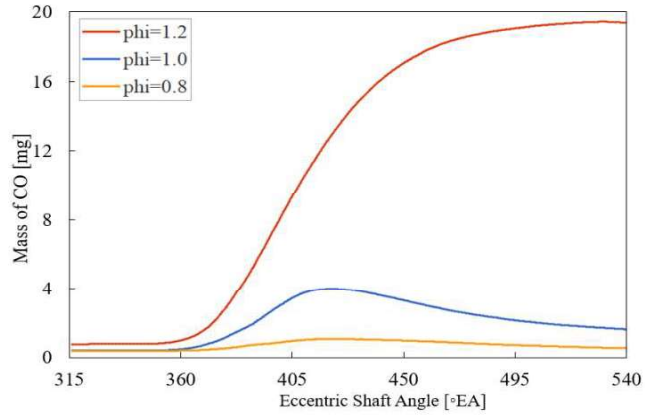


Figure 9. Comparison of mass of a) HC, b) soot, c) CO at working chamber for different cases.

Mass of HC emissions at the rich mixture conditions is the most as seen in Fig. 9a because rich mixture has the highest amount of fuel entering to the combustion chamber. Fig. 9b shows that as phi value increase, the soot emission increases.

The relation between equivalence ratio and exhaust emitted carbon monoxide (CO) is shown in Fig. 9c and Fig. 10. These results reveal that as phi value increase, the carbon monoxide (CO) emission increases. Carbon monoxide (CO) is produced from incomplete combustion of fuel. And oxygen (O_2) helps in better fuel combustion and reduces the emission of CO. In the complete combustion of fuel, only carbon dioxide (CO_2) is produced. In theory, CO should not be produced at a stoichiometric or lean mixtures, but in practice very little amount of CO is produced as seen Fig. 10.

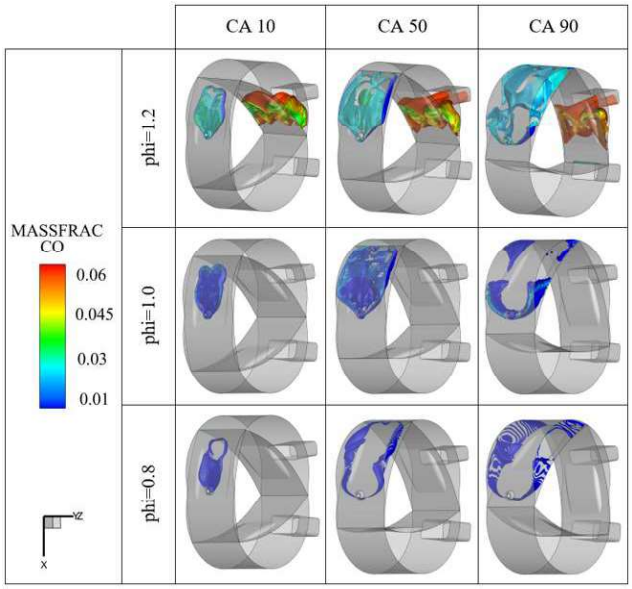


Figure 10. Iso surfaces of CO mass fraction in the combustion chamber for different mixture conditions at CA 10, CA50, and CA90.

4. CONCLUSION

In this study, the influence of fuel air equivalence ratio on combustion characteristics and emissions has been investigated.

The main findings of this study are listed below:

1. In rich mixtures, combustion duration is shortened, and ignition timing is advanced. On the contrary, in lean mixture conditions, combustion duration is prolonged and ignition timing is delayed.
2. Indicated work is higher at the stoichiometric mixtures. Rich mixtures have less air than the required quantity of air for the complete combustion of the fuel, so combustion gets worsened. Lean mixtures have insufficient fuel for complete combustion. For these reasons the in-cylinder pressure and mean in-cylinder temperature and indicated gross work in stoichiometric conditions are higher than those of other mixture conditions.
3. Leaning of the mixture reduces HC, CO and soot production mainly because of the lower carbon content of the total fuel-air mixture.

The main motivation behind this research is to contribute to Wankel engine designs, especially used in UAV's, in terms of the effect of fuel-air equivalence ratio. The relation between the equivalence ratio and combustion characteristics revealed in this paper and follow-on simulations of this study have been performing by different equivalence ratio variations for lean operation conditions. As a future study, the lean operating limits of the test Wankel engine will be determined and presented by minimizing cycle-to-cycle variations in lean mixtures.

ACKNOWLEDGMENT

The authors thank Vestel Defence Industry for their donation of the Wankel research engines, Bursa Technical University, High-Performance Computing Laboratory, and Bursa Uludag University, Internal Combustion Engine Laboratory and Convergent Science Inc. for providing the Converge license.

REFERENCES

[1].C. Ji, H. Wang, C. Shi, S. Wang, J. Yang, Multi-objective optimization of operating parameters for a gasoline Wankel rotary engine by hydrogen enrichment, *Energy Conversion and Management,* Vol. 229, 113732, 2021. https://doi.org/10.1016/J.ENCONMAN.2020.113732

[2]. J. Ribau, C. Silva, F. P. Brito, J. Martins, Analysis of four-stroke, Wankel, and microturbine based range extenders for electric vehicles, *Energy Conversion and Management*, Vol. 58, pp.120–33, 2012.

[3].A. O. Kutlar, Ö. Cihan, Investigation of Parameters Affecting Rotary Engine by Means of a One Zone Thermodynamic Model, *Journal of Energy Resources Technology*, Vol. 144(4), 2021. https://doi.org/10.1115/1.4052615

[4]. G. A. Danieli, J. C. Keck, J. B. Heywood, Experimental and theoretical analysis of Wankel engine performance, *SAE Technical Paper*, 780416, 1978. doi:10.4271/780416.

[5].T. J. Norman, *A performance model of a spark ignition Wankel engine*, Master Thesis, Massachussetts Institude of Technology, ABD, 1983.

[6]. J. M. Roberts, T. J. Norman, J. A. Ekcihan, J. B. Heywood, Computers Models for Evaluating the Premixed and DISC Wankel Engine Performance, *SAE Technical Paper*, 860613, 1986. https://doi.org/10.4271/860613.

[7]. G. A. Danieli, C. R. Ferguson, J. B. Heywood, J. C. Keck, Predicting the emissions and performance characteristics of a Wankel engine, *SAE Technical Paper*, 740186, 1974. https://doi.org/10.4271/740186.

[8].S. G. Paulos, Heywood JB. The effect of chamber geometry of a spark-ignition engine combustion, *SAE Technical Paper*, 830334,1983. https://doi.org/10.4271/830334.

[9].T. A. Bartrand, E. A. Willis, *Rotary engine performance computer program (RCEMAP and RCEMAPPC): User's guide*, NASA Contractor Report, 19940010719, 1993. https://ntrs.nasa.gov/citations/19940010719.

[10].L.Tartakovsky, V. Baibikov, M. Gutman, M. Veinblat, J. Reif, Simulation of Wankel engine performance using commercial software for piston engines, *SAE Technical Paper*, 2012-32-0098, 2012. https://doi.org/10.4271/2012-32-0098.

[11]. L. Finkelberg, A. Kostuchenkov, A. Zelentsov, V. Minin, Improvement of combustion process of spark-ignited aviation Wankel engine, *Energies*, Vol. 12(12), 2292, 2019. https://doi.org/10.3390/en12122292.

[12].S. Boughou, A. K. M. Mohiuddin, Combustion chamber design effect on the rotary engine performance- A review, *International Journal of Automotive Engineering,* Vol. 11(4), pp. 200–212, 2020. doi: 10.20485/jsaeijae.11.4_200.

[13].F. Amrouche, P. A. Erickson, S. Varnhagen, J. W. Park, An experimental analysis of hydrogen enrichment on combustion characteristics of a gasoline Wankel engine at full load and lean burn regime, *International Journal of Hydrogen Energy,* Vol. 43(41), pp. 19250–19259, 2018. https://doi.org/10.1016/J.IJHYDENE.2018.08.110

[14]. O. Badr, N. Alsayed, M. Manaf, A parametric study on the lean misfiring limit and knocking limits of gas-fuelled spark ignition engines, *Appl Therm Eng,* Vol. 18, 579e94, 1998.

[15]. Convergent Science. *CONVERGE Manual v3.0*, 1285, 2021.

[16].M. Peden, M. Turner, J. W. G. Turner, N. Bailey, Comparison of 1-d modelling approaches for Wankel engine performance simulation and initial study of the direct injection limitations, *SAE Technical Paper*, 2018-01-1452, 2018. https://doi.org/10.4271/2018-01-1452.

[17]. Ö. Cihan, O. A. Kutlar, Effect of leading and trailing spark plugs on combustion, fuel consumption and exhaust emission in a Wankel engine, *Arabian Journal for Science and Engineering,* Vol. 46(8), pp. 7471–7482, 2021. https://doi.org/10.1007/s13369-021-05456-3.

[18]. P. W. Hwang, X. C. Chen, H. C. Cheng, Influences of ignition timing, spark plug and intake port locations on the combustion performance of a simulated rotary engine. *Journal of Mechanics*, Vol. 32(5), pp. 579– 591, 2016. https://doi.org/10.1017/jmech.2016.39.

[19].J. Spreitzer, F. Zahradnik, B. Geringer, Implementation of a Rotary Engine (Wankel Engine) in a CFD Simulation Tool with Special Emphasis on Combustion and Flow Phenomena, *SAE Technical Papers,* 2015. https://doi.org/10.4271/2015-01-0382

[20]. M. Berckmüller, H. Rottengruber, A. Eder, N. Brehm, G. Elsässer, G. Müller, C. Schwarz, Potentials of a charged SI-hydrogen engine. *SAE Technical Paper,* 01-3210 2003, 2003. doi:10.4271/2003-01-3210.

[21]. S. Oh, C. Park, D. Nguyen, S. Kim, Y. Kim, Y. Choi, J. Lee, Investigation on the operable range and idle condition of hydrogen-fueled spark ignition engine for unmanned aerial vehicle (UAV), *Energy,* Vol. 237, 121645, 2021.

SYSTEMATIC STUDY OF FRICTION MODIFIERS FOR MOTOR GASOLINE, THEIR STRUCTURE, MECHANISM OF ACTION, EFFICIENCY EVALUATION AND ROLE IN THE PRODUCTION OF MODERN FUEL

Vsevolod D. Savelenko[1], Mikhail A. Ershov[1], Nikita A. Klimov[1, 2], Nikita O. Burov[1], David R. Aleksanyan[1, 2], Alisa E. Makhmudova[1], Tamer M.M. Abdellatief[1], Andrey A. Pimenov[3], Kirill A. Ovchinnikov[3], Ekaterina V. Podlesnova[3], Alexey V. Nizovtsev[3]

1. Department of Oil Refining Technology, Faculty of Chemical and Environmental Engineering, Gubkin Russian State University of Oil and Gas (National Research University), Moscow 119991, Russia; email: com@gubkin.ru
2. New Technologies Watch Center, LLC, Moscow, 117546, Russia; email: info@ntwc.ru
3. Gazpromneft Industrial Innovations, LLC, St. Petersburg, 197350, Russia; email: info@gazprom-neft.ru

Abstract

The share of gasoline with improved properties reaches up to 30% of the total production of gasoline in the world. The main component of the additive packages for these fuels is a detergent additive, however, to ensure a significant environmental, economic and power effect, additional input of substances that modify the surface of the fuel system elements and reduce friction losses is required. These substances are called friction modifiers and in recent years the importance of their use has increased significantly due to the tightening requirements for the efficiency of internal combustion engines and the increased share of gasoline engines with direct fuel injection. This paper presents the results of a systematic analysis of existing materials in the field of development and functional properties of friction modifiers in order to determine the magnitude of their real impact on fuel performance, i.e. the ability to increase power and reduce fuel consumption, thereby reducing the carbon footprint. In addition, the most common types of friction modifiers in commercial additives from various manufacturers are presented and existing approaches to the mechanism of action of these components are studied in order to highlight the most effective additive structure.

Keywords: Gasolines, Friction modifier, Multifunctional additive, Carbon footprint.

INVESTIGATION OF THE EFFECT OF DIESEL INJECTOR NOZZLE GEOMETRY ON COKING PHENEMONA

O. Özener[1], A. Ergenç[2], A. Kaya[3] and V. Gazi[4]

1. Yıldız Technical University, Department of Mechanical Engineering, İstanbul, Türkiye, email:oozener@yildiz.edu.tr
2. Yıldız Technical University, Department of Mechanical Engineering, İstanbul, Türkiye, emailaergenc@yildiz.edu.tr
3. ROBERT BOSCH Powertrain Solutions, R&D center, Engineering Nozzle and Research, Bursa, Turkey, alper.kaya@tr.bosch.com
4. ROBERT BOSCH Powertrain Solutions, R&D center, Engineering Nozzle and Research, Bursa, Turkey, veyzat.gazi@tr.bosch.com

Abstract

The deposits, which are called coking/soot and formed in the nozzle/hole structure of the common rail high pressure injection system injector nozzles used in diesel engines, have a significant effect on the hydraulic characteristics of the nozzle and the spray characteristics in the combustion chamber throughout the working life of the component. For this reason, it is important to examine the relationship between deposit formation in the injector nozzle and nozzle hole geometry in terms of internal combustion engine performance parameters. In this direction, to examine the effect of nozzle hole geometry, injector nozzles with 4 different nozzle hole geometries were designed. First the flow characteristics were simulated via using CFD techniques. Then these nozzles are manufactured and tested under accelerated test conditions. As a result of the study, it was observed that increased coking caused a decrease in the amount of injector spray/fuel as expected. It has been determined that the increase in rounding at the nozzle hole inlets increases the amount of deposits and decreases the amount of injected fuel/spray. The results obtained from study conducted in this direction helped to better understand the phenomenon of nozzle geometry resistant to coking phenomena.

Keywords: Coking, Diesel Engines, Injector, Nozzle

1 INTRODUCTION

Today stringent emission regulations exhibit new challenges in the development processes of diesel engines. It has become possible to meet emission regulations not only in the cylinder, but also by using exhaust treatment/filtering (after-treatment) systems (DPF, SCR, DOC etc..) systems on the exhaust line after in-cylinder combustion.

While trying to meet these challenging conditions, one of the important developments has been made on diesel injection systems. Fundamentally, reducing the injector nozzle diameters and increasing the injection pressures made it possible for diesel engines to produce greater power at the desired emission regulations. However, it has been observed that these modern injectors can cause a decrease in engine power output, especially due to deposit formation in long-term operations. Considering that direct injection systems that are used in modern engines today, it is known that characteristics of deposit formations in injectors adversely affects combustion and mixture formation and emission values, increases fuel consumption, and reduces engine power output.

The researchers have carried out both experimental and simulation studies, to examine the deposit formations in the injector nozzles with using the main parameter combinations or stand alone, that affect the hydraulic flow characteristics of the injector nozzle; nozzle hole diameter, nozzle hole geometry, conicity, nozzle hole inlet rounding, cavitation, nozzle tip temperature, etc. Along with the nozzle geometry, the nozzle tip temperature, especially the temperatures of >300°C and above causing thermal condensation, and Zn etc., which may be present in the fuel composition due to pollution. Substances play an important role as accelerating factors in the formation of deposits. [1-4]

Engine manufacturers, especially in recent years, tend to use more spray holes and therefore smaller hole diameters in nozzle design. This trend

obliges engine manufacturers to produce injectors with higher Cd (Coefficient of discharge) to achieve the same performance. Increasing the conicity factor or inlet rounding in the nozzle spray hole geometry, which provides injector production with higher Cd, reveals a nozzle structure that is more prone to deposit formation. Due to all these factors, the details of the formation of deposits in diesel injectors are being researched from new perspectives due to new boundary conditions emerging day by day. Case studies on the relationship between nozzle and spray geometry, coking phenomenon and engine performance for diesel injectors can also be found [5-10].

Within the scope of this study, injector nozzles with 4 different hole geometries were designed and produced, and post-production spray hydraulic measurements and spray photographs were performed. After this stage, the nozzles were tested in a 1.6-liter diesel engine in Yıldız Technical University engines laboratories in accordance with a specified engine cycle. 1ppm Zn to accelerate deposit/soot formation during engine tests added in diesel fuel was used.

2 METHOD

2.1 Test Injector Nozzles

Within the scope of the research, 4 different types of injector nozzle hole geometry were used. The number of hole outlets for all injector nozzles is 8 and the hole outlet diameters are the same. The injector types used are basically expressed in terms of the taper of the nozzle hole and the rounding ratio at the inlet of this hole. While the conicity value (k-factor) expresses the conicity that occurs depending on the inlet and outlet diameter values of the nozzle hole, rounding expresses the rounding made at the hole inlet with the help of a manufacturing process, in terms of the flow before the process and the flow after the process. Information on the conicity and rounding ratios of the hole types used in this direction is given below. All injectors with predetermined conicity were rounded until they could spray the same flow rate under the same conditions. Finally, injectors with 4 different hole geometries and similar flow efficiency that can spray the same flow rate under the same conditions (flow efficiency differences are quite low μ- standard deviation of =0,019) were produced. The characteristics of the nozzle types are given in Table 1, and the k-factor and flow efficiency (μ) are given in Figure 1. The rounding rate formula is given in the formula (1).

In order to optimize the working matrix and test costs, a full factorial test matrix approach is not preferred. It is known that the coking robustness of Type 1 is low under current operating conditions. Although it is known that the coking robustness of the type 2 nozzle is partially good, the production cost is higher. In this direction, Type 3 and Type 4 nozzle geometries, which are predicted to be produced with lower costs, were designed and added to the test matrix and a comparison was aimed. The conicity ratios in Type 3 and Type 4 are the same, and Type 4 nozzle geometry is designed to observe the effect of higher hole inlet rounding ratio in nozzles with the same conicity.

Table 1. Injector Types

Types	Conicity, k - factor	Rounding Rate (%)	μ
TYPE 1	1.5	22%	0.86
TYPE 2	3,5	15%	0.88
TYPE 3	0.5	31%	0.84
TYPE 4	0.5	43%	0.84

$$Rounding\ rate = \frac{Flow\ after\ process - Flo\quad before\ process}{Flow\ before\ process} \quad (1)$$

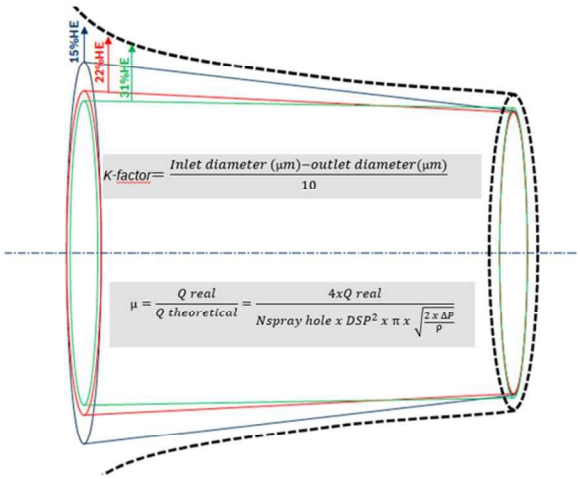


Figure 1. Explanation of injector nozzle parameters

2.2 Test System and Test Cycle

1,6-liter diesel engine was used in the Engines Laboratory of Yıldız Technical University Automotive Department. The specifications of the test engine are given in Table 2.

Table 2. Specifications of the test engine

Engine capacity	1.6 liters
Fuel injection System	Common line high pressure spray system (Common rail)
Injector type	Solenoid (CRI2.16)
Maximum spray pressure	1600 Bar
Engine maximum torque	215 Nm @ 2000 rpm
Engine maximum power	95 kW @ 3750 rpm

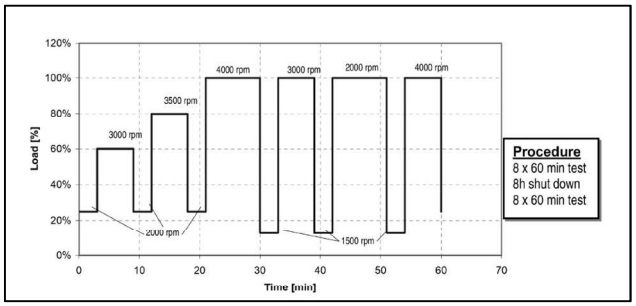


Figure 2. Test cycle

The engine test cycle developed by BOSCH was used as the engine test cycle. The engine speed and load conditions of the test cycle are given in Figure 2. During the tests, the relevant performance data of the engine were measured and recorded at 100% load-4000 rpm at the 29th minute of the cycle, which lasted for a total of 1 hour, and at 100% load-4000 rpm at the 59th minute. After the test cycle was repeated 8 times in succession, the engine was left to cool for 8 hours and then the test cycle was repeated 8 times again, and the test was completed. In this way, a test, finally 8+8+8, was completed in 24 hours.

2.3 Test Modules

Manufactured injectors have been tested within the framework of the designed test modules. Table 3 below shows which injectors are attached to which cylinder in the test modules. The purpose of each test module is given below.

i) Module 1: Detection of coking rate repetitively
ii) Module 2: Deposit/soot and spray geometry investigations for hole
    a. Module 2 - Test 1: Intra-hole deposit examination tests (destructive analysis)
    b. Module 2 - Test 2: Spray geometry inspection testing (spray layout analysis)
iii) Module 3: Evaluation of nozzle tip temperatures
iv) Module 4: Evaluation of injector and nozzle co-spraying characteristics

Tablo 3. Test modules

Module 1

TEST	S1	S2	S3	S4
1	Type1	Type1	Type1	Type1
2	Type2	Type2	Type2	Type2
3	Type3	Type3	Type3	Type3
4	Type4	Type4	Type4	Type4

Module 2

TEST	S1	S2	S3	S4
1	Type2	Type3	Type4	Type1
2	Type2	Type3	Type4	Type1

Module 3

TEST	S1	S2	S3	S4
1	Type1	Type2	Type3	Type4
2	Type4	Type1	Type2	Type3
3	Type3	Type4	Type1	Type2
4	Type2	Type3	Type4	Type1

Module 4

TEST	S1	S2	S3	S4
1	Type1	Type1	Type1	Type1
2	Type2	Type2	Type2	Type2
3	Type3	Type3	Type3	Type3
4	Type4	Type4	Type4	Type4

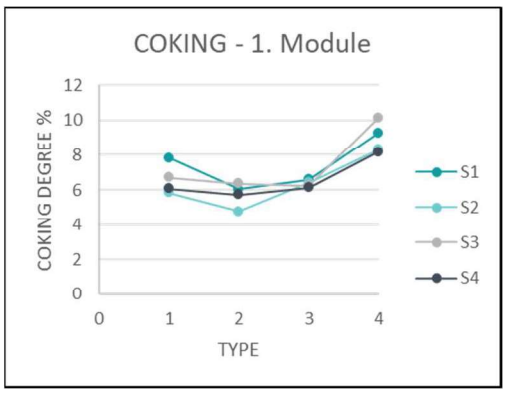
3 RESULTS

The results obtained after the tests are given below.

3.1. Coking Rate

Coking rate is defined as the percentage (%) of the difference in the amount that the injector can inject before and after the test under the same conditions, to the initial amount. Coking rates and

average coking rates obtained in Module 1 are given in Figure 3.



$$Coking = \frac{Flow\ without\ coking - Flow\ with\ coking}{Flow\ without\ coking} x100 \quad (2)$$

Figure 3. Coking rates (Module 1 Tests)

3.2. Spray Flow Change Due to Coking

For a TYPE 3 injector, the hydraulic flow behavior under the same injector voltage characteristic is given in Figure 4.

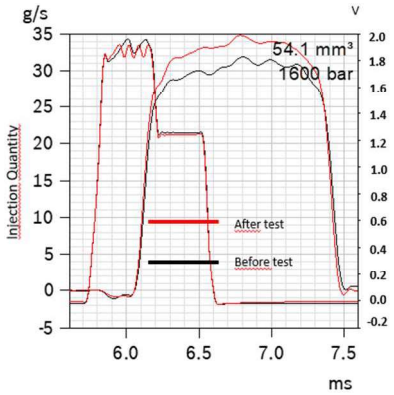
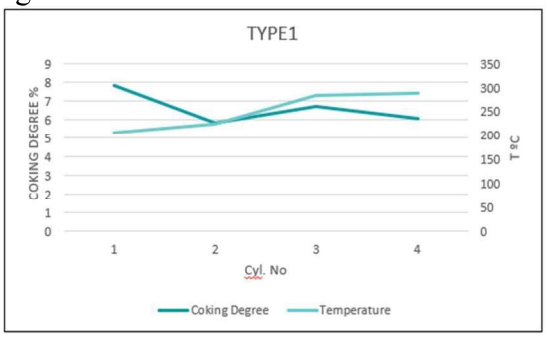
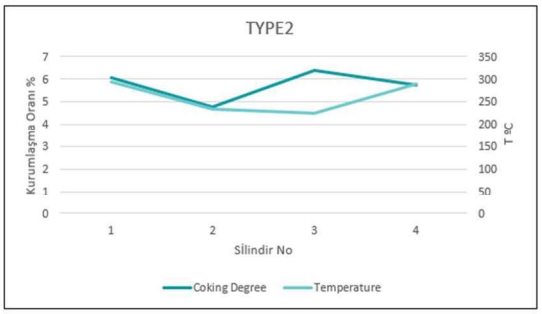


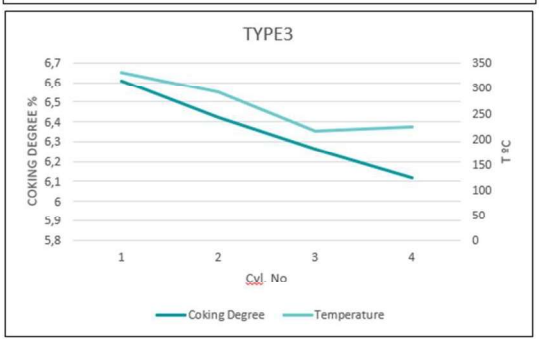
Figure 4. Hydraulic test spray flow variation (TYPE3)

3.3. Measured Nozzle Temperatures – Establishment Relationship

The relationships between the cure rates and the average nozzle temperatures obtained in the tests with thermo-injectors in Module 3 are given in Figure 5.







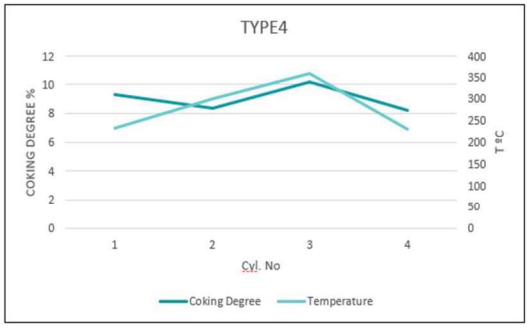


Figure 5. The relationship between nozzle temperatures and coking rates

3.4. Spray Geometry Studies

After test modules were completed, spray photographs were taken for all nozzle types and at 1600 bar pressures, and related spray geometry comparisons were made. Photographing example of TYPE 3 before and after the test is given in Figure 6. "t" represents the time elapsed after the start of spraying.

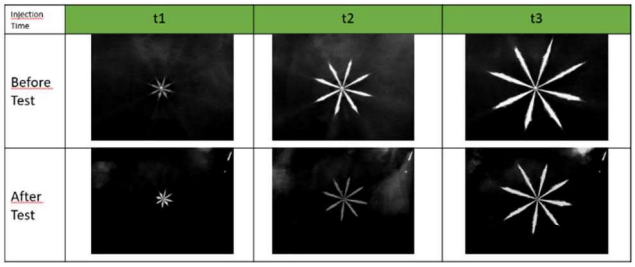


Figure 6. Spray photography (t3>t2>t1)

The spray photography studies were then digitized and analyzed. As a result of this study, the least spray length reduction was observed in Type 3 on average, and the spray length reduction percentages of all types are given in Figure 7.

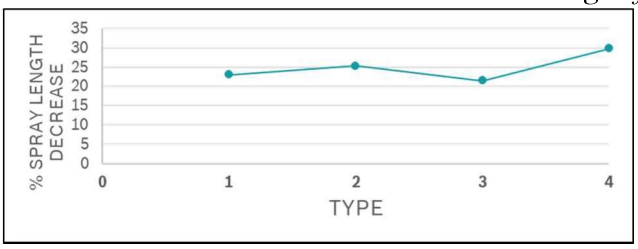


Figure 7. Average % reduction rates of spray lengths

3.5. Nozzle Hole Geometry - Drying - Engine Performance Relationship

During the tests performed for each nozzle type, the motor performance data were recorded and the changes in the motor torque depending on the nozzle hole geometry type are given in Figure 8.

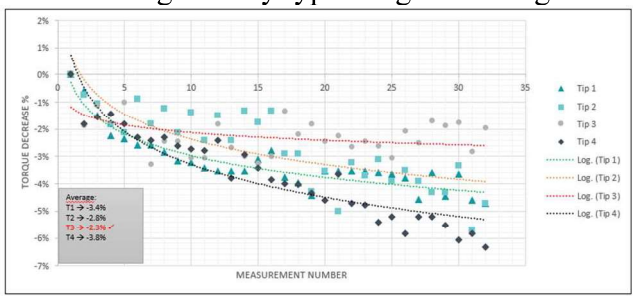


Figure 8. Torque drop during test cycle depending on nozzle hole types (Module 1)

4 CONCLUSIONS

When the results obtained as a result of the study are evaluated;

- According to the coking results of Module 1, TYPE3 shows a behavior between TYPE1 and TYPE2. (TYPE4 > TYPE1 > TYPE3 > TYPE2)

- When the injector hydraulic flow rates were compared under the same voltage characteristic after the rapid coking, it was observed that the coking caused a significant decrease in the injected fuel flow.

- No significant correlation was found when the coking rates and spray amount decreases were compared with the cylinder temperatures. For this reason, it has been evaluated that the temperature differences between the cylinders do not seriously affect the coking behavior.

- The spray geometries were examined, it was observed that there was less shortening in the spray lengths in the TYPE3 type. This case was evaluated as coking affected the spray form of the TYPE3 type less.

- TYPE3 was the hole geometry with the least torque drop across all modules.

- The relationship between the rounding process and sooting was evaluated as the increase in rounding at the hole entrances increases the amount of soot, decreases the amount of spraying, shortens the spray lengths significantly and causes a decrease in the torque of the engine.

- When the results of the study are evaluated in the light of all these data, it has been evaluated that especially in the markets where the fuel-induced sooting problem is high, especially the TYPE 3 nozzle geometry can be offered as a product with both low cost and high soot resistance.

ACKNOWLEDGEMENTS

This work was supported by Tübitak TEYDEB 1501 within the scope of the project numbered 3150777.

REFERENCES

[1] Tang, J., Pischinger S., Lamping, M., Körfer, T., Tatur, M., Tomazic, D. (2009), "Coking phenomena in nozzle orrifices of DI- Diesel engine", *Society of Automotive Engineers*, SAE ,2009-01-0837

[2] Argueyroller, B., Dehooks, S., Gastaldi, P., Lysiane G., Levy, F., Michel, A., Passerel. D., VR (2007), "Influence of injector nozzle design and cavitation on coking phenomenon", *Society of Automotive Engineers*, SAE ,2007-01-1896

[3] Ike moto, M., Omae, K., Nakai, K., Ueda, R., Kakehashi, N., Sunami, K., (2011) "Injection nozzle coking mechanism in common rail diesel engine", *Society of Automotive Engineers*, SAE, 2011-01-1818

[4] Birgel , A. , Laddommatos , N., Aleiferis , P., Zülch , S., Milanovic , N., Lafon , V., Orlovic , A., Lacey , P. Richards , P. (2008) " Deposit formation in holes of diesel injector nozzles : A critical Review ", *Society of Automotive Engineers* , SAE, 2008-01-2383

[5] Brunini, F., Falfari, S., Pelloni, P. (2014), "Influence of the diesel injector hole geometry on the flow conditions emerging from the nozzle", *Energy Procedia*, Vol.45, pg 749-758

[6] Mendoza, MC., Zhang, Q., Alan, CH., Reid, JF, (2001), "Injector Nozzle Coking With Oxygenated Diesel", *Society of Automotive Engineers*, SAE ,2001-01-2016

[7] Montanaro, A., Allocca, L., (2013), "Impact of the Nozzle Coking on Spray Formation for Diesel Injectors", *Society of Automotive Engineers*, SAE,2013-01-2546

[8] Rosberg, PA., Adlercreutz L., Aguilera, MG., Johansson T., Stensiö, L., Angstrom, HE., (2013), "Development of a Heavy duty Nozzle Coking Test", *Society of Automotive Engineers*, SAE ,2013-01-2674

[9] Mancaruso, E., Sequino, L., Vaglieco, BM., Ciaravino, C., (2013), "Coking Effect of Different FN Nozzles on Injection and Combustion in an Optically Accessible Engine", *Society of Automotive Engineers*, SAE ,2013 -01-2674

[10] Napolitano, P., Guido, C., Beatrice, C., Ciaravino, C., (2013), "Analysis of Nozzle Coking Impact on Emissions and Performance of a Euro5 Automotive Diesel Engine", *Society of Automotive Engineers*, SAE ,2013 -01-2674

DYNAMIC FLAME BEHAVIOR OF 30%H_2 30%CO 20%CO_2 20%CNG SYNTHETIC GAS MIXTURE DURING ACOUSTIC FORCING

Omer CAM[1,*], Harun YILMAZ[1] and Ilker YILMAZ[2]

1. Department of Aircraft Maintenance and Repair, Civil Aviation College, Erzincan Binali Yildirim University, Erzincan, Turkey; E-mails: ocam@erzincan.edu.tr, hyilmaz@erzincan.edu.tr
2. Department of Energy Systems Engineering, Faculty of Technology, Gazi University, Ankara, Turkey; E-mail: ilkeryilmaz@gazi.edu.tr

Abstract

The relationship between air-fuel mixture inlet velocity and flame propagation speed is of great importance for anchoring the flame to the burner lip in a stable manner. In order to achieve this flame stabilization, recirculation bubbles that occur in swirling flows inherently are used. However, these recirculation zones may not always ensure flame stability, and flame instabilities may arise. The aim of this study is to examine the effects of swirl number and equivalence ratio on dynamic behavior of 30%H_2 30%CO 20%CO_2 20%CNG mixture in a laboratory scale-premixed combustor. For this purpose, such mixture was tested at 2 different equivalence ratios (Φ) and 7 different swirl numbers (SN). In addition, the mixture flames were forced thermo-acoustically by two identical loudspeakers located downstream of the combustion chamber and placed on both sides symmetrically. Dynamic behavior of the flame was determined by measuring static and dynamic pressure, luminosity intensity and instantaneous flame images. As a result of the thermo-acoustic forcing, all tested flames flashed back at forcing frequencies related to natural acoustic modes of the combustor irrespective of the swirl number and equivalence ratio. However, back pressure value in burner varied depending on both parameters.

Keywords: Flame Instability; Dynamic Behavior; Swirl Number; Equivalence Ratio.

1 INTRODUCTION

Trying to reduce NO_x emissions by keeping pollutants such as CO, CO_2 and unburnt hydrocarbons (UHCs) at low levels brings many difficulties. One of the methods used to solve this problem is to send the fuel-lean reactants in a premixed way to the burner. Although there are many advantages in premixed combustion, problems may arise in combustion dynamics and these problems can cause an unstable vortex core by triggering instabilities within combustion chamber. Because, in lean premixed combustion systems, the flow is very sensitive to external disturbances, especially at flame blowout limits [1]. As a result of this instabilities and flow fluctuations, flashback and extinction can be observed.

The flow impinging to the swirler vanes adds a tangential velocity component to the flow. This velocity component forces the flow into a spiral motion. Consequently, this flow assures a more homogeneous and rapid mixing of the air/fuel mixture, and generally expands stable operating range in many combustion systems [2, 3]. In addition, studies have shown that swirl flows have large-scale effects on important parameters such as flame shape and stability, burning density, flow field etc. [4-7]. Although swirlers are frequently used in gas turbine combustors, studies examining the effect of swirl flows on combustion instability are very limited [3]. Because, high-cost test systems and equipment are required to examine dynamics of these complex combustors [8]. Furthermore, in numerical modeling of these systems, the basic equations of fluid physics should be customized and accurately defined in accordance with the operating conditions.

The flame, which exhibits temporal behavior during combustion, produces sound waves and these sound waves begin to spread in the radial direction (Figure 1). For unconfined flames, sound waves are damped by the atmosphere since these waves do not encounter any obstacles (in other words, they are not reflected). But, in today's combustion systems, the combustion chambers (closed environment) consist of complex structures. Due to the lack of

a natural damping mechanism, thermo-acoustic fluctuations resulting from the interaction between heat release and the combustion chamber acoustics generate a feedback loop (fluctuations of different types and intensities) [9]. If these fluctuations in the system do not dampen or decrease over time, flame interacts with combustion chamber and becomes unstable by itself [10]. High amplitude sound waves at different frequencies caused by pressure fluctuations can lead to serious damage to system elements [11]. Therefore, predicting the conditions in which instabilities occur is extremely important in understanding flame behavior. There are many studies in the literature investigating combustion dynamics on premixed swirling flames [12-19].

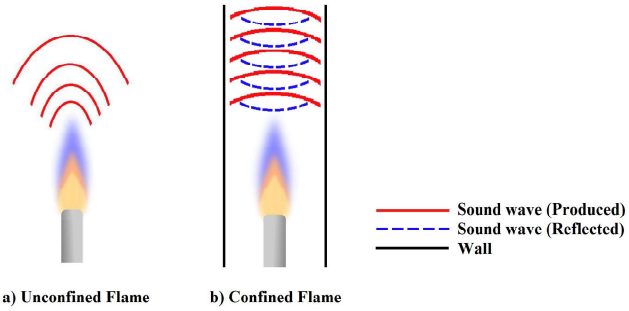


Figure 1. Propagation of sound waves in open and closed environment

In this study, the relationship between combustion instabilities and pressure fluctuations, i.e., flame stability characteristics, was experimentally investigated in a laboratory scale-swirl stabilized-premixed burner for 30%H_2 30%CO 20%CO_2 20%CNG synthetic gas mixture. Flame was acoustically forced with sound waves of different frequencies (0-300 Hz) via loudspeakers that act as mechanical actuators placed in the arms of the combustion chamber. By measuring luminous intensity, dynamic and static pressure, and analyzing instantaneous flame images, effects of equivalence ratio and swirl number on flame behavior were examined in detail.

2 EXPERIMENTAL SETUP

Figure 2 presents the schematic view of the experimental system. Experimental system shown in the Figure 2 can be divided into three main groups; gas supply line (1) to mix different gases and air in desired compositions, premixed-swirl stabilized burner (2) and combustion chamber (3). Air is provided from a compressor that has the capacity of 39 m^3/hour air supply. In addition, an extra 1000 lt (1 m^3) air tank is placed in the compressor unit to ensure that the compressor does not operate continuously. Besides, air filter and regulator are used in order to prevent inefficient operation of the mass flow controller. Mass flow controller (MKS 1579) used in the airline operates based on the pressure difference (40-49 psi) to send the desired flow rate to the premixer with high precision. Additionally, each fuel component was supplied from a high purity pressurized tank, and fuel mixtures were formed in the desired compositions via mass flow controllers.

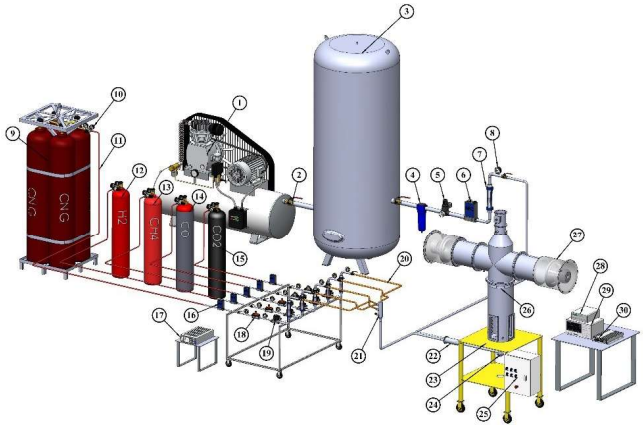


Figure 2. Schematic of experimental setup

1. Air Compressor (5.5 hp, 500 lt)
2. Global Gas Valve
3. Air Vessel (1 m^3)
4. Air Filter
5. Regulator (1 MPa to 0.3 MPa)
6. Air Mass Flowmeter Controller (MFC)
7. Float Type Flowmeter
8. Manometer
9. CNG Cylinder
10. High Pressure Regulator
11. High Pressure Rubber Hose
12. H_2 Cylinder
13. CH_4 Cylinder
14. CO Cylinder
15. CO_2 Cylinder
16. Fuel MFC
17. Vacuum System Controller
18. Pneumatic Regulator
19. Solenoid Valve
20. Braided Flexible Metal Hose
21. Fuel Collector
22. Pre-mixer
23. Portable Bench
24. Premixed Burner
25. Ignition and Solenoid Control Panel
26. Combustion Chamber
27. Loudspeaker
28. Signal Generator
29. Oscilloscope
30. Amplifier

Increasing the homogeneity of the fuel/air mixture can contribute to the reduction of NO_x emissions, increment in combustion efficiency, reduction of burner sizes, elimination of combustion instabilities and prolonging lifetime of the combustor components [20]. For this purpose, two main methods (active and passive mixing) have been developed by the researchers to mix fuel and air at the molecular level. The premixer used in the experimental setup passively operates. Fuel and air penetrate to the premixer through two different channels, pass through discs with fixed blades and perforations

in the premixer, and flow horizontally into the plenum chamber of the burner. The burner is designed to operate at thermal powers up to 10 kW. However, in the experiments conducted within the scope of this study, thermal power was kept constant (3 kW). All parts of the burner are designed to be easily assemble and disassemble. At the top of the burner, there is a gap for the swirl generator. In addition, luminosity and pressure measurement slots are placed on the burner. There are many studies [21-26] using this experimental setup. More information can be obtained if deemed necessary.

3 OPERATING CONDITIONS

Synthetic gases have a wide fuel composition range depending on the production method or the content of the raw material. In order to classify these gases, the volumetric ratio of H_2 to CO is used. In this study, this ratio (H_2/CO) was chosen as 1.0. Tests were carried out by changing the swirl number between SN = 0.2 and 1.6 at intervals of 0.2 and setting equivalence ratio as 0.8 or 1.0. Properties of the tested gas mixture are given in Table 1.

Table 1. Properties of tested gas mixture

Density (kg/m^3)	0.9413
Low Heating Value (MJ/kg)	15.138
Low Heating Value (MJ/m^3)	14.249
Wobbe Index (MJ/Nm^3)	17.680
Fuel Flow Rate	12.631*
Air Flow Rates at Φ=0.8 and 1.0	52.608 and 42.086*

* Flow rates are presented in SLPM

4 RESULTS AND DISCUSSIONS

Today, with integrated gasification combined cycle (IGCC) power plants using synthetic gases, 82% reduction in CO emissions and 24% reduction in NOx emissions have been achieved compared to conventional coal-based thermal power plants [27]. Meeting low emission standards and eliminating or reducing harmful components can make synthetic gases as a preferred energy source for today and future, which is the motive of this study.

Thermo-acoustic instabilities occur at frequencies related to natural acoustic modes of the combustion chamber [28]. For this reason, natural acoustic modes of the combustion chamber utilized in this study were initially determined by forcing the combustion chamber at different frequencies. Audio signals of the same phase and amplitude were sent to each loudspeaker placed in arms of the combustion chamber. Output power of the loudspeakers was kept constant in all experiments. The sound waves sent at constant amplitude and different frequencies interacted with the combustion chamber and caused high amplitude oscillations at 3 different frequency values between 0-300 Hz. In this way, natural acoustic modes of the combustion chamber were designated as 95-100 Hz, 170-175 Hz and 260 Hz (Figure 3).

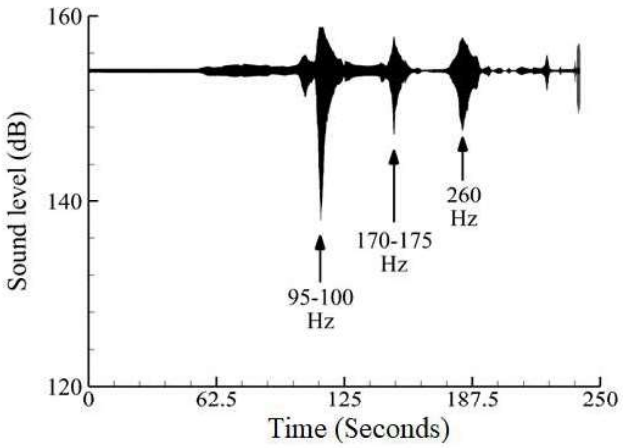


Figure 3. Sound level equivalents of pressure measurements

In thermo-acoustic forcing experiments, all flames showed similar behavior at all swirl numbers and equivalence ratios. From the beginning of the acoustic forcing, all flames moved upstream of the burner, and then flashed-back. However, pressure increment in burner plenum varied depending on the swirl number. Dynamic and static pressures and flame luminosities obtained during the thermo-acoustic forcing experiments are presented in Figure 4-5. The lowest pressure increment at both equivalence ratios were measured at SN = 0.4. Table 2 shows the highest measured pressure values as a result of the flashback. As seen, measured pressure values increase and reach up to 375.35 mbar (Φ=0.8 and SN=1.6) as swirl number increases.

At 0.8 equivalence ratio, flame luminosity slightly varies from the beginning of the acoustic forcing, and sharply decreases as a result of the

flashback occurrence at 0.2 swirl number. However, flame luminosity presents larger oscillations at higher swirl numbers (0.4, 0.6, 0.8 and 1.0). At 1.4 and 1.6 swirl numbers, flame luminosity starts to reduce from the beginning of the acoustic forcing and this decrement shows a linear behavior. At 1.2 swirl number, the trend of dependence of luminous intensity to acoustic forcing is similar to that of at lower swirl numbers (0.2 and 0.4). Durox et al. concluded that in swirling flames, a precessing vortex core (PVC) forms after exceeding SN = 0.45 [13], and PVC causes large amplitude of luminosity fluctuations in the combustion chamber [29] and may lead to flashback. Larger amplitude of luminosity fluctuations at higher swirl numbers are attributed to this phenomenon. Because vortex breakdown that occurs as a result of the formation of PVC forces the flame to propagate upstream and flashback occurs [30]. Compared to the 0.8 equivalence ratio, flame luminosity doesn't considerably change with acoustic forcing at 1.0 equivalence ratio at almost all swirl numbers tested except for 1.6 swirl number (Figure 4-5). Yet, flashback occurred at all tested cases.

Table 2. Properties of tested gas mixture

	Φ=0.8	**Φ=1.0**
SN=0.2	56.38	81.63
SN=0.4	41.88	36.01
SN=0.6	120.23	56.76
SN=0.8	130.61	162.2
SN=1.0	181.65	162.28
SN=1.2	242.38	232.39
SN=1.4	282.67	349.04
SN=1.6	375.36	357.21

While flame luminosity is expected to decrease with the swirl number increment, a non-monotonous behavior was detected (which is also the case for the effects of equivalence ratio). With the increase of equivalence ratio, a significant change was observed in flames structure (Figure 6). Flame lengths increased in all experiments performed at a stoichiometric ratio compared to Φ=0.8. Besides, the flames expanded in radial direction up to SN=0.4, and after SN=0.6 the flames were attached to the inside of the burner.

5 CONCLUSIONS

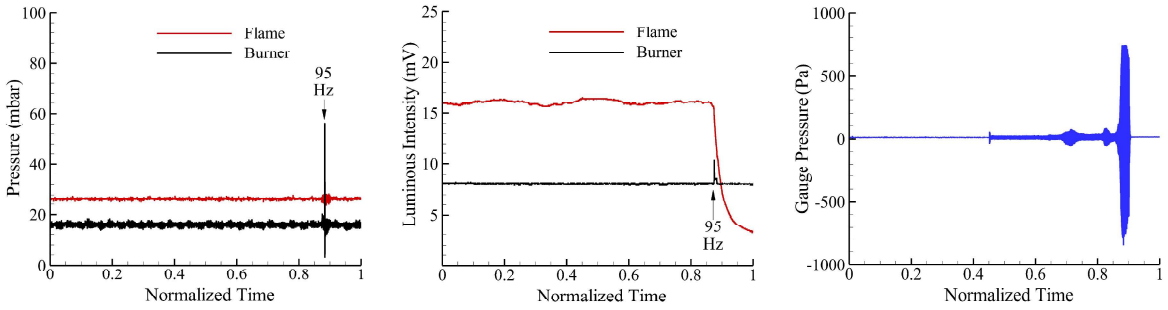
This study is based on the relationship between combustion instabilities and pressure fluctuations of a synthetic gas mixture (30%H_2 30%CO 20%CO_2 20%CNG), and the occurrence of flame extinction and flashback was researched on a premixed-swirl stabilized-laboratory scale burner. Flame was forced acoustically with sinusoidal sound waves of different frequencies (0-300 Hz) by means of loudspeakers placed in the arms of the combustion chamber. Dynamic/static pressure, luminosity intensity and instant flame images was measured and effects of equivalence ratio and swirl number on flame behavior were investigated in detail.

Results obtained from experimental studies:

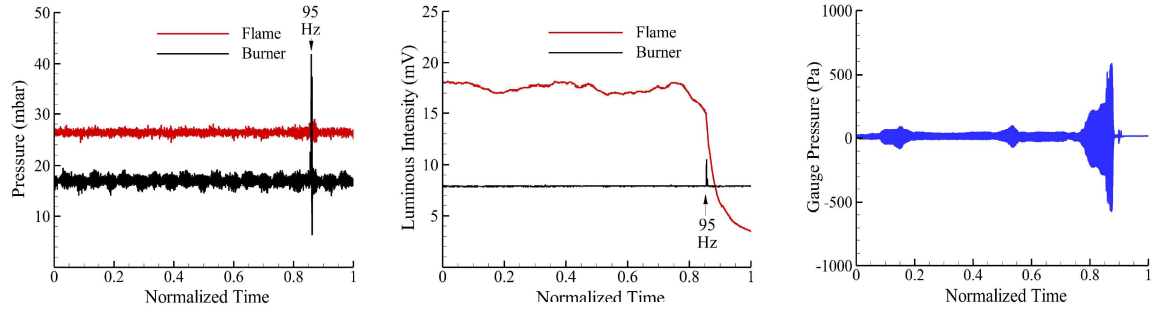
- It has been found that the combustion chamber resonates with high amplitude pressure fluctuations at three different frequency values (95-100, 170-175, 260 Hz).
- Pressure waves with an amplitude greater than 500 Pa were created in the combustion chamber at resonance frequencies.
- With the increase in the swirl number, the flame core started to move in the burner.
- The lowest pressure values at both equivalence ratios were measured at SN = 0.4.
- It has been determined that the swirl number does not have an effect on the flame behavior under thermo-acoustic forcing, but the pressure on the burner inner walls is higher (maximum pressure has been measured as 375.36 mbar at SN=1.6 and Φ=0.8) when flashback is occurred.

ACKNOWLEDGEMENTS

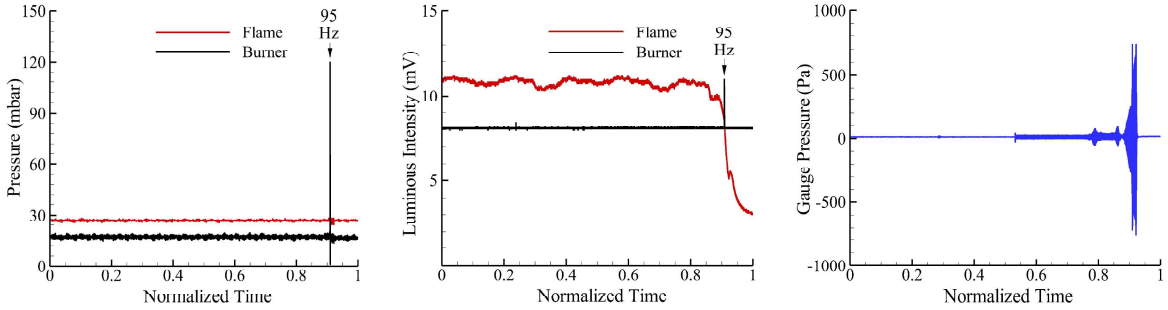
We would like to thank the Scientific and Technological Research Council of Turkey (TÜBİTAK-MAG-215M821) for its financial support.



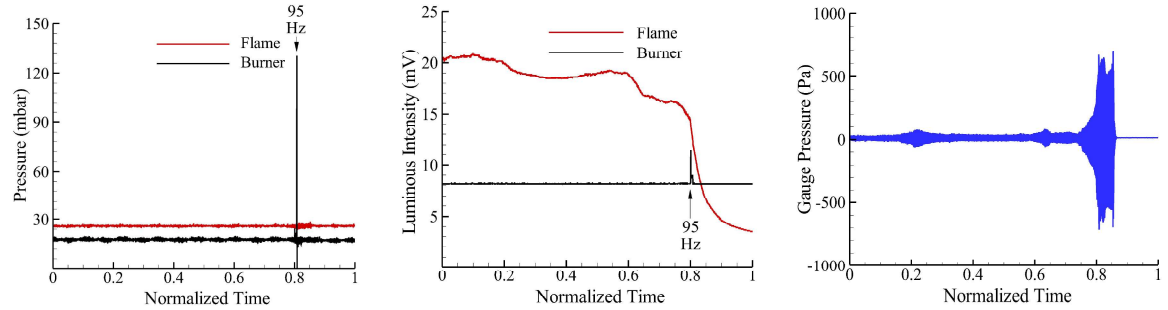
a) SN=0.2



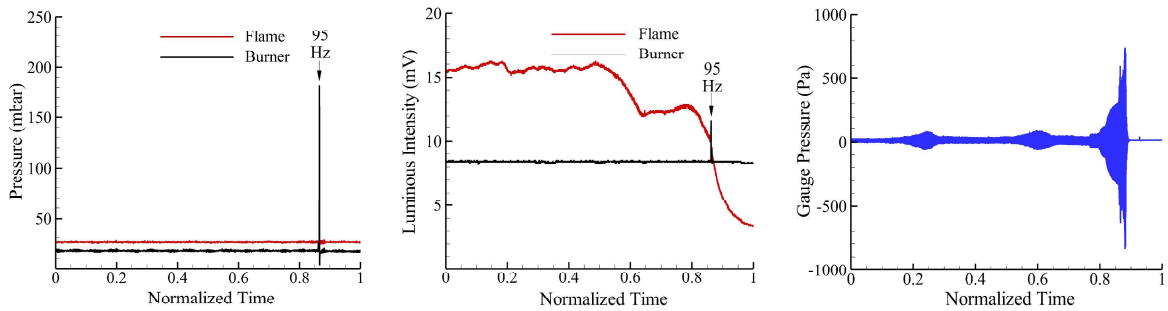
b) SN=0.4



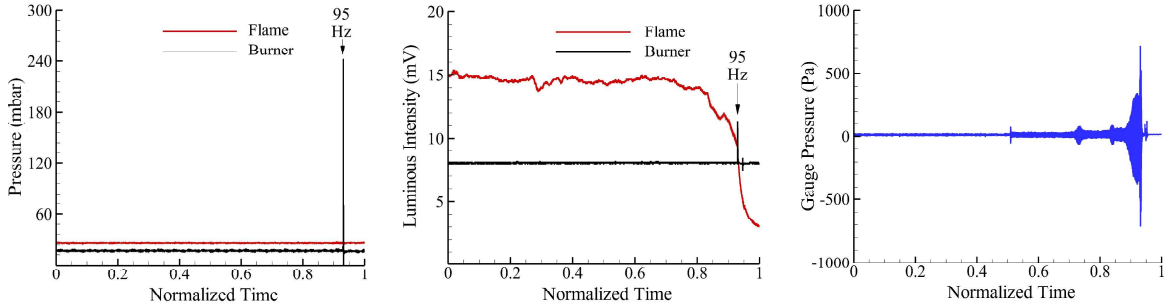
c) SN=0.6



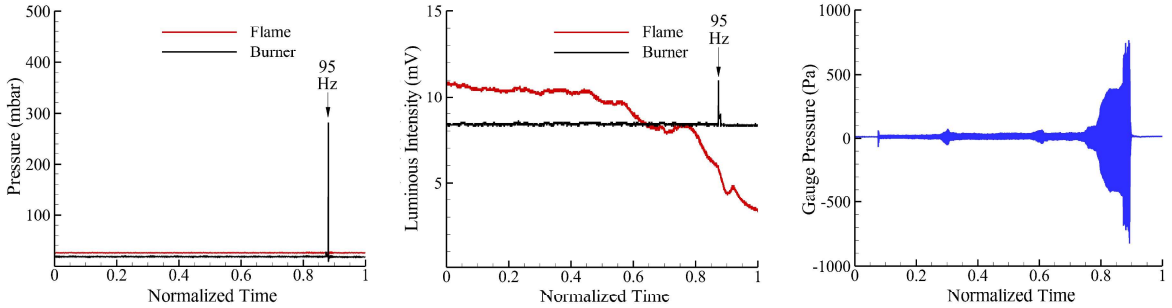
d) SN=0.8



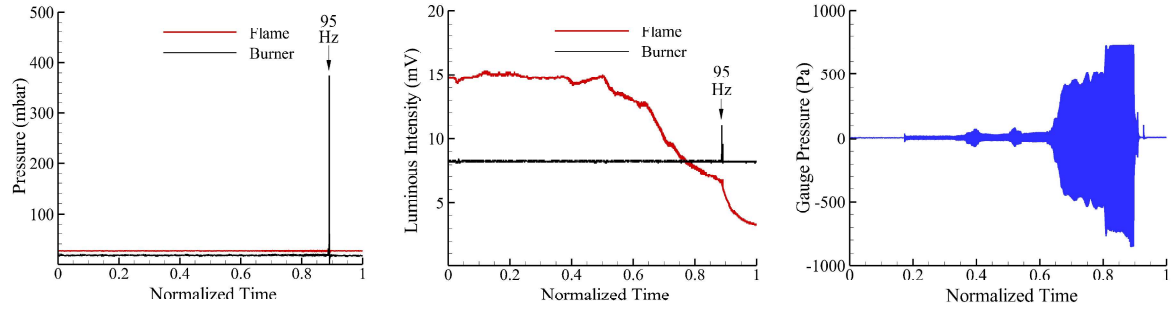
e) SN=1.0



f) SN=1.2

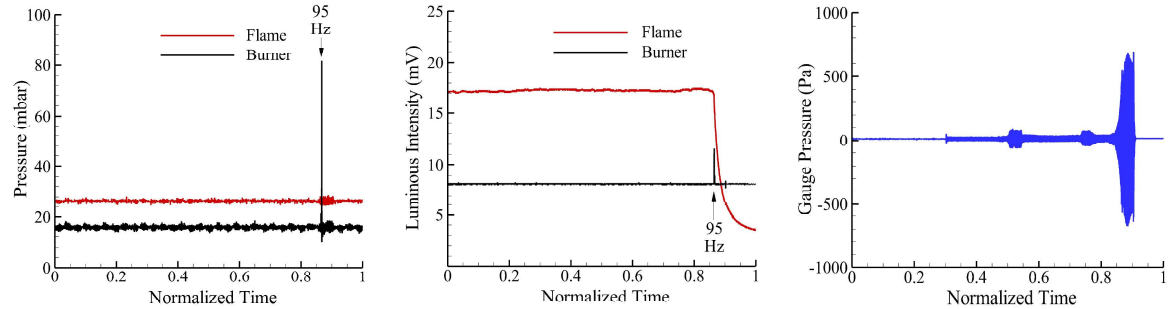


g) SN=1.4

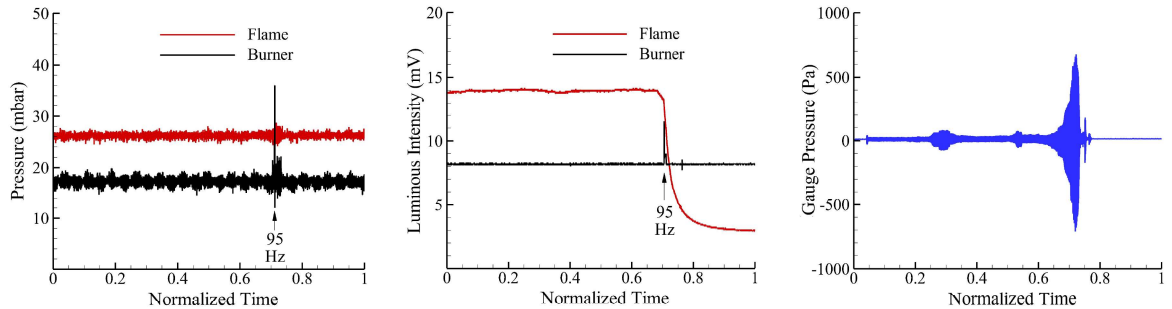


h) SN=1.6

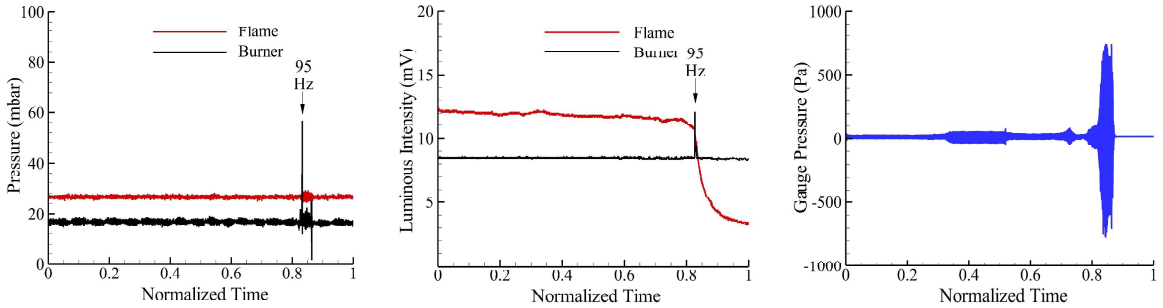
Figure 4. Pressures and luminous intensity profiles at Φ=0.8. ("flame" and "burner" indicates pressure sensor or photodiode located on combustion chamber and burner, respectively.



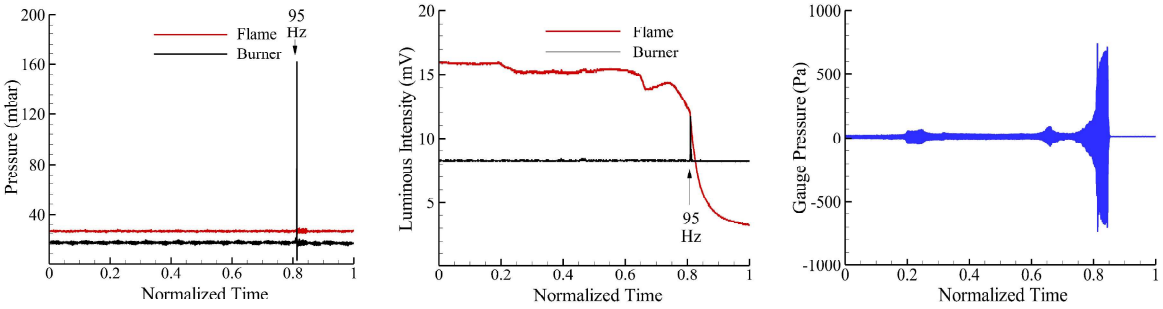
a) SN=0.2



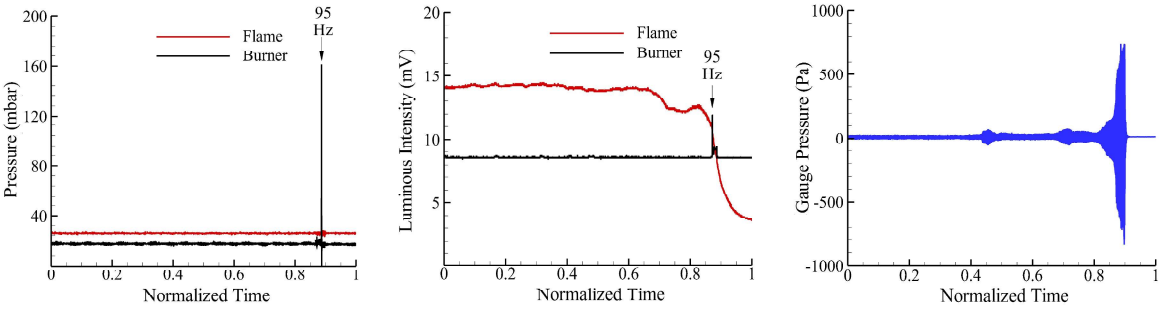
b) SN=0.4



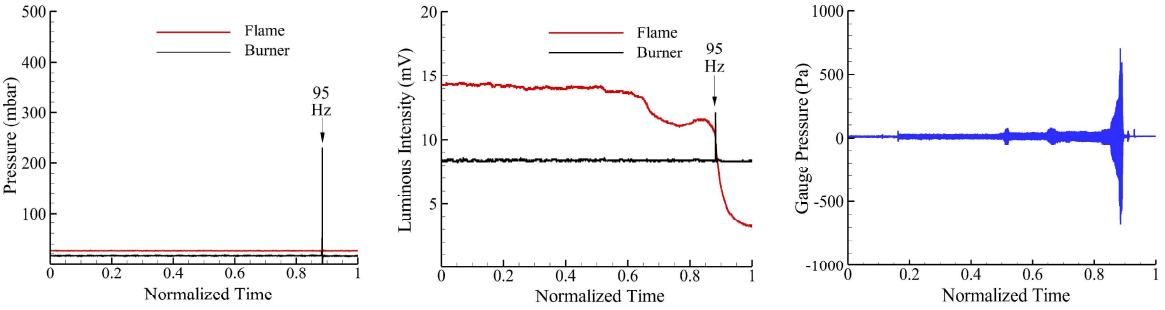
c) SN=0.6



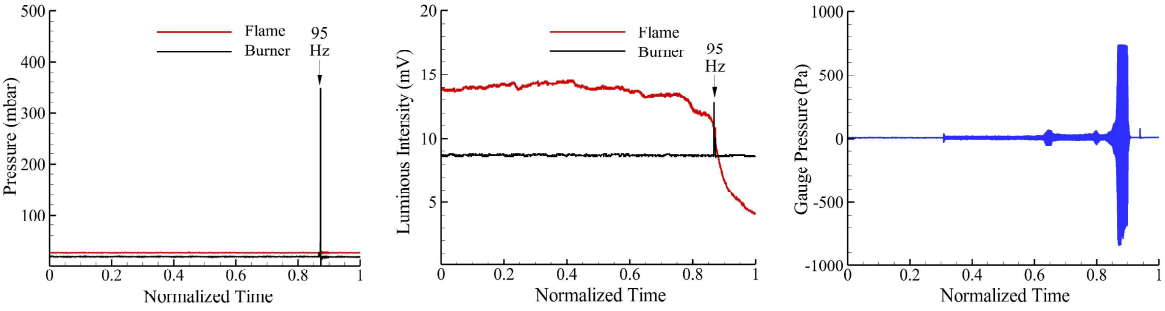
d) SN=0.8



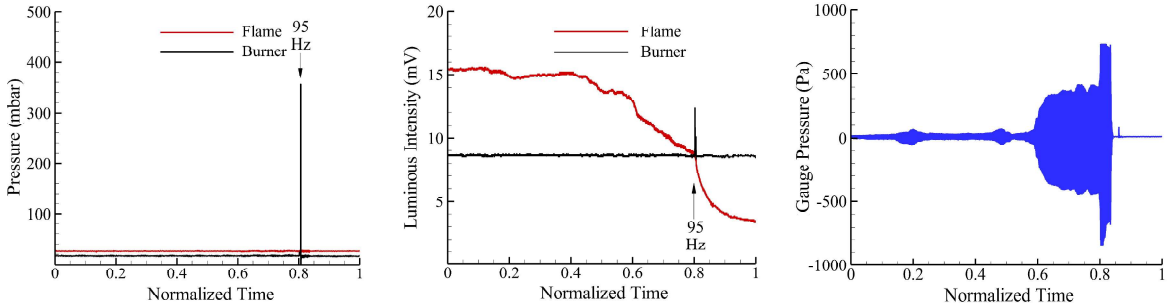
e) SN=1.0



f) SN=1.2

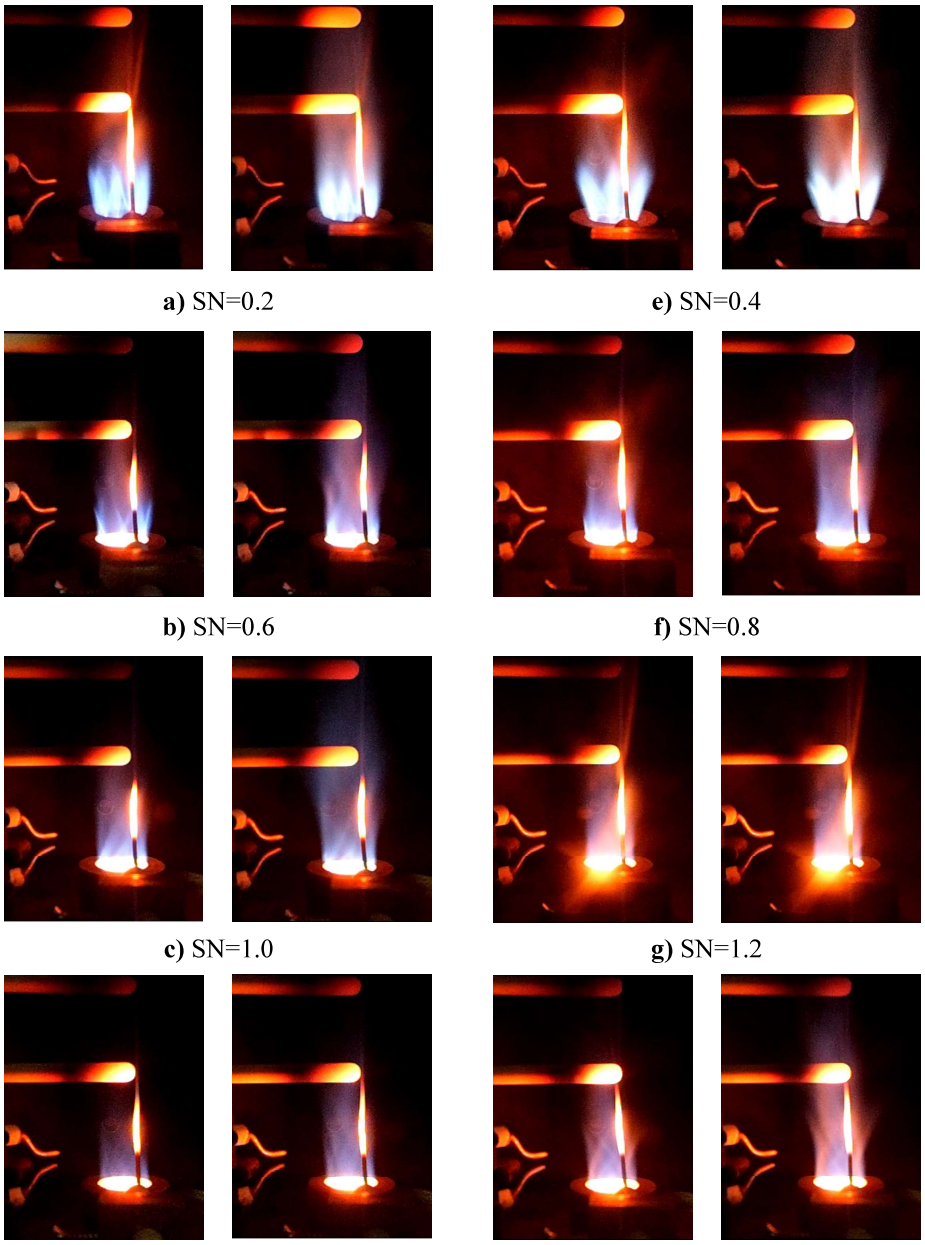


g) SN=1.4



h) SN=1.6

Figure 5. Pressures and luminous intensity profiles at Φ=1.0. ("flame" and "burner" indicates pressure sensor or photodiode located on combustion chamber and burner, respectively.



a) SN=0.2 **e)** SN=0.4

b) SN=0.6 **f)** SN=0.8

c) SN=1.0 **g)** SN=1.2

d) SN=1.4 **h)** SN=1.6

Figure 6. Instantaneous flame images. (Φ=0.8 on the left and Φ=1.0 on the right)

REFERENCES

[1] P. Palies, D. Durox, T. Schuller, S. Candel, The combined dynamics of swirler and turbulent premixed swirling flames, *Combustion and Flame, Vol.* 157(9), pp. 1698-717, 2010.

[2] N. Syred, J. M. Beér, Combustion in swirling flows: A review, *Combustion and Flame, Vol.* 23(2), pp. 143-201, 1974.

[3] A. K. Gupta, D. G. Lilley, N. Syred, *Swirl flows*, Tunbridge Wells, England, UK: Abacus Press, 1986.

[4] D. G. Lilley, Swirl flows in combustion: a review, *AIAA journal, Vol.* 15(8), pp. 1063-78, 1977.

[5] R. Thundil Karuppa Raj, V. Ganesan, Study on the effect of various parameters on flow development behind vane swirlers, *International Journal of Thermal Sciences, Vol.* 47(9), pp. 1204-25, 2008.

[6] F. Vashahi, S. Lee, J. Lee, Experimental analysis of the swirling flow in a model rectangular gas turbine combustor, *Experimental Thermal and Fluid Science, Vol.* 76, pp. 287-95, 2016.

[7] A. E. E. Khalil, A. K. Gupta, Distributed swirl combustion for gas turbine application, *Applied Energy, Vol.* 88(12), pp. 4898-907, 2011.

[8] C. Stone, S. Menon, *Combustion instabilities in swirling flows,* 37th Joint Propulsion Conference and Exhibit. pp.

[9] N. Syred, A review of oscillation mechanisms and the role of the precessing vortex core (PVC) in swirl combustion systems, *Progress in Energy and Combustion Science, Vol.* 32(2), pp. 93-161, 2006.

[10] S. Cheng, *Combustion instability theory,* In: Loh WHT, editor Jet, Rocket, Nuclear, Ion and Electric Propulsion. Springer; pp. 599-617, 1968.

[11] F. Culick, P. Kuentzmann, *Unsteady Motions in Combustion Chambers for Propulsion Systems*: NATO Research and Technology Organization Neuilly-Sur-Seine; 2006.

[12] R. S. Blumenthal, P. Subramanian, R. I. Sujith, W. Polifke, Novel perspectives on the dynamics of premixed flames, *Combustion and Flame, Vol.* 160(7), pp. 1215-24, 2013.

[13] D. Durox, J. P. Moeck, J.-F. Bourgouin, P. Morenton, M. Viallon, T. Schuller, et al., Flame dynamics of a variable swirl number system and instability control, *Combustion and Flame, Vol.* 160(9), pp. 1729-42, 2013.

[14] K. T. Kim, D. A. Santavicca, Interference mechanisms of acoustic/convective disturbances in a swirl-stabilized lean-premixed combustor, *Combustion and Flame, Vol.* 160(8), pp. 1441-57, 2013.

[15] R. C. Orbay, K. J. Nogenmyr, J. Klingmann, X. S. Bai, Swirling turbulent flows in a combustion chamber with and without heat release, *Fuel, Vol.* 104, pp. 133-46, 2013.

[16] S. Roux, G. Lartigue, T. Poinsot, U. Meier, C. Bérat, Studies of mean and unsteady flow in a swirled combustor using experiments, acoustic analysis, and large eddy simulations, *Combustion and Flame, Vol.* 141(1), pp. 40-54, 2005.

[17] E. Karlis, Y. Liu, Y. Hardalupas, A. M. K. P. Taylor, H2 enrichment of CH4 blends in lean premixed gas turbine combustion: An experimental study on effects on flame shape and thermoacoustic oscillation dynamics, *Fuel, Vol.* 254, pp. 115524, 2019.

[18] R. Mercier, T. F. Guiberti, A. Chatelier, D. Durox, O. Gicquel, N. Darabiha, et al., Experimental and numerical investigation of the influence of thermal boundary conditions on premixed

swirling flame stabilization, *Combustion and Flame, Vol.* 171, pp. 42-58, 2016.

[19] J. Zhang, A. Ratner, Experimental study on the excitation of thermoacoustic instability of hydrogen-methane/air premixed flames under atmospheric and elevated pressure conditions, *Int J Hydrogen Energ, Vol.* 44(39), pp. 21324-35, 2019.

[20] J. Zhang, *Micro injection fuel/air premixer/combustion*, *Agricultural and Mechanical College.* Louisiana State University; 95, 2007.

[21] H. Yilmaz, O. Cam, I. Yilmaz, Experimental Investigation of Flame Characteristics of H2/CO/CH4/CO2 Synthetic Gas Mixtures, *Combustion Science and Technology, Vol.*, pp. 1-23, 2020.

[22] H. Yilmaz, O. Cam, I. Yilmaz, A comparison study on combustion and emission characteristics of actual synthetic gas mixtures, *Fuel, Vol.* 263, pp. 116712, 2020.

[23] H. Yilmaz, O. Cam, I. Yilmaz, Experimental investigation of flame instability in a premixed combustor, *Fuel, Vol.* 262, pp. 116594, 2020.

[24] H. Yilmaz, I. Yilmaz, Effects of synthetic gas constituents on combustion and emission behavior of premixed H2/CO/CO2/CNG mixture flames, *Journal of the Energy Institute, Vol.* 92(4), pp. 1091-106, 2019.

[25] H. Yilmaz, I. Yilmaz, Combustion and emission characteristics of premixed CNG/H2/CO/CO2 blending synthetic gas flames in a combustor with variable geometric swirl number, *Energy, Vol.* 172, pp. 117-33, 2019.

[26] I. Yilmaz, H. Yilmaz, O. Cam, An experimental study on premixed CNG/H2/CO2 mixture flames %J Open Engineering, *Vol.* 8(1), pp. 32, 2018.

[27] T. Lieuwen, R. Yetter, V. Yang, *Synthesis Gas Combustion: Fundamentals and Applications*: CRC Press; 2009.

[28] J. O'Connor, V. Acharya, T. Lieuwen, Transverse combustion instabilities: Acoustic, fluid mechanic, and flame processes, *Progress in Energy and Combustion Science, Vol.* 49, pp. 1-39, 2015.

[29] C. Duwig, L. Fuchs, *Study of precessing vortex core during vortex breakdown using LES and POD*, *Fifth International Symposium on Turbulence and Shear Flow Phenomena.* Begel House Inc., 2007.

[30] C. Heeger, R. L. Gordon, M. J. Tummers, T. Sattelmayer, A. Dreizler, Experimental analysis of flashback in lean premixed swirling flames: upstream flame propagation, *Experiments in fluids, Vol.* 49(4), pp. 853-63, 2010.

EXPERIMENTAL ANALYSIS OF A HYDROGEN/DIESEL DUAL FUEL TEST CASE VIA IR IMAGING

C. Allouis[1,2], E. Mancaruso[1], R De Robbio[1], B.M. Vaglieco[1]

1. Institute of Science and Technology for Energy and Sustainable Mobility, STEMS-CNR, Napoli – Italy; email: christophe.allouis@stems.cnr.it
2. Middle East Technical University, Dept Mechanical Engineering, , Ankara - Türkiye: christop@metu.edu.tr

Abstract

Energy transition strongly leads researcher to find alternative fuel such as hydrogen to internal combustion engines. An immediate and transient solution is represented by the dual fuel (DF) technology. It can offer significant reduction of carbon dioxide and pollutant emissions. In this paper, DF operation was investigated in a single cylinder research engine. The engine run at 1500 rpm, while methane/hydrogen was injected in the intake manifold in front of the entrance of the tumble intake port. The aim of the study is to compare the DF hydrogen combustion with the DF methane combustion using Fast IR Imaging. We observed that IR camera was able to give combustion information and to follow the whole process for both DF hydrogen and methane, while identifying the combustion start point. Moreover, IR acquisitions for premixed hydrogen evidenced an unpredictably behavior of the mixture, leading to a specific Diesel injection strategy to avoid hydrogen auto-ignition at higher speed engine. Finally, premixed methane IR emission fully covered the combustion process, thus requiring a further image processing to get more information about the pilot and main injections.

Keywords: Dual fual, Hydrogen, IR imaging

1 INTRODUCTION

Energy transition leads researchers to find short term solutions to reduce fossil fuel consumption, especially for internal combustion engines (ICE). In the meantime, there is a tendency to improve engine performances. In this scenario, hydrogen, could be an interesting option in ICE [1]. Its carbon-free content, wide flammability limits and fast flame speeds represent attractive characteristics to reach the near-zero emission levels and to enhance the engine thermal efficiency. Its use in spark ignition (SI) engines is a huge constrain due to the low engine compression ratios thus limiting the thermodynamic efficiency. For compression-ignition engine, the spark ignition can be replaced by a pilot multiple fuel ignition to enhance a fast combustion when using gaseous fuel [2]. This dual-fuel concept, hydrogen-diesel direct injection, may reduce the limitations reported for hydrogen applications in SI engines. Moreover, the use of alternative fossil gaseous fuels in diesel engines presents some inconvenient, i.e. increased pressure drop, pre-ignition, and knocking, while enhancing positive effects concerning soot and NOx emission reduction.

Many studies about dual fuel engine are present in the literature especially about the operation and Reactivity Controlled Compression Ignition (RCCI) combustion [3]. The performances of hydrogen in a dual fuel compression ignition (CI) engine are compared to natural gas, liquefied petroleum gas (LPG) and synthetic gas [4]. The main conclusion concerned the high efficiency of hydrogen and LPG. On another hand, hydrogen suffers less from cyclic variations, emissions and smooth performance of the engine compared to other fuels. Its very low minimum flammability is a good asset under lean operation. Moreover, its thermodynamic and heat transfer characteristics enhance high compression temperatures thus improving the engine efficiency. Its high burning rates and low ignition energy levels come out to be a perfect candidate for high-speed and cold starting engine operating conditions [5]. The hydrogen auto-ignition represents another topic of investigation. Experiments were performed in a constant-volume combustion vessel over a broad range of thermodynamic conditions, including top dead centre (TDC) diesel engine conditions.

It has been demonstrated that the ignition delay is strongly affected by the fuel temperature and, at a lower level, by the O2 concentration, while H2O and CO2 concentrations influence is negligible [6]. Finally, another study involving hydrogen as unique fuel in a water-cooled single cylinder naturally aspirated four-stroke diesel engine, showed that the operating limits of the engine are significantly extended when the swirl chamber presented a smooth fuel leakage or by the use of a pilot fuel injection [7]. In that case, the NOx emissions presented a significantly higher concentration while operating a premixed hydrogen and air mixture at low equivalence ratios.

This paper presents preliminary studies on Methane/hydrogen-diesel dual fuel conditions were investigated in a single cylinder optically accessible research engine. The engine was operated at a constant engine speed (1500 rpm), and methane/hydrogen has been injected in the intake manifold in front of the entrance of the tumble intake port. The aim of the study is to compare the DF hydrogen combustion with the DF methane combustion. Premixed ratios up to 92 and 83 were used with methane and hydrogen, respectively. In-cylinder combustion pressures and cycle resolved optical diagnostics have been applied to detect infrared images from the combustion chamber, while measuring pollutant emissions.

2 EXPERIMENTAL SET-UP

Optical engine

The layout of the optical single cylinder CI engine used for this study is shown in Figure 1; while the engine specifications and injection systems are reported in Table 1.

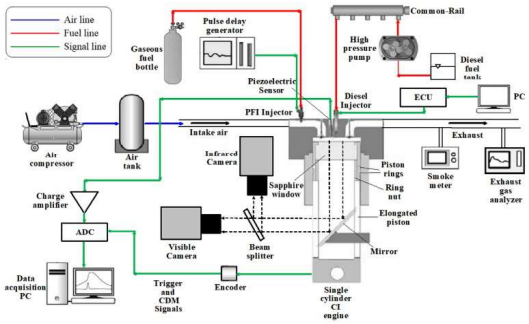


Figure 1. Optical single cylinder engine experimental setup.

Table 1. Optical engine and injection system characteristics.

Engine type	**4-stroke, single**
Stroke [mm]	92
Bore [mm]	85
Cylinder volume displacement	522
Combustion bowl volume [cm^3]	19.7
Compression ratio	16.5:1
Number of Valves	4
Exhaust Valve Open (EVO)	116° ATDC
Exhaust Valve Close (EVC)	340° BTDC
Inlet Valve Open (IVO)	344° ATDC
Inlet Valve Close (IVC)	132° BTDC
Diesel injection system	**Common rail**
Number of holes	7
Cone angle of fuel jet axis [deg]	148
Hole diameter [mm]	0.141
Hydrogen or Methane injection	**PFI**
Number of holes	1
Maximum injection pressure [bar]	5

The engine uses a conventional extended piston. A sapphire window of 46 mm diameter is located in the piston crown in order to have a good visualization of the in-cylinder combustion process. The bottom of the combustion bowl is flat; nevertheless, its volume and the wall shape are kept the same as the original metal engine by reducing the bowl bottom distance. A 45° visible-IR mirror inside the extended piston permits to grab the images reflected. Fast IR camera can record the entire combustion process, more details about engine setup can be found in [8-9]. The engine is equipped with the original four-cylinder modern common rail (CR) injection system, managed by a fully opened electronic control unit (ECU). The ECU controls the number of injections per cycle, the injection pressure, the injection start, and the energizing time of the injector. To inject the premixed fuel (hydrogen or methane) the intake manifold is provided with a commercial electronic port fuel injector (PFI) specifically designed for gaseous fuels. The injector is fed by a compressed gas bottle, and the injector pressure is set to the working condition of 5 bar via a pressure regulator. A delay generator manages the PFI synchronization with the engine cycle, while direct injection (DI) system is connected to the speed and phase sensors of the engine by means of the ECU. Acquiring signals from the encoder on the engine shaft allows to control the start and the duration of the premixed fuel injection. In this study, the gas is injected in front of the

entrance of the tumble intake port. Pure hydrogen or methane are premixed with the fresh air. Gas fuel injection is performed in the intake manifold once the exhaust valves are closed. The hydrogen supply line is composed by a pressure regulator, a flow meter, a hydrogen cylinder, a flow control valve, a flame arrester, and a flame trapper. The gas flowrate is measured by a Brooks® mass flow meter. The PFI signal is detected prior to reach the injector. To control the in-cylinder conditions, intake filtered and dehumidified air is controlled in terms of pressure and temperature. The Sensyflow FMT500-IG® is used to measure the mass flow rate of air. For each investigated operating condition, signals are digitalized and recorded at 0.2° crank angle (ca) increments. The average in-cylinder pressure is calculated from 200 consecutive combustion cycles. The heat release rate is calculated from the ensemble-averaged pressure data using the first law of thermodynamic and the perfect gas model [10]. Table 2 represents the properties of the tested fuels. The high research octane number (RON) of methane and hydrogen allows to operate with both high compression ratio and high boost typical of CI engines. Moreover, hydrogen presents the highest heating value, equivalence ratio in stoichiometric condition and wider flammability limits, enabling a further fuel consumption reduction. Its high flame speed value leads to a faster and more efficient consumption of the premixed charge.

Table 2. Fuel properties.

Feature	**Diesel**	**CH4**	**H2**
Density @ 15°C [kg/m^3]	833.1	0.678	0.0838
Viscosity at 40°C [mm^2/s]	3.141	-	0.0083
Cetane number	51.8	-	5-10
Research Octane Number	-	>120	>130
Low Heating Value [MJ/kg]	43	50	120
A/F st	14.54	17.24	34.4
Carbon [%, mol/mol]	85.22	75	0
Hydrogen [%, mol/mol]	13.03	25	100
Nitrogen [%, mol/mol]	0.04	-	0
Oxygen [%, mol/mol]	1.45	-	0
Flammability (Excess air ratio)	0.5-1.4	0.6-2.0	0.1-10
Flame velocity [m/s]	0.3	0.46	3

Finally, stable gaseous emissions, i.e. CO, CO_2, NO_x and THC, are measured with AVL DiCom 4000®. A volumetric gas measurement device calculated the percentage of CO and CO_2 gas amounts in exhaust, and the emission NO_x and THC expressed as ppm unit. Smoke measurements are taken by AVL 415S® as filter smoke number and/or mg/m^3 unit.

Optical setup

The scheme of the optical setup is presented in Figure 1. Acquisitions are performed by means of a beam splitter that divides the reflected image. IR imaging is performed using Telops FAST-IR 2K camera. The cooled high-performance indium antimonide (InSb) sensor has a matrix a 320x256 pixel in the spectral range of 3 – 5.5 µm. A 50-mm Janos lens is used for all experiments. A 70x70 pixels window size is selected to get an image recording speed of 10 000 frames per second. This allows to grab a frame every 0.9° crank angle at 1 500 rpm. Exposure time was set at 5 µs. The IR camera is equipped with a 4-position internal filter wheel. The first position has no filter, while the second position is equipped with a Neutral Density OD 1 filter. This filter reduces by 90% the incident light. It is used to prevent the FPA saturation. Further filters will be used, namely 4.2 µm and 3.9 µm to follow respectively the carbon dioxide and the burning mixture excluding mainly eventual soot emissions. The bandwidth tolerance of the filters is ± 50 nm.

Visible imaging analysis is performed by a 12-bit, high speed, complementary metal-oxide semiconductor (CMOS), monochrome camera. The camera used is the Photron Fastcam SA-X2®, presenting a 1024x1024 pixels resolution (pixel size of 20 x 20 µm^2). It is equipped with lens of 55 mm f/3.5. The resolution of images is 0.1 mm per pixel. With an image size of 115x115 pixel, the camera in cycle resolved mode can record 20 000 frames per seconds. It means that each frame is collected every 0.45° crank angle at 1500rpm. The images are acquired with an exposure time of 10 µs for all the tests and f-stop of the objective fixed at 22. To carry out a statistical analysis of the process, three repetitions are recorded and elaborated. Finally, it is worth to note that a delay generator is inserted to synchronize the Telops and Photron cameras with the engine speed.

3 TEST OPERATIVE CONDITIONS

The operative conditions of all test cases are reported in Table 3. Full Diesel at 1500 rpm acts as reference for both loads (2 and 5 bar). The first diesel cases are reproduced to assess the real performances of the research optical engine with respect to the 4-cylinder automotive engine. In fact, from Table 3, it is possible to observe that even if the reference case performed on the original engine achieves a brake mean effective pressure (BMEP), the research engine provides a lower indicated mean effective pressure (IMEP) due to the modifications made on it to get an optical access. However, it is worth to note that the engine runs continuously enhancing a near real heat exchange and EGR. For each case, two injections per cycle, from pilot and main were performed. The dual fuel mode is obtained by reducing the first main injection time and reaching a final identical injection time at the second one.

The study is performed keeping constant the IMEP of the engine running under traditional Diesel combustion. To do that, different quantities of methane and hydrogen are injected to reach the objective (Table 3). Gaseous fuel and air mass flow measurements allow to evaluate the equivalence ratio (φ) and the gaseous fuel energy contribution. This last parameter is represented by the premixed ratio (RP), obtained as follows:

$$RP = \frac{(m_p LHV_p)}{(m_p LHV_p + m_d LHV_d)} \times 100 \qquad (1)$$

where m_p and m_d are the mass flow rate of premixed fuel (hydrogen/methane) and directly injected fuel (diesel), respectively; whereas LHV_p and LHV_d are the lower heating values of the hydrogen/methane and diesel fuels. Namely, a RP equal to zero represents the normal diesel operation, and a RP higher than zero represents the dual fuel mode.

Table 3. Engine operating conditions

	Engine speed [rpm]	BMEP [bar]	SOI Pilot [°]	ET Pilot [µs]	SOI Main [°]	Inject press [bar]	VSA [%]	ET Main [µs]	M_{air} [kg/h]	EGR [%]	IMEP [bar]	RP [%]	φ mixture	φ premix fuel
Diesel	1500	2	-16	290	-6	615	66	545	15	58	1.7	0	0.18	-
DF CH_4								290	23.4	34	1.9	91	0.2	0.18
DF H_2									24.1	32	1.8	83	0.20	0.16
Diesel	1500	5	-11.6	269	0.3	867	61	570	22.8	39	5.0	0	0.26	-
DF CH_4								269	30.5	19	4.6	95	0.29	0.26
DF H_2									29.2	22	4.2	88	0.26	0.23

From Table 3, we can observe that the main part of energy is supplied by gaseous fuel. In fact, the concept of dual fuel combustion is based on the substitution of a great part of diesel fuel in order to reduce the particulate matter (PM) emissions. On another hand, the use of methane at low value of the equivalence ratio, enhances a slow flame propagation, causing a high amount of CO and THC. However, the multipoint ignition partly compensates this effect, and the addition of hydrogen to the fuel-air mixture is expected to further improve it too.

4 RESULTS AND DISCUSSIONS

Hydrogen autoignition recognition

The first phase of the tests regarded the evaluation of the hydrogen- in-cylinder interaction. The engine runs in motored condition without diesel injections, but hydrogen was injected into the intake manifold. Any combustion activity was detected by analyzing the IMEP of the motored cycles. Normally, in such conditions the IMEP assumes negative values because the work is done by the electric machine to move the optical engine. In the Figure 2 several peaks can be noted due to the spontaneous combustion of hydrogen. The boundary conditions seems to be of great impact on the possible autoignition of the premix charge of hydrogen and air. Table 4 reports the conditions under DF H2 mode. We observed that in 1.5% of the 200 acquired cycles results in hydrogen combustion event. This phenomenon is uncontrolled and should be investigated under higher speed engine. This conforms the necessity of diesel injection to control the combustion hydrogen in a compression ignition engine operating in dual fuel mode.

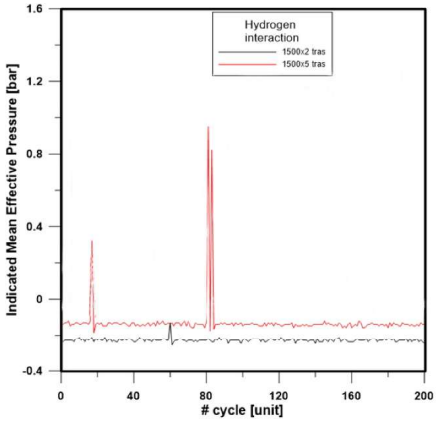


Figure 2. IMEP of 200 in-cylinder pressure cycles in motored condition.

Table 4. DF-H2 operating modes.

Engine speed	1500	1500
BMEP [bar]	2	5
m_air_motored	35.5	37.5
p intake [bar]	1.5	1.7
T intake [°C]	55	56
m_H2 [kg/h]	0.11	0.19
RP [%]	83	88
p @TDC [bar]	43	48

Dual Fuel combustion

The Figure 3 reports the in-cylinder pressure traces and the current injection signals of both PFI and DI fuels for a 2 bar load. The injection of gas occurs at the closure of the exhaust valves and lasts up to 80° and 78° crank angles for methane and hydrogen, respectively. Diesel fuel is injected via a pilot and a main injection of the same current duration near to the TDC. Figure 3.b represents a zoom in a narrower crank angle degree interval of the rate of heat release (ROHR) curves. We clearly observed, that the diesel combustion (black curve) presents two characteristic phases due to the pilot and main combustion. In this condition, the EGR level strongly affects the mixing, thus delaying the main combustion. The dual fuel combustions show a similar development, close to a SI engine. However, dual fuel hydrogen combustion reaches higher in-cylinder pressure peak, suggesting that a higher and probably more uniformly diffused heat release is obtained. Consequently, a higher in-cylinder temperature is reached. Concerning the ROHR curves for the DF, we observed that as soon as the pilot diesel fuel is ignited, the combustion starts to release heat, involving immediately the premixed fuel in the combustion process. In fact, both DF cases present an anticipated peak due to the pilot combustion with respect to conventional diesel. Despite a slightly higher peak and shorter combustion duration is noted for DF H_2 with respect to DF CH_4, no significant differences are observable in the evolution of the DF ROHR traces. It is likely to assume that the gaseous fuel type has a weak influence on the combustion at these equivalence ratios. A shorter combustion duration is detected for hydrogen.

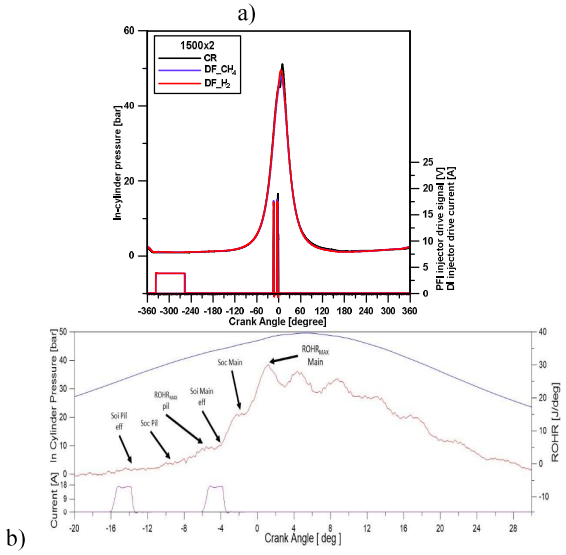


Figure 3. In-cylinder pressure curve, injectors' signals, and ROHR traces - OP 1500x2 - (b) zoomed view.

In Figure 4, a selection of unfiltered and filtered images recorded with the IR camera is reported for DF CH_4, for the operating condition 2 bars. The black and white images represent the images recorded with the Visible camera.

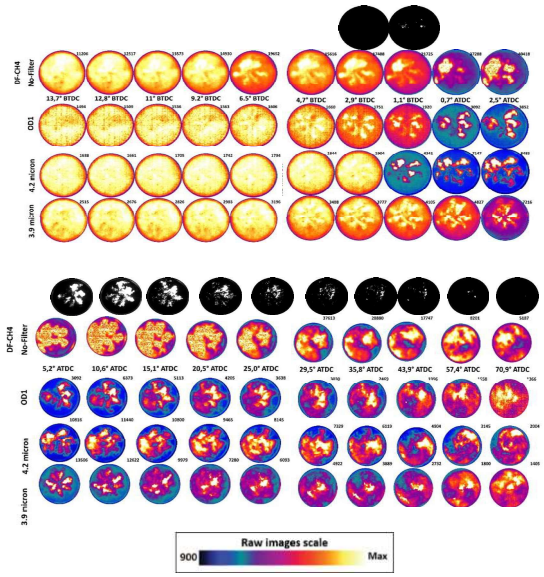


Figure 4. Full spectrum and filtered IR images of pilot injection for DF CH4 with different filters @2bars. Visible images are presented in black and white disks.

The evolution of pilot injection and combustion is illustrated. Since methane emits in the mid IR wavelength range, the camera detects high intensities in the background due to its high sensitivity. In that case, the pilot injection process is difficult to follow, although some bright spots emitted by the spreading jets can be recognized in the center of the images (see OD1 Raw). Moreover, the lack of structured shape in the 4.2 µm filtered images up to 6.5° BTDC indicates the absence of combustion. Combustion is detected 4.7° BTDC as indicated by the 4.2 µm filtered images, while the pilot unburned jets are well evidenced by the 3.9 µm filtered images. It is worth to note that the Visible camera starts to grab signal at 2.9° much later compared to the IR camera, and the signal intensity is low. The IR camera presents a better sensitivity and allows a good follow-up of the combustion process and the jet penetration. Moreover, it is still giving information, while the Visible camera is becoming blind, i.e. after 57.4° ATDC. Figure 5 presents a selection of unfiltered and filtered images recorded with the IR camera for DF H2, for the operating condition 2 bars and the same crank angles. The black and white images represent the images recorded with the Visible camera.

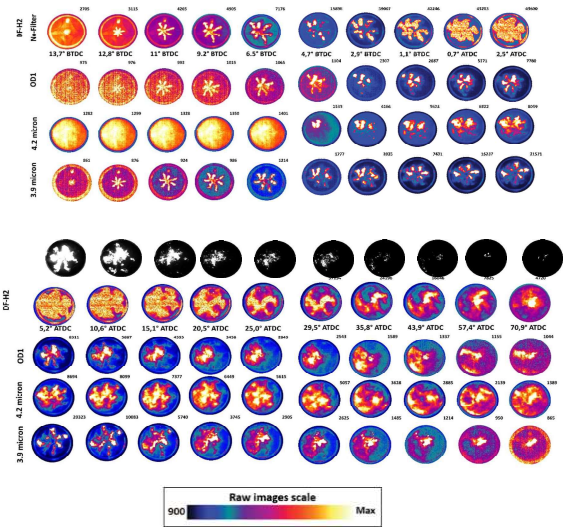


Figure 5. Full spectrum and filtered IR images of pilot injection for DF H2 with different filters @2bars. Visible images are presented in black and white disks.

As previously mentioned, hydrogen does not emit in the IR range, thus it was possible to follow the injection process. We can observe the seven jets are clearly distinguished, starting from the nozzle tip and moving toward bowl walls at 12.8°BTDC. Early jets are uniformly distributed along its axis and are successively following the swirl motion of the premixed mixture. This affects the beginning of combustion that starts 6.5°BTDC. In this phase the diesel fuel of pilot injection mixes with the premixed charge and starts to oxidation process. The fuel is transported in anticlockwise direction and is mainly concentrated in the center of the jet axis. This zone is easily indicated as the source of the autoignition as noticed at 6.5°BTDC. if we compare the behavior of the two DF, we observe that the DF H2 combustion is faster than for DFCH4. This result is expected due to the fast hydrogen kinetic. However, it is worth to note that the acquired IR images are of better quality in the case of DFH2. This is evidenced in the 3.9 µm images. In that case, we can observe the jets up to 15.1°ATDC due to a minor soot production during the combustion. These comments are still valid while increasing the pressure to 5 bars. For question of room, the images are not presented in this paper. However, the general tendency is unchanged. The pressure variation does not influence the potentiality of the IR imaging. At the end, an overall presentation of the pollutant emissions are presented in Figure 6. The minor production of particulate matter is confirmed for both DF modes. We obtain a maximum reduction of 94% compared to conventional diesel combustion. Concerning NOx emissions, the results have a strong dependency on the EGR rate and on the combustion evolution. At low load, both DF modes suffer from the critical intake conditions thus enhancing higher pollutant emissions. The addition of premixed fuel in the intake together with the necessity of not increasing the pumping loss reduce the quantity of recirculated exhaust gas (see table 3). The different EGR ratio is lower for the DF operations at low load, thus enhancing higher NOx concentration at the exhaust. The maximum reductions of NO_x emission compared to diesel combustion are of 28% for DF CH_4 and 32% for DF H_2. Since hydrogen is a carbon-free fuel, the CO_2 emissions drastically reduced, as expected, in the DF H_2 operation with a maximum reduction of 90%. Finally, HC emissions from the DF CH_4 cases are so high that they cannot be represented with the other case on the same figure. They were divided by 10^4 to be represented in Figure 6. They are mainly caused by the bad methane

consumption. In fact, the very low equivalence ratio reported in Table 3 does not allow an efficient flame propagation inside the combustion chamber. This strongly penalizes the DF CH_4 combustion since methane is a greenhouse gas with a global warming potential 25 times higher than CO_2. On the other hand, the use of hydrogen allows to drastically reduce both CO_2 and HC emissions at the exhaust pipe not only because it does not contain carbon, but also for its high flammability limits and higher flame speed. These factors mitigate the negative effects of critical operating conditions.

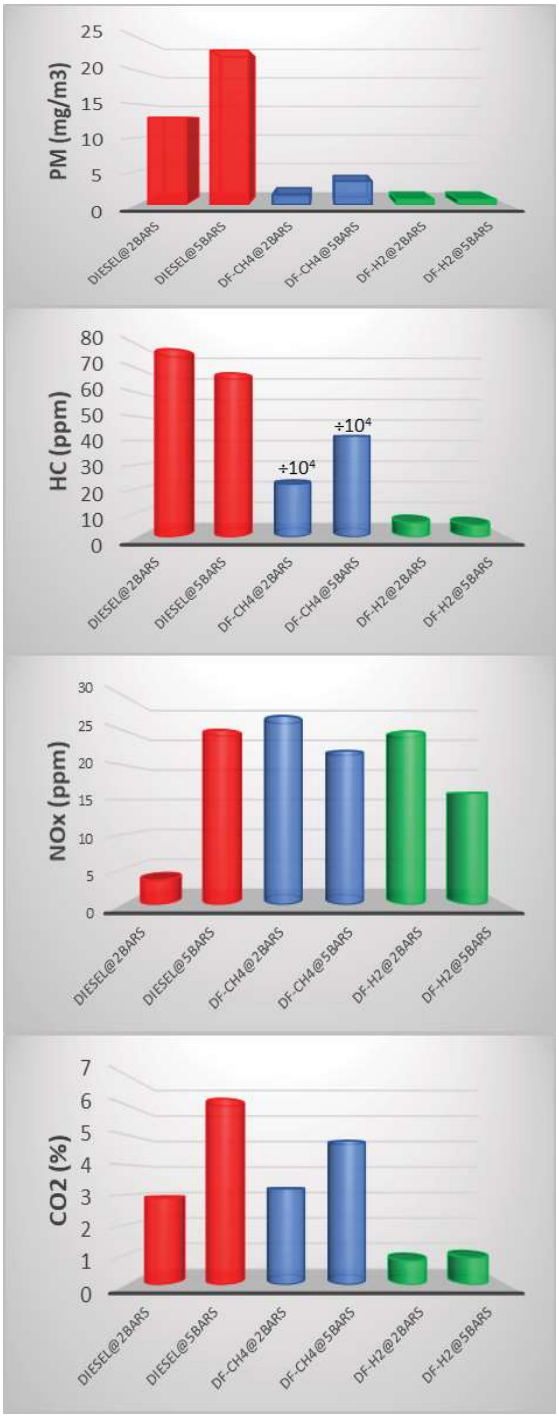


Figure 6. Pollutant emissions at the exhaust pipe.

5 CONCLUSIONS

Tests were performed to study Dual Fuel combustion by means of IR and Visible imaging in an optically accessible research compression ignition engine operated with hydrogen and methane, as premixed fuel in the intake manifold. These tests were performed at a constant engine speed, 1500 rpm, and two loads, 2 and 5 BMEP, while imaging was performed with the two cameras acquiring in a synchronous way according to a cycle resolved framework.

We observed that during DF modes, the in-cylinder combustion pressures showed a completely different behavior compared to diesel combustion. It is worth to note that, the ROHR evidences a uniform distribution close to the TDC due to the pilot and the main injections. Moreover, it was possible to observe some unpredictable self-ignition of hydrogen mixture without any diesel injection. The IR camera was capable to detect the whole combustion process, especially for the DF H_2. Diesel combustion emission remains higher in the infrared range than the hydrogen one. Moreover, the IR images were also in good agreement with the ROHR data. It is worth to note, that the methane IR emission strongly covers the on-going combustion process, requiring thus a post elaboration of the IR images to distinguish the pilot and main injections. An accurate image analysis allowed to identify geographically the combustion in the case of DF operations. Finally, DF conditions drastically reduced the PM emissions, while reducing NO_x emissions increasing the load. The CO_2 emissions decreased with DF operations, with a remarkable result in the case of Df H_2. A similar result is observed for the hydrocarbons emissions in the case of DF H_2.

ACKNOWLEDGMENTS

The authors gratefully acknowledge Mr. Carlo Rossi and Mr. Bruno Sgammato for their essential technical support

NOMENCLATURE

BMEP	Brake Mean Effective Pressure
CI	Compression Ignition

CMOS	Complementary Metal-Oxide Semiconductor
CR	Common Rail
DF	Dual Fuel
DI	Direct Injection
ECU	Electronic Control Unit
FCA	Focal Plane Array
ICE	Internal Combustion Engine
IMEP	Indicated Mean Effective Pressure
IR	Infrared
LPG	Liquefied Petroleum Gas
NEDC	New European Driving Cycle
PFI	Port Fuel Injector
PM	Particulate Matter
RCCI	Reactivity Controlled Compression Ignition
ROHR	Rate of Heat Release
RON	Research Octane Number
RP	Premixed Ratio
SI	Spark Ignition
TDC	Top Dead Center
THC	Total Hydrocarbons
VIS	Visible
VSA	Valve Swirl Actuator

REFERENCES

1. Onorati A, Payri R, Vaglieco B, et al. The role of hydrogen for future internal combustion engines. International Journal of Engine Research. 2022;23(4):529-540. doi:10.1177/14680874221081947
2. Pavlos Dimitriou, Taku Tsujimura, A review of hydrogen as a compression ignition engine fuel, International Journal of Hydrogen Energy, Volume 42, Issue 38, 2017, https://doi.org/10.1016/j.ijhydene.2017.07.232.
3. Watgave, S., Banapurmath, N., and Harari, P., "Comparative Study on Effect of Hydrogen and Hydrogen Blended Compressed Natural Gas on Compression Ignition Engine Operated under Homogeneous Charge Compression Ignition and Reactivity Controlled Compression Ignition Mode of Combustion," SAE Technical Paper 2021-28-0010, 2021, https://doi.org/10.4271/2021-28-0010.
4. D.B. Lata, Ashok Misra, S. Medhekar, Effect of hydrogen and LPG addition on the efficiency and emissions of a dual fuel diesel engine, International Journal of Hydrogen Energy, Volume 37, Issue 7, 2012, https://doi.org/10.1016/j.ijhydene.2012.01.014.
5. Robert W. Schefer, Christopher White, Jay Keller, Chapter 8 - Lean Hydrogen Combustion Derek Dunn-Rankin, Lean Combustion, Academic Press, 2008 https://doi.org/10.1016/B978-012370619-5.50009-1.
6. Hernández JJ, Salvador JB, Cova-Bonillo A. Autoignition of diesel-like fuels under dual operation with H2. Advances in Mechanical Engineering. June 2019. doi:10.1177/1687814019856781
7. Karagöz Y, Sandalcı T, Yüksek L, Dalkılıç AS, Wongwises S. Effect of hydrogen–diesel dual-fuel usage on performance, emissions and diesel combustion in diesel engines. Advances in Mechanical Engineering. August 2016. doi:10.1177/1687814016664458
8. De Robbio, R., Cameretti, M., Mancaruso, E., Tuccillo, R. et al., "Combined CFD - Experimental Analysis of the In-Cylinder Combustion Phenomena in a Dual Fuel Optical Compression Ignition Engine," SAE Technical Paper 2021-24-0012, 2021, https://doi.org/10.4271/2021-24-0012.
9. Mancaruso, E., Todino, M., and Vaglieco, B., "Analysis of Dual Fuel Combustion in Single Cylinder Research Engine Fueled with Methane and Diesel by IR Diagnostics," SAE Technical Paper 2019-01-1165, 2019, https://doi.org/10.4271/2019-01-1165.
10. Heywood, J.B., Internal Combustion Engine Fundamentals. Mc Graw-Hill, New York, 1988.
11. Mancaruso, E., Sequino, L. and Vaglieco, B.M., Evaluation of the vaporization energy of a fuel spray in a research engine using infrared imaging and 1D model. ICHMT International Symposium on Advances in Computational Heat Transfer, May 28-June 1, 2017.
12. Earle K. Plyler and Curtis J. Humphreys Infrared Emission Spectra of Flames Part of the Journal of Research of the National Bureau of Standards, Research Paper RP1890, Volume 40, June 1948
13. R.W. Schefer, W.D. Kulatilaka, B.D. Patterson, T.B. Settersten, Visible emission of hydrogen flames, Combustion and Flame 156 (2009) 1234–1241
14. Karmann S, Eicheldinger S, Prager M, Wachtmeister G. Optical and thermodynamic investigations of a methane and hydrogen blend fueled large bore engine. International Journal of Engine Research. 2022;23(5):846-864. doi:10.1177/14680874211066735
15. C. Lee, Y. Pang, H. Wu, J. J. Hernández, S. Zhang, F. Liu The optical investigation of hydrogen enrichment effects on combustion and soot emission characteristics of CNG/diesel dual-fuel engine Fuel 280 (2020) 118639

EFFECTS OF HYDROGEN AND EGR ON ENERGY EFFICIENCY IMPROVEMENT WITH ULTRA-LOW EMISSIONS IN A CRDI CI ENGINE FUELED WITH DIMETHYL ETHER (DME) UNDER HCCI MODE

Anilkumar Shere and K. A. Subramanian

Engines and Unconventional Fuels Laboratory, Department of Energy Science and Engineering, Indian Institute of Technology Delhi, New Delhi-110016, India; email: anilshere505@gmail.com or Anilkumar.Ramesh.Shere@ces.iitd.ac.in

Abstract

This research work was aimed at enhancing the energy efficiency with ultra-low emissions and extending the operating range (maximum torque limit) of dimethyl ether (DME) fueled homogeneous charge compression ignition (HCCI) engine through exhaust gas recirculation (EGR) and addition of hydrogen in order to control the combustion phasing at the rotational speed of 1400 rpm. In the neat DME mode, the possible maximum torque limit with controlled auto-ignition (CAI) was found as 8.4 Nm. Beyond 8.4 Nm, the knocking was observed. Addition of EGR extended the maximum torque limit 14 Nm (35% EGR) with retarding combustion phase and prolonged combustion duration. The hydrogen fuel was injected into the intake manifold along with DME during suction stroke at an optimized EGR rate. Hydrogen addition resulted in combustion phase retardation. The energy efficiency (EE) was enhanced to the maximum level with zero smoke emission, and ultra-low NO_x, CO and HC, and lower CO_2 emissions till 12% of hydrogen energy share (HES). Beyond 12% HES, the engine's performance deteriorated with a slight increase in emissions due to the knocking combustion. Thus, the combined strategy of EGR and hydrogen could effectively extend the operating range with ultra-low emissions levels.

Keywords: Homogeneous charge compression ignition (HCCI), Dimethyl Ether, Hydrogen, Knocking, EGR, Ultra-low emissions, Controlled auto-ignition (CAI).

1 INTRODUCTION

Diesel fuel (in compression ignition (CI) engines) is widely used in transportation, power generation, construction, and agricultural sectors. It leads to the emission of higher levels of harmful NO_x and smoke emissions, which violate the emission standard norms. The depletion of fossil fuels (due to an increase in consumption rate) directly affects the country's energy security. The dependency on fossil fuels can be reduced by adopting alternative renewable fuels, which may improve the energy security issue. The simultaneous reduction of NO_x and smoke emissions could be achieved by adopting an advanced mode of combustion technique [1, 2, 3].

The engine community has investigated many effective techniques and control strategies to improve the performance and reduce emissions from compression ignition (CI) engines. Dimethyl ether (DME) fuel can replace diesel fuel in conventional diesel engines due to its higher cetane number (~58), lower self-ignition temperature (235°C), and absence of the C-C bond (leading to zero-smoke combustion) in the structure with higher oxygen content (34.9% by mass) [4, 5, 6]. The combination of DME fuel (renewable alternative fuel) and homogeneous charge compression ignition (HCCI) mode (an advanced combustion technique) would reduce the dependency on fossil fuels with a simultaneous reduction of NO_x and smoke emissions and would sustain the life of the diesel engines.

The researchers have done numerous studies on the utilization of higher cetane number (CN) and octane number (ON) fuels under HCCI mode but the utilization of DME fuel has not been extensively investigated in the HCCI mode. Celebi et al. analyzed the combustion, performance, and emission characteristic of HCCI engines fueled with n-heptane and naphtha fuels at speeds between 800 rpm and 2000 rpm. It was reported that HC and CO emissions with naphtha fuel increased with reduced NO_x emission compared to n-heptane fuel. The engine's performance improved with retarded combustion and increased combustion duration with combustion stability with naphtha fuel compared to n-heptane fuel [7]. Lower

smoke and NO_x emissions with better performance of the HCCI engine fueled with biogas and diethyl ether (DEE) were reported experimentally by Feroskhan et al. [8]. Aydogan examined the impact of acetone addition to n-heptane fuel in the HCCI engine and reported that the probability of knocking tendency was eliminated due to the addition of acetone into n-heptane fuel [9]. Similar kinds of results were reported by other researchers, Jamsran et al. [10], Kocakulak et al. [11], Ardebili et al. [12], Bogrek et al. [13], Niklawy et al. [14], with the different alternative fuels under HCCI mode in CI engines.

From the detailed literature survey, achievement of zero smoke emission with ultra-low emissions and energy efficiency improvement in DME fueled HCCI engine has not been explored. The manuscript provides the scientific assessment of achieving ultra-low emissions and improved performance with controlled auto-ignition.

2 EXPERIMENTAL DETAILS

A single-cylinder water-cooled common-rail direct injection (CRDI) compression ignition (CI) engine was modified to operate on HCCI mode fueled with DME. The DME fuel in the gaseous form was injected into the intake port of the CRDI engine by using the port fuel injection system (PFIS) during the suction stroke. Further, the DME fueled HCCI engine was transformed into a dual-fuel mode by introducing hydrogen fuel (in gaseous form) in the intake manifold using a micro-controller fuel injection system during the suction stroke. The detailed specifications of the CRDI engine are listed in Table 1.

Table 1. Specifications of the CRDI CI engine

Details	Single-cylinder water-cooled common-rail direct-injection (CRDI)
Bore (mm) x Stroke (mm)	93 x 92
Swept volume (cc)	625
Compression Ratio (CR)	19:1
Power output	8.2 kW/11 hp at 3000 rpm
Maximum torque	36 Nm @ 1800 rpm

3 RESULTS AND DISCUSSION

The variation in the energy efficiency (EE) at 1400 rpm under DME-HCCI mode are shown in Figure 1. The EE of the engine under DME-HCCI mode increased significantly from 17.15% (without EGR) to 23.10% (35% EGR), and further increased to 26.90% (12% hydrogen energy share (HES)) with controlled auto-ignition. The higher cetane number of DME fuel (~58), with higher diffusivity and absence of C-C bond in structure and the highest calorific value (120 MJ/kg) of hydrogen fuel with higher flame speed (3.25 m/s) and wide flammability range (4 - 75% vol. in the air) results in the formation of a homogeneous mixture of DME, hydrogen and air under HCCI mode, leads to rapid combustion, which increases the energy efficiency of the HCCI engine.

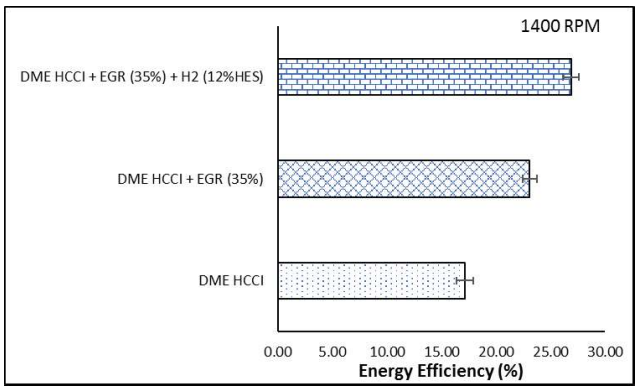


Figure 1. Energy efficiency variation without EGR, with EGR and with hydrogen addition in DME HCCI engine at 1400 rpm.

Figures 2 and 3 show the influence of EGR and hydrogen addition on smoke and NO_x emissions at 1400 rpm under DME-HCCI mode. Ultra-low NO_x (10-20 ppm) and zero smoke emissions were observed from DME-HCCI combustion. The uniform mixture of the charge (DME-hydrogen-air) and the absence of the C-C bond in DME and hydrogen structure results in quick and complete smokeless combustion. In DME-HCCI mode, the combustion temperature was below the level (below 2000 K), where the rate of production for NO becomes significant (which majorly occurs at high combustion temperature reaction between nitrogen and oxygen). NO_x emission reduced from 14.8 ppm (without EGR) to 7 ppm (35% EGR) and further increased to 20 ppm with hydrogen addition due to the higher flame speed and increased combustion temperature (12% HES) respectively.

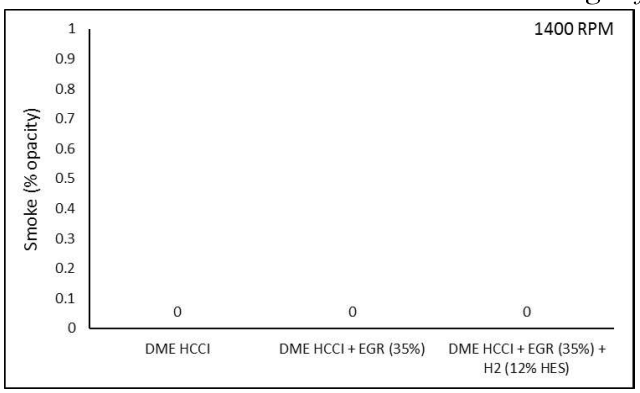


Figure 2. Smoke emission variation in DME HCCI engine with EGR and hydrogen addition at 1400 rpm.

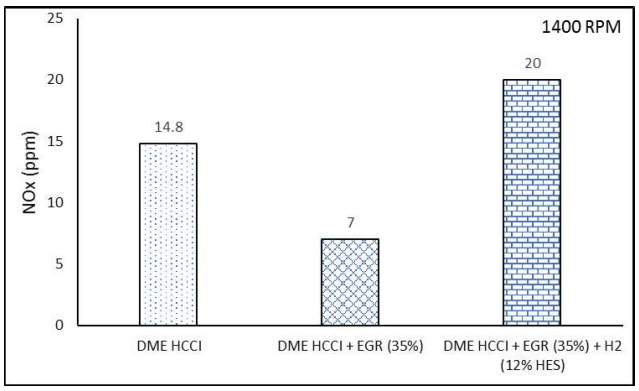


Figure 3. NO_x emission variation in DME HCCI engine with EGR and hydrogen addition at 1400 rpm

Figures 4 and 5 show the influence of EGR and hydrogen addition on CO and HC emissions at 1400 rpm under DME-HCCI mode. CO and HC emissions decreased from 0.53% vol. and 5.75 g/kWh (without EGR) to 0.41% vol. and 2.75 g/kWh (35% EGR) and further decreased to 0.06% vol. and 0.66 g/kWh (12% HES) i.e. near-zero level respectively. The near-zero level of CO and HC emissions could be due to shorter quenching distance (0.64 mm) and absence of carbon to carbon bond of hydrogen fuel results in the rapid oxidation of the charge.

Figure 6 shows the influence of EGR and hydrogen addition on CO_2 emission at 1400 rpm under DME-HCCI mode. CO_2 emission increased from 5.2% vol. (without EGR) to 6.8% vol. (35% EGR) due to the partial oxidation of CO to CO_2 and recirculation of the exhaust gas to the intake manifold of the engine, and further decreased to 1.8% vol. (12% HES) with hydrogen addition due to the higher flame speed of the hydrogen fuel in the charge.

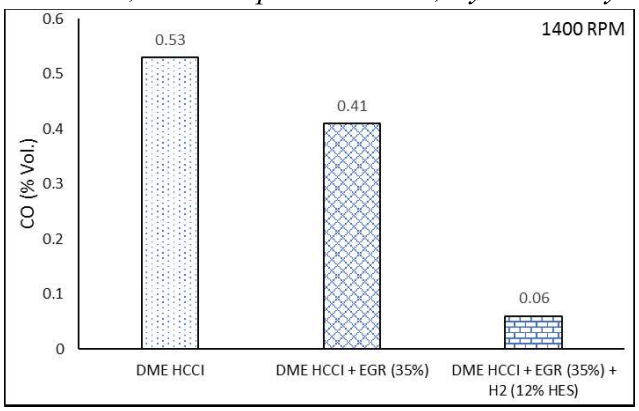


Figure 4. CO emission variation in DME HCCI engine with EGR and hydrogen addition at 1400 rpm.

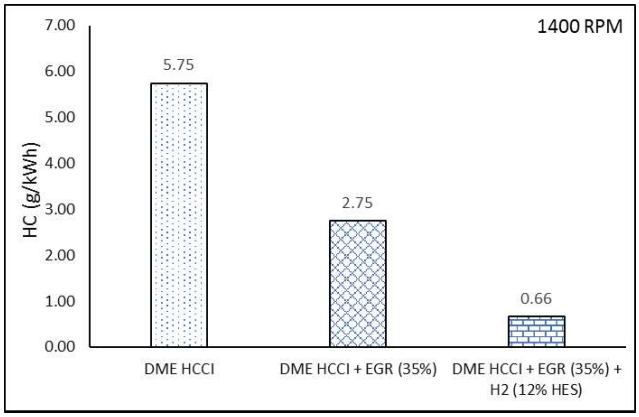


Figure 5. HC emission variation in DME HCCI engine with EGR and hydrogen addition at 1400 rpm.

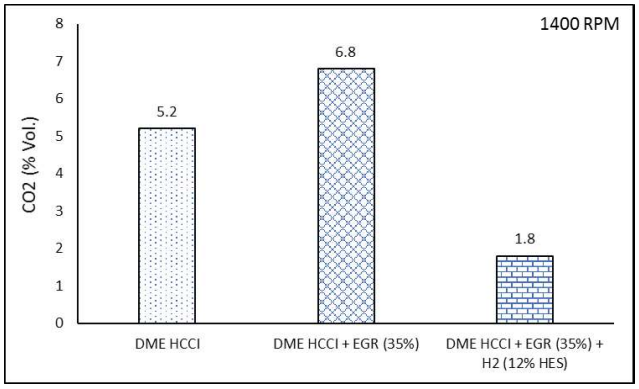


Figure 6. CO_2 emission variation in DME HCCI engine with EGR and hydrogen addition at 1400 rpm.

Figure 7 demonstrates the influence of EGR on the knock mitigation and extension of operating range at 1400 rpm under DME HCCI mode. The maximum torque limit was extended from 8.4 Nm (without EGR) to 14 Nm (35% EGR) under HCCI mode. As a result, cooled EGR was a promising strategy to mitigate the knocking

combustion and to extend the operating range of the HCCI engine with controlled auto-ignition.

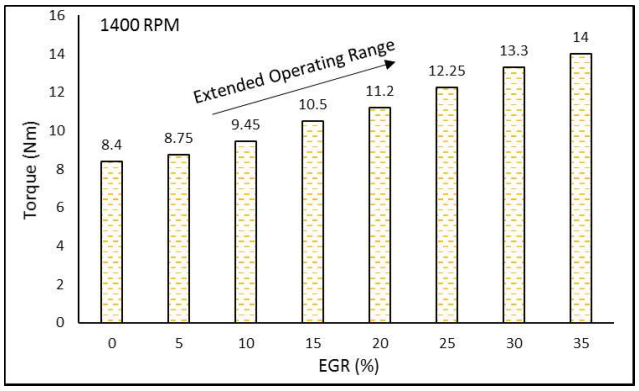


Figure 7. Extended operating range of the DME HCCI engine with cooled EGR application

4 CONCLUSIONS

The common rail direct injection compression ignition (CRDI-CI) engine was modified into homogeneous charge compression ignition (HCCI) mode fueled with dimethyl ether (DME). The results with neat DME under HCCI mode were compared with EGR and hydrogen addition at 1400 rpm, respectively. The main conclusions are drawn based on the above-mentioned experimental tests.

i. The energy efficiency of the engine under DME-HCCI mode increased significantly from 17.15% to 26.90% with hydrogen addition till 12% HES.

ii. Zero smoke emission (due to better homogeneity in DME-air charge) and ultra-low NO_x emission in the order of 10-20 ppm (due to lower combustion temperature) were observed from DME HCCI combustion with hydrogen addition.

iii. DME HCCI combustion with hydrogen addition showed ultra-low CO and HC emissions with lower CO_2 emission from the discharge of the HCCI engine.

iv. The operating torque limit in DME-HCCI mode was extended from 8.4 Nm to 14 Nm with cooled EGR application by mitigating the knock limit.

ACKNOWLEDGEMENTS

The authors would like to acknowledge IOCL R&D, India, for providing DME fuel funded by the Department of Science and Technology (DST), India.

REFERENCES

[1] M. Mofijur, M. M. Hasan, T.M.I. Mahlia , S.M.A. Rahman, A. S. Silitonga, H. C. Ong, Performance and emission parameters of homogeneous charge compression ignition (HCCI) engine: A review, *Energies*, Vol. 12, 2019. https://doi.org/10.3390/en12183557.

[2] M. Yao, Z. Zheng, H. Liu, Progress and recent trends in homogeneous charge compression ignition (HCCI) engines, *Progress in Energy and Combustion Science*, Vol. 35, pp. 398-437, 2009. https://doi.org/10.1016/j.pecs.2009.05.001.

[3] P. Kumar, A. Rehman, Bio-diesel in homogeneous charge compression ignition (HCCI) combustion, *Renewable and Sustainable Energy Reviews*, Vol. 56, pp. 536-550, 2016. https://doi.org/10.1016/j.rser.2015.11.088.

[4] S. H. Park, C. S. Lee, Applicability of dimethyl ether (DME) in a compression ignition engine as an alternative fuel, *Energy Conversion and Management*, Vol. 86, pp. 848-863, 2014. https://doi.org/10.1016/j.enconman.2014.06.051.

[5] C. Arcoumanis, C. Bae, R. Crookes, E. Kinoshita, The potential of di-methyl ether (DME) as an alternative fuel for compression-ignition engines: A review, *Fuel*, Vol. 87, pp. 1014-1030, 2008. https://doi.org/10.1016/j.fuel.2007.06.007.

[6] G. Thomas, B. Feng, A. Veeraragavan, M. J. Cleary, N. Drinnan, Emissions from DME combustion in diesel engines and their implications on meeting future emission norms: A review, *Fuel Processing Technology*, Vol. 119, pp. 286-304, 2014. https://doi.org/10.1016/j.fuproc.2013.10.018.

[7] S. Çelebi, C. Haşimoğlu, A. Uyumaz, S. Halis, A. Calam, H. Solmaz H, Operating range, combustion, performance and emissions of an HCCI engine fueled with naphtha, *Fuel*, Vol. 283, 2021. https://doi.org/10.1016/j.fuel.2020.118828.

[8] M. Feroskhan, V. Thangavel, B. Subramanian, R. K. Sankaralingam, S. Ismail, A. Chaudhary, Effects of operating parameters on the performance, emission and combustion indices of a biogas fuelled HCCI engine, *Fuel*, Vol. 298, 2021. https://doi.org/10.1016/j.fuel.2021.120799.

[9] B. Aydoğan, Combustion characteristics, performance and emissions of an acetone/n-heptane fuelled homogenous charge

compression ignition (HCCI) engine, *Fuel*, Vol. 275, 2020. https://doi.org/10.1016/j.fuel.2020.117840.
[10] N. Jamsran, H. Park, J. Lee, S. Oh, C. Kim, Y. Lee, Influence of syngas composition on combustion and emissions in a homogeneous charge compression ignition engine, *Fuel*, Vol. 306, 2021. https://doi.org/10.1016/j.fuel.2021.121774.
[11] T. Kocakulak, M. Babagiray, C. Nacak, A. Safieddin, A. Calam, H. Solmaz, Multi objective optimization of HCCI combustion fuelled with fusel oil and n-heptane blends, *Renewable Energy*, Vol. 182, pp. 827-841, 2022. https://doi.org/10.1016/j.renene.2021.10.041.
[12] S. Ardebili, H. Solmaz, A. Calam, D. İpci, Modelling of performance, emission, and combustion of an HCCI engine fueled with fusel oil-diethylether fuel blends as a renewable fuel, *Fuel*, Vol 290, 2021. https://doi.org/10.1016/j.fuel.2020.120017.
[13] A. Böğrek, C. Haşimoğlu, A. Calam, B. Aydoğan, Effects of n-heptane/toluene/ethanol ternary fuel blends on combustion, operating range and emissions in premixed low temperature combustion, *Fuel*, Vol. 295, 2021. https://doi.org/10.1016/j.fuel.2021.120628.
[14] W. Niklawy, M. Shahin, M. I. Amin, A. Elmaihy, Comprehensive analysis of combustion phasing of multi-injection HCCI diesel engine at different speeds and loads, *Fuel*, Vol. 314, 2022. https://doi.org/10.1016/j.fuel.2021.123083.

AN EXPERIMENTAL INVESTIGATION OF OXYGENATED FUELS BLENDING EFFECT ON GASOLINE ENGINE PERFORMANCE AND EMISSIONS

Mehrez Gassoumi[1], Zouhair Boutar[1], Ridha Ennetta[1], Hakan Serhad Soyhan[2]

1. Mechanical Modelling, Energy & Materials, National School of Engineers, Gabes University, Zrig, 6029, Gabes, Tunisia; email: ridha.ennetta@issig.rnu.tn
2. Mechanical Engineering Department, Engineering Faculty, Esentepe Campus, Sakarya University, Sakarya, 54187, Turkey; email: hsoyhan@sau.edu.tr

Abstract

In this study, the effects of three oxygenated fuels blends on the performance of a gasoline single-cylinder spark-ignition engine have been investigated experimentally. Experiments were conducted using a DIDACTA-T85 testbed under full load conditions and variable engine speed. Performance tests were performed by measuring the brake power (BP), brake torque (BT), brake mean effective pressure (BMEP), brake specific fuel consumption (BSFC), and brake thermal efficiency (BTE). The tested blends were G0, E10, A10, and M10, where G0 represents the base fuel, pure gasoline, and E10, A10, and M10 represent 10% by volume in gasoline of ethanol acetone, and methanol, respectively. Results showed that M10 gave better engine performance in BP, BT, and BMEP, while E10 performed better results in terms of BSFC and BTE. This study showed that oxygenated fuel blends could reduce significantly carbon monoxide emission (CO) at all engine speed. Carbon dioxide (CO2) levels was found to be increased at high engine speeds. A10 gave the lowest value in NOx emission at all engine speeds, however, it increases in the case of E10 and M10 blends.

Keywords: Engine, Gasoline, Oxygenated Fuel, Blends, Experimental Study

THE EFFECT OF THE ADDITION OF H, H+OH AND H+OH+O2 FROM THE INTAKE MANIFOLD ON EXHAUST EMISSION PARAMETERS IN A CI ENGINE USING DIESEL/DI ETHYL ETHER AS PILOT FUEL

S. Özer[1], E. Vural[2]

1. Muş Alparslan University, Faculty of Engineering and Architecture, Muş; email: s.ozer@alparslan.edu.tr
2. Aydın Adnan Menders University, Germencik Yamantürk Vocational School, Aydın; email: evural@adu.edu.tr

Abstract

This study examines the effects of adding H and OH from the intake manifold to an engine using diesel/di ethyl ether as a pilot fuel. The di ethyl ether fuel added to the diesel fuel was mixed volumetrically. Hydrogen gas, on the other hand, is formed by the hydrolysis of water by a hydrogen generator. The output parameter of hydrogen gas can be adjusted by controlling the current on the hydrogen generator. In this way, the amount of gas sent into the cylinder was discarded and reduced and the combustion parameters were tried to be adjusted. The gas obtained from the hydrogen generator can be taken separately as H and OH thanks to the capacity of the generator. Therefore, only the H and H+OH effects were observed separately in all studies. In addition, along with H and OH, additional oxygen was supplied from the intake manifold to improve the volumetric efficiency and exhaust emissions. The results obtained show that better results were obtained by adding H, H+OH and H+OH+O2 to the diesel ether pilot fuel.

Keywords: Diesel, Diesel fuel blends, hydrogen, combustion

1 INTRODUCTION

Motor vehicles are important machines that have become a part of the life of mankind. The power generation of these machines is provided by an internal combustion engine. Internal combustion engines convert chemical energy into kinetic energy. Fossil fuels are used as a chemical energy source in internal combustion engines. Generally, gasoline and diesel are used as liquid fuels in internal combustion engines, and LPG and its derivatives are used as commercial products as gas fuels. Motor vehicles sold as commercial products on the market are usually machines operated with the use of these fuels. This type of engine also releases dirty emissions from Tue exhaust by burning the fuel taken into the cylinder. Generally, with the combustion of fossil fuels in internal combustion engines, carbon dioxide (CO2), carbon monoxide (CO), hydrocarbon (HC), nitrogen oxides (NOx) and soot emissions are generated from their exhausts and disposed of. It is shown by many studies that the pollution caused by these emissions being above certain rates has harmful effects on the environment and human health. It is often stated that the global climate change, which has been expressed especially in recent years, is caused by exhaust emissions. For this purpose, academic studies on internal combustion engines have gained momentum in general in terms of reducing fuel consumption values and reducing exhaust gases [1-7]. In these studies, the use of fuels with biomass content, which will constitute an alternative to fossil fuels in general, is at the forefront [8-10]. It is reported that exhaust emissions are generally reduced in studies with fuels obtained from biomass.

Hydrogen gas is an important energy source that can be used as an alternative fuel. In recent years, studies on its use in internal combustion engines have gained momentum. In these studies, he focuses on the use of hydrogen instead of fossil fuels directly or for the reduction of exhaust gases [11-14]. In these studies, it is also reported that exhaust emissions decrease with the addition of hydrogen to internal combustion engines. In addition, disruptions in the storage of hydrogen are mentioned in these studies. For this reason, the necessity of producing hydrogen during use and using it directly is explained.

There has been an increase in commercial versions of devices called hydrogen generators in recent years, which will allow hydrogen to be used in engines that will be produced from the hydrolysis of water. For this reason, academic studies are conducting serious studies on the

investigation of the effects of the use of hydrogen (H) and hydroxyl (OH) obtained from hydrogen generators. It is mentioned that these studies [15-18] show that hydrogen can be produced from a hydrogen generator and that it is effective in reducing exhaust emissions in engines. However, it is mentioned that the use of hydrogen at low pressures creates some disadvantages.

2 MATERIALS AND METHOD

The experiments were carried out at Muş Alparslan University. The engine experiments were carried out in the experimental setup in 1.

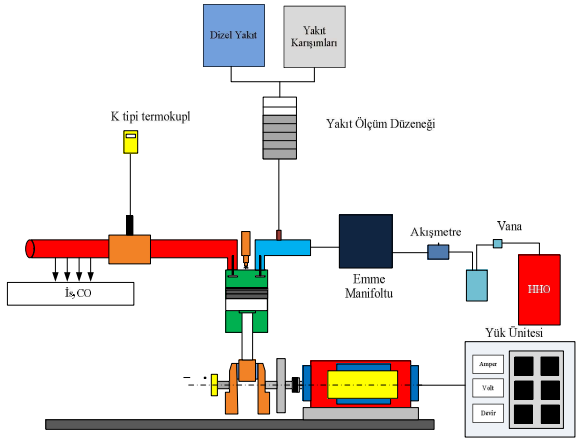


Figure 1. Schematic picture of the experimental setup.

The engine experiments were carried out in a single-cylinder compression ignition engine. The exhaust gas temperature was measured with a k-type thermocouple in the experimental setup, and the changes in soot emissions were measured with an exhaust gas analyzer. The H, H+HO gas supplied to the engine is produced by hydrolysis of water. The resulting gas is given from the intake manifold. The hydrogen generator allows the production of H and OH gases separately. All gases supplied to the engine are controlled by a flow meter and supplied to the engine as 5 LPM. In addition to the engine, oxygen is supplied from a tube. The amount of oxygen given was controlled and the amount of H+OH was given. Diethyl ether was added to diesel fuel at the level of 10% by volume. The engine was started with this fuel every time. This new fuel is given as the abbreviation DE10 in the charts. In the graphs, the new fuel mixtures formed by the addition of gases are given with the abbreviations DE10+(H), DE10+ (H+ OH), DE10+ (H+ OH+ O_2). The engine experiments were repeated at the engine speed of 3000 rpm, 1000 w and 2000 w engine load of the engine. The change of smoke opacity and NOx emissions during the experiments is given below.

The engine experiments were carried out in a single-cylinder compression ignition engine. The exhaust gas temperature was measured with a k-type thermocouple in the experimental setup, and the changes in soot emissions were measured with an exhaust gas analyzer. The H, H+HO gas supplied to the engine is produced by hydrolysis of water. The resulting gas is given from the intake manifold. The hydrogen generator allows the production of H and OH gases separately. All gases supplied to the engine are controlled by a flow meter and supplied to the engine as 5 LPM. In addition to the engine, oxygen is supplied from a tube. The amount of oxygen given was controlled and the amount of H+OH was given. Diethyl ether was added to diesel fuel at the level of 10% by volume. The engine was started with this fuel every time. This new fuel is given as the abbreviation DE10 in the charts. In the graphs, the new fuel mixtures formed by the addition of gases are given with the abbreviations DE10+(H), DE10+ (H+ OH), DE10+ (H+ OH+ O_2). The engine experiments were repeated at the engine speed of 3000 rpm, 1000 w and 2000 w engine load of the engine. The change of smoke opacity and NOx emissions during the experiments is given below.

3 RESULTS AND DISCUSSION

Figure 2 shows the change in NOx emissions of the addition of gases. With the addition of H, H+OH and H+OH+O2 supplied to diesel fuel from the intake manifold, there is an increase in NOx emissions. The highest increase rate in terms of NOx emissions occurred with the introduction of a H + OH+ O2 gas mixture at an engine load of 2000 W. As is known, the amount of oxygen taken in decreases with the delivery of gaseous fuels from the intake manifold in diesel fuels. In this case, it worsens the combustion inside the cylinder. It is aimed to increase volumetric efficiency and partially increase combustion by adding oxygen next to H+ OH gas from the intake manifold. The results obtained showed that NOx emissions were increased with the addition of oxygen. The

highest NOx data was measured as 156 ppm with a DE10 (H+OH+O2) gas mixture at an engine load of 2000 w, while the lowest NOx emission value was measured as 85 in a DE10 fuel mixture with a fuel mixture.

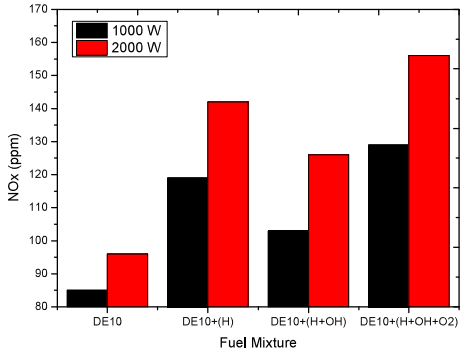


Figure 2. Change of NOx emission.

Figure 3 shows the change in soot emissions of the addition of gases. In diesel engines, soot emissions are described as the oxidation of non-combustible exhaust gases. With the addition of gases to the diesel / diesel ethyl ether fuel mixture used as pilot fuel, there is a tendency to reduce soot emissions in all engine loads. Along with the gas fuels taken into the cylinder, the combustion in the cylinder has partially improved and in this case has led to a decrease in soot emissions. The highest amount of reduction was achieved by using a DE10+(H+OH+O2) fuel mixture. It is possible to explain this situation by the fact that the amount of oxygen added partially improves combustion. The highest soot emission value was obtained as 12.1 at a 1000 w engine load with a DE10 fuel mixture, while the lowest soot emission value was obtained by using a DE10+ (H+OH+O2) fuel mixture as 7.6 at a 2000 w engine load.

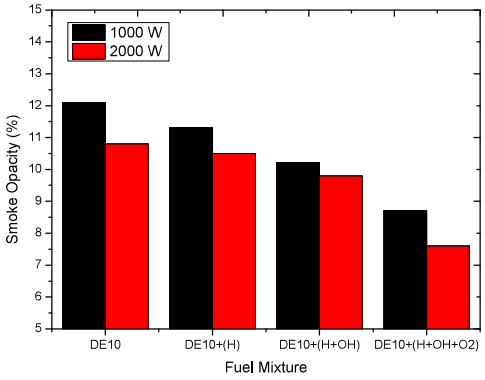


Figure 2. Change of smoke opacity emissions.

4 CONCLUSIONS

With the addition of H, H+OH and H+OH+ O2 to an engine that uses diethyl ether fuel added to diesel fuel as a pilot fuel, there is a decrease in NOx and soot emissions in all engine loads. With the addition of O2, the highest tendency to decrease in all engine loads was observed. The study is a preliminary study. In this respect, it will be expanded and improved with different engine loads and different fuel mixture ratios in the later stages of the study.

REFERENCES

1. Hongwen He∗, Yiwen Shou, Hao Wang, Fuel economyoptimizationofdieselenginefo rplug-inhybridelectric vehicle based onequivalentoperatingpoints, Control EngineeringPractice
2. Optimization of operating parameters for diesel engine fuelled with bio-oil derived from cottonseed pyrolysis Sakthivel Rajamohan Van Nhanh Nguyen a b , a , * * , Sidharth Suresh , Dirk Engel c a , Shanthinath Mallinathan , Shams Forruque Ahmed d , * a , Abbhijith Harigopal , Tri Hieu Le
3. Performance, combustion and emission characteristics investigations on a diesel engine fueled with diesel/ ethanol /n-butanol blends Zhiqing Zhang a,b,c, Jiangtao

Li a,c, Jie Tian a,c, Rui Dong a,c, Zhi Zou a,c, Sheng Gao a,c, Dongli Tan b,*

4. Performance, emission and combustion characteristics of a diesel engine fuelled with diesel/coconut shell oil blends S. Gowthaman * , K. Thangavel
5. Experimental and empirical analysis of a diesel engine fuelled with ternary blends of diesel, waste cooking sunflower oil biodiesel and diethyl ether Bukke Devaraj Naik a , Udayakumar Meivelu Santhoshkumar Annamalai d a , b , Vinoth Thangarasu , Vedharaj Sivasankaralingam
6. Experimental assessment of performance and emissions for hydrogen-diesel dual fuel operation in a low displacement compression ignition engine
7. Fuel injection strategy optimisation and experimental performance and emissions evaluation of diesel displacement by port fuel injected methanol in a retrofitted mid-size genset engine prototype
8. Impact on performance and emissions of the aspiration of algal biomass suspensions in the intake air of a direct injection diesel engine
9. The applicability of catalytic esterified biomass-pyrolysis-oil surrogates in diesel engine
10. Prediction of performance and emission characteristics of diesel engine fuelled with waste biomass pyrolysis oil using response surface methodology
11. Exploration of engine characteristics in a CRDI diesel engine enriched with hydrogen in dual fuel mode using toroidal combustion chamber
12. Cycle-to-cycle combustion analysis in hydrogen fumigated common-rail diesel engine
13. Effect of utilization of hydrogen-rich reformed biogas on the performance and emission characteristics of common rail diesel engine
14. Influence of hexanol/hydrogen additives with diesel fuel from CRDI diesel engine with exhaust gas recirculation technique: A special focus on performance, combustion, gaseous and emission species
15. Dual-fuel diesel engine run with injected pilot biodiesel-diesel fuel blend with inducted oxyhydrogen (HHO) gas
16. Effect of HHO gas enrichment on performance and emissions of a diesel engine fueled by biodiesel blend with kerosene additive
17. Performance & emission analysis of HHO enriched dual-fuelled diesel engine with artificial neural network prediction approaches
18. HHO enrichment of bio-diesohol fuel blends in a single cylinder diesel engine

THE EFFECT OF MULTIPLE INJECTION ON CI ENGINE POLLUTANT EMISSIONS AND GREEN HOUSE GASES

Arda ALBAYRAK[1], Onur GEZER[1], Orkun ÖZENER[1], Cihan BÜYÜK[2], Muammer ÖZKAN[1]

1. Department of Mechanical Engineering, Yildiz Technical University, Istanbul; email: albayrak.ard95a@gmail.com, ogezer@yildiz.edu.tr, oozener@yildiz.edu.tr, muaozkan@yildiz.edu.tr
2. TÜMOSAN Engine and Tractor Co. Topkapı/İstanbul; email: cihan.buyuk@tumosan.com.tr

Abstract

Nowadays, one of the most important cause of air pollution is pollutants originating from diesel engine. Diesel engine emissions are limited by strict regulations. Compliance with possible EURO VII regulations will become more difficult in the future. Manufacturers have to find innovative solutions to limit NO_x emissions while meeting market requirements. Having a reliable and consistent diesel combustion makes it easy to meet emissions targets, equipment endurance limits to ensure optimal engine performance and remain competitive in the market. Optimization tools are an essential to achieve the optimal fuel consumption. In this study, the non-linear behaviour of NO_x emission and fuel consumption were modelled by Gaussian regression method. Experimental data based on the multiple injection strategy in a CI engine were obtained by the way of dynamometer test and afterwards applied to Gaussian regression method. It was determined that the pilot and the main two stage injection reduced NO_x by %11.6 compared to the only main injection strategy. On the other hand, it is seen that fuel consumption increased by %1.5. The two pilot and main three stage injection configuration reduced NO_x emissions by %16 compared to the single main injection configuration. But, the fuel consumption value increased by 3.2%. Furthermore the effect of multiple injection on greenhouse gases CO_2 and N_2O is assessed from the obtained results.

Keywords: NO_x Emission, N_2O Emission, Multiple Injection, Gaussian Model, CI Engines

1 INTRODUCTION

In our age, one of the most important causes of air pollution is pollutants originating from road vehicles. While diesel engines were used only in heavy-duty vehicles until the 1970s, they have also been used in light-duty vehicles since the 1970s. Especially in the second half of the 2000s, with the commercialization of common-rail systems, diesel vehicles have become common at the passenger car park. Low fuel consumption makes diesel engines more attractive. In addition, they emit very low CO and THC emissions, but they are disadvantaged in terms of NO_x and PM emissions. Heterogeneous mixture formation is one of the important factor of these two emissions for diesel engines.

In diesel engines, NO_x emissions reveal mostly in the pre-mixed combustion phase [1]. The NO_x formed is a strong function of factors such as temperature, pressure, flame condition, reactant concentrations [2]. The basic mechanism of NO formation in diesel engines is defined by the Zeldovich mechanism, in addition, a small amount of NO is generated in the diffusion flame region. This is represented by the Fenimore mechanism, this NO_x generation mechanism occurs when hydrocarbon radicals react with nitrogen. Generated NO_2 emission is mainly due to the freezing of the reaction as a result of the mismatch between the reaction rate of the intermediate reactions and the chemical equilibrium state. NO_2 emission is strongly dependent on the initial amount of NO [3]. Most of the NO_x in diesel engines is NO, with lower amounts of NO_2 emits depending on engine speed and load. Compared to these two NO_x emissions, diesel engines emit little N_2O. Although it is released from road vehicles at a trace level, it is should be considered due to strong green house effect.

The after-treatment units which are DOC, DPF, SCR and/or LNT, become standard in current diesel engine system. Although NO_x conversion isn't the main purpose of DOC and DPF units, NO_x concentrations change at these units, due to the chemical reactions of other substances, temperature changes and usage of

NO_x as a consumable compound in the reaction (like passive DPF regeneration). SCR systems are an effective method for controlling NO_x emissions. Different catalysts have been developed to control of NO_x emissions at SCR systems [4]. Titanium-vanadium based SCR systems are commonly used. Despite the many advantages of vanadium-based catalysts, some problems arise during DPF regeneration. In addition, a toxic compound V_2O_5 may be released from the catalyst at high temperature regime [5]. Zeolite-based SCR systems are an advantageous to meet stricter emission regulations. Copper and ferrium reinforced Zeolite-based SCR systems are preferred due to both their NO_x reduction performance and superior thermal compatibility, these catalysts also perform better conversion efficiency at low temperature [6].

With the commercialization of common-rail systems, multi-phase fuel injection has become possible. Lee et al. [7] observed an extremely serious decrease in NO_x emissions as a result of better premixing with double pre-injection in their study carried on a heavy-duty diesel.

In this study, three different injection strategies were designed as only main injection, pre and main injection, two-stage pre injection and main injection. In order to observe the effect of the multi-stage injection strategy on NO_x emission, real-time measurements were taken at the engine operating points at engine test bench and test points were determined by the DoE method. These measurements were used to create the Gaussian regression model. By applying multiple injection strategy in diesel engines; the variation of fuel consumption, GHG effect and NO_x emissions were compared with the established model and experimental tests. In the study, it is aimed to investigate the green house gas effect of N_2O, which is minor part the NO_x emissions. N_2O takes values between 0.3-0.8% in diesel engine-out total NO_x emissions [8, 9]. However, the engine-out N_2O concentration differs in after-treatment systems, and even the N_2O concentration can increases. The aim of this study is to determine the behaviour of N_2O, whose concentration can increase during NO_x reduction.

2 METHODOLOGY

Black, gray and white box models are frequently used in NO_x modelling for diesel engines. Black box model establishes a relationship between existing input and output parameters without recourse to any physical principle [10]. Therefore, physical formulations are unnecessary to describing the system. Some physical equations are needed in gray box modeling [11].

In NO_x modelling in diesel engine, the exact formulation of the system in the combustion process is quite difficult due to the non-linear behaviour. For this reason, the black box model emerges as a more practical method if sufficient data are known.

Herringson et al. [12] created black-box model which evaluated fuel injected mass, injection timing, turbocharger condition properties, EGR ratio as inputs; IMEP, peak pressure, NO_x and PM were modelled as outputs. Similarly, Benatzky et al. [13] and Grahn et al. [14] also conducted studies with this method on the related subject. Gaussian regression model has gained importance in artificial neural network design in recent years. In this study, the Gaussian regression model was selected.

After the experimental design, data were taken from 200 different points in order to examine three different injection strategies as single phase, one pre and main phase, two pre and main phase injection. Comparative analyzes were carried out from 9 different points selected from here.

ETAS ASCMO program was used for modelling. It is aimed to obtain inputs that will contribute to the calculation of NO_x and fuel consumption values for the experimental data obtained after the creating of DoE. In order to model NO_x and fuel consumption outputs well, 12 different input parameters were considered. These are engine speed, engine torque, main injection quantity and timing, first pre injection quantity and timing, second pre-injection quantity and timing, rail pressure, intake air pressure, intake air mass quantity and engine cooling fluid temperature. In this part of the study, 90% of the data obtained from the test setup was used, while the remaining 10% was used for validation process.

3 EXPERIMENTAL PROCESS

In the study, a 4-cylinder, 4-stroke, 2 liter cylinder displacement volume, variable turbine geometry twin turbocharger unit diesel engine

was used. The technical specifications of the test engine are shown in Table 3.1.

Table 3.1. Engine Specification

Engine Specification	Values
Fuel Type	Diesel
Cylinder Number	4
Displacement Volume	2 liter
Bore	84 mm
Strok	90 mm
Compression Ratio	16.5

During the tests, the motor was braked with an 220kW braking capacity AVL DynoExact APA204/8 type AC dynamometer. The AVL PUMA program was used to operating the system to the desired operating conditions. AVL 735S device was used for fuel consumption measurement, it works with Corriolus principle, this device can use between 0 and 125kg/h range with 0.12% sensitivity. AVL 735C was used as the fuel conditioner and the fuel temperature was kept constant at 35°C. Air flow was measured with an ABB SensyFlow type flow meter. The MAP sensor was used to measure the intake air pressure. NO_x emission data is obtained by the AVL AMA i60. The schematic representation of the test setup is presented in Figure 3.1.

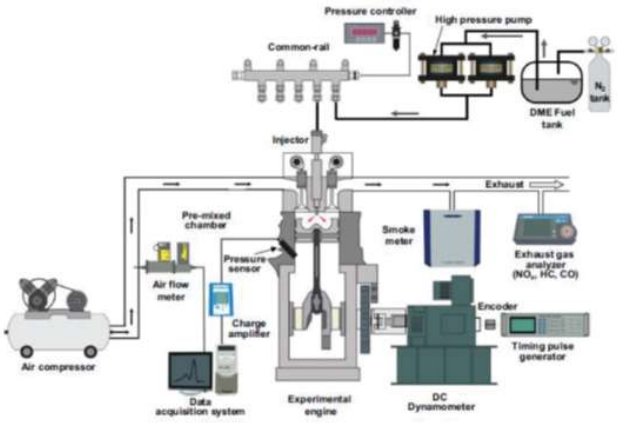


Figure 1. Schematic layout of engine test bench

3 RESULTS

In order to examine the effect of the injection strategy on fuel consumption and NO_x, 3 different injection configurations were examined for 200 different operating points selected previously. Meanwhile, in order not to affect the NO_x and fuel composition at changing operating points, all parameters were kept constant and only injection phasing was manipulated. The obtained data were divided into three different categories as A, B and C, as seen in Figure 4.1, depending on the normalized engine speed and normalized engine torque.

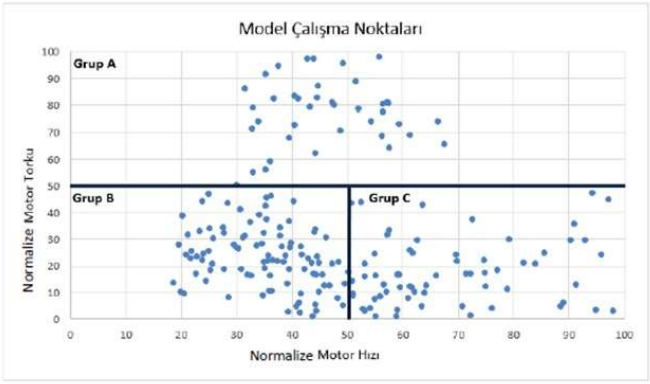
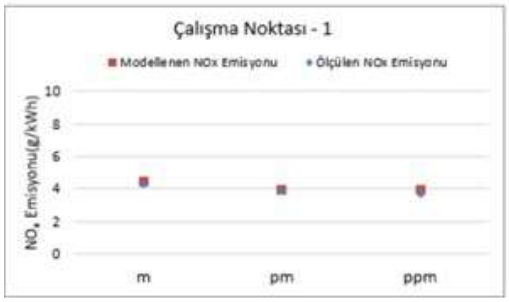


Figure 4.1. Categorization of test points with respect to normalized values

Single phase injection will be represented by "M", strategy consisting of a pre and main injection by "PM", two pre and main injection are presented with "PPM". Within the above distribution, 3 working points were selected in each group and data were taken at 9 different points. The selected data are represented in Table 4.1 in terms of normalized values.

Table 4.1. Representation of 9 determined operating points according to normalized values

Test Point	Group	Normalized Engine Speed	Normalized Engine Torque
1	A	56.40	68.67
2	A	44.03	96.98
3	A	33.13	78.71
4	B	20.43	38.49
5	B	29.60	27.84
6	B	44.10	32.56
7	C	61.35	25.82
8	C	76.28	3.93
9	C	93.10	29.38



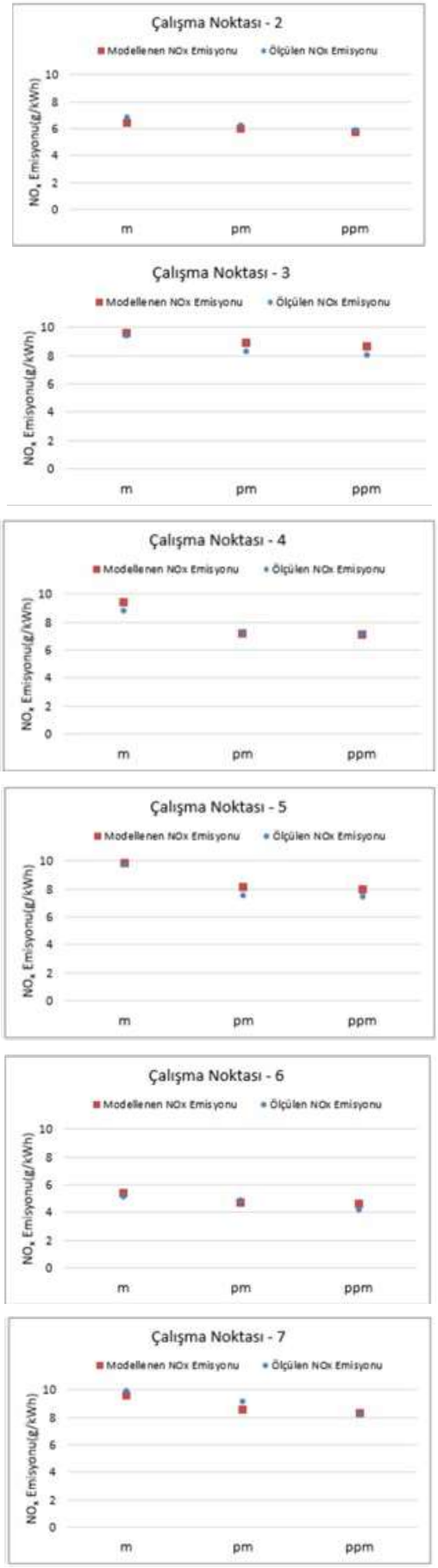


Figure 4.2. Specific NO_x emission values that occur according to different injection strategies

The greenhouse effect of a gas is measured with the global warming potential (GWP) and is compared to the effect of CO_2. The GWP of N_2O on the 100-year scale is 273 [15]. The ratio of N_2O, one of the nitrogen compounds in the exhaust of diesel engines, is quite low. However, N_2O formation may occur in SCR systems. In the SCR system, it is aimed to increase the concentration of NO_2 for more efficient NO_x conversion, during which N_2O formation also occurs. This mechanism, which is formed as a result of the reaction with ammonia, is indicated by equations (4.1) and (4.2).

$$8NO_2+6NH_3 \longrightarrow 7N_2O+9H_2O \qquad (4.1)$$

$$4NO_2+4NH_3+O_2 \longrightarrow 4N_2O+6H_2O \qquad (4.2)$$

In this study, it was assumed that 0.5% of the nitrogen compounds in the exhaust gases are N_2O. The conversion efficiency of zeolite-based SCR systems around 300°C is over 90% and conversion efficiencies up to close to 100% can be seen [16]. In this study, the SCR efficiency was assumed as 95%. In addition, in the case of using zeolite-based SCR, it has been observed that there is between 8% and 16% N_2O in the total nitrogen oxides at the exhaust system outlet [16]. In this study, it was assumed that 12% of the nitrogen oxides found at the SCR outlet were N_2O. Considering these rates, the engine output and Zeolite-based SCR output N_2O values are

presented depending on the injection strategy in Table 4.2 on a 100-year time scale.

Table 4.2. The amount of N_2O and CO_2 to be released from the engine and Zeolite-based SCR to the environment in a 100-year period

	GHG Emission	Injection Strategy		
		M	PM	PPM
Engine-out	CO_2 (ton)	742.2	766.5	780.7
Engine-out	N_2O (ton)	9.9	8.4	8.2
SCR-out	N_2O (ton)	11.8	10.0	9.8

With the studies and assumptions made, CO_2 and N_2O, which have greenhouse gas effects, are emitted with 752.1 tons of gas from the engine to the atmosphere over a 100-year period in the strategy when M is used. This value is 754 tons if the engine and the zeolite-based SCR system are used. PM strategy 774.9 tons of greenhouse gas from the engine releases to the atmosphere over a 100-year period. This value is 776.5 tons if the engine and only the zeolite-based SCR system are used. If PPM strategy is used, 788.9 tons of greenhouse gas from the engine releases into the atmosphere over a 100-year period. This value is 790.5 tons if the engine and zeolite-based SCR system are used.

5 RESULTS

When the results obtained from 3 different groups and 9 different points selected within the study were examined, the results mentioned in the following paragraphs were obtained.

For Group A, NO_x emissions decreased by 7% at PM strategy compared to M injection strategy, while fuel consumption increased by 1%. When the PPM strategy was applied in group A, NO_x emissions decreased by 9% on average and fuel consumption increased by 1.8% compared to the M strategy. At the B group operating points, the NO_x reduction in PM strategy decreased by 16% on average compared to the M strategy, and fuel consumption increased by 2% on average. An average of 18% NO_x reduction was observed in the PPM strategy compared to the M strategy at the operating points of Group B, and an average of 2.9% increase in fuel consumption was observed. At the C group operating points, NO_x emissions decreased by 12% and fuel consumption increased by 1.1% in PM strategy compared to M strategy. In the C group, NO_x emissions decreased by 21% on average in the PPM strategy compared to the M strategy, while fuel consumption increased by 4.9% on average.

It is seen from the literature data and the values in this study that NO_x emissions decrease in the phased injection strategy. The amount of N_2O released in the PM strategy decreased by 15.9% on average compared to the M strategy, and a 17.1% decrease was observed when the PPM strategy and the M strategy were compared. In the case of using zeolite-based SCR, the N_2O emission increase by an average of 16% compared to the engine output value.

Figure 1. Paper Layout

REFERENCES

[1] J. E. Dec, “A conceptual model of DI diesel combustion based on laser-sheet imaging,” in SAE Technical Paper Series, 1997.

[2] Y. Kitamura, A. Mohammadi, T. Ishiyama, and M. Shioji, “Fundamental investigation of NOx formation in diesel combustion under supercharged and EGR conditions,” in SAE Technical Paper Series, 2005.

[3] J. Klimstra and J. E. Westing, NO2 From Lean-Burn Engines-On Its Lower Sensitivity to Leaning Than NO. İn SAE Technical Paper 1995.

[4] T. V. Johnson, “Review of diesel emissions and control,” SAE Int. J. Fuels Lubr., vol. 3, no. 1, pp. 16–29, 2010

[5] Z. G. Liu, N. A. Ottinger, and C. M. Cremeens, “Methods for quantifying the release of vanadium from engine exhaust aftertreatment catalysts,” SAE Int. J. Engines, vol. 5, no. 2, pp. 663–671, 2012.

[6] B. Guan, R. Zhan, H. Lin, and Z. Huang, “Review of state of the art technologies of selective catalytic reduction of NOx from diesel engine exhaust,” Appl. Therm. Eng., vol. 66, no. 1–2, pp. 395–414, 2014.

[7] J. Lee, J. Jeon, J. Park, and C. Bae, “Effect of multiple injection strategies on emission and combustion characteristics in a single cylinder direct-injection optical engine,” in SAE Technical Paper Series, 2009

[8] P. Degobert, Automobiles and Pollution. Paris, France: Editions Technip, 1995.

[9] Control of Combustion Generated Nitrogen Oxide Emissions Technology Driven by “BOWMAN Department of Mechanical

Engineering Stanford University Stanford, CA 94305-3032 USA
[10] Q. Zhao and T. Hastie, "Causal Interpretations of Black-Box Models"," Journal of Business & Economic Statistics, vol. 39, no. 1

[11] J. Asprion, O. Chinellato, and L. Guzzella, "A fast and accurate physics-based model for the NOx emissions of Diesel engines"," Applied Energy, vol. 103, pp. 221–233, 2013.
[12] M. Henningsson, K. Ekholm, P. Strandh, P. Tunestål, and R. Johansson, "Dynamic mapping of diesel engine through system identification," in Identification for Automotive Systems, London: Springer London, 2012, pp. 223–239.
[13] C. Benatzky, S. Stadlbauer, S. Formentin, A. Schilling, and D. Alberer, "Indicated pressure-based data-driven diesel engine NOx modeling"," International Journal of Engine Research, vol. 15, no. 8, pp. 934–943, 2014
[14] M. Grahn, K. Johansson, and T. Mckelvey, "Data-driven emission model structures for diesel engine management system development'' International Journal of Engine Research, vol. 15, no. 8, pp. 906–917, 2014
[15] EPA. [Online]. Available: https://www.epa.gov/ghgemissions/understanding-global-warming-potentials. [Accessed: 12-Mart-2022].
[16] C. P. Cho, Y. D. Pyo, J. Y. Jang, G. C. Kim, and Y. J. Shin, "NOx reduction and N2O emissions in a diesel engine exhaust using Fe-zeolite and vanadium based SCR catalysts," Appl. Therm. Eng., vol. 110, pp. 18–24, 2017.

THE COMPARISON OF QUASI-STEADY EVAPORATION MODELS IN A SWIRL STABILIZED COMBUSTION CHAMBER

Deniz İmamoğlu[1], Özgür Ertunç[1], Altuğ M. Başol[2], M.Pınar Mengüç[3]

1. Fluid Dynamics & Spray Laboratory, Mechanical Engineering Department, Özyeğin University, Istanbul/Türkiye ; email: deniz.imamoglu@ozu.edu.tr
2. Mechanical Engineering Department, Özyeğin University, Istanbul/Türkiye
3. Center for Energy, Environment and Economy, Özyeğin University, Istanbul /Türkiye

Abstract

In this study, the effect of droplet evaporation on combustion has been investigated in a swirl stabilized combustion chamber with different quasi-steady single-component droplet evaporation models in Star-CCM+ 15.06.007-R8. Two different evaporation models, namely "Heat Transfer Limited Evaporation" and "Vapor Diffusion Limited Evaporation" based on the Abramzon-Sirignano droplet evaporation model, have been compared in Star-CCM+. These models differ from each other by the saturation state of the vapor at the droplet surface. Droplet heating before evaporation and evaporation rate has been studied by observing the droplet temperature and mole fraction of fuel in the simulations. JP-8 (Jet Propellent 8, $C_{11}H_{22}$, also designated as the A1 fuel) is used as fuel in the simulations. Particle temperature, temperature distribution, chemistry heat release rate indicator, and fuel mole fraction in the computational domain have been analyzed for combustion simulations. The remarkable differences caused by the evaporation models are the particle temperatures and the locations where combustion occurs.

Keywords: Droplet evaporation, Combustion, Numerical simulation

1 INTRODUCTION

The fuel droplet evaporation is essential in combustion efficiency, pollutant emissions, and ignition delays. A fuel droplet is heated, evaporates, and then burns when it encounters a high-temperature environment like a combustion chamber, providing the energy needed for propulsion [1]. Maxwell set the groundwork for the theory of droplet evaporation in a gaseous medium. Because the droplet radius and evaporation rate are constantly decreasing, Maxwell [2] argues that the evaporation of a droplet cannot be a stationary process. However, when the droplet density exceeds the vapor concentration in equilibrium with the droplet, the evaporation can be considered quasi-stationary [3].

Droplet evaporation depends on the type of fuel and how heat and mass transfer are modeled within the droplet and during its interaction with the environment. In [1], the fuels with different volatilities were compared experimentally to characterize the Nusselt and Sherwood numbers. It shows that the evaporation rate increases when the fuel volatility gets higher. Even in overheated ambient gases, an evaporating droplet's temperature stabilizes below the boiling point due to the cooling effect of evaporation. The steady-state temperature reached during the evaporation is equivalent to the wet-bulb temperature [4]. Numerous droplet evaporation models have been developed and implemented in different cases, such as single droplets in a hot stream or sprays in combustion chambers. In [5], the finite-gradient and zero gradient models for the preheat stage of liquid droplets are analyzed theoretically, containing the effects of transient heat conduction and evaporation. Sirignano [6] explain five droplet vaporization models for the quasi-steady gas phase, which are titled as d^2 law, infinite liquid conductivity model, conduction limit model, effective-conductivity model, and vortex model of droplet heating. In [7,8], he explained the effective-conductivity model formulated for transient liquid heating with circulation in the droplet for spray combustion calculations. Abramzon-Sirignano droplet heating and evaporation model for gas phase [8] is used in many studies for spray combustion and single droplet in hot stream calculations [9-14]. A comparative study has been done in [12] between experimental data and original Spalding, Borman-Johnson, and Abramzon-Sirignano droplet evaporation models. The study shows that the Abramzon-

Sirignano model results were the closest to experimental data. In another study [15], the heat transfer equation in [16] was improved and established for the evaporation model of fuel droplets. [15] found that [16] calculated higher evaporation rate due to giving extra heat to droplet by the heat transfer equation.

Apte et al. [9] evaluated the spray vaporization by Large Eddy Simulation (LES) approach's predictive capability. The results are noteworthy because they established a baseline level of accuracy in the simulation of complex flows on unstructured mesh under conditions similar to those in gas-turbine combustors. In another study, Snegirev et al. [10] developed two simple and accurate approaches for droplet evaporation to decrease the computational cost caused by the LES approach.

In the literature, the effect of mostly droplet evaporation modelling on single droplet or spray has been investigated. However, the studies on the relationship between combustion and droplet evaporation modelling are limited. In the present study, the effect of droplet evaporation on combustion has been investigated in a swirl stabilized combustion chamber with different quasi-steady single-component droplet evaporation models. The Lagrangian Model was used to track the fuel droplets on the background Eulerian flow. The heating and evaporation of fuel spray droplets have been observed and analyzed for each quasi-steady evaporation model. Droplet temperature, mole fraction of fuel's gas phase, and chemistry heat release rate indicator have been observed in the combustion simulations. This study shows that the combustion location and the high-temperature regions in the combustion chamber are affected by selecting droplet evaporation models in numerical simulations.

2 DROPLET EVAPORATION MODELS

The quasi-steady evaporation model allows the droplets to lose mass due to evaporation. The driving force for evaporation is the liquid-vapor system's departure from equilibrium. The liquid-vapor system consists of the droplet and the gas component of the continuous phase, specified as the droplet vapor. In addition to the driving force, the molecular diffusivity of the gas component and the Sherwood Number of the droplet are two other significant factors in determining the droplet evaporation rate.

Mass transfer occurs between the phases if the dispersed phase is volatile, soluble, or reactive. Interphase heat transfer occurs concurrently with this mass transfer. The temperature changes between the phases can also generate heat transfer. The particles of the dispersed material change in size because of interphase mass transfer.

The equation of mass conservation of a material particle is given by:

$$\frac{dm_p}{dt} = \dot{m}_p \tag{1}$$

where m_p is the mass of the particle and $\dot{m}_p$ *is* the rate of mass transfer to the particle. $\dot{m}_p$ is zero if the mass transfer does not occur, such as evaporation.

Quasi-steady single-component droplet evaporation assumes droplets to be internally homogeneous, consisting of a single liquid component such as a chemical species. The rate of change of droplet mass due to quasi-steady evaporation $\dot{m}_p$ can be written as [17],

$$\dot{m}_p = -g^* A_s \ln(1+B) \tag{2}$$

where B is the Spalding transfer number and g^* is the mass transfer conductance.

In Simcenter Star-CCM+, there are three different droplet evaporation models, such as "Super-Critical," "Heat Transfer Limited Evaporation," and "Vapor Diffusion Limited Evaporation," based on saturation pressure and critical temperature of droplets.

"Heat Transfer Limited Evaporation" is active when the vapor at the droplet surface is saturated and subcritical. It enforces a balance between latent heat transfer and other modes of heat transfer so that the droplet temperature remains at the saturation temperature at the droplet surface. The condition for a saturated vapor is that the surface equilibrium mole fraction of the vapor exceeds unity:

$$X_{v,s} = \frac{p_{sat}(T_p)}{p} \geq 1 \tag{3}$$

$p_{sat}(T_p)$ is the vapor saturation pressure at the droplet surface temperature. The transfer number is:

$$B = \frac{c_p(T-T_p)}{L} \tag{4}$$

where L is the latent heat of vaporization.

The mass conductance, g^* is,

$$g^* = \frac{kNu_p}{c_p D_p} \tag{5}$$

In this model, there is an "Equilibrium Boiling Mode." This mode ensures that the computed temperature of a droplet cannot exceed the saturation temperature at the droplet surface.

"Vapor Diffusion Limited Evaporation (VDL)" is active when the vapor at the droplet surface is subcritical and not saturated. The evaporation rate depends on the rate at which vapor can diffuse away from the droplet. Under this condition, the transfer number is [6],

$$B = \frac{Y_{v,s} - Y_v}{1 - Y_{v,s}} \quad (6)$$

where Y_v is the vapor mass fraction in the free stream and $Y_{v,s}$ is the equilibrium vapor mass fraction on the droplet's surface, which is,

$$Y_{v,s} = X_{v,s} \frac{W_v}{W_s} \quad (7)$$

where W_v and W_s are the molecular weights of the vapor and gas mixture at the droplet surface, respectively. The mass conductance, g^* is;

$$g^* = \frac{\rho D_v Sh_p}{D_p} \quad (8)$$

$Y_{v,s}$ term is the most critical parameter for the "Vapor Diffusion Limited Evaporation" model. The upper limit of $Y_{v,s}$ should be defined so that the transfer number in equation 6 is not an infinite value.

In Simcenter Star-CCM+, Sherwood and Nusselt numbers are defined with the Ranz-Marshall correlation. This correlation is suitable for spherical particles up to Re=5000 [18].

In [1], the energy balance during the evaporation was defined as,

$$Q_L = \Phi_{in} - \Phi_{vap} \quad (9)$$

where Q_L is the heat flux entering into the droplet, Φ_{in} is the convective heat flux comes from the gas phase, and Φ_{vap} is the heat flux because of the vaporization. Q_L can be higher than zero for the "Heat Transfer limited Evaporation" model with disabled "Equilibrium Boiling Mode" (HTL). It means that droplets can be heated up during combustion since the convective heat flux is higher than the vaporization heat flux. If "Equilibrium Boiling Mode" is enabled (HTLEB), Q_L cannot be higher than zero. Because the given droplet surface temperature is assumed as saturation temperature. In other words, the droplet surface cannot be heated up by the gas stream but give heat to the gas stream.

These three quasi-steady evaporation models have been used in the combustion simulations to observe the effect on combustion.

3 NUMERICAL MODELLING

In this study, numerical simulations were performed on Star-CCM+ 15.06.007 R8 version. The geometry scene of the computational domain is shown in Figure 1. The dimensions of geometry are taken from [19]. Before entering the combustor, ambient air is passed through a 12-vane radial swirler. A commercial pressure swirl nozzle delivered liquid fuel to the combustor with a 60° spray angle.

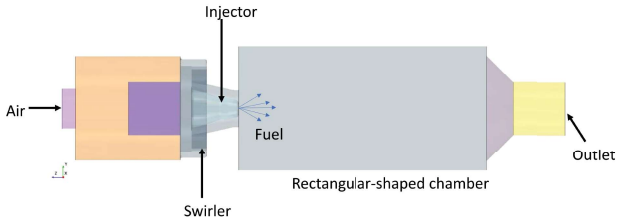


Figure 1. Geometry scene of the computational domain

In [19], the spray pattern is given as a semi-solid cone; but the injector is modeled as a solid cone in numerical simulations due to not existence of a semi-solid cone injector in Star-CCM+. Air and fuel flow rates are 5.93 g/s and 0.224 g/s, respectively. The boundary conditions of inlet and outlet are modeled as mass flow inlet and pressure outlet, respectively. The other boundary condition is defined as a wall. The fuel is Jet A-1 (JP-8), and the properties (Table 1) are taken from the literature [20-22]. Dynamic viscosity and specific heat of Jet A-1 are given temperature-dependent. Saturation pressure is calculated based on the Antoine equation as a function of temperature. Antoine equation is shown below;

$$log_{10}(p) = A - \frac{B}{C+T} \quad (10)$$

p is the absolute vapor pressure and A, B, C are Antoine coefficients specific to the substance.

Table 1. The properties of Jet A-1

Properties	Value
Density	812 kg/m^3
Elemental Composition	$C_{11}H_{22}$
Boiling Point	478.15 K
Surface Tension	0.0235 N/m
Thermal Conductivity	0.125 W/m·K

The Mesh scene of the computational domain is shown in Figure 2. Part-based mesh generation has been performed and generated approximately 2 million polyhedral mesh cells. Near the chamber walls and the swirler walls, prism layer meshes have been generated with a 1.1 stretching factor and 0.3 mm layer thickness. The number of prism layers has been set to five. In addition, mesh dependency has been done with three different meshed simulations, and the simulation with 2 million mesh has been selected due to low error and optimized computational time.

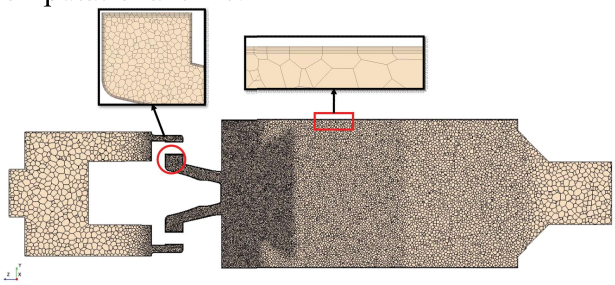


Figure 2. Mesh scene of the computational domain.

Numerical simulations have been divided into spray and combustion simulations. Firstly, spray simulations have been performed to validate the spray distribution with experimental data in [19] based on Sauter Mean Diameter (SMD) values. Spray simulations have been modeled as steady and realizable k-ε Two-layer turbulence is used as turbulence model. In [19], spray distribution and SMD measurements have been done without combustion and with the combustor windows removed to minimize the errors due to fuel build-up on the windows. In spray simulations, combustor walls were modeled as pressure outlets to represent this state of the experiments. Also, in the experimental study, the burner was positioned on a translation stage, and measurements were taken every 10 mm from 10⩽h⩽40mm and every 5 mm from -25⩽r⩽25mm to characterize the spray field. The spray measurements were done in a cylindrical volume with a 20 mm diameter [3]. r is the radial distance on the y-axis, and h is the distance from the injector on the z-axis in Figure 2.

In Simcenter Star-CCM+, particle data history is stored with the Particle Track File model. Particle diameter, particle temperature, particle velocity, and particle count data have been tracked during the spray simulations. At the end of the simulation, the track file has been exported, and SMD values have been calculated for all measurement locations.

Table 2. The injector properties

Properties	Value
Injector Type	Solid cone injector
Cone Angle	60°
Parcel Streams	1200
Velocity Magnitude	3.78 m/s
Particle Diameter	Rosin-Rammler Distribution

Injector properties are shown in Table 2. Rosin-Rammler distribution has been used for particle diameter in spray simulations. The Rosin-Rammler distribution was developed to describe the volume distribution of particles as a function of their diameter, $F_V(D_p)$ [23]. In Simcenter Star-CCM+, it is extended to be generic size distribution with a cumulative distribution function;

$$F(D)=1-e^{-\left(\frac{D}{D_{ref}}\right)^{q}} \quad (11)$$

in which parameters are the exponent, q, and the reference size D_{ref}.

Table 3 shows the Rosin Rammler Distribution parameters given to spray simulations. These parameters are adjusted based on the histogram of the volumetric frequency of particle diameters at the location (h= 20 mm & r=0 mm) from [19].

Table 3. Rosin-Rammler Distribution Parameters

Properties	Value
Minimum Diameter (D_{min})	8.26 µm
Maximum Diameter (D_{max})	559.49 µm
Reference Diameter (D_{ref})	302.00 µm
Exponent (q)	2.92

Accurate spray modeling is vital for liquid-fueled combustion simulations. There are two subsets of spray modeling: primary atomization and secondary atomization. In this study, primary and secondary break-up models have been selected, the Linearized Instability Sheet Atomization (LISA) and KHRT model, respectively. LISA model is for the thin liquid sheet at the nozzle exit that is created by the action of a pressure-swirl atomizer.

After the validation of spray distribution with experimental data in [19], combustion

simulations have been modeled and performed for different quasi-steady droplet evaporation models. In this study, flow is assumed to be steady, and the flame is non-premixed. Therefore, the flame the Steady Laminar Flamelet (SLF) model has been selected among the flamelet models for combustion simulations. The SLF model embeds steady diffusion flamelets in the turbulent flow. The assumption is that chemistry is fast compared to flow and mixing, so the flame is thin. The thermo-chemical state is parameterized by mixture fraction and the scalar dissipation rate. The chemical mechanism of the fuel has been obtained and imported to Star-CCM+ from [24-25].

In combustion simulations, firstly, the air was given in the combustor. After the convergence of airflow, a discrete phase (fuel) was introduced, and the combustion was started. After the energy and the mass flow rates are stabilized, the results have been analyzed.

4 RESULTS

Spray measurements were performed in a total of 28 locations throughout the spray. Measurement areas have been created with thresholds based on cylindrical coordinates at two different axes ((0,1,0) and (1,0,0)) in spray simulations. Two different axes are used to check spray measurements' direction dependency. The location of spray measurement for h=20 mm & r=0 mm is shown in Figure 3.

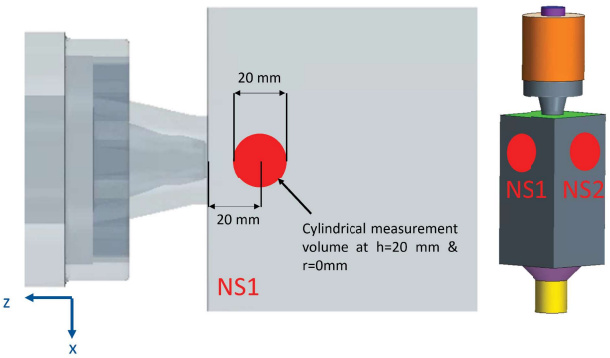


Figure 3. Spray measurement location at h=20 mm &r=0mm (The circle represents the area of intersection of the laser beam with the spray cone in experiments [19], so this method was used for calculations) and representation of NS1 and NS2 measurement volumes in numerical simulations.

SMD values were calculated with the equation,

$$SMD = 6\,\frac{\frac{4}{3}\pi(\frac{D_v}{2})^3}{4\pi(\frac{D_s}{2})^2} \tag{12}$$

where D is the particle diameter, v and s subscripts represent volume and surface respecitvely.

The comparison of SMD values with experimental data in [19] is shown in Figure 4. As the distance from the injector increases, SMD values calculated from the simulations are closer to experimental data. In spray simulations, SMD values at different radial distances seem uniform at h=10mm and h=20 mm. In addition, the average errors of NS1 and NS2 at all locations are 6.95% and 7.68%, respectively.

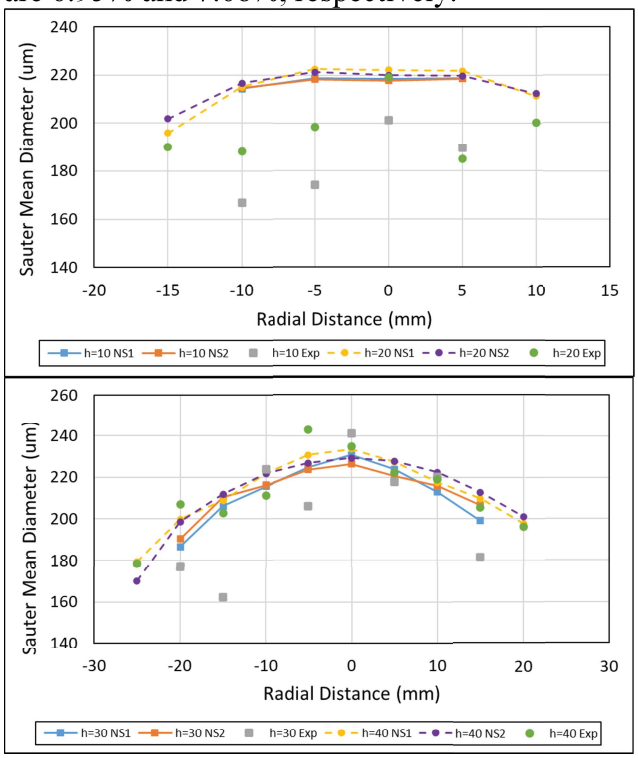


Figure 4. The comparison of SMD values with experimental data taken from [19] at different h and r locations.

Figure 5 shows the droplet temperature scene in the combustion chamber after combustion for three different evaporation models. Droplets heated up to 477 K for the HTL model. However, in the other models, droplets were not heated up. The maximum droplets' initial temperature is 288.15 K for HTLEB and VDL models. In the first two models (Figure 5a-5b), it is seen that droplets reach the outlet of the combustion chamber. In the last model, droplets could not reach the outlet due to the high vaporization rate. Since the equilibrium vapor mass fraction on the droplet's surface took the

upper limit value, the Spalding mass transfer number (Equation 6) got the higher value. Therefore, the evaporation rate increases proportionally to the mass transfer number (Equation 2).

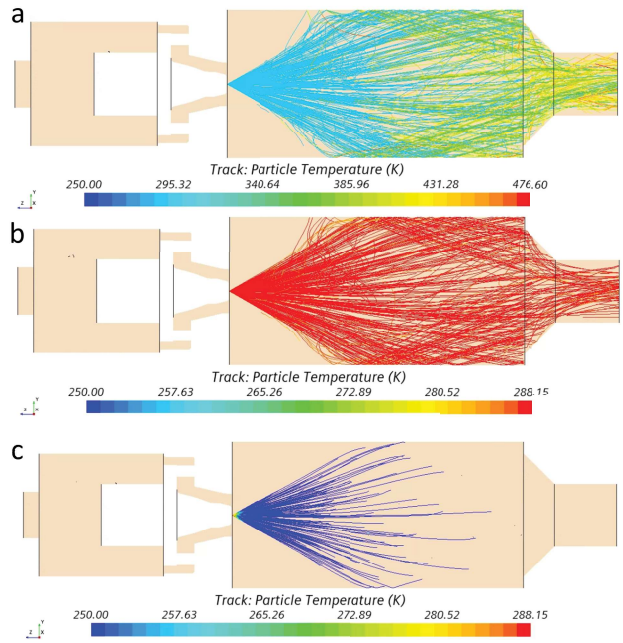


Figure 5. Droplet temperatures via particle track for a) Heat transfer limited evaporation with disabled Equilibrium Boiling Mode (HTL), b) Heat transfer limited evaporation with enabled Equilibrium boiling mode (HTLEB), c) Vapor diffusion-limited evaporation (VDL)

Figure 6 shows the mole fraction of the gas phase of the fuel after combustion. HTL and HTLEB models deliver similar fields of vapor fuel. However, the mole fraction of fuel in the VDL model is much higher than in the other models due to the higher vaporization rate.

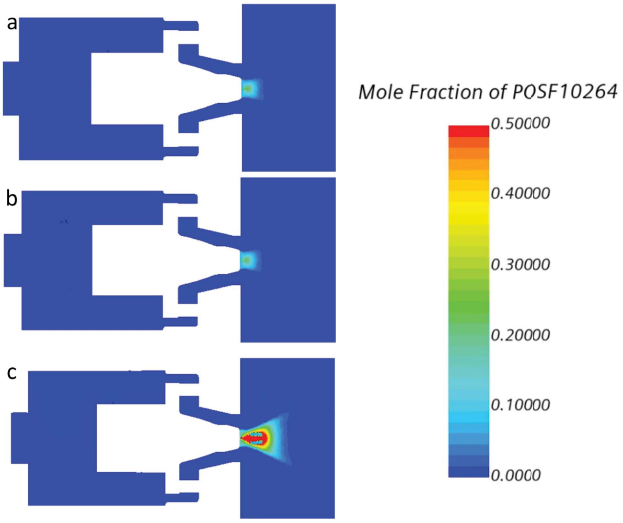


Figure 6. The mole fraction of Jet A-1 for a) HTL, b) HTLEB, c) VDL

Figure 7 shows the heat release rate indicator for each evaporation model. In the VDL evaporation model, heat generation is more intense than in the other two models. HTL and HTLEB models depict similar heat release rate indicator fields.

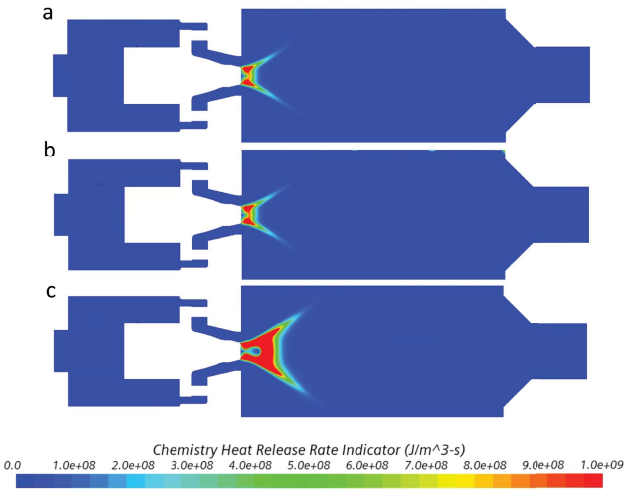


Figure 7. Chemistry heat release rate indicator in the combustion chamber for a) HTL b) HTLEB c) VDL

The temperature distribution in the combustion chamber is shown in Figure 8. Due to more intense heat generation in the VDL evaporation model, the high-temperature region reaches the middle of the combustion chamber. In the HTLEB model, the temperature on the walls of the combustion chamber is approximately 2000 K. The lowest outlet temperature is observed with the HTL evaporation model.

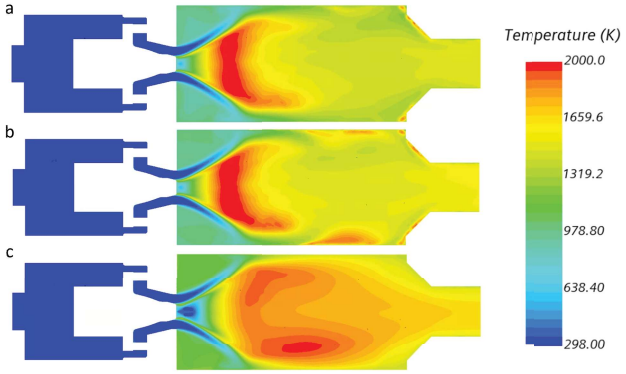


Figure 8. Temperature distribution in the combustion chamber for a) HTL, b) HTLEB, c) VDL

The tangential (out-of-plane) velocity fields are shown for all evaporation models in Figure 9. Figure 9 shows that these three different droplet evaporation models do not influence the velocity vectors.

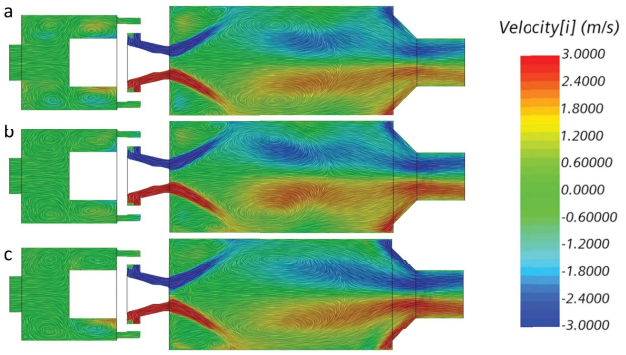


Figure 9. The tangential/out of plane velocity field in the combustion chamber for a) HTL b) HTLEB c) VDL

5 CONCLUSION

In this study, the effect of droplet evaporation on combustion has been investigated in a swirl stabilized combustion chamber with different quasi-steady single-component droplet evaporation models. Firstly, spray simulations have been done and the experimental data in [19] was validated with an average error of 6%. Then, the combustion simulations with different quasi-steady droplet evaporation models were performed and compared with each other.

In the HTL evaporation model, droplets were heated up by the gas stream, so droplet temperature increased up to boiling temperature of Jet A-1. However, in the HTLEB model, the maximum temperature of droplet was the initial temperature, 288.15 K. Because HTLEB model assumes that the vapor at the droplet surface is saturated, and "Equilibrium Boiling Mode" does not allow to exceed this temperature at the droplet surface. Furthermore, the droplet temperature can drop below initial temperature due to the cooling effect of evaporation. Enforced equilibrium is created by HTLEB evaporation model. In the VDL evaporation model, the equilibrium vapor mass fraction on the droplet's surface reaches the upper limit of 0.99999. So, the evaporation rate increases due to the high Spalding mass transfer number. In addition, the most intensive heat release rate was observed by the VDL evaporation model. For this reason, the average temperature in the combustion chamber is higher than in HTL and HTLEB evaporation models.

HTLEB evaporation model is unsuitable for combustion simulations since the initial droplet temperature is assumed to be saturation temperature. If the droplet is at the boiling point, this model can be used.

In future work, a detailed analysis must be done to decide which evaporation model is the most suitable model for combustion simulations among HTL and VDL. For this work, Large Eddy Simulations will be prepared and performed.

ACKNOWLEDGEMENTS

The authors gratefully acknowledge the Scientific and Technological Research Council of Turkey (TÜBİTAK) and TEI for providing financial support to this research with the 118C053 project. Special thanks for Taylor M. Rault for sharing information about experimental domain and fuel spray.

REFERENCES

[1] Deprédurand, V., Castanet, G., & Lemoine, F. (2010). Heat and mass transfer in evaporating droplets in interaction: Influence of the fuel. International Journal of Heat and Mass Transfer, 53(17–18), 3495–3502. https://doi.org/10.1016/j.ijheatmasstransfer.2010.04.010

[2] Maxwell, J. A Treatise on the Kinetic Theory of Gases. Nature 16, 242–246 (1877). https://doi.org/10.1038/016242a0

[3] Fuchs, Nikolai Albertovich. Evaporation and droplet growth in gaseous media. Elsevier, 2013.

[4] M.C. Yuen, L.W. Chen, On drag of evaporating liquid droplets, Combust. Sci. Tech. 14 (1976) 147–154.

[5] Kayser, R., & Bennett, H. S. (1977). Evaporation of a Liquid Droplet. J Res Natl Bur Stand Sect A Phys Chem, 81 A(2–3), 257–266. https://doi.org/10.6028/jres.081a.015

[6] Sirignano, William A. Fluid dynamics and transport of droplets and sprays. Vol. 2. Cambridge: Cambridge university press, 2000.

[7] Sirignano, W. A. (1983). Fuel droplet vaporization and spray combustion theory. Progress in Energy and Combustion Science, 9(4), 291–322. https://doi.org/10.1016/0360-1285(83)90011-4

[8] Abramzon, B., & Sirignano, W. (1988). Droplet vaporization model for spray combustion calculations. 32(9), 1605–1618. https://doi.org/10.2514/6.1988-636

[9] Apte, S. V., Mahesh, K., & Moin, P. (2009). Large-eddy simulation of evaporating spray in a coaxial combustor. Proceedings of the Combustion Institute, 32 II, 2247–2256. https://doi.org/10.1016/j.proci.2008.05.059

[10] Snegirev, A. Y., Talalov, V. A., Tsoi, A. S., Sazhin, S. S., & Crua, C. (2012). Advancement in turbulent spray modelling: The effect of internal temperature gradient in droplets. International Symposium on Advances in Computational Heat Transfer, 1065–1089. https://doi.org/10.1615/ICHMT.2012.CHT-12.650

[11] Snegirev, A., & Talalov, V. (2012). An accurate and simple approach to allow for the transient temperature gradient in a vaporizing droplet. American Society of Mechanical Engineers, Fluids Engineering Division (Publication) FEDSM, 1(PARTS A AND B), 587–598. https://doi.org/10.1115/FEDSM2012-72047

[12] Jafari, S., Khaleghi, H., & Maddahian, R. (2019). Comparative Analysis of a Single Fuel Droplet Evaporation. 53(1), 81–90. https://doi.org/10.22059/jchpe.2019.273934.1264

[13] Pinheiro, A. P., Rybdylova, O., Zubrilin, I. A., Sazhin, S. S., Sacomano Filho, F. L., & Vedovotto, J. M. (2021). Modelling of aviation kerosene droplet heating and evaporation using complete fuel composition and surrogates. Fuel, 305(August). https://doi.org/10.1016/j.fuel.2021.121564

[14] Both, A., Mira, D., & Lehmkuhl, O. (2022). Evaporation of volatile droplets subjected to flame-like conditions. International Journal of Heat and Mass Transfer, 187, 122521. https://doi.org/10.1016/j.ijheatmasstransfer.2022.122521

[15] P. Ni, "A fuel droplet vaporization model in a hot air stream," Appl. Math. Model., vol. 34, no. 9, pp. 2370–2376, 2010.

[16] S.K. Aggarwal, G. Chen, T.A. Jackson, G.L. Switzer, Vaporization behavior of fuel droplets in a hot air stream, Int. J. Heat Mass Tran. 34 (10) (1991) 2669– 2673.

[17] Spalding, D.B. 1960. "A standard formulation of the steady convective mass transfer problem," Int. J. Heat Mass Transfer, 1, pp. 192-207.

[18] Ranz,W.E., and Marshall,W.R. 1952. "Evaporation from drops Parts I and II," Chem. Eng. Prog., 48(3), p. 141.

[19] Rault, T. M., Vishwanath, R. B., & Gülder, Ö. L. (2021). Soot formation in turbulent swirl-stabilized spray flames in a model combustor fueled with n-butanol/Jet A-1 blends. Fuel, 287(June). https://doi.org/10.1016/j.fuel.2020.119452

[20] Colket, M., Heyne, J., Rumizen, M., Gupta, M., Edwards, T., Roquemore, W. M., Andac, G., Boehm, R., Lovett, J., Williams, R., Condevaux, J., Turner, D., Rizk, N., Tishkoff, J., Li, C., Moder, J., Friend, D., & Sankaran, V. (2017). Overview of the national jet fuels combustion program. AIAA Journal, 55(4), 1087–1104. https://doi.org/10.2514/1.J055361

[21] Edwards, T. (2003). Liquid fuels and propellants for aerospace propulsion: 1903-2003. Journal of Propulsion and Power, 19(6), 1089–1107. https://doi.org/10.2514/2.6946

[22] Edwards, T. (2017). Reference jet fuels for combustion testing. AIAA SciTech Forum - 55th AIAA Aerospace Sciences Meeting, 1–58. https://doi.org/10.2514/6.2017-0146

[23] Lefebvre, A.H., Atomization and Sprays, Taylor & Francis, Bristol PA,1989.

[24] H. Wang, R. Xu, K. Wang, C.T. Bowman, D.F. Davidson, R.K. Hanson, K. Brezinsky, F.N. Egolfopoulos, A physics-based approach to modeling real-fuel combustion chemistry - I. Evidence from experiments, and thermodynamic, chemical kinetic and statistical considerations, Combustion and Flame 193 (2018) 502-519.

[25] R. Xu, K. Wang, S. Banerjee, J. Shao, T. Parise, Y. Zhu, S. Wang, A. Movaghar, D.J. Lee, R. Zhao, X. Han, Y. Gao, T. Lu, K. Brezinsky, F.N. Egolfopoulos, D.F. Davidson, R.K. Hanson, C.T. Bowman, H. Wang, A physics-based approach to modeling real-fuel combustion chemistry - II. Reaction kinetic models of jet and rocket fuels, Combustion and Flame 193 (2018) 520-537. [4] Alluis, C., Beretta, F., D'Alessio, A., Borghese, A., "Ultraviolet absorption and fluorescence measurements in turbulent spray flames", *Proc. Comb. Inst.* 28:311-317 (2000).

EXPERIMENTAL AND COMPUTATIONAL PREMIXED LAMINAR FLAME PROPAGATION STUDIES FOR HYDROGEN CONTAINING FUELS

T.B. Kıymaz[1], D. Güleryüz[1], C. Allouis[1], İ. Gökalp[1], E. Saday[1,2], M. Karaca[3], B. Yılmaz[4], O. Kaya[5], O.C. Kocaman[6], S. Gümrük[6], B. Yazıcı[6], B. Sümer[6], F. Coşkun[7]

1. Department of Mechanical Engineering, Middle East Technical University, Ankara
2. Arçelik R&D Center, Istanbul
3. Department of Aerospace Engineering, Middle East Technical University, Ankara
4. Department of Mechanical Engineering, Marmara University, Ankara
5. PRO-SİS Engineering, Ankara
6. TÜBİTAK SAGE, Ankara
7. Yediç Engineering, Ankara

Abstract

The paper will summarise our recent experimental results obtained with the newly built spherical combustion chamber for laminar flame propagation studies, the flame flashback computations using the OPENFOAM 'reactingDNS' solver, and the ongoing studies on the development of a new laminar Bunsen flame burner to be explored by the laser induced Rayleigh scattering technique for laminar flame thickness measurements

Keywords: Laminar Flame Speed, Flame Flashback, Hydrogen Enriched Natural Gas, Premixed Flames

1 INTRODUCTION

Natural gas is one of the most widely used fossil fuels in the world for both industrial and domestic applications. However, natural gas contributes significantly to global warming due to the high amount of carbon it contains. The zero-emission target, which the whole world aims for, has pushed everyone to find renewable and cleaner energy sources instead of fossil fuels as an energy source. Hydrogen has become one of the most studied and supported areas among clean energy sources because it does not emit carbonaceous molecules that will contribute to global warming. . However, it cannot be replaced with natural gas fully due to different properties between two fuels. Considering the combustion devices used primarily in domestic applications, it will take a certain time to leave fossil fuels completely and start to use only hydrogen, because burning hydrogen has several risks and one of the main risks is the flashback phenomenon that could occur in premixed laminar flames. Due to this reason, studies for the hydrogen-enriched natural gas mixture (HENG) applications gain significant importance in recent years.

Laminar flame speed is a parameter which has crucial impacts on the burning characteristics of all combustion systems [1]. It is important for both laminar and turbulent flames, since the turbulent flame speed correlations are based on the laminar flame speed. There are numerous flame speed measurement techniques developed in combustion studies such as Bunsen flames, flat flames stabilized either by a stagnation plate or in counterflow opposed jets providing the twin flames configuration and the spherically expanding flames [2-6]. In this work, the spherical flame propagation method is used. In this method, a spherical flame propagates outwardly in a closed spherical combustion chamber following spark generated ignition in a homogenous quiescent fuel mixture [7]. Using the time variation of the flame front radius data obtained from the experiments, the laminar flame propagation speed can be determined. The advantage of this method is that laminar flame speed of mixtures at high pressures and high temperatures can be obtained more easily and more accurately compared to the other methods.

From the instantaneous images of the flame front, using the approach of Clavin and Joulin [8], stretched laminar flame burning velocity Vs can be obtain as the time derivative of the flame radius (Rf).

$$V_s = \frac{dR_f}{dt} \quad (1)$$

Flame stretch is defined as the fractional area change of a lagrangian surface element:

$$K = \frac{dA}{Adt} \tag{2}$$

The area is defined as the set of points which are located at the flame surface and has a the same normal velocity as the flame surface. For spherically expanding flame case [9,10]:

$$A = 4\pi R_f^2 \tag{3}$$

$$K = \frac{8\pi R_f}{4\pi R_f^2}\frac{dR_f}{dt} = \frac{2}{R_f}\frac{dR_f}{dt} = \frac{2V_s}{R_f} \tag{4}$$

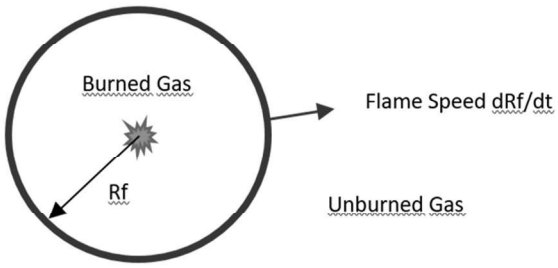


Figure 1. Representation of spherically expanding flame

Markstein [11] is proposed a relationship between stretched and unstretched burning velocities, using the flame stretch concept. If the spherical flame thickness is assumed as an infinitesimally thin and weakly stretched, for a unconfined and quasi-stable flame, the unstretched laminar burning velocity can be found using Markstein length relations. The linear theory relates the stretched laminar flame velocity to unstretched laminar flame velocity, using Markstein length and flame stretch. This method is considered to be accurate for moderate curvature and strain rates.

$$V_s = V_s^0 - LK \tag{5}$$

V_s^0 stands for unstretched laminar flame burning velocity and L is the Markstein length. Markstein length defines as the measure of flames response to stretch. It can be either positive or negative. Positive Markstein length results in decrease of stretched laminar burning velocity with increasing stretch and vice a versa. Smaller Markstein length means, the effect of the flame stretch on burning velocity will be not significant. Negative Markstein length also indication of a more unstable flame.

The unstretched laminar flame speed (S_L^0) can be obtained using the expansion ratio $\sigma = \frac{\rho_u}{\rho_b}$ where ρ_u is the unburned gas density and ρ_b is the burned gas density:

$$\frac{V_s^0}{S_L^0} = \sigma \tag{6}$$

An experimental setup including a specially designed Bunsen burner and laser Rayleigh scattering device is under development, to understand the laminar flame characteristics, other than laminar flame speed, of the combustion of the HENG mixtures. The Bunsen burner, which is specially designed for domestic applications, will experimentally model the laminar combustion and the Rayleigh scattering device provides the characteristics of combustion of HENG mixtures by measuring flame temperature, concentration, speed, and flame thickness.

2 SPHERICAL COMBUSTION CHAMBER EXPERIMENTAL SETUP

The experimental setup consists of a spherical combustion chamber (SCC), a schrilieren visiualization system, a fast camera and a data acquisition system. The focal length between the light source and the Schlieren mirror is set to 2 m. The same 2 m distance is used for the other Schlieren mirror and the knife edge. Two flat mirrors are used to reflect the flame image onto Schlieren mirrors. A high speed camera (Phantom) with 23000 fps and 720x640p resolution is used to collect the flame propagation images. A Nikkor 200mm f/4D IF-ED camera lens is mounted on the high speed camera. Collected data is transferred to the computer.
The detailed layout of the full SCC experimental set-up is shown in Fig.5. There are five different gas lines for Air, CH4, H2, CO and N2 and all the

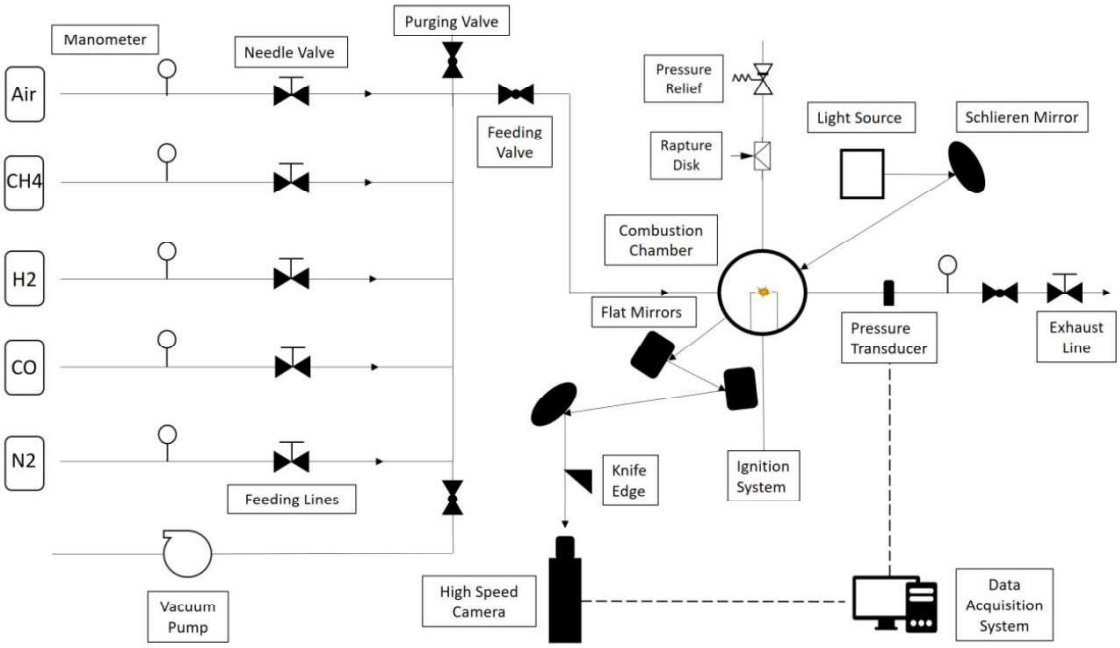


Figure 2. Layout of the Spherical Combustion Chamber Setup

gases are supplied from pressurized tanks to the gas lines with flexible hosepipes. On each line other than N2, there are manometers to observe the pressure on the gas line. A needle valve is located on each line. With these needle valves, the desired gas amount can be supplied to the combustion chamber precisely. For purging the gas line after each experiment, a globe valve is used. Two globe valves are located before and after the combustion chamber. The first one is for the feeding of the combustion chamber and second one for the exhaust line. A vacuum pump is connected to the feeding line to obtain vacuum conditions in the combustion chamber before each experiment. Gas flows to form the reactive mixture are introduced into the combustion chamber with respect to their partial pressures, from the lowest to the highest. A pressure transducer is used to read the pressure value inside the combustion chamber.

After each experiment, the gas lines are purged with N2. For safety reasons, a pressure relief valve and a rupture disk are connected to the combustion chamber. The pressure relief valve opens if the pressure inside the chamber

exceeds 105 bar and releases the pressure inside the chamber continuously to keep the pressure inside the chamber at 105 bar. The rupture disk bursts and releases the pressure inside the chamber immediately if the pressure inside the chamber exceeds 300 bars. The global flow monitoring system of the SCC facility is shown in Fig. 6.

Two tungsten electrodes are placed at the center of the combustion chamber with 1.5 mm distance to each other. To achieve the ignition of the mixture, a pulse generator connected to a DC source is used. A manual switch is used to power the pulse generator and create the ignition spark.

2.1 Preliminary Experimental Results

Preliminary experiments are performed for natural gas-air mixtures at 1 bar absolute pressure. Natural gas is used instead of methane for the first experiments. We assume that this is acceptable for literature comparisons since more than 96% of the natural gas mixture we used is CH4.

At the beginning of each experiment, a vacuum is created inside the spherical chamber using the vacuum pump. Fuel is then supplied to the SCC until the calculated partial pressure is obtained in the chamber. The amount of natural gas is adjusted using a needle valve and the fuel partial pressure inside the chamber is read from the computer using the pressure transducer. Air is

then supplied to the chamber until the total pressure reaches 1 bar. Following several experiments, 10 minutes settling time before ignition is found as optimal for the formation of a homogenous and stationary reactive mixture after air introduction. Ignition is then started, and the flame propagation dynamics is recorded using the high speed camera. Sample sequences of the obtained spherical flame propagation images are shown in Fig.3 for a stoichiometric natural gas and air mixture.

In the first figure of the sequence, the ignition pulse is seen at the center of the combustion chamber; this instance is labelled t=0. After ignition, the flame front starts to expand outwardly with time with a close spherical shape.

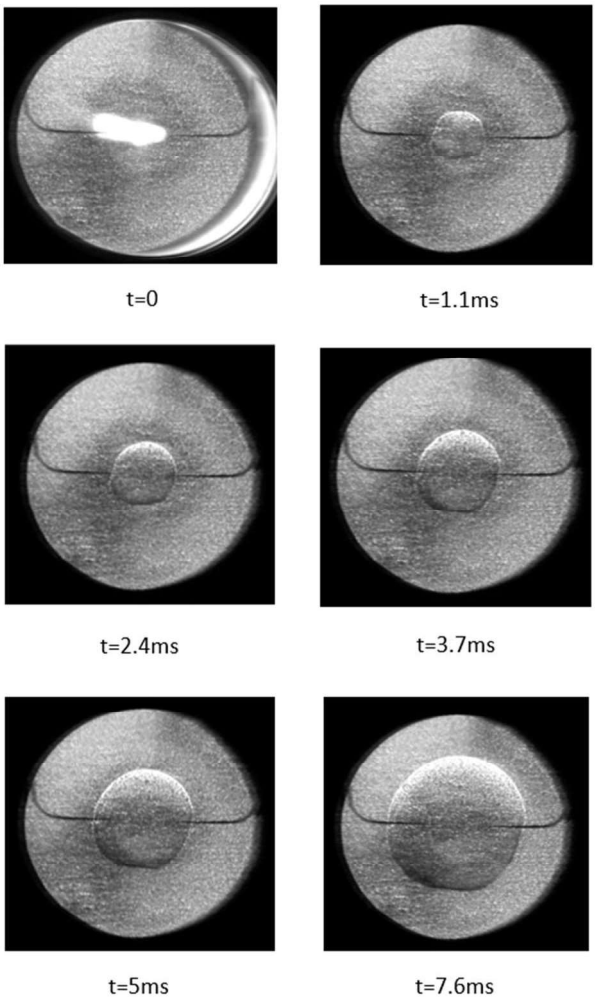
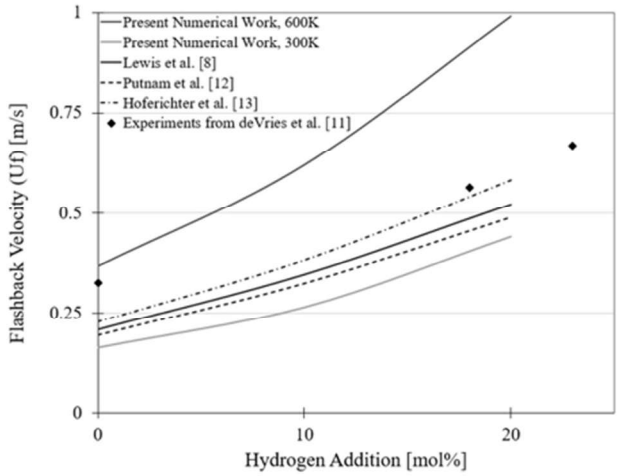


Figure 3. Sequences of flame propagation for a stoichiometric natural gas (96% CH4) and air mixture at atmospheric conditions

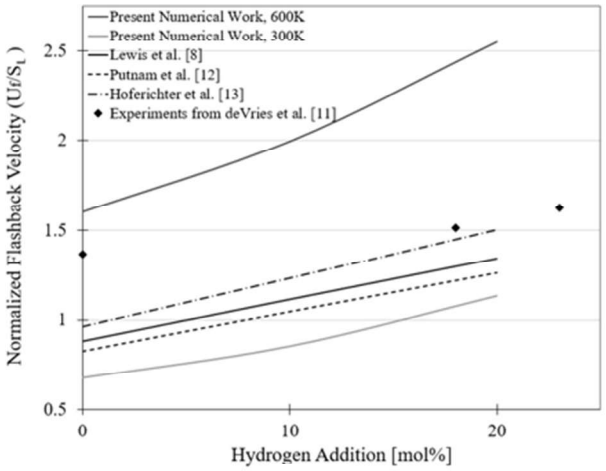
3. NUMERICAL STUDIES ON FLASHBACK

It is important to identify the hydrogen injection limits into the natural gas pipelines for safe hydrogen combustion applications in households. Flashback is defined as the flame propagation in the upstream direction into the unburned premixture. It happens when the laminar flame speed exceeds the inlet mixture bulk velocity, thus it is highly dependent on laminar flame speed. This is an unwanted phenomenon which may damage combustion systems. The purpose of this numerical work is to investigate the change in flashback limits with the addition of hydrogen to methane-air premixture.

The computations are performed using OpenFOAM, which is a open-source computational fluid dynamic software based on finite volume method. A 2D Bunsen burner with 1cm inner diameter is modelled, based on the experimental setup of de Vries et al [12]. Transient computations performed using 'reactingDNS' solver [13] with GriMECH 3.0 [14] for detailed chemistry and differential diffusion is taken into account. Details of the computational domain and numerical methodology can be found in [15]. Fig. shows the change of flashback limits with the addition of hydrogen to methane-air premixture for numerical, theorotical and experimental results. Flashback is observed at the velocities below the curves. Fig. 4a shows the flashback velocity increases with the addition of hydrogen to premixture for all cases. Fig. 4b shows the same results with a normalized value, which is obtained by dividing the flashback velocity to laminar flame speed. It shows that with the addition of more than 10% hydrogen, normalized flashback velocity is above 1 and increases (except for 300K wall temperature case). This result shows that, simple definitions only related with the laminar flame speed for flashback limits needs further investigation.



(a)



(b)

Figure 4. Comparison of experimental and calculated flashback limits

4.LAMINAR FLAME BUNSEN BURNER DESIGN

Laminar Bunsen flame is one of the most studied flames in the history. It can be used to capture most of the fundamental properties of the flames using different techniques, such as the laminar flame speed and flame thickness. In the flashback limits part, it is mentioned that the experimental results are taken from another work and there is no detailed information about the burner wall temperature, which effects the flashback limits tremendously. It is decided to build an experimental set up to collect data to validate these computations and also to provide safety guidelines to determine the safe limits for enriching natural gas domestic appliances with hydrogen.

An additional advantage of the Bunsen burner configuration is that it will permit determining the thickness of the laminar flame front for various hydrogenated fuel mixtures. The Rayleigh scattering measurement technique will be used for this purpose. Together with the laminar flame propagation velocity, the laminar flame thickness is the other important laminar flame property which determines the turbulent flame regimes. Since the hydrogen addition into natural gas (or methane) has an important effect on laminar flame thickness, it should be studied in detail.

Fig.5 shows the manufactured Bunsen burner and Fig.6 is the sketch of the cross sectional area. Co-axial burner is designed to sustain a pilot flame or an inerting gas flow to isolate the laminar flame from its surroundings and to diminish several potential flame instability sources, including those due the gravity induced buoyancy effects. The inner diameter of the burner exit is 10 mm and the burner is made of stainless steel. Sintered filters are placed in both main and pilot fuel passages, in order to laminarize and homogenize the incoming flow.

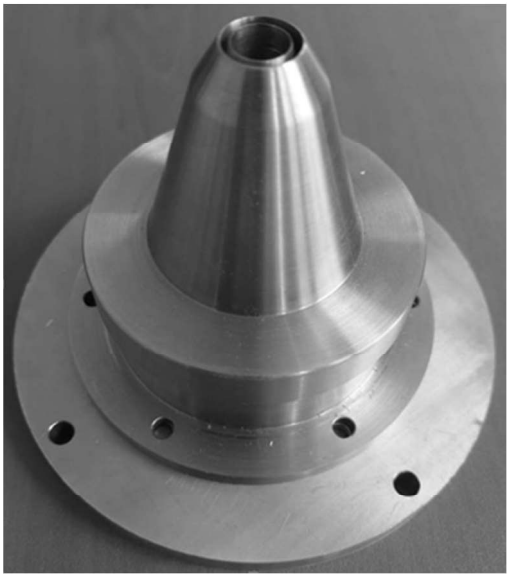


Figure 5. Designed co-axial Bunsen burner

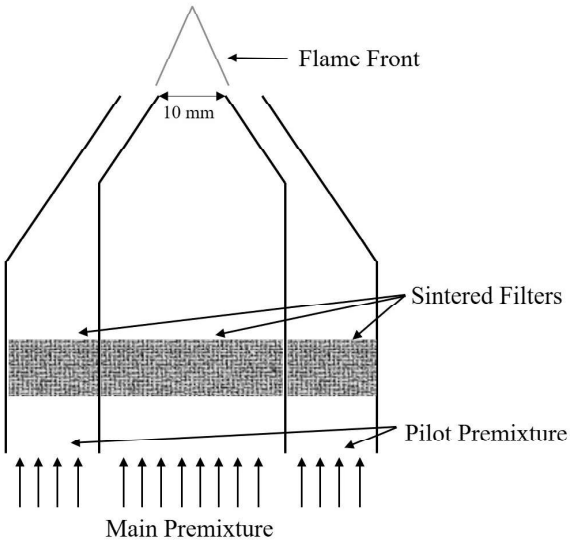


Figure 6. Schematic of the designed co-axial Bunsen burner

5. CONCLUSION AND FUTURE WORK

This work summarized our recent studies on laminar premixed flames. Spherical combustion chamber is installed and first experiments are performed successfully using natural gas and air premixture at atmospheric pressure. An accurate image processing method is under development for post-processing the flame images. The quality of the Schlieren images will be improved by changing one of the quartz window on system, since the surface quality is not sufficient enough. This creates optical noise for the images and leads to non-optimal image qualities. To capture the density differences better, the knife edge will be replaced by a pinhole. After that, unstretched laminar flame speed of hydrogen-natural gas-air premixture will be determined for various equivalence ratios and hydrogen addition rates. Also, high pressure experiments (up to 10 bars) will be performed as a second stage.

Flashback limits are presented for 2D numerical simulations up to 20% hydrogen addition to methane-air premixture. Results clearly shows that hydrogen addition increases the flashback risk. This is not only related with increasing laminar flame speed and it should be further investigated. To validate results, laminar Bunsen type burner is designed and presented in the last chapter. This setup will also be used for determining flame thickness of hydrogenated natural gas premixtures using Rayleigh scattering system. Installation of the experimental setup is in progress.

REFERENCES

[1] N. Peters (2000) Turbulent Combustion. Cambridge Monographs on Mechanics. Cambridge University Press

[2] Bouvet, N., Chauveau, C., Gökalp, I., Lee, S.-Y., & Santoro, R. J. (2011). Characterization of syngas laminar flames using the Bunsen burner configuration. International Journal of Hydrogen Energy, 36(1), 992–1005. https://doi.org/10.1016/j.ijhydene.2010.08.147

[3] Hu, S., Gao, J., Gong, C., Zhou, Y., Bai, X. S., Li, Z. S., & Alden, M. (2018). Assessment of uncertainties of laminar flame speed of premixed flames as determined using a Bunsen burner at varying pressures. Applied Energy, 227, 149–158. https://doi.org/10.1016/j.apenergy.2017.09.083

[4] Halter, F., Chauveau, C., Djebaïli-Chaumeix, N., & Gökalp, I. (2005). Characterization of the effects of pressure and hydrogen concentration on laminar burning velocities of methane–hydrogen–air mixtures. Proceedings of the Combustion Institute, 30(1), 201-208.

[5] Kelley, A. P., & Law, C. K. (2009). Nonlinear effects in the extraction of laminar flame speeds from expanding spherical flames. Combustion and Flame, 156(9), 1844–1851. https://doi.org/10.1016/j.combustflame.2009.04.004

[6] Kim, H. J., Van, K., Lee, D. K., Yoo, C. S., Park, J., & Chung, S. H. (2020). Laminar flame speed, Markstein length, and cellular instability for spherically propagating methane/ethylene–air premixed flames. Combustion and Flame, 214, 464–474. https://doi.org/10.1016/j.combustflame.2020.01.011

[7] Lewis B, Von Elbe G (2012) Combustion, flames and explosions of gases. Elsevier, London

[8] P. Clavin, G. Joulin, J. Phys. Lett. (1983) 44: L1–12.

[9] C.K. Law, Proc. Combust. Inst. (1988) 22: 1381–1402.

[10] N. Peters, Proc. Combust. Inst. (1986) 21: 1231–1250.

[11] G.H. Markstein (1964) Non-Steady Flame Propagation. Pergamon, New York, p. 22.

[12] De Vries, H. et al. (2017). The impact of natural gas/hydrogen mixtures on the performance of end-use equipment:

interchangeability analysis for domestic appliances. Applied Energy 208: 1007-1019. https://doi.org/10.1016/j.apenergy.2017.09.049

[13] Zhang, F., Bonart, H., Zirwes, T., Habisreuther, P., Bockhorn, H., & Zarzalis, N. (2014). Direct Numerical Simulation of Chemically Reacting Flows with the Public Domain Code OpenFOAM. High Performance Computing in Science and Engineering '14, 221–236. https://doi.org/10.1007/978-3-319-10810-0_16

[14] Smith Gregory P, Golden David M, Frenklach Michael,
Moriarty Nigel W, Eiteneer Boris, Goldenberg Mikhail,
Bowman C Thomas, Hanson Ronald K, Song Soonho,
Gardiner Jr William C, Vitali V. Lissianski, and zhiwei qin.
http://www.me.berkeley.edu/gri_mech/.

[15] Kıymaz, T. B., Böncü, E., Güleryüz, D., Karaca, M., Yılmaz, B., Allouis, C., & Gökalp, İ. (2022). Numerical investigations on flashback dynamics of premixed methane-hydrogen-air laminar flames. *International Journal of Hydrogen Energy*, *47*(59), 25022-25033.

Numerical Study on the Performance of a Flat-Tubular Solid Oxide Fuel Cell: The Effect of Burner Thermal Power and Furnace Geometry

Fethi Mustafa ÇİMEN[1], Serhat KARYEYEN[2] , Mustafa İLBAŞ[3]

1. Department of Energy Systems Engineering, Faculty of Technology, Gazi University, Ankara; email: fethimustafacimen@gazi.edu.tr
2. Department of Energy Systems Engineering, Faculty of Technology, Gazi University, Ankara; email: serhatkaryeyen@gazi.edu.tr
3. Department of Energy Systems Engineering, Faculty of Technology, Gazi University, Ankara; email: ilbas@gazi.edu.tr

Abstract

Considering the environmental effects of fossil fuels and the problem of climate change in the current century, the performance and emission values of combustion systems are of great importance. Solid oxide fuel cells (SOFCs) are promising devices as a highly suitable energy conversion tool, especially for high temperature applications. In this study, parametric analyzes were performed on the performance of a combustion chamber-SOFC hybrid system modeled on the basis of computational fluid dynamics. In the analyses, a SOFC with a flat-tube geometry, which has come to the fore with its many advantages especially recently, was modeled and the cell was fed with hydrogen. In this numerical study, the effect of burner thermal power and furnace/combustion chamber geometry have been investigated for the highest performance of the SOFCs. Thanks to the created combustion chamber geometry and burner thermal power, flame temperatures have become more uniform and have created a favorable environment for the operation of SOFCs. In addition, the power densities of the developed SOFC model under different operating conditions were examined and evaluated comparatively. The findings show that the hybrid SOFC-burner system is easily applicable in the future.

Keywords: Combustion Technique, Furnace Geometry, SOFC, CFD Modelling.

1 INTRODUCTION

The increase in population around the world has brought with it the demand for energy. This energy demand is mostly met by fossil fuels. However, as it is known, the use of fossil fuels by direct and inefficient systems raises the problem of global warming. The increase in global warming with each passing day directly affects the living life on earth. All these phenomena require turning to alternative options in energy systems. At this point, fuel cell technology is promising thanks to its high efficiency and not having harmful emissions.

Solid oxide fuel cells are distinguished from other fuel cell types because they are suitable for high operating temperatures and are preferred in many studies. In the literature, there are different studies focusing on various issues related to solid oxide fuel cells. Baldinelli et al. [1] investigated the performance of a SOFC stack using variable fuel compositions as the anode feeder. They also developed a performance estimation tool to examine SOFC performance in their study. They argued that the model could be used to properly evaluate the performance of any particular SOFC since the error rate in the estimation tool they developed was less than 1%. Saisirirat [2] has developed a hybrid SOFC-gas turbine model in MATLAB in his study. A detailed thermodynamic analysis of the created model was carried out. As a result of the study, it was concluded that fuel cell performance was significantly affected by temperature. Lorenzo and Fragiacomo [3] have created a stationary simulation model of a syngas-fed SOFC system in their study. In addition, they simulated SOFC system performance in Matlab environment. In the study, they investigated cell efficiency by making parametric analyzes with hydrogen and carbon monoxide rich fuel input. Cinti and Desideri [4] used urea as a fuel in their work. As a result of the study, it was observed that the theoretical efficiency of SOFC was reached up to 40-60%. In addition to these studies, there are many studies designed and conducted with various fuels and different systems related to SOFCs in the literature [5–12].

In this study, it is aimed to perform performance analyzes of fuel cells placed in some selected parts of the combustion chamber, depending on the temperature distribution in the combustion chamber. The focus of the study was the optimization of the fuel cell combustion chamber hybrid system and the increase in system efficiency.

2 MATHEMATICAL MODELING

In the study, a hybrid fuel cell-burner system was designed. In the combustion system, methane was used as fuel, and in the fuel cell system, the anode feed was made with hydrogen. Air was used as the oxidizer in both systems. Figure 1 shows the designed burner.

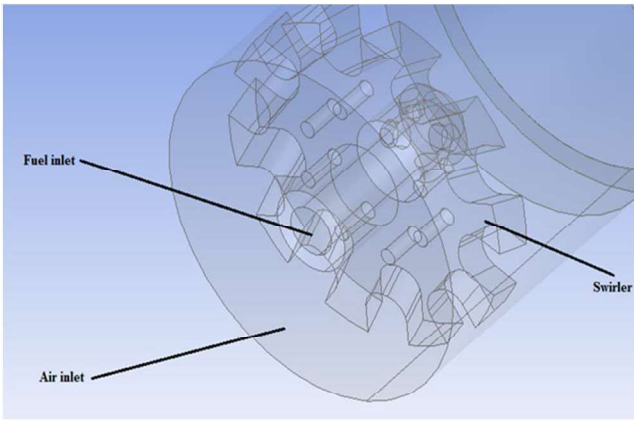
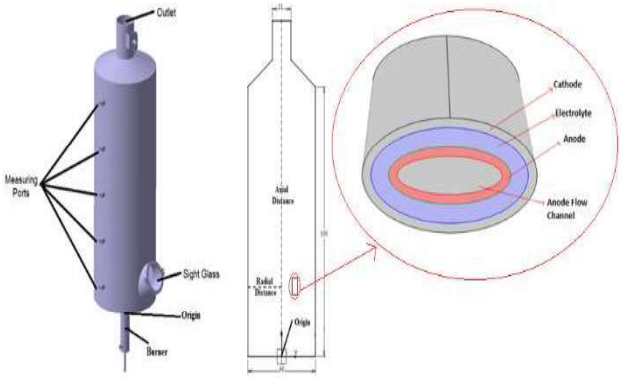


Figure 1. The Burner

Methane-air combustion analyzes were performed using the Ansys Fluent CFD code. Depending on the analysis results, the temperature data at the determined points in the combustion chamber were obtained. Based on these temperature data, the performance of a model flat-tube solid oxide fuel cell developed in COMSOL Multiphysics software was analyzed. Figure 2 shows the hybrid model created. In addition, the used parameters for the Burner-fuel cell system are given in Table 1.



(a) (b)

Figure 2. 3-D (a) and cross-sectional (b) view

Table 1. Design Parameters

Parameter	**Value**
Pressure	1[atm]
Inlet Temperature	1158, 1188, 1196, 1134, 1175 [K]
Cell length	30 mm
Initial cell polarization	0.05[V]
Anode inlet composition	Hydrogen
Cathode inlet composition	Air (79% N_2, 21% O_2)

3 RESULTS AND DISCUSSIONS

In the modeling process of the combustion system, combustion was carried out with an oxygen concentration of 21%, and the system power was determined as 10 kW in the first stage of the study. Then, the fuel flow was increased and the analyzes were made when the system power was 20 kW.

In Figure 3, the power outputs of the fuel cell models for the system with 10 kW burner power are given. Depending on the temperature distribution of the combustion chamber, the power curves obtained by the fuel cells placed at the 6 determined points of the combustion chamber are seen. Fuel cells are placed at radial distances of 2 cm and 3 cm in the system. Axial

distances were determined as 20 cm, 30 cm and 40 cm, respectively. The temperature values in the selected regions of the system were found to be 1041 K, 1013 K, 883 K, 705 K, 802 K and 779 K, respectively. When the graph is examined, it is seen that there is an obvious temperature difference in the combustion chamber. This has significantly affected the performance of fuel cells. The maximum and minimum powers of fuel cells are approximately 523 W/m^2 and 66 W/m^2.

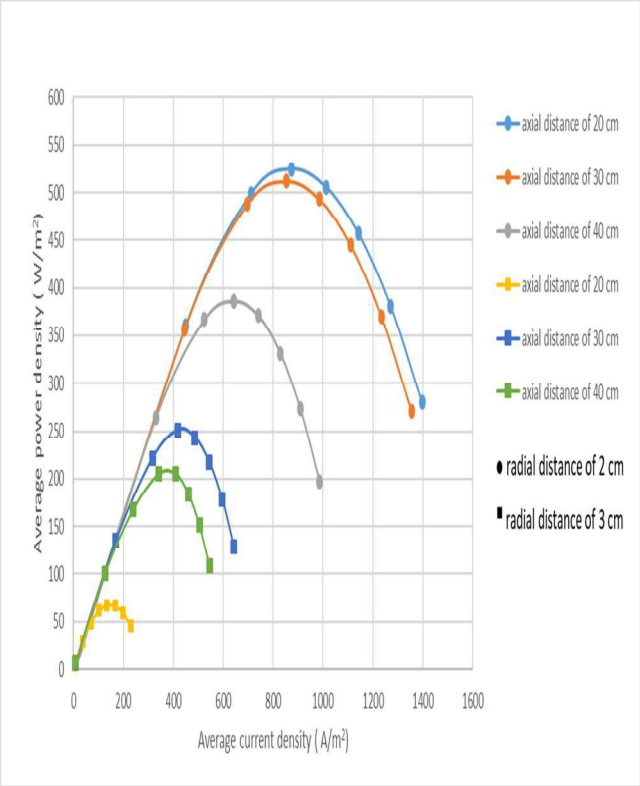


Figure 3. Power curves of the FT-SOFCs for the system with a burner output of 10 kW

Figure 4 shows the analysis results of the fuel cells placed at the same points for the case of increasing the system power to 20 kW. It is seen that increasing the system power causes an increase in the temperature values in the combustion chamber. As a result of this situation, the maximum power values of the fuel cells have increased and almost the same curves have been obtained. In these conditions, the maximum cell power of the fuel cells integrated into the system was found to be approximately 550 W/m^2.

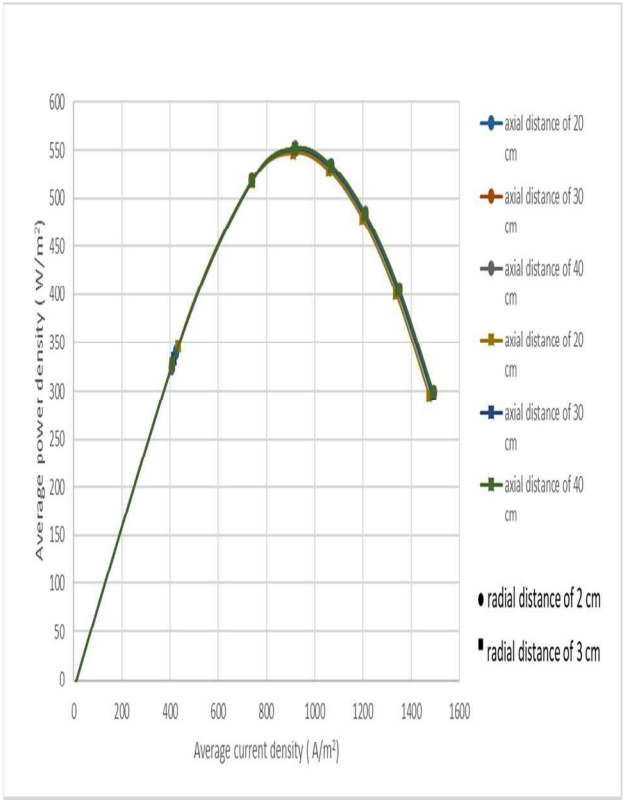
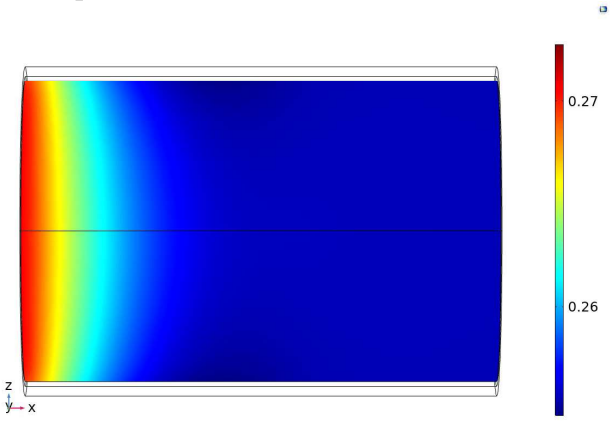
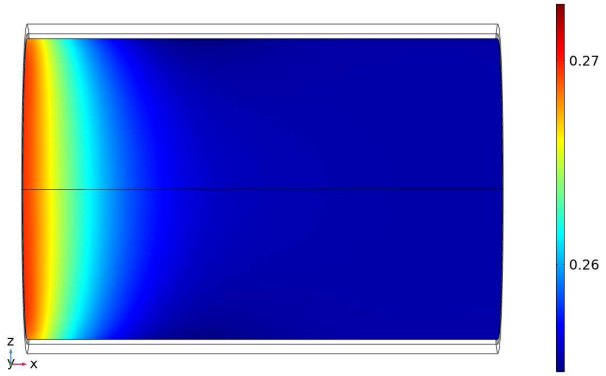


Figure 4. Power curves of the FT-SOFCs for the system with a burner output of 20 kW

Figure 5 shows the mole fraction of hydrogen supplied from the anode flow channel for 10 kW (a) and 20 kW (b) systems. As it can be understood from the previous power curves, the increase in the burner power has also increased the consumption rate of hydrogen since it affects the temperature distribution.



(a)



(b)

Figure 5. Mole fraction of hydrogen for 10 kW (a) and 20 kW (b) systems

4 CONCLUSIONS

In this study, the performance analysis of SOFCs, which are especially suitable for high temperature operations, was made. In the study, a hybrid model of SOFC-combustion system was created. The system is simulated for two different powers such as 10 kW and 20 kW to select the most suitable combustion chamber design and combustion conditions. The findings of the study can be stated as follows:

- SOFC performance changed significantly with temperature change.
- When the system power was determined as 10 kW, different power outputs were obtained from the cells placed at different points in the combustion chamber.
- A more uniform temperature distribution was obtained in the combustion chamber with a burner power of 20 kW.
- The high temperatures achieved uniformly in the combustion chamber allowed SOFCs to achieve not only similar but also high performance.

The results of the study also showed that with the increase of the burner power, the fuel cells can be placed in more distant regions from the center. This situation is expected to provide convenience in practice. In addition, it is foreseen that fuel cells will operate more effectively with lower burner power as a result of changes to be made in the geometry of the combustion chamber in future studies.

ACKNOWLEDGEMENT

We would like to thank Nigde Ömer Halisdemir University and Gazi University for the use of softwares.

REFERENCES

[1] A. Baldinelli, L. Barelli, G. Bidini, Performance characterization and modelling of syngas-fed SOFCs (solid oxide fuel cells) varying fuel composition, *Energy,* Vol. 90, pp.2070–84, 2015. https://doi.org/10.1016/j.energy.2015.07.126.

[2] P. Saisirirat, The Solid Oxide Fuel Cell (SOFC) and Gas Turbine (GT) Hybrid System Numerical Model, *Energy Procedia*, Vol. 79, pp. 845-50, 2015. https://doi.org/10.1016/j.egypro.2015.11.576.

[3] G. De Lorenzo, P. Fragiacomo, Energy analysis of an SOFC system fed by syngas, *Energy Convers Manag,* Vol. 93, pp.175–86, 2015. https://doi.org/10.1016/j.enconman.2014.12.086.

[4] G. Cinti, U. Desideri, SOFC fuelled with reformed urea, *Appl Energy,* Vol. 154, pp. 242–53, 2015. https://doi.org/10.1016/j.apenergy.2015.04.126.

[5] F.M. Cimen, B. Kumuk, M. Ilbas, Simulation of hydrogen and coal gas fueled flat-tubular solid oxide fuel cell (FT-SOFC), *Int J Hydrogen Energy*, Vol. 47, pp. 3429–36, 2022. https://doi.org/10.1016/j.ijhydene.2021.07.231.

[6] M. Ilbas, M.A. Alemu, F.M. Cimen, Comparative performance analysis of a direct ammonia-fuelled anode supported flat tubular solid oxide fuel cell: A 3D numerical study, *Int J Hydrogen Energy,* Vol. 47, pp. 3416–28, 2022. https://doi.org/10.1016/j.ijhydene.2021.10.080.

[7] O.A. Marina, C.A. Coyle, E.C. Thomsen, D.J. Edwards, G.W. Coffey, L.R. Pederson, Degradation mechanisms of SOFC anodes in coal gas containing

phosphorus, *Solid State Ionics,* Vol. 181, pp. 430–40, 2010. https://doi.org/10.1016/j.ssi.2010.01.018.

[8] J.P. Trembly, R.S. Gemmen, D.J. Bayless, The effect of IGFC warm gas cleanup system conditions on the gas-solid partitioning and form of trace species in coal syngas and their interactions with SOFC anodes, *J Power Sources,* Vol. 163, pp. 986–96, 2007. https://doi.org/10.1016/j.jpowsour.2006.10.020.

[9] M. Asmare, M. Ilbas, F.M. Cimen, C. Timurkutluk, S. Onbilgin, Three-dimensional numerical simulation and experimental validation on ammonia and hydrogen fueled micro tubular solid oxide fuel cell performance, *Int J Hydrogen Energy,* Vol. 47, pp. 15865–74, 2022. https://doi.org/10.1016/j.ijhydene.2022.03.057.

[10] M. Ilbas, S. Karyeyen, F.M. Cimen, Numerical investigation of combustion and flame characteristics for a model solid oxide fuel cell performance improvement, *Fuel,* Vol. 322, pp. 124188, 2022. https://doi.org/10.1016/j.fuel.2022.124188.

[11] A. Cuneo, V. Zaccaria, D. Tucker, A. Sorce, Gas turbine size optimization in a hybrid system considering SOFC degradation, *Appl Energy*, Vol. 230, pp. 855–64, 2018. https://doi.org/10.1016/j.apenergy.2018.09.027.

[12] Y.D. Lee, K.Y. Ahn, T. Morosuk, G. Tsatsaronis, Exergetic and exergoeconomic evaluation of an SOFC-Engine hybrid power generation system, *Energy*, Vol. 145, pp. 810–22, 2018. https://doi.org/10.1016/j.energy.2017.12.102.

NUMERICAL STUDY ON IMPACT OF COMBUSTOR METRICS OF TURBOPROP ENGINE USED IN AIR FREIGHTER

Mehmet Kirmizi[1], Hakan Aygun[2] and Onder Turan[3]

1. Aviation Higher Vocational School, Ege University, Turkey; email: mehmet.kirmizi@ege.edu.tr
2. Department of Aircraft Powerplant and Maintenance, Firat University, Turkey; email: haygun@firat.edu.tr
3. Faculty of Aeronautics and Astronautics, Eskisehir Technical University, Eskisehir, Turkey; email: onderturan@eskisehir.edu.tr

Abstract

Combustion chamber is the chief component of turboprop engine, and its parameters could affect the performance behavior of aero-engine, so it is particularly of high significance to examine parameters of combustor involving combustor efficiency (CE), combustor pressure ratio (CPR) and fuel to air ratio (FAR). In this context, a conceptual turboprop engine (CTE) that is very similar AE2100 turboprop are subjected to parametric cycle analysis at different flight conditions. With regard to analysis findings, specific fuel consumption of CTE decreases from 0.2438 to 0.2218 kg/kWh due to rising combustor efficiency. Moreover, thanks to lowering CPR in the combustor, SFC is prone to diminish from 0.2277 to 0.2193 kg/kWh. Lastly, the higher FAR leads to increase SFC from 0.1968 to 0.2472 kg/kWh whereas it makes thrust of CTE improvement from 14.27 to 14.41 kN. Moreover, the higher CE results in the higher thrust that changes from 14.4 to 14.34 kN whereas the lower CPR leads to increase net thrust from 13.97 to 14.5 kN. When considering these outcomes, it is clear that to enhance CPR and CE of the CTE make SFC lower, thereby the engine higher eco-friendly. It is thought that information from these assessments help in understanding how much the engine has improvement capacity that is hot topic followed by the related engineers.

Keywords: Turboprop, combustor, gas turbine performance

1 INTRODUCTION

With the enhancement of aerospace engineering, gas turbine engines used in aviation industry have experienced important developments that lead to increase overall efficiency, thereby lowering fuel consumption. When compared reciprocating engines, gas turbine engines have superiority such as higher power-to-weight ratio and reliability [1]. Especially, as usage of these systems increases in unmanned aerial vehicles that perform strategic tasks, the related engineers give great importance to the development of these systems.

Air freighter transportation is one of the leading sectors contributing countries' economies [2]. However, the raised aviation activities mean higher environmental pollution from aicraft engines. When considering that aviation CO_2 emissions were recorded as 915 million tonnes, it is significant to quantify environmental performance of aircrafts [3]. On the other hand, another anxiety from these aviation emissions is the emergence of various diseases. To enable sustainable environment, the related people should handle aviation field in holistic manner that includes positive and negative effects on human beings. Otherwise, although passenger or freighter could be transported expeditiously and comfortably, environmental concerns related to aviation may not be overcome. The main reason of environmental impact is to being released emissions of gas turbine engines that operate by burning fossil fuel or kerosene. In this context, fuel efficiency should be elevated as possible as since aviation sector utilizes about 3 % of total fossil fuel [4]. Undoubtly, more efficient engines or enhancement of exisiting ones can help in achieving this target. Moreover, to mitigate aircraft emissions, several attempts have been performed, which include Kyoto Protocol, emission trading system (as regionally) and CORSIA (as globally). Additionally, sustainable aviation fuels and electrical concepts for aircraft operation has been initiated to decrease dependence of fossil fuels by several well known companies [5].

Many scientists have addressed on negative impacts of aviation engines including piston-prop, turbojet, turboprop and turbofan engines. From

2000 year to nowadays, it could be cited a number of studies in where environmental impacts of gas turbine were searched. When considering novel studies, Balli et al. [6] investigated mini turbojet engine producing 125 N with environmental and economic aspects at four different RPMs. The authors stated that as the engine is operated higher RPMs, specific emission index goes down from 13.34 to 5.44 mPts/MJ whereas emission impact increases from 139.89 to 241.23 mPts/h due to raising fuel flow to combustor chamber. Moreover, Akdeniz et al. [7] dealt with several aspects including environmental impacts of turbofan engine generating thrust of 14.71 kN, whose combustion chamber enjoys the highest environmental impact since exergy efficiency is measured in it. Lastly, Topal and Turan addressed how combustor inlet temperature (CIT) and air to fuel ratio affect energy and exergy efficiencies. As CIT increases, both efficiencies of the combustor experience increment whereas adverse effect is seen at higher fuel to air ratio.

Main difference of this paper is to elaborate effects of three parameters regarding combustor of the turboprop engine. To investigate influences of combustor efficiency, pressure drop rato and FAR, parametric cycle equations are utilized by encoding MATLAB environment.

2 SYSTEM DESCRIPTION

Turboprop engine, which is the kind of gas turbine engine are generally equipped to military freighter airplane and regional commercial civil aircrafts. These engines were seen on aircraft soon after initialized jet age, which consist of two major parts such as core engine and propeller. Turboprop engines had come out the market so as to complement the shortcomings of turbojet and piston engines. Namely, turbojet consumes highly fuel, which means less endurance whereas piston engines have higher efficiency al lower altitude. The fuel power in turboprop is utilized to turn propeller whereas in turbojet to impel exhaust gases as quickly as possible. To efficiently make propeller operate, revolution speed of turbine that turn propeller is not kept same with each other by using reduction gearbox in turboprop engine, otherwise propeller could not withstand the forces acting on it. Main thrust is obtained from propeller which is turned by free turbine through reduction gearbox whereas appreciable one is produced through exhaust. Many heavy transport aircraft that operate moderate speeds not exceeding 0.7 Ma has been equipped with these engines, which leads to efficiently operation at most of flight phase [1]. When considering AE2100 engine, the specifications are presented in Table 1. Fig.1 illustrates cross-section of the engine with its major components. As can be understood, AE2100 engine consist of two shafts as well as air compressor, combustor, gas turbine and free turbine. Main applications of AE2100 turboprop are C130J, C27J and Saab 2000[8]. At sea level conditions and maximum power, this engine produces about power of 3400 kW whereas becomes 2650 kW at 0.59 Mach and altitude of 6.7 km.

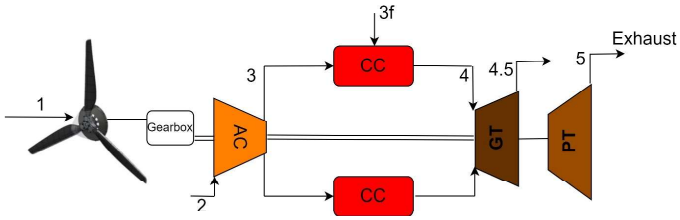


Figure 1. Two-dimensional illustration of AE2100 turboprop engine

Table 2. Several specifications regarding the turboprop as well as values of operation condition

Parameters	Value
Flight Mach number	0.59
Flight altitude (km)	6.7
Ambient temperature (K)	261.46
Ambient pressure (kPa)	54.15
Air mass flow ($kg.s^{-1}$)	9.68
Turbine inlet temp. (K)	1270
Compressor pressure ratio	16.6
Propeller efficiency	0.8
Shaft power (kW)	2651.4
Combustor pressure ratio	0.9<CPR<0.99
Burner efficiency	$0.9<\eta_{comb.}<0.99$
Fuel to air ratio (FAR)	0.0149<FAR<0.0189

3 MATERIALS AND BACKGROUND

3.1 Turboprop performance metrics

Prior to calculating specific fuel consumption and overall efficiency, equivalent shaft power should be measured by taking into consideration exhaust thrust power. It is written as [9, 10]:

$$ESP = SP + \tau_{core} V / \eta_{prop} \quad (1)$$

Exhaust thrust, as defined at other types of gas turbine, is calculated from conservation of momentum. It is presented as:

$$\tau_{core} = \dot{m}_a \left[(1+f) V_e - V_i \right] + \left(P_e - P_i \right) A_e \quad (2)$$

Specific fuel consumption of turboprop engine is ratio of fuel flow rate to equivalent shaft power. It is expressed as:

$$SFC = \frac{\dot{m}_f}{ESP} \quad (3)$$

Overall efficiency is ratio of equivalent shaft power to fuel power injected to the combustor. It is presented as:

$$\eta_{overall} = \frac{ESP}{\dot{m}_f LHV} \quad (4)$$

3.2 Combustor chamber parameters

Pressure ratio of combustor

When assumption the system as ideal, combustor pressure ratio is neglected. However, at real analyses, this parameter should be considered. CPR is ratio outlet pressure of combustor to inlet pressure. Pressure drop could mainly result from friction in the combustor wall.

$$\pi_{cc} = \frac{P_4}{P_3} \quad (5)$$

where π_{cc} is pressure ratio in the combustor.

To establish energy equations in the combustor so as to determine fuel to air ratio, the first law of thermodynamics should been subjected to the combustor.

$$\dot{m}_{core}(1+f) cp_h T_4 = \dot{m}_{core} cp_c T_3 + \eta_{cc} \dot{m}_f Q_{LHV} \quad (6)$$

where $\dot{m}_{core}$ is the air mass flow through the core section of the engine whereas cp_h represents specific heat for hot air gases and Q_{LHV} is lowering heat value of the fuel, which is 42800 kJ/kg. Also, T_4 is turbine inlet temperature.

The above equation is rearranged as follows:

$$f = \frac{\tau_\lambda - \tau_r \tau_{comp.}}{\eta_{cc} Q_{LHV} / (cp_c T_0) - \tau_\lambda} \quad (7)$$

where f is fuel to air ratio whereas η_{cc} is efficiency of combustion and τ_λ is enthalpy ratio for the combustor.

4 RESULTS AND DISCUSSION

In this section, performance behavior of turboprop engine depending on combustor parameters as well as flight conditions is presented. For this aim, AE2100 engine is subjected to parametric cycle analyses at Mach of 0.59 and altitude of 6.7 km. Main motivation of this study is to elaborate effects of combustor efficiency ranging from 0.9 to 0.99, pressure ratio of combustor changing from 0.9 and 0.99 and air to fuel ratio varying from 0.0149 to 0.0189.

Initially, Fig.2 demonstrates how performance of turboprop engine changes with combustor efficiency. As expected, the higher η_{comb} results in lowering fuel flow, which changes from 0.1803 to 0.1633 kg/s. Moreover, SFC of AE2100 experiences decrement from 0.2438 to 0.2218 kg/kWh. These findings validate that engine efficiency affects favourably from combustor with higher efficiency. Namely, thermal and overall efficiencies increase from 34.5 to 37.93 % and from 24.65 to 27.08 %, respectively.

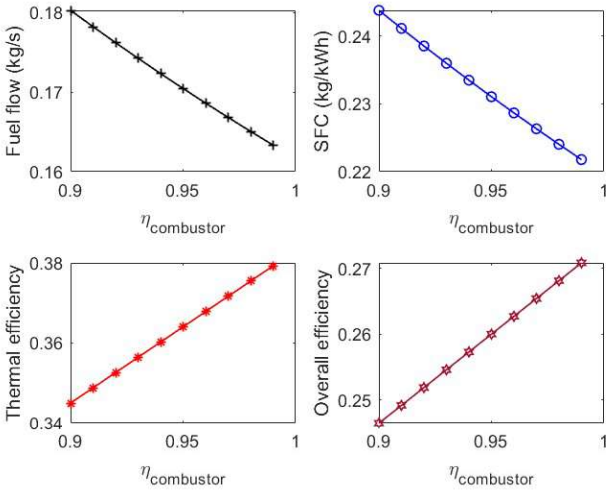


Figure 2. Variation of turboprop performance with respect to combustor efficiency

As for Fig.3, impact of pressure ratio in the combustor is presented. As seen in, although fuel flow does not change, which is measured as 0.1633 kg/s whereas SFC of the engine decreases from 0.2277 to 0.2193 kg/kWh, which corresponds to 3.68 %. As π_{comb} is elevated, thermal efficiency raises from 36.95 % to 38.35 % while overall efficiency experiences the decrement from 27.32 % to 26.95 %. The reason for this could be due to decreasing propulsive efficiency.

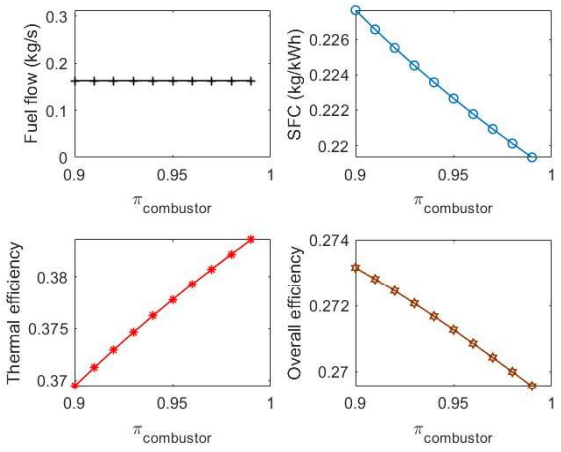


Figure 3. Variation of turboprop performance with respect to combustor pressure ratio

This figure emphasizes how fuel to air ratio affects performance of turboprop engine. When considering patterns in the figure, as the FAR is increased, fuel flow injected the combustor becomes higher. Namely, it raises from 0.1442 to 0.1830 kg/s. On the other hand, SFC of the engine is prone to raise from 0.1968 to 0.2472 kg/kWh. This increment corresponds to 25.6 %. However, thermal efficiency varies between 42.74 % and 34.02 %, which decreases by 8.72 %. Lastly, a decrement in the overall efficiency of the engine occurs by 6.22 % owing to increasing FAR, namely it diminishes from 30.52 to 24.30 %.

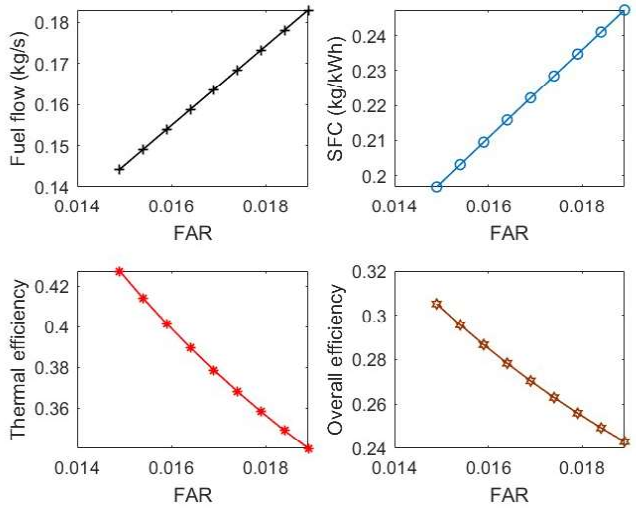


Figure 4. Variation of turboprop performance with respect to fuel to air ratio

Figs.5-6 present effect of flight conditions on the engine parameters mentioned above figures. As can be expected, fuel flow as well as SFC decrease with increment of altitude. However, efficiencies of the engine are not been affected as strict as other two parameters. In this context, as the altitude is elevated from 5 km to 6 km, fuel flow changes between 0.1922 kg/s and 0.1749 kg/s, which corresponds to 9 % whereas SFC of the engine slightly changes with elevated altitude. Namely, it diminishes from 0.2252 kg/kWh to 0.2231 kg/kWh. Similarly, effects of altitude on efficiencies are not discernable. In other words, thermal varies between 37.36 and 37.70 % whereas overall efficiency increases from 26.51 % to 26.86 %.

Finally, Fig.6 presents how relationship there is between Mach and performance metrics. As can be seen, the higher the Mach, fuel flow becomes greater, namely it ascends from 0.1411 kg/s to 0.1657 kg/s. In contrast, the higher Mach leads to lowering SFC from 0.2252 to 0.2214 kg/kWh which corresponds to 1.68 %. Lastly, efficiencies are more susceptible to variation of Mach. In this context, thermal efficiency raises from 37.35 % to 37.99 % while overall efficiency experiences decrement from 27.30 % to 27.06 %.

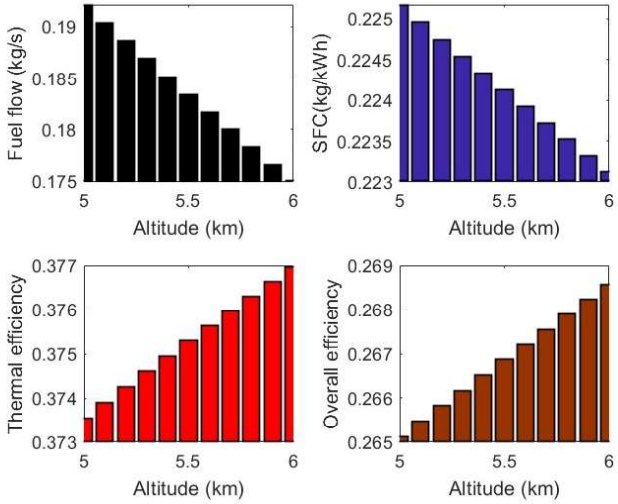


Figure 5. Variation of turboprop performance with respect to altitude

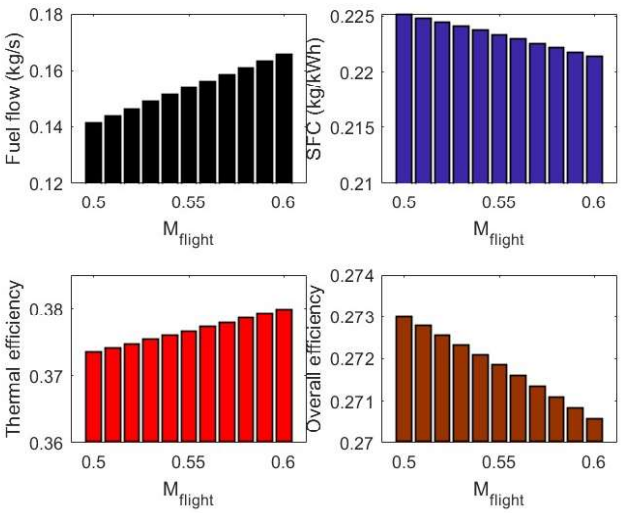


Figure 6. Variation of turboprop performance with respect to Mach number

5 CONCLUSIONS

In this paper, influences of combustor parameters of turboprop engine with two shafts as named AE2100 are investigated. For this aim, this engine is subjected to parametric cycle analysis so as to comprehend how variation of design variables affects AE2100 performance. Main novelty of this study is to investigate the first time effects of combustor efficiency, pressure ratio of combustor and fuel to air ratio regarding AE2100 turboprop. Moreover, it is tried that the relationship between flight conditions and the engine performance is revealed. Several important findings from this analysis can be point outed as follows:

Increasing of combustor efficiency results in enhancement of turboprop engine. Namely, as the η_{comb} raises from 0.90 to 0.99, SFC of the engine decreases by 9.02 % whereas overall efficiency improves by 2.43 %.

Due to varying CPR, magnitude of difference in performance of engine are not apparent. With effect of varying pressure drop ratio, SFC of the turboprop diminishes by 3.68 %, however overall efficiency decreases by 0.37 %.

As fuel to air ratio of the engine increases from 0.0149 to 0.0189, as expected, SFC of the engine changes by 25.6 %, which means that unless high power is required, setting high FAR leads to high fuel consumption, thereby lowering overall efficiency.

When considering altitude effects, SFC of the engine varies by 0.93 % whereas its overall efficiency has enhancement by 0.35 %.

Finally, Mach increases from 0.5 to 0.6, interestingly, SFC of the engine has improvement by 1.68 % whereas overall efficiency varies by 0.24 %. Compared with altitude, Mach effect is more dominant on performance of the engine.

Summarily, when considering that turboprop engines increases day by day due to civil and military needs, it is thoughout that the elaborated performans assessments help in mitigating environmental effects from engine, which diagnose the components that lead to deteriorating the engine performance. In other words, any attempt to enhance combustor parameters could mitigate SFC of the engine, thereby environmental impact. As a next study, exergetic aspects of turboprop engine by using different values of combustor parameters could be addressed.

References

[1] El-Sayed A.F., Aircraft propulsion and gas turbine engines. 2008: CRC press.

[2] Dinc A., Caliskan H., Ekici S., and Sohret Y. Thermodynamic-based environmental and enviroeconomic assessments of a turboprop engine used for freight aircrafts under different flight phases.Journal of Thermal Analysis and Calorimetry. 2022: pp. 1-15.

[3] https://www.atag.org/facts-figures.html.

[4] Baharozu E., Soykan G., and Ozerdem M.B. Future aircraft concept in terms of energy efficiency and environmental factors.Energy. 2017. 140: pp. 1368-1377.

[5] Zaporozhets O., Volodymyr V., and Synylo K. Trends on current and forecasted aircraft hybrid electric architectures and their impact on environment.Energy. 2020: pp. 118814.

[6] Balli O., Kale U., Rohács D., and Karakoc T.H. Exergoenvironmental, environmental impact and damage cost analyses of a micro turbojet engine (m-TJE).Energy Reports. 2022. 8: pp. 9828-9845.

[7] Akdeniz H.Y., Balli O., and Caliskan H. Energy, exergy, economic, environmental, energy based economic, exergoeconomic and enviroeconomic (7E) analyses of a jet fueled turbofan type of aircraft engine.Fuel. 2022. 322: pp. 124165.

[8] http://www.fi-powerweb.com/Engine/Rolls-Royce-AE-2100.html.

[9] Aygun H., Kirmizi M., and Turan O. Propeller effects on energy, exergy and sustainability parameters of a small turboprop engine.Energy. 2022. 249: pp. 123759.

[10] Balli O. and Hepbasli A. Energetic and exergetic analyses of T56 turboprop engine.Energy conversion and management. 2013. 73: pp. 106-120.

INVESTIGATION OF THE EFFECTS OF DIFFERENT RATES OF HEXANE BLENDED FUELS UTILIZED IN A CERAMIC-COATED DIESEL ENGINE ON HC, NO_X, AND SMOKE OPACITY BY TAGUCHI METHOD

E. Vural[1], S. Özer[2], S. Özel[3], M. Binici[4]

1. Aydın Adnan Menders University, Germencik Yamantürk Vocational School, Aydın; email: evural@adu.edu.tr
2. Muş Alparslan University, Faculty of Engineering and Architecture, Muş; email: s.ozer@alparslan.edu.tr
3. Bitlis Eren University, Faculty of Engineering and Architecture, Bitlis; email: sozel@beu.edu.tr
4. Bitlis Eren University, Faculty of Engineering and Architecture, Bitlis; email: mbinici@beu.edu.tr

Abstract

In this study, the impacts of different hexane and water blended diesel fuel rates on exhaust gas emissions (HC, NO_x, and Smoke Opacity) in ceramic-coated and uncoated diesel engines that were operated at different powers were investigated. Initially, experimental designs were created by the Taguchi method, and experiments were performed based on the resulting combinations. The experiment results were then tested and interpreted with ANOVA. The diesel fuel blends used in the experiments were 100% Diesel (D), 90% Diesel + 5% Water + 5% Hexane (D90W5H5) and 85% Diesel + 5% Water + 10% Hexane (D85W5H10). These fuels were used in two diesel engines, ceramic-coated and uncoated, and they were operated at engine powers of 2kW, 3kW, and 4kW for each fuel type. As a result of these experiments, the HC (ppm) and Smoke Opacity (%) from exhaust emissions were aimed to be lower, while the NO_x (%) ratio was higher. The experimental results showed that lower HC (ppm) and higher NO_x (%) values were achieved by the ceramic-coated diesel engine that used the D90W5H5 type of fuel and was powered at 4kW. The lower Smoke Opacity (%) was achieved by the ceramic-coated diesel engine which used the D85W5H10 fuel type and operated at 4kW power. The results of the experiments were tested with ANOVA, which showed that they were statistically significant ($P < 0.05$). Moreover, the models created for HC, NO_x, and Smoke Opacity have R^2 values which were above 95%, indicating the accuracy of these models. This experimental study was designed with the Taguchi method as a mixed level based on the orthogonal array L_{18} ($2^\wedge1\ 3^\wedge2$). The engine factor was defined as two levels, while the power and fuel factors were defined as three levels each. As a result of the mixed level Taguchi analysis, the highest signal-to-noise ratios for HC and NO_x gases were achieved by the ceramic-coated diesel engine which used the D90W5H5 fuel type and was powered at 4kW, while the highest signal-to-noise ratios for the Smoke Opacity were achieved by the ceramic-coated diesel engine which used the D85W5H10 fuel and powered at 4kW. For all experiments, the most effective factor in the results is power, while the fuel factor is the second, and the engine factor is the third most effective.

Keywords: Diesel, Diesel fuel blends, Diesel engine, Exhaust emissions, HC, NO_x, Smoke Opacity, Taguchi analysis, ANOVA

1 INTRODUCTION

Greenhouse gas emissions emanating from fossil fuels are among the most important environmental threats due to their effects such as climate change and deterioration of air quality [1]. For this reason, studies have been carried out to reduce the factors that cause air pollution in many types of internal combustion engines [2]. Diesel fuel, which is one of the fossil fuels, is used as the main fuel source in many vehicles due to its high efficiency [3]. The most significant problem of diesel engines is that they cause NO_x and particulate matter pollution emissions that threaten human health [4], and for this reason, regulations are being brought to reduce these emissions worldwide [5]. To reduce these emissions, some additives can be added to the diesel fuel [6] and some changes can be made to the diesel engine [7]. One of these substances, hexane, is an organic solvent [8] and is used in many industries around the world, such as oil processing [9].

There are some studies in the literature using a mixture of hexane and diesel fuel. In one of these studies, the emission, combustion, and performance values of the diesel engine were examined by mixing hexane and diesel fuel in different ratios, and it was determined that hexane-mixed diesel fuels reduced NO_x emission, while an increase in smoke emission was observed [7]. In another study, in which hexane was added to diesel fuel mixtures, improvements were observed in fuel quality and properties [10]. In another study investigating the effect of hexane on the performance and emission values of the diesel engine, there was a decrease in HC, CO, and Smoke Opacity emissions, while a slight increase in the NO_x emission value occurred [3]. On the other hand, according to the studies, the characteristics of the diesel engine along with the fuel are also effective on the emission values [11]. In a study in which the effect of ceramic-coated and uncoated diesel engines on exhaust emissions in terms of the characteristics of the engine was analyzed using the Taguchi method, HC emission values decreased in the ceramic-coated diesel engine, while the NO_x value was lower in the uncoated diesel engine [12]. The quality of the injected fuel, the air-fuel mixture in the combustion chamber, density, viscosity, and evaporation of the fuel play an important role in the effective operation of the engine [13]. There are also studies in which hexane is added to bio-diesel fuels, and the general purpose of using hexane in these studies is to reduce the viscosity of bio-diesel fuels to provide better combustion and reduce emission values [14-17].

In addition, by applying ceramic coating (for example, zirconia and silicon nitride) on the combustion chamber surfaces of diesel engines (piston, valve, etc.) with the thermal barrier coating method, lower thermal conductivity is created compared to conventional engines and therefore lower emission values can be achieved [18].

In this study, the aim is to analyze the HC, NOx, and Smoke Opacity ratios in ceramic-coated and uncoated diesel engines by adding hexane and water to diesel fuel at different rates. Taguchi optimization method was used as the analysis tool. There are studies examining the effects of diesel fuel mixtures using the Taguchi method [8, 12, 19-22].

2 MATERIALS AND METHOD

In this study, hexane and water were blended in different proportions with pure diesel fuel. These fuel blends were used in ceramic-coated and uncoated diesel engines at different powers. Experimental studies were carried out according to the experimental combinations obtained from the Taguchi optimization method. Experimental data were analyzed with ANOVA and the results were interpreted according to the signal-to-noise ratios obtained from the Taguchi method.

2.1 Diesel Engines and Fuel Blends

Two engines were used in this study, coated and uncoated. In the coated engine, the piston surface is coated with ceramic material by the plasma spray method. In this way, a thermal barrier layer was obtained on the piston surface. As fuel blends, there are three different types of fuels: 100% Diesel (D), 90% Diesel + 5% Water + 5% Hexane (D90W5H5) and 85% Diesel + 5% Water + 10% Hexane (D85W5H10). Each of these fuel types was operated in ceramic-coated and uncoated engines at 2kW, 3kW, and 4kW powers.

2.2 Taguchi Method

Taguchi method, which has a practical and robust structure, has been successfully applied in many studies for the creation of experimental designs of problems with multiple parameters. [23]. By using the orthogonal arrays given by the Taguchi method, the most suitable combination of experiments can be selected, and with this combination, less time and cost can be achieved by performing fewer experiments [8].

The results obtained from the experiments performed according to the orthogonal array given by the Taguchi method are converted into signal-to-noise ratios and the result with the highest value is determined as optimum. Signal-to-noise ratios, on the other hand, are found using the following formulas, depending on whether the desired result is “higher is better”, “lower is better” or “nominal is better” [24].

“Higher is better”

$$S/N = -10\ x\ log_{10}\left(\frac{1}{n}\sum_{i-1}^{n}\frac{1}{Y_i^2}\right) \quad (1)$$

"Lower is better"

$$S/N = -10\ x\ log_{10}\left(\frac{1}{n}\sum_{i-1}^{n} Y_i^2\right) \quad (2)$$

"Nominal the better"

$$S/N = -10\ x\ log_{10}\ (s\text{^}2) \quad (3)$$

Where Y_i = the result of the each experiment, i = number of repetitions

In this study, there are three control factors: fuel, engine, and power. Of these factors, fuel and power consist of three levels, while the engine factor consists of two levels. The control factors and levels used in the Taguchi analysis are given in Table 1.

Table 1. Control Factors and Levels

Control Factors	Level 1	Level 2	Level 3
Fuel	D	D90W5H5	D85W5H10
Power	2 kW	3 kW	4 kW
Engine	uncoated	coated	-

Since the levels of the factors are different, a mixed-level Taguchi design was used in this study [25].

2.3 Analysis of Variance (ANOVA)

ANOVA is a statistical method that is employed to analyze and interpret experimental results. With ANOVA, the effect of control parameters on the desired result can be determined as a percentage. It can also be determined whether these results are statistically significant [26].

3 RESULTS AND DISCUSSION

In this study, the Taguchi orthogonal array was first determined as L18 (2^1 3^2). Eighteen experiments were carried out according to this sequence and HC, NOx, and Smoke Opacity values were measured at the end of each experiment. Obtained experimental results were analyzed employing ANOVA, and it was examined whether they were statistically significant. Then, the experimental results were analyzed by the Taguchi method.

3.1 Experimental Results

Eighteen experiments were performed according to the Taguchi orthogonal array and the HC(ppm), NO_x (%), and Smoke Opacity (%) values obtained as a result of each experiment are given in Table 2.

Table 2. Experimental Results

No.	Engine	Power	Fuel	HC	NO_x	S.Op.
1	uncoated	2kW	D	157	111	11,6
2	uncoated	2kW	D90W5H5	141	124	10,8
3	uncoated	2kW	D85W5H10	143	116	10,3
4	uncoated	3kW	D	103	145	9,3
5	uncoated	3kW	D90W5H5	96	156	8,3
6	uncoated	3kW	D85W5H10	103	147	7,6
7	uncoated	4kW	D	45	215	7,6
8	uncoated	4kW	D90W5H5	39	224	7,1
9	uncoated	4kW	D85W5H10	45	219	6,4
10	coated	2kW	D	134	121	11,3
11	coated	2kW	D90W5H5	122	134	10,1
12	coated	2kW	D85W5H10	129	112	9,7
13	coated	3kW	D	101	157	8,9
14	coated	3kW	D90W5H5	74	165	7,6
15	coated	3kW	D85W5H10	79	137	7,1
16	coated	4kW	D	41	226	7,2
17	coated	4kW	D90W5H5	33	231	6,3
18	coated	4kW	D85W5H10	37	226	5,9

The variation of HC (ppm) values in coated and uncoated engines according to these test results is given in Figure 1.

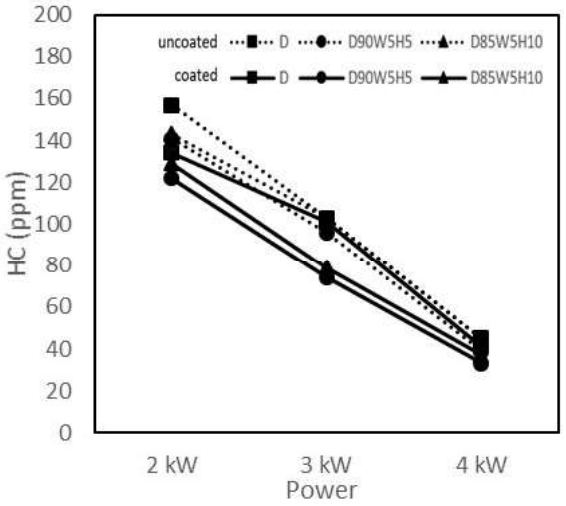


Figure 1. HC (ppm) Values in Uncoated and Ceramic-Coated Diesel Engines

As can be seen from Figure 1, HC emission decreases as the power in the engines increases for each fuel type. While the lowest emission values are reached utilizing the D90W5H5 fuel type, the D fuel type causes the highest HC emissions. In addition, the HC emission values in the ceramic-coated diesel engine are mostly lower than in the uncoated diesel engine. Another important point that stands out in the graphic is that the hexane-blended diesel fuel

types cause lower HC emissions than using only diesel fuel.

On the other hand, the change in NO_x emission follows the opposite situation compared to HC emission (Figure 2).

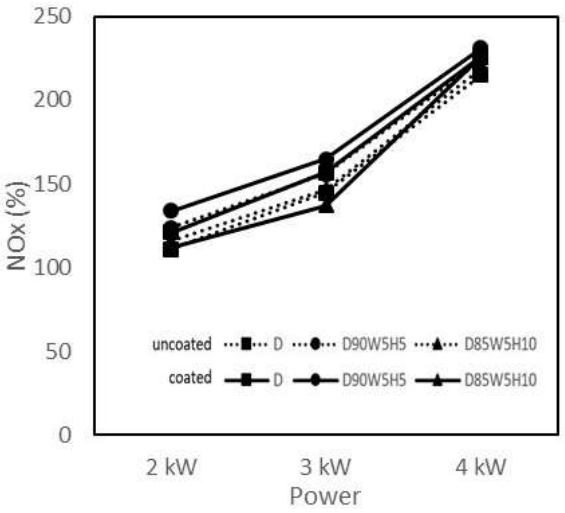


Figure 2. NO_x (%) Values in Uncoated and Ceramic-Coated Diesel Engines

In both engine types, as the power increases, NO_x emission increases. This is expected because the temperature in the engine combustion chamber increases as the power increases, and NO_x emissions also increase. Especially, this situation demonstrates itself more in the ceramic-coated diesel engine because the NO_x value will increase as the temperature is preserved more in the ceramic-coated engine [12]. But the striking point is that while pure diesel fuel causes less NO_x emission in the uncoated engine, 10% hexane blended fuel (D85W5H10) in the ceramic-coated engine causes less NO_x emission than pure diesel (D).

Finally, when the Smoke Opacity values are examined in Figure 3, it is seen that the emission decreases as the power increases and this decreases even more in the ceramic-coated engine. Another considerable point is that as the hexane ratio in the diesel fuel mixture increases, the Smoke Opacity emission decreases.

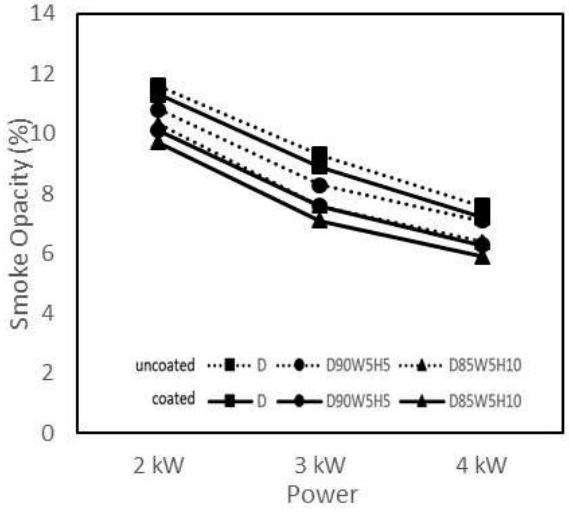


Figure 3. Smoke Opacity (%) Values in Uncoated and Ceramic-Coated Diesel Engines

3.2 ANOVA and Taguchi Analysis

The experimental design was created by using Taguchi orthogonal array to conduct experimental studies. In section 2.2, control parameters and levels have been mentioned. Engine factor consists of two levels, while fuel and power factors consist of three levels. For this reason, the mixed-level design method was employed while designing the Taguchi. After the design of the experiments was determined utilizing the Taguchi method, the experimental studies were carried out and the results were obtained for HC, NO_x, and Smoke Opacity emissions. These results were analyzed using the Taguchi method in the Minitab Trial version.

Initially, HC emission values were analyzed according to the "lower is the better" principle and signal-to-noise ratios were determined (Figure 4).

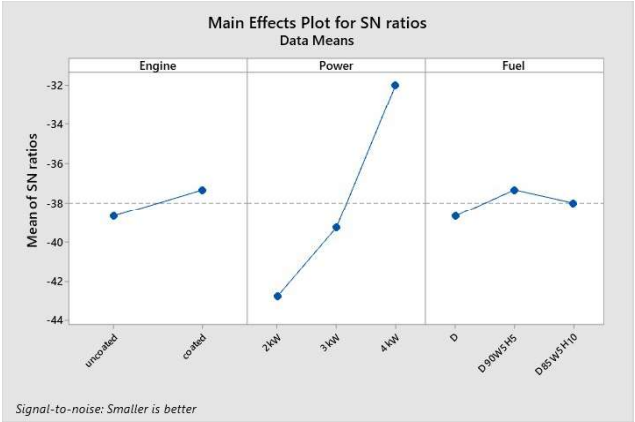


Figure 4. Graph of Signal-to-Noise Ratios for HC (ppm)

When Figure 4 is examined, it is seen that the ceramic-coated engine in Engine factor, 4 kW power in Power factor, and D90W5H5 fuel in Fuel factor give the highest signal-to-noise ratios. In other words, the lowest HC (ppm) emission can be achieved when each factor is operated at the levels that give these highest rates. Besides that, the most influential factor in the result is Power, while the others are Fuel and Engine, respectively.

When the HC experiment results were evaluated with ANOVA, each factor was found to be statistically significant (P<0.05) (Table 2).

Table 2. ANOVA Results for HC (ppm)

Source	DF	Seq SS	Adj SS	Adj MS	F	P
Engine	1	8,300	8,300	8,300	39,81	**0,000**
Power	2	361,587	361,587	180,794	867,05	**0,000**
Fuel	2	5,590	5,590	2,795	13,40	**0,001**
Residual Error	12	2,502	2,502	0,209		
Total	17	377,980				

In addition, the R^2 value of the model created for HC (ppm) was 99.34%. This shows that our model has reached a high accuracy value.

Another emission analyzed is NO_x values and the Taguchi analysis results are given in Figure 5. This analysis is based on the principle of "the higher the better". It may be desired that NO_x emission be less since it is a harmful gas to nature and human beings, but it was requested to be higher in the Taguchi analysis phase due to the issues stated in the Experimental Results section regarding NO_x.

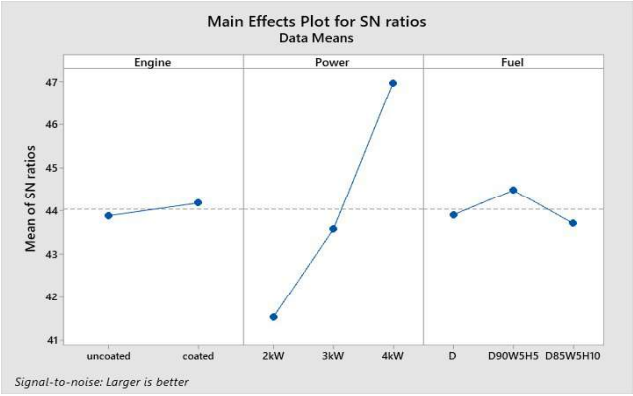


Figure 5. Graph of Signal-to-Noise Ratios for NO_x (%)

Looking at Figure 5, it can be seen that the highest signal-to-noise ratios are reached at the engine level in the Engine factor, at the 4 kW level in the Power factor, and at the D90W5H5 fuel level in the Fuel factor. In other words, each factor must be operated at these levels in order to reach higher NO_x values. While the most effective factor in NO_x emission values is Power, the others are Fuel and Engine factors, respectively.

When the ANOVA results for NO_x are examined, it is seen that other factors ($P < 0.05$) are statistically significant except for the Engine factor ($P=0.1 > 0.05$) (Table 3). In other words, the Engine factor does not have a significant effect on NO_x emissions.

Table 3. ANOVA Results for NO_x (%)

Source	DF	Seq SS	Adj SS	Adj MS	F	P
Engine	1	0,3925	0,3925	0,3925	3,17	**0,100**
Power	2	90,7507	90,7507	45,3753	367,01	**0,000**
Fuel	2	1,9483	1,9483	0,9742	7,88	**0,007**
Residual Error	12	1,4836	1,4836	0,1236		
Total	17	94,5751				

The R^2 value, which shows the accuracy of the model created for NOx emission, was 98.43%, meaning that the accuracy of the model is high.

Finally, when looking at the "lower is better" Taguchi analysis results for the Smoke Opacity emission values (Figure 6), it is seen that the coated engine in the Engine factor, 4 kW power in the Power factor, and D85W5H10 fuel level in the Fuel factor give the highest signal-to-noise ratios. In this case, it can be said that if the D5W5H10 fuel is utilized in a ceramic-coated diesel engine with a power of 4 kW, it will give a lower Smoke Opacity rate.

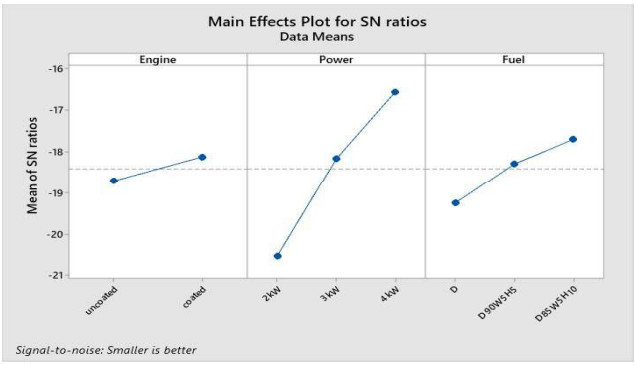


Figure 6. Signal-to-Noise Ratios Graph for Smoke Opacity (%)

The ANOVA results of the Smoke Opacity emission values given in Table 4 show that all factors are statistically effective in the results ($P < 0.05$). In addition, the R^2 value of the model created for this analysis was 99.16%, indicating that the model is highly accurate. Finally, in the ranking of the factors most affecting the Smoke Opacity emission values, Power is the first, Fuel is the second, and Engine is the third.

Table 4. ANOVA Results for NO_x (%)

Source	DF	Seq SS	Adj SS	Adj MS	F	P
Engine	1	1,5510	1,5510	1,5510	38,82	**0,000**
Power	2	47,6757	47,6757	23,8378	596,56	**0,000**
Fuel	2	7,3270	7,3270	3,6635	91,68	**0,000**
Residual Error	12	0,4795	0,4795	0,0400		
Total	17	57,0332				

4 CONCLUSIONS

- According to the experimental results, when the D90W5H5 fuel is operated at 4kW power in a ceramic-coated diesel engine, lower HC (ppm) emission is achieved, while NOx (%) emission is higher. Lower Smoke Opacity emissions are achieved when the ceramic-coated diesel engine is powered by 4 kW but with the D85W5H10 fuel.
- It has been observed that hexane and water blended diesel fuels in certain proportions reduce HC, NO_x, and Smoke Opacity emissions.
- Looking at the Taguchi analysis results, the desired lower HC and higher NO_x emissions are achieved when the Engine factor is at the coated level, the Power factor is at 4 kW, and the Fuel factor is at the D90W5H5 level. Smoke Opacity emission, on the other hand, reaches the desired lower level at the D85W5H10 fuel level, with only one difference.
- ANOVA results represent that the most important factor is Power in general, while the others are the Fuel and Engine factors, respectively.
- It was observed that all factors were statistically significant ($P < 0.05$) in all emission values, only the Engine factor did not give significant results in NOx emission ($P=0.1 > 0.05$).
- The R^2 values of the created models were higher than 95% and the accuracy rates were high.

REFERENCES

[1] Çelik, M. and Bayindirli, C., Enhancement performance and exhaust emissions of rapeseed methyl ester by using n-hexadecane and n-hexane fuel additives, *Energy*, 202, 117643, 2020.

[2] Datta, A. and Mandal, B. K., Numerical investigation of the performance and emission parameters of a diesel engine fuelled with diesel-biodiesel-methanol blends, *Journal of Mechanical Science and Technology*, 30(4), 1923-1929, 2016.

[3] Bayindirli, C. and Celik, M., Investigation of combustion and emission characteristics of n-hexane and n-hexadecane additives in diesel fuel, *Journal of Mechanical Science and Technology*, 33(4), 1937-1946, 2019.

[4] de Oliveira, A., de Morais, A. M., Valente, O. S., and Sodré, J. R., Combustion characteristics, performance and emissions from a diesel power generator fuelled by B7-ethanol blends, *Fuel Processing Technology*, 139, 67-72, 2015.

[5] Reşitoğlu, I. A., Altinişik, K., and Keskin, A., The pollutant emissions from diesel-engine vehicles and exhaust aftertreatment systems, *Clean Technologies and Environmental Policy*, 17(1), 15-27, 2015.

[6] Basha, S. A., and Gopal, K. R., A review of the effects of catalyst and additive on biodiesel production, performance, combustion and emission characteristics, *Renewable and Sustainable Energy Reviews*, 16(1), 711-717, 2012.

[7] Balamurugan, T., & Nalini, R., Experimental investigation on the effect of alkanes blending on performance, combustion and emission characteristics of four-stroke diesel engine, *International Journal of Ambient Energy*, 37(2), 192-200, 2016.

[8] Çelik, M., Bayındırlı, C., and Mehregan, M., Multi-objective optimization of a diesel engine fueled with different fuel types containing additives using grey-based Taguchi approach,

Environmental Science and Pollution Research, 29(20), 30277-30284, 2022.

[9] Xiao, X., Yan, B., Fu, J., and Xiao, X., Absorption and recovery of n-hexane in aqueous solutions of fluorocarbon surfactants, *Journal of Environmental Sciences*, 37, 163-171, 2015.

[10] Abdulvahitoğlu, A., and Aydın, K., Performance and exhaust emission characteristics of a CI engine fueled with synthesized fuel blends, *Energy Education Science and Technology Part A: Energy Science and Research*, 2, 699-710, 2012.

[11] Mangus, M., Kiani, F., Mattson, J., Tabakh, D., Petka, J., Depcik, C., ... and Stagg-Williams, S., Investigating the compression ignition combustion of multiple biodiesel/ULSD (ultra-low sulfur diesel) blends via common-rail injection, *Energy*, 89, 932-945, 2015.

[12] Özel, S., Vural, E., and Binici, M., Taguchi method for investigation of the effect of TBC coatings on NiCr bond-coated diesel engine on exhaust gas emissions, *International Advanced Researches and Engineering Journal*, 4(1), 14-20, 2020.

[13] Park, S. H., Kim, H. J., Suh, H. K., and Lee, C. S., Experimental and numerical analysis of spray-atomization characteristics of biodiesel fuel in various fuel and ambient temperatures conditions, *International journal of heat and fluid flow*, 30(5), 960-970, 2019.

[14] Fanse, T. S., A Green Project: Controlled Emissions from CI Engine through Different Blends of Bio-Diesel Fuel on Sustainability Basis, *International Journal of Research in Engineering, Science and Management*, 5(6), 39-44, 2022.

[15] Gad, M. S., Amin, A., and Mustafa, I., Experimental study of biodiesel-diesel blending using different processing technologies and feedstock, *Journal of Chemical Technology & Metallurgy*, 57(4), 2022.

[16] El-Seesy, A. I., Hassan, H., Dawood, A., Attia, A. M., Kosaka, H., and Ookawara, S.,. Investigation of the impact of adding titanium dioxide to jojoba biodiesel-diesel-n-hexane mixture on the performance and emission characteristics of a diesel engine, *In Internal Combustion Engine Division Fall Technical Conference*, Vol. 51982, p. V001T02A006., 2018.

[17] Sipayung, R., Optimization of biodiesel production from used cooking oil using modified calcium oxide as catalyst and N-Hexane as solvent, *Materials Today: Proceedings*, 2022.

[18] Caputo, S., Millo, F., Boccardo, G., Piano, A., Cifali, G., and Pesce, F. C., Numerical and experimental investigation of a piston thermal barrier coating for an automotive diesel engine application, *Applied Thermal Engineering*, 162, 114233, 2019.

[19] Alemayehu, G., Firew, D., Nallamothu, R. B., Wako, A., and Gopal, R., Operating Parameters Optimization for Lower Emissions in Diesel Engine with PCCI-DI Mode using Taguchi and Grey Relational Analysis, *Heliyon*, e09679, 2022.

[20] Sharma, A., Ansari, N. A., Singh, Y., Mustefa, I., and Vivekanandhan, C., Optimization of engine parameters using Polanga biodiesel and diesel blends by using Taguchi method, *Materials Today: Proceedings*, 5(14), 28221-28228, 2018.

[21] Natarajan, S., Pitchandi, K., and Mahalakshmi, N. V., Optimization of performance and emission characteristics of PPCCI engine fuelled with ethanol and diesel blends using grey-Taguchi method, *Journal of Thermal Science*, 27(1), 89-94, 2018.

[22] Rai, R. K. and Sahoo, R. R., Taguchi-Grey and ANOVA optimization techniques for engine performance with water in diesel emulsion fuels, *Heat Transfer*, 49(6), 3503-3530, 2020.

[23] Ng Chin Fei, Nik Mizamzul Mehat, and Shahrul Kamaruddin, Practical Applications of Taguchi Method for Optimization of Processing Parameters for Plastic Injection Moulding: A Retrospective Review, *International Scholarly Research Notices*, vol. 2013, Article ID 462174, 11 pages, 2013.

[24] Özel, S., Vural, E., & Binici, M., Optimization of the effect of thermal barrier coating (TBC) on diesel engine performance by Taguchi method, *Fuel*, 263, 116537, 2020.

[25] Babji, A., Rambabu, G., Naik, D. B., and Kumar, G. S., Optimization of Performance Parameters of a Variable Compression Ratio Diesel Engine with Hibiscus Cocos Nucifera Biodiesel using Taguchi Method, *International Journal of Ambient Energy*, 1-23, 2022.

[26] C. Vidal, V. Infante and P. Peças, P. Vilaça, Application of Taguchi Method in the Optimization of Friction Stir Welding Parameters of an Aeronautic Aluminium Alloy, *Int. J. Adv. Mater. Manuf. Charact*, 3, 21–26, 2013.

A PARAMETRİC STUDY TO OPTİMIZE THE TEMPERATURE OF HAZELNUT AND WALNUT SHELL GASIFICATION FOR HYDROGEN AND METHANE PRODUCTION

H. ÖZTAN[1], İ. KOÇYİĞİT ÇAPOĞLU[2], D. UYSAL[3], Ö. M. DOĞAN[4]

1. Gazi University, Faculty of Engineering, Chemical Engineering Department, Maltepe, Ankara, 06570, Turkey, e-mail: hazaloztan@gazi.edu.tr

2. Gazi University, Faculty of Engineering, Chemical Engineering Department, Maltepe, Ankara, 06570, Turkey,e-mail: iremkocyigit@gazi.edu.tr

3. Gazi University, Faculty of Engineering, Chemical Engineering Department, Clean Energy Research Center (CERAC), Maltepe, Ankara, 06570, Turkey, e-mail: duysal@edu.tr

4. Gazi University, Faculty of Engineering, Chemical Engineering Department, Maltepe, Ankara, 06570, Turkey, e-mail: mdogan@gazi.edu.tr

Abstract

The aim of this study is to optimize the temperature of hazelnut and walnut shells gasification in a updraft fixed bed reactor to produce hydrogen and methane gases. Steam was used as gasification agent to lead hydrogen releasing at a constant rate of 10 g/min. To optimize the gasification temperature fuels were gasified at 600℃, 650℃, 700℃, 750℃ and 800℃. The experimental results showed that the amount of hydrogen content in syngas increased with increasing temperature but amount of methane content decreased during both fuels gasification. The optimum gasification temperatures of hazelnut and walnut shells were obtained as 750℃ and 800℃, for producing hydrogen and the amount of hydrogen in produced syngas at optimum temperatures were obtained as 96.6% and 99.2%, respectively. Also, amount of methane in produced syngas was obtained as 99.9% (600℃) and 47.8% (650℃) for hazelnut and walnut shells, respectively. Lower gasification temperatures favoured the methane content instead of hydrogen in syngas. If the gasification temperature of biomasses is optimized, syngas composition can be arranged for different usage areas like hydrogen and methane or chemicals production.

Keywords: gasification, hydrogen, methane, biomass

1 INTRODUCTION

Regenerating technologies, young industries that are following up new techniques, increasing human population and activities have enhanced the global energy requirement [1, 2]. In addition to the increasing need for energy, the depletion of fossil resource reserves is the biggest problem of energy industries [3]. Researches to find alternative sources have gained momentum due to the depletion of fossil resource reserves. Among the renewable energy sources, the relationship of biomass with the sun and its easy and repeated production in the natural cycle draws attention in the search for new energy sources. Apart from taking part in energy production, the fact that an emission such as carbon dioxide, which affects global warming at the highest level, is less in the use of biomass compared to fossil fuels, brings biomass to the forefront in terms of an alternative energy source [4, 5].

When we look at the technologies that can produce energy, combustion and gasification processes, in which coal is used as raw material, are the most well-known processes today [6]. However, as it is known, when using traditional boiler-turbine systems in combustion processes, the efficiency is low due to undesired gas

emissions as a result of combustion, moisture and ash problems of low quality coals. In addition, the only product obtained in combustion processes is electrical energy. Contrary to these situations, the product obtained in gasification processes is a gas mixture containing a wide variety of combustible components. This gas product, which basically contains hydrogen and carbon monoxide, is called syngas, but can be used in suitable engines if desired [7], and can be considered as a very important raw material source for the chemical industry [8].

Syngas has the potential to produce hydrogen, which is the basic fuel for fuel cells, which are rapidly developing today. Hydrogen production is mainly based on the reforming of natural gas/naphtha or coal gasification. However, it is important for the industry that the systems are more sustainable in terms of raw material needs. For this reason, the use of biomass from renewable energy sources has come to the forefront for hydrogen production by gasification [9-11]. Also, syngas remarkably has methane. Methane is the main content of the natural gas and it should not be forgotten that it is also one of the fossil resources.

Turkey is the seventh-largest agricultural producer [12] and it has many hazelnut and walnut shells as waste of some food industries. In this study, hazelnut and walnut shells were used as biomass to produce syngas in an updraft fixed bed gasifier. Besides, optimum gasification temperature was investigated to obtain hydrogen and methane gases.

2 MATERIALS AND METHOD

2.1 Fuels

Hazelnut and walnut shells were used separately as fuels in the gasification experiments.

The experiments were carried out at a constant particle diameter as 1 mm. Proximate analyses of fuels are reported in Table 1.

Table 1. Proximate analysis of hazelnut and walnut shells

Proximate analysis (%)		
	Hazelnut shell	**Walnut shell**
% Moisture	9.31	7.13
% Ash	3.69	3.32
% Volatile matter	62.61	66.84
% Fixed carbon	24.39	22.71
TOTAL	100	100

2.2 Experimental Setup

Figure 1 shows the schematic diagram of the updraft fixed bed reactor and its auxiliary equipment. The reactor (3) is made of quartz glass and it has an internal diameter of 5 cm. The perforated plate (4) is used to distribute the steam homogeneously in reactor. The column is covered by an electrical resistance (2) for temperature control and indirect heating gasification was carried out. Steam at 100 °C was produced with a steam generator (1) and was sent to the reactor. The reactor was equipped with two condensers (8-9), temperature controller (5) and a thermocouple (6). There is a screw feeder (7) on the top of the column and there are three gas cleaning bottles with silica gel for the outlet gas (10). A vacuum pump (11) was used to get the gas sample. The gas samples were analyzed by SRI 310 model TCD gas chromatography device (12).

Gasification experiments of hazelnut and walnut shells (fuels) were carried out separately in this updraft fixed bed gasifier (reactor). The reactor was heated to five different temperatures: 600°C, 650°C, 700°C, 750°C and 800 °C. The reactor temperature was controlled with thermocouple. Steam was used as the gasifying agent and was fed to the reactor at a constant rate of 10 g/min. Fuels were fed to the reactor at a constant rate of 8 g/min by screw feeder. Produced gas was cooled by condensers and cleaned by silica gels in bottles to prevent the humidity within the gas which were analyzed by gas chromatography device. Gas samples were collected in gas sampling bags and these were analyzed with gas chromatography device in order to examine

amount of hydrogen, carbon monoxide, carbon dioxide, and methane gases in the produced syngas.

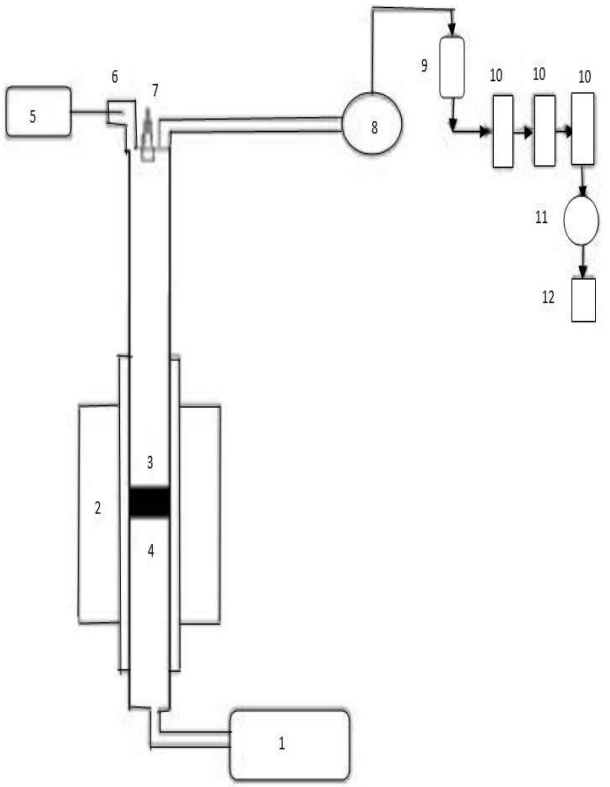


Figure 1. Schematic diagram of updraft fixed bed reactor and auxiliary equipment

3 RESULTS AND DISCUSSION

Gasification of hazelnut and walnut shells was carried out in an updraft fixed bed to optimize the temperature. The temperature interval was selected as 600-800℃ because of the gasification reactions and their thermodynamic behavior [13]. Gasification reactions that are given below are water-gas (1), water-gas shift (2), Boudouard (3) and methanation (4) and these reactions occur at high temperatures due to equilibrium conditions in gasifier [14].

Water gas reaction

$$C_{(s)} + H_2O_{(g)} \leftrightarrow CO_{(g)} + H_{2(g)}$$

$$\Delta H^{\circ} = + 131.38 \text{ kJ/mol} \quad (1)$$

Water gas shift reaction

$$CO_{(g)} + H_2O_{(g)} \leftrightarrow CO_{2(g)} + H_{2\,(g)}$$

$$\Delta H^{\circ} = - 41.15 \text{ kJ/mol} \quad (2)$$

Boudouard reaction

$$C_{(s)} + CO_{2(g)} \leftrightarrow 2CO_{(g)}$$

$$\Delta H^{\circ} = + 172.58 \text{ kJ/mol} \quad (3)$$

Methanation reaction

$$C_{(s)} + 2H_{2(g)} \leftrightarrow CH_{4(g)}$$

$$\Delta H^{\circ} = - 74.90 \text{ kJ/mol} \quad (4)$$

High temperatures for biomass gasification favor the hydrogen release [13, 15]. Experimental results showed that hydrogen concentration in produced syngas for hazelnut and walnut shell gasification increased as the temperature was increased. Hydrogen releasing is favored by high gasification temperatures owing to water-gas reaction (1) [14]. Water-gas reaction is the major reaction of carbonaceous materials to produce syngas when steam is used as the gasification agent especially. The optimum temperatures for hydrogen producing were obtained as 750℃ and 800℃ for hazelnut and walnut shell, respectively. The hydrogen concentrations for both fuels in this study were 96.6% and 99.2%.

Hydrogen concentrations that were obtained in experiments are presented in Figure 2. Fixed carbon content enhances the steam-char gasification and char reactivity to produce hydrogen [16]. Therefore, apart from gasification temperature, amount of fixed carbon in biomasses is important to utilize the materials as a fuel. Both hazelnut and walnut shell have high fixed carbon content (Table 1) and, also high hydrogen concentrations proved that hazelnut and walnut shells are quite utilizable fuels for hydrogen production.

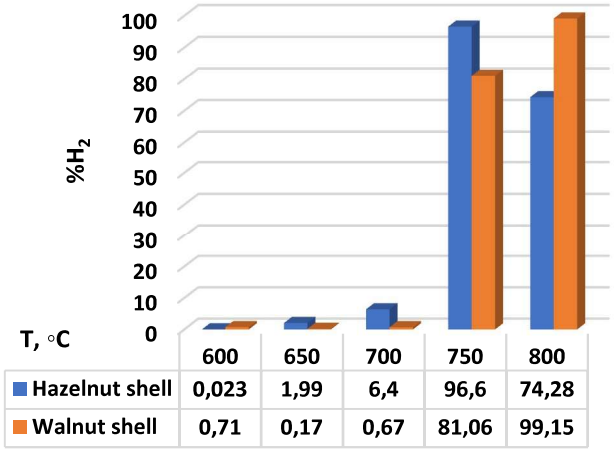


Figure 2. Hydrogen concentrations for hazelnut and walnut shell gasification

Carbon monoxide concentrations decreased when hydrogen increased for both results of fuels. This situation proved that the water-gas shift reaction (2) occurred during gasification. Water-gas shift reaction favors the hydrogen release in syngas, too [5, 17-20]. Also, carbon monoxide and carbon dioxide concentrations are affected due to Boudouard (3) and water-gas shift (2) reactions. Because Boudouard reaction consumes the carbon dioxide while water-gas shift produces it. Carbon monoxide and dioxide concentrations affected the gasifier conditions due to equilibrium and relationship between carbon monoxide and carbon dioxide is quite complex [21-23]. All compositions that were obtained in experiments are presented in Figure 3 and Figure 4.

A difference of 50°C was observed between the gasification temperature of the fuels for hydrogen releasing. This temperature difference could have been resulted from volatile content of fuels. Walnut shell has higher volatile matter content than that of hazelnut shell (Table 1) thus this volatile matter content decreased the temperature of gasification region in the reactor [5, 10, 24].

If volatile matter content is high in a biomass, methane releasing in syngas can occur. Also, lower gasification temperatures like 600°C and 650°C enhance the methanation reaction (4) thermodynamically [25]. Methane releasing was obtained in produced syngas because of high volatile matter content of fuels and supporting low gasification temperatures. The optimum temperatures for methane producing were obtained as 600°C and 650°C for hazelnut and walnut shell, respectively. The methane concentrations for both fuels in this study were 99.9% and 47.8%. Methane concentrations that were obtained in experiments are presented in Figure 5.

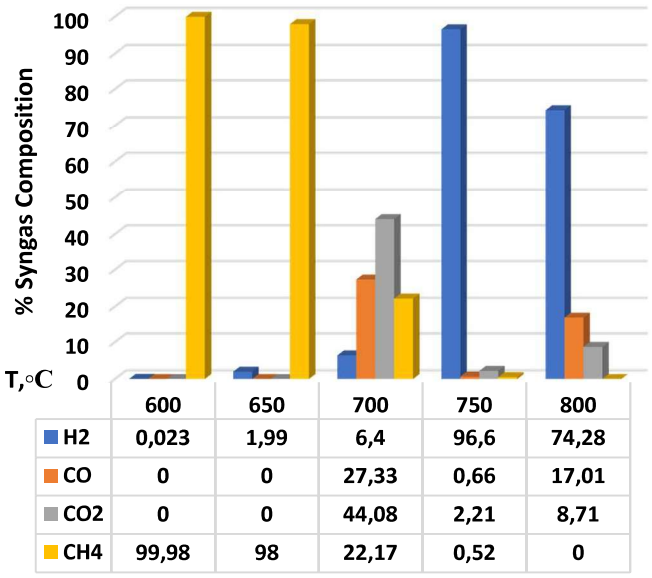


Figure 3. Syngas compositions for hazelnut gasification

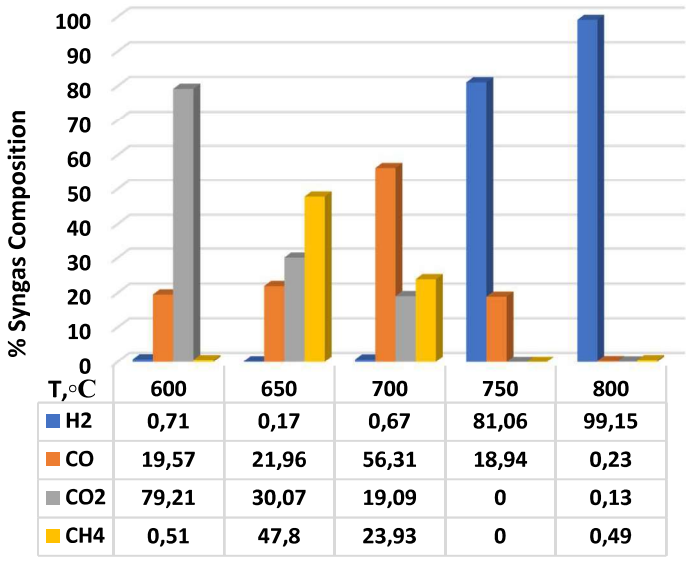
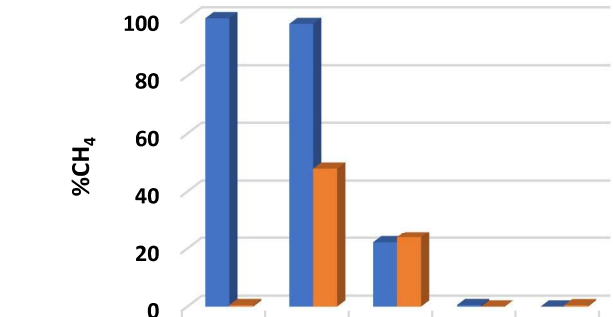


Figure 4. Syngas compositions for walnut gasification



T, ◦C	600	650	700	750	800
Hazelnut shell	99,98	98	22,17	0,52	0
Walnut shell	0,51	47,8	23,93	0	0,49

Figure 5. Methane concentrations for hazelnut and walnut shells

4 CONCLUSION

The experimental findings showed that as the gasification temperature was increased in gasification of hazelnut and walnut shells, hydrogen composition in the syngas increased, too. On the contrary, methane composition in the syngas decrease with increasing temperature. The high amount of carbon in the fuel is the biggest factor supporting the carbon conversion in gasification reactions. Hazelnut and walnut shells are notably important fuels for gasification processes to utilize biomasses due to their high fixed carbon content. Besides, thanks to gasification a solution is offered to eliminate the problematic storage process of hazelnuts and walnut shells which are sources of biomass.

ACKNOWLEDGEMENTS

We would like to express our sincere gratitude to Prof. Dr. Bekir Zühtü UYSAL for guiding us on this path with his valuable knowledge and constructive suggestions. Also, we would like to thank to Fatima Beyza YAĞIZ and Bedir TOPAL for their help getting some experimental data in this study. This study was supported by Gazi University Research Funding [Project No: 06/2007-26].

REFERENCES

[1] Faraji M, Saidi M. Process simulation and optimization of groundnut shell biomass air gasification for hydrogen-enriched syngas production. *Int. J. Hydrog. Energ*;47(28):13579-91,2022.

[2] Saidi M. Performance assessment and evaluation of catalytic membrane reactor for pure hydrogen production via steam reforming of methanol. Int. J. Hydrog. Energ;42(25):16170-85,2017.

[3] dos Santos RG, Alencar AC. Biomass-derived syngas production via gasification process and its catalytic conversion into fuels by Fischer Tropsch synthesis: A review. *Int. J. Hydrog. Energ*;45(36):18114-32,2020.

[4] Mallick D, Mahanta P, Moholkar VS. Co-gasification of coal and biomass blends: Chemistry and engineering. *Fuel*;204:106-28,2017.

[5] Ramos A, Monteiro E, Silva V, Rouboa A. Co-gasification and recent developments on waste-to-energy conversion: A review. *Renew. Sust. Energ. Rev.*;81:380-98,2018.

[6] (NETL) NETL. Fluidized Bed Gasifiers, https://www.netl.doe.gov/research/coal/energy-systems/gasification/gasifipedia/fluidizedbed; 2021 [accessed 18.08.2022].

[7] Khesa N, Mulopo J, Oboirien B. ASPEN Plus® reassessment of efficiency penalties associated with a pulverised coal oxy-combustion power plant-A case study. *CSCEE*;5:100189,2022.

[8] Ciferno J, Marano J. *Benchmarking Biomass Gasification Technologies for Fuels Chemicals and Hydrogen Production*. 2002.

[9] Vozniuk O, Tanchoux N, Millet J-M, Albonetti S, Di Renzo F, Cavani F. Spinel Mixed Oxides for Chemical-Loop Reforming: From Solid State to Potential Application. *Horizons Sust. Indust. Chem. Cataly*. :281-302,2019.

[10] Basu P. *Gasification Theory and Modeling of Gasifiers*. Biomass Gasification Design Handbook. 2010.

[11] Cao L, Yu IKM, Xiong X, Tsang DCW, Zhang S, Clark JH, et al. Biorenewable hydrogen production through biomass gasification: A review and future prospects. *Environ. Res.*;186:109547, 2020.

[12] Rincon L, Puri M, Kojakovic A, Maltsoglou I. The contribution of sustainable bioenergy to renewable electricity generation in

Turkey: Evidence based policy from an integrated energy and agriculture approach. *Energy Policy*;130:69-88, 2019.

[13] Emami Taba L, Irfan MF, Wan Daud WAM, Chakrabarti MH. The effect of temperature on various parameters in coal, biomass and CO-gasification: A review. *Renew. Sust. Energ Rev.*;16(8):5584-96,2012.

[14] Basu P. *Combustion and Gasification in Fluidized Bed.* Taylor and Francis Group; 2006.

[15] Emami-Taba L, Irfan MF, Wan Daud WMA, Chakrabarti MH. Fuel blending effects on the co-gasification of coal and biomass – A review. *Biomass and Bioenergy*;57:249-63,2013.

[16] Fermoso J, Arias B, Plaza MG, Pevida C, Rubiera F, Pis JJ, et al. High-pressure co-gasification of coal with biomass and petroleum coke. *Fuel Process. Technol.*;90(7-8):926-32,2009.

[17] Pinto F, Franco C, André RN, Miranda M, Gulyurtlu I, Cabrita I. Co-gasification study of biomass mixed with plastic wastes. *Fuel*;81:291-7,2002.

[18] Li K, Zhang R, Bi J. Experimental study on syngas production by co-gasification of coal and biomass in a fluidized bed. *Int. J. Hydrog. Energ.*;35(7):2722-6,2010.

[19] Ahmad AA, Zawawi NA, Kasim FH, Inayat A, Khasri A. Assessing the gasification performance of biomass: A review on biomass gasification process conditions, optimization and economic evaluation. *Renew. Sust. Energ. Rev.;*53:1333-47,2016.

[20] Güngör A, Ozbayoğlu, M, Kasnakoğlu, C, Bıyıkoğlu, A, Uysal, B Z Determination of air/fuel and steam/fuel ratio for coal gasification process to produce synthesis gas. J. *Environ. Sci. Eng.;*5(5):799-804,2011.

[21] Lahijani P, Zainal ZA, Mohammadi M, Mohamed AR. Conversion of the greenhouse gas CO2 to the fuel gas CO via the Boudouard reaction: A review. *Renew. Sust. Energ. Rev;*41:615-32,2015.

[22] Lapuerta M, Hernández JJ, Pazo A, López J. Gasification and co-gasification of biomass wastes : Effect of the biomass origin and the gasifier operating conditions. *Fuel Process. Technol.*;89:828-37,2008.

[23] Abuadala A, Dincer I, Naterer GF. Exergy analysis of hydrogen production from biomass gasification. *Int. J. Hydrog. Energ.;*35(10):4981-90,2010.

[24] Kunii D, Levenspiel, O. *Fluidization Engineering.* ABD: Buterworth- Heinemann Series in Chemical Engineering; 1991.

[25] Hedden K. The formation of methane from hydrogen and carbon at high temperatures and pressures. Proceedings of the fifth *Conference on Carbon*. Pergamon Press;125-31,1961.

THREE DIMENSIONAL NUMERICAL INVESTIGATION OF FLOW AND COMBUSTION CHARACTERISTICS IN AN AMMONIA FUELED MULTI-INLET CYCLONE COMBUSTOR

Mustafa Ilbas[1*], Assem Yerzhan[1], Mustafa Demirci[2]

1. Department of Energy Systems Engineering, Faculty of Technology, Gazi University, 06500, Teknikokullar, Ankara, Turkey

*Corresponding author e-mail: assem.yerzhan@gazi.edu.tr

Abstract

The cyclone combustors generally operate with high swirl numbers (3-20). The multi-inlet cyclone combustor that has been simulated in this study has 14 gas/air tangential inlets each of 9.525 mm ID and are inclined towards the front end of the combustion chamber by 30^0 in 2 symmetrical rows of seven. In this study, numerical modelling of a multi inlet cyclone combustor fueled by ammonia has been performed by using a CFD code. Boundary conditions are taken from the literature. The choice of the turbulent model is very important for complex highly swirling flows such as those generated by swirl combustors. In the multi-inlet cyclone combustor, very long residence times have been achieved. Two main flows are noticed in the combustion chamber, one spiralling towards the exit, the other towards the base plate where the boundary flow carries it into the central ascending flow. It is concluded that ammonia and ammonia added methane can be used as emerging fuels in the combustor by obtaining uniform temperature fields and low emissions.

Keywords: The Multi-Inlet Cyclone Combustor, CFD Modelling, Ammonia Combustion

1 INTRODUCTION

Energy plays an extremely important role in ensuring the sustainable and safe development of society. The sufficiency and reliability of providing electricity and heat to the growing needs of the economy and the population are of decisive importance. Traditional energy provides about half of the world's technogenic emissions of greenhouse gases and harmful substances into the environment [1].

Combustion is present continuously in our lives. It is a major source of energy conversion for power generation, transportation, manufacturing, indoor heating and air conditioning, cooking, etc. Its uncontrolled use may have damaging health effects through contamination of air and water [2].

However, achieving emission reduction targets requires the use of alternative, low-carbohydrate or non-carbon fuels in power generation and industrial sectors using combustion systems.

The urgency of the problem of searching for new energy carriers is determined primarily by the need for strict economy of oil products and, secondly, by the need to significantly reduce the toxicity of exhaust gases.

Among the many synthetic substances, only some alcohols, hydrogen and ammonia meet these requirements. According to the majority of world scientists, hydrogen should become the main alternative to hydrocarbon fuel, and the development of hydrogen technologies is considered the most promising.

Hydrogen is seen as the fuel of the future, allowing to solve energy and environmental problems. It has great advantages over fossil fuels. Its heat of combustion is almost three times higher than that of gasoline, and the energy required for ignition is 1.5 times less [3]. When hydrogen is burned in pure oxygen, the combustion products are absolutely harmless - water vapor; when burned in air, nitrogen oxides can be formed, but in smaller quantities than when burning conventional fuels. Hydrogen resources in nature are practically inexhaustible if water is used as a source. When hydrogen is burned, water is formed, which is again involved in the natural cycle.

At the same time, the use of ammonia as a secondary carrier of hydrogen converted into a non-cryogenic safe form is of great practical interest. The prospect of using ammonia as a fuel is due to a number of its positive properties. Ammonia has a higher energy density in terms of hydrogen content than gaseous, liquid hydrogen and metal hydrides, but has a lower calorific value compared to gasoline. Ammonia

is promising as a fuel due to its relatively low cost and virtually unlimited resource base. With the complete combustion of ammonia, only one harmful component is formed - NO_X, and its content is negligible [4].

In this research study, a multi-inlet cyclone combustor is modeled to burn these fuels. Some of the previous studies on this subject have been examined in the literature.

Tunçer investigated the laminar flame velocities of hydrogen-rich methane fuel with chemical kinetic simulations based on the GRI 3.0 mechanism. It was determined that hydrogen enrichment increased the flame as expected. The effect of hydrogen ratio and pressure on flame velocities and emissions was investigated. He found that increasing pressure reduces flame velocities, but in turn increases emissions. Emissions and flame rates increase with increasing hydrogen content. He focused on one- and zero-dimensional simulations. The focus in zero-dimensional simulations is the effect of equivalence coefficient fluctuations resulting from thermo-acoustic instability on lean flame extinction and emissions. In this study, it was observed that hydrogen-rich mixtures were more resistant to equivalence ratio fluctuations [5].

Yılmaz and İlbaş presented temperature distributions from turbulent chemical reactive flow in a model burner for hydrogen-methane fuel mixtures. Gas emissions were also obtained at the combustion chamber exit. Axial and radial temperature measurements were taken from six different distances and four distances, respectively. Experimental measurements were made at extreme air ratios of 1.2 and 1.7, two different thermal powers, 40 and 60 kW, and two different hydrogen-methane fuels. According to the results, it was determined that when the hydrogen content in the fuels is increased, the temperature level increases and the CO and CO_2 emissions decrease [6].

Medhat, Yehia, Khalil et al. have computationally evaluated its performance when a carbonless ammonia-hydrogen mixture is burned in a gas turbine-like combustor. The use of ammonia/hydrogen mixture provides increased flame stability and flame speed. Numerical two-dimensional model simulations of a turbulent flame containing a k-ε turbulence scheme that can be realized with the aid of a chemical mechanism on Reynolds Averaged Navier Stokes (RANS) were performed under various conditions. They chose a partially premixed combustion model with a flame release concept and took into account radiation effects. When the results were evaluated, they found that for constant operating conditions, such as a constant equivalence ratio of 0.8, increased hydrogen content resulted in increased NO emissions. Also, for constant ammonia/hydrogen concentrations, NO emissions increase with the equivalence ratio, then decrease under rich conditions, and NH_3 emissions are generally low. An equivalence ratio of less than 1.2 will be preferred to reduce the amount of unburned NH_3 formation [7].

Ayman M. Elbaz et al. in their article, they emphasize the importance of ammonia as an energy carrier and offer the basics of ammonia combustion. Measures to address the problem of low ammonia reactivity and its impact on NOx emissions are also presented. In this research work emphasizes the role of crucial reaction differences, the updates in the NO_x and De-NO_x pathways, NH_i recombination reactions and H_2NO chemistry. Various strategies have also been discussed to reduce NO emissions from the use of ammonia in gas turbines and industrial applications [8].

Kobayashi et al. In their paper, they discuss the successful use of ammonia as a fuel in gas turbines and in industrial furnaces. It also discusses the fundamental aspects of ammonia combustion, including characteristics of laminar premixed flames of a premixed. In addition, details are given on the combustion of ammonia to form NOx, NOx reduction processes, and testing of several models of ammonia oxidation kinetics.

Eventually, LES results for a gas turbine swirl burner are presented for the development of single-fuel ammonia gas turbines with low NOx emissions [9].

2 THE COMBUSTOR AND NUMERICAL METHOD

Cyclone combustors have been developed that give very good results with very low NO_x emissions. These combustors are mainly used to burn low calorific value fuels and previous studies have shown that such combustors provide efficient combustion systems for low calorific value gases. The multi-inlet cyclone combustor that has been simulated in this study is shown in Figure 1. It has 14 gas/air tangential inlets each of 9.525 mm ID and are inclined

towards the front end of the combustion chamber by 30^0 in 2 symmetrical rows of seven. The features of the multi-inlet cyclone combustor are as follows;

Diameter of the combustor exit : 76.20 mm
Diameter of the cyclone chamber : 152.4 mm
Total length of the combustor : 457.2 mm
Geometrical swirl number : Sg=7.91

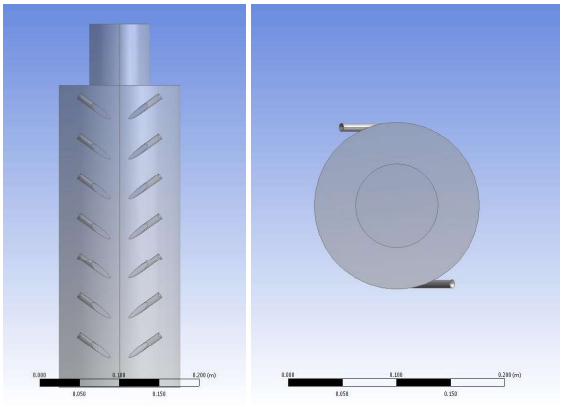


Figure 1. Multi-Inlet Cyclone Combustor

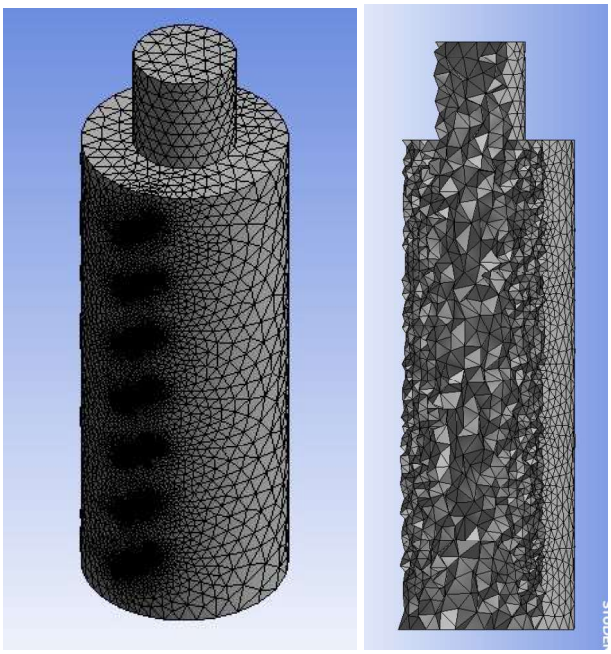


Figure 2. Mesh for the Multi-Inlet Cyclone Combustor

The cyclone combustor has been designed to be fully premixed and normally unlined. To provide a fully premixed combustor a copper tube of 20 mm ID with numerous entry holes was soldered into the main air supply tube. This design, due to the location of the main gas supply tube, which is far enough from the tangential inlets, gives good premixing of fuel and air, thus a more uniform combustion took place inside the cyclone combustor and the flame fully occupied the combustor body [10]. The mesh structure of the combustor is given in Figure 2.

3 RESULTS AND CONCLUSIONS

In this study, numerical analyzes of methane-air and ammonia-air mixtures were made using the ANSYS Fluent CFD code. Inlet velocities were calculated from the known volumetric flowrate according to mixture ratio. The boundary conditions were defined in terms of temperature and constant both for inlets and walls. The gas law was used to calculate the fluid density. The other physical constants of fluid were taken from the literature which are specific heat, thermal conductivity and viscosity. The computational default value was used for the operating pressure. Turbulence intensity was taken as to be default value of 10 %, Characteristic length scale was of 9.525e - 03m. Next the chemical species mass fractions at the inlet were defined by input of mass fractions of the Methane (CH_4), Ammonium (NH_3), Oxygen (O_2) and Nitrogen (N_2) according to mixture ratio. Inlet temperature of fluid was taken as to be 300 K in all cases. The turbulence model k - ε was used. The number of iterations was 2500. The results of modeling the combustion of a mixture of methane-air are shown in Figures 3 to 8.

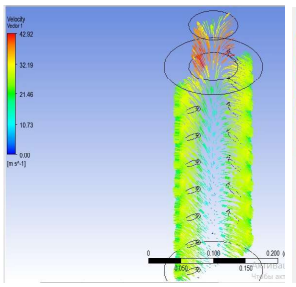


Figure 3. Velocity Distributions

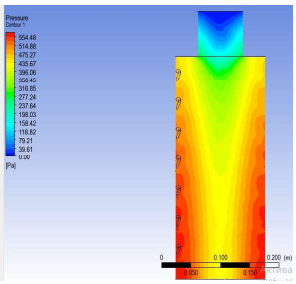


Figure 4. Pressure Distributions

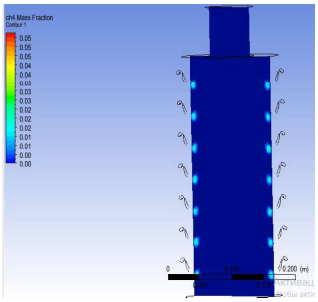


Figure 5. CH_4 Mass Fractions

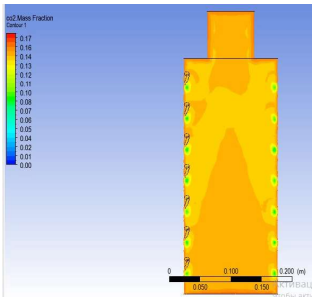


Figure 6. CO_2 Mass Fractions

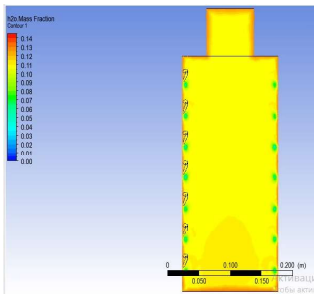


Figure 7. H_2O Mass Fractions

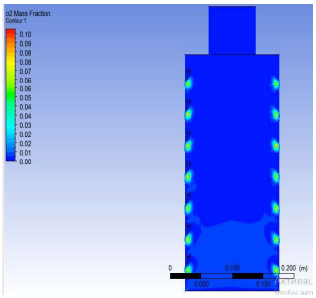


Figure 8. O_2 Mass Fractions

Figures 9-17 show the results of modeling the combustion of an ammonia-air mixture.

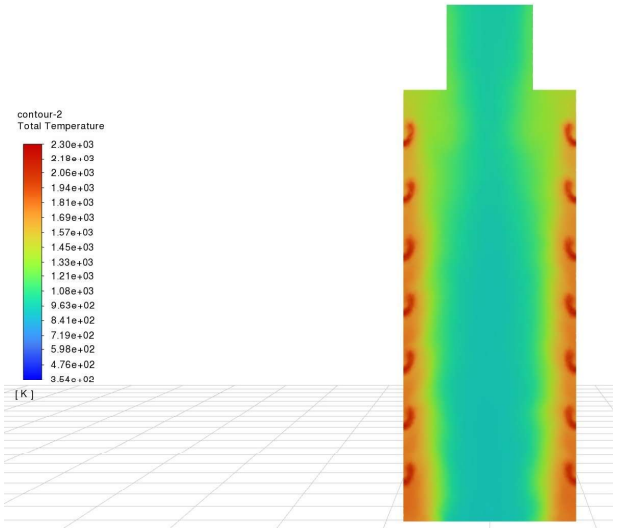


Figure 9. Temperature Distributions (K)

Figure 9 shows the temperature distribution when simulating the combustion of an ammonia-air mixture in a combustor.

The maximum temperature level was about 2300 K.

Uniform temperature distributions throughout the combustor length with the flame front being located next to the chamber wall. This can be explained by the location of the tangential inlets along the chamber and flame stabilization near the wall. Temperature levels are reduced (963 K) in the central core vortex region. This is because of the recirculation of slightly cooler burnt products from the exhaust zone.

The predicted turbulence distributions for isothermal conditions with the extended grid is given in Figure 12. At the inlet boundary, the inlet turbulence intensity was set at 10 % (default value of Fluent). Maximum value of turbulence is about 16 m^2/s^2 at the bottom wall inside the combustor main chamber and 28 m^2/ s^2 just outside the combustor exhaust.

Figures 5-8, 14-17 show the mass fractions of CH_4, NH_3, O_2, CO_2, H_2O and N_2.

The predictions show that methane and ammonia are consumed in the region very close to inlets. Furthermore methane and ammonia are consumed as soon as they enter the combustion chamber. The distributions of O_2, mass fractions (Figures 8, 15) and CH_4/NH_3 mass fractions were similar in shape. This was likely because of the premixing of the methane/ammonia and oxygen.

Figure 6 presents distributions of the predicted CO_2 mass fractions. The maximum predicted CO_2 level was 15 % which was produced from the conversion of CO to CO_2 in the second reaction. Distributions of the predicted H_2O mass fractions are given in Figures 7, 16. The maximum H_2O level was about 11 % and 20.7 % for these conditions and for N_2 (figure 17) about 10%.

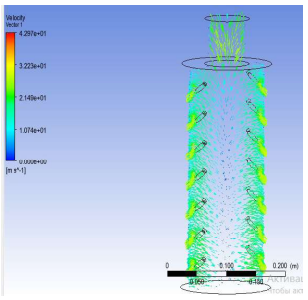


Figure 10. Velocity Distributions

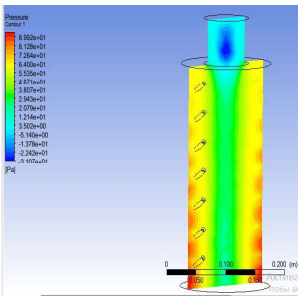


Figure 11. Pressure Distributions

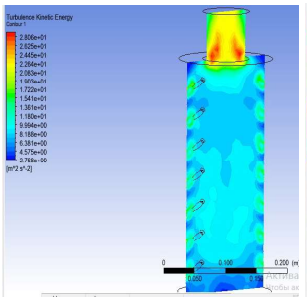


Figure 12. Turbulence Kinetic Energy

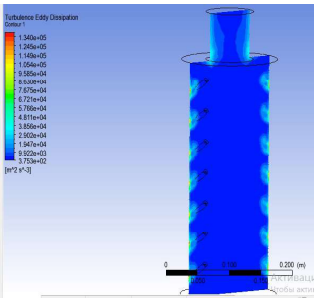


Figure 13. Turbulence Eddy Dissipation

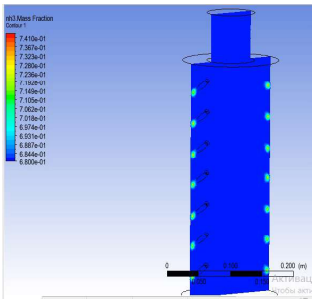


Figure 14. NH_3 Mass Fractions

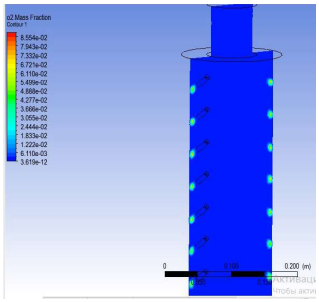


Figure 15. O_2 Mass Fractions

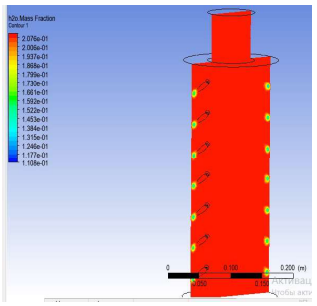


Figure 16. H_2O Mass Fractions

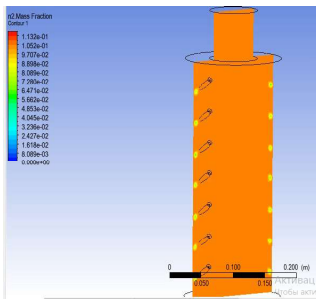


Figure 17. N_2 Mass Fractions

Based on the results obtained was concluded that ammonia and ammonia-added methane can be used as emerging fuels in the combustor by obtaining uniform temperature fields and low emissions.

REFERENCES

[1] B. N. Porfiriev, Alternative energy as a factor of environmental and energy security. *Journal of Regional, Vol. 2,* pp. 137-145, 2011.

[2] Sara McAllister, Jyh-Yuan Chen, A. Carlos Fernandez-Pello, *Fundamentals of Combustion Processes*, Springer, 2011.

[3] V. A. Legasov, *Atomic Hydrogen Energy and Technology*, Energoatomizdat, 1986.

[4] L. G. Kovalev, S. V. Zakharov. Possibilities of using ammonia as a carrier of hydrogen as a fuel for internal combustion engines. *Journal Vestnik. Vol. 4,* pp. 158-163, 2007.

[5] O. Tuncer, Chemical kinetic analysis of flame rates and emission values of hydrogen-enriched methane fuel, *Journal of Thermal Science and Technology, Vol. 29(2),* pp. 29-42, 2009.

[6] I. Yilmaz, M. Ilbas, An experimental study on hydrogen-methane mixtured fuels, *İnternational Communications in Heat and Mass Transfer*, Kayseri, 2007.

[7] Medhat, M., Yehia, M., Khalil, A., Franco, M.C., Rocha, R.C., A numerical prediction of stabilized turbulent partially premixed flames using ammonia/hydrogen mixture, *Journal of Advanced Research in Fluid Mechanics and Thermal Sciences, Vol. 87(3),* pp. 113-133, 2021.

[8] Ayman M. Elbaz, Shixing Wang, F. Guiberti, W. L. Roberts, Review on the recent advances on ammonia combustion from the fundamentals to the applications, *Journal Fuel Communications, Vol. 10,* pp. 1-26.

[9] H. Kobayashi, A. Hayakawa, K. D. Kunkuma, A. Somarathne, E. C. Okafor, Science and technology of ammonia combustion, *Proceedings of the Combustion Institute*, *Vol. 37,* pp. 109-133, 2019.

[10] M. Ilbaş, *Studies of ultra low NO_x burners*, PhD Thesis, School of Engineering, University of Wales, Cardiff, 1997

SYNTHESIS OF Pt/rGO CATHODE CATALYSTS FOR PEM FUEL CELLS THROUGH POLYOL AND COLLOIDAL METHODS

Tolga Kaan Kanatlı and Nezihe Ayas*

Department of Chemical Engineering, Faculty of Engineering, Eskisehir Technical University, Eskisehir, email: nazcan@eskisehir.edu.tr

Abstract

Hydrogen is a clean energy carrier that can be utilized in Proton Exchange Membrane (PEM) fuel cells to generate green electricity. In a PEM fuel cell, the hydrogen oxidation reaction (HOR) takes place at the anode, and the oxygen reduction reaction (ORR) at the cathode. ORR is much slower than HOR, therefore developing a potent catalyst for the cathode is of great importance. For this purpose, Pt/rGO (38 wt.%) catalysts were synthesized through polyol (at 190 °C) and colloidal methods (at room temperature), and the methods were compared. Catalysts were characterized through X-ray diffraction spectrometry (XRD), Thermogravimetric analysis (TGA) and Fourier transform infrared spectrometry (FT-IR). It was determined that the polyol method produces catalysts with higher Pt loading.

Keywords: Catalyst, Pt/rGO, Fuel Cell, PEM

1 INTRODUCTION

As the world population and industrialization increase, the power generation infrastructure of the planet is put under strain. This increase in power demand is being met mostly by fossil fuels, however, issues like climate change and the unsustainability of such fuel sources have pushed researchers into developing ways to utilize greener alternatives such as hydrogen.

When hydrogen reacts with oxygen to generate heat or power, the only product is water. Because of this reason, hydrogen is considered to be a clean energy carrier. Most of the hydrogen is produced through the steam reforming of methane, which is a costly process with a large carbon footprint. However, in previous studies by the authors, hydrogen-rich gas was successfully generated from biomass. Hydrogen generated through these methods is renewable and can help reduce carbon emissions [1].

Proton-Exchange Membrane (PEM) fuel cells utilize hydrogen to generate emission-free electricity. PEM fuel cells work at low temperatures (80 °C), and generate electricity directly, without the need for large steam turbines. This allows them to be light, and portable. Therefore, PEM fuel cells are especially valuable in the aerospace industry, however, they can also be used in powerplants for bulk energy generation [2].

In a PEM fuel cell, hydrogen is fed to the anode to undergo the hydrogen oxidation reaction in which the H_2 molecule breaks up into H^+ ions and electrons. The electrons travel away through the wires to power the connected devices, and the H^+ ions travel through the membrane to the cathode. After going through the circuits of the connected devices, electrons arrive at the cathode. The electrons, H^+ ions, and oxygen react in the oxygen reduction reaction to produce water. For these reactions to occur at low temperatures, highly potent catalysts loaded with Pt or its alloys like Pt-Ru and Pt-Au are used. ORR is a much slower reaction than HOR, therefore developing a potent catalyst for the cathode is of great importance [3].

Carbon black is the widely used support material for its high surface area and electron conductivity. Other support materials such as carbon nanotubes (CNT) [4], reduced graphene oxide (rGO) [5], titanium [3], and other conductive materials can also be used. rGO improves the corrosion resistance of the catalyst, has a large surface area, and is more conductive than carbon black. Marinoiu et al. used rGO support material at PEM fuel cells and reported superior electrochemical performance and stability [6].

PEM catalysts can be synthesized through many methods such as low-temperature precipitation, colloidal synthesis, sol-gel, impregnation, microemulsion, polyol, chemical vapor deposition (CVD), and electrochemical synthesis. The polyol method is the most widely used in the literature, however, the colloidal method is seldomly used on its own [7]. Therefore, a comparison of these methods was deemed necessary.

2 EXPERIMENTAL

2.1 rGO Synthesis

Reduced graphene oxide support material was synthesized through the modified hummers method which is the most common method used in the literature [8]. Graphite powder was mixed with H_2SO_4 and the mixture was stirred for 6 hours to produce graphite oxide. The produced graphite oxide was washed and centrifuged. Graphite oxide was then mixed with H_2SO_4 in an ice bath, and $KMnO_4$ was added. The mixture was then placed in a water bath and stirred at 35 °C for 2 hours. Afterward, H_2O_2 was added to help with the removal of $KMnO_4$, the mixture was washed with HCl and water and centrifuged. The resulting graphene oxide (GO) was dried in an oven at a low temperature (60 °C) for a day. Afterward, 100 mg GO was mixed with 100 mL water, and the mixture was sonicated for 90 minutes. The resulting reduced graphene oxide was centrifuged and dried.

2.2 Catalyst Synthesis Through Colloidal Method

40 wt.% Pt/rGO catalysts were synthesized through the colloidal method, similar to the one used by Fuente et al [7]. 20 mL Pt precursor (H_2PtCl_6) was mixed with 10 mL of isopropyl alcohol, then the pH was brought to 4 to produce a colloid mixture. A rGO - water mixture was added to the colloid mixture. Afterward, formaldehyde was added, and the mixture was stirred. In the end, the catalyst was washed with water and dried in an oven. A Pt loading of 40% was aimed.

2.3 Catalyst Synthesis Through Polyol Method

Microwave-assisted polyol method, similar to the one used by Kwok et al was utilized in this work [8]. Milestone Start S microwave synthesis unit was used at 500 W max power. A mixture of Pt precursor (H_2PtCl_6), NaOH and ethylene glycol (EG) was prepared. The mixture was brought to 190 °C and stirred for 20 minutes under reflux to produce a colloid. A rGO-EG solution was added to the colloid mixture and the system was stirred for 30 minutes. Afterward, it was heated to 190 °C and stirred for 35 minutes under reflux and the resultant catalyst was washed with water and centrifuged. The catalyst was dried overnight in an oven at 60 °C.

2.4 Catalyst Characterization

Crystalline structures of the catalysts were analyzed with a Rigaku Rint 2200 XRD device at a scanning angle of 0.02º, scanning speed of 8°/min, and in the range of 2θ = 5-85°. Debye Scherrer equation was used to determine crystalline sizes. Functional groups of the support material and catalysts were investigated with a Thermo Scientific Nicolet IS10 FT-IR device at a scanning speed of 64°/min, 4 cm^{-1} resolution in the range of 400-4000 cm^{-1}. Thermogravimetric analysis (TGA) of the catalysts and rGO was conducted by a Netzsch STA 6000 TGA device with an airflow rate of 50 mL/min, heating rate of 10 °C/min in the temperature range of 30-850 °C.

3 RESULTS AND DISCUSSION

3.1 FT-IR Results

FT-IR spectra of the support material and catalysts are given in Figure 1.

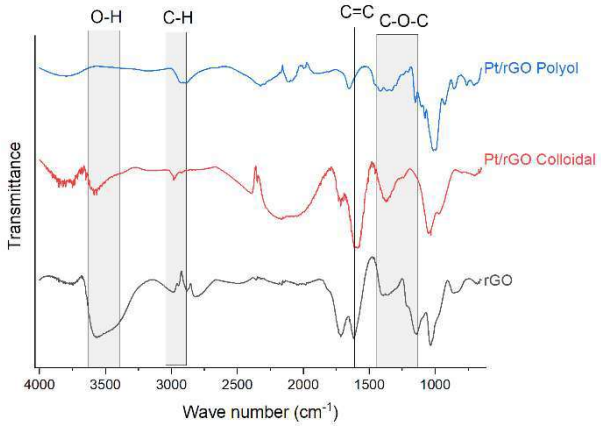


Fig 1. FT-IR spectra of rGO support and Pt/rGO catalysts

As seen in figure 1, rGO support material shows an O-H peak at 3600 cm^{-1} while the Pt/rGO catalysts show a much smaller peak. O-H functional groups create an easier binding route for mono atoms. This result shows that majority of the O-H functional groups got occupied by Pt molecules [9]. Catalyst synthesized through the polyol method doesn't have this peak, this means that the polyol method was more successful at loading Pt onto rGO.

Peaks between 1600-1050 cm^{-1} signify the C-O groups, and the peak at 1613 cm^{-1} shows the double bonded carbons. These peaks are caused by the graphene oxide support material, and they are similar to the peaks observed in the literature [10].

3.2 TGA Results

Both the support material (rGO) and the catalysts lost a considerable amount of mass between 350-580 °C. This loss is caused by the disintegration of the carbon mesh. Small amount of mass losses were observed with the rGO support material between 116-353 °C. In the literature, these losses are attributed to oxygen-containing groups that graphene oxide has [11]. The mass losses of the catalysts stabilized after 650 °C. The remaining mass of the catalysts at 850 °C signifies the Pt content of the catalyst. According to these results, Pt/rGO catalyst synthesized by the colloidal method has a Pt loading of 25 wt.%, and Pt/rGO catalyst synthesized by the polyol method has a Pt loading of 38 wt.%. These results show that the polyol method was a lot more successful at reaching the desired catalyst loading (40 wt.%).

3.3 XRD Results

XRD patterns of the rGO support and Pt/rGO catalysts can be seen in Figure 2.

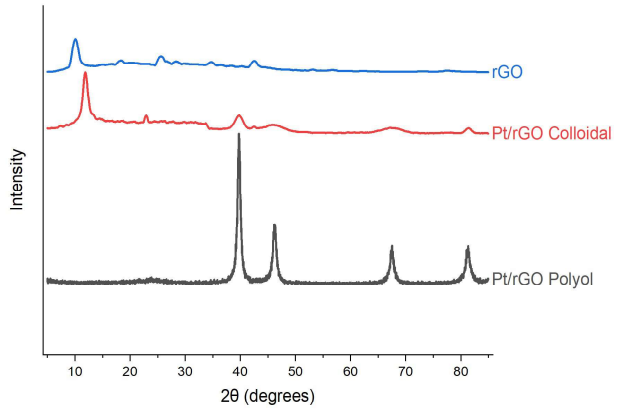


Figure 2. XRD Patterns of rGO support and Pt/rGO catalysts

Peaks at 2θ = 40, 46, 67.5 and 81.4° are the (1 1 1), (2 0 0), (2 2 0) and (3 1 1) peaks of the FCC Pt, respectively. The peak at 2θ = 26° is the characteristic peak of rGO, and the peak at 2θ = 12° is the characteristic peak of GO [12]. The existence of the GO peak shows that not all of the GO was reduced to rGO, however, this peak disappeared completely after the polyol process. Therefore, it can be said that the polyol process helped further reduce GO to rGO. Crystal sizes of the Pt particles were calculated, and they are found to be 10.08 nm for the polyol synthesis and 5.7 nm for the colloidal synthesis. In the literature, the ideal Pt crystal size for PEM fuel cells is reported to be between 2-5 nm. Catalyst synthesized by the colloidal method is close to this value, however, the polyol method resulted in undesirably high crystal size. This is caused because of the high synthesis temperatures used during the polyol method [12].

4 CONCLUSION

In this study, Pt/rGO catalysts were synthesized through polyol and colloidal methods, and the effectiveness of the methods were compared. TGA results show that the Pt loading was significantly higher (38 and 25 wt.%) for the polyol method. XRD patterns also show that the polyol method helped further reduce the graphitic support material into rGO, however, the Pt crystal size obtained by the colloidal method (5.7 nm) was smaller than the crystal size obtained by the polyol method (10 nm).

It is concluded that the polyol method yields catalysts with higher metal loading, however, the temperature of the polyol process should be controlled to obtain smaller crystal sizes.

ACKNOWLEDGEMENTS

This study was supported by Eskisehir Technical University Scientific Research Projects Commission under grant no: 21DRP148.

The authors acknowledge the support of Eskisehir Technical University Department of Material Science and Engineering for the XRD analysis.

REFERENCES

1. Kanatli, T. K. & Ayas, N. Gasification of sunflower seed pulp for the synthesis of hydrogen-rich products. 50, pp. 226–230. 2019.
2. Wang, C.-W. & Sastry, A. M. Mesoscale modeling of a Li-ion polymer cell. *J. Electrochem. Soc.* 154, pp. A1035--A1047. 2007.
3. Lim, A. *et al.* Polymer Electrolyte Membrane Unitized Regenerative Fuel Cells: Operational Considerations for Achieving High Round Trip Efficiency at Low Catalyst Loading. *Appl. Catal. B Environ.* 297, pp. 120458. 2021.
4. Zheng, Y. *et al.* Atomic platinum layer coated titanium copper nitride supported on carbon nanotubes for the methanol oxidation reaction. *Electrochim. Acta* 248, pp. 349–355. 2017.
5. Wang, J., Min, L., Fang, F., Zhang, W. & Wang, Y. Electrodeposition of graphene nano-thick coating for highly enhanced performance of titanium bipolar plates in fuel cells. *Int. J. Hydrogen Energy* 44, pp. 16909–16917. 2019.
6. Marinoiu, A. *et al.* Synthesis of well dispersed gold nanoparticles on reduced graphene

oxide and application in PEM fuel cells. *Appl. Surf. Sci.* 504, pp. 144511. 2020.
7. de la Fuente, J. L. G. *et al.* Functionalization of carbon support and its influence on the electrocatalytic behaviour of Pt/C in H2 and CO electrooxidation. *Carbon N. Y.* 44, pp. 1919–1929. 2006.
8. Kwok, Y. H., Wang, Y. F., Tsang, A. C. H. & Leung, D. Y. C. Graphene-carbon nanotube composite aerogel with Ru@Pt nanoparticle as a porous electrode for direct methanol microfluidic fuel cell. *Appl. Energy* 217, pp. 258–265. 2018.
9. Lagarteira, T. *et al.* The role of Pt loading on reduced graphene oxide support in the polyol synthesis of catalysts for oxygen reduction reaction. *Int. J. Hydrogen Energy* 45, pp. 20594–20604. 2020.
10. Gholivand, K., Sabaghian, M. & Eshaghi Malekshah, R. Synthesis, characterization, cytotoxicity studies, theoretical approach of adsorptive removal and molecular calculations of four new phosphoramide derivatives and related graphene oxide. *Bioorg. Chem.* 115, pp. 105193. 2021.
11. Farivar, F. *et al.* Unlocking thermogravimetric analysis (TGA) in the fight against “Fake graphene” materials. *Carbon N. Y.* 179, pp. 505–513. 2021.
12. Pak Hoe, L., Boaventura, M., Lagarteira, T., Kee Shyuan, L. & Mendes, A. Polyol synthesis of reduced graphene oxide supported platinum electrocatalysts for fuel cells: Effect of Pt precursor, support oxidation level and pH. *Int. J. Hydrogen Energy* 43, pp. 16998–17011. 2018.

THE EFFECT OF DIFFERENT CHARGING CONCEPTS ON HYDROGEN FUELLED INTERNAL COMBUSTION ENGINES

İ. Güler[1], O. Barış[2] and A. Yaşgül[3]

1. AVL Research and Engineering TR, Istanbul; email: ilker.guler@avl.com
2. AVL Research and Engineering TR, Istanbul; email: onur.baris@avl.com
3. AVL Research and Engineering TR, Istanbul; email: anil.yasgul@avl.com

Abstract

Hydrogen is the biggest candidate to be the fuel of the future in internal combustion engines with its chemical properties, environmental friendliness and being able to be produced from many different sources. Its carbon-free structure plays a key role for achieving the strict emission regulations. On the other hand, if the high amount of air flow demanded by hydrogen as a requirement of combustion stoichiometry cannot be achieved, NOx emissions that emitted after combustion become an important problem for the engine manufacturers.

The main aim of this study is determining the ideal boosting strategy for hydrogen fuelled internal combustion engines to meet the objectives such as fuel economy, high power density and low NOx emissions. A hydrogen fuelled internal combustion engine which is for heavy-duty-vehicle application and equipped with direct injection system has been modelled to achieve the aim. The results from the model were validated with dynamometer data. Several charging concepts have been investigated with model-based approach.

Keywords: Hydrogen, Engine Modelling, Boosting Strategy, Lambda

1 INTRODUCTION

From the beginning of the 21st century to the next twenty year, the world population has increased by about 26% as can be seen in [1]. This situation has also led to a demand growth to energy. In order to supply with this emerging energy need, the trend towards carbon-based fuels has caused to an increase of 39% in total greenhouse gas (GHG) emission values as carbon-dioxide (CO2) equivalent. When these increase items are analyzed by sector; industrial usage, electricity and heat production and, transportation are the leading ones as shown in [2].

To have a more livable planet and prevent global warming, the reduction of greenhouse gases released into the atmosphere has become a priority target for the whole world. In order to both achieve this goal and comply with strict emission regulations, the automotive industry has also turned to alternative fuels instead of carbon-based fossil fuels. Many researchers and engine manufacturers have emphasized that hydrogen is more suitable for use in internal combustion engines than other alternative fuels in terms of its unique physical and chemical properties [3, 4, 5, 6].

The comparison of hydrogen in terms of combustion properties, that is a candidate to replace fossil fuels in the future, with conventional fuels such as diesel and gasoline, which are widely used in internal combustion engines, are summarized in Table 1 from using the information from [7, 8, 9].

Hydrogen has extremely wide ignition limits compared to other conventional fuels which is very well suited for lean operation [10]. The most important factor triggering the formation of NOx emissions is the high temperature reached in the cylinder [11]. Lean mixture formation helps to reduce the combustion temperature thus near zero NOx emission aim can be achieved on H2 fuelled ICE [4]. Also another great benefit of lean mixture is of course a better overall engine efficiency because of the absence of flow losses (pumping losses) [12].

Table 1. Properties of Hydrogen Compared to Gasoline and Diesel

Property	Unit	Gasoline	Diesel	Hydrogen
Density	kg/m^3	760	833	0.09
Lower heating value	MJ/kg	43.5	42.5	120
Stoichiometric air demand	kg_{air}/kg_{fuel}	14.7	14.5	34.3
Mixture calorific value PFI (mixture aspirated)	MJ/m^3	3.76	-	3.19
Mixture calorific value DI (air aspirated)	MJ/m^3	3.83	3.77	4.52
Minimum ignition energy	mJ	0.24	0.24	0.02
Ignition limits	Vol % λ	1.0-7.6 0.4-1.4	0.6-5.5 0.5-1.3	4-76 0.2-10
Auto-ignition temperature	K	~623	~523	858
Laminar flame speed	cm/s	40-80	40-80	200
Quenching distance	mm	~2	-	0.64
Adiabatic flame temperature	K	2580	~2300	2480
Carbon content	%	84	86	0

At stoichiometric engine operation condition, hydrogen has the higher flame speed. This results in a more isochoric, thus thermodynamically more favourable combustion. On the other hand flame speed reduces on the lean mixture condition as explained in [13].

With the highest auto-ignition temperature relative to the common fuels, the resistance of hydrogen to knocking is expected to be high [9]. This feature also proves that hydrogen fuel is more suitable for use in spark ignition engines. However, since the minimum ignition energy value is very low, there is a risk of pre-ignition caused by hot spot if hydrogen fuel is used in spark ignition engines. Also, a non-platinum cold-rated spark plug should be used to avoid risks such as pre-ignition and backfiring in SI engine [14].

Hydrogen, which stands out thanks to its combustion characteristics and carbonless structure, is the biggest candidate to be the fuel of the future with its from different sources and enviromental-friendly production methods.

However, on H2 ICE, it is vital to determine the correct boosting strategy in order to keep emissions within regulation limits.

In this paper, conventional turbocharging concepts in the automotive sector are considered for H2 engine. The concepts that are investigated are as follows:

1. Fixed geometry turbocharger (FGT)
2. Variable geometry turbocharger (VGT)
3. 2-stage Turbocharging (2-stage)

FGT concept is the simplest and easiest solution to apply on an engine. It is also the most cost friendly option and therefore it is added to the list for consideration. This configuration is controlled via a wastegate, so there is active wastegate control.

VGT concept brings more flexibility across whole engine speed range, in which a smaller turbine is better for low speeds and high speeds require bigger turbine size. VGT can provide this by varying the turbine inlet geometry.

2-stage turbocharging is the most complex and costly one out of these options, but it is very advantageous considering high air requirements of hydrogen, which will be explained in more detail in thermodynamics part. 2-stage concept used in the model includes a mid-stage cooler as well. The smaller turbocharger is selected as a VGT for easier controllability and more flexibility. In this article, the first turbocharger that compresses the air is called the low pressure (LP) turbocharger and the second stage is called the high pressure (HP) turbocharger. It is explained here for more clarity for the following sections.

In addition to these, more advanced concepts such as e-turbo, e-boost or more advanced electrically assisted turbocharging systems can be modelled. However, these types of concepts are not widely available in the market. In addition, these all systems require higher voltage (48 V or higher), advanced electrical system and/or hybridization. For the sake of system simplicity, these concepts are left out of the scope of this paper, but these can be investigated as a next step if need arises.
Detailed comparison and conclusions out of this study will be given in the following parts of the paper but first the details of thermodynamic model will be explained.

2 THERMODYNAMIC MODEL

In this part; the important model details such as concepts that are selected will be explained.
The engine considered here is a heavy-duty inline engine, which is in a displacement widely used in the industry.
Thermodynamical model consists of one-dimensional (1D) model of the air path of the engine. Turbochargers are modelled using the measured performance maps of compressor and turbine parts.

For the investigation in this paper, low pressure direct injection concept hydrogen engine with spark ignition (SI) is simulated. Therefore, its compression ratio is lower compared to diesel similar to other heavy duty SI engines such as natural gas (NG) engines. There are also other injection concepts available such as multi-port injection (MPI) which is also spark ignited and high-pressure direct injection (HPDI) with diesel pilot or HPDI hydrogen only (ignited with glow plug or other support system). The reason why LPDI concept is selected because of its best compromise between parameters such as cost, risk, availability (of the injection system) and efficiency [15]. MPI concept is the cheapest among these concepts and easiest to adapt [16]. The injection system is relatively low pressure and less complex. One big disadvantage of MPI is backfire as can be seen in [15] In addition, it is mentioned in the same paper that the efficiency of the engine is lower compared to other concepts. Due to lower efficiency; its power density is also lower compared to other concepts. HPDI with diesel pilot is the concept, which is closest to diesel engine concept. The hydrogen is ignited with the means of a diesel pilot injection. Like diesel; the concept benefits from high compression ratio and therefore high thermal efficiency. However, since there is diesel pilot injection, there is also some amount of CO2 emitted from the engine. Other downside of the engine is the more complex and high pressure fuelling system required for both diesel and hydrogen. Another disadvantage of this system is the high cost related to its high-pressure injection system. Hydrogen only HPDI concept is generally considered to be troublesome and requires a lot of further work as stated in references [9, 17]. Therefore, it is left out of consideration. So, considering all the information available; it is concluded that the LPDI tends to have the best trade-off between all aspects considered.

Hydrogen combustion has different emission characteristics compared to diesel. As can be seen in reference [18]. Hydrogen tends to go to almost 0 engine-out NOx emission as excess air ratio (λ) goes above 2.4. Figure 1 from reference [18] clearly shows the behaviour and it is also stated in the paper explicitly. Similar conclusions and data are also shown in [19]. This will have the advantage to eliminate the NOx conversion catalyst (selective reduction catalyst- SCR) entirely or use a small and simpler one. This means that there can be a simpler and cheaper aftertreatment system (ATS). Therefore, it is chosen to investigate full load performance at high lambda.

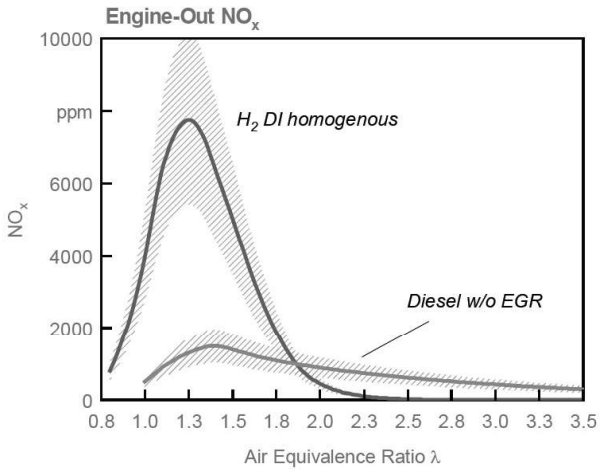


Figure 1 – Typical NOx behaviour of a hydrogen DI engine vs diesel.

Compared to engines in the market, this is a very high value and requires too much air. Therefore, instead of pumping all air into the cylinder, a cylinder mass ratio (CMR) is defined and it is targeted to 2.4. This is done because EGR is used in the model in all of the turbocharging concepts mentioned above. So the CMR includes both air and EGR divided by fuel mass and divided by stoichiometric air fuel ratio (AFR) of hydrogen as shown below.

$$CMR = \frac{\text{air flow} + \text{EGR flow}}{\text{fuel flow} * 34.33} \quad (1)$$

As stated in reference [20], high heat capacity of EGR will compensate even better than air to lower in cylinder temperatures and therefore also NOx emissions. It is clearly known that NOx is

directly related with high temperatures in cylinder as shown in [11]. In addition to these facts, tests are also performed to prove that CMR has similar effect on NOx emission as lambda and this behaviour is shown in Figure 2.

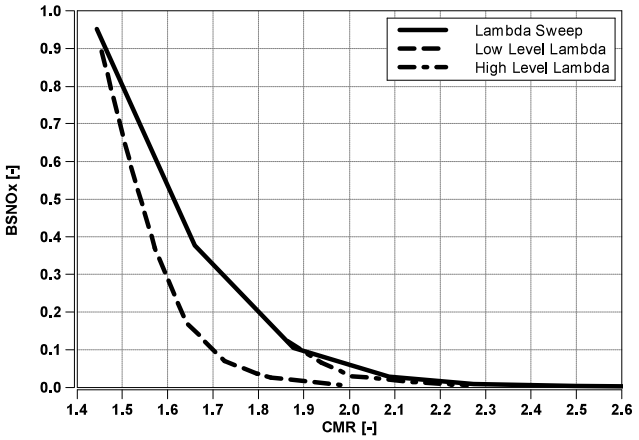


Figure 2 – NOx behaviour comparison including both Lambda and CMR

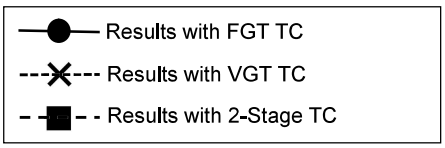
Since the selected target mass ratio (CMR) is significantly higher than typical diesel and gasoline engines, the question is whether there is a sufficient turbocharger able to supply the air flow demand. It is also the reason why different concepts are investigated in this paper in terms of their performance with such high mass ratio.
As the choice of the combustion model; SI Wiebe model is used. The combustion model is correlated with test engine data presented in [21]. Since the combustion process occurs within a homogenous mixture with spark ignition, it is well correlated using SI Wiebe function. In addition, limitations seen in tests are considered when determining the combustion timing in order to avoid abnormal combustion events due to hydrogens easy ignitability.

As mentioned earlier; EGR system is utilized. A high pressure EGR system between exhaust and intake boost system is used, which is one of the most common concepts. Also the EGR is cooled because hot EGR will drop the mass flow into the cylinder significantly at high loads. EGR is also beneficial for abnormal combustion events as investigated in reference [20]. In addition; some of the mass flow required for low NOx is supplied using EGR system, which in turn lowers airflow requirement from the turbocharger. So the range of airflow required from turbocharger will be lower and a smaller turbocharger can be selected, which will be also beneficial for transient response.

3. COMPARISON OF RESULTS

In this section, the comparison of steady state results between different turbocharger concepts will be shown.

As stated in the thermodynamic model section, this study has been performed by trying to reach CMR target 2.4 and this target has been achieved with all turbocharger concepts as can be seen below. In addition to that, all related results can be seen comparatively between concepts.



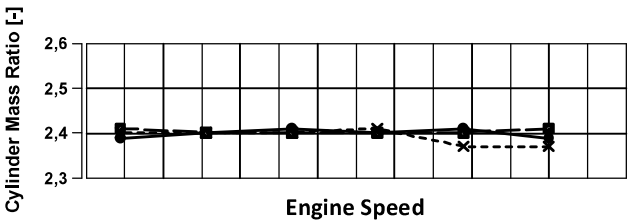


Figure 3 – CMR

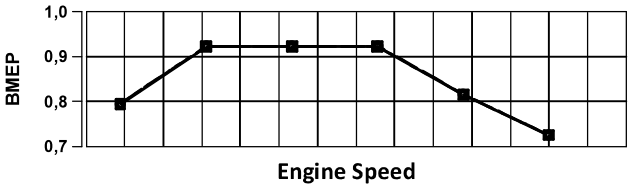


Figure 4 – BMEP

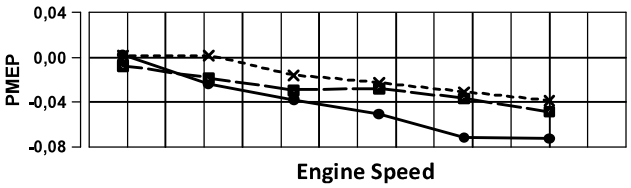


Figure 5 – PMEP

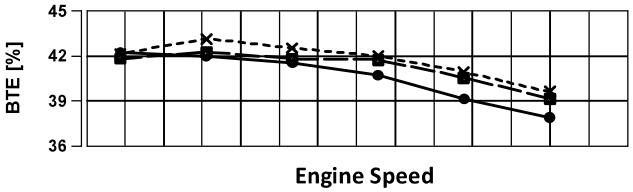


Figure 6 – BTE

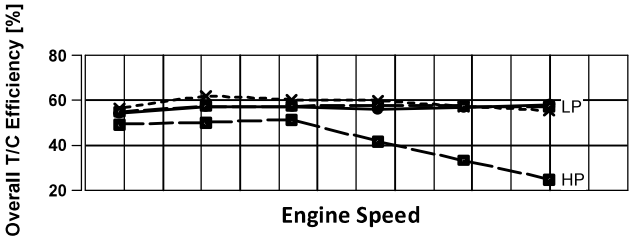


Figure 7 – Overall turbocharger efficiency

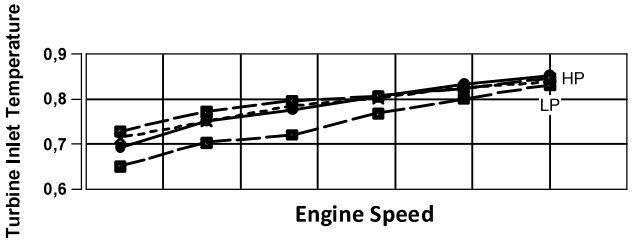


Figure 8 – Turbine inlet temperature

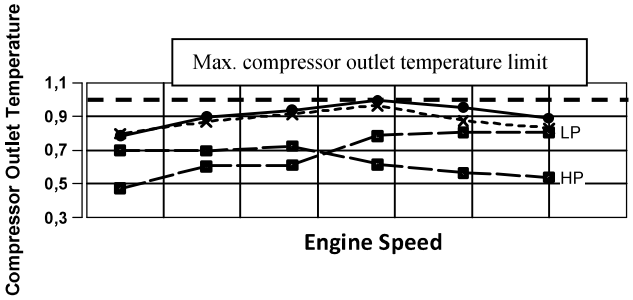


Figure 9 – Compressor outlet temperature

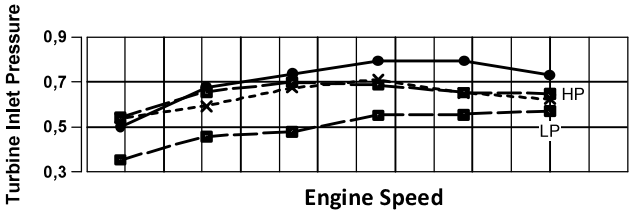


Figure 10 – Turbine inlet pressure

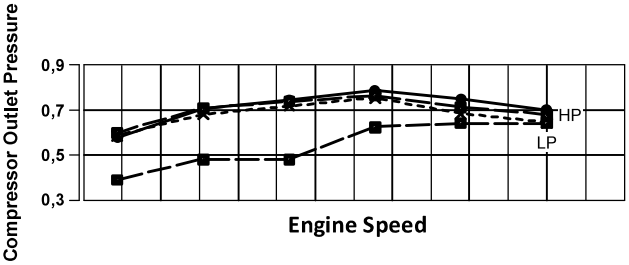


Figure 11 – Compressor outlet pressure

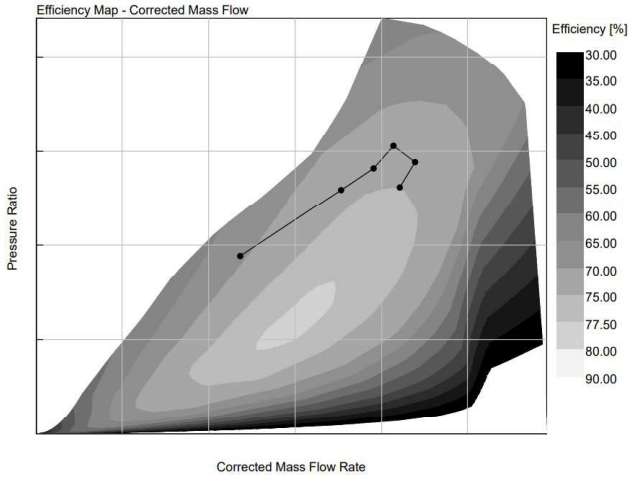


Figure 12 – Compressor map of FGT

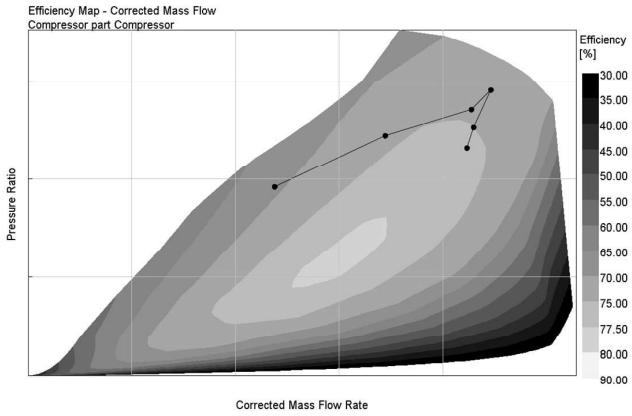


Figure 13 – Compressor map of VGT

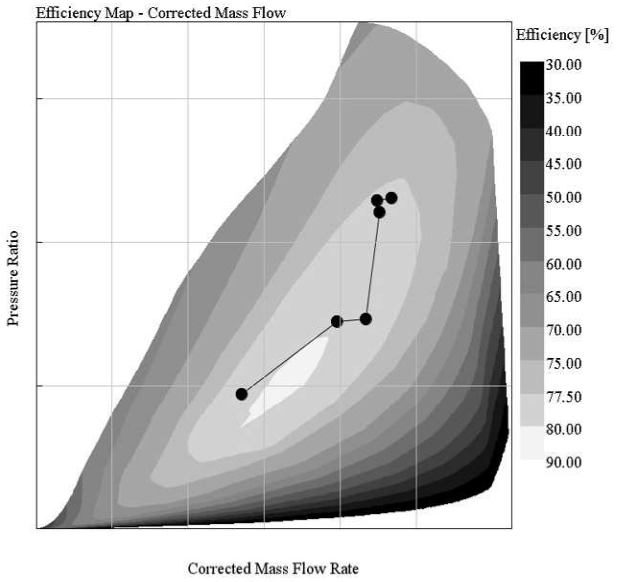


Figure 14 – LP compressor map of 2-stage TC

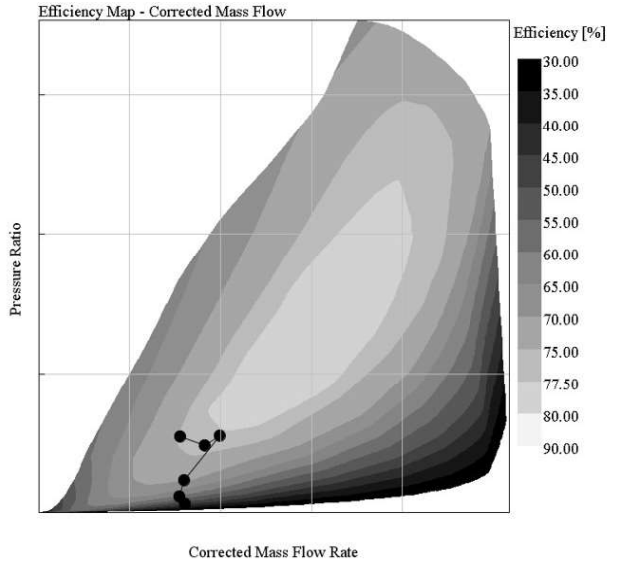


Figure 15 – HP compressor map of 2-stage TC

From BTE point of view, VGT turbocharger has the best efficiency in comparison to FGT and 2-stage configuration. This can be explained with the PMEP results especially at the low-end-speed region. FGT is the worst in PMEP, and 2-stage TC configuration is worse than VGT TC configuration at the low-end-speed region, because the size of high-pressure turbocharger of 2-stage charging system is lower than the size of VGT system. A smaller turbine results in a higher-pressure ratio and higher inlet pressure, which increases pumping work during exhaust stroke.

In addition to that, turbocharger limits are also important parameters to look deeply whether the performance of turbocharger is really able to achieve targets at sea level and high-altitude level, too. As can be seen, FGT is already at the limit even at the sea level (compressor outlet temperature), because CMR 2.4 target is a hard limit to provide boosted-air when the system has only the waste-gate to catch torque target.

VGT turbocharger system is better in comparison to the system with FGT charging, but this system is also close to the compressor outlet temperature limit. This could make the VGT's performance at high altitude questionable. Compared to FGT; VGT has more margin at higher engine speeds in compressor outlet temperature.

The system with 2-stage turbocharger can be the best option in terms of the high-altitude performance because it has very good margin to stay below the compressor outlet temperature limit in comparison to the systems with FGT and VGT. This means, system with 2-stage charging system can reach higher altitudes with same CMR levels without derating. This is the biggest advantage of 2-stage according to the analysis results.

Turbocharger speed is another important parameter and limit to understand turbocharger performance is enough for sea level and high altitude or not. As can be seen from compressor maps, all charging concepts have margin to reach the turbocharger speed limit at sea level. VGT is the less margin in terms of turbocharger speed amongst all charging systems, and this means the system with VGT has the least high-altitude potential in terms of turbocharger speed limit. However, in order to have an idea about high altitude potential, turbocharger speed limit and compressor outlet temperature should be considered together.

Regarding turbocharger efficiencies, it can be said that VGT has the highest efficiencies at most of the operation points. The system with FGT is also close to these efficiency levels and low-pressure turbocharger of 2-stage is also at same levels, where the high-pressure turbocharger of 2-stage looks worse than the others. It is because the low-pressure turbocharger is the more dominant one in terms of having higher compression ratios and that is why the results are closer to the centre of low-

pressure-charging compressor map. High-pressure stage has lower efficiency because of the lower pressure ratio.

As for transient performance, VGT is expected to respond faster than FGT turbocharger. However, having a smaller turbocharger on high pressure side, 2-stage turbocharging concept is expected to have the best transient response.

4. CONCLUSION

In this paper, different turbocharging systems are analysed for hydrogen engines with a very low engine-out NOx emission target. Here instead of lambda, CMR is taken as a target to enable low NOx emission with relaxed air charging requirement.

Following conclusion can be drawn about critical performance criteria:

- Full load target: All turbocharging concepts can achieve the target full load at sea level thanks to the CMR and EGR strategy
- NOx Emission: Low NOx emissions at steady state conditions are secured by targeting a CMR of 2.4 thanks to the characteristics of hydrogen combustion.
- Efficiency: VGT concept has the best brake thermal efficiency and FGT has the lowest. 2-stage has efficiency close to VGT at higher engine speeds. This is mostly related to pumping losses (PMEP).
- Altitude margin: 2-stage has well enough margin compared to VGT and FGT. FGT has almost no margin and VGT is limited at medium speed in terms of compressor outlet temperature and turbocharger speed.

From the conclusions drawn here, following applications can be supported with different charging strategies as shown in Table 1.

Table 2. Applications and possible use cases of different charging systems

	FGT	VGT	2-stage
Genset	X		
Long haul		X	X
Construction			X
Marine	X	X	
Off-road		X	X

As a next step, analyses for high altitude and transient load step can be performed for all of the concepts to get a clear picture with solid numbers.

ACKNOWLEDGEMENTS

The authors of this paper would like to thank to Abdullah Kılıçarslan, Taha Küçük for their efforts.

REFERENCES

[1] https://data.worldbank.org/indicator/SP.POP.TOTL

[2] https://ourworldindata.org/greenhouse-gas-emissions

[3] E. Kahraman, S. C. Ozcanlı, B. Ozerdem, An experimental study on performance and emission characteristics of a hydrogen fuelled spark ignition engine, *International Journal of Hydrogen Energy, Volume 32, Issue 12*, 2007

[4] C.M. White, R.R. Steeper, A.E. Lutz, ‘’The hydrogen-fueled internal combustion engine: a technical review,’’ *International Journal of Hydrogen Energy,Volume 31, Issue 10*, 2006

[5] W. Stockhausen, R. Natkin, D. Kabat, L. Reams et al., Ford P2000 Hydrogen Engine Design and Vehicle Development Program, *SAE Technical Paper 2002-01-0240*, 2002

[6] G. Kiesgen, M. Klüting, C. Bock, and H. Fischer, The New 12-Cylinder Hydrogen Engine in the 7 Series: The H2 ICE Age Has Begun, *SAE Technical Paper 2006-01-0431*, 2006

[7] Dr.-Ing. T. Pauer, Dipl.-Ing. H. Weller, Dr.-Ing. E. Schünemann, Prof. Dr. H. Eichlseder, Dr. P. Grabner, Dr. K. Schaffer, H2 ICE for Future Passenger Cars and Light Commercial Vehicles, *41. International Vienna Motor Symposium*, 2020

[8] T. Wallner, Efficiency and Emissions Potential of Hydrogen Internal Combustion Engine Vehicles, *Symposium on International Automotive Technology*, 2011

[9] H. L. Yip, A. Srna, A. C. Y. Yuen, S. Kook, R. A. Taylor, G. H. Yeoh, P. R. Medwell, Q. N. Chan, A Review of Hydrogen Direct Injection for Internal Combustion Engines: Towards Carbon-Free Combustion, *Appl. Sci. 2019, 9, 4842*, 2019

[10] T. Wallner, Efficiency and Emissions Potential of Hydrogen Internal Combustion

Engine Vehicles, SAE Technical Paper 2011-26-0003, 2011

[11] J. B. Heywood, *Internal Combustion Engine Fundamentals*, McGraw Hill, 1988.

[12] K. Rana, S. Natarajan, and S. Jilakara, Potential of Hydrogen Fuelled IC Engine to Achieve the Future Performance and Emission Norms, *SAE Technical Paper 2015-26-0050*, 2015.

[13] T. Wallner, Development of Combustion Concepts for a Hydrogen Powered Internal Combustion Engine, *PhD thesis, Graz University of Technology*, 2004.

[14] P. Huyskens, S. Van Oost, P. Goemaere, K. Bertels, The technical implementation of a retrofit hydrogen PFI system on a passenger car, *SAE Technical Paper 2011-01-2004*, 2011.

[15] Dr.-Ing. A. Kufferath, Dr.-Ing. E. Schünemann, Dr.-Ing. M. Krüger, Dipl.-Ing. M. Krüger, Dr. S. Jianye, Prof. Dr. H. Eichlseder, Prof. Dr. sc. techn. T. Koch, H2 ICE Powertrains for Future On-Road Mobility, *42nd International Vienna Motor Symposium*, 2021.

[16] A. Sommermann, F. Hinrichsen, T. Malischewski, D. Hyna, C. Karl, J. Schmitt M. McMackin, H. Bec, MAN H45 hydrogen engine: a robust and highly efficient technology for CO2-neutral mobility, *18th Symposium, Sustainable Mobility, Transport and Power Generation,* 2021

[17] A. Boretti, Hydrogen internal combustion engines to 2030, *International Journal of Hydrogen Energy 45 (2020) 23692-23703*, 2020

[18] Dr. E. Schutting, Dipl.-Ing. S. Roiser, Prof. Dr. H. Eichlseder, Ass. Prof. S. Lux, Dipl.-Ing. S. Kleiber, Hydrogen Engine Exhaust Aftertreatment, *43rd International Vienna Motor Symposium*, 2022.

[19] C. Bekdemir, E. Doosje, and X. Seykens, H2-ICE Technology Options of the Present and the Near Future, *SAE Technical Paper 2022-01-0472*, 2022

[20] S. Verhelst, J. De Landtsheere, F. De Smet, C. Billiouw, A. Trenson and R. Sierens, Effects of Supercharging, EGR and Variable Valve Timing on Power and Emissions of Hydrogen Internal Combustion Engines, *SAE International Journal of Engines , Vol. 1, No. 1 (2009), pp. 647-656*, 2009.

[21] Dr. P. Kapus, Dipl.-Ing. (FH) Dipl.-Ing. B. Raser, Dipl.-Ing. A. Arnberger, Dr. R. Heindl, Dipl.-Ing. M. Egert, N. Kunder MSc, Dr. G. Fraidl, Dipl.-Ing. M. Weißbäck, Dr. P. Grabner,, High Efficiency Hydrogen Internal Combustion Engine – Carbon Free Powertrain for Passenger Car Hybrids and Commercial Vehicles, *43rd International Vienna Motor Symposium*, 2022.

A NUMERICAL STUDY ON CO-FIRING OF BIOMASS-COAL BLENDS IN 100 kW LAB-SCALE SWIRL BURNER

C. Deniz Canal[1], Y.E. Boke[1] and A.C Benim[2]

1. Faculty of Mechanical Engineering, Istanbul Technical University, Istanbul; emails: cansudeniz@itu.edu.tr, boke@itu.edu.tr
2. Center of Flow Simulation (CFS), Department of Mechanical and Process Engineering, Duesseldorf University of Applied Sciences, Duesseldorf, Germany; email: alicemal@prof-benim.com

Abstract

Co-firing biomass with coal is an attractive option for CO_2 reduction and renewable energy source usage. The outstanding technology of CO_2 capturing is oxy fuel combustion using pure oxygen instead of air. In this research, the pulverized coal and biomass flame are investigated numerically. 2D numerical co-combustion calculations are carried out in a 100kW vertical down fired boiler, having swirl burner, by using commercial CFD code Fluent. The pulverized coal combustion model results are validated with experimental data. Afterwards, the specified model is used for biomass co-combustion model. RANS turbulence models were applied to simulation to find the better model for swirl burner. Five different blending ratios are examined as 100% coal, 75-25% biomass-coal, 50-50% biomass-coal, 25-75% biomass-coal and 100% biomass under oxy fuel atmosphere. Moreover, particle size distribution and kinetic rate variation on co-combustion mechanism are investigated.

Keywords: Co-firing, Biomass, Coal, Solid Fuel Combustion

1 INTRODUCTION

In the last decades, the climate has been changing due to greenhouse gases. As it is known, one of the gases that causes greenhouse gas effect is CO_2. Moreover, energy consumption is increasing continuously while energy sources are getting scarce. Combustion processes have been used to cover energy needs all around the world. As a fuel, coal is still among the most popular energy source as fossil fuel. However, renewable energy sources have been increasingly used to meet energy needs due to environmental issue in recent years. Combustion also plays an important role on the behalf of renewable energies. Biomass is the renewable energy source using combustion processes to convert into energy [1-6].

Co-firing biomass with coal is an alluring option for CO_2 reduction and renewable energy source usage. Another advantage of this process is that it could be implemented to existing coal-fired power plant with low cost. Furthermore, co-firing option is the least complicated way of using biomass instead of fossil fuels. Fuel properties are very important for combustion process. Moreover, the ratio of fuel blends is decisive for output of co-firing. The Sulphur content is very high in coal compared to biomass. Therefore, this kind of differences changes the emission gases content after co-firing [7-10].

There are three co-combustion methods as direct co-firing, indirect co-firing and parallel co-firing. Direct co-firing has an advantage on cost. It is also the most used methods for co-combustion. In second method, biomass firstly gasified before co-combustion. In this method, after gasification, gases should be cooled down and this led to high operational cost. In parallel co-firing option, coal and biomass burn separately. This option is used generally for paper industries [11].

A solid fuel particle has four combustion stages as evaporation, devolatilization, volatile combustion and char combustion. Firstly, water is evaporated from solid fuel. The volatile matter and tar are released from fuel particle in devolatilization step. Volatile gases are burnt with oxygen in volatile combustion step. Finally, char reacts with oxygen and produces CO and CO_2 in char combustion step. These steps occur simultaneously or progressively related to particle size and heating rate. The composition of char, gas and tar is dependent on different

parameters such as elemental analysis, particle size, and boiler temperature [12].

In this study, the coal and biomass co-firing are investigated numerically in the pulverized boiler having 100 kW power. The commercial CFD code Fluent is used in the modelling. The pulverized coal combustion model results are validated with experimental data. Afterwards, the specified model is used for biomass co-combustion model. Five different blending ratios are used as 100% coal, 75-25% biomass-coal, 50-50% biomass-coal, 25-75% biomass-coal and 100% biomass under oxy fuel atmosphere. Furthermore, particle size distribution and kinetic rate variation on co-combustion mechanism are investigated. The results of combustion model are given by the effect of turbulence on lab-scale burner, temperature distribution and gaseous emissions varying with various biomass sharing.

2 MODELLING

Ansys Fluent 18.0 is used as CFD code, which uses a finite volume method for discretization [13]. Coupled solver is used and a second order upwind scheme is utilized to discretize the convection terms. Least squares cell-based method is used for gradient calculations.

A Eulerian-Lagrangian approach is used for this case. The gas phase is solved as a continuum by solving the N-S Equations, while the particle phase is solved by tracking number of particles through the calculated flow field. Every 30th iteration particles are injected to boiler. Particles are assumed to have a spherical shape. Rosin-Rammler distribution is used for coal and biomass particle size distribution.

To model gas turbulence, RANS method is used. In the previous work [5], pulverized coal flame was investigated in same laboratory scale boiler having a different burner. Turbulent flow was modeled by using RANS models as S-KE, R-KE, RNG-KE and SST as well as RSM. RSM results were the best result comparing with experimental data. In addition to this, for burner having 100 kW power, RSM is also giving better performance according to other RANS model. The standard wall function is used for the near wall turbulence.

P1 radiation model is used for the radiative heat transfer mechanism. The Weighted Sum of Gray Gases Model calculates the absorption coefficient. Particle emissivity is assumed to be 0.9 and wall emissivity is assumed to be 0.7.

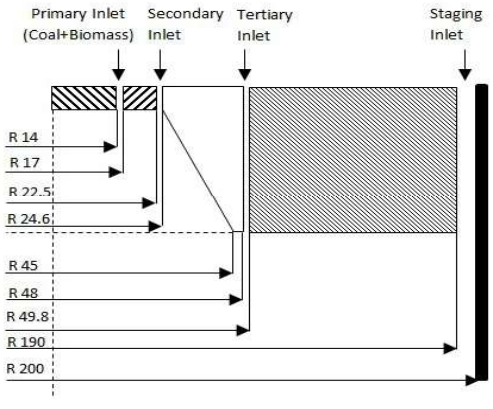
When the fuel particle enters the high temperature environment, evaporation and pyrolysis occur. Volatile matter burns homogeneously in the gas phase while the residual part named as char burns by heterogeneous reactions [3].

The prediction of volatile matter yield is determined by a devolatilization model. For this purpose, a two competing rates model is utilized for biomass devolatilization model. Kinetics/diffusion limited model is used for char combustion. The surface reaction rate is determined by kinetics or diffusion rate. For biomass fuel, kinetic rate of devolatilization and char combustion are taken from Li et.al [14] because of the similar ultimate and proximate analysis data. For the coal, the kinetic rate of devolatilization and char combustion are taken from Toporov et. al. [15].

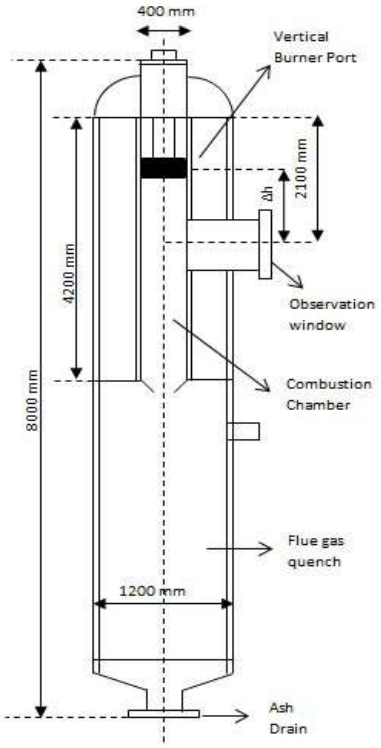
The gas phase combustion is assumed to happen by a global reaction scheme comprising two irreversible reactions. First of all, the volatile matter decomposes to CO and H2O. Secondly, CO is oxidized to CO2 [16]. Finite rate/Eddy Dissipation is used to model gas reactions in this study.

3 TEST CASE AND FUEL PROPERTIES

All experiments carried out at a test furnace of RWTH Aachen University [15]. The section view of Laboratory scale boiler and swirl burner are shown in Figure 1.



(a)



(b)

Figure 1. Section view of (a) swirl burner (b) laboratory scale combustion furnace

The pulverized fuel flame has a thermal power of 100 kW. Mass flow rate (MRF), the percentage of oxy environment, and temperature are given in Table 1.

Table 1. Operation conditions

	MFR (kg/h)	O_2/CO_2 (%)	T (K)
Primary Inlet	17.6	19/81	313.15
Secondary Inlet	26.6	21/79	333.15
Tertiary Inlet	1.5	21/79	333.15
Staging Inlet	54.9	21/79	1173.15

The coal and biomass are injected by the primary inlet of the burner. The primary inlet flow is not swirled. The swirl is imparted to the system by swirling the flow through the secondary inlet. The geometric swirl number is 0.958.

The proximate and ultimate analysis of the fuel are shown in Table 2. Coal is fed to system as rate of 6.5 kg/h. To achieve the same thermal power output, biomass should be fed into the system as a rate of 8.55 kg/h, if 100% biomass is used. Moreover, particle size distribution is given in Table 3. Rosin-Rammler distribution is fitted to the measured particle size distribution, shown in Fig 2. Yd is the mass fraction greater than d.

Table 2. Proximate and ultimate analysis.

	Coal		**Biomass**	
	AR	**DAF**	**AR**	**DAF**
C [w-%]	67.4	77,03	55.15	57.69
H [w-%]	4.24	4,85	5.52	5.77
O [w-%]	14.7	16,8	34.65	36.24
N [w-%]	0.86	0,98	0.25	0.26
S [w-%]	0.3	0,34	0.03	0.031
Water [w-%]	8.4	-	2.26	-
Ash [w-%]	4.1	-	2.14	-
Volatiles [w-%]	46.6	53,26	68.71	71.84
LHV [MJ/kg]	25.134	27.67	19.089	20.024
HHV [MJ/kg]	26.304	30.068	20.394	21,324

Table 3. Particle size distribution of coal and biomass.

Coal		
Dv(10) [µm]	**Dv(50) [µm]**	**Dv(90) [µm]**
6	25	75
Biomass		
Dv(10) [µm]	**Dv(50) [µm]**	**Dv(90) [µm]**
5	18	45

One can see that the matching CFD Inputs with Exp. Data is sufficiently good. However, there are some deviations. Their effect on results may be ignored.

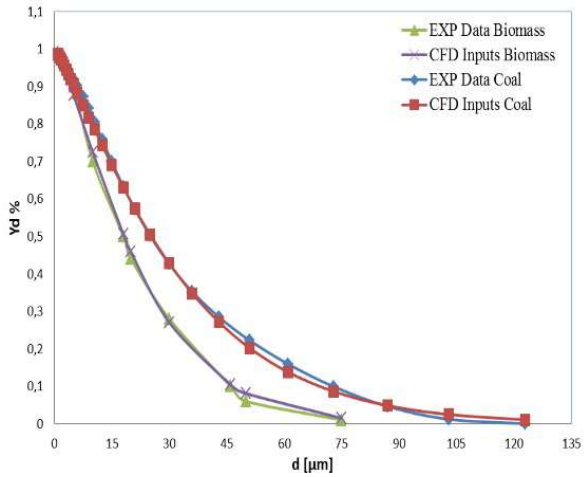


Figure 2. CFD inputs versus experimental data for particle size.

Devolatilization step for biomass is modelled by using two-competing rates considered by Kobayashi et al. [17] while for coal, single rate is used. Kinetics/diffusion-limited model is used for char combustion for both fuels. All kinetic data are given in Table 4.

Table 4. Kinetic data for coal and torrefied biomass.

Devolatilization kinetics		
	Coal* (Rhenish Lignite)	Biomass** (Torrefied)
A [s^{-1}]	2 x 10^5	5.48 x 10^3
E [kJ/mol]	49	59.8
A [s^{-1}]	-	2.15 x 10^7
E [kJ/mol]	-	147
Char reaction kinetics		
	Coal (Rhenish Lignite)	Biomass (Torrefied)
A [s^{-1}]	2 x 10^{-5}	56.3
Ea [kJ/mol]	79.4	78

*Kinetic data is taken from [15]
**Kinetic data is taken from [14]

4 SOLUTION DOMAIN AND BOUNDARY CONDITIONS

The problem is formulated as 2D-axisymmetric. Solution domain and boundary types are shown in Figure 3. Primary, secondary, tertiary and staging inlet are defined as mass flow rate as boundaries. Constant temperatures are prescribed at inlets, in accordance with the experimental data. Pressure outlet boundary condition is prescribed at the exit. The remaining boundaries are walls.

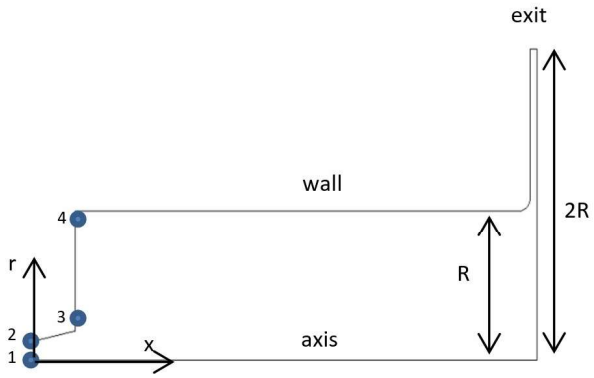


Figure 3. Solution Domain and BC types (1-Primary Inlet, 2-Secondary Inlet, 3-Tertiary Inlet and 4-Staging Inlet) "R" is defined as half diameter of furnace, 200 mm.

Mesh independency study was done in previous research for same furnace [5]. According to this study, generated grid having 35000 cells is shown in Figure 4.

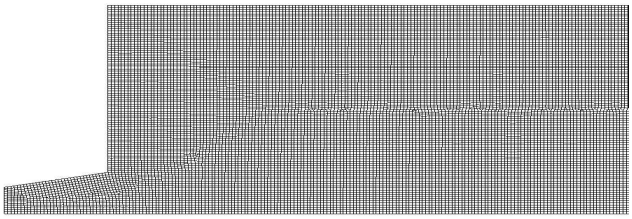


Figure 4. Generated mesh having 35,000 cells

5 RESULTS

Five different turbulence models are used to find best model fitting to this flow measurement. There are 5 different measurement stations through the furnace at x=0.025m, 0.05m, 0.2m and 0.3m. in Figure 5, the Experimental data is taken from x=0.025m as function of r. A similar study was done in previous work [5] in detail. According to that study, RSM gave better performance to predict turbulent rather than other TV models. As you can see in Figure 5, there is not a huge difference between models; however, RSM catches peak velocity value of the flame better than other models. RSM is also known as giving good results on swirling flows in literature [13].

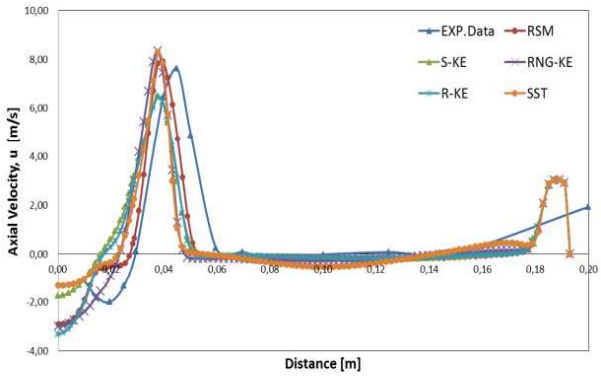


Figure 5. Axial velocity, u [m/s] experimental data versus numerical data.

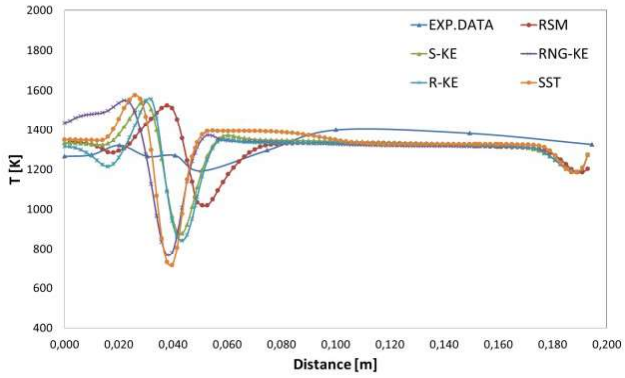


Figure 6. Temperature [K] experimental data versus numerical data.

One can see that minimum error between experimental data and calculated data for temperature can be observed in RSM model. Temperature increase trends are in agreement with the experimental data. Moreover, total temperature contour for 100% coal combustion is shown in Figure 7.

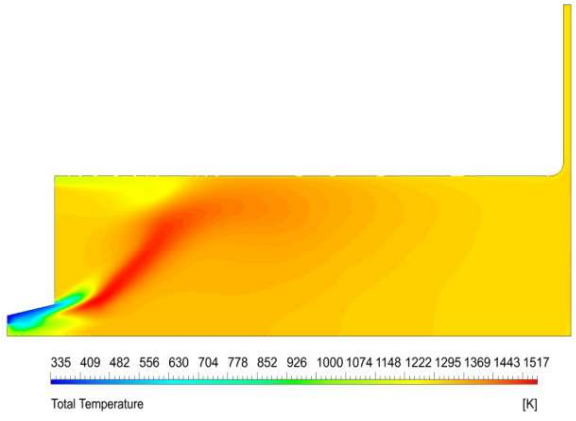


Figure 7. Temperature field for coal combustion.

Various co-firing ratios are investigated to determine the efficient blend ratio for easy implementation to existing coal-fired boiler. Coal and biomass are fed into same inlet. Torrefied biomass is used because it has a more similar composition to coal compared to other type of biomass. Feeding rates for blending are determined as 25% Biomass + 75% Coal, 50% Biomass + 50% Coal, 75% Biomass + 25% Coal, 100% Biomass. Temperature fields for each blending ratio are shown in Figure 8.

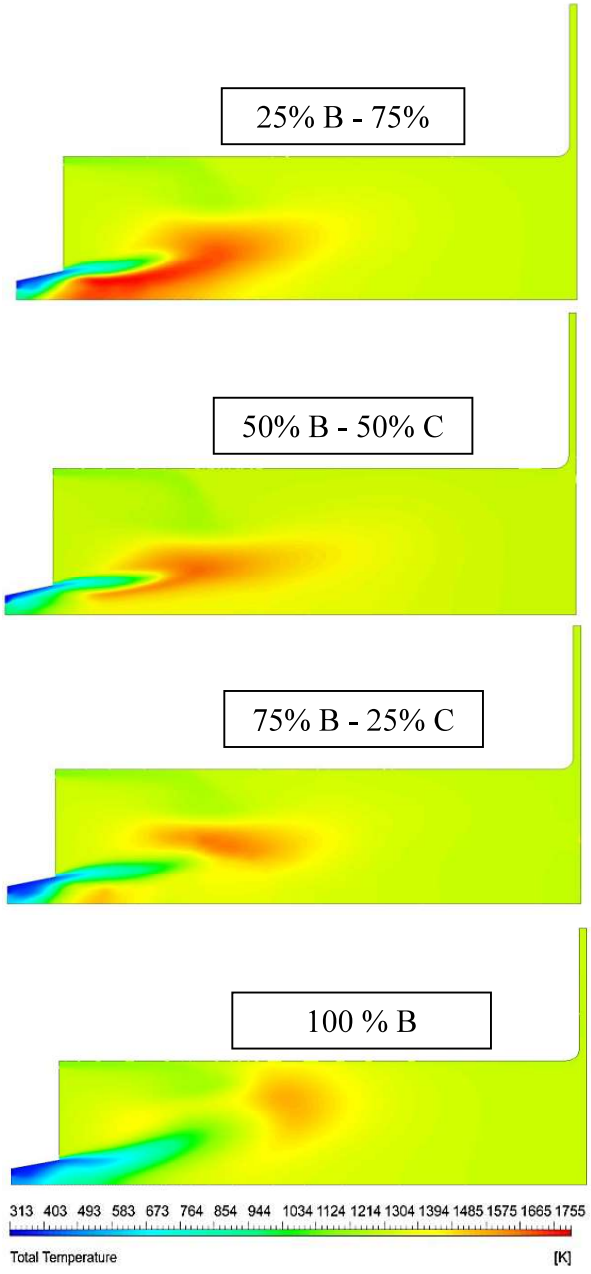


Figure 8. Temperature profiles for each co-firing ratio.

One can see that increasing the sharing percentage of torrefied biomass led to a decrease in peak flame temperatures, as shown in Figure 8. Specific values for peak flame temperature are 1800K for 25% Biomass/75% Coal, 1672K for 50% Biomass/50% Coal, 1660K for 75% Biomass/25% Coal and 1569K for 100% Biomass. While increasing biomass into the

blend, flame structure is occurring later. As expected, CO_2 mole fraction is decreased while increasing biomass content, shown in Figure 9.

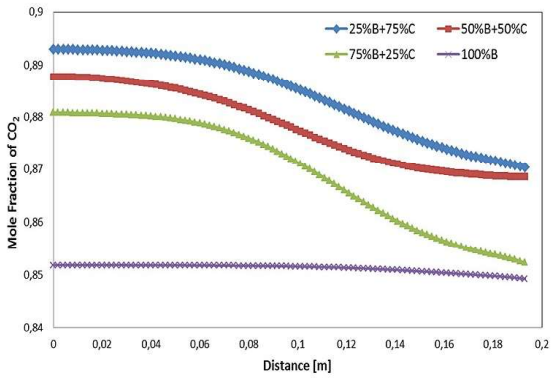


Figure 9. Mole fraction of CO_2 for each blending ratios (x=0.5m).

The discrete random walk model is used to model turbulent particle dispersion. An enough number of trials (M) need to be calculated to get meaningful results. Computational cost is directly affected by the number of trials. Therefore, optimum number should be found to obtain reasonable results with low computational cost. In this study, different trial numbers are used to investigate their effect on the results. M is chosen as 2, 5, 10 and 20. Temperature profiles along the axis are shown in Figure 10.

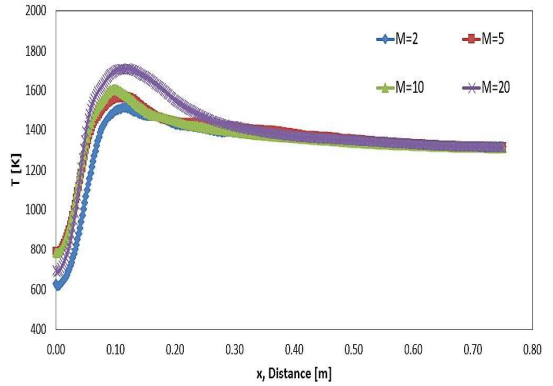


Figure 10. Temperature profiles along the axis, by defining various M values.

One can see that M equal to 10 gives the optimum results compared to other values. The temperature profile of M equals to 20, is quite similar to M=10. Number of size particle for coal and biomass is defined as 28 and 9, respectively.

6 CONCLUSION

Pulverized coal and biomass flame were investigated numerically. The Eulerian-Lagrangian model is used for model two-phase flow. For turbulence modeling, 5 different RANS model as S-KE, RNG-KE, R-KE, SST and RSM were used. Calculated axial velocity and static temperature values were compared with experimental data. As a conclusion, RSM gave better agreement with experimental data. Moreover, co-firing ratios are investigated in this study. While biomass ratio was increasing in blend, peak temperature of flame was decreasing. In addition to this, low emission was achieved as expected. The number of trials in the random walk model of turbulent dispersion was chosen as M=10, to optimize computational cost, which also gave acceptable results.

REFERENCES

[1] Lackner, M.;Winter, F.; Agarwal, A.K. (Eds.) Handbook of Combustion; Wiley: Chichester, UK, 2010.

[2] Deniz, C., Boke, Y.E, Aydin O, Benim, A.C. Computational Analysis of Pulverized Coal Co-Firing with Biomass In 150MWe Unit of Tuncbilek Thermal Power Plant. Journal of Thermal Sciences and Technology, Vol.41, pg. 37-50, 2021.

[3] Deniz, C., Boke, Y.E, Benim, A.C. Numerical analysis of pulverized biomass combustion, E3S Web of Conferences, 2021.

[4] Benim, A.C., Deniz, C., Boke, Y.E. Computational investigation of oxy combustion of pulverized coal and biomass in a swirl burner. Energy, Vol.238, Part C, 2021.

[5] Benim, A.C., Deniz, C., Boke, Y.E. A Validation Study for RANS Based Modelling of Swirling Pulverized Fuel Flames. Energies, vol.14, p.7323, 2021.

[6] Bhattacharyya, S.; Chattopadhyay, H.; Benim, A.C. Heat transfer enhancement of laminar flow of ethylene glycol through a square channel fitted with angular cut wavy strip. Procedia Eng., vol.157, p.19–28, 2016.

[7] Benim, A.C.; Pfeiffelmann, B.; Oclon, P.; Taler, J. Computational investigation of a lifted

hydrogen flame with LES and FGM. Energy, vol.173, pg.1172–1181, 2019.

[8] Jaseliunaite, J.; Povilaitis, M.; Stucinskaite, I. RANS- and TFC-based simulation of turbulent combustion in a small-scale venting chamber, Energies, vol.14, pg.5710, 2021.

[9] Pfeiffelmann, B.; Diederich, M.; Gül, F.; Benim, A.C.; Heese, M.; Hamberger, A. Computational and experimental investigation of an industrial biomass furnace. Chem. Eng. Technology, vol.44, pg.1538–1546, 2021.

[10] Rosendahl, L. (Ed.) Biomass Combustion Science, Technology and Engineering; Elsevier: Amsterdam, The Netherlands, 2013.

[11] Van L., Sjaak; Koppejan, J.; The Handbook of Biomass Combustion and Co-firing, pg.207, 2012.

[12] Fatehi, H.; and Xue-Song Bai. X. Gasification and Combustion of Biomass: Physical Description and Mathematical Modelling, Handbook of Clean Energy Systems, 2015.

[13] ANSYS Fluent Theory Guide, Rel. 2018 (ANSYS Inc., Canonsburg, 2018)

[14] Li, J.; Brzdekiewicz, A.; Yang, W.; Blasiak, W. Co-firing based on biomass torrefaction in a pulverized coal boiler with aim of 100% fuel switching. Applied Energy, vol.99, pg.344–354, 2012.

[15] Toporov, D.; Bocian, P.; Heil, P.; Kellermann, A.; Stadler, H.; Tschunko, S.; Förster, M.; Kneer R. Detailed investigation of a pulverized fuel swirl flame in CO2/O2 atmosphere. Combustion and Flame, vol.155, pg.605-618, 2008.

[16] Turns, S.R. An Introduction to Combustion, 3rd ed. (McGraw-Hill, New York, 2012)

[17] Kobayashi, H.; Horward, JB.; Sarofirm, AF. Coal devolatilization at high temperatures. Symposium on combustion, vol.16(1); pg.411-425, 1977.

FRAGMENTATION OF DROPLETS OF COAL-WATER SLURRIES CONTAINING PETROCHEMICALS UNDER DIFFERENT HEATING METHODS

D.V. Antonov[1], O.V. Vysokomornaya[1], K.Y. Vershinina[1], G.V. Kuznetsov[2] and P.A. Strizhak[2]

1. Research School of High-Energy Physics, Tomsk Polytechnic University, Tomsk, Russia, email: vysokomornaja@tpu.ru
2. School of Energy & Power Engineering, Tomsk Polytechnic University, Tomsk, Russia; email: pavelspa@tpu.ru

Abstract

This paper presents the experimental results on the integral characteristics of fragmentation of droplets of coal-water slurries containing petrochemicals heated on a substrate (300–600 °C), in an air flow (450–550 °C), and in a tubular muffle furnace (500–700 °C). The following fuel components were used: water, coal, coal processing waste (filter cake), used industrial turbine oil, sawdust, nut husks, stabilizers (neonol, starch, tween). Three modes of droplet heating before the ignition occurred: a monotonic decrease in size due to moisture evaporation; significant deformation of the surface during heating and destruction of the droplet with the separation of large fragments; and full breakup of the droplet into small fragments. We recorded the droplet breakup delay times and integral characteristics of secondary fragments (number, size, and surface area) in comparison with the same parameters of the initial droplet. The influence of a set of factors (temperature, heating scheme, and component composition of droplets) on the above characteristics was also established. Approximations for the established dependencies are obtained for the purpose of their use in mathematical modelling. the findings were compared with the earlier established characteristics of similar processes studied in experiments with emulsion droplets and two-component immiscible droplets containing liquid combustible and non-combustible components.

Keywords: coal-water slurries containing petrochemicals; droplets; fragmentation; breakup; delay times; secondary fragments /

1 INTRODUCTION

One of the most promising and effective methods for intensifying the processes of heating and evaporation of drops of liquids, slurries, solutions, emulsions, and various composite fuels is their fragmentation [1, 2]. Atomization of fuel droplets is typically classified into primary (by using sprayers and sprinklers) and secondary (directly in combustion chambers or heat exchangers) [3,4]. In some cases, it is ineffective to spray droplets beforehand, at the inlet of the corresponding heat exchanger or combustion chamber, because moving droplets may coalesce or high-temperature flue gases may entrain them or slow down the droplet flow. Moreover, quite a large volume of liquid remains on the chamber walls, thus deteriorating the heat exchange and evaporation. For these reasons, theoretical and experimental research is conducted to find ways to intensify the breakup (secondary atomization) of droplets within the heat exchange chamber [5]. Researchers are primarily interested in the breakup of heterogeneous droplets (emulsions, microemulsions, nanoemulsions, solutions, and slurries) typical of fuel technology, chemical production, etc. [6].

Energy-efficient ignition of fuel droplets in the combustion chambers of gasoline and diesel engines, furnaces of steam and hot water boilers, various furnaces and other industrial plants is an important problem both for the rational use of energy resources [7] and in terms of reducing the anthropogenic impact on the environment [8]. The intensification of heating and evaporation of liquid droplets significantly reduces the time interval preceding the ignition of the fuel, and also increases the completeness of its burnout [9]. One of the possible ways to increase the rate of heating and evaporation of fuel is to inject it into the combustion chamber in the form of an aerosol flow using nozzles, spray nozzles and adapters. However, in order to ensure the highest ignition efficiency, it is necessary to establish the optimal spray characteristics, which exclude the manifestation of the effects of intense coagulation of droplets, changes in the direction

of their movement, and entrainment by the gas flow from the combustion zone. Quite often, the viscosity of atomized fuels reaches the limit values, and then even high-pressure atomization does not provide a uniform atomization of the fuel. Promising technologies for dispersing inhomogeneous liquids are based on the use of droplet fragmentation, which consists in their disintegration as a result of using different schemes (collision with an obstacle or with neighboring drops, impact of a gas flow, micro-explosive decomposition upon heating). However, for the controlled application of the effects of fragmentation of fuel droplets during heating, it is necessary to experimentally establish the main regularities in the occurrence of this process and outcomes.

2 MATERIALS

Coal-water slurries with petrochemicals (CWSP) and without them (CWS) are liquid mixtures of several components, usually two to four. In general, a CWSP contains a solid and a liquid component. In particular, both the solid and the liquid parts may contain several combustible and noncombustible components or additives. The total mass fraction of solid components in the fuel composition varied from 40 wt% to 60 wt%. Waste (after a year of operation) turbine oil with a mass fraction of 0–10 wt% was used as a liquid combustible component. Distilled water (mass fraction of 40–60%) was a dispersed medium. The presence of combustible components and water in a mixture is a prerequisite for the implementation of micro-explosive fragmentation and, in general, droplet breakup. In addition to the materials listed above, components that improve the stability of slurries (neonol, starch, and TWEEN 80) were used. Their mass fraction varied in the range of 0.5–5 wt %.

3 EXPERIMENTAL TECHNIQUE

The experiments for recording the characteristics of CWS and CWSP droplet fragmentation used three heating schemes, similar to those used in [10]: in a heated air flow, on a heated substrate, and in a muffle furnace. The heating, evaporation, and fragmentation of CWS and CWSP droplets were recorded by a high-speed Phantom Miro C110 video camera (915 fps at 1280x1024; 12-bit 1.3 Mpx CMOS sensor). The videos were processed in the Phantom Camera Control software. During the processing, we recorded the droplet breakup onset delays, the initial sizes of droplets, as well as the sizes of secondary droplets after fragmentation. The droplet size was determined at the moment of their introduction into the heating zone. The systematic errors in the determining of the two key parameters did not exceed 0.001 s and 0.025 mm, respectively.

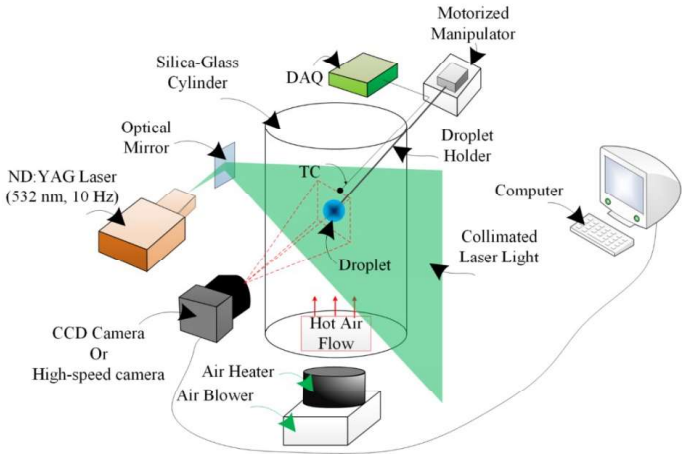


Figure 1. Scheme of experiments studying the CWS and CWSP droplet fragmentation in a heated air flow [10]

Heating in the heated air flow (Fig. 1) is implemented using an air heater (Leister LHS 61, maximum outlet air temperature 700 °C) and a high-pressure vortex blower (Leister Robust with air flow up to 1200 l/min at 20 °C) with regulation of the speed of heated air. The outlet nozzle was extended by a hollow cylindrical channel made of quartz glass. CWS and CWSP droplets were introduced into the channel on a holder in the form of a thin nichrome wire, 0.2 mm in diameter. The use of a nichrome wire minimized the support effects [11] on heating, evaporation, fragmentation, and ignition of CWS and CWSP droplets.

The temperature of gases in a glass cylinder was measured using a system consisting of a National Instruments 9219 high-speed data acquisition complex and two fast-response chromel-alumel thermocouples (temperature range of 0–1200 °C, accuracy of ±1 °C, and response time of 0.1 s). The high-temperature gas flow velocities (U_a) were measured using the Particle Image Velocimetry. The values of U_a were recorded immediately before the main experiment, *i.e.*, before introducing a droplet into the cylindrical channel. The error in the velocity U_a calculation did not exceed 2%. The temperatures (T_a) of the air flow in the convective heating scheme were relatively high,

so the U_a values could only be reliably recorded by PIV.

4 RESULTS AND DISCUSSION

In the experiments, we have determined the integral characteristics of fragmentation triggered by the heat supplied to a group of high-potential CWS and CWSP compositions in three schemes: in a heated gas flow, on a heated substrate, and in a muffle furnace. We have also established the droplet heating and fragmentation behaviour before ignition as well as the variation ranges of the characteristics under study Below the discussion of the key patterns and dependences is presented.

Heating regimes and conditions

Fig. 2 presents typical video frames of experiments involving the heating of CWS and CWSP droplets (50 wt% of flame coal, 45 wt% of distilled water, and 5 wt% of turbine oil): *a* – on a substrate (T_{sub} ≈ 500 °C), *b* – in a heated air flow (T_a ≈ 500 °C, U_a ≈ 2 m/s), *c* – in a tubular muffle furnace (T_a ≈ 500 °C)).

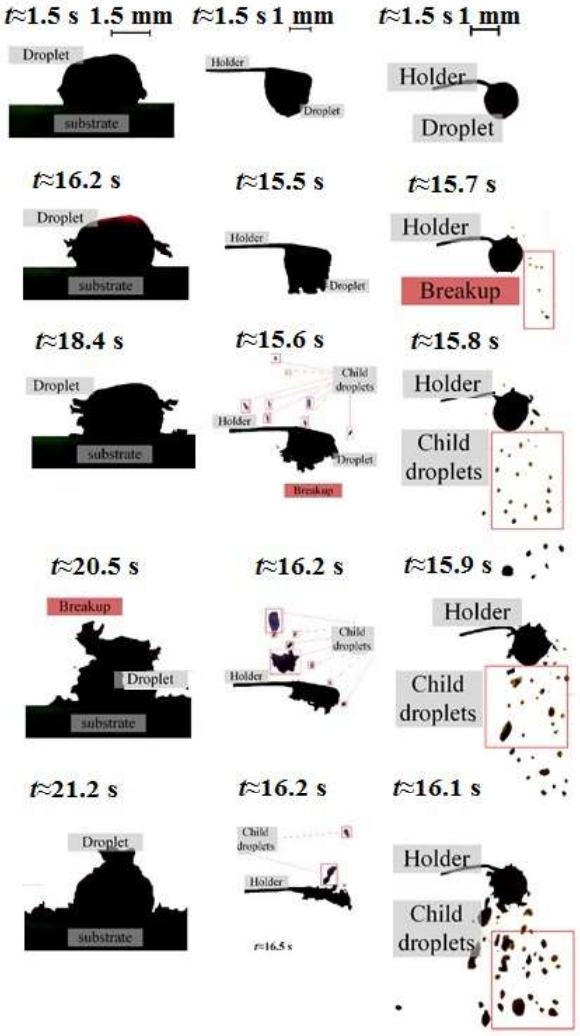
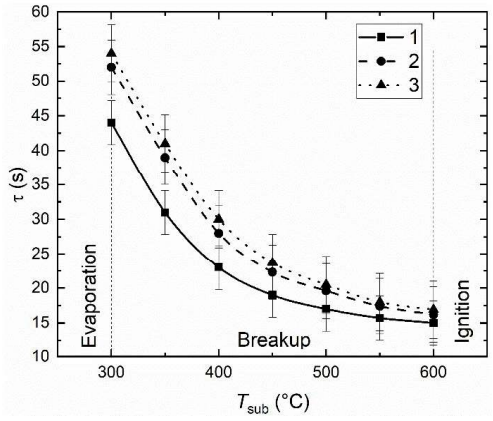


Figure 2. Typical video frames of experiments involving the heating of high-potential CWS and CWSP droplets (50 wt% of flame coal, 45 wt% of distilled water, and 5 wt% of turbine oil):*a* – on a substrate (T_{sub} ≈ 500 °C), *b* – in a heated air flow (T_a ≈ 500 °C, U_a ≈ 2 m/s), *c* – in a tubular muffle furnace (T_a ≈ 500 °C))

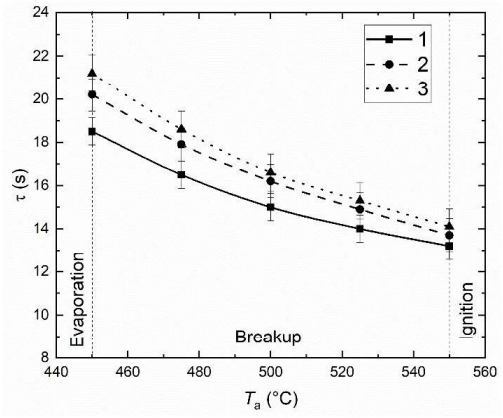
Compositions based on long-flame coal filter cake practically do not breakup. This is due to the fact that the chemical stabilizers and solvents contained in the filter cakes increase the surface tension and viscosity of the composition, and compress the fuel drop when heated. The latter is covered with a dense crust after the surface layers have dried. Droplets of coal-based slurries break up upon complete evaporation of moisture from the near-surface layers of the composition. The intensity of fragmentation (consists of shorter delay times, more secondary fragments, and smaller sizes of the latter) of fuel compositions became higher with increasing heating temperature. The experimental video frames (Fig. 2a) show that the heating scheme involving a heated substrate is not feasible in terms of maximum fragmentation – it typically provides a limited number of secondary fragments. In most cases, we only observed droplet swelling (i.e., vapor bubble nucleation) followed by the drying of the near-surface fuel droplet layers. With an increase in the flow rate from 2 to 4 m/s, an increase in the intensity of fragmentation occurs due to faster evaporation of moisture from the near-surface layers of the composition. At the same time, it was found that the decay delay time is significantly reduced (by more than 10%), and the number of secondary fragments changes insignificantly (less than 5%). This is because an increase in the speed of the incoming air flow contributes to an increase in the heat transfer coefficient. However, at high flow rates, the entrainment of small fragments from the lower surface of the drop slowed down, they pressed against the main drop. The detached fragments moved at a higher speed with an increase in the air flow rate. An analysis of the video frames showed that the droplets disintegrated when moisture evaporated only from the near-surface layer. Separated fragments of deep fuel layers after the complete destruction of the near-surface layer of the droplet evaporated intensively, behind them vapor plumes were formed in the process of movement in a heated medium. This suggests that the main

benefit of CWS and CWSP is in the simultaneous water evaporation, thermal decomposition of solid components, as well as gas-phase and heterogeneous combustion of fuel in the chamber. The totality of these processes reduces the gaseous anthropogenic emissions (first of all, the concentrations of sulfur and nitrogen oxides).

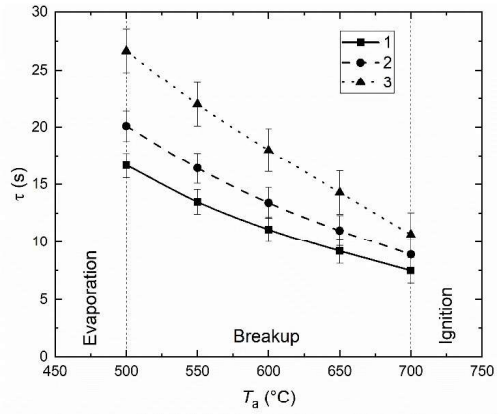
Fig. 3 shows the breakup delay times versus the temperature of the heated substrate (*a*), temperature of the incoming gas flow (*b*), and temperature in the muffle furnace (*c*) for the following compositions: *1* – 50 wt% of coal, 45 wt% of distilled water, and 5 wt% of turbine oil, *2* – 50 wt% of coal, 45 wt% of distilled water, and 5 wt% of sawdust, *3* – 50 wt% of coal, 45 wt% of distilled water, and 5 wt% of nut shells. Clearly, all the curves are nonlinear, which most likely stems from the nonlinear dependences of the rates of the liquid component evaporation and thermal decomposition of the solid part. In addition, the heterogeneous composition of droplets plays an important part, i.e., the uneven distribution of solid and liquid components in a droplet, which is typical of highly viscous slurry fuels.



a



b



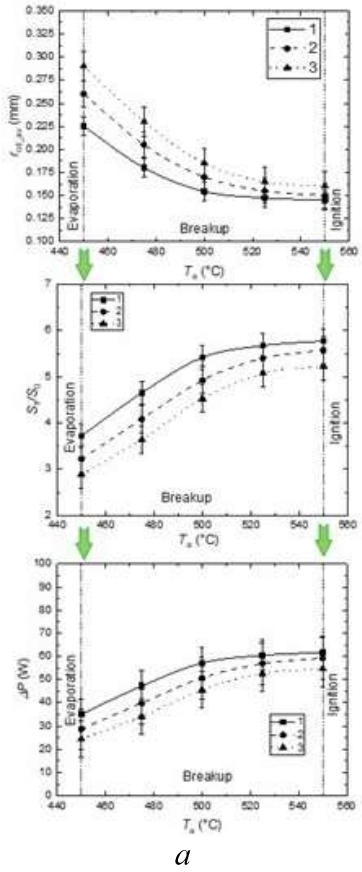
c

Figure 3. Droplet breakup delay times (R_{d0}≈0.8 mm) versus the temperature of the heated substrate (*a*), the temperature of the incoming gas flow (U_a≈2 m/s) (*b*), and the temperature in the muffle furnace (*c*) for the following compositions: *1* – 50 wt% of flame coal, 45 wt% of distilled water, and 5 wt% of turbine oil, *2* – 50 wt% of flame coal, 45 wt% of distilled water, and 5 wt% of sawdust, *3* – 50 wt% of flame coal, 45 wt% of distilled water, and 5 wt% of nut shells.

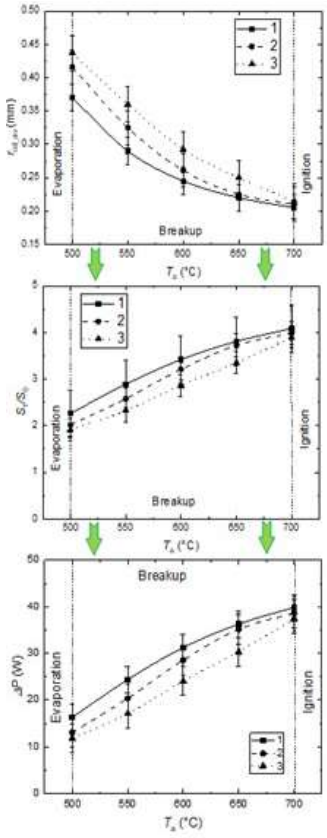
Main characteristics of the secondary fragments

Fig. 4 shows the average radius of secondary fragments (r_{cd_av}), S_1/S_0, and ΔP versus the temperature of the heating medium in a scheme with the air flow (*a*) and with a tubular muffle furnace (*b*) for the following compositions: *1* – 50 wt% of flame coal, 45 wt% of distilled water, and 5 wt% of turbine oil, *2* – 50 wt% of flame coal, 45 wt% of distilled water, and 5 wt% of sawdust, *3* – 50 wt% of flame coal, 45 wt% of distilled water, and 5 wt% of nut shells. For the composition with added turbine oil, a significant increase in the S_1/S_0 values (to 7) was recorded at above 500 °C. This result is associated with puffing and micro-explosion of the CWSP composition (50 wt% of flame coal, 45 wt% of distilled water, and 5 wt% or turbine oil) at high temperatures (above 500 °C). It is also noteworthy that the key characteristics of the secondary fragments of the three slurries established in the experiments (Fig. 4a) do not differ much when the temperatures of the medium reach about 550 °C. It has been established that the type of additive (oil, sawdust, husk) significantly affects the delay times for the decomposition of suspension droplets, but insignificantly affects the characteristics of secondary fragments. Most

likely, this is due to the fact that the proportion of additives does not exceed 5 wt %, and after the initial drop breaks down into dozens of fragments, only a small number of the latter (no more than 5%) contain additives.



a



b

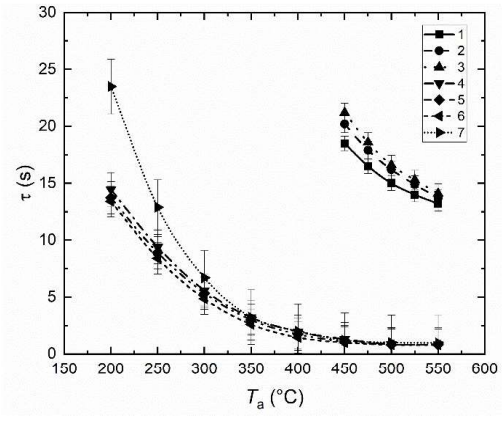
Fig. 4. Average radius of secondary fragments (r_{cd_av}), S_1/S_0, and ΔP versus the temperature of heating medium in a scheme with the air flow (*a*) and with a tubular muffle furnace (*b*) for the following compositions (R_{d0}≈0.8 mm): *1* – 50 wt% of flame coal, 45 wt% of distilled water, and 5 wt% of turbine oil, *2* – 50 wt% of flame coal, 45 wt% of distilled water, and 5 wt% of sawdust, *3* – 50 wt% of flame coal, 45 wt% of distilled water, and 5 wt% of nut shells

The results obtained illustrate that the fragmentation processes are realized, as a rule, before the moment of ignition of the fuel compositions. A temperature range of 450–700 °C was established, at which droplet decomposition was stably realized. This range corresponded to the so-called low-temperature ignition (up to 900 °C). In this temperature range, the formation of secondary fragments was recorded, the sizes of which depended on a group of factors (ambient temperature, air flow velocity, component composition of droplets, grinding fineness, heating scheme, etc.). The CWS and CWSP droplet breakup is most effective (maximum number of secondary fragments with the smallest size) when the high-temperature gas flows around the droplets. In actual fuel technologies, this happens when CWS and CWSP droplets move in a furnace chamber: in addition to water heating and boiling in the pores triggering the fragmentation, small particles of the solid component are entrained from the droplet surface by the gas flow. Predictably, the minimum size of secondary fragments in the experiments was equal to the minimum initial size of the coal particles in the composition. The largest increase in surface area was registered for compositions promising in terms of ecological, economic and energy indicators (Fig. 4). The maximum value of S_1/S_0 was about 7. After fragmentation, the secondary fragments were ignited at temperatures above 800°C.

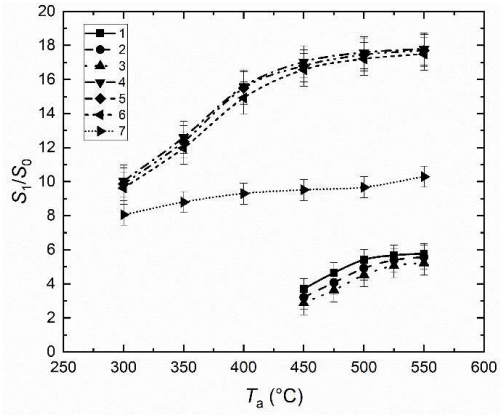
Comparison with experimental data for droplets without particles (miscible and immiscible droplets of fuel emulsions) and with solid particles in low concentrations

Fig. 5 compares the fragmentation delay times (τ) and S_1/S_0 when droplets with the following component compositions are heated in a heated gas flow: *1* – 50 wt% of coal, 45 wt% of distilled

water, and 5 wt% of turbine oil, *2* – 50 wt% of coal, 45 wt% of distilled water, and 5 wt% of sawdust, *3* – 50 wt% of coal, 45 wt% of distilled water, and 5 wt% of nut shells, *4* – 3 vol% of transformer oil and 97 vol% of distilled water.



a



b

Figure 5. Comparison of fragmentation delay times (τ) and S_1/S_0 when droplets with the following compositions are heated in a muffle furnace: *1* – 50 wt% of flame coal, 45 wt% of distilled water, and 5 wt% of turbine oil, *2* – 50 wt% of flame coal, 45 wt% of distilled water, and 5 wt% of sawdust, *3* – 50 wt% of flame coal, 45 wt% of distilled water, and 5 wt% of nut shells; *4* – 70 wt% of rapeseed oil, 29 wt% of distilled water, and 1 wt% of bituminous coal [12]; *5* – 70 wt% of rapeseed oil, 27 wt% of distilled water, and 3 wt% of bituminous coal [12]; *6* – 70 wt% of rapeseed oil, 25 wt% of distilled water, and 5 wt% of bituminous coal [12]; *7* – 70 wt% of rapeseed oil and 30 wt% of distilled water [12]

The comparison of experimental results (Fig. 5) on CWS/CWSP droplets with higher (over 40 wt%) and lower (under 5 wt%) concentration of coal particles in miscible/immiscible fuel droplets indicates that the surface area of all the fuels under study increases significantly due to fragmentation. In addition, Fig. 5 shows that droplets of miscible/immiscible fuel emulsions and droplets of fuel emulsions with low mass concentrations of particles broke up at lower temperatures, starting 250 °C, and the start of CWS/CWSP droplet breakup was only observed at above 500 °C. This can be explained by different breakup mechanisms. In the case of fuel emulsions, the key breakup mechanism is the superheating of the inter-component interface above the boiling (or nucleation) temperature of the low-boiling component (usually water). In the case of CWS/CWSP droplets, the breakup (fragmentation) occurred when all the moisture evaporated from the near-surface layers of the composition. Fig. 5 clearly shows the difference in the fragmentation ranges for fuel emulsion droplets and slurry droplets (CWS/CWSP).

The results of the experiments confirm the prospects for the development of technologies for supplying CWS/CWSP to boiler furnaces. As was mentioned above, the two most significant technological problems with CWS/CWSP combustion are as follows: (i) atomization of slurry fuels to droplet sizes less than 0.5 mm (in this case, combustion is initiated relatively simply); (ii) if fine spraying is not possible, then it is necessary to create conditions for the ignition of large (1.5–2.5 mm) droplets of slurries.

The experiments have shown (Fig. 5) that even at the temperatures of the medium that are as low as about 500 °C, the CWS and CWSP droplet breakup times do not exceed 1 s. At the same time, the surface area of all newly formed droplets after the breakup increases by more than four times; i.e., the temperatures of the medium of over 500 °C provide the conditions for the CWS/CWSP droplet ignition with the burnout times of no more than 1.5 s (according to [13]). Also, the characteristics of droplet ignition provide high efficiency of the whole combustion process for coal-water slurries with and without petrochemicals. In this case, there is no need in fine mist spraying of slurry fuels or larger-size furnaces (extended furnaces are usually installed). Moreover, fine mist spraying of coal-water slurries containing petrochemicals yields small particles of coal and wood of the necessary sizes with very short ignition delay times. At the same time, the smaller the particles, the more complete the fuel combustion and the

evaporation of water in the slurry. Thus, the combustion of solid and liquid components is arranged in a gas-vapor medium with a high concentration of water vapor, which significantly reduces the gaseous anthropogenic emissions.

CONCLUSIONS

Fragmentation of slurry droplets occurs within several modes: with complete evaporation of moisture from the near-surface layers of the composition (characteristic of CWS/CWSP droplets with a large proportion of the solid component); partial fragmentation or puffing (typical for slurries and fuel emulsions with an implicitly defined interface between two media; dispersion occurs due to the presence of vaporization microcenters on the surface of solid impurities (particles)); full fragmentation or micro-explosion (typical of fuel emulsions with a pronounced water/combustible component interface).

Fragmentation usually occurred before the ignition of the fuel compositions. The temperature range, in which droplets broke up consistently, corresponded to the low-temperature ignition (under 900 °C). Fifth, the CWS and CWSP droplet fragmentation depended on their initial sizes: the smaller the droplets were, the faster they broke up. Sixth, the CWS and CWSP droplet breakup is most effective (maximum number of secondary fragments with the smallest size) when the high-temperature gas flows around the droplets. In actual fuel technology, this happens when CWS and CWSP droplets move in a furnace chamber. Seventh, the coal particle grind is crucial for fragmentation: the minimum size of secondary fragments equals the minimum initial size of coal particles in a composition.

The experimental findings are important for the development of fuel technologies in the field of fuel injection in internal combustion engines and boiler unit furnaces. Fuel droplet fragmentation is the most effective with low-temperature ignition. High-temperature processes require primary atomization of CWS and CWSP at relatively low temperatures (250–900 °C) to provide the full breakup of fuel droplets into secondary fragments, which then should be supplied to the high-temperature combustion chamber interior.

ACKNOWLEDGEMENTS

The study was supported by a grant from the Ministry of Science and Higher Education of Russia, Agreement No 075-15-2020-806 (Contract No 13.1902.21.0014).

REFERENCES

[1] J. Shinjo, Xia J. Combustion characteristics of a single decane/ethanol emulsion droplet and a droplet group under puffing conditions. *Proceedings of the Combustion Institute,* Vol. 36, pp. 2513-2521, 2017.

[2] D.V. Antonov, M.V. Piskunov, P.A. Strizhak. Breakup and explosion of droplets of two immiscible fluids and emulsions. *International Journal of Thermal Sciences*, Vol. 142, pp. 30-41, 2019.

[3] D. Ogunkoya, S. Li, O.J. Rojas, T. Fang. Performance, combustion, and emissions in a diesel engine operated with fuel-in-water emulsions based on lignin. *Applied Energy*, Vol. 154, pp. 851-861, 2015.

[4] R.K. Gopidesi, P.S. Rajaram. A review on emulsified fuels and their application in diesel engine. *International Journal of Ambient Energy*, Vol. 43(1), pp. 732-740, 2022.

[5] K. Meng, Y. Wu, Q. Lin, F. Shan, W. Fu, K. Zhou, T. Liu, L. Song, F. Li. Microexplosion and ignition of biodiesel/ethanol blends droplets in oxygenated hot co-flow. *Journal of the Energy Institut*e, Vol. 92 (5), pp. 1527-1536, 2019.

[6] V. Ayhan, S. Tunca. Experimental investigation on using emulsified fuels with different biofuel additives in a DI diesel engine for performance and emissions. *Applied Thermal Engineering*, Vol. 129, pp. 841-854, 2018.

[7] B.S. Bidita, A.R. Suraya, M.A. Shazed, M.A.M. Salleh, A. Idris. Preparation, characterization and engine performance of water in diesel nanoemulsions. *Journal of the Energy Institute*, Vol. 89 (3), pp. 354-365, 2016.

[8] H. Taghavifar, S. Anvari, A. Parvishi. Benchmarking of water injection in a hydrogen-fueled diesel engine to reduce emissions. *International Journal of Hydrogen Energy*, Vol. 42 (16). pp. 11962-11975, 2017.

[9] S. Shen, K. Sun, Z. Che, T. Wang, M. Jia. Puffing and micro-explosion of heated droplets for homogeneous ethanol-propanol-hexadecane fuel and micro-emulsified ethanol-biodiesel-hexadecane fuel. *Applied Thermal Engineering*, Vol. 165, 114537, 2020.

[10] D.V. Antonov, M.V. Piskunov, P.A. Strizhak. Explosive disintegration of two-component drops under intense conductive, convective, and radiant heating. *Applied Thermal Engineering*, Vol. 152, pp. 409-419, 2019.

[11] D. Antonov, J. Bellettre, D. Tarlet, P. Massoli, O. Vysokomornaya, M. Piskunov, Impact of holder materials on the heating and explosive breakup of two-component droplets, *Energies*, Vol. 11 (12), 3307, 2018.

[12] D.V. Antonov, P.A. Strizhak, R.M. Fedorenko, Z. Nissar, S.S. Sazhin, Puffing/micro-explosion in rapeseed oil/water droplets: The effects of coal micro-particles in water, *Fuel*, Vol. 289, 119814, 2021.

[13] D.O. Glushkov, P.A. Strizhak, K.Y. Vershinina, Minimum temperatures for sustainable ignition of coal water slurry containing petrochemicals, *Applied Thermal Engineering*, Vol. 96, pp. 534-546, 2016.

EFFECTS OF HYDROGEN ENRICHMENT STRATEGY ON COMBUSTION AND EMISSIONS IN A GASOLINE FUELLED ROTARY ENGINE

Merve Küçük [1], Ali Sürmen[2] and Ramazan Şener[3]

1. Department of Mechanical Engineering, Bursa Technical University, Bursa, Turkey; email: merve.altay@btu.edu.tr
2. Department of Automotive Engineering, Bursa Uludag University, Bursa, Turkey; email: surmen@uludag.edu.tr
3. Department of Electronics and Automation, Batman University, Batman, Turkey; email: ramazan.sener@batman.edu.tr

Abstract

Due to recent developments in electric and hybrid vehicle technologies, there has been a growing interest in Wankel engines as an important future automotive power source. Wankel engine can contribute to enhance the power range of hybrid vehicles owing to its favourable power-to-weight ratio. Moreover, the advantages of hydrogen can be benefited by improving the combustion process with hydrogen enrichment on a gasoline fuelled Wankel engine. In this study, a CFD model was established to investigate the effects of hydrogen enrichment on combustion and emissions on a rotary engine. Hydrogen enrichment strategy was applied to a spark-ignition rotary engine model operating at the constant engine speed of 6000 rpm and wide-open throttle conditions. Simulation results revealed that the hydrogen enrichment process improved the engine performance and enhanced the fuel efficiency. Increasing the hydrogen fraction at the intake, reduced CO emissions while increased NO_x emissions.

Keywords: CFD simulation, Combustion, Emission, Hydrogen enrichment, Wankel engine.

1 INTRODUCTION

A Wankel engine invented in 1954 by the German mechanical engineer Felix Heinrich Wankel as an alternative to the conventional piston engine.

Due to their compact design, excellent power-to-weight ratio as well as smooth and quite running, Wankel engine have a wide range of applications from motorcycles to unmanned aerial vehicles [1-4]. Recent developments in electric and hybrid vehicle technologies refers to a use of rotary engines as a power source.

Ji et al. [5] investigated the injection strategy influences on the mixture formation and combustion process using a direct injection rotary engine CFD model.

Shi et al [6] carried out studies on a hydrogen-blended Wankel engine operating under the stoichiometric and lean conditions. They revealed that hydrogen addition increased pressure and decreased the combustion duration. Lean operation conditions contributed to get better emissions and high thermal efficiency.

Hydrogen enrichment has been investigated in many studies in the literature. However, only a few of these studies investigated hydrogen enrichment effects on combustion characteristics and performance using full engine CFD model with three chambers. The aim of this study is to present the effects of hydrogen enrichment on the combustion and gas flow characteristics and emissions of the Wankel engine. For this purpose, a full engine model with three chambers has been established and CFD analyses have been conducted. Hydrogen enrichment strategy has been applied to the Wankel test engine model operating at the constant engine speed of 6000 rpm and full-load condition. Based on this approach hydrogen mass fraction in the intake is increased from 0% to %5 and 10%, gradually. At the end of the study, the advantages and difficulties of hydrogen addition to a Wankel engine in terms of engine performance and clean environment are evaluated according to the simulation results.

2. MATERIALS AND METHODS

2.1. Model Description

CFD model represents the test Wankel engine that was supplied by Vestel Defence Industry. Demonstrations of the test Wankel engine and CAD model of it are shown in Fig. 1 and Fig. 2, respectively.

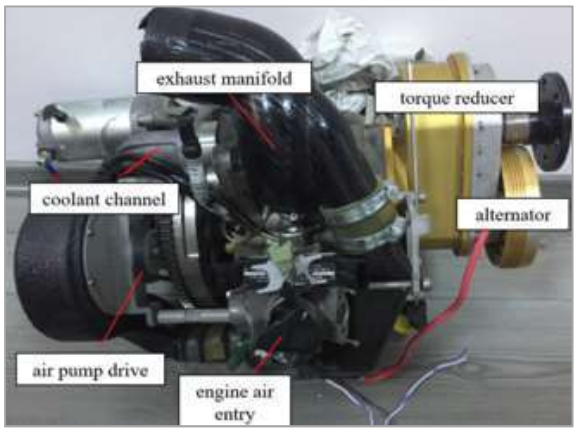


Figure 1. Demonstration of the test Wankel engine.

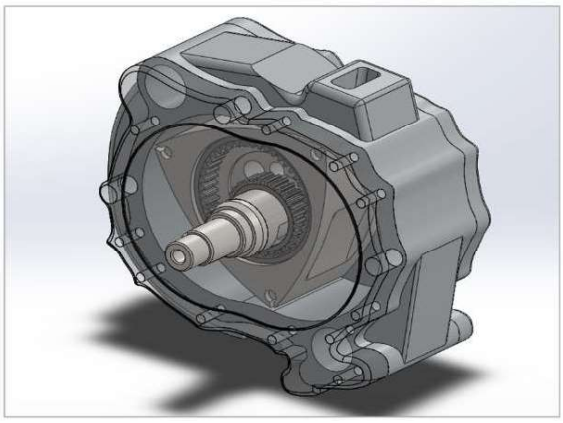


Figure 2. CAD model of the Wankel Engine.

A summary of the test engine specifications is presented in Table 1.

Table 1. Test engine specifications

Engine Type	Four-stroke Wankel engine
Radius, (R) [mm]	71.89
Amount of parallel transfer of trochoid, (a) [mm]	1.05
Generating Radius, (R_g)	72.94
Eccentricity, (e) [mm]	11.5
Width [mm]	7.44
k-factor	6.34

In this study, two cases fuelled with hydrogen-enriched gasoline and neat gasoline-fuelled cases were numerically investigated. Hydrogen mass fraction in the intake is 0% in Case A, which is a neat gasoline fuelled case. On the other hand, hydrogen mass fractions are 5% and 10% for Case B and Case C, respectively.

Some operating parameters and boundary conditions of the reference test engine are revealed in Table 2.

Table 2. Summary of the test engine operating parameters and boundary conditions.

Subject	Input
Inlet air temperature/pressure	300 K
Rotor/house wall temperature	488/443 K
Spark plugs wall temperature	600 K
Compression ratio	9.6
Spark plugs energy	0.03 and 0.04 J
Inlet/exhaust channel wall temperature	323/500 K
Wall boundary	No-slip
Mesh method	Modified cut-cell Cartesian
Intake and exhaust port	Pressures boundary condition
Rotor wall	Wall boundary condition
Pressure-Velocity coupling	PISO algorithm
Reaction mechanism	48 species and 152 reactions
Fuel mass $\dot{m}_{C_8H_{18}}$; $\dot{m}_{H_2}$(kg/h)	
Case A	11.89; 0.0000
Case B	10.80; 0.57
Case C	9.83; 1.19

Schematic illustration of the test engine surfaces can be found in Fig. 3.

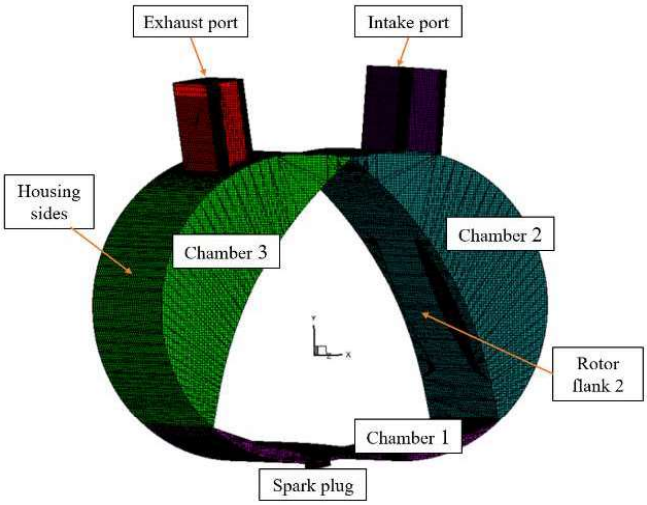


Figure 3. Schematic illustration of the test engine surfaces.

In this study, three dimensional CFD simulations have been carried out using Converge CFD software [7].

RNG k-ε model is more suitable for rotary engines [8-10]. Therefore, RNG k-ε turbulence model has been chosen in the simulations of the present study.

For primary reference fuel (PRF), a chemical reaction mechanism presented in Table 2 has been utilized [11].

SAGE combustion model has been preferred as a detailed chemical kinetics solver. CHEMKIN format has been used for the definition of chemical reaction equations. Isooctane (IC_8H_{18}) is selected as a fuel for the simulations.

Extended Zeldovich model has been used to obtain NOx formation. Hiroyasu model has been used as soot model [12].

Sub-models of the simulation are listed in Table 3.

Table 3. Sub-models of the simulation.

Subject	Input
Turbulent model	RNG k-ε
Wall Model	Wall heat transfer: O'Rourke and Amsden
	Near wall treatment: Standart Wall Function
Combustion model	SAGE (Adaptive Zoning)
NO_x model	Extended Zeldovich
Soot model	Hiroyasu-NSC

2.2. Experimental validation of the CFD model

Cartesian grid method has been preferred for the grid generation in the CFD model of the reference Wankel engine.

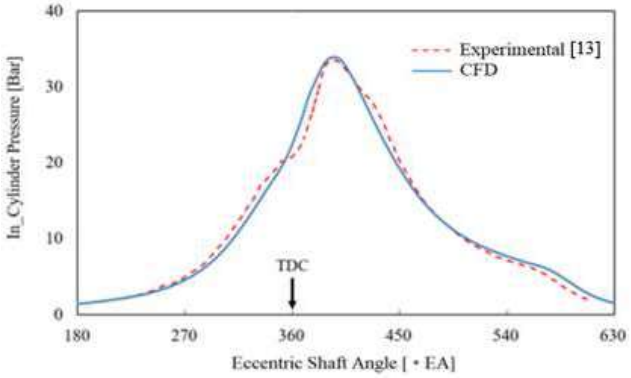
Mesh independence test has been performed for the base test engine. Four grid construction named coarse, medium, fine, and finer are tested as shown in Fig. 3a and Fig. 3b. These mesh structures are established with a base size of 4 mm, 3 mm, 2 mm, and 1 mm, respectively. Besides, fixed embedding and adaptive mesh refinement (AMR) techniques have been also applied to all the mesh structures.

Taking into account the simulation accuracy and computational cost, the mesh structure of "fine" is chosen.

As shown in Fig. 4a and Fig. 4b, pressure and HRR results, conducted at 6000 rpm are compatible with those of the experimental results [19]. So, the CFD model is assumed to be well-calibrated.

In the present study, CFD simulations of the four-stroke Wankel engine have been carried out using full engine model. In-cylinder pressure and heat release rate (HRR) results of the simulations are compared with the experimental results of Spreitzer et. al [13].

a.



b.

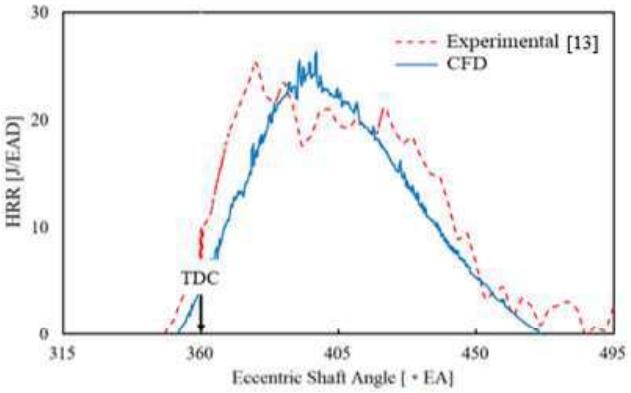


Figure 4. Validation of the CFD model with the experimental results. a. Pressure, b. HRR results versus eccentric shaft angle

As shown in Fig. 4a and Fig. 4b, pressure and HRR results, conducted at 6000 rpm are compatible with those of the experimental results. So, the CFD model is assumed to be well-calibrated.

3. RESULTS AND DISCUSSION

Neat gasoline fuelled Wankel engine case (Case A) was assumed as a base data and the results of other cases were compared with this base data. Simulations have been conducted using a full engine geometry with three combustion chambers.

CA10, CA50, and CA90 times of different cases are compared in Fig 6. The ignition advances for all the cases are kept the same (31°EA). CA10 of the Case A during the cycle is 367.04°EA and this value is advanced by 7.93°EA and 13.78°EA in

case B and Case C. CA90 of Case A during the cycle is 469.18°EA and this value is advanced by 13.98°EA and 27.56°EA in Case B and Case C, respectively. These results demonstrate that ignition is advanced and combustion duration is shortened at hydrogen blended cases proportional to the hydrogen mass fraction in the mixture. The combustion duration for the hydrogen blended Case B and C is shortened by 6.06°EA and 13.77°EA, respectively, compared to that of Case A [14].

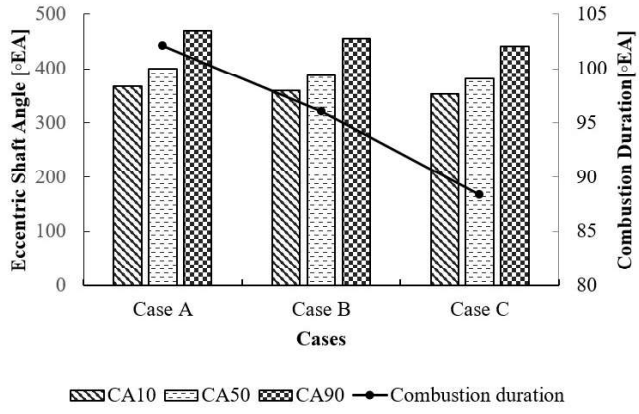


Figure 6. Comparison of CA10, CA50, and CA90 times of different cases.

In-cylinder pressure, average temperature, are plotted against eccentric shaft angle in Fig. 7. Hydrogen mass fraction in the intake for Cases A, B, and C are increased from 0% to %5 and 10%, gradually.

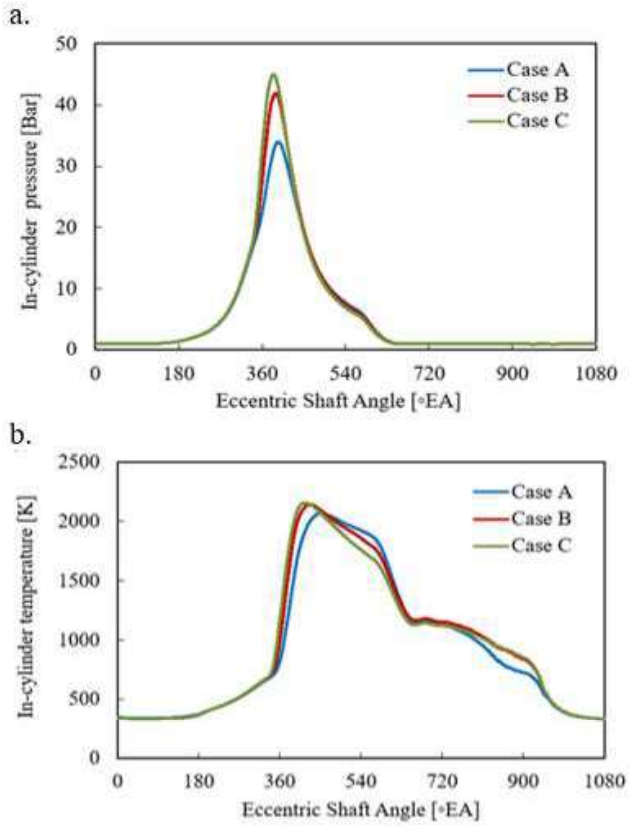


Figure 7. Comparison of a) pressure

Figure 7. Comparison of a) pressure, b) temperature.

The in-cylinder pressure and temperature increase by the hydrogen addition strategy, which leads to the shortened combustion duration and accelerated fuel burning speed, are shown in Fig.6.

Fig. 7a shows that the maximum pressure of the working chamber increases by 10.81% and 18.91% for hydrogen blended Case B and C, respectively, compared to Case A. Fig. 7b shows the effect of accelerated burning speed with increased hydrogen mass fraction, as first temperature increases rapidly and then shows a relatively sharp decrease.

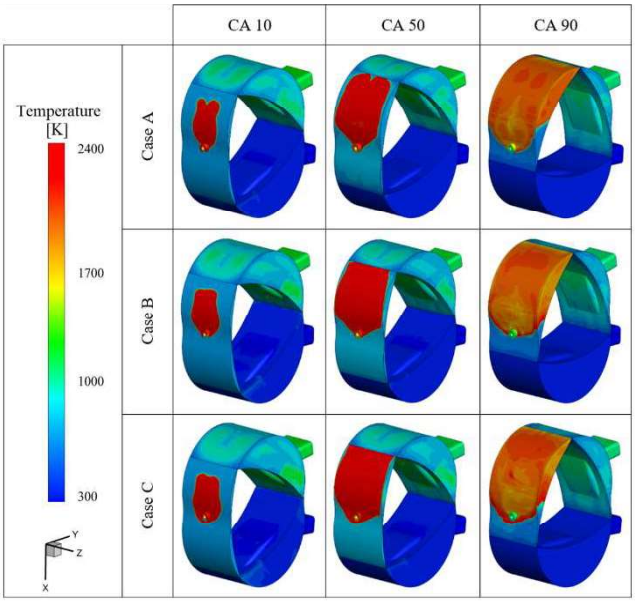


Figure 8. Temperature distribution for different cases at CA 10, CA50, and CA90.

The temperature distribution of rotor housing in 3D simulation is shown in Fig. 8. It is seen that the flame propagation is towards to the leading edge of the rotor and especially in Case A there are still cold regions (e.g., side walls of the housing) in the flame propagation direction because the flame cannot reach these regions yet. On the other hand, the flame can expand towards to the side walls of the housing in the hydrogen blended cases. Therefore, it can be said that hydrogen enrichment is very advantageous in Wankel engines because of its geometrical restrictions.

CONCLUSION

In this study, the effectiveness of the hydrogen enrichment strategy in a gasoline fuelled Wankel

engine is investigated. This study demonstrates the potential of the hydrogen enrichment strategy to increase engine performance and reduce emissions.

In future work, the benefits of the hydrogen enrichment strategy in the Wankel engine will be further improved by optimizing spark plug ignition timing, and spark plug positions. Moreover, the hydrogen direct injection technique will be applied to the full engine CFD model to improve the mixture formation and combustion process.

ACKNOWLEDGMENT

The authors thank Vestel Defence Industry for their donation of the Wankel research engines, Bursa Technical University, High-Performance Computing Laboratory, and Bursa Uludag University, Internal Combustion Engine Laboratory for their technical support, and Convergent Science Inc. for providing the Converge license.

REFERENCES

[1].Ö. Cihan, H. E. Doğan, O. A Kutlar, A. Demirci, M. Javadzadehkalkhoran, Evaluation of heat release and combustion analysis in spark ignition Wankel and reciprocating engine, *Fuel*, Vol. 261, 2020. https://doi.org/10.1016/j.fuel.2019.116479

[2]. H. Meng, C. Ji, S. Wang, D. Wang, J. Yang, Optimizing the idle performance of an n-butanol fueled Wankel rotary engine by hydrogen addition, *Fuel,* Vol. 288, 119614, 2021. https://doi.org/10.1016/J.FUEL.2020.119614

[3]. C. Ji, H. Wang, C. Shi, S. Wang, J. Yang, Multi-objective optimization of operating parameters for a gasoline Wankel rotary engine by hydrogen enrichment, *Energy Conversion and Management,* Vol. 229, 113732,2021. https://doi.org/10.1016/J.ENCONMAN.2020.113732

[4].J.Ribau, C. Silva, F. P. Brito, J. Martins, Analysis of four-stroke, Wankel, and microturbine based range extenders for electric vehicles, *Energy Conversion and Management*, Vol. 58, pp.120–33, 2012.

[5]. C. Shi, C. Ji., S. Wang, Y. Jinxin, W. Huaiyu, Experimental and numerical study of combustion and emissions performance in a hydrogen-enriched Wankel engine at stoichiometric and lean operations, *Fuel*, Vol. 291, 120181, 2021.

[6]. F. Amrouche, P. A. Erickson, S. Varnhagen, J. W. Park, An experimental analysis of hydrogen enrichment on combustion characteristics of a gasoline Wankel engine at full load and lean burn regime, *International Journal of Hydrogen Energy,* Vol. 43(41), 19250–19259, 2018.

[7]. Convergent Science. CONVERGE Manual v3.0 2021:1285.

[8]. C. Ji, C. Shi, S. Wang, J. Yang, T. Su, D. Wang, Effect of dual-spark plug arrangements on ignition and combustion processes of a gasoline rotary engine with hydrogen direct-injection enrichment, *Energy Convers Manage*, Vol. 181, pp.372–81, 2019.

[9]. C. Shi, C. Ji, S. Wang, J. Yang, Z. Ma, H. Meng, H. Potential improvement in combustion behavior of a downsized rotary engine by intake oxygen enrichment. Energy Convers Manage, 2020, 205:112433,2020.

[10]. O. O. Taskiran, A. T. Calik, A. O. Kutlar, Comparison of flow field and combustion in single and double side ported rotary engine, *Fuel,* Vol. 254, 115651, 2019.

[11]. P. K. Senecal, E. Pomraning, K. J. Richards, T. E. Briggs, C. Y. Choi, R. M. McDavid, Multi-Dimensional Modeling of Direct-Injection Diesel Spray Liquid Length and Flame Lift-off Length using CFD and Parallel Detailed Chemistry, *SAE Technical Paper*,01-1043, 2003.

[12]. R.I Issa, Solution of the implicitly discretised fluid flow equations by operator-splitting, *Journal of Computational Physics*, Vol. 62(1), pp.40-65, 1986.

[13]. J. Spreitzer, F. Zahradnik, B. Geringer, Implementation of a Rotary Engine (Wankel Engine) in a CFD Simulation Tool with Special Emphasis on Combustion and Flow Phenomena, *SAE Technical Papers,* 2015. https://doi.org/10.4271/2015-01-0382

[14].14 Z. Kan, Z. Hu, D. Lou, Z. Cao, J Cao, Effect of the altitude on the combustion characteristics of a low-compression-ratio diesel engine during the start-up process, *Proceedings of the Institution of Mechanical Engineers, Part D: Journal of Automobile Engineering*, Vol. 231(13), 1838–1847, 2017.

CHARACTERIZATION OF A PARTIALLY PREMIXED SWIRL BURNER USING OPENFOAM SIMULATIONS WITH A GLOBAL CHEMICAL KINETICS MECHANISM

Emre Böncü[1], Dilay Güleryüz[1], Tahsin Berk Kiymaz[1], Mehmet Karaca[2] , İskender Gökalp[1]

(1) Department of Mechanical Engineering, Middle East Technical University, Ankara

(2) Department of Aerospace Engineering, Middle East Technical University, Ankara

Abstract

To accelerate the CFD simulations involving swirl stabilized methane burners, a global chemical mechanism with only two chemical reactions was created by Franzelli et al [1]. This mechanism is called the "BFER's mechanism" and involves only the methane oxidation and CO - CO_2 equilibrium reaction. The advantage of using BFER's mechanism over using other detailed mechanisms such as GRI 3.0 is the much smaller reaction number of BFER's mechanism. BFER's mechanism only contains 6 species and 2 global reactions. On the other hand, for example, GRI3.0 mechanism is composed of 53 species and 325 reactions. Even the reduced versions of the GRI3.0 does not come close to the simplicity of the BFER's mechanism. BFER's correctly predicts laminar flame speed for the ranges of 300 to 700 K fresh gas temperature, 1 to 12 atmospheres of pressure and 0.6 to 1.5 equivalence ratios. In this study the ICARE swirl burner experimental setup geometry is simulated using BFER's mechanism with LES model using OpenFOAM. The numerical results are then compared with the experimental results to validate BFER's mechanism's use with OpenFOAM.

Keywords: Combustion, OpenFOAM, Methane

1 INTRODUCTION

To accelerate the CFD simulations involving swirl stabilized methane burners, a global chemical mechanism with only two chemical reactions was created by Franzelli et al [1]. This mechanism is called the "BFER's mechanism" and involves only the methane oxidation and CO - CO_2 equilibrium reaction. The advantage of using BFER's mechanism over using other detailed mechanisms such as GRI 3.0 is the much smaller reaction number of BFER's mechanism. BFER's mechanism only contains 6 species and 2 global reactions. On the other hand, for example, GRI3.0 mechanism is composed of 53 species and 325 reactions. Even the reduced versions of the GRI3.0 does not come close to the simplicity of the BFER's mechanism. BFER's correctly predicts laminar flame speed for the ranges of 300 to 700 K fresh gas temperature, 1 to 12 atmospheres of pressure and 0.6 to 1.5 equivalence ratios. In this study the ICARE swirl burner experimental setup geometry is simulated using BFER's mechanism with LES model using OpenFOAM. The numerical results are then compared with the ICARE experimental results from the experimental work of Mansouri et al. [2] to validate BFER's mechanism's use with OpenFOAM.

2 OPENFOAM CASE

The mesh used in the simulations consists of around 4 million elements and is fully hexahedral. From the air inlet 5.2 g/s of air is injected and swirled with the swirling blades. 0.24 g/s of methane is also injected from eight radial inlets downstream of the swirling blades. The centre fuel pipe is not modelled to keep the geometry simpler and appropriate for hexahedral meshing. The numerical domain is illustrated in figs. 1 and 2. The numerical domain is the replica of an existing experimental setup in ICARE facilities.

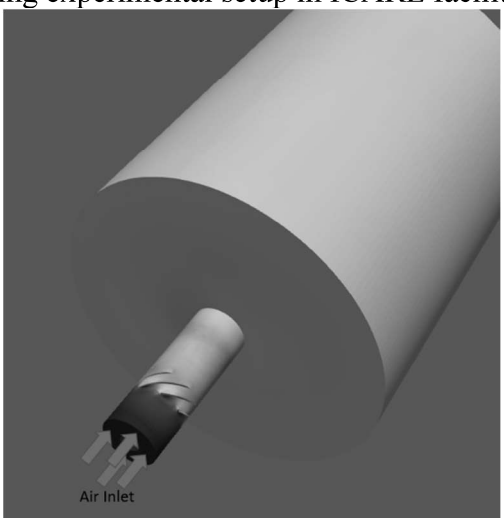


Figure 1. Numerical swirl burner domain coloured with static pressure contour

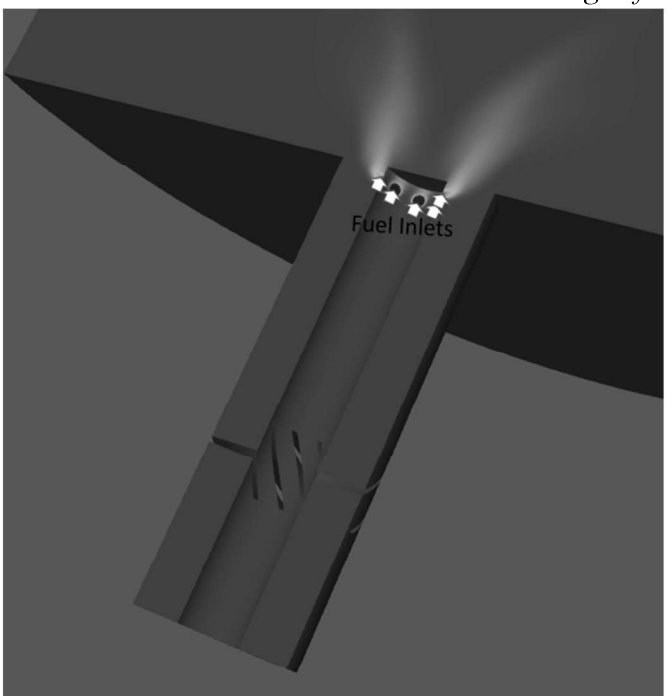


Figure 2. Numerical swirl burner domain clipped with an axial plane and coloured by mean methane mass fraction contour

3 NUMERICAL METHODOLOGY

In the area of swirl stabilized combustion CFD, LES has shown itself to be a very important tool. The reason for this mostly lies on the ability of LES to predict flows with highly curved streamlines. As one can imagine the swirl blades of any swirler geometry impose high curvature streamlines on the flow, which make it harder or even impossible for Reynolds Averaged Navier Stokes (RANS) simulations to predict certain flow features of swirl stabilizers. Especially important for predicting combustion characteristics is the existence and magnitude of the Central Toroidal Recirculation Zone (CTRZ), which occurs due to vortex breakdown and combines the hot exhaust gasses with the incoming fresh fuel-air mixture. This is the main mechanism in swirl flame stabilization. As such, prediction of the regions where negative axial velocity occurs, and the magnitude of this velocity component is of utmost importance for swirl stabilized combustion CFD. The inability of RANS simulations to predict this CTRZ have been observed in several studies such as "Assessment of the Performances of RANS Models for Simulating Swirling Flows in a Can-Combustor" by K. Khademi Shamami and M. Birouk [3]. In their study they found that most RANS simulations were not able to resolve the CTRZ properly and in some cases RANS simulations were not able to predict even the existence of CTRZ.

For these reasons LES model was chosen for the current study. The OpenFOAM solver reactingFOAM was chosen for the simulation. The Wall Adapting Local Eddy-viscosity (WALE) was used as the subgrid-scale (SGS) stress model. The accuracy of the LES simulation relies on the assumption that the smallest "large" eddies resolved by the CFD simulations lie in the inertial subrange of turbulent kinetic energy spectrum and as such the unresolved ones are isotropic enough to be modelled by the SGS viscosity models such as WALE.

Since the current numerical simulation uses OpenFOAM LES framework, it solves density-weighted filtered continuity equation, momentum equation and the transport equations for chemical species and enthalpy. These equations are illustrated in eqns. 1 to 4.

$$\frac{\partial \bar{\rho}}{\partial t} + \frac{\partial \bar{\rho}\tilde{u}_j}{\partial x_j} = 0$$

eqn. 1 (density-weighted filtered continuity equation)

$$\frac{\partial \bar{\rho}\tilde{u}_j}{\partial t} + \frac{\partial \bar{\rho}\tilde{u}_i\tilde{u}_j}{\partial x_j} = \frac{\partial \bar{\rho}}{\partial x_i} - \frac{\partial \tau_{ij}}{\partial x_j} + \frac{\partial \bar{\sigma}_{ij}}{\partial x_j} + f_i$$

eqn. 2 (density-weighted filtered momentum equation)

$$\frac{\partial \bar{\rho}\tilde{h}}{\partial t} + \frac{\partial \bar{\rho}\tilde{h}\tilde{u}_j}{\partial x_j} = \frac{\partial \bar{\rho}\tilde{p}}{\partial t} + \frac{\partial \bar{\rho}\tilde{p}\tilde{u}_j}{\partial x_j} - \frac{\partial q_j^h}{\partial x_j} - \frac{\partial \bar{q}_j}{\partial x_j} + \overline{\sigma_{\iota J}\frac{\partial u_\iota}{\partial x_J}} + \overline{\dot{\omega}_h} + \bar{s}_h$$

eqn. 3 (density-weighted filtered enthalpy equation)

$$\frac{\partial \bar{\rho}\widetilde{Y}_\iota}{\partial t} + \frac{\partial \bar{\rho}\widetilde{Y}_\iota\tilde{u}_j}{\partial x_j} = -\frac{\partial q_j^i}{\partial x_j} - \frac{\partial \bar{q}_j^i}{\partial x_j} + \overline{\dot{\omega}_\iota}$$

eqn. 4 (density-weighed filtered species equation)

Where $\bar{\blacksquare}$ operator means LES filtering operation, $\tilde{\blacksquare}$ operator means density-weighted averaging and is defined as $(\tilde{f} = \frac{\overline{\rho f}}{\bar{\rho}})$ and symbols ρ, u, Y_i, h, p represents density, velocity, mass fraction of i[th] chemical species, enthalpy and pressure. Furthermore $\tau_{ij} = \bar{\rho}(\widetilde{u_\iota u_J} - \tilde{u}_i\tilde{u}_j)$ which is the SGS stress tensor, $\bar{\sigma}_{ij}$ is the resolved molecular shear-stress tensor. $q_j^h = \bar{\rho}(\widetilde{hu_j} - \tilde{h}\tilde{u}_j)$ is SGS heat flux vector and q_j^i is the SGS mass

flux of the I[th] species calculated similar to the SGS stress and heat flux values. Their resolved counterparts being $\bar{q}_j$ and $\bar{q}_j^i$ respectively. Finally, $\overline{\dot{\omega}_\iota}, \overline{\dot{\omega}_h}, f_i$ and $\bar{s}_h$ are the filtered mass reaction rate of i[th] species, chemical reaction heat release, external forces such as gravity and external heat source/sink. Since gravity is neglected in this study $f_i = 0$.

Since WALE SGS viscosity model has been used for the simulation following equations are used in order to get to the τ_{SGS}.

$$\tau_{SGS} = 2\rho\nu_{sgs}S_{ij}^* - \frac{2}{3}\rho k_{sgs}\delta_{ij} \qquad \text{eqn. 5}$$

$$S_{ij}^* = \frac{1}{2}\left(\frac{\partial\tilde{u}_i}{\partial x_j} + \frac{\partial\tilde{u}_j}{\partial x_i} - \frac{1}{3}\frac{\partial\tilde{u}_k}{\partial x_k}\delta_{ik}\right) \qquad \text{eqn. 6}$$

For the chemistry-turbulence interaction Partially Stirred Reactor (PaSR) model was used.

For the meshing since OpenFOAM results seem to be highly sensitive to mesh qualities and because of the computational weight of the models used, a fully hexagonal mesh was constructed for both flow-oriented high quality meshes and a relatively low number of mesh count when compared to tetrahedral meshes. In fig. 3 and 4, the geometry partitioning methods used to mesh the domain are illustrated.

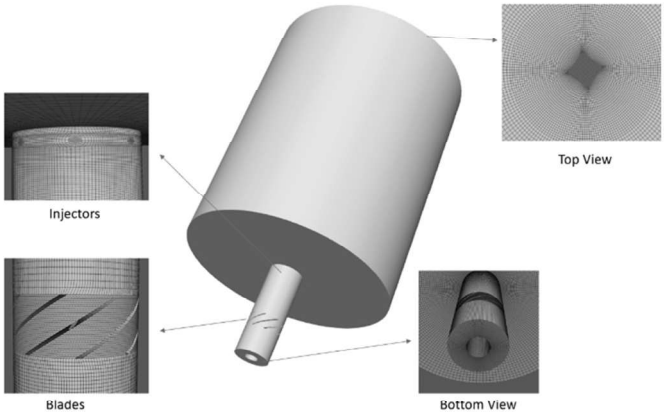


Figure 3. The illustration of geometry parting methods used in the meshing

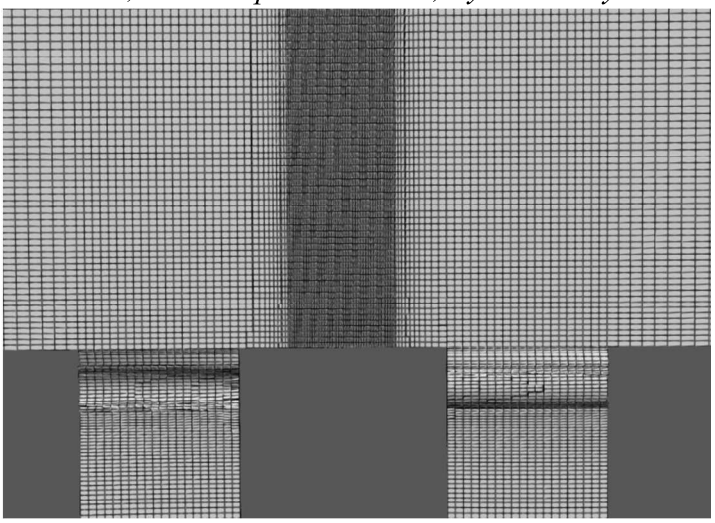


Figure 4. An axial slice of the hexahedral mesh

As seen from the figs. 2 and 3, the domain geometry is split into hexahedral pieces and these pieces are individually meshed with fully hexagonal cells. Since while partitioning, the flow directions were taken into consideration and the meshes were fully hexahedral and structured, the mesh has both high quality and low cell count.

4 RESULTS

The OpenFOAM simulation is conducted for 2.24 second of physical time and the results are averaged over a time window of 0.84 second to the end of the simulation. 0.84 seconds is higher than three times the flow through time, thus satisfies the condition for the averaging window. When the results are viewed it is seen that since the simulation is conducted for a long enough physical time the hot gasses had the time to fill the entire simulation domain. Which makes the temperature contour uniform and symmetric. The temperature contour of the results is given in fig 5.



Figure 5. Temperature contour of the results given in an axial slice of the domain

Also worth noting is the fact that the conical shaped maximum temperature region of the simulation is close to the experimental results. In some of the previous simulations which used GRI 3.0 mechanism, it was apparent that the maximum temperature regions were travelling all the way up to the outlet surface. Thus, it might be worthy to note that the BFER's mechanism is better at predicting temperature fields when compared to the previous GRI3.0 mechanism simulations of the same geometry. Furthermore, the existence of flame lift-off phenomenon is also predicted by the BFER's LES results. To illustrate this the mean chemical heat release contour is given in fig. 6

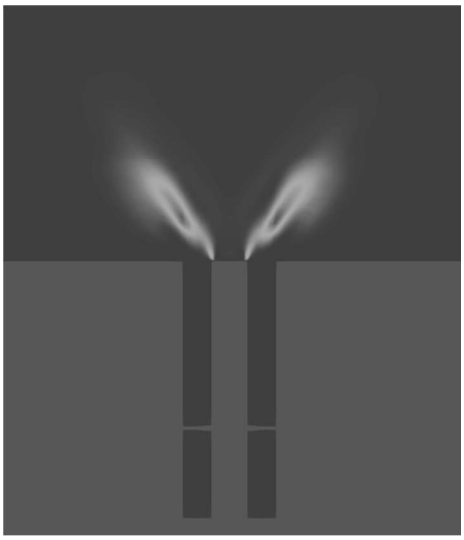


Figure 6. Mean Chemical heat release rate contour given in an axial slice

For further analyses the mean axial and tangential velocity values of the numerical results were compared with the experimental results of Mansouri et al. [2] which are gathered using the mentioned experimental setup in ICARE. The plots for these velocity magnitudes are given in figs. 7 to 10.

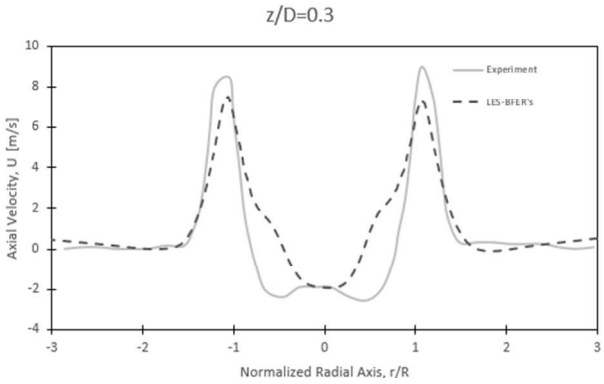


Figure 7. Axial velocity plots of the experiment and numerical simulation at 0.3 diameters distance

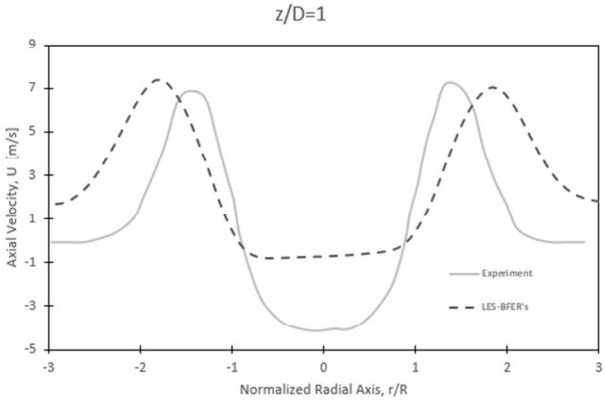


Figure 8. Axial velocity plots of the experiment and numerical simulation at 1 diameter distance

As seen from the axial velocity magnitude plots, for the plots at 0.3 diameter axial distance the numerical results are close to the experimental ones. it is apparent that the numerical results were able to predict the value of the minimum axial velocity in 0.3 diameter distance even though the size of the recirculation region is predicted to be smaller than the experimental results. However, for the plots at 1 diameter axial distance, there are significant differences between the two results. As seen from the plot the BFER's results did not capture the full extent of the central recirculation zone negative axial velocity value, when compared with the experimental results. This might have happened due to different

phenomena. One reason might be the mesh quality. Even though the simulation was conducted with the maximum number of meshes for the combustion simulation to finish within a reasonable amount of time, it might still have been too course for the LES simulation to capture enough turbulent motion. Consequently, this might have caused the over prediction of velocities within the central recirculation zone. This hypothesis must be tested by conducting the BFER's simulation with a refined mesh. A second possibility for the difference in results might be BFER's mechanisms inability to capture combustion induced vortex breakdown phenomenon. However, this is unlikely since the BFER's mechanism is tested and confirmed to be working for LES simulations of swirl combustors in Franzelli's article [1]. Furthermore, the swirler geometry used in the studies has a 1.4 swirl number. Which is generally too high for combustion induced vortex breakdown phenomenon. This implies the need for testing the BFER's mechanism by implementing the correction functions.

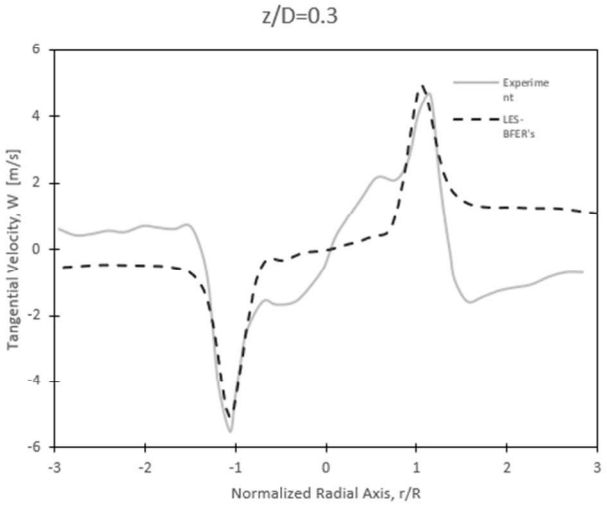


Figure 9. Tangential velocity plots of the experiment and numerical simulation at 0.3 diameters distance

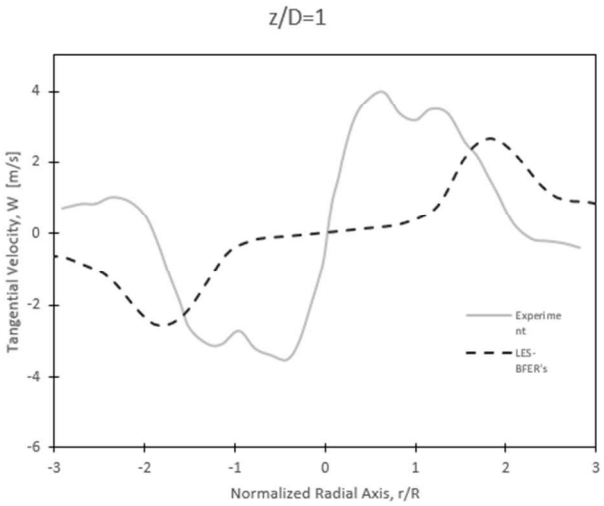


Figure 10. Tangential velocity plots of the experiment and numerical simulation at 1 diameter distance

The same phenomenon can be observed for tangential velocity plots also. For the plots at 0.3 diameter axial distance, the values for the LES and experimental results are very similar. However, for the plots at 1 diameter axial distance BFER's mechanism does not predict the same vortex strength the experiments.

5 CONCLUSIONS

BFER's mechanism is an attractive option for methane combustion because of its low computational cost when compared to other chemical mechanisms and the FFT analyses of the numerical results show logical results. Indicating that this sort of analyses is applicable to the simulations using BFER's mechanism and LES model. Finally, as a future work the simulation should be conducted with a higher mesh count to see the effects of mesh fineness.

REFERENCES

[1] Franzelli, B., Riber, E., Gicquel, L. Y., & Poinsot, T. (2012). Large eddy simulation of combustion instabilities in a lean partially premixed swirled flame. *Combustion and flame*, *159*(2), 621-637.

[2] Mansouri, Z., & Boushaki, T. (2018). Experimental and numerical investigation of turbulent isothermal and reacting flows in a non-premixed swirl burner. *International Journal of Heat and Fluid Flow*, *72*, 200-213.

[3] Shamami, K. K., & Birouk, M. (2008). Assessment of the performances of RANS models for simulating swirling flows in a can-combustor. *The Open Aerospace Engineering Journal*, *1*(1).

INVESTIGATIONS OF FLAME CHARACTERISTICS OF LPG USED IN THREE DIFFERENT SIZE HOUSEHOLD COOKERS

Berkay SAHIN[1], Nimeti DONER[1] and Mustafa ILBAS[2]

1. Gazi University, Engineering Faculty, Department of Mechanical Engineering, 06570 Ankara, TURKIYE. email: nimetidoner@gazi.edu.tr
2. Gazi University, Technology Faculty, Department of Energy Systems Engineering, 06570 Ankara, TURKIYE. email: ilbas@gazi.edu.tr

Abstract

In this study, the flame characteristics of cold flow and flame in a household cooker were experimentally investigated. Under laboratory conditions, flame temperatures, flow velocity, and gas emissions were measured for two flow rates (maximum and minimum). The pressure of the liquefied petroleum gas (LPG) used in the study is 2 to 3 bar and consists of a mixture of 70% butane and 30% propane. The household cooker has three cookers of different sizes, which are named Cooker 1, Cooker 2, and Cooker 3, depending on the diameter of the flame outlet. The outer diameter of the Cooker 1 is 8 cm, the outer diameter of the Cooker 2 is 7 cm, and that of the Cooker 3 is 5 cm. The reference points were determined for each cooker, and measurements were performed based on the reference point in the horizontal, vertical, and diagonal directions. The measurement range is between the reference point (0 cm) and 3 cm (including 3 cm) at intervals of 0.5 cm. The measured values are shown in the graphical figures.

Keywords: LPG, flame characteristics, gas velocity, flame temperature, gas emissions.

1 INTRODUCTION

LPG (Liquefied Petroleum Gas) is a colorless, odorless, combustible gas that is heavier than air, and is obtained by distilling crude oil in refineries or by separating it from natural gas and liquefying it under a certain pressure. LPG consists of hydrocarbons such as propane (C_3H_8), butane (C_4H_{10}) and their isomers or mixtures. LPG is preferable due to its low carbon emissions, higher heating value and efficiency, and is also more environmentally friendly than other fuels [1]. It is used as a fuel in many households, industries and vehicles, and due to these advantages, the consumption of LPG is increasing worldwide.

The nozzles of domestic cookers convert the potential energy of the resulting pressurised gas into kinetic energy. This turbulent, axisymmetric round jet radiates into the air that is at rest. Flame stability is defined as the ability of a flame to withstand a wind speed of 3 m/s [2]. In addition, there are mixed flames or diffusion flames in domestic cookers [3]. Dong et al. [4] studied the heat transfer effects of flame impingement of LPG in terms of Reynolds numbers (600-2500) at changing flow rates as a function of the distance between the burner and the top plate in the experimental setup using 14 thermocouples. They found that heat transfer increased at high Reynolds numbers and low equivalence ratios (0.7; 0.85). One of the first studies to investigate in detail the combustion characteristics of domestic cookers was also conducted by Ref. [5]. In this study, liquefied petroleum gas composed of 40% propane-C_3H_8 and 60% butane-C_4H_{10} was evaluated in terms of temperature, thermal efficiency, and CO emission for an unmixed (self-aspirating) and rotating flame on a burner of the same size through experimental studies. Li et al. [6] found through experimental and statistical studies that Reynolds number has a significant effect on both thermal efficiency and CO emission for LPG (70% butane and 30% propane). Lee, Hwang and Lee [7] found that LPG (main gas; propane) has the highest flame velocity at an equivalence ratio of 1.1 compared to other gases such as landfill gas and LNG. Anggarania et al. [8] investigated the combustion of LPG mixed with dimethyl ether (DME) at different volumetric ratios (5%, 10%, 15%, 20%, 25%, 30% and 50%) to explore alternative fuels that can be used in place of

LPG in domestic cookers applications. It was found that the thermal efficiency of LPG is affected by the blending condition. Kang et al. [9] conducted experimental and theoretical analyses of flame jet combustion characteristics when three different fuels (dimethyl ether, methane, and LPG) were used in a household stove. For each fuel flame, the Reynolds number increases with increasing burner diameter. While the flame height in the laminar region is proportional to the Reynolds number, the flame height in the fully developed region was found to remain constant. The flame width was found not to change significantly with flame jet velocity. It was concluded that the flame velocity and Reynolds numbers of dimethyl flames are lower than those of LPG flames. A recent study investigated the effects of different port shapes (such as rotating strips or circular ports) on the heating performance of different gases in a domestic cooker [10]. In this study, a structural design parameter was proposed based on the experimental results of the corresponding nozzle shapes. Wae-hayee et al. [11] studied the effects of the distance between the nozzle and the top plate on the heat transfer of a domestic cooker where LPG is used as fuel and found that the highest heat transfer occurs at the largest distance above the nozzle. In this study, a mixture of air and LPG was used as fuel, and the gas flow rates were 1.5, 4.5, and 5.5 g/min. They concluded that the highest heat transfer occurs when the flame hits the surface and that the total height can be reached at 70% of its length.

A study titled Access to Clean Cooking Energy and Electricity- Survey of States (ACCESS) was conducted in India in 2014-2015 on domestic cookers. This study surveyed household cookers and fuels in 8568 homes and 714 villages in 51 regions. It was found that LPG was used in households in 22% of the relevant regions [12]. Apart from this study, extensive research has also shown that the use of LPG in domestic cookers is crucial to the relationship between parameters such as health, climate, protection of environmental impacts, reduction of greenhouse gas emissions, protection of local health, and women's health [13]. In another study, the project of switching fuels to LPG for kitchen use was conducted in more than 50 million households in Indonesia over a period of five years from 2007 [14]. Shen et al. [15] determined that as the percentage of butane in the LPG increased, the thermal efficiency, combustion, and cooking performance increased. From these studies, the use of liquefied petroleum gas (LPG) with different gas mixtures in domestic cookers is widely used worldwide and it is important to determine its combustion characteristics. In our study, the flame characteristics of LPG (70% butane + 30% propane) in domestic cookers of different sizes were investigated in terms of flame temperatures and gas flow velocity.

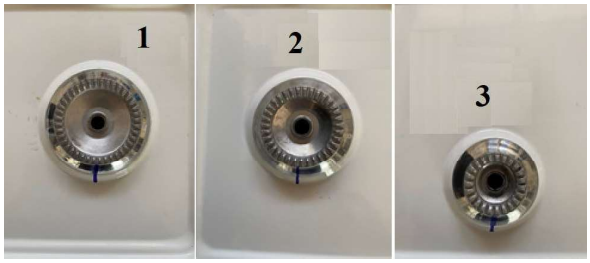
2 EXPERIMENTAL STUDIES

Household cookers are used in heating applications with multiple laminar mixed flame jets. Models with a circular cooker and numerous small ports are the most common and well-known types, producing thin-thickness low-velocity jets with a Reynolds number of 300-800.

Experimental studies were carried out using a 12 kg LPG tank, a household cooker with three different size cookers, a thermocouple for temperature measurements and an anemometer (the Geratech brand) for velocity, and emission measurements using the NOVAplus device. The most common model of household cookers, three different sized cookers with two gas flow rates, was used for the experiments on flame characteristics. The burners in the cookers shown in Figure 1 are the same and are 1 cm in diameter. The cookers are named Cooker 1, Cooker 2, and Cooker 3, respectively, according to the outer diameter. The outer diameter of the largest cooker is 8 cm, the outer diameter of the medium-size cooker is 7 cm, and the smallest outer diameter of the cooker is 5 cm. The maximum gas flow rate of Cooker 1 was measured as 0.6 l/min, and the minimum gas flow rate was defined as 0.25 l/min. The maximum flow rate of Cooker 2 was measured as 0.25 l/min and the minimum flow rate measured as 0.1 l/min. Cooker 3 has a maximum flow rate of 0.2 l/min and a minimum flow rate of 0.1 l/min. Cooker 1 consists of 40 ports, Cooker 2 consists of 35 ports and Cooker 3 consists of 23 ports. The flame characteristics of all cookers were measured from the reference points, and the reference points are shown in blue on the cookers.



(a)



(b)

Figure 1. (a) the household cooker used in our study and (b) cookers.

3 RESULTS and DISCUSSIONS

At minimum and maximum gas flow rates, from the reference point at intervals of 0.5 cm, by measure period of 10 minutes, temperature measurements were made in horizontal, vertical and diagonal directions for all nodes. The diagonal measurements of Cooker 1 at minimum and maximum flow rates are presented in Figure 2 and Figure 3, respectively. Measured flame temperatures for all cookers are given graphically in Figure 4.



0 cm



0.5 cm



1 cm



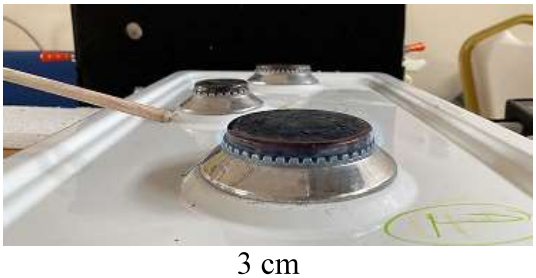
1.5 cm



2 cm



2.5 cm



3 cm

Figure 2. Temperature measurements of Cooker 1 at diagonal direction for minimum flow rate.

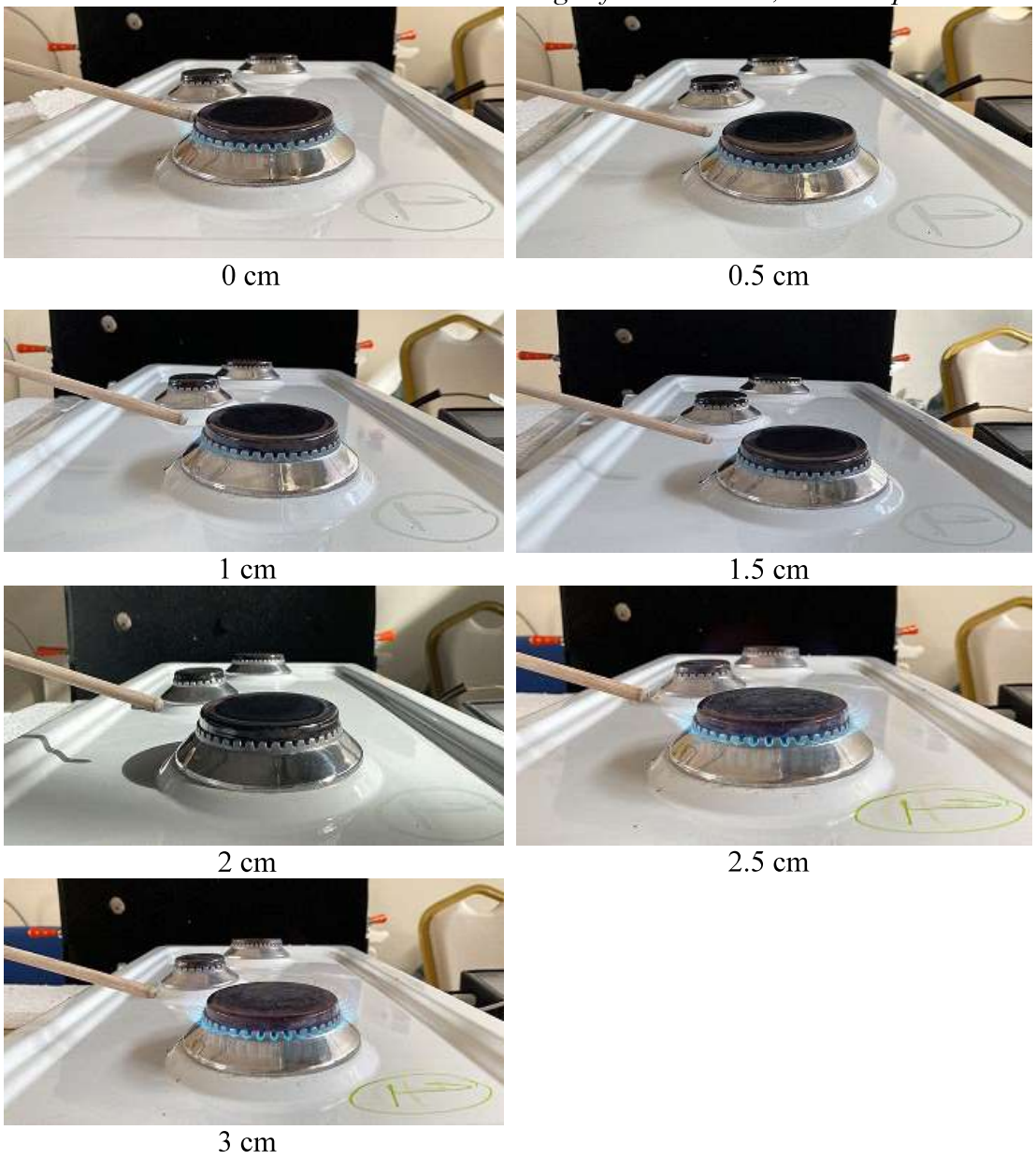
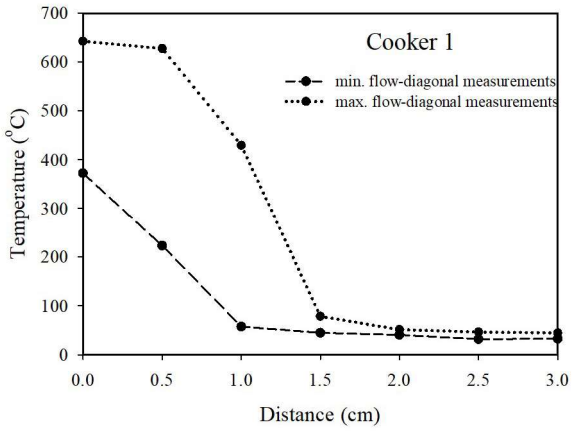
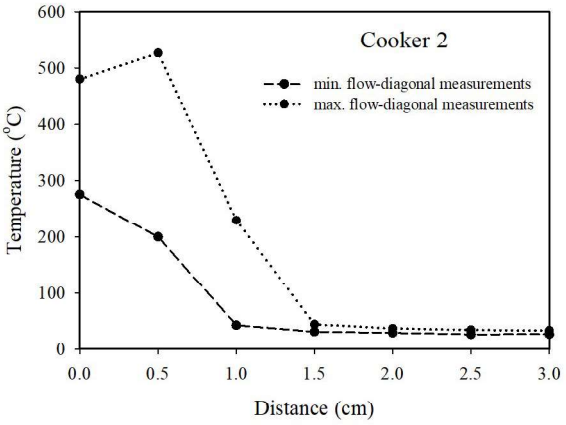


Figure 3. Temperature measurements of Cooker 1 at diagonal direction for maximum flow rate.

When the flame temperatures of all three cookers are measured, it can be seen that the temperatures at maximum flow rate are higher than the temperatures at minimum flow rate. The flame temperatures at the gas outlet are 650-680°C at maximum gas flow rate. These values continue in the distance range of 0-0.5 cm and gradually decrease after a distance of 1 cm, reaching about 50°C at 1.5 cm and further distances. The flame temperatures at the exit point decrease drastically as one moves away from the gas exit at minimum flow rate. Flame temperatures were found to be about 50°C at distances greater than 1 cm from the gas outlet.





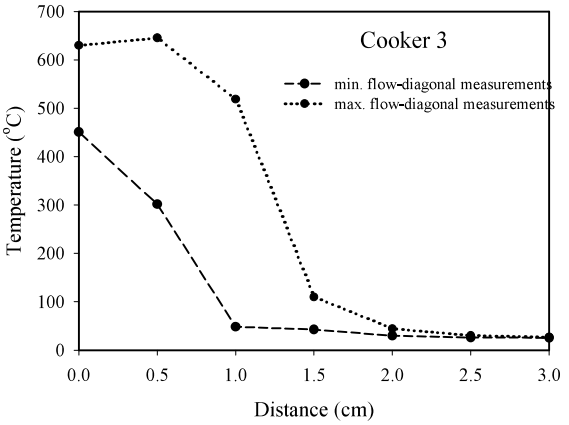
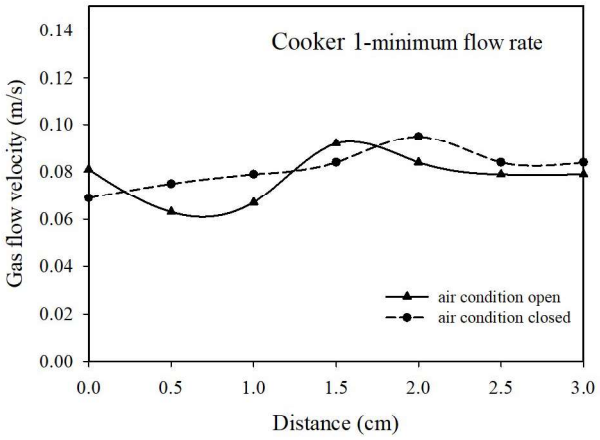
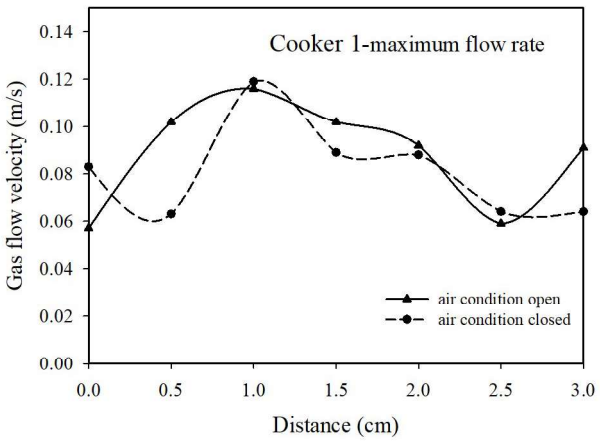
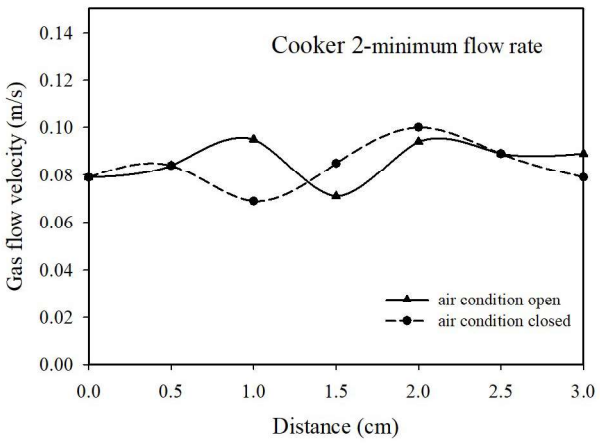


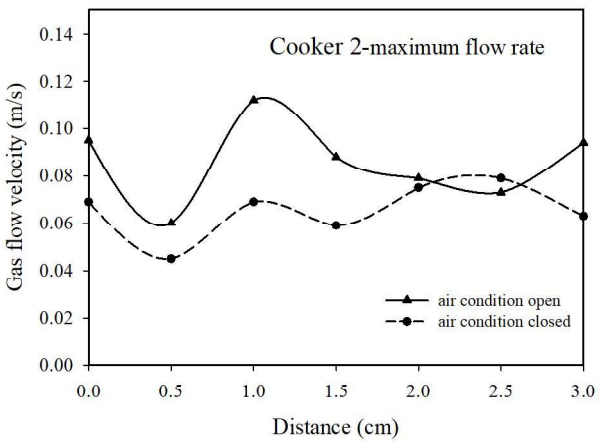
Figure 4. Flame temperatures in the household cookers.

From the studies in the literature, it appears that the gas flow velocity has a significant effect on the combustion characteristics. Moreover, compared to other fuel gases, liquefied petroleum gas has the highest flame gas velocity at an equivalence ratio of 1.1 [7]. For this reason, the gas flow velocities were measured for each cooker in the cold flow situation at the reference point in the diagonal direction for the open and closed ventilation conditions over a measurement period of 1.5 minutes. The results obtained are shown in Figure 5. Although our study is similar to the studies of Dong et al. [4] and Li et al. [6] on LPG, it differs in terms of the shape of the household cooker nozzle, flow rate, and gas pressure.









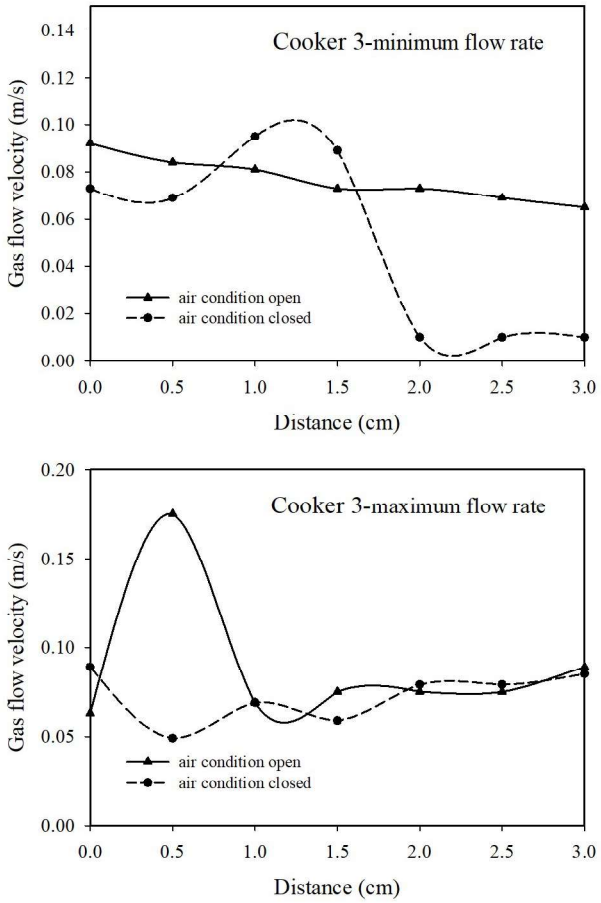


Figure 5. The gas velocities of the household cookers.

Gas flow velocities at the burners of all cookers were measured with open and closed ventilation using an anemometer. The images of the measurements are shown in Figure 6. The results obtained are listed in Table 1.

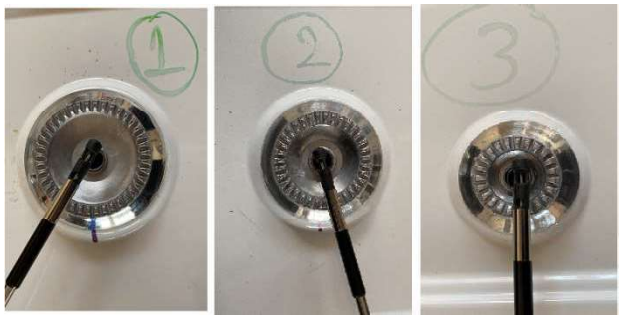


Figure 6. Measurements of gas velocities in the cookers.

For the minimum flow rate measurements for Cooker 1, the gas velocity was found to be 0.924 m/s with the vent open and 1.015 m/s with the vent closed. For the maximum gas flow rate, the gas velocity was 2.834 m/s with the ventilation on and 2.915 m/s with the ventilation off. From Table 1, it can be seen that the variation of the cooker gas flow velocities with the ventilation open and closed is evident for the maximum flow rate.

Table 1. The measurements of the flow velocity of cold flame at the output points.

Cooker	Flow rate	Gas velocity (m/s)	
		Air-vent open	Air-vent closed
1	min.	0.924	1.015
	max.	2.834	2.915
2	min.	1.22	1.18
	max.	2.04	2.25
3	min.	0.78	1.105
	max.	1.7	2.42

Emission measurements were made with the NOVAplus instrument in the diagonal direction at maximum flow in Cooker 1 over a measurement period of 1.5 minutes. The emission values are given in Figure 7. According to these results, the CO_2 emission (%) between the reference point and 1.5 cm was 12%, and it was found that it decreased to 11% for measurements between 1.5 cm and 3 cm. It was observed that the maximum value of CO (ppm) emissions occurred at the reference point and reached 7000 ppm, decreased linearly in the range of 0-1 cm, decreased to 6000 ppm, and a sudden decrease occurred in distances after 1.5 cm. For NOx measurements (ppm), a maximum value of 180 ppm was determined at the 0.5 cm point. There was a tendency for the NOx value to decrease after 0.5 cm, similar to the CO (ppm) curve after 2 cm and approached 0 (zero).

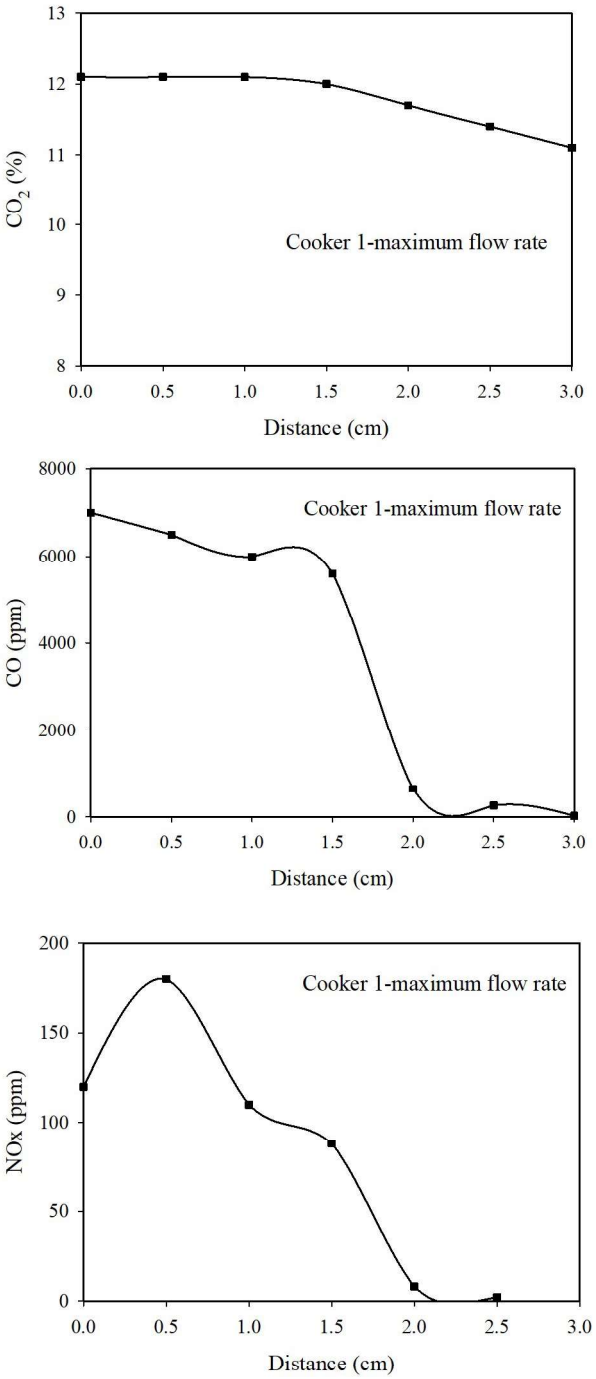


Figure 7. The CO_2, CO, and NOx emissions of the Cooker 1.

4 CONCLUSIONS

The flame characteristics of liquefied petroleum gas under normal combustion conditions were studied in household cookers. The experimental measurements were confirmed by repeating them several times. Our results are briefly given below:

The temperatures between maximum and minimum flow rates showed significant differences in all cookers. At distances after 1.5 cm from the reference point, for the maximum flow, the measured temperatures were almost equal in the horizontal and diagonal directions.

The maximum temperatures were determined at the reference point (0 cm) for the minimum flow rate for all examined cookers. At minimum flow, the temperatures measured in the horizontal and diagonal directions at the reference point (0 cm) were higher than the temperatures in the vertical direction. Significant temperature decreases were observed after a distance of 1.5 cm for the minimum flow rate. The measured temperatures in the horizontal and diagonal directions converge. At minimum flow, the changes in gas velocities of Cooker 1 and Cooker 2 are parallel. Significant differences were observed in the velocity measurements at the minimum and maximum flow rates of Cooker 3.

REFERENCES

[1]. S. McAllister, J.-Y. Chen, A.C. Fernandez-Pello, Fundementals of Combustion Process, Springer, 10–17, 2011.

[2]. S. Chander, A. Ray, Flame impingement heat transfer: a review. Energy Conversion Management, 46 (18–19), 2803–2837, 2005.

[3]. L. Gattei, A Study on the Fluid Dynamics of Domestic Gas Burners, Ph. Doctorate Thesis, University of Bologna, 2008.

[4]. L. L. Dong, C.S. Cheung, C.W. Leung, Heat transfer characteristics of an impinging butane/air flame jet of low Reynolds number. Experimental Heat Transfer, 14 (4), 265-282, 2001.

[5]. S. Jugjai, N. Rungsimuntuchart, High efficiency heat-recirculating domestic gas burners. Experimental Thermal and Fluid Science, 26, 581-592, 2002.

[6]. H.B. Li, T.T. Wong, C.W. Leung, S.D. Probert, Thermal performances and CO emissions of gas-fired cooker-top burners. Applied Energy, 83, 1326-1338, 2006.

[7]. C.E. Lee, C.H. Hwang, H.Y. Lee, A study on the interchangeability of LFG–LPG mixed fuels with LFG quality in domestic combustion appliances. Fuel, 87, 297-303, 2008.

[8]. R. Anggarania, C.S. Wibowo, D. Rulianto, Application of Dimethyl Ether as LPG Substitution for Household Stove. Energy Procedia, 47, 227-234, 2014.

[9]. Y.H. Kang, Q.H. Wang, X.F. Lu, X.Y. Ji, S.S. Miao, H. Wang, Q. Guo, H.H. He, J. Xu, Experimental and theoretical study on the flow, mixing, and combustion characteristics of dimethyl ether, methane, and LPG jet diffusion flames. Fuel Processing Technology, 129, 98-112, 2015.

[10]. Z. Chen, Y. Zhang, C. Qin, P. Duan, Combustion performance of domestic gas cookers with swirling strip-port and normal round-port on various natural gas compositions. Case Studies in Thermal Engineering, 13, 100366, 2019.

[11]. M. Wae-hayee, K. Yeranee, W. Suksuwan, C. Nuntadusit, Effect of burner-to-plate distance on heat transfer rate in a domestic stove using LPG. Case Studies in Thermal Engineering, 28, 101418, 2021.

[12]. C.F. Gould, J. Urpelainen, LPG as a clean cooking fuel: adoption, use, and impact in rural India. Energy Policy, 122, 395–408, 2018.

[13]. J. Goldemberg, J. Martinez-Gomez, A. Sagar, K.R. Smith, Household air pollution, health, and climate change: cleaning the air, Environmental Research Letters, 13 (3), 030201, 2018.

[14]. H. Budya, M. Arofat, Providing cleaner energy access in Indonesia through the megaproject of kerosene conversion to LPG. Energy Policy, 39, 7575−7586, 2011.

[15]. G. Shen, M.D. Hays, K.R. Smith, C. Williams, J.W. Faircloth, J.J. Jetter, Evaluating the Performance of Household Liquefied Petroleum Gas Cookstoves. Environmental Science and Technology, 52, 904–915, 2018.

EVALUATION ON HYBRIDIZATION OF HEAVY-DUTY LONG-HAUL DIESEL TRUCK POWERTRAINS

Yücel Karaca[1], Hasan Kubilay Yiğit[2], Caner Bayburtlu[3], Orkun Özener[4]

1. Yıldız Technical University, Mechanical Engineering, Istanbul, Turkey; email: karacayucel@outlook.com
2. Independent Researcher, Ankara, Turkey; email: hkubilayyigit@gmail.com
3. AVL Research and Engineering Turkey, Istanbul, Turkey; email: caner.bayburtlu@avl.com
4. Yıldız Technical University, Mechanical Engineering, Istanbul, Turkey; email: oozener@yildiz.edu.tr

Abstract

The main purpose of this study is to evaluate the potential benefits that can be obtained by applying various electrical components to 40 tons heavy-duty long-haul truck. A realistic base long-haul truck was modelled in a simulation environment with conventional drivetrain components, and on top of that, degrees of freedom were added to the system with electrical components and controllers, providing hybridization opportunities in terms of fuel economy improvement. The Heavy-Heavy-Duty Diesel Truck (HHDDT) and Vehicle Energy Consumption Calculator Long Haul (VECTOLH) cycles were examined. In addition to the base vehicle used in this study, each hybrid vehicle configuration was modelled on the AVL CruiseM™ using a representative internal combustion engine (ICE), battery pack and electric propulsion components. The hybridization of the long-haul truck provides fuel savings of up to 4.3% compared to the conventional vehicle. In addition, the same powertrain configuration provides a 28.7% reduction in tailpipe NOx emissions and a 17.9% reduction in urea consumption.

Keywords: Hybrid Powertrains, Heavy Duty Vehicles, HEV, Commercial Vehicles, Diesel Electrification

1 INTRODUCTION

Hybrid electric vehicles (HEVs) appear to be the fastest short-term action we can take to reduce the environmental impact of conventional ICE-powered powertrains. Hybridization ensures that an engine is sized correctly, by doing this we can reduce heat loss and increase efficiency [1]. Reduced ICE power can be obtained from the electric motor (EM). Especially at low speeds, EMs provide faster torque than their ICE counterparts. By doing this, startup performance can be improved even with a less powerful ICE [2]. Concepts related to HEV are explained in detail in the study of W. Enang and C. Bannister, and HEV control methods are mentioned. The methods were compared with speed cycles and fuel economy and emissions. A detailed cost savings analysis was not conducted in this study [3].

2 METHODOLOGY

2.1 Model Development

Dynamic models of the long-haul tractor and semi-trailer have been developed in AVL CruiseM. The simulation is mainly based on the longitudinal equation of motion of the vehicle created using the forces shown in the Figure 1. Details of vehicle parameters can be seen in Table 1.

Table 1. Model Parameters

Parameter	Unit	Value
Gross Vehicle Mass	kg	40000
Drag Coefficient	-	0.6
Coefficient Of Rolling Resistance	%	0.65
Frontal Area	m^2	8.5
Air Density	kg/ m^3	1,225
Gravitational Acceleration	m/s^2	9.81
Wheel Rolling Radius	m	0.5

In Figure 2, conventional vehicle powertrain layout and hybrid powertrain layout are visualized. In this study, the electric machine is placed between the gearbox and the main clutch, and this configuration is also known as the P2 hybrid configuration. A 13 L diesel engine model, whose maximum power is 465 PS and maximum torque is 2500 Nm, combined with an exhaust system model including diesel oxidation catalyst (DOC), diesel particulate filter (DPF) and selective catalytic reduction (SCR) has been implemented to the model. A 12-speed

automated manual transmission (AMT) model is used in the simulation.

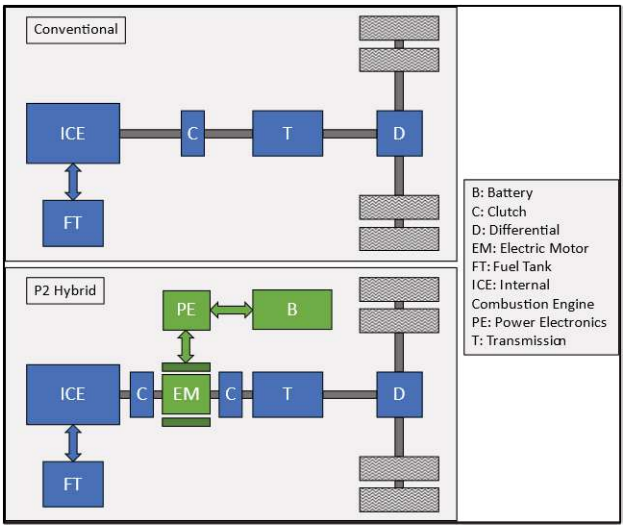


Figure 2. Arrangement of powertrain elements of the tractor. Conventional powertrain (top). Hybrid powertrain (bottom).

A look-up table-based engine control unit (ECU) converting ICE torque demand to engine actuator commands, a dosing control unit (DCU) determining the necessary amount of urea mass flow depending on the temperature of SCR and engine out nitro-oxides (NOx) mass flow, and a transmission control unit (TCU) determining the clutch position and gear shifts are also embedded to the model. The simulations are done with two different P2 hybrid configurations as well as conventional powertrain over Heavy-Heavy-Duty Diesel Truck (HHDDT) and Vehicle Energy Consumption Calculation Tool Long Haul (VECTOLH) cycles. The velocity and slope profile of these cycles are given in Figure 3.

Using two different electric motors; two different hybrid powertrain combinations, in which the EM and single ratio transmission are placed as a package between the two clutches between the internal combustion engine and the transmission, are examined. Details of electrical components can be seen in Table 2.

For result comparability, the maximum tractive effort of hybrid powertrains based on overall vehicle speed is limited to the conventional vehicle maximum traction curve. In addition, since there is no direct relationship between the battery state of charge (SOC) and the diesel fuel consumed, the cycles are simulated with an SOC deviation of ±0.1% between simulation start and simulation end, thus a SOC-independent fuel between different consumption comparison. arrangements can be made.

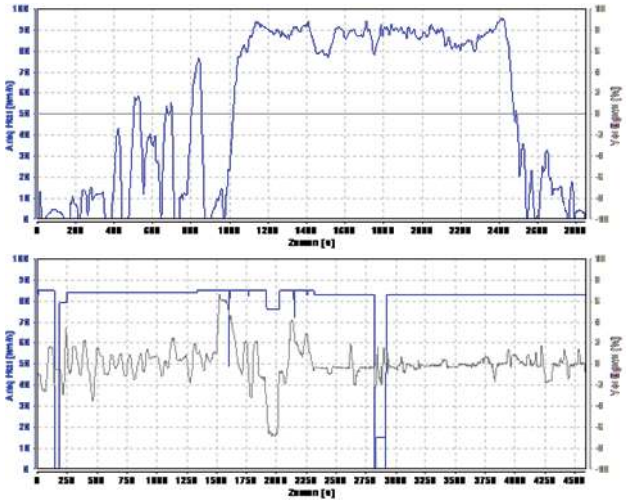


Figure 3. HHDDT (top) ve VECTOLH (bottom) test cycles

Table 2. Elements and details of hybrid architectures

		Config #1	Config #2
Electric Machine	-	EM1	EM2
Voltage	V	540	540
Max. Speed	rpm	6000	6000
Max. Torque	nm	400	400
Max. Power	kW	75	75
Transmission Rate	-	1:1	3:1
Battery	-	BAT	
Rated Voltage	V	540	
Total Capacity	kWh	32.5	

3 RESULTS AND CONCLUSION

The main factor affecting the distribution of these points is that the ICE-specific fuel consumption information is known by the hybrid controller and the operating points of the actuators are determined according to this information. The results obtained show that the additional degree of freedom given to the vehicle by the hybridization of the system contributes significantly to the fuel economy when used for the following purposes.

- Torque support to ICE
- ICE load point increase to achieve a better brake specific fuel consumption (BSFC)
- Idling or stopping ICE completely while driving

Table 3. HHDDT cycle results (Conventional vehicle-based improvements)

HHDDT		Config #1	Config #2
Reduction in fuel consumption	%	4.2	4.3
CO_2 (Exhaust pipe) reduction	%	4.8	5.1
NO_x (Exhaust pipe) reduction	%	28.7	23.8
Urea consumption is reduced	%	12.9	11.6
Energy recovered during braking	kWh	2.9	4.8
Energy recovered during torque boost	kWh	2.3	2.7
Average BSFC decline	%	1.9	1.8

Table 3. VECTOLH cycle results (Conventional vehicle-based improvements)

VECTOLH		Config #1	Config #2
Reduction in fuel consumption	%	2.0	1.5
CO_2 (Exhaust pipe) reduction	%	2.0	1.6
NO_x (Exhaust pipe) reduction	%	17.9	13.4
Urea consumption is reduced	%	5.7	3.4
Energy recovered during braking	kWh	4.2	6.0
Energy recovered during torque boost	kWh	5.6	6.1
Average BSFC decrease	%	0.2	0

Results in Table 3 and Table 4 show that configuration 2 gave the best results in both cycles. While a 4.3% fuel consumption reduction was observed in the HHDDT cycle, this figure was 2.0% in the VECTOLH cycle. In addition to fuel economy, it was observed that there was a significant reduction in exhaust emissions and NOx emissions were reduced by approximately 15-25% in both cycles.

ACKNOWLEDGEMENTS

AVL CruiseMTM program was used under AVL University Partnership Program (UPP).

REFERENCES

[1] K. David Huang and S.-C. Tzeng, "A new parallel-type hybrid electric vehicle," *Applied Energy,* vol. 79, no. 1 second. 51-64, 2004.

[2] J. Liu and H. Peng, "Modeling and Control of a Power-Split Hybrid Vehicle", *IEEE Transactions on Control Systems Technology,* vol. 16, no. 6, p. 1242 - 1251, 2008.

[3] W. Enang and C. Bannister, "Modelling and control of hybrid electric vehicles (A comprehensive review)," *Renewable and Sustainable Energy Reviews,* vol. 74, p. 1210-1239, 2017.

[4] European Commission Directorate-General for Mobility and Transport, "An Overview of the EU Road Transport Market in 2015", May 2017. [Online]. Available: https://ec.europa.eu/transport/sites/transport/files/mobility-package-overview-of-the-eu-road-transport-market-in-2015.pdf. [Accessed on 05 December 2020].

[5] European Environment Agency, "Emissions of Carbon Dioxide from Europe's Heavy Duty Vehicles", 12 April 2018. [Online]. Available: https://www.eea.europa.eu/publications/carbon-dioxide-emissions-from-europes. [Accessed on 5 December 2020].

[6] A. Taghavipour, NL Azad, and J. McPhee, "Design and evaluation of a predictive powertrain control system for a plug-in hybrid electric vehicle to improve fuel economy and emissions," *Proceedings of the Institute of Mechanical Engineers, Part D: Journal of Automobile Engineering. ,* skin. 5, no. 229, p. 624-640, 2014.

[7] AM Philips, M. Jankovic and KE Bailey, "Vehicle system controller design for a hybrid electric vehicle", *Proceedings of the 2000. IEEE International Control Applications Conference. ,* 2000.

[8] European Environment Agency, "Electric Vehicles in Europe", 26 September 2016. [Online]. Available: https://www.eea.europa.eu/publications/electric-vehicles-in-europe. [accessed 30 05 2021].

[9] AG Ulsoy, H. Peng and M. Çakmakçı, Automotive Control Systems, New York: Cambridge University Press, 2012.

A STUDY ON CAPTURING ACOUSTIC BEHAVIOUR IN CONFINED TUBE COMBUSTION USING OPTICAL TECHNIQUE

S.P. Choudhury[1] and S. Syam[1] and R. Joarder[1]

1. Department of Aerospace Engineering, Indian Institute of Technology Kharagpur, West Bengal, India; email: sibaprasad@iitkgp.ac.in

Abstract

A disturbance-free optical measurement technique is studied in this paper for capturing acoustic waves and measuring flame location for premixed propane-air combustion in a closed and half-open channel. The technique mainly measures the deflection of light ray due to the change in refractive index. The flame propagating inside closed or half-open channel changes its shape from a hemi-spherical flame to a flat flame (flame inversion) and in certain condition it forms a tulip flame. Initial pressure waves are generated from the ignition as well as by the flame front. These thermo-acoustic waves reflect from the end walls and lateral walls interact with each other and also with the flame front as they travel. The acoustic changes inside the combustion chamber and their effects on the tulip flame formation are studied by an optical technique. The optical measurement system uses a continuous laser, polarizer, analyzer, a photon detector and an oscilloscope. Flame front location and acoustic changes are captured using the technique. Signals for the acoustic are more pronounced when the laser is placed without the polarizer-analyzer system. Results also showed the phase changes in the acoustic signals.

Keywords: Tulip flame, Thermo-acoustic measurement, Optical technique, Laser

1 INTRODUCTION

Unstable combustion in tubes/channels, tanks, during transportation and storage or in combustion engines or in buildings leads to explosion causing damage to the properties and lives. Weak or strong pressure oscillations are generated due to this combustion instability, and in case of closed or semi-closed environment, the thermo-acoustic instability along with unsteady heat release can transform in to large amplitude pressure waves and deflagration-to-detonation wave (DDT). Combustion of premixed mixtures in closed or semi-closed channels also shows irregular flame front propagation and inversion of the flame front. In certain cases the flame shape changes forming cusp at the centre and flame acceleration near the wall forming a tulip shaped flame [1,2]. Many theories have been proposed to explain the phenomena of the tulip flame formation such as interaction of the self-generated shock wave with the flame front [3], Rayleigh-Taylor (R–T) instability [2,4], Darrieus-Landau (D–L) instability [5,6], reduction in flame surface area and squish flow [4,7]. Numerical study by Gonzalez et al. [8] reported the presence of a reverse flow in the burned gas region near the onset of the flame flattening. Choudhury et al. [9] from their experimental study on LPG-air premixed combustion also confirms the presence of the reverse flow in the burned gas region. Further, Ponizy et al. [10] concluded that the backward flow of the burned gas is the reason for the formation of the tulip flame. The presence of thermo-acoustic instability and its effect on the flame front is definitely one of the reason for the formation of the tulip flame in confined tube combustion [11,12]. Recently, Shen and Xiao [13] and Liberman et al. [14] from their numerical study suggests that the generation of the acoustic waves during the flame propagation and repeated interaction with the flame front have decisive role in the formation of the tulip flame. However, despite a large number of experimental, numerical and theoretical studies, there is still no clear explanation for the formation of the tulip flame.

The present paper tries to capture the acoustic behaviour and the flame dynamics using a laser based optical technique. It confirms the presence of the pressure waves inside the channel along with the flame front propagation. The optical technique also shows the strong pressure waves near the flame front inversion and its interaction with the flame front.

2 EXPERIMENTAL SETUP

The experiments are carried out on an un-cooled square cross-sectional chamber of dimension 40

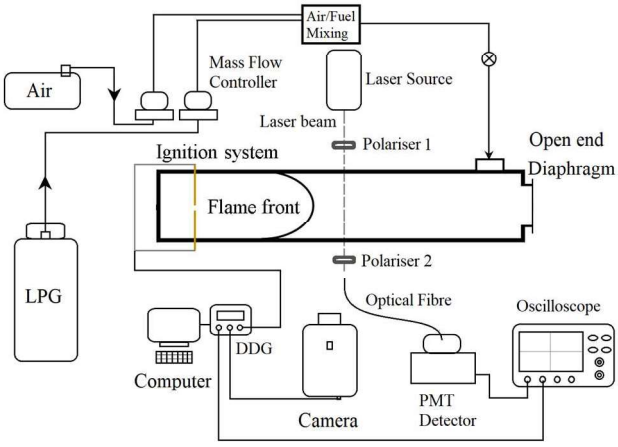


Figure 1. Schematic diagram of the experimental setup

× 40 mm^2 and 400 mm long. The chamber is made of acrylic sheet of 8 mm thick on the front and 15 mm on the top and bottom side. One end of the chamber is closed and other end is open. The open end is closed with a thin PVC diaphragm before each experiment and is allowed to break when a threshold pressure is reached during the combustion process. The premixed liquefied petroleum gas (LPG)-air mixture is fed in the channel using two separate mass flow controller. The equivalence ratio (ϕ) is 1.05. A schematic diagram of the experimental setup is shown in Figure 1. Details of the experimental setup are given in [9].

The optical measurement technique consists of a near-IR continuous laser (660 nm), a polarizer, an analyzer, objective lens (17 mm focal length), optical fibre and a photo detector (PMT detector). A photograph of the present set up with the optical detection system in place is shown in Figure 2. The laser beam crosses the chamber transversely (perpendicular to the side walls) through a polarizer (working wavelength range 450-750 nm, surface flatness ≤ 4λ at 633 nm, extinction ratio 4000:1, Newport Corporation). The laser crossing the combustion chamber falls on to an analyzer which filters the polarized light. The circular red spots in Figure 2 are the scattered laser beam from the polariser, from the channel side walls, and from the analyzer. An objective lens is used along the path of the laser light and focused on the head of an optical fibre mounted on the other side of the chamber to collect the refracted laser light. The Ø200 µm Core Multimode (from Thorlab) bare optical fibre is placed into to a photon multiplier tube (PMT) detector. The signal from the PMT detector is captured through an oscilloscope. The

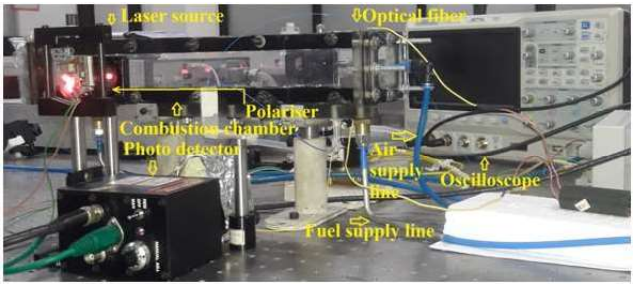


Figure 2. Experimental facility showing components of the optical measurement technique

ignition system and the oscilloscope are triggered with an external time unit (BNC 745 digital delay generator). The present experiments are carried out at an equivalence ratio of 1.05. The laser beam is placed at different axial locations of the channel to obtain the acoustic behaviour at those locations. It is determined from the numerical simulation with hydrogen-air as the fuel air mixture, the details of which is given elsewhere [15] and beyond the scope of this manuscript. The position of the flame front and acoustic waves are assumed to be similar for the two cases but with small variations as the premixed flame velocity in hydrogen air mixture combustion is higher than that of propane-air. The laser beam is placed at two different axial positions from the ignition source namely, 3.75 cm and 18.7 cm while the ignition source was placed at a distance of 5.0 cm from the left end wall (please refer to Figure 1). The vertical position of the beam is not important here as the objective of the present study is to capture the transversely oscillating acoustic waves and axially travelling flame front/acoustic wave.

3 THE PRINCIPLE OF ACOUSTIC WAVE AND FLAME FRONT DETECTION

Light can be considered as visible spectra of electromagnetic wave that travels at certain speed in vacuum. However, when light travels through a medium other than vacuum, it slows down and under certain conditions its state of polarization changes due to light-matter interaction. The speed of light through a medium is dependent on the density, refractive index and composition of the medium. Several real life dynamics or static activities [16,17] show that the refractive index (n) and density of the medium can modulate the light. This helps us understand the physics and engineer various devices. Light waves are transverse waves

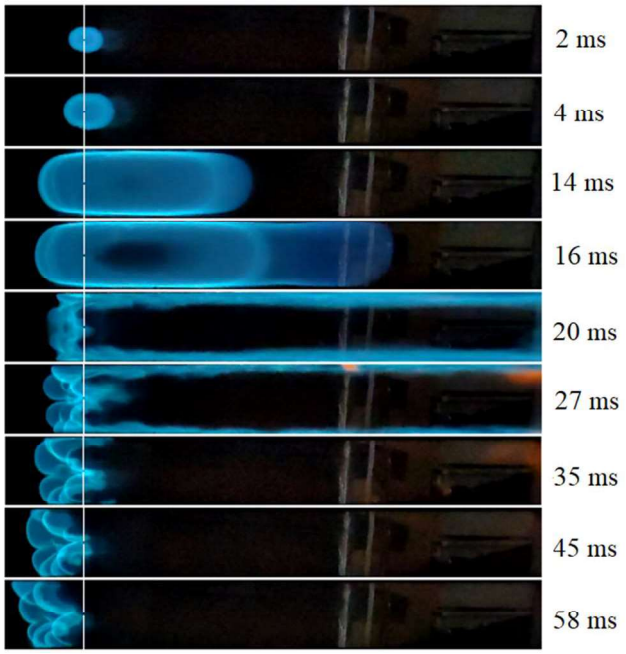


Figure 3. A series of high speed images for half-open channel combustion (open end in the right side).

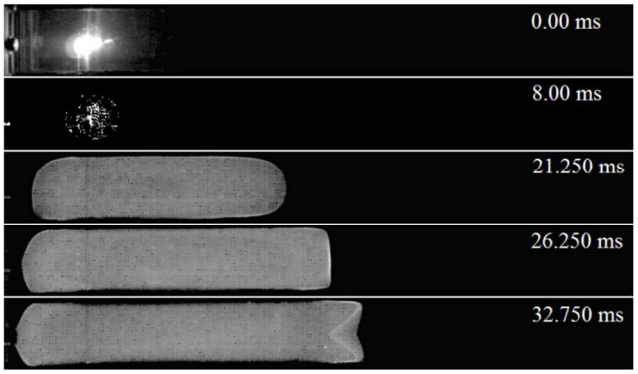


Figure 4. A series of high speed images for closed end channel combustion.

consisting of varying electric (E) and magnetic (B) fields that oscillate perpendicular to the direction of propagation and perpendicular to each other where the magnitude of electric field (E) is c (speed of light) times higher than that of the magnetic field (B). The oscillating electric field vector on the transverse plane can be filtered along a particular direction by a polarizer.

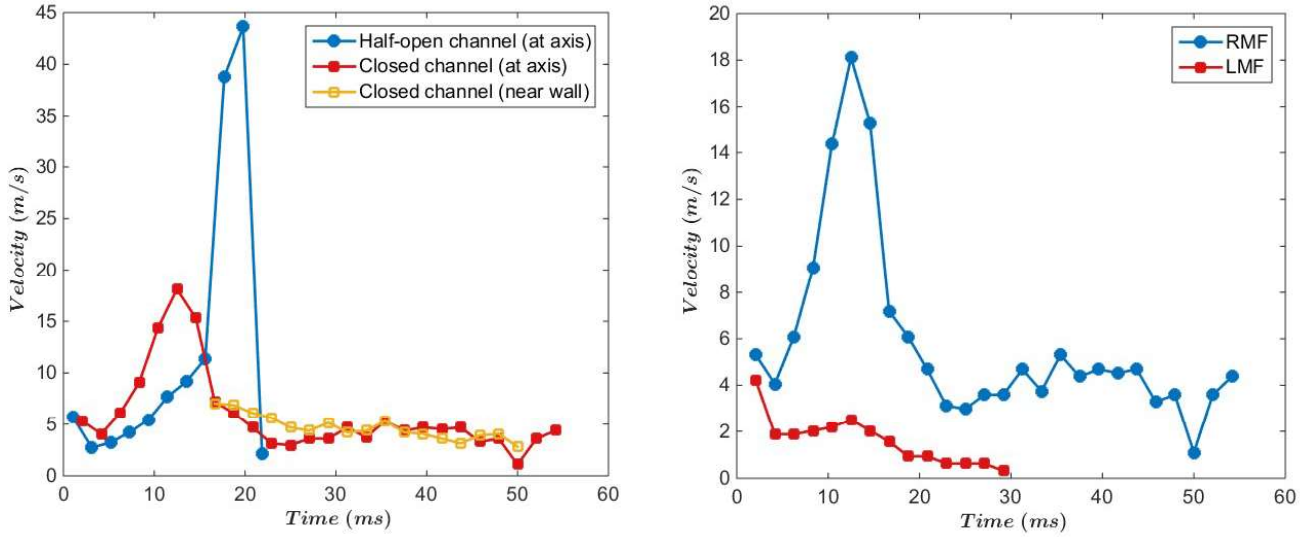
Time dependent rotation of the linearly polarized electric field vector of light due to dynamic change in the refractive index and density of the medium as a result of the burning of fuel-air mixtures has been investigated here. We demonstrated that the acoustic waves and the moving flame front can be detected with an open single optical beam based polarimetry technique. In the past, optical science communities used the light-matter interaction with linearly polarized electric field vector to study various physical phenomena [16,17,18] occurred in medium. Here, we have used the principle of cross polarized field vector along Z-scan and leakage of depolarized light field vector through the analyser due to polarization vector rotation under the influence of dynamic modulation of density and refractive index during the passage of the flame front and the acoustic waves. When there is no change in refractive index, the transversely polarized light would not pass the analyzer, therefore, no light would cross the analyzer and fall on detector. The light crossing the analyzer ensure that there is a modulation of the polarity of the light due to change in refractive index of the medium and the intensity of the depolarized light is measured by the detector. Intensity of the laser crossing the analyzer will be directly dependent on extent of the gradient of the refractive index or density of the medium.

4 RESULTS AND DISCUSSION

4.1 Flame Propagation in Half-Open and Closed Channel

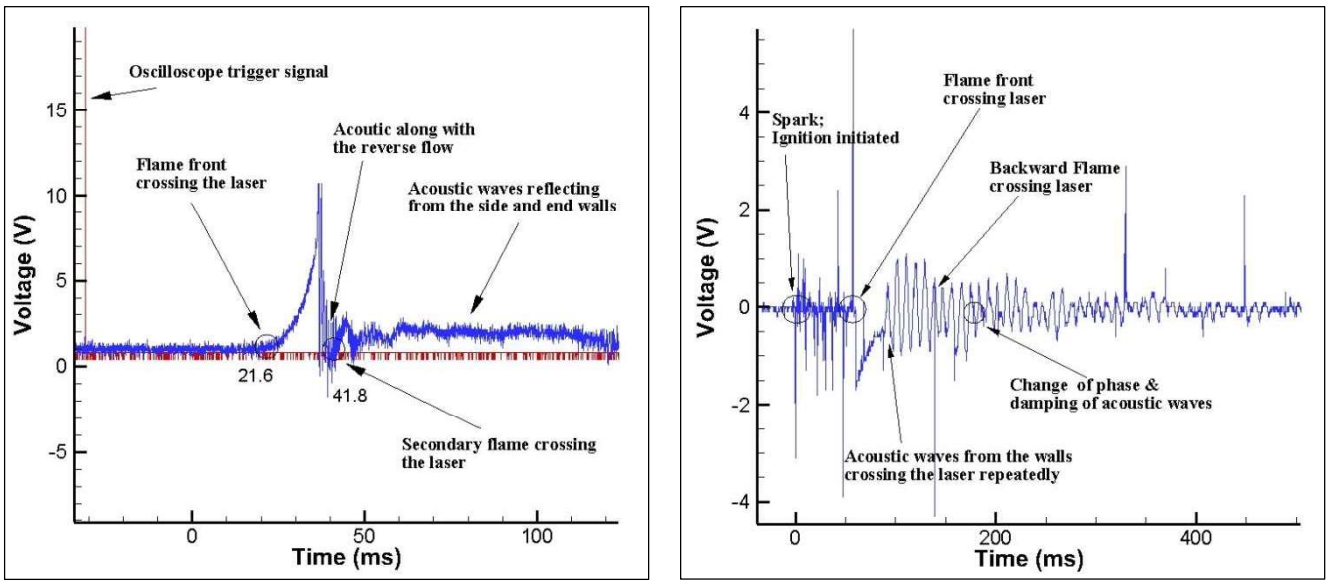
A series of photographs taken with the high speed camera for premixed LPG-air combustion (ϕ=1.0) in the closed and half-open channel are shown in Figure 3 and Figure 4. The flame propagation in half-open channel shows initial two stages of the flame propagation as observed by Clanet and Searby [2]. The flame exited the channel at t = 20 ms when the diaphragm broke. Classical tulip flame could not be observed as the opening vent is large compared to the cross-section of the chamber [9]. A distorted tulip flame is observed in the left side of the channel near the ignition side (closed end). This is because of the sudden exit of the burnt gas generating rarefaction wave inside the chamber. Figure 4 shows the flame dynamics for a premixed combustion in the closed channel. Flame propagation shows all the stages namely spherical flame expansion in the first stage, then the 'finger/capsule' shaped flame in the second stage. Third stage is the flame touching the walls of the channel, and then the flattening of the flame front or formation of the classical tulip flame. Flame flattening and formation of the classical tulip flame can be observed in the present case.

For the case of closed channel combustion, the velocity of the flame expansion along the axis, and velocity of the flame front moving in the left



(a) (b)

Figure 5. Velocity of flame front propagation (a)for half-open and closed channel combustion; (b)moving in right direction (RMF) and in left direction (LMF) in closed channel.



(a) (b)

Figure 6. Signal from the optical technique for axial distance X = 18.7 cm (from ignition point) (a)with polarizer and (b)without polarizer.

side (LMF) and right side (RMF) of the ignition are shown in the Figure 5. The velocity of the flame front travelling along the central axis of the channel and near the wall shows similar oscillating nature. It can be seen from the Figure 4 that the LMF is propagating at much lower speed compared to the RMF. LMF and RMF also oscillate in the same phase. Both the LMF and RMF are accelerating during the finger shaped flame expansion. Then, they started to decelerate simultaneously during the inversion of the flame (flat flame front at t = 26.50 ms). These phenomena and observations confirm the presence of acoustic waves which oscillate in the channel and affect the flame front transition. The pressure waves generated by ignition at the initial stage and by the spherical flame front later reflect back and forth from the end plate of the channel. These waves also reflect from the lateral walls and interact with each other repeatedly during the flame propagation [13,14].

4.2 Determination of Acoustic Waves and Flame Front

The current paper presents a non-destructive, non-intrusive and non-disturbing method to capture the acoustic phenomena and the flame front using an optical technique. The signals captured by the present method are shown in Figure 6. The results are obtained with the laser

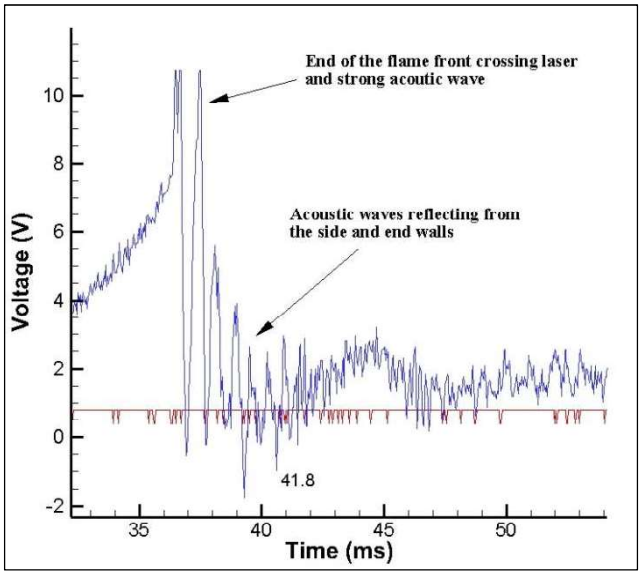


Figure 7. Zoomed view of the signal obtained for X = 18.7 cm.

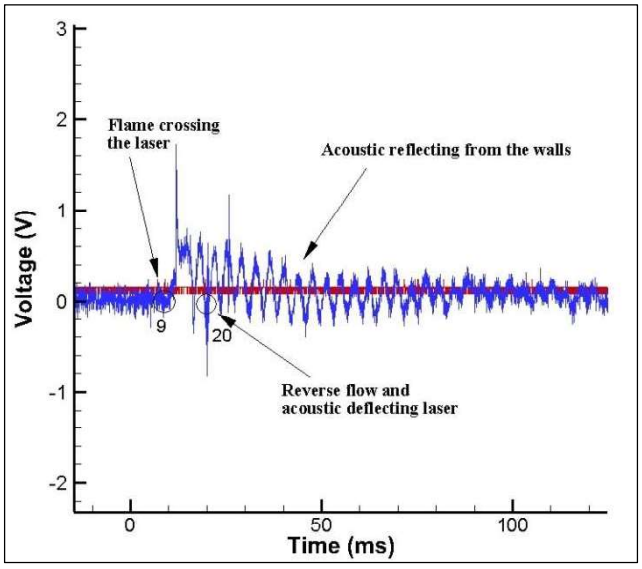


Figure 8. Signal from the optical technique for axial distance X = 3.75 cm (obtained using the polarizer-analyzer system).

crossing the combustion chamber at X = 18.7 cm (distance from the ignition point) where one is obtained with the polarizer-analyzer system (W-P) and other is without the use of the polarizer and analyzer (Wo-P). The flame inversion happens just before X = 18.7 cm. The flame front crossed the laser beam at t = 22.8 ms and a high peak in the signal is captured. The time of the ignition is t = 0 ms. The time of the ignition and flame front propagation are calculated from the frame rate of the high speed camera. The maximum error in calculating different timings of the stages of the flame propagation is 250-330 μs.

As the flame inversion occurs near X = 18.7 cm, the flame front became stationary at the axis and it started to propagate near the wall increasing the flame surface area. The same is seen as increasing voltage signal from 30–42 ms and another peak of the signal at t = 42 ms. Acoustic waves before and after the flame inversion are obtained as the high frequency (280-300 Hz) signals at later stage of the propagation. In case where the polarizer-analyzer system was used along the path of the laser beam (W-P), only the depolarized light (due to flame front or acoustic) could cross the analyzer. The intensity of the depolarized light will depend on the extent of the density gradient crossing the beam. Therefore, the flame front has higher voltage signal compared to the acoustic waves. A secondary flame due to burning of the fuel-air mixture in the left side of the chamber is also captured by the present technique.

The results obtained without the use of polarizer at X = 18.7 cm is shown in Figure 6 (b). The flame front crossing the laser and the acoustic phenomena is clearly observed from the voltage signal. Multiple peaks of voltage before the flame front reaching the laser beam are captured. These are the deflection of light due to the acoustic wave generated by the flame front and ignition source. The sinusoidal waves just after the flame front crossing the laser is the acoustic waves that is reflecting from the end walls and side walls. Due to repeated reflection from the side walls and interaction with each other, there is a change of phase in the signal and also a decrease in the signal strength over the time. The backward flame from the ignition end (closed end) is not pronounced in this case due to large signal from the acoustic wave. Figure 7 shows the zoomed view of the signal obtained for X = 18.7 cm, W-P when the flame surface crossed past the laser beam. As the stretched flame surface or high temperature region behind the flame tip crossed the laser, the peak suddenly decreased. The second peak at t = 37.5 ms is due to the backward flow pressure wave crossing the laser which is also interacting with the flame front. This is accompanied by the low and high frequency acoustic waves reflecting from the side walls. Acoustic signal are also present during the flame propagation from the secondary combustion.

Figure 8 shows the signal W-P for X = 3.75 cm. In the first stage of flame propagation the flame expands spherically before elongating in to a capsule shaped flame. During this stage, the

flame front is unaffected by the walls of the channel and there is no flame stretching or distortion of the flame front. The flame propagation speed (U_p) of the spherically expanding flame front is approximately 4 m/s and is much slower compared to the U_p in the second stage. The pressure waves travel ahead of the flame front as the laser beam is placed close to the ignition point. Flame crossed the laser beam at t = 9 ms. Strength of the signal due to the flame front is also low. Reverse flow due to secondary combustion near the closed end can also be observed from the results. Large oscillations of acoustic signal are observed at later stage. The oscillations of the signal are more pronounced similar to the signal obtained Wo-P. This could be due to the leakage of some amount of polarized light through the analyzer.

5 CONCLUSIONS

The optical measurement technique to capture the deflection of the laser beam due to the acoustic wave and the flame front is successfully employed for the premixed LPG-air combustion in a half-open channel at different axial location, and with and without the use of polarizer-analyzer system. Experiments are carried out at different locations (X = 3.75 cm and 18.7 cm) along the axis of the channel with and without the use of polarizer-analyzer system along the path of the laser beam. Deflection of light was measured as the change in the intensity of the light due to polarizer-analyzer system. It is found that the deflection of the light is higher due to the flame front than that of due to the acoustic waves because of the higher density gradient across the flame front. Acoustic waves are captured as low and high frequency signal depending on the laser beam location. When the laser is placed after the formation of the tulip flame (X = 18.7 cm), the signal strength is higher due to the larger flame surface area and lower flame propagation velocity in the onset of the inversion of the flame. Acoustic waves reflecting from the lateral walls near the flame front region was observed with the present technique. Time of the flame front propagation and inversion is also determined using the present optical technique. The present technique can help in capturing the acoustic behaviour during the flame propagation in a constant volume chamber. In addition, effect of the acoustic wave on the flame inversion and cause of the tulip flame formation can be further studied using this technique.

REFERENCES

[1] O. C. de C. Ellis and R. V. Wheeler, CCCCXXVI.—Explosions in closed cylinders. Part III. The manner of movement of flame, *Journal of the Chemical Society*, Vol. 0, pp. 3215-3218, 1928.

[2] C. Clanet, and G. Searby, On the 'Tulip Flame' Phenomenon, *Combustion and Flame*, Vol. 105, pp. 225-238, 1996.

[3] G. H. Markstein, A shock-tube study of flame front-pressure wave interaction, *Proceedings of the Combustion Institute*, Vol. 6, pp. 387-398, 1957.

[4] R. Starke and P. Roth, An experimental investigation of flame behavior during cylindrical vessel explosions, *Combustion and Flame*, Vol. 66, No. 3, pp. 249-259, 1986.

[5] V. Bychkov, V. Akkerman, G. Fru, A. Petchenko, and L.-E. Eriksson, Flame acceleration in the early stages of burning in tubes, *Combustion and Flame*, Vol. 150, pp. 263-276, 2007.

[6] M. Matalon, The Darrieus–Landau instability of premixed flames, *Fluid Dynamics Research*, Vol. 50, pp. 051412, 2018.

[7] D. Dunn-Rankin, P. K. Barr, R. F. Sawyer, Numerical and experimental study of "tulip" flame formation in a closed vessel, *Symp. (Int.) on Combustion*, Vol. 21, pp. 1291-1301, 1986.

[8] M. Gonzalez, R. Borghi, and A. Saouab, Interaction of a flame front with its self-generated flow in an enclosure: The "tulip flame" phenomenon, *Combustion and Flame*, Vol. 88, pp. 201-220, 1992.

[9] S. P. Choudhury and R. Joarder, High-speed photography and background oriented schlieren techniques for characterizing tulip flame, *Combustion and Flame*, Vol. 245, p. 112304, 2022.

[10] B. Ponizy, A. Claverie, B. Veyssi`ere, Tulip flame - the mechanism of flame front inversion, *Combustion and Flame*, Vol. 161, pp. 3051-3062, 2014.

[11] M. Gonzalez, Acoustic instability of a premixed flame propagating in a tube, *Combustion and Flame*, Vol. 107, pp. 245-259, 1996.

[12] A. S. Al-Shahrany, D. Bradley, M. Lawes, K. Liu, and R. Woolley, Darrieus–Landau and thermo-acoustic instabilities in closed vessel

explosions, *Combustion Science and Technology*, Vol. 178, pp. 1771-1802, 2006.
[13] T. Shen and H. Xiao, Numerical study of the stability of premixed flames propagating in half-open tubes, *Combustion Theory and Modelling*, Vol. 26, pp. 774-795, 2022.
[14] M. A. Liberman, C. Qian, and C. Wang, Early stages of flame dynamics in tubes and mechanism of tulip flame formation, *Proc. 28th International Colloquium on the Dynamics of Explosions and Reactive Systems*, Napoli, Italy, 2022.
[15] R. Joarder, S. P. Choudhury, S. Syam, N. Singh, and S. K. Biswas, Thermo-acoustics and its detection in a premixed flame, *arXiv preprint arXiv:2208.02146*, 2022.
[16] K. Taga, R. Hisatomi, Y. Ohnuma, Optical polarimetric measurement of surface acoustic waves, *Applied Physics Letters*, Vol. 119, 2021.
[17] G. Liu, J. Xiong, Y. Cao, Visualization of ultrasonic wave field by stroboscopic polarization selective imaging, *Optics Express*, Vol. 28, pp. 27096-27106, 2020.
[18] J. Yin, Q. Bai, B. Zhang, Sensitivity of polarized laser scattering detection to subsurface damage in ground silicon wafers, *Materials Science in Semiconductor Processing*, Vol. 144, 2022.

STUDY ON OH* CHEMILUMINESCENCE OF NH_3/AIR SWIRL FLAME

Danan Chen [1,2], Jun Li [1,2,3,*], Xing Li [1,2], Yijun Guo [1,2], Hongyu Huang [1,2,3], Noriyuki Kobayashi [4]

1. Guangzhou Institute of Energy Conversion, Chinese Academy of Sciences, Guangzhou 510640, China
2. School of Energy Science and Engineering, University of Science and Technology of China, Guangzhou 510640, China
3. Southern Marine Science and Engineering Guangdong Laboratory (Guangzhou), Guangzhou 511458, China
4. Department of Chemical Engineering, Nagoya University, Nagoya, Aichi 464-8603, Japan

Abstract

Ammonia (NH_3) is a carbon-free alternative fuel, and the use of chemiluminescence method to study its flame structure is a promising means. In this study, the OH* chemiluminescence distributions in NH_3/air swirling flames with different equivalence ratios, H_2 additions and ammonia cracking gas addition ratios were experimentally obtained. The OH distributions of NH_3/H_2 and NH_3/cracked gas under different conditions were compared. The results show that with the increase of equivalence ratio, the OH* radiation peak increases. The increase in equivalence ratio significantly enhanced the overall chemiluminescence intensity of OH*. In a lean fuel flame, the equivalence ratio effect is greater than the NH_3 dilution effect, while the two effects are comparable under equivalence and rich fuel conditions. The NH_3/H_2 flame is wider than that of NH_3/cracked gas, but the OH radiation peak is lower.

Keywords: OH* chemiluminescence, ammonia combustion, equivalence ratio, hydrogen addition level, swirl flame

1 INTRODUCTION

In recent decades, alternative and clean fuels have attracted increasing research attention given the energy crisis and pollutant emissions. Numerous candidates, such as biofuels, natural gas, ammonia (NH_3), and hydrogen (H_2), have been proposed as alternative fuels [1–3]. Among the candidates, ammonia is a carbon-free fuel with high energy density, easy liquefaction, and a hydrogen storage capacity of up to 17.8 (wt)% [4]. In industry, ammonia is mainly synthesized through the Haber-Bosch process under the conditions of high temperature and high pressure of 450-500℃ and 20MPa. The feedstock for the process is hydrogen from natural gas, coal or petroleum, and nitrogen from air [5]. In the future, renewable energy such as solar energy can even be used to synthesize ammonia, which not only eliminates the production of greenhouse gases such as carbon dioxide, but also is expected to produce ammonia through environmental protection processes [6]. Like propane, ammonia can be stored in liquid form at room temperature and 0.8MPa, and the cost per unit of stored energy is only one-third of that of hydrogen [7]. The existing ammonia production process and transportation technology will greatly reduce the investment cost, thereby improving the competitiveness of ammonia as an alternative fuel.

However, the efficient utilization of ammonia fuel is still very challenging. Compared with conventional hydrocarbon fuels, pure ammonia has lower laminar combustion velocity and heat value, longer ignition delay, higher energy required for ignition, and narrower flammability limit range [8-9]. These properties make the combustion of pure ammonia more difficult. Some scholars believe that hydrogen has the characteristics of fast combustion speed and low ignition energy, which can effectively solve the shortage of ammonia fuel. Experimental studies have shown that doping hydrogen can effectively improve the combustion of ammonia flames, including increasing the combustion speed and broadening the combustion limit. [10-12]. In addition, in terms of burner design, some scholars have studied the combustion performance of ammonia fuel in swirl burners [13-14].

For ammonia swirling flames, the process of flame stabilization and blowout depends to a large extent on the flow structure and the characteristics of the flame. Optical diagnostic

technology is a rapidly developing flame monitoring method based on chemiluminescence emission. The radiation emission generated by the de-excitation of excited radicals (such as OH*, CH*) can not only reflect the changes of the combustion phenomenon, but also provide characteristic parameters related to the combustion state of the flame [15-16]. By detecting and analyzing the emission information of these radicals, the flame structure and reaction characteristics can be obtained [17-18]. Li et al. [19] explored the OH* emission distribution in the flame under different gas flow rates using a UV imaging system, and the results showed that the OH* distribution is closely related to the oxygen flow rate and can be used to characterize the reaction zone in the flame.

However, there are few experimental studies on chemiluminescence of NH_3/air swirling flames in the literature. In this study, the chemiluminescence OH* distribution of NH_3/air premixed swirling combustion flames with different equivalence ratios, H_2 addition ratios and cracking gas addition ratios was obtained by using a CCD camera imaging system. The effects of the equivalence ratio and H_2 addition ratio on the distribution characteristics of the OH* layer and the combustion phenomenon were compared.

2 EXPERIMENTAL SETUPS

2.1 Combustion system

The experimental apparatus used in this study is shown in Figure 1. The swirl burner used in this experiment is 5 cm in diameter and 8 cm in height. Inside the burner are 10 vanes with a swirl angle of 45° and a swirl number of 0.778. The premixed gas of fuel and air enters the burner from four symmetrical inlets. In order to prevent the deformation of the blade due to excessive temperature, a water cooling device is added.

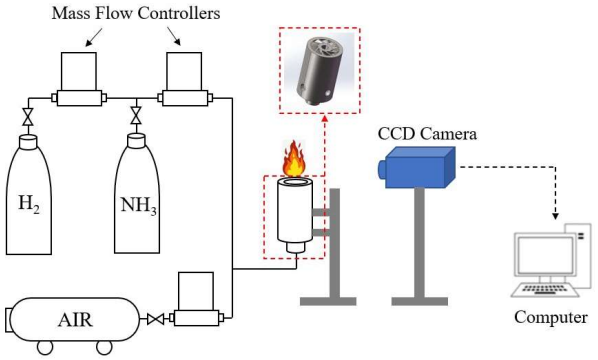


Figure 1. Experimental apparatus

For NH_3/air flames, the equivalence ratio (Φ) changed in the range of 0.8-1.2, so that the flame gradually transformed from fuel-lean to fuel-rich. The equivalence ratio is calculated by the following formula:

$$\Phi = \frac{m_{fuel}/m_{air}}{(m_{fuel}/m_{air})_{stoic}} \quad (1)$$

Where m_{fuel}/m_{air} is the mass ratio of gas based on the actual flow rate of fuel and air, and $(m_{fuel}/m_{air})_{stoic}$ is the stoichiometric ratio when the fuel is completely consumed.

NH_3 with a purity of 99.999% (Guangzhou Yigas Co., Ltd.), H_2 with a purity of 99.999% (Guangzhou Shenyinggas Co., Ltd.) and compressed dry air (21.0% O_2 and 79.0% N_2) were supplied from compression gas tank. NH_3, H_2 and air flows were regulated by commercial mass flow controllers (Azbil, CMS0050) with an accuracy of ±1.0% full scale. An air-cooled CCD Camera (FLI, e2v CCD47-10) with a specialized 50 mm focal length lens (F-stop = F/3.5) can capture light from 200 nm to 1000 nm was applied to obtain OH* chemiluminescence distributions.

The experimental conditions and Reynolds number are summarized in Table 1 and Table 2. The Reynolds number (Re) is calculated by the following formulas:

$$Re = \frac{D\bar{v}\rho}{\bar{\mu}} \quad (2)$$

$$\bar{\mu} = \frac{\sum y_i \mu_i M_i^{1/2}}{\sum y_i M_i^{1/2}} \quad (3)$$

where D is the equivalent nozzle diameter, ρ is the average density of fuel and oxidizer, u is the average velocity, and μ is the average viscosity of fuel and oxidizer. As calculated by formula (3), y_i is the mole fraction of component i, M_i is the molar mass of component i [20].

Table 1. Experimental conditions for adding hydrogen

Items	φ	v_{NH_3} (L/min)	v_{H_2} (L/min)	v_{air} (L/min)	X_{NH3}(%)	Re
1	1.2	4	1	13.9	80%	1910
2		3.5	1.5	13.4	70%	1820
3		3	2	12.9	60%	1730
4	1.0	4	1	16.7	80%	1600
5		3.5	1.5	16.1	70%	1520

6		3	2	15.5	60%	1440
7	0.8	4	1	20.8	80%	1390
8		3.5	1.5	20.1	70%	1310
9		3	2	19.3	60%	1240

Table 2. Experimental conditions for adding cracking gas

Items	φ	V_{NH3} (L/min)	V_{H2} (L/min)	V_{N2} (L/min)	V_{air} (L/min)	X_{NH3} (%)	Re
1	1.2	4	1	0.33	13.9	80%	1910
2		3.5	1.5	0.5	13.4	70%	1820
3		3	2	0.67	12.9	60%	1730
4	1.0	4	1	0.33	16.7	80%	1600
5		3.5	1.5	0.5	16.1	70%	1520
6		3	2	0.67	15.5	60%	1440
7	0.8	4	1	0.33	20.8	80%	1390
8		3.5	1.5	0.5	20.1	70%	1310
9		3	2	0.67	19.3	60%	1240

Table 1 and table 2 show the experimental conditions of adding hydrogen and cracking gas respectively. It can be seen that all laminar combustion flames are studied in this study. The equivalence ratios varied from 0.80 to 1.20, the addition levels of H_2 from ammonia varied from 60% to 80%.

2.2 Chemiluminescence measurement

The OH* chemiluminescence distributions of NH_3/air flames at various combustion conditions have been captured by an imaging system combined with a 1056*1027 CCD camera and an UV lens with a filter bandpass of 310 ± 10 nm. The OH* chemiluminescence distributions of NH_3/air flames were detected with a quartz filter band with UV permission of 310 ± 10 nm.

3 RESULTS AND DISCUSSION

3.1 Emission spectrum

A typical radiance distribution of OH* of NH_3/air flame is shown in Figure 2. This radiance distribution of OH* was obtained by the average of 10 times for the same flame within a CCD exposure time of 0.5s.

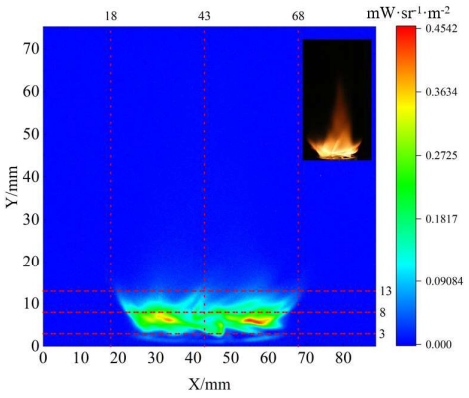


Figure 2. The radiance distribution of OH* of NH_3/air flame at X_{NH_3} = 80% and Φ = 0.8.

As can be seen from the direct shot in Figure 2, the NH_3/H_2 flame shows an orange/yellow tint, which is usually due to the emission of NH_2* excited radicals and superheated water vapor spectra. The main distribution area of OH* is between 3mm and 8mm on the surface of the inner burner.

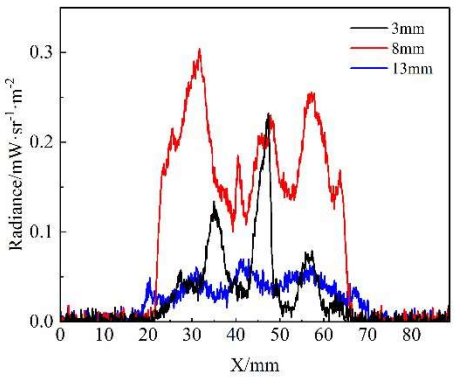


Figure 3. Radial OH* radiation distribution

As can be seen from Figure 3, each peak corresponds to the flame formed by each channel. When the horizontal position is 3mm, the OH* peak is narrowest and widest at 13mm, and the overall shape of the flame gradually expands downstream. The values of the OH* distribution peaks at 3mm and 8mm are higher than those at 13mm, which means that under this condition, the strong reaction zone of the flame is between 3mm and 8mm.

3.2 Effects of the equivalence ratio

Figure 4 shows the OH* distribution and straight-shot flame images representing three conditions of lean, rich, and equivalence. From the straight shot, as the equivalence ratio increases, the end of the NH_3/H_2 flame stretches longer, and a circulation zone is formed in the centre of the flame. The axial momentum force

is less than the back pressure created by the central recirculation. As the equivalence ratio increases, the OH radiance peak is larger. It can be seen from the OH* distribution diagram that the OH* distributions under these three conditions are quite different. Under the lean fuel condition, the overall flame is relatively stretched, the flame length of each channel is longer, and the OH* high concentration area is relatively dispersed. As the kinetic force increases, the change of the OH* concentration gradient is also more significant. In the equivalent condition, the OH* distribution is relatively concentrated. While in the rich fuel condition, the flame bottom has a relatively obvious rise, and the two ends of the flame bottom narrow, forming an "inverted cone" shape. The angle formed by the outer edge of the flame and the root of the flame is the smallest at equivalence, and the largest in fuel-rich conditions.

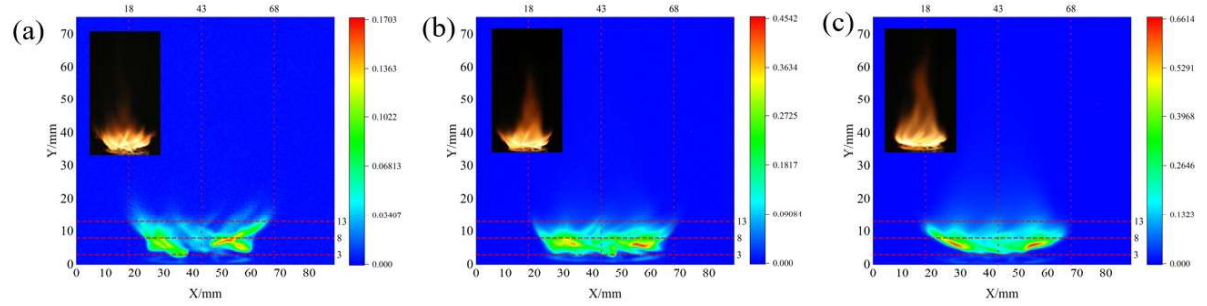


Figure 4. OH* distribution of X_{NH3}=80%-NH_3/H_2/air flame, (a) Φ=0.8, (b) Φ=1, (c) Φ=1.2

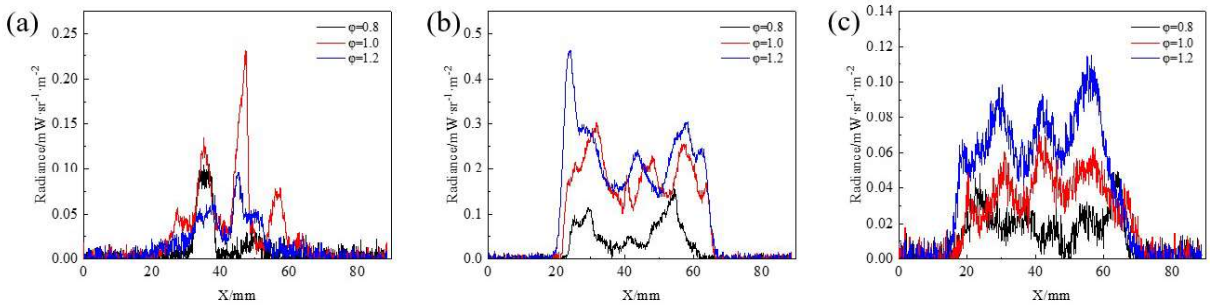


Figure 5. OH* distribution of X_{NH3}=80%-NH_3/H_2 flame at different radial positions, (a) 3mm, (b) 8mm, (c) 13mm

Figure 5 shows the OH* distribution of the X_{NH3}=80%, NH_3/H_2 flame at different radial positions. Figure 4 (a) shows that at 3 mm from the burner surface, the OH* intensity is the highest when the equivalent is 1, indicating that the intense reaction area of the flame is closer to the burner at this time. The width of the bottom of the flame is also the widest at equivalence, only about 22mm at the fuel rich. At 8 mm from the burner surface, the intensity peak increases with the equivalence ratio, and the flame width trend is the same, but the flame width and OH* peak are the largest for rich fuel, and the opposite is true for lean fuel. At 13mm from the burner surface, there is still a small amount of OH* distribution, and the trend is basically the same as that at 8mm.

3.3 Effects of the hydrogen addition levels

In order to explore the effect of different hydrogen addition ratios on the NH_3/H_2/air flame, the OH* distributions at different radial positions were obtained by adding 20%, 30% and 40% hydrogen, as shown in Figure 6. At 3mm from the burner surface, the peak value of OH* with X_{NH3}=60% is the highest, and the radial length is the longest, especially in rich fuel conditions, which means that when X_{NH3}=60%, the flame is closer to the burner surface. At X=8mm, the peak value of OH* with X_{NH3}=80% is the highest, the radial length is the smallest when the fuel is lean, but the radial length is the largest in the equivalent and rich fuel conditions. At X=13mm, the OH* peak value of X_{NH3}=80% is still the highest, indicating that the flame height is the highest

under this massacre ratio. In fuel-rich conditions, the flame exhibits an inverted cone shape, so at X=13mm, the radial length is longer.

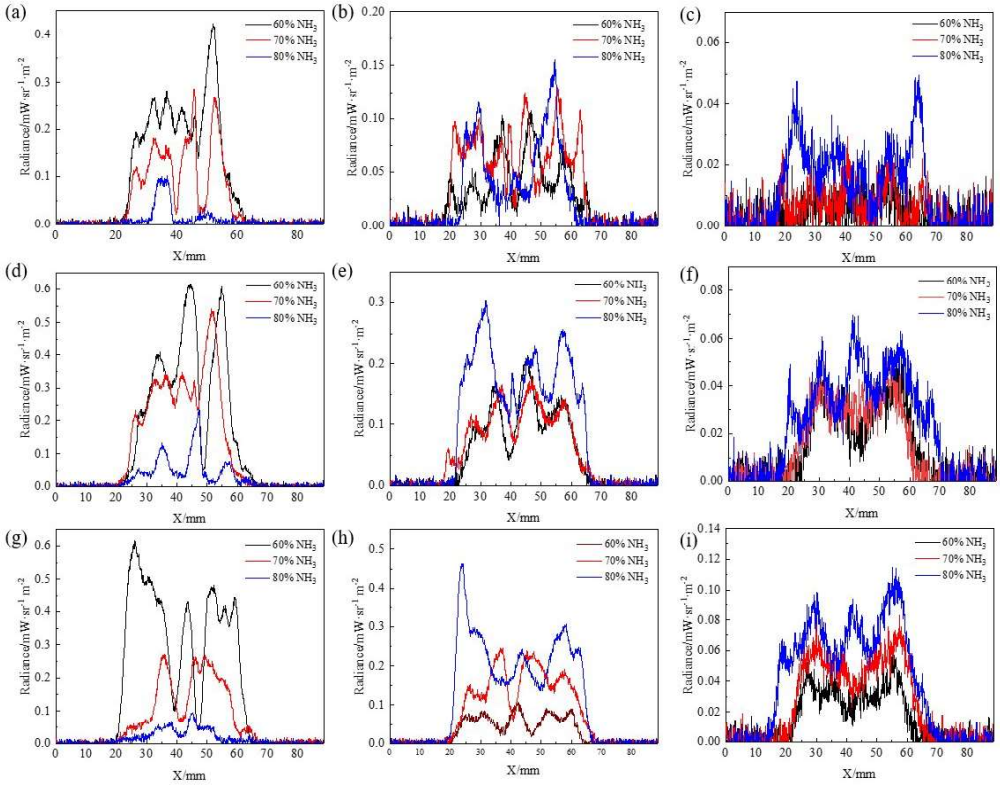


Figure 6. Comparison of OH* distribution of NH_3/H_2 flames at different radial positions

With the increase of NH_3 concentration, the OH* chemiluminescence intensity decreased rapidly, and the descending gradient gradually became larger, and did not tend to be stable, which is shown in Figure 7.

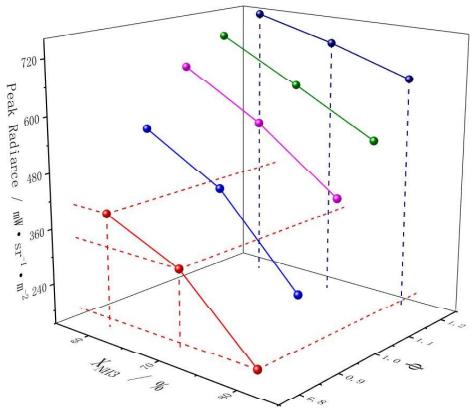


Figure 7. Chemiluminescent peak radiance of OH*

Compared with the equivalent and rich fuel, the radiance peak decreases with the increase of NH_3 concentration in the lean fuel condition. When Φ=0.8 and 0.9, the radiance decreases by 57.5% and 48.2%. The increase in equivalence ratio enhanced the overall chemiluminescence intensity of OH* more significantly, but this enhancement was limited by the rise of NH_3 concentration. Due to the thermal effect of NH_3, the flame temperature decreases, resulting in a decrease in the intensity of the chemical reaction. For lean fuel flames, the peak intensity increases by 28.3% when Φ=0.8 is increased to 0.9. The peak intensity decreases by 18% when X_{NH3} increases from 60% to 70%, which indicates that the overall equivalence ratio effect is greater than the NH_3 dilution effect in a lean flame, while the two effects are comparable in equivalence and rich fuel conditions.

3.4 Comparison with cracking gas

Ammonia is decomposed by the catalyst to generate H_2 and N_2 as shown in Equ. (4). The mixed combustion of cracking gas and ammonia not only improves the combustion performance of ammonia, but also reduces exhaust emissions [21].

$$NH_3 \rightarrow H_2 + N_2 \quad (4)$$

In order to understand the OH distribution and flame changes of the mixed combustion of ammonia and cracked gas, the components of the cracked gas were simulated in this paper, as shown in Table 2.

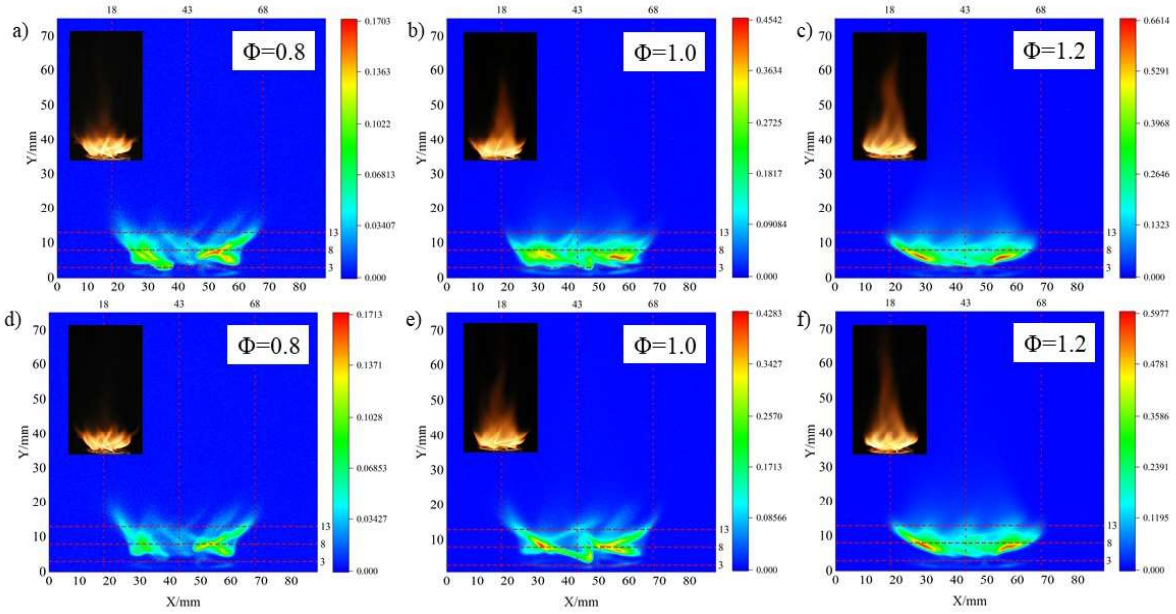


Figure 8. OH* distribution of NH_3/H_2 (a-c) and NH_3/crack gas (d-f)

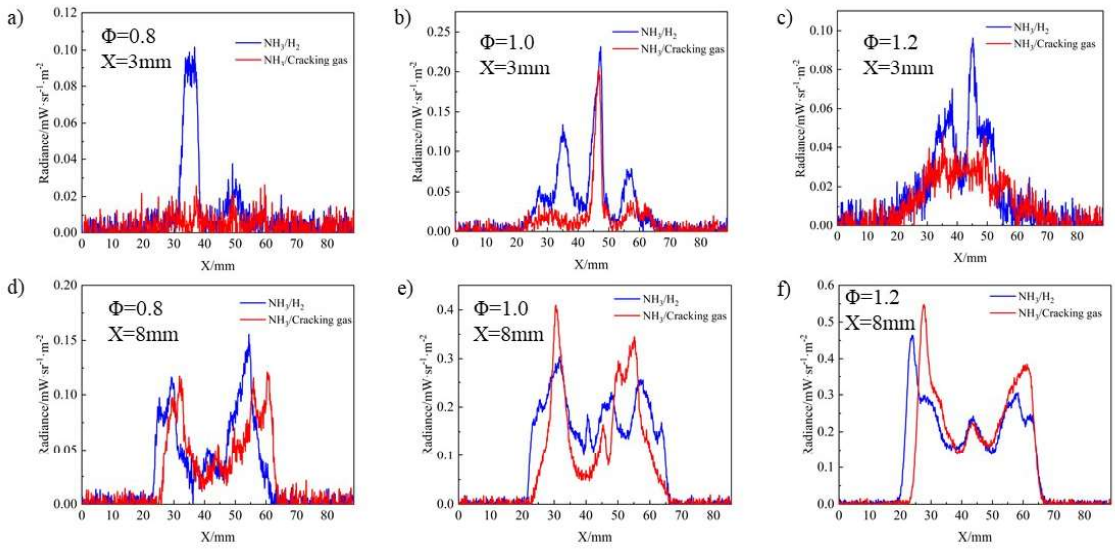


Figure 9. Comparison of radiance radial distribution of NH_3/H_2(a-c) and NH_3/cracking gas(d-f)

Figure 8 shows the OH* distribution of NH_3/H_2 (a-c) and NH_3/crack gas (d-f). It can be seen that the NH_3/H_2 flame center recirculation area is more obvious, and the OH* distribution is basically the same. The flame boundary slope of the NH_3/cracking gas is higher, while the high concentration area of OH* in the NH_3/H_2 flame is more prominent. Under the equivalent conditions, the OH* distribution of NH_3/H_2 flame is more concentrated and the peak value is higher, while the OH* distribution of NH_3/cracking gas flame is more dispersed, and the flame length has a certain stretch. In the equivalent condition, the OH* distribution of the NH_3/H_2 flame is more concentrated and the peak value is higher, while the OH* distribution of the NH_3/cracking gas flame is more dispersed, and the flame length is stretched.

Because there is little difference between the two cases when X=13mm, only the oh radial radiation distribution at 3mm and 8mm is compared in Figure 9. The OH* peak value of NH_3/H_2 flame is higher at lean burn, while the width of NH_3/H_2 flame is wider at 8mm. When equivalent, it can be seen from Figure 9(b) that the NH_3/H_2 flame distribution is more uniform. At 8mm, the NH_3/H_2 flame width is still wider, but the OH* peak of the NH_3/cracking gas flame is higher. When the fuel is rich, both flames are close to the burner surface but less intense. At 8mm, the NH_3/H_2 flame width is still wider, but the OH* peak of the NH_3/cracked gas flame is higher.

In conclusion, the flame width of NH_3/H_2 is wider, while the OH* peak of NH_3/cracking gas flame is higher.

4 RESULTS AND DISCUSSION

The effects of the equivalence ratio and the H_2 addition level on chemiluminescent distribution characteristics of OH* layer in ammonia/oxygen swirling flames were studied, the results are as follow:

With the increase of the equivalence ratio, the OH* radiance peak of NH_3/H_2 flame was larger, and a circulation zone was formed in the center of the flame.

The increase in equivalence ratio enhanced the overall chemiluminescence intensity of OH* more significantly, but this enhancement was limited by the rise of NH_3 concentration.

In a lean fuel flame, the overall equivalence ratio effect is greater than the NH_3 dilution effect, while both effects are comparable under equivalence and rich fuel conditions.

The flame width of NH_3/H_2 is wider, while the OH* peak of NH_3/cracking gas flame is higher.

ACKNOWLEDGEMENTS

This work was supported by Key Special Project for Introduced Talents Team of Southern Marine Science and Engineering Guangdong Laboratory (Guangzhou) (GML2019ZD0108), Leading Key Projects of Chinese Academy of Sciences (No. QYZDY-SSW-JSC038).

REFERENCES

[1] G W Crabtree, M S Dresselhaus, The Hydrogen Fuel Alternative, *Mrs Bulletin*, 33(4):421-428, 2008.

[2] T Mendiara, P Glarborg, Ammonia chemistry in oxy-fuel combustion of methane, *Combustion & Flame*, 156(10):1937-1949, 2009.

[3] J Lasocki, M Bednarski, Simulation of ammonia combustion in dual-fuel compression-ignition engine, *IOP Conf. Ser.: Earth and Environmental Science*, 214(1):012081, 2019.

[4] S Chiuta, R C Everson, H Neomagus, Reactor technology options for distributed hydrogen generation via ammonia decomposition: A review, *International Journal of Hydrogen Energy*, 38(35):14968-14991, 2013.

[5] B Brandhorst, Jr. Ammonia: It's Transformation and Effective Utilization, 6th International Energy Conversion Engineering Conference (IECEC), Cleveland, 2010.

[6] W Lu, M Xia, W Hong, Greening Ammonia toward the Solar Ammonia Refinery, *Joule*, 2(6), 2018.

[7] C Zamfirescu, I Dincer, Ammonia as a green fuel and hydrogen source for vehicular applications, *Fuel Processing Technology*, 90(5):729-737, 2009.

[8] J Li, HY Huang, N Kobayashi, Study on using hydrogen and ammonia as fuels: combustion characteristics and NOx formation, *Int J Energy Res*, 38:1214-23, 2014.

[9] A Ichikawa, A Hayakawa, Y Kitagawa, Laminar burning velocity and Markstein length of ammonia/hydrogen/air premixed flames at elevated pressures, *International Journal of Hydrogen Energy*, 40(30):9570-9578, 2015.

[10] J H Lee, J H Kim, J H Park, Studies on properties of laminar premixed hydrogen-added ammonia/air flames for hydrogen production, *International Journal of Hydrogen Energy*, 35(3):1054-1064, 2010.

[11] C S Mørch, A Bjerre, M P Gottrup, Ammonia/hydrogen mixtures in an SI-engine: Engine performance and analysis of a proposed fuel system, *Fuel*, 90(2):854-864, 2011.

[12] M F Ezzat, I Dincer, Development and assessment of a new hybrid vehicle with ammonia and hydrogen, *Applied Energy*, 219: 226-239, 2018.

[13] X Wei, M Zhang, Z An, J Wang, Z Huang, H Tan, Large eddy simulation on flame topologies and the blow-off characteristics of ammonia/air flame in a model gas turbine combustor, *Fuel*, ;298:120846, 2021.

[14] KDKA Somarathne, S Colson, A Hayakawa, H Kobayashi, Modelling of ammonia/air non-premixed turbulent swirling flames in a gas turbine-like combustor at various pressures, *Combust Theor Model*, 22(5):973–97, 2018.

[15] R W B Pearse, A G Gaydon, R W B Pearse, The identification of molecular spectra, *London: Chapman and Hall*, 1976.

[16] J Ballester, T García-Armingol, Diagnostic techniques for the monitoring and control of practical flames, *Prog Energ Combust,* 36:375–411, 2010.

[17] M Zhao, D Buttsworth, R Choudhury, Experimental and numerical study of OH* chemiluminescence in hydrogen diffusion flames, *Combust Flame*, 197:369–1337,2018.

[18] J Kojima, Y Ikeda, T Nakajima, Basic aspects of OH(A), CH(A), and C2(d) chemiluminescence in the reaction zone of laminar methane-air premixed flames, *Combustion & Flame*, 140(1/2):34-45, 2005.

[19] X Li, Z Dai, Y Xu, C Li, F Wang, Mode and hysteresis of laminar methane/oxygen inverse diffusion flame, *Acta Phys Sin*, 64:024704, 2015. (in Chinese).

[20] G Yan, C Hu, Q Guo, Chemiluminescence and Structure Characteristics in CH_4/O_2 Coflow Jet Diffusion Flames, *Energy Procedia*, 142:1059-1064, 2017.

[20] K Ryu, G E Zacharakis-Jutz, S C Kong, Performance enhancement of ammonia-fueled engine by using dissociation catalyst for hydrogen generation, *International journal of hydrogen energy*, 39(5): 2390-2398, 2014.

QUALITATIVE VISUALIZATION OF BUTANE AND HELIUM TRACERS IN AIR USING A DIGITAL BACKGROUND-BASED SCHLIEREN METHOD

F.U. Rückert[1], D. Hübner[1], D. Lehser-Pfeffermann[1] and M. Sauer[1]

1. University of Applied Sciences Saarbrücken (htw saar), Faculty of Economic Sciences, Campus Rotenbühl, Waldhausweg 14, 66123 Saarbrücken, Germany; email: frank.rueckert@htwsaar.de

Abstract

Fluid flow around aerofoil or turbine blades is responsible for operation and overall design of fluid machinery or airplane. Stall effects and turbulence behind blades are responsible for losses in efficiency. Because of this, exact knowledge of separation behaviour and vortex development of fluid flow around profile geometries are mandatory. For this reason, aerodynamic research focuses on investigations and visualization of turbulence around turbine blades. One possibility is to use a digitally generated background pattern together with a filtered video image to visualize differences in diffraction coefficient of the fluid. This so-called *Background Oriented Schlieren* (BOS) imaging is used to visualize flow and compare it against lift force measurements in our wind tunnel.

In addition to comparison of measured data, a qualitative comparison was also carried out. An adjustment experiment for further numerical simulations is prepared. This allows an evaluation of the effects resulting from the different approaches and to develop further approaches for future turbulence models which are needed for numerical simulation models. The experimental setup is explained, and different real time software filter methods are tested to get better quality of the visual results. Different background patterns are generated and tested for their suitability for BOS imaging.

Keywords: Turbulence, Fluid Flow, Background Oriented Schlieren Method, Visualization, Digital Filter

1 INTRODUCTION

Visualization and measurement of fluid flow is difficult because many important media are translucent, and wakes or swirls are difficult to be seen in the gas phase. [1] Other components like butane or helium are also translucent and can therefore not be identified in a mixture.

The *Schlieren* technique relies on the principle that the refractive index gradient of light in the measured flow field of gas is proportional to the density of each species and could be used to observe the boundary layer or swirls. [20] This phenomenon is known in the human observation as heat haze or mirage.

For optimization of fluid energy machines, the knowledge of stall effects at the blade or aerofoil is mandatory. Numerical simulation with *computational fluid dynamics* (CFD) can help, but turbulence models often lead to imprecise predictions and should be validated. [8, 19]

Although, *Schlieren* has been widely used in the observation of visual flow field, it still has many limitations. For example, traditional *Schlieren* measurement needs a relatively complicated system, is inflexible to use, and lead to relatively high costs. [2]

Problems like the deflection angle information in a certain direction, and in view of its dependence to the brightness of the light source, the uniformity of the flow field, the reflectivity of the lens, transmittance of the fluid to the light, depth of the cutting edge, size of the camera aperture, etc. occur. Because of this, traditional *Schlieren* are difficult to achieve. [9, 10]

At the beginning of the 21st century, *Richard and Meier*, et al. developed a new technique based on theory of the traditional *Schlieren* method. [11, 12, 18] Different from the traditional method, the deflection angle of a background ridge is obtained by comparing the pixel difference between two pictures taken before and after a time interval with a camera. This was called *Background Oriented Schlieren* (BOS) imaging.

Our new digital BOS system consists only of two parts: a random background and a digital camera. The lens system and the image plane represent the whole camera. The fluid flow is characterized by different refraction indices. By a digital comparison of the differences between the two pictures (*the stable background and the current image*), the displacement of each pixel on the background can be observed and

differences in refraction can be recalculated to flow information.

2 IMAGE PROCESSING AND FILTERING

Because digital image processing is time consuming and the quality of pre-filtering is important, we combined several calculation steps in one single matrix operation to fasten the process. Image processing is used to generate the background and optimizing the results.

We must investigate some basic concepts in image processing that appeared in the later paragraphs. In digital imaging, an image consists of pixels of different grayscales, and the distribution of grayscales in the image is an important feature of the image itself, e.g., the histogram describes the distribution in the image, which can intuitively show how many grayscales are at least in the image.

An image can be considered as waves. It consists of pixels, and for a grey scale image, each pixel has a colour value, distributed from 0 to 255. Every row of pixel value can be drawn in a curve. Each curve fluctuates up and down. In some areas, fluctuations are relatively small, and some areas suddenly show large fluctuations. Through comparison, it is obvious that where the curve fluctuates greatly, it is where the image is abrupt.

The image is essentially a superposition of various colour waves. In summary, the image is the fluctuation of colour: the large fluctuation means that the colour changes sharply; the small fluctuation means the smooth transition. Therefore, various indicators of the wave can be used to describe the image. Frequency is an indicator of the speed of fluctuation. The more fluctuations in a unit of time, the higher the frequency, and vice versa. The image processing is like signal processing. The filter can also be applied to maintain information with certain prospective and under certain circumstance. [3]

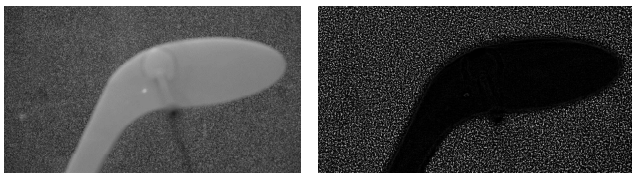


Figure 1: Original turbine blade image (*left side*); blade image through high-pass filter (*right side*)

Problems usually occurs by inhomogeneous lightning. The problem of light distribution can lower the original frequency of the background and cause loss of information. This problem can be removes with the help of a high-pass filter. [4]

In Figure 1 an original image of a turbine blade is compared with a high pass filtered image. This high-pass filter can conserve only mostly high frequency information from the illumination. So, the granularity can be emphasized. On the contrary, a low-pass filter blurs the detailed information and ignore some noise.

The biggest problem with random noise and regular noise is that they have scale limitations. The mismatch of the resolution of the camera sensor and that of the background can cause a loss of the detail and contrast in images. On one hand, when the pixel sensor has a worse resolution, random noise pattern will be down sampled in the imaging of the camera. As a result, the new pattern looks "*greyer*", which means it is more homogeneous and contains less information.

On the other hand, up-sampled noise pattern produces meaningless homogeneous regions when the camera has a better resolution. For each experiment of certain scales, a new background should be produced for the best result, which is to some extent a waste of processing time.

3 EXPERIMENTAL SETUP

Our method was tested with turbine blades on the small wind tunnel test rig. This *Eiffel-type* wind tunnel has an open setup and no air recirculation. [7] The blower is at the end of the tunnel in an outflow diffusor and has a power of 2.55 [kW] where flow velocities of about 25 [m/s] are possible to obtain.

In this setup, the flow guidance happens by means of a smoothing chamber with a rectifier, sieves, and a nozzle. Two force sensors can be used to measure forces like lift and drag forces acting on the examined object or blade. This is connected to a closed section of measurements. With a measuring length of 420 [mm] and nozzle cross-section of 292x292 [mm]. A digital camera was installed on the to visualize the turbulence. [15] Maybe the whole procedure can

be done with one simple smartphone app in future.

3.1 Wind Tunnel, Digital Camera, and Force Measurements

To visualize the air flow, we need a type of gas with different refractive index than air (n=1,000292 at 25 [°C]). [8] The following Figure 2 shows the setup construction. In this project, we tested a conduit to release butane (n= 1,3560000 at 25 [°C]) with a higher refractive index and helium (n=1,000034911 at 25 [°C]), which has a lower refraction index compared to air.

Additionally, hot air jets have been tested because refraction index of a gas changes with temperature. (*You can also find a movie at: https://youtu.be/DN9O2r7DcxQ*)

The position of the nozzle was through a hole on the acrylic sheet of the wind tunnel. The tracers have been released around the test object to observe the flow of air.

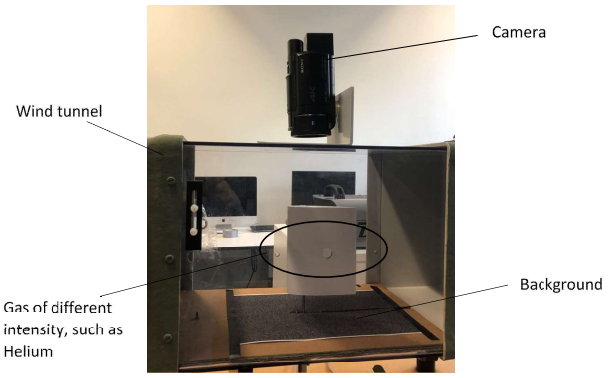


Figure 2: Experimental setup for the measurements of the Schlieren and forces on the aerofoils

The background pattern must be placed on the bottom of the tunnel. The camera should always be focused on the generated background pattern. The camera screen should cover about 80 [%] of the background. Normal HDMI has been used to connect the camera to a computer. Here a fast graphic card is needed. We used the *NVIDIA Quadro P600*. Slower GPU will lead to less resolution. The camera can send real-time data through a CAM LINK. On the computer, the real-data image is processed.

In each test, camera should be focused on the background. The camera's field of view should cover up to 4/5 of the background. Because the distance between the object and the camera is relative short, the edge of the object is blurred. However, when the gas flow is too small, we choose a smaller focus to obtain more effective area.

Additionally, to the *Schlieren* measurement a force measurement has been used to give a hint about pressure fields and acting forces around the blade.

We used a NACA0021 (*National Advisory Committee for Aeronautics*) aero foil design with boundary layer suction groves for our experiments. Lift and drag coefficients have been measured to different *angle-of-attacks* (AOA).

3.2 Software Tools and Digital Filter

Our software tool written in *Microsoft Visual Studio* is based on the former code of *Zilu Zhao* [0]. After an update, it can not only show the video image, but also can save pictures of original background, current image for later analysis in *particle image velocimetry* (PIV) and process images. Interpretation of the fluid flow is done by *PIVlab*. [4]

The tool is an open-source particle image velocimetry (PIV) software based on MATLAB. It can calculate the velocity distribution within image pairs, and derive, display, and export multiple parameters of the flow pattern. A user-friendly graphical user interface (GUI) makes PIV analyses and data post-processing fast and efficient. [17] MATLAB is a commercial mathematics software produced by *MathWorks*. It is a high-level technical computing language and interactive environment for algorithm development, data visualization, data analysis and numerical calculation. OpenCV (*Open-Source Computer Vision Library*) is a cross-platform vision library. [16]

3.3 Influence of Generated Backgrounds

The Background plays an important role for BOS. Inhomogeneous image detail can provide enough information for calculating and overserving the displacement of certain dots, or pixels on the background for better obtaining the visualization of optical flow.

Experts have proved that for outdoor experiments natural scenes could be helpful. As for indoor experiments, a random noise pattern or a regular dot pattern are often used. [18]

There are examples of three different background patterns in Figure 3.

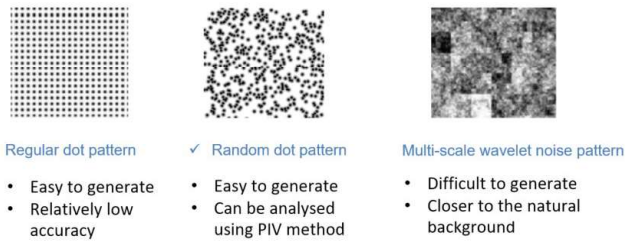


Figure 3: Different generated background patterns for *Background Oriented Schlieren Method* (BOS)

Therefore, a multi-scale pattern shows a better result by improving the accuracy and could save time for that because of the high-frequency content at all scales. A wavelet noise pattern of size 2^k x 2^k contains individual band-limited noise patterns at resolutions at 2^j x 2^j for $j<k$.

To generate a wavelet noise pattern, firstly, the noise pattern is down sampled by a factor two, then up sampled to the original resolution. The subtraction of the two picture up sampled to the resolution of 2^k x 2^k contains a narrow band of information. The uniformly sum of every pattern forms the wavelet noise pattern. [14]

Some tests on generating a multi-scale background are conducted, however, considering the PIV, the random dot pattern is chosen in this project. [0] The random dot pattern works best when the dot is the size of at least one pixel. A *MATLAB* routine is used to generate of the basic background. [0]

This program can automatically generate dots printed on a sheet of paper, so it is easier to place it opposite to the camera inside the tunnel. The dots are randomly seeded in the paper with a changeable number and size. It consists of three concentric circles, with grayscale decreasing from the inside out. It also can be used in *PIVlab* software to calculate the movement of the dots to visualize the wind movement. [5, 6]

Table 1. Camera and background setting

Camera resolution	1280x720
Number of dots	170000
Diameter	0,3
Background colour	Black

Table 2. Statistical analysis of generated background image and background setting

Area of dot in [pixel²]	2,33
Area of dot in[mm²]	0,07
Filled surface ratio [-]	0,19
Number of dots in query area of 8^8	10,30

In Table 2 is the analysis of the background. There are three parameters of this function. The number of dots in the whole pattern, the diameter of dots and the colour of background (*black or white*). For each sample, an analysis shows below to see if the parameters are suitable for the project. There are some common rules of parameters. Some sources indicate that in each query area around 10-20 [dots] should exist. Essentially, the filled surface ratio should be between 10-20 [%]. A pattern with white points on a black background is better for testing. Table 1 contains a list of the parameters chosen for this work.

The resolution of camera should be set as 1280x720 [pixel], excessively high resolution will cause the number of display frames to be too low. In terms of background design, in principle, the size of the dots is related to the resolution of the camera. The dots should at least be bigger as the size of one pixel in the camera. Although most papers [11, 13, 14] suggest an intensity of around 20 [%], a background with 50 [%] performs best when the gas flow is low.

3.4 Using PIV Algorithm for BOS

Although through subtraction the displacement of pixels can be observed, the characteristics of the flow movement cannot be quantized or calculated. Most scholars use cross-correlation in PIV technology to analyse pixel offset. This algorithm helps to analyse the speed and direction of the moves of the pixels by examining the similarity of two images and matching the same pixels on them. For every point, a vector show how it moves from the original position in the background pattern to the current location of the second picture.

PIVlab offers two opportunities of cross-correlation method for PIV evaluation, direct cross-correlation and fast Fourier transform based cross-correlation. The two-dimensional cross-correlation function is defined as follows:

$$R(x,y) = \sum\sum f1(i,j)f2(i-x,j-y) \quad (1)$$

Here *f2* is a function of the grayscale of each pixel of the background and *f1* is the function of the query area of the second picture.
R function shows the relativeness between the query areas of the two images. For example, we consider that the template *f1* is linearly shifted around in the sample *f2* without extending over edges of *f2*. For every sample shift, the sum of the products of all pixel intensities in the query area produces one value. And this value can be shown in a correlation plane. This is shown graphically in Figure 4. The largest value occurs at where the particle images in two images align with each other. The highest value in the correlation plane can be used as a direct estimate of the particle image displacement. [15]

In PIV, firstly, the size of a query area is selected, for example, 4 x 4 [pixel]. Assuming that the resolution of the image is 8 x 8 [pixel]. The two images are both divided into 25 query areas. For a random query area in the second image, it should be compared with all query areas in the first image to generate the cross-correlation plane. With all together 625 times comparisons, the match of each query area in the two images can be found.

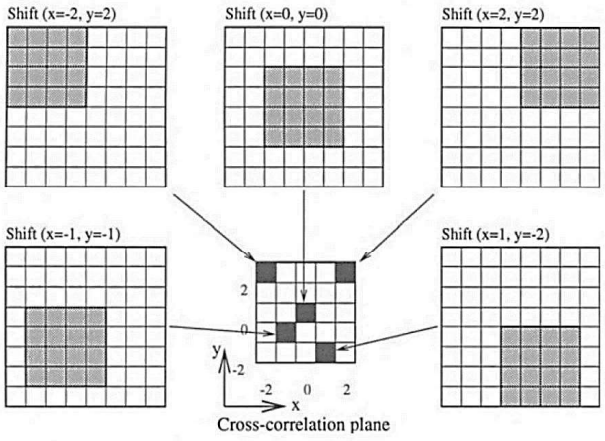


Figure 4: Example for formation of correlation plane, where 8 x 8 [pixel] sample represents f2, 4 x 4 [pixel] sample represent f1 [11]

Since the cross-correlation algorithm needs to interrogate the entire image space domain every iteration, the calculation amount is large. Therefore, *Fast Fourier Transform* (FFT) is proposed to add to the cross-correlation algorithm, which greatly improved the computational speed of the cross-correlation algorithm. The same query area is taken on the two images, and the pixel gradation function in the query area is fast Fourier transformed, then the best matching of the query interval is determined by the cross-correlation function, and finally the inverse Fourier transform and the speed in the corresponding query area are obtained. [11]
To find out the displacement *dx* and *dy*, we will involve knowledge in signal processing, such as Fourier transform. Firstly, we suppose image *f2* is obtained by shifting 1, then:

$$f2 = f1(x-\Delta x, y-\Delta y) \quad (2)$$

According to Fourier transform:

$$F2(u,v) = F1(u,v)e^{-2\pi j(u\Delta x+v\Delta y)} \quad (3)$$

According to the definition of the cross-correlation function:

$$Rccf(x,y) = f1(x,y)\cdot f2(-x,-y) \quad (4)$$

Calculate the Fourier transform, and because $F(u,v) = F1F^*1$:

$$Rccf(u,v) = F1(u,v)\cdot F^*2(u,v) \quad (5)$$

$$= F1F^*1e^{2\pi j(u\Delta x+v\Delta y)}$$

$$= F(u,v)e^{2\pi j(u\Delta x+v\Delta y)}$$

with F^* as the conjugate complex function of F. Invert the Fourier transform of the above formula:

$$Rccf(x,y) = F(x,y)\cdot\delta(x-\Delta x,y-\Delta y) = F(x-\Delta x,y-\Delta y) \quad (6)$$

It can be seen from the nature of the autocorrelation function that the peak of the function *F(x,y)* is at the origin, so the peak of *R(x,y)* appears at the point *(dx,dy)* that is, the function *f2(x,y)* offset. With the displacement *(dx,dy)*, we can obtain the speed and direction of the movement for each pixel and generate a plot of speed distribution. Others use determining optical flow. We will not go into details here.

4 COMPARISON OF DIFFERENT IMAGE PROCESSING METHODS

As already described, the filter for image processing in addition to the BOS is time-consuming. Therefore, we decided not to run both methods one after the other, but to combine them analytically first and perform the processing only once. This leads to a speed-up of the whole algorithm. Three different filters have been used.

4.1 High Pass Filter Method (HPF)

A *High-Pass Filter* (HPF) is a filter that detects an area of an image and then boosts the brightness of the pixel based on the difference in luminance between the pixel and the surrounding pixels. A function called *filter2D* in *OpenCV* helps to build a high pass filter to ignore the inhomogeneous lightning problem. The *Filter2D* is used to perform various linear or non-linear filtering operations on 2D images. The function applies an arbitrary linear filter to an image. Filtering is essentially convolution of kernel and image. [0] The function does compute correlation:

$$dst(x,y) = \sum_{\substack{0\le x'<kernel.cols \\ 0\le y'<kernel.rows}} kernel(x',y') * src(x+x'-anchor.x, y+y'-anchor.y) \tag{7}$$

Default value of anchor (-1, -1) means that the anchor is at the *kernel* center. In this project, the kernel is a 3 x 3 matrix:

$$kernel = \begin{pmatrix} 0 & -1 & 0 \\ -1 & 5 & -1 \\ 0 & -1 & 0 \end{pmatrix} \tag{8}$$

Suppose *src* to be the source matrix:

$$src = \begin{pmatrix} 127 & 2 & 4 & 7 \\ 25 & 4 & 56 & 1 \\ 28 & 20 & 42 & 1 \\ 1 & 1 & 1 & 1 \end{pmatrix} \tag{9}$$

For example, apply the filter2D function to the selected part in *src*, multiply two matrices:

$$dst = \begin{pmatrix} ? & ? & ? & ? \\ ? & -82 & ? & ? \\ ? & ? & ? & ? \\ ? & ? & ? & ? \end{pmatrix} \tag{10}$$

This equation has some special treatment for the edge data, and we would not go into details here. Performing this step on the image will have the effect of sharpening the edges. And so on. Since the background board is only black and white, the white spots on the black background can be well highlighted, and some light and shadow effects are avoided.

4.2 Blur Spatial Filter Method (BSF)

The *Blur Spatial Filter Method* (BSF) function in *OpenCV* helps by smoothening the image to make it more like a grayscale distribution rather than separate dots. It is essentially a low pass filter and has a similar calculation process. But this time, a spatial filter is used in the function:

$$kernel = \frac{1}{9}\begin{pmatrix} 1 & 1 & 1 \\ 1 & 1 & 1 \\ 1 & 1 & 1 \end{pmatrix} \tag{11}$$

For the same selected part:

$$src = \begin{pmatrix} 127 & 2 & 4 & 7 \\ 25 & 4 & 56 & 1 \\ 28 & 20 & 42 & 1 \\ 1 & 1 & 1 & 1 \end{pmatrix} \tag{12}$$

the new matrix looks like this:

$$dst = \begin{pmatrix} ? & ? & ? & ? \\ ? & 34 & ? & ? \\ ? & ? & ? & ? \\ ? & ? & ? & ? \end{pmatrix} \tag{13}$$

Through this, we obtain a different value for the same pixel.

4.3 Equalized Histogram Method (EH)

The *Equalized Histogram Method* (EH) or *EqulizaHist* helps to enhance image contrast by stretching out the pixel intensity range. The central idea is to change the grey histogram of the original image from a certain grey interval in the comparison set to a uniform distribution within the range. That is, mapping one distribution (*given histogram*) to another distribution (a wider and uniform intensity value distribution), so the intensity value distribution will be spread over the entire range.

To achieve the effect of equalization, the mapping function should be a cumulative distribution function. For the histogram *H(i)* its cumulative distribution *H'(i)* is:

$$H'(i) = \sum_{0 \le j \le i} H(j) \quad (14)$$

Then scale *H'(i)* to 0~255:

$$dst(i) = 225 \times H'(i) \quad (15)$$

For example, for an image like this:

$$src = \begin{pmatrix} 50 & 50 & 255 & 200 \\ 100 & 50 & 200 & 255 \\ 50 & 100 & 200 & 200 \\ 100 & 200 & 255 & 255 \end{pmatrix} \quad (16)$$

Here is the new image after mapping:

$$dst = \begin{pmatrix} 64 & 64 & 244 & 191 \\ 112 & 64 & 191 & 255 \\ 64 & 112 & 191 & 191 \\ 112 & 191 & 255 & 255 \end{pmatrix} \quad (17)$$

This function performs brightness *addition* and subtraction on each pixel to adjust the brightness of the picture. Entering a positive number will increase the brightness. On the contrast, a negative one will decrease the brightness. When the pixel value is greater than 255, the pixel turns out to be white. When the pixel value is less than 0, the pixel turns out to be black. This algorithm may cause a loss of information but has a positive effect when the image turns out to be too bright.

Table 3. An example of histogram equalization

Grayscale	Number of pixels	Cumulative probability	New grayscale
50	4	0,2500	64
100	3	0,4375	112
200	5	0,7500	191
255	4	1,0000	255

5 MEASUREMENTS OF TURBULENT FLOW

5.1 Turbulent Flow with Butane Tracer

The difference between refractive index of butane to air is much higher in comparison to helium. So, expected quality of measurements should be better. But flammability of butane is a problem for the setup in the wind tunnel. In Figures 5 and 6 measurements of a butane jet are presented. Firstly, we loaded at least two images (*see*: Figure 5), one image of the background and the several original current images. For an example geometry, we use a picture of the lighter to analyse.

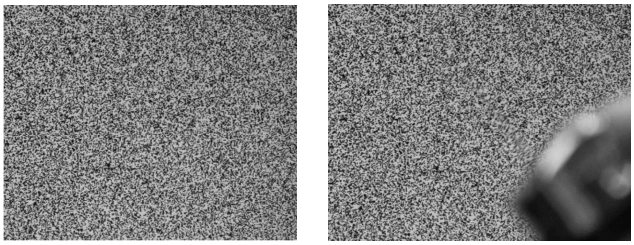


Figure 5: Background image (*left side*); current image with butane nozzle (*right side*)

Secondly, we should select the mask for the picture. During the test, the placed blocks or moving tubes will cause huge error. So, these parts should be deleted from the image. Since we use the original images, a pre-image processing should also be applied as the default value. [15, 20]

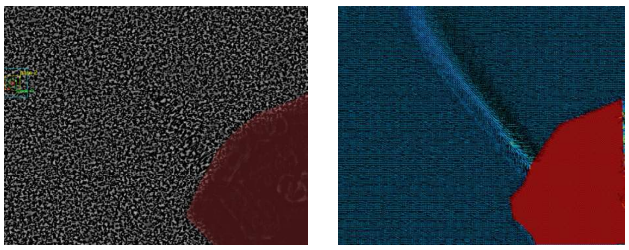


Figure 6: High pass filtered image with mask (*left side*); with butane tracer (*right side*)

Thirdly, we should set the PIV settings. In this test, we use all four pass filters, and the interrogation area should be decremented according to the size of the air. A larger interrogation area can capture higher velocity. After comparison, the display parameter *velocity magnitude* has a best result in all plots. It can be clearly seen from the figure that the flow of butane gas from the lighter.

5.2 Turbulent Flow with Helium Tracer

For each experiment, the result is documented with dates and serial numbers. In Figure 7 is a set of results for a NACA0021 aerofoil. The background dot density of this image is about 20 [%]. Because the profile is small, the selected interrogation area in PIVlab is also small, from

32 [pixel] to 4 [pixel]. The flow detachment is clearly visible after PIVlab processing.

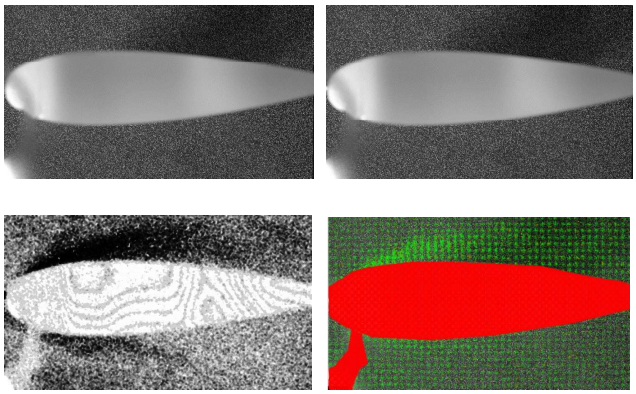


Figure 7: Background image (*upper left*); current dynamic image (*upper right*); processed image of BOS (*bottom left*); velocity plot with vectors generated by PIVlab (*bottom right*)

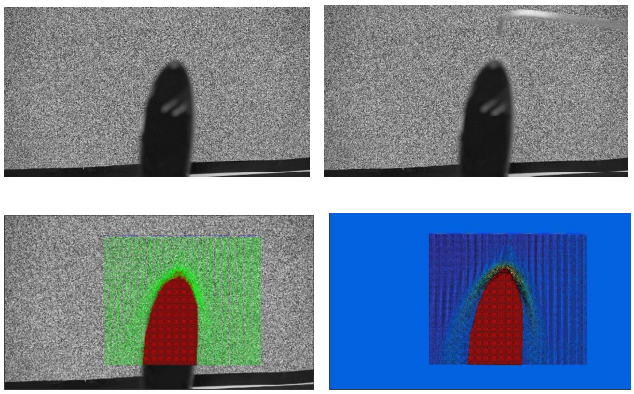


Figure 8: Background image (*upper left*); current dynamic image with helium nozzle (*upper right*); velocity plot with vectors with PIVlab (*bottom left*); magnitude velocity plot of PIVlab (*bottom right*)

As we can see from Figure 8, there are obvious black or green parts around the objects, which are the flow of helium. Laminar flow can be observed in the upper region, the rear gas is dispersed, and a little bit turbulence can be observed.

However, due to small gas contents, the stall effect was difficult to observe. Relatively high point density stores more information, which has a positive effect when gas flow is low.

In Figure 9 we see the helium plume on the turbine blade (*from Figure 1*) with helium tracer and background intensity of 50 [%].

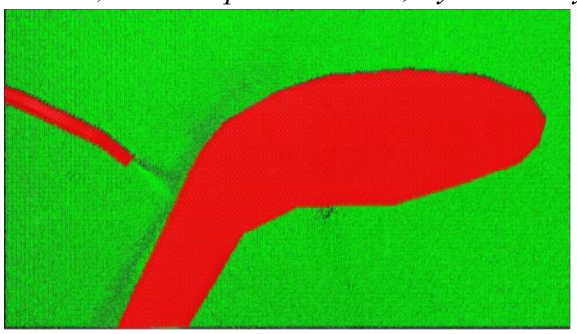


Figure 9: Velocity plot of a turbine blade geometry with helium tracer nozzle on right side and background intensity of 50 [%]

6 CONCLUSIONS AND OUTLOOK

The BOS method is very easy to conduct, cheap, and has advantages when applied to a measurement system. Experiments with fluid flow of butane tracers, helium tracers and hot air jets where conducted.

During experiments, a digital camera and an in-house programmed software tool have been used. As for image processing methods, the C++ program and *PIVlab* can both enhance the visual effect of the flow. It provides an opportunity of a real-time observation, while *PIVlab* can generate plots with more detailed information such as the magnitude speed, which is more suitable for experimental research.

Generally, a high-pass filter is required to avoid some illumination problems. Turbulence effects can be visualized for NACA0021 profiles as well as for alternative geometries. For improvements, a lightning system and an equipment that can create higher gas flow are recommended. In further study, a multi-scale wavelet noise pattern should be tried and compared with normal backgrounds.

In general, the experimental results are still relatively optimistic, there are two main defects in our experiments. The flow of gas can be observed, but details are harder to see. This is mainly due to the small amounts of helium or butane gas flow. Another problem is that illumination is still a strong interference factor, but it can be partly eliminated by high-pass filtering. For the above two defects, suggestions are to use equipment's that can generate lager flow of butane, helium, or hot air, such as heat gun and to add uniform lighting behind the test background, such as halogen lamps. In further

work we want to compare the measures against numerical simulations. [8]

ACKNOWLEDGEMENTS

We want to thank *University of Applied Sciences Saarbrücken* (*htw saar*) and the country of Saarland (*Germany*) for their financial support during *VisualFlow* project.

REFERENCES

[1] Dol, S. S., Nor M. A. M., and Kamaruzaman, M. H.: *An Improved Smoke-Wire Flow Visualization Technique.* Proceedings of the 4th WSEAS International Conference on Fluid Mechanics and Aerodynamics, Elounda, Greece, August 21-23, pp. 231-236., 2006

[2] S., Yarusevych, P., Sullivan, and J., Kawall. *On vortex shedding from an airfoil in Low-Reynolds-number flows.* Journal of Fluid Mechanics, 632, pp.245-271., 2009

[3] Lu, L. and Sick, V.: High-speed Particle Image Velocimetry Near Surfaces. Journal of Visualized Experiments, (76)., 2013

[4] Anon, PIV (*Particle Image Velocimetry*) Overview & Principle | SEIKA Digital Image. [online]; 2019

[5] Available at [Accessed 20 Aug. 2019].: https://www.seikadi.com/en/measurement/principle_of_piv.html

[6] PetaPixel. *Schlieren Photography Lets Us See an Invisible World.* [online] Available at: https://petapixel.com/2017/06/16/schlieren-photography-lets-us-see-invisible-world/ [Accessed 20 Aug. 2019].; 2019

[7] Westenberg-engineering.de. *Eiffel-Type Wind Tunnels.* Available at: http://www.westenberg-engineering.de/en/wind-tunnels/, 2019

[8] Cfdsupport.com. *Laminar vs. Turbulent Flow.* Available at: https://www.cfdsupport.com/ 2019

[9] Nuclear Power. *What is Reynolds Number - Definition of Reynolds Number?* Available at: https://www.nuclear-power.net; 2019

[10] Anon, SP-367 *Introduction to the Aerodynamics of Flight.* Available at: https://history.nasa.gov/SP-367/f48.htm [Accessed 20 Aug. 2019]., 2019

[11] Wang, G., Yang, Z., Meng, S., Wang, M., Zhong, Y.: *Application of quantitative background oriented schlieren in laminar axisymmetric flame temperature measurement.* J Exp Fluid Mech, 2016, 30(2): 103-110.

[12] Raffel, M., Willert, C. E., Wereley, S., & Kompenhans, J.: *Particle Image Velocimetry: a practical guide*; Springer. Edition: 2nd Publisher: Springer ISBN: 978-3-540-72307-3, 2013

[13] Atcheson, B., Heidrich, W. and Ihrke, I.: *An evaluation of optical flow algorithms for background oriented schlieren imaging. Experiments in Fluids,* 46(3), pp.467-476., 2008

[14] Moisy, F. (2009) Create BOS pattern. [online] [Accessed 20 Aug. 2019]. Available at: http://www.fast.upsud.fr/~moisy/ml/misc/makebospattern.m

[15] Zhao, Z. Turbulence *Visualization based on Schlieren Image,* 2018

[16] Docs.opencv.org.: Image Filtering — OpenCV 2.4.13.7 documentations. [online] Available at [Accessed 20 Aug. 2019]: https://docs.opencv.org/2.4/modules/imgproc/doc/filtering.html

[17] Thielicke, W. and Stamhuis, E.J.: PIVlab – Towards User-friendly, *Affordable and Accurate Digital Particle Image Velocimetry in MATLAB.* Journal of Open Research Software 2(1):e30, DOI: http://dx.doi.org/10.5334/jors.bl, 2014

[18] Richard, H., Raffel, M., Kompenhans, J., et al.: *Demonstration of the applicability of a Background Oriented Schlieren (BOS) method;* Conference: 10th Intern. Symposium on Applications of Laser Techniques in Fluid Mechanics, Lisbon, Portugal, July 2000

[19] Tinoco, E.N. *CFD Uncertainty and Validation for Commercial Aircraft Applications. In Computational Uncertainty in Military Vehicle Design* (pp. 20-1 – 20-36). Meeting Proceedings RTO-MP-AVT-147, Paper 20. Neuilly-sur-Seine, France: RTO. Available from: http://www.rto.nato.int; 2007

[20] Sendyka, B. Mitianiec, W., Noga, M.: *Study of combustion process with jet-ignition of propane-air mixtures;* Vol. 63; No 2; pp. 533-543; Bulletin of the Polish Academy of Sciences: Technical Sciences; 2015

INVESTIGATION OF SOOT FORMATION OF SWIRL-STABILIZED JET A-1 SPRAY FLAME WITH RANK CORRELATED SLW INCLUDING ETHYLENE AND ACETYLENE RADIATION

Berkay Halvaşi [1], Altuğ M. Başol, Özgür Ertunç and M. Pınar Mengüç

1. Mechanical Engineering Department Özyeğin University, İstanbul/Turkey;
email: berkay.halvasi@ozu.edu.tr

Abstract

Radiation effect in combustion chamber is significant, especially for sooting flames. Spectral radiation models that can account for the radiative effects in sooting flames need to be considered in detail, which necessitates the consideration of spectral gas models. This study numerically investigates the interaction between the radiation and soot formation on a swirl-stabilized jet A1 spray flame. A rank correlated spectral line-based weighted sum of gray gases (RC-SLW) global model is implemented in Ansys Fluent and used for the combustion modelling of a swirl-stabilized flame. RC-SLW model, including ethylene and acetylene radiation, shows considerable improvement in predicting soot volume fraction compared to the domain-based weighted sum of gray gases (WSGG) model in Ansys Fluent. Effect of RC-SLW model and effect of ethylene and acetylene radiation is investigated and compared to experimental data. Solving radiation with RC-SLW reduces error in soot production from 61% to 41% compared to WSGG when accounting CO2, CO and H2O as participating species. Error reduces less than 5% in the case that includes effects of ethylene and acetylene radiation and utilizes RC-SLW which shows that ethylene and acetylene radiation have a considerable effect on soot production for a swirl stabilized Jet A-1 spray flame.

1 INTRODUCTION

Swirl stabilized turbulent flames are frequently used in gas turbine engines combustion chambers. Those combustion chambers being the source of power of gas turbine engines need to be carefully designed. These designs should consider both performance of the engine and production of pollutants inside. Over last few decades a lot of research has been conducted to improve design of the gas turbine engines [1,2]. Thermal radiation plays an important role in many combustion systems (Internal combustion engines, gas turbines, furnaces, etc.) [3] and for gas turbine engine combustion chambers out of three heat transfer mechanisms, (conduction, convection and radiation) radiation plays an important role and affect flame shape and soot production. This predominant role requires it to be modelled accurately. Watanabe et al investigated the effect of radiation and equivalence ratio on n-decane spray flamen and found that soot formation is strongly affected by radiation [4]. Choi and Baek showed that radiation makes droplets to evaporate faster and shortens droplet trajectories which broadens high temperature zone [5].

Radiation is a complex problem and combining it with the complexity of simulating combustion systems, including multiphase flow, combustion chemical kinetics, and spray mechanics makes it even more difficult. There have been many advances to improve combustion simulations in the past decades, including advances in the solution of thermal radiation. Although there are advances in solving radiative transfer equations, solving radiation for a complete spectrum with complete accuracy and spatial resolution brings tremendous computational cost, making it non-viable without using any model to reduce computational cost.

The Radiative Transfer Equation (RTE) is integrodifferential in six independent variables (3 spatial and 2 directional, and wavenumber) [6]. There are several models used to simplify the solution of the spatial part of the radiative transfer equation (RTE), such as the General Spherical Harmonics (PN) method [7], and the Discrete Ordinates method [8-11]. Also, there are many global models to simply the spectral part of the RTE. Three main global models are the weighted sum of gray gasses (WSGG) [12], the spectral line-based weighted sum of gray gasses (SLW) [13-19], and the full spectrum k-distributions (FCK) [20,21] where WSGG is the simplest and fastest among the three.

SLW and FSCK, despite their difference in the way of approaching RTE solution they redistribute spectral data with absorption cross-section and normalize it with a plank blackbody distribution function. Only difference between them is the way they handle the integration of that function. Their convergence to be the same when their resolution (gray gas and quadrature number) is high enough. To use these models for non-uniform (non-isothermal, non-homogenous) medium, new methods that use scaling or correlation are used to adapt these spectral models [23,24,25].

In recent publications, it has been stated that SLW-based models yield more accurate results than WSGG [26]. Another study shows a significant difference between SLW and WSGG predictions of temperature and radiative heating [27]. The same study also stated that rank correlated spectral line-based weighted sum of gray gasses is as accurate as other SLW models and more robust to use in computational simulations.

Guo et al. [28] studied fuel preheating and showed that radiative heat transfer of C2H2 and C2H4 is non-negligible when considering ethylene laminar diffusion flames. Zheng et al. conducted numerical simulations that used statistical narrow-band correlated-k and showed that C2H2 and C2H4 affect soot production. Despite the studies for laminar diffusion flames, effect of C2H2 and C2H4 radiation for swirl stabilized spray flames is not broadly studied.

Recently, Lu-Yin Wang et. al. conducted experiment on a model combustor to investigate soot and flow field in a turbulent swirl-stabilized Jet-A1 spray flame [29]. Also, Rault et. al. investigated the effect of several different addition on soot and flow field for the same model combustor [30,31,32].

Guo et al. recently investigated different WSGG models for ethylene/air jet diffusion flame [33] and Shu Zheng et al. investigated the effect of C2H2 and C2H4 radiation on soot formation for ethylene/air laminar diffusion flames [34]. Effects of C2H2 and C2H4 will also be considered in this study.

The current study aims to investigate the interaction between the radiation and soot formation mechanisms on a sooting swirl stabilized Jet-A1 spray flame. Accordingly, the RC-SLW model has been implemented in Ansys Fluent, and its effects on soot formation are compared with the existing domain-based WSGG model in Ansys Fluent. Moreover, the effect of the acetylene (C2H2) and ethylene (C2H4) radiation are also included in the RC-SLW model, and their effects on soot formation are separately investigated.

2 RADIATIVE PROPERTY MODELS

Propagation of radiation in absorbing and emitting gaseous media along a path length s in a direction. Ω is characterized by the spectral radiation intensity $I_\eta(s,\Omega)$, which is governed by the Radiative Transfer Equation (RTE). In Eq. (1) η is the wavenumber, and $I_{b\eta}[T(s)]$ is the spectral Planck blackbody intensity at local gas temperature T(s).

$$\frac{\delta I_\eta(s,\Omega)}{\delta s} = -\kappa_\eta(s) I_\eta(s,\Omega) + \kappa_\eta(s) I_{b\eta}[T(s)] \quad (1)$$

2.1 RC-SLW Model

The weighted sum of gray gases (WSGG) utilizes non gray absorption coefficients (κ_k) for every gray gas that accounts. These gray gases also occupy a fraction of the Planck function weighted spectrum ($\alpha_k(T)$). Denison and Webb [14] used the relation between absorption coefficient (κ_k) and absorption cross section to make use of line by line data and created absorption line blackbody distribution functions (ALBDF) uses absorption cross sections as

$$F_s\left(C_{abs}, T_b, T_g, p, x_s\right) = \pi / (\sigma T_b^4) \sum_i \int_{\Delta\eta \in (C_{abs\eta}(T_g,p,x_s) < C_{abs})} I_{b\eta}(T_b) d\eta \quad (2)$$

As can be seen in Eq. (2), the sum is over all spectral regions $\Delta\eta$ for which $C_{abs,\eta}\left(T_g, p, x_s\right) < C_{abs}$. In the equation, $C_{abs,\eta}$ is spectral absorption cross-section, T_g is gas temperature, p is total pressure, x_s is the mole fraction of species s. ALBDF is a strictly increasing function that has a value between 0 and 1 with $C_{abs,\eta}$ increasing, which makes it invertible. The absorption cross-section is related to the absorption coefficient with Eq. (3).

$$C_{abs,\eta} = \frac{R_u T_g}{p x_s} \kappa_\eta \quad (3)$$

Where R_u is universal gas constant and κ_η is the absorption coefficient. SLW starts with spectral integration of the RTE, then solves it for directly integrated intensity for a finite number of the absorption cross-section values. It can be said that

instead of integrating over the whole spectrum, SLW model redistributes it using the Planck blackbody function and integrates over absorption cross-section. In rank correlated SLW (RC-SLW) model absorption line blackbody distribution function at a specified thermodynamic state which changes according to gas temperature, total pressure, and species mole fraction can be used to find the distribution at another thermodynamic state. F value for a specific absorption cross-section value at a specific state must give the same F for a different state. By using this relation inverse ALBDF can be used to find absorption cross section of a thermodynamic state using F value calculated for reference state.

RC-SLW method in Solovjov et al [22] is utilized for this study to model radiation properties. RC-SLW calculates gas radiative properties with steps written below:

1- It starts with division of C-variable to supplemental cross-sections $\tilde{C}_j^{ref}, j = 0, 1, \dots, n$. n here is the number of division (gray gases).

2- Calculations of corresponding F values for calculated $\tilde{C}_j^{ref}$s. Here $\phi_{\text{ref}} = \{T_{ref}, x_{ref}, p_{ref}\}$ is thermodynamic state of the reference stat.

$$\tilde{F}_j^{loc} = F(\tilde{C}_j^{ref}, \phi_{\text{ref}}, T_{loc}) \quad (4)$$

3- Calculate the local supplemental cross-sections $\tilde{C}_j^{loc}$

$$\tilde{C}_j^{loc} = C(\tilde{F}_j^{loc}, \phi_{loc}, T_{loc}) \quad (5)$$

4- Calculate the local weights of gray gases

$$a_j^{loc} = F\left(\tilde{C}_j^{ref}, \phi_{\text{ref}}, T_{loc}\right) - F\left(\tilde{C}_{j-1}^{ref}, \phi_{\text{ref}}, T_{loc}\right), \quad a_0^{loc} = F_0^{loc} \quad (6)$$

ALBDF is calculated from high resolution gas absorption cross-section and these calculations are conducted beforehand for various thermodynamic states and tabulated. For CO2, H2O, and CO, tabulated data that uses most up to date spectral database, HITEMP 2010 [35] has presented. For C2H2 and C2H4, HITRAN 2016 [36] database is used to create tabulated data. Both for C2H2 and C2H4 spectral range was 0 to 15000 and spectral resolution is $\Delta\eta = 0.005\, cm^{-1}$. Also, inverse ALBDF tables are created for all the gases.

Implemented RC-SLW model is validated using 1-D case. Case has two parallel plates at 0 K and composition of CO2, CO, and H2O ($X_{H_2O} = 0.2, X_{CO_2} = 0.1, X_{CO} = 0.03$) at 1000 K in between. As shown in Fig. 1, the comparison between LBL and SLW results show favorable agreements, especially for 10 and 16 gases.

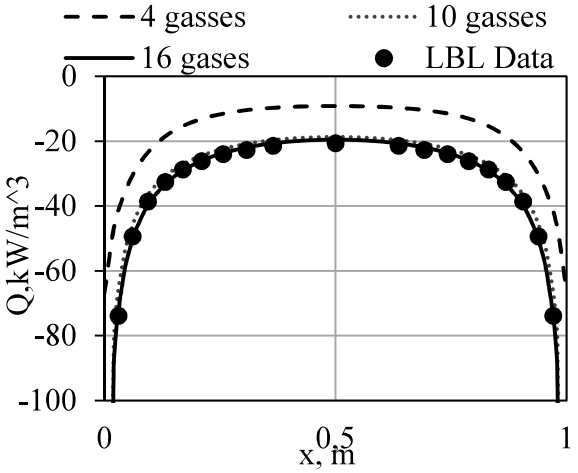


Figure 1. Comparisons of radiative source calculated by SLW and LBL models for $X_{H_2O} = 0.2, X_{CO_2} = 0.1, X_{CO} = 0.03$ at 1000 K

2.2 Soot radiative property model

Dependence of radiative property of soot particles on wavelength is much lower than gases. Therefore, soot radiative property can be considered gray [37]:

$$\kappa_{soot} = b1\rho_{soot} f_v [1 + b_T(T - 2000)] \quad (7)$$

In Eq. (7) κ_{soot} is soot absorption coefficient, T is temperature, ρ_{soot} is the soot density of 1800 kg/m^3, b_1 is 1232.4 m^2/kg and 4.8 x 10^{-4}K^{-1}. Soot particles are small in nature so T in the equation can be assumed same as local gas temperature. Total absorption coefficient is determined as:

$$\kappa_{total} = \kappa_{gases} + \kappa_{soot} \quad (8)$$

2.3 Numerical Models and Configurations

Swirl stabilized jet flame model combustor described by Wang et al. [29] and studied by Rault et al. [31] is numerically investigated. Flow domain can be seen in Fig. 2. Dimensions of the domain are 94x94x188 mm^3. Mesh sensitivity analysis is conducted and maximum difference between mesh with 2 million cells and 1.7 million cells with similar orthogonal quality is less than six percent. Thus, mesh with 1719987 cells with 0.24 minimum orthogonal quality is selected.

The governing equations have been solved using the pressure based, steady solver in Ansys Fluent 22R2. The pressure velocity coupling in the gas

phase has been accounted with the Couple algorithm.

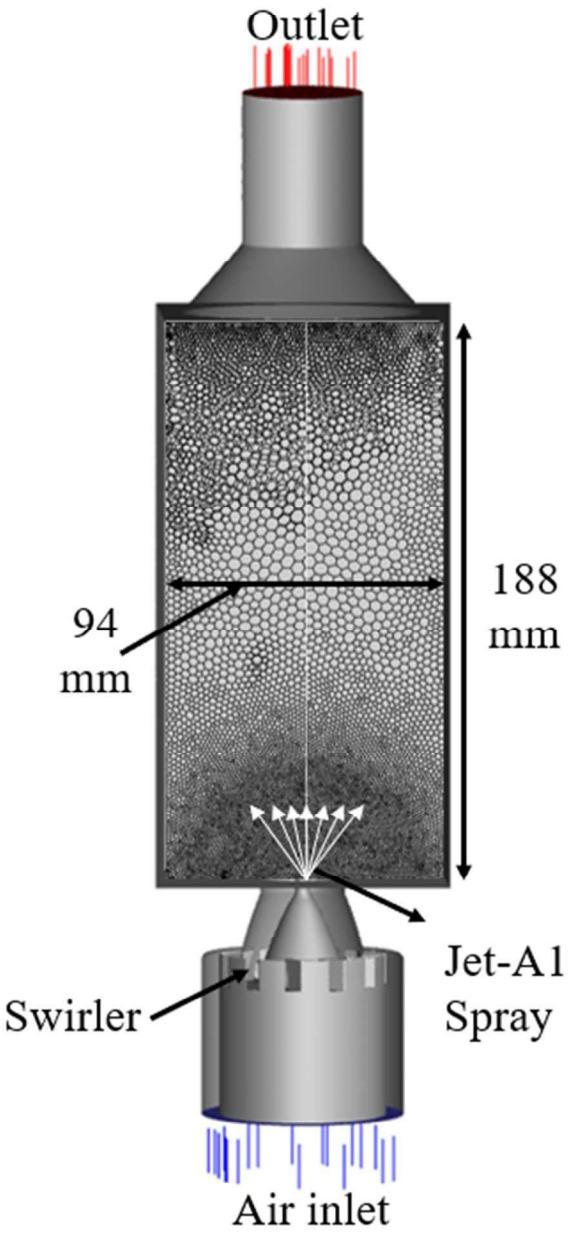


Figure 2. Flow domain and System mesh.

The Favre-averaged governing equations in the gas phase are solved and turbulent quantities are modelled using k-ω SST model.

A Jet-A1 spray at 300 K is injected into the domain at the rate of 0.224 g/s with rosin-rammler distribution created by the data presented. The Inlet air mass flow rate is 5.93 g/s and its turbulent intensity is 1.5%. Spray and gaseous phases interactions are handled with Eulerian-Lagrangian approach. Primary atomization is modelled using linearized instability sheet atomization (LISA) [38] and secondary breakup is modeled with Kelvin-Helmholtz Rayleigh-Taylor (KHRT) model [39]. Droplet drag coefficient is obtained with spherical law and droplet heating by convection and radiation vaporization is considered. Ranz Marshall [40, 41] is utilized to calculate convective heat transfer coefficient of droplets.

Combustion is modelled with steady-flamelets non-premixed combustion model and

[42,43] is used for combustion kinetics and method of moments is utilized to describe the soot particle dynamics. Nucleation process is modelled with Moss-Brokes model [44,45,46] and C2H2 and C2H4 is selected as both precursor and surface growth.

Radiation is modelled with Discrete Ordinates method and Theta and Phi are divided to four. Three different simulations are conducted. One of three simulations use RC-SLW with four and gray gases considering H2O, CO2, CO, C2H2 and C2H4 as participating species, other one utilizes RC-SLW with four gray gases considering H2O, CO2 and CO as participating species and last simulation uses a gray WSGG that considers only H2O, CO2 and CO. It adds a_j^{loc} values for gray gases together and solves only one radiative transfer equation. Table 1 shows all the case specifications. Using more than 4 gray gases for simulations to investigate the effect of gray gas number on RC-SLW were not possible due to the available computational resources.

Table 1. Information about cases.

Case	Radiation property	Participating gases	Gray gas number
1	RC-SLW	CO_2, CO, H_2O, C_2H_2, C_2H_4	4
2	RC-SLW	CO_2, CO, H_2O,	4
3	WSGG	CO_2, CO, H_2O,	1

3 RESULTS

Flow field of the simulations in Fig. 3 is similar to experiment with the exception of positions of big vortexes due to the modeling of turbulence. Through Figs. 4-10 temperature, the molar fractions of H_2O, CO_2, C_2H_2, and C_2H_4, and the soot volume fraction of Case 1 can be seen. Both C_2H_4 and C_2H_2 volume fractions are at considerably high levels, so their radiative effects need to be considered in the spectral radiation model. Comparison of 3 cases with experimental data published in Rault's work [31] can be seen in Fig. 10.

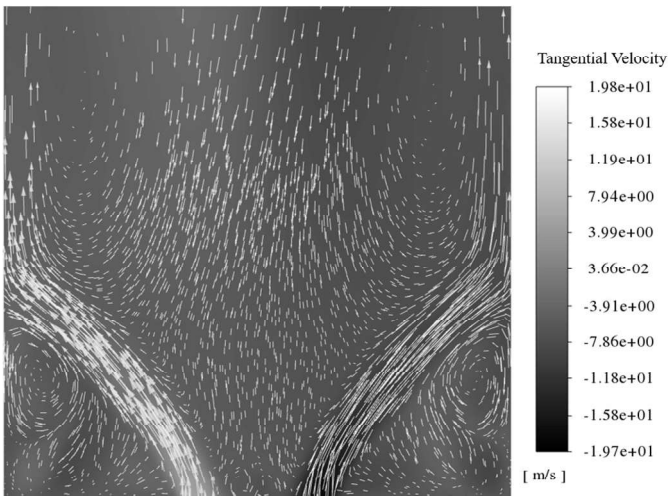


Figure 3. Flow field of the domain.

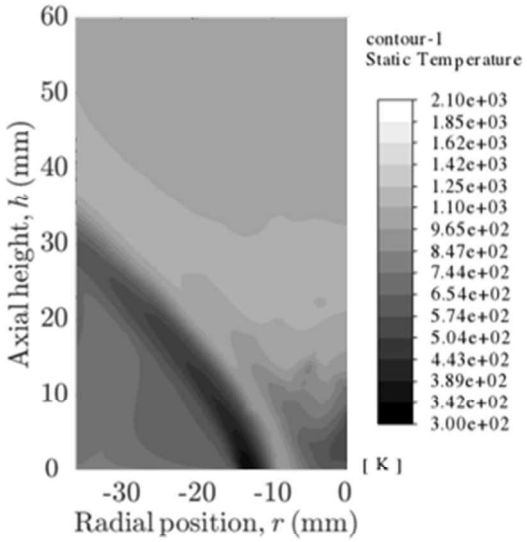


Figure 3. Temperature distribution of Case 1

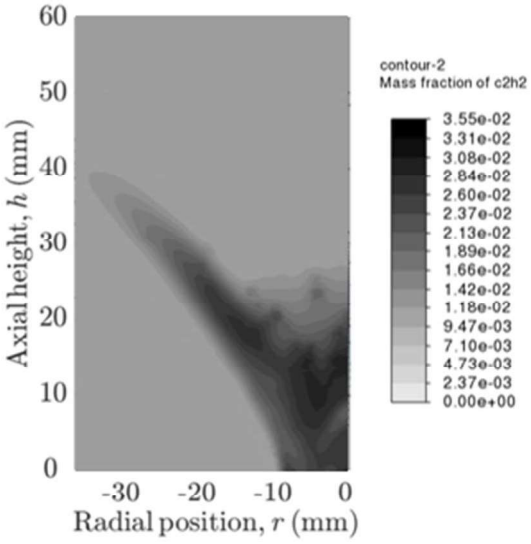


Figure 4. C2H2 mass fraction distribution of Case 1

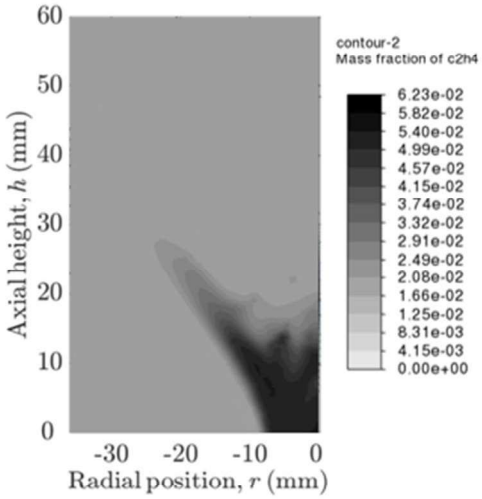


Figure 5. C2H4 mass fraction distribution of Case 1

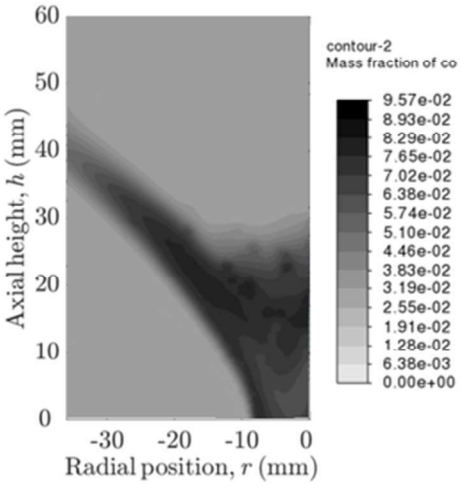


Figure 6. CO mass fraction distribution of Case 1

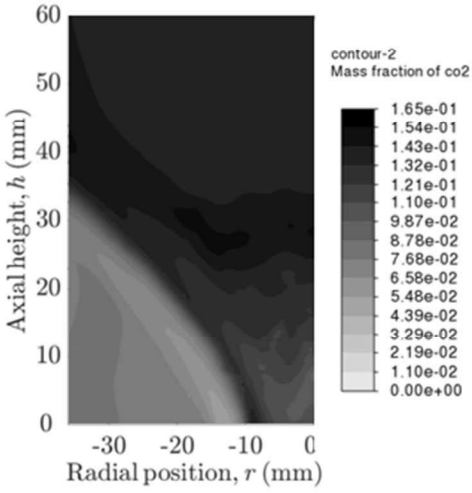


Figure 7. CO2 mass fraction distribution of Case 1

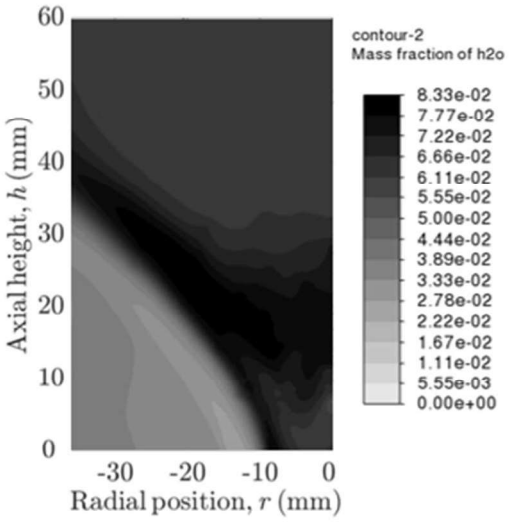


Figure 8. CO2 mass fraction distribution of Case 1

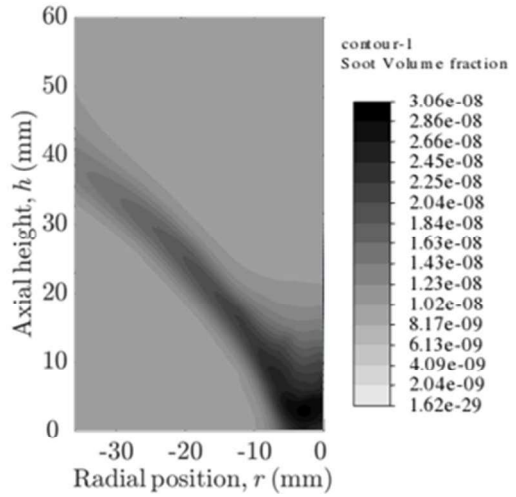


Figure 9. Soot volume fraction distribution of Case 1

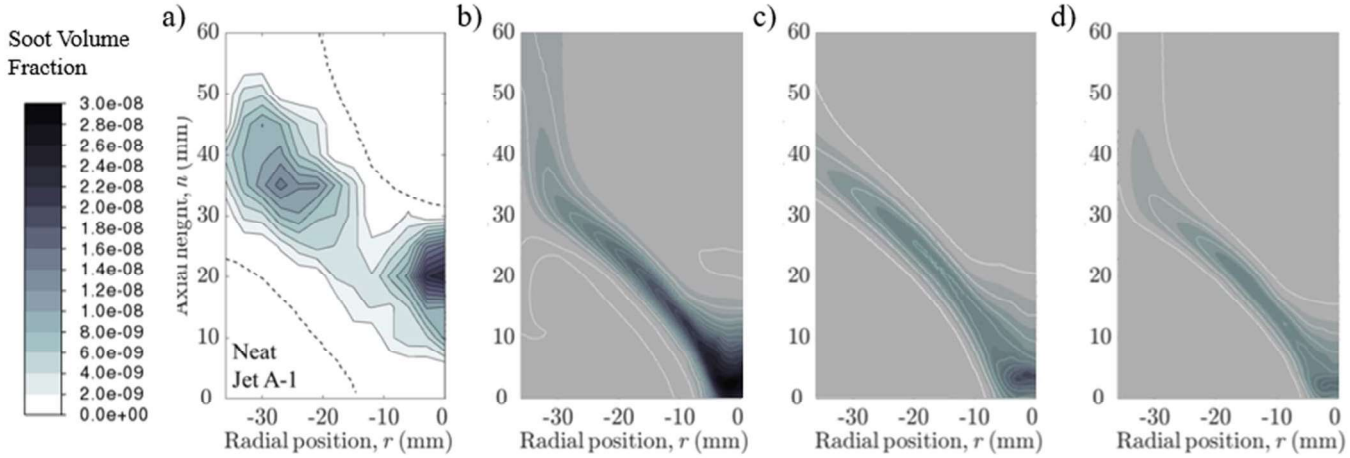


Figure 10. Soot volume fraction distribution of experiment [31] (a), Case 1 (b), Case 2 (c) and Case 3 (d)

As can be seen in Fig 10. soot volume fraction shapes of cases are quite similar to measurements. Only the position of maximum soot volume fraction point is about 1 cm lower in simulations compared to experiment and all cases have similar soot volume fraction propagation pattern.

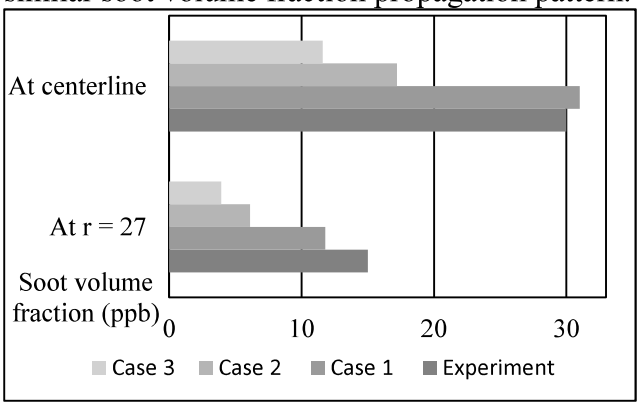


Figure 11. Maximum soot volume fraction values at the centerline and at r=27 mm.

Fig. 11 shows that despite the position of maximum soot volume fraction at the centerline simulations soot propagation behavior is similar to measurements.

Case 1 which utilizes RC-SLW and accounts CO, CO2, H2O, C2H2, C2H4 as participating gases shows minimum error in prediction of maximum soot volume fraction and its value is 31 ppb and its error in predicting domain maximum soot volume fraction is less than 5%.

Case 2 is like Case 1 utilizes RC-SLW but accounts only CO, CO2, H2O as participating species. Domain maximum soot volume fraction in Case 2 is lower than Case 1 and its value is 17.2 ppb. Not accounting acetylene and ethylene radiation brings error up to 42% in Case 2 and

shows that in addition to spectral solution of radiation which effects flame and soot formation with changing heat distribution, accounting acetylene and ethylene radiation also has a considerable effect on soot production.

Case 3 utilizes WSGG gray method by adding a_j^{loc} values of gray gasses and solving only one RTE. It also accounts only CO, CO2, H2O as participating species. WSGG used for Case 3 has the lowest domain maximum soot volume fraction value of 11.6 ppb and maximum error value of 61%.

4 CONCLUSION

This study implements the RC-SLW spectral global radiation model in Ansys Fluent using user-defined functions. The implementation is validated on a 1-D participating medium against line-by-line data. A validated radiation model is used to investigate the soot production behaviour of a swirls stabilized Jet A-1 spray flame. The developed RC-SLW model also accounts for the ethylene and acetylene radiation. The predictions of the RC-SLW model and existing domain-based WSGG in Fluent are compared against the experimental soot volume fraction data. The conclusions are listed below:

- Domain-based WSGG severely underpredicts (61%) the maximum soot volume fraction at the centerline of the flame.
- RC-SLW model, accounts only CO2, CO and H2O as participating gases captures peak soot volume fraction with a maximum error of 42% with 4 gray gases.
- RC-SLW model, including C_2H_2 and C_2H_4 radiation, captures peak soot volume fraction with a maximum error of 5% with 4 gray gases.
- Including the effects of C_2H_2 and C_2H_4 in the RC-SLW model considerably decreases error when capturing peak soot volume fraction.

Investigating effect of gray gas number on soot production and other hydrocarbons in a combustion environment is planned with increased computational resources.

ACKNOWLEDGEMENTS

Special thanks for Taylor M. Rault for sharing information about experimental domain and fuel spray.

The authors also gratefully acknowledge the Scientific and Technological Research Council of Turkey (TÜBİTAK) and TEI for providing financial support to this research with the 118C053 project.

REFERENCES

[1] B.L. Koff, "*Gas turbine technology evolution: A designer's perspective*", J. Propul. Power 20 (2004), pp. 577–595.

[2] V.K. Arghode and A.K. "*Gupta, Development ofhigh intensity CDC combustor for gas turbine engines*", Appl. Energy 88 (2011), pp. 963–973.

[3] J.R. Howell, M.P. Menguc, R. Siegel, Thermal Radiation Heat Transfer, CRC Press, 7th edition, 2020.

[4] H. Watanabe, R. Kurose, S. Komori, and H. "*Pitsch, Effects ofradiation on spray flame charac- teristics and soot formation*", Combust. Flame 152 (2008), pp. 2–13.

[5] C.E. Choi and S.W. Baek, Numerical analysis ofa spray combustion with nongray radiation using weighted sum ofgray gases model, Combust. Sci. Technol. 115 (1996), pp. 297–315.

[6] Modest MF. Radiative heat transfer. 3rd ed. New York: Academic Press; 2013.

[7] B. DAVISON, Neutron Transport Theory, Oxford Univer-sity Press, London ~1957!.

[8] Fiveland, W. A., "*A Discrete Ordinates Method for Predicting Radiative Heat Transfer in Axisymmetric Enclosures*", ASME Paper No. 82−HT−20, 1982.

[9] Fiveland, W. A., "*Discrete-Ordinates Solutions of the Radiative Transport Equation for Rectangular Enclosures*", J. Heat Transfer, vol. 106, pp. 699−706, 1984.

[10] Fiveland, W. A., "*Discrete Ordinate Methods for Radiative Heat Transfer in Isotropically and Anisotropically Scattering Media*", J. Heat Transfer, vol. 109, pp. 809−812, 1987.

[11] Fiveland, W. A., "*Three-Dimensional Radiative Heat-Transfer Solutions by the Discrete-Ordinates Method*", J. Thermophys. Heat Transfer, vol. 2, no. 4, pp. 309−316, 1988.

[12] T.F. Smith, Z.F. Shen, "*Evaluation of coefficients for the weighted sum of gray gases model*", *J. Heat Transf.* 104 (4) (1982) 602–608.

[13] M.K. Denison, B.W. Webb, M.K. Denison, "*A spectral line-based weighted sum of gray gases model for arbitrary RTE solvers*", J. Heat Transf. 115 (4) (1994) 1004–1012.

[14] M.K. Denison, B.W. Webb, "*The spectral line-based weighted-sum-of-gray- gases model in*

nonisothermal nonhomogeneous media", J. Heat Transfer 117 (2) (1995) 359–365.
[15] V.P. Solovjov, B.W. Webb, "*Global spectral methods in gas radiation: the exact limit of the SLW model and its relationship to the ADF and FSK methods*", J. Heat Transfer 133 (4) (2011). 042701(1–9).
[16] M.K. Denison, B.W. Webb, "*An absorption-line blackbody distribution function for efficient calculation of total gas radiative transfer*", J. Quant. Spectrosc. Radiat. Transfer 50 (5) (1993) 499–510.
[17] M.K. Denison, B.W. Webb, "*Development and application of an absorption line blackbody distribution function for CO2*", Int. J. Heat Mass Transfer 38 (10) (1995) 1813–1821.
[18] M.K. Denison, B.W. Webb, "*The spectral-line weighted-sum-of-gray-gases model for H2O/CO2 mixtures*", J. Heat Transfer 117 (3) (1995) 788–792.
[19] V.P. Solovjov, D. Lemonnie, B.W. Webb, "*SLW-1 modeling of radiative heat transfer in nonisothermal nonhomogeneous gas mixtures with soot*", J. Heat Transfer 133 (10) (2011). 102701(1–9).
[20] M.F. Modest, H. Zhang, "*The full-spectrum correlated-k distribution for thermal radiation from molecular gas-particulate mixtures*", J. Heat Trans. 124 (1) (2002) 30–38.
[21] Maurente A, Bruno AB, França FHR, Howell JR. "*Non-dimensional wavenumber in fullspectrum k-distribution computations with or without a reference state*". J. Quant. Spectr. Rad. Transfer 2017; 196:222-229.
[22] Solovjov, Vladimir P., et al. "*The rank correlated SLW model of gas radiation in non-uniform media.*" Journal of Quantitative Spectroscopy and Radiative Transfer 197 (2017): 26-44.
[23] Solovjov, Vladimir P., Brent W. Webb, and Frederic Andre. "*The rank correlated FSK model for prediction of gas radiation in non-uniform media, and its relationship to the rank correlated SLW model.*" Journal of Quantitative Spectroscopy and Radiative Transfer 214 (2018): 120-132.
[24] Solovjov, Vladimir P., et al. "*Locally correlated SLW model for prediction of gas radiation in non-uniform media and its relationship to other global methods.*" Journal of Quantitative Spectroscopy and Radiative Transfer 245 (2020): 106857.
[25] M.F. Modest, H. Zhang, "*The full-spectrum correlated-k distribution for thermal radiation from molecular gas-particulate mixtures*", J. Heat Trans. 124 (1) (2002) 30–38.
[26] Ali, H. Belhaj, F. Askri, and S. Ben Nasrallah. "*Comparative study of WSGG and SLW models coupled with control volume finite element method for non gray radiation prediction.*" International journal of thermal sciences 113 (2017): 73-82.
[27] Badger, J., B. W. Webb, and V. P. Solovjov. "*An exploration of advanced SLW modeling approaches in comprehensive combustion predictions.*" Combustion Science and Technology 194.2 (2022): 225-241.
[28] Guo, Hongsheng, et al. "*The flame preheating effect on numerical modelling of soot formation in a two-dimensional laminar ethylene-air diffusion flame.*" Combustion Theory and Modelling 6.2 (2002): 173.
[29] Wang, Lu-Yin, Cody K. Bauer, and Ömer L. Gülder. "*Soot and flow field in turbulent swirl-stabilized spray flames of Jet A-1 in a model combustor.*" Proceedings of the Combustion Institute 37.4 (2019): 5437-5444.
[30] Rault, Taylor M., Rahul B. Vishwanath, and Ömer L. Gülder. "*Influence of m-xylene addition to Jet A-1 on spray structure, flow field and soot production in turbulent swirl-stabilized spray flames in a model combustor*." Combustion and Flame 219 (2020): 258-267.
[31] Rault, Taylor M., Rahul B. Vishwanath, and Ömer L. Gülder. "*Soot formation in turbulent swirl-stabilized spray flames in a model combustor fueled with n-butanol/Jet A-1 blends.*" Fuel 287 (2021): 119452.
[32] Rault, Taylor M., Rahul B. Vishwanath, and Ömer L. Gülder. "*Impact of ethanol blending on soot in turbulent swirl-stabilized Jet A-1 spray flames in a model gas turbine combustor.*" Proceedings of the Combustion Institute 38.4 (2021): 6431-6439.
[33] Guo, Junjun, et al. "*Assessment of weighted-sum-of-gray-gases models for gas-soot mixture in jet diffusion flames*." International Journal of Heat and Mass Transfer 181 (2021): 121907.
[34] Zheng, Shu, et al. "*Effects of C2H2 and C2H4 radiation on soot formation in ethylene/air diffusion flames.*" Applied Thermal Engineering 183 (2021): 116194.
[35] L. S. Rothman, I. E. Gordon, R. J. Barber, H. Dothe, R. R. Gamache, A. Goldman, V.

Perevalov, S. A. Tashkun, J. Tennyson, "*HITEMP, the high-temperature molecular spectroscopic database*", J. Quant. Spectrosc. Radiat. Transfer 111, 2139-2150 (2010).
[36] I.E. Gordon, L.S. Rothman, C. Hill et al., "*The HITRAN2016 Molecular Spectroscopic Database*", Journal of Quantitative Spectroscopy and Radiative Transfer 203, 3-69 (2017).
[37] S. S. Sazhin, An Approximation for the Absorption Coefficient of Soot in a Radiating Gas, Manuscript. Fluent Europe Ltd., 1994
[38] D.P. Schmidt, I. Nouar, P.K. Senecal, C.J. Rutland, J.K. Martin, R.D. Reitz, and J.A. Hoffman, "*Pressure swirl atomization in the near field*", SAE Paper 1999-01-0496 (1999).
[39] M. A. Patterson and R. D. Reitz, "*Modeling the effects of Fuel Spray Characteristics on Diesel Engine Combustion and Emissions.*" SAE Technical Paper 980131, Society of Automotive Engineers, Warrendale, PA, 1998.
[40] W. E. Ranz andW. Marshall. "*Evaporation from drops—I*". In: Chemical Engineering Progress 48(4) (1952), 141—146.
[41] W. E. Ranz andW. Marshall. "*Evaporation from drops—II*". In: Chemical Engineering Progress 48(3) (1952), 173—180.
[42] Wang, Hai, et al. "*A physics-based approach to modeling real-fuel combustion chemistry-I. Evidence from experiments, and thermodynamic, chemical kinetic and statistical considerations.*" Combustion and Flame 193 (2018): 502-519.
[43] Xu, Rui, et al. "*A physics-based approach to modeling real-fuel combustion chemistry–II. Reaction kinetic models of jet and rocket fuels.*" Combustion and Flame 193 (2018): 520-537.
[44] S. J. Brookes and J. B. Moss. "*Prediction of Soot and Thermal Radiation in Confined Turbulent Jet Diffusion Flames*". Combustion and Flame. 116. 486–503. 1999.
[45] C. P. Fenimore and G. W. Jones. "*Oxidation of soot by hydroxyl radicals*". J. Phys. Chem. 71. 593–597.1967
[46] J. B. Moss, S. A. L. Perera,C. D. Stewart, and M. Makida. "*Radiation Heat Transfer in Gas Turbine Combustors*". In Proc. 16th (Int'l.) Symp. on Airbreathing Engines, Cleveland, OH. 2003.

THREE-DIMENSIONAL MODELLING OF AMMONIA/METHANE/AIR TURBULENT FLAMES IN A GENERATED PERFORATED BURNER AND FURNACE

Murat ŞAHİN[1], Mustafa İLBAŞ[2]

1. Mechanical Engineering Department, National Defence University, Ankara; email: msahin@kho.msu.edu.tr
2. Faculty of Technology, Gazi University, Ankara; email: ilbas@gazi.edu.tr

Abstract

This study concentrates on CFD modelling and entrainment effects to achieve distributed regime for ammonia fuel in a perforated burner. Entrainment without decreasing oxygen concentration in air was provided from the flame holder wall of the newly generated perforated burner at 10% and 20% entrainment rates in order to achieve ultra-low pollutant emissions levels. The results showed that the temperature distributions were achieved more uniform and the flame zones became more thinner for all cases studied. This provided more invisible or colorless flame appearance, and as a result of this, more uniform thermal field was achieved without substantial decrease in combustion performance. In terms of evaluation of distributed regime achievement on NOX emission levels, one can say that ultra-low emission levels were achieved with entrainment effects without decrease in oxygen concentration in air.

Keywords: Ammonia, combustion, burner, emission, entrainment

1 INTRODUCTION

With the rapid development of standards of life, the need for energy is increasing. In line with this increasing demand, there are some important problems that fuel, a significant source of energy production, can bring about. And at the very beginning of these problems are the emission values that have greatly jeopardized the future of our world and have recently been the focus of the focus. Many new combustion patterns have been developed, studied and continued to be done to aim to reduce emissions. Şahin [1], developed a perforated burner and studied combustion performance, entrainment effects and emission values on different synthesis gases. In this study, a perforated burner was designed and investigated for root oven gas, biogas and January gas at 10% to 20% to 30% drift rates respectively. As a result, a more homogeneous combustion has been achieved with increased entrainment rates, without a reduction in combustion performance, and it has been stated that the NOx and CO2 emission levels are dropped to ultra-low points outside the root oven gas. Ilbas et al. [2] using a burner that was non-premixed, they observed the effect of the oxidizer on NO emission and temperature when the ammonia was burned. Karyeyen ve Ilbas [3] studied for the turbulent flames of hydrogen-assisted synthesis gas mixtures for a new type of burner developed. The study examined the temperature and emission values of the low calorific synthesis gases derived from charcoal, in the improved burner. As a result, the temperature of the synthesis gases increased by the addition of hydrogen, and the NOX level was initially low owing to a low flame temperature, and it was stated that it increased by the addition of hydrogen. Furthermore, it has been emphasized that the addition of hydrogen on conversion from co2 emission to CO emission is significantly effective. In another study, Chen et al. [4] has implemented a new incineration system to a 300 MW down-fired boiler with a swirl burner. In the study, experiments were tried for 180-250-300 MW forces and a new NOX burn technology was applied to reduce emissions. With this system developed, they indicated a reduction in NOX level without increasing the amount of carbon in the ash. Jang et all. [5] has studied the effect of pulsed oscillating combustion on temperature and emissions in an industrial burner system. Measurements were taken at 3.32m axial distances within an oven with thermal capacity of 3 MW and radial directions at 0.15m intervals. As a result, NO generation in the oscillating flame has been reported to be reduced

by a maximum of 32% and heating performance improved by 9.8% in oscillating combustion. Yu et all. [6] has studied on thermal yield emissions for pre-mixed porous environment type burners. Three types of burners have been examined in the study; metal fiber (MF), ceramic (CM) and stainless-steel wing (SM). As a result of the investigations, MF has the lowest CO emission, SF lowest NOx emission and finally MF has the highest thermal efficiency. It has also been emphasized that the most suitable burner for condensed boiler is metal fiber (MF) burner according to certain standards. Increasingly, more and more study is being emerged in line with the needs of both emission improvement and to improve the quality of combustion.

Finally, the aim of this study is both to achieve uniform results without any changes in combustion performance, and reduction in emissions, with burners and entrainment structures developed in this study. The study conducted examinations for methane and ammonia. The results are obtained with the help of CFD simulations.

2 MATERIALS AND METHOD

In this study, 4 holes have been made that will have entrainment effect on the burner, as shown in figure 1, to improve the combustion quality and improve emission values.

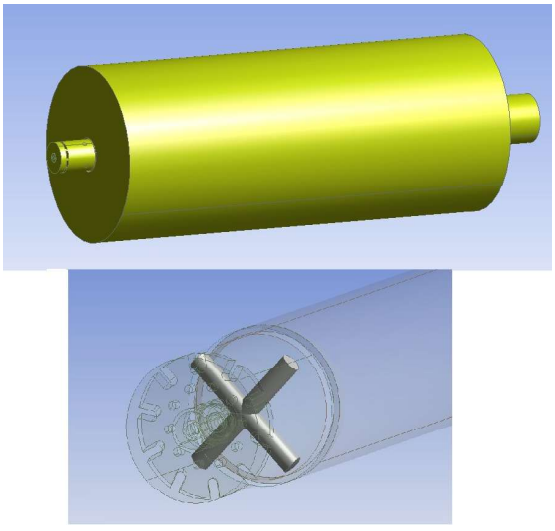


Figure 1. Schematic representation of the combustion chamber and burner structure

The emissions levels with entrainment applied from these created holes are predicted to be improved. Also, the burner dimension designed are 1 m long and 0.4 m in diameter.

The Ansys Fluent software has been used to simulate the study performed. Figure 2 shows the network structure applied to the structure that is designed. The tetrahedron mesh structure is applied to all areas of the design structure. It consists of 1509830 elements in total. For this network structure created, the highest Skewness value was 0.96478 and the lowest Orthogonal quality value was 0,058.

In this study, inspections were conducted for two cases, ammonia gas (100 NH3%) and methane gas (100 CH4%). The specified gases are followed by 10% and 20% entrainment effect respectively. Under these conditions, changes in temperature, speed and NOX emission values have been studied. The different axial positions of the combustion chamber were determined when performing the checks and the characteristics of the specified axial positions at 0.05m intervals of the radial distance were analyzed.

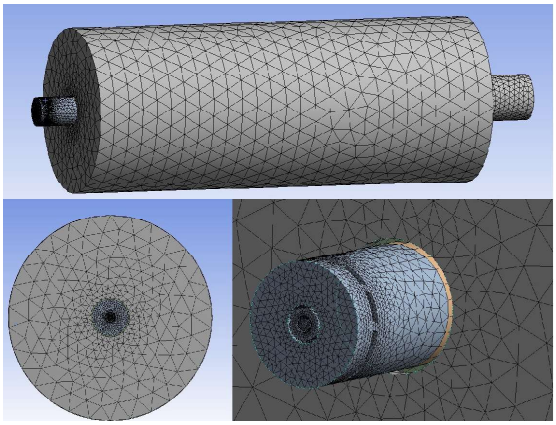


Figure 2. The mesh structure of the design model

In addition, the system modeling was applied the non-premixed combustion model, the standard k-u turbulence model, and the P-1 radiation model. Together, assumptions are accepted that the flow is stable, there is no surface radiation, there is gas radiation, there is no energy flow, and there is no slip boundary condition on the combustion chamber wall. The inlet temperatures for simulation are set to 300K. The presto method is applied for pressure parsing and the second-row wind top diagram is selected. Convergence criteria are set to $10-4$.

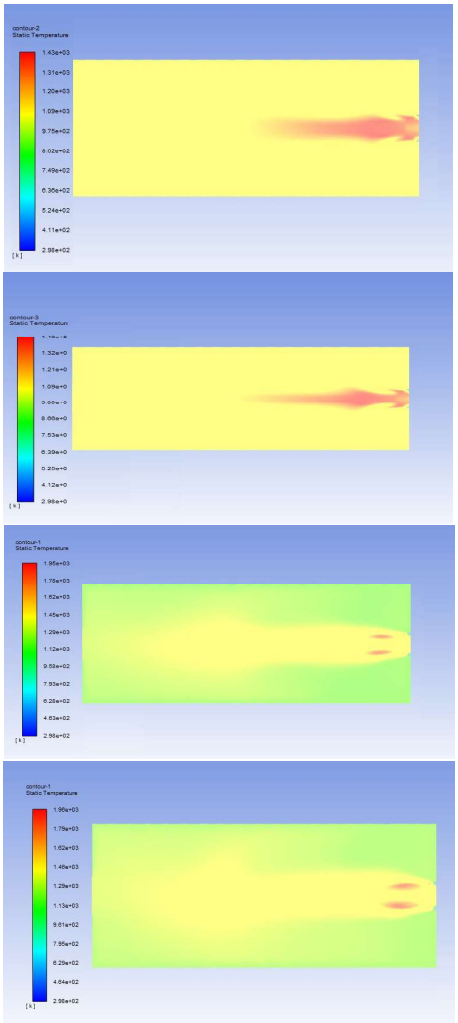
3 RESULTS AND DİSCUSSİON

This section shares the temperature, speed and NOX emission values at different radial distances in the prescribed axial lengths of the study. For axial lengths, 10cm, 30cm, 50cm,

70cm and 90cm are determined respectively. Radially, the values for each length point are taken into account in the 0.5cm ranges.

3.1 Temperature and velocity

Figure 3 shows contours of temperature variations based on different entrainment effect. In these figures, it can be said that at 20% entrainment effect, ammonia gas makes the flame thinner. In addition, the flame is almost lost in methane gas. Also, the increase in entrainment levels makes combustion more homogeneous. As can be seen from the figures, it is clear that at 20% entrainment effect, it is reduced distinction between temperatures. In addition, at 20% entrainment effect, higher temperatures were achieved compared to 10% entrainment effect for both ammonia and methane gas.



a)

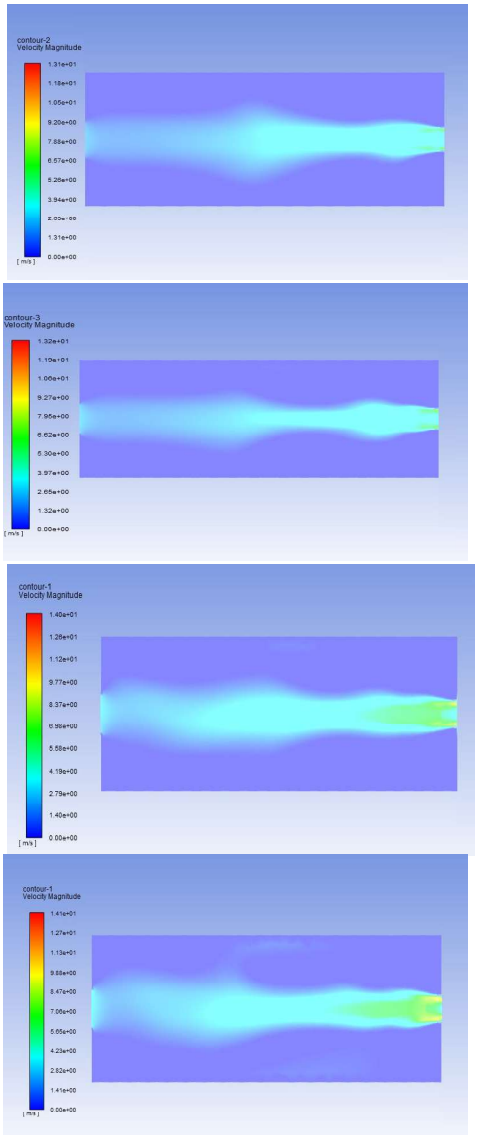
b)

c)

d)

Figure 3. a) temperature contours for ammonia combustion at 10% entrainment effect b) temperature contours for ammonia combustion at 20% entrainment effect c) temperature contours for methane at 10% entrainment effect d) temperature contours for methane at 20% entrainment effect

Figure 4 shows contours of velocity profiles resulting from combustion at 10% and 20% entrainment effect of ammonia gas and methane gas. In this context, both gases show that velocity profiles are get thinner at radial distance. There is also an increase in the velocity at the burner output with a 20% entrainment effect. This confirms that entrainment effect has an effect on the flow being faster. Finally, methane gas may indicate higher velocity at the burner outlet compared to ammonia gas.



a)

b)

c)

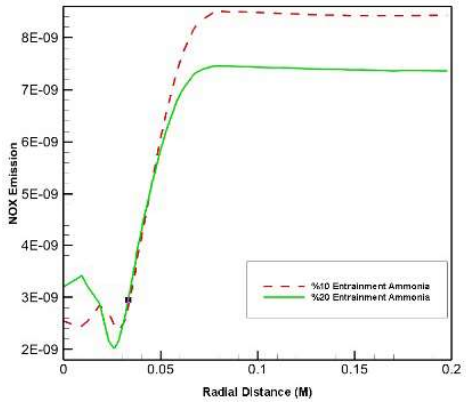
d)

Figure 4. A) Velocity contours for ammonia combustion at 10% entrainment effect b) Velocity contours for ammonia combustion at 20% entrainment effect c) Velocity contours for methane combustion at 10% entrainment effect d) Velocity contours for

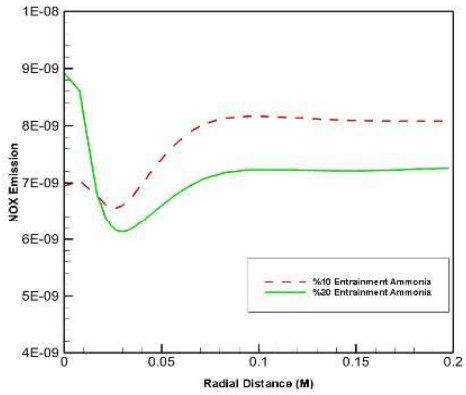
methane combustion at 20% entrainment effect

3.2 NOX Emission

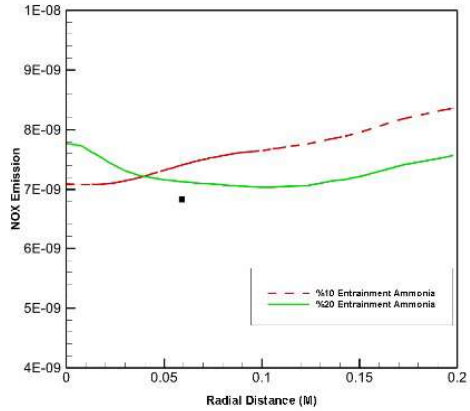
Figure 5 shows the graphs generated in the NOX emission values of the specified length ammonia gas. For a more habitable environment, reducing emission values is very important. At this point, as can be seen in the graph, there has been a reduction in NOX values without changing the oxygen concentration in the air by increasing the entrainment effect. With the used burner system, the NOX emission level are intended to be reduced to a minimum amount.



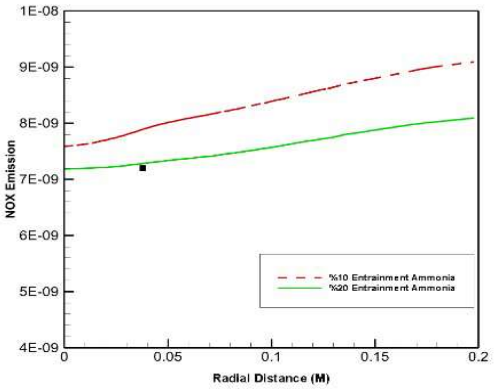
10 cm



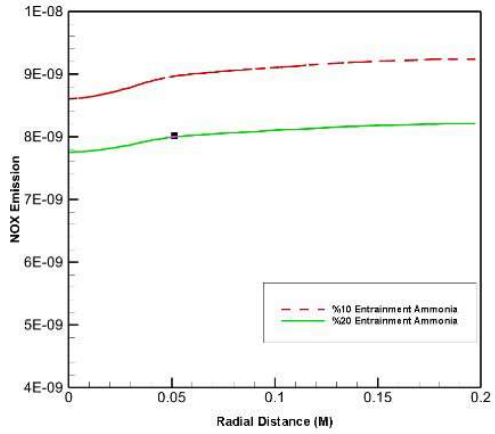
30 cm



50 cm



70 cm



90 cm

Figure 5. NOX emission variations of ammonia gas for radial distances at different axial distances

Unlike ammonia gas, methane gas is estimated to have a very small increase in NOX emissions due to an increase from 10% to 20%. These increases are estimated to have caused a slight increase in the number of NOX formations by the increase the combustion temperature of methane gas in consequence of increase of entrainment effect.

CONCLUSION

In this article, the studied of a designed burner with the CFD software of methane and ammonia gases have been studied on combustion temperature, speed and NOX emission. This burner is designed to achieve homogeneous combustion and low emissions without changing the combustion performance by having a 10% and 20% entrainment effect effect on the combustion chamber. At this point, the temperature and speed profiles for ammonia gas and methane gas were first examined. There has been a more uniform temperature distribution in terms of temperature. In ammonia gas, the flame has been seen with increase the entrainment effect, the flame is further thinned. In methane gas, the flame is almost invisible, along with the

entrainment effect. In addition, there has been a decrease in radial distance with the increase in entrainment effect in terms of speed profiles. As a result of the checks carried out, the effect of the entrainment effect on the flow rate during combustion is also very clear.

In terms of emission values, the NOX levels that may be the result of combustion have been analyzed. As a result of the study, with the increase in the entrainment effect, the reduction in NOX values in the ammonia gas are clearly seen. It is likely that it is very valuable to achieve these levels of reduction without any change in the air oxygen concentration. However, unlike ammonia gas, there have been very little increases in the NOX levels that have emerged along with the increase in the entrainment effect in methane gas. It can be stated that the burner structure, designed for these results, has positive results at both an improvement in emissions values and a uniform combustion.

ACKNOWLEDGEMENTS

The author gratefully thank to the National Defence University and Gazi University.

REFERENCES

[1] Sahin M., Entrainment effects on combustion characteristics of various syngases using a perforated burner, International Journal of Hydrogen Energy, Vol. 47, 15282-15295, 2022

[2] Ilbas, M., Kekul, O., Bektas, A., & Karyeyen, S., Oxidizer effects on ammonia combustion using a generated non-premixed burner, International Journal of Hydrogen Energy, Vol. 47, 12317-12337, 2022

[3] Karyeyen, S., & Ilbas, M., Turbulent diffusion flames of coal derived-hydrogen supplied low calorific value syngas mixtures in a new type of burner: An experimental study, International Journal of Hydrogen Energy, Vol. 42, 2411-2423, 2017

[4] Chen, Z., Wang, Q., Wang, B., Zeng, L., Che, M., Zhang, X., & Li, Z., Anthracite combustion characteristics and NOx formation of a 300 MWe down-fired boiler with swirl burners at different loads after the implementation of a new combustion system, Applied energy, Vol. 189, 133-141, 2017

[5] Jang, B., Oh, C., Ahn, S., Kim, Y., Park, J., Choi, M., & Sung, Y., Nitric oxide emission reduction and thermal characteristics of fuel-pulsed oscillating combustion in an industrial burner system, Energy, Vol. 216, 119263, 2021

[6] Yu, B., Kum, S. M., Lee, C. E., & Lee, S., Combustion characteristics and thermal efficiency for premixed porous-media types of burners, Energy, Vol. 53, 343-350, 2013

SYNTHESIS OF BENTONITE SUPPORTED Ni AND Ni-La CATALYSTS FOR THE STEAM REFORMING OF ACETIC ACID

Damla Dumlu, Ecem Ceylan, Merve Bayrakdar, Serkan Karadeniz, Tolga Kaan Kanatlı and Nezihe Ayas*

Department of Chemical Engineering, Faculty of Engineering, Eskisehir Technical University, Eskisehir; email: nazcan@eskisehir.edu.tr

Abstract

In this study, the production of the hydrogen-rich gas mixture by steam reforming of acetic acid (AA) was performed. Ni and Ni-La catalysts with bentonite support material were synthesized using the wet impregnation method with an active metal loading ratio of 30% by mass. The catalysts were characterized using X-ray diffraction (XRD), X-ray fluorescence (XRF), scanning electron microscope (SEM), Brunauer, Emmett, and Teller (BET) method, Fourier Transform Infrared Spectroscopy (FT-IR) and thermogravimetric analysis (TGA). Activity tests of the catalysts were carried out in a continuous flow tubular reactor at various temperatures (600-700 °C). Gas composition was determined by Micro-Gas Chromatography (μ-GC). The highest hydrogen yield (117.27 mol H_2/kg AA) was obtained at 600 °C with the 30% Ni-La/Bentonite catalyst.

Keywords: Acetic acid, Ni/Bentonite, Steam Reforming, Hydrogen

1 INTRODUCTION

With each passing day, energy demand is increasing. Due to the environmental hazards of fossil fuels such as carbon emissions and global climate change, there has been a shift toward alternative energy sources. Renewable energy sources are divided into two groups called primary and secondary sources. Hydrogen, a secondary energy source, is an energy carrier that has recently become prominent. Hydrogen has the highest energy content per unit mass. It releases only water vapor into the atmosphere when it is used as a fuel. Hydrogen can be produced from renewable and non-renewable sources [1]. Steam reforming is the most widely used method in the industry. Many sources like biomass, natural gas, and alcohol can be reformed using this method. Acetic acid (AA) was chosen because of its reliability and accessibility. The overall reaction of the steam reforming of AA is given in Equation (1) [2].

$$CH_3COOH + 2H_2O \rightarrow 2CO_2 + 4H_2 \quad (1)$$

Due to their high selectivity, nickel-based catalysts are preferred. In this study, Ni/Bentonite (Ni/Bent) and Ni-La/Bentonite (Ni-La/Bent) catalysts were synthesized using bentonite as the support material. Bentonite is an absorber and a swelling clay that is composed of mainly montmorillonite minerals. Moreover, it is a valuable adsorbent with an extensive surface area [3].

This study aims to improve the efficiency of the steam reforming process of acetic acid to produce hydrogen-rich gas. Consequently, 30 wt.% Ni/Bent and Ni-La/Bent catalysts were synthesized using the impregnation method. Bentonite support materials were pre-treated and calcined. Characterizations of the catalysts were carried out and activity tests were performed using the steam reforming method. The effect of reaction temperature and catalyst type on the hydrogen yield was investigated.

2 EXPERIMENTAL

2.1 Catalyst Preparation

Bentonite-supported Ni and Ni-La catalysts were synthesized by the impregnation method. An aqueous solution of active metal salts, $Ni(NO_3)_2$, $La(NO_3)_3$, and bentonite (calcined at 900 °C in dry airflow) was prepared and the impregnation method was applied for 3 hours at 60 °C. The final aqueous solution was aged for 24 hours and after that, it was oven-dried at 110 °C under air atmosphere. Finally, the catalyst was calcined at 600 °C for 6 hours under a dry air atmosphere [4].

2.2 Catalyst Characterization

The catalysts were characterized by XRD, XRF, SEM, BET, FT-IR, and TG analyses. XRD analyses were carried out to determine the crystalline structures of the catalysts with a Rigaku Rint 2200 XRD device at a scanning angle of 0.02°, scanning speed of 4°/min, and in

the range of 5°<2θ<85°. The chemical components of the catalyst have been determined by XRF analysis with Rigaku ZSX primus spectrometer. SEM analyses were performed to determine the surface morphology and chemical composition of catalysts with the ZEISS SUPRA 50 VP SEM device. Pore size, pore volume, and surface area of the catalysts were measured by a Micrometrics ASAP 2020 BET device. Functional groups of the catalysts and support material were investigated with a Thermo Scientific Nicolet IS10 FT-IR device at a scanning speed of 60°/min, 4cm^{-1} resolution in the range of 400-4000 cm^{-1}. Thermogravimetric analyses of the catalysts were conducted by using Netzsch STA 6000 TGA device with a nitrogen flow rate of 50 mL/min, and a heating rate of 10 °C/min in the temperature range of 30-850 °C.

2.3 Activity Tests

Activity tests of Ni/Bent and Ni-La/Bent catalysts were carried out in a continuous flow tubular reactor. 2 mL silicon carbide and 0.5 g catalyst were mixed to prepare the catalyst bed. The feed rate of the AA-water mixture (1:2 by volume) was constant at 0.12 mL/min, and the N_2 flow rate was 0.1 L/min for each experiment. The reaction temperatures were 600 and 700 °C. The composition of the gas mixture obtained from steam reforming was determined through μ-GC analysis.

3 RESULTS AND DISCUSSION

3.1 Catalyst Characterization

XRD Results

XRD patterns of the catalysts and support material are shown in Figure 1.

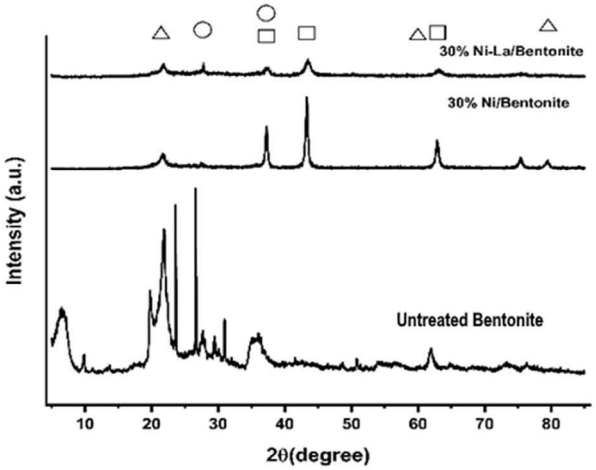


Figure 1. XRD patterns of Bentonite-supported catalyst
(○:Quartz, Δ:Montmorillonit, □:NiO)

XRD patterns of bentonite and bentonite-supported catalysts show that bentonite mostly contains peaks of montmorillonite and quartz minerals. Peaks of the montmorillonite were obtained at 2θ=21º, 62º, and 79º, and other characteristic peaks of quartz were obtained at 2θ=27º and 37º. Peaks of NiO were observed at 2θ= 37º, 43º, and 63º. The peak intensity of montmorillonite decreases as the amount of active metal loaded onto the support material increases [5].

The average crystal sizes of nickel at 37º, 43º, and 63º for 30% Ni/Bent catalysts were calculated. Also, for the 30% Ni-La/Bent catalyst, the crystal size of nickel at 43º and the crystal size of lanthanum at 27º and 77º were calculated. The crystal size of nickel metal was 18.79 nm for the 30% Ni/Bent catalyst. The crystal size of nickel metal was 9.68 nm, and the crystal size of lanthanum metal was 43.56 nm for the 30% Ni-La/Bent catalyst.

XRF Results

The chemical compositions (by mass) of bentonite and bentonite-supported catalyst were determined by XRF analysis. XRF results of the catalyst are shown in Table 1.

Table 1. XRF results of Ni/Bent catalysts

Component (wt. %)	Bent	30% Ni/Bent	30% Ni-La/Bent
NiO	-	35.30	21.60
La_2O_3	-	-	11.50
MgO	1.74	1.07	1.05
Al_2O_3	13.48	9.23	9.19
SiO_2	70.72	48.90	49.40
LOI*	7.86	1.46	1.98
Other**	6.20	4.04	5.28

*Loss of ignition

** Na_2O, P_2O_5, MnO, TiO_2, MoO_3, SO_3, Cr_2O_3, Fe_2O_3, Co_2O_3, CaO, K_2O

XRF spectroscopy of the catalysts shows that the targeted active metal ratios were successfully reached. Metal loadings are higher than the theoretical calculations because the loaded metals were in oxide form.

BET Results

BET results show that 30% Ni/Bent has a higher surface area and pore volume than 30% Ni-La/Bent however 30% Ni-La/Bent has a larger mean pore size. When the La and Ni metal were used together, the surface area and pore volume

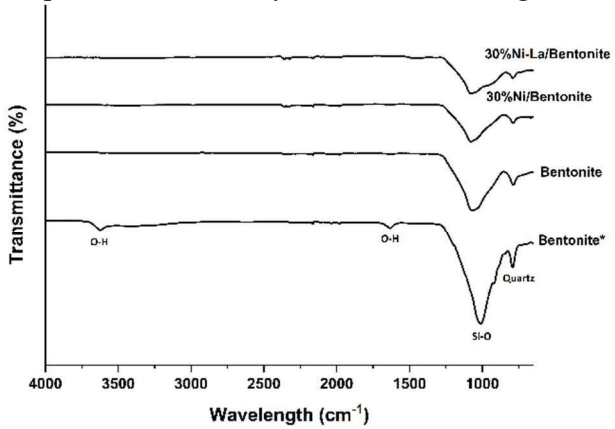
decreased, and the mean pore size increased. BET results of the catalysts are shown in Table 2.

Table 2. BET analysis results

Material	Surface Area (m^2/g)	Mean Pore Size (nm)	Pore Volume (cm^3/g)
30% Ni/Bent	33.26	8.87	0.07
30% Ni-La/Bent	18.10	10.35	0.05

FT-IR Results

The FT-IR spectra of bentonite and bentonite-supported catalyst were investigated. The bending vibration of Si-O corresponds to the band of 1011 cm^{-1}. The peaks of 1633 cm^{-1} and 3406 cm^{-1} were attributed to O-H bonding of water molecules and stretching vibration of the O-H groups in bentonite was observed at 3626 cm^{-1}. The bending vibration of Al-O-Al corresponds to the band of 923 cm^{-1}. The peak at 3382 cm^{-1} shows the H-O-H groups of water molecules that were adsorbed on the bentonite's surface [6]. FT-IR spectra of the catalyst are shown in Figure 2.



*Untreated Bentonite

Figure 2. FT-IR spectra of Bentonite and Bentonite-supported catalysts

SEM-EDS Results

SEM-EDS analyses were performed for 30% Ni/Bent and Ni-La/Bent catalysts. EDS analysis shows that the NiO contents were 75.17% and 28.90% for Ni/Bent and Ni-La/Bent catalysts, respectively. The NiO content obtained by the XRF analysis of Ni/Bent and Ni-La/Bent catalysts were %35.3 and %21.6, respectively. The results of the EDS and XRF analysis are different from each other because the EDS analysis is performed on a single point of the catalyst surface.

TG Analysis Results

TG analysis of bentonite and calcinated bentonite show that the mass losses were 2.5% and 1% respectively.

3.2 Activity Tests

Effect of the Catalyst Type

The effect of the catalyst type on gaseous product yield is shown in Figure 3.

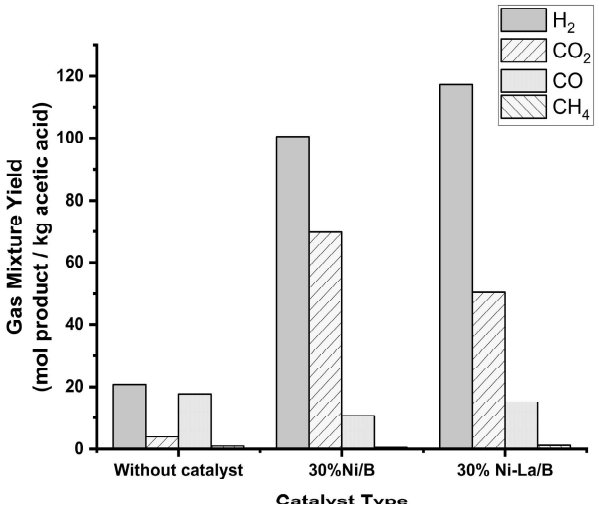


Figure 3. Effect of the catalyst type on gaseous product yield (600 °C, feed rate of 0.12 mL/min AA:H_2O, 0.1 L/min N_2)

Figure 3 shows that the Ni/Bent catalyst causes a 4 times increase in the hydrogen yield and the addition of La to the catalyst causes an even higher increase.

Effect of Reaction Temperature

The hydrogen yield of the 30% Ni-La/Bent catalyst reached its highest value at 600 °C and decreased when the temperature was increased. The highest hydrogen yield was obtained as 117.27 mol H_2/kg AA at 600 °C.

The effect of reaction temperature on the hydrogen yield is shown in Figure 4.

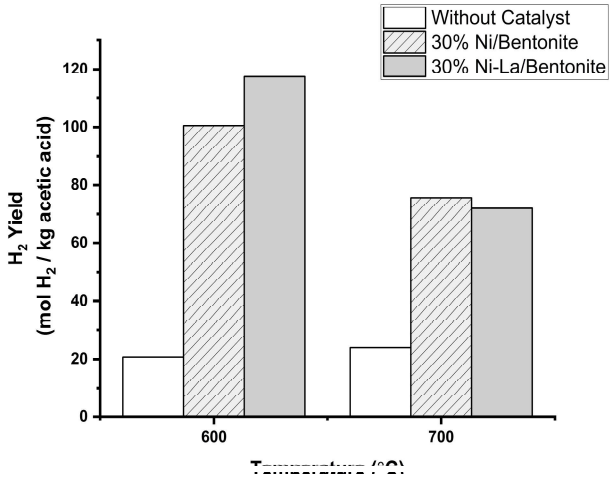


Figure 4. Effect of reaction temperature on gaseous product yield (Feed rate of 0.12 mL/min AA:H_2O, 0.1 L/min N_2)

4 CONCLUSION

In this study, the production of hydrogen-rich gas from acetic acid by using bentonite-supported catalysts was investigated. The effect of reaction temperature and catalyst type on hydrogen yield was examined by activity tests. The highest hydrogen yield was obtained as 117.27 mol H_2/kg AA at 600 °C for 30 wt.% Ni-La/Bent. It was determined that the hydrogen yield increased with the reaction temperature and when the catalyst was bimetallic.

ACKNOWLEDGEMENTS

This study was supported by TÜBİTAK 2209-A Research Project Support Programme for Undergraduate Students Commission under grant no: 1919B012102344.

REFERENCES

[1] F. Tutar and E. Mehmet, Geleceğin enerjisi: Hidrojen ekonomisi ve Türkiye. *Uluslararası İktisadi ve İdari İncelemeler Dergisi*, Vol. 6, 2011.

[2] G. Chen, J. Tao, C. Liu, et al., Hydrogen production via acetic acid steam reforming: a critical review on catalysts. *Renewable and Sustainable Energy Reviews*, Vol. 79, pp. 1091-1098, 2017.

[3] M. B. Yücel and Ö. Gül, Dünyada ve Türkiye'de Bentonit, *Maden Tetkik ve Arama Genel Müdürlüğü,* 2018.

[4] T. Başara, Determination of the synthesis and activity of the catalyst used in the method of production of H2 from methane, *Master's thesis, Eskişehir Technical University*, 2021.

[5] L. Zhirong, M. A. Uddin and S. Zhanxue, FT-IR and XRD analysis of natural Na-bentonite and Cu (II)-loaded Na-bentonite. *Spectrochimica Acta Part A: Molecular and Biomolecular Spectroscopy*, Vol. 79(5), pp. 1013-1016. 2011.

[6] Y. S. Chang, P. I. Au, N. M. Mubarak, et al., Adsorption of Cu (II) and Ni (II) ions from wastewater onto bentonite and bentonite/GO composite. *Environmental Science and Pollution Research*, Vol. 27(26), pp. 33270-33296, 2020.

CHAR REACTIVITY ASSESSMENT OF HIGH ASH COAL IN PACKED BED ENVIRONMENTS - EXPERIMENTAL INVESTIGATIONS

Shirish Kumar Sharma[1], Anand M Shivapuji[2], S. Dasappa[3]

1. Interdisciplinary Centre for Energy Research, Indian Institute of Science, Bangalore-560012, India
   Email: shirishs@iisc.ac.in
2. Centre for Sustainable Technologies, Indian Institute of Science, Bangalore-560012, India
   Email: anandms@iisc.ac.in
3. Centre for Sustainable Technologies, Indian Institute of Science, Bangalore-560012, India
   Email: dasappa@iisc.ac.in

Abstract

This paper addresses the char conversion phase as a part of the two-stage gasification, an emerging technology for generating high calorific gas. Control experiments are carried out to establish the char reactivity under relevant environments for the second stage of the reactor**.** The char is generated by subjecting coal chunks to an oxidative pyrolysis environment at 850 deg C in a furnace, closely imitating the condition of the reactor. Tight control is exercised over oxidative pyrolysis to ensure devolatilization only. The devolatilized char from oxidative pyrolysis is sized and segregated within 1.0 to 1.4 mm. In a representative packed bed furnace, 50 g of char particles are subjected to a controlled externally supported thermal environment at 800 degC with a continuous supply of pure steam. The evolved dry gas (post condensation at -6 deg C) flow rate was 1.3 +/- 0.3 LPM. The concentration of CO, CO_2, CH_4, and H_2 was 7, 26, 1, and 66 %, respectively. The steady rate of carbon conversion and reactivity of high ash coal char was 10.8 g/hr and 0.38 g/g-hr.

Keywords: high ash coal, two-stage gasification, char reactivity, packed bed

1 INTRODUCTION

High ash content in coal, by virtue of potential ash fusion and agglomeration renders conventional gasification approaches either impractical OR prohibitively expensive. Ash agglomeration and clinker formation, primarily due to high localized temperatures, are required to be addressed through appropriate technological interventions to enable the gasification of high ash coal [1,2]. To address these issues, research at the Indian Institute of Science focuses on staging the volatile release and char conversion phases, which have different conversion times. The challenge of high ash coal gasification has been addressed by separating the oxidation reactions and oxy-steam gasification zone into two stages. In stage one, an appropriate mechanism enables controlling the residence time of the coal in the mobile phase. The devolatilized char generated is subsequently transferred to the second stationary bed reactor for Oxy-steam gasification. The coal is fed in the highly mobile phase in the first stage, while in the second stage, the char in the form of the fixed bed collectively enables the handling of high ash coal without facing any ash fusion issues. The two separate but connected stages allow independent control over combustion and gasification reaction, which otherwise happen in close vicinity and affect each other in terms of temperature, gaseous environment, and material flow. A pilot scale gasification system of 150 kW thermal gasification capacity has been designed and tested with a range of high ash Indian coal. As one of the stages of this technology uses a fixed bed configuration for char steam gasification, the behavior of char in the reactor should be predicted for designing the reactor.

The rate of steam char reaction is a crucial parameter when deciding the size of the reactor. Generally, the kinetic parameters of TGA are taken as a measure of reactivity of coal/coal char. However, it poses limitations beyond particle size due to the diffusion-dominated process [3,4]. Further, the reactivity of solid fuel in fixed bed reactor conditions depends on many independent parameters like the composition of gaseous reactants, temperature, the composition of inorganic compounds in char, porosity, bed height, and extent of conversion [5]. In a packed bed reactor, many of those parameters varied

with time and space. This paper presents results from packed bed experiments for steam char reactions. These experiments are designed by simulating a portion of a pilot-scale fixed bed reactor for steam char gasification for high ash Indian coal.

2 MATERIAL AND METHODS

2.1 Materials

High ash Indian coal is used for preparing char. The value of moisture, volatile content, fixed carbon, and ash content of the coal are 10, 25, 42, and 23 on an absolute basis. The char is prepared through oxidative pyrolysis by subjecting a group of big chunks of coal (approximately 25-30mm) to a furnace maintained at 850 degC. As the first stage of two-stage gasification is also oxidative pyrolysis, this method of char preparation closely imitates the condition of the reactor. Immediately after the flaming, char particles are taken out and cooled by indirect heat transfer from flowing water at 5 ˚C. The final weight of the char is measured, and the weight loss during char preparation corresponds to the volatile content of the coal as per proximate analysis with an accuracy of ± 5%. After that, the char particles are sized and segregated to sizes between 0.5 to 1 mm. These particles are stored in an airtight container for further use. The different coal chunks are representatives of varying coal seams that have different chemical properties and inorganic contents. This method of bulk material preparation normalizes any form of inconsistencies in the coal char.

2.2 Experimental setup

The schematic diagram of the experimental setup is shown in figure 1. The packed char bed created inside a cylindrical steel reactor (100 x ⌀50 mm) is kept inside a controlled temperature furnace with four thermocouples placed height-wise at four locations in the char bed. The cylindrical reactor has a provision for providing steam from the bottom. Steam is generated by an electrically heated evaporative tube boiler and superheater. The feed water rate controls the flow of steam through a peristaltic pump. To optimize the steam utilization, the remaining excess steam after the char steam reaction is condensed with the help of a condenser maintained at 5 ˚C. The gas from the condenser passes through a cleaning unit consisting of an impinger bottle filled with iso-propyl-alcohol and held at -6 ˚C. For adsorption of remaining impurities and moisture of the generated gas, it is allowed to pass through the columns of silica gel and calcium chloride particles. The clean gas was sent to the gas analyzer (Sick Maihak S-715) for measuring the gas composition and flaring afterward. A three-way valve is kept between cleaning unit and gas analyzer that is used to divert the flow to gas flow measurement by bubble flow meter intermittently. The gas is again switched back to the gas analyzer quickly after taking flow measurements.

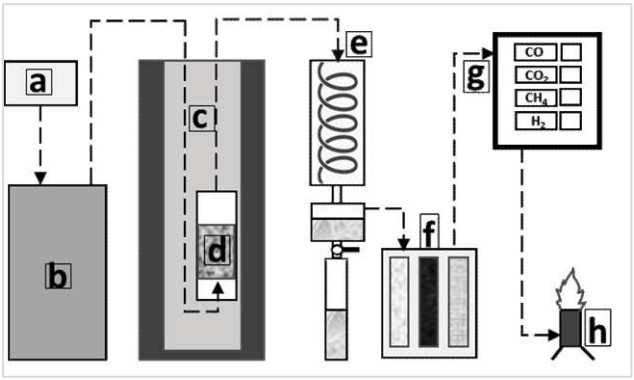


Figure 1: Schematic diagram (a) Peristaltic pump, (b)Boiler and superheater, (c) controlled temperature furnace, (d) Packed bed of char, (e) Condenser and condensate collection, (f) Cleaning columns, (g) Gas analyzer, and (h) flare

2.3 Methodology

The temperature-controlled furnace is switched on and allowed to reach 850 ˚C. Fifty grams of devolatilized char from high ash coal is placed inside the packed bed reactor over a fine mesh of 0.25 mm. The height of the char bed was 40 mm. The packed bed assembly is shifted inside the furnace after it attains 850 degC. Steam at 500 degC supplied to the bottom of the packed bed within 5 mins of placement of the packed bed reactor in the furnace. The steam is provided through the char bed at a rate of 7.2 g/min, controlled by a peristatic pump. The temperature of the bed at four locations is monitored. The experiment duration was 1 hr after reaching a steady temperature in the char bed. Gas generated by the reaction of char and steam is measured for flow rate and gas composition. The carbon conversion rate and reactivity of the char are determined by the flow rate of gas and composition.

2.4 Expressions

Carbon conversion rate is the rate of carbon leaving the reactor in the form of gaseous species like CO, CO_2, and CH_4. The expression for Rate of Carbon Conversion (CC) can be given by

$$CC = V * \sum_{i=1}^{3} X_{gas} * \rho_{gas} * \frac{MW_{carbon}}{MW_{gas}} \quad (1)$$

Where,

V = Total flowrate of gas generated

X_{gas} = Volume fraction of gas

ρ_{gas} = Density of gas

MW_{carbon} = Molecular weight of carbon

MW_{gas} = Molecular weight gas

And

i = 1 for CO

= 2 for CO_2

= 3 for CH_4

The reactivity of carbon is determined by dividing the carbon conversion rate by the instantaneous mass of carbon remaining at a given time step dt in the char bed. The instantaneous mass of carbon in the char is determined by subtracting cumulative carbon lost in the form of gas from the initial weight of carbon in the char till the point of interest.

$$\text{Reactivity} = \frac{1}{m}\left(\frac{dm}{dt}\right) \quad (2)$$

Where,

dm = mass loss in the form of carbon in the gas

m = remaining carbon in the char bed at given time step

3 RESULTS AND DISCUSSION

3.1 Temperature variation

The variation of the temperature inside the bed with time is shown in figure 2. It can be observed in figure 2 that the temperature in the char bed increases at all four locations with time and reaches to steady state within 10 min. The furnace temperature was set to 850 ˚C; however, at a steady state, the reactor temperature became asymptotic after going to 810 ˚C within 10 min. Hence there was a difference of 40 ˚C between the furnace temperature and the bed temperature throughout the next 1 hr. The reaction of char and steam is endothermic in nature. However, the effect of its endothermicity on the temperature was minimal with respect to the height of the char bed. There could be two reasons for the invariance of the temperature inside the bed; first, for the small height of 40 mm, the temperature effects are equally distributed by conductive and convective heat transfer, and secondly, there is enough heat pumped inside the reactor chamber from the conducting wall of the furnace that the endothermic effect of steam char reaction at any place of the reactor is compensated.

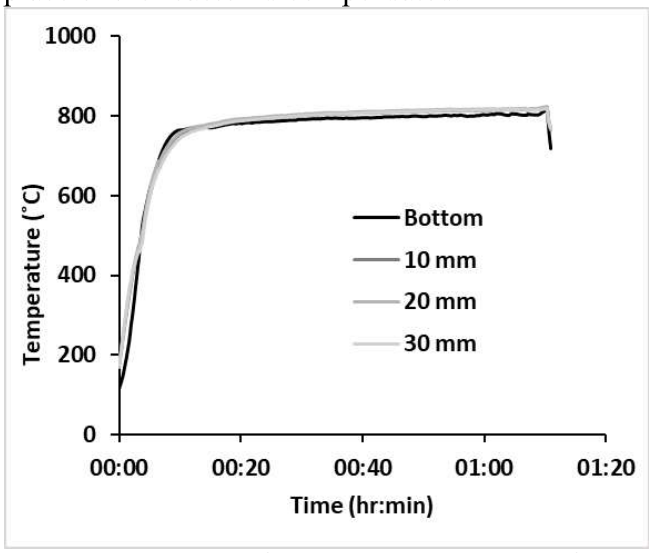


Figure 2: Variation of temperature with time at four different locations from the bottom

3.2 Gas composition

The steam reacts with the char and produces a mixture of CO, CO_2, CH_4, and H_2. The variation in the composition of gases with time is shown in figure 3. The gas composition remains stable after the initial transient phase. The concentration of CO, CO_2, CH_4, and H_2 at steady state were 7, 26, 1, and 66%, respectively. As the composition became constant after reaching a steady state, we can infer that the important elementary reactions, their intrinsic reaction rate, and contributions to gas generation also became constant.

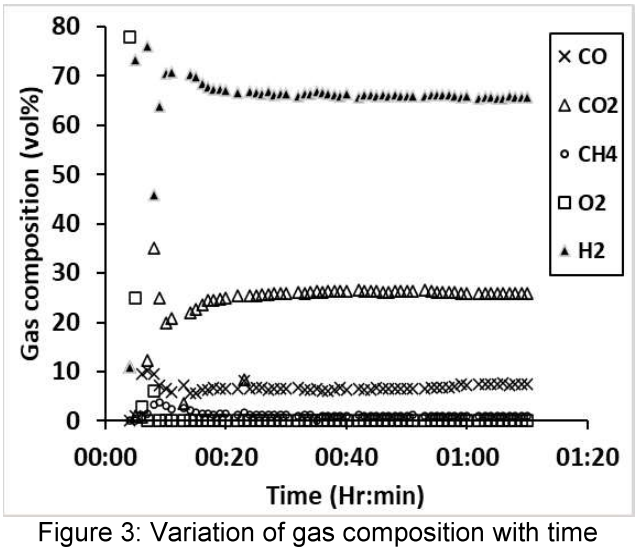


Figure 3: Variation of gas composition with time

The important reaction of a steam char gasification system is given below:

$C + H_2O \rightarrow CO + H_2$; Δh = 131 kJ/mol (a)

$CO + H_2O \rightarrow CO_2 + H_2$; Δh = -41 kJ/mol (b)

At the active sites of char, carbon reacts with steam and generates equal moles of CO and H_2, as mentioned in reaction (a). However, CO generated by reaction (a) further reacts with steam and produces CO_2 and H_2 given by reaction (b). Due to the combined effect of reactions (a) and (b), the H_2 concentration is higher than any other gaseous component. Reaction (b) is the Water gas shift reaction that is slightly exothermic and reduces the overall calorific value of gas. However, the higher H_2/CO is an essential requirement for synthesizing a specific class of chemicals [5, 6].

3.3 The flow rate of gas generated

Figure 4 shows the flow rate variation of gas generated from steam char reaction with time.

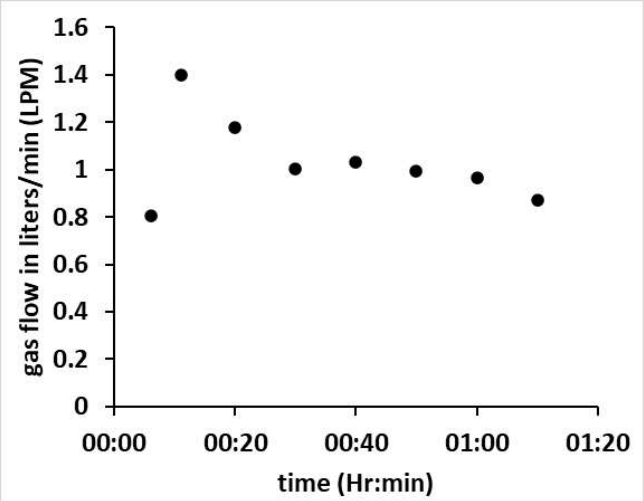


Figure 4: Variation of flowrate of gas with time

We can see in figure 4 that the flow rate of the gas increases rapidly after steam is supplied, peaks at 1.4 LPM at around 10 min, and then decreases slowly for the next one hr. We have seen in the previous discussion that the composition of the gas does not change during the experiments. In other words, the reactions at the carbon surface and their rates per unit mass are not changing, which results in consistent gas composition. However, the available mass of carbon decreases as the reaction proceeds forward. Therefore, it can be interpreted as the overall reaction system being scaled down with respect to the available mass of the carbon in the bed. Hence the yield of generated gas also decreases.

3.4 Rate of carbon conversion

The rate of carbon conversion is the rate at which carbon leaves the char bed due to the reaction of carbon and steam. In a practical case, the feed rate of fuel/carbon is decided based on the rate of carbon consumption or carbon conversion. Alternatively, carbon conversion rate is adjusted by the process parameters to achieve the required feed consumption.

With the help of gas flow rate and gas composition, the carbon conversion rate is determined, as shown in figure 5. The gas composition becomes invariable after an initial transient period of 10 min; therefore, the flow rate of gas governs the rate of conversion. The similarity in the trends of flow rate and rate of carbon conversion can be observed by comparing figures 4 and 5.

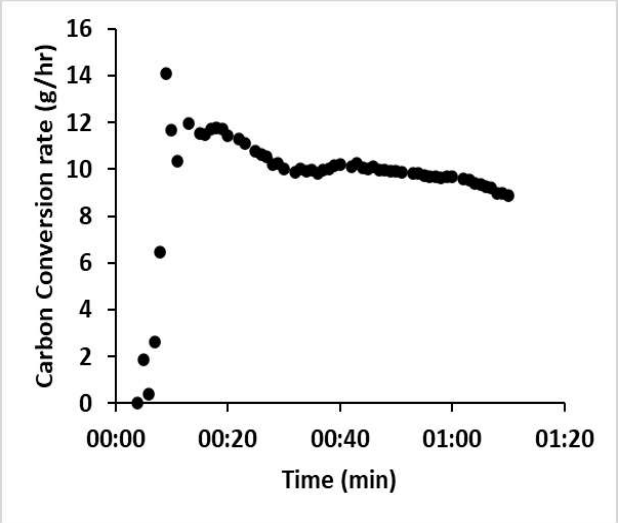


Figure 5: Variation of carbon conversion with time

Carbon conversion also decreases with the progress of the reaction, similar to the gas flow rate.

The dependence of the carbon conversion on the mass of available char is an indication of the volumetric participation of the bed in generating the gas. The probable reason for volumetric involvement of the char bed is explained as follows. Steam is supplied from the bottom of the char bed. At the constant temperature and set feed rate of steam in this experiment, the rate of reaction is not enough to consume all supplied steam, and hence the remaining steam passes on to the next layer and so on. This process has roughly imitated till the topmost layer, and therefore the entire bed

participates in producing gas. In other words, steam is available for reacting to each particle in the bed.

We have discussed the behavior of char bed as a whole in the last paragraph. However, it is also essential to understand how an individual char particle behaves for a given gaseous reactant like steam. One of the crucial aspects of the char steam reaction is the spatial distribution of reaction sites in the particle. At the individual particle level, one possible mechanism of the steam char reaction may be limited to the particle's surface. However, there is enough literature to show that a steam char reaction can be modeled as a volumetric reaction inside the particle, and there is minimal effect of particle size for a single char particle [7, 8].

This volumetric nature simplifies the approach for the scaling process. However, due to the small height of the bed, the effect of hydrogen inhibition and progressive dilution of the reactants by simultaneous generation of products cannot be captured in this work. Still, the process simulates the reactor condition better than a TGA experiment.

3.5 Reactivity of coal char

Char reactivity is determined by dividing the instantaneous carbon conversion rate by the quantity of carbon remaining in the bed. The determination of carbon remaining in the bed needs some analytical calculation. It can be found by the difference in initial carbon content in the bed and carbon gasified till a given time. To get the carbon converted/gasified till a given time, the carbon conversion rate is integrated over time, as shown in figure 6.

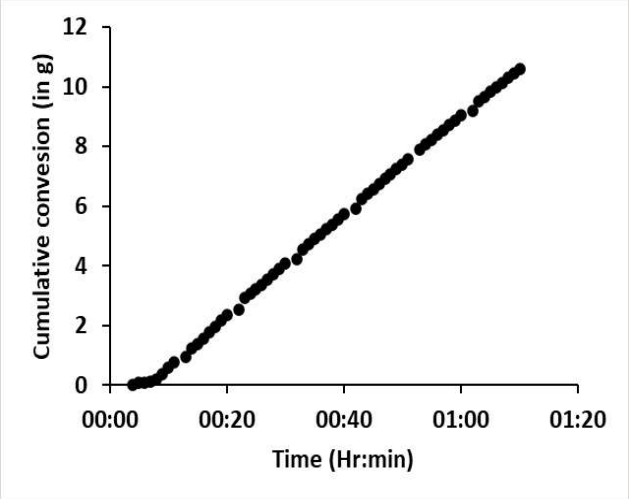


Figure 6: cumulative loss of carbon with time

The evolution of the average reactivity of the char bed with time is shown in figure 7.

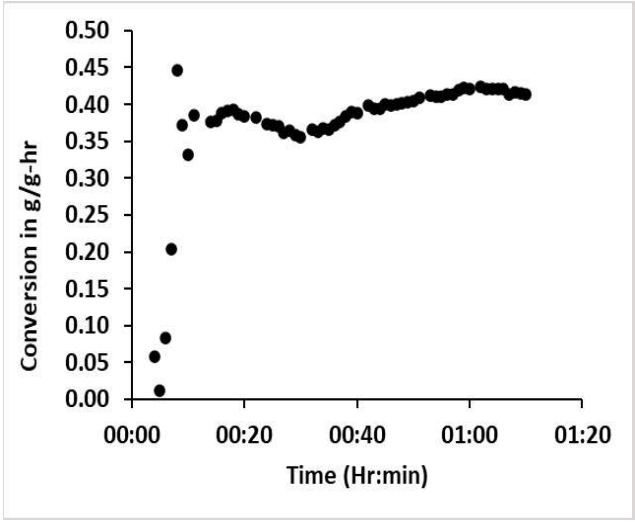


Figure 7: Variation of char reactivity.

In one hr of operation, 33% of carbon in char has been converted to gaseous species. In this range, the variation in reactivity is not much except a slight increasing trajectory which is in line with the literature [7]. The char reactivity dwells between 0.36- 0.41g/g-hr after reaching a steady state. The normalization with the instantaneous mass of carbon resulted in a stable number for the char's reactivity, unlike the carbon conversion rate decreasing continuously. The constant gas composition and a steady number of char reactivity establish volumetric participation of the char bed and reduce the complexity of the scaling.

4 CONCLUSION

The char reactivity of the of the steam char reaction is an essential parameter while designing the reactor. The general approach is to simulate the reactor by determining the reactivity of the char by TGA experiments. Controlled experiments have been carried out to replicate the reactor-like condition in a temperature-controlled packed bed with char as solid fuel and feed material. It has been found that the gas composition became stable with time, after initial transient period of 10 mins whereas the gas flow rate decreases gradually after reaching the peak. This behavior is attributed to constant elementary reactions, their intrinsic reaction rate, and contributions to gas generation. The reactivity calculated for experiments of one hr is found to be around 0.36-0.41 g/g-hr. The result from this

experiment can be used for scaling the system and for benchmark to verify the simulation results.

ACKNOWLEDGEMENTS

I thank the Department of Science and Technology, Government of India, for financial support for the work under the Flagship program "COAL 2017". I am also thankful to the Ministry of Education, Government of India, for the help in the form of the Scholarship during this work.

REFERENCES

[1] V. Krishnamoorthy, and S.V. Pisupati, "A critical review of mineral matter related issues during gasification of coal in fixed, fluidized, and entrained flow gasifiers". *Energies, 8(9), pp.10430-10463.* 2015.

[2] Raj Gupta, T. Wall, and L. Baxter, eds. Impact of mineral impurities in solid fuel combustion. Springer Science & Business Media, 2007.

[3] Y. Zhang, P. Geng, & Y. Zheng, "Exploration and practice to improve the kinetic analysis of char-CO2 gasification via thermogravimetric analysis". *Chemical Engineering Journal, 359, 298-304.* 2019.

[4] Q. Xu, S. Pang, & T. Levi, "Reaction kinetics and producer gas compositions of steam gasification of coal and biomass blend chars, part 1: Experimental investigation". *Chemical engineering science, 66(10), 2141-2148.* 2011.

[5] A. Ephraim, V. Pozzobon, O. Louisnard, D. P. Minh, A. Nzihou, & P. Sharrock, "Simulation of biomass char gasification in a downdraft reactor for syngas production". *AIChE Journal, 62(4), 1079-1091. 2016.*

[6] A. Singh, A. Gupta, N. Rakesh, A. M. Shivapuji, & S. Dasappa, "Syngas generation for methanol synthesis: oxy-steam gasification route using agro-residue as fuel". *Biomass Conversion and Biorefinery, 12(5), 1803-1818. 2022*

[7] C. Guizani, M. Jeguirim, R. Gadiou, F. J. E. Sanz, & S. Salvador, "Biomass char gasification by H2O, CO2 and their mixture: Evolution of chemical, textural and structural properties of the chars". Energy, 112, 133-145. 2016

[8] Jayaraman Kandasamy, and Iskender Gokalp. "Effect of char generation method on steam, CO2 and blended mixture gasification of high ash Turkish coals." *Fuel 153: 320-327. 2015*

COMBUSTION CHARACTERISTICS AND KINETICS OF BLENDS OF LIGNITE WITH EGGSHELL

Sena Erkent[1], Sema Yurdakul[1], Barış Gürel[2], Karani Kurtuluş[2], Savaş Özün[3]

1. Environmental Engineering Department, Süleyman Demirel University, Isparta; e-mail: senaaerkent7@gmail.com, semayurdakul@sdu.edu.tr
2. Mechanical Engineering Department, Süleyman Demirel University, Isparta; e-mail: barisgurel@sdu.edu.tr, karanikurtulus@sdu.edu.tr
3. Mining Engineering Department, Süleyman Demirel University, Isparta; e-mail: savasozun@sdu.edu.tr

Abstract

In this study, the co-combustion behavior of a local low calorific Turkish lignite with eggshell was investigated by a thermogravimetric analysis (TGA). Lignite was blended with eggshell in the range of 25–75 wt. % to examine their co-combustion characteristics and kinetics under the dry air atmosphere via a non-isothermal thermogravimetric method behavior at various heating rates of 5, 10, 15, and 20 °C/min. With the addition of eggshell, decomposition temperatures of the blends decreased. However, burnout temperatures increased. The combustion kinetics were calculated using isoconversional methods with Flynn−Wall-Ozawa− method. The activation energies of the lignite, 75lignite+25eggshell, 50lignite+50eggshell, 25lignite+75eggshell and 100egsheel samples were found to be 77.12 kJ/mol, 104.17 kJ/mol, 125.01 kJ/mol, 121.31 kJ/mol and 157.90 kJ/mol, respectively. In the study, comprehensive combustion index, flammability index and ignition index of the blends were also investigated. Consequently, with the addition of the eggshell into the lignite, ignition performance, flammability performance and comprehensive combustion behavior of the 50lignite+50eggshell, 25lignite+75eggshell and 75lignite+25eggshell blends were found to be better than a single lignite.

Keywords: TGA, Eggshell, Combustion characteristics, Fllyn-Wall-Ozawa

1 INTRODUCTION

Turkey ranks ninth in the world with a share of 1.5% in egg production [1]. In 2020, 19 297 591 000 chicken eggs were produced in Turkey and approximately 93 000 to 111 600 tons of waste eggshell was produced as a result of this production. Furthermore, the monthly produced waste eggshell amount coming from pasteurized egg producer companies in Turkey ranges from 40 to 180 tons. Among the eggshell disposal methods, the most basic ones are to send to landfills, mixing with soil, or to use as an additive to poultry feed. Among these alternatives, landfills seem to be the most suitable option as operating costs are taken into account. However, during the disposal of the eggshells in the landfills, some problems such as odor, flies etc. arising from microbiological deterioration are observed. In the meantime, if landfill is selected as a disposal option of the eggshells, the thermal value of the waste egg shells will not be utilized. Therefore, thermochemical processes can constitute an alternative to landfills for the disposal of waste eggshells.

Besides, Turkish lignites cannot be burned efficiently in conventional combustion systems due to their high moisture, ash and sulphur content and low heating value; it is understood that co-combustion of lignite and biomass wastes together in fluidized bed boilers will be the most environmentally friendly approach in the disposal of such wastes.

Therefore, this study was aimed at evaluating the thermal properties and activation energies of the waste egg shell and local Kale Lignite are co-combusted in a thermogravimetric analyzer.

2 MATERIAL AND METHODS

In this study, for the co-combustion experiments Kale lignite which is a local lignite was used. The waste egg shells obtained from the central cafeteria of Süleyman Demirel University were washed with tap water and then deionized water.

The washed eggshells were sieved to a particle size of 300-800 µm and stored in a desiccator until analysis. TG analyses were performed at four different heating rates (5 °C/min, 10 °C/min, 15 °C/min and 20 °C/min) under a dry air atmosphere. For the Thermogravimetric (TG) analysis, 5 different fuel mixtures were prepared; 100%eggshell; 100% lignite; 25% eggshell+75% lignite; 50% eggshell+50% lignite; 75% eggshell + 25% lignite. In this study, the Fllyn-Wall-Ozawa Method was used to calculate the activation energy of prepared fuel mixtures (Equation (1)). The slope of the curve obtained when the log (β) is plotted against 1/T at any conversion ratio will give 0.4567 E_a/R. As a result, E_a is calculated from the slope of this line [2].

$$\log \beta = \log (AEa/Rg(\alpha)) - 2{,}315 - 0{,}4567\ (Ea/RT)$$

In his equation, T is the temperature (K), β is the heating rate (K/min), Ea is the activation energy (kJ/mol), R is the universal gas constant (8.314 J/mol.K), A is the pre-exponential constant (min^{-1}) and α is the concentration of reactant (Equation (2)).

$$\alpha = (mo - mt)/(mo - m\infty) \qquad (2)$$

here, mo is the initial weight of the reactant, mt is its weight at time t, m∞ is the final weight of reactant g.

In the study, ignition performance, flammability performance and comprehensive combustion behavior of the fuel mixtures were calculated for multiple peaks to examine the co-combustion performance of the prepared fuel mixtures [3,4].

3 RESULTS

As shown in Figure 1, four regions were observed on thermograms of the raw egg shells.

The first stage at (~20 - 220 °C) is endothermic and related to physically adsorbed water on/in the egg shells and inner membrane.

The second (~ 220 - 492 °C) and third stages (~ 492 - 631 °C) are exothermic and attributed to decomposition of shell's organic matter and volatilization of membrane content, respectively. Around 600 °C, thermal decomposition of the membrane is completed. The last endothermic stage (~631 - 809 °C) is attributed to decomposition of calcium in the egg shells.

For blends, also four regions were observed. However, Lignite, Egg shell samples and their blends showed different thermal decomposition profiles in terms of peak, burnout and ignition temperatures. For 100%eggshell sample, the ignition index, flammability index and comprehensive combustion index were found to be 0.00092, 0.003621 and 0.00013, respectively. As heating rate increased, ignition index, flammability index and comprehensive combustion index of nearly all samples increased. Furthermore, with addition of egg shell into the lignite nearly for all blends, higher the ignition index, flammability index and comprehensive combustion index were calculated.

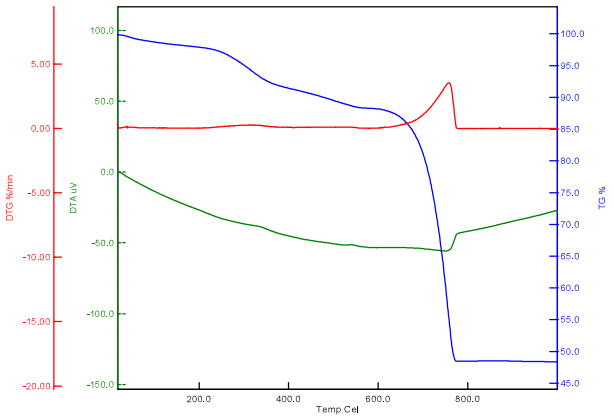


Figure 1. DTG curve of the Egg Shell @ 5 °C/min

In the study, the activation energies of the lignite, 75lignite+25eggshell, 50lignite+50eggshell, 25lignite+75eggshell and 100egsheel samples were calculated as 77.12 kJ/mole, 104.17 kJ/mole, 125.01 kJ/mole, 121.31 kJ/mole and 157.90 kJ/mole, respectively.

4 CONCLUSION

In this study, thermal properties and kinetics of the Egg Shell, lignite and their blends were examined.

Lignite, Egg shell samples and their blends showed different thermal decomposition profiles

in terms of peak, burnout and ignition temperatures.

With the addition of the ES into the lignite, ignition, flammability, comprehensive combustion and burnout index of the blends were found to be better than a single lignite.

Average activation energies of the Egg Shell and blends were in the range of 104.17 and 157.90 kJ/mol, respectively. Activation energy of the Kale lignite was 77.12 kJ/mol. Therefore, better combustion performance was observed with the addition of egg shells into the blends.

Therefore, this kind of studies will supply valuable design information about thermal decomposition properties and kinetics of Egg shell samples during their combustion or co-combustion.

ACKNOWLEDGEMENTS

The Authors would like to thank in advance both Remzi Akman and Muhammed Enes Önür for preparing the egg shell mixtures.

REFERENCES

[1] SGB, Tarım Ürünleri Piyasası, Tavuk Yumurtası, https://arastirma.tarimorman.gov.tr, 2021.

[2] X. Liu, M. Chen, M. and Y. Wei, Y. Kinetics based on two-stage scheme for co-combustion of herbaceous biomass and bituminous coal*, Fuel,* 143, pp.577-585, 2015.

[3] X. Jiang, C. Wang, X. Wang, Y. Liu, Z. Song, Q. Lin. Co-combustion of coal and carbonaceous wastes: Thermogravimetric analysis, *Energy Sources Part a Recovery Utilization and Environmental Effects,* 1–15, 2019.

[4] G.T. Marangwanda, D.M. Madyira, P.G. Ndungu and C.H. Chihobo, Combustion Characterization of Bituminous Coal and Pinus Sawdust Blends by Use of Thermo-Gravimetric Analysis, *Energies*, 14(22), p.7547, 2021.

PYROLYSIS AND COMBUSTION CHARACTERISTICS OF TEA STALK LIGNIN: EFFECT OF ORGANOSOLV AND SEQUENTIAL HYDROTHERMAL-ORGANOSOLV PRETREATMENTS

S. Başakçılardan Kabakcı[1], B. Karakurt Çevik[1] and G.S. Baş Berkem[2]

1. Energy Systems Engineering Department, Faculty of Engineering, Yalova University, Yalova; email: sibel.kabakci@yalova.edu.tr, basak.cevik@yalova.edu.tr
2. Polymer Engineering Department, Faculty of Engineering, Yalova University, Yalova; email: gamze.berkem@yalova.edu.tr

Abstract

In order to convert polysaccharides in lignocellulosic biomass to biofuel, lignin must be isolated by applying different pre-treatments. Although lignin-based chemicals, biofuels and materials are obtained by valorisation of lignin, it is seen that the most preferred method today is to recover the energy content of the lignin-rich fraction by thermochemical conversion. In the present study, lignin in tea stalk was isolated by glycerol-organosolv method and sequential hydrothermal-organosolv pre-treatments. Proximate and ultimate analyses, heating values, combustion and pyrolysis profiles/characteristics, volatiles released during combustion and pyrolysis of tea stalk lignin (TL) and hydrothermally pre-treated tea stalk lignin (HTL) were compared.

Keywords: Biorefinery streams, Biomass, Lignin, Combustion, Pyrolysis

1 INTRODUCTION

Due to the increasing pressure of climate change and the limited availability of natural resources, the processing of biomass into value-added chemicals, biofuels and bio-based materials is becoming increasingly important today. Biomass is living or recently lived (non-fossilized) biodegradable organic materials of plant, animal, and microorganism origin. This definition includes: 1) agricultural products, waste and residues, 2) energy plants and energy forestry products, 3) wood and wood processing wastes together with forest products and residues, 4) aquatic plants, 5) biodegradable fraction of household waste and, 6) food and food industry waste.

Although there are extensive biomass sources available, the processing of lignocellulosic biomass is important for both energy and environmental safety since it cannot be used as a food source. The basic building blocks of lignocellulosic biomass are cellulose, hemicellulose, and lignin. A lignocellulosic biomass contains approximately 40-60% cellulose, 10-40% hemicellulose and 15-30% lignin by weight, and these ratios vary according to the type of biomass [1]. While the diversity and amount of lignocellulosic biomass is a great advantage, its heterogeneous structure is the most important disadvantage. Pretreatment is essential for the valorization of cellulose, hemicellulose, and lignin. Often, this pretreatment involves both costly and energy-intensive processes [2].

The main purpose of the pretreatments, which can be classified as physical, physico-chemical, chemical, thermochemical, and biological, is to reduce the recalcitrance of lignocellulose structure and increase the accessibility of cellulase enzyme by reducing the particle size, breaking the lignin-hemicellulose bonds, dissolving hemicellulose, decreasing the crystallinity of cellulose [3]. In today's biorefineries (and also in pulp and paper industries), power and/or heat are obtained by burning the lignin fraction.

However, the valorization of hemicellulose and lignin in the lignocellulosic structure is very important for the development of bioeconomy. More than one pretreatment may be preferred to separately valorize the hemicellulose, cellulose and lignin fractions. The combined use of hydrothermal pretreatment and organosolv method can be given as an example of such application.

Hydrothermal pretreatment, which is a simple, environmentally friendly, and low-cost method, uses water as a solvent. Pretreatment is carried out under pressure (mostly autonomous) and at a temperature between 160-230 ^{o}C [4]. In this method (in which most of the hemicellulose is

degraded) swelling and partial hydrolysis of cellulose, partial decomposition and repolymerization of lignin are observed depending on the conditions of the hydrothermal pretreatment [3]. After hydrothermal pretreatment, the liquid fraction containing a high percentage of sugar can be converted into platform chemicals using different conversion methods [5]. The solid fraction is enriched with cellulose and lignin.

In the organosolv pretreatment, lignocellulosic biomass is brought into contact with a solvent in the presence of a catalyst. This process can be carried out under pressure, or it can be carried out at atmospheric pressure at relatively higher temperatures. The type of solvent, type of biomass, particle size of the biomass, biomass/solvent ratio, pretreatment conditions (temperature, pressure, mixing speed, time) affect the extent of delignification [6]. The cellulose-rich fraction is separated from the solution by filtration. Lignin is precipitated by diluting the organosolv solution with water. Solvent is often recovered from the solution [7].

Valorization of lignin is a subject that needs continuous research, as its unique structure allows to obtain more than one product with different properties. Recovery of lignin by pretreatment is also one of the most important steps in valorization. The present study includes a comparison of the thermal behavior (pyrolysis and combustion behavior), pyrolysis volatiles, combustion gases of lignin fractions obtained from tea stalks with one-step pretreatment (glycerol organosolv treatment) and two-step pretreatment (hydrothermal pretreatment and organosolv pretreatment).

2 MATERIAL AND METHODS

2.1 Lignocellulosic biomass

Tea stalk samples were supplied from a tea processing factory located in Rize. All tea stalk samples were dried (105 ºC for 24 h) before analyses and pretreatments to prevent samples from rotting and to provide better conditions for storage. After drying, the samples were ground and sieved to have a uniform particle size. Table 1 shows the proximate and ultimate analyses of tea stalk.

Table 1. Proximate and ultimate analyses of tea stalk samples.

Proximate analysis, (wt %, db)*			Ultimate analysis, (wt %, db)*			
FC	VM	A	C	H	N	S
25.1	71.1	3.8	46.6	5.5	2.6	0.1

FC: Fixed carbon, VM: Volatile matter, A: Ash, db: dried basis

* Proximate and ultimate analyses were done twice. Mean values were given in Table 1.

2.2 Organosolv pretreatment

Alkaline glycerol organosolv method, which we previously used for delignification [8], was modified in this study to increase the lignin yield. 20g tea stalk, 50 ml of 0.4 M NaOH solution and 150 ml glycerol were mixed in a three-necked glass reactor equipped with a reflux condenser and a thermocouple (that controls the set temperature of the heater). First the mixture was mixed for 30 min at 90 ºC, then the temperature was raised to 115 ºC. The mixture was continuously mixed for 90 min at this temperature. At the end of the treatment pulp was separated from the liquor. Pulp was washed with hot water (water at 55 ºC) for three times. The washing water and liquor were combined and diluted to 1L with hot water (water at 55 ºC). The pH was decreased to 2 by using 0.1 M H_2SO_4. As the lignin precipitated, the solution was centrifuged. Lignin was separated and dried.

2.3 Sequential hydrothermal pretreatment and organosolv pretreatment

Hydrothermal pretreatment of tea stalk was carried out in a 250 ml non-stirred, temperature-controlled, stainless-steel batch reactor. Hydrothermal pretreatment conditions were selected based on our previous study (pretreatment temperature: 220 ºC, residence time: 90 min, tea stalk/water ratio: 1 g/4 ml, amount of tea stalk: 10 g) [9]. After pretreatment, the reactor was cooled rapidly by using ice bath. Gases, which were formed during the pretreatment were not collected. The mixture was filtered to separate hydrochar. The hydrochar of tea stalk samples were washed with deionized water and then dried in an oven at 105 ºC for 24 h.

The hydrochar of tea stalk samples were delignified by using alkaline glycerol pretreatment as explained above.

2.4 Analyses

Proximate analyses of tea stalk, TL and HTL were done using thermogravimetry method as described in [10]. The ultimate analysis of all samples was carried by an elemental analyzer (LECO, CHNS-932).

The lower heating value (LHV) of TL and HTL were measured using IKA C5003 model bomb calorimeter based on ASTM D240. Fourier Transform Infrared (FTIR) spectra of samples were obtained using a spectrometer (Perkin Elmer Spectrum 100) coupled with a universal attenuated total reflectance (ATR) sampling device with a diamond crystal. The spectra were recorded with a resolution of 4 cm^{-1}, in the range from 400 to 4000 cm^{-1}.

To figure out pyrolysis profile, combustion profile and combustion characteristics of samples, thermogravimetric analyzer (Seiko, TG/DTA 6300) was used. Samples were heated from room temperature to 105 ºC with a heating rate of 10 ºC/min and kept for 10 min. Then, samples were heated up to 900 ºC with a heating rate of 40 ºC/min and maintained for 7 min. Ignition temperature of TL and HTL were determined by using intersection method where thermogravimetric analysis (TGA) and derivative thermogravimetric (DTG) curves were used together [11]. Burnout temperatures of TL and HTL were determined based on conversion method where the conversion reached 99% [11].

Evolved gases during pyrolysis and combustion (with a heating rate of 15 ºC/min from 25 ºC to 900 ºC under N_2 atmosphere for pyrolysis, with a heating rate of 15 ºC/min from 25 ºC to 900 ºC under air for combustion) were examined by using a thermogravimetric analyzer coupled with a FTIR (Perkin Elmer Pyris STA 600) (analyses were done at Central Laboratory of Middle East Technical University). The volumetric flowrate of N_2 was 45 ml/min. The temperature of the connection line was kept at 270 ºC to prevent condensation.

3 RESULTS AND DISCUSSION

3.1 Characterization of TL and HTL

Table 2 shows the proximate analyses, ultimate analyses and LHV of TL and HTL. Obviously, hydrothermal pretreatment prior to organosolv pretreatment changed the structure of lignin. Previous studies on hydrothermal pretreatment indicated that some of the lignin and hemicellulose in the lignocellulosic structure were dissolved due to hydrothermal conditions. Hemicellulose, which belongs to a group of heterogeneous polysaccharides, is hydrolyzed to oligosaccharides and acetic acid during hydrothermal pretreatment [12]. Acidic medium causes the cracking of glycosidic linkages in oligosaccharides to form pentoses and hexoses. Due to the hydrolysis of glycosidic linkages and loosening of cell wall lignin is partially dissolved even at very low hydrothermal treatment temperatures (120 ºC to 180 ºC) [4]. The degree of hemicellulose hydrolysis and lignin dissolution is directly related with pretreatment severity [12-14]. At severe hydrothermal conditions, the dissolved lignin might condense and it might repolymerize together with hemicellulose degradation products [15]. Therefore, it can be said that the application of the hydrothermal method before lignin extraction will change the structure of lignin. Similarly, in this study, it was observed that the structure of lignin changed. The carbon content and fixed carbon percentage of TL were higher. Due to high carbon content, the heating value of TL was also high. Hydrothermal-glycerol pretreatments produced lignin of low ash content due to partial dissolution of ash forming elements during hydrothermal pretreatment.

Table 2. Proximate analysis, ultimate analysis and LHV of TL and HTL.

	TL	HTL
Proximate analysis, (wt %, db)*		
FC	23.21	15
VM	75.25	84.82
A	1.537	0.18
Ultimate analysis, (wt %, db)*		
C	42.13	38.87
H	5.97	7.39
N	1.73	1.03
S	0.09	0.15
Heating Value, (MJ/kg)*		
LHV	17.91	16.85

FC: Fixed carbon, VM: Volatile matter, A: Ash, db: dried basis

* Proximate analyses, ultimate analyses and LHV analyses were done twice. Mean values were given in Table 2.

Using the elemental analysis and ash content given in Table 2, the oxygen content of TL and HTL was calculated as 48.54% and 52.38%, respectively. It can be said that the pretreatment carried out in two stages enriches the lignin with oxygenated functional groups. This enriching is slightly observed in FTIR spectra of HTL.

Functional groups that appear on the surface of TL and HTL were identified by FTIR spectra, which are given in Figure 1. The peaks were identified by comparing the FTIR spectra with the published data [16-24].

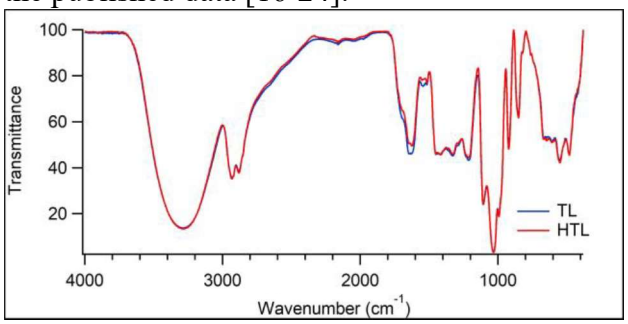
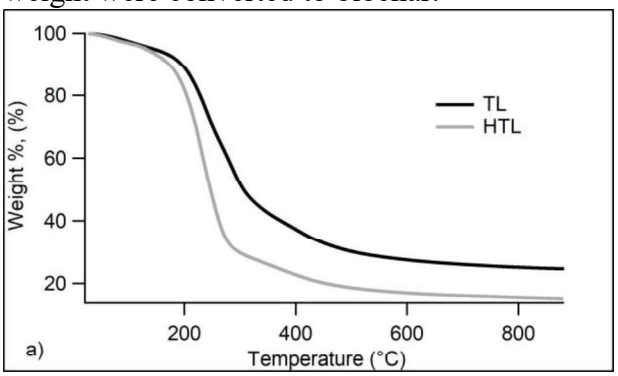


Figure 1. FTIR spectra of TL and HTL.

The FTIR spectra of TL and HTL were similar and both spectra exhibited vibrations that a typical lignin spectrum should have. The hydroxyl group of phenolic and aliphatic structure gave a characteristic absorption band (centered at 3280 cm^{-1}), which appeared in the wavelength range of 3200-3300 cm^{-1}. The stretching vibration of C-H bonds in alkyl groups (-CH_3, -CH_2, -OCH_3) was visible in both spectra at a wavelength of 2930-2932 cm^{-1} and 2880 cm^{-1}. The intensity of C=O stretching vibration (appearing at 1624-1640 cm^{-1}) was higher in the spectra of HTL. C=O stretching and aromatic skeletal vibration at a wavelength of 1590 cm^{-1} were noticeable in both spectra. Similarly, aromatic ring vibration (C=C in aromatic skeleton) was visible at 1516-1541cm^{-1}. The vibration of C-H in-plane deformation of lignin was seen in both spectra at a wavelength of 1425 cm^{-1}. C-O stretching of syringyl ring, stretching vibration of C-C and C-O bonds were detected in both FTIR spectra of TL and HTL at a wavelength of 1415-1420 cm^{-1} and 1212-1214 cm^{-1} respectively. C-C and C-O stretching of syringyl ring (a characteristic lignin peak) was noticed at a wavelength of 1320 cm^{-1} and 1240 cm^{-1}. The vibration of aromatic C-H deformation in syringyl ring at 1120 cm^{-1} appeared in both FTIR spectra. The stretching vibration of C-O, C=C and C-C-O bonds (at 1035 cm^{-1}) found in primary and secondary alcohols or aliphatic ethers was also seen in the spectra of both TL and HTL. Deformation vibration of C-H bonds in aromatic rings appeared at 920 cm^{-1} and 840 cm^{-1} in both spectra.

3.2 Pyrolysis Characteristics of TL and HTL

Thermogravimetric (TG) and differential thermo-gravimetric (DTG) curves of TL and HTL were shown in Figure 2. It can be seen from the thermal degradation curves that hydrothermal pretreatment before the organosolv treatment changes the lignin structure. Thermal degradation of both TL and HTL appeared at the temperature of 100-700 ºC, where several researchers reported similar temperature range [25-29]. Thermal degradation of TL occurred in three stages: 20-140 ºC (mainly evaporation of moisture), 140-370 ºC (primary pyrolysis) and 370-700ºC (carbonization stage). Maximum degradation rate was observed at 240 ºC in the primary pyrolysis stage, where a small shoulder appeared at 290 ºC. Based on DTG curve of HTL, hydrothermal pretreatment prior to organosolv treatment changed the thermal stability of lignin. Like TL's thermal degradation, thermal degradation of HTL occurred in three stages: up to 100 ºC (evaporation of water), 100-320 ºC (primary pyrolysis) and 320-700 ºC (carbonization). Having lower thermal stability, HTL had the highest reactivity in pyrolysis. At the end of the pyrolysis, 24.8% of TL and 15.2% of HTL by weight were converted to biochar.



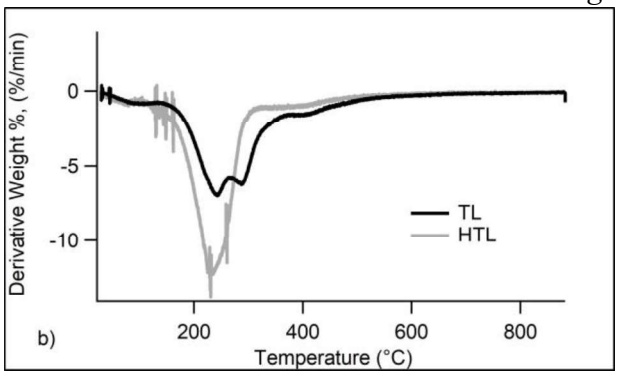


Figure 2. Pyrolysis profile of TL and HTL.

3.3 Pyrolysis Volatiles by TG-FTIR

Common functional groups detected by TG-FTIR were identified based on previous published data: stretching vibration of O-H due to H_2O (3400-4000 cm^{-1}), stretching vibration of C-H in CH_4 (2800-3200 cm^{-1}), stretching vibration of C=O in CO_2 (2217-2400 cm^{-1}), stretching vibration of C-O in CO (2030-2240 cm^{-1}), stretching vibration of C=O in compounds containing carbonyl groups such as acids, aldehydes, ketones (1680-1880 cm^{-1}), stretching vibration of C=C in aromatic hydrocarbons (1420-1600 cm^{-1}), stretching vibration of C-O-H in alcohols and phenols and alcohols (1000-1300 cm^{-1}), stretching vibration of C=O in CO_2 (586-780 cm^{-1}) [2, 30-36].

The FTIR spectra of pyrolysis volatiles of TL and HTL are shown in Figure 3 and Figure 4. The FTIR spectra shown in the graphs are those recorded at T_{max} (the temperature at which the maximum mass loss rate occurs), T_{low} (the temperature below 100°C), and T_{high} (the temperature at which the mass loss rate is almost constant). Although these temperatures were different in TL and HTL, vibrations of the same functional groups were observed in their spectra. Devolatilization of HTL started at lower temperatures compared to TL. The low temperature spectra (below 100 °C) of both TL and HTL showed the presence of O-H containing groups (due to evaporation of free water) and C=O containing carbonyl groups. Spectra recorded at T_{max} of both TL and HTL showed the presence of the same functional groups: O-H group (H_2O formation due to cleavage of -OH in the aliphatic side chains), C-H stretching (CH_4 formation due to cleavage of methoxy groups in the lignin structure), C=C stretching (formation of aromatic compounds due to cracking and rearrangement of unsaturated hydrocarbons and ring structures) and C-O-H stretching (formation of alcohols and phenols). As shown in previous studies on lignin [25, 28, 31], most of the volatiles formed in T_{max} in this study were composed of phenols and alcohols. Cleavage of methoxy bonds from benzene rings and decomposition of phenyl propane side chains of lignin are the reasons for the formation of methanol and phenols respectively [26, 37]. C=O stretching (due to CO_2 formation), which were detected in the spectra of T_{low}, T_{max} and T_{high}, indicated that the formation of CO_2 occurred in wide temperature range. CO_2 formation is due to cleavage of the carboxyl, carbonyl and ester groups of the side chains [25].

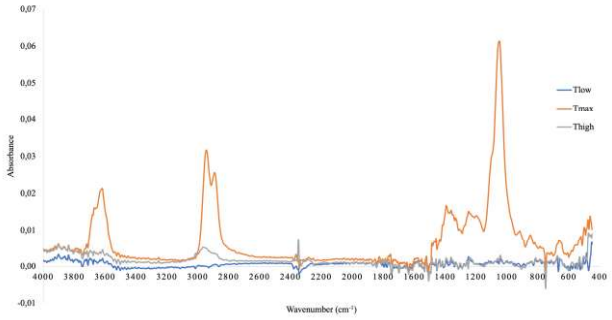


Figure 3. FTIR spectra of TL pyrolysis volatiles at T_{low}=91.16 ºC, T_{max}=259.92 ºC and T_{high}=473.57 ºC.

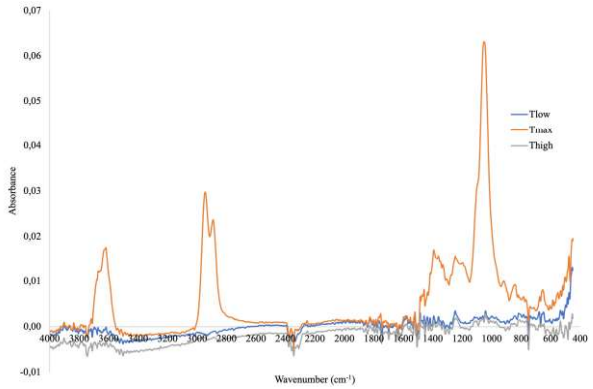


Figure 4. FTIR spectra of HTL pyrolysis volatiles at T_{low}=88.86 ˚C, T_{max}=253.02 ˚C and T_{high}=477.45 ˚C.

3.4 Combustion Characteristics of TL and HTL

The TG and DTG curves for the combustion of TL and HTL are given in Figure 5. The three classical steps of combustion were seen: drying (or moisture removal), formation and combustion of volatiles, combustion of char. Combustion took place over a wide temperature range for both TL and HTL. Combustion lasted up to 740 ºC for TL and 800 ºC for HTL. It is also seen from the combustion curves that

hydrothermal pre-treatment before the organosolv treatment modified the lignin structure. For HTL, devolatilization and combustion of volatiles were more reactive compared to TL. Contrarily, TL was more reactive in the char combustion stage. İgnition temperatures of TL and HTL were 200 ºC and 212.5 ºC respectively. The maximum mass loss rate for both TL and HTL was seen in the second stage where the devolatilization and combustion of volatiles were occurred. The temperature at which the maximum mass loss rate was observed was 240 ºC for TL and 280 ºC for HTL.

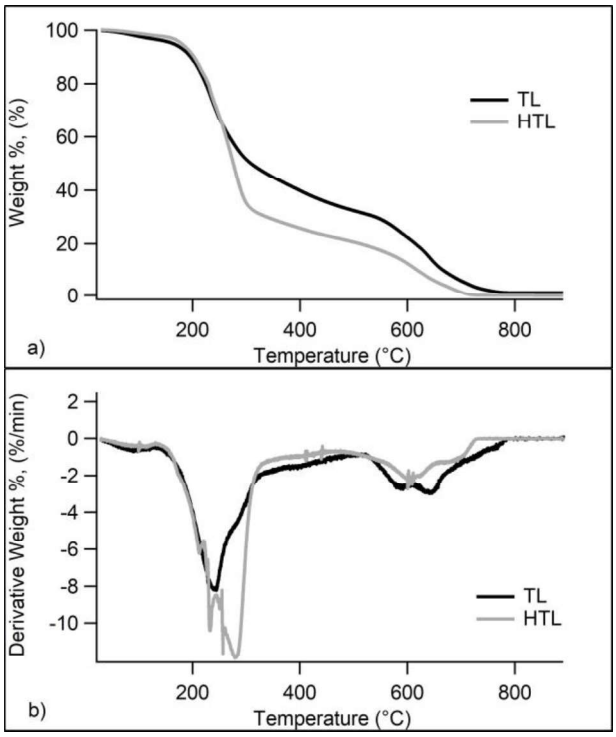


Figure 5. Combustion profile of TL and HTL.

FTIR spectra of gases formed by the combustion of TL and HTL are shown in Figure 6 and Figure 7. FTIR spectra are given for specific temperatures in accordance with the combustion stages: low temperature (T_{low}), temperature at which maximum mass loss rate is observed (T_{max}), high temperature at which oxidation of the char is observed (T_{high}). The -OH stretching due to H_2O removal from the samples was detected in both FTIR spectra at T_{low}. The spectra of TL and HTL recorded at T_{max} were quite similar: O-H stretching at 3600-3800 cm^{-1} (due to H_2O formation and cleavage of aliphatic hydroxy groups of lignin), C-H stretching at 2800-3000 cm^{-1} (CH_4 formation due to cleavage of methoxy group in the aliphatic branches of lignin), C=O stretching at 2200-2400 cm^{-1} (CO_2 formation due to cracking of carbonyl and carboxyl groups), C=O stretching at 1600-1800 cm^{-1} (formation of compounds containing carbonyl groups), C-O-H stretching at 1000-1300 cm^{-1} (formation of alcohols and phenols). As the intensity of the peak at a certain wavenumber is linearly dependent on concentration [38], it can be stated that formation of CO_2 and carbonyl containing compounds (such as acids, aldehydes) at T_{max} were less compared to other gases. As clearly observed from the FTIR spectra of TL and HTL recorded at T_{high}, dominant gases were CO_2 and CO at high temperatures. Compared to HTL, C=O (CO_2) stretching, and C-O (CO) stretching were more intense in the FTIR spectrum of TL recorded at T_{high}, which also revealed that there was more CO and CO_2 in the gas phase.

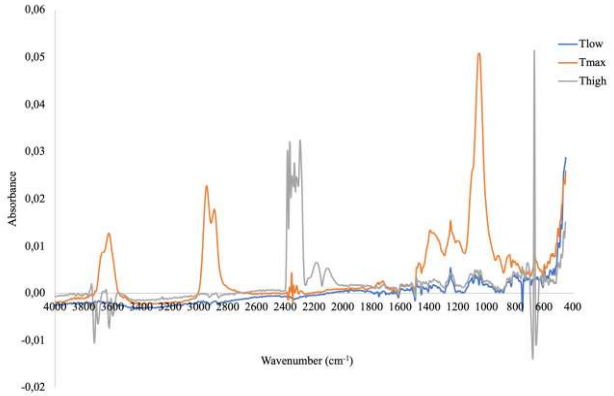


Figure 6. FTIR spectra of TL combustion emissions at T_{low}=89.82 ˚C, T_{max}=258.3 ˚C and T_{high}=659.78 ˚C.

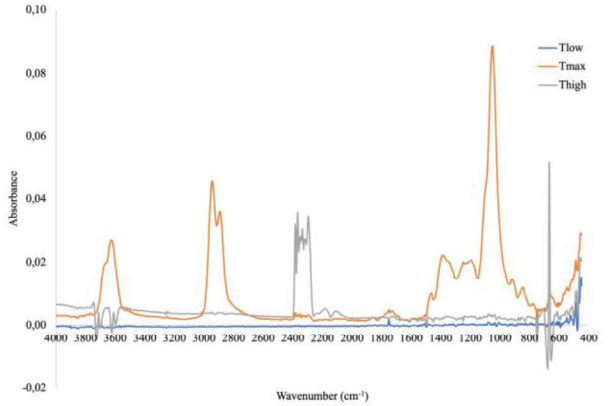


Figure 7. FTIR spectra of HTL combustion emissions at T_{low}=116.96 ˚C, T_{max}=295.59 ˚C and T_{high}=629.16 ˚C.

4 CONCLUSIONS

In this study, lignin was obtained from tea stalk by glycerol organosolv pretreatment and hydrothermal-organosolv pretreatment. Due to hydrolysis of hemicellulose and partial cleavage of lignin bonds during hydrothermal

pretreatment, the structure of precipitated lignin was modified. The carbon content of lignin obtained in two-step pretreatment was lower and the oxygen content was higher. Therefore, heating value of HTL was lower than that of TL. Due to dissolution of ash forming elements under hydrothermal pretreatment conditions, ash content of HTL was low. Lignin obtained in two-step pretreatment had lower thermal stability. Consistent with its pyrolysis behavior, the ignition temperature of the HTL was lower than that of the TL.

ACKNOWLEDGEMENTS

This research was financially supported by Yalova University Scientific Research Unit [Project No: 2020/AP/0007].

REFERENCES

[1] W. Schutyser, T. Renders, S. Van den Bosch, S.F. Koelewijn, G.T. Beckham, B.F. Sels, Chemicals from lignin: an interplay of lignocellulose fractionation, depolymerisation, and upgrading, *Chemical Society Reviews*, Vol. 47,pp. 852-908, 2018.

[2] S. Singh, C.F. Wu, P.T. Williams, Pyrolysis of waste materials using TGA-MS and TGA-FTIR as complementary characterisation techniques, *Journal of Analytical and Applied Pyrolysis*, Vol. 94,pp. 99-107, 2012.

[3] D. Sun, Z.W. Lv, J. Rao, R. Tian, S.N. Sun, F. Peng, Effects of hydrothermal pretreatment on the dissolution and structural evolution of hemicelluloses and lignin: A review, *Carbohydr. Polym.*, Vol. 281,pp. 2022.

[4] Q. Sun, W.J. Chen, B. Pang, Z.H. Sun, S.S. Lam, C. Sonne, Q. Yuan, Ultrastructural change in lignocellulosic biomass during hydrothermal pretreatment, *Bioresource Technology*, Vol. 341,pp. 2021.

[5] T. Scapini, M.S.N. dos Santos, C. Bonatto, J.H.C. Wancura, J. Mulinari, A.F. Camargo, N. Klanovicz, G.L. Zabot, M.V. Tres, G. Fongaro, H. Treichel, Hydrothermal pretreatment of lignocellulosic biomass for hemicellulose recovery, *Bioresource Technology*, Vol. 342,pp. 2021.

[6] Z.Y. Zhang, M.D. Harrison, D.W. Rackemann, W.O.S. Doherty, I.M. O'Hara, Organosolv pretreatment of plant biomass for enhanced enzymatic saccharification, *Green Chemistry*, Vol. 18,pp. 360-381, 2016.

[7] J.A. Ferreira, M.J. Taherzadeh, Improving the economy of lignocellulose-based biorefineries with organosolv pretreatment, *Bioresource Technology*, Vol. 299,pp. 2020.

[8] S.B. Kabakci, M.H. Tanis, Pretreatment of lignocellulosic biomass at atmospheric conditions by using different organosolv liquors: a comparison of lignins, *Biomass Conversion and Biorefinery*, Vol. 11,pp. 2869-2880, 2021.

[9] S.B. Kabakci, S.S. Baran, Hydrothermal carbonization of various lignocellulosics: Fuel characteristics of hydrochars and surface characteristics of activated hydrochars, *Waste Manage.*, Vol. 100,pp. 259-268, 2019.

[10] R. Garcia, C. Pizarro, A.G. Lavin, J.L. Bueno, Biomass proximate analysis using thermogravimetry, *Bioresource Technology*, Vol. 139,pp. 1-4, 2013.

[11] J.J. Lu, W.H. Chen, Investigation on the ignition and burnout temperatures of bamboo and sugarcane bagasse by thermogravimetric analysis, *Applied Energy*, Vol. 160,pp. 49-57, 2015.

[12] L.-P. Xiao, G.-Y. Song, R.-C. Sun, *Effect of Hydrothermal Processing on Hemicellulose Structure*, in: H.A. Ruiz, M. Hedegaard Thomsen, H.L. Trajano (Eds.) Hydrothermal Processing in Biorefineries: Production of Bioethanol and High Added-Value Compounds of Second and Third Generation Biomass, Springer International Publishing, 2017, pp. 45-94, 2017.

[13] B. Yang, C.E. Wyman, Effect of xylan and lignin removal by batch and flowthrough pretreatment on the enzymatic digestibility of corn stover cellulose, *Biotechnol Bioeng*, Vol. 86,pp. 88-95, 2004.

[14] W.-H. Chen, M.-H. Hsu, A.-Y. Wu, W.-S. Hwang, Efficient extraction and recovery of xylan and lignin from rice straw using a flow-through hydrothermal system, *Journal of the Taiwan Institute of Chemical Engineers*, Vol. 79,pp. 103-109, 2017.

[15] A. Moure, G. Garrote, H. Domínguez, *Effect of Hydrothermal Pretreatment on Lignin and Antioxidant Activity*, in: H.A. Ruiz, M. Hedegaard Thomsen, H.L. Trajano (Eds.) Hydrothermal Processing in Biorefineries: Production of Bioethanol and High Added-Value Compounds of Second and Third Generation Biomass, Springer International Publishing, 2017, pp. 5-43, 2017.

[16] F. Monteil-Rivera, M. Phuong, M.W. Ye, A. Halasz, J. Hawari, Isolation and characterization of herbaceous lignins for

applications in biomaterials, *Ind. Crop. Prod.*, Vol. 41,pp. 356-364, 2013.

[17] S.R. Wang, B. Ru, H.Z. Lin, W.X. Sun, Z.Y. Luo, Pyrolysis behaviors of four lignin polymers isolated from the same pine wood, *Bioresource Technology*, Vol. 182,pp. 120-127, 2015.

[18] L.B. Zhang, L.S. Yan, Z.M. Wang, D.D. Laskar, M.S. Swita, J.R. Cort, B. Yang, Characterization of lignin derived from water-only and dilute acid flowthrough pretreatment of poplar wood at elevated temperatures, *Biotechnology for Biofuels*, Vol. 8,pp. 2015.

[19] X. Tian, Z. Fang, R.L. Smith, Z. Wu, M. Liu, *Properties, Chemical Characteristics and Application of Lignin and Its Derivatives*, in: Z. Fang, J.R.L. Smith (Eds.) Production of Biofuels and Chemicals from Lignin, Springer Singapore, 2016, pp. 3-33, 2016.

[20] B. El Khaldi-Hansen, M. Schulze, B. Kamm, *Qualitative and Quantitative Analysis of Lignins from Different Sources and Isolation Methods for an Application as a Biobased Chemical Resource and Polymeric Material*, in: S. Vaz Jr (Ed.) Analytical Techniques and Methods for Biomass, Springer International Publishing, 2016, pp. 15-44, 2016.

[21] L.A. Panamgama, P. Peramune, Coconut coir pith lignin: A physicochemical and thermal characterization, *International Journal of Biological Macromolecules*, Vol. 113,pp. 1149-1157, 2018.

[22] A. Alzagameem, B. El Khaldi-Hansen, B. Kamm, M. Schulze, *Lignocellulosic Biomass for Energy, Biofuels, Biomaterials, and Chemicals*, in: S. Vaz Jr (Ed.) Biomass and Green Chemistry: Building a Renewable Pathway, Springer International Publishing, 2018, pp. 95-132, 2018.

[23] Z.Q. Ma, J.H. Wang, H.Z. Zhou, Y. Zhang, Y.Y. Yang, X.H. Liu, J.W. Ye, D.Y. Chen, S.R. Wang, Relationship of thermal degradation behavior and chemical structure of lignin isolated from palm kernel shell under different process severities, *Fuel Processing Technology*, Vol. 181,pp. 142-156, 2018.

[24] S.X. Li, M.F. Li, J. Bian, X.F. Wu, F. Peng, M.G. Ma, Preparation of organic acid lignin submicrometer particle as a natural broad-spectrum photo-protection agent, *International Journal of Biological Macromolecules*, Vol. 132,pp. 836-843, 2019.

[25] S.R. Wang, K.G. Wang, Q. Liu, Y.L. Gu, Z.Y. Luo, K.F. Cen, T. Fransson, Comparison of the pyrolysis behavior of lignins from different tree species, *Biotechnology Advances*, Vol. 27,pp. 562-567, 2009.

[26] Z.Y. Luo, S.R. Wang, X.J. Guo, Selective pyrolysis of Organosolv lignin over zeolites with product analysis by TG-FTIR, *Journal of Analytical and Applied Pyrolysis*, Vol. 95,pp. 112-117, 2012.

[27] D.L. Guo, S.B. Wu, G.J. Lyu, H.P. Guo, Effect of molecular weight on the pyrolysis characteristics of alkali lignin, *Fuel*, Vol. 193,pp. 45-53, 2017.

[28] T.P. Wang, H. Li, J.M. Yuan, W.X. Li, K. Li, Y.B. Huang, L.P. Xiao, Q. Lu, Structures and pyrolytic characteristics of organosolv lignins from typical softwood, hardwood and herbaceous biomass, *Ind. Crop. Prod.*, Vol. 171,pp. 2021.

[29] X. Lv, Q. Li, Z. Jiang, Y. Wang, J. Li, C. Hu, Structure characterization and pyrolysis behavior of organosolv lignin isolated from corncob residue, *Journal of Analytical and Applied Pyrolysis*, Vol. 136,pp. 115-124, 2018.

[30] J. Zhao, X.W. Wang, J. Hu, Q. Liu, D.K. Shen, R. Xiao, Thermal degradation of softwood lignin and hardwood lignin by TG-FTIR and Py-GC/MS, *Polymer Degradation and Stability*, Vol. 108,pp. 133-138, 2014.

[31] V. Volli, A.R.K. Gollakota, C.M. Shu, Comparative studies on thermochemical behavior and kinetics of lignocellulosic biomass residues using TG-FTIR and Py-GC/MS, *Science of the Total Environment*, Vol. 792,pp. 2021.

[32] H.Y. Huang, J.Y. Liu, H. Liu, F. Evrendilek, M. Buyukada, Pyrolysis of water hyacinth biomass parts: Bioenergy, gas emissions, and by-products using TG-FTIR and Py-GC/MS analyses, *Energy Conversion and Management*, Vol. 207,pp. 2020.

[33] C.X. Wang, H.B. Bi, Q.Z. Lin, X.D. Jiang, C.L. Jiang, Co-pyrolysis of sewage sludge and rice husk by TG-FTIR-MS: Pyrolysis behavior, kinetics, and condensable/non-condensable gases characteristics, *Renewable Energy*, Vol. 160,pp. 1048-1066, 2020.

[34] B.W. Lin, J.S. Zhou, Q.W. Qin, X. Song, Z.Y. Luo, Thermal behavior and gas evolution characteristics during co-pyrolysis of lignocellulosic biomass and coal: A TG-FTIR

investigation, *Journal of Analytical and Applied Pyrolysis*, Vol. 144,pp. 2019.
[35] J. Cao, G. Xiao, X. Xu, D.K. Shen, B.S. Jin, Study on carbonization of lignin by TG-FTIR and high-temperature carbonization reactor, *Fuel Processing Technology*, Vol. 106,pp. 41-47, 2013.
[36] S.B. Kabakci, B.K. Cevik, E.B. Ates, M.N. Borand, Increasing the energy density of high-moisture wastes of beverage industry by hydrothermal pretreatment: Comparison of thermochemical conversion behaviors, *International Journal of Energy Research*, Vol.,pp.
[37] Q. Khanh Tran, H. Vu Ly, H. Tae Hwang, J. Kim, S.-S. Kim, Study on pyrolysis of Organosolv lignin impregnated with alkali and alkaline earth metals: Kinetics, thermodynamics, and product characterization, *Fuel*, Vol. 329,pp. 125472, 2022.
[38] N.B. Gao, A.M. Li, C. Quan, L. Du, Y. Duan, TG-FTIR and Py-GC/MS analysis on pyrolysis and combustion of pine sawdust, *Journal of Analytical and Applied Pyrolysis*, Vol. 100,pp. 26-32, 2013.

ENERGY RECOVERY FROM SPENT COFFEE GROUND AND BREWERY SPENT GRAINS: A CIRCULAR ECONOMY APPROACH TO WASTE VALORIZATION

I.A. Idowu[1,2], L.J.R. Nunes[3], K.S Hashim[1] and A. Shaw[1]

1. Built Environment and Sustainable Technologies (BEST) Research Institute, Faculty of Engineering and Technology, Liverpool John Moores University, United Kingdom. i.a.idowu@ljmu.ac.uk, K.S.Hashim@ljmu.ac.uk, A.Shaw@ljmu.ac.uk
2. Low Carbon Eco Innovatory Unit, Liverpool John Moores University, United Kingdom i.a.idowu@ljmu.ac.uk
3. PROMETHEUS, Unidade de Investigação em Materiais, Energia e Ambiente para a Sustentabilidade, Escola Superior Agrária, Instituto Politécnico de Viana do Castelo, Rua da Escola Industrial e Comercial de Nun'Alvares, 4900-347 Viana do Castelo, Portugal leonelnunes@esa.ipvc.pt

Correspondence: leonelnunes@esa.ipvc.pt

Abstract

The circular economy assumes an increasingly important role towards the journey to net zero carbon emissions. While the UK is the first major economy to commit in law to net zero by 2050, through the set out landmark strategy and a vision for a decarbonised economy in 2050. Harnessing the waste resource for energy is crucial for a decarbonised economy. The present work addresses the management of brewery spent grains and coffee spent ground residues through incorporating of both material in the production of biomass pellets and their direct recovery, in an autonomous way, by combustion. It is also intended to evaluate its potential in comparison to other fuels derived from biomass using different conversion and recovery technologies. The results from incorporating these residues in processes such as the production of biomass pellets and other more conventional biomasses already presents more promising results. However, recovery through thermochemical conversion processes, such as pyrolysis, seems to be the scenario with the highest probability of success.

Keywords: brewery spent grains; spent coffee ground; circular economy; energy recovery; waste management; biomass energy.

1 INTRODUCTION

The circular economy assumes an increasingly important role in the daily lives of societies [1]. The recovery of waste generated in different industrial processes and the daily activities of populations contributes significantly to solving problems related to waste management, at the same time contributing to the creation of new value chains and reintroducing these material flows in new production chains [2]. These flows actively contribute to saving resources, both from the perspective of replacing virgin raw materials and the replacement of energy products, when circularization is done through energy recovery [3].

Agro-industrial waste constitutes a very significant percentage of waste generated in Europe. According to information on the European Parliament's official website (https://www.europarl.europa.eu/, accessed on 1 June 2022), 2.5 billion tonnes of waste are produced in Europe annually, from which 20 million tons correspond to waste generated in sectors associated with agriculture, forestry and fisheries. The use of this waste is a priority, justified by the inherent potential of this type of waste, which traditionally, over time, has been incorporated into the very processes where they were generated, as is the case of its use as fertilizer or introduced in animal feed, or still energetically valued [4].

Waste such as brewery-spent grains and coffee spent ground are two widespread types of waste generated in increasing amounts, given the increase in consumption associated with both beer and coffee [5].

Concerning energy recovery from both brewery-spent grains and coffee spent ground, perhaps because the amounts available until recently were easily manageable with the available processes, the focus was given more to more experimental processes, still underdeveloped and very focused on the recovery of waste as a means of increasing the efficiency of their production processes. For example, Géczi et al. [6] examined the technical and economic feasibility of energy recovery from brewery spent grains by aerobic and anaerobic digestion in the industrial unit itself to increase the efficiency and yield of the process. Byrne et al. [7] analysed the potential of various organic residues, including brewery spent grains. Coffee spent ground has also been studied with some persistence concerning energy recovery and more or less following the paths traced for brewery spent grains. In the case of coffee spent ground, the focus seems to be on biogas production, as shown, for example, by Vítěz et al. [8]. Other approaches also emerge, namely the analysis of the recovery potential using thermochemical conversion processes, such as pyrolysis, as presented by Kwon et al. [9], or by hydrothermal carbonization, as presented by Afolabi et al. [10].

The present work addresses the management of brewery spent grains and coffee spent ground residues through the possibility of incorporation in the production of biomass pellets and their direct recovery, in an autonomous way, by combustion. It is also intended to evaluate its potential compared to other fuels derived from biomass using different conversion and recovery technologies.

2 MATERIALS AND METHODS

2.1. Sampling and materials preparation

The biomass materials; Brewery Spent Grains (BSG) and Spent Coffee Grounds (SCG), were supplied by Love Lane Brewery Liverpool and Coffee Bean Shop Liverpool, UK, respectively. The brewery samples were provided in the form of a shaft, while the Coffee waste was provided in the form of particulate powder. The appearance of the samples as received is shown in Figure 1. The samples, when collected, were immediately stored in a freezer box to prevent microbial growth prior to analysis.

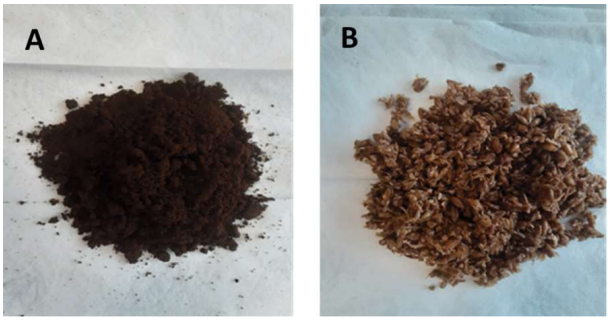


Figure 1: Digital photographs of (a) as received BSG (b) as received SCG.

2.1.1.Material preparation

The moisture content for biomass materials was determined using British Standard BS EN 14774-3:2009, both samples prepared were dried at a temperature of 105 ± 2 °C in an air atmosphere until a constant mass was achieved

and the percentage moisture is calculated from the loss in mass of the sample in previous research [5]. Initial moisture content for BSG and SCG was determined as 81.8 wt. % and 57.1 wt. % respectively (Idowu et al. 2021). 200g of BSG and SCG samples were measured in a 200 micron aperture mesh sieve and air dried in the laboratory at room temperature for five days. Samples were weighed after five days, and the moisture content for each sample measured was <10 wt.%. Prepared samples were placed in airtight paper bags prior to shipment to laboratory in Portugal for combustion analysis.

2.1.2 Laboratory characterization

The objective was to analyze the properties of the materials from a perspective of energy recovery. Therefore, the laboratory characterization of the collected materials was carried out according to the sequence presented in the standard ENPlus ®, enabling a direct comparison with other solid fuels derived from biomass. Table 1 presents the list of standards referred to in the standard ENPlus ® and where the laboratory procedures used are described.

Table 1. Standards used in the laboratory characterization tests.

Standard	**Description**
ISO 17225-1: 2014	Solid biofuels—Fuel specifications and classes—Part 1: General requirements.
ISO 16948: 2015	Solid biofuels—Determination of total content of CHNO.
ISO 16967: 2015	Solid biofuels—Determination of major elements—Al, Ca, Fe, Mg, P, K, Si, Na and Ti.
ISO 16968: 2015	Solid biofuels—Determination of minor elements—Ar, Cd, Co, Cr, Cu, Hg, Mn, Mo, Ni, Pb, Sb, V and Zn.
ISO 16994: 2016	Solid biofuels—Determination of total content of S and Cl.
ISO 18125: 2017	Solid biofuels—Determination of calorific value.
ISO 21404: 2020 (en)	Solid biofuels—Determination of ash melting behavior.

Elemental analysis (CHNO) was performed in the LECO CHN628 apparatus, in which the operating principle consists of weighing a sample in a tin foil that is later placed in the autoloader and then introduced into the furnace containing pure oxygen, with carbon, hydrogen, and nitrogen being completely oxidized and the CHN contents calculated. Oxygen content on a dry basis is calculated by difference. Thermogravimetric analysis (TGA) was performed using ELTRA THERMOSTEP equipment. One gram of each sample was introduced into crucibles and placed inside an oven, along with an empty reference crucible. As the temperature increased, crucibles were weighed on a precision scale. Moisture, volatile, and fixed carbon contents were determined throughout the heating process. Lastly, the final residue represented the ash content. A TITROLINE 7000 titrator from SI Analytics was used to determine the chlorine content. For this procedure, sample preparation involves previous digestion of the sample, performed in a SINEO MDS-6G microwave since titration requires a liquid sample. Chlorine content determination is achieved by potentiometric titration. The lower and higher heating values were determined using an adiabatic bomb calorimeter, model 6400

Automatic Isoperibol Calorimeter, by PARR INSTRUMENT. After each procedure, the equipment provides the corrected temperature increase that is later used to determine the heating value. The determination of ash fusibility consists of monitoring the behavior of ash melting along a temperature ramp. The samples, converted to ashes, were subsequently placed in a plastic dish, where two drops of ethyl alcohol were added and homogenized. Then, this paste was transferred to a mold, where a cylinder was compacted. Subsequently, the cylinders were placed on a zirconia lamella and then placed inside the chamber of the ash fusibility furnace, which in this specific case was an SYLAB IF 2000 g device. Inductively coupled plasma optical emission spectrometry (ICP-OES) was used to determine trace elements and sulphur. The equipment used was a THERMO SCIENTIFIC (iCAP 6000 series). A peristaltic pump delivered the digested samples to an analytical nebulizer and introduced them into the plasma flame that broke down the samples into charged ions, releasing radiation with specific wavelengths.

3. Results

3.1. Laboratory characterization

3.1.1. Spent coffee grains

The results obtained for the elemental analysis are shown in Figure 2.

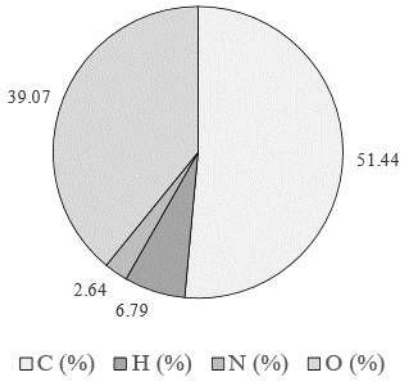


Figure 2. Obtained results from the elemental analysis (CHNO) of spent coffee ground samples.

The results obtained in the thermogravimetric analysis are shown in Figure 3.

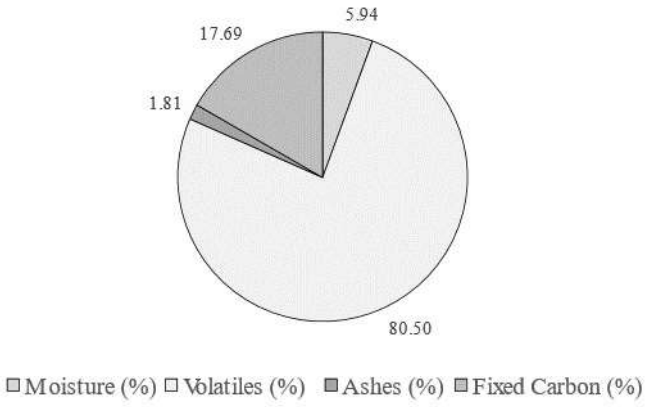


Figure 3. Thermogravimetric analysis of spent coffee ground samples.

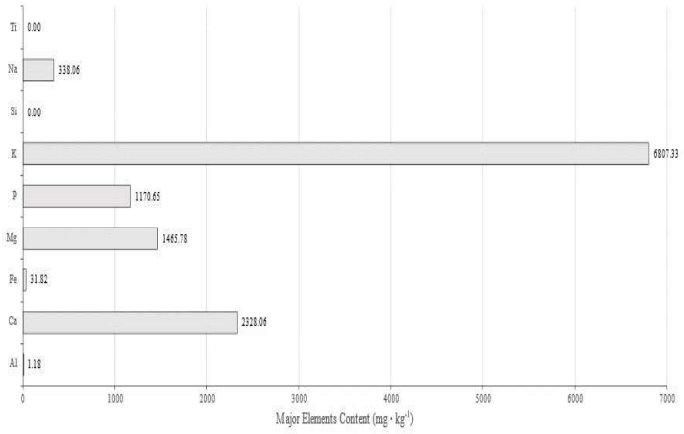


Figure 4. Chemical analysis by ICP-OES for the major elements ($mg \cdot kg^{-1}$).

The chemical analysis of the minor elements is shown in Figure 5.

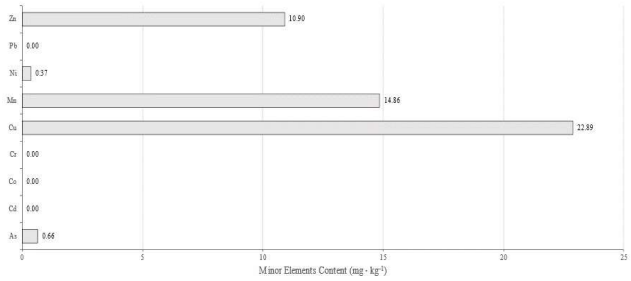


Figure 5 Chemical analysis by ICP-OES for minor elements (mg·kg^{-1}).

Table 2. Spent coffee ground ash fusibility temperatures (IDT – Initial Deformation Temperature; ST – Softening Temperature; HT – Hemispherical Temperature; and FT – Flow Temperature).

	IDT (ºC)	ST (ºC)	HT (ºC)	FT (ºC)
Mean	873	1011	1061	1167
Standard Deviation	12	3	3	4
Measurement Uncertainty	5	1	1	2

3.2.2. Brewery Spent Grains

The results obtained from the elemental analysis of brewery spent grains are shown in Figure 6.

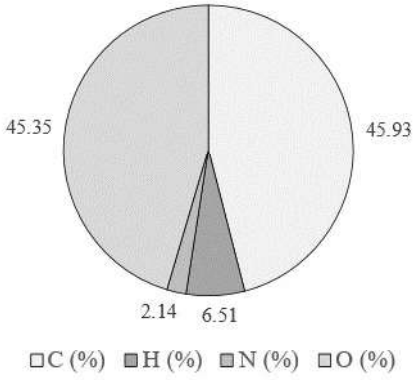


Figure 6. Results from elemental analysis (CHNO) of brewery spent grains samples.

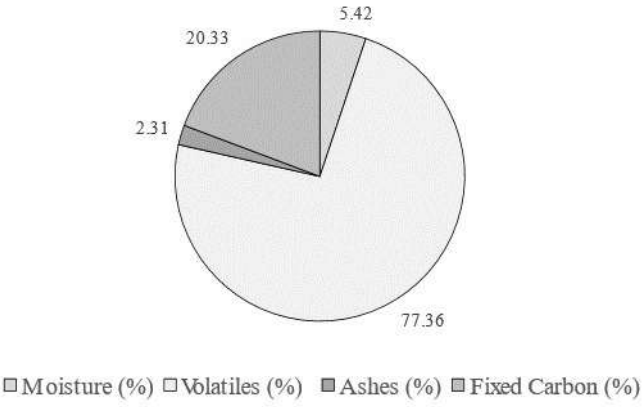


Figure 7. Thermogravimetric analysis of brewery spent grains.

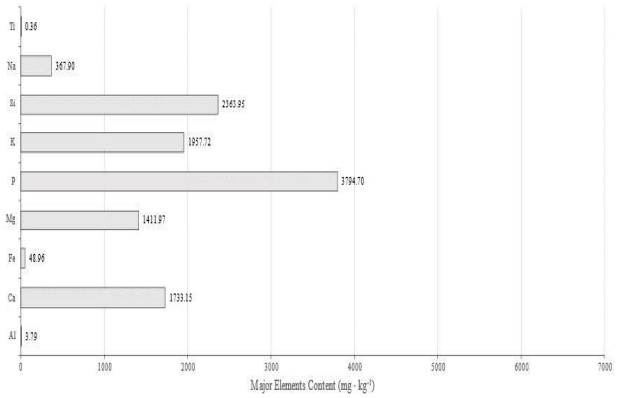


Figure 8. Chemical analysis by ICP-OES for major elements.

Table 3. Brewery spent grains ash fusibility temperatures (IDT – Initial Deformation Temperature; ST – Softening Temperature; HT – Hemispherical Temperature; and FT – Flow Temperature).

	IDT (ºC)	ST (ºC)	HT (ºC)	FT (ºC)
Mean	1159	1351	1498	1519
Standard Deviation	3	6	4	7
Measurement Uncertainty	1	2	2	3

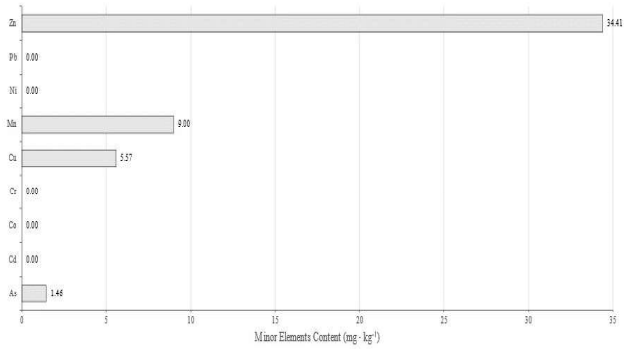
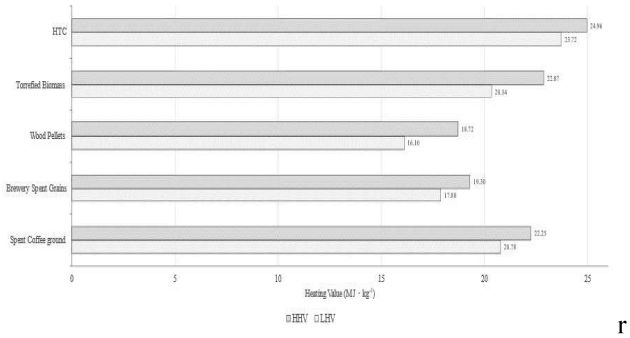


Figure 9. Chemical analysis by ICP-OES of minor elements from brewery spent grains.

Figure 10. Comparative analysis of lower and highe



r

calorific values of different types of biomass resulting from different conversion processes (torrefaction, densification, hydrothermal carbonization).

4. Discussion

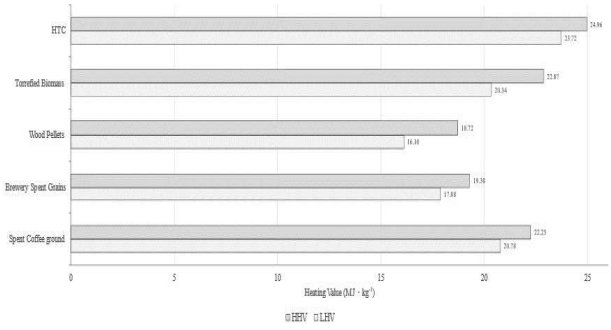
Several works refer to the valorisation of brewery spent grains, mainly, as mentioned, through the extraction, concentration, and production of compounds present in the residue. For example, Carvalheiro et al. [11] addressed the issue of oligosaccharide production by autohydrolysis of brewery spent grains. This perspective of processing in a biorefinery system, which in this specific case was used to produce xylooligosaccharides (XOS), seems to have been the preferred path for a wide range of works. An example of this is the work presented by Terrasan et al. [12], who addressed the production of xylanolytic enzymes, or by López-Linares et al. [13], who addressed microwave-assisted hydrothermal as greener pre-treatment of brewery spent grains for biobutanol production, or by Niemi et al. [14], who found that pre-hydrolysis with carbohydrases facilitates the release of protein from brewery spent grains, or by Montusiewicz et al. [15], who addressed the hydrodynamic cavitation of brewery spent grains diluted by wastewater, or the effect of a milling pre-treatment on the enzymatic hydrolysis of carbohydrates in brewery spent grains, presented by Niemi et al. [16], or by Nigam [17]. From the perspective of energy recovery, Chou et al. [18] conducted a pilot study on the influence of stirring and pH on anaerobes converting high-solid organic wastes to hydrogen. In other words, a more advanced approach and already thinking about a state-of-the-art fuel, which is also the path suggested by Poladyanet al. [18], who addressed hydrogen production by Escherichia coli using brewery waste. However, other approaches have tried to find solutions for the residues by adapting technologies and methodologies already applied to other residues of agro-industrial origin, such as through fermentation processes, aerobic and anaerobic digestion, or even by the application of technologies thermochemical conversion. Examples of this are the works presented by Čater et al. [19], Panjičko et al. [20], This wide range of energy recovery processes supports the idea that, preferably, this will be the path that may have the most potential, without forgetting, however, other forms of recovery, such as the use of these wastes in bioremediation processes [21-23]. From the point of view of energy

recovery processes by direct combustion, only one relevant work was found, presented by Celaya et al. [24], who analyzed the co-combustion of brewery spent grains and coal.

In the case of coffee spent ground, the existing works, in a significantly smaller number, approach practically the same perspectives as the works presented for brewery spent grains, with processing in a biorefinery system also showing some relevance here. For example, Zuorro and Lavecchia [25] refer to coffee spent ground as a valuable source of phenolic compounds and bioenergy, or Mussato et al. [26], who analyzed sugar metabolism and ethanol production by different yeast strains from the coffee industry wastes hydrolysates, or Kwon et al. [27]. They analyzed the sequential co-production of biodiesel and bioethanol with coffee spent ground. Also, in this case, the thermochemical conversion processes assume some prominence. For example, Zhang et al. [28] analyzed the torrefaction performance and energy usage of biomass wastes and their correlations with the severity index. However, as can be seen in the various references analyzed, the direct conversion by combustion of these materials, similarly to what was observed for brewery spent grains, does not seem to have aroused interest. For this reason, the present work assumes an innovative character.

The results show that both spent coffee ground and brewery spent grains have some potential for energy recovery through direct combustion techniques. As can be seen from the results obtained, the calorific value measured for the two materials analyzed is high, which may indicate, from the outset, good possibilities for energy recovery. The two materials analyzed present lower and higher calorific values, which, compared to other biomass resulting from other recovery processes, such as densification, torrefaction, or hydrothermal carbonization, present good conditions that justify their energy recovery. As shown in Figure 13, spent coffee ground and brewery spent grains can present a higher value than wood pellets, a product that does not undergo any chemical change process but only physical through the densification of the constituent material by mechanical pressing. Compared to torrefied biomass, spent coffee ground has an equivalent value, while brewery spent grains have a lower value. This approximation of spent coffee ground to torrefied material is justified since the coffee production process also involves torrefying the material. The material resulting from the hydrothermal carbonization process (HTC) presents values above (~ 2 $MJ \cdot kg^{-1}$) of the torrefied materials.

Figure 10. Comparative analysis of lower and highe



r calorific values of different types of biomass resulting from different conversion processes (torrefaction, densification, hydrothermal carbonization).

However, from the point of view of energy recovery, not only the calorific value is important, but as other parameters also play a decisive role in the efficiency of the thermal conversion processes, such as the ash content, the volatile content, or even the chemical composition of the ash. These parameters influence the kinetics of the oxidation reactions of materials, the release of energy, and how the by-products resulting from these reactions react with the surface of the thermal conversion equipment, as is the case of Cl and alkali metals. These chemical elements contribute significantly to corrosive, fouling, and slagging phenomena on equipment surfaces and ducts, so fuels, where these elements are abundant, are preferred over others where these levels are present in smaller amounts. The high content of N and S can also be considered a problem since their presence in fuels can lead to NO_x and SO_x, which result in gas emissions to the atmosphere, depending on the temperatures of the combustion chamber. Table 4 presents the limit values presented by the ENPlus ® standard, which is used to characterize the biomass materials used for energy recovery, and which allows a comparison with the most common forms of biomass used in the production of wood pellets, such as softwoods species (*Pinus pinaster*, *Pinus sylvestris*, ...), or species of the genus *Eucalyptus*.

Table 4. Comparison of ENPlus ® parameters with spent coffee ground and brewery spent grains.

Parameter	**Units**	**ENPlus ® reference values**	***Spent Coffee Ground***	***Brewery Spent Grains***
		A1 | **A2** | **B**		
Moisture	**%**	**≤ 10.0**	5.94	5.42
Ashes	%	≤ 0.7 | ≤ 1.2 | ≤ 2	1.81	2.31
LHV	$MJ \cdot kg^{-1}$	≥ 16.5	20.78	17.88
N	%	≤ 0.3 | ≤ 0.5 | ≤ 1.0	2.64	2.14
S	%	≤ 0.04 | ≤ 0.05	0.0530	0.0512
Cl	%	≤ 0.02 | ≤ 0.03	0.0039	0.0116
IDT	ºC	≥ 1200 | ≥ 1100	873	1159
As	%	≤ 1	≤ 0.01	≤ 0.01
Cd	%	≤ 0.5	≤ 0.01	≤ 0.01
Cr	%	≤ 10	≤ 0.01	≤ 0.01
Cu	%	≤ 10	≤ 0.01	≤ 0.01
Pb	%	≤ 10	≤ 0.01	≤ 0.01
Ni	%	≤ 10	≤ 0.01	≤ 0.01
Zn	%	≤ 100	≤ 0.01	≤ 0.01

As can be seen, most of the results fall within the limit values presented by the ENPlus ® standard. For example, the minor elements presented values significantly lower than those indicated in the standard, the same happening for the Cl content. The lower calorific value also falls within the limits of the norm, as it is significantly higher in both cases. On the other hand, the ash content presented by the brewery spent grains exceeds the limits of all the categories defined by the ENPlus ® standard, which are A1, A2 and B, which allow ash content of, respectively, ≤ 0.7%, ≤ 1.2% and ≤ 2%. Spent coffee ground could be included in Category B in ash content. However, when it comes to the N content, neither of the two products meets the limits imposed by the ENPlus ® standard since the limits imposed for each category are, respectively, ≤ 0.3%, ≤ 0.5%, and ≤ 1.0 %. Thus, spent coffee ground and brewery spent grains, with 2.64% and 2.14%, respectively, exceeded the permitted values by a large margin.

In this way, the use or even inclusion of these residues in the production process of wood pellets does not seem to be at all viable, especially from a conventional use perspective. The recovery of these residues in thermochemical conversion processes, such as torrefaction, pyrolysis, gasification, liquefaction, or others, could be possible since the fuels derived are not subject to the ENPlus ® standard and will be potentially used in industrial-type recovery processes. For example, torrefied products may follow the assumptions presented by ISO/TS 17225-8:2016 – Solid Biofuels – Fuel Specifications and Classes – Part 8: Graded thermally treated and densified biomass fuels. This standard includes different classes specifically for pellets produced by thermal processing of non-woody biomass, which is summarized in Table 5.

Table 5. Specifications of graded pellets produced by thermal processing of non-woody biomass presented in ISO/TS 17225-8:2016.

Property	Units	TA1	TA2	TA3
LHV	$MJ \cdot kg^{-1}$	≥ 18.0	≥ 17.0	Not specified
Ashes	%	≤ 5.0	≤ 10.0	Not specified
N	%	≤ 1.5	≤ 2.0	≤ 2.5
S	%	≤ 0.1	≤ 0.2	≤ 0.3
Cl	%	≤ 0.1	≤ 0.2	≤ 0.3

From the calorific value point of view, either of the two residues meets the requirements presented in the ISO/TS 17225-8:2016 standard. For the S and Cl contents, compliance is also verified. However, for the N contents, the two residues under analysis could only be included in the TA3 category, which refers to the processing of herbaceous biomass, fruit biomass and aquatic biomass. Most likely, these materials could not be used exclusively or even in combinations with each other but must be used in combination with other materials that allow a dilution of the less favorable parameters, as is the case of N.

5. Conclusions

The circular economy presents itself as the new paradigm of sustainable development, as it effectively contributes to the strengthening of two essential pillars of sustainability: the environmental and economic factors. Waste management has been a growing challenge, as current societies, eager for consumption, produce an increasing amount of waste that needs to be somehow disposed. The prospect of reintroducing this waste back into production cycles is, therefore, the best way to resolve the problem, as, on the one hand, it resolves the issue of the volume of waste to be managed, while on the other hand, it allows the saving of virgin resources. As seen in the literature review, much emphasis has been given to the recovery of these residues through bioremediation, use as a fertilizer, or as a substrate for crop growth. Concerning energy recovery, emphasis has been placed on fermentation and aerobic and anaerobic digestion. However, not much importance has been given to energy recovery through combustion, either directly or indirectly, through the incorporation of these materials in biomass densification processes, such as the production of biomass pellets, or even by

valorisation through thermochemical conversion processes. In this work, the physicochemical properties of brewery spent grains and coffee spent ground were analysed, verifying that their direct combustion may present some difficulties due to some chemical compounds that accelerate the corrosive processes of thermal conversion equipment. Alkali metals and Cl, also associated with the state in which the waste is, mainly due to the high moisture content of the production process, which would require pre-treatment through drying. On the other hand, incorporating these residues in processes such as the production of biomass pellets and other more conventional biomasses already presents more promising results. However, recovery through thermochemical conversion processes, such as pyrolysis, seems to be the scenario with the highest probability of success, given the ability of materials to homogenize, the elimination of the high content of volatile compounds and the concentration of fixed carbon that occurs in these processes, and which allow greater viability of products for applications of energy recovery by combustion, to be used as raw material in biorefinery processes, to be used as pre-treatment for gasification processes, for soil bioremediation, or to be used as a substrate for growing crops.

REFERENCES

1. Ghisellini, P., C. Cialani, and S. Ulgiati, A review on circular economy: the expected transition to a balanced interplay of environmental and economic systems. Journal of Cleaner production, 2016. 114: p. 11-32.
2. Geissdoerfer, M., et al., The Circular Economy–A new sustainability paradigm? Journal of cleaner production, 2017. 143: p. 757-768.
3. González-Sánchez, R., et al., Main dimensions in the building of the circular supply chain: A literature review. Sustainability, 2020. 12(6): p. 2459.
4. Pretty, J., et al., Policy challenges and priorities for internalizing the externalities of modern agriculture. Journal of environmental planning and management, 2001. 44(2): p. 263-283.
5. Idowu, I.A., et al., Enhancing the fuel properties of beverage wastes as non-edible feedstock for biofuel production. Biofuels, 2021: p. 1-8.
6. Géczi, G., et al., EXAMINATION OF ENERGY RECOVERY OF BREWERS'SPENT GRAIN II.-BIOLOGICAL PROCESS. Journal of Microbiology, Biotechnology and Food Sciences, 2021. 2021: p. 268-270.
7. Byrne, A., et al., Suitable biowastes for energy recovery. Sludge to energy Enterprises in Kampala (SEEK), Project, EAWAG Aquatic Research and Sandec, Dübendorf, Switzerland, 2015.
8. Vítěz, T., et al., On the spent coffee grounds biogas production. Acta Universitatis Agriculturae et Silviculturae Mendelianae Brunensis, 2016. 64(4): p. 1279-1282.
9. Kwon, E.E., S. Kim, and J. Lee, Pyrolysis of waste feedstocks in CO2 for effective energy recovery and waste treatment. Journal of CO2 utilization, 2019. 31: p. 173-180.
10. Afolabi, O.O., M. Sohail, and Y.-L. Cheng, Optimisation and characterisation of hydrochar production from spent coffee grounds by hydrothermal carbonisation. Renewable Energy, 2020. 147: p. 1380-1391.
11. Carvalheiro, F., et al., production of oligosaccharides by autohydrolysis of brewery's spent grain. Bioresource technology, 2004. 91(1): p. 93-100.
12. Terrasan, C.R.F., et al., production of xylanolytic enzymes by Penicillium janczewskii. Bioresource Technology, 2010. 101(11): p. 4139-4143.
13. López-Linares, J.C., et al., Microwave assisted hydrothermal as greener pre-treatment of brewer's spent grains for biobutanol production. Chemical Engineering Journal, 2019. 368: p. 1045-1055.
14. Niemi, P., et al., Pre-hydrolysis with carbohydrases facilitates the release of protein

from brewer's spent grain. Bioresource Technology, 2013. 136: p. 529-534.
15. Niemi, P., et al., Effect of a milling pre-treatment on the enzymatic hydrolysis of carbohydrates in brewer's spent grain. Bioresource Technology, 2012. 116: p. 155-160.
16. Nigam, P.S., An overview: Recycling of solid barley waste generated as a by-product in distillery and brewery. Waste management, 2017. 62: p. 255-261.
17. Chou, C.-H., et al., Pilot study of the influence of stirring and pH on anaerobes converting high-solid organic wastes to hydrogen. International Journal of Hydrogen Energy, 2008. 33(5): p. 1550-1558.
18. Poladyan, A., et al., Hydrogen production by Escherichia coli using brewery waste: optimal pre-treatment of waste and role of different hydrogenases. Renewable Energy, 2018. 115: p. 931-936.
19. Čater, M., et al., Biogas production from brewery spent grain enhanced by bioaugmentation with hydrolytic anaerobic bacteria. Bioresource technology, 2015. 186: p. 261-269.
20. Panjičko, M., et al., Biogas production from brewery spent grain as a mono-substrate in a two-stage process composed of solid-state anaerobic digestion and granular biomass reactors. Journal of Cleaner Production, 2017. 166: p. 519-529.
21. Abioye, P.O., A. Abdul Aziz, and P. Agamuthu, Enhanced biodegradation of used engine oil in soil amended with organic wastes. Water, Air, & Soil Pollution, 2010. 209(1): p. 173-179.
22. Chanzu, H.A., J.M. Onyari, and P.M. Shiundu, Brewers' spent grain in adsorption of aqueous Congo Red and malachite Green dyes: Batch and continuous flow systems. Journal of hazardous materials, 2019. 380: p. 120897.
23. Chanzu, H.A., J.M. Onyari, and P.M. Shiundu, Biosorption of malachite green from aqueous solutions onto polylactide/spent brewery grains films: kinetic and equilibrium studies. Journal of Polymers and the Environment, 2012. 20(3): p. 665-672.
24. Celaya, A.M., A.T. Lade, and J.L. Goldfarb, Co-combustion of brewer's spent grains and Illinois No. 6 coal: Impact of blend ratio on pyrolysis and oxidation behavior. Fuel Processing Technology, 2015. 129: p. 39-51.
25. Zuorro, A. and R. Lavecchia, Spent coffee grounds as a valuable source of phenolic compounds and bioenergy. Journal of Cleaner Production, 2012. 34: p. 49-56.
26. Mussatto, S.I., et al., Sugars metabolism and ethanol production by different yeast strains from coffee industry wastes hydrolysates. Applied Energy, 2012. 92: p. 763-768.
27. Kwon, E.E., H. Yi, and Y.J. Jeon, Sequential co-production of biodiesel and bioethanol with spent coffee grounds. Bioresource technology, 2013. 136: p. 475-480.
28. Zhang, C., et al., Torrefaction performance and energy usage of biomass wastes and their correlations with torrefaction severity index. Applied energy, 2018. 220: p. 598-604.

SWIRLER EFFECTS ON COLORLESS DISTRIBUTED COMBUSTION USING METHANE FLAME

A. ILBAS[1], M. B. OZDEMIR[2] and S. KARYEYEN[3]

1. Alparslan İLBAŞ, PhD Candidate of Faculty of Technology, Gazi University, Ankara; email: alparslan.ilbas@gazi.edu.tr
2. Mustafa Bahadır ÖZDEMİR, Faculty of Technology, Gazi University, Ankara; email: mbozdemir@gazi.edu.tr
3. Serhat KARYEYEN, Faculty of Technology, Gazi University, Ankara; email: serhatkaryeyen@gazi.edu.tr

Abstract

Colorless distributed combustion (CDC) is a promising combustion method for improving thermal efficiency and reducing environmental pollutions. This combustion method is often characterized by well-distributed reaction zones, which can potentially decrease hot temperature zones, resulting in NOx emission. The present study was carried out for an existing experimental combustion chamber with using numerical method to examine the effect of different swirl numbers on distributed conditions. In this study, the effect of the air reintroduced into the combustion chamber was investigated on the combustion conditions at different swirl numbers through a newly generated swirler during the non-premixed combustion of methane gas at an equivalent ratio of 0.83. According to the results obtained from the study, it was observed that increase in the swirl number provided combustion distribution throughout the combustion chamber, mitigated the local hot spots and resulted in a decrease in the NOx and CO pollutant emissions in the combustion products. It has been determined that the use of a swirler has contributed for achievement of CDC regime by providing well-distributed reaction zones.

Keywords: Distributed Combustion, Low NOx, Swirl Number, Swirler

1 INTRODUCTION

Nowadays, fossil fuels constitute our main energy sources. When the economic and industrial situations are examined, it is seen that it is not feasible to change this situation in the short term. Because of that, the number of investigations on burning with low pollutant and NOx have increased day by day.

Colorless distributed combustion (CDC or flameless combustion) is a novel method to enhance flame stability and thermal field uniformity, increase combustion efficiency, and reduce pollutants' emission [1]. CDC is achieved through the use of a carefully prepared fuel–oxidizer mixture along with reactive species [2].

In this study, methane was selected as the fuel in order to validate the modelling results. Methane is burned under no-swirl effect condition (condition that swirl number is 0) and with swirl effect (condition that swirl number is 1) conditions and investigated effect of increasing distributed combustion zone. Swirl effect on distributed colorless combustion characteristics such as temperature, velocity field, and emissions were examined. The main aim of the swirling flow is to achieve a stable flame and to provide a good mixing.

2 DETAILS OF MODELING

Methane fuel were consumed under two different conditions in the combustion chamber specified in Figure 1 [1]. The fuel required to obtain a thermal power of 10 kW has been calculated for all cases. In addition to this, the equivalence ratio for all cases was kept constant at 0.83. In order to compared distributed regime effect and to achieve distributed regime, swirler added air intake and swirler number is specified as 0 and 1. In this way, flameless combustion via swirler eddy on combustion characteristics of Methane fuel will be examined.

Combustor geometry, swirler position and relative data lines that are named as inletline, bottomline and outletline, are given Figure 1.

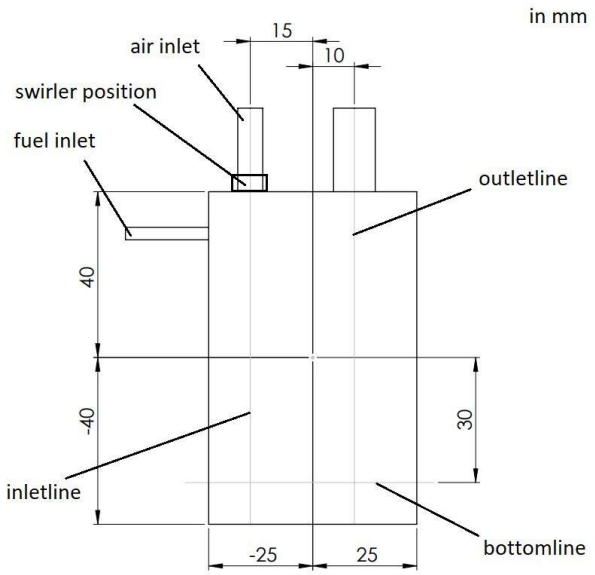


Figure 1. Combustor Geometry and Definitions

For all modelling, the non-premixed modelling with assumed-shape β-function Probability Density Function was selected as the combustion model. As a radiation model, P-1 have been used. The k-ε realizable turbulence model has also been selected for giving better results, in particular, for different velocity directions. In addition to combustion modelling, NOx post-processing has been implemented in the combustor for NOx prediction

2.1 Swirler Number Calculation

Swirler number was calculated as;

$$S = \frac{2}{3}\left(\frac{1-\left(d_h/d\right)^3}{1-\left(d_h/d\right)^2}\right)\tan\beta \quad (1)$$

Where, S is swirler number, d_h is generator hub diameter, d is the outer swirl generator diameter and β is exit angle of the swirl vanes

2.2 Validation

The experimental results reported by Gupta and Arghode [1] have been used for validation of the modelling results. The combustion chamber selected in the present study is the same as that one reported. In this way, the further modelling results will be meaningful in the present study.
The study that present by Gupta and Arghode[1], have experimental results at non-reaction conditions. Our analysis results showed good similarity with given experimental results.

3 RESULTS

Velocity, temperature and NOx formation graphs obtained in the combustion chamber for each condition are shown in Figure 2-10
Zero swirler angle conditions are shown dot line all graphs. The seamless line represents condition that equal swirler number is 1 at all graphs.
As part of the study, produced material mass flow rate calculated and shared with Table 1. Amount of total produced NOx is lower at condition that swirl number is 1.

Table 1. Outlet Section Mass Flow Rates

(kg/s)	S=0 Conditions	S=1 Conditions
NOx	-1,581E-07	-4,62523E-08
CH4	-6,374E-12	-5,4945E-10
N2	-3,032E-03	-3,026E-03
O2	-1,404E-04	-1,750E-04
H2O	-4,354E-04	-4,176E-04
H2	-1,783E-07	-7,007E-07
CO	-5,839E-06	-1,757E-05
CO2	-5,285E-04	-4,931E-04
OH	-5,792E-06	-4,290E-06
Total	-4,148E-03	-4,134E-03

3.1 Temperature Graphs

When inlet temperature graph is examined, condition that swirl number is 1, combustion started earlier than that of the condition that swirl number is 0. Less temperature level has been achieved for a swirl number of 1. This situation can be explained with distributed conditions. Also, air momentum distributed rotational and axial direction and the axial velocity of the air have decreased. This cause started to combustion an earlier position and more distributed combustion. In Figure 2, inletline temperature graph is given.

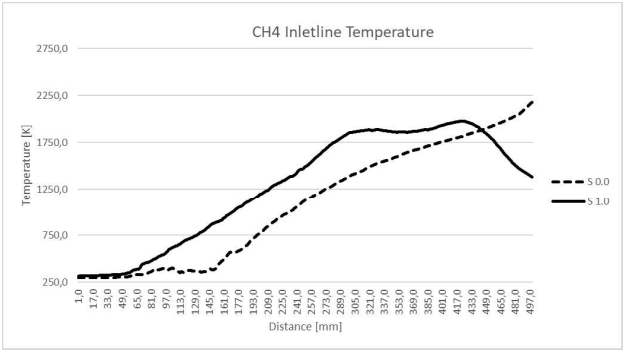


Figure 2. Inletline Temperature Graph

On the bottomline, for condition that swirl number is 1, there has been longer high temperature zones compared to that of a swirl

number of 0. This can be explained with axial air velocity difference. In Figure 3, bottomline temperature graph is given.

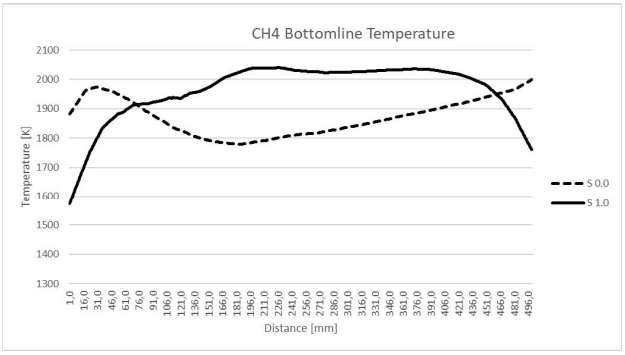


Figure 3. Bottomline Temperature Graph

On the outline, swirling effects on the temperature profiles can be seen due to mixing.

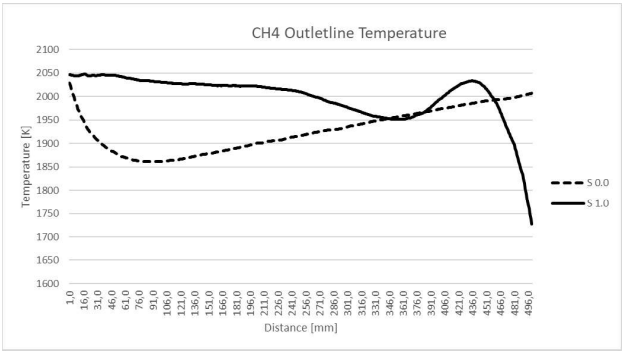


Figure 4. Outletline Temperature Graph

3.2 Velocity Graphs

According to below graphs, one can say that; the inletline axial velocity predicted for condition that swirl number is 1, is slower than that of the condition that swirl number is 0. The reason of this result, can be explained with total momentum divided into two directions at a swirl number of 1. Besides, inlet zone fluctuation at 0 swirl number is more. Those momentums contributed to achieve distributed conditions.

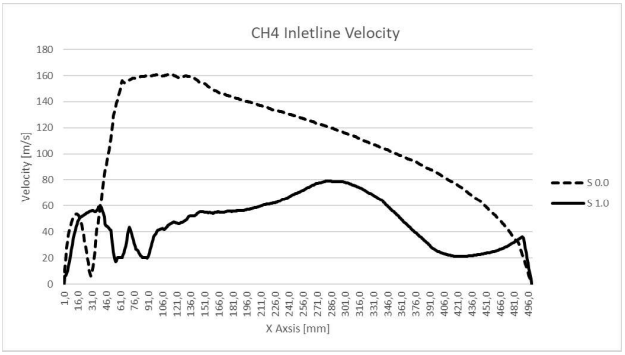


Figure 5. Inletline Velocity Graph

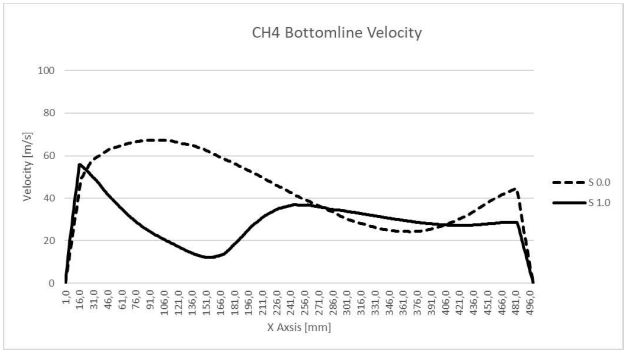


Figure 6. Bottomline Velocity Graph

Outletline velocity profiles for both conditions are seen in good agreement due to decrease in momentum effects.

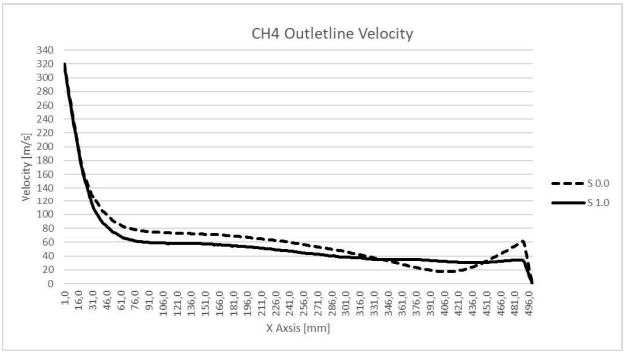


Figure 7. Outletline Velocity Graph

3.3 NOx Formation Graphs

According to the analysis, along the inletline, NOx levels predicted have been less level than other condition. For all graphs, condition that swirl number is 1, total NOx production remained at less levels. This graph is important to understand swirler effect on the combustion. In Figure 8, inletline NOx mass fraction graph is given.

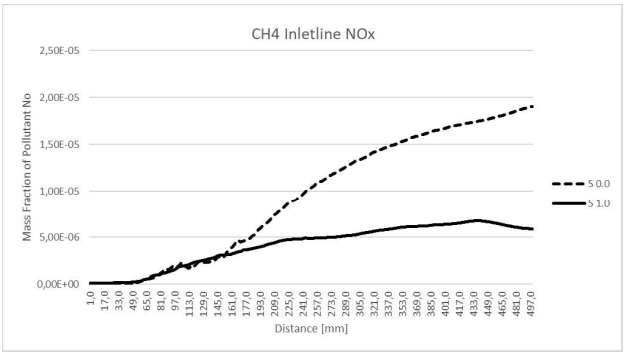


Figure 8. Inletline NOx Mass Fraction Graph

In Figure 9, bottomline NOx mass fraction graph is given.

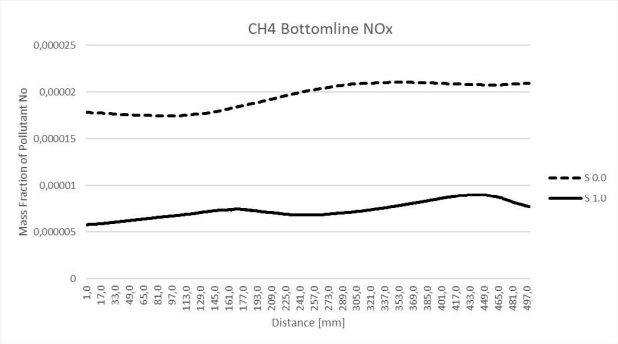


Figure 9. Bottomline NOx Mass Fraction Graph

In Figure 10, outline NOx mass fraction graph is given.

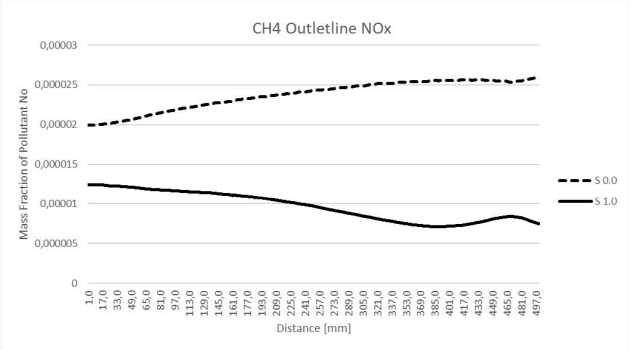


Figure 10. Outletline NOx Mass Fraction Graph

4 CONCLUSIONS

When the analysis results are examined, it is seen that the temperature distributions are more uniform in case of the swirl number is 1. The swirler eddy distributed reactants air flow changed combustion characteristics. Also, when examined outlet exhaust NOx level, combustion chamber with the swirler has less NOx pollutant than that of a swirl number of 0. The reason for this conclusion can be explained by swirl eddy caused more distributed zones, and this helps to achieve colorless distributed combustion conditions. When temperature distributions on combustion chambers are examined, for a swirl number of 1, thermal intensity regions have been wider than that of a swirl number of 1. This situation led to higher NOx formation due to thermal NOx mechanism. Therefore, it is understood that the swirler mitigated NOx formation and contributed to achieve colorless distributed combustion conditions.

ACKNOWLEDGEMENTS

The authors gratefully acknowledge Gazi University for its support because of permitting usage of Ansys Fluent Academic Computer Code.

REFERENCES

[1] A.E.E. Khalil, V.K. Arghode, A.K. Gupta, Novel mixing for ultra-high thermal intensity distributed combustion, Applied Energy, Vol. 105, pp. 327-334, 2013

[2] A.E.E. Khalil, A.K. Gupta, Internal entrainment effects on high intensity distributed combustion using non-intrusive diagnostics, Applied Energy, Vol 160, pp. 467-476, 2015.

[3] A. A. V. Perpignan, A. Gangoli Rao, D. J. E. M. Roekaerts, Flameless combustion and its potential towards gas turbines, Progress in Energy and Combustion Science, Vol. 69, pp. 28-62, 2018

[4] A. Ilbas, M.B. Ozdemir, S. Karyeyen, Investigation of colorless distributed combustion regime using a high internal recirculative combustor, International Journal of Hydrogen Energy, Vol. 47, Issue 24, pp. 12338-12353, 2022.

[5] Ø. Spangelo, Experimental and theoretical studies of a low NOx swirl burner, PhD Thesis, The Norwegian University of Science and Technology, 2004.

[6] M. Ilbas, S. Karyeyen, I. Yilmaz, Effect of swirl number on combustion characteristics of hydrogen-containing fuels in a combustor, International Journal of Hydrogen Energy, Vol. 41, Issue 17, pp. 7185-7191, 2016.

[7] S. Karyeyen, J.S. Feser, A.K. Gupta, Swirl assisted distributed combustion behavior using hydrogen-rich gaseous fuels, Applied Energy, Vol. 251, 113354, 2019.

[8] A.E.E. Khalil, A.K. Gupta, Thermal field investigation under distributed combustion conditions, Applied Energy, Vol. 160, pp. 477-488, 2015.

[9] F. Wang, X. Xie, Q. Jiang, L. Zhou, Effect of turbulence on NO formation in swirling combustion, Chinese Journal of Aeronautics, Vol. 27, Issue 4, pp. 797-804, 2014.

[10] A.E.E. Khalil, A.K. Gupta, Towards colorless distributed combustion regime, Fuel, Vol. 195, pp. 113-122, 2017.

NEW APPROACH TO EVALUATING THE FUNCTIONAL PROPERTIES OF DETERGENT ADDITIVES FOR MOTOR GASOLINES

Vsevolod D. Savelenko[1], Mikhail A. Ershov[1], Nikita A. Klimov[1, 2], Nikita O. Burov[1], David R. Aleksanyan[1, 2], Ulyana A. Makhova[1], Tamer M.M. Abdellatief[1], Andrey A. Pimenov[3], Kirill A. Ovchinnikov[3], Ekaterina V. Podlesnova[3], Alexey V. Nizovtsev[3]

1. Department of Oil Refining Technology, Faculty of Chemical and Environmental Engineering, Gubkin Russian State University of Oil and Gas (National Research University), Moscow 119991, Russia; email: com@gubkin.ru
2. New Technologies Watch Center, LLC, Moscow, 117546, Russia; email: info@ntwc.ru
3. Gazpromneft Industrial Innovations, LLC, St. Petersburg, 197350, Russia; email: info@gazprom-neft.ru

Abstract

Modern automobile gasoline is an extremely complex multi-component product that must not only supply energy to an internal combustion engine, but also keep its long and uninterrupted operation, which is ensured, among other things, by maintaining the cleanliness of the fuel system. To give gasolines a detergent ability, special detergents and multifunctional additives are included in them. The effectiveness of these additives is seen in extremely harsh and difficult-to-repeat operating conditions of the intake valve and combustion chamber, so the only way to evaluate their functional properties is engine rig tests. This paper proposes new approaches to assessing the detergent properties of gasolines containing additives that are not significantly expensive and use only laboratory equipment. The results of comparing the detergent efficiency of various commercially available and prototype samples of additives in the engine rig tests and proposed laboratory tests are given. The limits of applicability of the developed method are shown. The developed method can be used for screening samples of detergent additives in the process of their development and quality control of industrial batches, replacing expensive motor tests.

Keywords: Gasolines, Detergent additives, Multifunctional additives, Engine rig test.

RANS STUDIES OF MINIMUM IGNITION ENERGY OF STOICHIOMETRIC LAMINAR METHANE/AIR FUEL MIXTURES

***Vasudevan*, Sooraj PM, [£!]*Muppala*, Siva PR, *Heidari*, Ali and *Dembele*, Siaka**

Fire, Explosion and Fluid Dynamics (FEFD) Research Group
School of Engineering and the Environment
Faculty of Engineering, Computing and the Environment
Kingston University London
Roehampton Vale, Friars Avenue, London, UK, SW15 3DW
[!]s.muppala@kingston.ac.uk

Abstract
The aim of the European Commission is to achieve net zero carbon emissions by 2050. Despite the ban on oil and coal from its EU territory, natural gas, which consists of 70% to 90% methane, will remain a substantial source of energy in years to come, and the emitted CO_2 will be stored in depleted oil fields. This numerical study reports an evaluation of the lowest amount of energy for the methane-air stoichiometric mixture required to ignite the flame kernel and evolve into a self-sustainable flame. In this one parametric study, the ignition energy density is varied by keeping the kernel radius constant. The measurement of minimum ignition energy (MIE) helps to understand ignition delays, describe the ignition of sparks and, in general, and elucidate the combustion phenomena. Determining the explosive characteristics of hazardous chemicals requires knowledge of minimum ignition energy [9].

Keywords: Minimum Ignition Energy, RANS, OpenFOAM, Premixed methane/air mixtures

1 INTRODUCTION

The United Nations Sustainable Development Goals (SDGs) draw a compelling framework for the sustainable future of the planet earth. Energy sustainability is crucial to the success of Agenda 2030. Global energy's Sustainable Development Goal (SDG) 7 comprises three main objectives: to provide widespread, affordable, and dependable access to modern energy services; the achievement of this goal will considerably increase the proportion of renewable energy in the global energy mix [14]. Methane, the lightest hydrocarbon, arguably the cleanest hydrocarbon fuel, compared to petrol and diesel. The methane is a promising source of renewable energy because it can be synthesised through the anaerobic digestion of biomass [12]. Also methane can be converted to hydrogen, sustainability, provided CO_2 can be sequestrated. Using enthalpy calculations, the dissociation of methane to hydrogen is more energy economical than one water mole in electrolysis [4]. As a result, methane has extensive applications in both the domestic and industrial sector.

Spark ignition is a sophisticated mechanism that entails the interaction of chemical and physical reactions. The flame kernel is the initial step of flame inception in internal combustion, with many parameters, including mixture composition, initial temperature, and pressure, influencing the behaviour of the ignition [1]. One of the most fundamental challenges in combustion is the onset of a flame. It is either desired, as in gasoline engines, or avoided, as in explosive environments.. In both circumstances, knowing more about how the flame begins and spreads can lead to more applications. Initial flame propagation is the prime ignition sensitivity parameter; it is evaluated by taking the possibility of ignition into account [6]. Several studies have documented the flame kernel's development [13, 10, 11]. This enables the development of more efficient and safe engine

designs with enhanced fuel economy and reduced emissions.

Kravchik et al show that kernel growth happens in two stages. In the first, short stage, mass and energy are changed by the pressure wave and the expansion of the plasma kernel [7]. During the second stage, mass and energy are changed by diffusion and thermal conduction. However, there is a plethora of data on kernel parameters and minimum ignition energy (MIE) for various flammable combination of mixtures that may be accessed via ASTM-standardised experiments. One of the earliest detailed studies is by Lewis et al. who examined the influence of pressure, initial temperature, mixture stoichiometry, and ignition source volume for various fuels on MIE [8]. Cui et al. [2] carried out experiments to measure MIE for $CH_4/N_2/O_2$ mixtures with compositions to show that MIE is a strong function of pressure and temperature. Han et al. [5] numerically studied the spark ignition characteristics of CH_4/air mixtures, for temperatures 300 K, 1000 K and 2000 K by setting electrode gap to 1 mm, to measure minimum ignition energy (MIE) i.e. MIE, i.e. the energy required at which the flame develops successfully with 50% probability after the flame kernel ignition, are validated against experiments carried out by Lewis and von Elbe [8]. The same authors observed that the MIE curve shifts towards the leaner side with an increase in temperature. This finding substantiates experiments by Cui et al. [2] in that MIE decreases with increase in temperature.

In this study, MIE, of methane/air mixtures at atmospheric pressure is evaluated numerically, by solving unsteady conservation equations with one-step reaction mechanism using reactingFoam RANS solver. These flames are assumed to be spherically symmetric, which results in the considerable simplification of the case. The temperature and the species profiles are analysed to understand the evolution of the flame, until the flame temperature flattens after reaching the adiabatic temperature. The study do not take into account any heat losses.

.

2 GEOMETRY AND FORMULATION

The model geometry is a cuboid filled with methane/air stoichiometric mixture at standard atmospheric conditions, 300 K and 101.325 kPa, with a spherical ignition kernel at the centre. The spherical flame is expected to propagate symmetrically. The three-dimensional computational cubical domain measures 75 mm on each side, with 200 grid points in the x, y, and z directions, i.e. the resolution of the mesh is 0.1875 mm, as shown in Fig. 1. The kernel size is 0.5 mm in radius (radius of the flame kernel, r_s), so that it can have (1/0.1875=5.33) cells. Hexahedral mesh is opted for a more accurate flow field solution than tetrahedral mesh, for same number of cells [15].

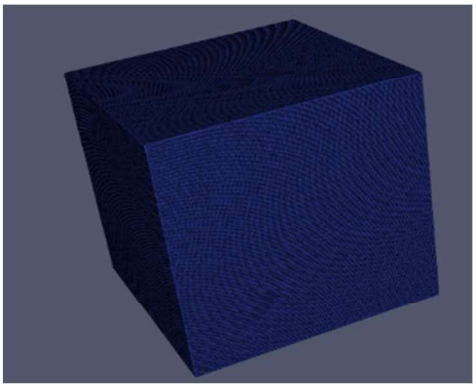


Figure 1: Cubical computational domain of side 75 mm with a spherical flame kernel of r_s= 0.5 mm at its centre, hexahedral mesh

The one-step methane/air reaction mechanism is

$$CH_4 + 2O_2 \rightarrow CO_2 + 2H_2O \quad (1)$$

The ignition energy is varied gradually by trial and error until MIE is attained.

3. NUMERICAL SOLVER, reactingFOAM

The cubical geometry is constructed using blockMeshDict utility where the vertices, number of grid points and boundaries are specified. Five boundaries are defined in this case such as top, left, right, bottom, frontAndBack. The boundary type is specified as patch. The spherical ignition kernel is set up using SetFiledsDict utility, in which the default scalar values such as mixture temperature, and composition of CH_4, O_2, and N_2 are set. All the transport equations are solved using the reactingFoam transient solver. Using the 'SphereToCell' command, the ignition temperature and other field values such as compositions of CH_4, pressure are pre-defined

for the flame kernel. The controlDict dictionary defines the numerical control of the whole

simulation, which identifies the start time, end time, and the deltaT (time step) of the simulation. Here, the time step is given as 0.01 The computational start time and end time are 0 and 10 s, respectively. Similarly, chemistry properties, combustion properties, momentum transport, thermo-physical properties and reactions are defined in the Constant folder. The Local Euler scheme is used for the time scheme as it is suitable for steady flows. The discretisation scheme used for gradient terms and divergence terms is the Gauss linear scheme.

4. NUMERICAL METHODOLOGY

There are three directories in OpenFOAM, for each numerical case, which are set as '0', 'system' and 'constant'. 'System' contains three files such as controlDict, with run control parameters that control the simulation. FvSchemes, where different discretisation schemes are used for time, divergence and gradient terms according to the type of simulation case and result required. fvSolution is where equation solvers, tolerances and other algorithm controls are set up. The geometry and mesh properties are defined in system/blockMeshDict. The minimum ignition energy density (q) is given with the help of fvOptions. Domain size is specified along with the number of gradient points. The boundaries are initialised as patch (general boundary) considering the flame development. '0' directory contains individual data required for particular fields. The fields can be initial values and boundary conditions that need to be defined to explain a problem. 'inletOutlet' boundary condition is specified . The most crucial part of simulating chemical reactions, is to determine the system's chemical and thermo-physical properties. Therefore, it is necessary to specify all the available chemical species and their associated models for computing physical properties. OpenFOAM needs species-specific information like molecular weight, density, enthalpy/internal energy, and transport characteristics. These quantities are obtained based on the thermo-physical models, selected from the existing list by the author. The model specified here is the laminar model from OpenFOAM libraries.

5. NUMERICAL RESULTS

The criterion of ignition success plays a crucial role in estimating the MIE. The point at which a flame kernel originates in a given location and develops consistently is regarded to be the point of successful ignition [6].

The minimum ignition energy density q is defined in the spherical flame geometry MIE

$$q = \frac{E}{V} \tag{2}$$

where

E is ignition energy

V is the ignition kernel volume

q is numerically evaluated by trial and error, starting with $1\text{^}10^6$ J/m^3 [16].

For spherical geometry, E is the total energy deposited at the centre of the gas mixture. The energy density q_s for the flame kernel.

$$q_s = \frac{E_s}{\frac{4}{3}\pi r_s^3} \tag{3}$$

where the letter s stands for sphere.

At the centre of the domain (r = 0), a volumetric constant heat source is applied from computational time, t = 0 to t = 0.2 s (ignition duration), confined to a cubical volume for which the size is determined by the ignition radius r_s = 0.5 mm so that there is adequate room to ensure that the domain's outer boundary does not interfere with the igniting process and the first phase of flame propagation

The present study shows the minimum ignition energy density, q, for a successful evolution of the flame is $q=1 \times 10^8 J/m^3$. Figure 2 shows the flame evolving up to the temperature contour as a function against time for the full computational time of 3.6 s, reaching the adiabatic flame temperature. The simulations

are run until the adiabatic flame temperature ~2230 K is achieved and remains constant, as shown in Figure 3.

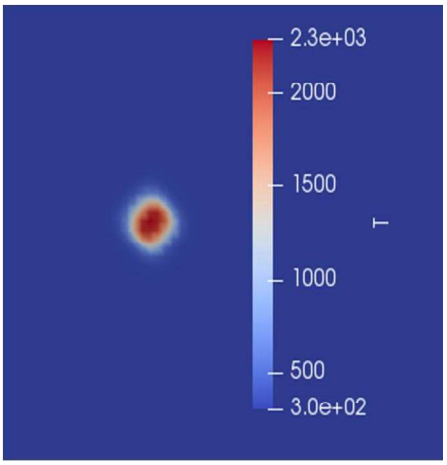


Figure. 2: Temperature (K) contour of premixed CH_4 /air mixture at the kernel flame radius r_s = 0.5 mm.

The same figure shows the flame temperature rises linearly from 300 k to 600 K, from t = 0 to t ~ 1.0 s then temperature shoots up to ~2500 K. Once the ignition is turned off, the slope of the temperature curve declines until t = 1 s, when it reaches a high of 2450 K. The flame temperature nearly stabilises at around T = 2230 K.

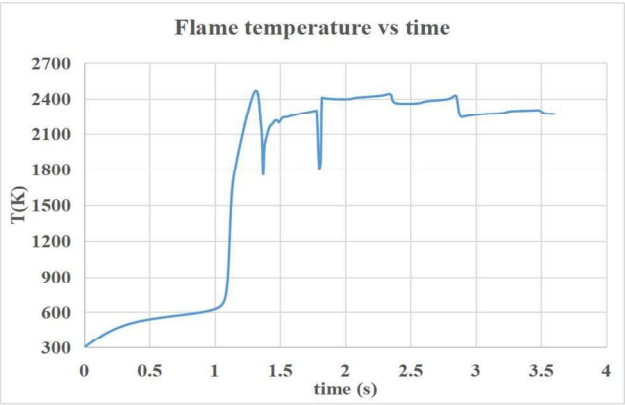


Figure. 3: Temperature (K) vs time (s) of premixed CH_4/air mixture at the kernel flame radius r_s = 0.5 mm

Figure 4 shows to the centre of the flame kernel (r = 0) to.the boundary of the domain (r = 37.5 mm). The temperature rises significantly inside the flame. The flame propagation can be visualised for the species methane and carbon dioxide, in Figures 5 and 6, respectively.

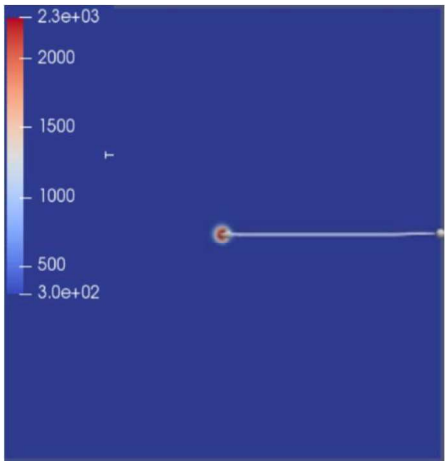


Fig.4a

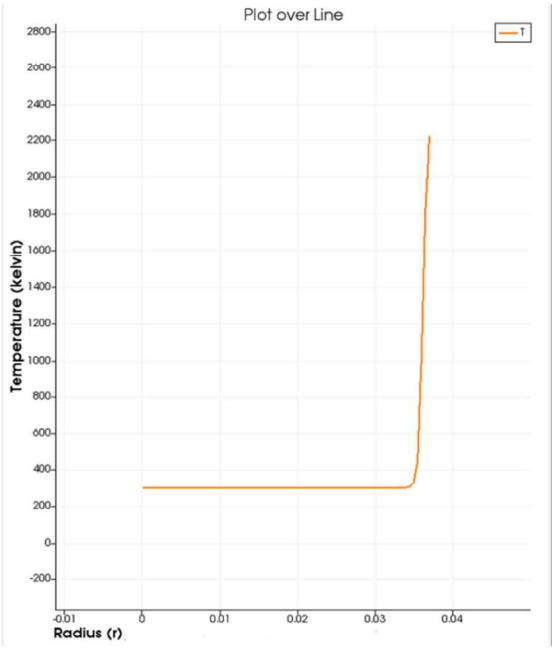


Fig. 4b.

Figure. 4a(top): shows the centre of the flame kernel r = 0 to the boundary r = 37.5 mm. The blue indicates unburned premixed CH_4 /air mixture, and red indicates the burned mixture. b) the plot showing temperature as a function of radius.

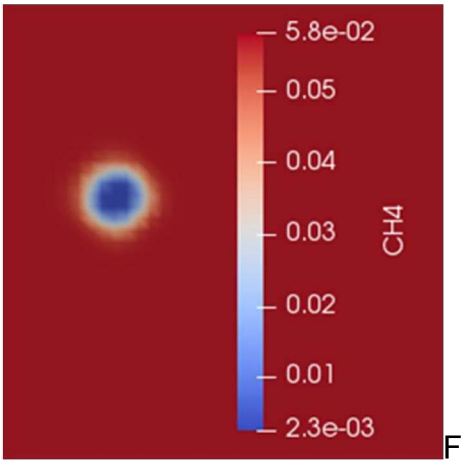


Fig.5a

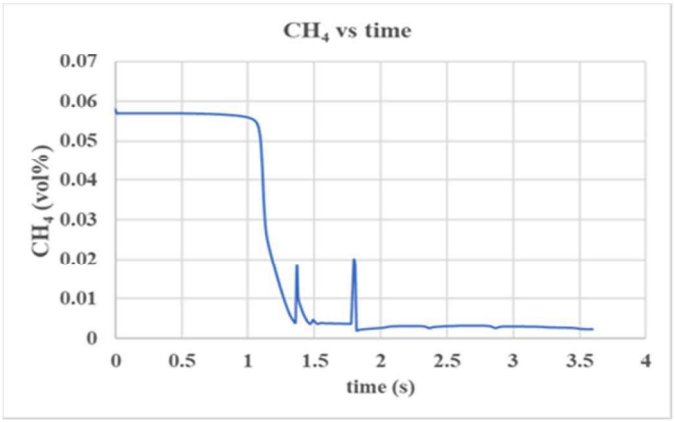


Fig. 5b

Fig. 5a&b: CH_4 contour (left) and plot over time methane is consumed for premixed CH_4 /air mixture at r_s = 0.5 mm (right). The sharp fall in the fuel indicates the reaction zone, at t = 1.1 to 1.4 s.

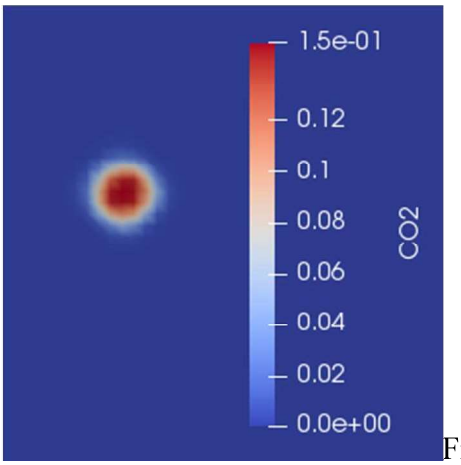


Fig.6a

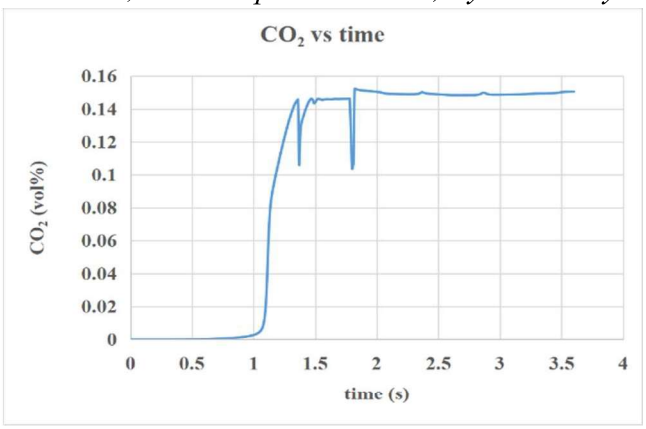


Fig.6b

Figure. 6a&b: CO_2 contour (left) and plot over time for premixed CO_2 at r_s = 0.5 mm

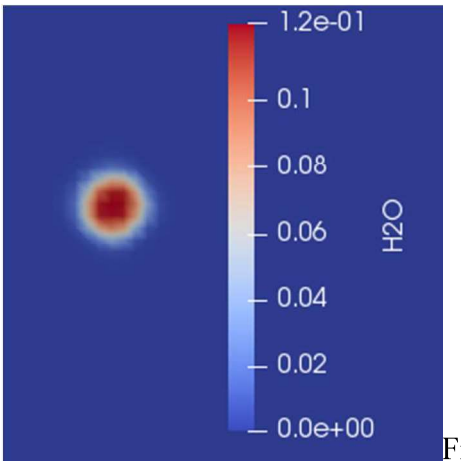


Fig.7a

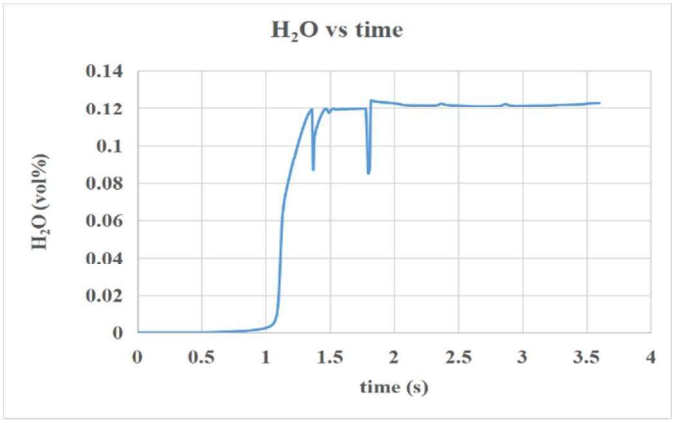


Fig.7b.

Figure. 7a&b: H_2O contour (left) and plot over time for H_2O at r_s = 0.5 mm

Figure 5 demonstrates the depletion of methane along with the propagation of flame. These results and this trend can be validated with the simulation results of methane/air simulation carried out using object-oriented software suite Cantera [3]. Figures 5, 6 and 7 show the variation in the

composition of CH_4, CO_2 and H_2O, respectively, over the full time steps.

6. CONCLUSION

In this RANS study, the minimum ignition energy and ignition characteristics of a successful stoichiometric methane-air flame were numerically studied using reactingFoam solver of free OpenFOAM source code using one-step methane mechanism. All the simulations were run until the temperature of the methane/air mixture stabilised at its adiabatic flame temperature of approximately 2230 K. The successful ignition of a spherical flame kernel was determined for minimum ignition energy density $q=1 \times 10^8 J/m^3$.

REFERENCES

[1] Y. Bianco, W. Cheng, and J. Heywood, 'The Effects of Initial Flame Kernel Conditions on Flame Development in SI Engine,' *SAE Technical Paper 912402*, 1991.

[2] G.Cui, W. Zheng, Z. Li, Y. Fu, Experimental study of minimum ignition energy of methane/air mixtures at elevated temperatures and pressures. *Fuel*. Volume 175, 1 July , pp. 257–263, 2016.

[3] G. G. David, K. M. Harry, S. Ingmar, L.S Raymond, and W. Bryan, Cantera: An object-oriented software toolkit for chemical kinetics, thermodynamics, and transport processes. www.cantera.org., 2016. (accessed 15 September 2022)

[4]. S. Furfari, *The hydrogen illusion*. Kindle edition. Page 71, 2021.

[5] J. Han, H. Yamashita, N. Hayashi, Numerical study on the spark ignition characteristics of a methane–air mixture using detailed chemical kinetics: Effect of equivalence ratio, electrode gap distance, and electrode radius on MIE, quenching distance, and ignition delay, *Combustion and Flame*, 157(7), 2010.

[6] J. L. Han, H. Yamashita, N. Hayashi, Numerical study on the spark ignition characteristics of hydrogen–air mixture using detailed chemical kinetics. *Int J Hydrogen Energy*, pp. 286–97, 2011.

[7] T. Kravchik, E. Sher, Numerical modelling of spark ignition and flame initiation in a quiescent methane-air mixture, *Combust. Flame*, pp.635–43, 1994.

[8] B. B. Lewis, G. von Elbe, *Combustion, Flames and Explosions of Gases*, 3/e, Academic Press, Florida, pp. 333–361, 1987.

[9] H. Lu, F. Liu, K Wang, G. Xu, J, Henry Numerical study on the minimum ignition energy of a methane-air mixture. *Fuel*. 285(119230), 2021.

[10] U. Pfahl, M. Ross, and J. Shepherd, Flammability Limits, Ignition Energy, and Flame Speeds in H_2-CH_4–NH_3-N2O–O2-N2 mixtures. *Combust. Flame*, 123, pp.140–158, 2000.

[11] S. Rabl, T. J. Davies, A. P. McDougall, R. F. Cracknell, Understanding the relationship between ignition delay and burn duration in a constant volume vessel at diesel engine conditions. *Proc. Combust. Ins*. 35(3), pp.2967–2974, 2015.

[12] C.A Sevillano, A. A Pesantes, E. P Carpio, E. J. Martinez, X. Gomez, Anaerobic Digestion for Producing Renewable Energy—The Evolution of This Technology in a New Uncertain Scenario. *Entropy*, 23(2):145, 2021.

[13] F. Scott, R. Van Dolah, M. Zabetakis, Flammability characteristics of the system H_2-NO-N_2O-air. *Proc. Combust. Inst*. 6, pp.540–545, 1957.

[14] United Nations Department of Economic and Social Affairs (UN DESA).Sustainable Development Goal 7: Ensure Access to Affordable, Reliable, Sustainable and Modern Energy for All**,** UN DESA, New York (2017). https://sustainabledevelopment.un.org/sdg7 (accessed 15 September 2022)

[15] T. Schneider, Y. Hu, X. Gao, J. Dumas, D. Zorin, D. Panozzo, A Large scale comparison of Tetrahedral and Hexahedral elements for solving elliptic PDEs with the Finite Element method,

Journal Computer Methods in Applied Mechanics and Engineering, pp 1-28, 2019.

[16] C. Wu, R. Schibi, U. Mass, Numerical studies on minimum ignition energies in methane/air and iso-octane/air mixtiures. *Journal of loss prevention in the process industries*, 72, pp. 1-11, 2021.

ANALYSIS OF CROSS-FLOW TUBE BANK ECONOMIZER-ASSISTED FOR H2S

Murat Sahin[1]

1. Mechanical Engineering Department, National Defence University, Ankara; email: msahin@kho.msu.edu.tr

Abstract

When biogas is produced, it has a high humidity ratio. This high humidity is also negative for the combustion process. Therefore, it is necessary to remove moisture from the inside before it combustion. Different heat exchangers are recommended in this sense. In this study, the developed cross-flow tube sets have been experimentally and numerically tested in it where they can be used for this purpose. The economizer and cooler efficiencies are calculated, and reported in order of values as 43% and 67%, with the help of the data obtained at the system's entry and exit point. These processes have helped both with more efficient combustion and use of less energy.

Keywords: Biogas, heat exchanger, tube bank, cross-flow, dryer

1 INTRODUCTION

With the rapid rise of the population, the demand for energy increases at that rate. Therefore, the search for resources that may be alternative to natural gas continues. One of the most important of these resources is biogas. Biogas are also very valuable for the study of climate change and zero carbon emissions. In addition, it is another focal spot in the efficiency of the fuel to be used. At this point, pre-combustion applications for fuels, may also be indicated to have a significant effect on efficiency. In this context, some energy conversion systems, such as heat transfer systems, are recommended. The literature contains several studies to improve this heat transfer systems.

Wang et. all (2016), have made a study to examine the heat transfer performance of cross-flow heat exchanger systems. In this study, they studied the heat transfer characteristics of cross-flow and trunk tube heat exchangers they used. As a result, they reported that the pipe inclination has no major effect on the flow rate and heat transfer, as well as a deterioration in heat transfer with reducing the crash angle. Rehim (2015) has conducted a study to examine the heat transfer and the flow status at fluid with turbulence at a heat exchanger that it has identified. In this study uses a staggered circular tube bank. As a result, the heat transfer aspect ratio in cross-flow tube bank type heat exchangers is dependent on unitless statements such as the Prandtl number and Reynolds number. Elmekawy et. all (2021), made CFD modelling for the tube-in-line heat exchanger model. In their study, they observed performance variations by adding a separator plate on a heat exchanger with a circular tube. As a result, it is stated that the effect of the pressure drop with the separator plate has decreased and the of Nusselts number has improved. Lavasani et. all (2014) made experimental study for a different heat exchanger model. In this study, they used a cam shaped tube bank and indicated that they installed the pipes in two systems with different longitudinal angle ratios. They also indicated that they have been able to acquire entrainment and heat transfer from the tubes placed in the second row. As a result, they have reported that the heat transfer and entrainment in the cam-shaped tubes is significantly based on the position of the tubes placed in the tube bank. Wang et. all (2002) have studied to examine the flat tube bank with wings connected to vortex generators. In this study, they reported that parameters such as the wing range, heat transfer and pressure drop have been analyzed. They also reviewed local and average heat transfer characteristics. As a result, it has been observed that the addition of wings has significantly affected the heat transfer. Similar to the study made in the article, Chen et. all (2022) designed a heat exchanger to take moisture from the air. The heat exchanger they designed is a reverse flow spiral, and they have made examine with 4.7 and 9 tube counts. As a result, they have reported that the spiral model is more efficient than the flat models, and the spiral hollow fiber

tube bank is better for heat transfer characteristics.

This study aims to dry the biogas produced by natural source before combustion, and then save energy with the heat recovery of hot biofuel. A different heat exchanger model is recommended for this operation. With this improved heat exchanger, the water in the biogas will be removed at the maximum level, increasing the temperature prior to the combustion process with heat recovery, saving the energy required. Experimental and numerical analysis of the required heat exchanger is performed and system efficiency is calculated.

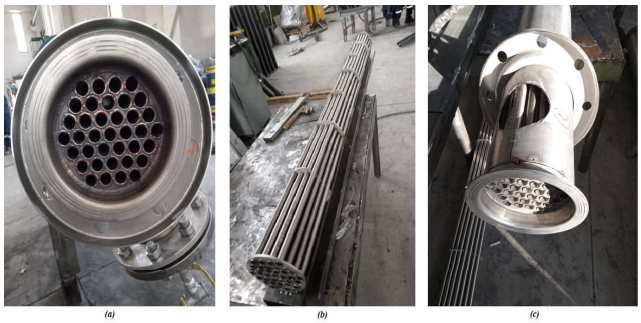
2 MATERIAL & METHOD

It is very important that the water in the biogas be purged before it goes into the combustion chamber. The system in this study is developed in order to remove the water in the biogas obtained from home sources. Table 1 refers to the biogas content used in the study.

Table 1. The substances contained by the biogas

	Biogas	Methane
CH_4	58	100
CO_2	40,57	-
N_2	1	-
H_2S	10 ppm	-
O_2	0,42	-

Figure 1 refers to the structure of the economizer used in the system. Number of 37 straight steel tubes with a diameter of 18 mm are used for each set of pipes. The outside pipe diameter is 139.7 mm and its thickness is 2 mm. The overall pipe and pipe sets have a length of 1000 mm. The system consists of economizer, cooler, chiller unit, separator and condensation tank. The humid biogas in the system circulates through the section between the shell pipe and the tube clusters. Cooling water in the chiller unit is used to dry the humid biogas around the tube clusters. Here, the dried biogas product is directed to the economizer, while condensation water is stored in the condensate tank. The aim of the biogas to be sent to the economizer is to increase the temperature of the dry biogas than the colder state and to restore heat from the damp biogas in the entry. The resulting biogas will be purified from water and sent to the combustion chamber with an elevated temperature. A blower is used to send the temperature-rising biogas into the combustion chamber. Thermocouples and moisture meters are used to store the data obtained.



Images of the heat exchanger examined in the study;
(a) front, (b) tube cluster, (c) overview

3 THEORETICAL ANALYSIS

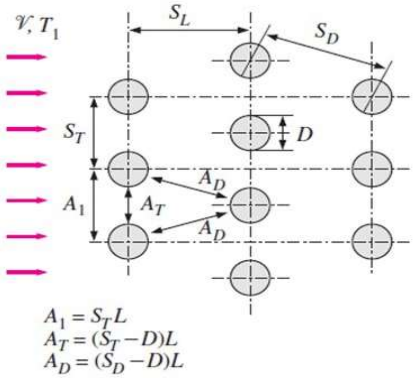


Figure 2. Schematic representation of the positioning of the tube bank [7]

Figure 2 shows the cluster of tubes carrying refrigerant fluid.

The following equation gives the angle between the tube banks. Where S_T is the cross pitch, S_L is longitudinal pitch, and S_D is refer to the cross pitch between the tube center.

$$S_D = \sqrt{S_L^2 + (S_T/2)^2} \quad (1)$$

The equation 2-3 shows A_1 and A_T.

$$A_1 = S_T L \quad (2)$$

$$A_T = (S_T - D)L \quad (3)$$

Here A_1 shows the distance between the two tube centers and A_T shows the distance between the two tube springs. D refers to the diameter of each tube.

In this system, the number of Reynolds is calculated based on the maximum speed (V_{max}). This is due, the maximum speed is dominant due to the flow characteristics in the tube banks.

$$RE_D = \frac{V_{max} D}{\mu} \quad (4)$$

In this equation μ refers to the dynamic viscosity of the fluid. Equation 5 is used for calculate the maximum velocity in the equation.

$$V_{max} = \frac{S_T}{2(S_D - D)} V \quad (5)$$

In this experiment, equation 6 is used to calculate the of Nusselt number. Here, it follows one of the correlations that Zukauskas has suggested and traditionally been used. [7]:

$$Nu_D = \frac{hD}{k} = CRe_D^m Pr^n (Pr/Pr_s)^{0.25} \quad (6)$$

Values based on the of m, C, and n Reynolds number in this equation. In addition, all parameters other than P_{rs} are calculated based on the average temperature of the fluid. The average temperature is given in equation 7.

$$T_m = \frac{T_{in} + T_{out}}{2} \quad (7)$$

Equation 8 is used to calculate the efficiency of the economizer used in the system. This equation is based on the LMTD (Logarithmic mean temperature difference) method.

$$\epsilon = \frac{Q}{Q_{max}} \quad (8)$$

Expressed in equation 8, Q shows real heat transfer and Q_{max} shows maximum heat transfer. Accordingly, the Q and Q_{max} is given in equation 9-10.

$$Q = \dot{m} c_p \Delta T = C\Delta T \quad (9)$$

$$Q_{max} = C\Delta T_{max} \quad (10)$$

The $C\Delta T_{max}$ in equation 10 indicates the difference between the inlet temperatures of fluids, while C indicates specific heat.

3.1 NUMERICAL STUDY

Ansys Fluent software is used to perform this study numerically.

Geometrically, shell pipe was designed as 168.3 mm. a total of 37 tubes, each 18 mm, are installed and positioned at an angle of 60 degrees. Biogas inlet and outlet pipe diameters are 114.3 mm. The system pipe length is also 2000 mm.

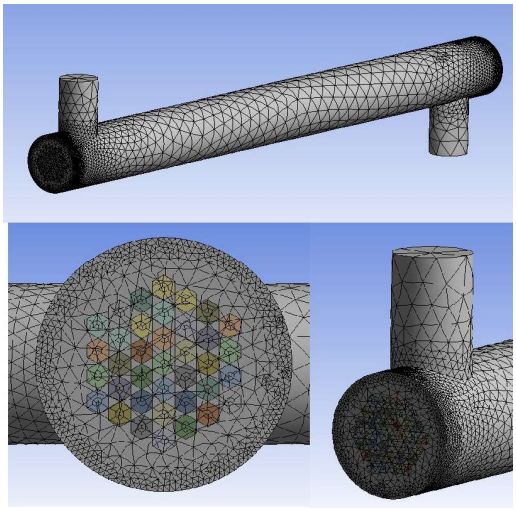


Figure 3. System numerical modelling and mesh structure used

Figure 3 refers to the system mesh structure. The standard tetrahedron mesh structure is used for the mesh structure. The outer tube surface is refined and the top and bottom parts of the cylinder surface are sized. Also, a total of 96360 elements were processed

K-epsilon standard turbulence model is accepted for simulation. Pipe material determined as steel and heat conduction coefficient received as 17 w/m2K. The outer tube thickness of 2 mm and the inner tube thickness is 5 mm. The flow rate for the simulation is considered 0.7 kg/s and simulated in 5000 iterations.

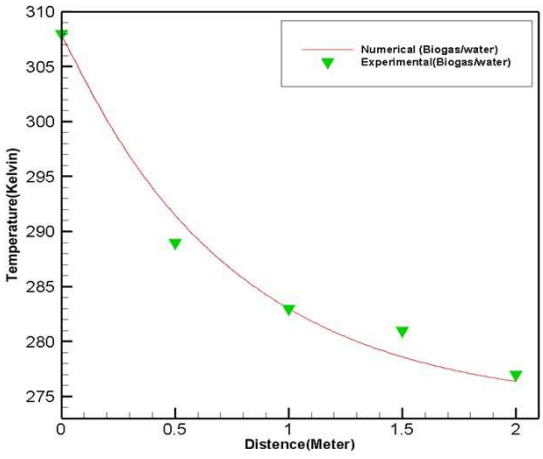


Figure 4. Variations in temperature obtained from experimental and numerical analysis depending on length

Figure 4 refers to the results of experimental and numerical studies that have been done. The graph shows temperature variations depending on length. The verification revealed that experimental and numerical data were very close

together. Depending on this result, the system may be recommended to be suitable for use.

4 RESULTS & DISCUSSION

The table below (table 2) shows the data obtained from the tests performed.

Table 2. Data obtained from the experiment

Equipment	Inlet Temperature (°C)	Exit Temperature (°C)
Economizer	40	35
Cooling water	1	3
Cooler	35	4
Separator	4	5
Dried biogas	75	40

The biofuel flow is 0.672 kg/s in the experiments carried out. In addition, the specific heat value of the biogas is 1.40 kJ/kgK and its density is 1.20 kg/m^3.

The horizontal length between each tube specified in the theoretical analysis section is 20 mm and the vertical length is 11.5 mm and the cross length is 15.24 mm.

Specific heat (C) was found as 0.9408 W/K as based on the thermophysical properties and temperature of biogas.

System efficiency is calculated, taking into account the data and values obtained. The Q and Q_{max} values are first need for system efficiency calculation. Equation 11-12 refers to these values.

$$Q_{max}= (0.9408)\ W/K*(75-5)\ K=65.856\ W \quad (11)$$

$$Q= (0.9408)\ W/K*(35-5)\ K=28.224W \quad (12)$$

Depending on the values calculated, system efficiency is shows in equation 13.

$$\epsilon=65.856/28.224=0.4285 \quad (13)$$

These calculations, based on the results of the experiments, indicate that the heat can be restored by 42.85% thanks to the economizer being developed. In addition, the cooler efficiency can be shared as 66.7%.

5 CONCLUSION

In this study, the process of pre-cooling and then pre-heating was experimentally and numerically examined to obtain a more efficient combustion from the biogas produced by natural resources. In the biogas cross-flow tube banks, gas fuel contained H2S are condensed at the condensation temperature and purified from water in the biogas. The cross-flow tube economizer, designed with subsequent operations, has confirmed that it is significantly employable at the heat recovery point for pre-heating after pre-cooling. The use of this system, recommended for the biogas at gas phase, can save up to 43% energy. In addition, system efficiency can be increased with different refrigerant fluids. This results in the energy and time required gain to reach the required ignition point in the burning of the biogas. In addition, in biogas cross-flow tube banks, H2S-content gas is condensed at fuel condensation temperature and free from water in.

ACKNOWLEDGEMENTS

The author gratefully thank to the National Defence University.

References

[1] Wang, Y., Gu, X., Jin, Z., & Wang, K.. Characteristics of heat transfer for tube banks in crossflow and its relation with that in shell-and-tube heat exchangers. International Journal of Heat and Mass Transfer, vol. 93, 584-594, 2016.

[2] Abdel-Rehim, Z. S., Heat Transfer and Turbulent Fluid Flow Over Staggered Circular Tube Bank, Energy Sources Part A-Recovery Utilization and Environmental Effects, vol. 37, 164-173, 2015.

[3] Elmekawy, A. M. N., Ibrahim, A. A., Shahin, A. M., Al-Ali, S., & Hassan, G. E.. Performance enhancement for tube bank staggered configuration heat exchanger–CFD Study. Chemical Engineering and Processing-Process Intensification, vol. 164, 108392, 2021.

[4] Lavasani, A.M., Bayat, H., and Maarefdoost, T., Experimental study of convective heat transfer from in-line cam shaped tube bank in crossflow, Applied Thermal Engineering, vol. 65, 85-93, 2014.

[5] Wang, L.B., Zhang, Y.H., Su, Y.X., and Gao, S.D., Local and average heat/mass transfer over flat tube bank fin mounted in-line vortex generators with small longitudinal spacing, Journal of Enhanced Heat Transfer, vol. 9, 77-87, 2002.

[6] Chen, J. C., Yang, Y., Yang, M., Zhuang, H. L., Deng, B., Low, E., & Huang, S. M.. Conjugate heat and mass transfer in a counter-

flow spiral hollow fiber membrane tube bank for liquid desiccant air dehumidification. International Journal of Thermal Sciences, vol. 177, 107550, 2022.
[7] Çengel, Y. A., Heat and Mass Transfer: A Practical Approach, McGraw Hill, 2006.

AN APPLICATION OF THE LOW-GREAT HEAT OF RECYCLING WATER OF FOOD INDUSTRY ENTERPRIESES FOR ELECTRIC GENERATION

Viktoriia.Karnaukh[1]

Prof. Dr. Hakan Serhad Soyhan[2], Prof. Dr. A.B. Buryukov[3], V.V.Varakuta[3]

[1]Department of Refrigerating and Trade Equipment, Donetsk National University of Economics and Trade, Donetsk, Schorsa str.3, karnaukh.vita0629@gmail.com
[2] Department of Mechanical Engineering, Sakarya University, Turkey, hsoyhan@sakarya.edu.tr
[3] Department of Department of Engineering Thermophysics, Donetsk National Technical University, Donetsk, Artema str.58, birukov.ttf@gmail.com

Abstract

Food industry enterprises can be classified as waste heat flows producer (with t_w ≤100°C). Frequently waste heat flows are not reused for their own needs. In this work recycling water (t_w=25…40°C) of food industry enterprises is taken into account as a source of high-level temperature for an Organic Rankine Cycle for generating electricity. The obtained efficiency of this installation is 3.4%, however, the obtained electricity is environmentally friendly and does not require using of fuels and other types of high-potential energy resources, it fully corresponds to the green energy conception.

Keywords: An Organic Rankine Cycle (ORC), waste heat energy source**,** recycling water, refrigerant, coefficient of performance, thermodynamic properties, R407C

Introduction

Current concerns over climate change call for measures to reduce greenhouse gases emissions, which will most likely include the following modifications of the current energy systems [1]:

- A decrease in the energy intensity of buildings and industry.
- A shift from fossil fuels toward electricity, e.g. for transportation and space heating.
- Clean power generation by a massive shift toward low-great temperature and renewable energies, comprising wind energy, biomass, geothermal and large hydro.
- A reinforcement of the grid capacity and inter-regional transmission lines to absorb daily and seasonal fluctuations.

According to the U.S. Department of Energy (U.S. DOE), manufacturing industries and power plants produce approximately 60% of the low-temperature waste heat [2].

In large-scale plants, a relatively low temperature heat is usually over abundant and often cannot be reintegrated entirely on-site or used for district heating. It is therefore rejected to the atmosphere. This causes two types of pollution: pollutants (CO2, NOx, SOx, HC) present in the flue gases generate health and environmental issues; heat rejection perturbs aquatic equilibriums and has a negative effect on biodiversity [3].

Food industry enterprises also can be classified as waste heat flows producer (with tw ≤100oC). Frequently waste heat flows are not reused for their own needs. They are usually discharged into the sewer system or local cooling towers. This applies to factories that produce alcohol, beer, dairy products, bakery products, etc. With a steady rise in energy prices, all this ultimately leads to an increase in unit costs for the production of final products and services.

Nowadays a wide range of modern technologies are employed to recover low-grade heat and many studies on them have been presented in the literature. [4-6]:

- Heat pump;
- Organic Rankine Cycle (ORC);
- Kalina cycle;
- Absorption cooling
- Stirling's engine;
- Goswami cycle;
- Heat pipes, etc.

The most wide spread techniques in the industry are heat pumps and ORC systems. Heat pumps transfer the low-grade heat at low temperature to a higher temperature by a compressor. Heat pumps have become the most common technology in newly built houses in many countries, but still only meet 7% of global building heating demand. Organic Rankine Cycle (ORC) is the recent type of an environmentally friendly leading technological system, applying the principle of the steam Rankine cycle, but can utilize relatively low-grade heat sources below 150°C. This system uses an organic substance as a working fluid; therefore it is named as 'Organic' Rankine. Organic Rankine cycles have been studied both theoretically and experimentally since the 1970s, and exhibit efficiencies lower than 10% for small-scale systems. Nowadays the ORC market is growing rapidly.

The most important feature of an ORC is its capability of utilization of various kinds of low-grade heat sources for power generation. Owing to its low operating temperature, an organic Rankine cycle can suitably recover heat from various sources: solar energy, geothermal energy, biomass products, surface seawater and waste heat from various thermal processes. According to the pie chart seen in **Figure**, the percentage of biomass energy source is 48%, the percentage of geothermal energy source is 31%, the percentage of **waste heats energy source is 20%** and the percentage of solar energy source is 1% [7].

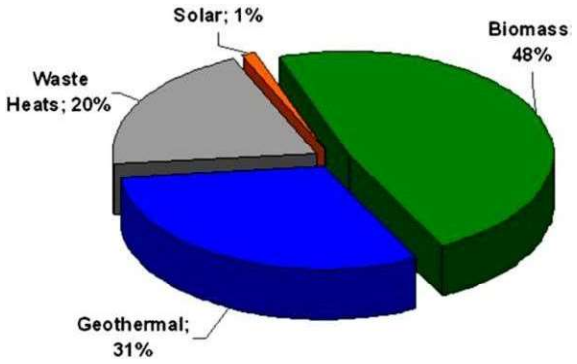


Figure 1. Pie chart of percentage of ORC energy sources [7].

Material and Method

The aim of this work is to analyze the possibility of generating electricity by an Organic Rankine Cycle through the use the recycling water systems of food industry enterprises as the primary source of high-great heat source.

It is known that heat engine (heat machine) operates between two reservoirs (levels) of different temperatures.

In this work recycled water (t_w=25…40^{o}C) of food production enterprises is taken into account as a source of high-level temperature.

Conceptually, the Organic Rankine Cycle is similar to a Steam Rankine Cycle in that it is based on the vaporization of a high pressure liquid which is in turn expanded to a lower pressure thus releasing mechanical work (Figure 2).

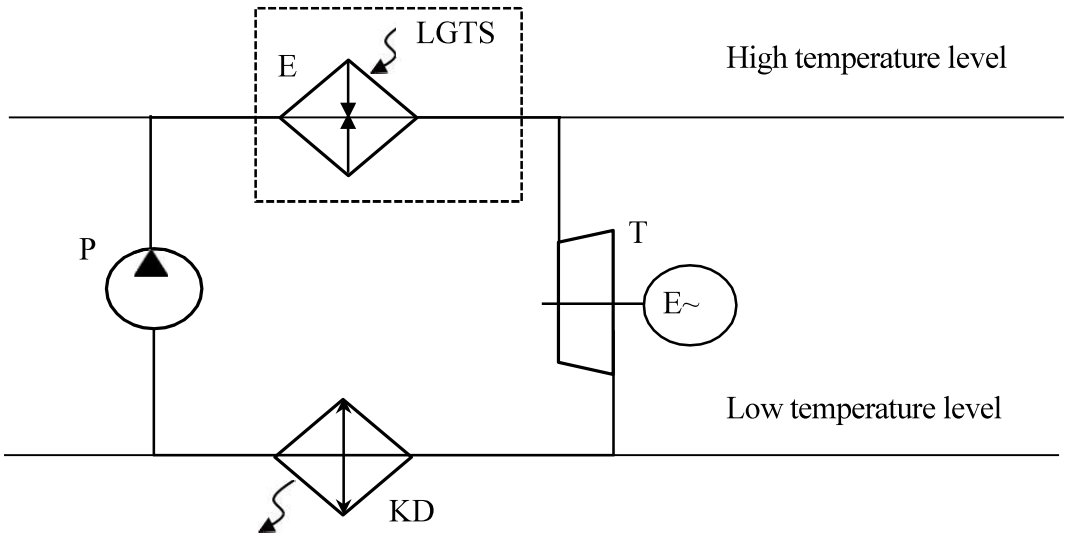


Figure 2. The layout of the basic Organic Rankine Cycle

The cycle is closed by condensing the low pressure vapor and pumping it back to the high pressure. Therefore, the Organic Rankine Cycle involves the same components as a conventional steam power plant (an evaporator, a work- producing expansion device-turbine, a condenser and a pump) [3]. However, the working fluid is an organic compound characterized by a lower ebullition temperature than water and allowing power generation from low heat source temperatures.
The main advantages and disadvantages of the ORC are presented in Table 1.

Table 1. The main advantages and disadvantages of the ORC

Advantages of the ORC	**Disadvantages of the ORC**
No superheating	Relatively small realizable capacities of installations (up to 5-6 MW) due to small heat drops
Low turbine inlet temperature	Decreasing the power when the cooling temperature rises above 12 °C
Compactness	Additional power losses when using an air condenser
Low evaporating pressure	Limited use of residual heat (only for heating or as a source of low-grade heat for heat pumps)
Modularity and adaptability to various heat sources	The maximum temperature of the heat source is limited by the chemical stability of the working fluid (because it undergoes chemical decomposition at high temperatures)
Proven technology with good maturity	Increasing the power of the installation requires an increase in the consumption of the working fluid, which increases the power of pumps and heat exchange equipment
Less complexity and less maintenance	The working fluids used are chemically unstable at high temperatures
Scalable and distributed generation system	Some working fluids are flammable, and can also have a negative impact on the ozone layer, such as some freons, which makes it necessary to exclude leaks
Low investment and maintenance costs	High cost of the working fluid compared to water
Market availability and well known suppliers	
Short commissioning time and good acceptance	

The working fluids of ORC are key point of high efficiency and applicability of ORC.

Therefore the following guidelines and indicators about working fluids should be taken into account:

- Thermodynamic performance: the efficiency and/or out put power should be as high as possible for given heat source and heat sink temperatures. This performance depends on a number of interdependent thermodynamic properties of the working fluid: critical point, acentric factor, specific heat, density, etc.
- Positive or isentropic saturation vapor curve (a negative saturation vapor curve (‘‘wet’’ fluid) leads to drop lets in the later stages of the expansion)
- High vapor density: this parameter is of key importance, especially for fluids showing a very low condensing pressure (e.g.siliconoils).
- Low viscosity**:** low viscosity in both the liquid and vapor phases results in high heat transfer coefficients and low friction losses in the heat exchangers.
- High conductivity is related to a high heat transfer coefficient in the heat exchangers.
- Acceptable evaporating pressure;
- High safety level: safety involves two main parameters—toxicity and flammability (The ASHRAE Standard 34).

ORC working fluids are: toluene; butane; pentane; ammonia refrigeration fluids (R245fa, R123, R1234yf, R407c, R123 et.al) silicone oils. Table 2 shows the basic properties for the some ORC working fluids including selected fluid R407C [8].

Table 2. The basic properties for the some ORC working fluids

Refrigerant/ parameter	**R744**	**R600a**	**R1234ze**	**R407C**
	Carbon Dioxide Natural refrigerants	Hydrocarbons HC Natural refrigerants	HFO Hydrofluoroolefins fluids/ fourth generation refrigerants	mixture of hydrofluorocarbons/ third generation refrigerant
Chemical formula	CO_2	C_4H_{10}	CF_3-CH=CHF	CH2F2/CHF2CF3/CH2FCF3
Molecular mass, kg/kmol	44.1	58.1	114.04	86.2
Normal Boiling Point at p=1atm, K	194.5	261.2	254.17	229.4

Critical Temperature, K	304.12	407.98	382.52	360.0
Critical Pressure (absolute), $p_{cp,}$ bar	72.75	36.846	36.4	46.2
Critical Density, kg/m^3	467.6	225.5	470.0	527.3
Ozon Depletion Potential,ODP	0	0.0	0	0.0
Global Warming Potential, GWP	1	0.01	7	1526
Safety class*	A1	A3	A2L	A1

The use of organic fluids, such as refrigerants, enables efficient and cost-effective power recovery of waste heat streams.

In our work the high temperature source (HTS) is the water of the circulating water supply system with a temperature of 30 ... 45 °C; the low temperature source (LTS) – a refrigerator –are rocks at a depth of 30 to 100 meters with an average temperature of plus 12 ° C or/and atmospheric air at the temperature below plus 12 °C. Refrigerant – R407C.

For further analysis, we accept the following parameters:

- temperature of HTS T_H = 313K or t_H = 40°C;
- temperature of water returned to the technological chain, T1 =27°C=300K;
- refrigerator temperature (LTS) T_L = 285K or t_L =12°C;
- heat flow Q =1MW=1000 kW;
- Electric generator efficiency ¤$_e$=0.95

A schematic picture of the simple or nonrecuperated organic Rankine cycle is shown in Figure 3 and consists of four major components: turbine, condenser, pump and evaporator.

The following processes take place in the simple (non-recuperated) ORC system (Figure 4). High-pressure vapor enters a turbine (state point 1). In the turbine mechanical energy is recovered through controlled expansion of high-pressure vapor and transferred into electrical energy through an electrical generator. The low-pressure vapor leaving the turbine at state point 5 enters a condenser where heat is rejected from the working fluid to and condensation takes place. The working fluid leaves the condenser as low-pressure, slightly sub-cooled liquid. (state point Б). A pump raises the pressure of the liquid to state point B and feeds it to an evaporator. In the evaporator heat is extracted from a waste heat source to preheat, evaporate and superheat the working fluid, thus modifying high pressure liquid into high pressure vapor (state point 1) ready to enter the turbine again.

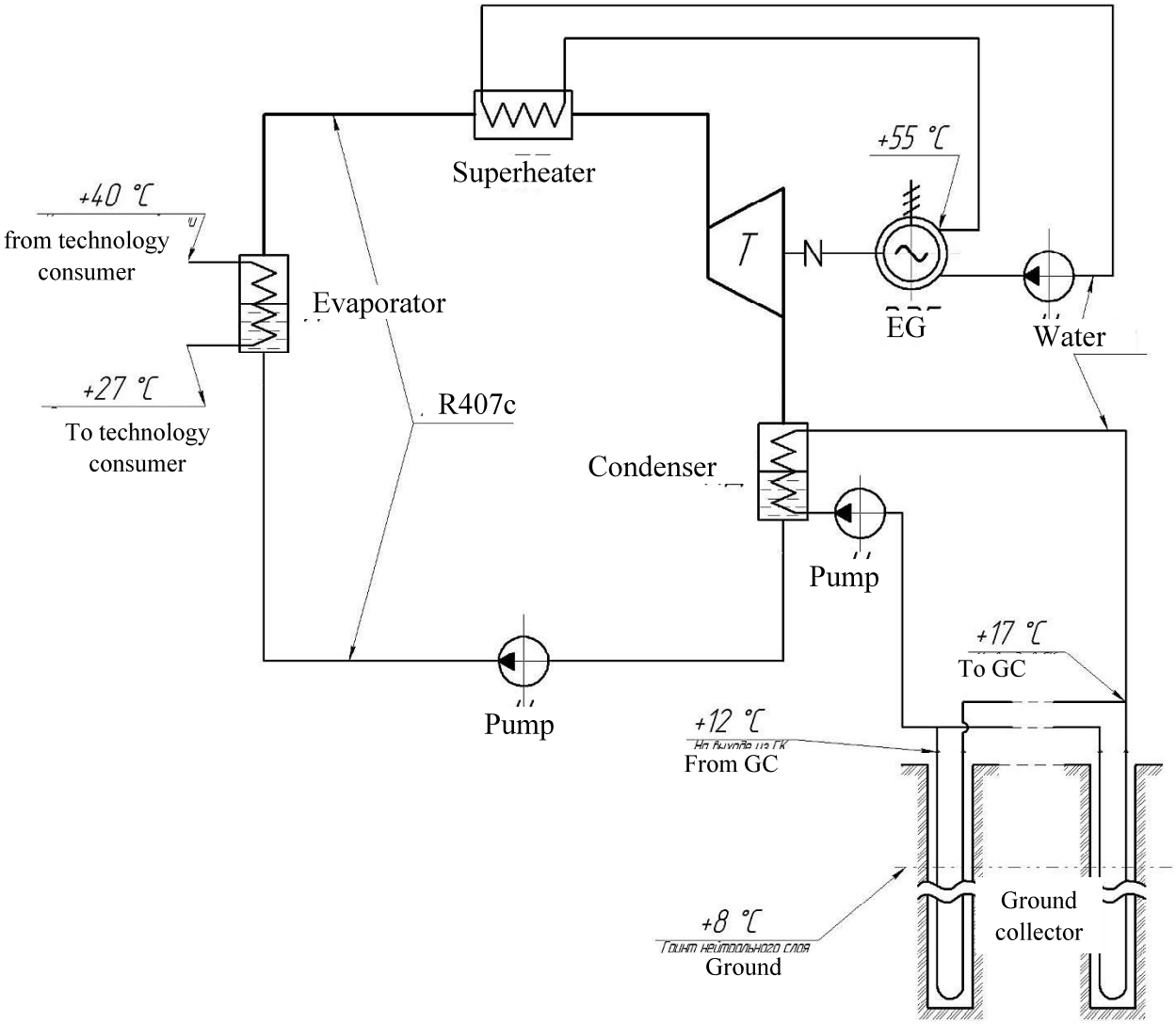


Figure 3. The layout of the Organic Rankine Cycle using the recycling water as high-great heat source

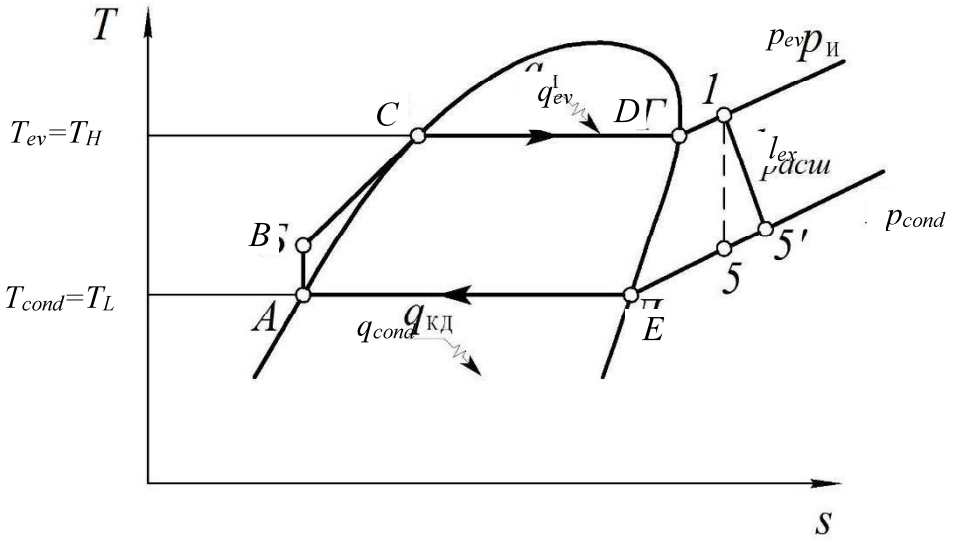


Figure 4. The thermodynamic cycle of ORC using the recycling water as low-great heat source in *T-s* diagram

An ORC cycle is consists of next processes:

A-C: Pressure increase in the condenser in the feed pump from pressure p_{cond} to p_{ev}; C-D-1: Isobaric heating, evaporation and overheating of the working fluid in the evaporator at pressure p_{ev};

1-5: Working fluid expansion in turbine from pressure p_{ev} *to* p_{cond} (theoretical);

1-5': Working fluid expansion in turbine from pressure p_{ev} *to* p_{cond} (polytropic process);

5 (5')-E-A: Isobaric heat release, complete condensation in the condenser at pressure p_{cond}.

Table 3. The main thermodynamical parameters of R407c in the points of the cycle

Point		**Temperature, °C**	**Pressure , MPa**	**Specific enthalpy, kJ/kg**	**Specific entropy, kJ/(kgK)**	**State**
A		+22	1,13	230,9	1,115	saturated liquid
Б		+22	1,49	232,2	1,115	Unsaturated liquid before the evaporator
B		+31	1,49	246	1,15	Saturated liquid at evaporating pressure
Г		35,8	1,49	328,6	1,42	Dry saturated steam before the superheater
1		+40	1,51	425	1,75	Superheated steam before the turbine
5		+22	0,944	419,89	1,75	Superheated steam at condensing pressure

Power at the generator clutch $N_{\sum}$:

$$N_{\sum}=G_V \cdot H \cdot \eta_m=36.9 \text{ , kW} \quad (1)$$

where G_v - steam flow rate through the turbine, kg/c; H – obtained heat drop, kJ/kg; η_m – coefficient of performance of generator clutch.

$$N_{\sum} = G_v \cdot H \cdot \eta_m = 36.9$$

Capacity of power generation, $N_{p.g.}$:

$$N_{p.g.} = N_{\sum} \cdot \eta_{p.g.} = 36.9 \cdot 0.92 = 34\,\text{kW} \quad (2)$$

where $\eta_{p..g.}$ =0.92 coefficient of performance of power generator.

Maximum efficiency of power generation, $\eta_{\max}$:

$$\eta_{\max} = \frac{N_{p.g.}}{Q} = \frac{34}{1000} = 0.034\,. \quad (3)$$

The feasibility of the proposed option for power generation is primarily based on the environmental effect, which consists of reducing greenhouse gases emissions (CO2, H2O) in terms of consumed conventional fuel *B* and water vapor losses during evaporation at the time of the annual operation cycle.

$M_{H_2O}^{CO_2eq} = 1.33$ ton; M_{CO_2} =294 ton

The total emission of greenhouse gases into the atmosphere can be expressed as:

$$M_{\sum} = M_{H_2O}^{CO_2eq} + M_{CO_2} = 1.33 + 294 = 295.33, \text{ton} \quad (4)$$

Total economic effect for the annual cycle is $C_{\sum} = 12.9 \cdot 10^5$ ruble $C_{\sum} = 3.8 \cdot 10^5 TL$

Calculated cost of the proposed energy complex is $C_{complex} = 63.13 \cdot 10^5$ruble

$C_{complex} = 18.6 \cdot 10^5 TL$

Payback period of the proposed energy complex is defined as:

$$P = \frac{C_{complex}}{C_{\sum}} = \frac{63.13}{12.9} = 4.9 \text{ years} \quad (5)$$

Conclusion

1. Organic Rankine Cycle (ORC) is the recent type of an environmentally friendly leading technological system. It has been investigated for electrical power production from low-great heat resource such as recycled water of food industry enterprises.

2. The obtained efficiency of this installation is less than 5%, however, the obtained electricity is environmentally friendly and does not require using of fuels and other types of high-potential energy resources, it fully corresponds to the green energy conception.

References

1. European Climate Foundation, 2010, EU Road map 2050. Available from: /http://www.roadmap2050.eu
2. Alireza Javanshir , Nenad Sarunac and Zahra Razzaghpanah Thermodynamic Analysis of ORC and Its Application for Waste Heat Recovery. J. Sustainability **2017**, 9, 1-26 Available from: https://www.researchgate.net/publication/320880783_Thermodynamic_Analysis_of_ORC_and_Its_Application_for_Waste_Heat_Recovery
3. Sylvain Quoilin a,n, Martijn Van Den Broek b,c, Se´ bastien Declaye a, Pierre Dewallef a, Vincent Lemort. Techno-economic survey of Organic Rankine Cycle (ORC) systems Available from: www.researchgate.net/publication/257569998_Techno-economic_survey_of_Organic_Rankine_Cycle_ORC_systems/download
4. Huijuan Chen. A review of thermodynamic cycles and working fluids for the conversion of low-grade heat/ Huijuan Chen, D. Yogi Goswami , Elias K. Stefanakos //J. Renewable and Sustainable Energy Reviews. – 2010. – Vol. 14. – P. 3059–3067. doi:10.1016/j.rser.2010.07.006 URL: https://www.sciencedirect.com/science/article/abs/pii/S1364032110001863.
5. Deepak Tiwari. Energy and Exergy Analysis of Organic Rankine Cycle Using Alternative Working Fluids/ Deepak Tiwari, Akhilesh Arora, Naushad Ahmad Ansari, Dr.A.F. Sherwani // IOSR Journal of Mechanical and Civil Engineering. ISSN: 2320-334X. –2015. – Vol. 12, Issue 1 Ver. II. – PP 85-92 . DOI: 10.9790/1684-12128592 URL: www.iosrjournals.org
6. Karnaukh, V.V. Trade-off working fluid selection for heat pumps / V.V. Karnaukh V.A. Mazur, A.B.Biryukov, K.A. Rzhesik // Proceedings of the IV International Scientific and Technical Conference "Energy Systems", Belgorod, 2019. doi:10.1088/1757-899X/791/1/012066 [Electronic Resource] – Access: https://iopscience.iop.org/article/10.1088/1757-899X/791/1/012066.
7. http://www.turboden.eu/en/rankine/rankine-advantages.php
8. Freon 407C Refrigerant (R-407C) Thermodynamic Properties (SI Units) [Электронный ресурс] – Доступ: https://www.freon.com/en/-/media/files/freon/freon-407c--thermodynamic-properties-si.pdf?rev=f57f78abcea24ae89e6d1bee8ede0007

DİZEL VE TRİETİL BORAT İLE KARIŞIMLARININ DAMLACIK YANMA DAVRANIŞLARININ İNCELENMESİ

Ahmet Alper Yontar[1] ve Mert Şevket Biçer[2]

1. Makine Mühendisliği Bölümü, Mühendislik Fakültesi, Tarsus Üniversitesi, Tarsus, Mersin; email: aayontar@tarsus.edu.tr
2. Makine Mühendisliği Ana Bilim Dalı, Lisansüstü Eğitim Enstitüsü, Tarsus Üniversitesi, Tarsus, Mersin; email: mert_bicer@tarsus.edu.tr

Özet

Dizel yanma ile enerji elde etme yöntemlerinde en sık kullanılan yakıtlardan birisidir. Bununla birlikte, dizel yakıtında rastlanan en büyük problem yanma sırasında açığa çıkan CO, NO_x ve diğer kirleticilerdir. Dizel gibi göz ardı edilemeyecek kadar büyük bir enerji kaynağını daha verimli kullanabilmek ve dizelin sebep olduğu sorunların üstesinden gelebilmek için püskürtme olayının kapsamlı bir şekilde anlaşılması gerekmektedir. Yakıt spreyi, çok sayıda küçük boyutlu damlacığın oluşturduğu bir bütün olduğundan dolayı damlacık yanmasının daha iyi anlaşılması spreyin bütünü için yorum yapabilmek için önemli bir husustur. Bu sebeple mevcut çalışmada dizel ile trietil borat yakıtlarının karışımlarının damlacık yanması detaylıca incelenmiştir. Deneysel olarak gerçekleştirilen çalışmada, yüksek hızlı kamera içeren arkadan aydınlatmalı görüntüleme sistemi ve kendinden aydınlatmalı görüntüleme sisteminden faydalanılmıştır. Yanmakta olan damlacık saniyede 1400 kare olacak şeklide kayıt altına alınmıştır ve özel bir algoritma kullanılarak görüntüler işlenmiştir. Böylece yakıtlara ait damlacık çapı değişimleri detaylıca incelenmiştir. Ayrıca termal kamera kullanılarak damlacığın yanmasına ait sıcaklık değişimleri anlık olarak incelenmiştir. Damlacık ömrü teşhisinin yapılmasında ve yorumlanmasında D^2 yasasından faydalanılmıştır. Gerçekleştirilen çalışma sonucunda yüksek trietil borat konsantrasyonuna sahip damlacıkların düşük tutuşma gecikmesine ve düşük yanma süresine sahip olduğu görülmüştür. Bunlara ek olarak trietil boratın damlacıkların yanma sıcaklarında büyük bir artışa neden olduğu gözlemlenmiştir.

Anahtar Kelimeler: Bor Türevli Yakıtlar, Damlacık Yanması, Trietil Borat, Dizel

1 GİRİŞ

Her geçen gün gelişen teknolojiye paralel olarak küresel enerji tüketimi de artmaya devam etmektedir. Sıvı hidrokarbon yakıtlar, katı yakıtlara göre bulunabilirliklerinin yanı sıra, bu yakıtların depolanmasındaki kolaylık ve esneklik nedeniyle enerji elde edilmesinde sıkça kullanılmaktadır. Bu nedenle, uygulamaların çoğunda sıvı yakıt oksitleyici ile karıştırılır ve küçük boyutlu damlacıklar halinde sprey şeklinde yakılır. Bu yanma şekli, dizel motorlar, roket motorları ve gaz türbinleri dahil olmak üzere çeşitli sistemlerin temelini oluşturmaktadır.

Dünya üzerindeki petrol rezervlerinin tükenmeye başlaması ile birlikte yakma sistemleri üzerinde kullanılan yakıtın miktarını azaltmaya yönelik çalışmalar da hız kazanmıştır.

Dizel yanma ile enerji elde etme yöntemlerinde önem arz eden bir yakıttır. Bununla birlikte, dizel yakıtında rastlanan en büyük problem yanma sırasında açığa çıkan CO, NO_x ve diğer kirleticilerdir. Dizel gibi göz ardı edilemeyecek kadar büyük bir enerji kaynağını kullanabilmek ve dizelin sebep olduğu sorunların üstesinden gelebilmek için araştırmacılar uzun yıllardır çalışmalarını devam ettirmektedir. Bu araştırma

konularında birçoğu ise yakıt spreyinin araştırılmasını kapsamaktadır.

Sıvı parçalanması ve damlacık oluşumu atomizasyon olarak bilinir. Sprey, birincil atomizasyon ve ikincil atomizasyon evrelerinden geçerek gelişimini tamamlar. Bu süreçler sonucunda püskürtülen yakıt farklı boyutlardaki damlacıklara ayrılır. Mevcut çalışma bu damlacıklar bütünün tek bir bileşenini oluşturarak davranışlarını incelemek üzerinedir. Bunun nedeni, yakıt spreyinin çok sayıda küçük boyutlu damlacığın oluşturduğu bir bütün olmasıdır. Bu nedenle, spreyin tek bileşeninin kapsamlı bir şekilde anlaşılması, daha genel sprey yapısını açıklamak için yardımcı olacaktır.

Literatürde damlacık dinamiğinin ve karakteristiğinin incelenmesi ile ilgili kayda değer sayıda çalışma bulunmaktadır ve bazılarından aşağıda bahsedilmiştir.

Raslavicius ve Bazaras [1], atmosferik basınç ve normal yerçekimi altında dizel damlacık yanmasını sayısal olarak inceledi. 770-860 K arasında değişen ortam sıcaklığının tutuşma gecikmesinde bir azalmaya neden olduğu çalışmanın ana odak noktası tutuşma gecikmesiydi ve damlacık boyutunun damlacık yanmasını önemli ölçüde geciktirdiği bulundu.

Rasid ve Zhang [2], yüksek hızlı kamera kullanarak dizel bazlı yakıt damlacıklarında is partikül kontaminasyonunun etkileri araştırmışlardır. Damlacık sıvı fazının görselleştirilmesiyle, yüzey distorsiyonu, üfleme ve mikro patlamalar detaylı şekilde incelenmiştir. Sonuç olarak damlacık yüzeyindeki is partikülleri bir kabuk oluşturarak saf dizel damlacığının yanma hızını %17 ve yanma fazının ömrünü %14 azaltmıştır.

Law vd. [3, 4], damlacık ısıtmanın ortaya çıkan yanma davranışı üzerindeki etkisi detaylıca araştırmıştır ve damlacık ömrü ve yanma davranışı üzerinde önemli ölçüde etkili olduğu gösterilmiştir. Tahmini damlacık ısıtma periyodu, toplam damlacık ömrünün yaklaşık %10-20'si olarak bulunmuştur.

Pan vd. [5], mikro yerçekimi altında yanma hızının damlacık boyutuna bağlı olduğunu gözlemledi. Daha büyük bir damlacığın (528 μm) küçük bir damlacığa (445 μm) göre daha kalın bir kurum kabuğu oluşturmuştur. Büyük damlacığın kurum kabuğunun damlacık yakma hızında gözle görülür bir azalmaya neden olduğu görülmüştür.

Faik ve Zhang [6], çok bileşenli yakıt damlacığının yanmasının yüksek hızlı arkadan aydınlatması ve gölge grafiği görüntülemesi ile sıvı faz dinamiği incelemesi gerçekleştirmiştir. Baz yakıtın dizel olduğu çalışmada biyodizel/dizel karışımları, suda dizel ve dizelde su emülsiyonları incelenmiştir. Arkadan aydınlatma sistemi ve gölge grafiği kurulumları kullanılarak çekirdeklenmenin, kabarcık oluşumunun, iç dolaşımın, şişirmenin, mikro patlamanın ve ikincil atomizasyonun uzaysal ve zamansal takibi izole edilmiş çok bileşenli yakıt damlacıkları için gerçekleştirilmiştir.

Sankaranarayanan vd. [7], RP-1 vekil yakıtının (RP-1-s), bileşenlerinin ve iki yeni enerjik yakıtın damlacık yanma davranışı araştırmıştır. Testler, asılı damlacık yöntemi kullanılarak ortam atmosferik koşulları altında gerçekleştirilmiştir. Sonuçlar, başlangıç çapı 1,3 mm olan bir damlacık için yanma hızı sabitlerinin, referans yakıtın yaklaşık 3.5, 1.24, 0.92 ve 0,96 katı olduğunu göstermektedir. Çalışma yakıtların enerji yoğunluklarının yanma hızıyla ilişkisi olmadığını göstermektedir.

Kobayasi [8], yüksek sıcaklıklı bir fırın içinde asılı duran 0,7-1,7 mm çapındaki damlacıkların hem buharlaşmasını hem de yanmasını izlemek ve görüntülemek için gölge grafiği görüntülemeyi kullandı. Bu yöntem kullanılarak elde edilen görüntüler yardımıyla farklı tek bileşenli ve çok bileşenli yakıtların yanma hızlarını değerlendirebildi.

Faeth vd. [9], bir yüksek basınç odası içinde asılı duran izole edilmiş dekan damlacıklarının yanmasını incelemek için 100 fps görüntüleme hızında gölge grafiği kullandı.

Faik vd. [10], gölge grafiği tekniği ve yüksek hızlı fotoğraf makinesi kullanarak, çok bileşenli dizel yakıtlarının damlacık davranışlarını 10 kat daha büyük görüntü elde ederek incelemişlerdir.

Literatür araştırmasında bor ve türevlerine dair damlacık çapında yanma konulu bir çalışmaya rastlanmamıştır.

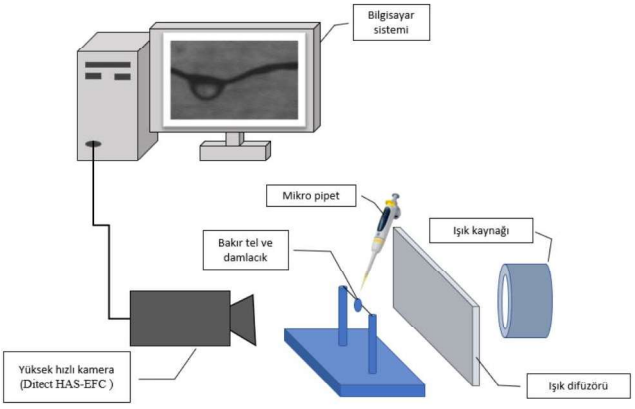
Mevcut çalışmalar ve elde edilen bilgiler doğrultusunda, bu çalışmada dizel ve bor türevli yakıtların damlacıklarının yanma davranmışları incelenmiştir. Gerçekleştirilen çalışma literatürde eksiği bulunan bor yanmasına dair bir bilgi kaynağı niteliğindedir.

2 DENEYSEL YÖNTEM

Nümerik metotlar ve simülasyon teknolojilerindeki gelişmelere rağmen damlacığın yanması sırasındaki mevcut parametreleri anlamak ve açıklamak için

kullanılabilecek en tutarlı yöntem deneysel çalışmalardır. Gerçekleştirilen ilk damlacık yanması çalışmalarından bu yana birincil olarak optik tanı yöntemlerine başvurulmuştur. Yanma süresinin çok kısa olmasından dolayı optik yöntemlerle deneysel veriler kayıt altına alınıp, detaylı incelemelerle veri takibi yapılmasıyla birlikte daha doğru sonuçlar elde edilebilir. Bunlara ek olarak optik tanı yöntemleri, deney alanına etkisi olamaması ve alevin yansımasını tam olarak kayıt altına alabildiği için damlacık yanması araştırmalarında en çok kullanılan yöntem olmaktadır. Bu sebeplerle, mevcut çalışmada deneye etkisi olmaması ve daha detaylı inceleme fırsatı sunduğundan dolayı arkadan aydınlatmalı görüntüleme sistemi ve termal kamera kullanılmıştır. Bu sistem Şekil 1'de de görüldüğü gibi damlacık süspansiyon sisteminin arkasına yerleştirilen bir ışık kaynağı sayesinde damlacığın keskin kenarlarını ortaya çıkarır. Buna ek olarak damlacığın iç dinamiklerini inceleme hususunda etkinliği kanıtlanmış bir yöntemdir.

Ayrıca mevcut çalışmada, elektrik arkı ateşleme yöntemi kullanılarak damlacık ateşlemesi gerçekleştirilmiştir. Elektrik arkı, gazların kıvılcım anında ortaya çıkması ile oluşan elektrik olayıdır. Elektrik arkı, sisteme herhangi bir kütle geçişine neden olmadığından ve buji ateşleme sistemiyle çok yakından ilgili olduğundan çalışma için avantajlı bir sistem olarak değerlendirilmiştir.



Şekil 1. Arkadan Aydınlatmalı Görüntüleme Sistemi

2.1 Yakıt Seçimi ve Karışım Oluşturma

Dizel ile oksijenli yakıtların harmanlanması CO emisyonlarını düşürmeye yarayan yöntemlerden birisidir. Trietil borat (TEB), $B(OCH_2CH_3)_3$ formülüne sahip renksiz bir sıvıdır. Borik asit ve etanolün bir esteridir [11]. Oksijence zengin içeriğe sahip ve bor elementi barındıran trietil borat, yüksek enerji içeriğine sahip bir yakıttır. Bu sebeple, dizel ile trietil borat karışımı kirletici sorununa uygun bir çözüm sunmaktadır. Tüm bunlar göz önünde bulundurularak, mevcut çalışmada dizel ve trietil borat yakıtlarının kullanılmasına karar verilmiştir.

Tablo 1. Yakıtlara Ait Özellikler [12, 13]

	Trietil borat	*Dizel*
Formül	$C_6H_{15}BO_3$	$C_{12}H_{23}$
Yoğunluk	0.858 g/cm³	0.840 g/cm³
Erime Noktası	188 K	267 K
Kaynama Noktası	391 K	493-673 K
Parlama Noktası	284 K	325 K
Molar kütle	145.99 g·mol^{-1}	202 g·mol^{-1}

Karışımlar kütlece ve yüzdesel olarak oluşturulmuştur. Kütlece oluşturulmasındaki en önemli neden yoğunluklarının çok yakın değerlere sahip olmasıdır. Ayrıca trietil boratın buharlaşma sıcaklığının çok düşük olması, dolayısıyla buharlaşması normal şartlar altında çok hızlı gerçekleştiğinden, deneysel hataların mümkün olabildiğince önüne geçilmiştir.

2.2 Damlacık Oluşturma

Mevcut çalışma için, damlacığı sabitlemek için damlacık süspansiyon yöntemi kullanılmıştır. Çünkü damlacık sıvı-faz dinamiğinin incelenmesi, damlacığın belirli bir konumda sabitlenmesini gerektirir. Aynı nedenle, yanma sırasında meydana gelen iç süreçlerin daha kolay takip edilebilmesi için damlacık boyutunun büyük olması gerekir. Yanma sırasında damlacık süspansiyonu için uygun olan herhangi bir malzemenin alev sıcaklığından daha yüksek bir erime noktasına sahip olması gerektiği açıktır. Yapılan öncü denemelerde farklı karışımlar denenmiş ve ortalama olarak 523 K yanma

sıcaklığına erişilmiştir. 1 mm kalınlığa sahip bakır (Cu) tel bu işlem için uygun bulunmuştur.

Karışımların adlandırmaları yapılırken yakıtları temsil edecek kısaltmalar ve karışım oranlarını temsil edecek sayılar kullanılmıştır. Dizel "D", trietil borat "TEB" olarak kısaltılmıştır ve sırasıyla ilk rakam dizel oranını, ikinci rakam trietil borat oranını temsil etmektedir. Örnek olarak; %10 dizel ve %90 trietil borat içeren bir karışım DTEB19 olarak isimlendirilmiştir.

Damlacık oluşturma işlemi, laboratuvar tipi bir mikro pipet kullanılarak gerçekleştirilir. Otomatik pipet, ayarlanabilir ya da belirli sabit miktarlarda ölçümleme ve transfer yapabilen cihazdır. Bu sayede 4.15±0.25 µl miktarlarında damlacık oluşturma işleminin yapılabilirliği sağlanmıştır. Belirtilen miktarlarda yakıt enjekte edildiğinde damlacığın simetrik olduğu kabul edilerek 2 mm çapında damlacıklar oluşturulmuştur.

2.3 Damlacık Analizi

Elde edilen görüntüler üzerinde öncelikle görüntü iyileştirme işlemi yapılmıştır. Görüntü iyileştirme, belirli uygulamalar için orijinalinden daha uygun bir görüntü elde etmek için görüntü işleme sürecidir. Bu süreç, verimli bilgisayar destekli analiz için görüntü kontrastını ve nesne netliğini geliştirerek gerçekleştirilir. Bununla birlikte, görüntü iyileştirme kriterleri bir standartta sahip değildir. Görüntü işleme uygulamasına bağlı olduğundan genellikle özneldir. Bu nedenle, mevcut çalışmada görüntü iyileştirme, ilk önce görüntüyü renkli formatından gri tonlamalı formata dönüştürerek gerçekleştirilir. Daha sonra işlenmeye hazırlanan görüntüler özel olarak oluşturulmuş bir kodlama algoritmasına tabi tutularak damlacıklara ait görsel veriler sayısal verilere dönüştürülmüştür.

Çalışma boyunca damlacık karakteristiklerini içeren veriler D^2 yasası dikkate alınarak işlenmiştir. Bu yasa aynı zamanda klasik damlacık yanması modeli olarak da bilinmektedir. Denklem 1 D^2 yasasını temsil etmektedir. Burada D damlacık çapını, t zamanı, D_0 damlacığın ilk çapını ve K ise yanma hızı sabitini temsil etmektedir. Damlacık çapı değişimi ve damlacıklara ait yanma hızı sabitleri bu denklemden faydalanarak hesaplanmıştır

$$D^2(t) = D_0^2 - Kt \quad (1)$$

Bahsi geçen denklem varsayımlar ile elde edildiğinden dolayı gerçek değerlerin değil yaklaşık değerlerin elde edilmesine yardımcı olmaktadır. Isıtma periyodu, kurum oluşumu ve radyasyon ihmal edilen durumlardandır. İhmal edilen durumlar deneysel sapmalarda büyük bir yüzdeyi temsil etmektedir. Buna göre, klasik damlacık yanma teorisinin kullanımıyla elde edilen değerler, kesin hesaplamalardan ziyade birincil tahmin amaçları için kullanılabilir.

3 SONUÇLAR VE DEĞERLENDİRME

Bu çalışmada dizel ve trietil borat damlacıklarının yanma davranışları yüksek hızlı kamera ile termal kamera vasıtasıyla incelenmiştir. Elde edilen görüntüler analiz edilerek yakıt damlacıklarının yanma süreci esnasında sergiledikleri davranışlar gözlenmiştir.

Bir damlacığın ömrü boyunca çap küçülmesi iki aşamadan oluşmaktadır. Aşama I olarak ifade edilen kısım, damlacıkta faz ayrımı, şişme-büzülme ve buharlaşma mekanizmalarının görüldüğü ısınma sürecidir. Aşama II kısmı ise buharlaşmanın şişme-büzülme döngüsünün önüne geçmesiyle başlar [14, 15].

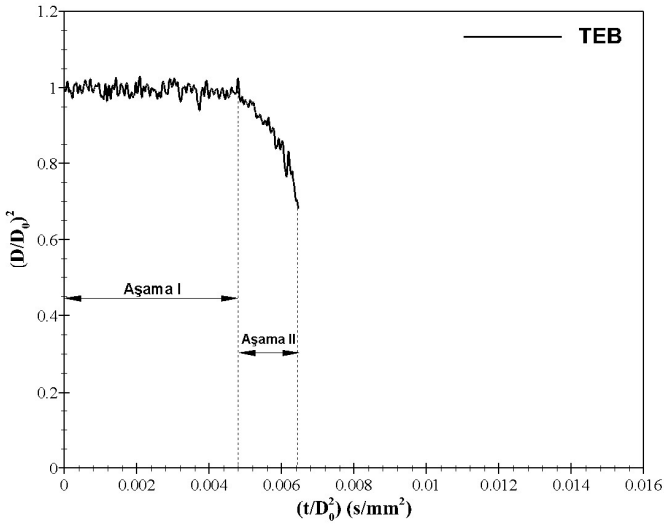
Dizel ve TEB ile karşılaştırıldığında; dizel yoğunluklu yakıt karışımlarına gelindikçe damlacık ömründe artış olduğu fark edildi. Bu, çok bileşenli karışımlardaki daha az uçucu bileşenin ısıtılması ve daha erken buharlaşmasıyla ilgilidir. Bu bileşenler damlacık içinde kaynamaya ve buharlaşmaya başlar ve buhar oluşumuyla artan iç basınç nedeniyle damlacık boyutunun artmasına neden olur [16].

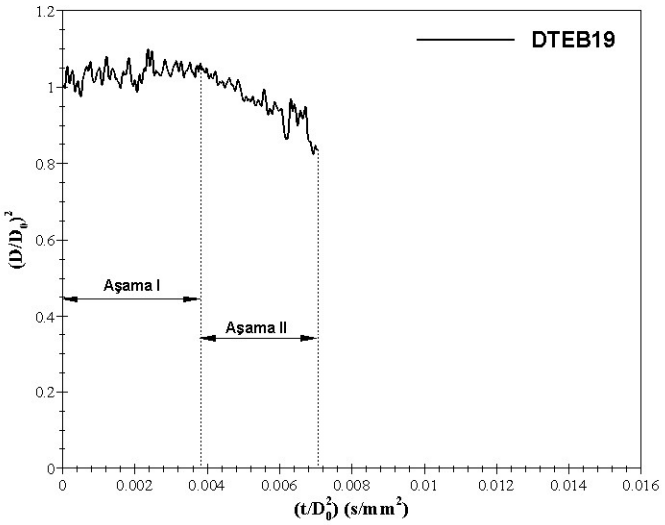
Tüm yakıtlar için Aşama I sürecinin şişme ve büzülme döngüsünden oluştuğu gözlemlenmiştir. TEB, dizele göre daha kararlı bir çap küçülmesi sergilemiştir. Tüm eğilimler incelendiğinde ise dizel için özellikle Aşama II başlangıcında yüksek şiddette salınımlar görülmektedir. Bu salınımlar damlacığın şekil değiştirdiğini göstermektedir. Bunun sebebi dizelin yapısında bulunan metil yapılarının yüksek salınımda şekil değişimlerine ve hızlı bir şekilde damlacığın tükenmesine sebep olmasıdır.

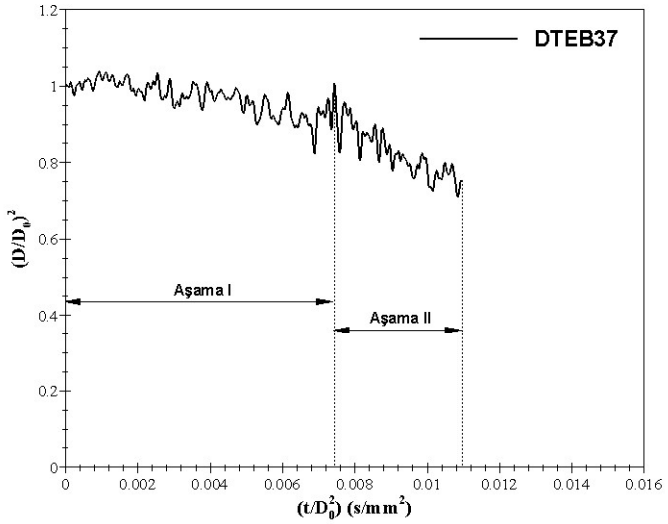
Dizel yakıt damlacığında sahip olduğu uzun karbon zincirlerinden dolayı Aşama I yanma sürecinin önemli bir kısmını oluşturmaktadır.

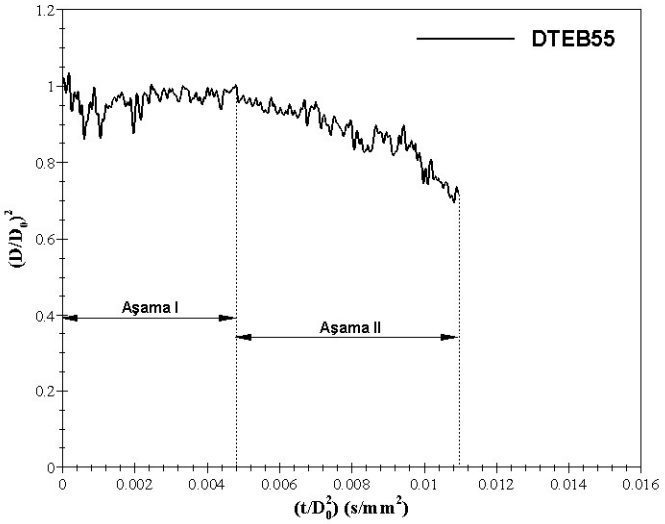
TEB'den dizele doğru gidildikçe Aşama I'de gözle görülür bir artış gözlemlenmiştir. Bu durum dizelin daha az uçucu olmasından kaynaklanmaktadır. Buharlaşma süresi artarak Aşama I süresini de arttırmıştır.

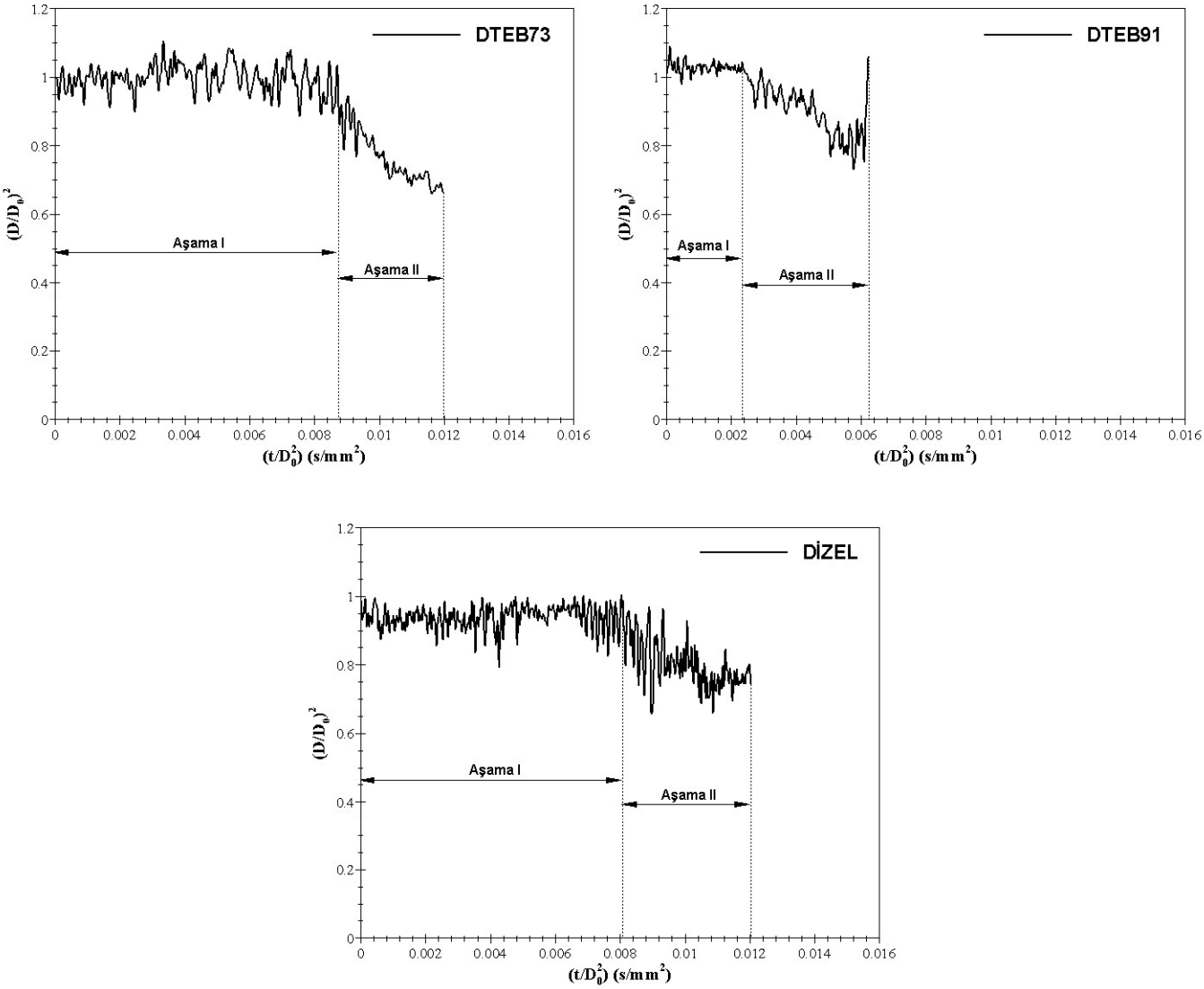
DTEB91 yakıtı üzerindeki deneyler üç kez tekrar edilmesine rağmen genel trende aykırı bir durum gözlemlenmiştir. Yakıt konsantrasyonu sebebiyle TEB yakıtı kısa süre içerisinde yanarak tükenmiştir. Geride kalan dizel herhangi bir ikincil atomizasyona, faz ayrımına veya mikro patlamaya maruz kalmamıştır. Başka bir tabirle saf dizel yakıtına benzer bir davranış sergilemiştir. Fakat diğer durumların aksine damlacığın uzun süre boyunca tel üzerinde salınımında artış gözlemlenmiştir. Bu duruma TEB yakıtının hızlıca yanarak tükenmesinin sebep olduğu düşünülmektedir. TEB yanarken açığa çıkan ısı damlacığın büyük bir kısmını oluşturan dizelin termofiziksel özelliklerinde küçük değer farkları yaratarak tel ile arasındaki adezyon kuvvetlerinin azalmasına ve akabinde yanmayı sonlandıracak kadar şiddetli salınım yapmasına neden olduğu düşünülmektedir [17].





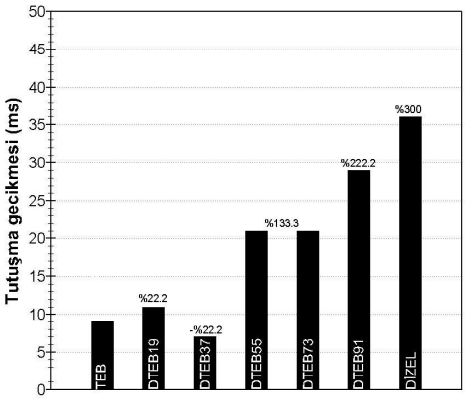






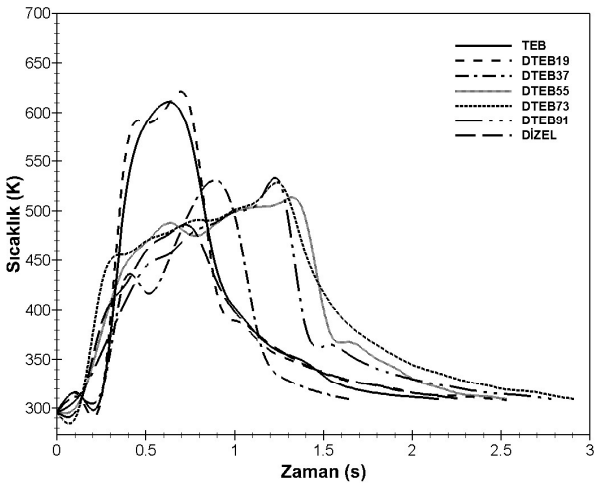
Şekil 2. Damlacık çapı değişimi grafikleri

Damlacık halindeki yakıtlara ait tutuşma gecikmesi değerleri ve artış oranları Şekil 3'te görülmektedir. İki saf yakıt damlası arasındaki tutuşma gecikme periyodu karşılaştırıldığında, dizelin tutuşma gecikmesi TEB'den %300 daha uzun sürmektedir. Bunun sebebi yakıtların buharlaşma sıcaklıklarıyla ilgilidir. Sıvı fazdaki yakıtın yanması için öncelikle gaz fazına geçiş yapması gerekmektedir. TEB yakıtının gaz faza geçişinin dizel yakıtına normal şartlar altında (298 K ve 1 atm basınç) daha hızlı gerçekleşmesi tutuşma gecikmesi süresini önemli oranda düşürmektedir. Buna ek olarak daha düşük oktan ve daha düşük setan sayısına sahip yakıtlarda düşük tutuşma gecikmesi eğilimi gözlemlenmiştir. Ayrıca yakıtların sahip olduğu kimyasal yapı daha karmaşık hale geldikçe bu durum tutuşma gecikmesinde artışa neden olmaktadır. Bünyesinde daha fazla metilen ve aromatik yapılar bulunduran dizel için tutuşma gecikmesi yüksek seviyededir. Buna karşılık metilen ve aromatik yapı bulundurmayan trietil boratın ise tutuşma gecikmesinin çok düşük seviyelerde olduğu görülmüştür.



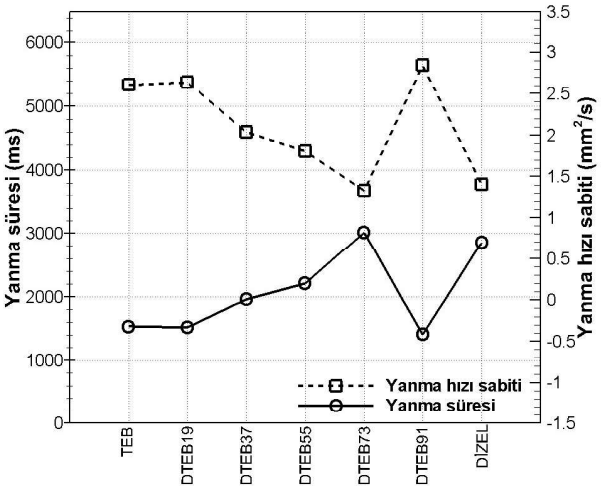
Şekil 3. Yakıtlara ait tutuşma gecikmesi değerleri

Mevcut çalışmada damlacık yanması sırasındaki alev sıcaklıkları termal kamera vasıtasıyla kaydedilmiştir. Termal kamera ölçüm yapılan bölgede maksimum sıcaklık değerini algılamaya odaklanmaktadır. Termal kamera üzerinde anlık olarak elde edilen veriler işlenerek alev sıcaklığı ve zaman arasındaki ilişki Şekil 4'te görülmektedir. Sıcaklık eğrileri incelendiğinde en yüksek alev sıcaklığına TEB'in sahip olduğu görülmektedir. En yüksek alev sıcaklığının test yakıtları içerisinde hidrojen/karbon oranı en yüksek olan TEB'de görülmüş olması beklenen bir durumdur. TEB'in atmosfer şartlarında ilk ateşleme anından maksimum sıcaklığa (~600 K) çok kısa bir sürede (~0.7 s) ulaştığı gözlemlenmiştir. En stabil maksimum alev sıcaklık trendi ise en uzun süre yanma davranışı sergileyen dizel yakıt damlacığında gözlenmiştir. Maksimum alev sıcaklıkları açısından yakıtlar karşılaştırıldığında; damlacıktaki TEB konsantrasyonu azaldıkça maksimum alev sıcaklığının düştüğü görülmektedir. Veriler incelendiğinde tüm yakıtlar için maksimum sıcaklık noktaları farklı zamanlara tekabül etmektedir. Bu durumun yakıtların kendine özgü reaktivitesiyle ilgili olduğu düşünülmektedir. Ayrıca TEB'in diğer yakıtlara oranlara daha erken bir sürede maksimum sıcaklık noktasına ulaşmasının yakıtın H/C oranı ve içeriğindeki yüksek oksijen miktarıyla ilgisi olduğu düşünülmektedir.



Şekil 4. Yakıtlara ait sıcaklık değerleri

Bir yakıt damlacığının yanma hızı, yakıtın ne kadar hızlı yandığının bir ölçüsüdür ve esas olarak sürekli buharlaşma ve yanma sürecinden etkilenir. Yanan bir damlacığın yanma hızı, damlacık yakma deneysel koşulu altında buharlaşan damlacık çapının zamansal değişiminin ölçülmesiyle belirlenebilir [18, 19]. Bu çalışmada yakıtlara ait yanma hızı sabitleri, damlacıkların yanma süresi durumları dikkate alınarak elde edilmiştir. Yüksek hızlı kamera ile elde edilen görüntüler incelenerek tutuşmanın başladığı an ile yanmanın sonlandığı an arasındaki süre hesaplanmıştır. Sonrasında ise Denklem 1'den faydalanılarak yanma hızı sabitine ulaşılmıştır. Şekil 5 incelendiğinde DTEB19 en yüksek yanma hızı sabitine sahiptir. Bu durum yakıtın oksijence zengin olmasıyla, metil köklerinin sayısının fazlalığıyla ve hidrojen/karbon oranıyla doğrudan ilişkidir. Yakıtın sahip olduğu oksijen miktarının ve hidrojen/karbon oranının artması yanma hızı sabitinde artışa neden olmaktadır. Bu durumu sıcaklık eğrilerini gösteren Şekil 4 de desteklemektedir. TEB yüksek reaktiviteye sahip bir bileşiktir. Bu durumdan dolayı yakıt hızlı bir şekilde tutuşarak tükenmektedir. Dizel ise kompleks iskelet yapısı sebebiyle reaktivitesi TEB'e göre düşüktür. Bu nedenle en düşük yanma hızı sabiti değerine sabit olduğu görülmüştür.



Şekil 5. Yakıtlara Ait Yanma Süresi ve Yanma Hızı Sabiti Değerleri

4 GENEL DEĞERLENDİRME

Bu çalışmada dizel ve TEB yakıt damlacıklarının yanma davranışı ve ikincil atomizasyon mekanizmaları kendi aralarında karşılaştırılmalı olarak sunulmuştur. Deneyler, damlacık boyutunda gerçekleştirilmiş olup normal yerçekimi, oda sıcaklığı ve atmosfer basıncı

koşullarında yapılmıştır. Temel bulgular şu şekilde özetlenmiştir:

- Tutuşma gecikmesi artışının, damlacık içerisindeki TEB konsantrasyonu artışıyla ters orantılı olduğu gözlemlenmiştir. TEB'in yakıt içerisindeki oranı arttıkça tutuşma gecikmesinde gözle görülür bir azalma olmuştur. Bu durum yakıtların tutuşma gecikmesinin kimyasal yapıdaki zincir sayısına, metil sayısına ve yapısında bulunan oksijen seviyesine bağlıdır. Yakıt içerisindeki metil ve oksijen sayısı arttıkça tutuşma gecikmesinde azalma görülürken, zincir uzunluğu artışının tutuşma gecikmesini arttırdığı görülmüştür.

- Yakıtların tükenme sürelerinin, yakıtların bağ türlerine göre değiştiği gözlemlenmiştir. Buna göre tutuşma gecikmesi en düşük olan yakıt TEB iken, en yüksek olan yakıt dizel olarak tespit edilmiştir. Ayrıca DTEB37 yakıtına ait tutuşma gecikmesi değerinin genel trende aykırı olduğu gözlemlenmiştir.

- Karışımdaki TEB konsantrasyonunun yanma sıcaklığı artışıyla doğru orantılı olduğu gözlemlenmiştir. Yanma sıcaklığı reaksiyon açısından önemli bir parametredir. Özellikle kirletici emisyonlardan biri olan partikül madde veya bir diğer adıyla is oluşumu sıcaklık artışıyla beraber azalma göstermektedir. TEB'in bu durum için de iyileştirici bir katkı maddesi olarak kullanılabileceği düşünülmektedir.

- DTEB91 yakıtına ait damlacık ömrü grafiği ve yanma hızı değerleri genel trende aykırı olmakla beraber veriler birbirini destekler niteliktedir. DTEB91 yakıtı için gerçekleştirilen üç ayrı deneyden elde edilen veriler birbirini doğrulamaktadır. Damlacığın yanması sırasında meydana gelen yüksek orandaki salınımın (mikro patlamalar, alev çekirdeki kopmaları vs.) damlacığın yanmasının sonlanmasına neden olduğu düşünülmektedir.

- Damlacık ömrü grafikleri incelendiğinde DTEB37 en fazla ikincil atomizasyona maruz kalan yakıt olmuştur. İkincil atomizasyon kısmı, toplam damlacık ömrünün küçük bir yüzdesini temsil eder. Ancak bu küçük yüzde, yakıt buharlaşmasını ve yakıt-hava karışımını artırmak için önemlidir. Hava-yakıt karışımının gelişmesi ise yakıt spreyinin genel yanma verimliliği için faydalıdır. Bu nedenle, bu süreyi artırmak yanma verimliliğini doğrudan arttıracaktır. Bu durum DTEB37 yakıtını diğer yakıtlardan daha önemli bir konuma getirmektedir.

- Karışım içerisindeki TEB konsantrasyonu arttıkça damlacık ömründe azalma gözlemlenmiştir. TEB doğrudan tutuşarak tükenme eğilimindedir ve bu diğer yakıtlara oranla daha hızlı gerçekleşmiştir. Bu durum yanmanın kısa sürmesi gerektiği durumlarda avantaj sağlayabilir.

KAYNAKÇA

[1] L. Raslavičius ve Ž. Bazaras, Variations in oxygenated blend composition to meet energy and combustion characteristics very similar to the diesel fuel. *Fuel Processing Technology*, *91*(9), 2010.

[2] A. F. A. Rasid ve Y. Zhang, Combustion characteristics and liquid-phase visualisation of single isolated diesel droplet with surface contaminated by soot particles. *Proceedings of the Combustion Institute*, *37*(3), 3401–3408, 2019.

[3] C. K. Law, Unsteady droplet combustion with droplet heating. *Combustion and Flame*, *26*(C), 17–22, 1976.

[4] C. K. Law ve W. A. Sirignano, Unsteady droplet combustion with droplet heating—II: Conduction limit, *Combustion and Flame*, *28*(C), 175–186, 1977.

[5] K. L. Pan, J. W. Li, C. P. Chen ve C. H. Wang, On droplet combustion of biodiesel fuel mixed with diesel/alkanes in microgravity condition, *Combustion and Flame*, *156*(10), 1926–1936, 2009.

[6] A. M. D. Faik ve Y. Zhang, Multicomponent fuel droplet combustion investigation using magnified high speed backlighting and shadowgraph imaging, *Fuel*, *221*, 89–109, 2018.

[7] A. Sankaranarayanan, S. Lal, I. N. N. Namboothiri, R. Sasidharakurup, A. Chowdhury ve N. Kumbhakarna, Droplet combustion studies

on two novel energetic propellants, an RP-1 surrogate fuel, and their blends, *Fuel*, *255,* 2019.
[8] K. Kobayasi, An experimental study on the combustion of a fuel droplet, *Symposium (International) on Combustion*, *5*(1), 141–148, 1955.
[9] G. M. Faeth, D. P. Dominicis, J. F. Tulpinsky ve D. R. Olson, Supercritical bipropellant droplet combustion, *Symposium (International) on Combustion*, *12*(1), 9–18, 1969.
[10] A. M. E. D. Faik, Y. Zhang ve S. de M. Hanriot, Droplet combustion characteristics of biodiesel–diesel blends using high speed backlit and schlieren ımaging, *Heat Transfer Engineering, 40*(13–14), 1085–1098, 2019.
[11] R. J. Brotherton, C. J. Weber, C. R. Guibert ve J. L. Little, Boron Compounds, 2000.
[12] Qi, D. H., Chen, H., Geng, L. M., & Bian, Y. Z., Experimental studies on the combustion characteristics and performance of a direct injection engine fueled with biodiesel/diesel blends. *Energy Conversion and Management*, 51(12), 2985-2992, 2010.
[13] Sigma-Aldrich Chemicals. *Triethyl borate 99 150-46-9*, Retrieved May 16, 2022.
[14] K. Pandey ve S. Basu, High vapour pressure nanofuel droplet combustion and heat transfer: Insights into droplet burning time scale, secondary atomisation and coupling of droplet deformations and heat release, *Combustion and Flame*, *209*, 167–179, 2019.
[15] W. Shang, S. Yang, T. Xuan, Z. He ve J. Cao, Experimental studies on combustion and microexplosion characteristics of n-alkane droplets, *Energy and Fuels*, *34*(12), 16613–16623, 2020.
[16] J. C. Lasheras, A. C. Fernandez-Pello ve F. L. Dryer, On the disruptive burning of free droplets of alcohol/n-paraffin solutions and emulsions, *Symposium (International) on Combustion*, *18*(1), 293–305, 1981.
[17] M. Ş. Biçer, Dizel ve Trietil Borat Yakıtları ile Karışımlarının Damlacık Yanma Davranışlarının İncelenmesi, 2022.
[18] M. Ghamari ve A. Ratner, Combustion characteristics of diesel and Jet-A droplets blended with polymeric additive, *Fuel*, *178*, 63–70, 2016.
[19] G. Singh, M. Esmaeilpour ve A. Ratner, The effect of acetylene black on droplet combustion and flame regime of petrodiesel and soy biodiesel, *Fuel*, *246*, 108–116, 2019.

GEOCHEMICAL ANALYSIS AND DESULFURIZATION OF BLACK GOLD FOR SUSTAINABLE USE IN THERMAL ENERGY SECTOR

Aliya Fazal[1]

1.Department of Chemistry, Fatima Jinnah Women University, Rawalpindi Pakistan

Abstract

Pakistan despite of having world's 7th largest lignite coal reserves of approximately 175 billion tons at Thar coal field of Thar Parker district of Sindh has only 02 power plants using local coal. Coal is an abundant and economical source of energy. It is accepted that coal is not only a dirty source of energy but main contributor to particulate matter, greenhouse gases, volatile organic compounds, and oxides of Sulfur. Sulfur is one of the most important quality parameters of coal especially in terms of coal rank/maturity and power generation. Combustion of coal having high content of sulfur leads to SOx emissions which have detrimental impacts on environment as well as on human health. High concentration of SOx can affect breathing, cause respiratory illnesses and aggravates existing heart and lung diseases. The present focus of the study is to analyze indigenous coal geochemistry which is broadly comprised of moisture, ash, volatile matter, fixed carbon, calorific value and total sulfur content of the Thar coal and its desulfurization by using nifty combinations of acidic ionic liquids. The proximate and ultimate analysis of 14 coal samples from Thar was done according to reported ASTM methods. The measured moisture content of coal samples was from 30-51 %. As moisture absorbs heat, so its high content reduces the relative heating efficiency of a coal upon combustion. The gross calorific value was in between 4984-6779 Btu/Lb suggesting it as Lignite-B type low quality fuel as it produces more smoke and less heat. Total sulfur content in 10 collected samples was <1% whereas 3 samples were of >1% category. The highest portion was found 11 % which reflects that it has undergone greatest degree of sulfurization. Coal was tested for desulfurization process through Extractive Catalytic Oxidative Desulfurization Strategy (ECODS). For this purpose, two ionic liquids (ILs) were synthesized based on 1-methyl piprazine as a cation with two acidic anions (dimethyl sulfate & Perchloric acid). Synthesized ILs were characterized using Fourier Transform Infrared Spectroscopy (FTIR), Nuclear Magnetic Resonance Spectroscopy - Proton (H^1 NMR), and Dynamic Scattering Calorimetry (DSC) for detailed insight into structural and functional characteristics of RTILs. The synthesized ILs were evaluated under optimized conditions for their desulfurization capabilities against Thar coal. Results have shown that these ILs have capacity for the removal of Sulfur content from coal which is recorded to be < 60 % at room temperature. These results have been supported from X-Ray Photoelectron Spectroscopy (XPS) as well as Gas Chromatography Mass Spectroscopy (GCMS). Hence, this study is an effort to design and develop cleaner and sustainable use of coal by reducing sulfur dioxide emissions.

Keywords: Coal desulfurization; Ionic liquids; climate adaptation

HİDROJEN KULLANILAN BİR DİZEL MOTORDA ÇEVRİMSEL YANMA DEĞİŞİMLERİNİN İNCELENMESİ

A. Şanlı[1] ve I.T. Yılmaz[2]

1. Gemi Makineleri İşletme, Piri Reis Mesleki ve Teknik Anadolu Lisesi, İstanbul; email: phdalisanli@outlook.com
2. Makine Mühendisliği, Teknoloji Fakültesi, Marmara Üniversitesi, İstanbul; email: ilker.yilmaz@marmara.edu.tr

Özet

Gelecekte petrol kökenli yakıt rezervlerinin azalacağı öngörülmektedir. Günümüz modern sıkıştırma ateşlemeli dizel motorlarında halen petrol kökenli yakıt olarak motorin kullanılmaktadır. Hidrojen yakıtı, sıkıştırma ateşlemeli dizel motorlarda gelecekte kullanılma potansiyeli olan ve çevreye en az zarar veren alternatif yakıtlardan biridir. Bu çalışmada, yüksek basınçlı yakıt püskürtme teknolojisine sahip dört silindirli bir dizel motorda hidrojen gazı emme kanalından fumigasyon yöntemiyle silindirlere verilerek sabit devirde (1750 d/dak) iki farklı motor yükünde (60Nm ve 100Nm) test edilmiştir. Hidrojen debisi, dakikada 10 litreden (H10) 50 litreye (H50) kadar 10 l/dak'lık artışlarla değiştirilmiştir. Yapılan yanma analizinde 200 çevrim için standart sapma ve çevrimsel değişim katsayıları incelendiğinde; 100 Nm'de krank açısına bağlı olarak silindir basıncında en az çevrimsel değişim H30 ve H40 oranlarında elde edilmiştir. Test motoru, düşük yükte çalıştırıldığında artan hidrojen miktarıyla birlikte maksimum silindir basıncının ve maksimum yanma sıcaklığının tüm çevrimlerde daha erken oluştuğu belirlenmiştir. 60 Nm'de en yüksek silindir basıncı H50 ile 365^o krank açısında 82,97 bar, 100 Nm'de dizel ile 374^o krank açısında 109,32 bar olarak belirlenmiştir. Düşük motor torkunda, H20 ile 375^o krank açısında 38,01 J/^{o} olarak elde edilen ısı dağılım oranı, yüksek torkta H50 ile 377^o krank açısında 70,39 J/^{o} olarak elde edilmiştir. Maksimum ısı dağılımı oranı değerleri tüm çevrimler için düşük yükte 371-377^o krank açısı aralığında değişirken, tork artışıyla birlikte değerler daha geniş bir krank açısı aralığında (370-379^o) elde edilmiştir. En yüksek yanma sıcaklıkları, düşük yükte H20 ile 390^o krank açısında 1571 K değerinde elde edilirken, yüksek torkta 392^o krank açısında H50 ile 2449 K değerinde elde edilmiştir. Aynı zamanda, 200 çevrim boyunca en yüksek sıcaklıklar düşük yükte 388-392^o krank açısı aralığında değişirken, yüksek yükte daha geniş krank açısı aralığında (386-393^o) değişmiştir. Ortalama indike basınç ve maksimum silindir basıncı için çevrimsel değişim katsayıları 100 Nm'de H50 çalışması haricinde tüm çalışma koşulları için %3'ün altında kalmıştır. Yapılan çalışma sonucunda, belirli çalışma şartları altında hidrojenin ortak hatlı dizel motorda çevrimsel değişimlerin azalmasına katkı sağladığı tespit edilmiştir.

Anahtar kelimeler: Hidrojen, Çevrimsel değişim, Yanma, Dizel

1 GİRİŞ

Dizel motorlar, ulaşım, jeneratör uygulamaları, tarım, denizcilik gibi birçok alanda kullanılmaktadır. Yakıt dönüşüm verimlerinin yüksek olmasının yanı sıra düşük oranda karbon monoksit (CO) ve yanmamış hidrokarbon (HC) emisyonları yayması önemli avantajlarıdır. Ancak, verimleri yüksek olmasına rağmen yüksek oranda partikül madde (PM) ve azot oksit (NO_x) emisyonu yaymaktadır. Bu emisyonların azaltılmasında kullanılan iyileştiricilerin artan maliyetleri ve motor performansını azaltması araştırmacıları farklı yöntemler geliştirmeye yöneltmiştir [1].

Hidrojen, karbon içeren emisyonları önemli oranda azaltmasından dolayı hem dizel hem buji ateşlemeli motorlarda sıklıkla tercih edilmektedir [2,3]. Alt ısıl değeri, alev ilerleme hızı, kendiliğinden tutuşma sıcaklığı ve difüzyon özelliği diğer yakıtlara nazaran daha yüksektir. Bunun yanı sıra, daha geniş alevlenme limitlerine ve daha düşük tutuşma enerjisine sahiptir [4]. Dizel motorlarda hidrojen, emme kanalından fumigasyon veya enjektörler aracılığıyla silindirlere gönderilmektedir. Diğer bir yöntem ise doğrudan silindirlere püskürtülerek kullanılmaktadır. Ancak, bu yöntem motorda önemli değişiklikler gerektiğinden ve artan maliyetlerden dolayı nadiren tercih edilmektedir. Dizel motorlarda

hidrojenin ana yakıt olarak kullanılmasında ateşleyici olarak, setan sayısı yüksek bir pilot yakıt (dizel veya biyodizel gibi) kullanılmaktadır. Pilot yakıt, sıkıştırma işlemi sonuna yakın bir zamanda yanma odasına püskürtülerek hidrojen ve hava karışımını tutuşturmaktadır. Emme kanalından hidrojen gönderilen yöntemlerde emilen hava miktarı azalmakta ve karışım zenginleşmektedir. Aynı zamanda, emme havasında yanıcı gaz bulunmasında ötürü geri tepme problemiyle karşılaşmamak için yüksek sıcaklığa maruz kalan kısımların iyi soğutulması gerekmektedir [5]. NO_x emisyon artışına neden olan yüksek alev hızı aynı zamanda kullanılan hidrojen oranıyla da artmaktadır. Düşük motor torkunda genel olarak NO_x emisyonları daha azdır. Bu durum silindir sıcaklıklarının düşük olmasından kaynaklanmaktadır [6].

Çevrimsel yanma değişimleri, motor performans ve emisyonlarına önemli oranda etki etmektedir. Aynı zamanda, motor titreşimlerinin temel sebeplerinden biri olduğu düşünülmektedir. Çevrimsel değişimler, silindirlerde meydana gelen fiziksel ve kimyasal olaylardan kaynaklanır. Çevrimden çevrime değişen bölgesel hava-yakıt oranı, önceki çevrimden kalan artık gaz miktarı, yanma odasında oluşan hava hareketleri, yakıt püskürtme basıncı ve miktarı, tutuşma gecikmesi gibi olaylar çevrimsel farklıkların temel sebepleridir [7]. Ortama indike basınçtaki küçük çevrimsel değişimler, çıkış gücünde önemli değişimlere neden olmaktadır [8].

Alternatif yakıtların içten yanmalı motorlarda çevrimsel değişimlere etkisi ile ilgili literatürde bazı araştırmalar karşımıza çıkmaktadır. Wang ve diğerleri [9], alternatif yakıt olarak dimetil eter kullanımının dizel motorda çevrimsel değişimlere etkisini incelemişlerdir. Maksimum basınç ve maksimum sıcaklık değişimlerinin tüm yakıt karışım oranları için %3 altında kaldığını tespit etmişlerdir. Maksimum basınç artış oranı değişiminin maksimum ısı dağılım oranına benzer olduğunu göstermişlerdir. Ceviz ve Yüksel [10], buji ateşlemeli motorda etanol miktarının çevrimsel değişimlere etkisini incelemişlerdir. Çalışmada, ortalama indike basınçta çevrimsel değişimler açısından en uygun etanol miktarının %10 olduğunu tespit etmişlerdir. Wang ve diğerleri [11], metanol-dizel çift yakıt karışımlarıyla çalıştırılan sıkıştırma ateşlemeli bir motorda düşük motor torkunda maksimum basınç ve maksimum sıcaklıklar için çevrimsel değişim katsayılarının arttığını gözlemlemişlerdir. Emme sıcaklığının düşük motor torkunda tüm çevrimsel değişim katsayı parametrelerine en etkili faktör olduğunu tespit etmişlerdir. Diğer taraftan, püskürtme zamanlamasının methanol-dizel çevrimsel çalışmalarına etkisiz bir parametre olduğu belirtilmiştir. Wang ve diğerleri [12], çeşitli doğalgaz-dizel karışım oranlarıyla çalıştırılan bir dizel motorda çevrimsel yanma analizi yapmışlardır. Artan doğalgaz miktarıyla birlikte, maksimum silindir basıncı, ortalama indike basınç ve krank açısına göre silindir basıncının arttığını tespit etmişlerdir.

Bu çalışmada, ortak hat yakıt püskürtme sistemine sahip dört silindirli ve dört zamanlı sıkıştırma ateşlemeli bir motor iki farklı motor torkunda değişik hidrojen akış oranlarıyla test edilmiştir. Elde edilen bulgular, çevrimsel farklılıklar açısından değerlendirilmiştir. Çevrimsel yanma değişimleri açısından iki farklı motor torkunda optimum hidrojen oranı araştırılmıştır.

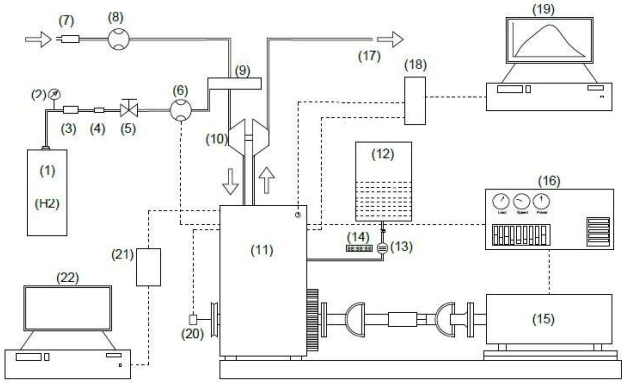
2 MATERYAL VE METOT

Çalışmada dört silindirli, dört zamanlı, turboşarjlı common-rail motor kullanılmıştır. Motor özellikleri Tablo 1'de verilmektedir. Test sistemi şeması Şekil 1'de verilmektedir. Motor torkunu ve devrini ayarlamak için elektrikli bir dinamometre kullanılmıştır. Testler boyunca dinamometrede oluşan yüksek hararet şehir şebeke suyu yardımıyla giderilmektedir. Motest yazılımı yardımıyla dinamometre ara yüzü kontrol edilebilmektedir. Motor emme havası akış oranı New Flow akış ölçer ile ölçülmüştür. Hidrojen gazı için 50 litrelik tüplerde Hatgaz AŞ'den temin edilen %99,999 saflıkta hidrojen gazı kullanılmıştır. Emme portunda bulunan bir karışım odasında emme havası ile karıştırılan hidrojenin akış oranı Sierra 5858E model akış ölçer ile ölçülmüştür. Her testte, dizel yakıt miktarı yakıt tankıyla bağlantılı olan ölçekli cam beher ve bir kronometre yardımıyla ölçülmüştür. Yanma odası basıncı, Optrand 33288 model kızdırma buji tipinde basınçölçer kullanılarak ölçülmüştür. Her deneyde toplanan silindir basınç sinyalleri National Instrument 6343 model veri toplama kartı üzerinden bir bilgisayara aktarılmıştır. Krank açısı, krank kasnağı eksenine bağlanan 360^o artımlı bir enkoder yardımıyla belirlenmiştir. Febris

yazılımında kaydedilen değerler çevrimsel yönden analiz edilmiştir.

Tablo 1. Test motoru özellikleri.

Motor tipi	Ortak hatlı, dört silindirli, turboşarjlı, sekiz supaplı
Enjeksiyon safhaları	Ön püskürtme ve ana püskürtme
Kurs mesafesi	80,5 mm
Silindir çapı	76 mm
Sıkıştırma oranı	16,9:1
Strok hacmi	1461 cm^3
Maksimum güç	48 kW @4000 d/dak
Maksimum tork	160 Nm @1750 d/dak



1.Hidrojen tüpü, 2. Basınç ölçer, 3. Regülatör, 4. Alev tutucu, 5. Kısma valfi, 6. Hidrojen akış ölçer, 7. Hava filtresi, 8. Hava akış ölçer, 9. Karışım odası, 10. Turboşarj, 11. Test motoru, 12. Yakıt tankı, 13. Ölçekli cam beher,14. Kronometre, 15. Dinamometre, 16. Dinamometre kontrol paneli, 17. Egzoz çıkışı, 18. Veri toplama kartı, 19. ve 22. Bilgisayar, 20.Enkoder, 21. Diagnostik kartı.

Şekil 1. Test şeması

Testler, sabit devirde (1750d/dak) iki farklı motor torku ve beş farklı hidrojen akış oranlarıyla yapılmıştır. Deneylerde kullanılan pilot yakıt, petrol ofisi yakıt istasyonlarından temin edilen Euro dizel yakıttır. Yakıt testleri, motor kararlı rejime ulaştığında yapılmıştır. Motor suyu giriş-çıkış sıcaklıkları 80±5^o C civarında sabit tutulmuştur. Soğutma suyu sıcaklıkları, egzoz gaz sıcaklığı, karter yağ sıcaklığı ve emme havası sıcaklığı K tipi termokupullarla ölçülmüştür. Testlerde, öncelikle normal dizel yakıt düşük ve yüksek motor torklarında referans yakıt olarak test edilmiştir. Daha sonra, hidrojen gazı düşük yükte emme portundan düşük akış oranlarından başlayarak kısma valfleri sayesinde kademeli olarak artırılmıştır. Geri tepme durumunda tüpe alev ulaşmaması için emme hattında alev tutucu kullanılmıştır. Daha yüksek hidrojen oranlarında çalışabilmek ve vuruntu oluşumundan kaçınmak için sıkıştırma oranı düşürülmüştür. Yakıt karışımları, hidrojenin hacimsel akış oranına göre isimlendirilmiştir. Örneğin, H10 sembolü 10 l/dak akış debisinde hidrojen akışını simgelemektedir. İstenen tork elde edilinceye kadar dizel yakıt miktarı artırılmaktadır. Hidrojen yakıt enerji paylaşım oranı, en yüksek hidrojen oranı (H50) için 60 Nm'de %29 ve 100 Nm'de %18'dir. Azalan hidrojen oranıyla birlikte dizel yakıt enerji paylaşım oranı artmaktadır. Her testte, motorun elektronik kumanda ünitesine bağlı bir diagnostik kart yardımıyla bir çevrimde püskürtülen dizel yakıt miktarı, emme havası sıcaklık ve akış oranları, gaz kolu açısı, common-rail basıncı gibi birçok farklı parametre bilgisayar ekranında aynı anda görülmektedir. Deneylerde kullanılan cihazların hata miktarları Tablo 2'de verilmektedir.

Tablo 2. Ölçülen bazı test değişkenlerinin doğrulukları

Ölçülen değişken	Hata miktarı
Tork, Nm	±0,25%
Devir, d/dak	±1%
Krank açısı	±1^o
Hidrojen debisi, l/dak	±1%
Dizel debisi, l/dak	±0,5%
Sıcaklık, ^{o}C	±1%
Silindir basıncı, bar	±0,5%

Deneylerde elde edilen silindir basıncı işlenerek yanma fazı hakkında önemli bulgulara ulaşılmaktadır. Birim krank açısı aralığında açığa çıkan ısı enerjisi (ısı dağılım oranı) termodinamiğin birinci kanunundan elde edilen aşağıdaki eşitlikle hesaplanmaktadır.

$$\frac{dQ_{Net}}{d\theta} = \frac{k}{k-1} P \frac{dV}{d\theta} + \frac{1}{k-1} V \frac{dP}{d\theta} \qquad (1)$$

Gaz sıcaklığı, referans bir noktadaki basınç, hacim ve sıcaklık değerleri kullanılarak ideal gaz kanununa göre aşağıdaki eşitlikten hesaplanmaktadır.

$$T_g = PV \frac{T_{ref}}{P_{ref} V_{ref}} \qquad (2)$$

Burada, ref alt indisi ile gösterilen değerler için emme supabının kapanma açısı olan 200^o krank

açısındaki (alt ölü noktadan sonra 20^o) basınç, silindir hacim ve gaz sıcaklığıdır.

Çevrimsel değişim katsayısı (ÇDK) herhangi bir yanma parametresi için hesaplanabilir. ÇDK, aşağıdaki bağıntıyla hesaplanmaktadır.

$$ÇDK = \frac{\sigma}{\bar{X}}100 \quad (3)$$

σ ve $\bar{X}$ sırasıyla standart sapma ve ortalama değeri ifade etmektedir. σ aşağıdaki eşitlikten hesaplanmaktadır.

$$\sigma = \sqrt{\frac{\sum_{i=1}^{n}(X_i-\bar{X})^2}{n-1}} \quad (4)$$

X_i herhangi bir yanma parametresi seçilebilir. n çevrim sayısıdır. Bu çalışmada, 200 çevrim için çevrimsel yanma analizi yapılmıştır.

3 BULGULAR VE TARTIŞMA

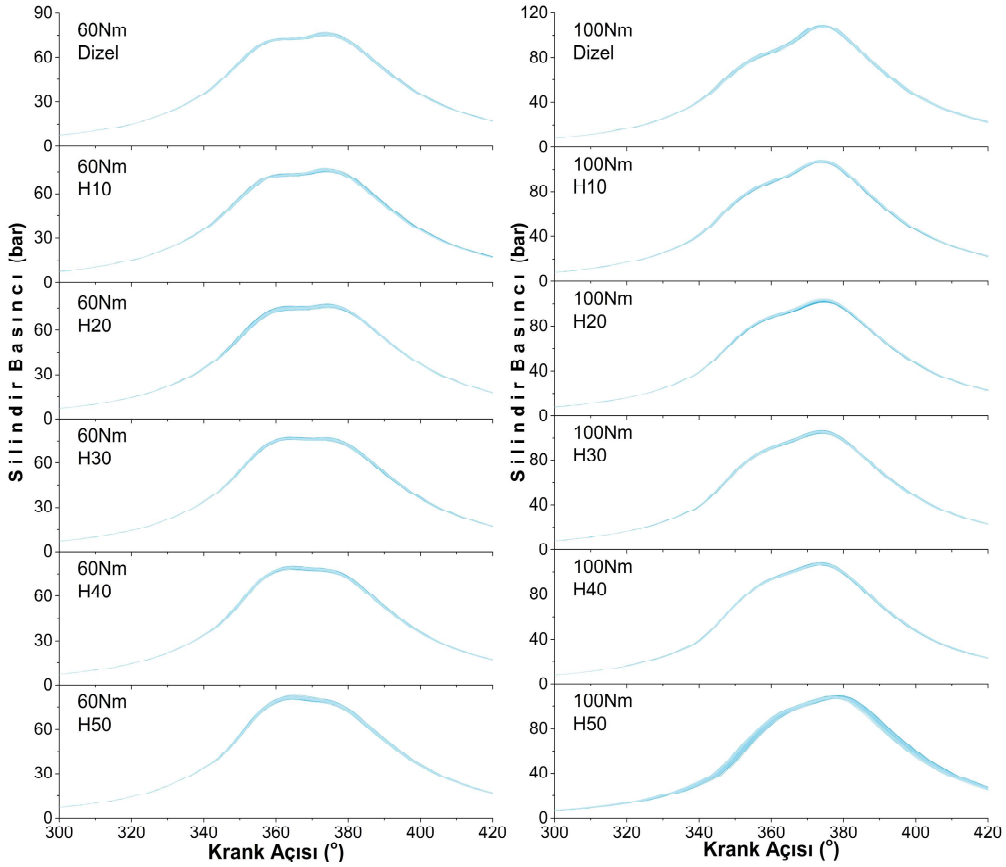
3.1 Çevrimsel Silindir Basıncı

Bu bölümde, hidrojen ve pilot dizel yakıtın yanması sonucu oluşan silindir basınç verileri 200 çevrim için verilmiştir. 60 Nm ve 100 Nm motor torklarında, her bir krank açısında oluşan silindir basınç değişimleri tüm hidrojen-dizel çalışmaları için Şekil 2'de verilmektedir. Şekiller incelendiğinde sıkıştırma periyodunda tüm silindir basınç eğrilerinde çevrimsel değişimlerin az olduğu görülmektedir. Ancak, yanma başlangıcından itibaren üst ölü nokta (ÜÖN) civarında çevrimsel değişimler artmaktadır. ÜÖN'den sonra yanma bitimine doğru çevrimsel değişimler azalmakta ve tüm silindir basınç eğrileri birbirine oldukça yakın bir eğilim göstermektedir. 60 Nm motor torku altında normal dizel çalışmasıyla kıyaslandığında, hidrojen-dizel yakıtlı çalışmalarda silindir basınç eğrilerinin çevrimden çevrime daha fazla değiştiği görülmektedir. En yüksek ve en düşük silindir basınçları arasındaki fark daha fazladır. Ancak, 100 Nm'de oluşan silindir basınçları incelendiğinde, H50 çalışması hariç diğer hidrojen-dizel çalışma durumlarında oluşan çevrimsel silindir basınç farklılıklarının normal dizel çalışmasından daha az olduğu görülmektedir. 100 Nm'de, H50 ile oluşan çevrimsel silindir basınçları önemli oranda değişmektedir. Bu değişimlerin, artan hidrojen ilavesi ve artan pilot dizel yakıt sonucu oluşan aşırı zengin karışımdan kaynaklandığı düşünülmektedir.

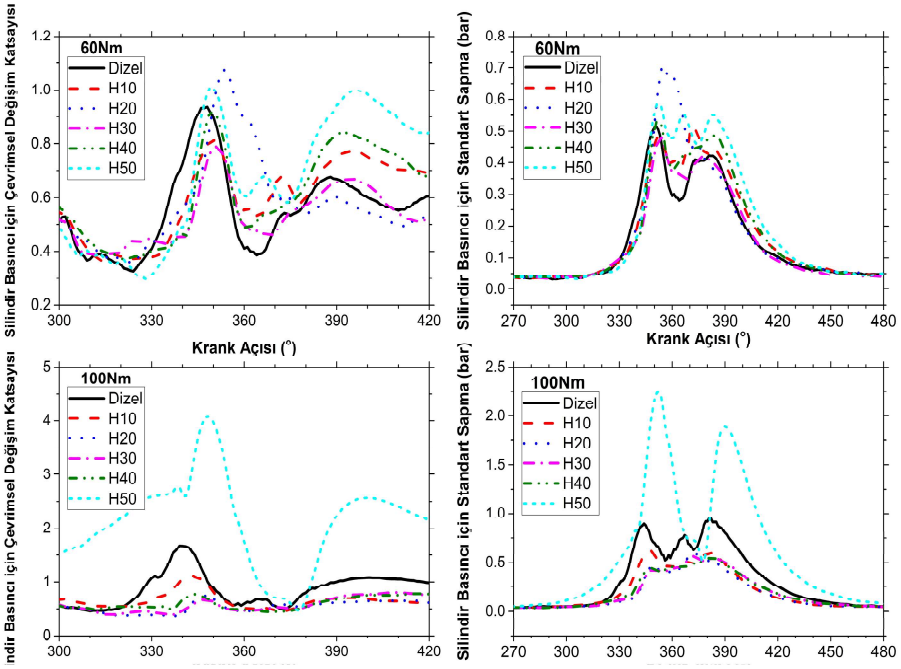
Dizel ve hidrojen-dizel karışımları için silindir basınç eğrilerinde çevrimsel değişimlerin boyutunun daha açık bir şekilde ortaya koyulabilmesi için krank açısına göre standart sapma ve çevrimsel değişim katsayısı (ÇDK) değişimlerinin ele alınması daha uygun olur. Şekil 3'de bu değişimler sunulmaktadır. Yukarıda tartışıldığı gibi 100 Nm'de H10, H20 H30 ve H40 çalışmalarında normal dizel yakıt çalışmasına göre silindir basıncında standart sapmanın daha az olduğu görülmektedir. Şekil 3'de açıkça görüldüğü gibi 100 Nm'de H50 çalışmasında çevrimsel değişim katsayısı değişimi diğer hidrojen oranlarına kıyasla oldukça yüksektir. Yüksek ÇDK değerleri, motor çıkış gücünde dalgalanmaların ve motor titreşimlerinin artacağı anlamına gelmektedir. Aynı zamanda, oluşacak yüksek basınç artış oranlarından dolayı vuruntu olacağı açıktır. Bu durum, motor çalışmasını ve dolayısıyla araç sürüş konforunu olumsuz yönde etkilemektedir.

Çevrimden çevrime değişimlerin incelenmesinde kullanılan diğer önemli göstergeler maksimum silindir basıncı-krank açısı ve maksimum silindir basıncı-çevrim sayısı değişimleridir. Farklı yüklerde dizel ve hidrojen-dizel yakıtlı çalışmalar için maksimum silindir basıncı-krank açısı değişimleri Şekil 4'de, maksimum silindir basıncı-çevrim sayısı Şekil 5'de gösterilmektedir. Test motoru düşük torkta çalışırken, normal dizel, H10 ve H20 yakıtları için maksimum silindir basınçları ÜÖN'den sonra 13-15^o krank açısı (KA) aralığında oluşmakta iken hidrojen oranı artışıyla birlikte maksimum silindir basınçlarının 8-11^{o}KA daha erken (364-365^{o}KA aralığından) oluştuğu görülmektedir. Aynı zamanda, 200 çevrim boyunca, artan hidrojen miktarıyla maksimum silindir basınç değerlerinin arttığı Şekil 4 ve Şekil 5'de açıkça gösterilmektedir. Sabit motor torkunda, hidrojen oranı artarken dizel yakıt miktarı azalmaktadır. Artan hidrojen miktarıyla ön karışım yanma prosesinde alev daha hızlı ilerler. Daha fazla miktarda hidrojen ve daha az miktarda dizel yakıt, ana püskürtme safhasından önce yakılır. Bu durumda, artan hidrojen oranıyla daha erken maksimum basınçlar gözlemlenir. Silindir hacminin daha küçük olması ve hidrojenin yüksek alev sıcaklığı, silindir basıncının daha fazla yükselmesine

neden olmaktadır. Ana püskürtme ile maksimum basınç değeri daha çok artar [13].

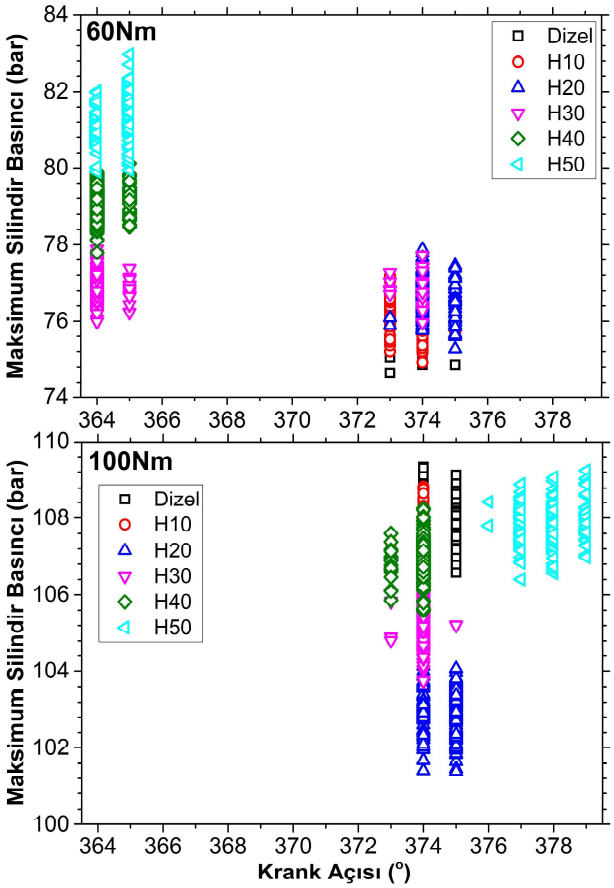


Şekil 2. Farklı hidrojen akış oranlarında ve farklı yüklerde çevrimsel silindir basınç değişimleri

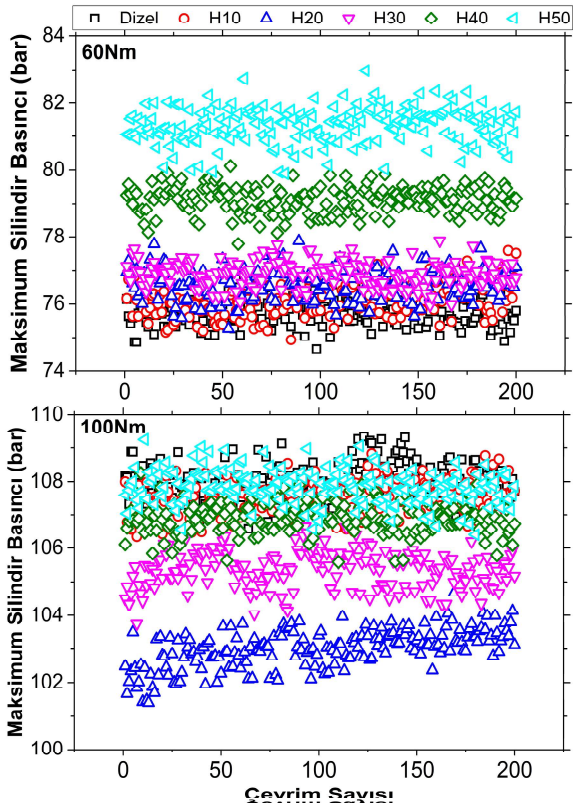


Şekil 3. Farklı hidrojen akış oranlarında ve yükler altında silindir basıncının standart sapma değişimleri

Diğer taraftan, artan yükle birlikte maksimum silindir basınçlarının geciktiği görülmektedir. 100 Nm'de yakıtların maksimum silindir basınçları 373-379^{o}KA aralığındadır. Yük artışı, ana safhada püskürtülen dizel yakıt miktarını artırmakta ve muhtemelen oluşan oksijen yetersizliğinden dolayı karışımın yanma fazını geciktirmektedir.



Şekil 4. Farklı hidrojen akış oranlarında ve yükler altında maksimum silindir basınç-krank açısı değişimleri



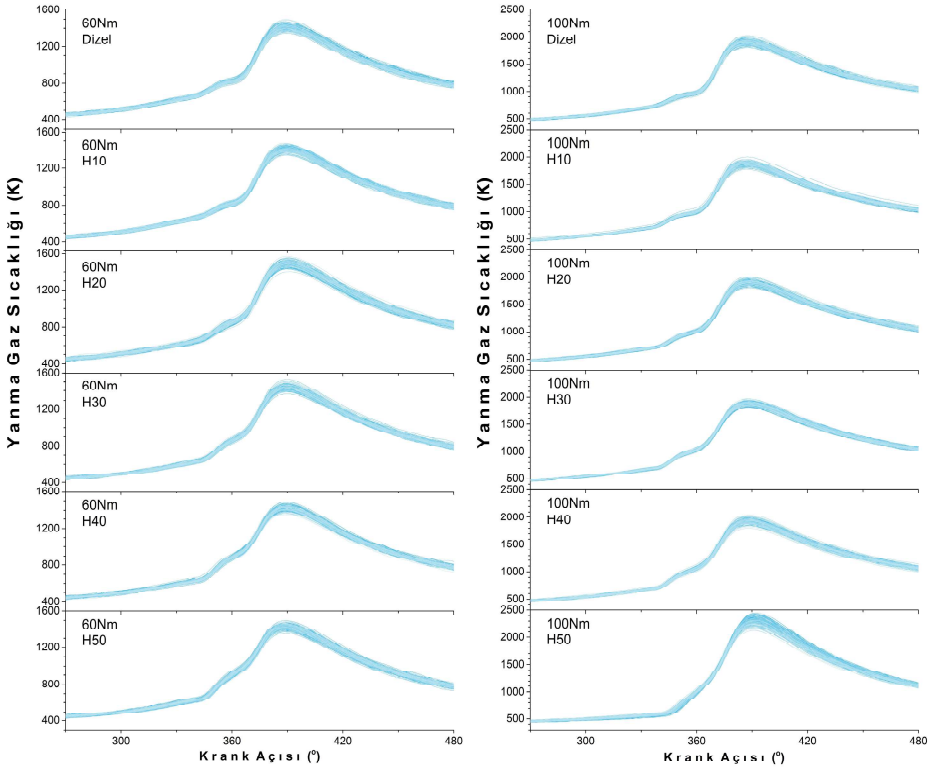
Şekil 5. Farklı hidrojen akış oranlarında ve yükler altında 200 çevrim boyunca maksimum silindir basınç değişimleri

60 Nm'de maksimum silindir basıncı H50 ile 365°KA'da 82,97 bar elde edilirken, 100 Nm'de normal dizel çalışması ile 374°KA'da 109,32 bar elde edilmiştir. Ayrıca, 100 Nm'de H50 yakıtıyla maksimum silindir basınç değerleri diğer yakıtlardan daha geç krank açılarında (376-379°KA) oluşmuştur. Aşırı hidrojen ilavesiyle birlikte emme havası azalmaktadır. Bunun yanında, artan yükle birlikte pilot dizel miktarındaki artış karışımı aşırı derecede zengin yapmıştır. Oluşan bu zengin karışım kısmen eksik yanmanın oluşmasına ve maksimum basıncın gecikmesine neden olmaktadır. Ayrıca, Şekil 2'de H50 ile oluşan çevrimsel değişimlerin kaynakları arasında düşünülmektedir.

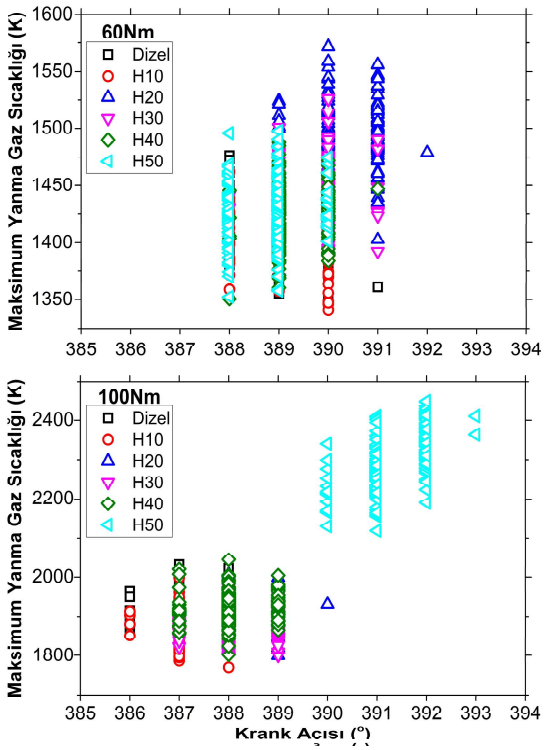
3.2 Çevrimsel Yanma Gaz Sıcaklığı

200 çevrim için krank açısına göre yanma gaz sıcaklığı değişimleri farklı yükler için Şekil 6'da verilmektedir. Düşük motor torkunda normal dizel ve hidrojen-dizel yakıtlı çalışmalar için yanma gaz sıcaklıkları 1400-1500 K civarında değiştiği görülmektedir. Artan yükle birlikte yanma gaz sıcaklıkları 2000 K üstüne çıkmıştır. Şekil 7'de maksimum yanma gaz sıcaklığı-krank açısı ve Şekil 8'de 200 çevrim boyunca meydana gelen maksimum yanma gaz sıcaklığı değişimleri gösterilmektedir. Şekil 7 incelendiğinde, düşük motor torkunda maksimum sıcaklıkların ÜÖN'den sonra 28-32°KA aralığında, yüksek motor torkunda ise maksimum sıcaklıkların 26-33°KA aralığında oluştuğu görülmektedir. Artan yükle birlikte maksimum sıcaklıkların oluştuğu KA aralığı genişlemektedir. Bunda H50 çalışma durumunun etkisi açıkça görülmektedir. Benzer durum daha önce belirtildiği gibi silindir basıncı için gerçekleşmiştir. Düşük motor torkunda H20 ile en yüksek sıcaklıkların, H10 ile en düşük sıcaklığın ÜÖN'den sonra 30°KA'da oluştuğu görülmektedir. Yüksek motor torkunda H50 ile en yüksek sıcaklıkların 392°KA'da, H10 ile en düşük maksimum sıcaklığın 388°KA'da oluştuğu görülmektedir.

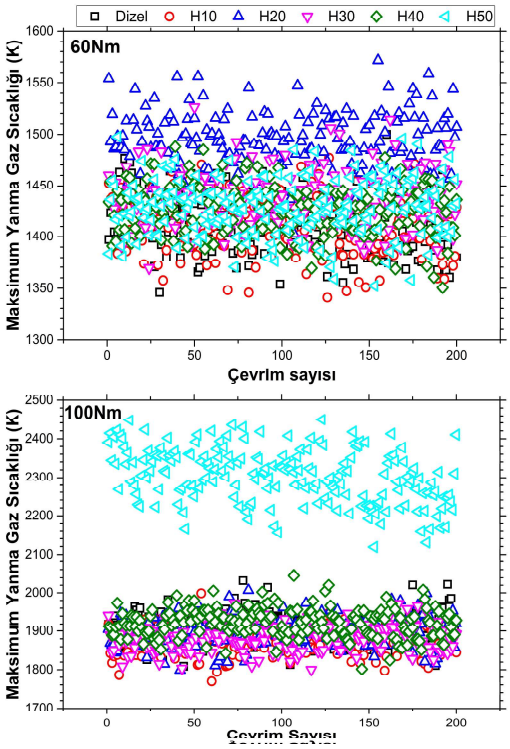
Ayrıca, Şekil 7 ve Şekil 8'den tüm yakıtlar için maksimum sıcaklıkların düşük torkta 1340-1571 K aralığında, yüksek torkta iken 1760-2449 K aralığında gerçekleştiği görülmektedir. Yüksek torkta, H50 çalışmasının yüksek sıcaklıkların oluşmasında daha etkili olduğu açıktır. Normal dizel ve H10'dan H40'a kadar olan çalışmalarda yaklaşık 1800-2000 K arasında benzer maksimum sıcaklıkların oluştuğu görülmektedir.



Şekil 6. Farklı hidrojen akış oranlarında ve farklı yüklerde çevrimsel yanma gaz sıcaklığı değişimleri



Şekil 7. Farklı hidrojen akış oranlarında ve yükler altında maksimum gaz sıcaklığı-krank açısı değişimleri



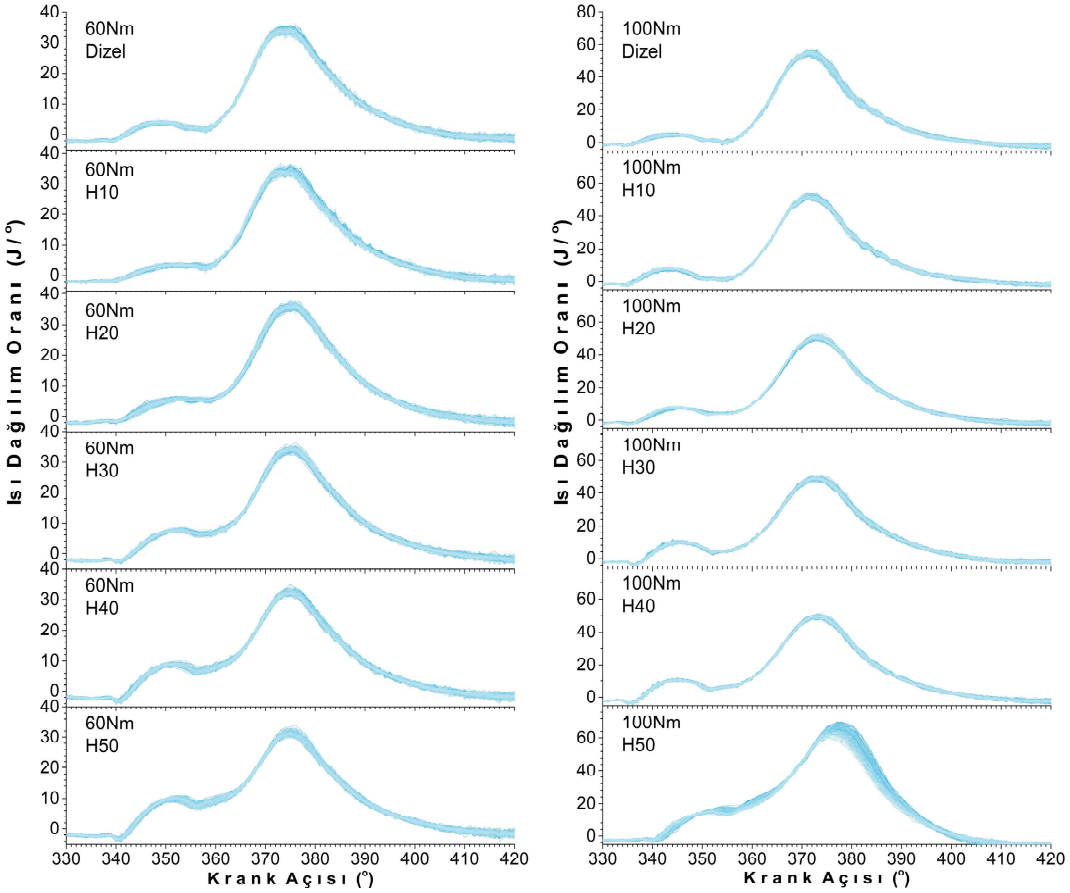
Şekil 8. Farklı hidrojen akış oranlarında ve yükler altında 200 çevrim boyunca maksimum gaz sıcaklığı değişimleri

3.3 Çevrimsel Isı Dağılım Oranı

Isı dağılım oranı (IDO), önemli yanma bulgularından biridir. Çift yakıt çalışma durumlarında, hidrojen varlığı normal dizel yanma fazını etkilemektedir. Sıkıştırma sonuna

doğru püskürtülen dizel yakıt, ön püskürtme safhasında kendiliğinden tutuşmakta ve oluşan alev çekirdeği hava-hidrojen karışımını tutuşturmaktadır. Püskürtme esnasında, eser miktarda hidrojen gazı dizel yakıta nüfuz etmektedir. Yanmayla birlikte IDO eğrisinde bir miktar yükselme gözlenmektedir. Yanmakta olan hava-hidrojen karışımına ana püskürtme safhasıyla birlikte daha fazla miktarda pilot dizel yakıt püskürtülür. Ana püskürtme safhasında, yine dizel yakıt içerisine hidrojen gazı nüfuz etmektedir. Hızla tutuşan dizel yakıtla birlikte karışımın kimyasal enerjisi artmakta ve IDO maksimum değerine ulaşmaktadır. Yanma işleminde, dizel yakıt ve hava-hidrojen karışımının önemli bir kısmı yanmaktadır [14]. Genişleme periyodunda, azalan yakıt miktarı ve artan hacimle birlikte IDO eğrisinde azalma meydana gelmektedir. Yanma sonunda, arta kalan yakıt karışımı kısmen egzoz yoluyla atılmakta veya bir sonraki çevrime katılmaktadır.

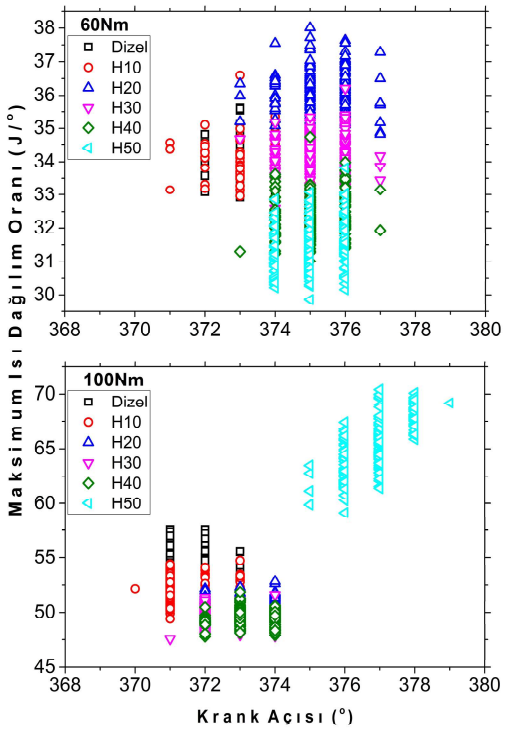
Şekil 9'da, farklı tork ve hidrojen akış oranlarında 200 çevrimde meydana gelen IDO değişimleri gösterilmektedir. Çevrimden çevrime IDO eğrilerinde değişim olduğu açıktır. Her iki motor torkunda, artan hidrojen oranıyla IDO eğrisindeki ön karışım safhasında oluşan pik değer artış göstermiştir. Sabit yükte, artan hidrojen oranıyla birlikte karışımın enerjisi artmaktadır. Ayrıca, 100 Nm'de dizel ve H10'dan H40'a kadar olan çalışmalarda IDO eğrilerinde oluşan çevrimsel değişimlerin 60 Nm'de oluşanlardan daha az olduğu görülmektedir. Yüksek torkta H50 ile IDO eğrilerindeki belirgin dalgalanma, yanma safhasında çevrimler arasında önemli farklılıkların olduğunu göstermektedir.



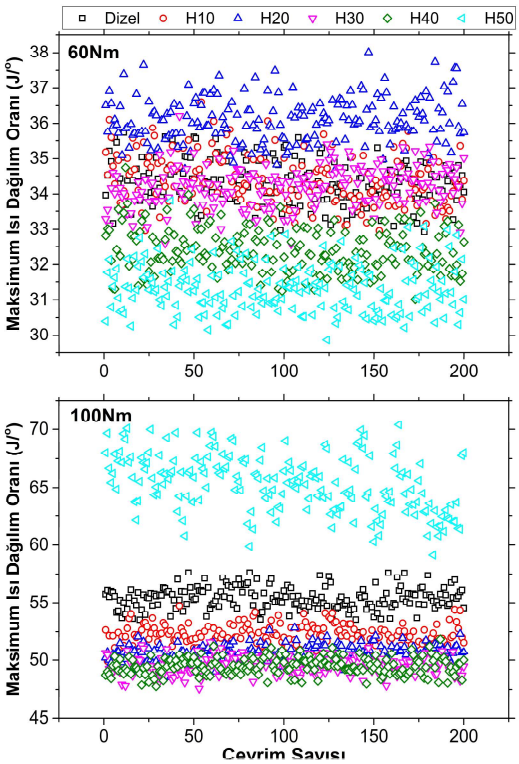
Şekil 9. Farklı hidrojen akış oranlarında ve farklı yüklerde çevrimsel ısı dağılım oranı değişimleri

Maksimum IDO değerleri ve meydana geldikleri krank açıları Şekil 10'da sunulmuştur. Şekil 10'da tüm hidrojen ilave oranları için düşük yükte, maksimum IDO değerlerinin 371-377°KA aralığında değiştiği görülmektedir. 60 Nm'de maksimum IDO, H20 ile 373-377° KA aralığında meydana gelirken, en düşük IDO değerlerinin H50 ile 374-376°KA aralığında meydana geldiği görülmektedir. Ayrıca, 60 Nm'de en düşük ve en yüksek IDO değerleri 375°KA'da meydana gelmiştir. Artan yükle birlikte maksimum IDO değerlerinin oluştuğu

krank açısı aralığı genişlemiştir (370-379°KA). 100 Nm'de maksimum IDO değerleri H50 ile önemli oranda artmıştır. En yüksek IDO değeri 377°KA'da, minimum IDO değeri H30 ile 371°KA'da meydana gelmiştir.

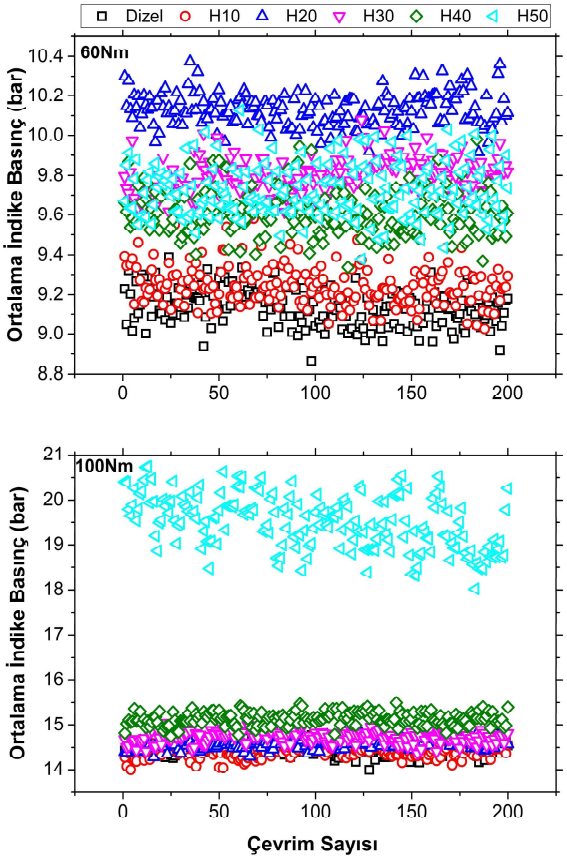


Şekil 10. Farklı hidrojen akış oranlarında ve yükler altında maksimum ısı dağılım oranı-krank açısı değişimleri



Şekil 11. Farklı hidrojen akış oranlarında ve yükler altında 200 çevrim boyunca maksimum ısı dağılım oranı değişimleri

Şekil 11'de 200 çevrim boyunca maksimum IDO değerlerinde meydana gelen değişim gösterilmektedir. 60 Nm'de dizel, H10, H20 ve H30 çalışmalarında maksimum IDO değerleri H40 ve H50 ile karşılaştırıldığında daha yüksektir. Dizel çalışmasından H40 ve H50 çalışmalarına geçildiğinde maksimum IDO değerleri kademeli olarak azalmıştır. 100 Nm'de 200 çevrim boyunca H10-H40 yakıtlarıyla elde edilen IDO değerlerinin normal dizelden daha az, H50 için ise daha fazla olduğu açıkça görülmektedir. Aşırı hidrojen ilavesinde, yanma esnasında oluşan aşırı gaz sıcaklığı ve basınç artış oranlarından dolayı IDO değerlerinin yükseldiği düşünülmektedir.



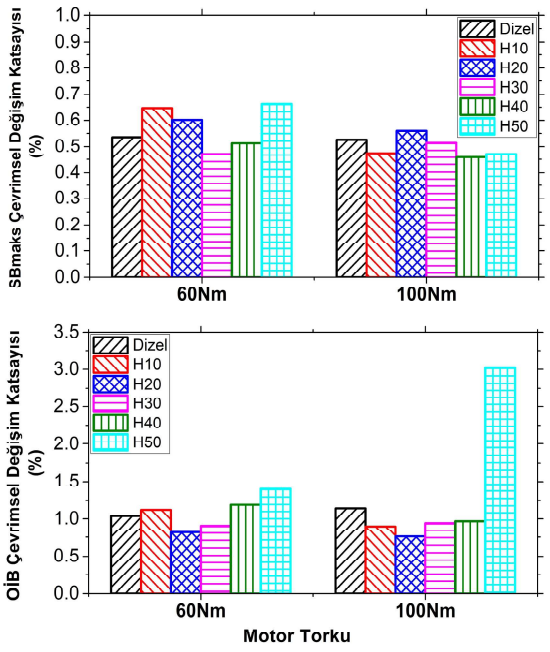
Şekil 12. Farklı hidrojen akış oranlarında ve yükler altında 200 çevrim boyunca OİB değişimleri

Şekil 12'de 200 çevrim boyunca OİB'de meydana gelen değişimler görülmektedir. 60 Nm'de dizel yakıta hidrojen eklenmesiyle OİB'de artış meydana gelmektedir. Dizel çalışmasına göre en yüksek OİB artışı H20 ile meydana gelmiştir. 100 Nm'de dizel ve H10'dan H40'a kadar olan çalışmalarda OİB değerlerindeki değişim benzer olup 14-15,5 bar arasındadır. Ancak, H50 çalışması ile OİB'de önemli oranda artış gözlenmiştir ve değerler 18-

21 bar seviyelerine çıkmıştır. Düşük ve yüksek yüklerdeki OİB'de meydana gelen değişimlerin, ortalama yanma gaz sıcaklığında meydana gelen değişimlere benzer olduğu gözlenmiştir.

Farklı oranlarda hidrojen ilavesi için her iki motor torkunda, maksimum basınç ve ortalama indike basınç (OİB) için ÇDK değerleri Şekil 13'de verilmektedir. Her iki ÇDK sonucunun maksimum değerlerin %3'den az olması daha iyi bir yanmanın ve daha düzenli motor çalışmasının göstergesidir. Grafikte, tüm yakıtlar için her iki motor torkunda silindir basıncının ÇDK değerleri %1'in altında olduğu görülmektedir. Normal dizel çalışmasındaki silindir basıncı ÇDK değerleri ile kıyaslandığında, düşük torkta H30 ve H40 yakıtları ile daha düşük değerlerde elde edilirken, yüksek torkta H10, H40 ve H50 ile dizelden daha az silindir basınç ÇDK değerleri elde edilmiştir.

Çevrimsel değişimlerin analizinde silindir basınç değerlerinden ziyade daha genel bir kabul olan OİB değerleri esas alınmaktadır. 100 Nm'de H50 hariç diğer tüm yakıtlarla %1,5'in altında değerler elde edilmiştir. 100 Nm'de H50 çalışmasıyla en yüksek OİB ÇDK değeri (%3) bulunmuştur. Bu değer, H50 yakıtı ile motorun 100 Nm'de nispeten daha düzensiz çalıştığını anlamına gelmektedir [8]. ÇDK OİB için, H20 en ideal çalışma durumudur.



Şekil 13. Farklı hidrojen akış oranlarında ve yükler altında silindir basıncı ve ortalama indike basınç için çevrimsel değişim katsayısı değişimleri

4 SONUÇ

Bu çalışmada, dört silindirli, turboşarjlı, ön püskürtme ve ana püskürtme safhasına sahip ortak hatlı bir dizel motorda emme havasına değişik oranlarda hidrojen ilavesinin çevrimsel yanma değişimleri incelenmiştir. Motor sabit devirde ve iki farklı yükte test edilmiştir. Elde edilen sonuçlar aşağıda özetlenmektedir.

Hidrojen ilavesi 100 Nm'de silindir basınç dalgalanmasını azaltmıştır. Yüksek oranda kullanılan hidrojen silindir basınç dalgalanmasını artırmıştır. Bu durumda, krank açısına göre silindir basıncı için standart sapma ve ÇDK fark edilebilir derecede artmıştır. Maksimum silindir basınç değerleri ÜÖN'den sonra 4-15°KA aralığında meydana gelmiştir. Artan hidrojen oranı, maksimum silindir basınçlarının daha erken krank açılarında oluşmasına sebep olmuştur.

Ortalama gaz sıcaklığındaki dalgalanmalar, silindir basıncına göre daha fazla bulunmuştur. 60 Nm'de en yüksek gaz sıcaklıkları H20 ile elde edilirken 100 Nm'de H50 ile elde edilmiştir. Maksimum gaz sıcaklığının meydana geldiği krank açısı aralığı, artan torkla birlikte artmıştır. Maksimum gaz sıcaklıkları 60 Nm'de ÜÖN'den sonra 28-32°KA aralığında oluşurken 100 Nm'de 26-33°KA aralığında oluşmuştur. Dizel çalışmasıyla kıyasladığımızda, hidrojen kullanımı maksimum gaz sıcaklıklarının daha geç oluşmasına neden olmuştur.

IDO'nun krank açısına göre dalgalanması silindir basıncına benzer şekilde gerçekleşmiştir. 60 Nm'de en düşük IDO H50 ile, en yüksek IDO H20 ile edilmiştir. 100 Nm'de en düşük IDO H30 ile en yüksek IDO H50 ile edilmiştir. Maksimum IDO için krank açıları 60 Nm'de ÜÖN'den sonra 11-17°KA aralığında 100 Nm'de 10-19°KA aralığında meydana gelmiştir.

Çevrimden çevrime OİB'de meydana gelen değişimler ortalama gaz sıcaklığında meydana gelen değişimlere benzemektedir. H50 ile yüksek yükte önemli OİB artışı meydana gelmiştir.

OİB için ÇDK H50 haricinde tüm yakıtlar için ideal değer aralığında (%0,7-1,4) bulunmuştur. Bu sonuçlardan anlaşılacağı üzere, her iki motor torkunda dizel ve H10'dan H40'a kadar olan hidrojen-dizel çift yakıt çalışmalarında common-rail dizel motor çevrimsel değişimler açısından stabil olarak çalışmaktadır. Her iki yükte, en düşük OİB ÇDK değeri H20 çalışmasıyla elde edilmiştir.

REFERANSLAR

[1] V. Chintala, K.A. Subramanian, A comprehensive review on utilization of hydrogen in a compression ignition engine under dual fuel mode, *Renewable and Sustainable Energy Reviews*, Vol.70, 472-491, 2017.

[2] T. Gatts, H. Li, C. Liew, S. Liu, T. Spencer, S. Wayne, N. Clark, An experimental investigation of H_2 emissions of a 2004 heavy-duty diesel engine supplemented with H_2, *International Journal of Hydrogen Energy*, Vol. 35, 11349-11356, 2010.

[3] J. Kim, K.M. Chun, S. Song, H.K. Baek, S. W. Lee, Hydrogen effects on the combustion stability, performance and emissions of a turbo gasoline direct injection engine in various air/fuel ratios, *Applied Energy,* Vol. 228, 1353-1361, 2018.

[4] İ. T. Yilmaz, The effect of hydrogen on the thermal efficiency and combustion process of the low compression ratio CI engine, *Applied Thermal Engineering,* Vol. 197, 117381, 2021.

[5] L.M. Das, Fuel induction techniques for a hydrogen operated engine, *International Journal of Hydrogen Energy*, Vol. 15(11), 833-842, 1990.

[6] M.S. Kumar, Use of hydrogen to enhance the performance of a vegetable oil fuelled compression ignition engine. *International Journal of Hydrogen Energy*, Vol. 28, 1143-1154, 2003.

[7] P. Kyrtatos, C. Brückner, K. Boulouchos, Cycle-to-cycle variations in diesel engines, *Applied Energy,* Vol. 171, 120-132, 2016.

[8] M.Y.E. Selim, Effect of engine parameters and gaseous fuel type on the cyclic variability of dual fuel engines, *Fuel*, Vol. 84(7-8), 961-71, 2005.

[9] Y. Wang, F. Xiao, Y. Zhao, D. Li, X. Lei, Study on cycle-by-cycle variations in a diesel engine with dimethyl ether as port premixing fuel, *Applied Energy,* Vol. 143, 58-70, 2015.

[10] M.A. Ceviz, F. Yüksel, Effects of ethanol-unleaded gasoline blends on cyclic variability and emissions in an SI engine, *Applied Thermal Engineering*, Vol. 25, 917-925, 2005.

[11] Q. Wang, B. Wang, C. Yao, M. Liu, T. Wu, H. Wei, Z. Dou, Study on cyclic variability of dual fuel combustion in a methanol fumigated diesel engine. *Fuel*, Vol. 164, 99-106, 2016.

[12] Z. Wang, X. Fu, D. Wang, Y. Xu, G. Du, J. You, A multilevel study on the influence of natural gas substitution rate on combustion mode and cyclic variation in a diesel/natural gas dual fuel engine, *Fuel*, 294, 120499, 2021.

[13] G.K. Lilik, H. Zhang, J. M. Herreros, D.C. Haworth, A.L. Boehman, Hydrogen assisted diesel combustion, *International Journal of Hydrogen Energy*, Vol. 35(9), 4382-4398, 2010.

[14] T. Tsujimura, Y. Suzuki, The utilization of hydrogen in hydrogen/diesel dual fuel engine, *International Journal of Hydrogen Energy*, Vol. 42(19), 14019-14029, 2017.

DISPOSAL OF RICE STRAW AND ITS CONVERSION INTO FERMENTABLE SUGAR AND ETHANOL BY ACID, ALKALI, ENZYMATIC AND BIOLOGICAL TREATMENTS

M. R. Khan[*1] and R. Batool[2]

1. Department of Environmental Science and Policy Lahore School of Economics Pakistan.
E- mail: drrafiq@lahoreschool.edu.pk, khanmr1939@yahoo.com
2. Department of Environmental Science and Policy Lahore School of Economics Pakistan
E-mail: rabiarahat 8@gmail.com

Abstract

Energy is a backbone for a country's socio-economic development. Shortage of energy sources particularly of fossil fuels is being faced by most of the countries of the world subsequently affecting the entire world status. That is why the experts all over the world are actively engaged in search of fossil fuel substitutes to overcome the shortage. Moreover, the fossil fuels are also considered as the major sources of the environmental pollution and thus less polluting fuels such as biofuels are likely to replace them. One of these biofuels popularly replacing gasoline is ethanol that can be produced from plant biomass encountered all over the globe as major component of agricultural wastes. Here the inquiry was focused on rice straw that is one of the most abundant crops produced in the developing countries including Pakistan and it is available almost throughout the year. Rice straw is rich in lignocellulose biomass and has great potential for sugar and bioethanol production. It was subjected to three different types of treatments to produce fermentable sugar such as glucose as food product and its subsequent conversion to ethanol as gasoline substitute. Pretreatment of rice straw was done using 5% HCl and 5% NaOH at 5 different temperatures. The treated rice straws were then subjected to the enzymatic treatment using enzyme cellulase with 5 different enzyme concentrations. Biological treatment of the treated rice straws for conversion of fermentable sugars into ethanol was accomplished using two organisms: Bacillus subtilis for production of fermentable sugar and saccharomyces cerevisiae for its transformation into ethanol. To check the symbiotic relationship between these organisms, both were grown together allowing them to react with rice straws. The research translated into significant production of fermentable sugars and ethanol with the conclusion that the rice straw offers a significant techno-economic potential for reducing the intensity of national and international food and energy problems.

Keywords: Disposal, Straw, Conversion, Fermentable, Sugar, Ethanol, by Acid, Alkali, Enzymatic, Biological Treatments, Bacillus, Saccharomyces cerevesae

1 INTRODUCTION

Energy deficit is a national as well as a global problem. The shortage of energy resources ultimately translates into its severe impact on socioeconomic status of the world economies that is facing an intense energy crisis indicated by the rise in the prices of energy reserves and a serious shortage in their availability [1]. The energy crisis is getting out of control due to the increase in world's population expected to reach 9.6 billion by the year 2050.. Currently, non-renewables like coal, oil and natural gas are being used as the major source of energy in the entire world. Today, 85% of the world's energy needs are fulfilled by fossil fuels. The ever growing population and energy demand are directly exploiting non-renewable resources and causing severe environmental damage. [2]. The fossil fuels are also considered as major sources of the environmental pollution and thus less polluting fuels such as biofuels are likely to replace them.

Biofuels are primarily produced from resources of biomass because these are sustainable, have the prospects of future, development, exhibit ability to have positive environmental impacts due to less release of carbon dioxide and sulfur, significant economic potential with expected increase in fossil fuel prices in future. Moreover, all biofuels are gaseous or liquids made from the plant materials and residues. These green fuels

are likely to play a significant role in decreasing the carbon emissions and helping in the increase of energy security. These are classified as bioethanol, biodiesel and biodiesel [3]. Consumption of oil and natural gas for the transportation is increasing with the increasing population, unfair distribution of resources, and development crisis [4].

Pakistan is a developing country and its economic development relies majorly on intensive energy demands and thus is also facing a noticeable energy crisis. More and more energy is demanded in future and the sources of energy which are mainly fossil fuels are running out of the nature's stock [3]. To reshape Pakistan economy, it is crucial to find ways that could replace the carbon emitting energy resources economically and efficiently with less carbon emitting energy resources. Renewable resources come from natural sources and biomass is the term which refers to the source of energy produced by photosynthesis and stored by plants. It includes crop residues, wood waste, fast growing plants, etc. The non-edible parts of biomass can be used as a sustainable energy source alternative to non-renewable energy sources and harmful when the burning of biomass causes increase in carbon dioxide emissions [4].

Lignocellulosic, biomass, being a dominant component of agricultural crops such as straw is a significant raw material to produce different high-value products like ethanol and other biofuels. The review of literature clearly signals that Bioethanol is a resource with less CO_2 emissions hence, does not trigger greenhouse effect as compared to traditional fossil fuels [5].

Rice straw which comes from rice cropping is considered as a significant stock for the production of bioethanol. This is because it contains almost 50% cellulose content and hemicellulose. Rice straw mainly contains cellulose content 32–47%, hemicellulose content 19–27%, lignins 5–24% and ashes around 18.8% [5]-[6]. Its biochemical analysis is given in Table1.

The rice straw waste, though it is used in many forms, its use to meet energy demands is still suppressed. Its utilization is done only 20% whereas, 50% of it is burnt by the farmers making their fields ready for the next

Table 1: Composition of rice straw

Composition	Rice straw (Wt. %)	Rice husk (Wt. %)
Cellulose	35.7	28.6
Hemicellulose	32	28.6
Lignin	22.3	24.4
Extractive matter	10	18.4

cultivation. Its burning in the fields causes incomplete combustion which ultimately leads to respiratory health impacts. It also harms insects and microbes beneficial for the soil's fertility. Thus, an urgent need is there to evaluate the rice straw economically so that farmers can get more profits for its collection and curb the burning of rice straw which creates pollution [6]. The efficient way of using wasted rice straw can be its conversion into biofuels by passing it through some physical and chemical processes [7].

Pretreatment for cellulosic biomass is considered as a key step towards low cost conversion into sugar and further into ethanol. The rigid structure of the cell wall of biomass makes it difficult to degrade hence, pretreatments release cellulose from amorphous hemicellulose and lignin. A number of studies have appeared on the international scene with this reference [8] to [].Among all chemical pretreatments use of alkali like sodium hydroxide (NaOH), Potassium hydroxide (KOH) and Sodium carbonate (Na_2CO_3) are considered more productive than others. Further the fermentable sugars obtained as above can be bio-converted into ethanol by microorganisms, mainly fungi which degrade cellulose. This makes the production of bioethanol economic, more environment friendly and renewable [5], [9].

Pakistan, in future, needs to diversify its sources of bioethanol production. Because Pakistan has number of potential sources in the form of residues of different crops like rice straw, rice husk, maize stalk, wheat straw, banana stalk and bagasse from sugar cane for bioethanol

production and thus Pakistan is also planning to reach the target of producing 2nd generation ethanol to 11.897million liter by 2030 [10]. Rice straw has a significant potential to produce ethanol as it has good quantity of cellulose and its disposal can also be done efficiently. In Pakistan, researches have been conducted to produce bioethanol from molasses as sugar cane is one of the major crops but rice straw is also abundantly available throughout the year, it has enough cellulosic content and can be a good alternative [11]. Of course, the increasing pressure on food commodities is causing the production of 1st generation biofuels unsustainable. Thus, to combat this issue residues of crops can provide a potential source of 2nd generation bioethanol production. In this scenario, crop residues can be the best solution [12].

The overview of production of sugar as a food material and ethanol as biofuel all over the globe and in Pakistan shows that there exists a handsome potential for production of fermentable sugars as food products and ethanol as alternative energy source. What Pakistan lacks is the intense efforts on the practical production of these socially significant products. Here an attempt is made to accelerate the intensity of this effort. Thus the goal and objectives were set as under and adequate work required at the laboratory level was carried out.

The goal of the research was to inquire at the laboratory level the prospects of production of fermentable sugar from rice straw in food context and ethanol in energy context. The objectives included collection of samples of rice straw, treatment of the rice straw with HCl/ NaOH, cellulase and fermentation of treated straws with Bacillus subtilis for conversion to fermentable sugar, fermentation of fermentable sugar to ethanol with Saccharomyces cerevisiae and fermentation of treated rice straw with Bacillus subtilis and Saccharomyces cerevisi.

2 MATERIALS AND METHODS

2.1 Rice Straw Samples

Rice straw samples were collected from the local fruit shops as they were easily approachable after getting convinced by the shop keepers that they get them from high yielding rice harvested fields near City of Lahore. The rice straw samples were thrashed to remove the sticking dust, air-dried and stored.in fruit boxes.

2.2 Microorganisms

Two types of microorganisms were used in the present study depending upon their availability at the time of research conducted and feasibility of biological growth and action due to weather conditions in Lahore Pakistan.

These were as under:

Bacillus subtilis for biological transformation of straw into sugar

Saccharomyces cerevisiae investigated for the conversion of fermentable sugar produced into ethanol.

2.3 Pre-treatment of Samples

The raw rice straw samples collected from various places of Lahore Pakistan were air dried and cut into 2 cm length with the help of metal scissors prior to the pre-treatment. The rice straw was treated with both mineral acid and alkali on different temperatures to study its transformation into sugar.

2.4 Pre-treatment of Rice Straw with 5 % HCl

10g of rice straw was soaked in 50 ml of 5% HCl solution at different temperatures; 30° C, 50o C, 60° C, 80° C and 100° C, overnight and filtered. The straw residue was preserved for further treatment and concentration of reducing sugar produced in the filtrate was estimated by Dinitrosalicyclic acid (DNS) method while absorbance was read in the spectrophotometer (SPECORD 200 plus) at 540 nm.as narrated above. The optical density was converted to mg/ml of sugar by comparing with the standard curve constructed using different concentrations of glucose (Fig. 1). The variation of sugar

produced was plotted against the temperature or shown by means of a line graph /bar diagram. The residue obtained from filtration was vacuum dried and kept for future experimentation at 4o C.

2.5 Pre-treatment of Rice Straws with 5% NaOH

10g of rice straw were soaked into 50 ml of 5%NaOH solution at 30° C, 50° C, 60° C, 80° C and 100° C overnight and filtered as done in case of treatment with HCl and the amount of reducing sugar in the solution was estimated by Dinitrosalicyclic Acid (DNS) Method spectrophotometrically.

2.6 Biological Treatment

Isolation of Bacillus subtilis

In order to grow *Bacillus subtilis*, nutrient agar and LB agar plates were made. The original colony of bacteria was taken and a loop full of bacteria was transferred onto newly made plates, which were solidified, a full loop inoculating tube was streaked onto the plate in order to see the grown fresh colonies of bacteria. The organism was transferred from a stored plate; the organisms were isolated and reproduced in lab for lab tasks. The streaked plates were carefully packed with Para film tape and left in the incubator for about 24 hours to let the bacteria grow. After 24 hours, the pure colony grown on the fresh agar plate was taken and transferred onto newly made nutrient agar slants. These slants were left in incubator for about 24 hours to let the bacteria grow. The whole experiment was done twice in laminar flow in order to avoid contamination.

In order to prepare inoculum, LB broth was made, according to the recipe mentioned earlier in which the grown bacteria were inoculated with the help of an inoculating loop. Ten test tubes were used each with 6 ml of LB broth in which bacteria were inoculated, taking all the precautionary measures to avoid contamination. All these steps were performed in laminar flow. The test tubes were then left for 24 hours to give bacteria time to grow on the slants. All the test tubes were left in tilted position. After 24 hours growth was recorded, it was then seen that there were bacterial cells in the bottom showing anaerobic strains of bacteria and aerobic on the top of the broth.

Treatment with Bacillus

The residues preserved after the treatment of rice straw treated with NaOH and HCl were taken in 15 test tubes (5g each) for NaOH and HCl separately, and 15 test tubes were made with 6 ml filtrate in each test tube separately for NaOH and HCl treated rice straws.

After that the filtrate test tubes were stored for later purpose, and residue test tubes were inoculated with 1 ml of LB broth inoculum prepared earlier with Bacillus subtilis in each treated rice straw test tube for NaOH and HCl. At every step a reference was created to compare the results.

Enzymatic Saccharification of Pretreated Rice Straw

The saccharification of biological and chemical pretreated rice straw was accomplished by Arrowzyme (commercial cellulase), procured from Anthem Cellutions. The straw was suspended in 0.1M sodium citrate buffer (pH 4.8) in a way to maintain the solid/liquid ratio of 1: 20 (w/v) after the enzyme addition. An enzyme loading of 30 filter paper units per gram of dry substrate (FPU/gds) was used for saccharification. Sodium azide (0.3%) was added in the reaction mixture to inhibit microbial growth during the enzymatic saccharification. The saccharification was carried in an orbital shaking incubator at 50°C, with continuous shaking at 100 r.p.m. For 72 hours. The aliquots were withdrawn after every 24 hour, centrifuged at 6,000 r.p.m. for 10 min and analyzed for reducing sugar by the method of Miller.

2.7 Estimation of Reducing Sugar

The reducing sugar was estimated by its color reaction with Dinitrosalyslic Acid (Bio-encyclopedia- Online) [13].

2.8 Preparation of Yeast (Saccharomyces cerevisiae)

Market purchased *Saccharomyces cerevisiae* was grown on PDA plates to obtain fresh yeast colonies. In order to inoculate the treated rice straws filtrate for ethanol production with *Saccharomyces cerevisiae*, inoculum, 10 flasks were used each with 50 ml of filtrate in which inoculum was added in equal quantities and 50 ml of water was inoculated with organism in order to have a reference check. After inoculation done in laminar flow, it was left at 32° C for 3 days, after which ethanol estimation was performed using potassium dichromate solution by colorimetric method.

After one-week incubation, ethanol estimation was again done in 50 ml of filtrate in each 10 iflasks, to estimate the amount of ethanol produced in the solution.

2.9 Fermentation of pretreated rice straw hydrolysate

The biomass of S. cerevisiae was transferred to saccharified hydrolysate, supplemented with 0.2% diammonium hydrogen phosphate, at 10% (v/v) and incubated at 30±2°C in a BOD incubator. The samples were withdrawn periodically after an interval of 24 hours, centrifuged at 6,000 r.p.m. for 10 min and analyzed for ethanol content by the method of Caputi and Wright [14].

3 RESULTS

The results of the study are presented below in different sections allotted according to the sequence of the experimentation.

Results of the Concentrations of Sugar Estimated by DNS Method in Filtrates of Rice Straw after Different Treatments

Pretreaatment with Acid

Different concentrations of reducing sugar in the filtrates after pretreatment of rice straw with HCl are compared in Fig 1.

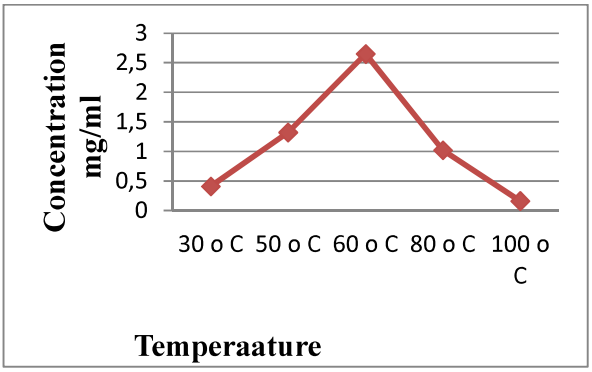


Fig. 1: Concentrations of reducing sugar in filtrates collected after pretreatment of rice straw with HCl at different temperatures.

The profile (Fig.1) exhibits that the amount of fermentable sugar increases with increase in temperature up to 60°C and then falls down with increase in temperature. The optimum conversion of rice straw into sugar takes place at 60°C (2.6480mg/ml)

Pretreatment with Alkali

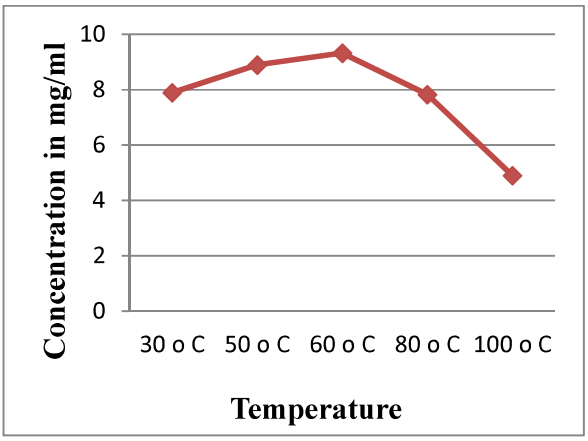


Fig. 2: Different concentrations of reducing sugar in the filtrates after pretreatment of rice straw with NaOH are compared in Fig2.

The profile (Fig. 3) shows that highest amount of reducing sugars was obtained in the filtrate of alkali treated rice straw at 60 °C kept for 2.5 hours (**9.3215mg/ml)**. There was also encountered a

color change with the increase in temperature that fortifies this conclusion.

Enzymatic Treatment

The concentrations of reducing sugar in filtrates of HCl and NaOH pretreated rice raws pretreated with Cellulase at 30°C are shown le 2 and profiles displayed in Fig. 3.

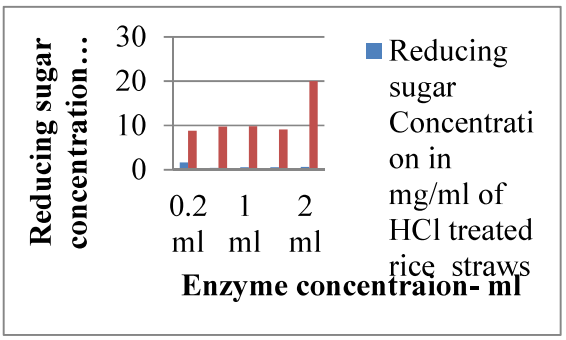


Fig. 3: Bar diagram for acid (blue bars) and alkali (red bars) treated rice straws at 30 ° C with different enzyme concentrations

The profile (Fig. 3) shows that optimum transformation of NaOH treated rice straw into sugars increases with increase of enzyme concentration up to 1ml at 30 ° C, whereas, it decreases with above this enzyme concentration. On the other hand, for acid treated rice straw exhibits a slow increase with increase of concentration up to 2ml.

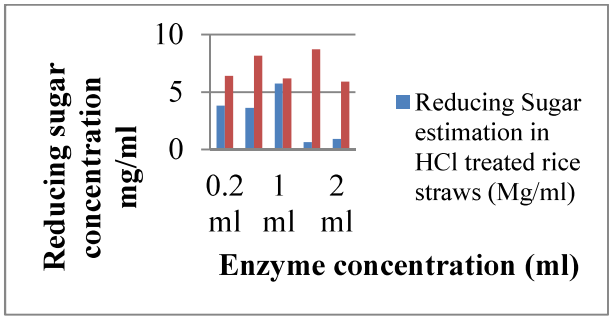


Fig. 4: Bar diagram for acid (blue bar) and alkali (red bar) treated rice straws at 60 ° C with different enzyme concentrations

The profile (Fig. 4) indicates significant production of sugars at 1.5 ml of enzyme concentration at 60 ° C.

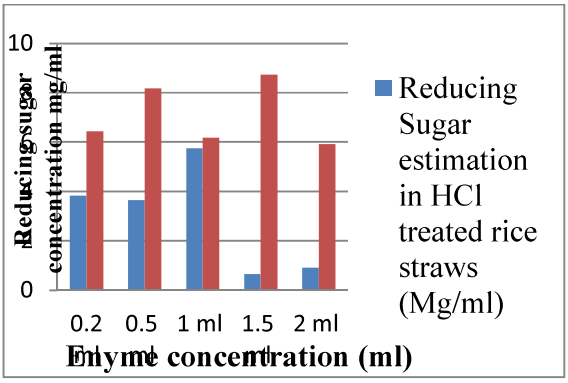


Fig.5: Bar diagram for non-treated rice straw= at different enzyme concentrations

The profile (Fig.5) indicates the production of sugars with NaOH treated rice straws, the highest point of sugars produced is seen at 1.5 ml of enzyme concentration which is about 9 mg/ml while HCl treated rice straw which has significant peak seen at 1 ml of enzyme concentration with about 6 mg/ml of reducing sugars.

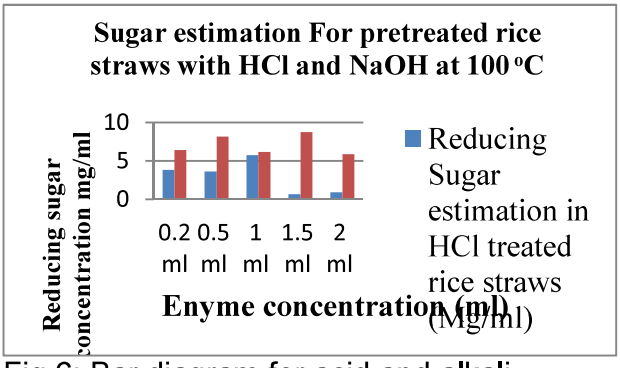


Fig.6: Bar diagram for acid and alkali treated rice straws at 100 ° C with different enzyme concentrations

The profile (Fig.6) indicates that the sugar produced with raw chopped rice straws with different enzyme concentrations. The highest point of production is seen at 1 ml of enzyme concentration with about 2.9 mg/ml of reducing sugars.

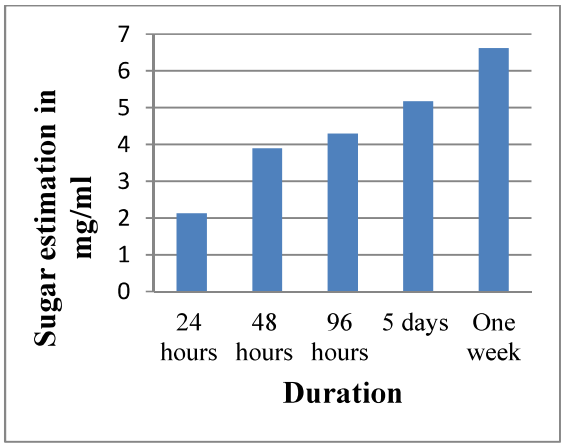


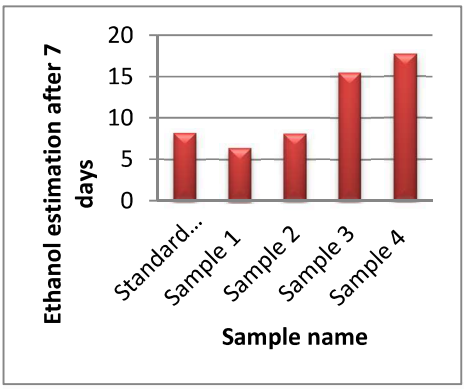
Fig.7: Bar diagram of Sugar estimation in NaOH treated rice straws with Bacillus subillis

The profile (Fig. 7) showing that organism Bacillus firstly consumed all the sugar available in the rice straw in order to grow, but later on reduced sugar in the filtrate when estimated. The profile exhibits that no significant transformation occurs in 24 hours. After 24 hours or lag phase the transformation started occurring and increased slowly with increase in concentration when the samples were kept for 4 days. The profile (Fig. 7) also shows that the highest amount of sugar was after 7 days.

Different concentrations of yeast samples for ethanol production are shown in Table 2.

Table 2: Yeast concentration samples for ethanol after 7days

Sample no.	Concentration
Standard solution	15 µl pure absolute ethanol+ 50 ml distilled water
Sample 1	10 ml sample + 40 ml distilled water
Sample 2	10 ml sample +40 ml distilled water
Sample 3	10 ml sample +40 ml distilled water
Sample 4	10 ml sample +40 ml distilled water
Sample 5	10 ml sample +40 ml distilled water



The profile (Fig.8) indicates high amount of ethanol

Fig.8: Bar diagram showing high amount of ethanol production when estimated after 7 days

The profile (Fig. 8) indicates high amount of ethanol production with yeast (*S. erevisiae*) when estimated after a period of 7 days' incubation. This shows that yeast is able to break the lignin bonds of rice straw and is able to produce significant amount of ethanol.

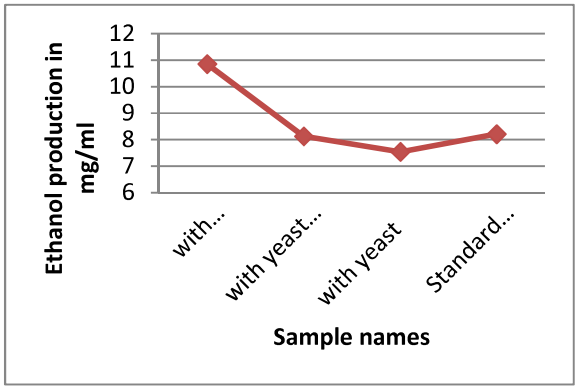


Fig.9: Line graph indicates highest peak for ethanol production with both yeast and bacterial inoculum together.

The profile (Fig.9) indicates symbiotic relationship between yeast and bacteria that the ethanol production is highest with both of these organisms when incubated together.

4 DISCUSSION

The research work reported here was a multipurpose exercise with different dimensions of aim and objectives reported below

The research proves to be a promising work for the disposal of rice straw that is a big source of solid waste along with extraction of economic benefits such as its transformation into sugar in context of the food problem and subsequent transformation of the fermentable sugar produced into ethanol in energy context. The success achieved on the laboratory level endorses that it was an attempt to link an environmental problem with an economic problem. The discussion on different methods of transformation follows.

The study indicates that hydrochloric acid is capable of transforming rice straw into sugar but not to a desirable extent perhaps due to inhibition of the hydrolysis of cellulose by the major constituent of straw by itself or by some other products of hydrolysis. The optimal sugar yield of rice straw filtrate of processed straw was 2.6480 mg/ml .

Our subsequent of transformation by treatment with alkali (NaOH) was quite promising and yield under similar process conditions was 9.3215mg/ml at 60 °C that was almost 4 times of yield by treatment with acid. The reason is that treatment with alkali removes hemicellulose and lignin concurrently. Thus our results of pretreatment with alkaline solutions are in agreement with results reported by Takano et al [7]. The purpose of treatment with acid and alkali was to open some active sites in structure of cellulosic component of straw to make it a better substrate for enzymatic and biological transformations.

The results of enzymatic transformation of rice straw by commercial cellulase were remarkably significant as indicated by effect of different concentrations of enzyme on the substrate as indicated by Fig, 4 to 6 that exhibit different amounts of fermentable reducing sugars in mg/ml produced from the liquid medium of rice straw at different temperatures, The highest yield of sugar in filtrate of rice straw was 20 mg/ml with NaOH treated rice straw at 30°C respectively. The rice straws pretreated with alkali showed better results. The yield of sugar decreased with the increase in temperature; may be due to the partial deactivation of the enzyme at higher temperature.

The raw untreated straw was also given enzymatic treatment and the highest amount of sugar produced was about 3mg/ml that is around one seventh of the highest sugar produced from alkali treated rice straw (20mg/ml) and almost equal to the sugar produced from acid treated straw. The comparison indicates that alkali opens some active sites on the cellulosic component of the straw by removing from it some structural components probably lignins while acid is unable to do so. The overall yield may be 20+20 = 40 mg percent if recovered separately.

The results of biological transformation of rice straw by laboratory isolated and characterized *Bacillus Subtilis* organism were remarkably significant as indicated by effect of different concentrations of *B. subtilis* inoculum respectively on the substrate as indicated by Fig.7 that exhibit different amount of fermentable reducing sugars in mg/ml produced from the fermentation medium of rice straw with

bacterial inoculum. The rice straws pretreated with alkali showed better results and the amount of fermentable sugar produced was the highest after 7 days fermentation.

The subsequent transformation by biological transformation of sugars into ethanol with *S.cerevisae* (yeast inoculum) treatment with alkali (NaOH) treated rice straws was quite promising and yield of ethanol under similar process conditions was 17.6704 mg/ml. The purpose of treatment with yeast was to determine the feasibility of transformation of fermentable sugars into ethanol that is a promising future petrol substitute. When analysis was conducted after 3 days of inoculation, the results were not satisfactory, but when analyses were done after about 7 days, the results indicated high amount of ethanol production with yeast (*S.cerevisae*) as shown in Fig 8.

The profile (Fig.9) indicates symbiotic relationship between yeast and bacteria, as the ethanol production is highest with both of these organisms when incubated together.

The results of biological transformation of rice straw by laboratory isolated ***Bacillus subtilis*** and ***S.cerevisae*** organisms grown together were remarkably significant. Symbiotic relationship is seen in between these two organisms i.e.; yeast and bacteria. The data obtained showed ethanol production is highest with both of these organisms when incubated together. The yield of ethanol per 50 ml of rice straw filtrate was 10.8543 mg/ml respectively. The rice straws pretreated with alkali showed better results.

To convert the fermentable monomeric sugars into ethanol in energy context the yields of sugar per 100 g straw were calculated to determine potential of production of sugar and ethanol were calculated.

According to a recent study held in Pakistan [3], Pakistan produces 2 million metric ton rice straw annually. Around 42,274 metric tons /year of rice straw only is consumed to produce 12,682 kl of ethanol for biofuel consumption. It is because of lack of farmer's interest, behavior, and low amount of money offered to them for rice straw. The production can be increased with more usage of rice straws utilizing the data obtained from this study to produce more ethanol. Only 60% of farmers are willing to sell their rice straw due to utilization otherwise, such as in burning, and other ways of their interest. Burning of rice straw can pollute the air as it produces different air pollutants. It is eco-friendly to consume it for ethanol production and to use ethanol for energy generating purposes.

5 CONCLUSION

The study concludes that rice straw can be disposed effectively with economic benefits such as energy and food by primary treatment with NaOH followed by biological treatment. The highest amount of fermentable sugars (ethanol) is seen in alkali treated rice straws when inoculated with the cocktail of microorganisms, *S. cerevisae* and *B. subtilis* altogether. There exists a significant potential of this waste to energy conversion in Pakistan. From the 2 million metric tons of rice straw produced per annum.

Maximum sugar produced with these processes= 200,000 +66,241 = 266,241 tons per arum

Potential of ethanol produced

Ethanol produced from yeast (Saccharomyces *cerevisiae*) =176,704

Ethanol produced from yeast (Saccharomyces *cerevisiae*) and *Bacillus subtilis* grown together = 108,543 ton per Annum

Maximum ethanol produced with these processes= 285,247 tons per arum

6 REFERENCES

1. Naseem & J. Khan, Impact of Energy Crisis on Economic Growth of Pakistan. *International Journal of African and Asian Studies,* 7, 2015
2. S. Pathak, Energy Crisis: A Review. *Journal of Engineering Research and Applications,* 4(3), pp.845-851, 2014.
3. M. S. Javed, R. Raza, I. Hassan, R. Saeed, N. Shaheen, J. Iqbal, & S. F. Shaukat, The energy crisis in Pakistan: A possible solution via biomass-based waste. *Journal of Renewable and Sustainable Energy,* 2016.

4. L. Caspeta, N. A. Buijs, & J. Nielsen, The role of biofuels in the future energy supply. *Energy & Environmental Science*, *6*(4), 1077, 2013.
5. E. Belal, Bioethanol production from rice straw residues. *Brazilian Journal of Microbiology*, 44(1), pp.225-234, 2013.
6. A. Satlewal, R. Agrawal, S. Bhagia, P. Das, & A. J. Ragauskas, Rice straw as a feedstock for biofuels: Availability, recalcitrance, and chemical properties. *Biofuels, Bioproducts and Biorefining*, *12*(1), pp.83-107, 2017.
7. M. Takano, K. & Hoshino, Bioethanol production from rice straw by simultaneous saccharification and fermentation with statistical optimized cellulase cocktail and fermenting fungus. *Bioresources and Bioprocessing*, *5*(1), 2018.
8. P. Binod, R. Sindhu, R. R. Singhania, S. Vikram, L. Devi, S. Nagalakshmi, A. Pandey, Bioethanol production from rice straw: An overview. *Bioresource Technology*, *101*(13), pp.4767-4774, 2010.
9. S. Kim, S. Lee, J. Lee, Y. Jung, L. Thapa, J. Kim, S. Kim, Pretreatment of rice straw with combined process using dilute sulfuric acid and aqueous ammonia. *Biotechnology for Biofuels, 6*(1), 109, 2013.
10. M. Tayyab, Bioethanol production from lignocellulosic biomass by environment-friendly pretreatment methods: review. *Applied ecology and environmental research*, *16*(1), 225-249, 2018.
11. T. Ali, J. Huang. J. Yang, An Overview of Biofuels Sector of Pakistan: Staus and Policies. *International Journal of Economics and Resources*, 2, pp.69-76, 2012.
12. A.W. Bhutto, K. Harijan, K. Qureshi, A. A. Bazmi, & A. Bahadori, Perspectives for the production of ethanol from lignocellulosic feedstock – A case study. *Journal of Cleaner Production,* 95,pp.184-193, 2015.
13. Bioencyclopedia, Biotechnology Methods/ Biochemistry, Estimation of Reducing Sugars by the Dinitro Salicylic Acid (DNS) Method (Online) (DNS Method)
14. A. Caputi and Wright. Collaborative Study of the Determination of Ethanol in Wine by Chemical Oxidation *Journal of Association of Official Analytical Chemists*, Volume 52, Issue 1, 1 January 1969, Pages 85–88, https://doi.org/10.1093/jaoac/52.1.85 (Published 01 February 2020)
15. M. Irfan, M. Nadeem, & Q. Syed, Ethanol production from agricultural wastes using Sacchromyces cervisae. *Brazilian Journal of Microbiology*, *45*(2), pp.457-465, 2014.
16. N. Yoswathana, P. Phuriphipat, P. Treyawutthiwat, & M. N. Eshtiaghi, Bioethanol Production from Rice Straw. *Energy Research Journal*, *1*(1), 26-31, 2010.
17. N. K., Aggarwal, V. Goyal, A. Saini, A. Yadav, & R. Gupta, Enzymatic saccharification of pretreated rice straw by cellulases from Aspergillus niger BK_{01}. *3 Biotech,* 7(3), 2017.

AN INVESTIGATION ON SOME CRITICAL FUEL PROPERTIES OF BIODIESEL FUELS OF DIFFERENT GENERATIONS

F. Yasar[1] and H. Sanli[2]

1. Vocational School of Technical Sciences, Department of Refinery and Petro-chemistry, Batman University, Batman; email: fevzi.yasar@batman.edu.tr
2. Corlu Vocational School, Department of Automotive Technology, Tekirdag Namik Kemal University, Tekirdag; email: hsanli@nku.edu.tr

Abstract

Biodiesel is a critical alternative energy source since it has the potential to be used in all transportation sectors (road transport, maritime transport, railway transport and airway transport). The use of biodiesel fuels especially in airway transportation by mixing them with jet fuel in certain proportions is a very popular issue. However, a biodiesel fuels' physico-chemical fuel properties are of vital importance for their long-term usage in modern technology systems, which are very susceptible to fuel quality, without any problems. The fuel properties of biodiesel fuels produced from different feedstocks vary considerably. In this study, some critical fuel properties such as viscosity, density, cold filter plugging point, cetane index and flash point of 13 different biodiesel fuels of different generations were compared with each other.

Keywords: Alternative Energy, Biodiesel, Fuel Property, Feedstock,

1 INTRODUCTION

The importance of energy for the sustainable development of countries and the continuation of daily life becomes more critical every year. As a result of the dependence on fossil energy resources, some countries having own petroleum and natural gas resources may use these advantages as a political blackmail in international relations. Transportation sector is one of the biggest energy consumption areas and main causes of environmental pollution. Therefore, the use of alternative energy in the transportation sector is a very important issue.

Biodiesel is a domestically producible, sustainable and environmentally friendly alternative diesel engine fuel. It is also compatible with the existing fuel distribution network and fuel station infrastructure, and does not require any significant modification in diesel engines [1]. In many countries including Turkey, it is mandatory to blend biodiesel with petro-diesel in certain proportions. Biodiesel can be produced from lots of feedstocks such as vegetable oils, waste frying oils, waste animal fats and algae oil. Biodiesel fuels produced from edible vegetable oils are classified as the first generation biodiesel. Waste frying oils, waste animal fats or inedible oil based biodiesel fuels are defined as the second generation biodiesel fuel. Another biodiesel feedstock that is more recent than other feedstocks is algae. A biodiesel fuel of algae oil origin is called as the third generation biodiesel [2].

The impact of the feedstock type, which is used in biodiesel production, on the sustainability of the biodiesel industry and on the cost of biodiesel is very important. In addition, since the fatty acid distribution of the feedstock remains almost the same during the transesterification reaction, the physico-chemical fuel properties of the biodiesel fuel vary significantly according to the feedstock from which it is produced [3]. Therefore, it is very important to determine the different generation biodiesel fuels' critical fuel properties that directly affect the performance, combustion and exhaust emission characteristics of a diesel engine.

2 MATERIALS AND METHODOLOGY

In order to determine the some critical physico-chemical fuel properties of different generation biodiesel fuels of various origin, biodiesel fuels were produced from 11 different feedstocks (covering 3 different biodiesel generations) such as safflower oil, sunflower oil, hazelnut oil, rapeseed oil, corn oil, soybean oil, olive oil, palm oil, cottonseed oil, waste frying oil and algae oil. In the production of all biodiesel fuels, transesterification reaction conditions of 6:1 molar ratio of methanol: feedstock, 1% KOH

(w/w), 60 °C of reaction temperature, 1 hour of reaction duration, and 600 rpm of mixing speed were stayed constant. In order to characterize and compare the biodiesel fuels of different generations; produced biodiesels' some critical fuel properties such as kinematic viscosity (KV), density (D), cold filter plugging point (CFPP), cetane index (CI) and flash point (FP) were determined. In this study, biodiesel fuel could not be produced from waste animal fats due to the difficulties experienced in accessing feedstock. Nevertheless; for including biodiesel fuels obtained from these very important feedstocks in this study, the above-mentioned fuel properties of biodiesel fuels produced from waste fleshing oil and waste chicken fat were quoted from Ref [4].

3 RESULTS AND DISCUSSION

KV, D, CFPP, CI and FP values of 13 different biodiesel fuels of different origin were given in Table 1.

Table 1. Some Critical Fuel Properties of Biodiesel Fuels of Three Generations

Biodiesel Fuel	KV (mm^2/s)	D (kg/m^3)	CFPP (°C)	CI	FP (°C)
Sunflower Oil Biodiesel	4.45	891.46	-6	51.39	176
Hazelnut Oil Biodiesel	4.77	879.94	-10	57.70	184
Rapeseed Oil Biodiesel	4.84	885.24	-10	55.83	180
Corn Oil Biodiesel	4.32	879.52	-9	55.48	176
Soybean Oil Biodiesel	4.11	875.83	-9	51.50	170
Olive Oil Biodiesel	4.84	890.48	-6	57.09	182
Safflower Oil Biodiesel	4.13	887.85	-9	53.74	174
Palm Oil Biodiesel	4.55	885.15	8	56.40	172
Cottonseed Oil Biodiesel	4.36	884.36	3	55.82	178
Waste Frying Oil Biodiesel	6.65	891.31	9	50.54	180
Waste Chicken Fat Biodiesel	5.30	889.70	3	52.30	169
Waste Fleshing Oil Biodiesel	4.70	876.70	10	58.80	168
Algae Oil Biodiesel	4.49	880.25	-10	55.90	142

3.1 Kinematic Viscosity

Viscosity is one of the most critical fuel properties since it directly affects the atomization quality. High viscosity deteriorates the fuel atomization and causes higher fuel droplets from the injector, leading to insufficient air-fuel mixture formation inside combustion chamber. This situation negatively influences the combustion phenomenon and exhaust emissions [5]. The upper kinematic viscosity limit given in the European Biodiesel Standard (EN 14214) is 5.0 mm^2/s at 40 °C while this limit is 6.0 mm^2/s in American Biodiesel Standard (ASTM D-6751).

As can be seen in Table 1, KV values of just waste frying oil biodiesel and waste chicken fat biodiesel fuels were higher than 5 mm2/s. Among 13 biodiesel fuels, the highest KV belonged to waste frying oil biodiesel. This should be expressed that waste frying oil was obtained from a fast-food facility. Waste frying oil feedstock was of palm oil origin. High saturated fatty acid content of palm oil and high polarity-high molecular weight degradation products resulted from deep-fat frying process may cause this high viscosity value. Despite the high KV value of waste chicken fat biodiesel, KV of waste fleshing oil was lower than 5 mm^2/s. Algae oil biodiesel fuel's viscosity value was very close to those of vegetable oil based biodiesels.

3.2 Density

Density is effective in the secondary and tertiary breakdown of the injected fuel. Thus, it influence atomization process, combustion phenomenon and consequently exhaust emissions. PM and NO_x emissions generally increases with increasing fuel density. Moreover, since an injection system sprays as much fuel as the discharged volume when the injector needle is lifted, the mass of fuel injected into the combustion chamber will increase as the fuel density increases [6].

Density specification given in EN 14214 is between 860-900 kg/m^3 (at 15 °C). As be understood from Table 1, density values of all biodiesel fuels met the specified value. The lowest (876.70 kg/m^3) and the highest density (891.46 kg/m^3) values belonged to waste fleshing oil biodiesel and sunflower oil biodiesel fuels, respectively. The density of algae oil

biodiesel (880.25 kg/m^3) and hazelnut oil biodiesel (879.94 kg/m^3) were very close to each other.

3.3 Cold Filter Plugging Point

Although there is no certain temperature value in EN 14214 to specify cold flow characteristics, cold flow quality of a biodiesel fuel is a very critical property. In general, three concepts (cloud point, pour point, and cold filter plugging point) are used to characterize the cold-flow quality of liquid fuels. The cloud point is the first temperature at which the crystal cloud, which is an indicator of the onset of freezing, is seen on the fuel surface. As the temperature drops, the crystallization increases, and consequently the fluidity of the fuel decreases. The pour point is defined as the lowest temperature that fuel continues to flow. The cold filter plugging point (CFPP) is the temperature at which the pumped fuel cannot pass through the fuel filter as a result of crystallization, and it is more accurate to use the CFPP value for internal combustion engines [7].

Among 13 different biodiesel fuels, algae oil biodiesel, hazelnut oil biodiesel and rapeseed oil biodiesel had the lowest CFPP value (-10 °C). CFPP value of safflower oil biodiesel, soybean oil biodiesel and corn oil biodiesel were - 9 °C. Waste chicken fat biodiesel and cottonseed oil biodiesel had the same CFPP (3 °C). CFPP values of waste fleshing oil biodiesel (10 °C), waste frying oil biodiesel (9 °C) and palm oil biodiesel (8 °C) were too high. This result can be explained by these biodiesel fuels' high saturated fatty acid content, leading to poor flow quality. This should be strongly underlined that CFPP values of all biodiesel fuels regardless of its generation and feedstock origin were too high compared with that of petro-diesel. In order to use biodiesel fuels in cold weather conditions without any problems, their unacceptably poor cold flow properties should be improved by various strategies such as cold flow depressants, etc. very close to each other.

3.4 Cetane Index

Cetane number is a critical fuel feature since it directly affects almost all engine characteristics. Cetane number is the most important indicator of a diesel fuel's self-ignitability. It has a very distinct effect on ignition delay which can be defined as the time interval between the start of fuel injection and the start of combustion. Ignition delay time decreases with increasing cetane number, thus limiting the rapid increase in cylinder pressure and temperature values during premixed- controlled combustion phase. In addition, cetane number significantly influences exhaust emissions such as NO_x [8]. The cetane number of a fuel is measured by using a cetane engine. However, since the cetane engine is very expensive, it can only be used in a very limited number of research centres. In addition, the determination of the cetane number is time-consuming and labour-intensive. Instead of cetane number, the cetane index (CI) can be calculated with a negligible margin of error by using the distillation temperatures and density value of the related fuel.

In this study, CI values of biodiesel fuels apart from waste animal fat-based biodiesels were calculated. Waste chicken fat biodiesel and waste fleshing oil biodiesel's cetane number values were quoted from Ref [4]. The lowest CI value (50.54) and the highest CI value (58.80) belonged to waste frying oil biodiesel and waste fleshing oil biodiesel, respectively. CI values of algae oil biodiesel (55.90), cottonseed oil biodiesel (55.82), corn oil biodiesel (55.48) and rapeseed oil biodiesel (55.83) were very close to each other.

3.5 Flash Point

The flash point is described as the lowest temperature at which the fuel vapour ignites when it comes into contact with the flame. Although it is generally considered in terms of transportation safety, it can also be accepted as an indicator of fuel volatility which directly affects easy start in cold weather, combustion and emissions. As a result of the high viscosity and low volatility properties of a diesel fuel, problems may occur in easy cold-start and ignition delay time. In addition, high flash point temperature may cause to soot formation inside the combustion chamber [9].

According to EN-14214, flash point of a biodiesel fuel must be higher than 101 °C. As can be seen in Table 1, all biodiesel fuels met this specification. Hazelnut oil biodiesel had the highest flash point temperature of 184 °C, whereas algae ail biodiesel had the lowest flash point temperature of 142 °C.

REFERENCES

[1] M. Canakci and H. Sanli, Biodiesel production from various feedstocks and their effects on the fuel properties, *Journal of Industrial Microbiology and Biotechnology*, Vol. 35, pp. 431-441, 2008.

[2] S. Tayari, R. Abedi and A. Rahi, Comparative assessment of engine performance and emissions fueled with three different biodiesel generations, *Renewable Energy*, Vol. 147, pp. 1058-1069, 2020.

[3] F. Yasar, Comparison of fuel properties of biodiesel fuels produced from different oils to determine the most suitable feedstock type, *Fuel*, Vol. 264, 116817, 2020.

[4] E. Alptekin, M. Canakci, A.N. Ozsezen, A. Turkcan and H. Sanli, Using waste animal fat based biodiesels-bioethanol-diesel fuel blends in a DI diesel engine, *Fuel*, Vol. 157, pp. 245-254, 2015.

[5] H. Sanli, An experimental investigation on the usage of waste frying oil-diesel fuel blends with low viscosity in a common rail DI-diesel engine, *Fuel*, Vol. 222, pp. 434-443, 2018.

[6] F. Yasar, Biodiesel production via waste eggshell as a low-cost heterogeneous catalyst: Its effects on some critical fuel properties and comparison with CaO, *Fuel*, Vol. 255, 115828, 2019.

[7] G. Dwivedi and M.P. Sharma, Impact of cold flow properties of biodiesel on engine performance, *Renewable and Sustainable Energy Reviews*, Vol. 31, pp. 650-656, 2014.

[8] Y. Kidoguchi, C. Yang, R. Kato and K. Miwa, Effects of fuel cetane number and aromatics on combustion process and emissions of a direct-injection diesel engine, *JSAE Review*, Vol. 21, pp. 469-475, 2000.

[9] H. Sanli, E. Alptekin and M. Canakci, Using low viscosity micro-emulsification fuels composed of waste frying oil-diesel fuel-higher bioalcohols in a turbocharged-CRDI diesel engine, *Fuel*, Vol. 308, 121966, 2022.

HOMOJEN DOLGULU SIKIŞTIRMA ATEŞLEMELİ BİR MOTORDA HAFİF NAFTA-BENZİN KARIŞIMI KULLANIMININ MOTOR PERFORMANSI VE EMİSYONLARINA ETKİSİ

S. Çelebi[1], U. Demir[2] and C. Haşimoğlu[3]

1. Sakarya University of Applied Science, Arifiye Vocational School, Motor Vehicles and Transportation Technologies Dep., Sakarya, email: scelebi@subu.edu.tr
2. Bilecik Şeyh Edebali University, Mechanical Engineering Department, Bilecik; email: usame.demir@bilecik.edu.tr
3. Sakarya University of Applied Science, Technology Faculty, Mechanical Engineering Dep., Sakarya, email: canhasim@subu.edu.tr

Özet

Bu çalışmada, HCCI modda çalışan bir dizel motorda hafif nafta ve benzin yakıt karışımları kullanımının motor performansına etkileri deneysel olarak araştırılmıştır. Karışım oranı olarak %50 hafif nafta %50 benzin karışımı test edilmiştir. Deneylerde motor yükü, yakıt tüketimi ve silindir içi basınç ölçümleri alınmıştır. Farklı hava fazlalık katsayısı için deneyler yapılmıştır. Farklı hava fazlalık katsayısına göre HCCI modda iki farklı devir ve bu yakıt karışım oranı için çalışma aralığı belirlenmeye çalışılmıştır. En düşük yakıt tüketimi 0,230 gr/kWh ile 11 ms enjektör açıklığında, HFK 2,88 ve1100 d/dk motor hızında elde edilmiştir. En yüksek moment ise 13,43 Nm ile 14 ms enjektör açıklığı ve HFK 2,07 ve 1100 d/dk motor hızında elde edilmiştir. Maksimum güç 1,54 kW ile maksimum momentin oluştuğu değerlerde oluşmuştur. Motor, 1100 d/dk motor hızında HFK 2,07-2,88 aralığında, 1300 d/dk motor hızında HFK 2,4-2,71 aralığında çalışmıştır. HCCI modda herhangi bir ön ısıtma uygulamadan motorun bu aralıkta çalıştığı görülmüştür. Motor hızının ve HFK'nın artması ile yakıt tüketimi, HC emisyonu ve CO emisyonlarında artış meydana gelmiştir. HFK'nın azalması ve motor hızının düşmesi ile maksimum güç, tork ve egzoz gaz sıcaklığında artış meydana gelmiştir.

Anahtar kelimeler: HCCI Motor, Nafta, Çalışma aralığı

1 GİRİŞ

Yük taşımada kullanılan taşıtların sayısı gün geçtikçe artmaktadır. Eurostat raporuna göre 2017 yılında AB-28'de kayıtlı 4,3 milyon araç mevcutken bu değer 2016'ya göre % 2,1, 2013'e göre% 2,8 artmıştır [1]. Bu taşıtların yanında ulaşım için kullanılan taşıtların sayısı da gün geçtikçe artmaktadır. Uluslararası ulaşım istatistikleri raporuna göre toplamda dünya üzerinde 2015 yılında üretilen motorlu araç sayısı 2014 yılına göre %1,6 artışla 95.175.000 adet olarak bildirilmiştir [2].

Küresel enerji talebi, 2017 yılında %2,1 artarak, güçlü küresel ekonomik büyümenin de artmasına neden olmuştur. Bu durum bir önceki yılın oranının iki katından daha fazla arttığı anlamına gelmektedir. Enerji talebindeki artışın çoğu petrol, gaz ve kömürle karşılanmıştır.

Küresel enerji talebindeki büyümenin %70'inden fazlası petrol, doğal gaz ve kömürle karşılanırken, yenilenebilir enerji kaynakları kalan kısmı oluşturmaktadır. Enerji verimliliğindeki gelişmeler geçen yıl yavaşlamıştır. Bu eğilimlerin bir sonucu olarak, küresel enerjiye bağlı karbondioksit emisyonları, üç yıl sabit kaldıktan sonra 2017'de %1,4 oranında artmıştır [3,4].

Motorlu araç üretimindeki ve kısmen buna bağlı olarak enerji taleplerindeki artışın olumsuz etkilerini önleyebilmek için içten yanmalı motorlarda yeni yanma modelleri üzerine araştırmalar yapılmaktadır. Alternatif yakıt olarak alkoller, biyodizel vb. yakıtlar geniş bir araştırma alanına sahiptir. Fakat buji ateşlemeli motorların kısıtlı ısıl verimi ve sıkıştırma oranlarından ve sıkıştırma ateşlemeli motorların PM ve NO_x emisyonlarını azaltma zorunluluğundan dolayı alternatif oluşturmak için araştırmalar yapılmaktadır. Bu araştırmalar motor verimliliğini arttırmaya ve egzoz emisyonlarını azaltmaya yönelik olmaktadır. Bu zorlukları giderebilmek için düşük sıcaklık yanması olarak bilinen homojen dolgulu sıkıştırma ateşlemeli, kısmi dolgulu sıkıştırma ateşlemeli, reaktif kontrollü yanma ateşlemeli yanma modelleri yüksek ısıl verim ve düşük partikül madde ve azot oksit emisyonları için

umut vadeden yanma modelleridir [5]. Benzin-hava karışımının yanabilmesi için kullanılan HCCI motorun çalışmasına ait fiziksel ve teknik prensip uzun süredir bilinmektedir. Bu teknoloji benzinli motor verimliliğini dizel motorun verimliliğine yaklaştırmak için bir yol sunar. Bu teknikte benzin hava karışımı dolgunun sıkıştırılmasından sonra kendiliğinden tutuşma işlemi sonucunda ateşlenir. Soğuk çalışma ve aşırı yükleme durumlarında buji kıvılcımına ihtiyaç duyulmaktadır. Ancak motor düşük yükte çalışıyorsa, kontrollü homojen dolgulu sıkıştırma ateşlemeli sistem çalıştırılabilir. HCCI teknolojisiyle çalışan bir motorun yakıt tüketimi dizel motorun özgül yakıt tüketimininkine benzer. Ayrıca NO_x oluşumu çok düşük seviyelerde olduğundan bu emisyonları önlemek için pahalı sistemlere gerek yoktur [6]. HCCI yanması yüksek ısıl verim sağlayabilir çünkü ısı yayma işlemi kıvılcım ateşlemeli motora göre daha hızlıdır. Motor yükünün aşırı hava ve/veya egzoz gazı resirkülasyonu yoluyla kontrolü pompalama kayıplarını azaltır, çünkü çevrim daha düşük sıcaklıkta gerçekleşmektedir [7]. HCCI motorların yüksek CO ve HC emisyonları, yanma fazı kontrolündeki güçlükler, yüksek motor yüklerinde vuruntu, düşük motor yüklerinde alev sönmesi ve sınırlı çalışma aralığı gibi bazı dezavantajları bulunmaktadır [8]. Bu sorunların üstesinden gelebilmek için HCCI motorlarda yapılan çalışmalar genel olarak yanma fazının kontrolü alanına yoğunlaşmıştır. HCCI motorlarda şu parametreler üzerine çalışmalar yapılmaktadır, emme havası sıcaklığı ve basıncı, EGR oranı, enjeksiyon zamanlaması ve basıncı, alternatif yakıtların HCCI yanması [8,9,10].

Nafta, hafif ve ağır olmak üzere iki farklı şekilde rafinerilerde bulunmaktadır. Nafta, endüstride çözücü ve hammadde olarak kullanılmaktadır. İçten yanmalı motorda nafta kullanımı ile ilgili az sayıda çalışma vardır. R. Vallinayagam ve diğerleri [11] Nafta ve dizelin yakıtlarının HCCI yanmasına geçişte yanma homojenliği üzerine etkisini araştırmışlardır. Bu çalışmada farklı yanma modlarında nafta ve dizelin arasındaki yanma ve emisyon davranışları araştırılmıştır. Araştırma oktan sayısı 60 olan yakıtlar için sıkıştırma ateşlemeli moddan homojen dolgulu sıkıştırma ateşlemeli moda geçişte yanma homojenliği ve fiziksel özelliklerin etkisi araştırılmıştır. Isı salımı ve yanma görüntülerinden, nafta ve PRF60'ın, dizel karışımları ile karşılaştırıldığında, ön karışımlı yanmanın daha gelişmiş olduğu görülmüştür. CI yanma işleminde is konsantrasyonunun daha yüksek olduğu, PPC modunda is emisyonlarının sıfıra yakın olduğu görülmüştür. Ayat Gharehghani [12], HCCI modda doğalgaz, etanol ve metanol yakıtlarının yük sınırlarını araştırmıştır. Sonuçlar, denklik oranlarının 0,3'ten fazla olduğu karışımlar ve 430 K'dan daha yüksek emme havası sıcaklıkları için doğal gazın uygun bir seçim olduğunu, bu durumda etanol ve metanolün vuruntuya ve ayrıca kabul edilemez düzeyde NO_X emisyonlarına neden olduğunu ortaya koymuştur. Mohammed Djermouni ve diğerleri [13] HCCI motorda LPG ve LNG yakıtlarını karşılaştırmıştır. Kompresör basıncı ve denklik oranı gibi çalışma parametrelerin genel sistem performansı üzerine etkileri tartışılmıştır. Rakesh Kumar Maurya ve diğerleri [14] Bu çalışma, hidrojen HCCI operasyonu için kimyasal kinetik ve yapay sinir ağı (ANN) kullanarak RI (ringing intensity-gürültü) karakterizasyonu ve tahminini sunmaktadır. Çalışmanın ilk bölümünde, denklik oranının (4), giriş sıcaklığının (Tivc) ve motor hızının gürültü yoğunluğu üzerindeki etkisi kimyasal kinetik model kullanılarak incelenmiştir. Yanzhao An ve diğerleri [15] düşük oktan sayılı benzin ile çalışan sıkıştırma ateşlemeli bir motorda HCCI ve PPC yanması araştırılmıştır. CONVERGE ® kullanılarak tam zamanlı motor çevrimi simülasyonları oluşturulmuştur ve kimyasal kinetikler ile birleştirilmiştir. HCCI ve PPC yanma modlarında elde edilen simülasyon ve deney verileri iyi bir uyum göstermiştir. Tamamen önceden karıştırılmış HCCI modu ÜÖN'dan 180 derece erken enjeksiyon zamanlamasında yanma sıcaklığı 1600K'in altında olduğunda elde edilebilir. Burada is ve NO_x oluşumları da başarıyla önlenebilmiştir. A.O. Hassan ve diğerleri [16] motor hızı ve EGR'nin HCCI motor performansına ve emisyonlara etkisini araştırmışlardır. Hava-yakıt oranının artması HCCI yanmasının avantajlarından biri olarak düşünülebilir. Silindir içinde seyreltilmiş ön karışım yanma sıcaklığını düşürür böylece NO_x emisyonları düşürülmektedir. Analiz, HCCI modundaki HC ve CO'nun motor hızına büyük ölçüde bağlı olduğunu göstermektedir. HC emisyonu, motor devrinden CO ve NO_x emisyonlarından daha çok etkilenmiştir.

HCCI motorlarda kullanılabilirliği araştırılan yakıtlar önceki çalışmalarda Nafta, PRF60, dizelin, doğalgaz, LPG, LNG, etanol, metanol, RFC, RON20, RON40 vb. olarak görülmektedir. HCCI motorunun çalışma aralığı kullanımını sınırlayan önemli bir faktördür. HCCI motorda kullanılacak olan yakıtın rafineriden elde edilebilmesi yakıta ulaşma açısından bir avantaj olarak görülebilir. Bu çalışmada hafif naftanın HCCI motorunda kullanımının silindir içi basınç, motor gücü, fren özgül yakıt tüketimi, ısıl verim, ortalama efektif basınç değerlerine etkisi parametrik olarak incelenmiştir. Bu çalışmanın önceki çalışmalardan farkı, sıkıştırma ateşlemeli bir motor HCCI modunda çalıştırılmış 15 deney noktasında çalışılmış ve silindir içi basınç, fren özgül yakıt tüketimi ve motor çalışma sınırları elde edilmiştir.

2 MATERYAL VE METOT

2.1 Deneylerde kullanılan yakıt

Deneylerde hafif nafta ve benzin yakıtları kullanılmıştır. Deneyler Gazi Üniversitesi Otomotiv Mühendisliği Bölüm Laboratuvarlarında gerçekleştirilmiştir.

Hafif nafta ve benzin yakıtlarının özellikleri Tablo 1'de gösterilmiştir.

Tablo 1. Deneylerde kullanılan yakıtların teknik özellikleri

	Hafif nafta	Benzin
Kendiliğinden tutuşma sıcaklığı [°C]	280-470	246-280
Yoğunluk [kg/cm^3 at 20 °C]	642	720-775
Kaynama noktası [K]	32-402	210
Araştırma oktan sayısı	64.5	95
Alt ısıl değer [kJ/kg]	48500	46400

2.2 Deney Düzeneği ve Metodoloji

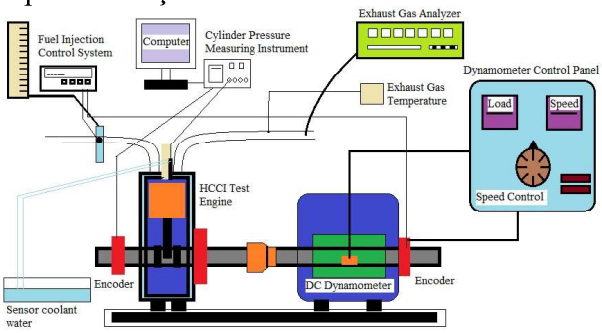
Deneylerde kullanılan motorun özellikleri Tablo 2'de verilmiştir.

Tablo 2. Deney motorunun teknik özellikleri

Test motoru	Lombardini LDA450
Silindir sayısı	1
Silindir çapı x kurs boyu (mm)	85 x 80
Sıkıştırma oranı	17,5/1
Maksimum döndürme momenti	1700 d/dk'da 28,5 Nm
Maksimum güç	5,5 kW
Enjektör püskürtme basıncı (dizel)	183 bar
Enjektör püskürtme basıncı (nafta)	3 bar
Püskürtme zamanı (krank açısı)	Üst ölü noktadan 28° önce

Hafif nafta, motora eklenen elektronik enjeksiyon sistemi ile emme manifolduna püskürtülmüştür. Deneylerde kullanılan yakıt enjektörünün püskürtme karakteristiği belirlenmiştir. Bu karakteristik verilerine göre yakıt tüketimi miktarı hesaplanmıştır.

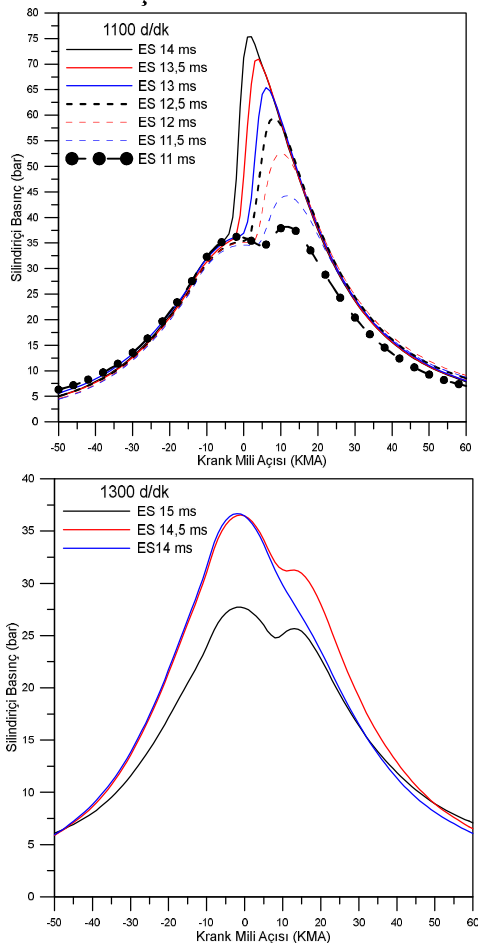
Enjeksiyon zamanlaması yakıt sisteminin ÜÖN sensöründen aldığı veriye göre sabit bir noktada gerçekleştirilmiştir. Enjeksiyon süreleri ise düzenekteki enjektör açık kalma süresinin ayarlanması için geliştirilen kontrol paneli üzerinden ayarlanmıştır. Deneyler 1100 ve 1300 d/dk motor hızlarında ve farklı enjektör açık kalma sürelerinde gerçekleştirilmiştir. Deneylerden elde edilen sonuçlar grafiklerde rapor edilmiştir.



Şekil 1: Deney düzeneğinin şematik görünüşü

3 DENEYSEL SONUÇLAR

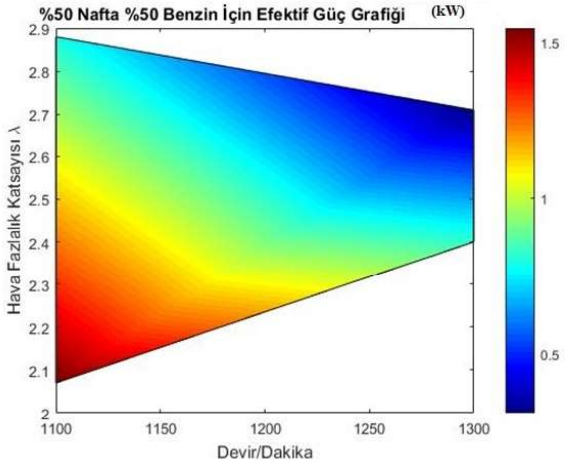
Deneylerde silindir içi basınç, kuvvet, emisyon ve egzoz gaz sıcaklığı ölçülerek sonuçları bu bölümde verilmiştir.



Şekil 2. Krank açısına bağlı silindir içi basınç değişimi

Şekil 2'de 1100 ve 1300 d/dk motor hızları için farklı enjeksiyon açık kalma sürelerine göre silindir içi basınç grafiğinin değişimi görülmektedir. Enjeksiyon süresindeki artışın daha fazla yakıt püskürtülmesini sağlayarak HFK değerini azalttığı ve karışımın zenginleşmesi sebebiyle maksimum basıncın yükselmesine sebep olduğu düşünülmektedir.

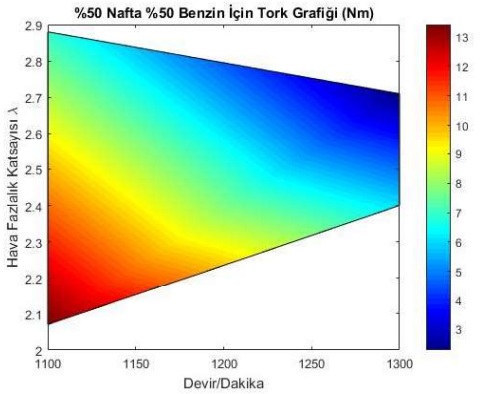
HFK değeri olarak 1100 d/dak için 2,07-2,88 ve 1300 d/dk için 2,4 ile 2,71 arasında motorun sorunsuz bir şekilde çalıştığı görülmüştür. Enjeksiyon süresinin 14 ms olarak gerçekleştiği durum HFK 2,07 olduğu değerin karşılığı olarak maksimum basıncın 75 bar civarına yükseldiği ve HFK 2,88 değeri yani enjeksiyon süresinin 11 ms olduğu değer maksimum basıncın 40 bar civarında olduğu 1100 d/dk'da görülmektedir. 1300 d/dk için enjeksiyon süresinin 15 ms olduğunda 37 bar civarında maksimum basınç oluşmuştur. HFK'nin artması ile yanmanın gerçekleşmemesi ve HFK'nin azalması ile motorda vuruntu oluştuğu gözlemlenmiştir.



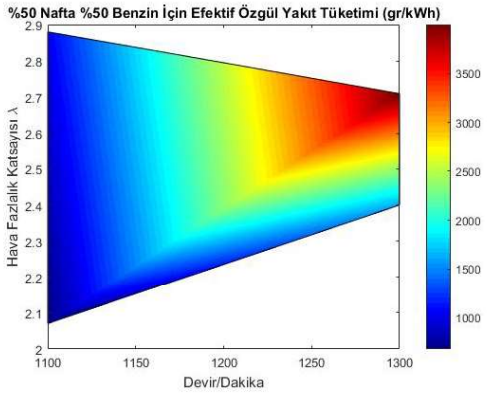
Şekil 3. HFK ve motor hızına göre efektif güç değerinin değişimi

Şekil 3'de HFK ve motor hızına göre efektif güç değişimi görülmektedir. Bu değerler göz önünde bulundurulduğunda ise maksimum gücün 1100 d/dk için HFK 2,1-2,4 aralığında verdiği söylenebilir. Motor hızının artması ve HFK'nin artması ile motor gücünde düşüş olduğu anlaşılmaktadır.

Şekil 4'de HFK ve motor hızına göre tork değişimi görülmektedir. Bu grafik göz önünde bulundurulduğunda ise maksimum torkun maksimum güç ile benzer bir grafik oluşturduğu söylenebilir. Motor hızının artması ve HFK'nin artması ile motor torkunda 4 Nm değerine kadar düşüş olduğu görülmektedir.

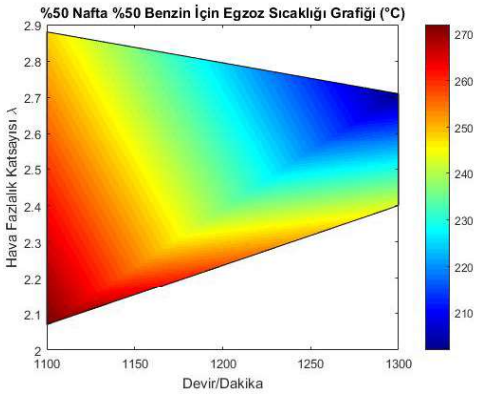


Şekil 4. HFK ve motor hızına göre tork değerinin değişimi



Şekil 5. HFK ve motor hızına göre efektif özgül yakıt tüketimi değerinin değişimi

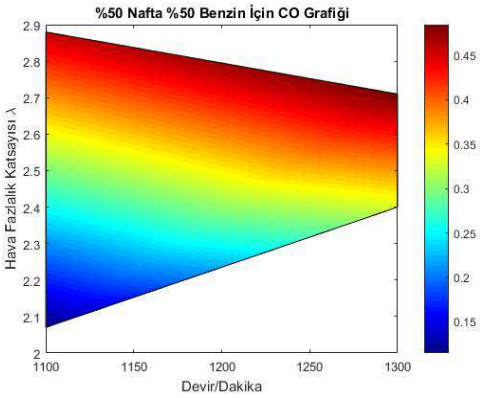
Şekil 5'de HFK ve motor hızına göre efektif özgül yakıt tüketimi değişimi görülmektedir. Maksimum efektif özgül yakıt tüketiminin motor hızının artması ve HFK'nin artması ile de artış gösterdiği görülmektedir. Buradan da anlaşıcağı üzere maksimum tork ve gücün oluştuğu yerde daha az yakıt tüketimi oluşması nedeniyle motorun HFK 2,1-2,5 arasında yaklaşık 1000-1500 gr/kWh değeri ile 1100 d/dk'da yakıt tüketiminin en iyi değerleri verdiği görülmüştür. Motor hızının ve HFK'nin artması ile yakıt tüketimi artarak maksimum 3500 gr/kWh değerine kadar yükseldiği görülmektedir.



Şekil 6. HFK ve motor hızına göre egzoz gaz sıcaklığı değerinin değişimi

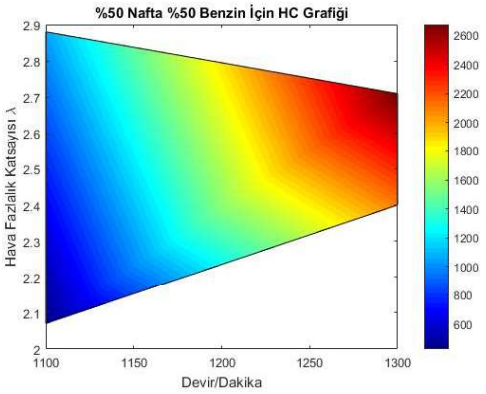
Şekil 6'da HFK ve motor hızına göre egzoz gaz sıcaklığı değişimi görülmektedir. Maksimum egzoz gaz sıcaklığının maksimum güç ile benzer bir grafik oluşturduğu söylenebilir. Motor

hızının artması ve HFK'nin artması ile egzoz gaz sıcaklığında düşüş meydana gelerek 210 ^{o}C kadar düşmüştür. 1100 d/dk ve HFK 2,1 değeri için 270 ^{o}C egzoz gaz sıcaklığı oluşmuştur.



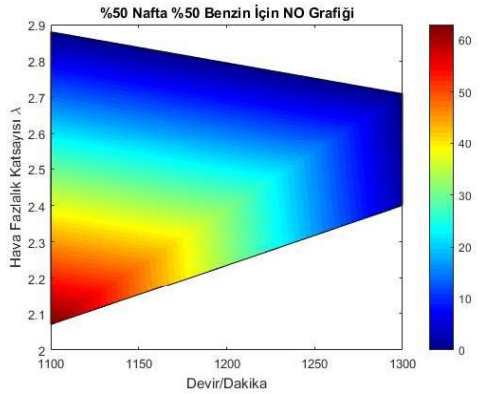
Şekil 7. HFK ve motor hızına göre CO emisyon değerinin değişimi

Şekil 7'de HFK ve motor devrine göre CO emisyon değişimi görülmektedir. Maksimum CO emisyonu motor devrinin ve HFK'nin artması ile artış göstermiştir. Buradan da anlaşıcağı üzere maksimum tork ve gücün oluştuğu yerde yanma veriminin arttığı söylenebilir. Bu sebeple HFK'nin atması ile tam yanmama gerçekleşmekte ve CO emisyonu artmaktadır. 1100 d/dk'da HFK 2.1 için %0,15 değerinde gerçekleşirken HFK 2,88 değeri için %0,45 değerine yükselerek tam tamına üç katına yükselmiştir.



Şekil 8. HFK ve motor hızına göre HC emisyon değerinin değişimi

Şekil 8'de HFK ve motor hızına göre HC emisyon değişimi görülmektedir. Maksimum HC emisyonu motor hızının ve HFK'nın artması ile artış göstermiştir. Buradan da anlaşıcağı üzere maksimum tork ve gücün oluştuğu yerde yanma veriminin arttığı söylenebilir. Bu sebeple HFK'nın artması ile yanma tam gerçekleşememekte ve yanmamış HC emisyonu artmaktadır. 1100 d/dk'da HFK 2,1 için 600 ppm değerinde gerçekleşirken HFK 2,88 değeri ve 1300 d/dk için 2600 ppm değerine yükselerek dört katındanda fazla yükselmiştir.



Şekil 9. HFK ve motor hızına göre NO_x emisyon değerinin değişimi

Şekil 9'da HFK ve motor hızına göre NO_x emisyon değişimi görülmektedir. Maksimum tork ve maksimum güç ile benzer bir grafik oluşturduğu söylenebilir. Motor hızının artması ve HFK'nin artması ile NO_x emisyonu 0 ppm değerine kadar düşmüştür. HFK 2,1 ve 1100 d/dk için 60 ppm değerine kadar yükselmiştir. Özellikle HCCI mod ile NO_x emisyonu oluşması motorun bu sınırlarda çalıştırılması gerektiğini göstermektedir.

4 DEĞERLENDİRME

Dizel bir motor port enjeksiyon dönüşümü ile HCCI modda çalıştırılarak herhangi bir ön ısıtma işlemi veya başka bir ek katkı sağlanmadan motorun çalışma aralığı %50 hafif nafta ve %50 benzin karışımı için araştırılmıştır.

Yapılan çalışma sonucunda özellikle motorun maksimum güç ve tork değeri verdiği aralıkta minimum yakıt tüketimi sağlandığı maksimum güç ve torkun oluştuğu durumda NO_x ve egzoz gaz sıcaklığında artışm meydana geldiği görülmüştür. Ayrıca motor hızının ve HFK değerinin artması ile yakıt tüketiminin kötüleştiği HC ve CO emisyonlarında ise artış meydana geldiği gözlemlenmiştir.

REFERENCES

1. https://ec.europa.eu/eurostat/statistics-explained/index.php/Road_freight_transport_by_vehicle_characteristics#Vehicle_fleets

2. National transportation sttistics 2017 Bureau of Transportation Statistics U.S. Department of Transportation http://www.princeton.edu/~alaink/Orf467F17/NTS_Entire_2017Q2.pdf

3.https://www.iea.org/newsroom/news/2018/march/global-energy-demand-grew-by-21-in-2017-and-carbon-emissions-rose-for-the-firs.html

4.https://www.iea.org/newsroom/news/2018/march/global-energy-demand-grew-by-21-in-2017-and-carbon-emissions-rose-for-the-firs.html.

5. Investigation of effect of compression ratio on combustion and exhaust emissions in A HCCI engine Alper Calam, Hamit Solmaz, Emre Yılmaz, Yakup _Içingür, Energy 168 (2019) 1208 -1216
6. Michal Puškár , Melichar Kopas, System based on thermal control of the HCCI technology developed for reduction of the vehicle NO_x emissions in order to fulfil the future standard Euro 7, Science of the Total Environment 643 (2018) 674-680
7. Jacek Hunicza, Maciej Mikulski, Investigation of the thermal effects of fuel injection into retained residuals in HCCI engine, Applied Energy 228 (2018) 1966–1984
8. Hyun Kwon Noh, Soo-Young No, Effect of bioethanol on combustion and emissions in advanced CI engines: HCCI, PPC and GCI mode – A review Applied Energy 208 (2017) 782–802
9. S.V. Khandal , N.R. Banapurmath , V.N. Gaitonde, Performance studies on homogeneous charge compression ignition (HCCI) engine powered with alternative fuels, Renewable Energy 132 (2019) 683e693
10. Mina Nishi , Masato Kanehara, Norimasa Iida, Assessment for innovative combustion on HCCI engine by controlling EGR ratio and engine speed Applied Thermal Engineering 99 (2016) 42–60
11. R. Vallinayagam, Yanzhao An∗, S.Vedharaj, Jaeheon Sim, Junseok Chang, Bengt Johansson, Naphtha vs. dieseline – The effect of fuel properties on combustion homogeneity in transition from CI combustion towards HCCI, Fuel 224 (2018) 451–460
12. Ayat Gharehghani, Load limits of an HCCI engine fueled with natural gas, ethanol, and methanol, Fuel 239 (2019) 1001–1014).
13. Mohammed Djermouni, Ahmed Ouadha, Comparative assessment of LNG and LPG in HCCI Engines, Energy Prodecia 139 (2017) 254-259
14. Rakesh Kumar Maurya*, Mohit Raj Saxena, Characterization of ringing intensity in a hydrogen-fueled HCCI engine, i n t e r n a t i o n a l journal o f hydrogen energy 43 (2018) 9423 - 9437
15. Yanzhao An, Mohammed Jaasim, Vallinayagam Raman, Francisco E. Hernandez Perez, Jaeheon Sim, Junseok Chang, Hong G. Im, Bengt Johansson, Homogeneous charge compression ignition (HCCI) and partially premixed combustion (PPC) in compression ignition engine with low octane gasoline, Energy 158 (2018) 181-191
16. A.O. Hassan, Ahmad Abu-jrai, Ala'a H. Al-Muhatseb, Farrukh Jamil, Impact of EGR and engine speed on HCCI engine performance and tail pipe emissions, Energy Procedia 136 (2017) 208-212

Microwave Assisted Biomass-Based Electrode Material Production for Supercapacitor Applications

Musa ALTINIŞIK[1], Tülin AVCI HANSU[2] and Murat AKDEMİR[3*]

1. Musa ALTINIŞIK, Faculty of Engineering, Siirt University, Siirt; email: musa.altnsk56@gmail.com
2. Tülin AVCI HANSU, Faculty of Engineering, Siirt University, Siirt; email: tulin.hansu@siirt.edu.tr, tulinn_avci@hotmail.com
3. Murat AKDEMİR, Faculty of Engineering, Siirt University, Siirt; email: muratakdemir@siirt.edu.tr

ABSTRACT

Recently, supercapacitors have been considered as a solution to eliminate the energy storage problem. Supercapacitors are the most important group of electrochemical energy storage systems designed to quickly store and transfer energy. While statically storing energy can store more energy than conventional capacitors, they can transfer this energy much faster than electrochemical batteries [1]. Electrode base material and activation play the most important role in determining supercapacitor performance [2]. In our previous study, the capacity of supercapacitor electrodes produced using *Quercus infectoria (Qui)* biomass was 89 F/g [3]. In this study, in order to increase the capacitance and stability of the electrodes obtained from Qui biomass, produced activated carbon was exposed to microwave at various powers and durations, and four different electrodes were developed. The microwave powers and durations applied to the produced materials are given in Table 1.

Table 1. The microwave powers and durations applied to activated carbon for electrode types

Electrode material	Power (W)	Duration (min.)
MAQ-1	500	10
MAQ-2	750	10
MAQ-3	1000	10

MAQ-4	500	20

The energy storage capacity, stability and energy-power density of the supercapacitor were determined by using cyclic voltammetry curves (CV), impedance curves (EIS) and charge-discharge curves (GCD) obtained as a result of electrochemical characterization. In Table 2, the electrochemical performance measurements of each electrode material at a current density of 1 A/g are given. As can be seen from Table 2, the MAQ-4 supercapacitor electrode material gave the highest capacitance with a value of 283.90 F/g.

Table 2. The electrochemical performance measurements of each electrode at 1 A/g

Electrode material	**Capacitance (F/g)**	**IR drop (mV)**	**R_s (Ω)**	**R_{ct} (Ω)**
MAQ-1	231.04	32	0.30	6.06
MAQ-2	125.69	11	0.09	4.48
MAQ-3	213.84	14	0.01	7.48
MAQ-4	283.90	12	0.04	8.86

The electrodes obtained by applying 500W for 20 min. exhibited the highest capacitance value at 1 A/g current density (MAQ-4). Electrochemical characterization results of The MAQ-4 supercapacitor cell are given in Figure 1. The CV and GCD curves of the all supercapacitors resemble the ideal curves. Since there is no metal oxide or polymer-based material in the active material used, redox deviations did not occur and showed a typical electrical double layer capacitor (EDLC) feature [4, 5]. However, the applied microwave power and duration had different effects on the capacitance and empedance of the electrodes. When the power of the microwave applied to the material was increased from 500W to 750W, the capacitance, impedance of the electrodes, and voltage drop on the material decreased. When the power was increased to 1000 W, the capacitance and impedance of the electrodes increased again. When the amount of applied time increased, a two-way positive effect was

created, resulting in an increase in capacitance values and a decrease in voltage drops on the electrodes. As a result, it was seen that the the microwave power and duration had a significant effect on the capacitance values and voltage drop occured on the electrodes. MAQ-4 electrode looks attractive with its high capacitance values and low electrode empedance.

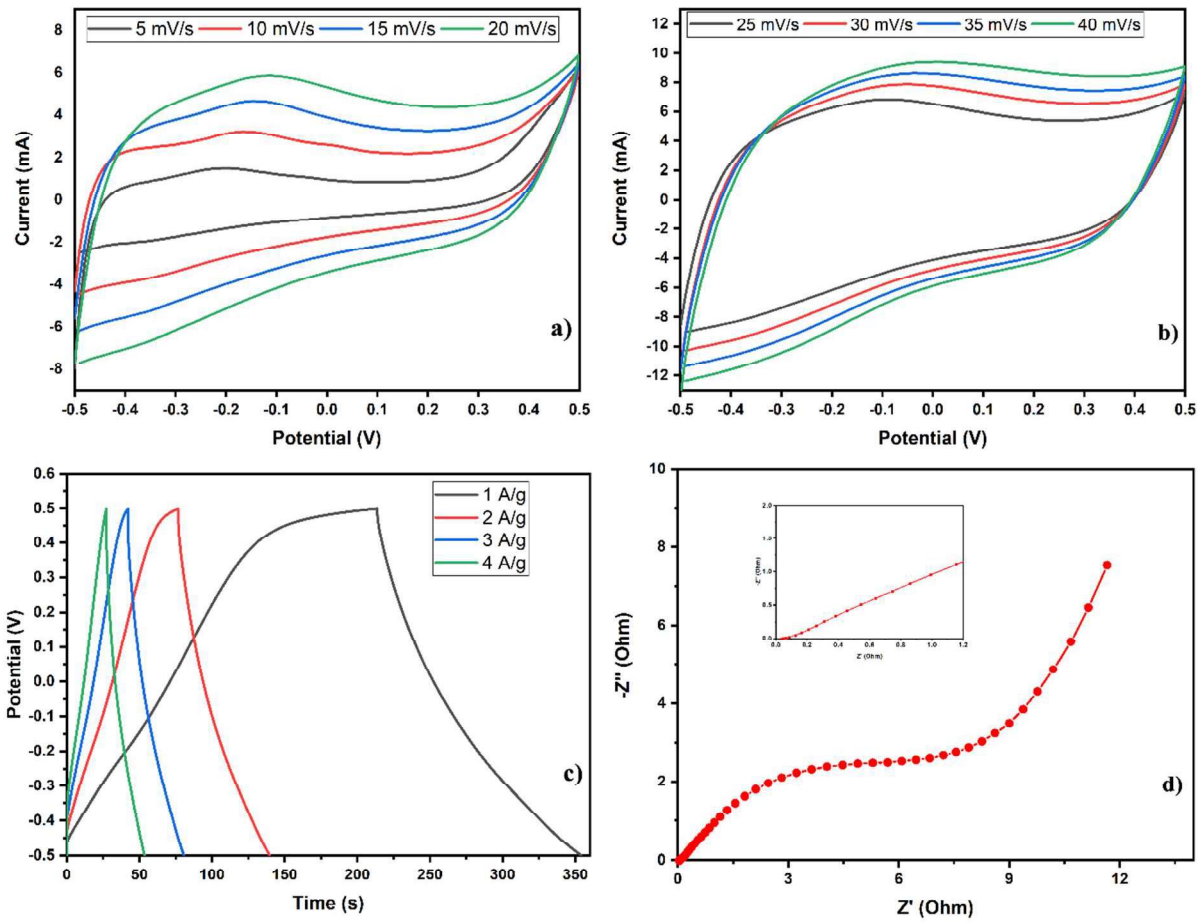


Figure 1. Electrochemical characterization results of the MAQ-4 supercapacitor cell

References

1. Pandolfo, A. G., & Hollenkamp, A. F. (2006). Electrochemical capacitors–scientific fundamentals and technological applications. *J Power Sources*, 157, 11-27.

2. Inal, I. I. G., Akdemir, M., & Kaya, M. (2021). Microcystis aeruginosa supported-Mn catalyst as a new promising supercapacitor electrode: A dual functional material. *International Journal of Hydrogen Energy*, 46(41), 21534-21541.

3. Akdemir, M. (2022). Electrochemical performance of Quercus infectoria as a supercapacitor carbon electrode material. *International Journal of Energy Research*, 46(6), 7722-7731.

4. Özarslan, S., Atelge, M. R., Kaya, M., & Ünalan, S. (2021). A Novel Tea factory waste metal-free catalyst as promising supercapacitor electrode for hydrogen production and energy storage: A dual functional material. *Fuel*, *305*, 121578.

5. Özarslan, S., Atelge, M. R., Kaya, M., & Ünalan, S. (2021). Production of dual functional carbon material from biomass treated with NaOH for supercapacitor and catalyst. *Energy Storage*, *3*(5), e257.

DÜŞÜK GİRDAP ÜRETEÇLİ BRÜLÖRÜN KULLANILDIĞI BİR DOĞALGAZ KAZANINDA YANMA VE EMİSYONLARIN NUMERİK İNCELENMESİ

M.S. Cellek[1], A. Pınarbaşı[2], G. Coskun[3]

1. Makine Mühendisliği Bölümü, Bingöl Üniversitesi, Bingöl e-mail: mscellek@bingol.edu.tr
2. Makine Mühendisliği Bölümü, Yıldız Teknik Üniversitesi, İstanbul e-mail: alipnrbs@yildiz.edu.tr
3. Makine Mühendisliği Bölümü, Sakarya Üniversitesi, Sakarya e-mail: gcoskun@sakarya.edu.tr

Özet

Doğal gaz yakıtlı kazanlar çevreci ve verimli yanma sağlamaları sebebiyle günümüzde ısıtma sistemlerinde kullanımı oldukça yaygındır. Bu kazanların yanma veriminin daha iyi ve emisyonların daha düşük olması için çalışmalar devam etmektedir. Maliyetlerinin yüksek ve imalat sürelerinin uzun olması sebebiyle deneysel çalışmalarla yapılan iyileştirmeler yavaş ilerlemektedir. Bu sebeple CFD simülasyonlarıyla yapılan iyileştirme çalışmaları tercih edilmektedir. CFD ile yapılan yanma simülasyonlarının daha doğru sonuç vermesi için kullanılan türbülans ve yanma modellerinin doğru seçilmesi oldukça önemlidir. Bu çalışmada bir doğalgaz kazanında yanma ve emisyonları farklı türbülans ve yanma modelleri ile incelenmiştir. Simülasyonlarda kullanılan türbülans modelleri sırasıyla Standard k – ε, Realizable k – ε, RNG k – ε ve RSM modelleri iken, yanma modelleri ise Eddy Dissipation Model (ED), Finite Rate/Eddy Dissipation (FR/ED), Eddy Dissipation Concenpt (EDC), Non-Premix Combustion (NPC) ve Partial-Premix Combustion (PPC) yanma modelleridir. Sayısal simülasyonlar ile elde edilen sonuçlar deneysel veriler ile karşılaştırıldığında Realizable k-ε türbülans modelinin diğer türbülans modellerine kıyasla daha iyi NOx emisyon tahmininde bulunduğu anlaşılmıştır. Yanma modellerinde ise PPC ve ED yöntemlerinin NOx tahmininde daha başarılı oldukları gözlemlenmiştir.

Anahtar Kelimeler: *Doğal gaz kazanı, CFD, Yanma, Türbülans modeli, Yanma modeli*

1 GİRİŞ

Silva ve arkadaşları [1] 2 boyutlu eksenel simetrik bir silindirik yanma odasında doğalgazı metan olarak ele alıp, metan-hava iki basamaklı reaksiyon mekanizması ile Eddy Breakup – Arrhenius modeliyle yakmışlardır. Bu çalışmada yanma odası ısıl radyasyonu bölgesel bir yaklaşımla çözümlenmiştir. Bu yaklaşımda dalga boyu o bölgedeki gaz özelliklerine bağlıdır. Bu gaz özellikleri Weighted-Sum-of-Gray-Gases-Model (WSGGM) ile çözümlenmektedir. Yanma odası diferansiyel denklemler hacimsel kontrol yaklaşımıyla çözülmüştür. Bu çalışmada literatürden elde edilmiş deneysel verilerin simülasyonu yapılmış ve yanma odası içerisinde CH_4, T, O_2, CO ve CO_2 sonuçları eksenel ve radyal yönlerde iki durum için karşılaştırılmıştır. Yanma odası boyunca iki durum arasında farklılıkların gözlemlendiği özellikle CO_2 için belirgin farklılıkların olduğu görülmüştür. Fakat reaktantların püskürtüldüğü noktanın 1.1 m mesafesinde, nümerik ve deneysel sonuçların birbiriyle iyi derecede uyumlu olduğu ifade edilmiştir. Ren et al. [2], EDC ve PDF yanma modelleri ile ön karışımsız alevi simüle etmişlerdir. Farklı türbülans modellerinin ön karışımsız alevlerin HAD çözümü üzerindeki etkisini ele alan çeşitli çalışmalar bulunmaktadır. Frassoldati ve ark. [3], yavaş yanma rejiminde Reynolds stres modeli (RSM), k – ε ve modifiye edilmiş k – ε ($C_{\varepsilon 1}$=1:6) türbülanslı modellerin metan/hidrojen alevi üzerindeki etkisini karşılaştırmışlardır. RSM ve modifiye edilmiş k – ε modellerinin deneysel sonuçlarla iyi bir uyum sağladığı gösterilmiştir. Ziani ve ark. [4], Olasılık Yoğunluğu Fonksiyonu (PDF) yaklaşımını kullanarak CH_4-H_2 yakıt karışımının ön karışımsız türbülanslı yanmasını sayısal yöntemlerle modellemişlerdir. k – ε modeli, değiştirilmiş k – ε modeli ve RSM modeli olmak üzere üç farklı türbülans modeli ile simülasyonlar yapmışlardır. Sonuç olarak modifiye edilmiş k – ε türbülans modelinin bu tür alevleri simüle etmek için ideal olduğu sonucuna ulaşmışlardır. Pfeiler ve Raupenstrauch [5], hava ile çevrili olarak birlikte akan, ön karışımsız bir metan alevinin 2 boyutlu eksenel simetrik ve 3 boyutlu simülasyonu üzerine realizable k – ε ve RSM türbülans modellerinin performanslarını incelemişlerdir. 2B eksenel simetrik simülasyonunda realizable k – ε ve 3B

simülasyoda RSM türbülans modeli sonuçların beklenmedik şekilde benzer sonuçlara ulaştığını görmüşlerdir. Khaldi et al. [6], teğetsel olarak püskürtülen toz haline getirilmiş kömür ile yakılan fırınının akış alanını ve yanma özelliklerini araştırmak için sayısal bir çalışma gerçekleştirmiştir. Yanma sırasında doğru tahminler elde etmek için farklı türbülans modelleri kullanılmışlardır. Çalışmalarında RNG k-ε modelinin hız ve sıcaklık alanlarını tahmin etmek için en verimli türbülans modeli olduğu belirtmişlerdir. Yapılan literatür araştırması her bir türbülans modelinin farklı uygulamalarda iyi sonuçlar verebildiğini göstermektedir. Genelleme yaparak en iyi türbülans modelini ortaya koymanın güç olduğu sonucuna varılmaktadır.

Bu çalışma ise, düşük girdap akışlı bir brülörün kullanıldığı doğalgaz kazanında türbülans ve yanma modelleri sonuçları deneysel sonuçlarla karşılaştırılarak, en uygun modellerin belirlenmesi hedeflenmektedir.

2 DENEYSEL YÖNTEM

Deneysel çalışma Şekil 1 de görülen ECO 45 G C 3B brülörlü ve dairesel formadaki doğal gaz kazanı kullanılarak yapılmıştır. Deney başlangıcında brülöre giren doğal gaz debisi, hava debisi ölçülerek brülörün ısıl yükü belirlenmiştir (1085 kW). Sonrasında baca gazı emisyonları ve gerekli sıcaklık ölçümleri yapılmıştır. Test kazanında doğal gazın yanma sonucu gaz emisyonları, sıcaklığı ve hava fazlalık değeri ölçümü için NOVA marka emisyon ölçüm cihazı kullanılmış ve CO_2, O_2 ve NOx değerleri ölçülmüştür. Deneysel çalışma sırasında hava fazlalık katdsayısı, λ=1.20 olarak alınmıştır.



Şekil 1. Testler için kullanılan ECO 45 G C 3B brülörü ve kazanı [7,8]

Ayrıca emisyon ölçüm cihazında NO, NO_2, NOx, CO, CO_2 ve SO_2 gibi emisyonlar ölçülebilmekte ve hava fazlalık katsayısı, çiğlenme sıcaklığı baca gazı sıcaklıkları gibi sonuçlar gösterilmektedir. Burada okunan NOx emisyonun da NO ve NO_2 emisyonları toplamına eşit olması nedeniyle toplam NOx belirsizliği de Kline ve McClintock yöntemine göre aşağıdaki şekilde hesaplanabilir:

$$\mathrm{NOx} = \mathrm{NO} + \mathrm{NO_2} \tag{1}$$

$$w_{NOx} = \pm\left[\left(\frac{\partial NOx}{\partial NO} w_{NO}\right)^2 + \left(\frac{\partial NOx}{\partial NO_2} w_{NO_2}\right)^2\right]^{\frac{1}{2}} \tag{2}$$

$$w_{NOx} = \pm\left[(1w_{NO})^2 + \left(1w_{NO_2}\right)^2\right]^{1/2} \tag{3}$$

3 NÜMERİK YÖNTEM

3.1 Türbülanslı Akışın Modellenmesi

Türbülanslı akışlar karmaşıklığı nedeniyle birçok araştırmacının ilgisini çekmiş ve yapılan çalışmalar sonucunda modeller geliştirilmiştir. Gerçekte bu akışları modelleyebilmek çok zor ve neredeyse imkânsızdır. Çünkü akış karmaşık, rastgele ve anlık olarak değişmektedir. Fakat günümüzde gelişmiş CFD programlarıyla uygulamalar da türbülanslı akışlar yaklaşık olarak modellenebilmekte ve tahmin edilebilmektedir. Fluent programı bünyesinde bulunan türbülans modellerinden Standard k-ε modeli, Realizable k-ε modeli ve RNG k-ε modeli yaygın olarak kullanılan k-ε türbülans modelleri olarak bilinmekte ve en gelişmiş türbülans modelleri arasında görülmektedir. Türbülans modellerinde k türbülans kinetik enerjisi ve ε disipasyon (yayınım) oranını temsil ederken, Standard k-ε modeli, Realizable k-ε modeli ve RNG k-ε modelleri arasındaki temel farklılıklar da türbülanslı vizkozitenin hesaplanma yöntemi, k-ε türbülans yayılımıyla ilgili olan Prandtl sayıları ve ε denklemindeki üretim ve tüketim terimleridir [9].

3.1.1 Standard k-ε Modeli

Standard k-ε modeli türbülansın iki deklemle tanımlandığı en basit ve en temel modeldir. Bu modelde türbülans hızı ve uzunluk skalası iki ayrı tranport denkleminin çözümüyle birbirinden bağımsız olarak belirlenebilmektedir. Launder ve Spalding tarafından önerilen bu model, doğru tahmin, ekonomiklik ve sağlamlığı dolayısıyla türbülanslı endüstriyel akış ve ısı transfer uygulamalarında oldukça popülerdir [10]. Yarı ampirik bir model olmakla birlikte jet akışları ve kanal akışlarının modellenmesinde tercih edilmektedir [11].
Zamanla k-ε modelindeki eksiklikler tespit edilerek düzeltme ve eklemeler yapılarak iki ayrı k-ε modeli geliştirilmiştir [10].

3.1.2 Realizable k-ε Modeli

Yüksek dönümlü ve girdaplı türbülanslı akışların modellenmesinde Standard $k-\varepsilon$ modeli iyi bir tercih değildir. Bunun yerine türbomakinalarda akışın dönümlülüğünü, brülör ve yakıcılarda girdapları göz önüne alabilecek Realizable $k-\varepsilon$ modelinin kullanılması daha uygundur. Bu modelin düşük girdap sayışı ($S<0.5$) türbülanslı akışlarda kullanılması önerilmektedir [10].

3.1.3 RNG k-ε Modeli

Düşük girdap sayılı ($S< 0.5$) türbülanslı akışlarda önerilen Realizable $k-\varepsilon$ ile birlikte kullanılabilen bir başka model de RNG $k-\varepsilon$ modelidir. Bu modelin de girdap üreteçli brülör ve siklon tipi yakıcılarda Standard $k-\varepsilon$ yerine kullanılması önerilmektedir [10].

RNG metodu matematiksel teknikler kullanılarak anlık Navier-Stokes denklemlerinden türetilmektedir. Bu modelde analitik türev Standard $k-\varepsilon$ modeldekinden farklı sabitler kullanılarak sonuçlar vermektedir. Dahası taşınım dekleminde k ve ε için farklı ve ilave terimler içermektedir [11].

3.1.4 Reynolds Stress Modeli (RSM)

Reynolds Stress Modeli diferansiyel taşınım denklemlerini kullanarak her bir Reynolds gerilmenin hesaplanmasını içerir. Reynolds gerilmeleri daha sonra Reynolds ortalama momentum denkleminin kapalı formunu elde etmek için kullanılır. Reynolds gerilme taşınım denklemleri tam momentum denkleminin momenti alınarak türetilebilir [12]. Reynolds Stress Modeli düşük girdap sayılı türbülans akışlarında kullanılan Realizable $k-\varepsilon$ ve RNG $k-\varepsilon$ türbülans modellerinin aksine yüksek girdaplı ($S> 0.5$) akışlar için kullanılması önerilmektedir [10]. Reynold Stress, geri dönüş bölgesinin meydana geldiği ters akış gradyenlerini tespit etmede diğer iki yöntemden daha başarılı olduğu ayrıca denklemlerinde bulunan stres komponentleri sayesinde akışın anizotropik davrandığı düşük hızlı ters akış bölgelerinde hız profillerini daha gerçekçi tespit ettiği ifade edilmektedir. Bu modelin handikapları ise yakınsamadaki zorluklar ve çözümleme süresinin diğer modellere göre daha fazla olmasıdır [10].

3.2 Yanmanın Modellenmesi

Kimyasal türler için korunum denklemlerinin çözümü her bir türün yerel kütle kesri, her bir tür için Fluent programı ile konveksiyon-difüzyon denkleminin çözümü ile tahmin edilir. Korunum denkleminin genel formu şu şekilde ifade edilebilir [9].

$$\frac{\partial}{\partial t}(\rho Y_i) + \nabla \cdot (\rho \vec{v} Y_i) = -\nabla \cdot \vec{J}_i + R_i + S_i \qquad (4)$$

Bu denklemde ilk ifade her bir türün kütle kesrinin değişimini, ikinci ifade türlerin konveksiyonunu ifade eder. Denklemin sağ tarafındaki ilk terim difüzyon değişim oranını, ikinci terim kimyasal reaksiyon sonucu türlerin net üretimini ifade eder. Son terim ise diğer kaynakların değişimini ifade eder [12].

Kimyasal türlerin korunum denkleminde reaksiyon hızı R_i, şu üç şekilde hesaplanır [7]:

- Laminer sonlu-hız modeli (Laminar Finite-Rate Model)
- Girdap Ayrışma Modeli (Eddy Dissipation Model)
- Girdap Ayrışma Konsepti (Eddy Dissipation Concept)

3.2.1 Girdap Ayrışma Modeli (Eddy Dissipation Model)

Çoğu yakıtlar hızlı yanma eğilimindedir ve toplam reaksiyon hızı türbülans karışımı tarafından kontrol edilir. Ön karışımsız alevlerde, türbülans yakıt ve oksitleyiciyi reaksiyon bölgesi içinde karıştırır. Ön karışımlı alevlerde, türbülans soğuk reaktantları ve sıcak ürünleri reaksiyon bölgesi içinde yavaşça karıştırır. Bazı uygulamalarda karışım sınırlı, karmaşık ve bazen bilinmezdir, bu durumlarda kimyasal kinetik hızı güvenli bir şekilde ihmal edilebilir. Fluent, Eddy Dissipation olarak bilinen Magnussen ve Hjertager'ın çalışmalarına dayanan bir türbülans-kimyasal etkileşim modeli geliştirmiştir. Her bir i türünün r reaksiyonu dolayısıyla üretim hızı, $R_{i,r}$, aşağıdaki iki denklemde küçük olana göre belirlenir [9].

Reaktantların kütle fraksiyonunu için:

$$R_{i,r} = \nu'_{i,r} M_{\omega,i} A \rho \frac{\epsilon}{k} min\left(\frac{Y_R}{\nu'_{R,r} M_{\omega,R}}\right) \qquad (5)$$

Ürünlerin kütle fraksiyonunu için:

$$R_{i,r} = \nu'_{i,r} M_{\omega,i} AB \rho \frac{\epsilon}{k} \frac{\sum P Y_P}{\sum_j^N \nu''_{i,r} M_{\omega,j}} \qquad (6)$$

Burada,
Y_P= Herhangi bir ürün türünün kütle kesri, P
Y_R = Belirli bir reaktantın kütle kesri, R
A= Bir ampirik sabiti, 4'e eşittir
B= Bir ampirik sabiti, 0.5'e eşittir

Denklem 5 ve 6'de kimyasal reaksiyon hızı, Spalding modeli [13] olan Eddy Break-up yanma modelindeki gibi büyük girdap karıştırma zaman ölçeği k/ε tarafından hükmedilir. Yanma türbülansın varlığında $k/\varepsilon > 0$ gelişir ve yanmayı başlatacak bir tutuşturucuya ihtiyaç duyulmaz. Bu durum ön karışımsız alevler için geçerlidir. Fakat ön karışımlı alevlerde, reaktantlar hesaplama bölgesine girer girmez yanmaya başlar. Bu durumun önüne geçmek için ANSYS Fluent ayrıca Finitre-Rate Eddy Dissipation modelini geliştirmiştir. Burada Hem Arrhenius ve eddy dissipation reaksiyon hızları hesaplanır ve reaksiyon hızı en düşük olana eşit olur. Uygulamada Arrhenius hızı alev tutucundan önce reaksiyonu önleyen bir anahtar görevini görür. Alev tutuştuğunda, girdap ayrışma hızı (Eddy Dissipation rate) genellikle Arrhenius hızından daha küçük olmakta ve reaksiyon karışım oranı ile sınırlanmaktadır [9].

3.2.2 Sonlu-Hızlı/Girdaplı Dağılım Modeli (Finite Rate/Eddy Dissipation)

Eddy Dissipation modeli, reaksiyonların hızlı olduğunu ve sistemin tamamen karıştığını varsaymaktadır. Eğer durum tam olarak böyle değilse, sonlu oranda kimya ile birleştirilebilir. FLUENT'de buna sonlu-hızlı / girdaplı dağılım modeli (Finite Rate / Eddy Dissipation) denir. Bu durumda kinetik hız, girdap dağılım modeli tarafından öngörülen reaksiyon hızına ek olarak hesaplanır. Sonuçta en yavaş reaksiyon hızı kullanılır [9].

- Türbülans düşükse, karışım yavaştır ve bu reaksiyon hızını sınırlar.
- Türbülans yüksekse fakat kinetik hız düşükse, bu da reaksiyon hızını sınırlandırılacaktır.

Bu model çeşitli sistemler için kullanılabilir ancak model sabitleri A ve B, her bir sistemdeki her reaksiyon için ampirik olarak ayarlanmalıdır. Bir ve iki basamaklı yanma işlemleri için sırasıyla 4 ve 0.5 varsayılan değerleri olarak belirlenmiştir. Model, reaksiyonların devam etmesi için her zaman bir ürünün mevcut olmasını gerektirir. Eğer bu istenmiyorsa ürününün başlangıç kütle kesri ve model sabiti ayarlanmalıdır [12].

3.2.3 Girdap Ayrışma Konsepti (Eddy Dissipation Concenpt)

Eddy Dissipation Concept modeli Eddy Dissipation modelinin geliştirilmiş bir versiyonudur ve türbülanslı akışlarda detaylı kimyasal mekanizma içermektedir. Bu model, reaksiyonun küçük bir türbülans yapısında (fine-scale) gerçekleştiğini kabul eder. Eddy Dissipation Concept modeli detaylı kimyasal mekanizmaları türbülanslı reaksiyon akışları içine dâhil eder [9]. Fakat bu detaylı kimyasal mekanizmaların çözümü her zaman zor, sayısal hesaplamaları çok maliyetli ve çözümleri uzun sürmektedir.

3.2.4 Ön Karışımsız Yanma Modeli (Non-Premixed Combustion)

Yakıt ve havanın reaksiyon bölgesine ayrı ayrı gönderilmesiyle oluşan yanma ön karışımsız yanma olarak ifade edilir. Pulverize kömür ve

içten yanmalı dizel motorlarındaki yanma bu yanma modeline örnek olarak gösterilebilir [9].

Belirli varsayımlarla termokimya tek bir parametreye indirgenebilir. Bu parametre karışım kesri veya fraksiyonudur. f ile gösterilen karışım fraksiyonu, yakıt akışından kaynaklanan kütle fraksiyonudur. Diğer bir değişle, yanmış ve yanmamış yakıt akım elementlerinin (C, H ve diğerleri) tüm türler (CO_2, H_2O, O_2 ve diğerleri) içerisindeki yerel kütle kesridir. Bu yaklaşımda kimyasal reaksiyonundaki atomik elementler korunduğundan son derece mükemmel bir yaklaşımdır. Karışım fraksiyonu korunan skalar bir büyüklüktür ve bu yüzden onun taşınım denklemi bir üretim terimi içermez. Yanma basitleştirilerek bir karışım problemine indirgenir ve non-linear olan ortalama reaksiyon hızlarından kaynaklanan zorluklar ortadan kalkmış olur. Karışım sağlandığında, kimya denge modeli ile kimyasal denge olarak modellenebilir. Daimi difüzyon flama (flamalet) modeli ile kimyasal denge yaklaşımı sergilenebilir veya daimi olmayan (kararsız) difüzyon flama modeliyle kimyasal dengeden önemli ölçüde ayrılır [9].

Ön karışımsız yanma modeli karışım fraksiyonları için taşınım denklemlerin çözümlerini kapsar ve her bir tür için bir denklem çözülmez. Bunun yerine türlerin konsantrasyonları tahmin edilen karışım fraksiyon alanları elde edilir. Kimya ile türbülans etkileşimi Olasılık Yoğunluk Fonksiyonu (PDF-Probability Density Function) ile göz önüne alınır [7,12].

3.2.5 Kısmi-Ön Karışımlı Yanma Modeli (Partially Premixed Combustion)

ANSYS Fluent, ön karışımsız ve ön karışımlı yanma modellerini temel alarak kısmi-ön karışımlı yanma modelini (Partially Premixed Combustion) geliştirmiştir. Kısmi ön karışımlı yakma sistemleri, üniform ol[mayan yakıt-oksitleyici karışımıyla (eşdeğerlik oranları) ön karışmış alevlerdir. Difüzyon pilot alevleri olan fakir ön karışımlı yakıcılar, soğutma havası jetleri ve iyi derecede ön karıştırılmamış girişleri olan alevler bu yanma modeli için birer örnek sayılabilirler. ANSYS Fluent programında bu modelin üç farklı alt uygulaması mevcuttur. Bunlar kimyasal denge, daimi difüzyon alevciği (flamelet) ve alevcik üretim manifoldudur [9].

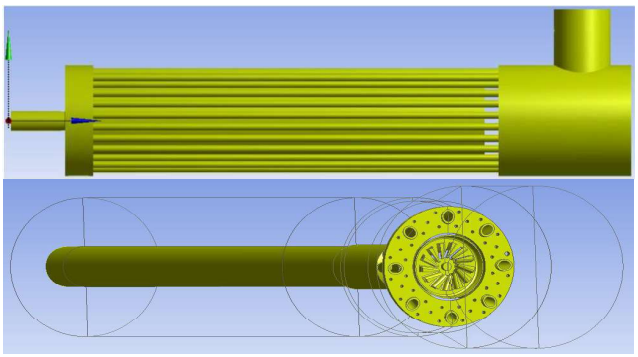
Kısmi ön karışımlı yanma modeli, ön karışımsız ve ön karışımlı yanma modellerini temel alması dolayısıyla bu modelde de termokimya tek bir parametreye indirgenir bu karışım kesri ifadesidir. Reaksiyon bölgesine giren ikincil bir yakıt veya kimyasal reaksiyona girebilecek olan farklı bir tür akımı söz konusu olduğunda girenlerin karışım kesirleri toplamı bire eşit olması gerekmektedir [9].

Karışım kesrinden başka sayısal hesaplamalarda göz önüne alınan başka bir ifade de gelişim değişkenidir (progress variable, c). Hava-yakıt karışımının, önceden belirlenen bir sınır koşuldaki durumunum tarif edilmesi amacıyla yararlanılmaktadır [15]. Alev ortalama reaksiyon ilerlemesini gösteren c değeri 0 ve 1 arasında değişmektedir. Alev formu üzerinde c=0 bölgesi yanmamış reaktanların olduğu, c=1 olduğu bölgede ise yanmış ürünlerin olduğu anlaşılmaktadır. Türbülanslı ön karışım alevde dalgalanan bir alev için c değeri 0 ile 1 arasında değişmektedir [9].

3.3 Kazan ve Brülör Geometrisinin Akış Hacimleri ve Ağ yapısı

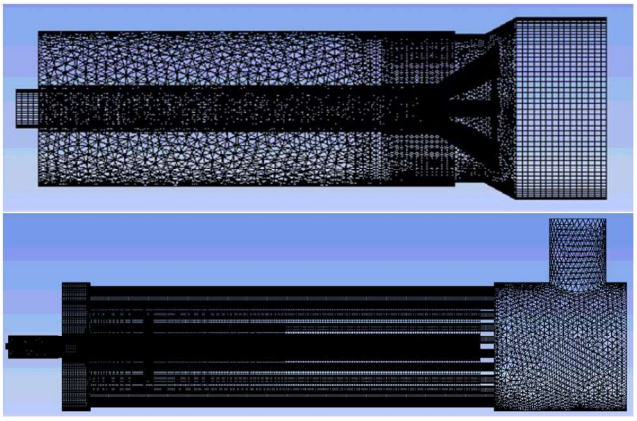
Simülasyon çalışmalarında sayısal analizleri gerçekleştirebilmek için yapılması gereken ilk adım olarak kazanın 3 boyutlu akış hacmi modellenmiştir. Kazan ve brülör geometrilerinin 2 boyutta çalışmaya uygun olmaması nedeniyle 3 boyutlu yanma analizleri gerçekleştirilmiştir. Öte yandan, türbülanslı, girdaplı ve karmaşık akışları daha iyi gözlemleyebilmek için 3 boyutlu çalışmalar daha gerçekçi olsa da analiz sürelerinin uzun sürmesi ve yakınsama noktasında bazı zorlukların ortaya çıkması üstesinden gelinmesi gereken handikaplardır [16].

Şekil 2'de test kazanı, brülör ekipmanlarından yakıt borusu, girdap üreci, disk ve bunların 3 boyutlu olarak hazırlanana montajı görselleri verilmiştir.



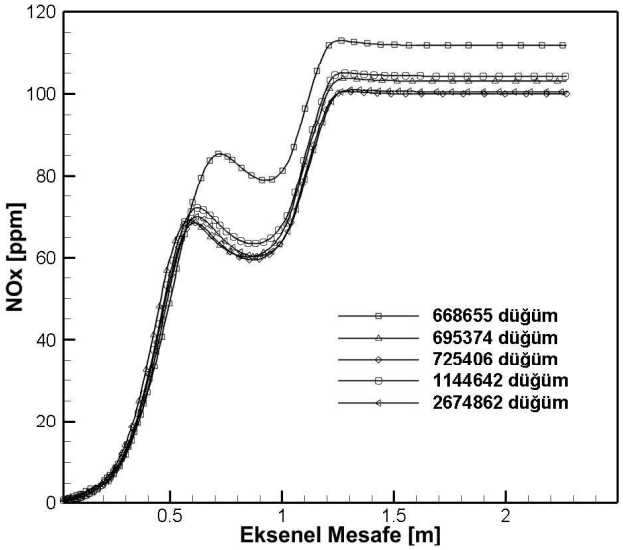
Şekil 2. 2.80 m kazan uzunluğu için test kazanının akış hacmi, brülör yakıt borusu, nozullar, girdap üreteci ve diskinin görselleri.

Brülör kazan için oluşturulmuş sayısal ağ Şekil 3'te gösterilmiştir. Kazan ve brülörün tam ve periyodik olarak modellenmesi için brülör ve kazan geometrileri her iki model için hazırlanmıştır. Toplam ağ sayısını azaltmak için periyodik model (1/4 model) kullanılmıştır [16].



Şekil 3. Brülör geometrisine (üst) ve kazan dâhil tüm hacme ait ağ yapısı (alt)

Yapılan çözümlerin ağdan bağımsızlığını ortaya koymak amacıyla 5 farklı düğüm sayısında (668655, 695374, 725406, 114642 ve 2674862) sayısal ağlar oluşturulmuştur. Farklı düğüm sayılarında yapılan çözümlerde kazan çıkışında elde edilen NOx emisyon sonuçları kazan eksen çizgisi üzerinde Şekil 4 'te karşılaştırılmıştır [16].



Şekil 4. Farklı düğüm sayılarında kazan eksen düzlemindeki NOx emisyon değişimleri [17]

Şekil 4 yardımıyla eksenel mesafesi üzerindeki NOx emisyonlarının değişimi incelendiğinde ise düğüm sayısının NOx seviyeleri üzerindeki etkisi daha belirgindir. Bu farkın sebebi NOx emisyonlarının sıcaklık seviyesine karşı çok hassas olması ve sıcaklıklar arasındaki küçük bir farkın NOx seviyelerinde belirgin bir sapmaya neden olduğudur. Buna rağmen 695374, 725406 ve 114642 düğüm sayılarında NOx seviyeleri birbirine yakın değerler almaktadır. Mesh bağımsızlığı çalışmasında 725406 ve 1144642 düğüm sayılarıyla periyodik modelleme ile doğal gaz yanması sonuçları karşılaştırıldığında NOx emisyonları bakımından standart sapmanın %1 'in altında olduğu hesaplanmıştır. Düşük düğüm sayısında ağ ile çalışmak, hem çözücü performansı hem de çözüm süresi üzerinde etkili olması dolayısıyla düğüm sayısı olarak periyodik model için 725406 düğüm sayısı tercih edilmiştir [16].

3.4 Fiziksel Özellikler, Sınır Şartları ve Çözüm Metodu

Bu çalışmada sayısal analiz ve hesaplamalar için NOx hesaplama modülünü de bünyesinde barındırılan, kapsamlı bir CFD uygulama alanına sahip ANSYS Fluent 16 [9] programı seçilmiştir. Brülör girişinde yakıt ve hava hızlarıyla yapılan hesaplamalarda Mach sayısının 0.2'den küçük olması nedeniyle, brülör girişlerinde, yoğunluk sıkıştırılamaz ideal gaz varsayımı yapılmış ve türlerin yoğunluğu belirlenmiştir [18].

Doğal gaz-hidrojen karışımları için soğurma (emilim) katsayısı, doğal gaz-hidrojen yakıt karışımları için 0.5, saf hidrojen için 0.45 alınmış, saçılma katsayıları da bu yakıtlar için 0.01 m^{-1} olarak seçilmiştir [19]. Ayrıca, doğal gaz ve metan soğurma katsayıları için Wsggm-domain-based kullanılmışken, her iki durumda da kullanılan saçılma katsayıları ise 1e-09 alınmıştır [20]. Brülör giriş sınır şartları olarak genellikle kütlesel debi kullanılmış, kazan çıkışı için basınç çıkışı sınır koşulları tanımlanmıştır [16].

Bu çalışmada kullanılan brülörde düşük girdap sayısı (S <0.5) söz konusu olması dolayısıyla, türbülans modellerinin karşılaştırılması dışındaki yanma modellerinin karşılaştırılmasında Realizable k-ε türbülans modeli kullanılmıştır [16]. P1, Rosseland, Discrete Ordinates (DO) ve Discrete Transfer (DTRM) modelleri arasında uygun olan radyasyon modelini seçmek için optik kalınlık aL güzel bir ipucudur. Burada a soğurma

(emilim) katsayısı, L ise uzunluk ölçeğidir. Brülör-kazan uygulamalarında, L yanma odası (ocak) çapına eşit alınır. P1 modeli $aL > 1$ uygulamalarında, Rosseland modeli $aL \gg 1$ uygulamalarında kullanılması önerilirken, $aL < 1$ uygulamaları için DTRM ve DO modellerinin kullanılması daha elverişlidir ve önerilmektedir [21]. DO modelinin kullanımı yüksek hesaplama maliyeti ve işlemci yoğunluğu gerektirse de, diğerlerinin yanı sıra dağınıklık (Scattering), parçacık etkisi, yarı şeffaf duvarlar, speküler duvarlar, gri olmayan radyasyon ve yerel ısı kaynakları uygulamalarında kullanılabilir olması gibi birçok avantajdan dolayı tercih edilebilir [22]. Tüm bu avantajları yanında aL < 1 olması dolayısıyla radyasyon hesaplamaları için DO modeli (aL <1) kullanılmıştır [16].

Akış alanındaki girdaptan veya dönmeden kaynaklanan yüksek dereceli dönme akışı eksenel ve radyal yönde büyük basınç gradyenlerinin meydana gelmesine neden olur. Bu tür akışlar çözüm sürecinde istikrarsızlıklara neden olabilir ve akışın tam modellenememesi veya çözümün yakınsayamamasına neden olabilir. Dönme akışlarında yer alan basınç gradyanlarının tespit edilip modellenebilmesi için çok uygun bir yöntem olan PRESTO!, girdaplı ve dönme akışları için bir çözüm stratejisi ortaya koyabilmektedir [19]. Bu çalışmada üç boyutlu akış alanını ayrıklaştırmak için PRESTO! yöntemi tercih edilmiştir. Basınç ve hız çifti için de COUPLED yöntemi kullanılmıştır. Akış alanının fiziğini tanımlamak için, daimi şartlar altında Reynolds ortalama Navier-Stokes denklemleri kütle, momentum, enerji ve skalar taşınımı için kullanılmıştır [16].

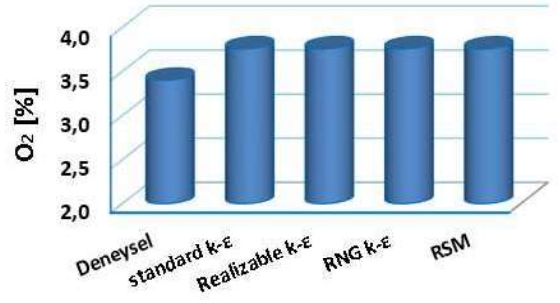
4 DENEYSEL VE HAD SONUÇLARIN KARŞILAŞTIRILMASI

Bu bölümde verilen ilk verilerde türbülans modellerinden en yaygın kullanılan 4 yöntem ile ilgili HAD analizlerinin sonuçları deneysel sonuçlar ile karşılaştırılmıştır. Bu modellerin kullanılmasıyla yanma ve emisyonların değişimi incelenmiştir. Sonrasında faklı yanma modelleri ile ilgili HAD analizleri sonuçları yine deneysel sonuçlar ile birlikte verilmiştir. Elde edilen tüm sonuçlar ışığında doğal gazın modellenmesinde en uygun türbülans ve yanma modelleri belirlenmiştir [16].

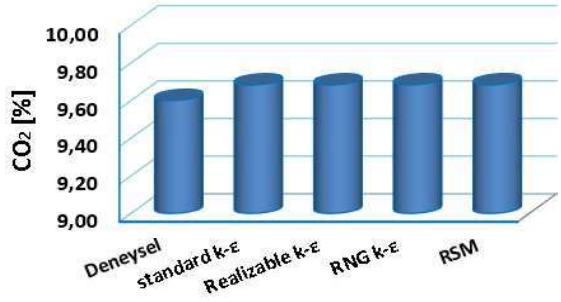
4.1 Türbülans Modellerinin İncelenmesi

HAD simülasyonunda yanmanın doğru bir şekilde modellenebilmesi için gerekli koşullardan biri olan doğru türbülans modelinin seçilmesidir. Bu seçim HAD analizlerin doğruluğu ve güvenirliği bakımından son derece önemlidir.

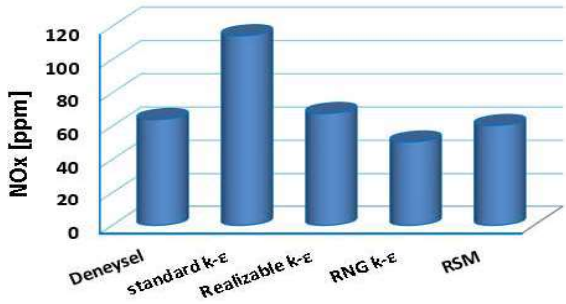
Farklı türbülans modellerinin sıcaklık ve NOx emisyonları kazan egzozu çıkışındaki etkileri Şekil 5'te verilmiş ve sonuçlar karşılaştırılmıştır. Yapılan inceleme de deneysel çalışmada ölçülen %CO_2 ve %O_2 seviyeleri HAD simülasyonlarından daha düşük değerler almakta ve bu değer farkı yaklaşık olarak CO_2 için %8, O_2 için de %10.5 civarında çıkmaktadır (Şekil 5(a),(b)). Ayrıca kullanılan türbülans modellerinin CO_2 ve O2 seviyeleri üzerinde kayda değer bir fark yaratmadığı görülmektedir. Son olarak deneysel çalışmada ölçülen NOx seviyesi ile farklı türbülans modellerinin kullanılmasıyla hesaplanan NOx seviyeleri Şekil 5(c)'de görülmektedir. Yapılan incelemede Standard k-ε modeli NOx seviyesini deneysel sonuçtan ve diğer tüm modellerden daha yüksek tahmin etmekte, hesaplanan değerin deneysel modele göre hata oranı %78.6 olduğu belirlenmiştir. Realizable k-ε model sonucu ise deneysel model ile iyi bir uyum sergilemekte ve hata oranı %5.2 seviesinde kalmaktadır. RSM model sonucu ise Realizable k-ε model sonucundan sonra en iyi ikinci sonuçtur ve hata oranı %5.6'dır. RNG k-ε modeli ise NOx emisyonu Realizable ve RSM modellerinden daha düşük hesaplamakta ve bu modelin hata oranı %21 olarak hesaplanmıştır. Bu sonuçlardan da görüleceği üzere düşük girdap sayısında S < 0.5, Realizable k-ε modeli RNG k-ε ve Standard k-ε modellerinden daha iyi emisyon sonucu vermektedir. Her ne kadar RSM modeli yüksek girdap sayısında (S > 0.5) kullanılması önerilse de düşük girdap sayılarında da iyi sonuçlar verdiği görülmektedir. Analizlerin yakınsayabilmesi ve deneysel sonuçlarla olan uyumu dolayısıyla Realizable k-ε modelinin tüm analizler için iyi bir seçenek olduğu görülmektedir [16].



(a)



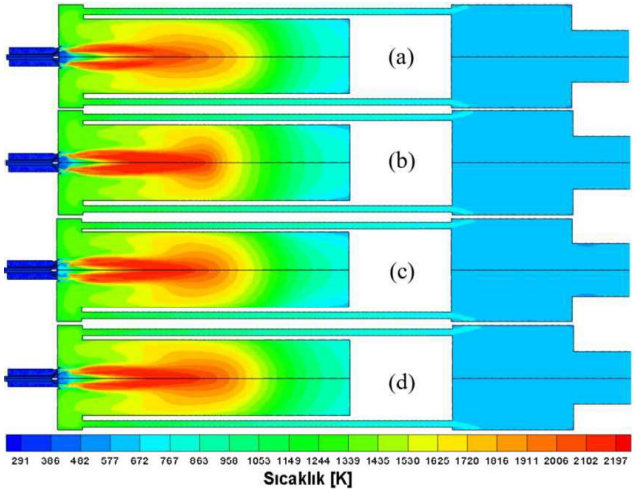
(b)



(c)

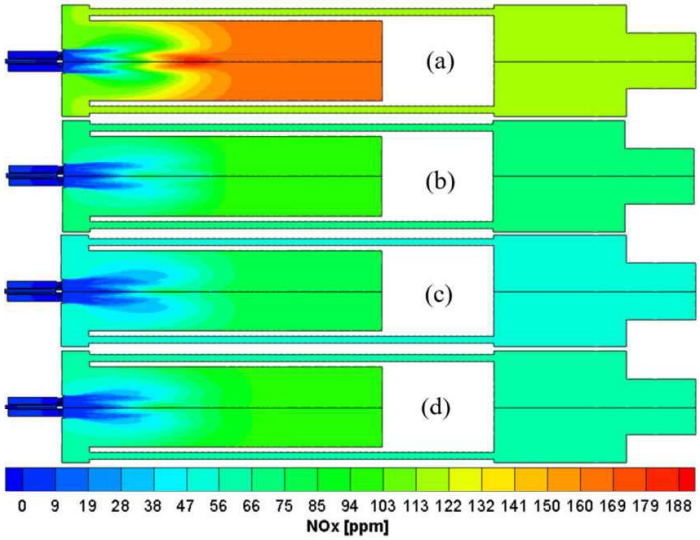
Şekil 5. Deneysel ve farklı türbülans modellerinin kullanıldığı HAD simülasyonlarında sıcaklık (a) ve CO_2 (b) emisyonlarının karşılaştırılması

Şekil 6'da dört farklı türbülans modelinin kullanılmasıyla kazan içerisinde oluşan sıcaklık dağılımları görülmektedir. Yapılan incelemede Realizable $k-\varepsilon$ modeli dışındaki türbülans modellerinde alev formları birbirine çok benzemekte ve alevler ocak içerisinde yayılmaktadır. Realizable $k-\varepsilon$ modelinde ise alev sonunda alev daha dairesel bir form almaktadır. Yanma sırasında en yüksek sıcaklık değeri Standard $k-\varepsilon$ modelinde (2196.28 K) oluşurken, en düşük maksimum sıcaklık değeri RSM modeli (2163.77 K) ile oluşmaktadır. Realizable ve RNG $k-\varepsilon$ modellerinde ise yaklaşık olarak aynı maksimum sıcaklık değerleri (2173 K) elde edilmiştir. En uzun alev formu RSM modeli ile oluşurken en kısa form Realizable $k-\varepsilon$ modelinin kullanılmasıyla oluşur. Alev çapları ise birbirne yakın değerler almaktadır. Her bir modelde kazan çıkışına doğru sıcaklıkların düştüğü görülmektedir [16].



Şekil 6. (a) Standard $k-\varepsilon$, (b) Realizable $k-\varepsilon$, (c) RNG $k-\varepsilon$ ve (d) RSM tübülans modellerinin kullanılmasıyla kazan eksen düzleminde oluşan sıcaklıklar

Şekil 7'de dört farklı türbülans modelinin kullanılmasıyla NOx emisyon oluşumları aynı skala üzerinde karşılaştırılmıştır. Şekiller incelendiğinde en yüksek NOx seviyesinin Standard $k-\varepsilon$ modelinin kullanılmasıyla oluştuğu, en düşük değerlerin de RNG $k-\varepsilon$ modeli ile oluştuğu görülmektedir. Bu durumda kullanılan türbülans modelleriyle ocak içerisinde oluşan maksimum alev sıcaklıklarının NOx üzerinde etkili olduğu fakat tek etken olmadığı görülmektedir. Çünkü Realizable ve RNG $k-\varepsilon$ modellerinde maksimum alev sıcaklıkları aynı değerleri alırken NOx değerleri arasında 17 ppm'lik bir fark oluşmaktadır [16].



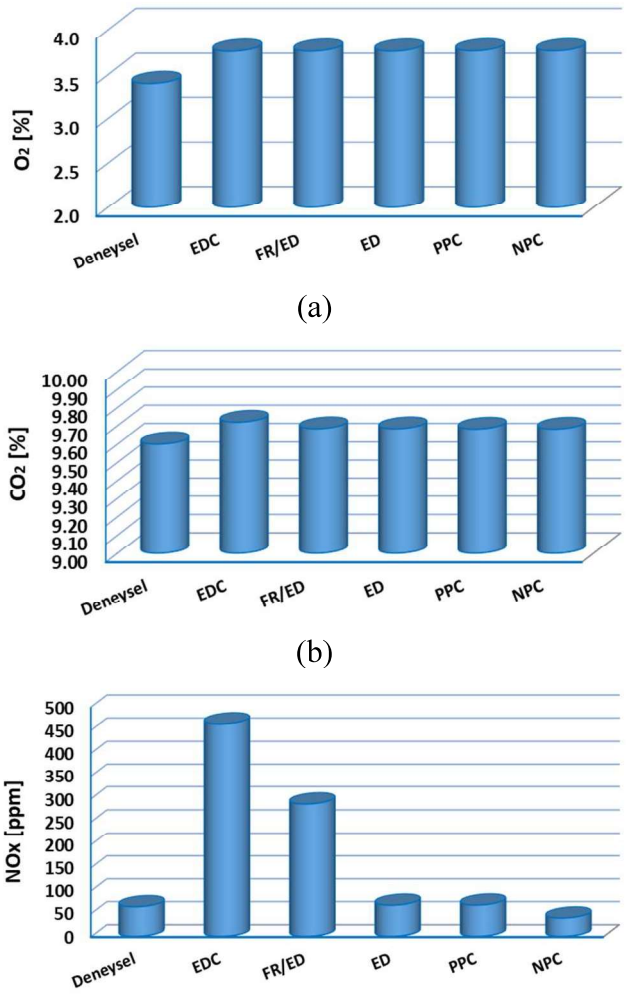
Şekil 7. (a) Standard $k-\varepsilon$, (b) Realizable $k-\varepsilon$, (c) RNG $k-\varepsilon$ ve (d) RSM) türbülans

modellerinin kullanılmasıyla kazan eksen düzleminde oluşan NOx emisyonları

4.2 Yanma Modellerinin İncelenmesi

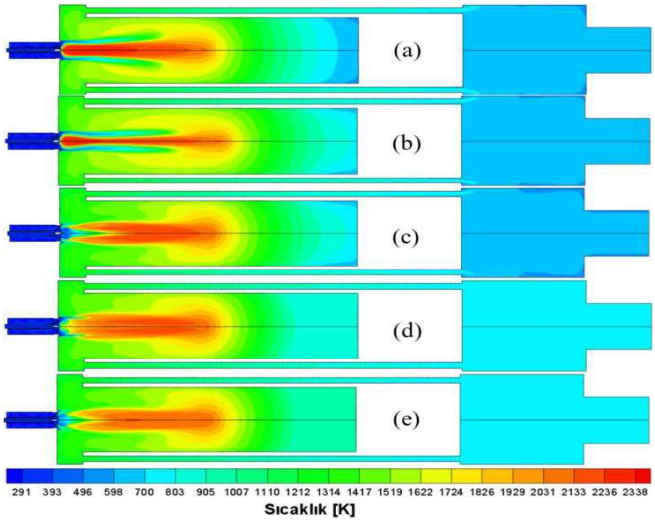
HAD analizleri için ANSYS Fluent yazılımında birden çok yanma modeli mevcuttur ve bunların seçimi yakıt-oksitleyici karışım şekli, laminer ve türbülanslı alevler, yakıtın hızlı yanma eğilimi, reaksiyonun hızlı gelişip gelişemeyeceği ve kullanılan kimyasal kinetik mekanizmasına bağlıdır. ANSYS Fluent yazılımında bulunan EDC, FR/ED, ED, PPC ve NPC yanma modelleri ile doğal gaz karışımı, 1085 kW brülör ısıl yükünde λ=1.2 hava fazlalık değeri için 2.1 m kazan ocak uzunluğunda ve 0.58 m ocak çapında Realizable $k-\varepsilon$ türbülans modeli kullanılarak modellenmiştir. Yapılan simülasyonlar sonucunda kazan çıkışı gaz emisyon sonuçları deneysel sonuçlar ile karşılaştırılmıştır [16].

Şekil 8 (a)'da % O_2 miktarını, Şekil 8(b)'de yanma sonu gazlarındaki % CO_2 miktarını göstermektedir. Grafikler incelendiğinde her iki türün HAD simülasyon sonuçları deneysel sonuçlardan daha yüksek oldukları görülmektedir. Sonuçlar arası hata oranları CO_2 gazı için en fazla %1.76 ile EDC modeliyle ve O_2 gazı için en fazla % 7.44 ile NPC modeliyle oluşmaktadır. En önemli yanma emisyonlarından olan NOx'un gaz çıkışındaki seviyeleri Şekil 8(c)'de görülmektedir. Şekilden görüleceği üzere EDC ve FR/ED modelleri NOx seviyesini deneysel seviyeden oldukça yüksek tahmin etmişlerdir. Bu iki modelin hata oranları sırasıyla %611 ve %342,73'tür. Öte yandan NPC yanma modeli deney sonucu dâhil en düşük NOx tahmini gerçekleştirmiştir. Bu modelin deneysel sonuca göre hata oranı %39'dur. Deneysel çalışma şartlarında farklı yanma modelleriyle yapılan analizlerde NOx emisyonu bakımından deneysel sonuçlarla en uyumlu model ED ve PPC modelidir. Bu iki modelde hata oranları sırasıyla %3.66 ve % 4 'dir [16].



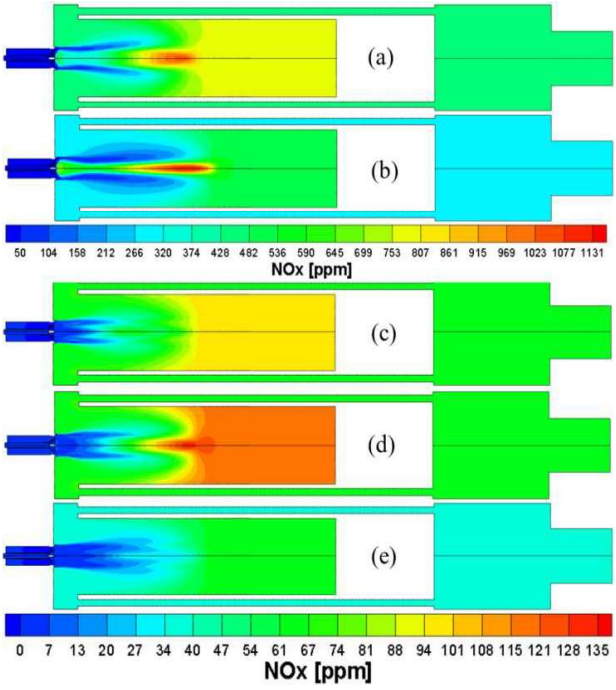
Şekil 8. Deneysel ve farklı yanma modellerinin kullanıldığı HAD simülasyonları için (a) sıcaklık ve yanma emisyonları (b) NOx, (c) CO_2, (d) O_2 ve (e) CO karşılaştırılması

Doğal gazın beş farklı yanma modeli ile modellenmesi sonucunda kazan içerisinde elde edilen sıcaklık dağılımları Şekil 9'da görselleştirilmiştir. Yapılan incelemede EDC ve FR/ED modellerinin kullanılmasıyla alev bölgesinde oluşan sıcaklıkların, ED, PPC ve NPC modellerine göre daha yüksek oldukları görülmektedir. Bunun nedeni EDC ve FR/ED modellerinde doğal gaz mekanizmasının (2 basamaklı uyarlanmış metan mekanizması) iki adımlı olması nedeniyle normal şartlarda oluşması beklenen birçok ara ürünün oluşumunu ihmal etmesi ve özgül ısıların olmasından daha yüksek değerde olmasıdır. Fakat ocak son kısmında ve kazan çıkış bölgesine PPC ve NP modellerinin kullanılmasıyla oluşan sıcaklıklar EDC, FR/ED ve ED modellerin kullanılmasıyla oluşan sıcaklıklardan daha yüksek değerler almaktadır [16].



Şekil 9. Farklı yanma modellerinin kullanılmasıyla ((a) EDC, (b) FR/ED, (c) ED, (d) PPC ve (e) NPC) kazan eksen düzleminde sıcaklık dağılımları

Şekil 10'da beş farklı yanma modeli ile modellenen doğal gazın yanması sonucu kazan boyunca oluşan NOx seviyesinin değişimini göstermektedir. EDC ve FR/ED yanma modellerinin kullanılmasıyla oluşan NOx seviyesi diğer modellerden çok daha yüksek olması nedeniyle iki farklı skala kullanılmıştır [16].



Şekil 10. Farklı yanma modellerinin kullanılmasıyla ((a) EDC, (b) FR/ED, (c) ED, (d) PPC ve (e) NP) kazan eksen düzleminde oluşan NOx dağılımları

Birinci skala yardımıyla EDC ve FR/ED modelleri kullanılmasıyla oluşan NOx değerleri karşılaştırılmış, ikinci skala yardımıyla da ED, PPC ve NPC modellerinde oluşan NOx emisyonları karşılaştırılmıştır. Şekiller incelendiğinde EDC, FR/ED ve kısmen PPC modelinde alev çekirdek bölgesinde NOx oluşumları görülebilmektedir. ED ve NPC modellerinde ise bu durum görülememektedir. Çekirdek bölgesi dışında NOx seviyeleri, bu bölgelerin daha düşük sıcaklıklarda olması ve NOx oluşum mekanizmalarının tamamlanması nedeniyle sabit değerlerde kaldıkları görülmektedir. Yapılan incelemede EDC modeli ile en yüksek NOx emisyonu oluşurken, en düşük NOx emisyonun da NPC modelinin kullanılmasıyla elde edildiği görülmektedir [16].

5 SONUÇLAR VE TARTIŞMA

Bu çalışmada 1085 kW brülör ısıl yükünde λ=1.2 hava fazlalık değerine sahip düşük girdap sayısına sahip bir brülörün bir doğal gaz kazanında doğalgaz yakılarak emisyon verileri elde edilmiştir. Aynı sistemin HAD yöntemi ile yapılan analizlerinde Standard $k-\varepsilon$, Realizable $k-\varepsilon$, RNG $k-\varepsilon$ ve RSM türbülans modelleri kullanılarak en uygun türbülans modelinin belirlenmesi hedeflenmiştir.

Ayrıca Eddy Dissipation Model (ED), Finite Rate/Eddy Dissipation (FR/ED), Eddy Dissipation Concenpt (EDC), Partial-Premix Combustion (PPC) ve Non-Premix Combustion (NPC) yanma modelleri ile de en uygun yanma modeli belirlenmeye çalışılmıştır. Yapılan HAD analizleri sonucunda elde edilen sonuçlar şu şekilde sıralanabilir:

- Dört farklı türbülans modeli ile yapılan sayısal analizler sonucunda, düşük girdap sayısındaki brülör ve kazanın modellenmesinde NOx tahmininde Realizable $k-\varepsilon$ modelinin en uygun türbülans modeli olduğu tespit edilmiştir.

- Dört farklı yanma modeli kullanılarak yapılan HAD analizleri sonucunda NOx deneysel verilerileriyle en iyi uyum sağlayan modelin Partial-Premix Combustion (PPC) modeli olduğu anlaşılmıştır.

- EDC ve FR/ED modellerinde kullanılan doğal gaz mekanizmasının iki adımlı olması nedeniyle normal şartlarda oluşması beklenen birçok ara ürünün oluşumunu ihmal etmesi ve özgül ısıların normalden daha yüksek değerde olmasından dolayı bu modellerle yapılan simülasyonlarda alevin çekirdek bölgesinde daha yüksek yanma sıcaklığına ulaştığı ve bu sebeple NOx değerlerinin deneysel sonuçlara göre çok daha yüksek çıktığı anlaşılmaktadır.

TEŞEKKÜR

Bu çalışma Yıldzı Teknik Üniversitesi Teknopark ve Termo-Heat Isı San.A.Ş tarafından desteklenen "Sanayi tipi brülör-kazan sisteminde yanma emisyonların incelenmesi " adlı Doktora Tezinden türetilmiştir. Her iki kuruma ve çalışanlarına teşekkür etmeyi bir borç biliriz.

REFERANSLAR

[1] Da Silva, C.V., Vielmo, H.A. ve Franca, F.H.R., (2006). "Numerical Simulation of the Combustion of Methane and Air in a Cylindrical Chamber", Therm. Eng., 5:13–21.

[2] Z. Ren, G.M. Goldin, V. Hiremath, S.B. Pope Simulations of a turbulent non-premixed flame using combined dimension reduction and tabulation for combustion chemistry Fuel., 105 (2013), pp. 636-644

[3] A. Frassoldati, P. Sharma, A. Cuoci, T. Faravelli, E. Ranzi Kinetic and fluid dynamics modeling of methane/hydrogen jet flames in diluted coflow. Appl. Therm. Eng., 30 (2010), pp. 376-383

[4] L. Ziani, A. Chaker, K. Chetehouna, A. Malek, B. Mahmah Numerical simulations of non-premixed turbulent combustion of CH4/H2 mixtures using the PDF approach Int. J. Hydrogen Energ., 38 (2013), pp. 8597-8603

[5] C. Pfeiler, H. Raupenstrauch Application of different turbulence models to study the effect of local anisotropy for a non-premixed piloted methane flame Comput-Aided Chem. Eng., 28 (2010), pp. 49-54

[6] W. Jerzak, M. Kuźnia Experimental study of impact of swirl number as well as oxygen and carbon dioxide content in natural gas combustion air on flame flashback and blow-off
J. Nat. Gas Sci. Eng., 29 (2016), pp. 46-54

[7] Termo-Heat Isı San Tic A.S.
https://www.ecostar.com.tr/
https://www.termo-heat.com/

[8] MS Cellek, A Pinarbasi, Effects Of Thermal Load And Excess Air Coefficient On Combustion Products In A Natural Gas-Fired Burner-Boiler, 5th International Conference On Advances In Mechanical Engineering, Istanbul, (2019).

[9] ANSYS Inc. (2015). ANSYS Fluent Theory Guide-Release 16.0, Canonsburg, USA.

[10] Fluent Inc., (2005). Fluent 6.2 User Guide, 2A.

[11] İ. Yılmaz, Model Bir Yakıcıda Hidrojen-Metan Karışımının Yanmasının Sayısal Ve Deneysel İncelenmesi, Doktora Tezi, Erciyes Üniversitesi Fen Bilimleri Enstitüsü, Kayseri, (2006).

[12] A. Bakker, Modeling Chemical Reactions with CFD, Reacting Flows - Lecture 10,http://www.bakker.org/dartmouth06/engs199/10-react.pdf, 30 Temmuz 2017.

[13] D.B. Spalding, Mixing And Chemical Reaction In Steady Confined Turbulent Flames, In 13th Symp. (Int'l.) on Combustion, 23-29 August (1970),University of Utah, Salt Lake City.

[14] F. Özdemir, Tunçbilek Termik Santrali'nin 5. Ünite Kazanındaki Alev Oluşumunun Sayısal Modellemesi, Yüksek Lisans Tezi, İTÜ Fen Bilimleri Enstitüsü, İstanbul, (2014).

[15] M.O Özçelik, Doğrudan Ateşlemeli, Kanatlı Borulu Isı Değiştiricinin Modellenmesi, Yüksek Lisans Tezi, İTÜ Fen Bilimleri Enstitüsü, İstanbul, (2012).

[16] MS Cellek, Sanayi tipi brülör kazan sisteminde yanma emisyonlarının incelenmesi,

Fen Bilimleri Enstitüsü, Doktora Tezi, YTU, 2017

[17] MS Cellek, A Pinarbasi, Investigations on performance and emission characteristics of an industrial low swirl burner while burning natural gas, methane, hydrogen-enriched natural gas and hydrogen as fuels, International Journal of Hydrogen Energy, (2018), 1194-1207.

[18] A. Colorado, ve V. McDonell, Prediction Of NOx Emissions From Premixed Natural Gas And Hydrogen Enriched Flames Stabilized With A Low-Swirl Burner", Fall Tech. Meet. West. States Sect. Combust. Institute, WSS/CI 2013 Fall Meet., Paper 084IC-0015, Colorado State University in Ford Collins, 7-8 October (2013), Colorado.

[19] M. Ilbas, The Effect Of Thermal Radiation And Radiation Models On Hydrogen-Hydrocarbon Combustion Modelling", Int. J. Hydrogen Energy, (2005) 30:1113–1126.

[20] ANSYS Inc., Tutorial: 2D Simulation of A 300 KW BERL Combustor Using the Magnussen Model, (2010).

[21] ANSYS Inc., ANSYS FLUENT Choosing a Radiation Model, https://www.sharcnet.ca/Software/Fluent6/html/ug/node583.htm, 28 Nisan 2016.

[22] Fluent Inc., (2005). Fluent 6.2 User Guide, 2B.

AĞIR HİZMET TİPİ BİR DİZEL MOTORDA DİZEL VE DOĞALGAZ KARIŞIMLARININ MOTOR PERFORMANSI VE EGZOZ EMİSYONLARI ÜZERİNE ETKİLERİNİN DENEYSEL İNCELENMESİ

Volkan Sabri KÜL[1] and Selahaddin Orhan AKANSU[2]

1. Makine Mühendisliği Bölümü, Erciyes Üniversitesi, Kayseri, Turkiye email: volkanskul@gmail.com
2. Makine Mühendisliği Bölümü, Erciyes Üniversitesi, Kayseri, Turkiye email: akansu@erciyes.edu.tr

Özet

Bu çalışmada, 11.670 cc motor hacmine sahip altı silindirli ağır hizmet tipi bir dizel motor, %35 dizel ve %65 doğal gaz karışımı ile çalıştırılmıştır. Maksimum yük altında yapılan deneylerde motor 660 d/d sabit motor devrinde çalıştırılmıştır. Doğal gaz, motor emme manifoldu vasıtasıyla 1,5 bar basınçta hava ile önceden karıştırılarak yanma odasına iletilmiştir. Motorun çift yakıtla sabit motor devrinde ve maksimum yük altında çalıştırılması sonucunda motor performansı ve egzoz emisyon değerleri incelenmiştir. Bu çalışmada elde edilen bilgilerin literatüre katkı sağlaması amaçlanmaktadır.

Anahtar Kelimeler: Dizel, Doğal Gaz, Çift Yakıt, CNG, Egzoz Emisyonları.

Abstract

In the present study, a six-cylinder heavy-duty type diesel engine with an engine displacement of 11,670 cc was powered by a mixture of 35% diesel and 65% natural gas. In the experiments carried out under the maximum load, the engine was operated at a constant engine speed of 660 rpm. Natural gas was conveyed to the combustion chamber as pre-mixed with together air via the engine intake manifold at 1.5 bar pressure. Engine performance and exhaust emission values were investigated as a result of running the engine with dual fuel at constant engine speed and under maximum load. It is aimed that the information obtained in the present study will contribute to the literature.

Keywords: Diesel, Natural Gas, Dual Fuel, CNG, Exhaust Emissions.

1 GİRİŞ

Dünyada artan enerji ihtiyacı ve petrol rezervlerinin azalması ulaşım ve taşımacılık alanlarında kullanılan araçlarda alternatif yakıtların kullanımı ihtiyacını doğurmuştur. Doğal gaz içten yanmalı motorlarda kullanılabilecek en iyi yakıtlar arasında ön plana çıkmaktadır. Doğal gaz, yüksek oktan sayına sahip olması ve doğal gaz kaynaklarının zenginliğinden dolayı alternatif yakıt olarak ön plana çıkmaktadır [1].

Bu çalışmada yakıt olarak önce %100dizel, daha sonra %35dizel - %65 doğal gaz (NG) karışımı kullanılmıştır. Deneyler 660 d/d sabit devirde maksimum tork olan 386 Nm'de gerçekleştirilmiştir. Doğal gaz 1,5 bar basınç ile emme manifoldundan hava ile ön karışımlı bir şekilde yanma odasına ulaştırılmıştır. Motor performans ve egzoz emisyon verileri ölçülerek doğal gaz karışımının performas ve egzoz emisyonlarına etkisi incelenmiştir.

2 YÖNTEM

Bu çalışmada motor testleri 11,670 cc motor hacmine sahip, altı silindirli dizel motor ile gerçekleştirilmiştir. **Tablo 1**'de test motorunun teknik özellikleri verilmiştir. Motor deneyler boyunca 660 d/d sabit motor hızında çalıştırılmıştır. 660 d/d'da motorun ürettiği maksimum tork 386 Nm olarak elde edilmiştir.

İlk olarak motor %100 dizel yakıt kullanılarak 660 d/d ve 386 Nm tork altında çalıştırılmış, motor performans ve egzoz emisyon değerleri ölçülüp kaydedilmiştir. Daha sonra motor emme manifoldundan hava ile beraber doğal gaz ön karışımlı olarak yanma odasına ulaştırlmıştır. %35 dizel - %65 doğal gaz yakıt karışımı kullanılrak motor yine aynı devir ve tork altında çalıştırılmış, performans ve egzoz emisyonları ölçülmüştür. Daha sonra iki durum karşılaştırmalı olarak değerlendirilmiştir.

Tablo 1. Test Motoru Özellikleri

Deney Motoru	NİSSAN PE6H ağır hizmet tipi dizel motor
Silindir çapı	133 mm
Silindir strok boyu	140 mm
Silindir sayısı	6
Motor hacmi	11670 L
Maksimum Güç	234 Hp
Maksimum Devir	2300 d/d
Sıkıştırma oranı	16.5
Enjeksiyon zamanı	16° KMA ÜÖN'dan önce
Enjeksiyon basıncı	200 kg/cm² (2850 psi)
Ateşleme sırası	1-4-2-6-3-5
Supap boşluğu (Soğuk)	Emme 0.4 mm, Egzoz. 0,4 mm

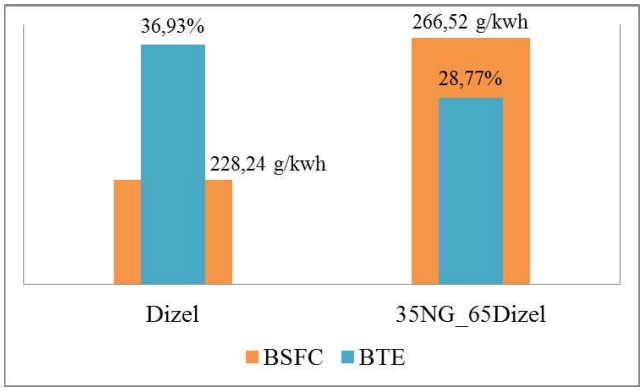


Şekil 1. Test Motoru

Yakıt tüketimi ölçümünde hassas terazi kullanılmıştır ve her 5 dk'da değer alınmıştır. Doğal gaz akış kontrolü için ALICAT marka kütle akış ölçer kullanılmıştır. Piston içi basınç ölçümü PCB 113B22 model silindir içi basınç sensörü ile yapılmıştır. Egzoz emisyon ölçümleri Bosch BEA 060 model analizör ile gerçekleştirilmiştir. Diğer motor performans verileri PCS marka motor test sistemi kullanılarak elde edilmiştir.

3 BULGULAR VE TARTIŞMA

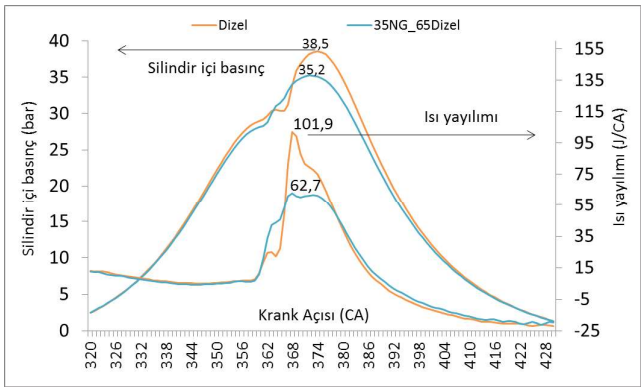
Fren termal verimi (BTE) ve Özgül yakıt tüketim (BSFC) değerleri **Şekil 2**'de verilmiştir. Çift yakıt ile çalışmada özgül yakıt tüketimi dizel yakıta kıyasla %16,8 oranında artış göstererek çift yakıt ile çalışma yakıt ekonomisi açısından kötüleşme göstermiştir. Bununla birlikte fren termal verimde %8,16 oranında düşüş göstermiştir. Çift yakıt ile çalışmada fren termal veriminin azalması ve özgül yakıt tüketimin artması yanmanın kötüleştiğini ve eksik yanma gerçekleştiğini göstermektedir. Doğal gaz yüksek oktan sayısına sahip olduğu için dizel yakıta göre yanmaya karşı daha dirençlidir [2]. Doğal gazın tam yanabilmesi için yakıtın yanma odasında yeterince süre gereklidir. Geç enjeksiyon başlama zamanı doğal gazın tam yanaması için silindir içerisinde yeterince kalmamasına neden olmuş ve bu durum Fren termal verini düşürmüştür [3]. Buna bağlı olarak özgül yakıt tüketimide artmıştır. Başka bir açıdan bakacak olursak doğal gaz ile yanmalarda sıkıştırma oranının artırılması özgül yakıt tüketimini düşürebilir ve fren termal verimini artırabilir [4] veya buji eklenerek doğal gazın tam yanması sağlanabilir fakat bu çalışmada amacımız buji kullanmadan çift yakıt ile verimli yanmayı araştırmaktır.



Şekil 2. BTE ve BSFC Değişimi

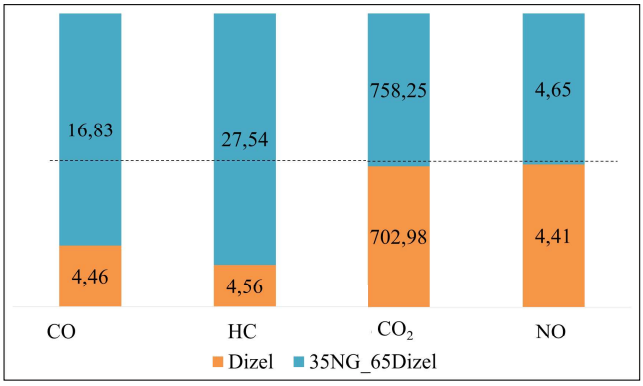
Şekil 3'te silindir içi basınç ve ısı yayılım değerleri gösterilmiştir. %35 dizel - %65 doğal gaz (35NG_65Dizel) yakıt karışımının silindir içi basıncı dizel yakıt yanmasına göre %8,6 daha azdır. Silindir içinde düşük basınç oluşması fren termal verimini ve özgül yakıt tüketimini kötüleştirmiştir. Genişleme zamanında çift yakıt yanmasının ısı yayılımı dizel yakıta göre daha fazladır. Bu durum çift yakıt ile yanmada geçikmiş yanma olduğunun göstergesidir [5]. Geç enjeksiyon başlama zamanı doğal gaz

karışımlı yakıtta geç yanmaya neden olduğu düşünülmektedir.

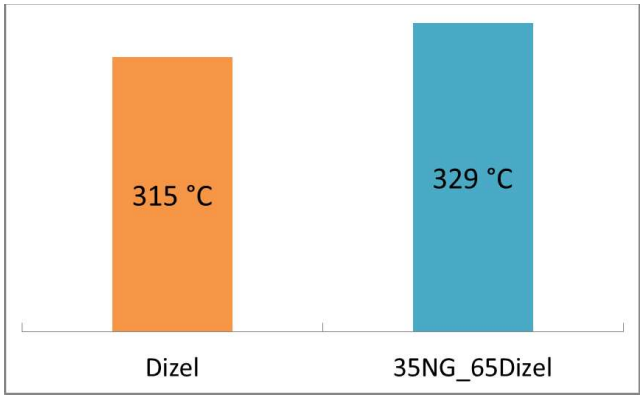


Şekil 3. Silindir İçi Basınç (bar) ve Isı Yayılımı (J/CA)

Şekil 4'te 660 d/d ve 386 Nm maksimum tork değerinde dizel ve %35Dizel - %65 Doğal gaz karışımlı yakıtların emisyon değerlerinin karşılaştırması verilmiştir. CO ve HC çift yakıtlı yanmada sırasıyla 12,37 ve 22,98 g/kwh artmıştır. Doğal gaz karışımlı yanmada yanma odasına giren yakıt miktarının tamamı yanmaya katılamamış ve egzozdan atılmıştır, böylece HC oranı dizel yakıt ile yanmaya göre artmıştır. Diğer bir taraftan doğlagaz karışımlı yanmada yanmanın eksik olmasından dolayı CO, CO_2'ye dönüşemeden egzozdan atılmıştır [6, 7]. Doğal gaz karışımlı yakıtta geç yanmanın oluşmasından dolayı HC ve CO miktarı dizele göre önemli miktarda artmıştır. Doğal gaz karışımlı yanmada dizel yakıta göre CO_2 ve NO sırasıyla %7,7 ve %5,4 oranında artış göstermiştir. **Şekil 5**'te görüldüğü gibi doğal gaz karışımlı yanmada egzoz sıcaklığı dizele göre 14°C daha fazladır. NO oranın doğal gaz karışımlı yanmada artmasına bu durumun neden olduğu düşünülmektedir. Doğal gaz karışımlı yanmada geç yanmanın oluşması egzoz sıcaklığını artmış olabileceği düşünülmektedir.



Şekil 4. Emisyon Değerleri (g/kwh)



Şekil 5. Egzoz Sıcaklığı (°C)

TEŞEKKÜR

Bu çalışma yapılırken daha önce FBG-2014-5234 proje numaralı destek ile alınan ekipmanlar kullanılmıştır, bu yüzden Erciyes Üniversitesi Bilimsel Araştırma Projeleri Birimi'ne ve deneylerde kullanılan CNG'nin (Sıkıştırılmış Doğal Gaz) tedariki konusunda desteklerini esirgemeyen Naturelgaz Sanayi Ve Ticaret A.Ş. ye çok teşekkür ederim.

REFERENCES

[1] Papagiannakis, R. G., Rakopoulos, C. D., Hountal as, D. T., & Rakopoulos, D. C. 2010. Emission characteristics of high speed, dual fuel, compression ignition engine operating in a wide range of natural gas/diesel fuel proportions. *Fuel*, 89(7), 1397-1406.

[2] Demirci, O. K. & Çınar, C. (2019). The Investigation of the Effects of Using Natural Gas on the Performance and Exhaust Emissions in an HCCI-DI Engine. *Gazi University Journal of Science* Part C: Design and Technology, 7 (2), 317-330.

[3] Meng, X., Tian, H., Long, W., Zhou, Y., Bi, M., Tian, J., & Lee, C. F. F. (2019). Experimental study of using additive in the pilot fuel on the performance and emission trade-offs in the diesel/CNG (methane emulated) dual-fuel combustion mode. *Applied Thermal Engineering*, 157, 113718.

[4] Singh, R., & Maji, S. (2012). Performance and exhaust gas emissions analysis of direct injection cng-diesel dual fuel engine.

International Journal of Engineering Science and Technology, 4(3), 833-846.

[5] Salvà, E. P, Gallo, W. L. R. (2013). Determination of the apparent heat release for diesel engine. *22nd International Congress of Mechanical Engineering* (COBEM 2013).

[6]Liu, J., Yang, F., Wang, H., Ouyang, M., & Hao, S. (2013). Effects of pilot fuel quantity on the emissions characteristics of a CNG/diesel dual fuel engine with optimized pilot injection timing. Applied Energy, 110, 201-206.

[7] Pulkrabek, W W. Engineering Fundamentals of the Internal Combustion Engines, Novi Bios, 2021.

EXPERIMENTAL INVESTIGATION OF DIESEL-BIODIESEL-ETHANOL BLENDS ON A COMPRESSION IGNITION ENGINE PERFORMANCE

F. Hamdi[1], I. Yahya[1], Z. Bouttar[1], R. Ennetta[1] and H.S. Soyhan[2]

1. Mechanical Modelling, Energy & Materials, National School of Engineers, Gabes University, Zrig, 6029, Gabes, Tunisia; email: ridha.ennetta@issig.rnu.tn
2. Mechanical Engineering Department, Engineering Faculty, Esentepe Campus, Sakarya University, Sakarya, 54187, Turkey; email: hsoyhan@sau.edu.tr

Abstract

The main objective of this research work is to study, experimentally, the mechanical and thermochemical characteristics of a compression ignition engine fuelled by diesel fuel and biodiesel mixture and then by diesel-biodiesel-ethanol mixture. The obtained results are compared with those of the engine fed by pure diesel fuel. This experimental investigation was carried out on a single cylinder four-stroke and air-cooled diesel engine under full load conditions.

Three fuel mixtures have been tested: pure diesel fuel (B0), 90% of diesel blended with 10% of biodiesel (B10) and a mixture constituted by 88.5% of pure diesel, 2.5% of ethanol and 10% of biodiesel (B10E2.5).

Biodiesel was produced by direct esterification of sunflower oil using microwave assisted heating reactor developed in our lab.

During the first step, we have investigated the effect of B10 on the engine performance and emissions, comparatively to B0.

Addition of biodiesel improved slightly the engine power (BP) with an average percentage of 6%. The brake mean effective pressure (BMEP) presented a remarkable increase at low and medium speeds which reached 16% compared to that given by B0. However, at high speeds this percentage decreased to about 4%.

The specific fuel consumption (SFC) of B10 showed a decrease compared to that given by B0 for a speed lower than 1400 rpm then this behaviour is reversed giving higher values when the engine speed is increased. The SFC rise for B10 reaches 40% at 2400 rpm.

The break thermal efficiency (BTE) obtained with B10 was higher than that of B0 for engine speeds lower than 1500 rpm but a decrease by about 10% has been observed beyond this speed.

Concerning the engine emissions, a significant improvement, compared to B0, has been noticed for B10, characterized by a decrease in exhaust gas temperature (EGT) which reached 20% at 2000 rpm; an important decrease in CO emission which exceeds 40% regardless the engine speed, a decrease in CO_2 with about 30% at low speeds and reaches 50% at high speeds, and finally a decrease in NOx emission varying from 34% to 46%.

In the second step, we have substituted 2.5% and 10% of pure diesel fuel by ethanol and biodiesel, respectively. The new mixture (B10E2.5) showed an improvement in the engine SFC, especially at low and medium speeds which reached 10% compared to B0. No change was observed in BP and its values were comparable to those given by B0. BMEP decreased comparatively to B10 but remained higher than that given by B0. Addition of ethanol improved the BTE by an increase of 5%.

Ethanol presence caused an increase in CO emissions at low speeds, but a significant decrease was observed at high speeds reaching 50% at 2500 rpm.

It is important to notice that the addition of ethanol gave the greatest CO_2 reduction at the whole speeds range which reached 60% at 2000 rpm. In addition, by adding ethanol, a significant decrease in NOx emissions was observed, especially at low and medium speeds. This reduction reached 70% at 2000 rpm compared to that given by B0.

Keywords: Diesel engine, biodiesel, Ethanol, Experimental study.

MICROWAVE-ASSISTED SYNTHESIS OF Pt/C CATALYST AT HIGH TEMPERATURES FOR PEM FUEL CELLS

Serkan KARADENİZ and Nezihe AYAS*

Department of Chemical Engineering, Faculty of Engineering, Eskisehir Technical University, Eskisehir, email: nazcan@eskisehir.edu.tr

Abstract

Parametric investigation on synthesis of Pt/C catalysts with Pt loading of 20% were carried out by microwave assisted polyol method. Commercial Vulcan XC-72 was selected as catalysts support material. A Teflon reaction vessel that is suitable for high pressure and temperature applications was used. Catalyst synthesis reactions were carried out at various temperatures (140-200 ^{o}C) that are higher than the normal boiling point of polyol mixture. The catalysts were characterized by X-ray diffraction analysis and Fourier transform infrared spectroscopy. XRD results show that size control of Pt nanoparticles was possible by controlling the reaction duration and temperature. FTIR spectra were recorded to investigate chemical interactions on the catalysts surface.

Keywords: PEM, Pt/C, Polyol, Microwave heating

1 INTRODUCTION

Proton Exchange Membrane fuel cells (PEMFC) has attracted great attention in the recent years due to their potential for wide range of applications ranging from small scale portable uses to large scale industrial areas. One of the main factors that affect the performance of a PEMFC is the electrocatalyst. Platinum (Pt) metal loaded on high surface area carbon material is the main type of catalyst used in PEMFC. Pt has the highest catalytic activity towards both oxygen reduction reaction and hydrogen oxidation reaction [1]. Due to its high cost, investigation of more efficient ways to utilize Pt has been an important topic of interest [2].

Vulcan XC-72 is one of the main types of carbon supports used for synthesis of Pt/C electrocatalysts due to its good electrical conductivity and high surface area [3].

One of the various methods for synthesis of Pt/C catalyst is the polyol method. In the polyol method, ethylene glycol (EG) is used as both solvent and reducing agent. The mechanism regarding the reduction of Pt and its deposition on carbon support is a well-studied topic [4].

In order to synthesize a Pt/C electrocatalyst with high dispersion and high surface area, many parameters of the polyol process can be controlled [5]. Another parameter affecting the polyol process is the method of heating. Two of the main ways for providing the energy required for synthesis reactions are conventional and microwave assisted heating.

Microwave assisted synthesis is an effective method that offers uniform and rapid heating of polyol mixture. As the polyol mixture is heated uniformly, Pt crystallizes faster and a more homogeneous nucleation occurs [3]. The polyol mixture is usually prepared by using EG-platinic acid and sodium hydroxide (NaOH) solutions. Depending on the concentration of NaOH solution, boiling point of the EG-NaOH mixture is lower than the boiling point of pure EG. This situation poses a challenge on working at high temperatures. By using a closed reaction vessel, it is possible to work on elevated temperatures that are higher than the mixture's boiling point under normal conditions.

Reaction temperature and duration have important roles in the nucleation process of Pt nanoparticles. If the reaction is allowed to continue for too long at high temperatures (overtime heating), coalescence of the formed particles can occur [6]. To achieve the ideal size distribution for Pt nanoparticles, reaction temperature and duration needs to be controlled.

In this study, Pt/C catalysts with 20% metal loadings were synthesized by microwave assisted polyol process. A closed reaction vessel was used to achieve elevated temperatures above the normal boiling point of the EG-platinic acid mixture. As the normal boiling point of this mixture was determined to be ~140 °C, effect of

various reaction temperatures in the range of 140-200 °C were studied.

2 EXPERIMENTAL

Analytical grade chemicals were used without any pre-treatment. Chloroplatinic acid hexahydrate (%99,95) was purchased from Erdes. Ethylene glycol was used as reducing agent and solvent for polyol process. NaOH pellets was used to prepare the 3 M NaOH aqueous solution. Concentrated hydrochloric acid (HCl) aqueous solution was used to prepare 1 M HCl solution. Vulcan XC-72 was used as the carbon support material.

2.1 Synthesis of Pt/C electrocatalysts

Vulcan XC-72 was used as carbon support and Chloroplatinic acid hexahydrate ($H_2PtCl_6.6H_2O$) was used as Pt precursor. Required amount of $H_2PtCl_6.6H_2O$ was added to 30 mL of EG and the mixture was magnetically stirred for 30 minutes. The pH was adjusted to 12 by using 3 M NaOH aqueous solution. EG-platinic acid mixture was transferred into a 100 mL modified PTFE (TFM, Milestone) reactor. Reactor was then sealed and placed into Milestone Start S microwave synthesis unit. Reactor's temperature was controlled by a thermocouple placed into the reactor via a thermowell. The mixture was heated to desired temperature by continuous microwave heating. A heating rate of 10 °C/min was used for all experiments. The mixture was held at desired temperature for 35 minutes. After that, mixture was left to cool down to 80 °C. Then the reactor was opened and calculated amount of Vulcan XC-72 was added to the mixture. Reactor was then sealed back and the mixture was held at 80 °C for 5 minutes under microwave heating. The reactor was re-opened and the pH of the mixture was adjusted to 2 by using 1 M HCl. The black mixture was then filtered, washed with deionized water and dried at 105 °C for 24 hours in an oven. Synthesized Pt/C catalyst was calcinated at 200 °C for 2 hours under N_2 atmosphere, as reported in literature [5], using a heating rate of 10 °C/min. Synthesized catalysts are denoted as Pt/C-T, where T is the reaction temperature in °C.

2.2 Physical Characterization

X-ray diffraction (XRD) patterns were recorded on a Rigaku XRD MiniFlex 600 using Cu Kα radiation, 5 °/min scan rate, step size of 0.02° in the range of 5° < 2θ < 85°. Debye-Scherrer equation was used to determine the crystallite size of Pt from XRD patterns. Debye-Scherrer equation is given as Equation 1, where D is the mean size of crystallite in nm, λ is the wavelength of X-ray, B is full width at half maximum of the peak broadening in radians, and θ is the angle of the peak.

$$D = (0.94\lambda) / (B\cos\theta) \quad (1)$$

Mean size of crystallites was calculated by using the Pt peaks of (111), (220) and (311).

Fourier transform infrared (FTIR) spectra of synthesized catalysts and Vulcan XC-72 were recorded using Thermo Fisher Scientific-Nicolet IS10 spectrometer in ATR mode. Spectra were recorded in the range of 650-4000 cm^{-1}, at 4 cm^{-1} resolution and 16 scans.

3 RESULTS AND DISCUSSION

Physical Characterization

XRD patterns of the synthesized Pt/C catalysts and Vulcan XC-72 are given in Figure 1. It was determined that the peak at 25° corresponds to (002) structure of the Vulcan XC-72. Peaks at 2θ=39°, 46°, 68° and 81° belong to Pt. These peaks are (111), (200), (220) and (311) diffraction peaks of face centred cubic Pt, respectively.

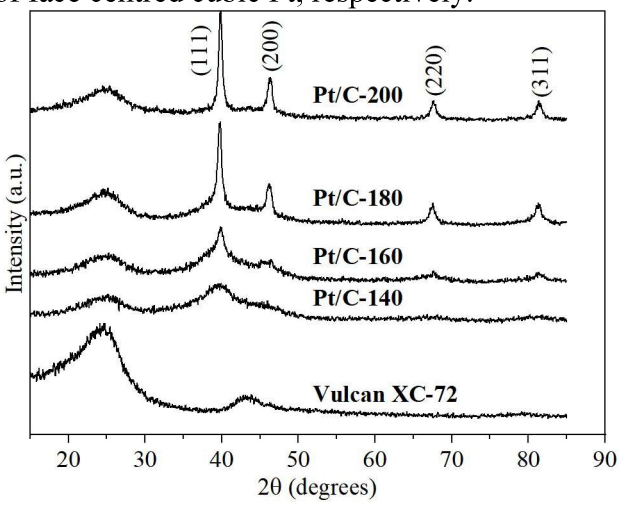


Figure 1. XRD patterns of Pt/C catalysts synthesized at different temperatures

Average crystallite sizes of Pt calculated from peaks of (111), (220) and (311) from XRD patterns are given in Table 1. Crystallite size of Pt/C-140 catalyst from (220) peak could not be calculated due to peak broadening.

Crystallite sizes of Pt/C electrocatalysts show a near-linear increase with reaction temperature. Pt/C-140 and Pt/C-160 have crystallite sizes of 1.95 and 4.98 nm respectively, which is in the ideal range of 2-5 nm. Pt/C-180 and Pt/C-200 have crystallite sizes of 10.82 and 13.20, which is

well above the ideal size range. Main cause of this result was determined to be overtime heating effect, which causes the formed Pt nanoparticles to coalesce as the synthesis reaction proceeds. This unwanted effect can possibly be eliminated by shortening the reaction duration.

Table 1. Average crystallite sizes calculated from XRD patterns of Pt/C

Temperature (°C)	**Crystallite Size (nm)**			**Average Crystallite Size (nm)**
	(111)	*(220)*	*(311)*	
140	1.83	-	2.07	1.95
160	5.00	2.29	7.66	4.98
180	12.19	9.97	10.30	10.82
200	16.10	11.75	11.76	13.20

Future works are planned on this topic, including experimental design studies to optimize electrocatalyst synthesis parameters at elevated temperatures.

FTIR spectra of synthesized Pt/C catalysts are given in Figure 2.

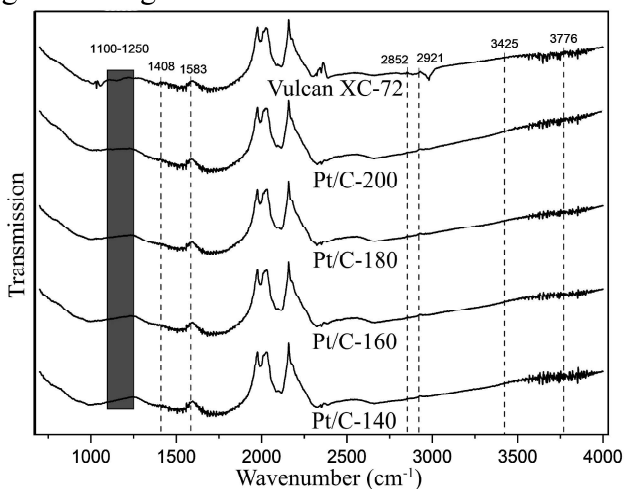


Figure 2. FTIR Spectra of Pt/C catalysts

In line with the data obtained from literature, vibrations at 1100-1250 band, 1583, 2852-2921 cm^{-1} are attributed to C-O, C=O, and C-H vibrations, respectively [5].

4 CONCLUSIONS

In this study the effect of working at elevated temperatures on the microwave assisted polyol method was studied. The crystallite sizes of the Pt/C increases with the increasing synthesis temperature. Various surface interactions on the Pt/C electrocatalysts were investigated and determined from FTIR spectra. Further study on this topic including experimental design and electrochemical activity tests to optimize working parameters of catalyst synthesis process is ongoing.

ACKNOWLEDGEMENTS

This study was supported by Eskisehir Technical University (ESTU) Scientific Research Projects Commission under grant no 21DRP140. The authors gratefully acknowledge ESTU Materials Science and Engineering Department for their equipment support during XRD analysis.

REFERENCES

[1] E. Zagoraiou, N. Shroti, and M. K. Daletou, "Development of Pt-Co catalysts supported on carbon nanotubes using the polyol method—tuning the conditions for optimum properties," *Mater. Today Chem.*, vol. 16, p. 100263, Jun. 2020, doi: 10.1016/j.mtchem.2020.100263.

[2] T. Lagarteira, S. Delgado, C. Fernandes, C. Azenha, C. Mateos-Pedrero, and A. Mendes, "The role of Pt loading on reduced graphene oxide support in the polyol synthesis of catalysts for oxygen reduction reaction," *Int. J. Hydrog. Energy*, vol. 45, no. 40, pp. 20594–20604, Aug. 2020, doi: 10.1016/j.ijhydene.2020.02.022.

[3] Y. Devrim, E. D. Arıca, and A. Albostan, "Graphene based catalyst supports for high temperature PEM fuel cell application," *Int. J. Hydrog. Energy*, vol. 43, no. 26, pp. 11820–11829, Jun. 2018, doi: 10.1016/j.ijhydene.2018.03.047.

[4] H.-S. Oh, J.-G. Oh, and H. Kim, "Modification of polyol process for synthesis of highly platinum loaded platinum–carbon catalysts for fuel cells," *J. Power Sources*, vol. 183, no. 2, pp. 600–603, Sep. 2008, doi: 10.1016/j.jpowsour.2008.05.070.

[5] J. Qi, L. Jiang, M. Jing, Q. Tang, and G. Sun, "Preparation of Pt/C via a polyol process – Investigation on carbon support adding sequence," *Int. J. Hydrog. Energy*, vol. 36, no. 17, pp. 10490–10501, Aug. 2011, doi: 10.1016/j.ijhydene.2011.06.022.

[6] Y. Li, X. Zhu, Y. Chen, S. Zhang, J. Li, and J. Liu, "Rapid synthesis of highly active Pt/C catalysts with various metal loadings from single batch platinum colloid," *J. Energy Chem.*, vol. 47, pp. 138–145, Aug. 2020, doi: 10.1016/j.jechem.2019.12.004.

[7] L. Pak Hoe, M. Boaventura, T. Lagarteira, L. Kee Shyuan, and A. Mendes, "Polyol synthesis of reduced graphene oxide supported platinum electrocatalysts for fuel cells: Effect of Pt

precursor, support oxidation level and pH," *Int. J. Hydrog. Energy*, vol. 43, no. 35, pp. 16998–17011, Aug. 2018, doi: 10.1016/j.ijhydene.2018.05.147.
[8] N. R. Elezović, B. M. Babić, N. V. Krstajić, L. M. Gajić-Krstajić, and Lj. M. Vračar, "Specificity of the UPD of H to the structure of highly dispersed Pt on carbon support," *Int. J. Hydrog. Energy*, vol. 32, no. 12, pp. 1991–1998, Aug. 2007, doi: 10.1016/j.ijhydene.2006.09.042.
[9] L. Calvillo, V. Celorrio, R. Moliner, A. B. Garcia, I. Caméan, and M. J. Lazaro, "Comparative study of Pt catalysts supported on different high conductive carbon materials for methanol and ethanol oxidation," *Electrochimica Acta*, vol. 102, pp. 19–27, Jul. 2013, doi: 10.1016/j.electacta.2013.03.192.
[10] S. Song, Y. Wang, and P. K. Shen, "Pulse-microwave assisted polyol synthesis of highly dispersed high loading Pt/C electrocatalyst for oxygen reduction reaction," *J. Power Sources*, vol. 170, no. 1, pp. 46–49, Jun. 2007, doi: 10.1016/j.jpowsour.2007.04.012.
[11] Z. Liu, L. Hong, M. P. Tham, T. H. Lim, and H. Jiang, "Nanostructured Pt/C and Pd/C catalysts for direct formic acid fuel cells," *J. Power Sources*, vol. 161, no. 2, pp. 831–835, Oct. 2006, doi: 10.1016/j.jpowsour.2006.05.052.
[12] J. Liu, J. Yin, B. Feng, F. Li, and F. Wang, "One-pot synthesis of unprotected PtPd nanoclusters with enhanced catalytic activity, durability, and methanol-tolerance for oxygen reduction reaction," *Appl. Surf. Sci.*, vol. 473, pp. 318–325, Apr. 2019, doi: 10.1016/j.apsusc.2018.12.072.

Influence of Two-Stage Fuel Injection Timing for Combustion and Emissions under Different Engine Loads in a Direct Injection Diesel Engine

H. Enes Fil[a], S. Orhan Akansu[a]

[a] Department of Mechanical Engineering, Engine Laboratory, Faculty of Engineering, Erciyes University, 38039 Kayseri, Turkey (E-mail: *h.enesfil@erciyes.edu.tr*)

Abstract

Population growth and the development of the world economy increase the demand for oil. This situation has led scientists to search for alternative fuels and new combustion technologies that reduce emissions. In this study, the effect of a two-stage injection system on engine performance and emissions was investigated. Experiments were carried out in a diesel engine with two cylinders, four strokes, and an injection system converted from a mechanical to a common rail type system. In the experiments, pure diesel fuel was used at three different loads (0%, 25%, and 50%) conditions and different first and second injection advances. Experimental results showed that the thermal efficiency was highest when the second injection advance was 351 CAD at all load conditions. It has been shown that CO emissions increase from 335 CAD, where the second injection time starts, to the last injection advance. While there is no significant change in HC emissions at 20 Nm load, but there is uncertainty at 10 Nm load. On the other hand, NO emissions decrease significantly as the second injection time closes to the TDC.

DESIGNING A NEW BELL-TYPE PRIMARY AIR NOZZLE FOR A LARGE-SCALE CIRCULATING FLUIDIZED BED BOILERS

Mustafa Metin Çam[1] , Cenk Çelik[2], Mansour Al Qubeissi [3] Hakan Serhad Soyhan [4],

1. TUBITAK Marmara Research Center, Gebze, Kocaeli, 41470, Turkey; email: metin.cam@tubitak.gov.tr
2. Department of Mechanical Engineering, Umuttepe Campus, Kocaeli University, Kocaeli, 41040, Turkey; email: cenkcelik@kocaeli.edu.tr
3. Faculty of Engineering, Environment and Computing, Coventry University, Coventry CV1 2JH, United Kingdom; email: ac1028@coventry.ac.uk
4. Department of Mechanical Engineering, Engineering Faculty, Esentepe Campus, Sakarya University, Sakarya 54050, Turkey; email: hsoyhan@sakarya.edu.tr

Abstract

Well-organized engineering systems are critical in terms of economic and environmental effects. Circulating Fluidized Bed (CFB) technology is one of them in clean energy productions. CFB boilers enable widely using solid fuel and operating low emission. Primary air nozzles are auxiliary equipment critical role in fluidizing that is combustion efficiency, and internal consumption of energy in CFB boiler. In nozzle designing, even a minor flaw can lead to undesirable consequences such as increasing pressure losses, nonuniform air distribution, and backflow of bed material. Therefore, they need to be designed wisely. Although, there are certain types of nozzles used for air distribution at the bottom of the CFB boilers, bell-type nozzles are commonly preferred. In this work, the bell-type primary nozzle used in the Turkish lignite-fired ÇAN Thermal Power Plant (CTPP), which has two 160 MWe CFB boilers, was taken as referenced. The bell-type primary air nozzle was newly designed through computational fluid dynamics (CFD). The inner head of the bell-type nozzle geometry was redesigned by opening slots, rather than existing holes. With the newly designed bell-type nozzle, the velocity at the outlet orifices was maintained and a decrease of 3.92 kPa was achieved in the total pressure loss. Hence, if it is used, the energy consumption of primary fans at full load in CTPP Unit I will be reduced by 20%, resulting in 3.1 GWh/year savings in internal electricity consumption.

Keywords: Nozzle, Circulating fluidized bed, Computational fluid dynamics

1 INTRODUCTION

Fluidized bed technology is one of the most suitable combustion systems in terms of bringing lignite to energy production [1]. The most important advantage of fluidized bed combustion technology is that it enables low-calorific solid fuels such as lignite and bio-waste to be combust in high efficiency and low NOx and SO2 emission values, especially compared to the traditional pulverized combustion system [2,3]. Fluidized bed combustion system consist of three groups according to their working principle. In [4] these are;

- bubbling fluidized beds (BFB),
- circulating fluidized beds (CFB),
- pressurized fluidized beds (PFB).

CFB is the most widely used technology among them. In[5], it was stated that CFB boiler technology has been developed considerably over the past 20 years, its installed power capacities were increased up to 600 MWe in a single unit, and its use has increased rapidly in the world.

In CFB boilers, about 40-60% of the total combustion air, which is primary air, is fed from the bottom part of the combustion chamber by the air distributor grate and the remaining air (secondary air) is fed from an upper level of the air distributor grate [6].

CFB boiler's air grate main purpose is to distribute the primary air uniformly in the combustion chamber. Therefore, its design has great importance in terms of combustion efficiency in the CFB boilers. Due to the defects of distributor grate

design, many problems may be occurring in the boiler operation. The common problems are;

- nonuniform fluidization,
- pressure drop increasing,
- plugging and breaking,
- backflow of bed material,
- shortening of service life,
- abrasion of solid particles in the bed [7].

There are three different types of air distributor plate used in the fluidized bed boilers. These are;

- perforated plate,
- nozzle,
- scatter tube.

Nozzles is more safety design and commonly used as an air distributor in CFB boilers [8]. The minimum required pressure drop across the air distributor may vary depending on the nozzles structure, windbox geometry and characteristic feature of the CFB boiler [9].

While the low-pressure drop in the nozzle reduces the resistance against the backflow of the bed material into the windbox, the high-pressure drop increases the internal energy consumption due to the fan load. Internal energy consumption is a major cost factor in any process using fluidized beds and can sometimes eliminate the advantages of this type of combustion systems [10].

In the literature, there are very limited and specific studies on the primary air nozzle used in CFB boilers, and the results of some of them are mentioned as follows. For instances, Yang et al. [11] and Huang et al.[12] developed a new type of nozzle design sensitive to flow rate in their studies. By per-forming the performance tests in the experimental setup of the nozzle, the pressure drop characteristic curve depending on the flow rate was obtained. They stated that the new type nozzle has 60% less pressure drop compared to the standard bell-type air nozzle. However, they stated that the resistance of the nozzle against the main problems such as unbalanced air distribution, backflow to windbox, and material wear should be investigated with additional experimental and CFD analysis. In an-other study, Mirek [13] purposed to develop a new type of nozzle geometry through CFD analysis and an experimental approach for a 235 MWe CFB boiler. He designed the new type of nozzle geometry by targeting two basic criteria. The first criteria was to obtain a uniform gas velocity profile within the nozzle. The second criteria was to perform a geometric design that would resist the reverse direction of flow in the event of strong negative pressure. Thus, with the novel nozzle design achieved a 545 Pa in pressure drop improvement compared to the existing arrowhead nozzle in the CFB boiler. Omer and Weng [14] measured the pressure drop of each of 500 nozzles in a 105MWt CFB boiler and making the bed pressure drop map out in their study. Accordingly, the effect of non-uniform primary air distribution on the solid-gas mixture throughout the boiler was investigated by CFD modeling. It was stated that nozzles are subject to excessive wear and clogging, often in certain areas on the large-scale boiler bottom of the bed, causing non-uniform primary air distribution. Mirek and Klajny [15] stated that the backflow of the bed material into the air plenum was eliminated with the new type of nozzle developed instead of the arrow type nozzle used in the 466 MWe CFB boiler. The number of outlet orifices, which were two in the existed nozzle, were four in the new type of nozzle and obtained uniform air distribution in the nozzle by enhancing the inner geometry of the nozzle through CFD analysis. As a result of this study, while increasing the velocity outlet of the nozzle orifice from 64 m/s to 90 m/s, pressure drop and internal energy demand were the same as in the old primary air distribution system. In [16], the thermal efficiency has been increased from 86.4% to 91.8% using the new bell-type nozzle for a CFB boiler of steam capacity 220 tons/hour. The authors improved the novel bell-type nozzle geometry through CFD analysis. Hence, they provided an 18.9% improving in pressure drop compared to a conventional bell-type nozzle and making 66% upgrading in flow uniformity, and also preventing bed material back-flow by designing the orifices 30° downwards. Huang et al. [17]improved the design of the bell-type nozzle used in the air distributor of a 480 t/h CFB boiler through CFD analysis. Within the scope of the design, the risk of clogging was reduced by giving a special shape to the nozzle orifice outlet and thus the service life was extended.

In the abovementioned literature, there is research on the enhancement of the nozzle design and its effects on the CFB boilers. These studies are quite limited in the literature and vary according to the characteristic features of the CFB boilers. In this work, the bell-type primary air nozzle used in the 160 MWe CTPP CFB boiler is investigated. Firstly, the bell-type primary air nozzle is numerically modeled using commercial CFD software from

ANSYS Fluent®. Secondly, the model is validated by comparing the data measured in the CFB boiler unit under the same operational conditions. Then, primary air nozzle geometry was designed newly by opening 8 slots (instead of the original 16 holes) on the inner head in the model to minimize the pressure drop. Additionally, the effects newly designed nozzle on pressure and velocity profile were investigated with help of the CFD analysis. Finally, it was presented that the pressure drop at the bell-type primary air nozzle contributes to the CTPP Unit I in terms of electricity consumption.

2 METHODOLOGY

2.1 System definition

Çan Thermal Power Plant (CTPP) consists of two units, Unit I and Unit II the same technical specifications. The total electric power of units is 160 MWe capacity. Unit I is taken as a reference in this study. Unit I measure 50 m in height, 7.9 m in width, and 14.5 m in depth CFB boiler with a steam generation capacity of 462 tons/hour [18]. Further details of the CTPP are summarized in **Table 1**.

Table 1. Characteristic properties of CTPP Unit I.

Unit		
Power of electric	160	MWe
Efficiency, boiler	92	%
Fuel, lignite	130	tons/hour
Lignite, LHV	2900	kcal/kg
Furnace Bed Area		
Nozzle, type	bell-type	
Nozzles, pcs.	741	
Dense bed, floor area	49,6	m2
Dense bed, height	6,24	m
Dense bed, temp.	850	°C

The dense bed zone of the CFB boiler is conical in shape and expands upwards, its height 6.24 meters. Approximately 43% of the combustion air fed to the boiler is primary air and is fed from the bed floor. The remaining combustion air is secondary air fed to the system by air ducts at 2 levels, 1 and 5 meters respectively above the bed floor. While the unit is operating at 100 % capacity, the fresh air taken by the primary air fans first passes through the rotary type heat exchanger and the temperature of the air is increased about 287 °C. Then it transfers to the wind box located in the bottom part of the CFB boiler. Finally, primary air 69.2 kg/s feed to the CFB boiler through 741 nozzles located at the bottom of the combustion chamber.

The bell-type primary nozzles used for primary air distribution in CTPP boiler consist of three essential parts that can screw to each other. First part is a pipe connected to the bottom of the bed, 73 mm in diameter. Second part is inner head, 70 mm in diameter. Third part is cover, 150 mm in diameter. The inner head of the nozzle has 16 holes at two levels with a diameter of 12 mm, and there are eight orifices with a diameter of 20 mm on the cover as shown in **Fig.1.**

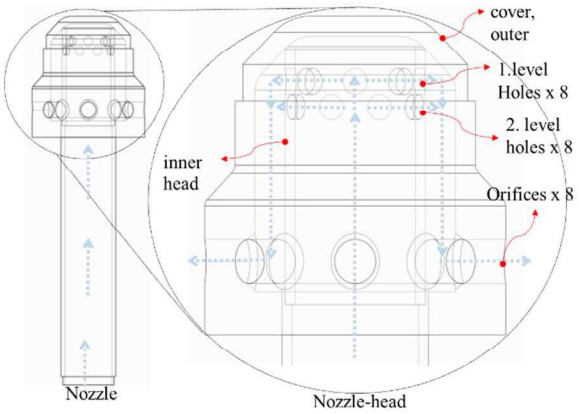


Fig. 1. Schematic diagram of the bell-type nozzle.

2.2 CFD Model

The bell-type nozzle was firstly drawn in 3D CAD software. After that, the 3D air-flow volume of the nozzle was generated. Then, boundary layers were defined such as mass flow inlet, pressure outlet, fluid, and wall surfaces on the airflow volume After that, this nozzle airflow volume was used in the FLUENT meshing tool for the meshing study.

The effect of the mesh numbers at the nozzle flow volume on the total pressure drop is as given in **Fig. 2.** Accordingly, When the numerical solution time and the rate of change in pressure drop is considered the number of 1753803 mesh elements might be acceptable for this study. For this reason, approximately this mesh number was taken as reference in all other numerical analyzes.

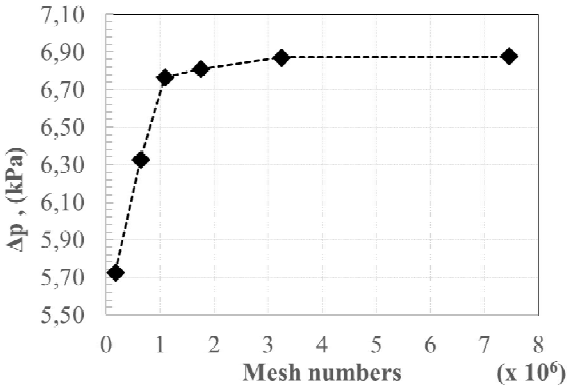


Fig. 2. Mesh independence study of the bell-type nozzle.

In the meantime, the polyhedral mesh was used in this mesh independence study because of providing good accuracy in a shorter time [19]. Inflation layer meshing was also applied to the boundary layer region with ten layers to capture the flow separation and pressure drop with sufficient number of polyhedral mesh elements.

2.3 Physical properties of the CFD model

In this work, k–ε turbulence model was used to analyze the problem. This model can be formulated with the equations given below, and the turbulence kinetic energy (k), turbulence dissipation rate (ε) can be calculated from these equations. At this equations, Gk represents the turbulent kinetic energy produced by the main velocity gradient and σk, σϵ are the turbulent Prandtls numbers. The model constants used in this equation are C1ϵ = 1,44, C2ϵ = 1,92, σk = 1,0, σk =1,3.

$$\nabla\rho k = \nabla \cdot \left[\left(\mu + \frac{\mu_t}{\sigma_k}\right) \cdot \nabla k\right] + G_k - \rho\varepsilon \qquad (1)$$

$$\nabla\rho\varepsilon = \nabla \cdot \left[\left(\mu + \frac{\mu_t}{\sigma_\varepsilon}\right) \cdot \nabla \varepsilon\right] + C_{1\varepsilon}\frac{\varepsilon}{k}G_k - C_{2\varepsilon}\rho\frac{\varepsilon^2}{k} \qquad (2)$$

Turbulent viscosity is expressed by the equation given below.

$$\mu_t = \rho C_\mu \frac{k^2}{\varepsilon} \qquad (3)$$

The difference of the Realizable k–ε model from the Standard and RNG k–ε model is that in turbulent viscosity balance, the C_μ coefficient is variable, not constant. The realizable k–ε model is suitable for flows at boundary conditions under strong pressure gradients and flows with separation and recombination [20].

Defined in the FLUENT solver that the flow rate entrance the nozzle is 0.0934 kg/s at the nominal load. In the model, air was selected as the fluid and air properties were entered temperature at 287° C, density ρ_a = 0.632 kg/m^3 and dynamic viscosity μ_a = 2.89E-05 Pa.s. Nozzle inlet section, "mass flow inlet" outlet sections, "pressure outlet" and all other surfaces were defined in the model as wall boundary condition. In the model, the hydraulic diameter was D and the turbulence density was estimated with values of 4.6%. The numerical algorithm was used Coupled. The second-order discretization was utilized in that it presents higher-order accuracy, especially for complex flows involving separation.

2.3 Validation of the CFD model

The characteristic working curve of the existed bell-type nozzle was derived through CFD analysis under the airflow rates corresponding to boiler loads. Accordingly, the effect of the inlet airflow rate on the pressure drop and orifices velocity outlet is given in **Fig. 3.**

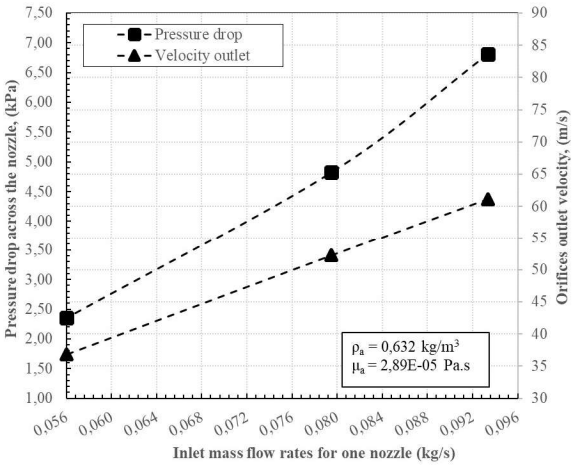


Fig. 3. Characteristic curve of the existed bell-type nozzle.

It is determined that the average pressure drop in the primary distribution nozzle grid obtained from on-site measurements under the same temperature and mass flow rates at the CTPP boiler operating full load validated the pressure loss value of 6.8 kPa obtained through CFD analysis.

3 RESULTS AND DISCUSSION

Design of the inner head holes of the bell-type air nozzle used in the CTPP boiler cause high velocity field and turbulence which increase the pressure drop in the nozzle. Therefore, the inner head holes

geometry has been changed to reduce the pressure drop at the nozzle and improve the velocity field in this study. Thus, the inner head of the nozzle is newly designed by opening 2x4 slots at 2 levels, 39 mm length and 12 mm diameter instead of 16 holes as seen in **Fig. 4.** After the airflow volume was extracted from the 3D newly designed solid model, performing mesh study and then pressure and velocity parameters were obtained through the CFD analysis.

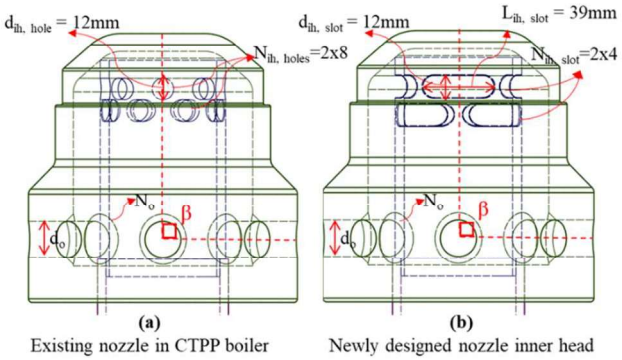


Fig. 4. Geometric view of the existed and newly designed bell-type nozzle.

As a result of CFD analysis, a comparative view of the pressure and velocity field contours of existing and newly designed nozzle models are given in **Figs. 5. and 6.** Accordingly, when the total pressure distribution contour is investigated, it is seen that pressure at the inner head of the bell-type air nozzle used in CTPP boiler is around 6.8 kPa. At the same time, it is seen that as the flow progresses from the nozzle arms to the orifice outlet, the pressure decreases and becomes zero at the orifice outlet. Additionally, it was determined that the pressure was very low in the upper wall of the orifice and in the near region. On the other hand, in the newly designed nozzle, the total pressure decreased by 2.9 kPa with the decrease of flow velocities at the outlet of the inner head slots.

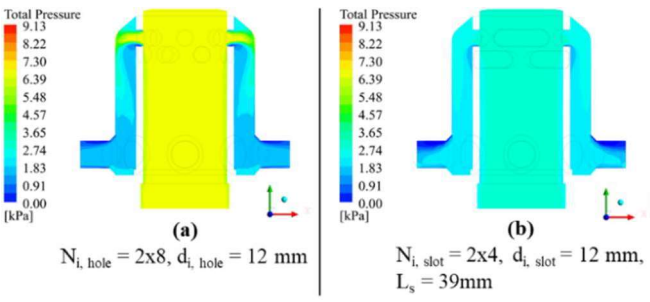


Fig. 5. Contours of total pressure distribution (a) existing nozzle in CTPP Boiler (100% load); (b) newly designed nozzle model (100%load).

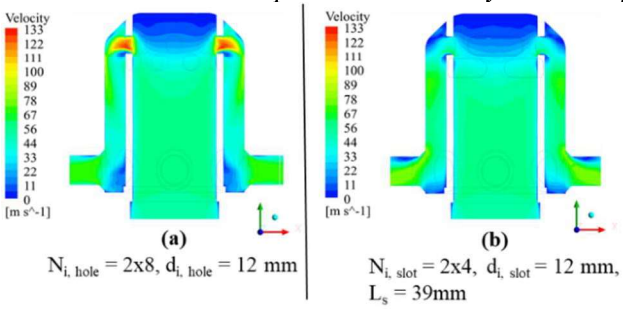


Fig. 6. Contours of velocity distribution (a) existing nozzle in CTPP Boiler (100% load); (b) newly designed nozzle model (100%load).

When the velocity field contour is examined, it has been determined that the flow velocity of the CTPP boiler's nozzle is around 129 m/s at the holes of inner head exit, while this value has decreased to 55 m/s in the new model. This resulted in a significant decrease in pressure loss. In the meanwhile, flow velocities are averaged 61 m/s at the orifice outlet of both nozzles. The dead zone was relatively reduced in the newly designed nozzle according to the existed nozzle, particularly in the regions close to the orifice entrance.

4 CONCLUSION

As stated in [21], a 1 kPa decrease in nozzle pressure drop in CTPP, will reduce the energy consumption in primary fans by 4.65%, and save 720,667 kWh/year of electricity consumption. With the newly designed bell-type nozzle model, it was achieved that, the pressure loss was reduced from 6.81 kPa to 2.89 kPa, while the velocity at the orifice outlet can be maintained at 61 m/s. Hence, the energy consumption in primary fans by 20% will decrease and save 3.1 GWh/year in internal electricity consumption at the CTPP Unit I at the full load. On the other hand, uniformity of velocity distribution at the orifice channel and lower limit of pressure drop at the distribution grate are critical for fluidizing and resist of backflow in boiler operation. Therefore, these parameters are needs to be also considered to enhance nozzle geometry.

REFERENCES

[1] Yue G, Cai R, Lu J, Zhang H. From a CFB reactor to a CFB boiler – The review of R&D progress of CFB coal combustion technology in China. *Powder Technology* 2017; 316:18–28.

[2] Li PW, Chyang CS, Ni HW. An experimental study of the effect of nitrogen origin on the

formation and reduction of NOx in fluidized-bed combustion. *Energy* 2018; 154:319–27.
[3] Ke X, Engblom M, Yang H, Brink A, Lyu JF, Zhang M, et al. Prediction and minimization of NOx emission in a circulating fluidized bed combustor: A comprehensive mathematical model for CFB combustion. *Fuel* 2022;309:122133.
[4] Arjunwadkar A, Basu P, Acharya B. A review of some operation and maintenance issues of CFBC boilers. *Appl. Therm. Eng.* 2016; 102:672–94.
[5] Huang Z, Deng L, Che D. Development and technical progress in large-scale circulat-ing fluidized bed boiler in China. *Front Energy 2020*; 14:699–714.
[6] Basu P, Nag PK. Heat transfer to walls of a circulating fluidized-bed furnace. *Chem Eng Sci* 1996; 51:1–26.
[7] Guo Q, Werther J, Hartge E-U. Investigation into maldistribution in a circulating fluidized bed. *China Particuology* 2003;1:145–50.
[8] Shukrie A, Anuar S, Oumer AN. Air distributor designs for fluidized bed combustors: A Review. Engineering, *Technology & Applied Science Research* 2016; 6:1029–1034.
[9] Vakhshouri K, Grace JR. Effects of the plenum chamber volume and distributor geometry on fluidized bed hydrodynamics. *Particuology* 2010;8:2–12.
[10] Basu P. Circulating Fluidized Bed Boilers Design. 1th ed. *Springer Cham* 2015.
[11] Yang HR, Huang ZM, Yue GX, Lu JF. Characteristics of a float nozzle designed for circulating fluidized bed boilers. *Chemical Engineering & Technology* 2007;30:1398–1400.
[12] Huang ZM, Yang HR, Liu Q, Wang Y, Lu JF, Yue GX. Characteristics of a modified bell jar nozzle designed for CFB boilers. *Proceedings of the 20th International Conference on Fluidized Bed Combustion* 2010; 492–495.
[13] Mirek P. Designing of primary air nozzles for large-scale CFB boilers in a combined numerical-experimental approach. *Chemical Engineering and Processing: Process Intensification* 2011; 50:694–701.
[14] Omer A, Weng M. Effect of primary air maldistribution due to nozzle wear on CFBC performance. *Fuel Processing Technology* 2018; 173:191–196.
[15] Mirek P, Klajny M. Air nozzle design criteria for protection against the backflow of solids in CFB boilers. *Applied Thermal Engineering* 2018; 141:503–515. 018.06.006.
[16] Liu X, Zhu G, Asim T, Zhang Y, Mishra R. The innovative design of air caps for improving the thermal efficiency of CFB boilers. *Energy* 2021; 221:119844.
[17] Huang Z, Deng L, Che D. Experimental and CFD simulation studies on bell-type air nozzles of CFB boilers. *Applied Sciences* 2019; 9: 3805.
[18] Gürel B. Designing particle and water natural circulation system for combustion low quality lignite in the circulating fluidized bed boiler (CFBB) and investigation of the combustion characteristics (Ph.D. Thesis). *Süleyman Demirel University, Institute of Science and Technology* 2018.
[19] Zhang H, Tang S, Yue H, Wu K, Zhu Y, Liu C, Liang B, Li C. Comparison of computational fluid dynamic simulation of a stirred tank with polyhedral and tetrahedral meshes. *Iranian Journal of Chemistry and Chemical Engineering* 2020;39:311–319.
[20] Ansys I. Ansys Fluent Theory Guide. In: Ansys I, ed. 15.0 ed. *The United States of America*; 2013.
[21]Çam MM, Cenk Ç, Türkmen AC. Numerical investigation of the effect of nozzle design on pressure loss and energy consumption in a circulating fluidized bed boiler. *23rd congress on thermal science and technology*, GAZİANTEP, 2021; 951-960.

EVALUATİON OF THE EFFECT OF SYSTEM PARAMETERS ON HYDROGEN PRODUCTION IN STEAM-METHANE REFORMERS

Kubilay BAYRAMOĞLU[1], Can COSKUN[2], Zuhal OKTAY COSKUN[3]

1. Bulent Ecevit University, Department of Marine Engineering, Zonguldak; email: kubilay.bayramoglu@beun.edu.tr
2. Izmir Democracy University, Department of Mechanical Engineering, Izmir; email: can.coskun@idu.edu.tr
3. Izmir Democracy University, Department of Mechanical Engineering, Izmir; email: zuhal.oktay@idu.edu.tr

Abstract

Variable renewable energy sources are used to minimize unwanted gases such as CO_2, NO_X and hydrocarbons, which are formed as a result of the combustion of fossil fuels. In recent years, the use of hydrogen as a fuel has increased its importance due to the absence of carbon atoms in its structure and its high combustion potential. However, hydrogen cannot be used sufficiently because it is not found in pure form in nature and it is difficult to store. In this study, the production of hydrogen by steam-methane reformer with exhaust waste heat was evaluated numerically. In the study, the effect of thermal conditions such as different exhaust temperatures, variable methane-vapor gas mixture temperatures and on the hydrogen production of both exhaust and methane-water vapor mixture at variable velocity were evaluated. Finally, the effect of variable steam/methane ratio on hydrogen production was evaluated parametrically. The study was carried out in steady-state conditions with the computational fluid dynamics method. As a result of the study, it was determined that the hydrogen production increased with increasing temperature, but the increasing flow rate decreased the hydrogen production. Increasing steam-methane ratio also increases hydrogen production. In parametric studies, the amount of hydrogen formation was increased up to about 2000 ppm.

Keywords: Hydrogen production, Waste heat, Methane-steam reformer, Sustainability, Combustion, Chemical kinetics

1 INTRODUCTION

Climate change has become a major concern in recent years. Climate change is generally caused by harmful gases resulting from combustion. In order to reduce harmful gases, the parties signed the Kyoto Protocol [1] and the Paris agreement [2]. Today, approximately 81% of fossil fuels are used in power generation machinery, while renewable energy sources such as biogas, biofuels, nuclear, solar, water and wind are used at a rate of 19% [3]. In recent years, the use of hydrogen as a renewable energy carrier has increased its importance to reduce emissions and increase the power obtained. The use of hydrogen does not cause CO_2 emissions due to the absence of carbon atoms in its structure, and it is also more advantageous than traditional fuels thanks to its high combustion energy and low ignition temperature [4-5]. Hydrogen is not found in nature as a fuel in its raw form. Therefore, for hydrogen to be used as a fuel, it must be produced with different techniques. The main ones of these techniques are to obtain hydrogen from biogas, methane or electrolysis [6-8). In recent years, different studies on obtaining hydrogen have been presented. Song et al. [9] proposed a new hydrogen production system called the electric, SMR (E-SMR) process, combining PTG technology with the traditional SMR process. Quirino et al. [10] applied a statistical approach based on experimental design and response surface methodology for a better understanding of reformer behaviour. Luo et al. [11] produced electricity by producing hydrogen through electrolysis with wind energy. Hasan and Genç, [12] conducted a cost analysis of producing hydrogen by electrolysis from solar and wind-assisted hybrid systems for different configurations.

In this study, the effects of different exhaust and reformer temperatures, velocity and H_2O/CH_4 ratios on hydrogen production with the help of waste heat recovery were evaluated. The study was carried out numerically as steady state with computational fluid dynamics (CFD). In the study, temperature and hydrogen production values and distribution were evaluated parametrically.

2 METHODOLOGY

Within the scope of the study, the process of obtaining hydrogen from waste exhaust heat is given in Fig. 1. While some of the waste exhaust expands directly in the turbine, some of it is used for the evaporation of the water to be used in the formation of hydrogen. The temperature required to obtain hydrogen is also provided from the exhaust line. Methane gas is supplied to the reformer with steam and hydrogen is obtained with the exhaust gas temperature.

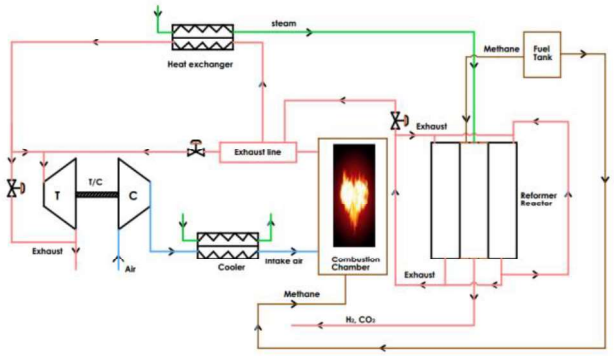


Figure 1. Basic Hydrogen Production System Design

2.1 Governing Equations

The turbulence model used in the study is Reynolds averaged Navier-Stokes (RANS) based models and this model has a complex physics. RANS equations are models with zero, one, and two equations, known as quadratic convergence models. Two-equation turbulence models are the most studied models for the last forty years. RANS equations are a complete model for the turbulent nature of the flow and to accurately predict turbulent flow [13]. The parameters used in the Reynolds mean expression are expressed as the sum of the mean and the instantaneous fluctuations in the full Navier-Stokes equations [14]. Reynolds expresses any parameter expression as in Eq (1).

$$\phi = \overline{\phi} + \phi' \tag{1}$$

where ϕ denotes any scalar quantity, ϕ' denotes the mean value of this magnitude, and $\overline{\phi}$ denotes the fluctuation value. These quantities can be variables such as velocity, pressure, temperature. Conservation of mass is presented in Eq. (2) for steady-state conditions.

$$\frac{\partial \rho}{\partial t} + \nabla \cdot (\rho \vec{v}) = 0 \tag{2}$$

where ρ is the gas density. The momentum equation, also known as the Navier-Stokes equation, is presented in Eq. (3).

$$\frac{\partial}{\partial t}(\rho \vec{v}) + \nabla \cdot (\rho \vec{v} \vec{v}) = -\nabla \cdot \rho + \nabla \cdot (\bar{\bar{\tau}}) + \rho \vec{g} + \vec{F} \tag{3}$$

In the given equations, $\vec{g}$ is the gravity and F is the body force. The energy equation for the computational model is given in Eq. (4).

$$\nabla \cdot \vec{u}(p + \rho \cdot h_f) = \nabla \cdot \left[k_{eff} \cdot \nabla T - \left(\sum h_j - \overrightarrow{J_j}\right) + \bar{\bar{\tau}} \cdot \vec{v}\right] + S_f \tag{4}$$

where, h_f is the heat convection coefficient, k_{eff} is the heat conduction coefficient.

RANS based k-e turbulence model is used in the numerical model. The RANS-based Standard k-ε turbulence model is governed by transport equations containing k and ε terms. The transport equations and model constants are calculated for the numerical model. The two-equation k-ε turbulence model allows to determine both the turbulence length and the time scale by solving two separate transport equations [15-16].

The following reaction sets are used to obtain H_2 with waste heat. The reaction given in Eq. (5) expresses the mixture of methane and water vapor given to the reactor. As a result of this reaction, CO and H_2 are formed. However, in this statement, it is desired that the CO components be destroyed. Therefore, by Eq. (6), known as water shift reaction, CO components combine with water vapor and turn into H_2 and

CO_2 components. The expression given in Eq. (7) expresses the reformer reaction [17-18].

$$CH_4 + H_2O \Leftrightarrow CO + 3H_2 \quad (5)$$

$$CO + H_2O \Leftrightarrow H_2 + CO_2 \quad (6)$$

$$CH_4 + 2H_2O \Leftrightarrow 4H_2 + CO_2 \quad (7)$$

The Arrhenius expression for each methane steam reformer reaction is expressed as Eq. (8).

$$k = Ae^{\frac{-E_a}{R_u T}} \quad (8)$$

Where, A is the frequency expression, E_a is the activation energy, R_u is the Universal gas constant and T is the ambient temperature [19-20]. The temperature change given in the equation provides the determination of the reaction rate by solving the energy equation throughout the system.

2.2 Boundary Conditions

The numerical model boundary conditions are given in Figure 2. On the 3D model, the exhaust and reformer gases are modelled as counter flow to increase heat transfer. The model's red-coloured area represents the exhaust inlet and the blue area represents the reformer outlet. The Green Area is modelled as an adiabatic wall.

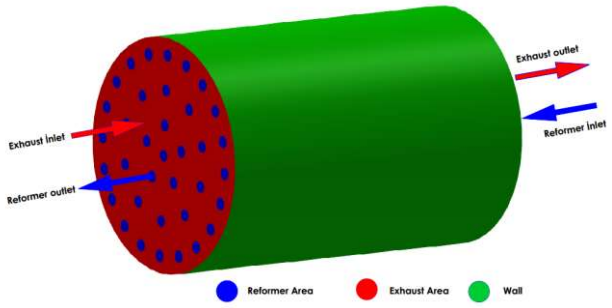


Figure 2. Boundary Conditions

The chemical kinetic coefficients of the reformer reactions defined in Eq. (5-7) in accordance with the Arrhenius equation defined in Eq. (8) are given in Table 1.

Table 1. Reformer Chemical Kinetics Coefficient

Equations	*A*	*E_a [J/mol]*
5	4.22×e15	240100 J/mol
6	1.96×e6	67130 J/mol
7	1.02×e15	243900 J/mol

The numerical geometry of the reformer used to obtain hydrogen is presented in Figure 3. The model given includes a single reformer tube inside the reactor. The Red Area represents the exhaust domain, and the blue Area represents the reformer domain.



Figure 3. Numerical Model Boundary Conditions

Variable parametric studies have been carried out to examine the process of obtaining hydrogen with waste heat. The system boundary conditions are given in Table 2.

Table 2. Boundary Conditions

Parameter	**Boundary conditions**	**Units**	**Value**
Exhaust velocity inlet	Velocity (T=1000 K)	m/s	1
			2.5
			5
			10
	Temperature (V=5 m/s)	K	1000
			800
			600
Exhaust pressure outlet		kPa	100
Reformer velocity inlet	Velocity (T=500 K)	m/s	0.75
			1
			2.5
			5
	Temperature (V=1 m/s)	K	300
			400
			500
Reformer pressure outlet		kPa	100
CH_4:H_2O		-	1
			2
			3
			4
			5

3 RESULTS AND DISCUSSION

Hydrogen production was investigated with different parametric studies with methane-steam reformers from numerical studies. Parametric studies were carried out at variable temperatures, velocity and water vapor methane ratios.

3.1 Effect of Different Exhaust and Reformer Velocity on Temperature and Hydrogen Production

The effect of different exhaust velocities on hydrogen production due to heat transfer was investigated in the numerical model, which was modelled as counter flow at 500 K temperature of the water vapor-methane gas mixture, the exhaust temperature of which was determined as 1000 K. Figure 4 shows the effect of reformer temperature taken from the center line at different exhaust velocities.

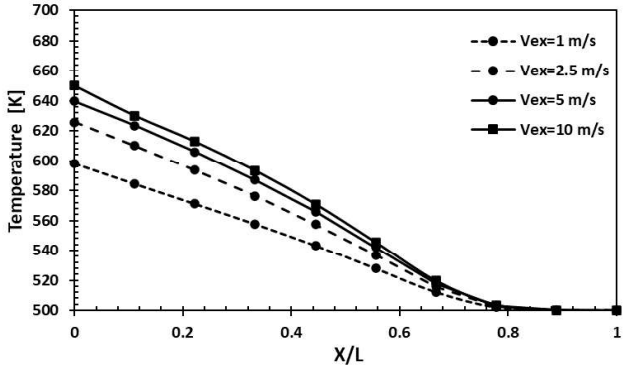


Figure 4. Effect of Different Exhaust Velocities on Reformer Temperature

It has been shown that increasing reformer exhaust velocity increases heat transfer. The highest reformer temperature was obtained at an exhaust velocity of 10 m/s. In the parametric exhaust velocities, the reformer velocity was taken as 1 m/s. Increasing reformer temperature also directly affects the amount of hydrogen formed in the reformer. Figure 5 shows the amount of hydrogen formed at different exhaust velocity.

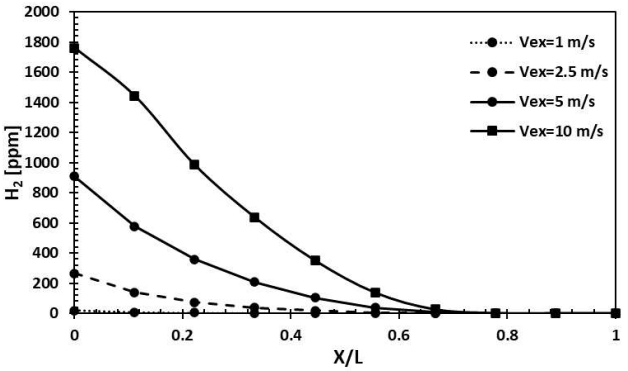


Figure 5. Effect of Different Exhaust Velocities on Hydrogen Production

As given, the highest hydrogen production was determined as approximately 1800 ppm at 10 m/s exhaust velocity. As the velocity decreases, both temperature and temperature-dependent hydrogen production decrease. For an exhaust velocity of 1 m/s, hydrogen generation approaches almost zero.

The temperature and hydrogen distribution for different exhaust velocities on the 2D model is presented in Figure 6. Since the exhaust flow and the reformer flow are in opposite flow, it is seen that the exhaust temperature decreases along the reformer tube from the beginning, on the other hand, the temperature at the reformer outlet also increases. The temperature change does not change the heat transfer much at low exhaust velocities. This is due to the small displacement of the exhaust throughout the system. At high exhaust velocities, the temperature causes more heat to occur in the exhaust area, which in turn increases the heat transfer.

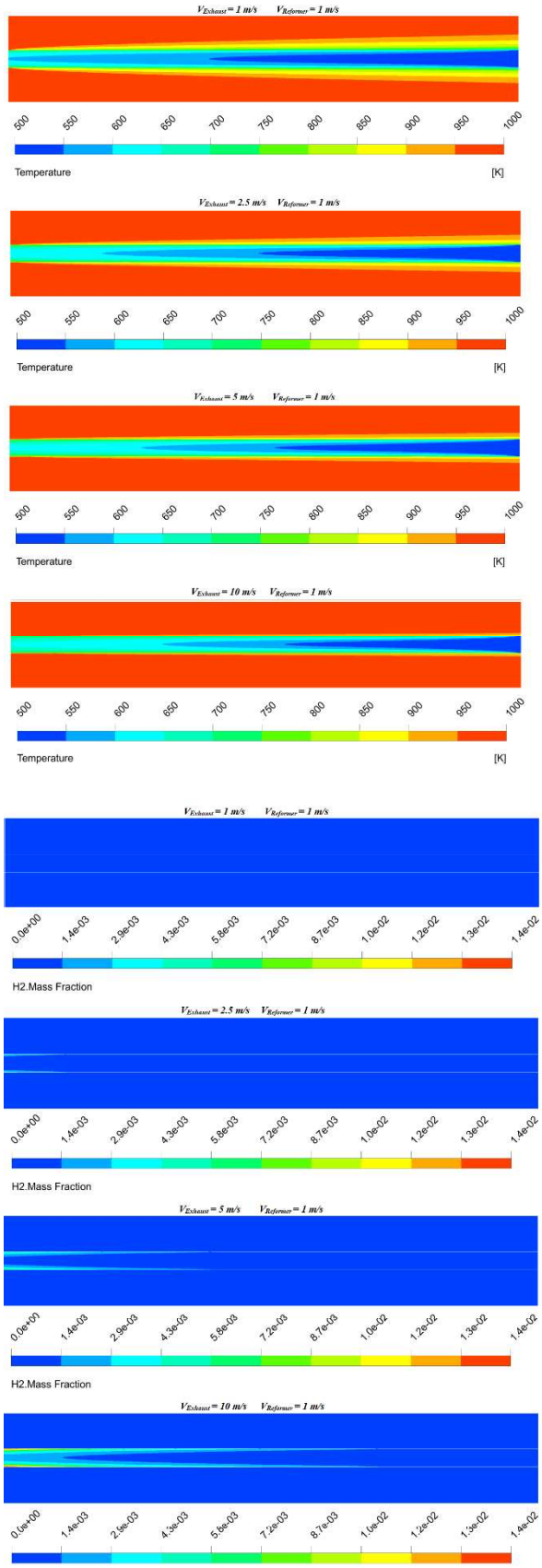


Figure 6. The Temperature and Hydrogen Distribution at Different Exhaust Velocities

The effect of the flow of different methane-water vapor mixtures in the reformer at different velocity on temperature and hydrogen production was investigated. Figure 7 expresses the temperature change at four different reformer velocity. The temperature causes the temperature to increase at low reformer velocities, unlike the exhaust velocity.

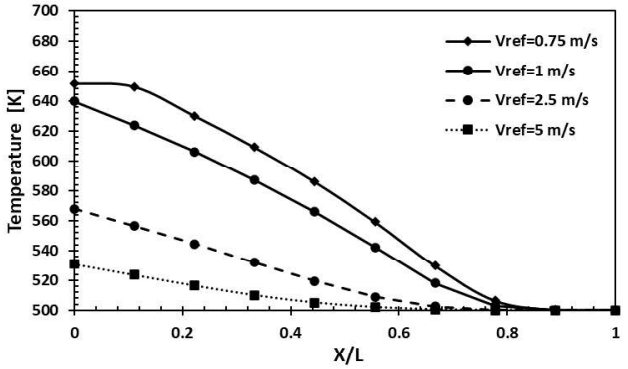


Figure 7. Temperature Change at Different Reformer Velocity

While at 0.75 m/s reformer velocities the flow has reached temperatures from 500 K to 650 K, this value is around 530 K at 5 m/s reformer velocity. Considering the hydrogen production, hydrogen production is the highest at low reformer velocity and is around 3200 ppm. Figure 8 represents hydrogen production at different reformer velocity. Due to the low heat transfer at reformer velocity of 5 m/s and above, hydrogen production approaches zero. In the analyses made, the exhaust velocity is assumed to be 5 m/s.

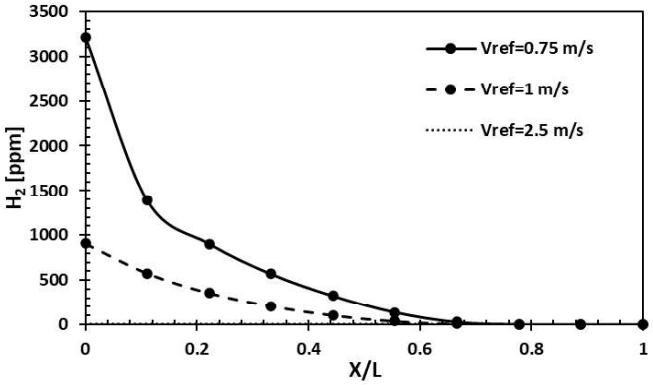


Figure 8. Hydrogen Production at Different Reformer Velocity

3.2 Effect of Different Exhaust and Reformer Inlet Temperatures on Temperature and Hydrogen Production

In this section, variable exhaust and reformer temperature effects heat transfer and hydrogen production. Figure 9 represents the change of

reformer temperature for three different exhaust temperatures. At 1000 K exhaust temperatures, the reformer temperature ranged from 500 K to 640 K. At 600 K exhaust temperatures, this value was determined as 530 K.

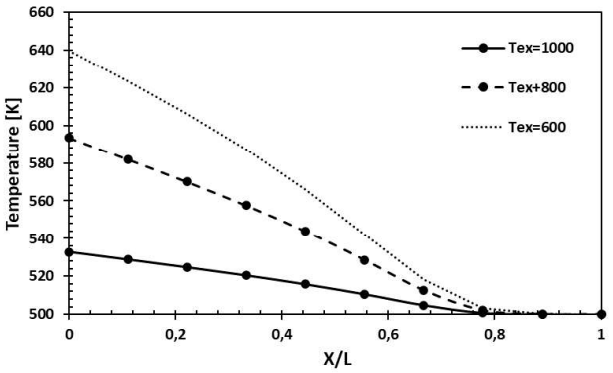


Figure 9. Change of Reformer Temperature with Variable Exhaust Temperatures

Figure 10 represents the hydrogen exchange at different exhaust velocities. Hydrogen production was achieved at 1000 K exhaust temperatures at 900 ppm levels. However, hydrogen production does not occur at 800 K exhaust temperatures and at lower exhaust temperatures.

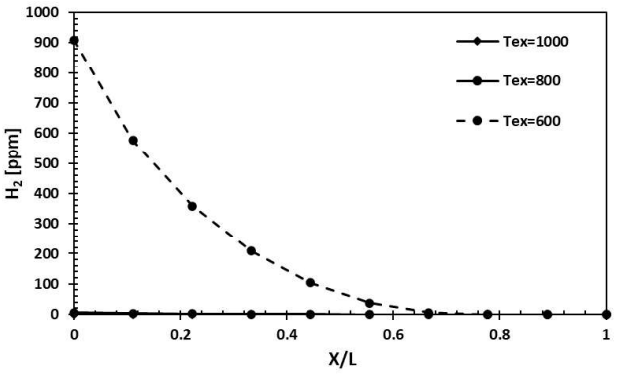


Figure 10. Hydrogen Production with Variable Exhaust Temperatures

In Figure 11, the effect of different reformer inlet temperatures on reformer temperature and hydrogen production is evaluated. For reformer inlet temperatures of 300 K, 400 K and 500 K, the reformer outlet temperatures were determined as 430 K, 550 K and 640 K, respectively. These values were obtained for 1000 K exhaust temperatures.

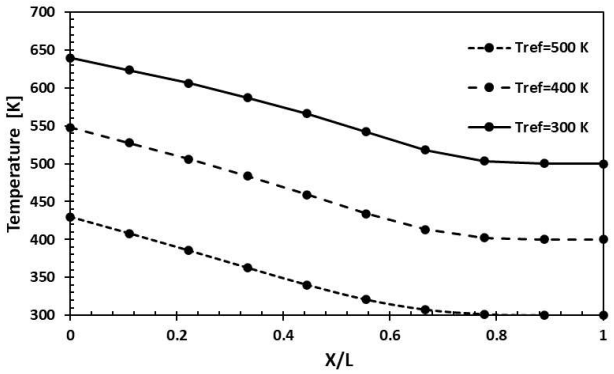


Figure 11. Change of Reformer Temperature with Variable Reformer Temperatures

Figure 12 represents hydrogen formation at different reformer inlet temperatures. While hydrogen formation at 500 K exhaust temperatures is around 900 ppm, hydrogen formation is negligible at 400 K and 300 K inlet temperatures.

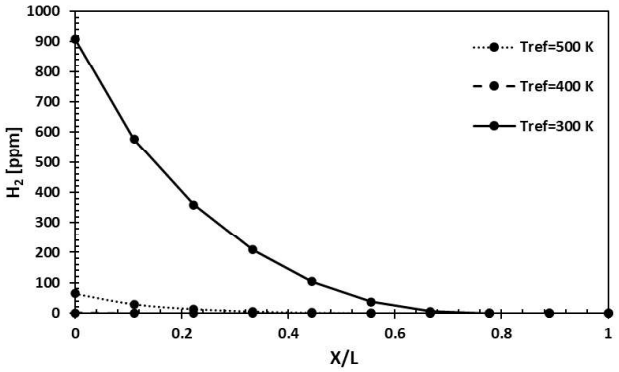


Figure 12. Hydrogen Production with Variable Reformer Temperatures

3.3 Effect of Inlet Temperatures on Temperature and Hydrogen Production at Variable H_2O:CH_4 Ratios

The effect to the hydrogen formation of reformer mixture at variable H_2O:CH_4 ratios is given in Figure 13. It was determined that the amount of hydrogen production increased with increasing H_2O:CH_4 ratios. Hydrogen production, which was about 1100 ppm in the case of a H_2O:CH_4 ratio of 5, decreased to about 500 ppm when this ratio was 1.

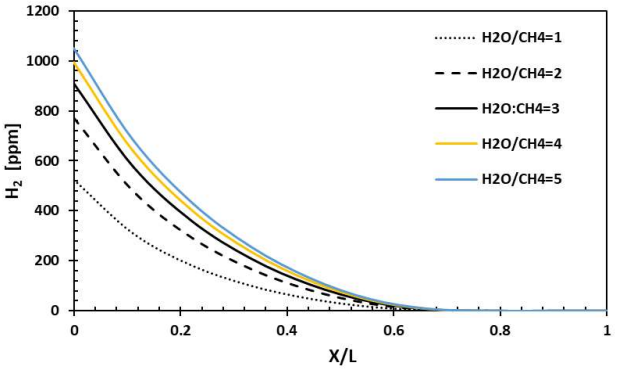


Figure 13. Hydrogen Production at Different H_2O:CH_4 Ratios

4 CONCLUSION

In this study, hydrogen production from exhaust waste heat was investigated parametrically according to variable exhaust and reformer velocity, temperature and reformer gas ratios. The studies were evaluated numerically by the Computational Fluid Dynamics (CFD) method. The following findings were reached within the scope of the study.

- ✓ Since the heat transfer is lower at low exhaust velocities, the reformer outlet temperature and hydrogen production are minimal. While hydrogen production at 1 m/s exhaust velocity is negligible, hydrogen production at 10 m/s exhaust velocity is determined as approximately 1800 ppm. Contrary to the exhaust velocity, heat transfer and hydrogen formation are higher at low reformer velocities. At reformer velocities of 0.75 m/s, hydrogen production is around 650 ppm.

- ✓ At high exhaust and high reformer velocity, the temperature and hydrogen formation in the middle of the reformer pipe center are higher. In the study, analyzes were carried out at 1000 K, 800 K and 600 K exhaust temperatures and at 300 K, 400 K and 500 K reformer temperatures, and the highest hydrogen formation occurred at 1000 K exhaust and 500 K reformer temperatures.

- ✓ Numerical analyses were carried out for three different ratios of H_2O:CH_4 mixture at the reformer inlet and it was determined that the amount of hydrogen formation increased with increasing H_2O:CH_4 ratios. The highest hydrogen formation was determined as approximately 1100 ppm when the H_2O:CH_4 ratio was 5.

REFERENCES

[1] Freedman, M., Jaggi, B., 2005. Global warming, commitment to the Kyoto protocol, and accounting disclosures by the largest global public firms from polluting industries. *The International Journal of Accounting* 40, 215–232. doi:https://doi.org/10.1016/j.intacc.2005.06.004

[2] Agreement, P., 2015. Paris agreement, in: *Report of the Conference of the Parties to the United Nations Framework Convention on Climate Change* (21st Session, 2015: Paris). Retrived December. p. 2017.

[3] Fan, L., Li, C., van Biert, L., Zhou, S.-H., Tabish, A.N., Mokhov, A., Aravind, P.V., Cai, W., 2022. Advances on methane reforming in solid oxide fuel cells. *Renewable and Sustainable Energy Reviews* 166, 112646. doi:10.1016/j.rser.2022.112646

[4] Gunasekar, P., Manigandan, S., Praveen, P.K., 2020. Hydrogen as the futuristic fuel for the aviation and aerospace industry – *review. Aircraft Engineering and Aerospace Technology* 93, 410–416. doi:10.1108/AEAT-07-2020-0145

[5] Kanimozhi, B., kumar, G., Alsehli, M., Elfasakhany, A., Veeman, D., Balaji, S., thiran, T., Praveen Kumar, T.R., Sekar, M., 2021. Effects of oxyhydrogen on the CI engine fueled with the biodiesel blends: A performance, combustion and emission characteristics study. *International Journal of Hydrogen Energy*. doi:10.1016/j.ijhydene.2021.08.054

[6] Ebrahimi, A., Ghorbani, B., Ziabasharhagh, M., Rahimi, M.J., 2021. Biomass gasification process integration with Stirling engine, solid oxide fuel cell, and multi-effect distillation. *Journal of Thermal Analysis and Calorimetry* 145, 1283–1302. doi:10.1007/s10973-020-10314-9

[7] Gür, T.M., 2016. Comprehensive review of methane conversion in solid oxide fuel cells: Prospects for efficient electricity generation from natural gas. *Progress in Energy and Combustion Science* 54, 1–64. doi:10.1016/j.pecs.2015.10.004

[8] Teramoto, K., Iwai, H., Kishimoto, M., Kawaguchi, T., Takemoto, M., Saito, M., Yoshida, H., 2020. Direct reforming of Methane–Ammonia mixed fuel on Ni–YSZ anode of solid oxide fuel cells. *International Journal of Hydrogen Energy* 45, 8965–8974. doi:10.1016/j.ijhydene.2020.01.073

[9] Song, H., Liu, Y., Bian, H., Shen, M., Lin, X., 2022. Energy, environment, and economic analyses on a novel hydrogen production method by electrified steam reforming with renewable energy accommodation. *Energy Conversion and Management* 258, 115513. doi:10.1016/j.enconman.2022.115513

[10] Quirino, P.P.S., Amaral, A., Manenti, F., Pontes, K.V., 2022. Mapping and optimization of an industrial steam methane reformer by the design of experiments (Doe*). Chemical Engineering Research and Design* 184, 349–365. doi:10.1016/j.cherd.2022.05.035

[11] Luo, Z., Wang, X., Wen, H., Pei, A., 2022. Hydrogen production from offshore wind power in South China. *International Journal of Hydrogen Energy*. doi:10.1016/j.ijhydene.2022.03.162

[12] Hasan, M.M., Genç, G., 2022. Techno-economic analysis of solar/wind power based hydrogen production. *Fuel* 324, 124564. doi:10.1016/j.fuel.2022.124564

[13] Rodriguez, S., 2019. Applied Computational Fluid Dynamics and Turbulence Modeling, *Applied Computational Fluid Dynamics and Turbulence Modeling*. doi:10.1007/978-3-030-28691-0

[14] Reynolds, O., 1894. On the Dynamical Theory of Incompressible Viscous Fluids and the Determination of the Criterion, *Philosophical Transactions of the Royal Society of London* 186, 123–164.

[15] Bayramoğlu, K., 2018. HAD (Hesaplamalı Akışkanlar Dinamiği) Yöntemiyle Gemi Dizel Motorlarinda Yanma Analizi. *Dokuz Eylul Üniversitesi.*

[16] Wilcox, D.C., 2006. Turbulence Modeling for CFD.

[17] Upadhyay, M., Lee, H., Kim, A., Lee, S. hun, Lim, H., 2021. CFD simulation of methane steam reforming in a membrane reactor: Performance characteristics over range of operating window. *International Journal of Hydrogen Energy* 46, 30402–30411. doi:10.1016/j.ijhydene.2021.06.178

[18] Xu, J., Froment, G.F., 1989. Methane steam reforming, methanation and water-gas shift: I. Intrinsic kinetics. *AIChE Journal* 35, 88–96. doi:10.1002/aic.690350109

[19] McAllister, S., Chen, J.-Y., Fernandez-Pello, A.C., 2011. *Fundamentals of Combustion Processes*. doi:10.1007/978-1-4419-7943-8

[20] Yim, S.D., Kim, S.J., Baik, J.H., Nam, I.S., Mok, Y.S., Lee, J.H., Cho, B.K., Oh, S.H., 2004. Decomposition of urea into NH_3 for the SCR process. *Industrial and Engineering Chemistry Research* 43, 4856–4863. doi:10.1021/ie034052j

TYRE PYROLYTIC OIL BLENDS IN A STATE-OF-THE-ART COMPRESSION IGNITION ENGINE: TOWARD FUEL-OPTIMIZED COMBUSTION

J. Hunicz[1], M. Mikulski[2] and A. Rybak[1]

1. Lublin University of Technology, Faculty of Mechanical Engineering, Nadbystrzycka 36, 20-618 Lublin, Poland; email: j.hunicz@pollub.pl
2. University of Vaasa, School of Technology and Innovation, Wolffintie 34, FI-65200 Vaasa, Finland; email: maciej.mikulski@uwasa.fi

1 INTRODUCTION

The end-to-end efficiency and environmental impact of the pyrolysis oils as diesel substitutes are currently on the high agenda of worldwide research [1,2]. Pyrolysis enables environmentally sound processing of various materials to engine fuel, often taking advantage of their different chemical makeup [3]. End-of-life tyres pose a particular challenge in utilization, yet provide large energy density to make their pyrolysis economically feasible [4].

On the end-user side, most of the knowledge regarding combustion and emissions of tyre pyrolitic oil (TPO) comes from legacy (pre-Euro standard) engine platforms operating in non-optimal combustion conditions [5]. Murugan et al. [6], working on a direct-injection engine, observed a monotonic increase in NO_X, THC and CO emissions as the TPO content in the mixture was increased. This was explained by the aromatics content, higher viscosity and lower volatility of TPO. Ilkiliç and Aydin [7], performed experiments with a similar engine. They found that blends up to 35% TPO can be used effectively without any engine modifications. Frigo et al. [8] conducted tests on a similar platform using TPO blends of 20% and 40% in diesel fuel (DF). It was observed that there was no significant difference in engine performance and emission values when using 20% TPO admixture, but there was a deterioration in engine combustion characteristics when TPO content was increased to 40%.

Tests on modern automotive engines are narrowed down to small TPO additives, not exceeding 10%, and mostly done using factory, diesel-optimized calibration maps. For instance, Martinez et al [9] tested a diesel blend with 5% TPO in a 2-litre 4-cylinder turbocharged car engine. At high loads, no differences were noticed between pure DF and fuel containing TPO. However, in the low-load range, the TPO additive affected negatively thermal efficiency and increased hydrocarbon emissions. The TPO additive also increased NO_X emissions and exhaust smoke regardless of load. An increase in combustion duration was also noted.

This paper presents a research approach aimed at understanding the TPO effect on combustion and emissions in modern diesel engines and providing the background for dedicated engine calibration for efficient and clean TPO combustion. The TPO used in the study is from a fully identifiable source. A complex analysis of the fuel injection strategy and variable exhaust gas recirculation (EGR) rates under fully controlled thermal conditions was carried out. The work further provides insight into relevant non-legislated emissions that can influence the decision on fuel-market intake.

2 TEST FUELS

The TPO used to compose the engine test sample, was manufactured using an industry-scale (8-ton feed capacity), rotary kiln reactor operating in the intermittent feed mode. Compressed and packaged light-duty vehicle tyres were fed directly to the reactor without any pre-processing. The TPO was discharged from the reactor as vapour and after condensation subjected to 2-step filtration. The distillation process removed light fractions which reduce the flashpoint. Table 1 shows the most important properties of the tested TPO and DF as a reference.

The binary mixtures with TPO content of 20% and 40%, denoted as TPO20 and TPO40 respectively, were subjected to engine tests. The selection of final engine blends was guided by a more in-depth consideration of blending strategies. At this point, it is enough to say that the primary targets for the blends were to achieve acceptable sulphur content, flash point and viscosity while balancing the anticipated demand for individual TPO fractions concerning different fuel quality requirements. To this end,

the present study took the possible applications of the fuels in off-road machinery, according to the premise highlighted in the introduction. Thus the respective EPA, ASTM D975 standard No. 4 was used as guidance for engine fuel quality targets.

The fuel samples were subjected to physical and chemical analysis. This followed the respective standards for testing DF and alternatives. A comprehensive discussion of the fuel analytics methods, including their accuracy, the reader can find in the previous work by the authors [10].

Table 1. Fuel analytics

Parameter	DF	TPO	TPO20	TPO40
Density @ 15°C [kg/m^3]	826	948	844	867
Viscosity @ 40 °C [mm^2/s]	2.3	15.3	3.0	3.9
Flashpoint [°C]	61	90	61	61
Sulphur content [mg/kg]	6,1	5000	1154	2265
Water content [mg/kg]	11	410	86	141
Higher heating value [MJ/kg]	44.8	44.7	44.7	44.8
Cetane index	40.1	32.6	38.2	36.1

3 THE ENGINE TEST METHODS

Experimental works were performed at the Lublin University of Technology. Four-stroke, single-cylinder AVL research engine type 5402 CR DI served as the research object. The engine had a displacement of 510 cm^3 and a compression ratio of 17:1. Table 2 lists the governing parameters of the tested engine, and Fig. 1 provides a detailed diagram of the test stand.

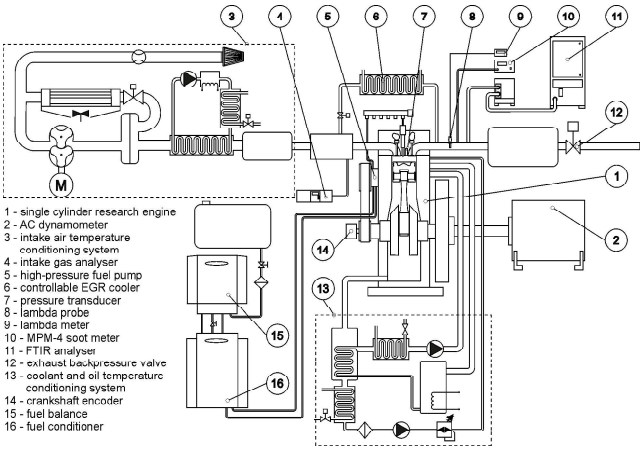


Figure 1. Diagram of the engine test stand

The fuels were examined according to the ISO 8178 type D2 test for stationary engines. The test comprised 5 operating points representing a load sweep performed at a rated engine speed of 1500 rpm. Engine calibration was created for the reference DF and aimed at minimum overall emissions with constrained high indicated thermal efficiency. To achieve this, a split injection strategy was realized including early pilot injection and main injection close to the top dead centre (TDC) to directly control the start of combustion. Note that such a combustion system is propitiatory to state-of-the-art diesel engine technology. The engine calibration details for all operating points are provided in Table 3.

Table 2. Research engine specifications

Type	AVL 5402
Configuration	4-stroke, 1-cylinder
Bore	85 mm
Stroke	90 mm
Displacement	510.5 cm3
Compression ratio	17:1
No. of valves	4
Swirl ratio	1.7:1
Combustion chamber	Mexican hat
Max. fuel pressure	180 MPa
Injection system	CR, Bosch CP4.1
Boost compressor	El. driven Eaton M45
EGR system	high-pressure, cooled
Engine management	AVL-RPEMS, ETK7-Bosch
Intake valve opening	712 CAD
Intake valve closing	226 CAD
Exhaust valve opening	488 CAD
Exhaust valve closing	18 CAD
Max. IMEP	2.4 MPa

Table 3. Engine operating conditions and control parameters

Load [%]	10	25	50	75	100
IMEP [MPa]	0.2	0.5	0.8	1.1	1.4
MAP [kPa]	100	125	140	155	175
λ [-]	5.2	2.8	2.0	1.7	1.55
SOI1 [CAD]	342	342	340	340	340
SOI2 [CAD]	356	356	354	354	354
Fuel pressure [MPa]	50	60	70	80	80
Pilot fuel quantity [mg]	1.5	1.6	1.7	1.7	1.7
Pilot fuel fraction [%]	20	10	7	5	3.7

The second stage of the research was performed at a single operating point, at IMEP of 0.5 MPa,

which corresponds to the point in the test which has a high contribution to the overall test emissions. To investigate fuel behaviour at variable control parameters, fuel start of injection timing (SOIs) was shifted earlier and later concerning baseline conditions shown in Table 3. Additionally, variable EGR rates were applied at constant boost pressure.

4 RESULTS HIGHLIGHTS

4.1 Fuel to fuel differences at standard calibration

It is evident from Fig. 2 that in the high load regime, TPO samples did not affect CO, HC or NO_X emissions, which are comparable to DF within the limits of statistical relevance. Thus, these quantities are not influenced by the fuel composition and remain sensitive to engine control parameters affecting combustion. The Elevated particulate matter (PM) emissions along with high aromatic and SO_2 concentrations, observable across all operating points, are primarily attributed to TPO's chemical makeup.

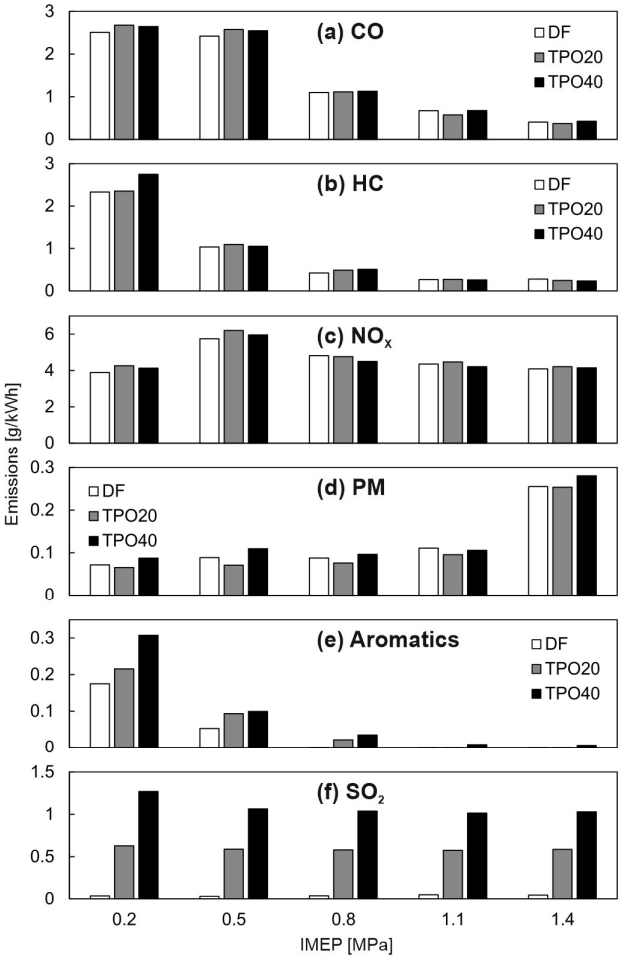


Figure 2. Indicated specific emissions at reference conditions

Focusing on the 0.5 bar IMEP point, foreseen for recalibration, Fig. 2 implies CO and NO_X emissions from TPO20, elevated from the DF baseline by respectively 6% and 7%. For TPO40 those differences are much smaller – an order of 2%. PM emissions for TPO40, on the other hand, are significantly higher compared to DF (order of 22%). For TPO20, PM emissions are reduced by the same order of magnitude. Hence, combustion–wise TPO20 and TPO40 exhibit the opposite sides of NO_X/PM trade-offs.

Detailed HRRs for this operating point, with DF and TPO40, are illustrated in Fig. 3. Note that despite the same SOI, the pilot fuel ignition is substantially delayed for TPO-containing fuels. For TPO40 versus DF, this delay is an order of 2 crank angle degrees (CAD) and originates from a substantially lower cetane index and lower volatility, influencing the ignition delay of TPO. The fuel-to-fuel differences in the main combustion phase diminish, however, as the start of combustion here is controlled diffusively.

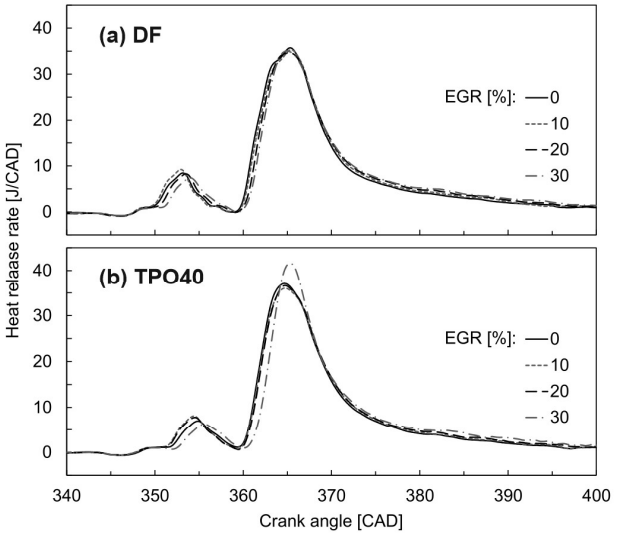


Figure 3. HRR for DF and TPO40; 0.5 MPa IMEP, reference conditions

According to the same reasoning, the addition of EGR primarily affects the premixed pilot combustion phase. The effects, despite substantial, are however non-monotonic. According to Fig. 3b, for instance, the mid-range EGR additions (up to 20%) can stimulate pilot fuel HRR, while heavy EGR can suppress it considerably.

4.2 Emission optimization for TPO

To provide an overall picture of fuels' response to control parameters, emission indicator (E) was calculated using the following formula:

$$E = \frac{CO}{CO_{min}} + \frac{HC}{HC_{min}} + \frac{NOx}{NOx_{min}} + \frac{PM}{PM_{min}} - 4 \quad (1)$$

and depicted in Fig. 4. The symbols of chemical compounds represent indicated emissions, whereas the minimum values (denominators) are determined for DF and can be read from Figs. 5a and 6a. The emission indicator is zero if all components of Eq. 1 are at the minimum level achievable for DF. Obviously, the minimum emission points for different fuels do not coincide on the EGR/SOI maps.

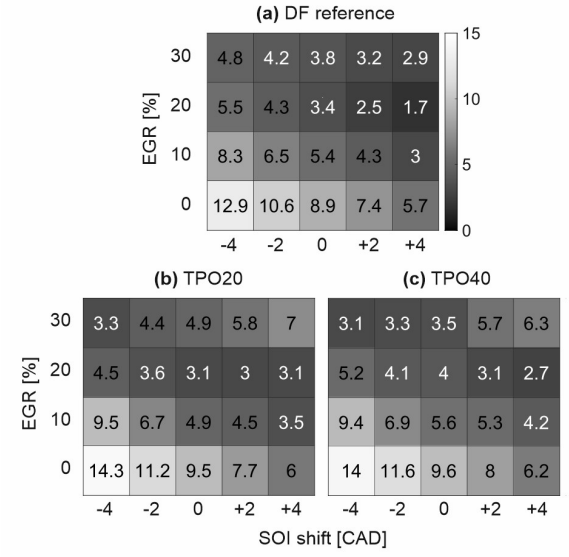


Figure 4. Emission indicator values for DF, TPO20 and TPO40 at variable SOIs and EGR rates

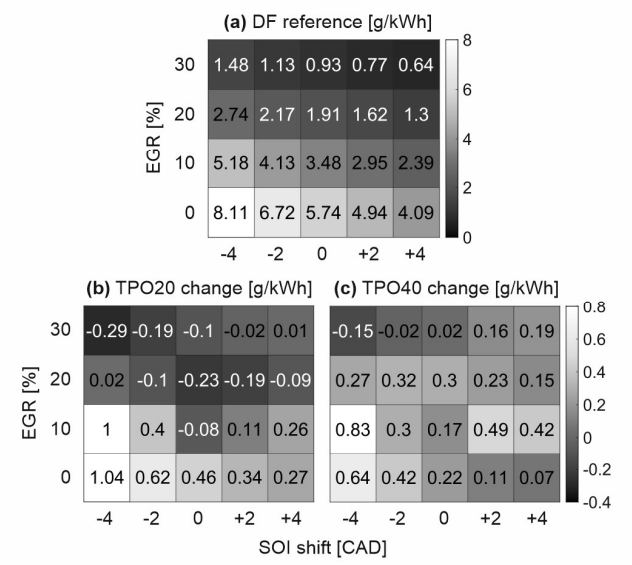


Figure 5. Indicated specific emissions of NO_X at variable SOIs and EGR rates; TPO results expressed as relative to DF

For DF, the emission indicator map is almost solely shaped by the NO_X, as this changes in the largest span. However fuel-to-fuel differences are mostly influenced by PM emissions. Generally higher emission indicators of TPO result from its chemical propensity to create soot. Nevertheless, the emission maps clearly show premixed combustion regimes, where both NO_X and PM are produced to a lesser extent.

Comparing DF and TPOs, one can note that, emission-wise DF prefers delayed injection and mild-EGR. In contrast, if TPO is added, the comparable emission indicators, at the level of 3, can be achieved at a wider area of the control map.

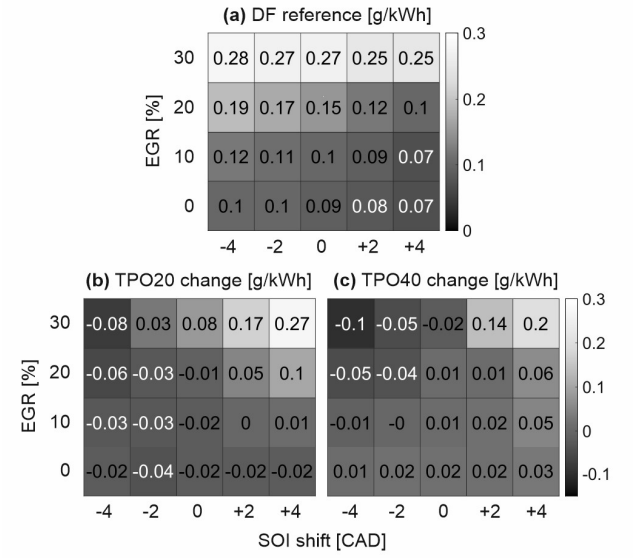


Figure 6. Indicated specific emissions of PM at variable SOIs and EGR rates; TPO results expressed as relative to DF

ACKNOWLEDGEMENTS

The research was financed in the framework of the project Lublin University of Technology, Regional Excellence Initiative, funded by the Polish Ministry of Science and Higher Education (contract No. 030/RID/2018/19).

The authors wish to thank AVL List GmbH for making the simulation software available in the framework of the AVL University Partnership Program.

REFERENCES

[1] O. Azeta, A. O. Ayeni, O. Agboola, and F. B. Elehinafe, A review on the sustainable energy generation from the pyrolysis of coconut biomass, *Sci. African*, vol. 13, p. e00909, 2021,

[2] M. B. Figueirêdo, I. Hita, P. J. Deuss, R. H. Venderbosch, and H. J. Heeres, Pyrolytic lignin: a promising biorefinery feedstock for the production of fuels and

valuable chemicals, *Green Chem.*, vol. 24, no. 12, pp. 4680–4702, 2022,

[3] H. Yaqoob, Y. H. Teoh, M. A. Jamil, and M. Gulzar, Potential of tire pyrolysis oil as an alternate fuel for diesel engines: A review, *J. Energy Inst.*, vol. 96, pp. 205–221, 2021,

[4] H. Aydin and C. Ilkiliç, Optimization of fuel production from waste vehicle tires by pyrolysis and resembling to diesel fuel by various desulfurization methods, *Fuel*, vol. 102, pp. 605–612, 2012,

[5] M. Mikulski, M. Ambrosewicz-Walacik, J. Hunicz, and S. Nitkiewicz, Combustion engine applications of waste tyre pyrolytic oil, *Prog. Energy Combust. Sci.*, vol. 85, 2021,

[6] S. Murugan, M. C. Ramaswamy, and G. Nagarajan, Assessment of pyrolysis oil as an energy source for diesel engines, *Fuel Process. Technol.*, vol. 90, no. 1, pp. 67–74, 2009,

[7] C. Ilkiliç and H. Aydin, Fuel production from waste vehicle tires by catalytic pyrolysis and its application in a diesel engine, *Fuel Process. Technol.*, 2011,

[8] S. Frigo, M. Seggiani, M. Puccini, and S. Vitolo, Liquid fuel production from waste tyre pyrolysis and its utilisation in a Diesel engine, *Fuel*, vol. 116, pp. 399–408, 2014,

[9] J. D. Martínez, J. Rodríguez-Fernández, J. Sánchez-Valdepeñas, R. Murillo, and T. García, Performance and emissions of an automotive diesel engine using a tire pyrolysis liquid blend, *Fuel*, vol. 115, pp. 490–499, 2014,

[10] M. Mikulski, J. Hunicz, K. Duda, P. Kazimierski, T. Suchocki, and A. Rybak, Tyre pyrolytic oil fuel blends in a modern compression ignition engine: A comprehensive combustion and emissions analysis, *Fuel*, vol. 320, p. 123869, 2022,

[11] G. F. Hohenberg, Advanced approaches for heat transfer calculations, in *SAE Technical Papers*, 1979, p. 790825.

[12] S. Kline and F. McClintock, Describing Uncertainty in Single Sample Experiments, *Mech. Eng.*, vol. 75, pp. 3–8, 1953.

[13] A. C. Johansson, R. Molinder, T. Vikström, and H. Wiinikka, Particle formation during suspension combustion of different biomass powders and their fast pyrolysis bio-oils and biochars, *Fuel Process. Technol.*, vol. 218, p. 106868, 2021,

[14] J. Hunicz, J. Matijošius, A. Rimkus, A. Kilikevičius, P. Kordos, and M. Mikulski, Efficient hydrotreated vegetable oil combustion under partially premixed conditions with heavy exhaust gas recirculation, *Fuel*, vol. 268, p. 117350, 2020,

Dunaliella Salina Microalgae Obtained as an Effective Material for Double Applications: Supercapacitor and Hydrogen Production

Rıdvan ÇETİN[1,2], Mustafa KAYA[3], Murat AKDEMİR[2*], Muhammet Ali ARSERİM[1]

1. Department of Electrical and Electronics Engineering, Faculty of Engineering, Dicle University, 21280 Diyarbakır, Turkey
2. Department of Electrical and Electronics Engineering, Faculty of Engineering, Siirt University, 56100 Siirt, Turkey
3. Department of Chemical Engineering, Faculty of Engineering, Siirt University, 56100 Siirt, Turkey

***Corresponding Author:** Murat AKDEMİR, (e mail: muratakdemir@siirt.edu.tr)

ABSTRACT

The consumption of fossil fuels has increased in the modern era due to rising demand for energy based on industrialization and population growth. The significant increase in fossil fuel usage causes a reduction in the amount of fossil fuel reserves and affects the environment negatively [1]. The increased usage of fossil fuels to meet the rising energy demand also increases the interest in renewable energy sources [2-3]. One of the sources that can be shown as an alternative to fossil fuels is hydrogen energy [4]. To produce hydrogen gas from NaBH4 solution, a catalyst is must be used [5]. Organic materials such as algae can be used directly as catalysts without any precious metals and support materials. Due to their simpler development and quicker growth than other plants, as well as the ability to use CO_2 gas emitted into the environment as a nutrition, microalgae are favoured as catalysts [6]. The catalyst made from microalgae, known as Cap-Cat, has been studied for use in producing hydrogen and as an electrode material for supercapacitors [7-8]. Due to their high power density supercapacitors, which are rapidly emerging as a developing technology among energy storage devices [9], have a higher energy density than other capacitors. Additionally, supercapacitors have high efficiency, high capacity for charge/discharge current and a wide temperature range [10]. In this study, the catalyst obtained from the microalgae which name is *Dunaliella salina* is used both in hydrogen production and as a supercapacitor electrode material. In addition to carbonization, microalgae is converted into activated carbons at different burning temperatures (300 °C, 400 °C, 500 °C) and burning times (30 min., 45 min., 60 min.) with $ZnCl_2$, KOH and H_3PO_4 activators at different concentrations (10%, 20%, 30%) as in table 1. Taguchi orthogonal

arrays L9 (3 4) is used while performing these experiments for determining optimal values of parameters for cost-effective optimization. Table 2 lists the tests that were conducted.

Table 1. Parameters for experiments

	Activation Material	Amount of Activation Material	Burning Temperature (^{O}C)	Burning Time (min)
1	$ZnCl_2$	10%	300	30
2	KOH	20%	400	45
3	H_3PO_4	30%	500	60

Table 2. Experimental design with with Taguchi ortogonal arrays

Experiment Number	**Activation Material**	**Amount of Activation Material**	**Burning Temperature (^{O}C)**	**Burning Time (min)**
1	$ZnCl_2$	10%	300	30
2	$ZnCl_2$	20%	400	45
3	$ZnCl_2$	30%	500	60
4	KOH	10%	400	60
5	KOH	20%	500	30
6	KOH	30%	300	45
7	H_3PO_4	10%	500	45
8	H_3PO_4	20%	300	60
9	H_3PO_4	30%	400	30

Methanolysis experiments were performed in the presence of 2.5% $NaBH_4$, 10 ml methanol, 30 ^{o}C and 0.1 g catalyst. The methanolysis performance of the catalysts obtained from *Dunaliella salina* microalgae is given in Figure 1. As seen in the figure, sample number 9 completes the methanolysis reaction in the shortest time under the same conditions. In the calculations, the initial rate (R_o) was calculated as 5154.2 kj/mol and the initial velocity of all samples are given in Figure 1.

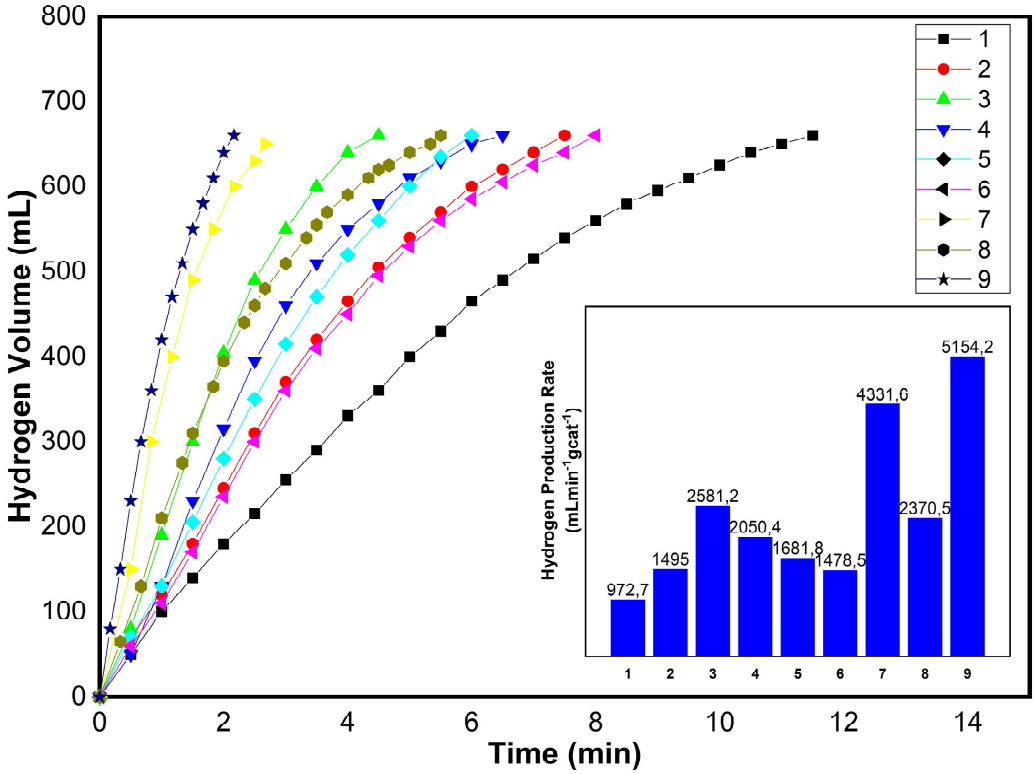
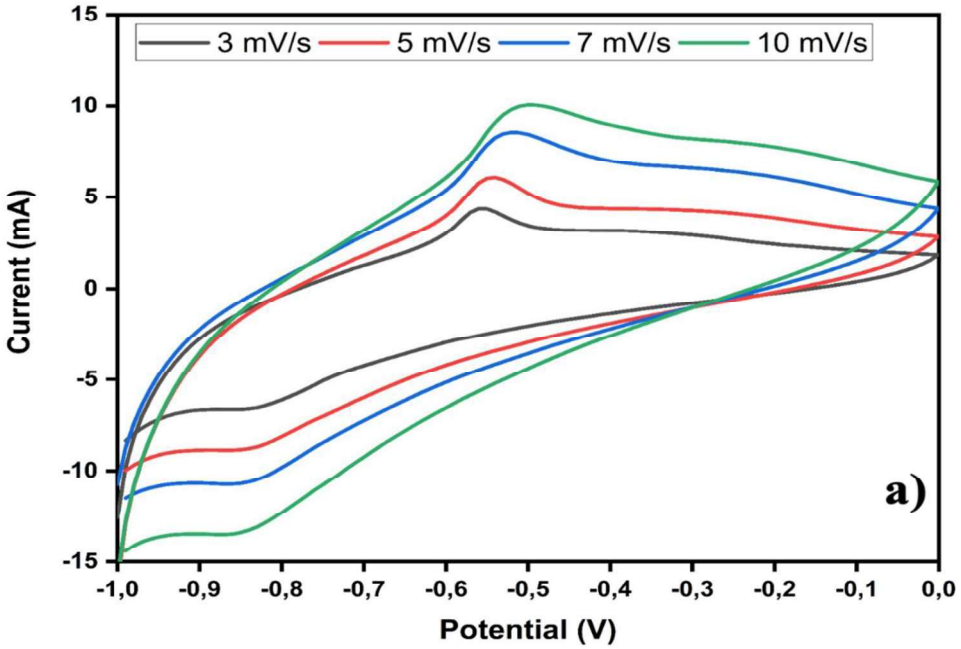


Figure 1. Hydrogen production volumes vs time from methanolysis of $NaBH_4$

Activated carbon material in which gave the best results in hydrogen production (experiment number 9) was used as a supercapacitor electrode and it's electrochemical properties were investigated. The energy storage capacity, stability and energy-power density of the supercapacitor were determined with the help of cyclic voltammetry curves (CV), impedance curves (EIS) and charge-discharge curves (GCD). The capacitance values of the electrode at different curerent density are given at Table 3 and CV curves of the produced supercapacitor are given in Figure 2. The electrochemical results of the produced electrode show similar properties to the ideal supercapacitor curves and a high capacitance value of 405.8 F/g was obtained at a current density of 1 A/g. Moreover, the equivalent series resistance (R_s) and the load transfer resistance (R_{ct}) of the electrode were measured 0.3 Ω and 6.06 Ω . The produced material has shown good results both for hydrogen production as a catalyst and for supercapacitor applications as electrode material.

Table 3. The capacitance value and voltage drop at different curerent density

Current density (Ag^{-1})	Capacitance (F/g)	IR drop(mV)
1	405,8	102
2	194,34	102
3	175,05	102
4	86,59	102
5	46,65	102



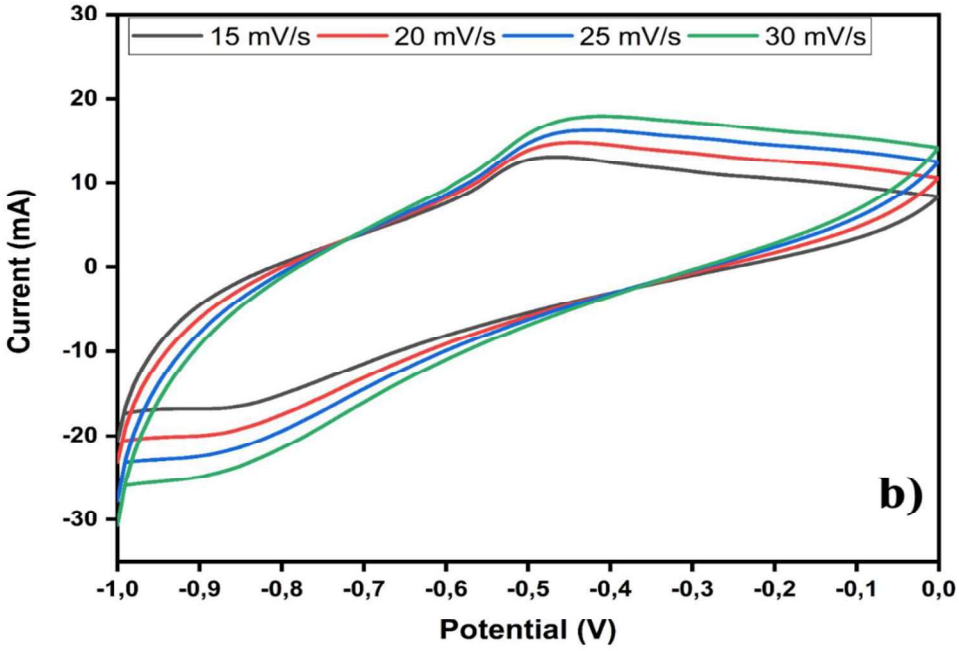


Figure 2. CV curves of the produced supercapacitor

REFERENCES

[1]. Farhad, S., Saffar-Avval, M., & Younessi-Sinaki, M. (2008). Efficient design of feedwater heaters network in steam power plants using pinch technology and exergy analysis. International journal of energy research, 32(1), 1-11.

[2]. Youm, I. S. J. S., Sarr, J., Sall, M., & Kane, M. M. (2000). Renewable energy activities in Senegal: a review. Renewable and Sustainable Energy Reviews, 4(1), 75-89.

[3]. Hiemstra-van der Horst, G., & Hovorka, A. J. (2009). Fuelwood: the "other" renewable energy source for Africa?. Biomass and bioenergy, 33(11), 1605-1616.

[4]. Yusaf, T., Laimon, M., Alrefae, W., Kadirgama, K., Dhahad, H. A., Ramasamy, D., ... & Yousif, B. (2022). Hydrogen energy demand growth prediction and assessment (2021–2050) using a system thinking and system dynamics approach. *Applied Sciences*, *12*(2), 781.

[5].Jeong, S. U., Kim, R. K., Cho, E., Kim, H. J., Nam, S. W., Oh, I. H., ... & Kim, S. H. (2005). A study on hydrogen generation from NaBH4 solution using the high-performance Co-B catalyst. *Journal of Power Sources*, *144*(1), 129-134.

[6]. Rangabhashiyam, S., Behera, B., Aly, N., & Balasubramanian, P. (2017). Biodiesel from microalgae as a promising strategy for renewable bioenergy production—a review. *J. Environ. Biotechnol. Res.*, *6*(4), 260-269.

[7].Akdemir, M., Avci Hansu, T., Caglar, A., Kaya, M., & Demir Kivrak, H. (2021). Ruthenium modified defatted spent coffee catalysts for supercapacitor and methanolysis application. *Energy Storage*, *3*(4), e243.

[8].Karakaş, D. E., Akdemir, M., Atabani, A. E., & Kaya, M. (2021). A dual functional material: Spirulina Platensis waste-supported Pd-Co catalyst as a novel promising supercapacitor electrode. *Fuel*, *304*, 121334.

[9]. Dubey, R., & Guruviah, V. (2019). Review of carbon-based electrode materials for supercapacitor energy storage. *Ionics*, *25*(4), 1419-1445.

[10]. Wang, S., Wei, T., & Qi, Z. (2008). Supercapacitor energy storage technology and its application in renewable energy power generation system. In Proceedings of ISES World Congress 2007 (Vol. I–Vol. V) (pp. 2805-2809). Springer, Berlin, Heidelberg.

OPTIMIZATION OF HYDROGEN PRODUCTION WITH THE ALUMINIUM-WATER REACTION

R. N. Mutlu[1*], E. Eroğlu[1,2] J. Kandasamy[1], H. Ü. Toffoli[2] and İ. Gökalp[1]

1. Department of Mechanical Engineering, Faculty of Engineering, Middle East Technical University, Ankara.
2. Department of Physics, Middle East Technical University, Ankara.

Email*: nmutlu@metu.edu.tr

Abstract

The paper will present our recent results on the optimization rules between the main aluminum hydrolysis parameters for hydrogen generation. Hydrolysis of light metals such as aluminum is a known hydrogen generation process. Once the Al – water reactions are activated, hydrogen is readily generated with a very high efficiency. This is also a sustainable process as the generated aluminum oxide can be recycled to the Al metal. In this study the combination of the parameters of aluminum-water reactions, which are (i) the solution concentration (1-4 M NaOH), (ii) the solution temperature (25-80 °C), (iii) the amount of aluminum (mg) and (iv) the diameter of aluminum wire (0.6-1 mm), are optimized. The hydrogen evolution rate ($mlmin^{-1}$) is measured for different conditions by establishing a relationship between the parameters with the central composite design approach. The maximum and minimum hydrogen evolution rates are determined. The optimization of the parameters allows predicting the hydrogen evolution rates at any point in the parametric space.

Keywords: Hydrogen, Hydrolysis, Aluminum, Aluminum Wire

This work is financially supported by the Scientific and Technological Research Council of Turkey (TÜBITAK), Grants No: 118C291 and 118C287).

USE OF HYDROGEN-BIOGAS MIXTURE AS FUEL IN COMMON-RAIL DIESEL ENGINE WITH THERMAL BARRIER COATING

A. Şanlı[1], İ.T. Yılmaz[2], M. Akçay[3] and M. Gümüş[2]

1. Piri Reis Vocational and Technical Anatolian High School, İstanbul; email: ali_sanlixl@hotmail.com
2. Faculty of Technology, Marmara University, İstanbul; email: ilker.yilmaz@marmara.edu.tr, mgumus@marmara.edu.tr
3. Faculty of Engineering and Architecture, Muş Alparslan University, Muş; email: m.akcay@alparslan.edu.tr

Abstract

In this study, combustion characteristics of biogas, and hydrogen-enriched biogas were experimentally analysed and compared with baseline diesel fuel. In study a four cylinder, four stroke, water cooled, turbocharged, Common-Rail diesel engine with and without thermal barrier coated pistons was used. Experiments were carried out at fixed engine load (50 Nm) and fixed engine speed (1750 rpm). Results showed that cylinder pressures and heat release rates for all fuels under the low heat rejection (LHR) engine were higher than those of the standard (STD) engine. For dual-fuel modes heat release rates and cumulative heat releases were comparatively earlier than diesel fuel mode. A larger amount of the fuel was burned closer to the TDC for dual-fuel mode.

Keywords: Common-rail, thermal barrier coated piston, dual-fuel, biogas, hydrogen enrichment

1 INTRODUCTION

Nowadays, the research and development of alternative fuels has become mandatory due to the limited life of petroleum reserves and the negative effects of emissions released using petroleum-derived fuels on the environment. One of the candidates that has recently been seen as an alternative to conventional fuels is biogas.

The biogas can be used in transportation and stationary power machines for supplying the energy requirement. It is yielded by anaerobic fermentation of organic raw materials and has similar contents to the natural gas, which mainly contains methane of 50-60%, carbon dioxide (CO_2) of 30-40%, and small amounts of other gases such as hydrogen sulphide, nitrogen, carbon monoxide, oxygen, water vapor, ammonia, hydrogen and so on [1].

Gaseous fuel-diesel dual-fuel mode can be applied to increase brake thermal efficiency (BTE), and to decrease nitrogen oxide (NO_x) and particulate emissions being among the main problem of the diesel engines [2,3]. However, CO_2 presence in biogas leads to lower flame propagation speed and combustion enthalpy.

The enrichment or combination with the gases having higher flame speed such as hydrogen can significantly improve the combustion characteristics of the biogas [4].

Coating the parts of the engine's combustion chamber generally enhances the engine performance because of decreasing the heat transfer to the cooling, meaning that converting the heat energy released by fuel into the more sufficient work [5]. Parts of the combustion chamber can be insulated by materials with a lower thermal conductivity coefficient. Not only combustion gases temperatures but also exhaust temperatures can increase [6].

In this study, the use of biogas and hydrogen-enriched biogas in the LHR and STD engines was investigated. Tests were carried out at 50 Nm engine load and 1750 rpm engine speed. The study aimed to reveal the combustion properties of biogas and hydrogen-enriched biogas in LHR and STD diesel engines.

2 MATERIAL AND METHOD

In this study, a 4-cylinder, water cooled, turbocharged, Common-Rail diesel engine was used. An eddy-current dynamometer with water cooling was used to control the speed and load of the engine. Speed, load, gas flow rates and temperatures at specific points of the test engine were watched in control panel of the

dynamometer. One of the test fuels contained 80% methane and 20% CO_2 by volume in this study. After the tests, 50% of the CO_2 volume in the biogas was replaced with the same volume of hydrogen gas. Thus, 80% methane, 10% CO_2, and 10% hydrogen by volume were obtained. They were mixed with intake air in a mixing chamber before the engine turbocharger. Flame arresters were fixed on gas line to prevent the flame propagations of methane and hydrogen in case of possible backfire. In-cylinder pressure was measured by Optrand pressure transducer fixed on the first cylinder of the engine. A Kubler incremental encoder was used to determine the crank shaft angle. Signals collected from the cylinder and the encoder passed on National Instruments 6343 model data acquisition card. 200 consecutive pressure data with 1 °CA resolutions were sampled for each test and averaged to eliminate the effects of cycle-by-cycle variations.

8% Yttria Stabilized Zirconia was used as a main coat and nickel-aluminum (Ni-Al) as a bond coat for the coating of the piston bowls. Thickness of main and bond coats were 400 µm and 100 µm, respectively. Atmospheric plasma spray method was used for the coating application. This application was made by a commercial company. Detailed information about the test engine was given in the previous study of the authors [7]. Experimental instrumentation system is illustrated in Figure 1.

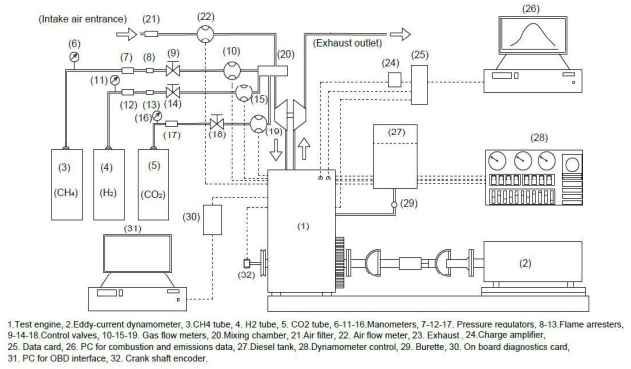


Figure 1. Schematic of experimental instrumentation.

3 RESULTS AND DISCUSSION

The variations of cylinder pressures based on cylinder volume for test fuels under STD and LHR engines are shown in Figure 2.

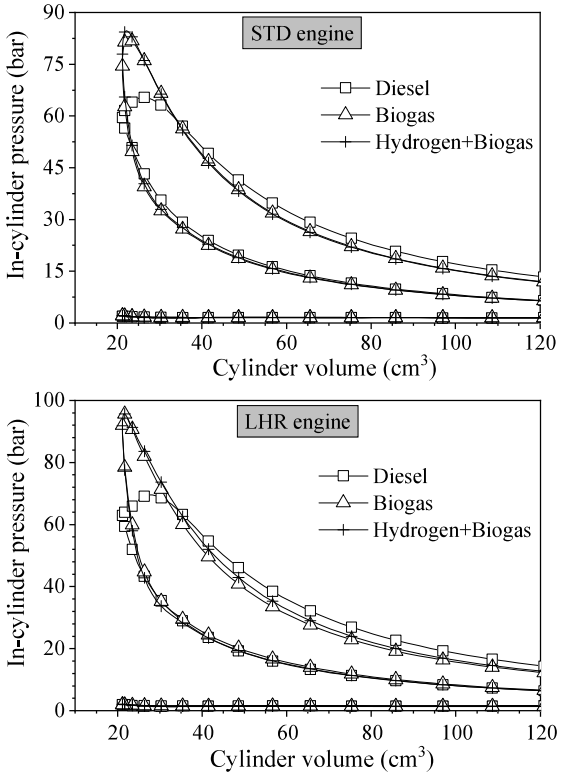


Figure 2. Indicator diagrams for STD and LHR engines

It was observed that instant combustion occurred with dual-fuel modes and the combustion process occurred almost at a constant volume. Due to constant volume combustion, higher in-cylinder pressures were achieved in dual-fuel modes compared to conventional diesel fuel mode [2, 8]. Cylinder pressures of all fuels for the LHR engine were slightly higher than corresponding ones for the STD engine.

The variations of heat release rates (HRR) based on crank angle for the test fuels under STD and LHR engines are presented in Figure 3. It was observed from Figure 3 that heat release occurred earlier with dual-fuel modes than diesel fuel mode. Pre-injection of diesel fuel into the cylinder ignited the gas fuel-air mixture. Due to the sudden combustion of gas fuel in the cylinder, a significant part of the heat release took place before the main diesel fuel injection for dual-fuel modes. Slightly higher heat release values were generally obtained with hydrogen-enriched biogas. This is explained by the higher flame speed and instant combustion of hydrogen [9,10]. Higher HRR values were obtained for each test fuel with LHR engine compared to STD engine.

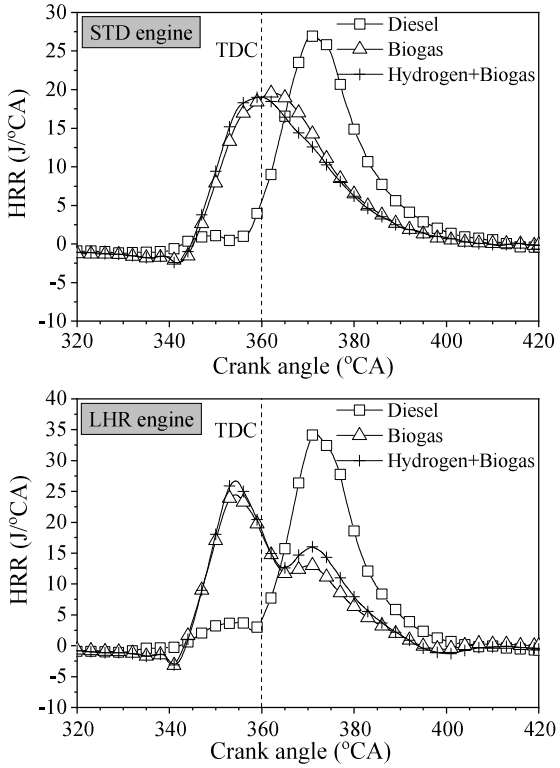


Figure 3. HRR values for STD and LHR engines

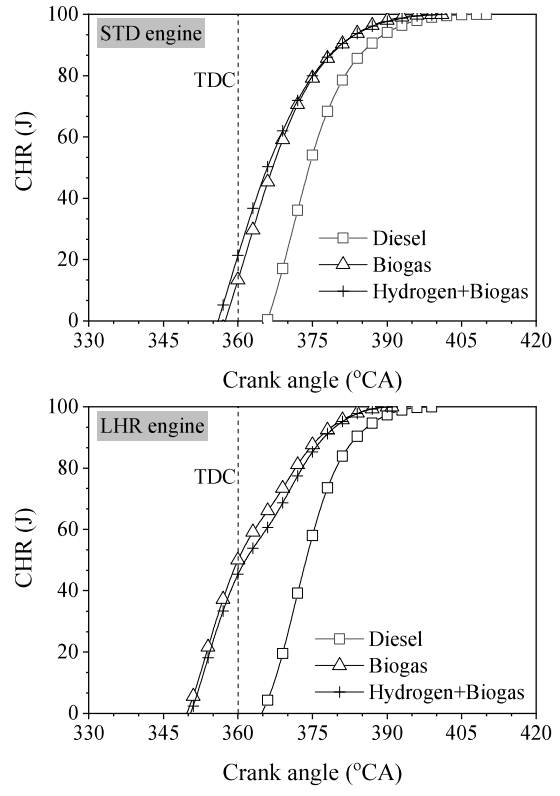


Figure 4. CHR values for STD and LHR engines

CHR variations for the test fuels under coated and uncoated modes are presented in Figure 4. The values presented in here were normalized CHR values. It revealed that the CHRs of the dual-fuel operations showed a faster premixed combustion phase, as the mixture was burned homogeneously and was triggered in several cores by the pre-injection of diesel fuel.

For dual-fuel modes a larger amount of the fuel was burned closer to the TDC. LHR engine clearly showed earlier combustion phases for all fuels as compared to those of the STD engine.

4 CONCLUSIONS

As alternative gaseous fuels, biogas and hydrogen-induced biogas were separately run in LHR engine and STD diesel engine. Combustion and performance characteristics of the engine were investigated in this study. Main conclusions obtained from this study are summarized below.

The combustion process occurred almost at a constant volume with dual-fuel modes.

Higher in-cylinder pressures were achieved in dual-fuel modes compared to conventional diesel fuel mode.

In-cylinder pressures under LHR engine were always higher than STD engine.

The significant part of the heat release took place before the main diesel fuel injection with dual-fuel mode.

Slightly higher heat release values were generally obtained with hydrogen-enriched biogas.

Earlier CHR occurred with dual-fuel modes compared to conventional diesel fuel mode.

REFERENCES

[1] S. S. Kalsi and K. A. Subramanian, Effect of Simulated Biogas on Performance, Combustion and Emissions Characteristics of a Bio-diesel Fueled Diesel Engine, *Renewable Energy*, Vol. 106, pp. 78-90, 2017.

[2] I. T. Yilmaz and M. Gumus, Investigation of the Effect of Biogas on Combustion and Emissions of TBC Diesel Engine, *Fuel*, Vol. 188, pp. 60-78, 2017.

[3] X. Shan, Y. Qian, L. Zhu and X. Lu, Effects of EGR Rate and Hydrogen/Carbon monoxide Ratio on Combustion and Emission Characteristics of Biogas/Diesel Dual Duel Combustion Engine, *Fuel,* Vol. 181, pp. 1050-1057, 2016.

[4] H. S. Tira, Impact of Alternative Fuels and Hydrogen-Enriched Gaseous Fuel on Combustion and Emissions in Diesel Engines, *Ph.D. Thesis*, Birmingham University, UK. 2013.

[5] G. Venkadesan and J. Muthusamy, Experimental investigation of Al_2O_3/8YSZ and CeO_2/8YSZ plasma sprayed thermal barrier coating on diesel engine, *Ceramics International*, Vol. 45, pp. 3166-3176, 2019.

[6] M. Civiniz, C. Hasimoglu, F. Şahin and M. S. Salman, Impact of Thermal Barrier Coating Application on the Performance and Emissions of a Turbocharged Diesel Engine, *Proc. ImechE. Part D. J. Auto. Eng.*, Vol. 222, pp. 2447-2455, 2008.

[7] I. T. Yılmaz, Effect of using dual fuel (biogas-diesel) on the performance and emissions of a low heat rejection diesel engine, *Ph.D. Thesis*, Marmara University, Turkey, 2015 [in Turkish].

[8] N. Saravanan, G. Nagarajan, C. Dhanasekaran, K. M. Kalaiselvan, Experimental investigation of hydrogen port fuel injection in DI diesel engine. *International Journal of Hydrogen Energy*, Vol. 32, pp. 4071–4080, 2007.

[9] Y. Karagöz, İ. Güler, T. Sandalcı, L. Yüksek, A.S. Dalkılıç, S. Wongwises, Effects of hydrogen and methane addition on combustion characteristics, emissions, and performance of a CI engine, *International Journal of Hydrogen Energy*, Vol. 41, pp. 1313-1325, 2016.

[10] N. Saravanan, G. Nagarajan, G. Snajay, C. Dhanasekaran, K.M. Kalaiselvan, Combustion analysis on a DI diesel engine with hydrogen in dual fuel mode, *Fuel*, Vol. 87, pp. 3591–3599, 2008.

A THERMODYNAMIC APPROACH TO CALCULATE THE MEAN TURBULENCE INTENSITY OF CNG AND GASOLINE FUELS IN A RESEARCH ENGINE

H.E. Doğan[1], A. Demirci[1], O.A. Kutlar[2], Ö. Cihan[3], H. Arslan[2]

1. Faculty of Engineering, Karamanoğlu Mehmetbey University, Karaman, Türkiye; email: hemredogan@kmu.edu.tr; arahmandemirci@kmu.edu.tr
2. Faculty of Mechanical Engineering, İstanbul Technical University, İstanbul, Türkiye; email: kutlar@itu.edu.tr; arslanh@itu.edu.tr
3. Faculty of Engineering, Hakkari University, Hakkari, Türkiye; email: omercihan@hakkari.edu.tr

Abstract

Combustion is the main parameter that affects efficiency and exhaust gas emissions in internal combustion engines. Recently, due to the increasing use of alternative fuels and leaning mixtures in spark ignition engines, different studies have been carried out to increase the burning rates. Compressed natural gas (CNG) is a promising alternative fuel with its high H/C ratio and widespread current infrastructure. In this study, the burning rates of gasoline and CNG were investigated quantitatively by calculating the mean values of turbulent burning speeds instead of qualitatively as is usually done. A three-zone quasi-dimensional thermodynamic model based on the measured cylinder pressure was created to calculate turbulent burning speeds. In MR shapes, it was determined that the turbulent burning speed decreased after it reached a maximum value in the combustion period. In the flat geometry, without any bowl, speed continuously decreased different from the other designs. Although the burning rate of gasoline was higher than CNG in the stoichiometric mixture, CNG burned faster than gasoline in the ultra-lean mixture. Using a quasi-dimensional thermodynamic model, mean values of the turbulent burning speeds and turbulence intensity might be calculated without having any optical observation and CFD analysis.

Keywords: Combustion chamber design, Turbulent burning speeds, Quasi-dimensional model, Low temperature combustion, CNG.

1 INTRODUCTION

Numerous studies have been conducted on increasing burning speed with alternative fuels such as CNG, LPG and Hydrogen [1,2]. With high H/C levels of compressed natural gas (CNG) and the existence of distributed infrastructure, it is the most promising alternative fuel [3]. If the compression ratio (ε) is about 14 without knocking, CNG might be 10% more efficient than gasoline [4]. In addition, usage of CNG could decrease the CO_2 emission by 15–20% due to higher H/C ratio of CNG [5]. The most effective method to reduce NO emissions is burning at low temperatures. Working with an ultra-lean mixture is a method used to reduce the temperature. Therefore, except for THC, all exhaust emissions could be reduced under the ultra-lean mixture conditions ($\lambda = 1.6 - 1.7$).

With an increase in burning speed, it is possible to work with lean mixtures. Furthermore, this change increases the efficiency value [6]. Changing the shape of the combustion chamber is one of the methods used to accelerate the combustion process [7]. With the combustion chamber design, the direction and intensity of air motion can be changed [8]. The diameter of the cylindrical bowl on the piston reveals regionally different intensities of turbulence [9].

In this study, three different geometries were formed on the piston crown in such a way that the compression ratio would be fixed. The effect of this change in the combustion chamber was evaluated, not over the burn durations as is usually done, but over the turbulent burning speeds with the help of a model, which was created using thermodynamic approaches. Rassweiler & Withrow [10] conducted the first study in this area. They divided the combustion chamber into two different sections by using cylinder pressure data, and an approach was

propounded to determine the volume and mass of a burned and unburned zones. Later, Lancaster et al. [11] proposed a developed approach that considered heat release as a basis. In recently, the approach of dividing the combustion chamber into different sections with quasi or single dimensional models continues to be used [12]. Nowadays quasi or single dimensional simulation programs are still used to calculate the parameters related to the combustion process [13]. However, these methods generally describe the process with many equations, and they are sometimes difficult to understand and practice [14]. In this study, the process is mainly defined based on shapes. With this method, the effect of different combustion chamber geometries and different fuels on turbulent burning speeds were examined. The ratio of the consumption speed to the laminar speed is an indicator of the flame surface areas or turbulence intensity in the combustion chamber. This speed ratio was directly defined as the wrinkling factor in some studies [15,16]. In addition, the mean turbulence intensity in the combustion chamber was determined with the approaches in the thermodynamic model, which is based on the Damköhler principle [17,18].

2 EXPERIMENTAL METHOD

2.1 Research Engine

An Antor 3LD 450 single cylinder spark-ignition engine was used in the experiments. The engine was based on a direct-injection and water-cooled diesel engine which was converted to a port fuel spark ignition engine [19]. The technical data of this engine may be seen in Table 1. In addition, a mini control unit (ECU) and software were developed in the laboratory to control this research engine [20]. The fuel pressure was kept at 1.0 bar for gasoline and 2.0 bar for CNG, and the injection timing was set to 50°CA after top dead center in the intake period.



Figure1. Produced combustion chamber geometries. Cylindrical bowl (*left*), MR (*centre*) and Flat (*right*)

Table 1. Research Engine Specifications

Engine specification	
Engine name	Antor 3LD450
Cylinder number	1
Fuel	Gasoline, CNG
Compression ratio	12
Engine volume, cm^3	454
Bore, mm	85
Stroke, mm	80
Fuel system	Electronically controlled, PFI
Ignition system	Electronically controlled, spark ignition
Charging	Naturally aspirated

2.2 Combustion Chamber Geometries

The pistons of the engine were purchased without any geometry on the piston crown. Designed geometries were manufactured by the machining process on the piston crown (Figure1), and the desired compression ratio ($\varepsilon = 12$) was set.

2.3 Measurement Systems

In the experiments, a 70 kW eddy-current engine brake dynamometer was used, and the engine torque was measured with a load-cell. Except for cylinder pressure, at each experiment, all the measured physical data was recorded during 90 seconds by the laboratory control system. An AVL GU21D piezoelectric transducer was used to measure the cylinder pressure. Exhaust gas emissions were carried out with a Horiba Mexa 7500. The experiments were carried out in different relative air/fuel ratios (λ=1.0, λ=1.30 and λ=1.6) and with a constant speed, 1500 rpm. The spark advance and air mass flow rate were selected as a constant value in all experiments.

3 THERMODYNAMIC MODEL

In this study, the combustion chamber was divided into three zones (Burned, Newly Burned and Unburned) and mean values of the basic parameters such as mean global consumption and turbulence intensity were calculated with the created model. Each calculation step in this model consists of 6 sub-steps (Figure 2). The basic starting point of the thermodynamic model is the Rassweiler – Withrow approach. As is known, this method is widely used in the calculation of heat release rate. In this study, heat release rate

was calculated with the Equation 1, which was based on the pressure increase created by the burning of fuel.

$$Q_{1_2} = \frac{1}{k-1} V_2 \left[p_2 - p_1 \left(\frac{V_1}{V_2} \right)^k \right] \quad (1)$$

The established model started by calculating the heat release rate, which was extracted from measured cylinder pressure data. In the following process, calculations continued with the instantaneous cylinder volume, the heat release rate, and the total mass of charge that entered the cycle. Detailed information about the model and the thermodynamic equations are given in the Ref [21].

The speed ratio of consumption speed to laminar burning speed was obtained in the model. According to the first approach proposed by Damköhler, this ratio can give information about the level of mean turbulence intensity [17]. The mean value of the turbulence intensity can be obtained from the speed ratios in Equation 2. The mean turbulence intensity could be calculated with Equation 2. A study [22] in the literature with both gasoline and CNG was used in the calculation of laminar burning speed.

$$\frac{S_T}{S_L} = 1 + 3.0 \left(\frac{u'}{S_L} \right)^{5/6} \quad (2)$$

4 RESULTS

An interpretation could be made about the speed of the combustion process by looking at the heat release rates. However, this assessment is usually qualitative. In all designs, gasoline burned faster than CNG at the stoichiometric mixture. The heat release rate data is a basic input parameter for the crated thermodynamic model.

The variation of turbulent consumption speed, which was calculated with the created thermodynamic model, was examined in this section. The MR design showed the highest values in consumption speed for both fuel types. During the combustion process, the burning speeds of the flat design decreased continuously, while the speed of the MR and CB firstly increased and then started to decrease (Figure 3). Considering that the spark advances, relative air/fuel ratio and air flow rate were constant in these experiments, the reason for this change was the turbulence created by the combustion chamber geometries.

There were some differences between the consumption speed of natural gas and gasoline. Gasoline fuel has a higher consumption speed at the stoichiometric mixture (Figure 3).

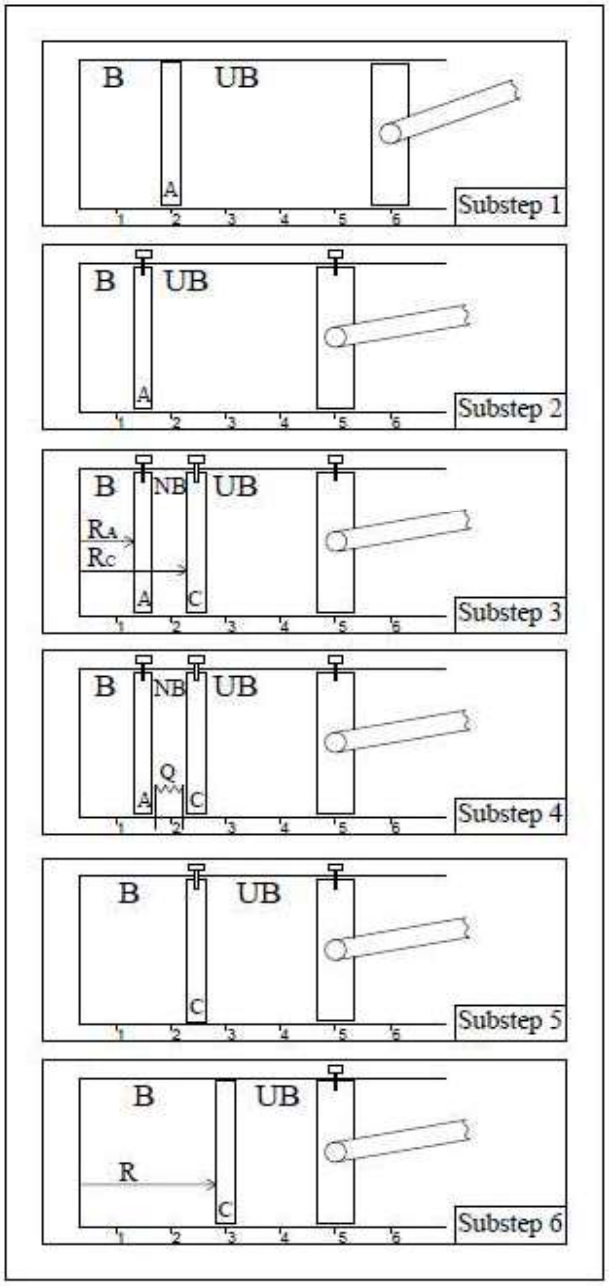


Figure 2. Schematic illustration of calculation sub-steps related to a thermodynamic model

Consumption speeds decreased in the lean mixture compared to the stoichiometric mixture, as expected. However, contrary to the stoichiometric mixture, the consumption speed of natural gas was higher than the consumption speed of gasoline in the ultra-lean mixture (λ=1.6) (Figure 4). The decrease in cylinder pressure, which was due to the leaning of the mixture, limited the decrease in the laminar burning speed of the CNG. Consumption speeds at ultra-lean

mixture were also investigated with the model. Since stable operation was not possible with flat geometry under these conditions, only MR and CB were compared.

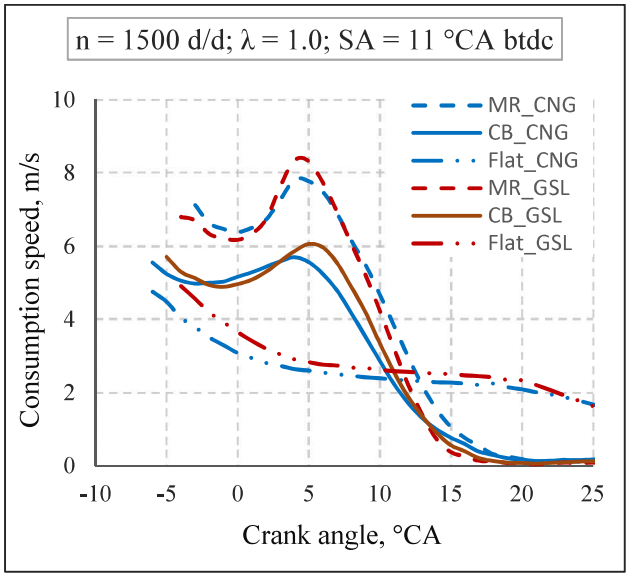


Figure 3. Variation of consumption speeds for different fuels and combustion chambers

In addition, it was not possible to ensure that CNG and gasoline run at the same spark advance in the ultra-lean mixture. As seen in (Figure 4), the MR design still increased the burning speed over a period. Under these conditions, the cycle to cycle variations (Net IMEP) were below 5%. If it is desired to operate with ultra-lean mixtures, turbulence intensity should be increased. In the MR design, it was observed that the consumption speed of CNG was clearly higher when both fuels had the same spark advance (Figure 4).

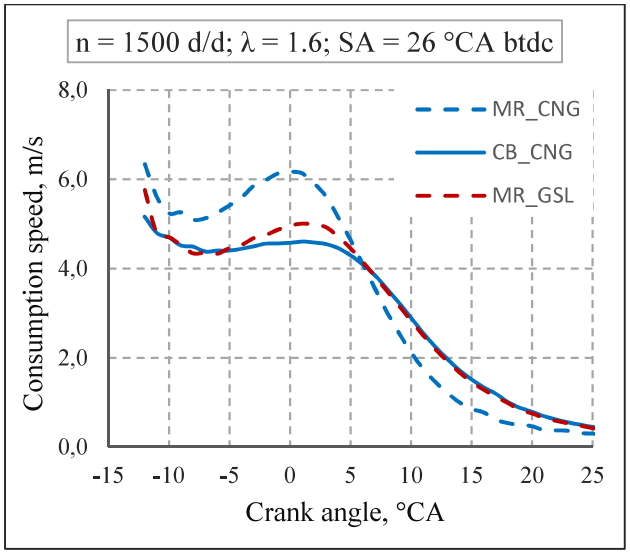


Figure 4. Consumption speeds of different chamber shapes in ultra-lean mixture

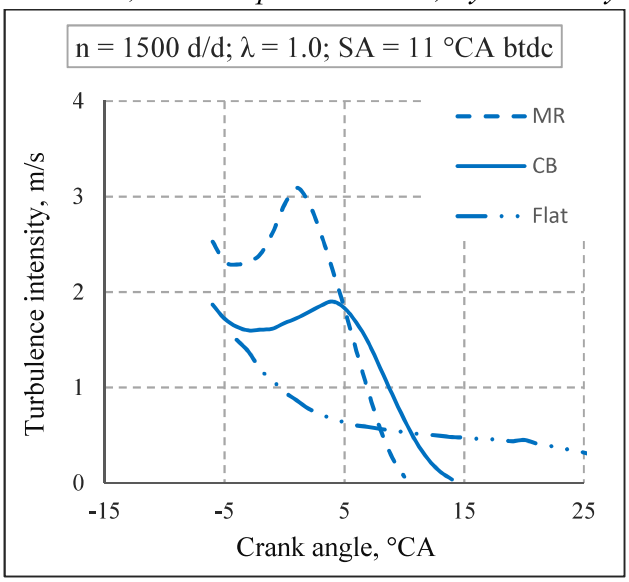


Figure 5. Variation of the calculated mean turbulence intensity

The mean value of turbulence intensity was calculated by Equation 2, which was given in section 3. As seen in Figure 5, the combustion chamber designs affected the mean turbulence intensity. Engine speed also has a significant effect on the calculated values. It is possible to reach turbulence intensity around 10 m/s at 2500-3000 rpm. It should be emphasized once again that this calculated turbulence intensity reflects the mean values. Otherwise, the turbulence intensity is higher values in the local region.

5 CONCLUSION

In this study, the combustion characteristics of different combustion chamber geometries and different fuels were investigated. A quantitative result has been revealed on turbulent burning speeds with the help of a created thermodynamic model instead of a qualitative evaluation based on burn duration, which is usually preferred in experimental studies. The generated quasi-dimensional thermodynamic model uses the experimentally measured cylinder pressure. Gasoline has a higher mean consumption speed than natural gas under stoichiometric conditions. However, this situation was reversed with the leaning of the mixture. In the designs that increase turbulence intensity, both flame propagation and consumption speeds were higher. In operating conditions with lean mixture, the combustion chamber geometry must be designed to create a certain amount of squish/tumble motion.

As a result, the mean value of turbulent burning speeds and turbulence intensity could be

calculated with the help of the quasi-dimensional thermodynamic model. Explaining the created model with geometric shapes and calculating with simple thermodynamic equations made it pretty understandable and useful.

ACKNOWLEDGEMENTS

The authors wish to thank TUBITAK (Scientific and Technological Research Council of Turkey) for their support of the scientific research (Project No. 218M232). Finally, The Authors also are grateful to Prof. Dr. Rafig Mehdiyev for his contribution of selection and design of combustion chamber geometries.

REFERENCES

[1] J. K. Pandey and G. N. Kumar, Effect of variable compression ratio and equivalence ratio on performance, combustion and emission of hydrogen port injection SI engine, *Energy*, Vol. 239, pp. 1-10, 2022.

[2] C. Wu, K. Deng and Z. Wang, The effect of combustion chamber shape on cylinder flow and lean combustion process in a large bore spark-ignition CNG engine, *J Energy Inst*, Vol. 89, pp. 240*247, 2016.

[3] F. Königsson, P. Stalhammar and H. E. Angstrom, Characterization and potential of dual fuel combustion in a modern diesel engine, *SAE Tech. Pap.*, 2011-01–2233, pp. 1-13, 2011.

[4] M. L. Poulton, Alternative fuels for road vehicles. Southampton, WIT Press/Computational Mechanics, Boston, UK, 1995.

[5] A. A. Yontar and Y. Dogu, Experimental and numerical investigation of effects of CNG and gasoline fuels on engine performance and emissions in a dual sequential spark ignition engine, *Energy Sources, Part A: Recovery, Utilization, and Environmental Effects*, Vol. 40, pp. 2176-2192, 2018.

[6] Z. Ran, D. Hariharan, B. Lawler and S. Mamalis, Experimental study of lean spark ignition combustion using gasoline, ethanol, natural gas, and syngas, *Fuel*, Vol. 235, pp. 530-537, 2019.

[7] S.G. Poulos and J. B. Heywood, The effect of chamber geometry on spark-ignition engine combustion, *SAE Tech. Pap.*, 830334, pp. 1-24, 1983.

[8] A. O. Hasan, H. Al-Rawashdeh, A. H. Al-Muhtaseb, A. Abu-jrai, R. Ahmad and J. Zeaiter, Impact of changing combustion chamber geometry on emissions, and combustion characteristics of a single cylinder SI (spark ignition) engine fueled with ethanol/gasoline blends, *Fuel*, Vol. 231, pp. 197-203, 2018.

[9] B. Yan, L. Tong, H. Wang, Z. Zheng, Y. Qin and M. Yao, Experimental and numerical investigation of the effects of combustion chamber reentrant level on combustion characteristics and thermal efficiency of stoichiometric operation natural gas engine with EGR, *Appl. Therm. Eng.*, Vol. 123, pp. 1473-1483, 2017.

[10] G. M. Rassweiler and L. Withrow, Motion pictures of engine flames correlated with pressure cards, *SAE Tech. Pap.*, 380139, pp. 185-204, 1938.

[11] D. R. Lancaster, R. B. Krieger, S. C. Sorenson and W. L. Hull, Effects of turbulence on spark-ignition engine combustion, *SAE Paper*, 760160, pp. 689–710, 1976.

[12] E. Conte and K. Boulouchos, A quasi-dimensional model for estimating the influence of hydrogen-rich gas addition on turbulent flame speed and flame front propagation in IC-SI engines, *SAE Tech. Pap.*, 2005-01-0232, pp. 1-13, 2005.

[13] B. Afkhami, Y. Wang, S. A. Miers and J. D. Naber, Development of a turbulent burning velocity model based on flame stretch concept for SI engines. *J Energy Inst.*, Vol. 93, pp. 2444-2455, 2020.

[14] I. Altin and A. Bilgin, Quasi-dimensional modeling of a fast-burn combustion dual-plug spark-ignition engine with complex combustion chamber geometries, *Appl. Therm. Eng.*, Vol. 87, pp. 678-687, 2015.

[15] B. Renou and A. Boukhalfa, An experimental study of freely propagating premixed flames at various Lewis numbers, *Combust. Sci. Technol.*, Vol. 162, pp. 347-370, 2001.

[16] P. Clavin, and F. A. Williams, Effects of molecular diffusion and of thermal expansion on the structure and dynamics of premixed flames in turbulent flows of large scale and low intensity. *J. Fluid Mech.*, Vol. 116, pp. 251-282, 1982.

[17] S. R. Turns, An introduction to combustion: concepts and applications, *MCGraw Hill*, New York, USA, 2000.

[18] A. Ratzke, T. Schöffler, K. Kuppa and F. Dinkelacker, Validation of turbulent flame speed models for methane-air mixtures at high pressure gas engine conditions, *Combust. Flame*, Vol. 162, pp. 2778-2787, 2015.

[19] O. A. Kutlar, A New method to decrease the fuel comsumption at part load conditions of four stroke ottocycle (rochas) engine (skipperiod engine), PhD Thesis, Istanbul Technical University, 1999.
[20] Ö. Tekeli, Designing and production ignition and injection units of a gasoline engine with skip cycle, MsC Thesis, Istanbul Technical University, 2013.
[21] H. E. Doğan, Investigation of different combustion chamber geometries with natural gas and gasoline fuel, PhD Thesis, Istanbul Technical University, 2019.
[22] R. Amirante, E. Distaso, P. Tamburrano and R. D. Reitz, Laminar flame speed correlations for methane, ethane, propane and their mixtures, and natural gas and gasoline for spark-ignition engine simulations, *Int. J. Engine Res.*, Vol. 18, pp. 951-970, 2017.

EXPERIMENTAL INVESTIGATION ON EXPLOITING THE BIOFUELS BLEND AND IMPROVING ITS USABILITY BY ADDING TiO_2 NANOPARTICLES

Abdülvahap ÇAKMAK[1]

1. Department of Motor Vehicles and Transportation Technologies, Kavak Vocational School, Samsun University, Samsun; email: abdulvahap.cakmak@samsun.edu.tr

Abstract

Biofuels are clean and renewable fuels produced from various local bioresources. In the energy field, biofuels have gained significant importance because they reduce exhaust emissions and alleviate the dependence on oil imports. However, biofuels can decrease the performance of the engines as they have poorer fuel properties than petroleum fuels, which is a significant drawback of biofuel use. On the other hand, using nanoparticles as a fuel additive is a feasible way to overcome performance issues and exploit biofuels' advantages more. In the current study, an experimental investigation is carried out to improve biofuel usability by adding TiO_2 nanoparticles to the base fuel. The combustion, performance, and emissions characteristics of a conventional diesel engine fuelled with TiO_2-doped biofuels-diesel blends are established. TiO_2 nanoparticles are added to a biofuel-diesel combination (B25) at 50, 100, and 150 ppm concentrations by implementing a mechanical stirrer and ultrasonication process. Biofuel is made by mixing biodiesel, waste cooking oil, and ethanol at a volumetric ratio of 0.6, 0.2, and 0.2, respectively. The test engine is operated at a fixed speed of 1500 rpm, and loads of 0.1, 0.2, 0.3, and 0.4 MPa brake mean effective pressure. Results reveal that the inclusion of TiO_2 nanoparticles in B25 fuel brings overall improvement in combustion, performance, and exhaust emission characteristics. Moreover, B25+TiO_2 nanofuels considerably decrease brake-specific fuel consumption, up to 7.9%, compared to base fuel without nanoparticles. At the same time, TiO_2 doped fuels yield a maximum reduction in CO emission and smoke opacity by 31.9% and 26.2%, while a maximum rise in NO emission by 30.8% is detected relative to base fuel. Consequently, it can be inferred that using nanoparticles upgrades the biofuel's performance, speeding up switching from fossil fuels to biofuels. Nevertheless, regarding metallic nanoparticles' usability, there are serious impediments to be passed over, such as high fuel costs and hazardous effects of nanoparticles on human and environmental health.

Keywords: Biofuels, Combustion, Diesel, Emissions, Nanofuel, Nanoparticles, TiO_2

1 INTRODUCTION

It is a fact that future petroleum production will not meet growing fuel needs because the energy demand is continuously increasing, and petroleum reserves are extinguishing. In addition, the fact that oil reserves are in limited geography causes political crises and induce oil prices to rise incessantly. This situation has happened recently again due to the Russia-Ukraine war. Fortunately, biofuels produced from local renewable sources can make it possible to deal with such difficult situations. In other words, replacing fossil fuels with biofuels can reduce some drawbacks of fossil fuel use, including pollutant emissions, depletion of the limited oil reserves, dependence on foreign suppliers, and unstable prices. Therefore, it is requisite to switch to biofuels from petroleum fuels gradually.

Bioethanol and biodiesel are the most commonly used liquid biofuels for internal combustion engines, and these biofuels can take the place of petroleum fuels [1]. However, the significant technical drawback of biofuels is that they have poor physicochemical fuel properties, causing performance loss in engines developed for petroleum-based fuel [2]. As a result, scientists have increased their efforts to improve biofuels' performance and promote their usability.

Nanoparticles with large surface areas, high thermal conductivity, and catalytic activity are unique fuel additives, assisting efficient combustion and lowering exhaust emissions [3]. Therefore, nanoparticles have emerged as an efficient solution to improve diesel engine

emission and performance [4]. As a result, the application of metal nanoparticles as a fuel additive to diesel engine fuels has recently increased [5].

The impact of nanoparticles on the combustion, performance, and emissions of diesel engines has been investigated in the research primarily conducted in the last decade. For example, Bello et al. [6] explored the CI performance and soot characteristics of the engine fuelled with diesel fuel, including titanium dioxide nanoparticles. Results stated that higher engine performance is acquired with TiO_2-doped fuel. Additionally, nanoparticles were found capable of inhibiting PM formation due to enhanced chemical reactivity.

Sundar et al. [7] studied the usability of the neat plastic oil with TiO_2 nanoparticles added as an additive at 100, 150, and 200 ppm concentrations in a diesel engine. They observed a significant improvement in engine performance and emissions for TiO_2 nanoparticles doped- neat plastic oil.

Praveen et al. [8] investigated the engine characteristics of a diesel engine run with B20 mixed with TiO_2 nanoparticles in concentrations of 20, 40, 60, and 80 ppm and found encouraging results. A substantial decrease in specific fuel consumption, smoke, HC, and CO emissions occurred by adding nanoparticles. But a marginal increase in NOx emissions was also observed.

Vigneswaran et al. [9] found that adding TiO_2 nanoparticles to water-in-diesel emulsion fuel improves engine performance; thermal efficiency increases by 5.6%, along with a substantial decrease in CO, HC, and smoke emissions with nano-emulsified fuels.

In a recent study [10], authors analyzed the energy, exergy, exergoeconomic, exergoenvironmental, and sustainability aspect of a diesel engine fuelled with a diesel-ethanol-nanoparticles combination. They reported that the diesel-ethanol blend, including TiO_2 nanoparticles, performs better for aspects of energy and exergy efficiencies and environmental impact than pure diesel fuel. However, the exergoeconomic analysis showed that nano fuel prepared with TiO_2 nanoparticles increases the cost of brake work per unit exergy by 48.4% compared to diesel fuel. Consequently, cheap biofuels such as waste cooking biodiesel are recommended rather than ethanol to decrease the high cost.

There is a further need to perform a scientific investigation to improve the performance and emissions of diesel engines, considering the utilization of biofuels with nanoparticles.

Although studies have been performed so far and offer significant contributions to the literature, most of these studies typically consider only one type of fuel (diesel, alcohol and biodiesel or their blends). Therefore, this investigation is specially conducted for a diesel-biofuel combination including various biofuels. This study aims to research the characteristics of a diesel engine fuelled with nanofuel created by mixing biodiesel, waste cooking oil and ethanol, and neat diesel along with TiO_2 nanoparticles.

2 MATERIALS AND METHODS

Four fuel blends are prepared and subjected to engine tests in this experimental study. All test fuels have a constant biofuel fraction of 25% by volume. The biofuel fraction makes up 15% canola oil biodiesel, 5% ethanol, and 5% waste cooking oil. A reference fuel named RF is prepared by mixing the biofuels and diesel fuel. Three test fuels, TF1, TF2, and TF3, are created by adding 50 ppm, 100 ppm, and 150 ppm TiO_2 nanoparticles to the reference fuel. The fuel composition and nanoparticle dosage are presented in Table 1. The same basic fuel properties of these fuels are shown in Table 2.

Table 1. Fuel Composition by Volume Percent

Components	RF	TF1	TF2	TF3
Diesel	75	75	75	5
Biodiesel	15	15	15	15
Ethanol	5	5	5	5
Waste cooking oil	5	5	5	5
TiO_2 concentration (ppm)	0	50	100	150

A schematic representation of the experimental test setup is illustrated in Figure 1. The details of this unit are given in the following. A four-stroke, single-cylinder, liquid-cooled, direct injection diesel engine is employed for engine tests. The test engine operates at a fixed speed of 1500 rpm and has different torque outputs. It produces a maximum torque of 21.8 Nm and a full brake power of 3.5 kW. For the experimentation, no modification is made, and it is operated at standard compression ratio and injection timing. An Eddy current dynamometer

with a water-cooled system is connected to the engine output shaft to load the engine. The dynamometer has a 10 kW absorption capacity and a maximum rotation speed of 10000 rpm. A loading unit is utilized to adjust the dynamometer load, and its value is measured by a load cell. In addition, the volumetric flow rate of the intake air and fuel is gauged with an air flow transmitter and a fuel flow transmitter, respectively.

A piezoelectric pressure transducer with a 0-34.5 MPa measuring range is employed to detect cylinder pressure. The crankshaft sensor monitors the position and rotational speed of the crankshaft. The cylinder pressure is recorded with a one ºCA interval over 100 consecutive cycles. Data over experimentation time is monitored and collected by a data logger (NI) and then stored in the computer. The experimental data is further processed in "*ICEngineSoft 9.0 V*" software to determine engine performance and combustion details. The captured cylinder pressure data is processed according to the first law of thermodynamics to calculate the heat release rate. For this, it is assumed that the gas mixture inside the engine cylinder obeys the ideal gas law and is uniform in temperature, pressure, and chemical composition [11].

$$\frac{dQ_{NHR}}{d\theta} = \frac{k}{k-1} P \frac{dV}{d\theta} + \frac{1}{k-1} V \frac{dP}{d\theta} \qquad (1)$$

In Equation (1), k $\left(= c_p/c_v\right)$ is the specific heat ratio of the gas mixture. θ and P is the measured crank angle and instantaneous cylinder pressure, respectively. Finally, V is the instantaneous cylinder volume.

Table 2. Some Basic Fuel Properties

Property	RF	TF1	TF2	TF3
Density@15 ˚C, kg/m^3	839.3	839.2	839.5	839.2
Flash Point, ˚C	24	24	24	24
Cetane index	53.4	53.7	53.6	54.1
T10, ˚C	196.5	196.9	198.2	200.3
T50, ˚C	289.2	290.7	290.7	291.7
T90, ˚C	347.0	348.7	348.8	349.3

BOSCH BEA 550 emissions device is wielded to measure smoke opacity, carbon monoxide (CO), and nitrogen oxide (NO). This device determines the smoke opacity by measuring the absorbed light by exhaust gases passing through the exhaust gas optical duct with an accuracy of 0.01 m^{-1}. In order, the measurement accuracy for the CO and NO is ±0.005% and ±1 ppm. Engine tests are carried out at the speed of 1500 rpm and loads of 0.1, 0.2 0.3, and 0.4 MPa brake mean effective pressure (bmep). The selected loads are equivalent to 25%, 50%, 75%, and 100% engine load, respectively. Once steady-state conditions are set, engine tests are started, and each test is repeated at least three times to minimize errors. Emissions are measured and recorded with an interval of 40 s during five minutes, and the averaged values are considered for comparison.

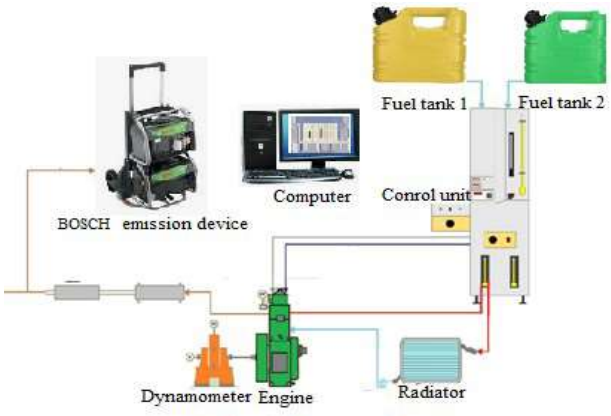


Figure 1. The engine test setup layout

3 RESULTS AND DISCUSSIONS

The investigated combustion parameters include cylinder pressure (CP), net heat release rate (NHR), and pressure rise rate (PRR). These combustion characteristics are determined at an engine load of 0.4 MPa and presented graphically in the following Figures. Figure 2 illustrates the recorded maximum cylinder pressure and its crank angle (CA) position for fuels. In addition, it is seen that adding TiO_2 nanoparticles to reference fuel (RF) slightly increases the maximum cylinder pressure value. As a result, the peak CP for RF, TF1, TF2, and TF3 are 5.30, 5.38, 5.53, and 5.42 MPa, respectively, occurring at 7 °CA aTDC. The increase in cylinder pressure can be ascribed to the effects of nanoparticles on combustion. Nanoparticles homogenize the fuel-air mixture thanks to their large surface area; nanoparticles' catalytic impact on chemical reactions brings more excellent combustion and hence high cylinder pressure [12], [13]. Bello et al. [6] reported similar results in their study where cylinder pressures for TiO_2-doped fuels are higher than that of diesel fuel. The main reason for this improvement in-cylinder pressure is

attributed to the high thermal conductivity of the nanoparticles that upgrades the fuel-air mixing process.

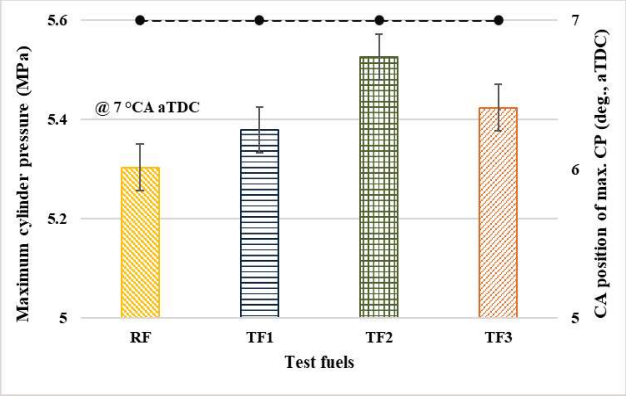


Figure 2. Maximum CP and its CA location for fuels

The maximum heat release rate and its crank angle position for fuels are shown in Figure 3. Adding 50 ppm TiO_2 nanoparticles to reference fuel increases the maximum net heat release rate twice compared to reference fuel. TF1 gives a heat release rate of 41.9 J/˚CA at 5 ˚CA bTDC. Further, TF2 and TF3 also raise the maximum heat release rate value by 67.9% and 57.1% compared to RF. Moreover, all fuels' peak heat release rate occurs at 5 °CA bTDC. The heat release rate is linked to combustion speed [11]. TiO_2 nanoparticles can accelerate chemical reactions between the fuel and air molecules and thus combustion, resulting in a quick heat release. Therefore, nanoparticle-doped fuels offer a higher maximum heat release rate than reference fuel. The maximum pressure rise rate and its crank angle position for fuels are presented in Figure 4. The determined maximum pressure rise rate is 0.36, 0.37, 0.34, and 0.32 MPa/°CA at 5 °CA bTDC for RF, TF1, TF2, and TF3, respectively. TF1 increases the PRR somewhat while TF2 and TF3 slightly diminish the maximum value of PRR compared to reference fuel. In addition, all fuels present a lower maximum PRR than 1 MPa/°CA, which is the limit of diesel engine knocking. This outcome shows that the diesel engine can withstand wear, pressure, or damage and run smoothly when fueled with these fuels.

Figure 5 illustrates the brake-specific fuel consumption (bsfc) for fuels. The variation of bsfc with engine load at a fixed engine speed matches typical reciprocating engine characteristic. In other words, bsfc decreases as the engine load increases owing to rising brake power and combustion efficiency. At all brake mean effective pressures, reference fuel presents the highest bsfc, whereas test fuels with TiO_2 nanoparticles diminish the bsfc due to improved combustion inside the cylinder. TF1, TF2, and TF3 provide an overall decrease in bsfc by 0.79%, 1.40%, and 3.91% compared to RF. Adding TiO_2 nanoparticles to reference fuel can improve the fuel cetane index and fuel atomization, enhancing engine performance. Nanoparticles can extend the fuel spray penetration inside the cylinder, yielding a more homogeneous fuel-air mixture [14]. In addition, TiO_2 nanoparticles have high thermal conductivity [15], which can increase convective heat transfer between the droplets of fuel and gas molecules, providing effective fuel evaporation and mixing process. Therefore, better combustion occurs, and a lower bsfc is accomplished [16]. Many researchers have observed similar results; El-Seesy et al.[17], Soudagar et al. [18] and Mujtaba et al. [19] have found a decrease in bsfc with nanoparticle addition to fuels.

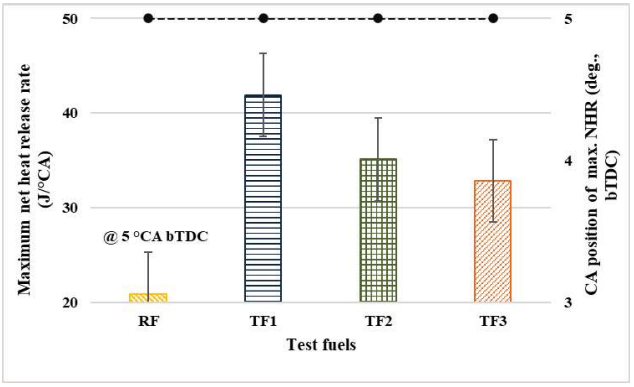


Figure 3. Maximum NHR and its CA location for fuels

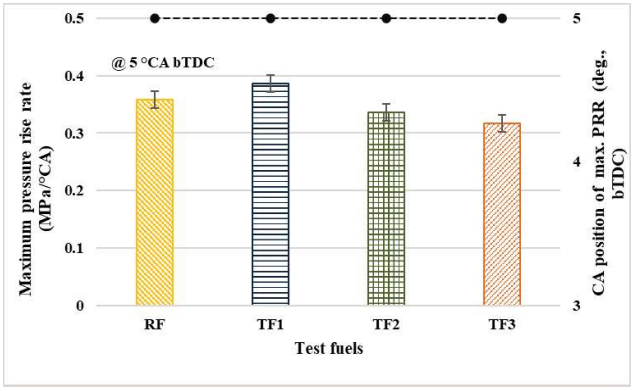


Figure 4. Maximum PRR and its CA location for fuels

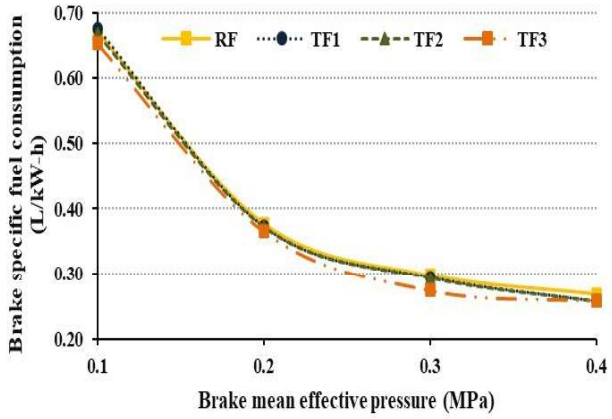


Figure 5. Brake-specific fuel consumption for fuels

The recorded exhaust gas temperature for all fuels is shown in Figure 6. It is seen that the exhaust gas temperature rises with an increase in engine load since the amount of fuel combusted per cycle augments. Moreover, adding TiO_2 nanoparticles to reference fuel raises the exhaust temperature. It is determined that the average exhaust gas temperature for TF1, TF2, and TF3 is high by 1.3%, 1.8%, and 2.1%, respectively, compared to reference fuel. It is attributed to the catalytic effect of nanoparticles, which results in enhanced combustion rate and, thus, high gas temperature. One other possible reason for high exhaust gas temperature for nanoparticles doped fuels can be less heat loss occurs by radiation. As seen in Figure 9, test fuels decrease the soot emissions that increase the heat transfer to the cylinder walls through radiation inside the cylinder. Solid carbon particles (PM) are mainly generated in the cylinder during the diffusion combustion stage [11]. It is when the combustion temperature reaches the maximum; thus, considerable heat loss occurs with radiation [20]. Therefore, a high concentration of soot emissions further increases the radiative heat transfer, resulting in low exhaust gas temperature. Besides, the exhaust gas temperature is affected by the fuel's calorific value and vaporization enthalpy [21]. However, those fuel properties are expected to not change significantly with the nanoparticle addition. Therefore, the effect of the fuel properties mentioned above on exhaust temperature can be too small to be worth consideration.

The variation of CO emissions with bmep for all fuels is shown in Figure 7. It is seen that the amount of CO emission decreases as the bmep increases. It is because higher in-cylinder temperature boosts the conversion of CO into CO_2. However, CO emission for TF1 and TF2 present an increasing trend at maximum bmep case because rich mixture combustion produces higher CO emission. The addition of TiO_2 nanoparticles to reference fuel significantly can enhance fuel oxidation on account of the catalytic effect of nanoparticles, providing a substantial CO reduction. The maximum decrease in average CO emission by 21.9% is observed for 100 ppm nanoparticle concentration compared to reference fuel. Adding 50 ppm and 150 ppm TiO_2 also reduces the CO emission by 14.1% and 3.1%, on average. Distinct researchers [7], [22], [23] found a similar trend of CO emission for TiO_2 nanoparticle-doped fuels.

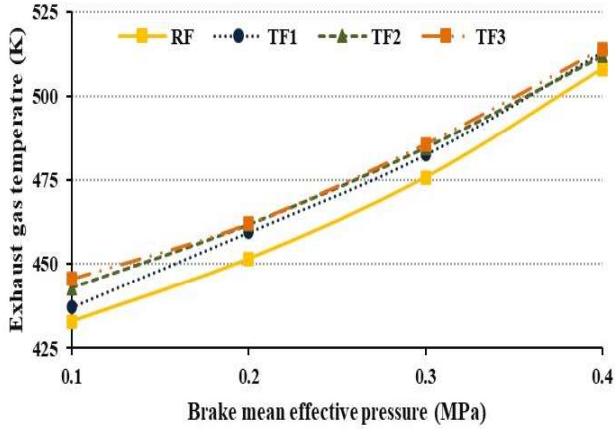


Figure 6. Exhaust gas temperature for fuels

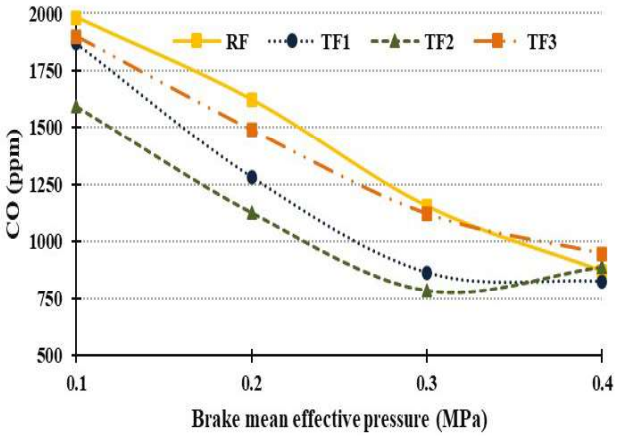


Figure 7. CO emission for fuels

The variation of NO emission of fuels concerning bmep is presented in Figure 8. The graph displays an upward trend in NO emission with an increase in bmep irrespective of fuel

type. It is related to cylinder temperature; high combustion temperature leads to more NO emissions [24]. TiO_2-doped fuels generate more NO emissions than the reference fuel. As the concentration of TiO_2 in the fuel blend increases, the NO emission further increases. The increment in NO emission with nanoparticles can be ascribed to high cylinder pressure and heat release rate due to improved combustion because of the catalytic effect of nanoparticles. Örs et al. [23], Praveen et al. [8], and Al-Hartomy et al. [25] reported a similar increase in NOx emissions for various TiO_2-doped fuels.

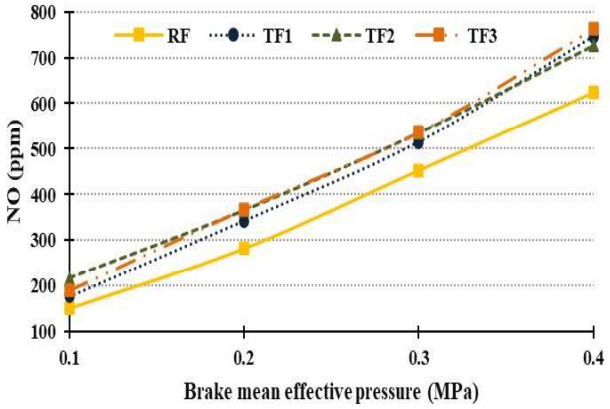


Figure 8. NO emission of fuels

Figure 9 illustrates the chancing in smoke opacity with bmep for test fuels. Due to decreasing air-to-fuel ratio, smoke opacity increases as engine load increases. Therefore, the maximum smoke opacity is measured at bmep of 0.4 MPa by 0.9, 1.0, 0.8, and 0.7 m^{-1} for RF, TF1, TF2, and TF3, respectively, and the overall reduction in exhaust smoke opacity is 2.2%, 4.2%, 19.6%, in the same order for TiO_2 doped test fuels. The addition of nanoparticles to reference fuel decreases the overall smoke opacity of exhaust gases. The reduction in smoke opacity for test fuels may be due to the large surface area to volume ratio of nanoparticles, increasing the rate of evaporation, mixing, and combustion. Moreover, due to the high thermal conductivity of the nanoparticles [7], the evaporation of fuel droplets existing in the rich regions can be accelerated, bringing better mixture formation, and producing fewer particle matters. Most of the generated soot particles within the engine cylinder burn during the expansion stroke when the temperature and oxygen concentration is high, and there is sufficient oxidation time [11]. However, the turbulence intensity significantly affects the soot oxidation rate [11]. Nanoparticles can also increase the turbulence level in the cylinder [26]; therefore, the smoke opacity decreases.

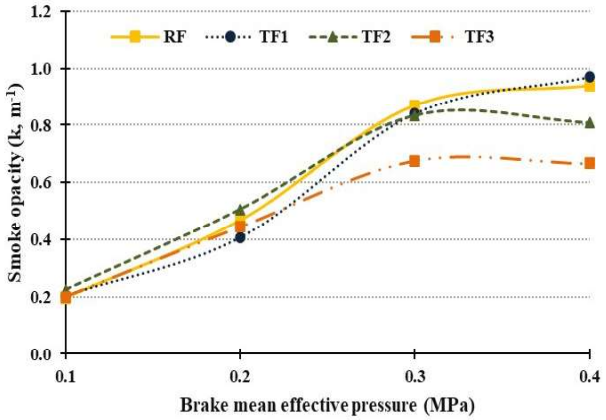


Figure 9. Smoke opacity for fuels

4 CONCLUSIONS

This research investigates the combustion, performance, and exhaust emissions parameters of a direct injection diesel engine run on TiO_2-doped biofuel-diesel blends under varying bmep conditions. Based on the experimental results, the following conclusions are derived.

- The performance and emissions characteristics investigated of the engine have the same tendencies with the bmep but with different magnitudes for reference fuel and nanoparticle-added fuels.
- The biofuel-diesel blends, including TiO_2 nanoparticles, can be directly used in existing diesel engines without needing a retrofit.
- Brake-specific fuel consumption for nanoparticles doped fuels decreases compared to the fuel without nanoparticles. For example, TF3, including 150 ppm TiO_2 nanoparticles, yields the highest decrease in brake-specific fuel consumption by 3.9%, on average.
- All fuels containing nanoparticles enhance the cylinder pressure and heat release rate. The rate of pressure rise rate data indicates that those fuels are not causing engine knocking, and hence the addition of nanoparticles to engine fuels could keep the engine durability.
- An inclusion of TiO_2 nanoparticles to base fuel ensures a reduction in the CO emission and smoke opacity by 31.9%

and 26.2%, except for NO emission, which increases by 30.6%.

- TiO_2 nanoparticles are influential additives for improving the engine's performance and emissions fuelled with a diesel-biofuel mixture composed of biodiesel, waste cooking oil, and ethanol.
- Although favorable results are obtained with TiO_2 nanoparticles, the health consequences of the nanoparticles emitted by exhaust gases are a big challenge to be succeeded. Besides, a new emission control system is required to capture nanoparticles in exhaust gases.
- For nanoparticle-doped biofuel-powered engines, NO_X emission should be mitigated and may require an additional NO_X emission control strategy.
- Currently, the price of metallic nanoparticles in the market is very high, which makes the nano fuel expensive. However, the overall benefits of using nanoparticles doped biofuels are much higher in terms of cost.
- The effect of TiO_2 on the performance of after-treatment devices can be investigated in future research.

REFERENCES

[1] M. Puškár, J. Živčák, M. Kočišová, M. Šoltésová, and M. Kopas, "Impact of bio-renewable energy sources on reduction of emission footprint from vehicles," *Biofuels, Bioprod. Biorefining*, vol. 15, no. 5, pp. 1385–1394, 2021.

[2] T. N. Verma *et al.*, "A comprehensive review of the influence of physicochemical properties of biodiesel on combustion characteristics, engine performance, and emissions," *J. Traffic Transp. Eng. (English Ed.*, vol. 8, no. 4, pp. 510–533, 2021.

[3] J. D. Ampah *et al.*, "Progress and Recent Trends in the Application of Nanoparticles as Low Carbon Fuel Additives—A State of the Art Review," *Nanomaterials*, vol. 12, no. 9, p. 1515, 2022.

[4] A. T. Hoang *et al.*, "Understanding behaviors of compression ignition engine running on metal nanoparticle additives-included fuels: A control comparison between biodiesel and diesel fuel," *Fuel*, vol. 326, p. 124981, 2022.

[5] V. Saxena, N. Kumar, and V. K. Saxena, "Multi-objective optimization of modified nanofluid fuel blends at different TiO2 nanoparticle concentration in diesel engine: Experimental assessment and modeling," *Appl. Energy*, vol. 248, pp. 330–353, 2019.

[6] Y. H. Bello *et al.*, "Investigating the engine performance, emissions and soot characteristics of CI engine fueled with diesel fuel loaded with graphene oxide-titanium dioxide nanocomposites," *Fuel*, vol. 269, p. 117436, Jun. 2020.

[7] S. P. Sundar *et al.*, "Feasibility study of neat plastic oil with TiO2 nanoadditive as an alternative fuel in internal combustion engine," *J. Therm. Anal. Calorim.*, vol. 147, no. 3, pp. 2567–2578, 2022.

[8] A. Praveen, R. L. Krupakaran, G. Lakshmi Narayana Rao, and B. Balakrishna, "An assessment of the TiO2 nanoparticle concentration in the C. inophyllum biodiesel blend on the engine characteristics of a DI diesel engine," *Int. J. Ambient Energy*, pp. 1–14, 2021.

[9] R. Vigneswaran, D. Balasubramanian, and B. D. S. Sastha, "Performance, emission and combustion characteristics of unmodified diesel engine with titanium dioxide (TiO2) nano particle along with water-in-diesel emulsion fuel," *Fuel*, vol. 285, p. 119115, 2021.

[10] Ü. Ağbulut, C. Uysal, E. J. C. Cavalcanti, M. Carvalho, M. Karagöz, and S. Saridemir, "Exergy, exergoeconomic, life cycle, and exergoenvironmental assessments for an engine fueled by diesel–ethanol blends with aluminum oxide and titanium dioxide additive nanoparticles," *Fuel*, vol. 320, p. 123861, 2022.

[11] J. B. Heywood, *Internal combustion engine fundamentals.* New York: McGraw-Hill, 1988.

[12] S. Kumar, P. Dinesha, and I. Bran, "Experimental investigation of the effects of nanoparticles as an additive in diesel and biodiesel fuelled engines: a review," *Biofuels*, vol. 10, no. 5, pp. 615–622, Sep. 2019.

[13] A. T. Hoang, "Combustion behavior, performance and emission characteristics of diesel engine fuelled with biodiesel containing cerium oxide nanoparticles: A review," *Fuel Process. Technol.*, vol. 218, p. 106840, 2021.

[14] G. Balaji and M. Cheralathan, "Effect of CNT as additive with biodiesel on the performance and emission characteristics of a DI diesel engine," *Int. J. ChemTech Res.*, vol. 7, no. 3, pp. 1230–1236, 2015.

[15] Q. Xu *et al.*, "Experimental study on synergistic enhancement of thermal performance of a closed two-phase thermosyphon by a TiO2 nanofluid doped with Al2O3," *Case Stud. Therm. Eng.*, p. 102192, 2022.

[16] A. I. EL-Seesy, H. Kosaka, H. Hassan, and S. Sato, "Combustion and emission characteristics of a common rail diesel engine and RCEM fueled by n-heptanol-diesel blends and carbon nanomaterial additives," *Energy Convers. Manag.*, vol. 196, pp. 370–394, Sep. 2019.

[17] A. I. El-Seesy, A. M. A. Attia, and H. M. El-Batsh, "The effect of Aluminum oxide nanoparticles addition with Jojoba methyl ester-diesel fuel blend on a diesel engine performance, combustion and emission characteristics," *Fuel*, vol. 224, pp. 147–166, 2018.

[18] M. E. M. Soudagar *et al.*, "Effect of Sr@ZnO nanoparticles and Ricinus communis biodiesel-diesel fuel blends on modified CRDI diesel engine characteristics," *Energy*, vol. 215, p. 119094, 2021.

[19] M. A. Mujtaba *et al.*, "Comparative study of nanoparticles and alcoholic fuel additives-biodiesel-diesel blend for performance and emission improvements," *Fuel*, vol. 279, p. 118434, 2020.

[20] W. W. Pulkrabek, *Engineering Fundamentals of the Internal Combustion Engine*. New Jersey: Prentice Hall, Inc., 1997.

[21] I. A. Resitoglu, "The effect of biodiesel on activity of diesel oxidation catalyst and selective catalytic reduction catalysts in diesel engine," *Renew. Sustain. Energy Rev.*, vol. 148, p. 111286, 2021.

[22] S. Ge *et al.*, "Performance, combustion and emission characteristics of the CI engine fueled with Botryococcus braunii microalgae with addition of TiO2 nanoparticle," *Fuel*, vol. 317, p. 121898, 2022.

[23] I. Örs, S. Sarıkoç, A. E. E. Atabani, S. Ünalan, and S. O. O. Akansu, "The effects on performance, combustion and emission characteristics of DICI engine fuelled with TiO2 nanoparticles addition in diesel/biodiesel/n-butanol blends," *Fuel*, vol. 234, pp. 177–188, Dec. 2018.

[24] M. Puškár and M. Kopas, "System based on thermal control of the HCCI technology developed for reduction of the vehicle NOX emissions in order to fulfil the future standard Euro 7," *Sci. Total Environ.*, vol. 643, pp. 674–680, 2018.

[25] O. A. Al-Hartomy, M. A. Mujtaba, A. Al-Ghamdi, J. Iqbal, and S. Wageh, "Combined effect of Phoenix dactylifera biodiesel and multiwalled carbon nanotube–titanium dioxide nanoparticles for modified diesel engines," *Int. J. Environ. Sci. Technol.*, vol. 19, no. 1, pp. 515–540, 2022.

[26] A. Suhel, N. Abdul Rahim, M. R. Abdul Rahman, and K. A. Bin Ahmad, "Engine's behaviour on magnetite nanoparticles as additive and hydrogen addition of chicken fat methyl ester fuelled DICI engine: A dual fuel approach," *Int. J. Hydrogen Energy*, vol. 46, no. 27, pp. 14824–14843, 2021.

DETONASYON MOTORUNA SAHİP ROKETLERDE ÖN-DETONATORDE FARKLI HİDROJEN-KARBON ORANLARINA SAHİP YAKITLARIN ŞOK DALGASI ÜZERİNDEKİ ETKİSİNİN İNCELENMESİ

Ahmet Alper YONTAR[1] ve Mehmet Ali ADIGÜZEL[2]

1. Ahmet Alper YONTAR, Mühendislik Fakültesi, Tarsus Üniversitesi, Tarsus, Mersin; email: aayontar@tarsus.edu.tr
2. Mehmet Ali ADIGÜZEL, Makine Mühendisliği Anabilim Dalı, Tarsus Üniversitesi, Tarsus, Mersin; email: mehmet_adiguzel@tarsus.edu.tr

Özet

İtki sistemleri günümüzün en önemli konularından biridir. Sivil havacılıktan savunma sanayisine kadar birçok alanda kilit taşıdır. Roket motorlarında artan maliyetlerin azaltılması ve tüketilen yakıt miktarının fazla olması bu alanı sürekli gelişime açık tutmaktadır. Roket motorlarının verimini arttırmanın iki yolu vardır. Bunlar çevrim ve üretim yöntemidir. Günümüzde geleneksel roket motorlarında çevrimi değiştirmeden üretim yöntemini iyileştirmek ne yazık ki verimi arttırmak konusunda sınırlıdır. Çevrimin değişmesi üretim yöntemlerini iyileştirmekten çok daha fazla verimi arttıracaktır. Uzaya veya dünyanın herhangi bir yerine taşınan devasa ağırlıklar için tonlarca yakıt tüketilmektedir. Bu yüzden verimde yapılacak %1'lik bir iyileştirme bile hem maliyet hemde emisyonlar bakımından çok büyük geri kazanımlar sağlayacaktır. Detonasyon motorları PDE (Pulse Detonation Engine) ve RDE (Rotating Detonation Engine) olmak üzere ikiye ayrılır ve DDT (Deflagration to Detonation Transition) alev dalgasının detonasyon dalgasına dönüşmesi mantığıyla çalışır. Detonasyon motorları bir ön-detonator yardımıyla şok dalgası oluşturmakta ve bu şok dalgasını kullanarak önündeki yanmamış yakıtın basınç ve sıcaklığını yükselterek ilerlemektedir. Daha sonra bu şok dalgası ana detonatora ait yanma odasına girmekte ve çeşitli şok dalgaları(eğik şok, Mach diskleri vb.) oluşturmaktadır. Ana detonatorden çıkan yüksek basınç ve sıcaklıktaki gaz bir nozulda genişletilerek itki kuvveti elde edilmektedir. Bir ön-detonator sürücü ve sürünen olmak olmak üzere iki bölümden ve bu bölümleri ayıran bir diyaframdan oluşmaktadır. Sürücü bölgesinde yanmış hava-yakıt bulunurken sürünen bölgede yanmamış hava-yakıt karışımı bulunmaktadır. Diyaframın ortadan kaldırılmasıyla oluşan şok dalgası önündeki yanmamış yakıtın basınç ve sıcaklığını arttırıp yakarak ilerlemektedir. Bu çalışmada farklı yakıtlar kullanılarak ön-detonatorde şok dalgası oluşum süresi, şok sonrası basınç, sıcaklık ve hız değişimlerinin sayısal modelleme yöntemiyle incelenmesi amaçlanmıştır.

Anahtar kelimeler: Detonasyon, Ön Detonator, Ana Detonator, Şok Dalgası.

1 GİRİŞ

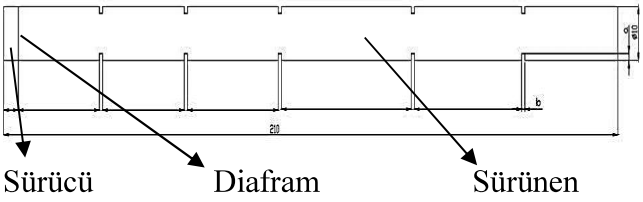
Detonasyon motorları bir ön-detonator kullanarak şok dalgası oluşturmakta ve bu şok dalgası önündeki yanmamış yakıtın basınç ve sıcaklığını yükseltip yakarak ilerlemektedir. Bu amaçla yola çıkan mühendisler Amerika ve Sovyet Rusyanın 1960'larda ki uzay yarışında gölgede kalan detonasyon motorlarına yönelmişlerdir. Günümüzdeki teorik çalışmalar detonasyon motorlarının geleneksel roket motorlarından %1-20 arasında daha verimli olduğunu göstermektedir [1]. Detonasyon motorları PDE (Pulse Detonation Engine) ve RDE (Rotating Detonation Engine) olmak üzere ikiye ayrılır ve DDT (Deflagration to Detonation Transition) alev dalgasının detonasyon dalgasına dönüşmesi mantığıyla çalışır [2]. Ön-detonatorden çıkan şok dalgası ana detonatora girerken (eğik şok, Mach diskleri vb.) gibi çeşitli şok dalgalarını meydana getirmektedir [3]. Bir ön-detonator sürücü ve sürünen olmak olmak üzere iki bölümden ve bu bölümleri ayıran bir diyaframdan oluşmaktadır [4]. Ön detonatorde oluşturulan detonasyon dalgası ana detonatore aktarılır. Ana detonatorden elde edilen yüksek basınç ve sıcaklıktaki gaz bir nozulda genişletilerek itki kuvveti elde edilmektedir. Bu çalışmada Ø10x210mm sahip bir ön-detonatorde etan, etilen ve kerosen kullanılarak şok oluşma süresi, şok sonrası basınç, sıcaklık ve hız değerlerinin incelenmesi amaçlanmıştır.

Detonasyon motorları hakkında yapılan literatür çalışmaları incelendiğinde; Liu ve arkadaşlarının iki boyutlu olarak modellenmiş dönel detonasyon motorunda akış alanını ve basınç kazancı

performansını incelemişlerdir. Açık kaynaklı yazılım OpenFOAM programında analizleri gerçekleştirmişlerdir. Analiz sonucunda giriş alan oranının 1'den küçük olduğu durumlarda üçgen yapılı gaz katmanları farklı boyutta çizgili dağılım sergilemiş ve yanma odası basınç kazanç oranını da azalttığını tespit etmişlerdir [5]. Liu ve arkadaşlarının yapmış oldukları diğer bir çalışmada ön karışımlı dönel detonasyon motorunda stokiyometrik şartlarda hidrojen-hava karışımını 3-D sayısal analiz çalışmasında gerçekleştirmişlerdir. Hesaplama çalışmasında tek adımlı Arrhenius kimya modelini Euler denklemleri ile birleştirmişlerdir. Yanma odası çevresindeki şok dalgalarının saat yönünün tersine döndüğünü tespit etmişlerdir. Ayrıca yansıyan şok dalgaları motorların stabilitesini etkilerken dönel detonasyon motorlarında itme performansının düşmediğini bulgulamışlardır [6].

2 GEOMETRİ VE MESH

Geometri Ø10x210mm boyutunda ve türbülansı arttırmak için 5 engelden oluşmaktadır (Şekil 1).

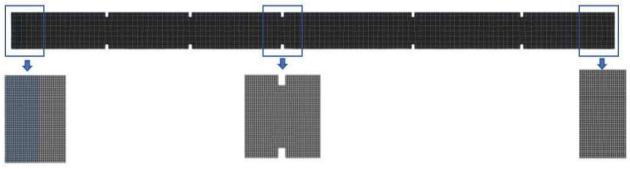


Şekil 1. Ön Detonatör Geometri

Mesh parametreleri Tablo 1 de mevcut olup literatürde kabul edilebilir aralıktadır. Oluşturulan ağ yapısı Şekil 2'de görülmektedir. Analiz basınç tabanlı çözücüde k-epsilon türbülans modeli seçilmiştir. Yanma modeli olarak türlerin taşınması yönteminde ideal gaz yoğunluk modeli ile çözülmüştür. Başlangıç parametreleri hibrit ve yama olup, method olarak birinci derece çözücüde zaman adımı 1.5e-07s ve iterasyon sayısı 30000'de gerçekleştirilmiştir.

Tablo 1. Mesh Parametreleri

Mesh Parametreleri	Değerler
Element Quality	0.95-1.00
Aspect Ratio	1.00-1.10
Skewness	1.30e-10-5.10e-2
Ortagonal Quality	0.99-1.00
Elements	60000



Şekil 2. Mesh Yapısı

Yapılan çalışmada baz alınan temel denklemler aşağıda sıralanmıştır.

Kütlenin Korunumu:
Sıkıştırılabilir akış için

$$\frac{\partial p}{\partial t} + \nabla \rho \vec{V} = 0 \qquad (1)$$

Momentumun Korunumu:
Büyük 'D' materyal türevi ifade eder.

$$\frac{D(\rho h)}{\partial Dt} + \vec{V}\nabla\left(\overrightarrow{\rho V}\right) = -\nabla \mathrm{p} + \rho\vec{g} + \mu\nabla^2\vec{V} \qquad (2)$$

Enerjinin Korunumu:

$$\frac{D(\rho h)}{\partial Dt} = \frac{Dp}{Dt} + \nabla(k\nabla T) + \emptyset \qquad (3)$$

$\emptyset$ yitim katsayısıdır. Viskoz kuvvetlere karşı yapılan işi sembolize eder.

$$\emptyset = (\tau\nabla)\vec{V} = \tau_{ij}\left(\frac{\partial Vi}{\partial xj}\right) \qquad (4)$$

Hal Denklemi:
İdeal gaz yasası

$$p = \rho RT \qquad (5)$$

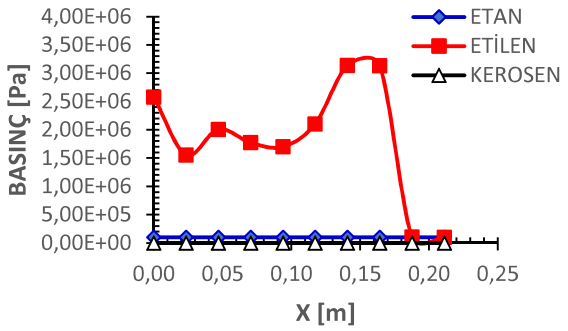
Yakıtların C/H oranlarının baz alınarak elde edilen basınç ve sıcaklıkların değişimi Tablo 3. te verilmiştir.

Tablo 3. Yakıtlara Ait Parametreler

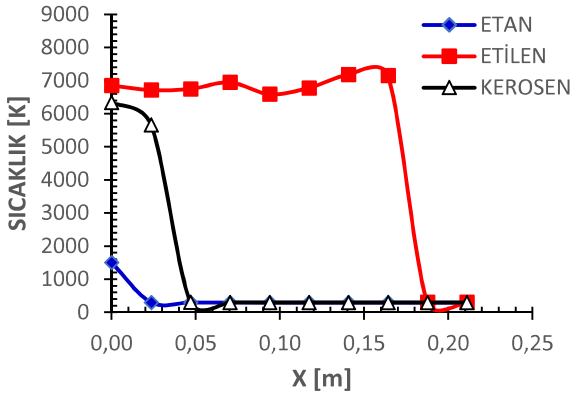
Yakıt	Parametreler		
	P	T	(C/H)
Etilen	27.1	26.5	0.50
Kerosen	45.1	26.2	0.52
Etan	23.5	26.4	0.33

3 UYGULAMA VE DEĞERLENDİRME

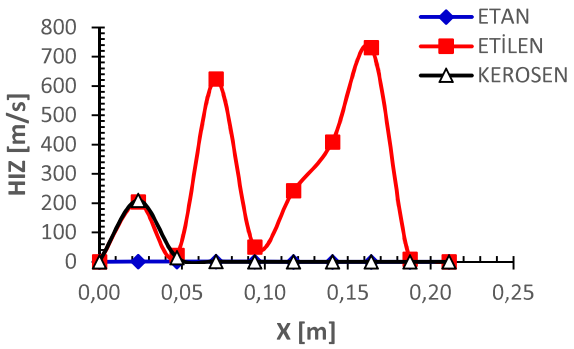
Şok dalgası etilen ve kerosende sırasıyla 0.294, 0.346 milisaniyede oluşurken etanda 0.765 milisaniyede oluştuğu gözlemlenmiştir. Şekil 3, Şekil 4 ve Şekil 5 grafikleri şok dalgasının 0.354 milisaniyedeki değerleri olup şokun önündeki yanmamış yakıt-hava karışımının basınç sıcaklık ve hızını arttırarak ilerlediğini göstermektedir.



Şekil 3. Basınç-Konum

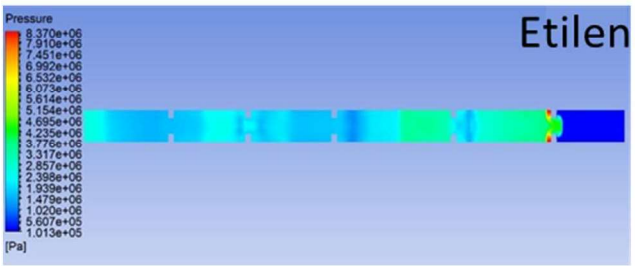


Şekil 4. Sıcaklık-Konum

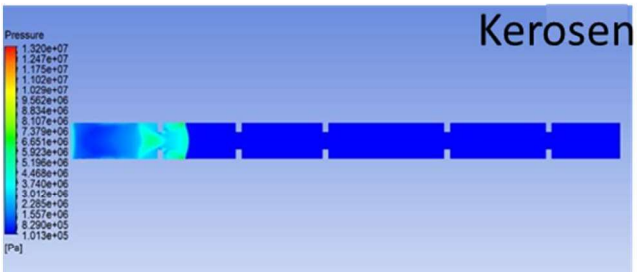


Şekil 5. Hız-Konum

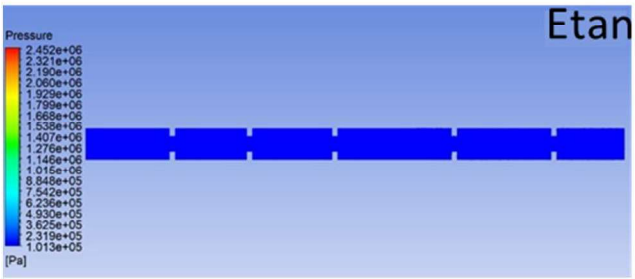
Şekil 6, Şekil 7 ve Şekil 8 şok dalgasının 0.354 milisaniyedeki değerleri olup sırasısyla etilen, kerosen ve etanın basınç konturlarını belirtmektedir.



Şekil 6. Etilen - Basınç Değişimi

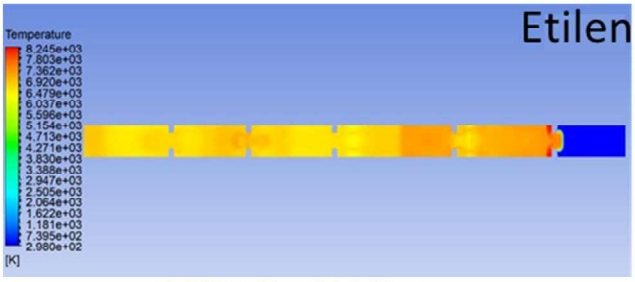


Şekil 7. Kerosen - Basınç Değişimi

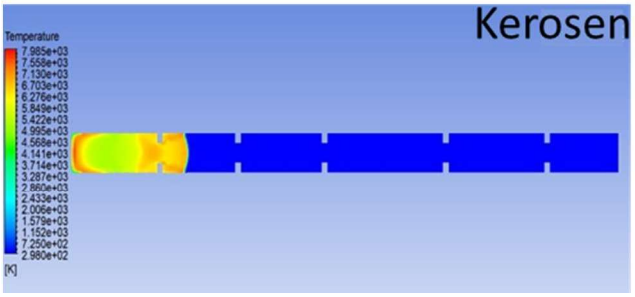


Şekil 8. Etan - Basınç Değişimi

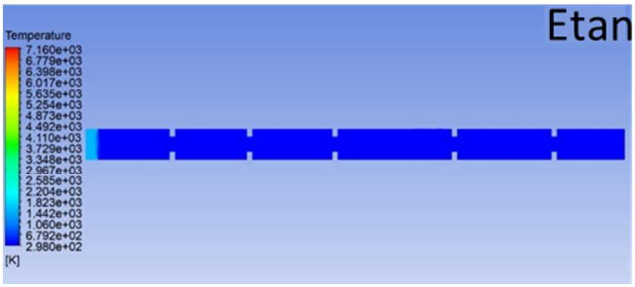
Şekil 9, Şekil 10 ve Şekil 11 şok dalgasının 0.354 milisaniyedeki değerleri olup sırasıyla etilen, kerosen ve etanın sıcaklık konturlarını belirtmektedir.



Şekil 9. Sıcaklık Konturu

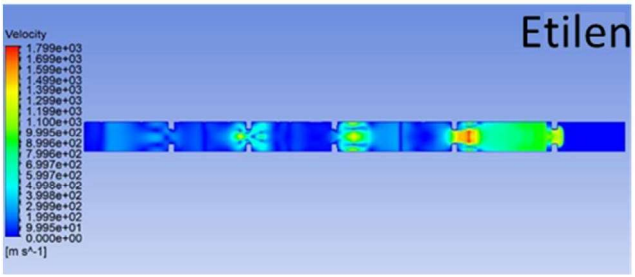


Şekil 10. Sıcaklık Konturu

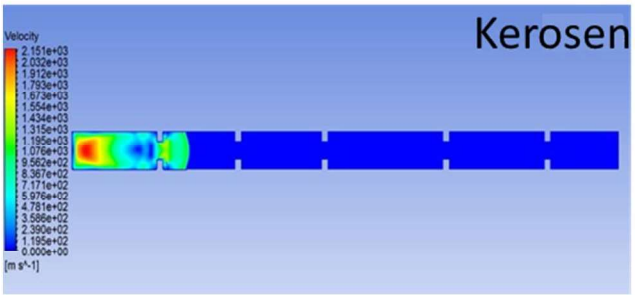


Şekil 11. Sıcaklık Konturu

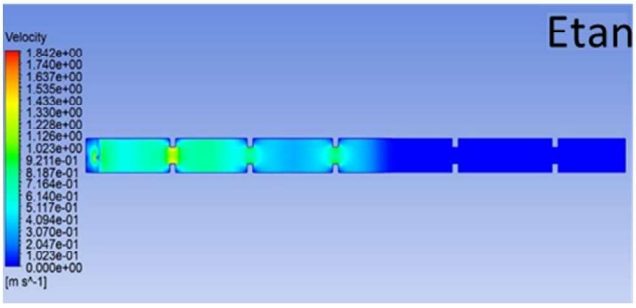
Şekil 12, Şekil 13 ve Şekil 14 şok dalgasının 0.354 milisaniyedeki değerleri olup sırasısyla etilen, kerosen ve etanın hız konturlarını belirtmektedir.



Şekil 12. Etilen – Hız Değişimi



Şekil 13. Kerosen - Hız Değişimi



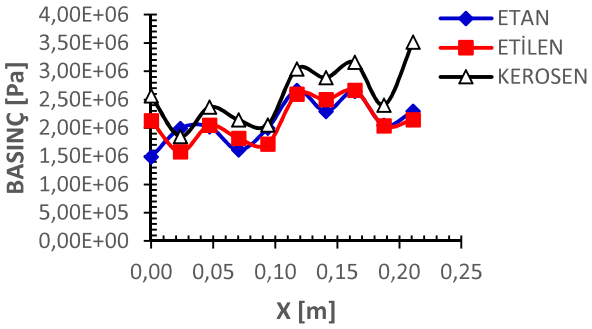
Şekil 14. Etan - Hız Değişimi

Şok dalgasının oluşmasının yakıtlara göre değişimi Tablo 2'de gösterilmiştir. Şok dalgası en hızlı etilende oluşmuş olmasına rağmen şokun en son oluştuğu etan ön-detonatorü en hızlı terk eden yakıt olmuştur.

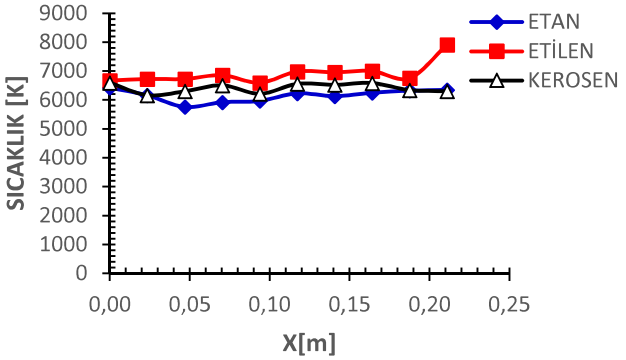
Tablo 2. Şok Dalgası Oluşum Süreleri

Yakıt	Başlangıç	Bitiş	Fark (ms)
Etilen	0.294	0.363	0.069
Kerosen	0.347	0.419	0.072
Etan	0.704	0.765	0.061

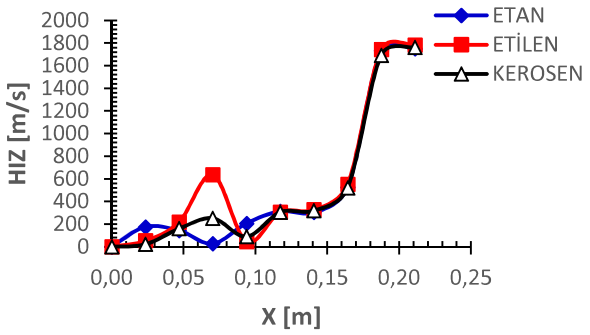
Şekil 15, Şekil 16 ve Şekil 17 şok dalgasının ön-detonator boyunca sırasıyla basınç, sıcaklık ve hız değerlerinin değişimini göstermektedir.



Şekil 15. Basınç-Konum

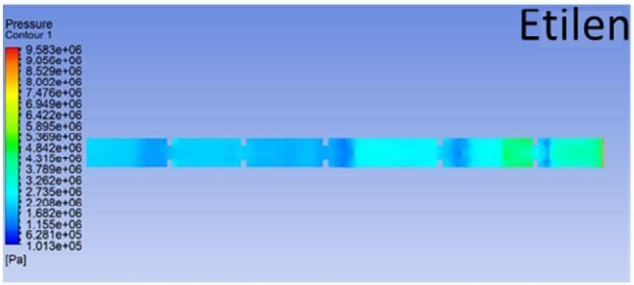


Şekil 16. Sıcaklık-Konum

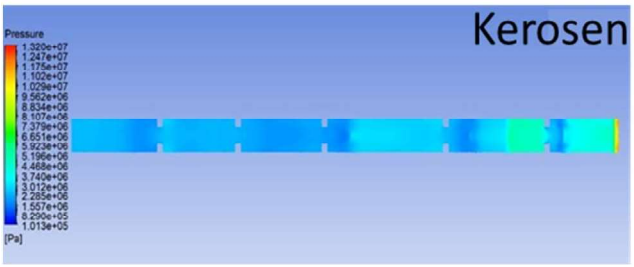


Şekil 17. Hız-Konum

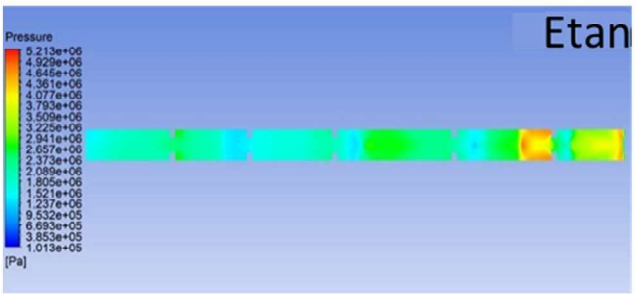
Şekil 18, Şekil 19 ve Şekil 20 şok dalgasının ön-detonator boyunca sırasıyla etilen, kerosen ve etanın basınç konturlarını belirtmektedir.



Şekil 18. Etilen - Basınç Değişimi

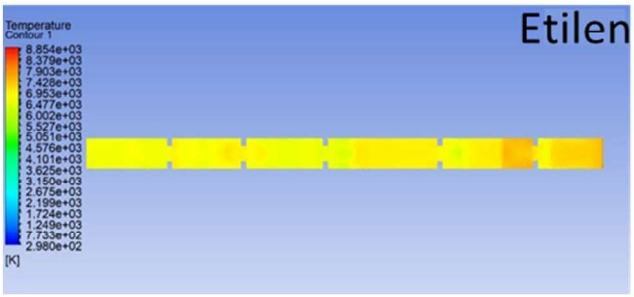


Şekil 19. Kerosen - Basınç Değişimi

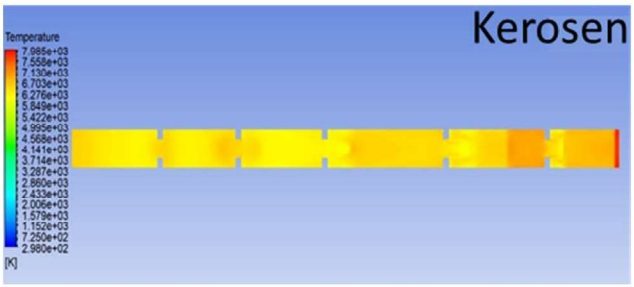


Şekil 20. Etan - Basınç Değişimi

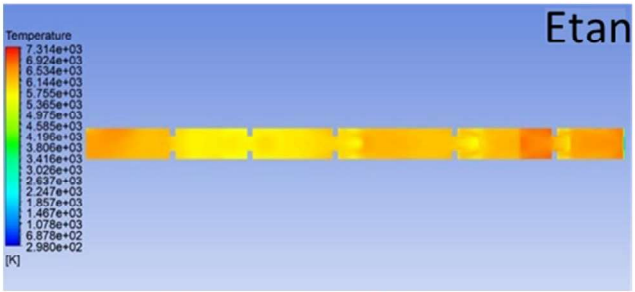
Şekil 21, Şekil 22 ve Şekil 23 şok dalgasının ön-detonator boyunca sırasıyla etilen, kerosen ve etanın sıcaklık konturlarını belirtmektedir.



Şekil 21. Etilen - Sıcaklık Değişimi

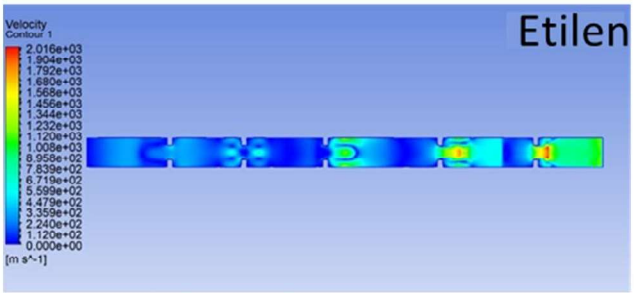


Şekil 22. Kerosen - Sıcaklık Değişimi

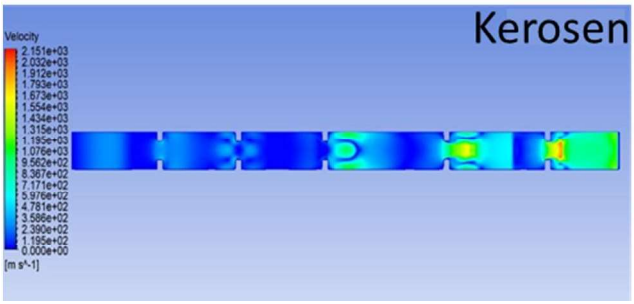


Şekil 23. Etan - Sıcaklık Değişimi

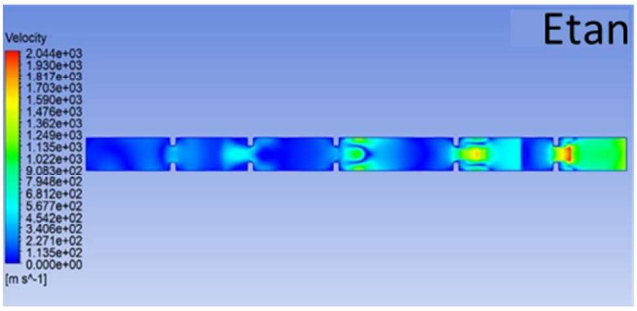
Şekil 24, Şekil 25 ve Şekil 26 şok dalgasının ön-detonator boyunca sırasıyla etilen, kerosen ve etanın hız konturlarını belirtmektedir.



Şekil 24. Etilen - Hız Değişimi



Şekil 25. Kerosen - Hız Değişimi



Şekil 26. Etan - Hız Değişimi

4 SONUÇ

- Yapılan analizler sonucunda şok dalgasının en hızlı etilen en yavaş ise etan yakıtında oluştuğu tespit edilmiştir.
- Azalan C/H oranının şokun oluşumunu geciktirdiği gözlemlenmiştir.
- C/H oranının artışı yakıtlarda şokun basıncını arttırırken sıcaklığın birbirine yakın kaldığını göstermiştir.
- Şok dalgası en hızlı etilende oluşmuş olmasına rağmen şokun en son oluştuğu etan ön-detonatorü en hızlı terk eden yakıt olmuştur.
- Şok dalgası etilen ve kerosende sırasıyla 0.294, 0.347 milisaniyede oluşurken etanda 0.704 milisaniyede oluştuğu gözlemlenmiştir.
- Şok dalgası oluştuktan sonra en hızlı 0.061 milisaniye ile etan, 0.069 milisaniye ile etilen ve 0.072 milisaniye ile kerosen ön-detonatoru terk ettiği saptanmıştır.
- Basınç 45.1 kat ile en yüksek kerosende oluşmuştur.

Bu çalışmada yakıtların birbirine göre avantajları ve dezavantajları sonuçlar kısmında tartışılmıştır. Bu ve benzeri çalışmalar ışığında tasarlanan ön-detonatorler ana detonatorler için büyük önem arz etmektedir. Dünyanın birçok yerinde hızlı gelişme gösteren bu alanda çalışmalara başlamak ülkemizde havacılık ve uzay teknolojilerinin geleceği açısından büyük bir öneme sahiptir.

TEŞEKKÜR

Araştırmacılar bu bildiri çalışmasının gerçekleştirilmesine olanak sağlayan Tarsus Üniversitesi Yanma Laboratuvarı'na teşekkür eder.

KAYNAKÇA

[1] Kumar, R. (2019). Pulsed Detonation Engine Nozzle Design and Analysis (Doctoral dissertation, The University of Texas at Arlington).

[2] Lee, J. H. S. (2008). The Detonation Phenomenon. Cambridge: Cambridge University Press.

[3] Panicker, P. K. (2008). The development and testing of pulsed detonation engine ground demonstrators (Doctoral dissertation, The University of Texas at Arlington).

[4] Tsuboi, N., Asahara, M., Kojima, T., & Koichi Hayashi, A. (2017). Numerical Simulation on Rotating Detonation Engine: Effects of Higher-Order Scheme. Detonation Control for Propulsion, 77–107.

[5] Liu, X.-Y., Chen, Y.-L., Yao, S.-B., & Wang, J.-P. (2019). Numerical Study of Reverse-Rotating Wave in the Hollow Rotating Detonation Engines. The Proceedings of the 2018 Asia-Pacific International Symposium on Aerospace Technology (APISAT 2018), 1677–1684.

[6] Liu, X.-Y., Luan, M.-Y., Chen, Y.-L., & Wang, J.-P. (2020). Flow-field Analysis and Pressure Gain Estimation of a Rotating Detonation Engine with Striped Distribution of Reactants. AIAA Propulsion and Energy 2020 Forum

TERMİK SANTRALLERDE YANGIN GÜVENLİĞİNİN BİR ÖRNEK ÜZERİNDEN İNCELENMESİ

Elif ÇATAKLI[1], Ekrem BÜYÜKKAYA[2], Gökhan COŞKUN[3]

1. Yangın ve Yangın Güvenliği Bölümü, Fen Bilimleri Enstitüsü, Sakarya Üniversitesi, Serdivan, Sakarya; email: elif.catakli@ogr.sakarya.edu.tr
2. Makine Mühendisliği Bölümü, Mühendislik Fakültesi, Sakarya Üniversitesi, Serdivan, Sakarya; email: ebkaya@sakarya.edu.tr
3. Makine Mühendisliği Bölümü, Mühendislik Fakültesi, Sakarya Üniversitesi, Serdivan, Sakarya; email: gcoskun@sakarya.edu.tr

Özet

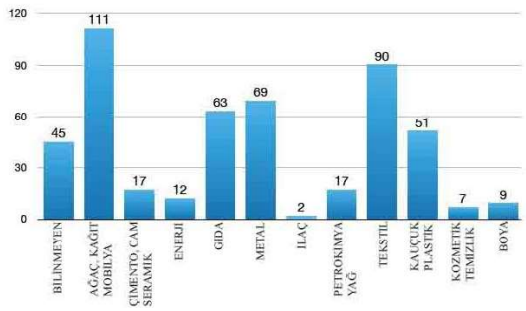
Endüstriyel yapılar, tehlikeli madde barındırdıkları için yangın açısından riskli bölümlerdir. Büyük endüstriyel kazaların oluşmasında asıl sebep yangın, patlama ve toksik yayılımdır. Bu sebeple yangın güvenlik önlemlerinin yeterli olup olmadığı periyodik olarak kontrol edilerek yüksek farkındalık oluşturulmalıdır. Bu çalışmada endüstriyel yapıları temsilen termik santrallerin yangın riskli bölümleri irdelenmiştir. Yangın güvenliği açısından alınan aktif güvenlik önlemleri ve pasif güvenlik önlemlerinin üzerinde durulmuştur. Örnek bir termik santralin yangın güvenlik önlemleri incelenerek genel kapsamda öneriler sunulmuştur.

Anahtar Kelimeler: Yangın, Yangın Güvenliği, Termik Santrallerde Yangın

1 GİRİŞ

Yeterli miktardaki oksijen, ısı ve yanıcı malzemenin brleşmesiyle meydana gelen yanma, kimyasal bir reaksiyondur. Yangın, bu üç unsurdan yanıcı malzeme ya da oksijenden birinin bitmesiyle sonlanır. Başlangıç, gelişim ve tam gelişmiş şekilde ilerler. Başlangıç evresinde ısı yayılımı az, alevler sönür, duman salınımı azdır. Gelişme evresinde alevler gözle görülür hale gelir ve diğer bölgelere sıçrama olur. Tam gelişmiş evrede ise yangın tamamen yayılır [1].

Bir binanın yangın riski o binanın türüne bağlı değişkenlik göstermektedir. Buna bağlı olarak alınan önlemler de farklılaşmaktadır. Yangın riski yüksek olan endüstriyel yapıların da kendi içerisinde risk oranları değişir [2]. TMMOB Kimya Mühendisleri Odasının yayınladığı "2020 Patlama Raporu"na göre yangın ve patlamaların sektörel dağılımları Şekil 1'de verilmiştir [3].



Şekil 1- Sektörel Dağılım [3]

Tehlikeli yerlerde patlama oluşma riski daha yüksek olduğundan öncelikle bu bölgeler sınıflandırılmalıdır. Alınacak önlemler sınıflandırmaya göre belirlenir. Tablo 1'de sınıflandırma verilmiştir [4].

Tablo 1- Tehlikeli Yerlerin Sınıflandırılması [4]

Bölge 0	Gaz, buhar ve sis halindeki yanıcı maddeler ile havanın karışmasıyla oluşan patlayıcı ortam	Sürekli Uzun süreli Sık
Bölge 1	Gaz, buhar ve sis halindeki yanıcı maddeler ile havanın karışmasıyla oluşan patlayıcı ortam	Ara sıra
Bölge 2	Gaz, buhar ve sis halindeki yanıcı maddeler ile havanın karışmasıyla oluşan patlayıcı ortam	Yok Kısa süreli
Bölge 20	Havada asılı kalan tutuşabilir tozlar	Sürekli Uzun süreli Sık
Bölge 21	Havada asılı kalan tutuşabilir tozlar	Ara sıra
Bölge 22	Havada asılı kalan tutuşabilir tozlar	Yok Kısa süreli

Not: Tabaka, tortu, yığın halinde tutaşabilir tozların olduğu yerler, patlayıcı ortam oluşturabilecek başka kaynak gibi görülmeli.

Kömür yakan termik santrallerde yangın riskinin yüksek olduğu bölümler kömür taşıma bantları, kömür bekleme alanları, kömür depolama alanları, kömür öğütme değirmenleri, elektrik üretim türbinleri ve jeneratörlerdir.

Kömür taşıma bantları ulaşımı zor bölgelere kurulduğundan olası yangın başlama anı hemen fark edilemeyebilir. Bant sahasına düşen kömür tozları statik elektrik yoluyla yangın çıkarabilmektedir.

Kömür depolama alanlarında adyabatik basınç ve ortamın nemine bağlı oluşan ekzotermik reaksiyon yoluyla okside olan kömür kızışma yoluyla yangın çıkarabilmektedir.

Kazanların bacasında kömür tozu birikmeleri yangın riski oluşturmaktadır [5].

Tablo 2'de kömürün patlama karakteristikleri verilmiştir [6].

Tablo 2- Kömürün Patlama Karakteristiği [6]

Kendi kendine tutuşma sıcaklığı	°C	540
Minimum tutuşma enerjisi	mJ	>1000
LEL	g/m^3	60
Maksimum patlama basıncı	bar	8
Toz patlama sabiti	bar.m/s	117

Yangın anında yan ürünler oluşur ve ortamdaki sinerjik etki ile ölüme neden olan birden fazla durum meydana gelir. Tablo 3'te yangın anında ölüme neden olaylar verilmiştir [7].

Tablo 3- Yangın Anında Ölüme Neden Olan Olaylar [7]

Ölüm Nedeni	Ölüm Oranı (%)
Duman	36
Yanma + Zehirlenme	25
Yanma	19
Kalp krizi, felç, düşme	7
Diğer	7
Boğulma	3
Bronş yangısı	3

Yanma anında ortama salınan gazlardan oluşan duman, sadece insan hayatını fizyolojik olarak etkilemez. Görüş mesafesini azalttığı için tahliyeyi olumsuz etkiler. Yangın anında bir mahal içerisindeki duman miktarı ise havalandırmaya bağlıdır. Dumanın içeriğinde bulunan zehirli gazlar 3 grupta incelenir;

1. grup boğucu etkili zehirli gazlar,
2. grup tahriş edici zehirli gazlar,
3. grup kanı zehirleyip sinir sistemini tahrip eden zehirli gazlar.

Gazların zehirlilik sınırları PEL (izin verilen maruz kalma değeri) ve STEL (aksi belirtilmedikçe 15dk için aşılmaması gereken değer) ile ifade edilmektedir. Bu değerler pmm (1 m^3 havada bulunan maddenin mililitre miktarı) ile belirtilmektedir. Tablo 4'te zehirli gaz kapsamında karbonmonoksit, karbondioksit, hidrojen sülfür, hidrojen klorür, hidrojen siyanid, hidrojen florür gazlarının zehirlilik sınır değerleri verilmiştir [7].

Tablo 4- Bazı Gazların Zehirlilik Sınır Değerleri [7]

Gazın İsmi	Formül	PEL (ppm)	STEL (ppm)
Karbonmonoksit	CO	50	1200
Karbondioksit	CO_2	5000	50000
Hidrojen Sülfür	H_2S	10	100
Hidrojen Klorür	HCL	5	50
Hidrojen Siyanid	HCN	10	50
Hidrojen Florür	HF	3	30

Örnek termik santrali için yüksek yangın riskli yerler hidrojen üretim tesisi, amonyak depolama tesisi, yardımcı kazan tesisleri ve polishing sistemi olarak belirtilmiştir. Yüksek riskli yerler kırmızı işaretlidir. Hidrojen üretim tesisleri, amonyak depolama tesisleri, yanıcı-patlayıcı gaz depolama alanları bu kategoridedir. Orta riskli bölümler sarı işaretlidir. Kazanlar, türbinleri trafo-mcc-elektrik odaları, kömür tesis ve depoları, atölyeler bu kategoridedir. Düşük riskli bölümler mavi işaretlidir. Mutfaklar, yemekhaneler, idari binalar bu kategoridedir.

Bölge-20; toz kaynaklarının içi, besleme hunileri, silolar, siklonlar, filtreler, toz nakil sistemleri, karıştırma tesisleri, değirmenler, kurutucular, torbalama ekipmanlarıdır.

Bölge-21; toz kaynaklarının çevresi ve dış kısmı, patlayıcı ortamların dış kapakları, dolup yerlerinin yakın çevresi, besleme bantları, numune alma noktaları, kamyon yükleme döküm istasyonları, bant aktarma noktalarıdır.

Bölge-22; arıza durumunda toz yayma ihtimali olan filtreler, nadir açılan aletlerin çevresi, toz ürün içeren torbalanmış malzeme depoları, torbalama işlemiyle önlem alınan Bölge-21 kısımlarıdır [8].

2 YANGIN GÜVENLİĞİ

Binaların Yangından Korunması Hakkında Yönetmelik'te belirtildiği üzere binanın yapımında kullanılan malzemelerin yanıcılık sınıfları göz önünde bulundurulmalıdır. Yangının yayılmasını önlemeye yardımcı olan duvar, kapı ve pencere gibi elemanların kendine has uygulama standartları mevcuttur. Dekorasyon amaçlı kullanılan malzemelerin de yanmaya direnci fazla olanları seçilmelidir. Bir binada acil durum anında tahliye amaçlı kullanılan kaçış yolları, proje aşamasında tasarlanmalıdır. Kaçış yollarında bulunan kapılar kilitli olmamalıdır ve dışa doğru açılmalıdır. Yangına 120 dakika dayanımlı yapılmalıdır. Yapıda çıkan yangını sınırlandırma amaçlı konpartımanlamaya başvurulur. Bu sayede yapıdaki diğer mahaller yangından korunmuş olur [9].

Belirtilen risk değerlendirmesine göre alınacak önlemler de farklılık göstermektedir. Bu kapsamda kullanılacak ekipman kategorileri;

Bölge-0 ve Bölge-20: Kategori-1,

Bölge-1 ve Bölge-21: Kategori-1 ve Kategori-2,

Bölge-2 ve Bölge-22: Kategori-1, Kategori-2 ve Kategori-3 şeklindedir [4].

Kömürün kırıldığı mahallerde kömür tozundan kaynaklanabilecek yangınları önleme amaçlı toz toplama üniteleri bulunmaktadır. Şekil 2'de toz toplama kanalı gösterilmiştir [8].



Şekil 2- Toz Toplama Kanalı [8]

Tozun etrafa yayılmasını ve havada asılı kalmasını engellemek için düzenli olarak su ile nemlendirme ve yıkama işlemleri yapılmaktadır. Şekil 3'te örnek işletmenin sulama yapılan alanı gösterilmiştir [8].



Şekil 3- Sulama ile Temizlenen Alan [8]

Santral içerisindeki kimyasal maddelerin depolandığı alanlar sınırlandırılarak güvenli bölge oluşturulmaktadır. Personel harici girişler yasak olup dikkatli kullanım sağlanmaktadır. Şekil 4'te örnek tesiste sınırlandırılan depolama alanı gösterilmiştir.



Şekil 4- Kimyasal Depolama Alanı Genel Görünüm [8]

Kömürün işlenme ve taşınma bölümleri gibi yüksek yangın riskli alanlar sprinkler söndürme sistemleri kullanılarak, yüksek gerilimin dönüştürücülerle işlenerek eletrik üretimi ve dağıtımının sağlandığı şalt sahalarında su jeti soğutma ve yangın monitörleri kullanılarak, iç mekan panolar, elektrik ve trafo odalarında IG-01 / IG-541 argon gazlı söndürme sistemleri kullanılarak yangın güvenliği sağlanmaktadır. Sızdırmazlık testleri ile sertifikalandırılmıştır.

Liman içerisinde ve rıhtımda tam teşekküllü "Fire Fighting Vessel" olarak adlandırılan yangın söndürme amaçlı gemiler bulundurulmaktadır.

İtfaiye Amirliğince yangın hidrantı ve yangın duvar vanaları, taşınabilir yangın söndürme cihazları aylık periyotlarda, hidrant ve vana hortumları yıllık periyotlarda, kontrol edilmektedir. Taşınabilir yangın söndürme cihazlarının %10 yedek olarak stokta bulundurulmaktadır.

Itfaiye Amirliği tesise özel olarak araçlar, solunum setleri, yüksekte çalışma için koruyucu donanımlar, kurtarma ekipmanları, yangın hortumları, kompresör ve aspiratörler, haberleşme, aydınlatma ve görüntüleme araçları, yangın dolapları bulundurmaktadır. Kapalı ve kısıtlı alanda çalışma, yüksekte güvenli çalışma, alevli ve simüle yangınla mücadele, arama ve kurtarma ve temel ilkyardım eğitimleri vermektedir.

Tüm tesis çalışanlarına temel iş sağlığı ve güvenliği harici her yıl düzenli olarak teorik ve uygulamalı "Yangın ve Acil Durum Eğitimi" verilmektedir.

Tesiste yıllık periyotlarla araç ve personel kurtarma kapsamında "Acil Durum Tatbikatları" yapılmaktadır.

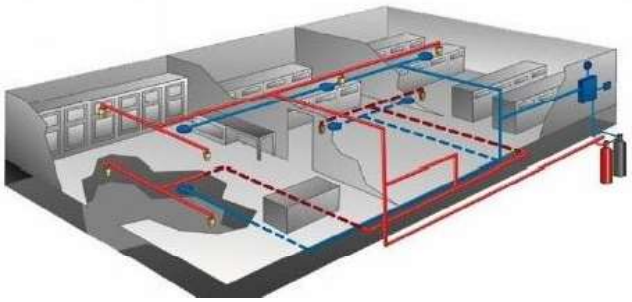
Patlama tehlikesi yüksek olan hidrojen üretim binasında hidrojen tanklarının emniyet duvarı ile çevrelenmesi ve çalışanların antistatik iş kıyafeti kullanması ile yangın güvenliği sağlamaktadır.

Mutfak ve yemekhane davlumbaz söndürme sistemi ve sprinkler söndürme sistemi ile yangından korunmaktadır. Şekil 5'te örnek bir sulama sistemi gösterilmiştir [10].



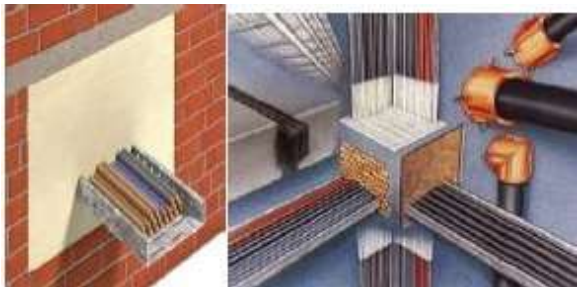
Şekil 5- Sprinkler Yangın Söndürücü [5]

Santrallerde yangın riski yüksek olan kontrol odaları, yangın ihbar sistemi ve FM-200 söndürücüyle korunmaktadır. Otomatik gazlı söndürme sistemlerinde, yangın söndürme amaçlı oksijen oranı azaltılırken çalışanların sağlığını tehlikeye atmamaya dikkat edilmelidir. Söndürme sisteminde, maddenin kurulduğu hacim içinde eşit dağıldığına emin olunmalıdır. Şekil 6'da kontrol odası için örnek bir yangın ihbar ve FM-200 söndürme sistemi gösterilmiştir [5].



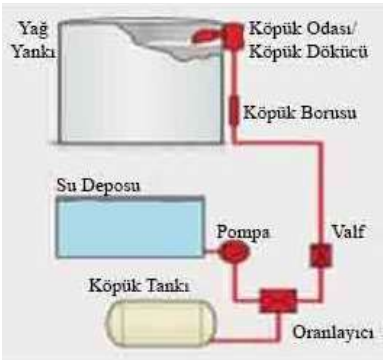
Şekil 6- Yangın İhbar ve FM-200 [5]

Santrallerde elektrik kaynaklı yangınların engellenmesi için kablo kanallarının duvardan geçtiği yerlerde oluşan açıklıklara yanmaz mastik, köpük, sıva gibi yalıtım malzemeleriyle kapatılmalıdır. Bu sayede duman ve ısı sızdırmazlığı sağlanır ve yangın yayılımı engellenir. Şekil 7'de kablo kanallarının çevresine yangın bariyeri kurulması gösterilmiştir [5].



Şekil 7- Yangın Bariyerleri [5]

Köpüklü yangın södürme sistemleri, sprinkler sisteme benzer ancak debi konsantresi en az 15 dakika olarak tasarlanmalıdır. NFPA 16 standardına göre su sprinkler sistemleri için belirtilen özelliklerin köpük söndürücüde bulunması kabul edilmektedir. Köpüklü söndürücülerde yüksek genleşmeli konsantre kullanılıyorsa su ile doğru oranda karıştırılması, hızlı ve etkin bir söndürme sağlar. Şekil 8'de fuel-oil deposu için kullanılan köpüklü yangın söndürme sistemi gösterilmiştir [11].



Şekil 8- Köpüklü Söndürücü Sistemi [5]

3 SONUÇ VE DEĞERLENDİRMELER

Yangın ve patlama oluşturma ihtimali yüksek olan kimyasal maddelerin sık kullanıldığı yapılarda yangın risk değerlendirmeleri be bu değerlendirmelere bağlı güvenlik önlemleri alınmasına özen gösterilmelidir. Yangın güvenlik önlemleri kapsamında ülkemizde geçerli olan "Binaların Yangından Korunması Hakkında Yönetmelik" ve NFPA yangın standartları kullanılmaktadır.

Endüstriyel yapılar için ise T.C. Çevre ve Şehircilik Bakanlığı'nın yayımlamış olduğu SEVESO II Direktifinin Uygulama Kapasitesinin Arttırılması İçin Teknik Yardım Projesi kapsamında "Büyük Endüstriyel Kaza Risklerinin Azaltılması (BEKRA) İşletmeciler İçin Rehber"e uyulması gerekmektedir.

Yapının projelendirme aşamasında düşünülmesi gereken pasif yangın güvenlik önlemleri, malzeme seçimi, yangının yayılmasını önleyen kompartımanlar oluşturma ve tahliyeyi kolaylaştırmaya dayalıdır.

Inşaatın bitimiyle sonradan yapıya eklenen her türlü yangın algılama, yönlendirme ve söndürme sistemleri aktif yangın güvenliğidir.

Termik santraller yerleşim yerlerine uzak birimler olduğundan kendi özellerinde düzenli eğitimlerin verildiği itfaiye birimleri barındırırlar. Bu birimler 6331 sayılı İş Sağlığı ve Güvenliği Yasası'na ve NFPA 600 standardına uygun olmalıdır.

Tesislerdeki yangın sistemleri belirtilen sürelerine göre düzenli olarak denetlenmelidir.

TEŞEKKÜR

Bu çalışmadaki bulgular için yazarlar Zonguldak Eren Enerji'ye teşekkür ederler.

KAYNAKLAR

[1] Bilal, F., Yangın Güvenli Yapı Tasarımı-Genel Bilgiler, İZODER Isı Su Ses ve Yangın Yalıtımcıları Derneği.

[2] Beyhan, F., Çetin, S. Performansa Dayalı Yangın Güvenli Tasarımı, TÜYAK Uluslararası Yangın ve Güvenlik Sempozyumu ve Sergisi Bildiriler Kitabı, 170-184, 2017.

[3] TMMOB Kimya Mühendisleri Odası İstanbul Şubesi. Endüstriyel Yangınlar ve Patlamalar, 2020.

[4] Resmi Gazete (30 Nisan 2013). Çalışanların Patlayıcı Ortamların Tehlikelerinden Korunması Hakkında Yönetmelik, Sayı: 28633.

[5] Kozacı, C., Kömür Yakıtlı Termik Santrallerde Yangın Tehlike Kaynakları Riskler ve Kontol Önlemleri, TMMOB Makine Mühendisleri Odası, 2017.

[6] Üçüncü, K., Toz Patlamalarından Korunma Rehberi, Risk Yönetim Derneği 2020.

[7] Kök, F., Yangında Açığa Çıkan Gazların, İnsan Sağlığına Vereceği Zararın Engellenmesi, Ulusal Çevre Bilimleri Araştırma Dergisi, 3(2): 83-94, 2020.

[8] Eren Enerji Zonguldak Şube. Eren Enerji Zonguldak Şube Patlamadan Korunma Dokümanı, Zonguldak, 2020.

[9] Temizalan Uçar, A., Endüstriyel tesislerde yangın güvenliği ve bir fişli kablo üretim tesisinin yangın güvenliği açısından değerlendirilmesi, yüksek lisans tezi, İstanbul Yeni Yüzyıl Üniversitesi Sağlık Bilimleri Enstitüsü, İstanbul, 2019.

[10] Durkut, Ş., Eren Enerji Elektrik Üretim AŞ. Ve Liman İşletmesi Yangın Risk Değerlendirme Raporu, Zonguldak, 2018.

[11] Şiranlı, O., Kimyasal Tesislerde Temel Yangın Riskleri ve Uygulanan Yangın Korunum Sistemleri, TÜYAK Uluslararası Yangın ve Güvenlik Sempozyumu ve Sergisi Bildiriler Kitabı, 194-208, 2017.

ÇİFT YAKITLI DOĞALGAZ-DİZEL BİR MOTORDA ENJEKSİYON STRATEJİSİNİN PERFORMANS VE EMİSYONLARA ETKİSİNİN İNCELENMESİ

Mustafa Deniz Altınkurt[1], Menno Merts[2], Martin Tunér[2], Ali Türkcan[1]

1. Department of Automotive Engineering, Kocaeli University, 41380 Izmit, Turkey; email: deniz.altinkurt@kocaeli.edu.tr
2. Department of Energy Sciences, Lund University, Ole Romers Vag 1, Lund 22363, Sweden

Özet

Petrol türevi yakıtların tükenmekte olması ve çevreye verdiği zararlar içten yanmalı motorlarda alternatif yakıtların kullanılması gerekliliğini ön plana çıkarmıştır. Çift yakıtlı yanma stratejisinde motor üzerinde fazla değişikliğe gidilmeden doğalgaz, alkoller, hidrojen vb. alternatif yakıtlar yüksek miktarlarda ve yüksek sıkıştırma oranlarında kullanılabilir. Bu çalışmada kullanılan çift yakıtlı yanma stratejisinde yüksek oktanlı doğal gaz emme manifolduna püskürtülmüş ve hava ile homojen karışarak silindire alınmıştır. Yüksek reaktiviteli yakıt olan dizelle tutuşma ve yanma kontrolü sağlanmıştır. Bu sayede tüm karışımda fakir ve homojen yanma sağlanabildiğinden düşük sıcaklıkta yanma gerçekleşmekte, düşük NO_x ve is emisyonları elde edilebilmektedir. Fakat yakıt-hava karışımının fazlaca fakirleştiği düşük motor yüklerinde yanma kötüleşmeye ve yanmamış HC ve CO emisyonları problem olmaya başlar. Bu çalışmada düşük yüklerdeki bu problemleri incelemek adına çift yakıtlı bir motorda dizel enjeksiyon stratejilerinin emisyon ve performans parametrelerine etkileri incelenmiştir. Tek dizel enjeksiyonu ve çift dizel enjeksiyonu farklı enjeksiyon zamanlarında karşılaştırılmıştır. Motor testleri sonucunda maksimum silindir gaz basıncı (P_{maks}) çift enjeksiyon kullanılarak kısmen azaltılarak yakın değerlerde indike ortalama efektif basınç (IMEP) elde edilebilmiştir. HC ve CO emisyonları çift enjeksiyon testlerinde bir miktar yüksek elde edilse de, erken ve geç ikinci enjeksiyon zamanlarında daha düşük değerler ölçülmüştür. Çevrimsel farklılıklar da erken enjeksiyon zamanlarında sınır limitin yakınına veya altına çekilebilmiştir.

Anahtar kelimeler: Çift yakıtlı yanma, doğal gaz, enjeksiyon stratejisi, emisyonlar

1 GİRİŞ

Günümüzdeki karayolu taşıtlarına baktığımızda ağır ticari araçların (kamyon, tır vb.) oranı sayıca azdır. Fakat küresel ulaşım sektörü sera gazı emisyonları baz alındığında, ağır ticari araçlar bu emisyonların yaklaşık üçte birinden sorumludur [1, 2]. Aynı anda farklı alternatif yakıtların (alkol yakıtlar, doğal gaz vb.) tek motor üzerinde pratik olarak kullanılabildiği uygulamaların sayısının artması, hem fosil yakıtların tükenmekte olması hem de kirletici emisyonların azaltılması açısından önem arz etmektedir. Bu yüzden emisyonlar açısından gelecek vaat eden düşük sıcaklıkta yanma stratejilerinin daha çok incelenmesi gerekmektedir. Bu çalışmada da kullanılan çift yakıtlı yanma stratejisinde, yüksek oktanlı (düşük reaktiviteli) doğal gaz, alkol gibi yakıtlar emme manifolduna püskürtülür, havayla karışarak silindire alınır ve sıkıştırma zamanı boyunca sıkıştırılır. Sıkıştırma sonunda reaktivitesi yüksek olan yüksek setanlı pilot yakıt ise (dizel, biyodizel, dimetil eter, n-heptan vb.) az miktarda püskürtülerek karışım tutuşturulur. Bu yakıtların kütlesel oranlarının, pilot yakıt püskürtme zamanı ve sayısının değiştirilerek karışım reaktivitesinin kontrol edildiği yanma stratejisi ise reaktivite kontrollü sıkıştırma ile ateşleme (RCCI) olarak adlandırılmaktadır.

Öncelikle neden dizel pilot-doğal gaz çift yakıtlı yanma çalışılmakta olduğunu açıklayacak olursak kısaca aşağıdakileri söyleyebiliriz. Doğalgaz içinde en yüksek oranda bulunan metan, düşük C/H oranı ile birlikte sera gazı emisyonlarını 20%'nin üzerinde azaltma potansiyeline sahiptir. Büyük çaplı (large bore) çift yakıtlı gemi motorlarında ise gaz operasyonu kullanımı ve fakir yanma konsepti sonucu motor çıkışından oldukça düşük miktarlarda is ve doğrudan IMO Tier3 NO_x regülasyonunu sağlayacak şekilde düşük NO_x emisyonları elde edilebilmektedir. Çift yakıtlı yanmanın diğer avantajları, dizel yanmaya yakın seviyelerde güç ve tork, düşük NO_x ve is emisyonları, pilot püskürtme sayesinde doğalgaz bujili yanmaya göre çoklu tutuşma noktaları ile daha robust bir tutuşma sağlanması sayılabilir.

Çift yakıtlı yanma stratejilerinin dezavantajları ise düşük motor yüklerinde yanmanın

kötüleşmesi, artan uHC ve CO emisyonları, çevrimsel farklılıkların artması, düşük silindir sıcaklıkları ve fakir karışım sonucu oluşan alevin sağlıklı ilerleyememesi olarak sayılabilir. Ayrıca enjeksiyon zamanı kontrol aralığının çok dar bir bandda olduğu önceki çalışmalarda görülmüştür. Yüksek yüklerde: artan silindir içi sıcaklıklarla birlikte, artan NO_x ve vuruntulu yanma riski fazla oranda oluşmaya ve problem oluşturmaya başlar.

En son literatür çalışmalarından güncel durumu özetleyebiliriz. Yousefi vd. [3] enjektör ray basıncı ve çoklu enjeksiyon stratejilerinin birlikte kullanımının etkilerini ağır ticari bir motorda incelemişlerdir. Çift yakıtlı yanma stratejisiyle dizel motora yakın ve bazen daha yüksek seviyelerde yakıt enerji çevrimi elde edilebilmekte ve güncel dizel motorlara kısmen daha basit modifikasyonlarla uyarlanabilmektedir [4-8]. Fakat bu yanma modu, düşük yüklerde fakir doğal gaz-hava karışımının alev ilerlemesini olumsuz etkilemesinden dolayı yüksek yanmamış metan emisyonları ve düşük termal verim dezavantajlarına sahiptir [9]. Önceden yapılmış çalışmalar yakıt ortak hattı (rail) basıncını artırmanın termik verimi iyileştirdiğini ve yanmamış HC ve CO emisyonlarını azalttığını göstermiştir. Artan basınçla birlikte iyileşen yakıt parçalanması ve azalan tutuşma gecikme süresi emisyonların azaltılması sonucunu doğurur. Bu nedenle, hem erken direkt enjeksiyon (DI) hem de artan yakıt püskürtme basıncı, dizel yakıt ile doğal gaz-hava karışımı arasında daha iyi bir karışma sağlar. Bunun yanısıra, dizel DI zamanının erkene alınması ve yakıt hattı basıncının arttırılması genellikle yüksek basınç artış oranı ve artan NO_x emisyonlarına yol açar [10–12]. Liu vd. [13] düşük devirli gemi motorunda tutuşma karakteristikleri ve basınç salınımlarını incelemişlerdir. Simülasyon sonuçlarından basınç salınımlarının pilot enjeksiyonunun geciktirilmesi ile arttığını görmüşlerdir. Zhao vd. [14] 6 silindirli common rail bir motoru dizel-doğal gaz modu konfigürasyona çevirerek ön enjeksiyon stratejisinin etkilerini deneysel olarak incelemişlerdir. Sonuçlar tutuşma fazının ana enjeksiyonla kontrol edildiğini göstermiştir.

Bu çalışmada deneysel sonuçlar incelenecek, daha sonraki çalışmalarda hesaplamalı akışkanlar mekaniği (CFD) modelleme çalışmaları tamamlandığında karşılaştırma yapılacaktır. CFD simülasyonları ile birlikte reaksiyon ilerlemesi ve sıcaklık dağılımı sonuçları, düşük yüklerdeki problemlerin daha detaylı incelenmesini sağlayacak, enjeksiyon parametrelerinin emisyon oluşumuna etkileri de görülecektir. Ayrıca çalışmada da incelenen gemi motorlarının büyük boyutu nedeniyle optik motor testleri oldukça zor olup, CFD tercih sebebidir. CFD simülasyonları sayesinde yanmanın başlangıcında pilot yakıtın dağılımı, CH2O bileşiği sayesinde düşük sıcaklıkta yanma reaksiyonları ve emisyonların silindir içi dağılımı görüntülenebilmektedir.

Literatür çalışmalarından görüldüğü üzere motor enjeksiyon kontrol parametrelerinden dizel enjeksiyon basıncı, enjeksiyon zamanı ve sayısının performans ve emisyonlara etkileri sınırlı sayıda çalışmada incelenmiştir. Bu çalışmada incelenen çoklu enjeksiyon stratejilerinde iki adet enjeksiyon kullanılmış olup hem birinci hem ikinci enjeksiyon zamanı geniş aralıkta değiştirilerek test edilmiştir. Daha önceki tek enjeksiyon uygulamalarında enjeksiyon zamanı avansının termik verim, HC ve CO emisyonlarını düşük yüklerde azaltabildiği, fakat basınç artış oranı ve NO_x emisyonlarında artışa neden olduğu görülmüştür. Çift enjeksiyon uygulamasıyla ise bu dezavantajlar giderilerek HC, CO emisyonları ve çevrimsel farklılıkların iyileştirilmesi hedeflenmiştir.

Literatür çalışmalarını incelediğimizde, dizel çoklu enjeksiyon stratejilerinin çift yakıtlı yanmaya etkisinin özellikle daha fazla çalışmayla incelenmesi gerektiğini, özellikle ağır ticari ve orta devirli large bore (büyük çaplı) gemi motorlarında kapsamlı çalışılmadığını görebiliriz. Bu çalışmada doğal gaz-dizel çift yakıtlı bir motorda tek ve çift dizel enjeksiyon stratejilerinin motorun maksimum basınç, çevrimsel farklılıklar ve emisyon parametrelerine etkileri incelenmiştir.

2 MATERYAL VE METOT

Bu çalışmada Wärtsilä W20DF model, altı silindirli su soğutmalı, gemi ve jeneratör uygulamalarında kullanılan büyük çaplı orta devirli motor kullanılmıştır. Test motoru özellikleri Tablo 1'de verilmiştir. Araştırma amacı gereği altı silindirli motorun sadece volan tarafındaki birinci silindiri aktif olup diğer silindirlerde yakıt enjeksiyonu ve yanma gerçekleşmemektedir.

Tablo 1. Test motoru özellikleri

Wärtsilä	**W20DF**
Çap x Strok	200x280
Silindir hacmi	8.8 L
RPM	900
Sıkıştırma oranı	13.4
Ray basıncı (dizel)	2300 bar'a kadar
Doğal gaz	MPI
Dizel enjektör	9x0,295 µm

Test motorunun kontrol edilebilen parametreleri özet olarak Tablo 2'de verilmiştir. Test sisteminde emme basıncı hava tankında bulunan valf kontrolü ile, emme havası sıcaklığı emme havası ısıtma sistemiyle, supap zamanları ve lifti elektrohidrolik aktüatör mekanizması ile kontrol edilebilmektedir. Egzoz geri basıncı gerçek şartlardaki turbonun etkisini verebilmek adına iki adet geri basınç valfi ile kontrol edilebilmiştir. Dizel enjeksiyonu ise SCANIA XPI common rail yakıt basınç pompası sayesinde çevrim başına 3 adete kadar enjeksiyon yapılabilmekte ve enjeksiyon zamanı kontrol edilebilmektedir. Yakıt hattı basıncı da ayrıca kontrol edilebilmektedir. Doğal gaz enjeksiyon süresi ve zamanı da kontrol edilebilmekte olup bu çalışmada ikisi de sabit tutulmuştur.

Tablo 2. Motor Kontrol Parametreleri

Kontrol parametreleri
Emme basınç ve sıc. (P&T)
Supap zamanları&lifti
Egzoz geri basıncı
Dizel yakıt hattı basıncı
Enjeksiyon zamanı ve süresi
NG zamanı ve süresi

Tüm motor testlerinde motor devri ABB model elektrik dinamometre ile sabit tutulmuştur. Motorun en düşük emisyonlar ve en yüksek termik verimi sağladığı yaygın kullanılan çalışma aralığı lambda global değeri 2 olup, bu çalışmada bu değer kullanılmıştır. Doğalgaz enjeksiyon zamanı ve süresi sırasıyla -330° aTDC ve 3600 µs olarak sabit tutulmuştur. Her motor testi kaydında 300 çevrimin ortalaması alınmıştır. %18 emme hava valfi açıklığında ve yaklaşık 6.5-7 bar IMEP'te düşük yük motor testleri gerçekleştirilmiştir. Emme havası giriş sıcaklığı 40 °C'de kontrol edilmiştir. Tablo 3'teki deneysel prosedür şemasında görüldüğü üzere NG enerji giriş oranı yaklaşık %85 değerinde sabit tutulmuştur ve dizel çift enjeksiyon şartlarında dizel kütle oranı 0.5'te test edilmiştir. Tüm testlerde yakıt enjeksiyon basıncı 1700 bar'da sabit tutulmuştur. Enjeksiyon zamanları birinci ve ikinci enjeksiyon için sırasıyla SOI_1 ve SOI_2 olarak verilmiştir. Enjeksiyon zamanları tabloda ve grafiklerde üst ölü noktadan önce (ÜÖNÖ) cinsinden gösterilmiş ve değişken enjeksiyon aralıkları tire sembolü ile ayrılmıştır. Aşağıda doğalgaz enerji oranı ve dizel kütle oranının hesaplanmasında kullanılan formüller verilmiştir. Burada m kütleyi, LHV ise ilgili yakıtın alt ısıl değerini ifade etmektedir.

$$\text{Doğalgaz enerji oranı (\%)} = \frac{m_{CH4}\, x\, LHV_{CH4}}{m_{CH4}\, x\, LHV_{CH4} + m_{Dizel}\, x\, LHV_{Dizel}} \text{ x } 100 \quad (1)$$

$$\text{Dizel kütle oranı (-)} = \frac{m_{Dizel-Enj1}}{m_{Dizel-Enj1} + m_{Dizel-Enj2}} \quad (2)$$

$$COV_{imep}(\%) = \frac{\sigma_{imep}}{\overline{imep}} \times 100 \quad (3)$$

Tablo 3. Motor test prosedürü

Test koşulları:	**SOI_1 (ÜÖNÖ)**	**SOI_2 (ÜÖNÖ)**
1. Dizel referans	25 - 4	-
2. Çift yakıt modu- tek pilot	70 - 4	-
3. Çift yakıt modu- çift pilot	75 - 45	Değişken

Çevrimsel farklılıklar 300 çevrimin IMEP verisinin standart sapma (σ_{imep}) ve ortalama değerleri ($\overline{imep}$) üzerinden COV_{imep} (coefficient of variation of IMEP) hesaplanarak yukarıda formül 3'te verilmiştir. Dizel motorlar için, kararlı yanma ve iyi sürüş için kabul edilen maksimum limit %5 bu çalışma için de kullanılmıştır [15]. Emisyon verileri HORIBA MEXA 9400 emisyon cihazı ile egzoz hattı üzerinden ppm (parts per million: milyonda bir

parça) cinsinden ölçülmüştür. Motor test sistemi ile ilgili daha fazla detaylı bilgiye [16] kaynaklarından ulaşılabilir.

3 BULGULAR VE TARTIŞMA

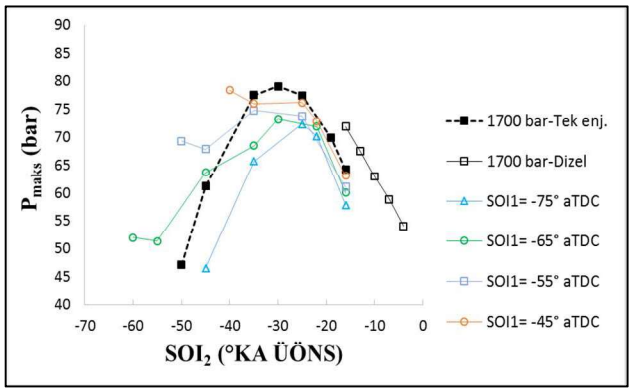
Bu bölümde deneysel çalışmalardan elde edilen sonuçlar değerlendirilecek ve çıkarımlar özet olarak yapılacaktır. İlk olarak silindir içi basınç verilerinden hesaplanan maksimum basınç (P_{maks}) ve ortalama indike efektif basıncı (IMEP) verim sonuçları değerlendirilmiştir. Daha sonra çevrimsel farklılıklar ve emisyon karakteristikleri ele alınarak değerlendirmeler yapılmıştır. Çoklu enjeksiyonlar için tüm grafiklerde farklı çizgi renkleri farklı birinci enjeksiyon zamanını (Üst Ölü Noktadan sonra-ÜÖNS) belirtmekte olup, x ekseni ikinci enjeksiyon (SOI_2) değişimini göstermektedir. Tek enjeksiyon şartları için x ekseni yalnızca tek enjeksiyon zamanını göstermektedir.

3.1 Silindir içi basınç karakteristikleri

Bu bölümde silindir gaz basıncı ölçümlerinden hesaplanan maksimum silindir gaz basıncı (P_{maks}) incelenmiştir. P_{maks} verileri Şekil 1'de enjeksiyon zamanına karşılık çizdirilmiştir. P_{maks} genel olarak tutuşma gecikmesine ve ön karışımlı yanma fazında salınan ısı miktarına bağlıdır [17]. Daha önceden de motor üzerinde yapılan çalışmalarda görüldüğü gibi [16] normal dizel enjeksiyon zamanı aralığında enjeksiyon zamanının gecikmesi ile yanma fazı genişleme zamanına ilerlemekte ve P_{maks} düşmektedir.

Yaklaşık 30 °KA civarında yanma ÜÖN civarına geldiğinden en yüksek değerlere ulaşılmaktadır. Enjeksiyon zamanına daha fazla avans verildikçe hem tek hem de çoklu enjeksiyonda karışımdaki seyrelme etkisi daha fazla olduğundan yanma başlangıcı gecikmekte ve yanma fazı tekrar genişleme zamanına ilerlemeye başlamaktadır. Bunun sonucunda P_{maks} tekrar düşmeye başladığı görülmektedir. Bu durum tek enjeksiyonda oldukça belirgin olup, çift enjeksiyon grafiklerinde ise benzer eğilim görülmektedir.

Çift enjeksiyon kullanımının silindir içi P_{maks} değerlerini özellikle -35 °KA'na kadar önemli ölçüde azalttığını söyleyebiliriz. Daha erken SOI_2 zamanlarında, özellikle iki enjeksiyon birbirine yakın zamanlarda gerçekleştiğinde, P_{maks}'ın bir miktar arttığını görebiliriz.

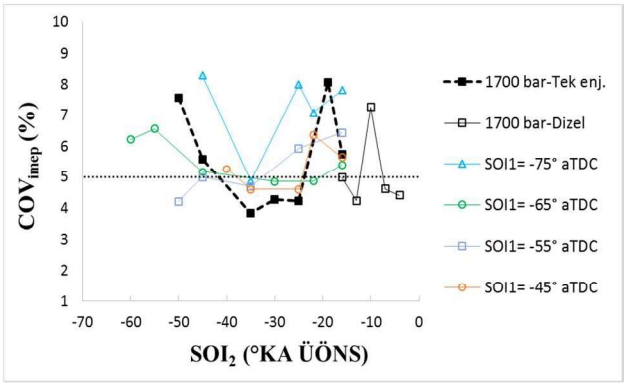


Şekil 1. Enjeksiyon zamanı-P_{maks} grafiği

P_{maks}'ın çok fazla artması bir sonraki kısımda görülebileceği gibi NO_x emisyonlarının artışını tetiklemektedir. Aynı SOI_2 şartlarında SOI_1'in etkilerini grafik üzerinden incelediğimizde, SOI_1'in erkene alınmasının P_{maks}'ı azalttığı açıkça görülebilir. Karışma süresinin artarak lokal eşdeğerlik oranlarının azalması ve yanma fazının gecikmesi bunun nedenleri olarak sayılabilir. İleride yapılacak çalışmalarda birinci enjeksiyon zamanı kontrolüyle yanma ve emisyonların kontrol edilebileceği sonucuna varabiliriz.

3.2 Çevrimsel farklılıklar ve emisyonlar

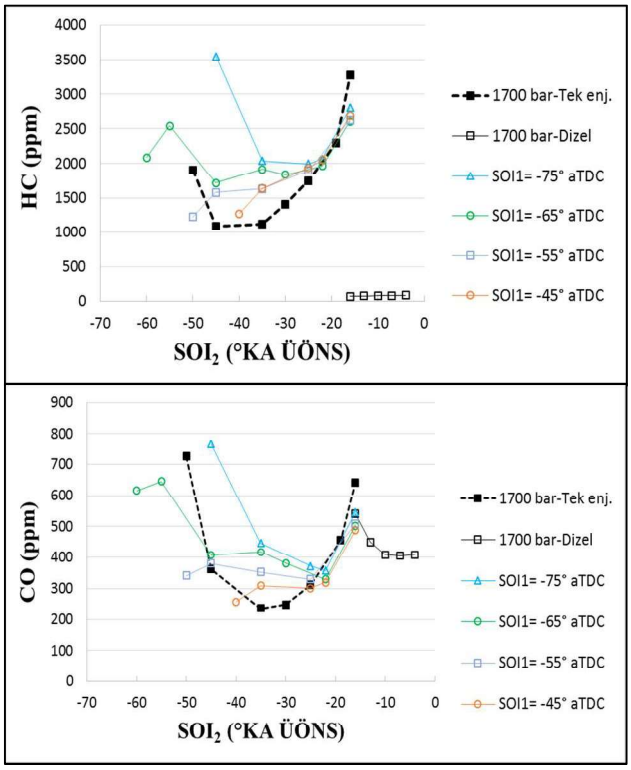
Bu bölümde IMEP'teki çevrimsel farklılıklar COV_{imep} üzerinden değerlendirilerek yanma kararlılığı incelenmiş ve devamında kirletici emisyon verileri değerlendirilmiştir.



Şekil 2. Çevrimsel farklılıkların enjeksiyon zamanıyla değişimi

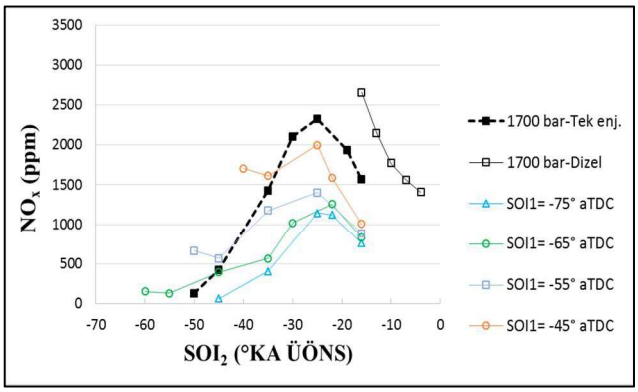
COV_{imep} verileri Şekil 2'de enjeksiyon zamanlarına karşılık verilmiştir. Yanma kararlılığı motorun stabil çalışması için önemli bir gösterge olup %5 değeri bu motorlar için sınır değer olarak kabul edilmekte, bu seviyenin üzeri yanma kararlılığının bozulmaya başladığını göstermektedir [15]. Grafiklerdeki eğilimlere bakıldığında genel olarak en az değerlerin orta enjeksiyon zamanlarında elde edildiği, çok erken yada çok geç enjeksiyon zamanlarına gidildiğinde silindir içi basınç ve sıcaklıkların

azalmasıyla yanma kararlılığının bozularak çevrimsel farklılıkların artmaya başladığı görülmektedir. En düşük ölçülen değer tek enjeksiyonda olup buna en yakın değerler referans dizel yanma ve orta dereceli SOI_1 avansı kullanılan -55/-50 °KA çift enjeksiyon şartında görülmüştür. Birinci enjeksiyon daha erken yapıldıkça çevrimsel farklılıkların hızla arttığı ve kararlı yanmanın elde edildiği aralığın daraldığı görülmüştür. İlk enjeksiyon -65 ve sonraki açılarda yapıldığında COV_{imep} değerlerinin artması engellenmiş, özellikle birbirine yakın enjeksiyon yapıldığında düşüş etkisi daha belirgin olmuştur. Bu durum emisyonlarda da kendini göstermiştir.



Şekil 3. HC ve CO emisyonları

Şekil 3'te yanmamış HC ve CO emisyonları verilmiştir. Her iki grafiğe bakıldığında COV_{imep} verileri ile benzer bir eğilim görülebilir. Yanma kararlılığının bozulduğu bölgelerde HC ve CO emisyonları da ani artışlar göstermiştir. Çift enjeksiyon kullanımında en düşük HC ve CO emisyonları SOI_1'in geç yapıldığı zamanlarda tek enjeksiyona yakın seviyelere çekilebilmiştir. Doğalgaz-dizel çift yakıtlı yanma modu ile CO emisyonları dizel yanmadan daha düşük elde edilmiş olup en düşük değerler tek enjeksiyon ile elde edilmiştir. HC emisyonları çift yakıt modunda metan gazının supaplardan kaçması veya piston segmanı üstü-silindir duvarı arası bölgelere alevin yeterince ilerleyememesi (soğuk çeperlerle birlikte) nedeniyle dizel yanmaya kıyasla daha fazla ölçülmüştür. Çift yakıtta dizel yanmaya kıyasla erken yapılan enjeksiyonun tüm emisyonlar açısından optimum aralığı verdiği görülebilir.



Şekil 4. NO_x emisyonlarının enjeksiyon zamanları ile değişimi

Şekil 4'te NO_x emisyonları verilmiştir. Bilindiği üzere NO_x emisyonları içten yanmalı motorlarda yanma sıcaklığı 1800 K ve üzerine çıkmaya başladığında hızla artmaya başlar. P_{maks} değerlerinin görüldüğü aralıklar aynı zamanda yüksek silindir içi sıcaklıkların elde edildiği bölge olduğundan NO_x emisyonları da SOI_2'nin -30 ve -20 olduğu aralıkta yüksek çıkmıştır. Daha geç ikinci enjeksiyon zamanlarında dizel yanmaya benzer şekilde yanma fazının genişleme zamanına ilerlemesi maksimum sıcaklıkları da azaltmış ve NO_x azalmıştır. İkinci enjeksiyon erken zamanlara alındığında da dizelin daha homojen dağılarak yanma fazının gecikmesi düşük NO_x emisyonu elde edilmesini sağlamıştır. İlk enjeksiyonun da erkene alınmasıyla emisyon eğilimi aşağı yönlü olarak elde edilmiştir. -65 veya -75 SOI_1 zamanında regülasyon sınırları (yaklaşık 200 ppm ve altı) altında NO_x elde edilebilmiştir. En güncel literatür çalışmalarında önerildiği gibi [18] sonraki çalışmalarda farklı enjeksiyon basınçları da kullanılarak bu aralıkların daha detaylı incelenmesi hedeflenmektedir.

4 SONUÇLAR

Bu çalışmada çift yakıtlı doğal gaz-dizel yanmalı bir motorda farklı pilot dizel enjeksiyon stratejileri kullanılarak incelenmiştir. Tek ve çift dizel enjeksiyonunda enjeksiyon zamanlarındaki değişimin motor performans, çevrimsel farklılıklar ve emisyonlar üzerindeki etkileri incelenmiştir.

Çalışma sonucunda hem maksimum silindir gaz basıncı hem de yanma kararlılığının pilot dizel

enjeksiyon zamanları ile kontrol edilebildiği görülmüştür. Birinci enjeksiyon zamanının NO_x ve HC emisyonlarını iyileştirme potansiyeli görülmüştür. İkinci enjeksiyonun uygun zamanda seçilmesi ile tek enjeksiyon şartı ile karşılaştırılabilir çevrimsel farklılıklar ve emisyon değerleri gözlemlenmiştir. Bu çalışma daha fazla parametre (farklı enjeksiyon basıncı, motor yükleri vb.) eklenerek deneysel olarak genişletilecek ve yanma simülasyonları ile silindir içi yanma ve emisyon oluşumu süreçleri detaylı olarak incelenecektir.

TEŞEKKÜR

Bu çalışma, Tübitak 2214-A Yurt Dışı Doktora Sırası Araştırma Burs Programı desteği ile İsveç-Lund Üniversitesi'nde gerçekleştirilmiştir. Yazarlar Lund Üniversitesi-Yanmalı Motorlar bölümü laboratuvar çalışanlarına ve teknisyenlerine teşekkür eder. Ayrıca test motorunu sağladığı için Wärtsilä'ya teşekkür ederiz.

KAYNAKLAR

[1] Barbosa F., Heavy Duty Diesel Emission Standards Regulation Evolution Review - Current Outcomes and Future Perspectives, SAE Technical Paper, 2019-36-0174, 2020.

[2] Mertens J., Belmans R., Webber M., Why the Carbon-Neutral Energy Transition Will Imply the Use of Lots of Carbon. C. 2020; 6(2):39.

[3] Yousefi A., Guo H., Birouk M., Liko B., On greenhouse gas emissions and thermal efficiency of natural gas/diesel dual-fuel engine at low load conditions: Coupled effect of injector rail pressure and split injection, Applied Energy, 2019, 242, 216-231.

[4] Ahmad Z., Aryal J., Ranta O., Kaario O., Vuorinen V., An optical characterization of dual-fuel combustion in a heavy-duty diesel engine, SAE Tech Paper, 2018-01-0252, 2018.

[5] Yousefi A., Birouk M., Guo H., An experimental and numerical study of the effect of diesel injection timing on natural gas/diesel dual-fuel combustion at low load, Fuel, 2017.

[6] Zheng J., Wang J., Zhao Z., Wang D., Huang Z., Effect of equivalence ratio on combustion and emissions of a dual-fuel natural gas engine ignited with diesel, Appl Therm Eng, 2019, 146, 738–51.

[7] Yousefi A., Guo H., Birouk M., Effect of diesel injection timing on the combustion of natural gas/diesel dual-fuel engine at low-high load and low-high speed conditions, Fuel, 2019, 235, 838–46.

[8] Merts M, Derafshzan S, Hyvönen J, Richter M, Lundgren M, Verhelst S. An optical investigation of dual fuel and RCCI pilot ignition in a medium speed engine. Fuel Communications, 2021;9, 100037.

[9] Yousefi A., Guo H., Birouk M., Effect of swirl ratio on NG/diesel dual-fuel combustion at low to high engine load conditions, Appl Energy, 2018, 229, 375–88.18

[10] Zhang C., Zhou A., Shen Y., Li Y., Shi Q., Effects of combustion duration characteristic on the brake thermal efficiency and NOx emission of a turbocharged diesel engine fueled with diesel-LNG dual-fuel, Appl Therm Eng, 2017, 127, 312–8.

[11] Ryu K., Effects of pilot injection pressure on the combustion and emissions characteristics in a diesel engine using biodiesel-CNG dual fuel, Energy Convers Manage, 2013, 76, 506–16.

[12] Guo H., Liko B., Luque L., Littlejohns J., Combustion performance and unburned hydrocarbon emissions of a natural gas – diesel dual fuel engine at a low load condition, Proc ASME 2017 intern combust engine div fall tech conf (ICEF2017) Oct 15–18, 2017, Seattle, Washington, USA. 2017. p. 1–9.

[13] Liu H., Li J., Wang J., Wu C., Liu B., Dong J, et al., Effects of injection strategies on low speed marine engines using the dual fuel of high-pressure direct-injection natural gas and diesel, Energy Sci Eng, 2019, 7(5), 1994–2010.

[14] Zhao G., Jia Q., Yao C., Song E., Lu C., Sun J., Effect of pre-injection strategy on combustion and emission characteristics of dual-fuel engines, Trans CSICE, 2020, 01, 19–26.

[15] Gürgen S., Ünver B., Altın İ., Prediction of cyclic variability in a diesel engine fueled with n-butanol and diesel fuel blends using artificial neural network, Renewable Energy, 2018, 117, 538-544.

[16] Valladolid P. G., Tunestål P., Monsalve-Serrano J., García A., Hyvönen J., Impact of diesel pilot distribution on the ignition process of a dual fuel medium speed marine engine, Energy Conversion and Management, 2017, 149, 192-205.

[17] Alptekin E., Canakci M., Ozsezen A. N., Turkcan A., Sanli H., Using waste animal fat based biodiesels–bioethanol–diesel fuel blends in a DI diesel engine, Fuel, 2015, 157, 245-254.

[18] Niki Y., Rajasegar R., Li Z., Musculus M. P., Garcia Oliver J. M., Takasaki K., Verification of diesel spray ignition phenomenon in dual-fuel diesel-piloted premixed natural gas engine, International Journal of Engine Research, 2022, 23(2), 180-197.

NUMERICAL INVESTIGATION OF THE EFFECT OF OPERATING TEMPERATURES ON A PLANAR SOLID OXIDE FUEL CELL

Süleyman ALTINDAL[1], Eren Gürkan EROL[1], Barış GÜREL[1], Sema YURDAKUL[2]

1. Süleyman Demirel University Mechanical Engineering Department
2. Süleyman Demirel University Environmental Engineering Department

Abstract

Recent developments in the energy field have led to the introduction of commercially available fuel cells. KOYH (Solid Oxide Fuel Cells) provide a scalable route to clean hydrogen fuel. Fuel cells can provide higher electrical conversion efficiency compared to traditional technologies such as coal-fired power plants and power generators based on internal combustion engines.

In this study, it is aimed to numerically investigate the planar KOYH for different operating temperatures (600,700,800,900,1000°C).

As a result of the study, it was seen that the average fuel cell power increases as the average current density increases at low operating temperatures. While the average current density is 5000-6000 A/m2, the highest average cell power is reached. It has been observed that the average current density increases as the voltage decreases at low temperatures. The highest current density and the highest average fuel cell power were obtained at 600°C.

Keywords: Solid oxide fuel cell, flow field, numerical modeling, current density

1 INTRODUCTION

Fuel cells are one of the cleanest and most efficient technologies for generating electricity. Since there is no combustion, there are none of the contaminants commonly produced in boilers and furnaces. For systems designed to consume hydrogen directly, the only products are electricity, water and heat. Fuel cells are an important technology for a potentially wide variety of applications, including on-site electrical power for residential and commercial buildings; car, truck, ; It is used for supplemental or auxiliary power to support personal, public and commercial transportation and aircraft systems.

Various fuel cells are at different stages of development. The most common classification of fuel cells is based on the type of electrolyte used in the cells and includes:

1) Polymer electrolyte fuel cell (PEFC),
2) Alkaline fuel cell (AFC),
3) Phosphoric acid fuel cell (PAFC),
4) Molten carbonate fuel cell (MCFC)
5) Solid oxide fuel cell (SOFC).

In general, the choice of electrolyte determines the operating temperature range of the fuel cell. The operating temperature and useful life of a fuel cell determine the physicochemical and thermomechanical properties of the materials used in the cell components (i.e. electrodes, electrolyte, interconnect, current collector, etc.). Aqueous electrolytes are limited to temperatures of about 200 °C or lower due to their high vapor pressure and rapid degradation at elevated temperatures. The operating temperature also plays an important role in determining the required degree of fuel treatment. In low-temperature fuel cells, all fuel must be converted to hydrogen before entering the fuel cell. In addition, the anode catalyst in low-temperature fuel cells (mainly platinum) is strongly poisoned by CO. In high-temperature fuel cells, CO and even CH4 can be internally converted to hydrogen or even directly oxidized electrochemically.

The electrolyte in this fuel cell is a solid, non-porous metal oxide, usually ZrO2 stabilized with Y2O3. The cell operates at 600-1000 °C, where ionic conduction of oxygen ions takes place. Typically, the anode is Co-ZrO2 or Ni-ZrO2 cermet and the cathode is Sr-doped LaMnO3.

In Solid Oxide Fuel Cells, since the Electrolyte is solid, the cell can be cast in various shapes such as tubular, planar or monolithic. The robust ceramic structure of the unit cell reduces any corrosion problems in the cell. The solid electrolyte also allows for precise design of the three-phase boundary and prevents electrolyte movement or overflow at the electrodes.

The high temperature of SOFC has its drawbacks. There are thermal expansion mismatches between materials and sealing between cells is difficult in flat plate configurations. The high operating temperature places severe constraints on material selection and results in demanding manufacturing processes. Corrosion of metal chimney components (such as interconnects in some designs) is a challenge.

1.1 Cell Components

The main components of a single COCP cell include electrolyte, cathode and anode. Fuel cell stacks contain an electrical interconnect that connects individual cells in series or in parallel. The electrolyte is made of a ceramic such as yttria-stabilized zirconia (YSZ) and acts as a conductor of oxide ions. The oxygen atoms are reduced by electrons to oxide ions on the porous cathode surface and then flow from the ceramic electrolyte to the fuel-rich porous anode, where the oxide ions react with the fuel (hydrogen) to release the electrons [1]. Interconnection serves to conduct electrons through an external circuit.

1.1.1. Electrolyte Materials

In an SOFC, the electrolyte is exposed to both oxidizing (air-side) and reducing (fuel-side) species at elevated temperatures; therefore, long-term successful COFC operation requires electrolytes to have:

(1) Sufficient ionic conductivity — electrolyte materials must have an ionic transfer number close to unity, that is, the electronic conductivity in the electrolyte must be low enough to achieve high energy conversion efficiency. Also, oxide ion conductivity must be high to minimize ohmic loss;

(2) Dense structure - to achieve maximum electrochemical performance, the electrolyte must be gas-tight; and

(3) Stability - the electrolyte is exposed to both air and fuel at high temperature and must be chemically stable in them. Also, the coefficients of thermal expansion must match at the electrolyte/electrode interfaces.

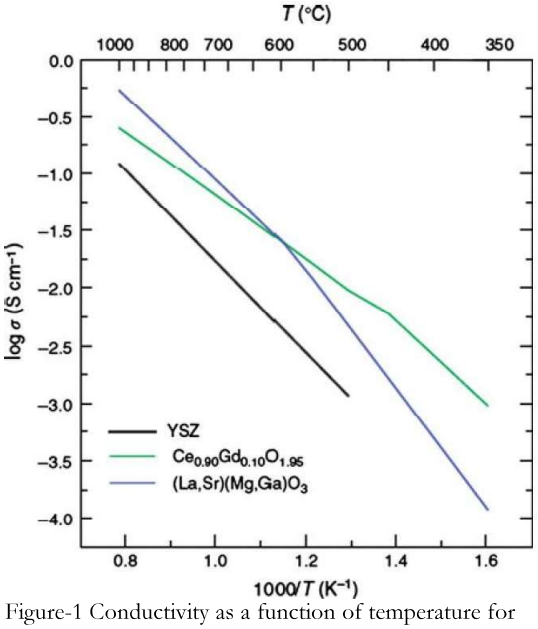


Figure-1 Conductivity as a function of temperature for yttrium-stabilized ZrO2 (YSZ), gadolinium-doped CeO2 and (La, Sr) (Mg, Ga) O3 (LSMG).

Typical electrolyte materials for COFPs are low-valent element-substituted oxides, sometimes called acceptor additives, and form oxygen vacancies through charge compensation. Yttrium stabilized ZrO2 (YSZ) is the most common material to meet these requirements; acceptor doped CeO2 and perovskite structure oxides were also investigated as electrolyte materials [2].

A graph of ionic conductivity as a function of temperature for common COYP electrolyte materials is shown in Figure 2. Although YSZ shows the lowest ionic conductivity in Figure 1, it remains the only material shown to provide long-term stability. Up to approximately 80,000 hours at 1000 °C under cell operating conditions. A typical approach to minimizing ohmic loss for the use of YSZ in the CT regimen is to reduce the thickness of the YSZ electrolyte. Another approach to reduce ohmic loss is to improve the ionic conductivity of a ZrO2-based electrolyte. Sc doped zirconia shows higher conductivity than yttrium doped ZrO2; however, the cost and known aging of Sc-doped ZrO2 poses difficulties in using this material for commercial SFCs.

1.1.2. Cathode Materials

The cathode material is very important because the electrochemical reduction of O2 on the cathode requires a series of elementary reactions and involves the transfer of more than one

electron. The cathode should have the following properties: high electronic conductivity, chemical and dimensional stability in environments encountered during cell production and cell operation, thermal expansion compatibility with other cell components, compatibility with the electrolyte and minimal reactivity, and interconnection with which it comes into contact, and high for oxygen molecule dissociation and oxygen reduction. a catalytic activity [3]. Finally, the cathode must have a stable, porous microstructure so that gaseous oxygen can diffuse easily across the cathode to the cathode/electrolyte interface. These stringent electrochemical and mechanical requirements greatly restrict the number of suitable candidate materials.

1.1.3. Anode Materials

The anode must be an excellent catalyst for the oxidation of the fuel and must be: stable in the reducing environment, electronically conductive, and have sufficient porosity to allow gas species to enter and exit the electrolyte/anode interface where the fuel oxidation reaction takes place. Other requirements include matching the coefficient of thermal expansion with that of the electrolyte and interconnect material; chemical stability with electrolyte and interconnection; and applicability for use with various fuels and impurities (such as sulfur) [4]. In addition, cost-effectiveness is always a factor in the commercialization of SFCs. In the early stages of COIP development, the anode materials were precious metals (such as Pt and Au) and transition metals (such as Fe and Ni). However, these candidates cannot meet the above-mentioned strict requirements for the anode in SMPs. For example, Ni is an excellent catalyst; however, it has a high coefficient of thermal expansion (13.4 9 10-6 / °C) and exhibits a microstructure thickening due to metal aggregation through grain growth. It has been found that the Ni-YSZ composite can prevent the sintering of nickel particles, reduce the effective coefficient of thermal expansion of Ni, and achieve better adhesion of the anode with the electrolyte. Currently, Ni-YSZ cermet is the most widely used anode material.

1.1.4. Sealing Materials

In planar SFC stacks, gaskets are critical and must prevent (or at least sufficiently minimize for acceptable performance) the leakage of both fuel and oxidant gases from the flue to the outside environment, as well as to ensure mixing of fuel and oxidant gases within the flue. The successful development of sealants and the concepts for planar SOFCs are probably the most important issues for the long-term performance stability and lifespan of planar SFC stacks and hence their commercialization at competitive costs. The primary challenge in gasket development lies in the various stringent requirements that effective gaskets must meet. First, an effective seal must be thermochemically stable under the stack's operating conditions, be electrically insulating, and have a thermal expansion appropriate to the fuel cell components [5]. In addition, the gasket must be compatible with other components and formed at a low enough temperature to avoid damaging the cell components, and must also not migrate or flow from the designated sealing zone during sealing or cell operation. It is also necessary to develop a sealing system that can withstand the thermal cycling between the cell operating temperature and room temperature. To meet these requirements, a number of different sealing approaches have been developed with some success, such as rigid, bonded gaskets (eg, glass ceramics and solders), conformal gaskets (eg, viscous glasses), and compressive. Gaskets (eg mica-based composites); Multiple sealants can be used between different components in any stack design.

1.1.5. Interconnecting Materials

An interconnector provides the electrical connection between cells and provides air and fuel separation within the cell stack. Typical requirements for an interconnect material include: high electronic conductivity with low ionic conductivity chemical stability in both fuel and air; a suitable thermal expansion to other cell components; high mechanical strength, high thermal conductivity and chemical stability compared to other cell components. Additionally, ease of fabrication must be taken into account when considering a stack design [6]. To meet these requirements, doped

lanthanum chromite was used as an interconnect for cells intended to operate at approximately 1000 °C. Lanthanum chromite is a p-type conductor; Its conductivity is due to the small polaron that jumps from room temperature to 1400 °C at oxygen pressures as low as 10-18 atm. Conductivity increases as lower valence ions (eg Ca, Mg, Sr, etc.) are substituted at La3 or Cr3+ sites. In cells intended to operate at lower temperatures (800°C), it is possible to use oxidation-resistant metallic materials for the interconnection [7]. Compared to lanthanum chromite ceramic interconnects, metal alloys offer advantages such as improved manufacturability, significantly lower raw material and manufacturing costs, and higher electrical and thermal conductivity. To be useful in interconnecting applications, however, metal alloys must meet additional requirements, particularly resistance to surface oxidation and corrosion in binary atmospheres (exposure to oxidizing atmospheres on one side and reducing atmospheres on the other). An oxide protective layer formed during oxidation in situ or ex situ by a coating technique can provide resistance to surface oxidation and corrosion. As a result, the oxide should have the following properties: slow growth kinetics, adequate electrical conductivity, strong adhesion to the underlying alloy even under severe thermal cycling conditions, and good chemical compatibility with the electrodes without significant diffusion or evaporation of components that could affect electrode performance or oxide integrity.

2. SOFC DESIGN

Over the years, various SCF designs have been researched and developed by configuring the three active components of the cell, the electrolyte and the two electrodes, in different geometric configurations. The two most common designs are planar and tubular, and they come in many variations. These are explored below.

2.1. Planar SOFC Design

In the planar design, a series of cell components are configured as thin, flat plates, then electrically connected to create the desired electrochemical performance. A schematic of a general planar SFC design is shown in Figure 3. Planar cells can be electrolyte supported, electrode supported or metal supported. Planar solid oxide fuel cell design is shown in Figure 2. Each of these designs can also have a number of interesting variants; For example, the planar COFC may be in the form of a circular disk fed with fuel from the central axis, or it may be in the form of a square or rectangular plate fed from the edges. Planar designs offer several potential advantages, including simpler and cheaper fabrication processes and higher power densities than tubular cells described in the next section. However, planar designs require high-temperature gas-tight seals between components in the KOYP stack; such seals are not required in tubular cells. Seal development remains the most challenging area in the successful commercialization of planar SMPs. An important feature of the planar design lies in the configuration of the gas flow and gas manifold, which plays an important role in minimizing the use of seals, improving fuel usage, managing even temperature and current distribution to reduce thermal stresses, and improving stability. Generally, the interconnect is ribbed on both sides to allow cross-flow, co-flow, or counterflow configurations.

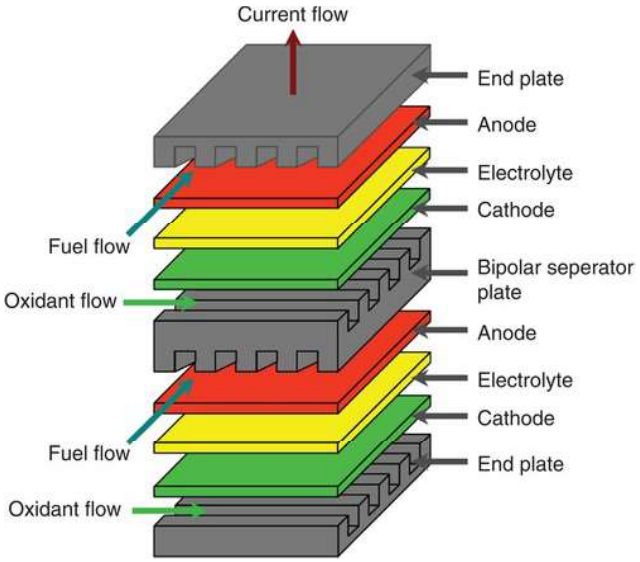


Figure 2 Düzlemsel katı oksit yakıt hücresi tasarımı

2.2. Tubular SOFC Design

Tubular COFCs can be of large diameter (15 mm) or much smaller diameter (5 mm), called microtubular cells. Also, the tubes can be flat and joined together to provide higher power density and easily printable surfaces for depositing the electrode layers. In a typical tubular COFC as shown in the Siemens Westinghouse design shown in Figure 5, the cell

tube is porous doped lanthanum manganite produced by extrusion/sintering and is closed at one end. Cell components, dense YSZ electrolyte, porous Ni-YSZ anode and doped lanthanum chromite interconnect are deposited in thin layers by atmospheric plasma sputtering.

For cell operation, the oxidant (air or oxygen) is delivered through an alumina injector tube placed inside the cell. The oxidant is discharged near the closed end of the cell and flows through the annular space formed by the cell and the coaxial injector tube. Fuel flows out of the cell from the closed end and is electrochemically oxidized as it flows into the open end of the electricity generating cell. At the open end of the cell, deoxygenated air leaves the cell and is burned with partially depleted fuel. Typically, 50–90% of the fuel is used in the electrochemical cell reaction. Some of the discharged fuel is recirculated in the fuel stream and the remainder is burned to preheat the incoming air and/or fuel. The electrochemical performance of a tubular cell (2.2 cm diameter, 150 cm active length) at 800, 900 and 1000 °C with 89% H2 fuel with 11% H2O (85% fuel usage) and air as oxidant are shown in Figure 6 . Such tubular cells have a power density of about 0.2 W/cm2 at 1000 °C.

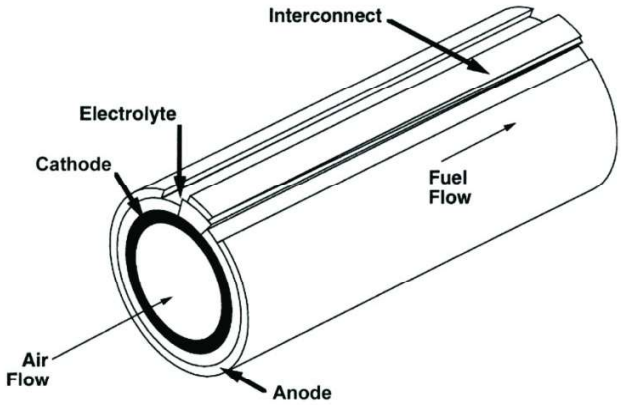


Figure 3 Tubular solid oxide fuel cell design

Tubular solid oxide fuel cell design is shown in Figure-3. The major advantage of tubular cells over planar cells is that they do not need any high temperature seals to isolate the oxidant from the fuel, making the performance of tubular cell stacks very stable over long periods (several years). However, their areal power densities are much lower (about 0.2 W/cm2) compared to planar cells (up to 2 W/cm2 for single cells and at least 0.5 W/cm2 for stacks) and higher production costs. The volumetric power density is lower for tubular cells than for planar cells. In order to increase the power density and reduce the physical size and cost of tubular SFC stacks, alternative tubular geometry cells have been explored. Such alternating geometry cells combine all the advantages of tubular SFCs, such as not requiring high-temperature sealing, while providing higher area and volumetric power densities.

A single COMP, whether planar or tubular, usually produces a voltage of less than about 1 V. Therefore, a series connection of single cells, a stack is created to achieve higher power. In the graphic below, the voltage-current density and power-current density of a Tubular SMP are shown in Figure-4.

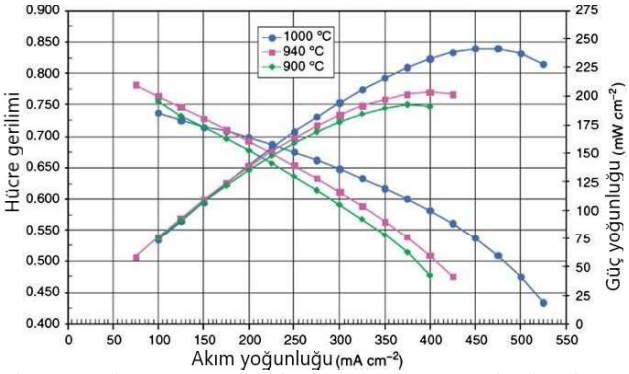


Figure 4 Voltage-current density and power-current density plots of a tubular SFC

3. METHOD

Solid oxide fuel cell design will be made in 3D in Solidworks software. Interconnector with 1.5x1.5mm flow area will be preferred in the design. Electrode lengths of 0.04mm and electrolyte lengths of 0.19mm were chosen. Below is the solid oxide fuel cell geometry.

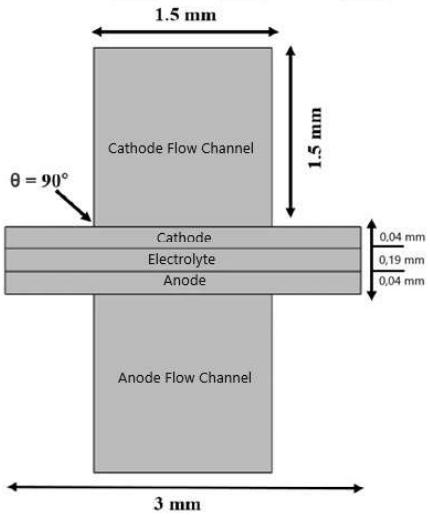


Figure 5 SOFC model dimensions studied

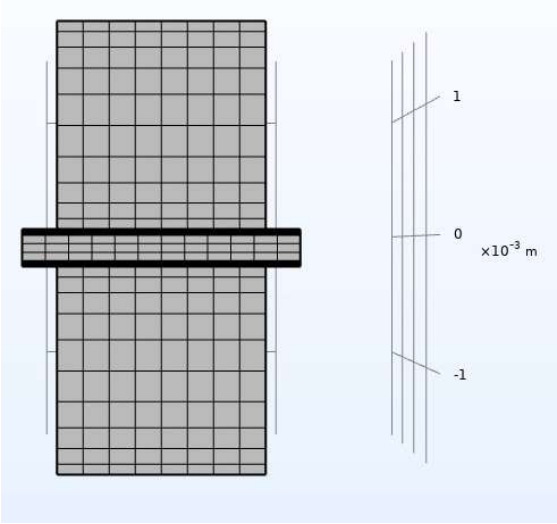


Figure 6 SOFC numerical mesh view

Table 1 Experiment sample table

Anode Material	Cathode Material	Electrolyte Material	Interconnector Geometry	Operating temperature
NiO/YSZ	LSM/YSZ	YSZ	Rectangle prism	600°C
NiO/YSZ	LSM/YSZ	YSZ	Rectangle prism	700°C
NiO/YSZ	LSM/YSZ	YSZ	Rectangle prism	800°C
NiO/YSZ	LSM/YSZ	YSZ	Rectangle prism	900°C
NiO/YSZ	LSM/YSZ	YSZ	Rectangle prism	1000°C

While other parameters are at optimum values at different temperatures, the effect on battery performance is given in Figure-7 and Figure-8. As the temperature increases, battery performance also increases.

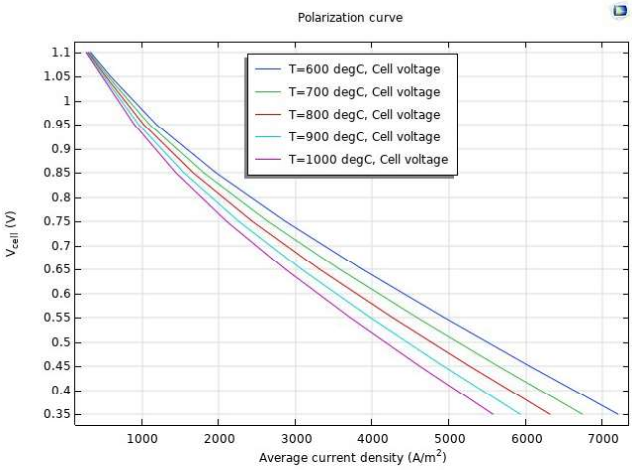


Figure 7 Polarization Curve

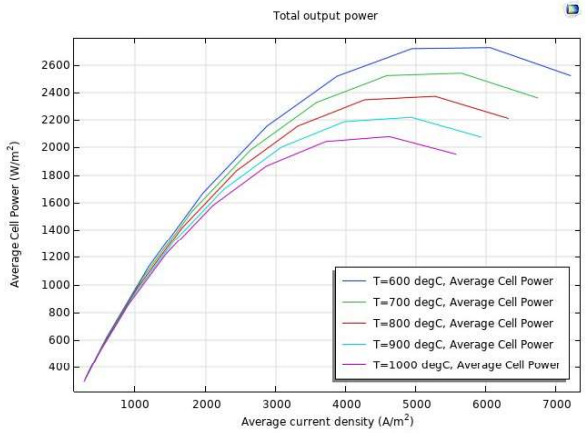


Figure 8 Power Output Curve

4. CONCLUSION

In this study, the SOFC cell model is introduced. The effect of the power produced in the SOFC system at different operating temperatures on the efficiency has been investigated. The following main results were obtained:

The cell voltage decreases with an increase in current density, while the power density of the SOFC stack increases with an increase in SOFC operating temperature and current density.

Increases in SOFC operating temperature result in improved SOFC operating efficiency as a result of improved power output at higher operating temperature.

The electrical efficiency decreases as the current density increases and increases at the high operating temperature of the SOFC.

REFERENCES

[1] D. Jaimes, V. McDonell and S. Samuelsen, Numerical investigation of a dual-stage off-gas burner to support high pressure and high temperature solid oxide fuel cell/gas turbine (SOFC/GT) hybrid systems,, Cleaner Engineering and Technology,, 2021.

[2] P. Pianko-Oprych, T. Zinko and Z. Jaworski, Modeling of thermal stresses in a microtubular Solid Oxide Fuel Cell stack, Journal of Power Sources, 2015.

[3] A. K. Sleiti, Performance of tubular Solid Oxide Fuel Cell at reduced temperature and cathode porosity, Journal of Power Sources, 2010.

[4] G. Pongratz, V. Subotić, C. Hochenauer, R. Scharler and A. Anca-Couce, Solid oxide fuel cell operation with biomass gasification

product gases: Performance- and carbon deposition risk evaluation via a CFD modelling approach, Energy, 2022.

[5] S.-S. Wei, T.-H. Wang and J.-S. Wu, "Numerical modeling of interconnect flow channel design and thermal stress analysis of a planar anode-supported solid oxide fuel cell stack," *Energy,,* 2014.

[6] M. Andersson, T. K. A. S. Hironori Nakajima, T. Koshiyama, H. Paradis, J. Yuan and B. Sundén, "Comparison of humidified hydrogen and partly pre-reformed natural gas as fuel for solid oxide fuel cells applying computational fluid dynamics," *International Journal of Heat and Mass Transfer,* 2014.

[7] M. F. Serincan, U. Pasaogullari and P. Singh, "Controlling reformation rate for a more uniform temperature distribution in an internal methane steam reforming solid oxide fuel cell," *Journal of Power Sources,* 2020.

ALIŞVERİŞ MERKEZLERİNDE İNSANLARIN ACİL DURUM TAHLİYE DAVRANIŞLARININ DENEYSEL VE SİMÜLASYON YÖNTEMLERİYLE İNCELENMESİ

Koray Uluç[1], Gökhan Coşkun[2] ve Ekrem Büyükkaya[3]

1. Yangın ve Yangın Güvenliği Yüksek Lisans Öğrencisi, Sakarya Üniversitesi, koray.uluc1@ogr.sakarya.edu.tr
2. Doç Dr, Makine Mühendisliği Bölümü, Sakarya Üniversitesi, gcoskun@sakarya.edu.tr
3. Prof Dr, Makine Mühendisliği Bölümü, Sakarya Üniversitesi, ebkaya@sakarya.edu.tr

Özet

Bu çalışmanın konusu; örnek bir Alışveriş merkezi yangında can güvenliği performansının, bilgisayar destekli programlar yardımı ile farklı yangın senaryoları için tespit edilmesi ve çıkan sonuçların irdelenmesidir. Yasal mevzuatlar ülkemizde yangın tahliye olanaklarının sadece yönergesel yöntemler ile boyutlandırmasına müsaade etmektedir. Bu yöntem ile tasarlanmış bir binada bina tahliye performansının ölçülmesi bir zaruret değildir. BYKHY gereği tüm binalarda senede en az bir sefer tahliye tatbikatı yapılmalıdır, AVM binalarında ise yönetmelikte yer almasına karşın uygulanabilir olmadığı için tam tahliye tatbikatı hiçbir zaman yapılmamaktadır. Bu nedenlerden ötürü AVM binaları sıradan ofis, fabrika gibi binalara nazaran yangında tahliye performansı öngörülebilir veya kontrol edilebilir yapılar değildir. Yönergesel olarak tasarlanan bir can güvenliği sisteminin performans bazlı bir ölçüm metodu kullanılarak değişik senaryolar için sınanması, ve senaryolar arasındaki performans farklarının incelenebilmesi bu çalışmanın öne süreceği görüşlere dayanak oluşturacaktır.

Anahtar kelimeler: Tahliye, Acil durum, Alış veriş merkezi, Can güvenliği, Duman, Yangın, Simülasyon, Adım hızı, Zehirlenme

1 GİRİŞ

Güncel AVM mimarilerinde sıkça kullanılan atriumlar BYKHY [1] gereği duman kontrol sistemleri ile korunmalıdır, fakat bu tip sistemlerin boyutlandırılabilmesi için yürürlükteki yönetmelikte ve referans standartlarda yangın mühendisliği bakış açısı ile tutarlı olabilecek yönergesel tasarım kriteri bulunmamaktadır. Bu gibi durumlarda tasarım aşamasında CFD destekli yangın simülasyonları kullanılması gerekmektedir. Bu simülasyonların hesap başlangıç kriterinin içerisinde GGTS, gerekli güvenli tahliye süresi değeridir. Öyle ki gerekli tahliye süresi bulunacak bu süre boyunca yaşanabilir ortam kriterlerinin sağlanabilmesi için olası yangında ne kadar duman atılacağı hesaplanabilecektir. Bu değerin sağlanabilmesi ise dizayn aşamasındaki bir AVM de bulunan Atrium bölümü için ancak tahliye performansı bilgisayar simülasyonu ile ölçülmüş ise belirlenebilir. Bu değer çok önemli bir can güvenliği sisteminin tasarım başlangıç kriteri olacağı için gerçek durumu yansıtabilecek şekilde hesaplanabilmesi ve olası olumsuzlukların dikkate alınabilmesi hayati önemdedir. Bu tip sistemlerin tasarlanmasında her zaman olası olumsuzluklar ve beklenmeyen durumlarda göz önünde bulundurularak belirli bir tölerans ile tasarım yapılması gereklidir. MGTS, yani mevcut güvenli tahliye süresi her zaman GGTS üzerinde bir süre olmalıdır. Mühendislik nosyonu gerekliliği olarak optimum güvenli sistemlerin tasarlanması amaç olduğu için olası koşulların olabildiğince netleştirilebilmesi hem güvenli tasarımların yapılmasına hem de aşırı tasarımlardan kaçınılabilmesine olanak sağlayacaktır. hızları üzerindeki etkisi de göz önünde bulundurulacaktır.

2 YANGINDAN KORUNUM SİSTEMLERİ STRATEJİLERİ, TASARIMDA KULLANILAN YÖNETMELİKLER VE STANDARTLAR

2.1 Yangından Korunum Stratejileri

Yangından korunum temelde iki şekilde sağlanabilir;

Tutuşmanın önlenmesi en etkili ve maliyet avantajlı korunum stratejisidir, bu stratejiyi yalnız başına kullanmak proseslerin ve ortam koşullarının nadir olarak izin verebileceği bir

durumdur. Isı kaynakları ile yanıcı malzemeleri tümü ile ayırabilmek ve yangın riskini sıfıra indirgemek çoğu zaman mümkün olmamaktadır, bu gibi durumlarda diğer yangından korunum stratejisini geliştirmek gerekmektedir "Yangının etkisini yönet" Bu strateji artık yangının oluştuğunu ve etkilerinin minimum seviyeye indirilmeye çalışıldığı aşmadır. Bu aşamada yangını yönetmek ve maruz kalanları kontrol altına almak yangınla yapılan mücadelede başarı sağlanmasını sağlayacaktır.



Şekil 1. Yangın güvenliği konsepti

Yangının algılanması sonrası tahliye süresinin uzun tutulabilmesi yani MGTS süresinin uzun tutulabilmesi etkili bir söndürme sisteminin ve duman kontrol sisteminin mevcudiyeti ile doğru orantılıdır. Her ne kadar otomatik söndürme sistemleri kullanılsa dahi her zaman yeterli kapasitede manuel müdahale olanakları da binada tesis edilmiş olmalıdır, unutulmamalıdır ki insan çoğu zaman en iyi yangın algılama sistemidir ve eğitimli personel yangına müdahalede özellikle yangının başlangıç aşamasında çok daha etkilidir.

2.2 Yönergesel Tasarım Metodu

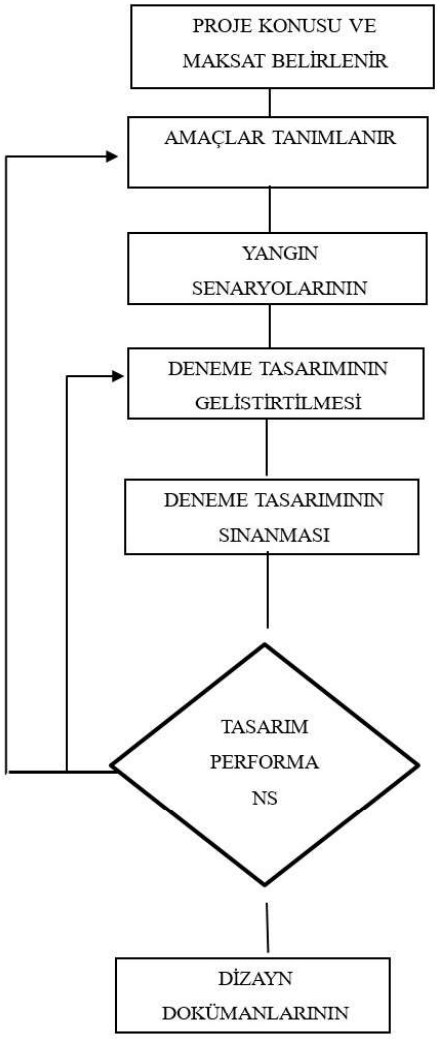
Ülkemizde kullanılabilir tek tasarım yöntemi bu tasarım yöntemdir, bu yöntemde önceden belirlenmiş ve tarif edilmiş tasarım kurallarına bağlı kalarak bina tasarlanır kural dışı tasarımlar ve daha önceden yapılmamış yerleşkeler tasarlamak ancak uzun süreçli standart revizyonları ile hayata geçebilir, bu yöntemde alternatif yangından korunum sistemleri kullanılması mümkün değildir. Bu nedenlerden hayal gücü ve güncel teknoloji ile sınırlı estetik mimari tasarımlara, günün koşullarına göre çok hızlı değişim gösteren endüstriyel bina tasarımlarına yönergesel tasarım metodu kullanılarak her zaman cevap verebilmek mümkün olmamaktadır. Yönergesel tasarım kriterleri bina özelliklerini önceden konulmuş sınırlar dâhilinde tutmayı amaç edinmiştir, bu kriterler haricinde tasarım yapılmasını engellemektedirler.

2.3 Performans Bazlı Tasarım Metodu

Performans bazlı tasarımda tasarlanmak istenen sistem ve maruz kaldığı etmenler bilimsel yöntemler ile hesaplanarak tasarımın amacına uygun olup olmadığı kontrol edilir, yapılan tasarım uygun değil ise geliştirilerek tekrar sınanır ve bu süreç uygun tasarıma ulaşana kadar tekrarlanır.

Can güvenliğinin amaç olarak edinildiği tasarımlarda ise performans bazlı tasarımın en basit olarak ifadesi olası yangında ortamdaki Mevcut Güvenli Tahliye Süresi (MGTS) ile Gereken Güvenli Tahliye Süresinin (GGTS) bilimsel yöntemler ile hesaplanarak yerleşkenin yangına karşı güvenli olmasını sağlamaktır.

MGTS > GGTS koşulu yerleşkenin güvenli olduğu durumdur.



Şekil 2. Performans bazlı Tasarım adımları

2.4 Yangından Korunum Sistemlerinin Tasarımında Kullanılan Standartlar

Yönetmelikler tasarımın hangi standartlara göre yapılacağını tarif eden kanunlar, tüzükler ile belirlenmiş tasarım, işletme, bakım, kurulum, kapsam, sorumluklar gibi konuların bütününü teşkil eder. Yönetmelikler konu ettikleri konularda anayasa, kanun ve tüzüklerin altında standartların üzerindedirler.

Ülkemizde binaların yangından korunması hakkındaki yönetmelik (BYKHY) 2002 senesinden bu yana bulunmakta olup en son revizyonunu 2021 senesinde geçirmiştir.

Standartlar ise bir tasarım yöntemlerini, tasarımın nasıl yapılacağını, tasarım kriterlerini ihtiva eden dokümanlardır. Genellikle yönetmelikler tasarım kriterleri içermeden ilgili sistem tasarımları için ilgili standartları belirtmektedir fakat BYKHY içerisinde Türk standartlarında belirtilen tasarım kriterlerine uyun olmayan tasarım kriterleri de verilmiştir, bu gibi durumlarda yönetmelik standartların üzerinde olduğu için BYKHY gereklilikleri tasarımlarda uygulanmalıdır.

BYKHY öncelikli olarak TS standartlarının kullanılmasını bu standartlarda yer almayan konularda EN Avrupa standartlarının kullanılmasını bu standartlarda da yer almayan konularda ise yurt dışı standartların kullanılmasını istemektedir.

Yurt içinde kullanılan test kuruluşu TSE Türk standartları enstitüsüdür, TSE yangından korunum sistemleri bakımından birçok alanda test ve sertifikalandırma hizmeti verebilmekle beraber eksik kalınan noktalarda öncelikle EN standartları sonrasında yurt dışı standartları sıkça kullanılmaktadır. Maalesef yangından korunum sistemleri bakımından ülkemiz standartları ve yönetmeliği güncel, kapsamlı tasarım kriterleri içermediği için ülkemizde tasarımcılar sıklıkla NFPA, UL, FM, SFPE gibi Amerika birleşik devletleri kökenli standartlar, kodlar ve kaynaklar kullanmaktadırlar.

3 YANGIN TAHLİYE SİSTEMLERİ TASARIMI KRİTERLERİ

Yangın durumunda tahliye olanaklarının sağlanması can güvenliğinin temini bakımından çok önemlidir. Mimari olarak yangından kaçış yolları güvenliği temini yanı sıra yangın tahliye olanaklarının yardımcı elektromekanik tesisatlar sayesinde yangın durumunda kullanılabilir kalması temin edilmelidir.

3.1 Yangin Tahliye Olanakları Bölümleri

Yangın tahliye olanakları üç ana temelde değerlendirilir [2];

- Çıkışa ulaşım
- Çıkış
- Çıkıştan tahliye

Çıkışa ulaşım:

Kat bazında güvenli yangın hollerine kadar ulaşımı kapsar ve çıkışa kadar maksimum seyahat mesafesi, tek yönde zorunlu seyahat mesafesi, ölü koridor maksimum uzunluğu, çıkışa ulaşım koridoru yapısal özellikleri, çıkışa ulaşım yolu üzerindeki kapıların özellikleri, çıkışların birbirinden minimum uzaklığı gibi kriterler üzerinden standartlarda ön görülen limitlerde binalar tasarlanmalıdır.

Çıkış:

Çıkış, çıkıştan tahliye ile çıkışa ulaşım arasındaki bölümdür. Bu bölüm tek katlı bir binada sadece çıkış kapısı iken çok katlı binalarda yangın holü kapısından başlayıp yangın holü, yangın merdiveni kapısı, yangın merdiveni ve tahliye katı çıkış kapısının özelliklerini kapsar.

Çıkış tahliye:

Çıkış tahliye yangın merdiveninden çıktıktan sonra en yakın güvenli halka açık yola çıkana kadarki bölümü ifade eder. Yangın merdiveninden binayı tahliye eden insanların çıkıştan çıktıktan sonra tehlikeye maruz kalmadan ve sıkışmadan güvenli bir yola çıkması gereklidir.

4 DUMAN KONTROL SİSTEMLERİ

Duman atım sistemlerinin tasarlanmasında amaç tahliye süresini olabildiğince uzatmakla birlikte yangına müdahale edecek itfaiye personelinin binaya girişini ve yangının merkezini tespit etmesine olanak sağlamaktır.

Mülkün korunmasına yönelik tasarlanan yangından korunum sistemlerinde, yangına manuel müdahalenin geç olacağı ve can güvenliği riskinin düşük olduğu yangınlarda, eğer sprinkler sistemleri var ise, yangına sprinkler sistemi ile müdahale edilmesine olanak tanımak ve duman egzozunu otomatik olarak yapmamak daha uygun bir yangın ile savaşma stratejisidir.

Zira duman egzoz yapılırken ortama taze hava verilmesi bir zorunluluk olup yanmayı körükleyecek oksijen girişine müsaade edilmiş ve olası yangının oksijene doyurulması ile daha verimli yanmasına neden olunur.

Duman tahliye sistemleri cebri veya doğal duman atım sistemleri olabilmektedir. Cebri duman atım sistemleri duman egzoz fanları marifeti ile ortamdan dumanın çekilmesi taze havanın da ortama doğal veya cebri yöntemlerle verilmesi neticesinde çalışırlar.

Her iki yöntemde de dumanın atılabilmesi için ortama taze hava girişi olması vazgeçilmez bir gerekliliktir. Taze hava ortama bina cidarından sızıntı ile girebilse de bu oran atılan dumana nazaran çok küçük bir değerdir, bu nedenle NFPA92 gerekliliği olarak en az %95 oranında taze hava beslemesi yapılabilmelidir [6].

4.1 Isı Salınım Oranı (ISO)

Duman kontrol sistemlerinin tasarımında ısı salınım oranı (ISO) karar verilmesi çok önemli olan bir tasarım başlangıç parametresidir. Hali hazırda küçük ölçekte çeşitli malzemelerin ısı yayma oranları laboratuvarlarda ölçülerek eğrileri ile birlikte kayıt altına alınmıştır fakat bir mağazada çıkan yangının birçok farklı yanıcı malzemeyi farklı zamanlarda tutuşturacağı her bir grubun farklı ısı salınım eğrileri olacağı ve belirli zaman diliminde kümülatif eğrinin nasıl olacağı konusunda parametreleri çokluğu nedeni ile bilimsel dökümü yapılmış bir eğri mevcut değildir. BS 7346-4 (Components for smoke and heat control systems- Part 4: Functional recommendations andcalculation methods for smoke and heat exhaust ventilation systems, employing steady state design fires —Code of practice) Tablo 1 [8] dikkate alınır ise, mağaza içerisinde çıkan bir yangın için standart tepki süreli sprinkler kullanılması halinde hesaba sokulması gereken ısı salınım oranı 0,625MW/m²'dir. Yangının yayılım alanı ise 10m² alınmalı yangının çapı 12m alınmalıdır. Yangını toplam 10m² yayıldığı düşünüldüğünde hesaba sokulması gereken toplam yangın yükü 6,25MW olarak bulunmaktadır.

Bu bildiride kullanılacak en yüksek yangın yüklü senaryolarda sprinklersiz ortam için oksijen yeterliliği üzerinden maksimum yangın yükü hesaplaması yapılacaktır.

4.2 Yaşanabilir Ortam Kriteri

Duman kontrol sistemlerinin amacı GGTS (Gerekli güvenli tahliye süresi) süresince yaşanabilir ortam koşullarını sağlayabilmektir ancak bu şekilde binayı tahliye edecek herkesin güven içerisinde tahliyeyi gerçekleştirebileceğinden emin olunabilir.

Optik olarak yoğun duman, çıkış seçimini ve kaçış kararlarını etkiler, yol bulma yeteneği ve yolcuların hareket hızı duman konsantrasyonuna (optik yoğunluk) bağlıdır.

İnsanlı yapılan deneylerde, İnsanların dumanla dolu bir koridorda yürümesi istendiğinde, Jin [5] tahriş edici olmayan duman (Duman gözleri ve üstü solunum yollarını tahriş eder.) içinde yürüme hızının duman yoğunluğu ile azaldığını ve 0,5 OD/m optik yoğunlukta (tükenme katsayısı 1,15) yürüme hızının yaklaşık 1,2 m/s'den (dumansızken ki hız) 0,3 m/s'ye kadar azaldığını göstermiştir. Bu şartlar altında yapılan testte insanlar zifiri karanlıktaymış gibi davranmışlar ve yollarını duvarlar boyunca dokunarak bulmuşlardır [20].

Günümüzde bu değerlendirme kriterlerinin yanına dumanda oluşan zehirli gazların etkisinin değerlendirilmesi de girmiştir. Aynı zamanda FED (Fractional Effective Dose) yani kısmi etkili doz değerleri de izlenmektedir. Çeşitli kaynaklara göre FED Kabul edilebilir sınırları değişiklik göstermektedir.

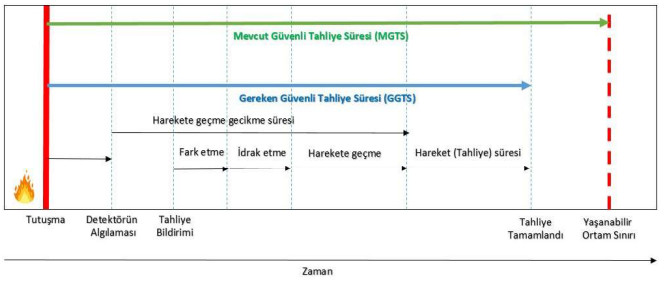
4.3 MGTS ve GGTS

Performans bazlı tasarımda Mevcut güvenli tahliye süresi (MGTS) ve gerekli güvenli tahliye süresinin (GGTS) analizi yapılarak binanın

güvenli olup olmayacağına karar verilebilmektedir.

MGTS yangının başlangıcından yangının etkileri nedeni ile ortam koşullarının elverişsiz hale gelmesi neticesinde yerleşkeden tahliye yapacak kişilerin etkisiz, hareketsiz kalacağı tahmin zamana kadar geçecek süreyi tariflemektedir.

GGTS yangının başlangıcından itibaren tüm kişilerin güvenli bir alana tahliye etmesi için gerekli tüm süreyi ifade etmektedir [3].



Şekil 3. MGTS ve GGTS Kavramları

Gerekli güvenli tahliye süresi hesabı tutuşmadan sonra eğer otomatik bir yangını algılama sistemi mevcut ise dedektörlerin yangını algılama süresinin harekete geçme süresi ile ve tahliye süresi ile toplanması ile bulunmaktadır.

Harekete geçme süresi ise içerisinde fark etme süresi, idrak etme süresi ve harekete geçme sürelerini içermektedir.

Tahliye süresi yapılacak simülasyon sonucu belirlenir, sonuçta hesaplanan gereken güvenli tahliye süresi (GGTS) yani binanın tamamen tahliye edilmesi için yangının başlangıcından itibaren geçen sürenin Mevcut güvenli tahliye süresinden (MGTS) az olup olmalıdır.

Harekete Geçme Süresi

Harekete Geçme Süresi: İnsanların yangın çıktığını anladıktan sonra harekete geçme için karar aldığı süredir. SFPE el kitabı [7] Tablo 3.13.'de de belirtildiği üzere toplam 3 dakikalık bir harekete geçme süresi gecikmesi kayıt edilmiş ses ile sesli anons sistemi kullanılan bir AVM binası için uygun bir yaklaşımdır.

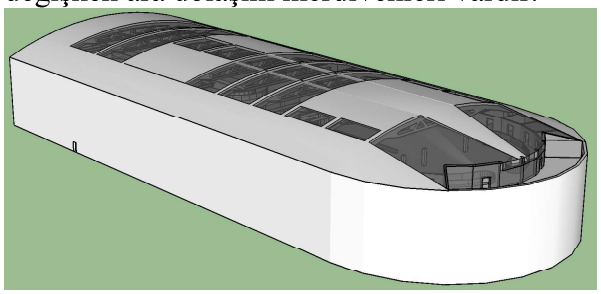
5 MATERYAL VE METOT

Tahliye Süresi

Tahliye hızları gerçek hayatta insanların fiziki kondisyonları, cinsiyeti, kıyafeti, eşlik ettikleri kişiler, yaş ve maruz kaldıkları dış etmenlere göre değişiklik göstermektedir, tahliye hızları çıkışa ulaşım yolları üzerinde geniş alanlarda, kapılarda, düz koridorlarda, sıkışık düzende ve rahat yürüme koşullarında da farklılık göstermektedir. Bu konuda SFPE el kitabında [7] belirtilen deneysel sonuçlar edinilmiştir. Tahliye simülasyonda kullanılan Pathfinder programı SFPE modunda tahliye hesapları yaptırılarak kullanılmıştır, SFPE modunda tahliye hızı yoğunluğun bulunan bölgenin ve SFPE temel diyagramına bağlı bir hız eğrisinden çekilen fonksiyondur.

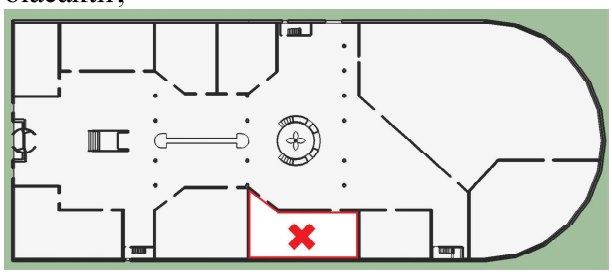
Simülasyon Yapılacak AVM Mimarisi

Simülasyon yapılacak AVM örnek binası bir girşi 3 normal kat olmak üzere toplam 4 kattan oluşmaktadır, AVM de tüm katlara hitap eden toplam 3 adet yangın merdiveni ve katlar arası değişken ara dolaşım merdivenleri vardır.



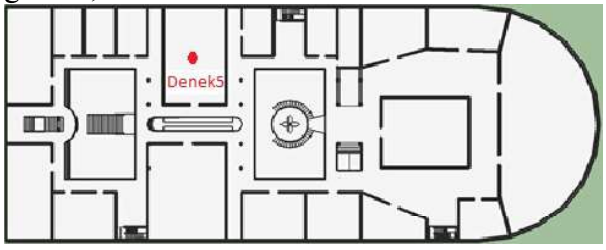
Şekil 4. AVM Dıştan görünüş

Yangın başlangıç noktası AVM binası giriş katında yer alan aşağıdaki oyuncakçı mağazası olacaktır;

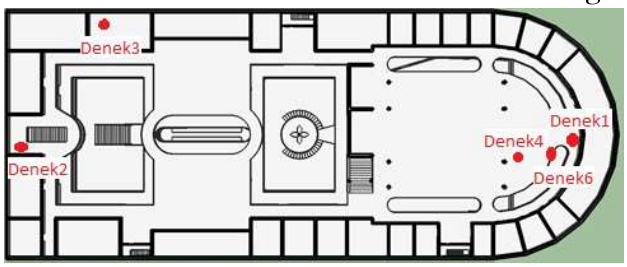


Şekil 5. Yangın merkezi

Simülasyonda incelenen deneklerin kat planındaki başlangıç pozisyonları aşağıdaki gibidir;



Şekil 6. İkinci kat planı



Şekil 7. Üçüncü kat planı

Yangın Senaryosu

Atrium bölgesinde çıkacak yangın ve bu yangın için çeşitli senaryolar ile simülasyon başlangıç kriterlerinin oluşturulmasında SFPE 5. Addition kullanılmıştır [7].

YANGIN LOKASYONU	OTOMATİK SÖNDÜRME	DUMAN EGZOZ SİSTEMİ	SENARYO NO	SENARYO OLASILIK
Atriuma açılan mağaza	Evet (0,7)	Evet (0,7)	S01	0.49
		Hayır (0,3)	S02	0.21
	Hayır (0,3)	Hayır (0,3)	S03	0.09
		Evet (0,7)	S04	0.21

Şekil 7. Senaryo olasılık ağacı

Atriumlarda duman kontrol sisteminin sadece CFD çalışması yapılarak tasarlanmasının mümkün olduğu bu tezin önceki bölümlerinde belirtilmiştir, bu nedenle yapılacak analizde duman egzoz sistemi kapasitesi en kötü senaryolar dikkate alınarak S04, S02 ve S03 senaryoları için irdelenecek duman kontrol sisteminin ve sprinkler sisteminin bu tip binalarda can güvenliği bakımından önemi irdelenecektir.

Simule Edilecek Yangın Özelliği

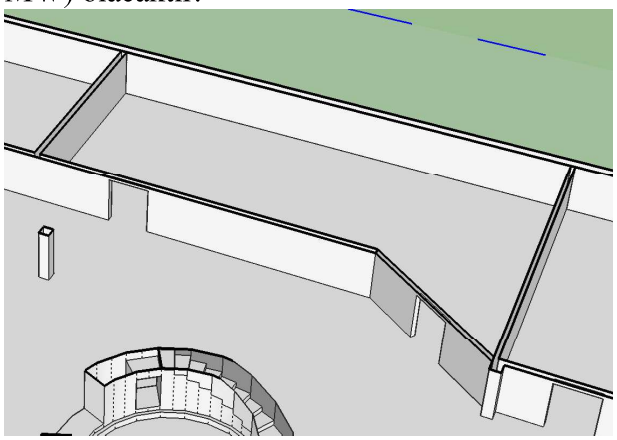
Mağazanın içinde oluşabilecek pik yangın yükü için doğal havalandırma sınırı aşağıdaki Walton ve Thomas 2008 denklemi kullanılarak hesaplanabilir [7];

$$Qvl = 1500 \frac{kw}{m^{5/2}} A_0 \sqrt{h_0}$$

(5.1)

Qvl=Doğal havalandırma ile sınırlı yangın büyüklüğü (kW)
h_0= Açıklığın yüksekliği (m)
A_0= Açıklığın alanı (m^2)

Modelde yangının çıkacağı alan olarak belirlenen oyuncak mağazasının iki adet kapısı vardır, kapılar 2,4 metre yüksekliğinde ve 2 metre genişliğindedir.
Formül üzerinden hesaplandığında her iki kapıdan girebilecek taze hava miktarı ile bu alanda klima santrallerinin yangın ihbar üzerine durması ile sadece kapılardan doğal hava sirkülasyonu olacağı kabulü ile 14.400kw (14,4 MW) olacaktır.



Şekil 8. Yangın çıkan mağaza kapıları

Simule Edilecek Duman Tahliye Sistemi Özellikleri

Simülasyonda çatıya yerleştirilmiş 2 adet duman egzoz fanı kullanılacaktır her bir egzoz fanının debisi sabit olarak 33,3m^3/saniye (119.880m^3/saat) olacak toplam debi 66.6m^3/saniye (239.760m^3/saat) olacaktır. Duman egzoz fanları yangını merkezindeki duman detektörlerinden herhangi birisi aktive olduktan sonra 30 saniyelik bir bekleme süreci sonrasında devreye girecektir.
Taze hava bina zemin katında bulunan 4 adet kapının yangın anında otomatik olarak açılması ile sağlanacaktır.

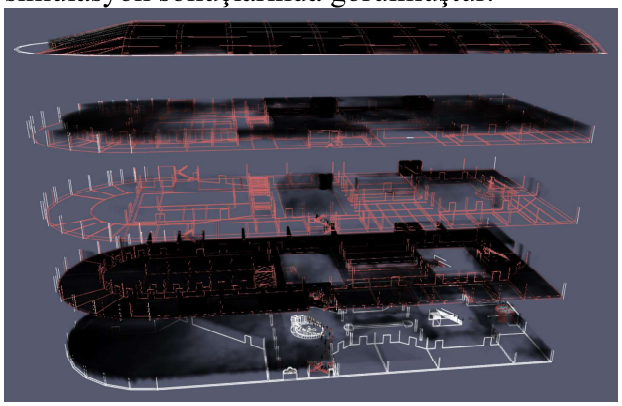
6 SONUÇLAR VE ÖNERİLER

6.1 Sonuçların Genel Planlar Üzerinden Değerlendirmesi

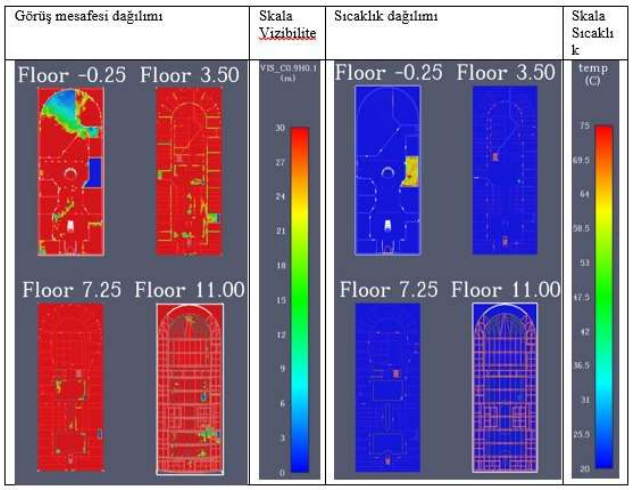
S02 Senaryosu yani sadece sprinkler sisteminin çalıştığı bu nedenle yangın yükünün 6,25MW ile sınırlı kaldığı senaryo can güvenliği bakımından en güvenli senaryo olarak belirlenmiştir, simulasyonun sonunda 675. Saniyede görüş mesafesi (Vizibilite) ve baş mesafesindeki sıcaklık değerleri aşağıdaki gibi hesaplanmıştır;

Görüş mesafesinin 5-10 metre civarlarında olması BS PD 7974-6:2019 'a göre uygundur [4]. Yangın merkezi hariç bina genelinde görüş

mesafesinin 5 metre altına düşmediği simülasyon sonuçlarında görülmüştür.

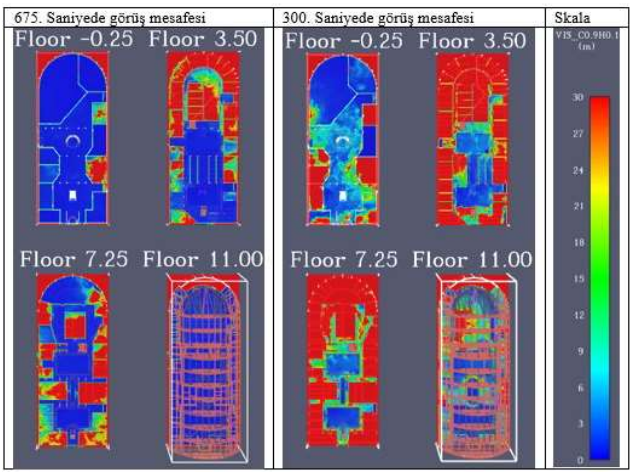


Şekil 9. Senaryo 2, 650. Saniye duman yayılımı(Görselde katlar birbirinden ayrılarak gösterilmiştir.)



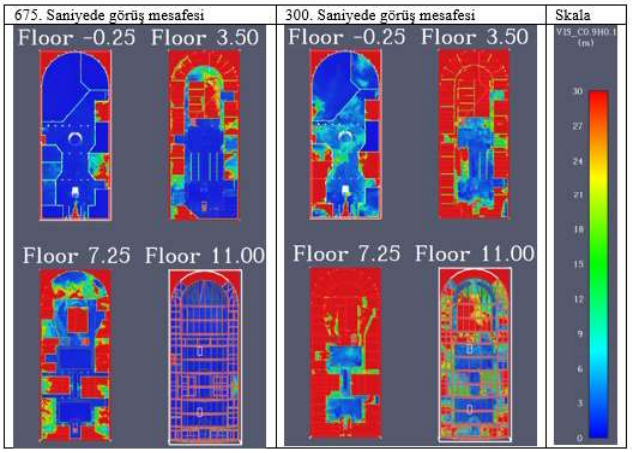
Şekil 10. Senaryo 2, senaryosu 675. Saniye görüş mesafesi ve sıcaklık değerleri

S03 Senaryosunda, duman egzoz sisteminin ve sprinkler sisteminin aktif olmadığı senaryoda görüş mesafeleri aşağıdaki görseldeki gibi olmuştur;



Şekil 10. Senaryo 3, senaryosu vizibilite (görebilirlik) mesafeleri

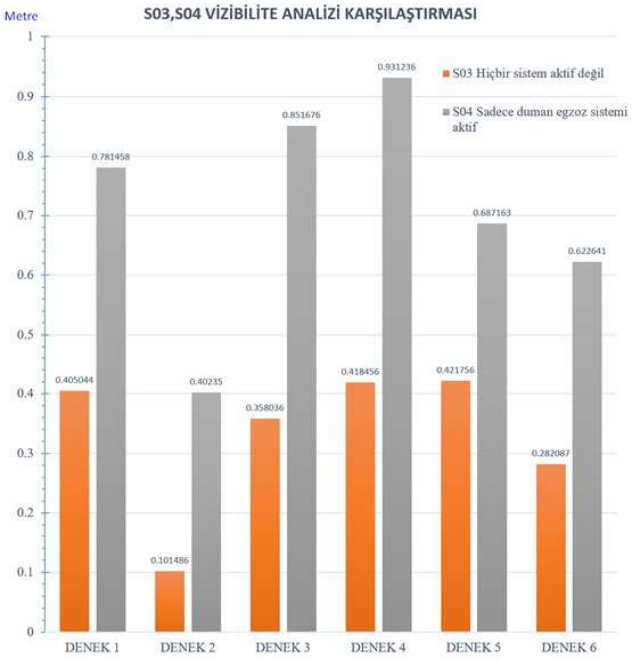
S04 Senaryosunda, sadece duman egzoz sisteminin aktif olduğu senaryoda görüş mesafeleri aşağıdaki görseldeki gibi olmuştur;



Şekil 11. Senaryo 4, senaryosu vizibilite (görebilirlik) mesafeleri

6.2 Sonuçların Denekler Üzerinden Değerlendirmesi

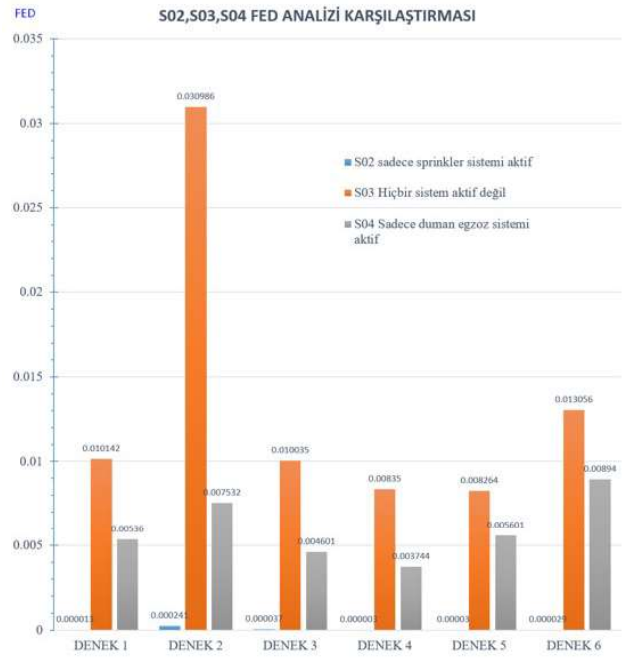
Yapılan incelemede S02 senaryosu için vizibilite konusunda hiçbir denek için kritik eşiğin aşılmadığı görülmüştür, S03 ve S04 senaryolarında ise her denek için vizibilite sınırlarının aşıldığı tespit edilmiştir;



Şekil 12. Senaryo 3-4 Vizibilite Karşılaştırması

Her iki senaryo da vizibilite bakımından gerekli kabul değerlerini sağlamamasına rağmen duman kontrol sisteminin varlığı denekler geneline bakıldığında misli oranında pozitif yönde etki sağlayabilmiştir.

Senaryolara göre FED (Kısmi etkili doz) karşılaştırması;
675. Saniye sonunda tahliye eden insanlardaki Fed oranları senaryolara kıyasla aşağıdaki gibidir;



Şekil 13. FED analizi Karşılaştırması

6.3 Çalışma Sonuçlarının Değerlendirmesi

Çalışma sonucunda;

Bu tip bina yangınlarında duman kontrol sistemi tasarımı bakımından görülebilirlik sınırının FED kriterinden daha konsarvatif bir tasarım verisi olduğu değerlendirilmiştir.

Duman kontrol debisinin yetersiz seçilmesi durumunda bile FED bakımında pozitif etkinin kayda değer oranda görülebileceği değerlendirilmiştir.

Yetersiz bir duman kontrol sistemi görülebilirlik (Vizibilite) konusunda duman kontrol sistemi yoksunluğu durumu ile benzer sonuçlar vereceği görülmüştür.

Sprinkler sisteminin kullanımının duman kontrol sistemi kullanımına nazaran daha etkin bir can güvenliği önlemi olduğu görüşü kuvvetlenmiştir.

REFERANSLAR

[1] Binaların Yangından Korunması Hakkında Yönetmelik -(09/07/2015)-29411, 2015
[2] NFPA 101: Life Safety Code, 2018 Edition
[3] ISO/TS 29761:2015 Fire safety engineering — Selection of design occupant behavioural scenarios
[4] BS PD 7974-6:2019 Application of fire safety engineering principles to the design of buildings – Part 6: Human factors. Life safety strategies. Occupant evacuation, behaviour and condition (Sub-system 6)
[5] JIN, T. Visibility through fire smoke. Part 5. Allowable smoke density for escape from fire. Report of Fire Research Institute of Japan. 1976, No.42, 12
[6] NFPA 92 Standard for smoke control systems
[7] SFPE Handbook of Fire Protection Engineering-5th Edition-Morgan J_2015-2016.
[8] H. Nelson, “Performance-Based Fire Safety,” in Proceedings: 1996 International Conference on Performance-Based Codes and Fire Safety Design Methods, Society of Fire Protection Engineers, Bethesda, MD (1996).
[9] H. Nelson, “Performance-Based Fire Safety,” in Proceedings: 1996 International Conference on Performance-Based Codes and Fire Safety Design Methods, Society of Fire Protection Engineers, Bethesda, MD (1996).

REAKTİF KONTROLLÜ SIKIŞTIRMA İLE ATEŞLEMELİ BİR MOTORUN PERFORMANS VE EMİSYON PARAMETRELERİNİN İNCELENMESİ

Ahmet Kaya[1], B. Albayrak Çeper[2], Nafiz Kahraman[2] ve S.Orhan Akansu[1]

1. Mühendislik Fakültesi, Erciyes Üniversitesi, Kayseri
2. Havacılık ve Uzay Bilimleri Fakültesi, Erciyes Üniversitesi, Kayseri

Özet

Günümüzde içten yanmalı motorlara sahip taşıtlar için çok sıkı emisyon değerleri düzenlenmiştir. Ayrıca dünyada fosil yakıt rezervlerinin sınırlı olması ve her geçen gün daha da azalması büyük bir problem haline gelmektedir. Bütün bu olumsuz durumların önüne geçmek amacıyla alternatif yanma modellerinin araştırılmasında Reaktif Kontrollü Sıkıştırma ile Ateşlemeli motorlar ön plana çıkmaktadır. Bu çalışma kapsamında dizel bir motorda standart dizel yanması ile RCCI yanma modu için motor deneyleri gerçekleştirilmiştir. Deneylerde düşük reaktiviteli yakıt olarak benzin yakıtı, yüksek reaktiviteli yakıt olarak dizel yakıtı (motorin) kullanılmıştır. Deneysel parametre olarak farklı benzin dizel yakıt oranları, sabit devirlerdeki deneylerde tekrar edilmiştir. Deneylerde motor momentinin en yüksek 2000-2500 d/d aralığında olduğu tespit edilmiştir. 2000 d/d motor devri deney verisi olarak ele alınmış ve EGR uygulaması test edilmiştir.

Anahtar Kelimeler: RCCI, Hesaplamalı Akışkanlar Dinamiği, EGR, Emisyon

1 GİRİŞ

İçten yanmalı motorlardan salınan emisyon değerlerinin ilgili emisyon standartlarının NOx, CO, HC ve partikül emisyonları için uyguladığı maksimum müsaade edilen seviyelerde sağlanması için motorlar üzerindeki çalışmalar güncelliğini koruyarak artmaktadır. Hem taşıt kaynaklı egzoz emisyonlarının azaltılması hem de içten yanmalı motorların verimlerini arttırabilmek için konvansiyonel yanma türlerinin dışında farklı yanma modları üzerinde araştırmalar sürdürülmektedir. Bu alternatif yanma modları arasında homojen dolgulu sıkıştırma ile ateşlemeli (HCCI), kısmi ön karışımlı yanma (PPC), ön karışımlı sıkıştırma ile ateşlemeli yanma (PCCI) ve reaktif kontrollü sıkıştırma ile ateşlemeli yanma (RCCI) bulunmaktadır [1]. Son yıllarda, yanma koşullarını iyileştirmek amacıyla geliştirilen motorlardan bir tanesi, düşük silindir sıcaklıkları ve aynı zamanda yüksek sıkıştırma oranı sayesinde yüksek verimler elde edilebilen HCCI motorlarıdır. Diğer bir motor çalışma koşulu ise bir miktar ön karışımın dizel yakıtıyla ateşlendiği PCCI motorlarıdır [2]. RCCI modu, HCCI ve PCCI'yi geliştirmek için yakıt oranı ve ateşleme zamanı düzenlenmesi ile reaktif geçişlerini başlatma ve ateşleme kontrolü sağlanmaya çalışılır. Amaç yüksek termal verim, düşük NOx ve PM (partikül madde) emisyonu sağlamaktır [3]. Wang ve arkadaşları [4], direkt enjeksiyonlu (DI) yakıt özelliklerinin çift yakıtlı RCCI yanma işleminde tek silindirli, ağır hizmet tipi bir dizel motor üzerindeki etkilerini araştırmak için deneysel bir araştırma yapmışlardır. Setan sayısı (CN) 34 ila 100 arasında değişen dört direkt enjeksiyonlu yakıtın yanma ve emisyon özellikleri farklı yanma sınır koşulları altında incelemişlerdir. Setan sayısı 34/43/56/100 olan yakıtları RCCI operasyonunda yanma ve emisyon özellikleri farklı yanma koşulları altında incelemişlerdir. RCCI yanmasının, daha gelişmiş SOI zamanlaması, daha fazla egzoz gazı devridaimi (EGR) ve daha yüksek ön karışım oranı sağladığını tespit etmişlerdir.

Pandian ve Anand [5], çalışmalarında RCCI işleminin, tarım ve elektrik üretim uygulamalarında kullanılan küçük, tek silindirli bir dizel motor kullanarak daha yüksek fren ısıl verim ile birlikte sıfıra yakın azot oksitleri (NOx) ve duman emisyonlarını elde etmek için en umut verici bir yanma stratejisi olarak ortaya çıktığını belirtmişlerdir. Mevcut çalışmada, bir mekanik yakıt enjeksiyonunu, esnek bir common rail direkt enjeksiyonlu dizel sistemi ve düşük basınçlı bir benzin portlu yakıt enjeksiyon sistemi ile değiştirerek hafif hizmet dizel motorunda RCCI stratejisini uygulanmaya çalışılmıştır. Ayrıca piston sıkıştırma kabındaki modifikasyonlar sayesinde motor sıkıştırma oranını azaltmışlardır. Elde edilen sonuçlar, motorun

tüm yük aralığında RCCI modunda çalıştırılabileceğini ve konvansiyonel yanmaya kıyasla maksimum yanma ile %14,2 fren ısıl verim artışı, sıfıra yakın NOx ve duman emisyonlarında çalışabileceğini göstermiştir. Benajes ve arkadaşları [6], optimize edilmiş RCCI ve çift yakıtlı dizel-benzinli yanma stratejilerini birleştirerek tam yüke kadar temiz ve verimli motor çalışması elde etmeyi amaçlamışlardır. Deneysel çalışmada, RCCI çalışma aralığının daha yüksek yüklere doğru uzatılması amacıyla motorun sıkıştırma oranını 17.5:1'den (stok) 15.3:1'e düşürmek için piston haznesi hacmini arttırmışlardır. Çalışmalarında konvansiyonel dizel yanma ile karşılaştırılması, bu çift yakıtlı stratejinin tüm motor haritasındaki NOx sıkıştırma ateşlemeli motor emisyonlarını azaltmada ve aynı zamanda düşük yük bölgesinde duman emisyonlarının eşzamanlı olarak azaltılmasında büyük bir potansiyele sahip olduğunu ortaya koymuşlardır. Li ve arkadaşları [7], RCCI motorlarının verimliliği üzerine incelemelerde bulunmuşlardır. RCCI motorların daha yüksek ısıl verim ve çok düşük NOx ve PM emisyonları sağlayabildiğini bulmuşlardır. Ayrıca bu çalışmada kontrol edilebilirlik sorunlarını da ele almışlardır. Benajes ve arkadaşları [8], RCCI yanmasında karışım ve kendi kendine tutuşma işlemlerini dizel ve benzin yakıt kullanarak deneysel ve sayısal olarak incelemişlerdir. Port enjeksiyonu ve direkt enjeksiyon yapılarak sıkıştırma ile ateşlemeli bir motorda tek boyutlu püskürtme modelini kullanarak analiz yapmışlardır. Konvansiyonel dizel yanmasına göre RCCI yanmasında NOx emisyonlarında bir miktar, duman emisyonlarında ise ciddi bir azalma tespit etmişlerdir.

2 YÖNTEM VE MATERYAL

Deneysel çalışma Erciyes Üniversitesi Motorlar laboratuarında motorun modifikasyonu ile sisteme EGR hattı ve tüp bağlantılarının tamamlanması ile gerçekleştirilmiştir. Deney motoru öncelikle saf dizel yakıtı ile çalıştırılmış veriler kaydedilmiştir, akabinde benzin-dizel yakıtları ile testler gerçekleştirilmiştir. Deney motorunda Benzin yakıtının motor içerisine verilmesini sağlamak için emme manifoldu üzerine yakıt enjektörü monte edilmiştir. Enjektörün pulse miktarını ayarlayabilmek için sistem üzerine kontrol kartı takılmıştır. Deneyde kullanılacak tek silindirli dört zamanlı motor saf dizel yakıt ile yapılan deneyler haricinde benzin-dizel yakıtı ile farklı devirlerde çalıştırılarak veriler toplanmıştır. Deneyler sabit devirde 2000 d/d için tekrar edilmiştir. Silindir içerisinde oluşan basınç değerleri osiloskop ve enkoder yardımıyla Picoscope 6 programı içerisine aktarılarak veriler bilgisayar ortamına aktarılmıştır. Deneylerde test motoru olarak tek silindirli dört zamanlı Antor marka 4LD820 model dizel motor kullanılmıştır. Tablo 1'de motora ait özellikler verilmiştir. Egzoz gazı emisyon cihazı yardımıyla deneylerde elde edilen emisyonlar değerlendirilmiştir (Tablo 2).

Tablo 1. Deney Motoru Özellikleri

Tip	4LD 820
Silindir Sayısı (Adet)	1
Silindir Hacmi (cm3)	817
Silindir Çapı (mm)	102
Strok (mm)	100
Sıkıştırma Oranı	17:1
Motor Devri (d/d)	2600 (3000)
Motor Gücü (BG)	15/(17)
Maksimum Tork (kgm)	5@1600rpm

Tablo 2. Emisyon Cihazı Ölçüm Aralıkları

CO	0…10 %Vol
CO2	0…20 %Vol
HC	0…20000 ppmVol
O2	0…21 %Vol
NOx	0…5000 ppm
Lambda	0…5

Deneysel çalışmada 50 kW'lık bir hidrolik dinamometre kullanılmış ve dinamometrenin ölçtüğü değerler ise PC 101BMS kontrol panosu yardımıyla okunmuştur. Deneylerde kullanılan yakıtlara ait özellikler Tablo 3'de verilmiştir.

Tablo 3. Deney Yakıt Özellikleri[9]

Özellik	**Birim**	**Benzin**	**Motorin**
Kimyasal formül	-	C_6H_{14}-C_7H_{16}	$C_{13}H_{28}$
Yoğunluk(15°C ta)	kg/m^3	727	829
Alt ısıl değeri	kj/kg	42000	42900

Deneysel sisteme ait görüntü şekil 1'de verilmektedir.



Şekil 1. Deneysel sistem

RCCI yanmasında ön karışım oranının etkisini gözlemlemek için gerçekleştirilen deneylerde rp hesabı için eşitlik (1) den faydalanılmıştır.

$$R_p = \frac{\dot{m}_b.H_b}{\dot{m}_b.H_b + \dot{m}_d.H_d}.100 \quad (1)$$

Rp: Benzin yakıtının yüzde oranı [%]
m_b: Benzin yakıtı kütlesel debisi (g/s)
m_d: dizel yakıtın kütlesel debisi (g/s)
Hu_b: Benzin alt ısıl değeri (kj/kg)
Hu_d: Ddizel alt ısıl değeri (kj/kg)

EGR uygulanan deneylerde EGR oranı aşağıda verilen denklemle bulunmuştur.

$$EGR = \frac{(CO_2)_{\text{emme manifoldu}} - (CO_2)_{\text{çevre}}}{(CO_2)_{\text{egzoz manifoldu}}}.100$$

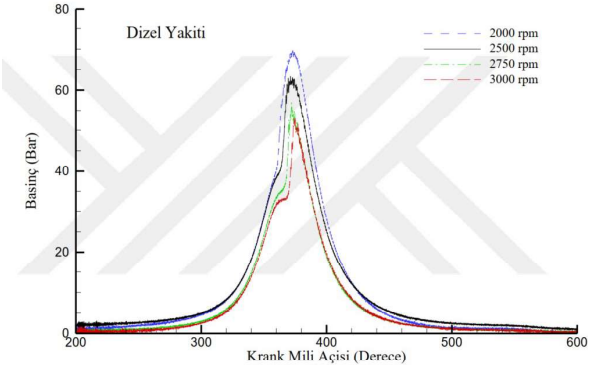
Burada,
EGR: Motora geri gönderilen egzoz gazı miktarı (%),
$(CO_2)_{\text{emme manifoldu}}$: Emme manifoldunda bulunan CO_2 miktarı (hacimsel, %),
$(CO_2)_{\text{çevre}}$: Ortamda yani atmosferde bulunan CO_2 miktarı (hacimsel, %),
$(CO_2)_{\text{egzoz manifoldu}}$: Egzoz gazı içinde bulunan CO_2 miktarı (hacimsel, %) olarak verilmiştir.

Atmosferde hacimsel olarak CO_2 miktarı çok çok az olduğu için formülde ihmal edilebilir. Ayrıca emisyon cihazının hassasiyeti ortamdaki CO_2 miktarını ölçmek için yeterli değildir. Dolayısıyla çevredeki CO_2 miktarı sıfır kabul edilerek formül güncellenirse aşağıdaki denklem elde edilir.

$$EGR = \frac{(CO_2)_{\text{emme manifoldu}}}{(CO_2)_{\text{egzoz manifoldu}}}.100$$

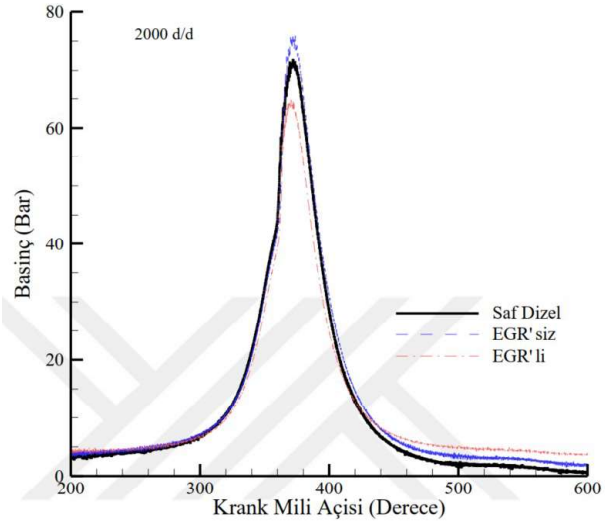
3 BULGULAR

Dizel yakıtına ait farklı devir değerlerine göre silindir içi basınç değişimleri Şekil 2'de görülmektedir. Şekil 3'de görüldüğü üzere silindir içi basınç maksimum 2000 d/d motor hızında, minimum 3000 d/d motor hızında görülmüştür. Motor hızı arttıkça silindir içi basıncın azaldığı tespit edilmiştir. Maksimum basıncın 2000 d/d motor hızında olmasına bağlı olarak genişleme sürecinde elde edilen yüksek basınçtan dolayı maksimum motor momenti ve efektif güç bu devirde çıkmıştır.



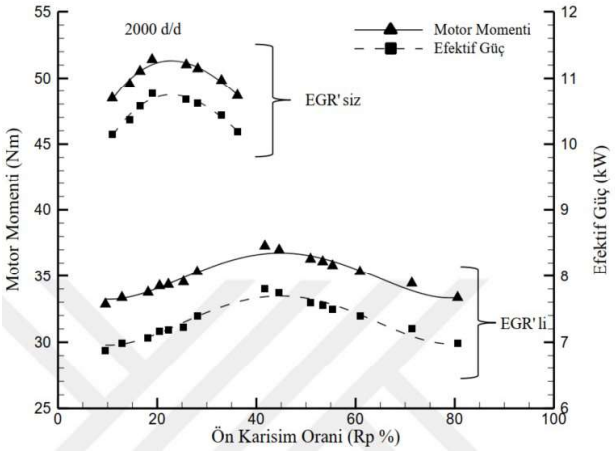
Şekil 2. Farklı devirler için basınç değişimleri

Şekil 3'de görüldüğü üzere silindir içi maksimum basınç RCCI modunda EGR'siz durumda, minimum basınç ise RCCI modunda EGR uygulandığı durumda görülmüştür. RCCI modunda silindir içi basıncın tek dizel yakıtlı duruma göre arttığı fakat EGR uygulanması durumunda silindir içi basıncın tek dizel yakıtlı durumdan da daha düşük basınca sahip olduğu görülmüştür. Maksimum basıncın EGR'siz durumda olmasına bağlı olarak genişleme sürecinde elde edilen yüksek basınçtan dolayı maksimum motor momenti ve efektif güç EGR'siz durumda elde edilmiştir.



Şekil 3. Krank mili açısına bağlı basınç değişimleri

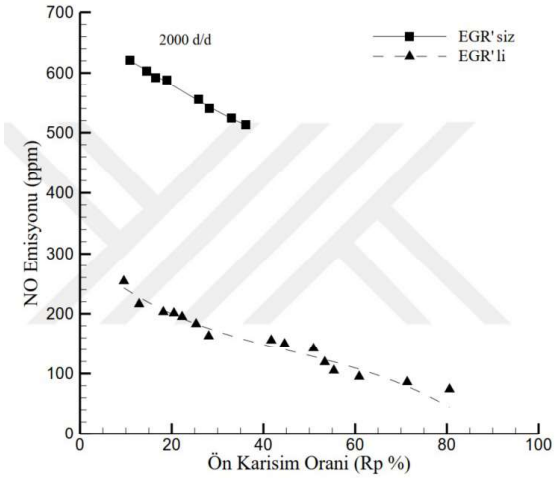
Şekil 4'de EGR'li ve EGR'siz durumda karışım oranına bağlı motor momenti ve efektif güç değerleri görülmektedir. EGR'li durumda EGR'siz duruma göre hem motor momenti hem de efektif güç değerleri daha düşük çıkmıştır. Bunun sebebi, EGR uygulandığı durumda açığa çıkan ısının birazını egzoz gazlarının soğurması sonucu silindirde açığa çıkan maksimum ısının azalmasına bağlı olarak silindir içi basıncın azalması sayılabilir. Ayrıca, genişleme strokunda çevrimden elde edilen iş miktarını azalttığı için EGR'li deneylerde motor momenti ve efektif güç değerleri daha düşük çıkmıştır



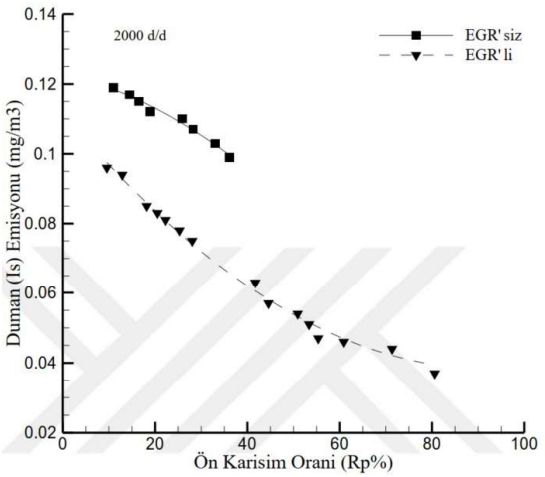
Şekil 4. Rp ile moment ve güç değişimleri

Şekil 5 ve Şekil 6'da Rp oranı ile NO ve İs emisyon değişimleri görülmektedir. Bu şekillerden ön karışım oranı (R_P) arttıkça NO ve is emisyonlarında azalma meydana gelmektedir. Ayrıca EGR uygulamasının da NO ve is emisyonlarını iyileştirdiği görülmektedir. Literatürde de benzer sonuçlara ulaşıldığı görülmüştür [6, 22].

Xu ve arkadaşları [10], yaptıkları çalışmalarında genel eğilim açısından benzin oranının artmasıyla NOx ve kurum emisyonları önemli ölçüde azaldığını belirtmişlerdir. Ancak %58 benzin oranı için NOx ve kurum emisyonunda büyük bir artışla karşılaşmışlardır. Benzin oranının artmasıyla hava-yakıt oranı azaldığından NOx emisyonunun da azaldığını belirtmişlerdir. Ayrıca silindir içi sıcaklık yükseldiği için kurumun azaldığından bahsetmişlerdir.



Şekil 5. Rp ile NO emisyon değişimleri



Şekil 6. Rp ile duman emisyon değişimleri

4 SONUÇLAR VE BULGULAR

Bu çalışma kapsamında tek silindirli dizel bir motorda standart dizel yanması ile RCCI modu için deneysel çalışmalar gerçekleştirilmiştir. Deneysel parametre olarak farklı benzin dizel yakıt oranları, tam motor yükünde ve sabit devirde deneyler tekrar edilmiştir. Deneylerde motor momentinin 2000 d/d civarında en yüksek olduğu tespit edilmiş ve ilerleyen aşamalarda 2000 d/d deney verisi olarak kullanılmıştır. Deneylerde daha sonra çift yakıtla 2000 d/d motor devrinde EGR uygulaması yapılmıştır. Elde edilen sonuçlar grafikler halinde sunulmuştur.

RCCI modunda 2000 d/d motor hızında hem EGR'siz hem de EGR'li deneyler yapılmıştır. EGR uygulaması yapılmasının motor performansı ve emisyonlar üzerindeki etkileri irdelenmiştir. EGR uygulanmadan benzin ön karışım oranı maksimum %36,16 olarak uygulanabilmiştir. Daha yüksek ön karışım oranlarına motor vuruntu yaptığı için çıkılmamıştır. Ancak EGR kullanımıyla motor içi basınç düşürülerek %80,58 oranında benzin ön karışım oranına çıkılmıştır. EGR'siz durumda %18,97 benzin ön karışım oranında, EGR'li durumda %41,7 benzin ön karışım oranında motor momenti maksimum değere ulaşmıştır. EGR'siz durumda benzin ön karışım oranı %18,97 oranından %36,16 oranına çıkınca motor momenti ve efektif güç değerlerinde %5,6 oranında azalma meydana gelmiştir. EGR'li durumda benzin ön karışım oranı %41,7 oranından %80,58 oranına çıkınca motor momenti ve efektif güç değerlerinde %11,7 oranında azalma meydana geldiği görülmüştür. Bu azalmanın karışımdaki dizel yakıt miktarının azaldığından dolayı olduğu söylenebilir. EGR uygulanması halinde %50,91 oranından daha yüksek oranlarda EGR'siz en düşük özgül yakıt tüketiminden daha yüksek özgül yakıt tüketim değerleri ortaya çıktığı için eğer EGR uygulanacak ise %50,91 benzin ön karışım oranını aşmamak gerektiği görülmüştür. EGR'siz maksimum motor momentinin elde edildiği %18,97 benzin ön karışım oranında %7,4 oranında EGR uygulaması yapıldığında motor momentindeki %34,4 oranındaki azalmayla özgül yakıt tüketimi %39,7 oranında azalmıştır. Ayrıca deneylerde EGR oranı arttığında özgül yakıt tüketiminin arttığı görülmüştür. Artan EGR oranının karışımı fakirleştirmesiyle açığa çıkan maksimum ısı miktarının azalmasının özgül yakıt tüketimini arttırdığı söylenebilir. Benzin ön karışım oranı arttıkça hem EGR uygulandığı deneylerde hem de uygulanmadığı deneylerde efektif verimin gittikçe azaldığı tespit edilmiştir. Bu durumun, benzin yakıtının alt ısıl değerinin dizel yakıtının alt ısıl değerine göre daha düşük olduğu için yakıt karışımında benzin yakıtı arttıkça karışımın ortalama alt ısıl değerinin düşmesiyle gerçekleştiği söylenebilir. Silindir içi sıcaklık düştükçe genişleme strokunda basınç düşeceği için yapılan iş azalır ve efektif verim düşer. Hem EGR'li durumda hem de EGR'siz durumda benzin ön karışım oranı arttıkça NOx ve is emisyonları önemli ölçüde azalmıştır. Bunun sebebi karışımın benzin oranı arttıkça silindir içi sıcaklıkların daha düşük olmasıdır. Ayrıca EGR kullanılmasıyla NO ve is emisyonlarında dikkate değer azalmalar meydana gelmiştir. EGR'siz maksimum motor momentinin elde edildiği %18,97 benzin ön karışım oranı referans alındığında %7,4 oranında EGR uygulaması yapıldığında efektif güçteki %34,4 oranındaki azalmaya karşılık NO emisyonunun %65,5 oranında azaldığı ve duman emisyonunun da %24,1 oranında azaldığı deneylerde görülmüştür.

5 TEŞEKKÜR

Yazarlar, Erciyes Üniversitesi Bilimsel Araştırma Projeleri Birimi'nin (proje no: FBA-2018-8289) mali desteği için minnettardır.

6 KAYNAKLAR

1. Uyumaz, A., Solmaz, H., Boz, F., Yılmaz, E., Polat, S., 2017. Reaktif kontrollü sıkıştırma ile ateşlemeli (RCCI) bir motorda lamdanın yanma karakteristiklerine etkileri. Afyon Kocatepe Üniversitesi Fen Ve Mühendislik Bilimleri Dergisi, 17 (2017): 035903 (1146-1156).

2. Aydın, M., 2016. Çift Yakıtlı Sıkıştırmalı Ateşlemeli Bir Motorda Yanmanın Üç Boyutlu Modellenmesi. İstanbul Teknik Üniversitesi, Yüksek Lisans, İstanbul, 133s.

3. Işık, M. Z., & Aydin, H. 2019. Investigation on the effects of gasoline reactivity controlled compression ignition application in a diesel

generator in high loads using safflower biodiesel blends. Renewable Energy, 1481(18): 31209-6.

4. Wang, H., Zhao, X., Tong, L., Yao, M., 2018. The effects of DI fuel properties on the combustion and emissions characteristics of RCCI combustion. Fuel, 227: 457-468.

5. Pandian, M. M., Anand, K., 2018. Experimental optimization of reactivity controlled
compression ignition combustion in a light duty diesel engine. Applied Thermal Engineering, 138: 48-61.

6. Benajes, J., García, A., Monsalve-Serrano, J., Boronat, V., 2017. Achieving clean and efficient engine operation up to full load by combining optimized RCCI and dual-fuel diesel gasoline combustion strategies. Energy Conversion and Management, 136: 142-151.

7. Li, J., Yang, W., Zhou, D., 2017. Review on the management of RCCI engines. Renewable and Sustainable Energy Reviews, 69: 65-79.

8. Benajes, J., Molina, S., García, A., Belarte, E., Vanvolsem, M., 2014. An investigation on RCCI combustion in a heavy duty diesel engine using incylinder blending of diesel and gasoline fuels. Applied Thermal Engineering, 63:66-76.

9. Çelik, O., 2019. Atık Taşıt Lastiklerinden Elde Edilen Pirolitik Yağın Reaktivite Kontrollü Sıkıştırma Ateşlemeli Motorlarda Kullanımının Deneysel Olarak Araştırılması. Fırat Üniversitesi Fen Bilimleri Enstitüsü, Yüksek Lisans Tezi, Elazığ, 98 s.

10. Xu, Y., Kang, H., Gong, J., Zhang, S., Li, X., 2018. A study on the combustion strategy of gasoline/diesel dual-fuel engine. Fuel, 225: 426-435

NUMERICAL INVESTIGATION OF COMBUSTION AND FLAME CHARACTERISTICS IN A SWIRL BURNER/FURNACE FOR A MODEL THERMOELECTRICAL GENERATOR(TEG) PERFORMANCE

Mustafa Ilbas[1],Sumeyye Akyildiz[2], Serhat Karyeyen [1], Ahmet Aktas [1]

1. Gazi University, Faculty of Technology, Department of Energy Systems Engineering, 06560, Teknikokullar, Ankara, Turkey
2. Graduate School of Natural and Applied Science, Gazi University, 06560, Teknikokullar, Ankara, Turkey email: sumeyye.akyildiz@gazi.edu.tr

Abstract

This paper performs computational fluid Dynamics (CFD) techniques and MATLAB Simulink to investigate the flame characteristics in the combustion chamber and thermoelectrical generator (TEG) performance. TEG converts thermal energy into electrical energy with the Seebeck effect, using the temperature difference between its two surfaces. In this study, temperatures and flame characteristics in the combustion chamber were obtained using the CFD Analysis program. The performance of the TEG model was analyzed using MATLAB Simulink depending on variable temperature values. The main objective of this research is to analyze the flame characteristics to serve as a reference for the performance of the model TEG. The generated swirl burner was modeled under conventional combustion conditions. The temperature zones obtained from combustion were used to initiate and sustain the thermoelectrical generator. The effect of the use of TEG on flame characteristics was numerically investigated. TEG performance values for different temperatures were also analyzed and interpreted. Flame deviations were observed in the areas where TEG was placed on the wall.

Keywords: Combustion and Flame, CDC, TEG, Numerical Analysis

1 INTRODUCTION

Energy requirements are constantly rising over the world due to the increase in heating, electricity, and other usages.

Today, as a result of rapid industrialization, the amount of CO2 released into the atmosphere is increasing by the day. Concerns have been raised about global warming and climate change as a result of this situation. Despite the fact that fossil fuel reserves are limited, one of the primary causes of global warming, their consumption continues in this century. Studies on the efficient use of fossil fuels are becoming increasingly important in order to prevent the escalation of environmental problems.

Burners are divided into premixed and diffusion (non-premixed) burners. Reactants are mixed before the reaction is initiated in premixed flames as well as fuel and oxidizers enter the combustion chamber as separate streams in diffusion flames. Both of them are commonly used to burn natural gas or methane which is a significant component of natural gas in any combustion system. [1]

As a promising alternative energy technology, thermoelectric generation has evoked substantial attention in renewable energy research because of its unparalleled merits, such as no pollution, no moving parts, no maintenance cost, and long service life. Due to the advantages of simple structure and convenient installation, the common way to directly convert heat energy into electrical energy is to use a thermoelectric generator (TEG)

Most researchers utilize computational fluid dynamics (CFD) simulations to solve the temperature distributions in TEG systems and then calculate output power based on the mean surface temperature obtained.[2]

Y.Zhao et al. proposed a thermoelectric generator system with heat transfer fluid circulation, using the heat transfer fluid after heat exchange with the exhaust to the generator to complete the thermo-electric conversion. As a result of by analyzing the parameters on the system performance and the fluid parameters, they obtained the optimum heat transfer fluid flow rate at maximum net output power in the new system. [3]

To improve the efficiency of thermoelectric systems based on hydrocarbon fuel combustion microscale, Z.Zhao et al. Simulation models with variable temperature parameters have been proposed by The results show that the two-stage thermoelectric module design reduces combustion chamber thermal efficiency while increasing thermoelectric module conversion efficiency significantly. Therefore, the overall efficiency of the two-stage system is much higher than the single-stage system. The greater height and cross-sectional area of the thermoelectric leg help improve efficiency, but is not conducive to miniaturization of the micro thermoelectric generator. [4]

Hiranandan et al. studied the development of a numerical model for a thermoelectric generator integrated with a novel micro combustor to predict the thermoelectric performance of the system. The novelty of the work lies in the development of a numerical model to predict and analyze the system's thermal characteristics and thermoelectric performance with numerical simulations. To improve its flame stability and thermal characteristics over other combustors, the combustor has backward-facing steps and a recirculating cup. Following the thermal analysis of the micro combustor, the model for predicting the power output from the thermoelectric modules is validated and then integrated by using a separate sub-routine. A maximum open-circuit voltage of 8 V was reported for the integrated system.[5]

2 METHODOLOGY

Under conventional conditions, high temperatures are reached in the combustion chamber by burning different types of fuel. Electricity can be generated by using the TEG system to evaluate the waste heat generated at the end of combustion. The main objective of this research is to analyze the flame characteristics as a reference for the performance of the model TEG.

2.1 Combustion Modeling

Computational fluid dynamics modeling was performed through an existing gas burner for methane combustion in order to model the combustion. Methane-air combustion was selected to model in the existing burner and the combustion chamber through Ansys Fluent CFD code [6] and the used combustion chamber is shown in Figure 1.

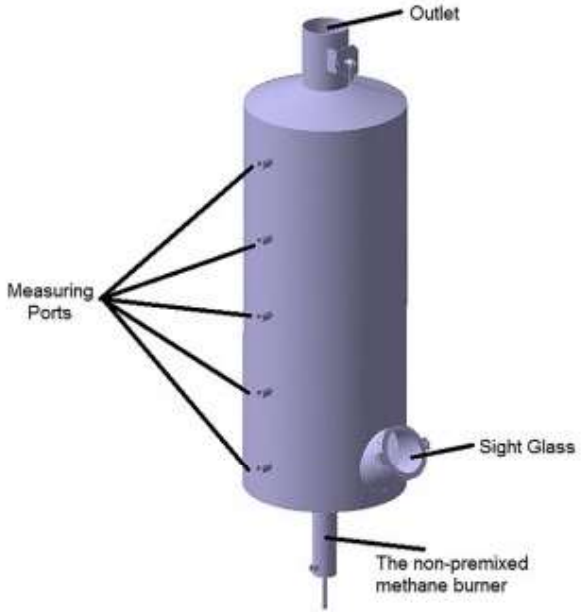


Figure 1. Combustion chamber

The diffusion burner involves two stream regions coaxially, one of which is the air stream and the other is fuel stream.Inlet temperatures of the oxidizers and fuels were of 295 K, and it was supposed that combustion occurring in all cases were under atmospheric conditions. And the heat transfer coefficient was selected as 20 W/m^2 K. All combustion cases were planned for 20 kW thermal power and an equivalence ratio of 0.83.

Mesh structure was thickened, especially at the location of the burner and swirling area. Since combustion reactions begin in this area, increasing the frequency of mesh structure is critical. Mesh pattern, which were used in this study are illustrated in Fig. 2

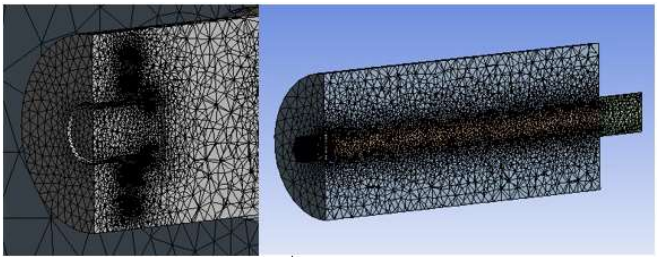


Figure 2. Mesh

2.2 Thermoelectric generator

The thermoelectric device is an electrical circuit that consists of thermal materials that convert the heat into electricity by two different semiconductor materials conducted to each other by a conducting plate which would make one of them negatively charged (n-type) and the other positively charged (p-type). An electrical current will flow in the circuit if any temperature difference existed between the TEM's sides according to the Seebeck effect.

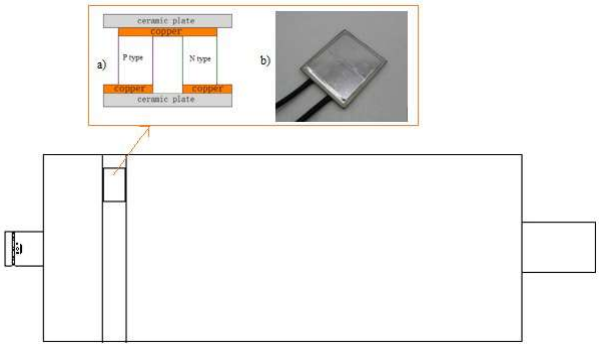


Figure 3. a) TE module b) Used TEG module

Figure 3 depicts the combustion chamber and TEG used for modeling. The combustor has a length of 100 cm and a diameter of 40 cm.

The energy balance for TEG module in given by Eq. (1).

$$E_{in} - E_{out} = 0 \tag{1}$$

The rate of energy in E_{in} is the rate of heat transfer from the combustor wall into the TEG while the hot side heat absorption is the rate of energy out. Thermal resistance, R_{conv}, is given by Eq. (2):

$$R_{con,w} = \frac{1}{h_w} A_{TEG} \tag{2}$$

where h_w is coefficient of convective heat transfer (W m^{-2} K^{-1}) which can be given by Eq (3)

$$h_w = Nu_w \frac{K_w}{Dh} \tag{3}$$

where K_w is the hot water thermal conductivity (W m^{-1} K^{-1}) and Dh represents the hydraulic diameter of the combustor.

The conduction resistance between the combustor surface wall and the internal surface of TEG may be given in terms of wall thickness, t (m), thermal conductivity, K (W m^{-1} K^{-1}), and TEG area.

$$R_{con} = \frac{t}{K * A_{TEG}} \tag{4}$$

The rate of heat flux to the TEG from the combustor wall could be evaluated in terms of hot temperature, T_w, and TEG hot side temperature, T_h as

$$Q_h = \frac{T_w - T_h}{R_{conv,w} + R_{cond,w}} \tag{5}$$

Table 1. The TEG module specifications

Hot side temperature /Th	600
Cold side temperature /Tc	30
Open circuit voltage (V)	13,30
Matched load resistance (Ohms)	2,05
Matched load output (V)	6,65
Matched load output current (A)	3,27
Matched load output power (W)	21,7
Heat flow across the module (W)	273
Heat flow density (W cm-2)	7,1
AC resistance (Ohms)	0,7-1,1

The performance of the TEG model was analyzed using MATLAB Simulink depending on variable temperature values. In this case, TEGs are modeled to be placed on the wall along the y-axis in a selected section of the combustion chamber and their effects on combustion are observed.

In TEG applications, the maximum output from the TEG withdrawal of power is always desired. TEG maximum current max I is when the load voltage VL = 0.

$$V = \alpha \Delta T \tag{6}$$

Here, V TEG open circuit voltage (V), $\propto$ Seebeck constant (V/K) and ΔT is the temperature difference (K). ΔT between the hot and cold surface is the difference ($\Delta T = TH - TC$)

The electrical power (W) from the P TEG system and Q_h TEG is the heat given to the system. A TEG is a temperature-dependent voltage.

$$I = \frac{V^2}{R_{int} + R_l} \tag{7}$$

I current (A), R_{int} internal resistance (Ω), and RL load is the resistance (Ω). The power supplied to the load by the TEG is:

$$P = \frac{V^2}{(R_{\text{int}} + R_L)^2} R_L \qquad (8)$$

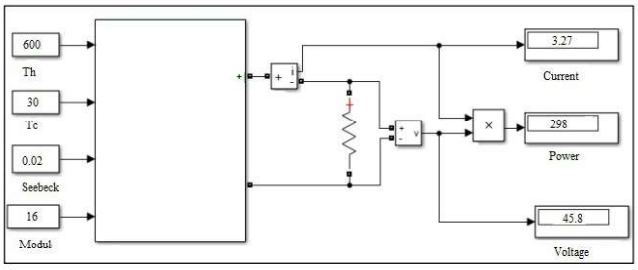


Figure 4. Matlab/Simulink simulation

Figure 4 demonstrates a TEG simulation in Matlab/Simulink. Voltage, current, and power values are calculated using this simulation at various temperatures. In this study, 16 TEGs were connected in series to generate 298 W of power.

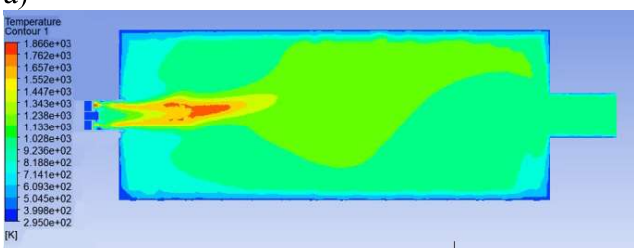
3 RESULTS AND DISCUSSIONS

In this study the temperature distributions were obtained from the modeling results under conventional conditions. TEGs were placed at part of the wall of the combustion chamber where methane was burned, and power analysis was made in this case. The obtained temperature profiles have been inputs for modeling a TEG created using Matlab Simulink.

Figure 5 shows the results of methane combustion under conventional combustion conditions and a combustion system with TEG placed in a region under the same conditions. With adding TEG, the maximum temperature of 1860 K drops to 1826 K.

The effect of the system on the flame changes as the area where the TEG has been placed changes. A region near the flame was chosen for this study, and the effect of TEG on the flame was observed. In addition, due to the deviation in the flame, the wall temperature increased in one region and a uniform distribution could not be obtained. Better results can be obtained by analyzing the TEG system under CDC conditions for a more uniform distribution.

a)



b)

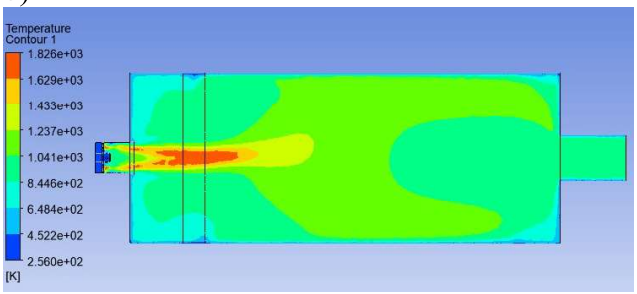


Figure 5. Contours showing temperature fields for (a) conventional combustion condition, (b) TEG placed condition

When the temperatures along the axis are compared, the temperature along the axis reached lower values in the system where TEG was placed.

As seen in Figure 6, when the temperatures along the axis were compared, the temperature along the axis reached lower values in the system where the TEG was placed.

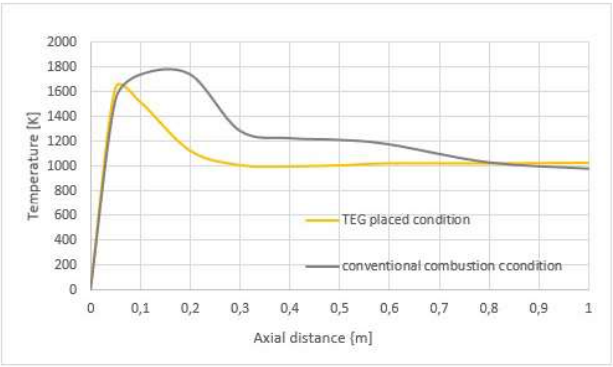
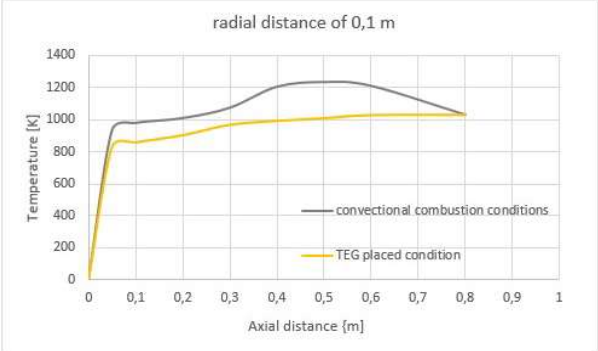


Figure 6. The axial temperature profiles

a)



b)

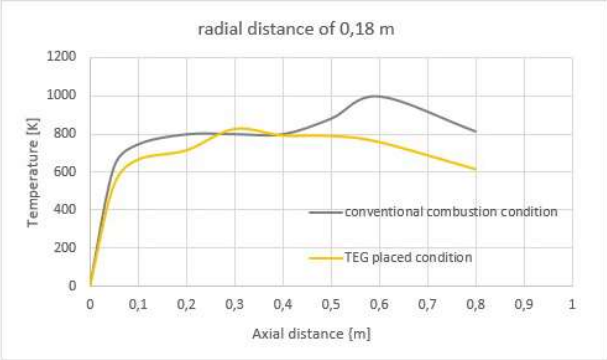


Figure 7 The radial temperature profiles for (a) 0.1 m, (b) 0.18 m

Figure 7 shows the temperatures in the radial and at a distance of 0.1 and 0.18 radially As can be seen from the graphics, the temperature values also decreased in the radial direction in the system where TEG was placed. The wall temperature obtained from here will be the source for the hot side of the TEG.

The power obtained for the TEG modules placed on the wall is calculated as 298 W.

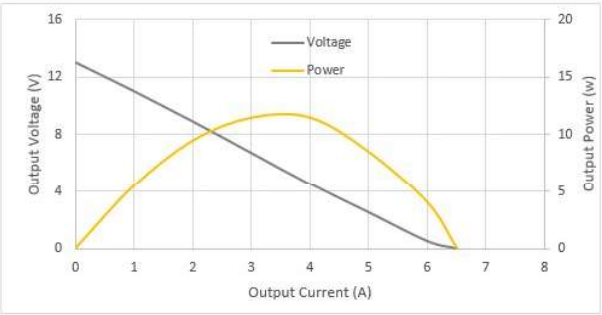


Figure 7 Power and Voltage Output

The relation between power and voltage is shown in Figure 7. In case the number of TEGs are increased, the power can be increased by connecting them in parallel and in series.

4 CONCLUSIONS

In this paper, temperatures and flame characteristics in the combustion chamber and the performance of the TEG model were analyzed using the CFD Analysis program and MATLAB Simulink program respectively. The effect of the use of TEG on flame characteristics was numerically investigated. TEG performance values for different temperatures were also analyzed and interpreted. Flame deviations were observed in the areas where TEG was placed on the wall.

REFERENCES

[1] Van Oijen JA, De Goey LPH, Roekaerts DJEM. *International Combustion Institute Winter School on Combustion*, Lecture Note, 2016.

[2] Fernandez P., Armas O., Thermal analysis of a thermoelectric generator for light-duty diesel engines *Appl.Energy*, 226 (2018), pp. 690-702

[3] Zhao Y, Lu M, Characteristics analysis of an exhaust thermoelectric generator system with heat transfer fluid circulation, *Appl. Energy*, 304 (2021), Article 117896

[4] Zhao Z.,Zuo Z., Performance optimization for a combustion-based micro thermoelectric generator with two-stage thermoelectric module, *Appl Therm Eng*, 198, s. 117464

[5] Hiranandani K.,Aravind B.,Development of a numerical model for performance prediction of an integrated micro combustor-thermoelectric power generator , *Energy,* Volume 192

[6] Karyeyen S. Combustion characteristics of a non-premixed methane flame in a generated burner under distributed combustion conditions: a numerical study. *Fuel* 2018;230:163–71.

CHARACTERISTICS OF THE GAS HYDRATES IGNITION PROCESS

O.S. Gaidukova[1] and P.A. Strizhak[2]

1. Research School of High-Energy Physics, Tomsk Polytechnic University, Tomsk, Russia; email: osy1@tpu.ru
2. School of Energy & Power Engineering, Tomsk Polytechnic University, Tomsk, Russia; email: pavelspa@tpu.ru

Abstract

Gas hydrates are an alternative and environmentally friendly energy source increasingly in the focus of scientific attention. The physicochemical processes behind gas hydrate combustion are studied experimentally with a view to improving the combustion efficiency and reducing gas emissions. Our experiments focused on the impact of furnace temperature on dissociation rates and concentrations of anthropogenic gas emissions. Characteristics of the gas hydrates ignition process

Keywords: Gas hydrate, ignition, ignition delay times, anthropogenic gas emission.

1 INTRODUCTION

Gas hydrates are an innovative clean alternative energy resource to replace conventional fuels. They are crystalline compounds formed by natural gas at low temperature and high pressure [1].

The study of the patterns of gas hydrates ignition and combustion is an important direction in the hydrates study. The processes of gas hydrates ignition and combustion are accompanied by multiple phase transformations, which adds new research interests in the physics and combustion chemistry field. The gas hydrates combustion process differs from conventional solid or liquid fuels in that gas hydrate is exposed multicomponent heterogeneous combustion [2]. A literature analysis has shown that the results of experimental and theoretical studies of the gas hydrates ignition processes characteristics under different heating schemes, limited in applicability, have so far been obtained. The studies results with varying key initial parameters over a wide range are important for the gas hydrate combustion technologies development, as well as for optimizing combustion parameters in order to increase the efficiency of gas hydrate fuel combustion.

The purpose of this work was a gas hydrate ignition process experimental study under the influence of radiative heat flux.

2 EXPERIMENTAL PROCEDURE

The ignition and combustion of methane hydrate, methane-propane hydrate, methane-ethane hydrate, and methane-isopropanol hydrate were studied experimentally and theoretically. Gas hydrate was a powder with a particle (granule) size R_d = 0.25 mm.

The experimental setup for studying the ignition of gas hydrates is schematically represented in Figure 1 [3]. Before the experiment, all the hydrate samples were removed from a Dewar vessel with liquid nitrogen and put into a tank. The tank had a temperature below – 100 °C, which prevented the gas hydrate from dissociating. The mass of the powder and tablets was measured by the gravimetric method on an electronic balance *3*. After measuring their mass, we placed the gas hydrate samples in a fine thin-walled metal mesh *4* and moved it into the center of the muffle furnace *1* with the help of a positioning mechanism *2*. The temperature in the center of the muffle furnace was measured by a chromel-alumel thermocouple. The air temperature in the center of the muffle furnace was ranged from 550 to 1000 °C. The concentration of the emitted gases from the combustion was measured using a Test 1 laboratory gas analyser *5*. The gas composition recording involved the following sequence of steps. After placing the hydrate sample into the muffle furnace, we inserted the gas analyzer probe into the opposite orifice and then sealed the orifice with a thick layer of a heat insulation material. The flue gases from the combustion were carried through the modular probe and a system of filters to the gas analyzing unit. This unit contains a set of sensors. Each of them is meant for measuring the concentration of a certain component of the gas mixture. As the fuel was burning, the PC monitor *7* showed the variation trends of the component concentrations

for the gas mixture with a delay caused by the sensor response time.

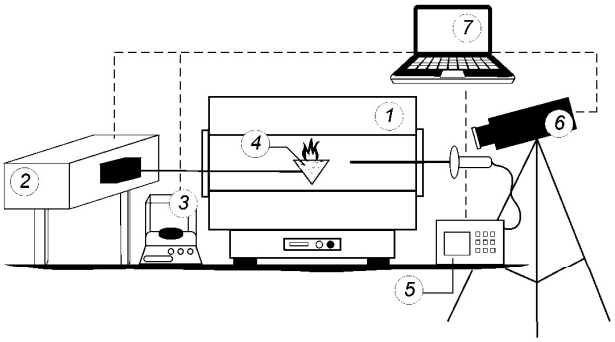


Figure 1. Scheme of the setup for studying the fuel ignition behavior on radiative heating: *1* – muffle furnace; *2* – positioning mechanism; *3* – electronic balance; *4* – metal holder with a fuel sample; *5* – gas analyzer; *6* – high-speed video camera; *7* – laptop.

3 RESULTS AND DISCUSSION

Table 1 presents the double gas hydrate (methane-propane) ignition delay times under radiative heating obtained experimentally and theoretically with varying heating source temperature from 700 to 1000 °C.

Table 1. Double gas hydrate ignition delay times under radiative heating with varying heating source temperature from 700 to 1000 °C (hydrate particle size R_d = 0.25 mm).

Heating temperature, °C	Ignition delay times, s (experimental study)	Ignition delay times, s (theoretical study)
700	0.014	0.0154
800	0.007	0.0069
900	0.003	0.0033
1000	0.001	0.0017

Table 1 shows that the ignition delay times of gas hydrates (methane-propane) go down from 0.014 s to 0.001 s with an increase in the heating source temperature. The ignition delay times obtained experimentally and theoretically differ on average by up to 15%. With a heating source temperature over 900 °C, the ignition delay times are one-third of those at 800 °C. At high temperatures of the heating source (over 900 °C), higher gas hydrate dissociation rate (decomposition into gas and water) sharply accelerates the exothermic reaction, thus reducing the ignition delay times. A decrease in the ignition delay times by several orders of magnitude suppresses the formation of water vapor around the fuel sample. As mentioned earlier, water vapor significantly changes the reaction behavior of some elementary reactions (chemical effect), which leads to a reduction in flame temperature and slows down combustion.

Table 2 presents the experimental data on the autoignition temperature of several types of gas hydrates in the furnace [4]. The lowest temperature corresponds to the methane-propane hydrate, while methane hydrate shows the highest temperature. It is important to factor in the autoignition temperature value when calculating the combustion stability of various gas hydrates.

Table 2. Limited autoignition temperature of gas hydrates in a furnace.

Several types of gas hydrates	Autoignition temperature, °C
Methane gas hydrate	661
Methane-ethane hydrate	611
Methane-isopropanol hydrate	655
Methane-propane hydrate	570

The presence of ethane, propane, and isopropanol in gas hydrates may have a significant impact on the fuel combustion behavior, in particular, on the composition of gases released from the combustion. In addition, the combustion of gas hydrates is notable for the high concentration of water vapors in the flame, which significantly affects the combustion kinetics and elementary chemical reactions. To minimize the harmful emissions while maintaining the energy-related, economic, and technological combustion parameters, it is necessary to examine the influence of inputs (hydrate composition, its combustion method, and temperature conditions) on the concentration of components in flue gases. Fig. 2-5 shows the average and maximum concentrations of CH_4, H_2, CO, and CO_2 released from the combustion of gas hydrates with different component

compositions (heating temperature T_g = 1050 °C).

According to the data obtained (Fig. 2), the combustion of pure methane hydrate was notable for the maximum CH_4 concentrations. The addition of heavy hydrocarbons, such as ethane, propane, and isopropanol, reduced the emissions of unburned CH_4 by 60%.

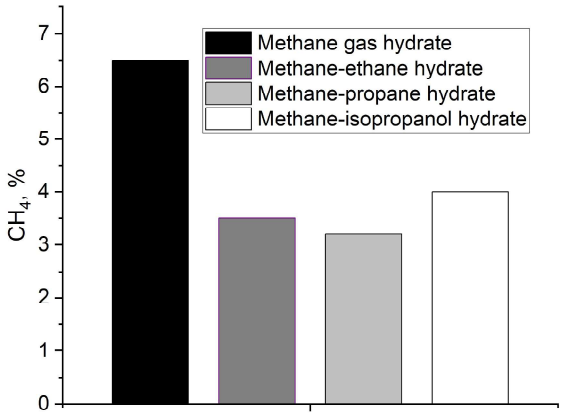


Figure 2. Average concentrations of CH_4 released from the combustion of gas hydrates with different component compositions (T_g = 1050 °C).

The heavy hydrocarbons react with water vapor to form a larger amount of free hydrogen compared to methane steam reforming. As a result, the H_2 concentrations increased by 10–55% for double hydrates (Fig 3). The decrease in the proportion of unburned CH_4 can be attributed to the methane substitution by heavier hydrocarbons and increased reactivity of the blend.

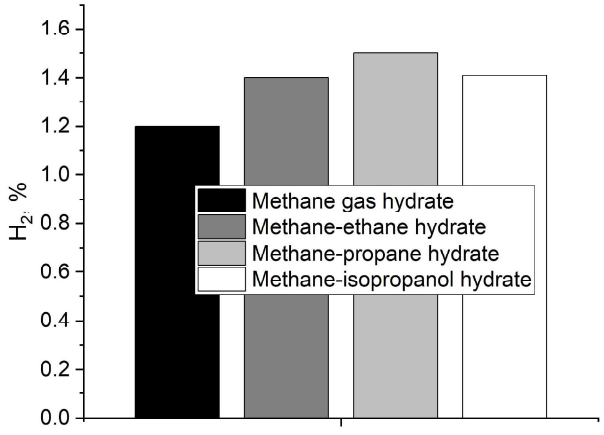


Figure 3. Average concentrations of H_2 released from the combustion of gas hydrates with different component compositions (T_g = 1050 °C).

Methane enrichment with higher hydrocarbon gases was found to reduce CO concentrations (Fig. 4) by 31%. Lower CO emissions for gas hydrates containing higher alkanes must be related to the high-temperature combustion of richer fuel mixtures (carbon content in hydrates increases due to enrichment with ethane, propane, or isopropanol), faster reactions, and ultimately more efficient combustion.

In addition, unlike alkyl radicals (C_2H_5, C_3H_7) formed during the combustion of larger hydrocarbon fuels, methyl radical (CH_3) does not undergo thermal decomposition. It only undergoes oxidation, so chain branching is even slower for methane. However, mixing methane with higher hydrocarbons that promote chain branching or decomposition may significantly affect the methane ignition in the case of premixing.

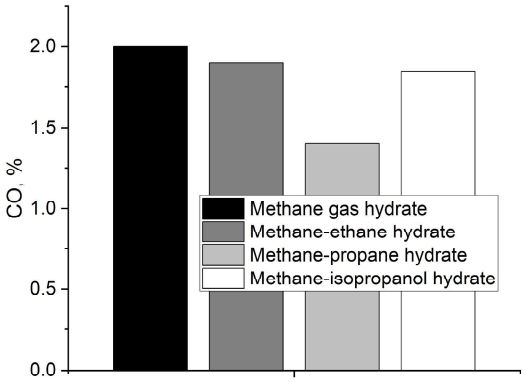


Figure 4. Average concentrations of CO released from the combustion of gas hydrates with different component compositions (T_g = 1050 °C).

The use of ethane, propane, and isobutane was found to increase CO2 emissions (Fig. 5). The methane-isopropanol blend showed the highest concentrations. The values observed for a methane powder and methane-isopropanol mixture differed by 44%. According to isopropane steam reforming, C_3H_8O and water vapor interacted to form carbon dioxide, whereas the resultant of reactions between other hydrocarbons and vapor was carbon monoxide. This can be attributed to higher content of carbon in the blend due to the addition of higher alkanes. Also, higher combustion efficiency of the blends—and hence a reduction in the proportion of unburned methane and carbon

monoxide—had a corresponding effect on the carbon dioxide yield. Increased concentrations of this gas once again confirm the theory that methane hydrate enrichment with higher hydrocarbons increases the degree of the gas burnout and promotes the involvement of a greater amount of carbon in the combustion reactions.

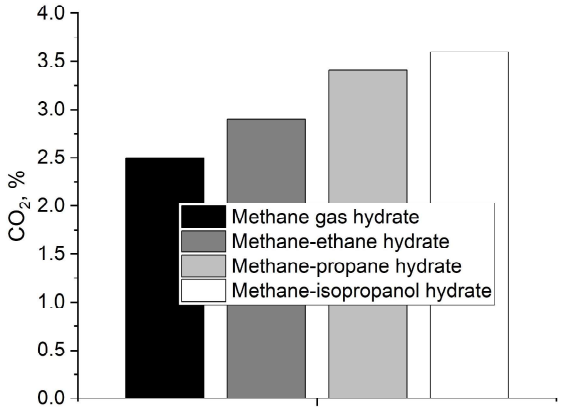


Figure 5. Average concentrations of CO_2 released from the combustion of gas hydrates with different component compositions (T_g = 1050 °C).

4 CONCLUSIONS

The impact of temperature in the furnace on the concentration of gas emissions was studied experimentally and theoretically. The concentrations of the most harmful emissions (CO_2) in flue gases were found to increase with a temperature increase from 750 °C to 1050 °C. A strong upsurge in the flammable gas concentrations (H_2 and CO) was also observed with an increase in the furnace temperature. Effective thermal conditions were found for the environmentally promising combustion of hydrates in power plants, which would minimize the emissions while maintaining the acceptable energy parameters of the process. The component composition of hydrates is instrumental here. In particular, the combustion of methane-ethane hydrate produces the highest NO_x concentrations (at 1050 °C). The maximum CO_2 concentrations were observed from the combustion of methane-isopropanol.

ACKNOWLEDGEMENTS

This research was supported by TPU development program Priority 2030 (Priority-2030-NIP/EB-006-0000-2022).

REFERENCES

[1] Y. Li, N. Wu, C.Q. He, Z. Sun, Z. Zhang and X. Hao. Nucleation probability and memory effect of methane-propane mixed gas hydrate, *Fuel*, Vol. 291, Article number 120103, 2021.

[2] Y.C. Chien, D. Dunn-Rankin. Combustion characteristics of methane hydrate flames. *Energies*, Vol. 12, Article number 1939, 2019.

[3] D.V. Antonov, I.G. Donskoy, O.S. Gaidukova, S.Ya. Misyura, V.S. Morozov, G.S. Nyashina, P.A. Strizhak. Dissociation and combustion of mixed methane-ethane hydrate, *Fuel*, Vol. 325, Article number 124771, 2022.

[4] D. Antonov, O. Gaidukova, G. Nyashina, D. Razumov, P. Strizhak. Prospects of Using Gas Hydrates in Power Plants, *Energies,* Vol. 15 (12), Article number 4188, 2022.

HASTANE BİNALARINDA YANGIN ANINDA KULLANICILARIN TAHLİYESİNİN SİMÜLASYON DESTEKLİ İNCELENMESİ

Furkan Kadı[1], Gökhan Coşkun[2] ve Ekrem Büyükkaya[3]

1. Yangın ve Yangın Güvenliği Yüksek Lisans Öğrencisi, Sakarya Üniversitesi, furkan.kadi1@ogr.sakarya.edu.tr
2. Doç Dr, Makine Mühendisliği Bölümü, Sakarya Üniversitesi, gcoskun@sakarya.edu.tr
3. Prof Dr, Makine Mühendisliği Bölümü, Sakarya Üniversitesi, ebkaya@sakarya.edu.tr

Özet

Bu çalışmada, hastane binalarında yangın anında kullanıcıların tahliyesinin simülasyon destekli olarak incelenmesi konusunda HAD tabanlı yangın simülasyonu Pyrosim ve tahliye simülasyonu Pathfinder programları kullanılarak, yatay tahliye, asistanlı tahliye gibi hastane binalarına özel tahliye olanaklarının irdelenmesi hedeflenecektir. Yangın simülasyonunda ilgili yönetmelik ve standartlarda belirtilen yangın yükleri baz alınarak hesaplama yapılacaktır. Hastane binalarında bulunacak yaşam destek ünitesine bağlı, medikal gazlara muhtaç, hareket kabiliyetleri sınırlı vb. hastaların yangın anında tahliyesi incelenecek, örnek bir hastane mimarisi üzerinden tahliye olanaklarının yeterliliği araştırılacaktır. Yapılacak tahliye simülasyonunda hastane ortamında bulunabilecek çeşitli hareket kabiliyetlerine sahip bina kullanıcılarının durumları göz önünde bulundurulacaktır. Bu bağlamda tahliye simülasyonu programında kullanıcı grupları oluşturularak gerçek duruma en yakın veriler elde edilmesi hedeflenecektir.Yangın simülasyonu yazılımında hazırlanacak örnek yangın durumu tahliye simülasyonu yazılımına aktarılacak ve bu programda mimari üzerinde yerleştirilmiş olan bina kullanıcılarının tahliye süreleri, görüş mesafeleri ve maruz kalınan sıcaklık değerleri irdelenecektir.

Anahtar kelimeler: Tahliye, Yangın, Hastane, Sağlık, Simülasyon, Can güvenliği

1 GİRİŞ

Hastane binaları acil durum tahliye olanakları bakımından, içerisinde bulundurduğu kullanıcıların özel durumları sebebiyle diğer kullanım amaçlı binalara göre daha katı şartlara tabidir. Hastanelerde olası bir yangın durumunda kendi imkânlarıyla çıkışlara ulaşabilecek kişilerin yanı sıra bir veya daha fazla sayıda refakatçi eşliğinde tahliye edilmesi gereken hareket kabiliyeti kısıtlı hastalar, medikal gazlara ve diğer yaşam destek ünitelerine bağlı hastalar gibi kullanıcıların da tahliyeleri düşünülerek tasarım yapılmalıdır.

Yönetmelikler ve standartlar yapıları gereği yönergesel (prescriptive) dökümanlardır. Dünyada ülkemiz de dâhil olmak üzere pek çok ülke yangından korunum sistemleri tasarımında yönetmelik ve standartlara bağlı kalınmasını zorunlu kılar. Ancak, özellikle son yıllarda sayıları artmış olan bazı ülkeler ise yönetmelik ve standart üzerinden tasarımın yanı sıra performans bazlı(performance-based) tasarımı da kullanmaktadır. Performans bazlı tasarım ya da performansa dayalı tasarım olarak adlandırılan bu metot kısaca, genel uygulama yerine, uygulama yapılacak binanın belirli özelliklerini dikkate alarak binalarda yangından korunma ve can güvenliği sistemleri tasarlamak için bilim ve mühendisliğin uygulanmasıdır denilebilir.

Bu çalışmada hastane binaları hakkında öncelikle yerel yönetmelik olan Binaların Yangın Korunması Hakkında Yönetmelik(BYKHY-(09/07/2015)-29411, 2015) hükümleri açıklanacaktır. BYKHY' de konu hakkında fazla detay olmadığından uluslararası standartların hastane binaları ile ilgili maddeleri incelenecektir. Sonrasında ise performansa dayalı tasarım kullanılarak çeşitli senaryolarda hastanede bulunan kullanıcıların yangın durumuna maruziyetleri incelenerek sonuçlar yorumlanacaktır.

Bu çalışmada bir hastane binasında olası bir yangın incelenecek olup, aynı yangın dört farklı senaryo üzerinden irdelenerek, her bir senaryonun can güvenliği açısından artıları ve eksileri ortaya konulmaya çalışılacaktır. Çalışma kapsamında yangın dumanının görüş mesafesi ve dolayısıyla bina kullanıcıların binayı tahliye hızları üzerindeki etkisi de göz önünde bulundurulacaktır.

2 YANGINDA TAHLİYE BİLEŞENLERİ

Türkiye' de bulunan tüm binalar yangında tahliye olanakları bakımından BYKHY gerekliliklerini yasal olarak sağlamak zorundadır. Yine yönetmelikte belirtildiği üzere, yönetmelikte hakkında yeterli hüküm bulunmayan husularda öncelikle Türk standartları ve Avrupa standartları kullanılmalıdır. Yine yeterli bilgi edinilememesi durumunda ise uluslararası geçerliliği kabul edilen standartlar kullanılabilir [1].

Tahliye konusu üç ana başlık altında incelenmelidir. Bunlar çıkışa ulaşım, çıkış ve çıkıştan tahliye olarak özetlenebilir.

2.1 Çıkışa Ulaşım

Çıkışa ulaşım kısmı bir binada her bir katta güvenli yangın hollerine kadar ulaşımı kapsar ve çıkışa kadar en fazla seyahat mesafesi, tek yönde zorunlu seyahat mesafesi, ölü koridor en fazla uzunluğu, çıkışa ulaşım koridoru yapısal özellikleri, çıkışa ulaşım yolu üzerindeki kapıların özellikleri, çıkışların birbirinden minimum uzaklığı gibi kriterleri içerir.

Yağmurlama sistemi bulunmayan hastane binalarında tek yönde en çok seyahat mesafesi 15 m, iki yönde en çok seyahat mesafesi ise 30 m olabilir. Yağmurlama sistemi bulunan hastane binalarında ise tek yönde en çok seyahat mesafesi 25 m, iki yönde en çok seyahat mesafesi ise 45 m olabilir [1]. NFPA 101' e göre ise yeni inşa edilecek hastane binalarında yağmurlama sistemi yapılmasının zorunludur. Bu sebeple yağmurlama sistemi olmayan hastaneler için tahliye mesfesi verilmemiştir. Yağmurlama sistemi bulunan hastane binalarında tek yönde en çok seyahat mesafesi 30 m, iki yönde en çok seyahat mesafesi ise 61 m olabilir [2].

2.2 Çıkış

Tahliye bileşenlerinden olan çıkış bölümü yangın güvenlik holleri, yangın merdivenleri ve kapılardan meydana gelir. Bu başlık altında hol ve merdiven özellikleri, sahanlıklar, yer kaplamaları, basamak boyutları, trabzanlar gibi bileşenlerin özellikleri incelenir.

2.3 Çıkıştan Tahliye

Çıkıştan tahliye, yangın merdiveninden çıktıktan sonra en yakın güvenli yola veya toplanma alanına ulaşana kadarki bölümü ifade eder. Yangın merdiveninden binayı tahliye eden insanların çıkıştan çıktıktan sonra tehlikeye maruz kalmadan ve sıkışmadan güvenli bir yola çıkması önemlidir. Kaçış merdivenlerinin kapasite ve sayı bakımından en az yarısının doğrudan bina dışına açılması gerekir. Kaçış merdiveninin, zemin düzeyindeki dışarı çıkışın görülebildiği ve engellenmediği hol, koridor, fuaye, lobi gibi bir dolaşım alanına inmesi hâlinde, kaçış merdiveninin indiği nokta ile dış açık alan arasındaki uzaklık, kaçış merdiveni bir kattan daha fazla kata hizmet veriyor ise 10 m'yi aşamaz. Yağmurlama sistemi olan yapılarda bu uzaklık en fazla 15 m olabilir. Dışa açık alanın, kaçış merdiveninin indiği noktadan açıkça görülmesi ve güvenlikli bir şekilde doğrudan erişilebilir olması gerekir. İç kaçış merdivenlerinden boşalan kullanıcı yükünü karşılayacak yeterli genişlikte dışa açık kapı bulunması şarttır [1].

3 HASTANE BİNALARI İÇİN ÖZEL ŞARTLAR

Hastane binaları BYKHY' e göre Orta Tehlike 1 sınıfına girmektedir[1]. Bu açıdan bakıldığında hastaneler için öngörülen yangın riski oteller, okullar, ofisler gibi bina sınıflarıyla aynıdır. Hastaneler için farkı yaratan durum ise bina kullanıcıların yukarıda saydığımız diğer binaların kullanıcılarına göre daha savunmasız pozisyonda olmalarıdır.

Hastaneler içerisinde bulundurduğu yaşam destek ünitesine bağlı, medikal gazlara muhtaç, hareket kabiliyetleri sınırlı vb. hastalar nedeniyle yangından korunum sistemleri bakımından kritik binalardır. Bu bakımdan gerek yurt içi standart ve yönetmeliklerde, gerekse de uluslararası standartlarda hastene binaları için birtakım özel şartlar talep edilmektedir.

3.1 BYKHY Gereklilikleri

Bedensel veya zihinsel bir hastalığın veya yetersizliğin tedavisinin veya bakımının yapıldığı veyahut küçük çocuklar, nekahet hâlindeki kişiler veya bakıma muhtaç yaşlıların bakımları için kullanılan ve dört veya daha fazla kişinin yatırılabildiği binaları veya binaların bu amaçla kullanılan bölümleri sağlık hizmeti amaçlı binalar sınıfında değerlendirilir. Hastaneler, huzurevleri, çocuk bakım ve rehabilitasyon merkezleri, dispanserler ve benzeri yerler bu sınıfa girer. Sağlık ocakları, özel klinikler, revirler, teşhis ve tedavi merkezleri ve tıbbi laboratuvarlar da bu sınıftan sayılır [1].

Hastane binalarında en fazla kompartıman alanı 1500 m^2 dir. Ancak binada uygun yangın kontrol sistemleri(otomatik algılama, yağmurlama sistemi, duman tahliye sistemi ve benzeri) yapılmış ise kompartıman alanı 2 katına çıkarılabilir. Buna göre bu sistemlerin bulunduğu hastane binalarında en fazla kompartıman alanı 3000 m^2 olabilir [1].

Sağlık yapıları kapsamında olan, hastanelerde, yaşlılar için dinlenme ve bakım evleri ve bedensel ve zihinsel engelliler için olan bakım evlerinde aşağıda belirtilen şartlara uyulmalıdır.

a) Kullanıcı yükü 15 kişiyi aşan herhangi bir hasta yatak odası veya süit oda için birbirinden uzakta konuşlandırılmış 2 kapı bulunması gerekir.

b) Hastanelerin ve bakımevlerinin 300 m2'den büyük olan yatılan katlarının her biri, en az yarısı büyüklüğünde iki veya daha fazla yangın kompartımanına ayrılır veya korunumlu yatay tahliye alanları teşkil edilir. Yatay tahliye alanlarının hesaplanmasında kullanıcı yükü 2,8 m^2/kişi olarak dikkate alınır. Hastanelerde koridor genişlikleri 2 m'den az olamaz [1].

Yangına en az 60 dakika dayanıklı ve duman geçişi önlenmiş yatay tahliye alanı sağlanan hastane gibi yerlerde kaçış uzaklığı, yatay tahliye alanına götüren koridorun çıkış kapısına kadar olan ölçüdür. Her yatay tahliye alanından en az bir korunumlu kaçış yoluna ulaşılması gerekir [1].

3.2 NFPA101 Gereklilikleri

Diğer birçok bina ve kullanım gruplarından farklı olarak, bir hastane binasında en az istenen acil durum, hastaların toptan taşınması veya tahliyesidir. Bu nedenle "yerinde savunma" stratejisi kullanılmaktadır. Yerinde savunma stratejisi "toplam konsept" yaklaşımı kullanılarak uygulanır. Buna göre hastaneler ve diğer sağlık hizmeti amaçlı binalar, bina sakinlerinin tahliyesini gerektiren bir yangın acil durumu olasılığını en aza indirecek şekilde tasarlanmalı, inşa edilmeli, gerekli bakımları muntazam yapılmalı ve işletilmelidir[2].

Hastaların bir sağlık tesisindeki düşey tahliyesi, verimsiz ve zaman alıcı bir süreçtir. Özellikle kritik bakım alanlarındaki hastalar(yoğun bakım, ameliyathane vb.) yaşam destek ekipmanına bağlıdırlar, bu da hastanın hareketini zorlaştırır ve bazı durumlarda imkânsız hale getirebilir. Bu nedenle, bina kullanıcılarının düşeyde tahliyesini zorunlu hale getirecek bir yangın olasılığını en aza indiren bir yerinde savunma stratejisi uygulanmalıdır. Hastaların tek bir kat seviyesindeki güvenli alanlara yatayda tahliyesini sağlamak ve herhangi bir yangına maruz kalan bina kullanıcılarının sayısında yönetilebilir ve başa çıkılabilir bir sınır sağlamak için bariyerlere ihtiyaç vardır. Düşeyde tahliye olanakları (özellikle merdivenler), hastaların tahiyesiyle doğrudan ilgisi olmayan, ziyaret için orada bulunan insanlar ile hastaların tahliyesinde direkt rol almayan hastane personeli için tahliye olanağı olarak düşünülürken ve hastaların tahliyesi için ise son çare olarak düşünülmelidir.

Yatayda tahliye kavramı kısaca, olası bir yangın durumunda bina kullanıcılarının aynı katta bulunan yangın dayanımlı komşu kompartımana geçerek tahliye edilmesidir denilebilir. Bu sayede düşeyde tahliyenin mümkün olmadığı veya çok zor uygulanabileceği binalarda alternatif bir tahliye metodu olarak vazife görür.

Yatay çıkışlar, duman bariyerleri üzerinde yer alan kapılardan çıkışla karıştırılmamalıdır. Duman bariyerlerindeki kapılar sadece dumana karşı geçici koruma sağlamak için tasarlanmıştır; yatay çıkışlar ise dumandan anında koruma sağlamanın yanı sıra nispeten uzun bir süre yangına karşı koruma sağlar. Böylece yangın kontrol altına alınıncaya kadar bina kullanıcılarının güvende kalması sağlanabilir.

Yatay tahliye olanağı olarak hizmet edecek duvarlar en az 120 dakika yangın dayanımlı olmalıdır[3]. Bu duvarda gerçekleştirilecek tüm tesisat(mekanik veya elektriksel) geçişleri, uygun tipte yangın durdurucu uygulamalarla kapatılarak duvarın yangın dayanımını koruması sağlanmalıdır. Kanal geçişlerinde yangın damperi kullanılmalıdır. Yatay tahliye bölmeleri arasında yer alacak duvar üzerinde bulunacak kapılar en az 90 dakika yangın dayanımlı ve duman sızdırmaz olmalıdır[3]. Kapılarda otomatik kapanma düzeneği bulunmalıdır. Operasyonel nedenlerle, özellikle koridorlar gibi normal zamanlarda da yoğun kullanılan yollar üzerindeki kapılar manyetik tutucular vasıtasıyla açık tutulabilirler. Ancak alarm durumunda, binanın yangın algılama ve ihbar sistemine bağlı bir kontrol modülü vasıtasıyla bu manyetik tutucuların enerjisi kesilerek manyetiklik özelliklerini kaybetmesi ve dolayısıyla kapıların kapanması sağlanmalıdır.

3.3 Hastane Binalarını Diğer Binalardan Ayıran Etmenler

Hastane binalarını diğer binalardan ayıran en önemli faktör içerisinde bulunan kullanıcıların durumudur. Hastane binalarında yoğum bakımda medikal ekipmanlara ve gazlara bağlı hastalar, entübe hastalar, narkoz etkisinde bulunan hastalar, yatağa bağımlı hastalar, hareket kabiliyeti kısıtlı hastalar, tek başına tahliyeye olamayacak olan hastalar, ayakta tedavi edilen hastalar, muayene için gelmiş hastalar, ziyarete gelmiş olan hasta yakınları, hastane sağlık personeli, hastane güvenlik personeli, hastane teknik ve temizlik personeli, idari personel vb. bulunabilir.

Burada saydığımız bina kullanıcılarından ayakta tedavi edilen hastalar, muayene hastaları, ziyaretçiler, hastane personelleri dışında kalanlar olası bir acil durumda tahliye konusunda yardıma muhtaç kişilerden oluşmaktadır ve sayıları bir hayli fazla olabilir. Öte yandan ziyarete gelmiş hasta yakınları da binayı çok iyi tanımamaları sebebiyle yangın durumunda risk grubunda yer alacaktır.

Hastaların çoğu ayakta ya da yaşam destek ekipmanları ile ve güvenli tahliye için dışarıdan yardıma ihtiyaç duyacaktır. Bu nedenle, kısmi olabilecek güvenli tahliyeye, yani yangının çıktığı kattaki hastaları ve yangın katının üstündeki ve altındaki katlardaki hastaları hareket ettirme veya tamamen tahliye, yani tüm bina kullanıcılarının güvenli tahliyesi için özel dikkat gösterilmelidir.

4 PERFORMANSA DAYALI TASARIM

Performansa dayalı tasarım kısaca; kabul edilen yangın güvenliği amaç ve hedeflerine, yangın senaryolarının belirleyici ve/veya olasılıklı analizine, kabul edilen mühendislik araçlarını, metodolojilerini ve performans kriterlerini kullanarak yangın güvenliği amaç ve hedeflerine göre tasarım alternatiflerinin nicel değerlendirmesi olarak tanımlanabilir [4].

Yönetmelik ve standartların kesin bir şekilde çerçevesini oluşturduğu yönergesel yaklaşımda, mühendis ve mimarların tasarım ve imalat özgürlüğü sınırlıdır. Bu yönergesel tasarımın bir dezavantajı olarak söylenebilir. Diğer konuların yanı sıra, bina yükseklikleri, taban alanları, yangından korunma sistemleri, tahliye planları ve alt sistemler (elektrik, mekanik ve sıhhi tesisat), zaman zaman hem tasarım hem de imalatta yaratıcılığı engelleyen yerel ve uluslararası yönetmelik ve standartların kuralları dâhilinde yapılmalıdır. Bina sahipleri, mimarlar, tasarımcılar ve mühendisler, projelerini tamamlamak ve can güvenliği ve yangından korunma hedefini karşılamak için bu düzenlemelere uymalıdır.

Yönergesel tasarımın bir diğer dezavantajı da genellikle yapılacak işin maliyetinin yüksekliğidir. Günümüzde maliyetler, belki de her zamankinden daha çok dikkat edilmesi gereken konuların başında gelmektedir. Performansa dayalı tasarımda bir binanın spesifik özellikleri göz önünde bulundurularak çalışma yapılabilmekte ve bölüm bölüm farklı yangından korunum sistemlerinin gereklilikleri irdelebilmektedir. Bu durumda daha riskli bir bina bölümünde alınması gereken ek tedbirler ile az riskli bir bölümde alınması gereken tedbirler farklılık gösterebilmektedir.

4.1 Performansa Dayalı Tasarım Kriterleri

Tahliye Süresi, SGTS ve GGTS Kavramları

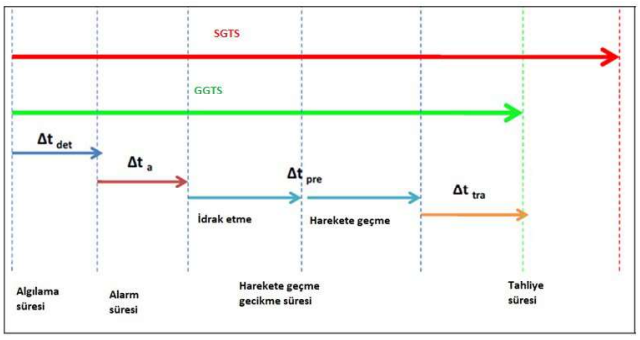
Peformansa dayalı tasarımda en önemli parametrelerden biri tahliye süresidir. Gerek yönetmelik ve standartların koyduğu kurallara uygun yapılan yönergesel tasarımda, gerekse de performansa dayalı tasarımda amaç bina kullanıcılarının olası bir yangın anında güvenli bir şekilde binadan tahliye edilmelerini sağlayabilmektedir. Bunu sağlayabilmek adına bina tahliye olanakları, binada kullanılan yapı malzemeleri, otomatik ve manuel yangın söndürme sistemleri, yangın algılama sistemleri, duman kontrol sistemleri gibi tahliye esnasında çalışacak veya tahliyenin güvenli bir ortamda yapılmasını sağlayacak önlemler alınması gerekir. Bu sayede tüm bina kullanıcılarının tahliyesi için gerekli zaman sağlanmaya çalışılır.

SGTS(available safe escape time / sağlanabilen güvenli tahliye süresi), bir yangın sırasında bir bina kullanıcısı için, tutuşma zamanı ile koşulların, kişinin ehliyetsiz kalacağı tahmin edildiği, yani güvenli bir sığınağa veya güvenli bir yere kaçmak için etkili bir eylemde bulunamayacak hale geldiği zaman arasındaki hesaplanan zaman aralığı olarak tanımlanmaktadır.

GGTS(required safe escape time / gerekli güvenli tahliye süresi) ise bir bina kullanıcısının tutuşma anında bulunduğu yerden güvenli bir

sığınağa veya güvenli bir yere seyahat etmesi için gereken hesaplanmış süre olarak tanımlanır [5].

Bir yangın sırasında SGTS > GGTS durumu tahliyenin güvenli olduğunu gösterir ilk veridir. Bu sebeple yapılan tüm tasarımlarda bu durumun sağlanması hedeflenir.



Şekil 1. SGTS ve GGTS Kavramları

$$T_{GGTS}=\Delta t_{det}+\Delta t_a+(\Delta t_{pre}+\Delta t_{trav}) \quad (1)$$

GGTS süresi hesaplanırken; yangının dedektörler tarafından algılanması, tahliye alarmının devreye girmesi, bina kullanıcılarının yangını fark etmesi ve idrak etmesi ile bir çıkışa ulaşıncaya kadar geçen tahliye süreleri dikkate alınmalıdır. Bu sürelerin toplamı GGTS(gerekli güvenli tahliye süresi) değerini verir.

Ortam Sıcaklığı

Isıya maruziyetin hayati tehlikeye yol açabileceği üç temel yol vardır. Bunlar hipertermi, vücut yüzeyi yanıkları ve solunum sistemi yanıklarıdır.

Yangınlarda ısıya maruz kalmaya bağlı yaşam tehdidinin modellemesinde kullanım için sadece iki kriteri dikkate almak gerekir:

- Cildin ikinci derece yanma eşiği
- Hiperterminin zihinsel bozulmaya neden olabilecek seviyede olduğu ve bu nedenle hayatta kalmayı tehdit ettiği durumlara maruz kalma [11].

Ortamın ısınması sonucu vücut sıcaklığı da zamanla artış gösterecektir. Normal vücut sıcaklığı kabul edilen 37 ºC' nin 39 ºC' ye kadar olan artışı normal kabul edilebilir. Zira yoğun spor yapılan bir anda da vücut sıcaklığı bu değerlere ulaşılabilmektedir. Ancak bu değer 40 ºC' yi aşarsa bilinçte bulanıklaşma başlayabilmektedir. 42,5 ºC üzerindeki değerler ise hızlı bir tedavi uygulanmazsa ölümcül olabilmektedir. Ciltte 0,1mm derinlikte 44,8 ºC sıcaklık hissedilmesi durumunda yanıklar oluşmaya başlayacaktır [4].

Cildin radyant ısıya maruziyeti için dayanıklılık sınırı yaklaşık 2,5 kW · m^{-2} 'dir. Bu olay ısı akışı seviyesinin altında, dayanıklılığı önemli ölçüde etkilemeden maruz kalma 30 dakika veya daha uzun süre tolere edilebilir [6].

Bu seviye ve üzerindeki radyant ısı, ciltte ağrıya ve ardından birkaç saniye içinde yanmalara neden olur, ancak daha düşük akılar 5 dakikadan fazla tolere edilebilir. İnsanların kaçmak için sıcak bir duman katmanının altından geçmesinin gerektiği durumlarda, limit değer yaklaşık olarak 200 ºC kabul edilir [7].

Görüş Mesafesi

Genel olarak, üç faktör görüş mesafesi ile yakından ilgilidir: çevresel koşullar, görülecek nesnenin koşulları ve kişinin görme yeteneği [4].

Kişinin görme yeteneği; kişinin yaşı, görme bozukluğu veya görme engeli olup olmamasına göre değişiklik gösterir. Özellikle hastane gibi her görme yeteneğinde insan bulunabilecek binalarda, yönlendirme işaretlerinin mümkün olduğunca görülebilir olması sağlanmalıdır. Bu faktör bina tasarımcıları ve işletmecilerinin kontrol edebileceği bir faktör değildir. Dolayısıyla ancak diğer iki faktör ile desteklenerek güvenlik altına alınması sağlanabilir.

Yangın sonrası duman oluşumu ve buna bağlı olarak görülebiliriğin azalması, binada bulunan kişilerin tahliye esnasındaki yürüme hızlarını dumanın yoğunluğuna ve tahriş ediciliğine bağlı olarak etkiler. Çeşitli standartlarda ve teknik dokümanlarda farklılık göstermekle birlikte, bir yangın durumunda görüş mesafesinin en az 5 ila10 m olacak şekilde kalması hedeflenir [8].

Isı Salınım Oranı

Bir yangını nicel olarak tanımlayan temel özelliği ısı salınım oranıdır. Isı salınım oranı (ISO; heat release rate) performansa dayalı tasarımda, tasarımın başlangıç değişkenlerinden biridir.

Prensip olarak, efektif yanma ısısı teori veya test ile belirlenebilir. Uygulamada ise, efektif yanma ısısı sabit değilse, deneysel teknikler normalde doğrudan ISO'nun ölçülmesini içerir. Bu bağlamda çeşitli test metotları kullanılmaktadır.

Bunlar tam ölçekli test, orta ölçekli test ve tezgâh ölçekli testtir. Gerçeğe en yakın sonuçların elde edilebileceği test tipi ise tam ölçekli testlerdir.

Hastane binaları için, gerek içerisinde bulunan birbirinden farklı kullanım amaçlı alanlar, gerekse de barındırdığı faklı yanıcılık sınıfına sahip malzemeler sebebiyle dünyaca kabul görmüş tek bir ısı yayılım değeri mevcut değildir. Bunun yerine yangının başladığı bölümün yangın yükü (hasta yatak odası, elektrik odası vb.) ya da yanacak malzemenin (elektrik panosu, hasta yatağı vb.) yangın yükü baz alınarak hesaplamalar yapılmaktadır.

5 MATERYAL VE METOT

Bu çalışmada yangın HAD tabanlı Pyrosim programıyla simüle edilecek, tahliyede ise Pathfinder programı kullanılacaktır. Bu iki programın entegrasyonuyla hem tahliye süreleri görülebilecek hem de yangının sonucu görünürlük, ortam sıcaklığı gibi veriler elde edilebilecektir.

Acil durumlarda bina sakinlerinin tepkilerini yönlendiren değişkenler karmaşıktır, ancak her bireyin kendine özgü bir deneyimi olmasına rağmen, bina kullanıcılarından oluşan gruplar düşünüldüğünde, bir dizi ortak durum ve gelişen senaryolar belirlenebilir. Davranış aşamaları için nicel veriler, özellikle uyarı ve kaçışa başlama öncesi süreler, yangın olayları sırasında yangın güvenliği yönetimi ve bina kullanıcısının davranışının gözlemlenmesiyle ve tasarım davranış senaryolarının ana kategorileri için gözlemlenen tahliyelerle elde edilmiştir. Bunlar daha sonra, kaçış ve tahliye sürelerinin tahmini için basit ama sağlam bir yöntem sağlamak için seyahat süresi hesaplamalarıyla birleştirilir [8].

Davranışsal senaryoların her biri için, güvenlik yönetimi stratejilerine ve mevcut uyarı sistemine bağlı olarak alarm ve ön seyahat süreleri için varsayılan süreler türetilebilir; bu değerlendirmede kullanıcı farkındalığı, kullanıcı aşinalığı, kullanıcı yoğunluğu, binanın mimari olarak karmaşıklığı gibi parametreler göz önünde bulundurulmuş ve buna göre tıbbi bakım uygulanan binalar D sınıfı bina olarak değerlendirilmiştir [8].

Binanın yangın algılama ve ihbar sistemi seviyesi, bina karmaşıklık oranı, bina yangın güvenliği tedbirlerinin kalitesi(eğitilmiş personel sayısı, yeterli acil tahliye olanaklarına sahip, uygun otomatik algılama ve ihbar sistemine sahip vb.) gibi etmenlere bağlı olarak bir tahliye öncesi bekleme süresi belirlemektedir. Bu çalışmada tahliye öncesi bekleme süresi 15 saniye olarak alınmıştır [8].

Modellenecek olan yangının bir hasta yatak odasında başladığı varsayılacaktır. Yangın yükü ile ilgili değerler buna göre belirlenmiştir. Buna göre meydana gelecek olan yangının yangın yükü yoğunluğu 230 MJ/m^2 olarak alınacaktır. Bir yatak odasının alanı yaklaşık 10 m^2 olduğundan yangın yükü yoğunluğu 2300 kW olarak alınacaktır [9].

Yangın büyüme hızı BS PD 7974-1’ e göre hızlı olarak seçilmiştir. Bu durumda hız sabiti 0,047 $kW.s^{-2}$ olmaktadır. Buna göre, yangının 1055 kW a ulaşması 150 saniye sürrecektir. Yapılan hesaplamayla senaryoya konu yangının pik noktası olan 2300 kW’ a ulaşmasının 221 saniye süreceği tespit edilmiştir [11]. Yangın simülasyonu yazılımında yangın büyüme senayosu bu şekilde girilmiştir.

Simüle edilecek yangında yanan malzeme poliüretan_GM27 olarak seçilmiştir. Bunun sebebi bu malzemenin karbon monoksit salınımının yüksek olmasıdır [4].

Yapılan bu çalışmada; bulunan yapısal ve yapısal olmayan elemanlar ile bilgisayar performansı ve optimum sonuca ulaşma isteği göz önünde bulundurularak ağ boyutları 0,25x0,25x0,25 m olarak seçilmiştir. Buna göre kullanılan toplam mesh sayısı 589.760 adet olmuştur.

Bina yağmurlama(sprinkler) tesisatı Orta tehlike 1 sınıfına göre tasarlanacaktır. Kullanılacak sprinkler K faktörü metrik 80, aktivasyon sıcaklığı 68 ºC olacaktır. Sprinklerler hızlı tepkili olarak seçilmiştir ve buna göre reponse time index değerleri 50 olarak girilmiştir. Sprinkler başına atılacak debi 5 L/dk, sprinkler başına tasarım debisi ise 0,5 bar olacaktır. [10]. Bina duman egzoz sisteminde kullanılacak fan kapasitesi 18000 m3/h olarak alınmıştır.

Yangın simülasyonun HAD tabanlı Pyrosim yazılımı, tahliye simülasyonunda ise Pathfinder yazılımı kullanılacaktır. Tahliyeler yazılımdaki SFPE modunda yapılmıştır.

Toplam 4 farklı senaryo iredelenecektir;

Birinci senaryoda hem sprinkler tesisatı hem de duman egzoz sistemi bulunan bir hastane binası yangını modellenecek ve tahliye incelenecektir.

İkinci senaryoda sprinkler tesisatı bulunmayan, ancak duman egzoz sistemi bulunan bir hastane binası yangını modellenecek ve tahliye incelenecektir.

Üçüncü senaryoda sprinkler tesisatı bulunan, ancak duman egzoz sistemi bulunmayan bir hastane binası yangını modellenecek ve tahliye incelenecektir.

Dördüncü senaryoda hem sprinkler tesisatı hem de duman egzoz sistemi bulunmayan bir hastane binası yangını modellenecek ve tahliye incelenecektir.

6 SONUÇLAR VE ÖNERİLER

6.1 Tahliye Sürelerinin Kıyaslanması

Acil durum tahliye süreleri binanın kullanım amacı ve bina kullanıcıların profillerine göre farklılıklar göstermektedir. Hastane binası gibi, içerisinde tahliye için desteğe muhtaç veya medikal cihazlara ve medikal gazlara bağımlı kişilerin bulunabileceği yerlerde tahliye sürelerinin çok kısa olması mümkün olmayacaktır. Bu bakımdan yönetmelik ve standartlarda tahliye mesafeleri diğer binalara nazaran daha kısa tutulmuş ve yatayda tahliye gibi alternatifler üretilmiştir.

Tablo 1. Tahliye Sürelerinin Karşılaştırılması

Senaryo no	Tahliye süresi (sn)
1	626
2	628
3	638
4	646

Denklem 1 bu noktada uygulanabilir, örnek olarak senaryo 1 değerleri göz önünde bulundurulacak olursa;

Yangının başladığı noktaya en yakın duman dedektörü 18. Saniyede algılama yapmıştır. En yakın ikinci duman dedektörün algılama süresi ise 28 saniye olmuştur. İkinci dedektör algılama yaptığında bina alarm sistemi devreye girecektir.

T_{GGTS} = 18 + 10 + (15 + 583)= 626 saniye olmaktadır.

Bu durumda SGTS>GGTS şartının sağlanabilmesi için SGTS en az 627 saniye olmalıdır. Yatay tahliyede, yangın dayanımlı bariyerin diğer tarafına geçildiğinde 2 saat yangın dayanımlı bölmede bulunacağından SGTS süresi 7200 saniye olacaktır.

Görülebileceği üzere bina kullanıcılarının toplam tahliye süresi senaryo bazında majör değişiklikler göstermemiştir. Bu da yatay tahliye imkânının sağladığı bir veri olarak değerlendirilebilir.

6.2 Görüş Mesafelerinin Kıyaslanması

Hastane binalarında, kat koridorlarında tavan yükseklikleri genellikle çok fazla olmadığından, olası bir yangında dumanın görüş mesafesine ve dolayısıyla da tahliye hızına etkisini minimuma indirgemek adına çeşitli sistemler teçhiz edilmesi istenmektedir. Bunlara örnek olarak duman egzoz sitemi ve sprinkler sistemini verebiliriz.



Şekil 2. Senaryo 1'de 240.saniyede göz hizasında koridordaki duman yoğunluğu

Görüş mesafesi değeri ortamda bulunan yangın dumanı yoğunluğuna göre değişiklik gösterecektir. Görüş mesafesi değerlendirmesi zeminden 1,8m yükseklikte yapılmıştır.

Tablo 2. Görüş Mesafelerinin Karşılaştırılması

Senaryo no	Kişi no	Zaman(sn)	Görüş mesafesi (m)
1	48	668	0,080
2	48	668	0,078
3	7	662	0,072
4	48	670	0,072

Tablo 2 her bir senaryoda görüş mesafesinin en düşük olduğu anları ve en düşük görüş mesafesine sahip bina kullanıcısını göstermektedir. Tüm senaryolarda 240. saniyeden itibaren görüş mesafesi 1 metrenin altına düşmeye başlamaktadır. Bu durumun tahliye açısından zorluk yaratacağı açıktır.

Burada sıcak duman tavanda birikip daha sonrasında zemine doğru çökmeye başlayacağından ayaktaki insanlar eğilerek çıkışa doğru ulaşmaya çalışabilecektir.



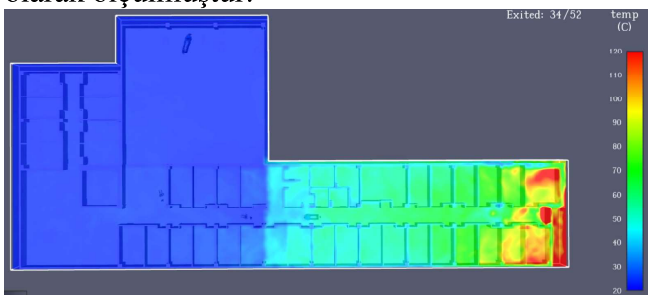
Şekil 3. Senaryo 4'te 221.saniyede duman yoğunluğu

Hedeflenen değer olan 5 metre görüş mesafesi değerinin altına çok hızlı bir şekilde inilmektedir. Her ne kadar simülasyon sonuçlarında tahliye süreleri uygun görünse de duman yoğunluğunun sebep olduğu görüş mesafesi değerlerinin çok çok düşük olması insanların tahliyesini olumsuz yönde etkileyebilecektir.

6.3 Ortam Sıcaklıklarının Kıyaslanması

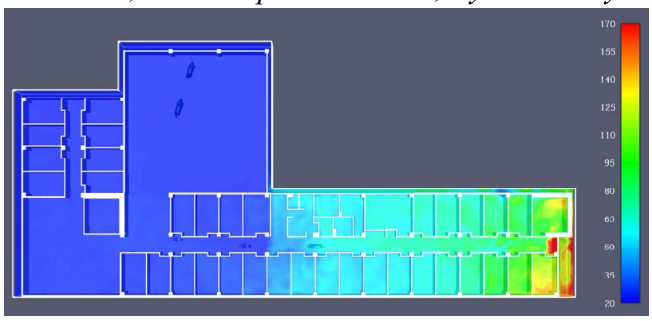
Her bir senaryo için yangının başladığı koridorda sıcaklık seviyeleri ölçülmüştür. İnsanların tahliyesi için kabul edilmiş olan üst eşik değer olan 200 ºC hiçbir senaryoda aşılmamıştır. Bu bakımdan tahliyeyi etkileyeceği öngörülen teorik sıcaklık değerinin altında kalınmıştır.

Duman egzoz sistemi ve sprinkler tesisatı bulunan ilk senaryoda en yüksek sıcaklık 120 ºC olarak ölçülmüştür.



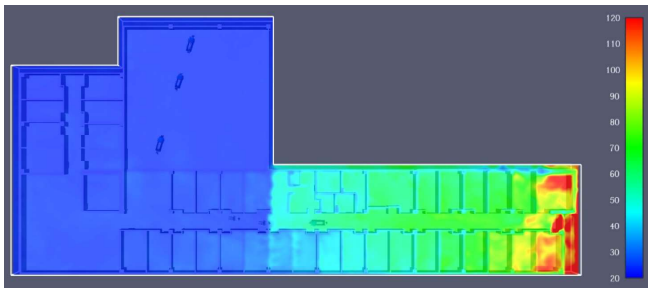
Şekil 4. Senaryo 1'de 500.saniyede koridorda oluşan sıcaklık değerleri

Duman egzoz sistemi bulunan ve sprinkler tesisatı bulunmayan ikinci senaryoda en yüksek sıcaklık 170 ºC olarak ölçülmüştür.



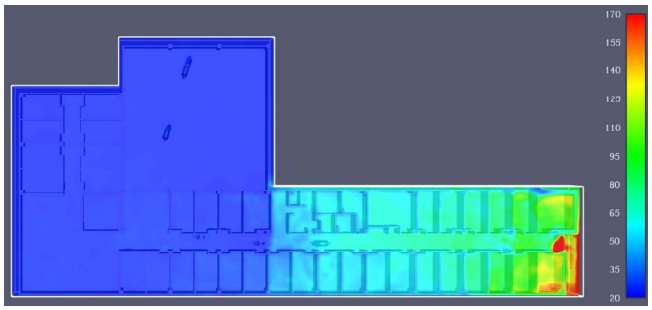
Şekil 5: Senayo2'de 500.saniyede koridorda oluşan sıcaklık değerleri

Duman egzoz sistemi bulunmayan ve sprinkler tesisatı bulunan üçüncü senaryoda en yüksek sıcaklık 120 ºC olarak ölçülmüştür.



Şekil 6: Senayo3'te 500.saniyede koridorda oluşan sıcaklık değerleri

Duman egzoz sistemi ve sprinkler tesisatı bulunmayan dördüncü senaryoda en yüksek sıcaklık 170 ºC olarak ölçülmüştür.



Şekil 7: Senayo4'te 500.saniyede koridorda oluşan sıcaklık değerleri

Dört senaryodan alınan verilere bakıldığında, sprinkler tesisatı bulunmayan senaryo 2 ve senayro 4' te sıcaklık 170 ºC olurken; sprinkler tesisatı bulunan senaryo 1 ve senaryo 3' te ise 120 ºC olmuştur. Bu durum sprinkler tesisatının ortam sıcaklığı üzerindeki etkisini ve güvenli tahliyeye sıcaklığı belirli bir değerin altında tutarak sağladığı katkıyı ortaya koymaktadır.

Sprinkler tesisatı bulunan iki senaryoda, yangının çıktığı noktaya en yakın olan sprinkler 20. saniyede aktive olmuştur.

Tahliye simülasyonu yazılımından alınan veriler doğrultusunda binadaki kişilerin maruz kaldığı

sıcaklık değerleri aşağıdaki tabloda özetlenmiştir.

Tablo 3. Maruz Kalınan Sıcaklıkların Karşılaştırılması

Senaryo no	Kişi no	Zaman(sn)	Sıcaklık (^{0}C)
1	60	451	46,7
2	58	490	52
3	58	419	50,2
4	57	387	57

Tablo 3' e göre en yüksek sıcaklıklara maruz kalan kişi senaryo 4' te 57 numaralı bina kullanıcısı olmuştur. Bu kişi hastabakıcılardan biridir ve pek çok kez yangın mahaline geri dönerek asiste edilmesi gereken hastaların tahliyesini sağlamıştır.

Yukarıdaki değerler 44,8 ºC' nin üzerinde olduğundan 57 nolu bina kullanıcısının vücut yanıklarına maruz kalması kuvvetle muhtemeldir.

6.4 Öneriler

Elde edilen sonuçlar ışığında yatay tahliye seçeneğinin; tahliye açısından dezavantajlı olan, yardıma muhtaç kişilerin bulunma ihtimali yüksek olan bir hastane binasında ne kadar avantaj sağladığı, tüm senaryolarda benzer tahliye sürelerinin elde edilmesiyle ortaya çıkmıştır. Ülkemizde güncel yönetmelik ve standartlarda yatay tahliye olanağı bulunmayan bina tipleri için de kullanılabilmesi uygun olacaktır. Bu konu yeni yönetmelik ve standartlar hazırlanırken göz önünde bulundurulmalıdır ve kullanımının yolu açılmalıdır. Bu sayede tahliye mesafeleri ve süreleri bağlamında tasarruf sağlanabilecek ve can güvenliği seviyesi, mevcut durumdan daha yüksek hale getirilebilecektir.

Uygulanan tüm senaryolarda görüş mesafeleri hedeflenen değerin altında kalmıştır. Yoğun dumanın görüş mesafesini azaltmasının bir sonucu da yönlendirme işaretlerinin görülmesinin zorlaşması olacaktır. Zemin seviyesinde ek yönlendirme işaretleri yerleştirilerek bu risk azaltılabilir.

Yangın sırasında ortam sıcaklığının mümkün olduğunca düşük tutulması ve dolayısıyla bina kullanıcılarının bu sıcaklıktan etkilenme oranlarının minimuma indirilebilmesi için sprinkler(yağmurlama) sistemi çok önemli bir görevi yerine getirmektedir. Sprinkler tesisatı mal ve bina güvenliğine katkısının yanı sıra can güvenliğine de büyük katkılar sunmaktadır. Yönetmelik ve standartların zorunlu kıldığı bina tiplerinde yasal zorunluluk olarak sprinkler sistemleri kurulmaktadır. Bunlar dışında kalan bina tipleri için sprinkler tesisatı kurulması, genellikle ilk yatırım maliyet açısından yatırımcıya yük olarak görülmektedir. Bu düşünce yatırım maliyeti açısından bakıldığında doğru gibi görünse de can güvenliği açısından bakıldığında yanlış olarak değerlendirilebilir.

Binada yangından korunum sistemlerinin bulunması elbette önemlidir. Ancak belki de daha önemli olan nokta ise bu sistemlerin işletilmesidir. Ülkemizde ne yazık ki yangından korunum sistemlerinin periyodik test ve bakımları büyük oranda ihmal edilmektedir. Yangından korunum sistemleri işletme ömürleri boyunca belki hiç çalışmayacak, belki sadece bir kez çalışacaktır. Önemli olan, bu sistemlere ihtiyaç duyacağımız o tek seferde hepsinin çalışmaya hazır ve tasarımına uygun şekilde görev yapabilecek durumda olmasını sağlamaktır. Bunu sağlamanın yolu ise tasarımın doğru bir şekilde yapılmasının yanı sıra periyodik test ve bakımlarının doğru ve zamanında yapılmasıdır. Yangın pompaları, sprinkler tesisatı, yangın dolabı tesisatı, itfaiye su alma ağzı tesisatı ve çevre hidrant tesisatı gibi sistemlerin bakımları için günümüzde en kapsamlı ve detaylı içerikler NFPA 25 bakım formlarında bulunmaktadır. Bu formlar kullanılarak yapılan bakım ve testler sayesinde sistemler her an çalışmaya hazır durumda tutulabilir. Yangın algılama ve ihbar sistemi bakımları için ise TS EN 54 prosedürleri takip edilmelidir.

Performansa dayalı tasarımın kullanılmasıyla yönergesel tasarımın müsaade ettiği kısıtlı tasarımlar ve esnek olmayan seçenekler dışında farklı alternatifler ortaya çıkarılarak, hem can ve mal güvenliği artırılıp hem de bina tasarım maliyetleri düşürülebilmektedir. Bina tasarım maliyetleri mimari, inşai, mekanik ve elektriksel olarak farklı kategorilerde ele alınması uygun olacaktır. Buna göre yatay tahliye olanağı kullanılarak mimari ve inşai açıdan gerekli olan ekstra çıkış kapısı ve merdiven sayısı azaltılabilmektedir. Mekanik sistemler açısından bakıldığında, kullanılacak sprinkler tesisatı ve duman egzoz sistemi kapasiteleri performansa

dayalı tasarım metoduyla düşürülebilmektedir. Elektriksel olarak ise yangın algılama ve ihbar sistemleri tasarımında avantajlar elde edilebilmektedir. Bir bütün olarak bakıldığında performansa dayalı tasarım, tasarımcıya daha özgür düşünebilme ve yaratıcı fikirleri ortaya koyabilme imkânı tanır. Bu da tasarımcıya bir yandan mesleki tatmin sağlarken, diğer yandan yangından korunum sistemlerinin günbegün olumlu yönde gelişmesi ve yeni teknolojilerin ortaya çıkması hususunda katkı vermektedir.

REFERANSLAR

[1] Binaların Yangından Korunması Hakkında Yönetmelik -(09/07/2015)-29411, 2015.

[2] NFPA 101: Life Safety Code, 2018 Edition

[3] NFPA 5000: Building and Construction Safety Code, 2018 Edition

[4] SFPE Handbook of Fire Protection Engineering-5th Edition-Morgan J_2015-2016.

[5] ISO/TS 29761:2015 Fire safety engineering — Selection of design occupant behavioural scenarios

[6] ISO 13571:2012 Life-threatening components of fire — Guidelines for the estimation of time to compromised tenability in fires

[7] BS 7899-2:1999 Assessment of hazard to life and health from fire - Part 2: Guidance on methods for the quantification of hazards to life and health and estimation of time to incapacitation and death in fires

[8] BS PD 7974-6:2019 Application of fire safety engineering principles to the design of buildings – Part 6: Human factors. Life safety strategies. Occupant evacuation, behaviour and condition (Sub-system 6)

[9] BS EN 1991-1-2:2002 Eurocode 1: Actions on structures Part 1-2: General actions – Actions on structures exposed to fire

[10] TS EN 12845:2015+A1:2019 Sabit yangın söndürme sistemleri - Otomatik sprinkler sistemleri – Tasarım, kurulum ve bakım

[11] BS PD 7974-1:2019 Part 1: Initiation and development of fire within the enclosure of origin (Sub-system 1)

EVALUATION OF BINARY NANOPARTICLES TO OXYGENATED FUEL WITH ETHANOL AND N- BUTANOL ON COMBUSTION BEHAVIOR

M.R. Atelge[1], Esenay Arslan[2], Nafiz Kahraman[3], Sebahattin Ünalan[4*]

1. Siirt University, Department of Mechanical Engineering, Siirt, 56100, Turkey
2. Kayseri University, Department of Electricity and Energy, Kayseri, 38010, Turkey
3. Erciyes University, Department of Aerospace Engineering, Kayseri, 38010, Turkey
4. Erciyes University, Department of Mechanical Engineering, Kayseri, 38010, Turkey

Abstract

This study revealed that oxygenated fuel with ethanol and n- butanol blend reduced the calorific value of the tested fuels, as a result, BTE decreased by 5.6% according to baseline fuel under the full loading conditions. However, this reduction is mostly covered with in-cylinder pressure increment. Linearly, the reduction should have been higher, however, the pressure inside the combustion chamber increased by 0.7% compared to conventional diesel. Moreover, the drawback was eliminated by using a binary nano additive inside the liquid fuel. The maximum pressure increased by 1.9, and 2.9% for D100TiO75Gp50, and D80n-B10E10TiO75Gp50, respectively, compared to D100. The increment leads to thermal efficiency improvement for the same fuels. The BTE was noticed to be 32.2, and 31.5% for D100TiO75Gp50, and D80n-B10E10TiO75Gp50, respectively at the full load while the BTE of conventional diesel was recorded as 30.5%. For future evaluation, the second law efficiency should be investigated for all tested fuels. Moreover, the emissions of mentioned fuels need to study further.

Keywords: Nano additive, Graphene Nanoplates; TiO2 Alcohols, Combustion

1 INTRODUCTION

Finding methods that could create a viable pathway for the decarbonization of internal combustion engines has recently attracted attention. The use of fossil fuels is highly dependent on the transportation industry. Yet, in recent decades, scientists have extensively examined forms of sustainable energy, such as biodiesel for internal combustion engines. Alcohols rank as one of the best choices for renewable fuel sources in internal combustion engines. In the literature, renewable alcohol fuels like methanol, ethanol, and n-butanol have drawn more attention as alternate pure fuels and fuel mixes for diesel engines. The decarbonization of the automotive market and the energy security of nations are both improved when alcohols like ethanol and butanol are combined with diesel. In addition, the high heat of vaporization suggests a drop in the temperature of the intake air and fuel and an increase in volumetric efficiency. High laminar flame speeds also benefit from a reduction in combustion time and an increase in brake thermal efficiency.

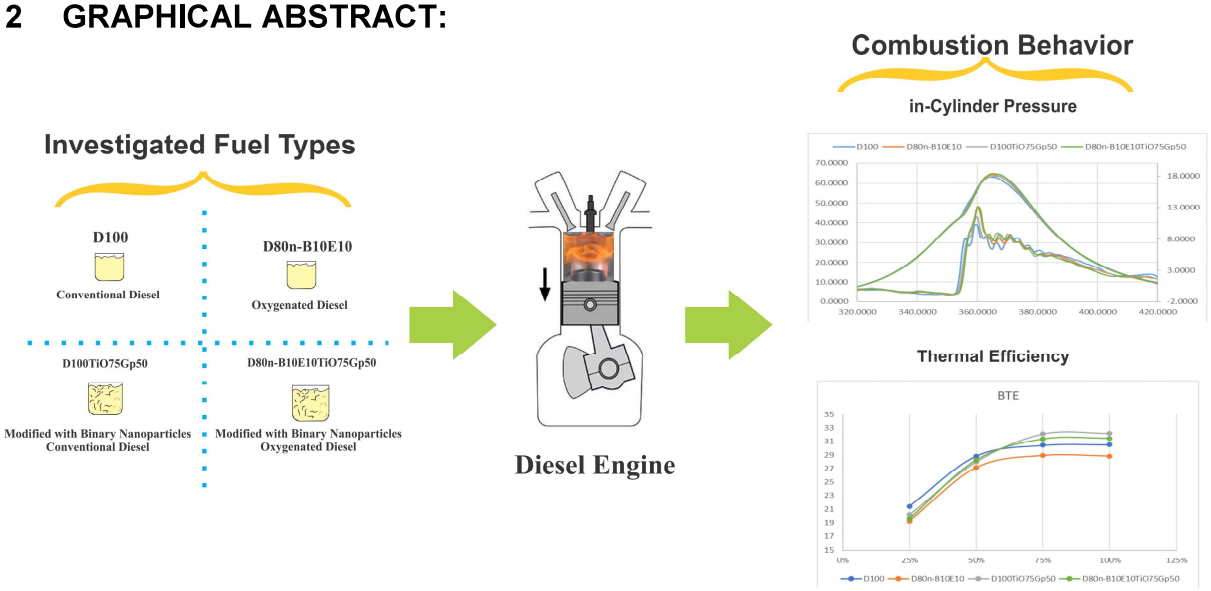
Modifying liquid fuels with nanomaterials has been described in the literature as the most effective practice in fuel research. Scientists are currently looking at nano additive fuels since advancements in nanotechnology make it easier to obtain nanoparticles. According to research, the fuel's physicochemical qualities have been improved by the nanoparticle additives. An innovative and promising fuel additive that improves engine performance is the use of nanoparticles in diesel fuels. The additional nanoparticles boost heat conductivity, increase microexplosions that result in microscopic fuel drops, and function as a catalyst in the combustion process. As a result, the nano additive enhances the efficiency of the diesel engine. Diesel or biodiesel has been used to study a variety of nanoparticles, including metal, metal oxide, and carbon nanotubes. Due to the thermophysical features of nanofluids, a high surface-to-volume ratio, catalytic activity during ignition, and a rise in heat and mass transport qualities, the addition of nanoparticles enhance the heat release performance of fuels.

The literature research mentioned above indicates that CI engines are the most popular engines because of how fuel-efficient they are. Both alcohol mixtures and the use of nanoparticles have undergone in-depth research as they help to enhance emissions and fuel efficiency. However, not enough details, including various nano additive materials,

particularly both metallic and non-metallic nanomaterials, have been released in oxygenated diesel, a blend of diesel and alcohols. Thus, the purpose of this study is to provide pertinent knowledge on ternary mixes of diesel (80% v/v), ethanol (10% v/v), and n-butanol (10% v/v). To close this gap, improved fuels containing these ternary blends were also tried. In order to modify diesel, 50 ppm graphene nanoplates and 75 ppm TiO2 with and without alcohols were examined. Extensive investigations were carried out to ascertain engine performances in the CI engine, including brake thermal efficiency (BTE), brake specific fuel consumption (BSFC), and heat release rate (HRR).

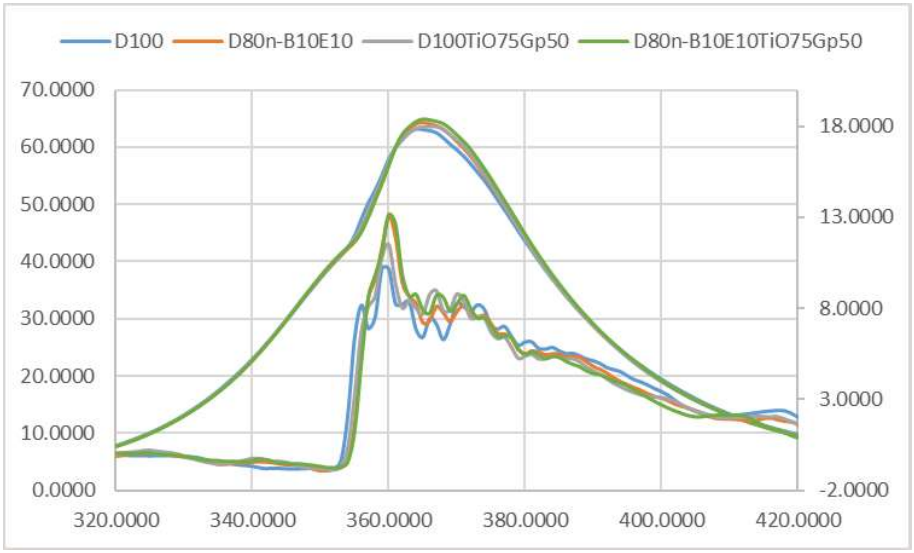
This study revealed that oxygenated fuel with ethanol and n- butanol blend reduced the calorific value of the tested fuels, as a result, BTE decreased by 5.6% according to baseline fuel under the full loading conditions. However, this reduction is mostly covered with in-cylinder pressure increment. Linearly, the reduction should have been higher, however, the pressure inside the combustion chamber increased by 0.7% compared to conventional diesel. Moreover, the drawback was eliminated by using a binary nano additive inside the liquid fuel. The maximum pressure increased by 1.9, and 2.9% for D100TiO75Gp50, and D80n-B10E10TiO75Gp50, respectively, compared to D100. The increment leads to thermal efficiency improvement for the same fuels. The BTE was noticed to be 32.2, and 31.5% for D100TiO75Gp50, and D80n-B10E10TiO75Gp50, respectively at the full load while the BTE of conventional diesel was recorded as 30.5%. For future evaluation, the second law efficiency should be investigated for all tested fuels. Moreover, the emissions of mentioned fuels need to study further.

2 GRAPHICAL ABSTRACT:

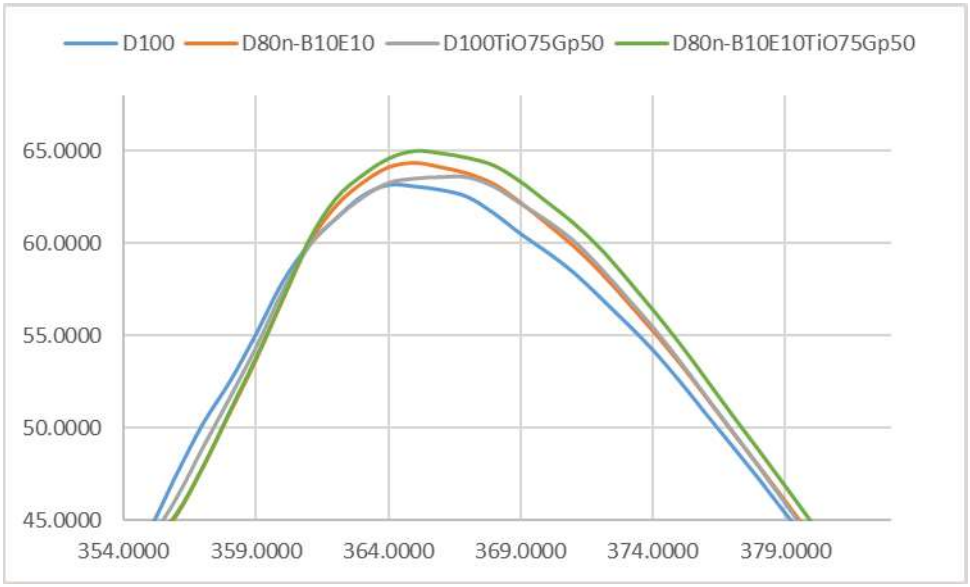


3 RESULTS

Figure 1 presents the in-cylinder pressure versus the crank angle at the full load for all tested fuels. The results revealed that the highest pressure was observed to be 64.99 bar for D80n-B10E10TiO75Gp50 while the maximum pressure for D100 was noticed as 63.15 bar. The inside cylinder pressure increased 0.7, 1.9, and 2.9% for D80n-B10E10, D100TiO75Gp50, and D80n-B10E10TiO75Gp50, respectively, comparison to D100.



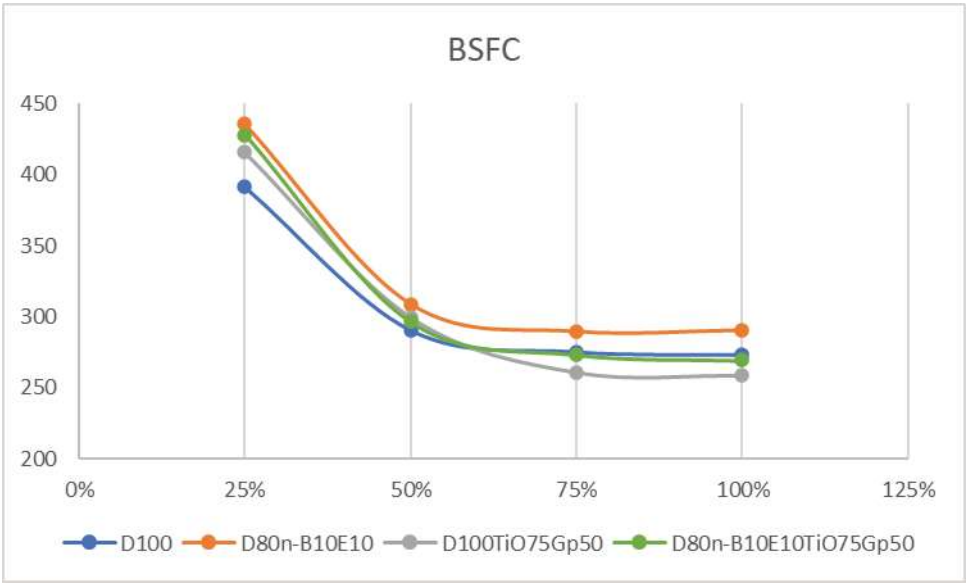
a



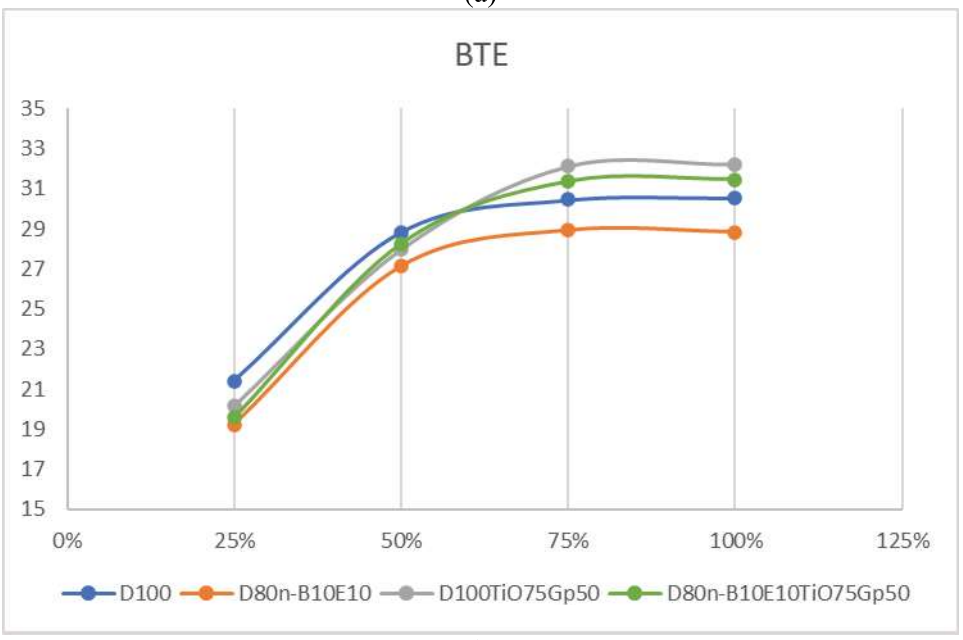
b

Figure 1. Variation of in-cylinder pressure and HRR versus the crank angle at 100% load (a) and scale up of pressure (b)

Figure 2 shows the BSFC and BTE for all investigated fuels according to applying load conditions. The highest fuel consumption was obtained from D80n-B10E10 as expected because n-Butanol and ethanol have lower calorific values than diesel fuel. At the full load, the BSFCs for D100, D80n-B10E10, D100TiO75Gp50, and D80n-B10E10TiO75Gp50 were calculated to be 273, 290.3, 258.5, and 269.2, respectively. On the other hand, the thermal efficiency showed the opposite trend with BSFC as expected. The BTEs was noticed to be 30.5, 28.8, 32.2, and 31.5% for D100, D80n-B10E10, D100TiO75Gp50, and D80n-B10E10TiO75Gp50, respectively at the full load. The improvement of BTE according to D100 was calculated as 5.5 and 3% for D100TiO75Gp50, and D80n-B10E10TiO75Gp50 at 100% load while BTE of D80n-B10E10 decreased by 5.6% under the same conditions.



(a)



(b)

Figure 2. Variation of BSFC (a) and BTE (b) as performance parameters at different loading conditions for all fuels

REFERENCES

[1] J. Han, W. He, L.M.T. Somers, Experimental Investigation of Performance and Emissions of Ethanol and n-Butanol Fuel Blends in a Heavy-Duty Diesel Engine, Frontiers in Mechanical Engineering, 6 (2020) 1-16.

[2] A.I. El-Seesy, M. Nour, A.M.A. Attia, Z. He, H. Hassan, Investigation the effect of adding graphene oxide into diesel/higher alcohols blends on a diesel engine performance, International Journal of Green Energy, 17 (2020) 233-253.

[3] A.I. El-Seesy, H. Hassan, L. Ibraheem, Z. He, M.E.M. Soudagar, Combustion, emission, and phase stability features of a diesel engine fueled by Jatropha/ethanol blends and n-butanol as co-solvent, International Journal of Green Energy, 17 (2020) 793-804..

[4] Arslan, E., Atelge, M. R., Kahraman, N., & Ünalan, S. (2022). A study on the effects of nanoparticle addition to a diesel engine operating in dual fuel mode. Fuel, 326, 124847.

[5] Atelge, M. R. (2022). Experimental study of a blend of Diesel/Ethanol/n-Butanol with hydrogen additive on combustion and emission and exegetic evaluation. Fuel, 325, 124903.

[6] Atelge, M. R. (2022). Investigation of a ternary blend of diesel/ethanol/n-butanol with binary nano additives on combustion and emission: A modeling and optimization approach with artificial neural networks. Fuel Processing Technology, 229, 107155.

[7] Atelge, M. R., Arslan, E., Krisa, D., Al-Samaraae, R. R., Abut, S., Ünalan, S., ... & Kıvrak, H. D. (2022). Comparative investigation of multi-walled carbon nanotube modified diesel fuel and biogas in dual fuel mode on combustion, performance, and emission characteristics. Fuel, 313, 123008.

[8] M.K. Yesilyurt, T. Eryilmaz, M. Arslan, A comparative analysis of the engine performance, exhaust emissions and combustion behaviors of a compression ignition engine fuelled with biodiesel/diesel/1-butanol (C4 alcohol) and biodiesel/diesel/n-pentanol (C5 alcohol) fuel blends, Energy, 165 (2018) 1332-1351.

[9] M.A. Mujtaba, M.A. Kalam, H.H. Masjuki, M. Gul, M.E.M. Soudagar, H.C. Ong, W. Ahmed, A.E. Atabani, L. Razzaq, M. Yusoff, Comparative study of nanoparticles and alcoholic fuel additives-biodiesel-diesel blend for performance and emission improvements, Fuel, 279 (2020) 118434.

[10] I. Örs, S. Sarıkoç, A.E. Atabani, S. Ünalan, S.O. Akansu, The effects on performance, combustion and emission characteristics of DICI engine fuelled with TiO2 nanoparticles addition in diesel/biodiesel/n-butanol blends, Fuel, 234 (2018) 177-188.

ELEKTRİKLİ ARAÇLARDA BATARYA YANGINLARINA GENEL BAKIŞ

M.I. Karamangil[1], A. Sürmen[2] ve M. Tekin[3]

1. Otomotiv Mühendisliği, Müh. Fak., Bursa Uludağ Üni., Bursa; email: ihsan@uludag.edu.tr
2. Otomotiv Mühendisliği, Müh. Fak. Bursa Uludağ Üni., Bursa; email: surmen@uludag.edu.tr
3. Otomotiv Mühendisliği, Müh. Fak., Bursa Uludağ Üni., Bursa; email: mervetekin@uludag.edu.tr

Özet

Trafiğe kayıtlı hibrit ve elektrikli taşıt sayısı hem dünyada hem de ülkemizde her geçen gün artmaktadır. Kirletici emisyon üretmemeleri, işletme maliyetlerinin düşük olması, sessiz çalışmaları gibi birçok avantaj sunan elektrikli araçlar bazı problemleri de birlikte getirmektedir. Bunlardan bir tanesi de yangın riskleri ve yangın sırasında çıkan ısıl yüklerin fazla olmasıdır. Klasik araçlarda çıkan yangınlar ve bu yangınlara müdahale yöntemi bilinmekle birlikte elektrikli bir araç yangınına nasıl müdahale edilir, kaza yönetimi nasıl olmalıdır en azından ülkemiz için henüz tam olarak netleşmemiş bir konudur. Bu çalışmada sırasıyla elektrikli bir araçta batarya yangınlarının çıkış sebepleri, farklı batarya türlerinin yangına etkisi ve yangına müdahale yöntemleri anlatılacaktır. Lityum iyon bataryalarda anot malzemesi olarak grafit yerine $Li_4Ti_5O_{12}$ (Lityum Titanat Oksit) veya başka metaller (Si, Sn, Sb, Ge vs..) ve bu metallerin lityum ile alaşım yapabilen bileşenlerinin kullanımı, katot malzemesi olarak LCO (Lityum Kobalt Oksit) veya NCM (Nikel Kobalt Mangan) yerine $LiFePO_4$ (Lityum Demir Fosfat) kullanımı, elektrolit malzemesi olarak daha kararlı lityum tuzları, elektrolit katkı maddeleri ve yanıcı olmayan solvent kullanımının yangın riskini azalttığı görülmüştür.

Anahtar Kelimeler: Lityum–iyon batarya, yangın, ısıl sürüklenme

Abstract

The number of hybrid and electric vehicles registered to traffic is increasing day by day both in the world and in our country. Electric vehicles, which offer many advantages such as not producing polluting emissions, low operating costs, and quiet operation, also bring some problems. One of them is the fire risks and the high thermal heat during the fire. Although the fires in classical vehicles and the method of prevention to these fires are known, how to intervene in an electric vehicle fire and how the accident management should be is an issue that has not yet been fully clarified, at least for our country. In this study, the causes of battery fires in an electric vehicle, the effects of different battery types on fire and fire prevention methods will be explained respectively. In lithium-ion batteries, $Li_4Ti_5O_{12}$ (Lithium Titanate Oxide) or other metals (Si, Sn, Sb, Ge etc.) and components of these metals that can alloy with lithium are used instead of graphite, the use of $LiFePO_4$ (Lithium Iron Phosphate) instead of LCO (Lithium Cobalt Oxide) or NCM (Nickel Cobalt Manganase) as cathode material, the use of more stable lithium salts as electrolyte material, electrolyte additives and non-flammable solvents reduce the risk of fire.

Keywords: Lithium-ion battery, fire, thermal runaway

1 GİRİŞ

Elektrikli ve hibrit araçlardaki lityum iyon batarya yangınları klasik araç yangınlarıyla karşılaştırıldığında az sayıda olmakla birlikte, açığa çıkan ısıl yük, toksik gaz salınımı ve yüksek voltaj riskleri nedeniyle önemli hale gelmektedir. Ayrıca yangına müdahale şekilleri de klasik araçlardan farklı olmaktadır. Örneğin Tesla'nın Megapack diye isimlendirilen 13 tonluk elektrik santrali olarak kullanılan bataryasında çıkan yangını 150 itfaiyeci 4 günde ancak söndürebilmiştir, [1]. Bir Tesla Model S araç yangınında açığa çıkan ısıl yük aracın altındaki yolu eritmiştir, [2]. Bu nedenle bataryalı araçlara mahsus yangın sonrası termo-fiziksel ve termo-kimyasal ortamın tanımlanması ve yangın müdahale donanımlarının ona göre belirlenmesi gerekir. Örneğin: fiziksel temas ve kimyasal soluma durumunda ortaya çıkabilecek sağlık problemlerini engelleyici donanımlar (maskeler), elektriği kesmek için yalıtımlı lastik ayakkabı, yalıtımlı eldiven, elektrolit sızıntısına müdahale durumunda asit ve alkali önleyici eldivenler, koruyucu gözlük gibi ilave ekipmanlar kullanılmalıdır. Elektrikli araçların kaza anında hızlı tanı ve akabinde müdahale

öncesi teknik detay tanı alametlerinin uygulanabilir bir teknikle oluşturulması gerekmektedir.

Lityum iyon batarya hücrelerinin birbirine yakın yerleştirilmiş elektrotlardan oluşması kısa devre olasılığını arttırır. Ayrıca hücrelerin yanıcı bir sıvı elektrolitle dolu olması, ısınan elektrolitin kaynaması ve hücre dışına sızması yangın riskini arttıran diğer bir ana faktördür. Elektrolitler çok sayıda yanıcı malzeme ve zararlı kimyasal içerir, bu nedenle her koşulda yangına neden olabilirler. Ancak üreticiler, bataryayı yangın duvarları ile ayıran küçük hücrelere bölerek sorunu çözmeye çalışmaktadırlar. Böylelikle yangının en azından komşu parçalara sıçraması geciktirilebilir. Bazı mühendisler daha az yanıcı ve daha az zararlı kimyasala sahip daha az riskli elektrolitler üretmektedir. Elektrikli bir araç yangını sırasında, her ikisi de insanlar için ölümcül olan karbon monoksit ve hidrojen siyanür gibi bazı inanılmaz derecede toksik gazlar da dahil olmak üzere 100'den fazla organik kimyasal üretilebilir.

Bir batarya paketindeki tüm hücreler ısıl sürüklenmeye (**thermal runaway –TR-**) maruz kalabilir. Isıl sürüklenme, 60 °C ve üstünde yangına sebep olan, durdurulamayan bir zincir reaksiyonudur. Bir hücredeki ısıl sürüklenme, bitişik batarya hücrelerinin tutuşmasına neden olacak kadar ısı üretir ve böylece her hücrede tekrar tekrar alevlenen bir yangın meydana gelir. Üreticiler, elektrikli araçlarda ısıl sürüklenmenin yarattığı etkileri engellemek ve azaltmak için farklı yöntemler tasarlamaktadırlar.

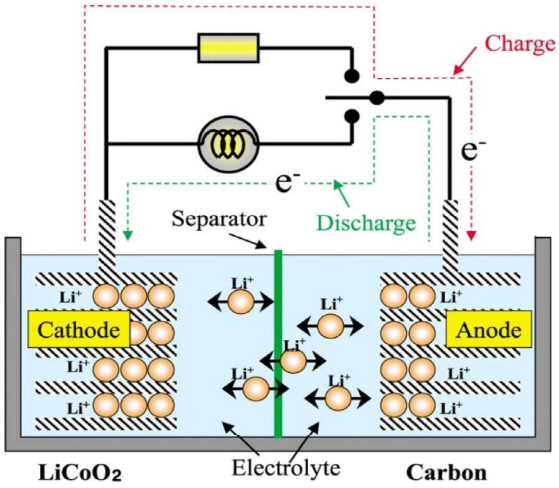
Lityum iyon batarya 15-45 °C arasında çok daha dar bir çalışma aralığına sahiptir. Bu sıcaklık aralığından çıkmamak oldukça önemlidir. Sıvı veya hava kullanan soğutma yönetimi ve izleme, bataryanın, aracın ve yolcuların güvenliği için şiddetle tavsiye edilir.

Elektrikli ve hybrid araçlar, tipik olarak 100 ila 600 volt arasında değişen yüksek voltajlı elektrik sistemlerine sahiptirler. Batarya paketleri, sızdırmaz muhafazalara yerleştirilmiştir ve hücreleri aşırı şarj, titreşim, aşırı sıcaklıklar, kısa devre, nem, yangın, çarpışma ve suya daldırma gibi koşullara maruz bırakan test standartlarını karşılarlar. Üreticiler bu araçları, **bir çarpışma veya kısa devre** algıladıklarında elektrik sistemini devre dışı bırakan yalıtımlı yüksek voltaj hatları ve güvenlik özellikleri ile tasarlarlar.

Bu çalışmada, bir lityum iyon bataryanın temel elemanları ve bunların yangına olan etkileri izah edildikten sonra, batarya yangınlarına neden olabilecek mekanik, elektriksel ve termal hasar durumları detaylı bir şekilde incelenmiştir. Son olarak bir hücreyi ısıl sürüklenemeye götüren süreç ve elektrikli araç kaza yönetimi anlatılmıştır.

2. Lityum-İyon Batarya Yapısı

Bir lityum-iyon batarya 4 ana bileşenden oluşur. Bu bileşenler 1. Anot, 2. Katot, 3. Elektrolit ve 4. Seperatör'dür, Şekil 1. Lityum iyonlarının anotla katot arasındaki değiş-tokuş hareketi nedeniyle bu bataryaya **-Sallanan sandalye tipi batarya-** adı verilir, [3].



$$\textbf{Katot:}\quad LiCoO_2 \underset{\leftarrow\ Discharge}{\overset{Charge\ \rightarrow}{\rightleftharpoons}} Li_{(1-x)}CoO_2 + xLi^+ + xe^-$$

$$\textbf{Anot:}\quad 6C + xLi_+ + xe^- \underset{\leftarrow\ Discharge}{\overset{Charge\ \rightarrow}{\rightleftharpoons}} Li_xC_6$$

$$\textbf{Reaksiyonlar:}\quad LiCoO_2 + 6C \underset{\leftarrow\ Discharge}{\overset{Charge\ \rightarrow}{\rightleftharpoons}} Li_{(1-x)}CoO_2 + Li_xC_6$$

Şekil 1: Lityum iyon bataryanı çalışma prensibi [4]

Anot Malzemesi:

Anot malzemesi olarak çoğunlukla grafit kullanılır. Grafit lithium plating'e (lityum biriktirme, deposition) daha yatkındır. Bu ise anot üzerinde dentritlere (çıkıntılara) neden olur. Bu dentritler seperatöre zarar verebilir. Bu nedenle enerji kapasitesi grafite göre düşükte olsa $Li_4Ti_5O_{12}$ kullanımı veya başka metaller (Si, Sn, Sb, Ge vs..) ve bu metallerin lityum ile alaşım yapabilen bileşenleri üzerine çalışılmaktadır.

Katot Malzemesi

Katot malzemesi olarak çoğunlukla $LiCoO_2$ (LCO), $LiMn_2O_4$ (LMO), $Li(Ni_xCo_yAl_z)O_2$ (NCA) ve $Li(Ni_xCo_yMn_z)O_2$ (NCM) gibi lityum metal oksitler kullanılır. LCO veya NCM yerine $LiFePO_4$ kullanmak yangın riskini azaltır. Çünkü organik elektrolitlerle reaktivitesi daha düşük dolayısıyla daha az ısı salınımı gerçekleşir.

Daha yüksek enerji kapasitesine ve daha yüksek voltaja sahip katot malzemeleri tercih edilir.

Elektrolit Malzemesi:

Elektrolit malzemesi genelde organik solventlerden ve lityum tuzlarından oluşur. Organik solvent olarak ethylene carbonate (EC), diethyl carbonate (DEC), propylene carbonate (PC), ethyl methyl carbonate (EMC) ve dimethyl carbonate (DMC) gibi maddeler kullanılır. Özellikle EC (146 °C), DMC (18 °C) ve EMC (23 °C) diğer solventlere göre daha düşük parlama noktasına sahiptirler ve bu nedenle kolayca ateşlenebilirler. Lityum tuzu olarak ise lithium hexafluorophosphate ($LiPF_6$), lithium hexafluoroarsenate monohydrate ($LiAsF_6$), lithium perchlorate ($LiClO_4$) ve lithium tetrafluoroborate ($LiBF_4$) kullanılır, [5-9].

Organik çözücüler birer hidrokarbondur dolayısıyla yanıcıdırlar. Elektrolitin kütle oranı, hücre kütlesinin yaklaşık %10'u kadardır, [10, 11].

Yangın emniyeti açısından daha kararlı lityum tuzları, elektrolit katkı maddeleri, yanıcı olmayan solventler ile polimer ve solid state elektrolitler tercih edilir.

Seperatör Malzemesi:

Seperatör serbest lityum iyonlarının transferine izin verir ve dahili kısa devre (internal short circuit – ISC-) riskini engellemek adına anot ile katot arasında bir yalıtım görevi görür. Seperatör elektrokimyasal olarak aktif bir malzeme olmamakla birlikte batarya güvenliği açısından son derece önemlidir. Seperatör hasar görürse, hücre ISC nedeniyle ısıl sürüklenme durumuna geçebilir. İyon transferinde önemli bir rol oynar, hücre ömrünü ve performansını belirler. Seramik katkılı seperatörlerde bozulma sıcaklığı 250 °C ye kadar çıkar, [12, 13].

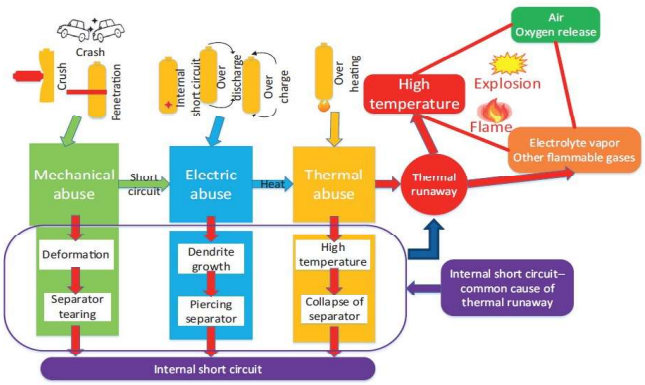
3. Elektrikli Araç Batarya Yangını Çıkış Sebepleri

Üretici tarafından tavsiye edilen sınırlar içinde depolanır ve çalıştırılırsa, lityum iyon bataryaların (LIB'lerin) arıza oranının 40 milyonda 1 olduğu tahmin edilmektedir [14]. Ancak aşırı şarj, harici ısıtma ve mekanik kötüye kullanım gibi öngörülemeyen durumlar bu arıza olasılığını önemli ölçüde arttırabilmektedir. Ticari LIB hücrelerine çeşitli güvenlik cihazları dahil edilmiş olsa da, birçoğu hücre üreticileri ve ürünlerinde LIB teknolojisini kullanan şirketler için önemli olumsuz etkilere neden olan çok sayıda yüksek profilli batarya arızası/kazası olmuştur. Bu kazaların temel nedenleri Şekil 2'de gösterildiği gibi üç grupta toplanabilir:

1. Mekanik hasar
2. Elektriksel hasar
3. Termal hasar

Mekanik hasar olarak batarya muhafazanın zarar görmesi, hücrelerin sıkışması, ezilmesi, delinmesi ve bükülmesi durumlarını, **elektriksel hasar olarak** aşırı şarj, aşırı deşarj, yüksek güç çıkışı (high C-rate) ve iç kısa devre durumlarını ve **termal hasar olarak** da kendi kendine ısınma (self-heating) ve dışarıdan bir ısı kaynağının sebep olduğu ısınma olaylarını sayabiliriz. Mekanik hasar durumunda bataryada meydana gelen deformasyon separatörün yırtılmasına, elektriksel bir hasar durumunda bataryadaki dentrit oluşumu seperatörün delinmesine, termal hasar durumunda batarya içerisindeki yüksek ısı oluşumu seperatörün çökmesine neden olur. Dikkat edilirse her üç hasar durumunda da seperatör zarar görmektedir. Seperatörün zarar görmesi anot ile katot arasındaki yalıtıma son verdiği için kısa devreye ve kısa devrede yangına götüren bir elektron akışına sebep olmaktadır.

Özellikle sıcak günlerde veya büyük batarya paketlerinde normal çalışma koşulları altında bile bataryada üretilen ısı tamamen uzaklaştırılamamaktadır. Artan batarya sıcaklığı, diğer istenmeyen parazitik reaksiyonları tetikleyerek, batarya ısı üretiminin kontrol edilemediği noktada yangına neden olabilmektedir.



Şekil 2: Bir lityum-iyon bataryada yangına sebep olan durumlar

Şekil 2'de dikkat edilirse mekanik, elektriksel ve termal her üç hasarda netice itibariyle bataryada ısıl sürüklenme sürecini başlatmakta ve bu süreç batarya yangını ile sonuçlanmaktadır.

Thermal Runaway hücre içerinde ekzotermik reaksiyonlar tarafından üretilen ısı, çevreye olan ısı kayıpları tarafından dengelenmediğinde meydana gelir. Bu biriken ısı, sıcaklık artışını tetikler ve bu da reaksiyon hızlarında üstel bir artışa neden olur. İdeal koşullarda, ısı hücreden uzaklaştırılır. Ancak, thermal runaway durumunda, ısının hücreden atılma hızından birkaç kat daha yüksek bir oranda ısı hücre içerinde üretilir. Lityum iyon bataryada (LIB), mekanik, elektriksel veya termal hasar nedeniyle batarya içinde istenmeyen bir sıcaklık artışı meydana gelebilir. Isı üretim hızı, çevreye ısı yayılım hızını aşarsa, sıcaklık yükselmeye devam eder. Bazı kritik sıcaklıklara, özellikle seperatörün çökmesine neden olan sıcaklığı ulaştığında hücre bozulur. Batarya sıcaklığının giderek daha yüksek bir oranda yükselmeye devam ettiği sıcaklığa kritik denge sıcaklığına "**Temperature of No Return – Geri dönülemez sıcaklık**" denir.

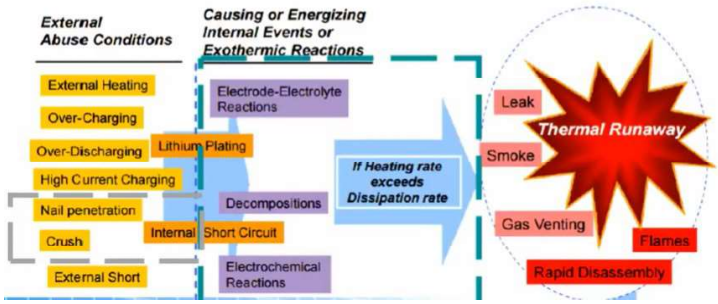
Ayrıca, yüksek bir ortam sıcaklığı, **self-accelerating decomposition temperature (SADT)** neden olabilir. Yani bu durumda bataryayı, bileşenleri arasındaki elektrokimyasal reaksiyonlardan ötürü ısı üreten bir **reaksiyon sistemine** benzetebiliriz.

Thermal runaway olayını hücre sıcaklığındaki kontrolsüz artışın neden olduğu bir dizi kontrolsüz ekzotermik reaksiyonun tezahürü ve buna bağlı olarakta **hücre içindeki ısı salınımın ivmelenmesi** olarak tanımlayabiliriz. Süreç hücreden gaz, şarapnel ve partikül çıkışı, duman ve yangın ile tamamlanır, [15].

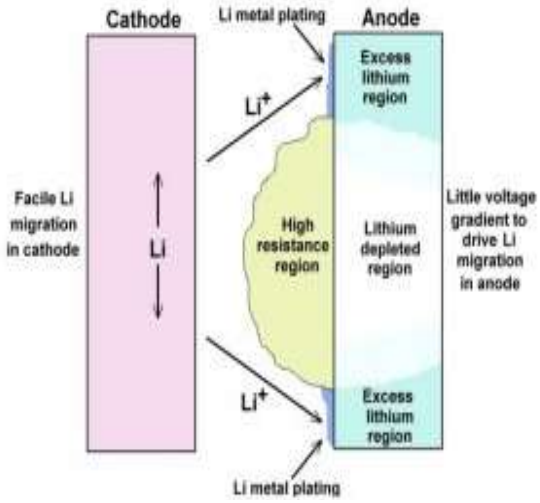
Şekil 3'te ise bir bataryayı thermal runaway'e götüren süreç farklı bir boyutta gösterilmiştir. Şekil 3'te thermal runawaya götüren süreçlerden birinin lithium plating (lityum birikmesi) olduğu görülmektedir. Lithium plating'in oluşma sebebi:

1. Yüksek şarj akımı lityum iyonlarının anot içine nüfuz etmeye zorlar.
2. Düşük sıcaklıkta şarj etmektir.

Lithium plating'i önlemenin en basit iki yolu, şarj sırasında aşırı voltajı (hücre başına 4,2 voltun üzerinde) ve düşük sıcaklıkta (15 ºC'nin altında) şarj ve deşarjı önlemektir. Şekil 4'de Lithium plating oluşumu gösterilmiştir.



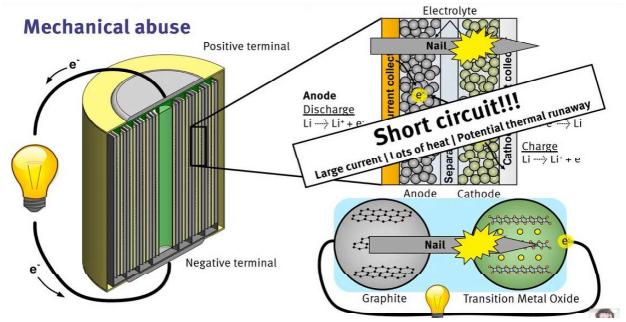
Şekil 3: Bir bataryayı thermal runaway'a götüren süreç, [16]



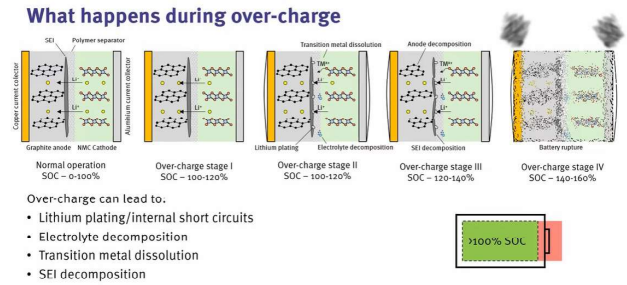
Şekil 4: Lithium plating oluşum, [17]

Genellikle hafif bir kısa devre kendi kendine deşarjın yükselmesine neden olabilir ve deşarj enerjisi çok düşük olduğu için çok az ısı üretilir. Ancak, yeterli mikroskobik metal parçacığı bir noktada birleştiğinde, büyük bir elektrik kısa devresi gelişebilir ve bu durumda pozitif ve negatif plakalar arasında yanmaya neden olan büyük bir akım akar.

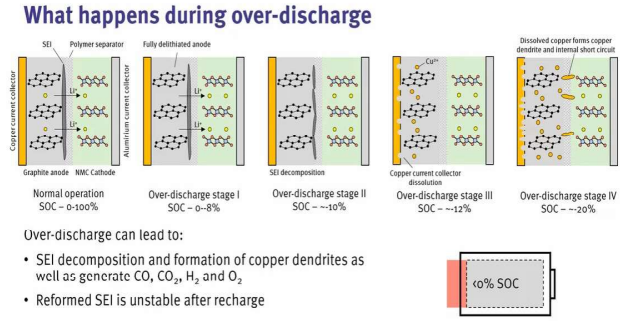
Şekil 5'te mekanik, elektriksel ve termal hasara örnekler verilmiştir.



a. Çivi batması



b. Aşırı şarj (Over-charge)



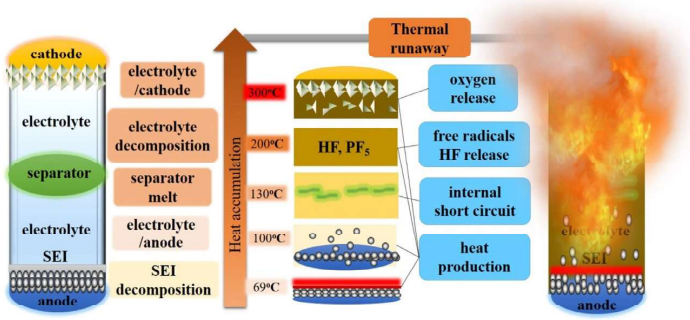
c. Aşırı deşarj (Over-decharge)

Şekil 5: Mekanik, elektriksel ve termal hasara örnekler

3. 1 Thermal Runaway'ye (TR) neden olan ısı kaynakları ve temel reaksiyonlar:

Bir bataryayı thermal runaway sürecine götüren ısı üretimi iki kısımda değerlendirilebilir. Şekil 6'da bir hücrede sıcaklık artışına bağlı olarak gerçekleşen olaylar özetlenmiştir.

1. Normal çalışma esnasında (şarj/deşarj) ısı üretimi
2. Sıcaklık artışına bağlı olarak gerçekleşen reaksiyonlar ve ısı üretimi
   - LIB içindeki yüksek sıcaklıktaki elektrokimyasal reaksiyon süreci çok karmaşıktır.
   - Solid Electrolyte Interphase (SEI) tabakasının bozulması, elektrolit ile anot malzemesi arasındaki reaksiyon, seperatörün erimesi, elektrolitin bozulması, elektrolit ile katot malzemesi arasındaki reaksiyon ve anot ile bağlayıcı arasındaki reaksiyon.
   - Bu reaksiyonların birçoğu paralel olarak gerçekleşir.



Şekil 6: $LiCoO_2$ /graphite hücresine ait thermal runaway süreci

Şekil 6'da HF (Hidrojen Florür) hidroflorik asit formunda doku ile temas ettiğinde aşındırıcı, delici ve son derece tehlikeli bir gazdır. Gaz ayrıca korneanın hızlı yıkımı ile körlüğe neden olabilir. PF_5 (Phosphorus pentafluoride) ise zehirli bir gazdır.

Şekil 6'da sırasıyla gerçekleşen olaylar:

i. SEI (Solid Electrolyte Interphase layer) Katmanının Bozulması

Katı elektrolit ara fazı grafit anot üzerinde oluşan ince bir katmandır. Sıcaklık yükseldiğinde TR reaksiyonunun ilk adımı SEI tabakasının bozulmasıdır. Bu tabakanın

bozulması yaklaşık 60 °C de başlayabilir. Daha sona 90-120 °C arası CO_2 salınımı başlar, [18-21].

ii. Anotla Elektrolit Arasındaki Reaksiyon

SEI katmanının bozulması batarya iç sıcaklığını arttırır ve anot elektrolit reaksiyonunu başlatır.

Organik çözücüler lityum ile reaksiyona girerek C_2H_4, C_3H_6 ve C_2H_6 gibi yanıcı hidrokarbonlar serbest kalır.

$$2Li + C_3H_4O_3\ (EC) \rightarrow Li_2CO_3 + C_2H_4$$

$$2Li + C_4H_6O_3\ (PC) \rightarrow Li_2CO_3 + C_3H_6$$

$$2Li + C_3H_6O_3\ (DMC) \rightarrow Li_2CO_3 + C_2H_6$$

iii. Seperatörün Çökmesi ve ISC oluşumu

Polietilen (PE) ve Polipropilen (PP) seperatörler sırasıyla 135 °C ve 166 °C'de erir. Seramik kaplı seperatörler ise sıcaklık 200 °C'nin üzerinde dayanım gösterirler. Sıcaklık arttıkça seperatör büzülür, bu durumda anotla katot birbirine temas eder ve kısa devre gerçekleşir. LIB'da, eğer seperatör kademeli olarak büzülür ve küçük bir alanda ISC oluşursa hücre yüksek sıcaklığa maruz kalır ve kendi kendine deşarj olur.

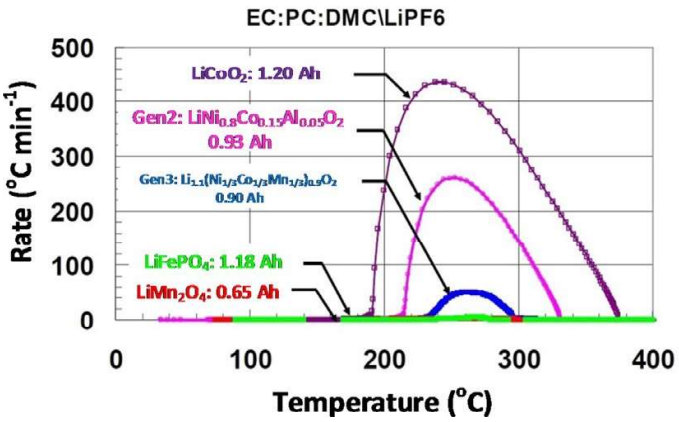
ISC TR'in önemli bir tetikleyicisidir. Ancak, ISC olmadan da TR şartları oluşabilir.

Katot tarafından salınan oksijen, lityumlu anot ile reaksiyona girer ve 274.2 °C'de 87.8 W/g ısı akışı ile büyük miktarda ısı üretir, [22].

iv. Katotun bozulması ve elektrolit ile reaksiyonu

Daha yüksek sıcaklıklarda katot bozulmaya başlar ve oksijen salar. EC/DEC solventinde, kendi kendine devam eden ekzotermik reaksiyonlar için başlangıç katot bozulma sıcaklığı LCO, $Li(Ni_{0.1}Co_{0.8}Mn_{0.1})O_2$ ve LFP tipi bataryalar için sırasıyla 150 °C, 220 °C ve 310 °C'dir (tümü 4.2 V'a şarj edilmiştir), [23]. Şekil 7'de 18650 tipi hücre için ölçülmüş kendi kendine ısınma oranları (sef-heating rate) gösterilmiştir. Buna göre katot malzemesi termal reaktivitesi en yüksekten en düşüğe doğru LCO > NCA > NCM > LMO > LFP şeklindedir.

İyileştirilmiş katot stabilitesi sayesinde kendi kendine ısınma pik değerlerinin azaldığı görülmektedir.



Şekil 7: 18650 tipi hücre için ölçülmüş kendi kendine ısınma oranları (sef-heating rate). Geliştirilmiş katot kararlılığı sayesinde azaltılmış kendi kendine ısınma pik değerleri, [14].

Farklı katot malzemelerinin bozulma sıcaklık değerleri Tablo 1'de verilmiştir.

Tablo 1: Farkı katot malzemelerinin elektrolitlerle yaptığı reaksiyon özellikleri (birden fazla değer farklı çalışmalardan alınan sonuçları göstermektedir.)

Katot	Kaynak	Bozulma sıcaklık aralığı [°C]#	Elektrottan salınan ısı oranı (J/g)
LCO	[24]	200-500	450
NCA	[25]	160*	850±100
	[26]	200*	793
LMO	[27]	225-400	350
	[24]	150-300	450
	[28]	89*	2014,3
LFP	[29]	190-285	290
	[30]	180*	145

[24] $LiCoO_2$ ve 1 M $LiPF_6$ + PC/EC/DMC (1:1:3) elektrolit ve $Li_{0,1}Mn_2O_4$ ve 1 M $LiPF_6$ + PC/EC/DMC (1:1:3) elektrolit; solventlerin oranı hacimsel veya kütlesel olarak belirtilmemiştir.
[25] $Li_x(Ni_{0,8}Co_{0,15}Al_{0,05})O_2$ (4,2 V vs Li) ve 1 M $LiPF_6$ + EC/DEC (1:2) elektrolit; solventlerin oranı hacimsel veya kütlese olarak belirtilmemiştir.
[26] $Li_x(Ni_{0,8}Co_{0,15}Al_{0,05})O_2$ (4,2 V vs Li) ve 1 M $LiPF_6$ + EC/DMC (1:1 vol.) elektrolit
[27] $Li_xMn_2O_4$ (5,0 V vs Li) ve 1 M $LiPF_6$ + EC/DMC (1:1 vol.) elektrolit
[28] $Li_xMn_2O_4$ (4,3 V vs Li) ve 1 M $LiPF_6$/EC+DEC (1:1 wt%) elektrolit
[29] $Li_{0,05}Fe_2PO_4$ (4,3 V vs Li) ve 1 M $LiPF_6$ + EC/DMC (1:1 wt%) elektrolit
[30] %100SOC karbon kaplı $LiFePO_4$ ve 1,2 M $LiPF_6$ + EC/EMC (3:7 wt%) elektrolit
kolon: * bozulma başlangıç sıcaklığını belirtir, * işareti yoksa bozulma sıcaklık aralığı belirtilmiştir.

3.1.1 Farklı katot malzemelerinde meydana gelen bozulma reaksiyonları:

LCO'nun Bozulması

LCO, nispeten zayıf termal kararlılığa sahip LIB için en eski ticari katot malzemesidir. LCO'nun ayrışma yolları [31-33]:

$Li_xCoO_2 \rightarrow xLiCoO_2 + 1/3(1-x)Co_3O_4 + 1/3(1-x)O_2$

$Co_3O_4 \rightarrow 3CoO + 0.5O_2$

$CoO \rightarrow Co + 0.5O_2$

$Li_{0,45}CoO_2$ + elektrolit (PC/EC/DMC(1/1/3) + $LiPF_6$ (1M)) reaksiyonunun ayrışmasında, Biensan [24] ısı salınımının 450 J/g olduğunu ölçmüştür ve reaksiyon sıcaklık aralığı 220–500 °C ve O_2 salınımının sıcaklığı 230 °C olarak belirlenmiştir.

NCA'nın Bozulması

NCA ($LiNiCoAlO_2$) katodunun ayrışması [34,35]:

$$Li_x(Ni_{0,8}Co_{0,15}Al_{0,05})O_2(R3m) \rightarrow \frac{1+x}{3}[Li_{\frac{3x}{1+x}}(Ni_{0,8}Co_{0,15}Al_{0,05})_{\frac{3}{1+x}}O_4] + (Fd3m) + \frac{1-2x}{3}O_2$$

$$Li_x(Ni_{0,8}Co_{0,15}Al_{0,05})O_{\frac{4(1+x)}{3}}(Fd3m) \rightarrow [Li_x(Ni_{0,8}Co_{0,15}Al_{0,05})O_{1+x}] + (Fm3m) + \frac{1+x}{6}O_2$$

NCM'nin Bozulması

NCM katodunun özellikleri Ni, Co ve Mn atomlarının oranına bağlıdır. Genel olarak, yüksek Ni içerikli NCM'ler yüksek elektrik kapasitesine sahiptir ancak termal stabilitesi düşüktür, [36].

Bak ve ark. [37] farklı Ni, Co ve Mn içeriğine sahip yüklü $Li(Ni_xMn_yCo_z)O_2$ katot malzemesinin termal kararlılığını araştırmış ve daha fazla Ni ve daha az Co ve Mn'nin, daha düşük faz geçişi başlangıç sıcaklığına ve daha büyük miktarda oksijen salınımına neden olduğunu bulmuşlardır.

Roder [38,39] NMC için aşağıdaki ayrışma reaksiyonunu önermiştir:

$$NCM(R3m) \xrightarrow{\Delta T, solv.\rightarrow} (mn, Ni)O(Fm3m) + CoO + Ni + O_2$$

$LiMn_2O_4$'nın Bozulması

$LiMn_2O_4$'ün ayrışması aşağıdaki reaksiyonlarla temsil edilebilir [40,28]:

$Mn_2O_4 \rightarrow Mn_2O_3 + 0,5O_2$

$Li_{0,2}Mn_2O_4 \rightarrow 0,2LiMn_2O_4 + 0,8Mn_2O_4$

$3Mn_2O_4 \rightarrow 2Mn_3O_4 + 2O_2$

$LiMn_2O_4 \rightarrow LiMn_2O_{4-y} + y/2O_2$

$LiMn_2O_4 \rightarrow LiMnO_2 + 1/3Mn_3O_4 + 1/3O_2$

$LiFePO_4$'nın Bozulması

$LiFePO_4$ nispeten güvenli bir katot malzemesidir ve güvenlikteki gelişme, $(PO_4)^{3-}$ polianyonun güçlü P–O kovalent bağ yapısına atfedilir. Bazı araştırmacılar, $LiFePO_4$'ün yüksek sıcaklıkta oksijen salmadığını söyler. Bununla birlikte, net bir kanıt olmaksızın $FePO_4$'ün aşağıdaki gibi ayrışabileceği de öne sürülmüştür [41]:

$2Li_0FePO_4 \rightarrow Fe_2P_2O_7 + 0.5O_2$

v. Elektrolitin Bozulması

Salınan oksijen solventlerle reaksiyona girer, örneğin DMC için:

$3O_2 + C_3H_6O_3$ (DMC) $\rightarrow 3CO_2 + 3H_2O$

Lityum da organik solventle reaksiyona girer, Örneğin EC için:

$2Li + 2EC \rightarrow LiO(CH_2)_4OLi + 2CO_2$

$LiPF_6 \rightarrow LiF + PF_5$

$LiO(CH_2)_4OLi + PF_5 \rightarrow LiO(CH_2)_4F + LiF + POF_3$

Sıcaklık 200 °C'yi aştığında elektrolit ekzotermik olarak bozulur ve karbondioksit, flor gazları ve hidrokarbonlar salmaya başlar.

$C_2H_5OCOOC_2H_5 + PF_5 \rightarrow C_2H_5OCOOPF_4 + HF + C_2H_4$

$C_2H_4 + HF \rightarrow C_2H_5F$

$C_2H_5OCOOPF_4 \rightarrow PF_3O + CO_2 + C_2H_2 + HF$

$C_2H_5OCOOPF_4 \rightarrow PF_3O + CO_2 + C_2H_5F$

$C_2H_5OCOOPF_4 + HF \rightarrow PF_4OH + CO_2 + C_2H_5F$

vi. Bağlayıcı ile ilgili reaksiyon

Batarya sıcaklığı 260 °C'nin üzerinde olduğunda, bağlayıcı madde katot malzemesi ve Li_xC_6 ile reaksiyona girebilir.

PVDF bağlayıcı içeren LCO katot malzemesinde, bağlayıcı LCO'nun termal reaktivitesini artırabilir. Yüksek sıcaklıkta, aktif malzeme ile bağlayıcı arasındaki arayüzde yüzey Co_3O_4 oluşumu ve Co iyonlarının çözünmesi hızlanır.

Hidrojen florürün (HF), LCO'nun bozulma reaksiyonunda rol oynadığı bulunmuştur.

$$4LiCo^{III} \rightarrow Co^{IV}O_2 + Co^{II}Co_2^{III}O_4 + 2Li_2O \xrightarrow{4HF \rightarrow} 4LiF + 2H_2O$$

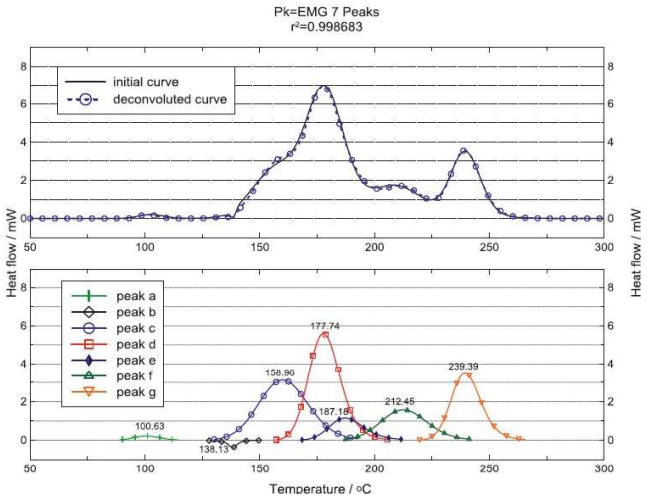
Bir anotun PVDF-heksafloropropen ile reaksiyonunun ısısı 1220 J/g dır.

$$-CH_2 - CF_2 \xrightarrow{base \rightarrow} -CH = CF - + HF$$

$$-CH_2 - CF_2 + Li \rightarrow LiF \pm CH = CF - + 0{,}5H_2$$

3.2.2 Tüm Hücrenin Termal Analizi

Şekil 8'de ısı üretimine en büyük katkı katodun ayrışmasıdır ve ikinci en büyük katkı ise katotla-anot arasındaki ISC'dir.



Pik	Baş. Sıcaklığı (°C)	Reaksiyon	Isı salınım miktarı (mJ)	Özgül ısı salınımı (J/g)#
a	89,06	SEI tabakasının bozulması	-1077,66	-44,90*
b	127,79	Separatörün erimesi	943,74	224,70***
c	129,35	Katot–anot materyallerinin kısa devresi	-25615,66	---
d	158,08	$LiCoO_2$'nin orantısızlaşması	-29340,06	-488,18**
e	169,16	Lityum (Li_xC_6'daki)-elektrolit reaksiyonu	-6652,43	-277,18*
f	188,29	$LiCoO_2$'nin ileri düzeyde bozulması	-12072,59	-200,88**
g	220,65	Termal bozulma sonucu oluşan elektrolit ürünlerinin oksidasyonu/PVDF içeren termal reaksiyonlar	-17251,04	-718,79*/ -287,04**
Toplam			-91155,69	

kolon: *,**,*** sırasıyla anot, katot ve seperatör kütlesine bölünerek elde edilen özgül ısı salınımı. Ekzotermik ısı negatiftir.

Şekil 8: 0,2 °C/dak ısınma hızında, tam hücre sıcaklığına karşı ısı akışının başlangıç ve çözülmüş ısı akışı eğrileri. Sistem 60,1 mg Li_xCoO_2, 24,0 mg Li_xC_6, 23,8 mg 1,0 mol/L $LiPF_6$/EC + DEC elektrolit, 4,2 mg ayırıcı, 11,2 mg Al ve 18,0 mg Cu akım toplayıcı içerir, [42].

4 Kaza Yönetimi

Basit bir elektrikli araç kazasında kontak anahtarını kapatmak ve düşük voltajlı akü bağlantısını kesmek yeterli olabilmektedir. Batarya deforme olmuş veya hasar görmüş ise bataryanın sıcaklığı gerçek zamanlı olarak izlenmeli ve anormal sıcaklık artışı durumunda, yangını ve patlamayı önlemek için fiziksel soğutma yapılması gerekmektedir.

Aracın çekici ile çekilmesi sırasında da batarya sıcaklığının izlenmesi gerekir. Burada da anormal sıcaklık artışı durumunda soğutma yapılması gerekebilir.

Kaza yapan aracın bataryasından elektrolit sızıntısı olması durumunda tespit yapılarak uyarı alanı tanımlanmalıdır.

Az miktarda sıvı elektrolit sızıntısı olduğunda, yangın kaynağından uzak durulmalı, elektrolit toplanarak ya hava geçirmez bir kaba konulmalı ya da yakılmalıdır. Çok miktarda sıvı elektrolit sızıntısı olduğunda ise bunları toplamalı ve tehlikeli kimyasallara göre işlemden geçirmeli ve zehirli gaz HF'yi (hydrofluoric acid) işlemek için kalsiyum glukonat solüsyonu eklemelidir. Elektrolitin insan vücudu ile temas etmesi durumunda hemen o kısım su ile 10-15 dakika kadar yıkanmalıdır. Ağrı varsa %2,5 kalsiyum glukonat merhem sürülebilir veya ağrıyı azaltmak için %2-2,5 kalsiyum glukonat solüsyonuna batırılabilir, [43].

Araç servise götürülmeden önceki zaman dilimi süresince içerisine su girmemeli ve korozyon riski olmayan güvenli bir yerde tutulmalıdır. Su girme ve korozyon riskini önlemek için gerekirse su geçirmez örtü ile kaplanmalıdır.

Yüksek voltaj kesilmeden önce hasarlı bir araç binalardan veya diğer araçlardan en az 15 m uzağa yerleştirilmelidir. Aksi takdirde hasarlı araç bataryasında başlayacak güçlü bir yangın diğer araç bataryalarının da yanmasına neden olabilecek termal şok etkisi oluşturabilir.

Su içerisinde de bataryanın patlama riski vardır. Farklı su seviyelerinde araca müdahaleler farklılık gösterir.

Üreticiler elektrikli araçlarını, bir çarpışma veya kısa devre algıladıklarında elektrik sistemini devre dışı bırakan yalıtımlı yüksek voltaj hatları ve güvenlik özellikleri ile tasarlamakta ve araçları için acil müdahale kılavuzları yayınlamaktadırlar.

Bir batarya yangınının söndürüldükten birkaç saat veya birkaç gün sonra tekrar başlayabileceği unutulmamalıdır.

5 Sonuç

Bir elektrikli araç yangını bataryanın mekanik, elektriksel veya termal bir hasar sonucu thermal runaway sürecine girmesi ile başlamaktadır. Her üç durum için süreç aşağıdaki gibi özetlenebilir.

1. ***Mekanik:*** Deformasyonun sebep olduğu seperatör yırtılması, kısa devre ve TR
2. ***Elektriksel:*** Aşırı şarj ve aşrı deşarjın neden olduğu dentrit oluşumu, seperatörün delinmesi, kısa devre ve TR
3. ***Termal:*** Seperatörün erimesi, malzemelerin deformasyonu ve TR

Ayrıca aşağıdaki tespitler yapılabilir:

- ✓ Bir kaza sırasında seperatörün göreceği zarar kısa devre alanını etkiler, bu alan ne kadar büyük olursa TR'e o kadar erken ulaşılır.
- ✓ Gaz çıkışı ile TR arasında geçen süre bataryadan bataryaya farklılık gösterir.
- ✓ TR'ye eşlik eden olaylar farklılık arz edebilir. Gaz çıkışı veya yangın veya duman veya bunların kombinasyonları gözlemlenebilir.
- ✓ Bataryadan salınan gazlar yanabilir özelliktedir, zehirli ve tahriş edicidir. Bu nedenle solunmamalıdır. (HF: körlüğe neden olabilir).
- ✓ Batarya yaşlandıkça yangın riski artar.
- ✓ BMS'in hücre yönetimi önemlidir. Örneğin Tesla'nın bir aracında 7000 hücrenin yönetimi sözkonusudur.

6 Kaynaklar

[1] https://www.indyturk.com/node/394696/ekonomi%CC%87
[2] https://tr.motor1.com/news/127753/olumcul-tesla-model-s-kazasinda-cikan-yangin-guvenlik-konusunda-endiseleri-arttirdi/
[3] Wang Q, Mao B, Stoliarov SI, Sun J. "A review of lithium ion battery failure mechanisms and fire prevention strategies" *Progress in Energy and Combustion Science* vol. 73, pp. 95–131, 2019.
[4] Nishi Y. The development of lithium ion secondary batteries. *Chem Rec* Vol. 1, pp. 406–13, 2001.
[5] Wang Q, Jiang L, Yu Y, Sun J. Progress of enhancing the safety of lithium ion battery from the electrolyte aspect. *Nano Energy* Vol. 55, pp. 93–114, 2018.
[6] Li Q, Chen J, Fan L, Kong X, Lu Y. Progress in electrolytes for rechargeable Li-based batteries and beyond. *Green Energy Environ* Vol. 1, pp. 18–42, 2016.
[7] Dahbi M, Ghamouss F, Tran-Van F, Lemordant D, Anouti M. Comparative study of EC/DMC LiTFSI and LiPF 6 electrolytes for electrochemical storage. *J Power Sources* Vol. 196, pp. 9743–50, 2011.
[8] Li F, Gong Y, Jia G, Wang Q, Peng Z, Fan W, et al. A novel dual-salts of LiTFSI and LiODFB in $LiFePO_4$ - based batteries for suppressing aluminum corrosion and improving cycling stability. *J Power Sources* Vol. 295 pp. 47–54, 2015.
[9] Zeng Z, Wu B, Xiao L, Jiang X, Chen Y, Ai X, et al. Safer lithium ion batteries based on nonflammable electrolyte. *J Power Sources* Vol. 279, pp. 6–12, 2015.
[10] Ribière P, Grugeon S, Morcrette M, Boyanov S, Laruelle S, Marlair G. Investigation on the fire-induced hazards of Li-ion battery cells by fire calorimetry. *Energy Environ Sci* Vol. 5, pp. 5271–80, 2012.
[11] Ping P, Wang Q, Huang P, Li K, Sun J, Kong D, et al. Study of the fire behav- ior of high-energy lithium-ion batteries with full-scale burning test. *J Power Sources* Vol. 285, pp. 80–9, 2015.
[12] Zhang H, Zhou MY, Lin CE, Zhu BK. Progress in polymeric separators for lithium ion batteries. *RSC Adv* Vol. 5, pp. 89848–60, 2015.
[13] Orendorff CJ. The role of separators in lithium-ion cell safety. *Electrochem Soc Interface* Vol. 21, pp. 61–5, 2012.
[14] Doughty DH, Roth EP. A general discussion of Li ion battery safety. *Elec- trochem Soc Interface* Vol. 21, pp. 37–44, 2012.
[15] https://ul.org/what-we-do/electrochemical-safety/getting-started-electrochemical-safety/what-thermal-runaway
[16] https://www.youtube.com/watch?v=G5-gdx3IleU

[17] https://www.upsbatterycenter.com/blog/lithium-plating/

[18] Zhao L, Watanabe I, Doi T, Okada S, Yamaki J-I. TG-MS analysis of solid elec- trolyte interphase (SEI) on graphite negative-electrode in lithium-ion batter- ies. *J Power Sources* Vol. 161, pp.1275–80, 2006.

[19] Aurbach D, Zaban A, Ein-Eli Y, Weissman I, Chusid O, Markovsky B, et al. Recent studies on the correlation between surface chemistry, morphology, three-dimensional structures and performance of Li and Li-C intercalation anodes in several important electrolyte systems. *J Power Sources* Vol. 68, pp. 91–8, 1997.

[20] Richard M, Dahn J. Accelerating rate calorimetry study on the thermal sta- bility of lithium intercalated graphite in electrolyte. I. Experimental. *J Electrochem Soc* Vol. 146, pp. 2068–77, 1999.

[21] Yang H, Bang H, Amine K, Prakash J. Investigations of the exothermic reactions of natural graphite anode for Li-ion batteries during thermal runaway. *J Electrochem Soc* Vol. 152, pp. A73-A9, 2005.

[22] Liu X, Ren D, Hsu H, Feng X, Xu GL, Zhuang M, et al. Thermal runaway of lithium-ion batteries without internal short circuit. *Joule* Vol. 2, pp. 2047–64, 2018.

[23] Jiang J, Dahn JR. ARC studies of the thermal stability of three different cathode materials: LiCoO2; Li[$Ni_{0.1}$ $Co_{0.8}Mn_{0.1}$]O_2; and $LiFePO_4$, in $LiPF_6$ and LiBoB EC/DEC electrolytes. *Electrochem Commun* Vol.6, pp. 39–43, 2004.

[24] Biensan P, Simon B, Peres J, De Guibert A, Broussely M, Bodet J, et al. On safety of lithium-ion cells. *J Power Sources* Vol. 81, pp. 906–12, 1999.

[25] Wang Y, Jiang J, Dahn J. The reactivity of delithiated Li(Ni1/3Co1/3Mn1/3)O_2 , Li($Ni_{0.8}Co_{0.15}Al_{0.05}$)O_2 or $LiCoO_2$ with non-aqueous electrolyte. *Electrochem Commun* Vol. 9, pp. 2534–40, 2007.

[26] Huang Y, Lin YC, Jenkins DM, Chernova NA, Chung Y, Radhakrishnan B, et al. Thermal stability and reactivity of cathode materials for Li-ion batteries. *ACS Appl Mater Interfaces* Vol. 8, pp. 7013–21, 2016.

[27] Zhang Z, Fouchard D, Rea J. Differential scanning calorimetry material studies: implications for the safety of lithium-ion cells. *J Power Sources* Vol. 70, pp. 16–20, 1998.

[28] Wang Q, Sun J, Chen C. Thermal stability of delithiated $LiMn_2O_4$ with elec- trolyte for lithium-ion batteries. *J Electrochem Soc* Vol. 154, pp. A263-A7, 2007.

[29] Martha SK, Haik O, Zinigrad E, Exnar I, Drezen T, Miners JH, et al. On the thermal stability of olivine cathode materials for lithium-ion batteries. *J Elec-trochem Soc* Vol. 158, pp. A1115-A22, 2011.

[30] Joachin H, Kaun TD, Zaghib K, Prakash J. Electrochemical and thermal studies of carbon-coated $LiFePO_4$ cathode. *J Electrochem Soc* Vol. 156, pp. A401-A6, 2009.

[31] Jiang J, Dahn JR. ARC studies of the thermal stability of three different cath- ode materials: $LiCoO_2$; Li[$Ni_{0.1}Co_{0.8}Mn_{0.1}$]O_2; and $LiFePO_4$, in $LiPF_6$ and LiBoB EC/DEC electrolytes. *Electrochem Commun* Vol. 6, pp. 39–43, 2004.

[32] MacNeil D, Dahn J. The reaction of charged cathodes with nonaqueous solvents and electrolytes: I. $Li_{0.5}CoO_2$. *J Electrochem Soc* Vol. 148, pp. A1205-A10, 2001.

[33] Arai H, Tsuda M, Saito K, Hayashi M, Sakurai Y. Thermal reactions between delithiated lithium nickelate and electrolyte solutions. *J Electrochem Soc* Vol. 149, pp. A401-A6, 2002.

[34] Ping P, Kong D, Zhang J, Wen R, Wen J. Characterization of behaviour and hazards of fire and deflagration for high-energy Li-ion cells by over-heating. *J Power Sources* Vol. 398, pp. 55–66, 2018.

[35] Feng X, Ouyang M, Liu X, Lu L, Xia Y, He X. Thermal runaway mechanism of lithium ion battery for electric vehicles: a review. *Energy Storage Mater* Vol. 10, pp. 246–67, 2017.

[36] Gong J, Wang Q, Sun J. Thermal analysis of nickel cobalt lithium manganese with varying nickel content used for lithium ion batteries. *Thermochim Acta* Vol. 655, pp. 176–80, 2017.

[37] Bak SM, Hu E, Zhou Y, Yu X, Senanayake SD, Cho SJ, et al. Structural changes and thermal stability of charged $LiNi_xMn_yCo_zO_2$ cathode materials studied by combined in situ time-resolved XRD and mass spectroscopy. *ACS Appl Mater Interfaces* Vol. 6, pp. 22594–601, 2014.

[38] Huang P, Ping P, Li K, Chen H, Wang Q, Wen J, et al. Experimental and modeling analysis of thermal runaway propagation over the large format energy storage battery module with $Li_4Ti_5O_{12}$ anode. *Appl Energy* Vol. 183, pp. 659–73, 2016.

[39] Röder P, Baba N, Wiemhöfer HD. A detailed thermal study of a Li[$Ni_{0.33}Co_{0.33}Mn_{0.33}$]O_2/$LiMn_2O_4$ - based lithium ion cell by accelerating rate and differential scanning calorimetry. *J Power Sources* Vol. 248, pp. 978–87, 2014.

[40] Spotnitz R, Franklin J. Abuse behavior of high-power, lithium-ion cells. *J Power Sources* Vol. 113, pp. 81–100, 2003.

[41] Röder P, Baba N, Friedrich K, Wiemhöfer H-D. Impact of delithiated Li 0 FePO 4 on the decomposition of $LiPF_6$ -based electrolyte studied by accelerating rate calorimetry. *J Power Sources* Vol. 236, pp.151–7, 2013.

[42] Ping P, Wang Q, Huang P, Sun J, Chen C. Thermal behaviour analysis of lithi- um-ion battery at elevated temperature using deconvolution method. *Appl Energy* Vol. 129, pp. 261–73, 2014.

[43] Electric Vehicle Safety Guide, China Association of Automobile Manufacturers (CAAM), China Automotive Power Battery Industry Innovation Alliance, China Electric Vehicle Charging Infrastructure Promotion Alliance, 2019.

WASTE HEAT RECOVERY IN AN ORIGINAL DESIGN COMMERCIAL CONVECTION OVEN

Z. Kahraman[*,1], M. Hacı[1], K. İçibal[1] and H.S. Soyhan[2,3]

1. Öztiryakiler Madeni Eşya San. ve Tic. A.Ş, R&D Technology Center, Büyükçekmece, İstanbul, Türkiye; email: zkahraman@oztiryakiler.com.tr
2. Fire and Combustion Research Centre, Esentepe Campus, Sakarya University, Sakarya, Türkiye
3. Team-San Co., Sakarya University, Teknokent, Serdivan, Sakarya, Türkiye

Abstract

Commercial convection ovens are used in commercial kitchens for the traditional cooking of various dishes, with fan and hot air blowing structures in different models and capacities. With the increase in energy prices in recent years, consumers have turned to energy-saving products, and in this direction, studies on energy efficiency are increasing in many areas. In this study, for the first time in our country, the energy required for heating the water in the steam generator of the original designed commercial convection oven prototype working with gas (G20 – natural gas) was achieved with the flue gas waste heat recovery system. Tests and evaluations have been conducted concerning EN 203-1 and EN 203-2-2 standards on an innovative gas commercial oven prototype. In addition to the development of a uniquely designed flue gas waste heat recovery system for the environmentally friendly innovative commercial oven to contribute to energy savings with studies based on R&D systematics, the reduction of pollutant emissions compared to our existing gaseous commercial convection ovens has been achieved through activities within the scope of university-industry cooperation.

Keywords: Commercial convection oven, waste heat recovery, energy efficiency

1 INTRODUCTION

Commercial cooking ovens are used as electric or gas (natural gas or LPG) in different models and capacities of all cooking establishments. Studies on energy recovery systems about energy efficiency have found a vast place in kitchens in recent years [1-4].

In our country, there is no study on a product that uses waste heat in the field of commercial ovens. When the publications on gas and electric convection ovens are examined, there are studies mainly on household convection ovens [5-9].

A test geometry was developed by Park and the working group concerning an actual product, including the oven cavity, fan casings, fans, and burners. Experimental data confirmed the simulations; they stated that the most significant temperature difference was 2.5%, and the difference in mean temperature was 0.44%. A total of 15 different cases were examined using different hole positions in the fan casing. The different hole positions changed the direction of the velocity vector in the holes, and as a result, the flow pattern and temperature distribution inside the oven cavity also changed significantly. Thermal performance was evaluated according to the oven cavity's average temperature and temperature homogeneity. The distribution of the temperature and velocity vector in the vertical plane in the center of the fan case is given in Figure 1. according to two different situations (the first case is open on all inner surfaces, and in the second case, the hole on the lower right is closed) [5].

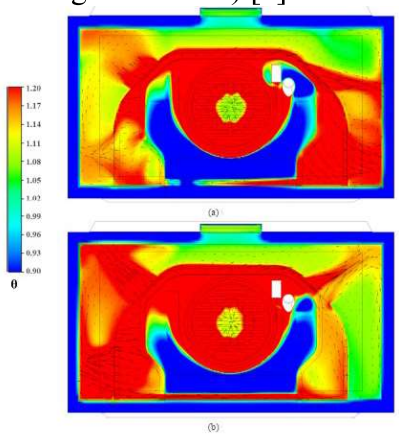


Figure 1. Distribution of the temperature and speed vector according to two different situations in the vertical plane in the center of the fan casing [5].

Various studies related to baking ovens are summarized below [10-16];

T.M. Various evaluations were made by Alkhamis and his team on using waste heat in the kitchen oven. In this study, they investigated waste heat recovery from flue gas using a coil-type heat exchanger (Ø1 cm copper pipe) designed and manufactured in a diesel fuel-fired oven on the university campus. As a result of the studies, they emphasized that more than 60% heat recovery can be achieved by utilizing the waste heat of the chimney and that studies in this direction should be developed [10].

C.O. Diaz-Ovallea and his working group emphasized the importance of a preheating step in convection ovens to achieve a uniform temperature. They stated that the energy consumption increased during the preheating phase and was proportional to the preheating time. The preheat time depends on the set point temperature. Evaluations were made with 3-D computational fluid dynamics (CFD) simulations and experimental measurements at different temperatures and geometric variants of the baffle in front of the fan. Analyses were conducted to reduce the preheating time in a convection oven using CFD. The geometry of the pilot scale convection oven is given in Figure 2 [11].

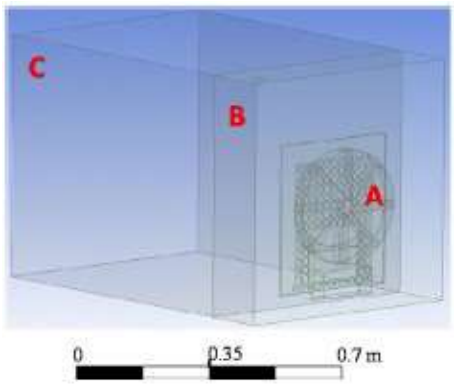


Figure 2. Pilot scale convection oven geometry [11].

Although studies on waste heat recovery systems have gained importance in recent years, studies in various fields are also increasing [17-24].

C. Forman and his working group evaluated the waste heat temperatures, including the sector shares of waste heat distribution in various sectors, in 3 different ranges below 100°C, between 100 and 299°C, and above 300°C.

Sectoral shares of waste heat distribution are given in Figure 3. [17].

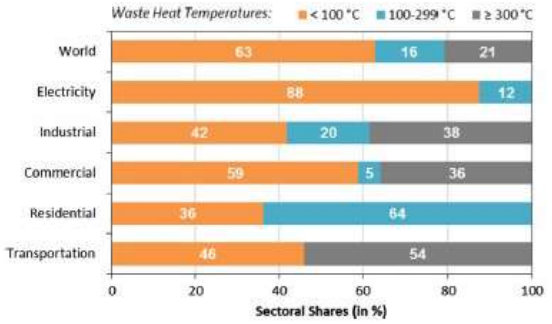


Figure 3. Sectoral shares of waste heat distribution [17].

Brückner and his working group evaluated industrial waste heat's heating and cooling applications. They examined the technical and economic potentials of heat conversion technologies. Possible sources of waste heat at different industrial processes and operating temperatures and low-temperature processes that can be provided with waste heat are evaluated. They noted the need for more research on heat exchange technologies to recover waste heat, focusing on system integration, design, and market applications.

The classification of waste heat recovery technologies is given in Figure 4 [18].

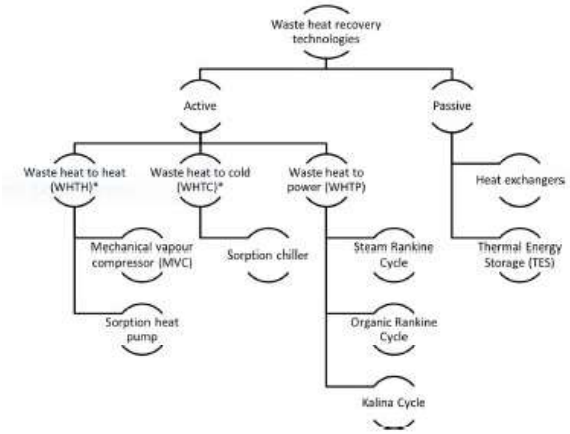


Figure 4. The classification of waste heat recovery technologies [18].

2 MODELING

With the studies based on R&D systematics, the original design studies of the combustion system, heater pipes, and chimney part of the innovative prototype were carried out. Simulation studies were used effectively in the design verification phase to ensure the most efficient combustion conditions of the designed combustion system and heater pipes compared to natural gas.

Combustion analyses were carried out by parametric study for different operating conditions. In the originally designed commercial convection oven prototype, the most suitable design was obtained for the combustion system, heater pipes, and the flue waste gas heat recovery. As a result of the experiments, the most effective working range of the system was determined.

2.1 Model Validity

The uniquely designed combustion system of the gas commercial convection oven prototype has a boundary layer on the wall areas. Studies were carried out by applying "sweep mesh" to a particular flow region.

The initially designed combustion system model of the innovative prototype consists of the following parts;

- combustion chamber,
- heater pipes,
- chimney part.

Various views of the existing gas model commercial convection oven before the R&D activities are given in Figure 4.

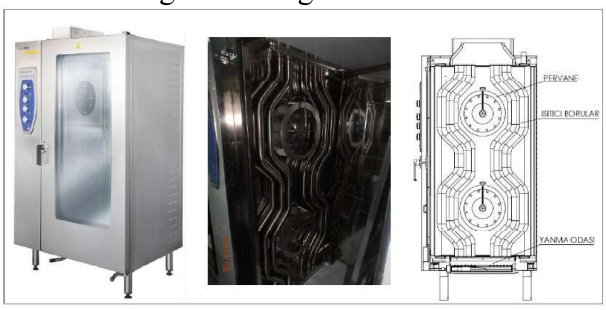


Figure 4. Various views of the existing gas commercial convection cooking oven.

The heat generated from the burners forming the combustion system through simulation studies is blown in by two 300 mm diameter fans. The air velocity entrained into the oven was taken as 0.15 m/s, and two conditions and four different heat transfer values were investigated. The heat was transferred to the ambient air by convection, and the temperature of the prototype oven interior unit was examined.

Examples of simulation studies in the combustion system of the designed initially commercial convection oven prototype are given in Figure 5-8.

Single burner commercial convection oven prototype analyses are given in Figure 5 and Figure 6.

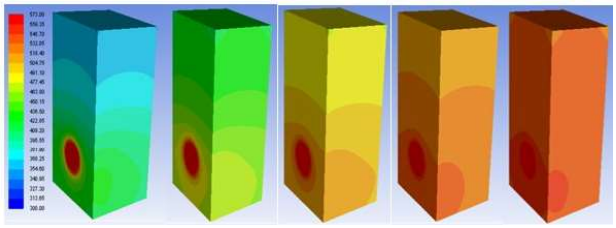


Figure 5. Simulation of temperature change during the first 5th, 10th, 20th, 30th, and 40th seconds of the adiabatic oven prototype (single burner).

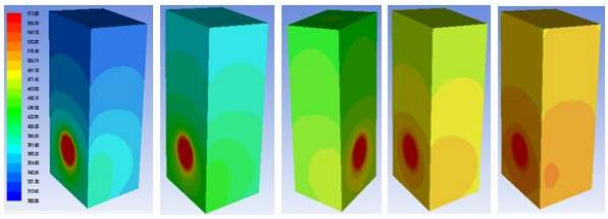


Figure 6. Simulation of temperature change at 5th, 10th, 20th, 30th and 40th seconds (single burner) with a convection coefficient of 0.1 (W/m^{2}K).

Double burner commercial convection oven prototype analyses are given in Figure 7 and Figure 8.

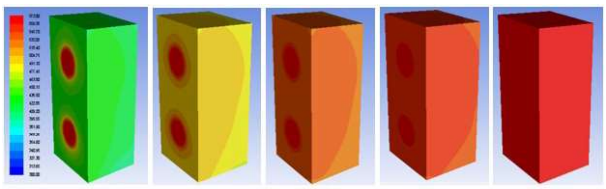


Figure 7. Simulation of temperature change during the first 5th, 10th, 16th, 20th, and 30th seconds of the adiabatic oven prototype (double burner).

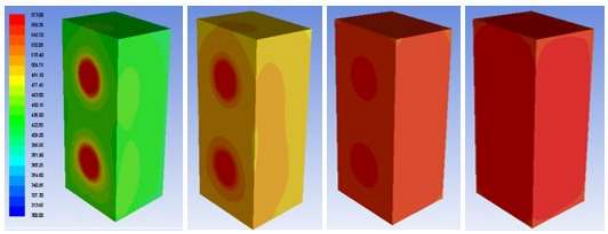


Figure 8. Simulation of temperature change at 5th, 10th, 20th and 30th seconds (double burner) with a convection coefficient of 0.1 (W/m^{2}K).

The simulation data determined that the double burner system provides a more homogeneous temperature distribution compared to the single burner system.

As a result of the design verification studies, the drawing of the original designed gas commercial convection oven prototype shown in Figure 9. was obtained.

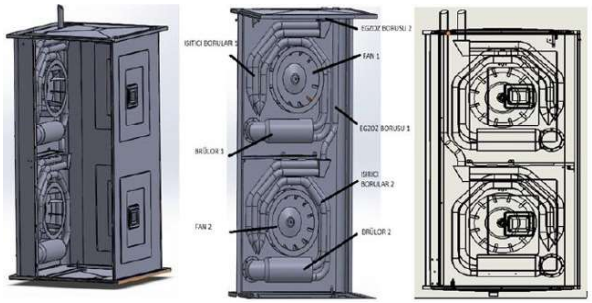


Figure 9. The original design gas commercial convection oven prototype draft drawing.

Following the design verification data, the manufacturing and assembly stages of the originally designed prototype were completed. After this stage, the testing and evaluation stage started.

3 EXPERIMENTAL STUDIES

The originally designed commercial convection oven prototype's main body is stainless steel (AISI 304).

The chemical composition of the AISI 304 stainless steel material is given in Table 1.

Table 1: Chemical composition (%) of AISI 304.

	Elements			
Chemical composition (%)	C	Si	P	S
	0.053	0.047	0.031	0.002
	Elements			
	Ni	Cr	Mn	Cu
	8.05	18.11	1.05	0.07

The visual of the test phase with the gas analyzer for the commercial convection oven prototype is given in Figure 10.



Figure 10. The test phase image of the initially designed gas commercial convection oven prototype with a gas analyzer.

To increase energy efficiency in the innovative commercial oven prototype, temperature measurements were made with a thermal camera on the innovative prototype shown in Figure 11.

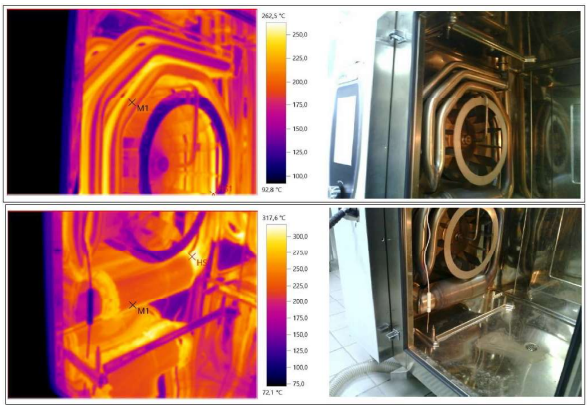


Figure 11. Temperature measurements with a thermal camera in the combustion system of a prototype commercial convection oven with a unique design.

The visuals of the flue gas temperature on the originally designed commercial convection oven prototype are given in Figure 12. and Figure 13.



Figure 12. Test photograph of flue gas temperature measurement (up to 307°C) of a standard model gas commercial convection oven.



Figure 13. Test photograph of flue gas temperature (max. 145.2°C) measurement of a prototype gas commercial convection oven with the original design.

While the flue gas temperature of the standard convection oven was measured as max. 307°C, the flue gas temperature of the uniquely designed commercial convection oven prototype was measured as max. 145.2°C.

With the initially designed prototype, the "combustion chamber", which is one in the existing gas commercial convection cooking oven heater unit, was increased to two; while the number of propellers was not changed, the length of the heater pipes that circulate the exhaust gases in the heater unit was increased.

In the originally designed system, the heating pipes circulated as two sections were then combined at a single point, and these combined gases were recirculated in the system and recirculated in a way to evaporate the water in a chamber that could be found in the boiler and it was designed to make the most of the heat obtained.

4 RESULTS

With the design verification studies, an effective placement was made for the double burner in the commercial convection oven prototype working with natural gas, and the flue gas path circulating in the system was increased with a unique design.

The time to reach the standard firing temperature provided in the current gas commercial convection oven conditions is reduced in the innovative prototype with a unique design, thus contributing to its efficient operation. Thus, it contributed to the savings in fuel consumption of the initially designed prototype. This reduction in fuel consumption has also resulted in improvements in total pollutant emissions.

According to the analysis results at the test and evaluation phase with the innovative prototype, data were obtained to ensure a 30% reduction in pollutant emission values and fuel consumption.

In the initially designed gas commercial convection oven prototype, the flue gas temperature was reduced by 52.7% compared to the existing system.

With the test and evaluation studies, the commercial convection oven prototype that provides flue gas waste heat recovery was successfully obtained in line with international standards (EN 203-1 and EN 203-2-2). With this study, for the first time in our country, the gas commercial convection oven prototype has been obtained by R&D systematics to reduce pollutant emissions and energy performance.

ACKNOWLEDGEMENTS

This study was prepared from the project study numbered 3160092 within the scope of TÜBİTAK-TEYDEB 1501 coded Industry Research Technology Development and Innovation Projects Support Programme. We would like to thank TÜBİTAK-TEYDEB Transport, Defense, Energy and Textile Technologies Group (USETEG) for their contribution to the project work.

REFERENCES

[1] K. Subramanian, S.S. Chopra, C.M. Wharton, W. Yonge, J. Allen, R. Stevens, S. Fahy, P. S. Milindi, Mapping the food waste-energy-water-emissions nexus at commercial kitchens: A systems approach for a more sustainable food service sector, *Journal of Cleaner Production*, Vol. 301, 126856, 2021.

[2] I. Schestak, J. Spriet, D. Styles, A.P. Williams, Emissions down the drain: Balancing life cycle energy and greenhouse gas savings with resource use for heat recovery from kitchen drains, *Journal of Environmental Management*, Vol. 271, 110988, 2020.

[3] Y. Wang, C. Shen, P. Sun, C. Li, C. Zhang, Utilization of waste heat from commercial kitchen exhaust for water heating and dish drying, *Journal of Building Engineering*, Vol. 32, 101788, 2020.

[4] K. Wang, N. Li, J. Peng, X. Wang, C. Wang, M. Wang, A highly efficient solution for thermal compensation of ground-coupled heat pump systems and waste heat recovery of kitchen exhaust air, *Energy and Buildings*, Vol. 138, pp. 499-513, 2017.

[5] S. H. Park, Y. H. Kim, Y. S. Kim, Y. G. Park, Man Yeong Ha, Numerical study on the effect of different hole locations in the fan case on the thermal performance inside a gas oven range, *Applied Thermal Engineering*, Vol. 137, pp. 123-133, 2018.

[6] U. Kokolj, L. Skerget, J. Ravnik, A numerical model of the shortbread baking process in a forced convection oven, *Applied Thermal Engineering*, Vol. 111, pp. 1304-1311, 2017.

[7] J. Smolka, Z. Bulinski, A. J. Nowak, The experimental validation of a CFD model for a heating oven with natural air circulation, *Applied Thermal Engineering*, Vol. 54, pp. 387-398, 2013.

[8] H. Mistry, S. Ganapathi-subbu, S. Dey, P. Bishnoi, J. L. Castillo, Modeling of transient natural convection heat transfer in electric ovens, *Applied Thermal Engineering*, Vol. 26, pp. 2448-2456, 2006.

[9] H. Mistry, S. Ganapathi-subbu, S. Dey, P. Bishnoi, J. L. Castillo, A methodology to model flow-thermals inside a domestic gas oven, *Applied Thermal Engineering*, Vol. 31, pp. 103-111, 2011.

[10] T. M. Alkhamis, M. A. Alhusein, M. M. Kablan, Utilization of waste heat from the kitchen furnace of an enclosed campus, *Energy Conversion and Management*, Vol. 39, pp. 1113-1119, 1998.

[11] C. O. Diaz-Ovallea, R. Martinez-Zamoraa, G. Gonzalez-Alatorreb, L. Rosales-Marinesc, R. Lesso-Arroyoda, An approach to reduce the preheating time in a convection oven via CFD simulation, *Food and Bioproducts Processing*, Vol. IO2, pp. 98-106, 2017.

[12] M. J. Blikra, D. Skipnes, A. H. Feyissa, Model for heat and mass transport during cooking of cod loin in a convection oven, *Food Control*, Vol. 102, pp. 29–37, 2019.

[13] M. Pinelli, A. Suman, Thermal and fluid dynamic analysis of an air-forced convection rotary bread-baking oven by means of an experimental and numerical approach, *Applied Thermal Engineering*, Vol. 117, pp. 330-342, 2017.

[14] J. K. Carson, J. Willix, M. F. North, Measurements of heat transfer coefficients within convection ovens, *Journal of Food Engineering*, Vol. 72, pp. 293–301, 2006.

[15] E. Bottani, A. Volpi, An analytical model for cooking automation in industrial steam ovens, *Journal of Food Engineering*, Vol. 90, pp. 153–160, 2009.

[16] A. Garg, L. Malafronte, E. J. Windhab, Baking kinetics of laminated dough using convective and microwave heating, *Food and Bioproducts Processing*, Vol. II5, pp. 59-66, 2019.

[17] C. Forman, I. K. Muritala, R. Pardemann, B. Meyer, Estimating the global waste heat potential, *Renewable and Sustainable Energy Reviews*, Vol. 57, pp. 1568-1579, 2016.

[18] S. Brückner, S. Liu, L. Miro, M. Radspieler, L. F. Cabeza, E. Lavemann, Industrial waste heat recovery technologies: An economic analysis of heat transformation technologies, *Applied Energy*, Vol. 151, pp. 157-167, 2015.

[19] O. Farhat, J. Faraj, F. Hachem, C. Castelain, M. Khaled, A recent review on waste heat recovery methodologies and applications: Comprehensive review, critical analysis and potential recommendations, *Cleaner Engineering and Technology*, Vol. 6, 100387, 2022.

[20] Y. Men, X. Liu, T. Zhang, A review of boiler waste heat recovery technologies in the medium-low temperature range, *Energy*, Vol. 237, 121560, 2021.

[21] S. Mukherjee, A. Asthana, M. Howarth, R. Meniell, Waste heat recovery from industrial baking ovens, *Energy Procedia*, Vol. 123, 321-328, 2017.

[22] Z. Y. Xu, R. Z. Wang, C. Yang, Perspectives for low-temperature waste heat recovery, *Energy*, Vol. 176, 1037-1043, 2019.

[23] A. Kumar, D. Rakshit, A critical review on waste heat recovery utilization with special focus on Organic Rankine Cycle applications, *Cleaner Engineering and Technology*, Vol. 5, 100292, 2021.

[24] H. Jouhara, N. Khordehgah, S. Almahmoud, B Delpech, A. Chauhan, S. A. Tassou, Waste heat recovery technologies and applications, *Thermal Science and Engineering Progress*, Vol. 6, 268-289, 2018.

EVALUATION OF NATURAL GAS CONSUMPTION IN TURKEY

S.Y. Kandemir[1], E. Güler[2] and M.H. Ahmadi[3]

1. Faculty of Engineering, Bilecik Şeyh Edebali University, Bilecik, Turkey; email: syerel@gmail.com
2. Faculty of Engineering, Bilecik Şeyh Edebali University, Bilecik, Turkey; email: ezgi.guler@bilecik.edu.tr
3. Faculty of Mechanical Engineering, Shahrood University of Technology, Shahrood, Iran; mohammadhosein.ahmadi@gmail.com

Abstract

Natural gas, one of the primary energy sources, has been a preferred energy source in recent years due to its ease of use, low cost, and environmental friendliness. The share of natural gas in electricity generation, domestic heating, and industrial activities are pretty high. In this study, Fourier Analysis, Winters Method, and Seasonal Autoregressive Integrated Moving Average (SARIMA) model were used to estimate monthly natural gas consumption in Turkey. It was aimed to obtain predicted monthly natural gas consumption data via the most appropriate forecasting method. One hundred thirty-two monthly data sets between January 2010 and December 2020 were divided into modeling and test sets. Models were prepared for each forecasting method using the modeling set between January 2010 and December 2017. The resulting forecasting models were applied to the data within the test set. The prediction success of the forecasting models has been measured by mean absolute error (MAE), mean square error (MSE), and means absolute percentage error (MAPE) performance evaluation criteria. With the "MAE: 344.390; MSE: 218024.354; MAPE: 9.401%" values for the test set, it was concluded that Winters' Method is the most appropriate forecasting method. Therefore, the Winters' Method made monthly natural gas consumption estimation for the 60 months (between January 2021 and December 2025).

Keywords: Estimation, Fourier analysis, Monthly Natural Gas consumption, SARIMA model, Winters' Method.

1 INTRODUCTION

Energy resources are one of the essential inputs in the economic development of countries. Energy is an essential indicator of countries' powers and developments in the world of global competition [1,2]. Despite the rapidly increasing world population, there was a rapid increase in energy consumption, making it necessary to use the existing energy more planned [3,4]. Due to the depletion of energy resources in today's economies, energy must be obtained both less costly and used rationally. In this context, the countries' national energy policies should be designed to provide timely, reliable, cost-effective, environmentally friendly, and high-quality [5].

Natural gas, which is non-polluting environmentally friendly compared to oil and solid fuel, an energy source, is used in many electricity generations and industry areas, especially in heating, due to its high combustion efficiency, being easily storable [6]. Natural gas consumption varies seasonally. Demand for natural gas is significantly higher in winter than in summer.

Forecasting is essential for natural gas consumption, which may vary depending on the time factor. Estimations should be made via various statistical methods. Most of the demand forecasting studies in the literature are performed "annually". However, since natural gas consumption estimation is under the effect of seasonality, it is not preferred to estimate via annual studies [7]. Therefore, demand for natural gas in Turkey with the selected demand forecasting methods in this study was estimated monthly.

This study evaluated forecasting models using Turkey's 132-month natural gas consumption data between January 2010 and December 2020. Forecasting methods are Fourier Analysis, Winter's multiplicative Method, and Seasonal Autoregressive Integrated Moving Average (SARIMA) model. Mean square error (MSE) and mean absolute error (MAE) model performance criteria were calculated. According to the results of model performance criteria, the most appropriate forecasting method was obtained. The following months' predicted

natural gas consumption data were calculated using the most appropriate forecasting method.

2 MATERIAL AND METHODS

2.1 Data Source

In this study, monthly natural gas consumption data was determined as the dependent variable, months of the year where the independent variable. The natural gas consumption data from "January 2010 to December 2020 (132 months)" have been retrieved from http://www.jodidb.org/ [8].

2.2 Forecasting Methods

Fourier Analysis

Fourier analysis involves the empirical approach to a function containing trigonometric terms using discrete time series. For the Fourier analysis to be applied in a discrete-time series, it must be defined with few observations. When the problem is considered as one-dimensional time series, the Fourier series is determined according to yt (observation value at time t) against increasing values of t (time) variable. This analysis is called "curve fitting with sinusoidal functions" [9,10]. The Fourier analysis regression equation is reached using the obtained regression coefficients in Eq. 1.

$$\hat{y}_t = a_0 + 2\sum_{k=1}^{K} a_k \cos(wkt) + 2\sum_{k=1}^{K} b_k \sin(wkt) + e \quad (1)$$

Where;

a_0, a_k, and b_k: These parameters are to be determined from the model and the angular frequency w is related to the basic period t ($wT=2\pi$);

T: Period;

N: Number of observations;

k: This value depends on N;

$\hat{y}_t$: It gives the predicted value at any time t,

e: The random error at time t.

Matrix equations are required to obtain a_0, a_k, and b_k parameters in the regression model. Matrix equations are given in Eq. 2, Eq. 3, Eq. 4, and Eq. 5, respectively. Matrix A is called a matrix of coefficients, and matrix G is called an observation matrix. N and n matrices are product matrices. The x matrix is the unknowns matrix [11].

$$A = \begin{pmatrix} 1 & 2\cos(wt_0) & 2\sin(wt_0) \\ 1 & 2\cos(wt_1) & 2\sin(wt_1) \\ \vdots & \vdots & \vdots \\ 1 & 2\cos(wt_{N-1}) & 2\sin(wt_{N-1}) \end{pmatrix} \quad (2)$$

$$n = A^T G \quad (3)$$

$$N = A^T A \quad (4)$$

$$x = N^{-1} n = [a_0 \quad a_1 \quad b_1 \quad a_2 \quad b_2 \quad \dots \quad a_k \quad b_k]^T \quad (5)$$

The regression model equation formed by the "least-squares approach" in Fourier Analysis is given in Eq. 1.

Winters' Method

Winters' Method is frequently used to predict future values for time series showing seasonality. In the Winters' Method, there are three different smoothing parameters related to the model's smoothing constant (α), trend smoothing constant (β), and seasonal smoothing constant (γ), respectively [12]. Winters' Method is examined in 4 types according to the calculation of seasonal indices. These models are multiplicative, additive, modified, and extended [13]. The multiplicative model was used in this study. In the models, seasonality is related to the trend, and proportions are made to reach the seasonally smoothed series [10]. The smoothing parameters were taken as 0.2. Winters' multiplicative method equations are below with Eq. 6, Eq. 7, and Eq 8 [14, 15]. The forecasting equation is given in Eq.9.

$$\text{Level: } y_t^l = \alpha \frac{y_t}{I_{t-L}} + (1-\alpha)(y_{t-1}^l + b_{t-1}) \quad (6)$$

$$\text{Trend: } b_t = \beta(y_t^l - y_{t-1}^l) + (1-\beta) b_{t-1} \quad (7)$$

$$\text{Seasonal: } I_t = \gamma \frac{y_t}{y_t^l} + (1-\gamma) I_{t-L} \quad (8)$$

$$f_{t+m} = (y_t^l + b_t m) I_{t-L+m} \quad (9)$$

Where;

y_t: The observed series,

y_t^l: The smoothed value of the series for the period t,

I: The length of the seasonal cycle (adjustment factor),

L: Season length in a certain period,

b_t: The trend estimation value for the t period of the series gives the seasonal estimate value

for the t period of the series. While $t-1$ sub-index shows the relevant parameter value of the previous month,

$t-L$: Sub-index shows the parameter value of the previous period,

f_{t+m}: The forecast for m-periods into the future

Seasonal Autoregressive Integrated Moving Average (SARIMA) Model

The SARIMA (Seasonal ARIMA) model is often used to follow seasonal influence. The model is built considering the seasonal nature of the time series. The general SARIMA model is expressed as SARIMA (p, d, q) (P, D, Q)$_s$ [16]. The general equation of SARIMA (p, d, q) (P, D, Q)$_s$ model is given in Eq. (10). It can be recognized the symbols as p being "non-seasonal AR order," d being "non-seasonal differencing," q being "nonseasonal MA order," P being "seasonal AR order," D being "seasonal differencing," Q being "seasonal MA order," and S is "time span for recurring seasonal pattern" [17].

$$\varphi(B)\varphi(B^s)(1-B)^d(1-B^s)^D(Z_t-\mu)=\theta(B)\theta(B^s)\varepsilon_t \quad (10)$$

Where;

$\varphi(B)=1-\varphi_1 B-\varphi_2 B^2-\cdots-\varphi_P B^p$:

The order p of AR term;

$\theta(B)=1-\theta_1.B-\theta_2.B^2-\cdots-\theta_P.B^p$:

The order q of MA term;

$\varphi(B^s)=1-\varphi_1 B^s-\varphi_2 B^{2s}-\cdots\varphi_P B^{Ps}$:

The order P of seasonal AR term;

$\theta(B^s)=1-\theta_1 B^s-\theta_2 B^{2s}-\cdots\theta_Q B^{Qs}$:

The order Q of seasonal MA term;

ε_t ~ $(0,\sigma^2)$;

d : It is a non-negative integer,

s : It is the integer always greater than one,

Note that $\mu=0$, if $d>0$ *or* $D>0$ [18].

Akaike Information Criterion (AIC) and Bayesian Information Criterion (BIC) are also crucial for SARIMA (p, d, q) (P, D, Q)$_s$ models. In this paper, BIC was used. BIC says to select the SARIMA (p, d, q) (P, D, Q)$_s$ model, which minimizes. In Eq. (11); lnL is the natural logarithm of the predictive likelihood function. $k=p+q$ is the total number of parameters, and n is the number of observations in the model.

$$BIC=-2\,lnL+2kln(n) \quad (11)$$

The model with the minimum values of BIC can be considered as the best SARIMA (p, d, q) (P, D, Q)s model [19, 20]. For the selection of the most suitable SARIMA model, the Residual Autocorrelation Function (ACF) and Residual Partial Autocorrelation Function (PACF) graphs are also examined [21].

2.3 Model Performance Criteria

In the literature, forecasting models' performance efficiency is evaluated using criteria such as MAE, RMSE, MSE, MAPE, etc. [22, 23]. This study used MAE, MSE, and MAPE criteria to evaluate the success of three forecasting models. These criteria are calculated using Eq. (12-14).

$$MAE=\frac{1}{n}\sum_{t=1}^{n}|y_t-\hat{y}_t| \quad (12)$$

$$MSE=\frac{1}{n}\sum_{t=1}^{n}(y_t-\hat{y}_t)^2 \quad (13)$$

$$MAPE=\frac{1}{n}\sum_{t=1}^{n}\frac{|y_t-\hat{y}_t|}{y_t}x100\% \quad (14)$$

Where;

y_t : the actual value at a time (t),

$\hat{y}_t$: the predicted value of the model.

n : the number of observation data [24].

3 ANALYSIS RESULTS

This study examined natural gas consumption data in "modeling set" and "test set" groups. Forecasting models were created for the data set in the modeling set, and the created forecasting models were applied to the test set. The data set for the 96 months from January 2010 to December 2017 were accepted as the modeling. Data for the 36 months from January 2018 to December 2020 were the test set. The graph of the monthly natural gas consumption dataset is given in Figure 1.

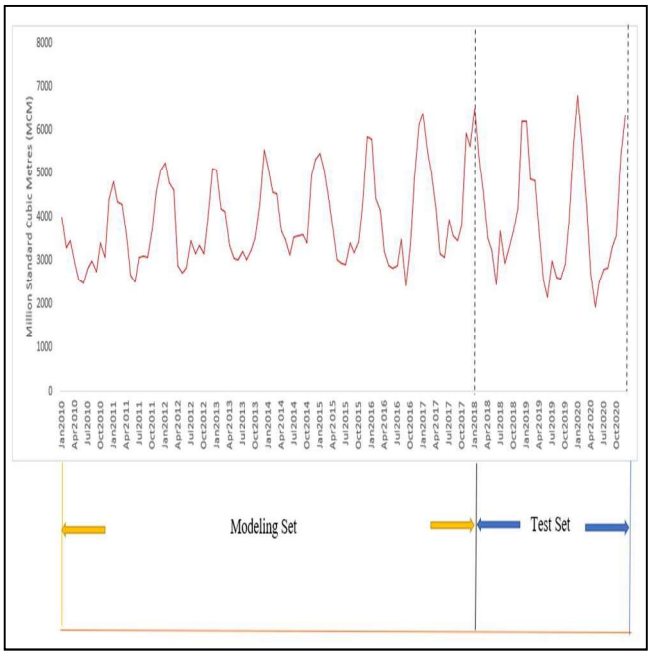


Figure 1. Actual Natural Gas consumption values in Turkey (January 2010-December 2020)

This study used different forecasting methods described in Section 2 to evaluate natural gas consumption. These methods are Fourier Analysis, Winters' Method, and the SARIMA model.

The Fourier analysis used sinus and cosine matrix transformations as an estimation tool [9]. In the Fourier series, "w" is the only variable affecting the results. This study shows significant yearly seasonality since natural gas consumption data, T = Period = 12.

Winters' Method, α, β, and γ parameters were determined as 0.2, respectively [25, 26]. The parameter values are automatically determined as 0.2. [27]. There are also studies where these parameters have been optimized, and the model has been established [28]. In this paper, α, β, and γ parameters were taken as 0.2, considering the general judgment.

In applying the SARIMA model, a selection can be made from several alternative models specified [24]. In this paper, BIC values were considered for selecting the best among some SARIMA models whose parameters were determined. The residues' ACF and PACF plots were examined for the obtained model, and the model's suitability was investigated. Alternative SARIMA models and normalized BIC values obtained are given in Table 1.

Table 1. Normalized BIC values of alternative SARIMA models

Some of the Alternative SARIMA Models	Normalized BIC Values
SARIMA(1,1,1) $(0,1,0)_{12}$	12.377
SARIMA(1,1,1) $(1,1,0)_{12}$	12.321
SARIMA(1,1,0) $(0,1,0)_{12}$	12.407
SARIMA(1,1,2) $(0,1,0)_{12}$	12.442
SARIMA(1,1,1) $(1,0,1)_{12}$	12.347
SARIMA(1,1,0) $(1,1,0)_{12}$	12.338

As seen in Table 1, the model produced in terms of the minimized BIC value (12.321) was SARIMA(1,1,0) $(1,1,0)_{12}$. The residual ACF plots and PACF of SARIMA(1,1,0) $(1,1,0)_{12}$ were given in Figure 2.

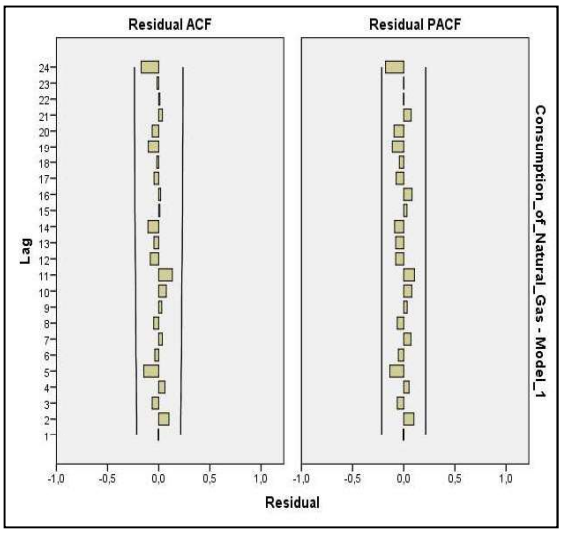


Figure 2. Residual ACF and PACF plots of the SARIMA(1,1,0) (1,1,0)12 model

There was no excess value in the plots in Figure 2 [29]. For this reason, the SARIMA(1,1,0) $(1,1,0)_{12}$ model was said to have a good fit.

These three different forecasting methods were applied to the monthly natural gas consumption data in the modeling set shown in Figure 1, and the models were defined in this way. The data in the test set was used to evaluate the performance of the built forecasting models. The performance of forecasting methods as graphically was given in Figure 3 for the test set.

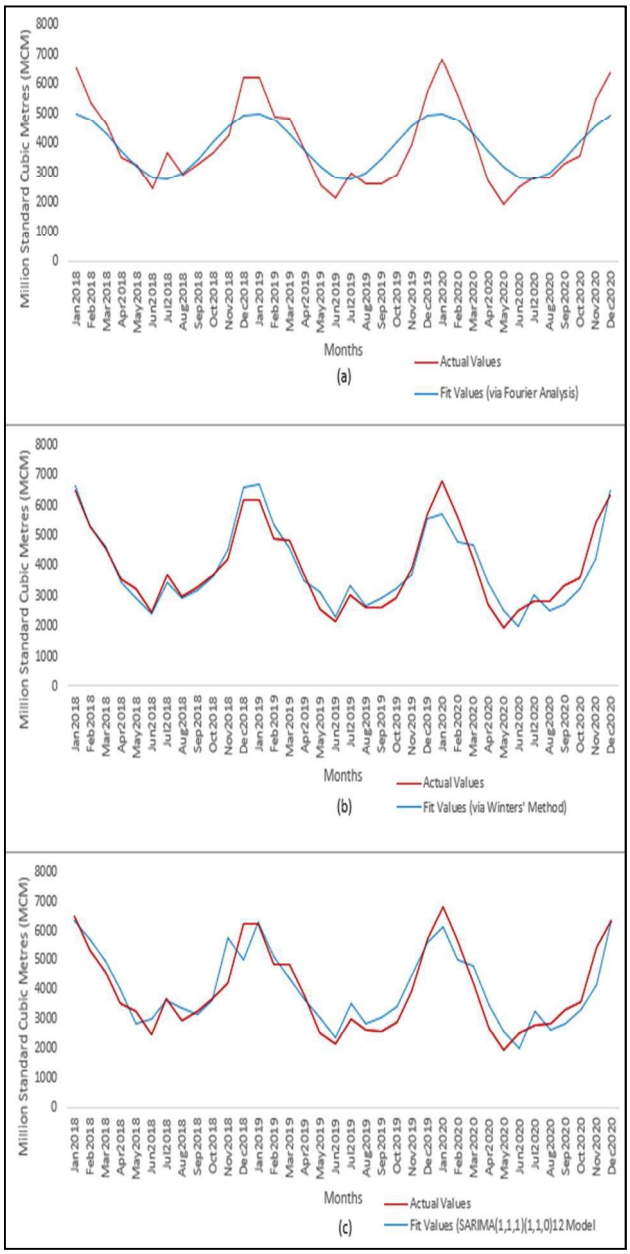


Figure 3. Obtained fit values via forecasting models for the test set

MAE, MSE, and MAPE were calculated from the model performance evaluation criteria defined in Section 2. The purpose of calculating MAE, MSE, and MAPE values in both modeling and test set was to interpret the changing criteria values. The calculation results are given in Table 2. The modeling set's MAE, MSE, and MAPE values were smaller than the test set and gave meaningful results indicating the modeling's success. Also, such a result was encountered because the number of periods in the test set was less.

Table 2. Model performance evaluation criteria for modeling and test set

Criteria	Fourier Analysis	Winters' Method	SARIMA Model
MAE	429.896	266.203	321.309
MSE	306757.183	126726.369	181397.284
MAPE	11.461%	6.913%	8.408%
	Test Set		
Criteria	Fourier Analysis	Winters' Method	SARIMA Model
MAE	605.088	344.390	443.759
MSE	593513.859	218024.354	338414.297
MAPE	15.796%	9.401%	12.704%

Although other evaluation criteria are essential, at this point, especially the MAPE values have been examined in detail. Because the MAPE values have value ranges for the quality of the forecasting models. For MAPE value;

if it is below 10%, “High”

if it is between 10% and 20%, “Good”

if it is between 20% and 50%, “Reasonable”

if it is above 50%, “Insufficient” model accuracy is mentioned [30].

Winters' Method has a high estimation success level (Test set MAPE value: 9.401%; MAE Value: 344.390; MSE Value: 218024.354). This paper's primary purpose is to select the best model among the forecasting methods used and estimate Turkey's future natural gas consumption. In this context, the predicted values were obtained using the Winters' Method for the 60 months between January 2021 and December 2025. The predicted natural gas consumption values are given in Table 3.

Table 3. Predicted Natural Gas consumption values (MCM) (January 2021- December 2025)

Months/Years	2021	2022	2023	2024	2025
Jan	6640	6830	7020	7210	7400
Feb	5302	5453	5604	5755	5906
Mar	4537	4666	4796	4925	5054
Apr	3359	3454	3549	3644	3740
May	2737	2725	2800	2875	2950
Jun	2650	2814	2892	2969	3046
Jul	3402	3498	3594	3690	3786
Aug	3260	3352	3443	3535	3626
Sep	3419	3515	3611	3707	3803
Oct	3768	3873	3979	4084	4189
Nov	5203	5348	5494	5639	5784
Dec	6464	6644	6824	7004	7184

4 CONCLUSION

The demand for energy in the global world has made it necessary to tend to different energy sources. In this respect, it is vital to evaluate natural gas production and consumption, one of the primary energy sources. In this study, different forecasting methods were evaluated to estimate the natural gas consumption in Turkey. For this purpose, 132 months period data were obtained between January 2010 and December 2020. The data was divided into modeling set (January 2010-December 2017) and test set (January 2018-December 2020), and the analyses were detailed. The methods used for the forecasting models were Fourier Analysis, Winters' Method, and the SARIMA model. Each of these methods has been examined separately according to the algorithm structure.

Since it is desired to minimize the deviation from error, forecasting methods with minimized model performance evaluation criteria are used. When the model performance criteria were examined for the test set, the Winters' Method was the “appropriate forecasting method” for the monthly natural gas consumption data set. This decision was made by comparing model performance criteria values. Significantly, the finding of "MAPE value: 9.401% (“high” accuracy)" was revealed that determining Winters' Method as an estimation tool would be more advantageous than other forecasting methods. For this reason, the monthly natural gas consumption data for the 60-months between January 2021 and December 2025 were estimated using the Winters' Method. As a result, It is thought that this study will contribute to decision-makers in the energy sector in terms of comparing alternative forecasting methods used in forecasting natural gas demand.

REFERENCES

[1] E. Güler, S. Y. Kandemir, E. Açıkkalp, Evaluation of the Efficiencies of the Energy Distribution Companies in Turkey with DEA, *Bilecik Seyh Edebali University Journal of Science*, Vol. 7(1), pp. 66-79, 2020.

[2] E. Güler, S. Y. Kandemir, E. Açıkkalp, M. H. Ahmadi, Evaluation of sustainable energy performance for OECD countries, *Energy Sources, Part B: Economics, Planning, and Policy*, 1-24, 2021.

[3] S. Akgül, S. Yıldız, The estimation of natural gas consumption, *Journal of Social Sciences and Humanities,* 5(1), 440-452, 2013.

[4] C. Yıldız, and H. Açıkgöz, Forecasting diversion type hydropower plant generations using an artificial bee colony based extreme learning machine method, *Energy Sources, Part B: Economics, Planning, and Policy*, pp.1-19, 2021.

[5] O. F. Demirel, S. Zaim, A. Calışkan, P. Özuyar, Forecasting natural gas consumption in Istanbul using neural networks and multivariate time series methods, *Turkish Journal of Electrical Engineering & Computer Sciences*, Vol. 20(5), 695-711, 2012.

[6] O. Kaynar, S. Taştan, F. Demirkoparan, Natural gas consumption forecast with artificial neural networks, *Journal of Economics and Administrative Sciences*, Vol. 25, pp. 463-474, 2011.

[7] H. A. Es, Monthly natural gas demand forecasting by adjusted seasonal grey

forecasting model, *Energy Sources, Part A: Recovery, Utilization, and Environmental Effects,* Vol. 43(1), pp. 54-69, 2021.

[8] Gross Inland Deliveries in Turkey (Observed Natural Gas Consumption), http://www.jodidb.org/ (accessed 10 March 2021).

[9] E. Güler, S. Y. Kandemir, 2020. Forecasting Models for PM10 Concentrations in Bozüyük, Bilecik (Turkey). *Proceedings of ICCESEN-2020*, Online-Turkey, 21-25 October 2020.

[10] E. Özkan, E. Güler, Z. Aladağ, Selection of the appropriate forecasting method for electric energy consumption data. *Journal of Industrial Engineering*, Vol. 31(2), pp. 198-214, 2020.

[11] E. Yükseltan, A. Yücekaya, A. H. Bilge, and E. A. Aktunç, Forecasting models for daily natural gas consumption considering periodic variations and demand segregation. *Socio-Economic Planning Sciences,* Vol. 74, 100937, 2021.

[12] A. E. Gürel, U. Ağbulut, and Y. Bicen, Assessment of machine learning, time series, response surface methodology and empirical models in prediction of global solar radiation. *Journal of Cleaner Production*, Vol. 277, 122353, 2020.

[13] L. F. Tratar, and E. Strmčnik, The comparison of Holt–Winters method and Multiple regression method: A case study, *Energy*, Vol. 109, pp. 266-276, 2016.

[14] S. Makridakis, and S.C. Wheelwright, McGee V.E., Forecasting: methods and applications., New York: Wiley, 1998.

[15] A. A., Davidescu, S. A. Apostu, A. Paul, Comparative analysis of different univariate forecasting methods in modelling and predicting the Romanian unemployment rate for the period 2021–2022. *Entropy*, Vol. 23(3), pp. 325, 2021.

[16] E. Afrifa-Yamoah, B. Saeed, and A. Karim, SARIMA modeling and forecasting of monthly rainfall in the Brong Ahafo Region of Ghana World, *Environment*, Vol. 6, pp. 1–9, 2016.

[17] I. M. Almanjahie, Z. C. Elmezouar, M. B. Baig, and I. Ahmad, Modeling of water consumption in Saudi Arabia using classical and modern time series methods. *Arabian Journal of Geosciences,* Vol. 14(6), pp. 1-8, 2021.

[18] S. Ray, S. S. Das, P. Mishra, and A. M. G. Al Khatib, Time series SARIMA modelling and forecasting of monthly rainfall and temperature in the south asian countries. *Earth Systems and Environment*, Vol. 1-16, 2021.

[19] F. Okyere, L. Kyei, Behavioral Pattern of ordinance marriages in Accra metropolis: An application of multiplicative SARIMA model. International Journal of Modern Mathematical Sciences, 12(2), 112-125, 2014.

[20] J. Arlt, and P. Trcka, Automatic SARIMA modeling and forecast accuracy, *Communications in Statistics-Simulation and Computation*, pp.1-22, 2019.

[21] M. Akpinar, and N. Yumusak, Daily basis mid-term demand forecast of city natural gas using univariate statistical techniques. *Journal of the Faculty of Engineering and Architecture of Gazi University,* Vol. 35(2), pp. 725-741, 2020.

[22] A. Mohanasundaram, B. Narasimhan, and G.S. Kumar, Transfer function noise modelling of ground water level fluctuation using threshold rainfall-based binary-weighted parameter estimation approach, *Hydrol Sci J*, Vol. 62(1), pp. 36–49, 2017.

[23] Çoban, V., Güler, E., Kılıç, T., Kandemir, S.Y., Precipitation forecasting in Marmara region of Turkey. *Arabian Journal of Geosciences*, Vol. 14(2), pp. 1-10, 2021.

[24] M. Zhai, W. Li, P. Tie, X. Wang, T. Xie, H. Ren, ..., L. Qiu, Research on the predictive effect of a combined model of ARIMA and neural networks on human brucellosis in Shanxi Province, China: a time series predictive analysis, *BMC Infectious Diseases,* Vol. 21(1), pp. 1-12, 2021.

[25] A. V. Metcalfe, and P. S. Cowpertwait, Introductory time series with R (p. 2). Springer-Verlag New York, 2009.

[26] S. Raha, and S. K. Gayen, Simulation of meteorological drought using exponential

smoothing models: A study on Bankura District, West Bengal, India. SN Applied Sciences, Vol. 2(5), pp.1-24, 2020.

[27] https://support.minitab.com/en-us/minitab/18/help-and-how-to/modeling-statistics/time-series/how-to/winters-method/before-you-start/example/ (accessed 01 April 2021)

[28] R. Rasmussen, On time series data and optimal parameters. *Omega*, Vol. 32(2), pp. 111-120, 2004.

[29] B. G. Tabachnick, and L. S. Fidell, 2013. Using multivariate statistics: International edition. *Pearson*, 2012.

[30] X. Ma, and Z. Liu, Application of a novel time-delayed polynomial grey model to predict the natural gas consumption in China. *Journal of Computational and Applied Mathematics*, Vol. 324, pp. 17-24, 2017.

HAVACILIK SEKTÖRÜNDEKİ YANGIN ALGILAMA ve SÖNDÜRME SİSTEMLERİNİN PROJELENDİRME, KURULUM ve İŞLETİM SÜREÇLERİNİN YÖNETİLMESİ

Onur MAMMACIOĞLU [1], Cemil ÖZKALAY [2], Gökhan COŞKUN [3], Hakan Serhad SOYHAN [4]

1. Sakarya Üniversitesi Fen Bilimleri Enstitüsü Yangın ve Yangın Güvenliği ABD/Sakarya email: mammacioglu@outlook.com.tr
2. Sakarya Üniversitesi Fen Bilimleri Enstitüsü Yangın ve Yangın Güvenliği ABD/Sakarya email: cemilozkalay@gmail.com
3. Sakarya Üniversitesi Fen Bilimleri Enstitüsü Yangın ve Yangın Güvenliği ABD/Sakarya email: gcoskun@sakarya.edu.tr
4. Sakarya Üniversitesi Fen Bilimleri Enstitüsü Yangın ve Yangın Güvenliği ABD/Sakarya email: hsoyhan@sakarya.edu.tr

Özet

Bu çalışmada, havacılık endüstrisinde gelişmelerin beraberinde getirdiği risklerin öncesinde ve sonrasında karşımıza çıkabilen yangınlara karşı alınan tedbirlerin, hangi oranda başarıya ulaştığı örnek olayda elde edilen bilgiler ve tecrübeler ışığında incelenmiştir. Yangın, meydana gelişi ve sonuçları değerlendirildiğinde disiplinlerarası bir alandır. Bu kapsamda yangın senaryolarının oluşturulmasında genellikle bilgisayar destekli modellemeler ve hesaplamalar ile bütünleşmiş mimari ve mühendislik uygulamaları esas alınmaktadır. Ancak sahadaki uygulamaları esnasında ortaya çıkabilen olumsuz insan davranışları, çevre koşulları vb. etmenler ile karşı karşıya kalındığında hesaplamaların ne ölçüde başarılı olacağı irdelenmemektedir. Günümüzde yangın yönünden alınan emniyetlerin sahadaki uygulamalarının denetlenmesi, genellikle müşavir firmalarında çalışan tecrübeli mühendis veya teknisyenler tarafından yapılmaktadır. Ancak yangın alanının disiplinlerarası oluşundan kaynaklanan, pozitif bilim ile acil durum senaryolarını aynı anda operasyonel çerçevede incelenmesi göz ardı edilmektedir. Günümüz teknolojisinin bizlere sunduğu otomatik yangın algılama ve söndürme sistemlerinin kurulumu yüksek maliyetlere neden olmaktadır. Bu yüzden tercih edilen sistemin meydana gelebilecek yangınlara karşı yeterli, gerekli ve makul çözümler üretmesinin yanı sıra aşırı mühendislik uygulamalarından da kaçınılması gerekmektedir. Yangınlara karşı alınan tedbirler can, mal ve çevrenin korunması bakımından önemi tartışılmaz sistemlerdir. Bu çerçevede yüksek maliyetli bu sistemlerin kurulması kendi başına yeterli olamamaktadır. Çünkü her ne kadar programlama ile bizlerin gözü kulağı olan bu sistemler aynı zamanda yalnız başlarına var olamayacak kadar bizlere muhtaçtır. Bu yüzden sistemlerin ehil personel tarafından bakımlarının yapılması ve ilgili binada bulunan bireylere, sistemi nasıl kullanılacağına dair verilecek eğitimler, yangına karşı alınacak tedbirler için ödenen maliyetler kadar önem kazanmaktadır.

Anahtar Kelimeler: Sivil Havacılık, Yangın, Yangın Algılama ve Söndürme Sistemleri, Yangına Karşı Alınması Gereken Tedbirler

Abstract

In this study, the success rate of the measures taken against fires, which may occur before and after the risks brought by the developments in the aviation industry, has been examined in the light of the information and experience obtained in the case study. Fire is an interdisciplinary profession when its occurrence and consequences are evaluated. In this context, architectural and engineering applications integrated with computer-aided modeling and calculations are generally taken as basis in the creation of fire scenarios. However, It is not scrutinized to what extent the calculations will be successful when faced with factors like negative human behaviors, environmental conditions, etc. that may occur during their application in the field. Today, the audit of the field applications of the safety taken in terms of fire is usually carried out by experienced engineers or technicians working in accountant companies. However, due to the interdisciplinary nature of the fire profession, the simultaneous examination of positive science and emergency scenarios in an operational framework is ignored. The installation of automatic fire detection and

extinguishing systems offered to us by today's technology causes high costs. For this reason, it is necessary to avoid over-engineering practices as well as producing adequate, necessary and reasonable solutions against possible fires of the preferred system. The measures taken against fires are systems whose importance is indisputable in terms of protecting life, property and the environment. Within this scope, the establishment of these high-cost systems is not sufficient on its own. Because although these systems, which are our eyes and ears with programming, are also in need of us so that they cannot exist on their own. Therefore, the maintenance of the systems by qualified personnel and the training to be given to the individuals in the relevant building on how to use the system are as important as the costs paid for the measures to be taken against fire.

Keywords: Civil aviation, Fire, Fire Detection and Extinguishing Systems, Measures to be Taken Against Fire

1 GİRİŞ

Binaların Yangından Korunması Hakkındaki Yönetmeliğinin (BYKHY) amacı ilgili yönetmeliğin birinci maddesinde, *"kamu kurum ve kuruluşları, özel kuruluşlar ve gerçek kişilerce kullanılan her türlü yapı, bina, tesis ve işletmenin, tasarımı, yapımı, işletimi, bakımı ve kullanımı safhalarında çıkabilecek yangınların en aza indirilmesini ve herhangi bir şekilde çıkabilecek yangının can ve mal kaybını en aza indirerek söndürülmesini sağlamak üzere, yangın öncesinde ve sırasında alınacak tedbirlerin, organizasyonun, eğitimin ve denetimin usul ve esaslarını belirlemektir."* şeklinde ifade edilmiştir.

Binaların Yangından Korunması Hakkındaki Yönetmeliğin birinci maddesinin özüne inersek; yangını meydana gelmeden önce önlemek, önlenememiş ise en az hasar ile yangını söndürmemiz gerektiğidir. Yönetmelik içerisinde belirtilen tüm hususlar sözel olarak algılamanın kolay olduğu ifadelerdir. Bu ifadelerin kolay anlaşılır olmasının nedeni yangının tüm insanlığın ortak düşmanı olmasıdır. Ancak bu çerçevede vandalist düşünceler ile zarar vermek ya da sonuçlarından fayda sağlamak amacıyla gerçekleştirilen kundakçılığı tenzih ediyoruz.

Günümüz dünya yaşamı insanlığa birçok teknolojik gelişmeleri sağlamaktadır. Bu teknolojik gelişmeler, endüstriyel tesislerin ve akıllı robot teknolojilerinin insanoğlunun hayatındaki yerini de arttırmıştır. Bu teknolojik tesislerin yapay zekâ algoritmaları ile birleşmesi, bu tesislerin insandan bağımsız olarak çalışabilme yetisi kazanmasını sağlamıştır. Bu gelişmeler insanlığın yaşamına büyük kolaylıklar ve faydalar getirmenin yanısıra tesisin çalışma prensiplerine bağlı olarak güvenlik önlemleri hakkında alınması gereken tedbirleri ve uygulamaları arttırıp, çeşitlendirmektedir. Teknolojik gelişmeler ile aynı doğrultuda ilerleyen tıp alanındaki gelişmeler, insanlığın varoluşundan bu yana içinde barındırdığı hayatta kalma iç güdüsüne hitap eden gelişmelerin mümkün kılınmasını sağlamıştır. İç güdüsel bu durum insanlığın temelinde, çağlar öncesinden bu yana bulunsa da, hayatta kalmak terimi altına alacağımız teknolojik gelişmeler insanlığın son yüz yılında yeni kilometre taşlarını ardı ardına koymuştur. Bu duruma örnek verecek olursak, günümüzde dünyada önemli yer tutan iş güvenliği standartları bu iç güdünün bir ürünü olarak karşımıza çıktığı görüşü doğmaktadır.

2 YANGIN ALGILAMA VE İHBAR SİSTEMLERİ

Yangın algılama ve ihbar sistemleri, Binaların Yangından Korunması Hakkındaki Yönetmelik tarafından belirlenmiş standartlara uygun olarak belirli özellikteki binalara kurulması şarttır. Bu kapsamda kurulması gereken sistemin hangi esaslarda projelendirilmesi gerektiği aynı yönetmeliğin *"Binalarda kurulan elektrik tesisatının, kaçış yolları aydınlatmasının ve yangın algılama ve uyarı sistemlerinin, yangın hâlinde veya herhangi bir acil hâlde, binada bulunanlara zarar vermeyecek, panik çıkmasını önleyecek, binanın emniyetli bir şekilde boşaltılmasını sağlayacak ve güvenli bir ortam oluşturacak şekilde tasarlanması, tesis edilmesi ve çalışır durumda tutulması gerekir."* ifadesi ile yönetmelik maddeleri arasında yerini almıştır.



Şekil 1. Yangın Algılama ve İhbar Sistemi

Yangın Algılama ve ihbar sistemleri genellikle iki türde üretilir. Bunlar konvansiyonel ve adresli yangın algılama ve ihbar sistemlerdir. Konvansiyonel yangın algılama ve ihbar sistemleri 1 veya 2 katlı, oda veya bölme sayısı çok bulunmayan yerleşke veya depo benzeri yapılarda ve 20-30 kadar dedektörün bir bölge oluşturabileceği binalar için uygundur.

Adresli yangın algılama ve ihbar sistemleri ise; çok katlı ve çok odalı/bölmeli olan gökdelen, hastane, otel, birleştirilmiş eğitim ve simülatör merkezleri gibi yapılarda tercih edilen sistemlerdir. Konvansiyonel sistemler yangın ihbarlarını bölgesel olarak verirken, adresli sistemler ihbarlarını noktasal olarak verebilmektedir. Adresli sistemlerin kullanımı daha etkin ve zaman kazandırıcı özellikte olmasının yanısıra işletme ve idameleri daha maliyetli iken; konvansiyonel sistemler maliyet yönünden daha elverişlidir.

3 YANGIN SÖNDÜRME SİSTEMLERİ

Yangın söndürme sistemleri sulu, temiz gazlı ve kuru kimyasallı söndürme sistemleri olarak üç ana bölüme ayrılmıştır. Ancak her bir sistem de kendi içerisinde birden fazla bölüme ayrılmıştır. Bu ayrılmanın sebebi ihtiva ettikleri söndürme maddeleri ya da yangına müdahale etme yöntemleridir. Yangın söndürme sistemleri, algılama sistemleri ile eş zamanlı çalışması gereken sistemlerdir. Yangın algılama ve söndürme sistemlerinin beraber çalışması gerektiğine dair ifade BYKH Yönetmelikte "*Binada otomatik yağmurlama sistemi bulunuyor ise, yağmurlama başlığının açılması hâlinde yangın uyarı sisteminin otomatik algılama yapması sağlanır. Bu amaçla, her bir zon hattına su akış anahtarları tesis edilir ve bu akış anahtarlarının kontak çıkışları yangın alarm sistemine giriş olarak bağlanır.*" ve "*Binada veya yapıda otomatik veya el ile çalışan diğer gazlı, kuru kimyevi tozlu veya benzeri sabit söndürme sistemi bulunuyor ise, bunların devreye girdiğinin yangın alarm sistemi tarafından otomatik olarak algılanması gerekir. Bunu sağlamak üzere, söndürme sistemlerinden, söndürme sisteminin devreye girdiğini bildiren kontak çıkışları yangın alarm sistemine giriş olarak bağlanır.*" maddeleri ile yönetmeliktekini yerini almıştır.



Şekil 2. Yangın Söndürme Sistemi Pompa Grubu

Sulu söndürme sistemleri A sınıfı yangınlarla mücadele edebilecek özellikte iken, Kuru kimyasallı söndürme sistemleri A, B ve C sınıfı yangınlarla mücadele etmek üzere tesis edilmiştir. Temiz gazlı söndürme sistemleri ise; günümüz teknoloji ürünü olan bilgisayar sistem odaları, kontrol odaları, UPS odaları, simülatör odaları, kablo kanalları, türbin bölgeleri, müze ve arşivler, denizcilik sektöründe ise motor ve pompa odaları gibi buna benzer elektronik veya korunma hassasiyeti taşıyan binalarda kullanılmaktadır.

4 HAVACILIK SEKTÖRÜNDE YANGIN ALGILAMA VE SÖNDÜRME SİSTEMLERİNİN YERİ VE ÖNEMİ

Günümüz dünyasında yangın alanında bu tür gelişmeler yaşanırken, havacılığa kazandırılan yeni uçak ve sistemlerle uyumlu binalarda yangından korunma programları kapsamında son teknoloji ürünü yangın algılama ve söndürme sistemlerinden yoksun kalması düşünülemez. Bu kapsamda, havacılık sektöründe çalışan personelin de bu teknolojik gelişmeler ile doğru orantılı olarak bu sistemler hakkında gerekli bilgi ve beceriye de sahip olmalıdır.



Şekil 3. Sulu/Köpüklü Yangın Söndürme Sistemi

İthal veya yerli tedarikçileri ya da milli imkanlarla üretilmiş olsun, yangın algılama ve söndürme sistemlerinin kurulması yüksek maliyetler ile mümkün olabilmektedir. Ancak kurulum aşamasında yüksek maliyetlere sahip bu ürünler periyodik bakım ve onarım işlemlerinden mahsun bırakılır ise; işe yaramayan ve sürekli yanıltıcı ihbar veren, daha ötesi bu ihbarlar dolayısıyla söndürme sistemleri aktif olarak milyon dolarları bulabilecek hasarlara sebep olabilmektedir. Bu kapsamda göz önünde bulundurulması önem arz eden hususlar aşağıda sıralanmıştır.

a. Yeterli, gerekli ve makul çözüm üretecek uygun bir proje seçilmelidir.

b. Projenin seçilmesi safhasında yalnızca kurulum maliyetinin değil, bu sistemlerin bakım onarım ve idame planlarının oluşturulmalıdır. Bu sistemlerin en az 20 yıl maliyet etkin bir şekilde kullanılması hedeflenmelidir.

c. Projenin seçilmesi safhasında karar merkezinde mühendisler, yangın danışmanları ve itfaiye personeli yer almalıdır.

ç. Projenin kurulumu esnasında ulusal ve uluslarası normlara uygun tesis edildiğinin kontrol edilmelidir.

d. Proje ve yazılan teknik şartname esastır ancak sahada oluşabilecek değişkenler göz önüne alınarak, basma kalıp çözümler yerine gerçekçi ve çözüm odaklı sonuçlara yönelmek ve kurulum sürecini dinamik yönetilmelidir.

e. Projelendirme safhasında alınması gereken emniyet tedbirine karar verme sürecinde problem yaşanması halinde AŞIRI MÜHENDİSLİK uygulamaları kaçınılmaz olmaktadır. Aşırı mühendislik, bilgisizliğin ve yorum yapamamamın karşılığıdır. Bu durum nedeniyle yangın algılama ve söndürme sistemlerinde, gereksiz maliyet artışına sebep olmaktadır. Bu yüzden makul, yeterli ve gerekli çözümler ile yangın emniyetinin sağlanması önem arz etmektedir.

f. Projenin gerçekleştirilme safhasında yalnızca mühendisler, yangın danışmanları ve itfaiye personeli değil, sistemi kullanması planlanan personelinde sürece dahil edilmesi sağlanmalıdır.

g. Binanın yapısal bütünlüğünü korumak adına kurulması planlanan yangın söndürme sistemi ile özellikli koruma oluşturulan alanların yangın algılama ve söndürme sistemi projeleri ayrı ayrı değerlendirilmelidir. Buna örnek verecek olursak; binanın elektrik pano odasına gazlı söndürme sistemi kurulmuş ise bu sistem yalnızca elektrik pano odasındaki yangına müdahale etmek üzere tasarlanmıştır. Odaya ayrıca kurulması planlanan sulu söndürme sistemi ise; binanın yapısal bütünlüğünü korumak üzere tasarlanmıştır. Bu noktadan hareketle, kurulması planlanan bu iki sistem birbirini yedekler nitelikte DEĞİLDİR.

Sistemlerin projelendirilmesi esnasında yönetmelik içerisinde hangi binalara yangın algılama ve ihbar sistemi kurulması belirtilmiş iken; kurulacak sistemin niteliği ve kullanım amacına göre uygunluğu tamamıyla projeyi oluşturan mühendislere bırakılmıştır. Bu durumda tüm karar (eğer tip proje yapılmayacaksa) projeyi oluşturacak mühendise kalmaktadır. Ancak bu karar verme safhasını kolaylaştıracak bir takım sorulara, verilecek uygun cevaplar ile doğru karar vermek mümkündür.

1- Yapıyı oluşturan malzemeler nelerdir?
2- Yangın güvenliği oluşturulacak yapının içerisindeki maddelerin kalorifik değeri kaçtır?
3- Kitle halinde patlama olasılığı var mı?
4- Yapının havalandırma durumu nedir?
5- Yapının içerisindeki maksimum elektrik enerjisi yükü nedir?
6- Özellikli bir bölme oluşturulmalı mı?
7- Özel korumaya muhtaç alan var mı?
8- Binanın kullanım amacı uygun bir yangın algılama/söndürme sistemi var mı? Maliyet etkin mi?
9- Kurulacak söndürme sisteminin ikincil hasar oluşturma potansiyeli var mı?

5 SONUÇ

Kurulan son teknoloji ürünü yangın sistemleri her ne kadar kendi kendilerine çalışabilse de, insan denetimine muhtaç sistemlerdir. Çünkü yangın gibi can güvenliğini doğrudan etkileyebilecek hadiseler, makinaların inisiyatifine bırakılması sistemlerin gerektiğinde çalışmamasına neden olabilmektedir. Bunun yanısıra denetimsiz bir sistem zamansız ve gereksiz yere aktif hale gelmesi maddi hasarlara sebep olabilmektedir.

Bu konu hakkında temel referans kaynağı *NFPA (Ulusal Yangından Korunma Derneği) 20: Standart for the Installation of Stationary Pumps for Fire Protection* dokümanı bizlere otomatik olarak yangına müdahale eden yangın söndürme sistemlerinin yangın sonrasında durdurulmasının bireyler tarafından yapılması gerektiğini ifade etmektedir. Bu noktadan hareketle yangın algılama ve söndürme işlemi yapan milyonluk sistemlerin, bireylerin kontrolü ve denetimi olmadan yeterli verimi veremeyeceği insan eğitiminin de ne kadar önemli olduğu konusunu tekrar gündeme getirmektedir.

Yangın söndürme sistemleri projelendirilirken sulu/köpüklü yangın söndürme sistemleri (ıslak/kuru borulu, baskın, ön tepkimeli sistemlerin tamamı) aynı zamanda bölgeye kurulması planlanan yangın hidrant sisteminden ayrı branşmanlarda tesis edilmelidir. Yangın hidrant sistemi ile sağlanan yüksek basınçlı su boru hattına aynı zamanda hava girişine neden olmaktadır ve bu durum kılcal nitelikte değerlendirebileceğimiz bina içi söndürme sistemlerindeki fleksi boru çıkışlarına ekstra yük bindirerek bina içi sistemlerde kaçak veya patlaklara neden olmaktadır. Bunun yanı sıra bina içi sistemlerdeki köpük tanklarının karıştırma ve valf sistemlerine zarar vererek köpüklü söndürme sistemlerinin çalışmamasına veya verimsiz çalışmasına neden olabilmektedir.



Şekil 4. Yangın Söndürme Hattı Basınç Düzenleyicisi

Kapalı devre su basınçlandırma sistemlerinde endişe edilen en önemli konu havadır. Yangın söndürme sistemlerinde sisteme hava girişine neden olan yollar genellikle; pompanın su basma noktası, hidrant çıkışları ve boru hattı içerisindeki suyun çözünmesi ile meydana gelmektedir. Sistem içinde kontrolsüz havanın bulunması istenmez çünkü sisteme giren hava, su gibi kontrol edilemezse saha elemanlarında malzeme yorgunluğuna ve sonunda arızalara neden olmaktadır. Bu durum yüksek metrajlı alanlarda kaçınılmaz olan bir durum olsada bununla başa çıkmanın yolu sisteme giren havayı tahliye etmektir. Yangın söndürme hatlarında ana boru üzerinde uygun yerlere tesis edilecek hava tahliye vantuzu ve basınç düşürücü/düzenleyici aparatlar hava sorunu ile başa çıkılmasını sağlayacaktır. Tesis edilmesi planlanan hava tahliye vantuzları ve basınç düzenleyici sistemlerin yerleri belirlenirken genellikle hattın topografik olarak en yüksek yeri ya da hattı bölümlendirecek şekilde projelendirilmelidir.



Şekil 5. Hava Tahliye Vantuzu

İnsanların yangın konusunda eğitilmesi, öncelikle bireylerin ikna edilmesi ile başlamaktadır. Çünkü yangın algılama, ihbar ve söndürme sistemleri gerek projesel hatalar, gerek ise uygunsuz saha elamanları nedeniyle insanların başını ağrıtan sürekli yanlış ve yanıltıcı ihbarlar veren ve problem çıkarıcılar olarak görülmektedir. Ana sebep olarak olarak belirlediğimiz projesel hatalar ve uygunsuz saha elemanı problemleri sıraladığımız maddeler aracılığıyla çözüme kavuşacaktır.

Yangın algılama, ihbar ve söndürme sistemleri üzerine bireylerin, sistemi başlı başına problem olarak görmek yerine onun çalışma prensibini ve alınması gereken aksiyonları hap bilgi olarak almaları bu sistemlerin aslında o kadar da anlaşılması güç karmaşık yapılar olmadığını bizlere göstermektedir. Sistemler hakkında verilecek olan eğitimlerin niteliği onu kullanacak insanların sistemi benimsemesi ve uygulaması ile birleştiğinde kazan-kazan şeklinde yorumlanabilecek bir kazanım olacaktır.

KAYNAKLAR

[1] Binaların Yangın Korunması Hakkında Yönetmelik, 2018.

[2] Mammacıoğlu, O., Soyhan, H., S., (2019) Duman Dedektörlerinin Çalışma Prensipleri Ve Test İşlemlerinin İncelenmesi, Uluslararası Yakıtlar Yanma ve Yangın dergisi, 7, 17-21. Erişim adresi: https://dergipark.org.tr/fce.

[3] NFPA (Ulusal Yangından Korunma Derneği) 20: Standart for the Installation of Stationary Pumps for Fire Protection, 2019 Edition.

[4] Stowell, M., Frederick, Essentials of Fire Fighting and Fire Department Operations Sixth Edition, Oklahoma State University Fire Protection Publications, 1174-1216, 2015.

[5] Prof. Dr. Soyhan, H., Serhad, Özkalay, Cemil, Can, Kadir, Mammacıoğlu, Onur, Yangın ve Yaşam, Cenevre Yayınları, V-VI, 2018.

[6] Sulu - Köpüklü Yangın Söndürme Sistemi, www.google.com/görseller Erişim Tarihi: 12.08.2022.

[7] Yangın Algılama ve İhbar Sistemi, www.google.com/görseller Erişim Tarihi: 12.08.2022.

EXPERIMENTAL AND COMPUTATIONAL PREMIXED TURBULENT FLAME PROPAGATION STUDIES FOR HYDROGEN CONTAINING FUELS

Dilay Güleryüz[1], Emre Böncü[1], Tahsin Berk Kıymaz[1], Christophe Allouis[1], İskender Gökalp[1], Mehmet Karaca[2], Barış Yılmaz[3], Oğuz Kaya[4], Fatih Coşkun[5]

1. Department of Mechanical Engineering, Middle East Technical University, Ankara
2. Department of Aerospace Engineering, Middle East Technical University, Ankara
3. Department of Mechanical Engineering, Marmara University, İstanbul
4. Pro-Sis Engineering, Ankara
5. Yedic Engineering, Ankara

Abstract

Reduced emission requirements and increased efficiency demands strongly constrain today the design of new combustors. Emission requirements indicate the use of hydrogen as a potential solution. Hydrogen flames strongly differ from natural gas flames in terms of flame propagation velocity, thickness, and temperature. Such parameters also affect the flame stability and flashback propensity of both laminar and turbulent hydrogen flames. This research program concerns experimental and numerical studies of high-pressure turbulent lean premixed flames of natural gas-hydrogen-air mixtures. The newly developed experimental facility is a high-pressure optically accessible combustion chamber capable of hosting several burners. The ongoing work concerns a turbulent Bunsen type burner where the turbulence is triggered by perforated plates. Laser induced Rayleigh scattering measurements will be implemented for instantaneous scalar field measurements in the turbulent flames brush to deduce all the relevant parameters to model the turbulent burning rate for various natural gas – hydrogen blends. Large eddy simulations of the high-pressure turbulent burner are also developed; they will be validated by the experimental results.

Keywords: Premixed Flame, Turbulence, High pressure, Rayleigh scattering, LES

INTRODUCTION

Turbulent premixed combustion usually takes place within high pressure environments, such as gas turbines. The reduction in carbon emissions forces the research towards hydrogenated fuels. It is crucial to study the effect of hydrogen mixtures in high pressure flames.

The experimental and numerical investigation of lean turbulent premixed flames of the hydrogenated mixtures is the objectives of this research program. The newly built experimental facility and the ongoing numerical studies are described in this work. The grid resolution limitations of the large eddy simulations are discussed. The numerical simulations consider RANS modelling for the non-reacting turbulent flow. The simulation results are used for mesh validation for large eddy simulations. The results are also compared with the previous experimental data.

EXPERIMENTAL WORK

2.1 Experimental Setup

The high-pressure combustion chamber

The high-pressure combustion chamber consists of two superposed modules. It allows the experimental characterization of the turbulent premixed flame created using a Bunsen type burner. Each module has internally 600 mm height and 300 mm diameter and are made of stainless steel. The modules are cooled with water pipes surrounding the internal walls of the chamber. The maximum operating pressure is 9 MPa.

A Bunsen burner where the turbulence is controlled by perforated plates is used in the present work. The turbulence intensity can be adjusted by mounting various perforated plates, while the aim is to create a homogenous and isotropic turbulence structures. Both modules have 4 windows, however only three of them has optical access. The quartz glasses are on the bottom module. The three quartz windows allow optical observations and laser

induced measurements within the turbulent flame brush.

The Bunsen burner is mounted on top of a moving mechanism actuated with a stepper motor that allows the burner to move axially. The system is assisted with two pistons that utilize the internal pressure of the chamber to drive its movement. The burner is replaceable in the combustion chamber setup; therefore, other turbulent burners can be mounted on the blind flange on the bottom of the lower chamber module.

Laser Induced Rayleigh Scattering for Turbulent Flame Characterization

Principle of Rayleigh Scattering

Rayleigh scattering technique utilizes the diffusion of photons by elastic collisions with small particles, here the gaseous medium molecules, which are smaller than the incident light's wavelength. The total intensity of the scattered light is therefore directly proportional to the number of molecules, hence the instantaneous density.

Laser induced Rayleigh scattering technique allows to make measurements of the local instantaneous gas density without causing any perturbation in the flame. By applying several statistical analyses to the Rayleigh scattering signal, the characteristic time scales of the scalar field can be determined leading to characterize the turbulent flame brush using the progress variable approach [REF].

The Rayleigh scattering system can be arranged for one-point or two-point measurements. One-point measurements provide the temporal properties of the flamelet dynamics, while two-point measurements provide spatial statistics.

Examples of one and of two-point Rayleigh scattering arrangements are given in Fig. 1.

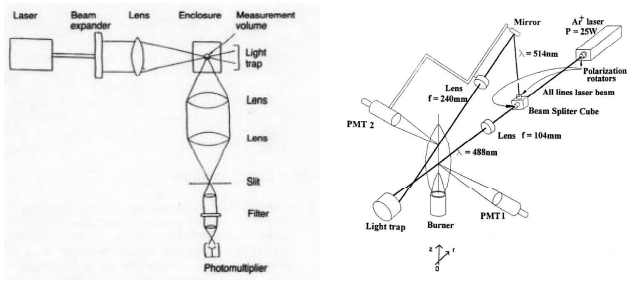


Fig. 1. a) One-point [1] and b) Two-point [2] Rayleigh scattering arrangement

In the experiments, the laser induced Rayleigh scattering technique will be used to deduce the relevant temporal and spatial statistics of the turbulent flame brush, such as flamelet crossing frequencies, the transit time that a flamelet puts to cross over its own thickness and the probability density distributions of these times. Progress variable data of the scalar field and the burning time fractions will be calculated from the temporal statistics. Global parameters such as flame surface density and mean reaction rate will be deduced from the statistical data from the Rayleigh scattering setup.

Rayleigh Scattering system

The Rayleigh scattering system consists of the laser, the camera and its intensifier and the planar light sheet optics. The pulsed Q-smart 850 laser provides 850 mJ pulsed energy with a repetition rate of 10 Hz. The HiSense Zyla intensified Camera has 49 fps frame rate. It is also planned that two photomultiplier tubes will be used at 532 nm for the temporal and scalar statistics measurements. The Rayleigh system is shown in Fig. 2.

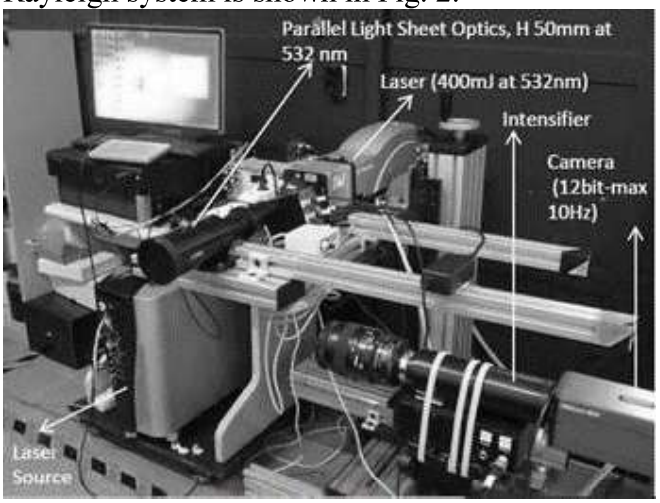


Fig. 2. Rayleigh Scattering setup.

1. NUMERICAL WORK

1.1. Burner Geometry and Numerical Domain

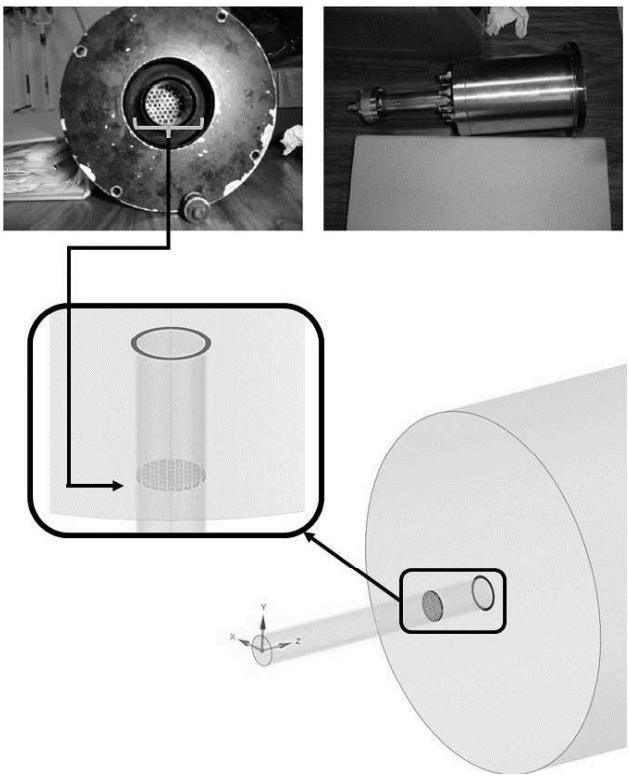


Fig.3. The burner geometry

The burner and combustion geometries are modelled using the actual set-up dimensions. The perforated plate is 1 mm thick and is located 50 mm upstream of the burner exit. The pilot flame surrounds the burner and issues from an annular section of 2 mm thickness. The combustion chamber is modelled as 300 mm in diameter and 600 mm in height.

The transient nature of the turbulent flame is to be modelled with the large eddy simulations (LES) approach. The following sections summarize the preparation and computation steps of the reacting large eddy simulations.

Non-Reactive Simulations

The non-reacting flow field is investigated for different meshes in the same configuration. The non-reacting flow is modelled using Reynolds Averaged Navier Stokes (RANS) computations. The RANS computations will be used as an input for Large Eddy Simulations (LES).

The first important step of LES is the establishment of a grid-independent mesh. The mesh should be able to solve both turbulence characteristics and the reacting flow parameters. For a complete LES, the constituent equations should be free from flow-dependent specifications. Solution-adaptive methods are common in LES practice to reach flow-independent meshing.

According to Pope [3], the turbulence resolution level is measurable by the resolved fraction of the turbulent kinetic energy. Capturing 80% of the total modelled kinetic energy with the mesh is the first step for a successful LES simulation.

The mesh is generated according to the y+ requirements of the domain. The first simulations are performed using the RANS k-ε turbulence model, therefore the requested y+ value is in the order of 1 or less.

The corresponding wall distance is calculated as follows:

$$Re = \frac{\rho U_{free\ stream} L_{boundary\ layer}}{\mu} = 29980$$

$$C_f = [2\log_{10}(Re)_x - 0.65\,]^{-2.3} = 7.68e-3$$

$$\tau_w = C_f \frac{1}{2}\rho U^2_{free\ stream} = 0.0179 \text{ (Schlichting)}$$

$$u_* = \sqrt{\frac{\tau_w}{\rho}} = 0.122$$

$$y = \frac{y^+ \mu}{\rho u_*} = \frac{1 \cdot 1.82e-5}{1.205 \cdot 0.11117} = 1.23e-4\ m$$

In order the wall distance to be less than 1.23e-4 m, the largest mesh size near the wall in the burner region is estimated as 0.3 mm. This is about 3 times higher than the desired y+ value on the wall. The y+ simulations are recalculated with the help of a steady simulation using k-epsilon RANS simulations. The y+ values were correct, therefore, globally, the mesh can be assumed to be appropriate in terms of y+.

Another requirement of a good LES-mesh is to resolve 80% of the modelled turbulent kinetic energy in the domain [3]. Air is selected as the working fluid in the domain for non-reacting RANS simulations. As a third step, the flame thickness is calculated. The flame thickness is calculated here to provide insight for the mesh dimensions in the possible flame areas, using the Zeldovich formulation [4]:

$$\delta_L = \frac{\lambda}{\rho_u C_p S_L^0} = \frac{\alpha}{S_L^0}$$

The Zeldovich thickness is calculated as 0.2 mm for a premixture with 0.6 equivalence ratio. When constructing the mesh, this thickness is also considered.

Three different meshes are constructed for the cold flow simulations, consisting of 2.1 million, 6.5

million and 19.1 million cells respectively. The mesh is specifically refined for the perforated plate simulations, wall regions and the expected flame regions according to the mentioned mesh criterion.

Non-Reactive RANS for Mesh Calculations

From the cold flow RANS results, the turbulent length scales are calculated. The standard k-epsilon turbulence model is employed for calculating the initial turbulence field. The CFD software Fluent solves two equations for the turbulence kinetic energy and its dissipation rate:

$$\frac{\partial}{\partial t}(\rho k) + \frac{\partial}{\partial x_i}(\rho k u_i) = \frac{\partial}{\partial x_j}\left[\left(\mu + \frac{\mu_t}{\sigma_k}\right)\frac{\partial k}{\partial x_j}\right] + G_k + G_b - \rho\varepsilon - Y_M + S_k \quad (1)$$

$$\frac{\partial}{\partial t}(\rho \varepsilon) + \frac{\partial}{\partial x_i}(\rho \varepsilon u_i) = \frac{\partial}{\partial x_j}\left[\left(\mu + \frac{\mu_t}{\sigma_\varepsilon}\right)\frac{\partial \varepsilon}{\partial x_j}\right] + C_{1\varepsilon}\frac{\varepsilon}{k}(G_k + C_{3\varepsilon}G_b) - C_{2\varepsilon}\rho\frac{\varepsilon^2}{k} + S_\varepsilon \quad (2)$$

where, G_k is the generation of turbulence kinetic energy due to mean velocity gradients, G_b is the generation of turbulence kinetic energy due to buoyancy, Y_M is the contribution of the fluctuating dilatation in compressible turbulence to the overall dissipation rate and $C_{1\varepsilon}, C_{2\varepsilon}, C_{3\varepsilon}$ are constants of 1.44, 1.92 and -0.33, respectively. σ_k and σ_ε represent the turbulent Prandtl numbers for k and ε, which are 1.0 and 1.3 respectively, while S_k and S_ε are user defined source terms in Fluent. Turbulent viscosity is modelled as:

$$\mu_t = \rho C_\mu \frac{k^2}{\varepsilon} \quad (3)$$

where C_μ is constant equal to 0.09.

From the RANS results, the integral length scale is calculated as [5]:

$$I_0 = 0.09^{0.75}\frac{k^{3/2}}{\varepsilon} \quad (4)$$

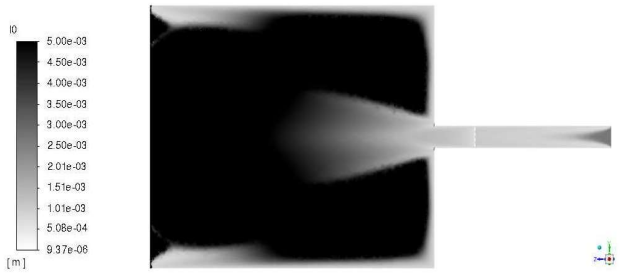


Fig.4. Integral length scale distribution for the initial (2.1M) mesh.

At the burner exit and just before the perforated plate, the integral length scale is calculated as 1 mm. The mesh is refined to be about one third of the integral length scale at those sections, therefore 0.3 mm near the perforated plate and the burner exit, in a gradually increasing manner with growth rate of 1.2. For y+ requirements, near the burner walls, the mesh size is restricted to 0.75 mm. With these conditions, a mesh consisting of 6.5 million elements is generated for LES calculations.

The RANS results of the 6.5M mesh are used for re-calculating the turbulent kinetic energy capture rate presented by the integral length scale is presented in Fig. 5.

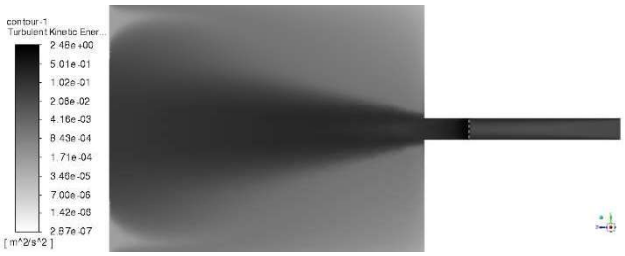


Fig. 5. Turbulent kinetic energy captured by the 2.1M mesh.

This mesh is re-evaluated by the following ratio:

$$M_I = \frac{I_0}{\Delta}$$

where Δ is the local mesh cell size. The regions where $M_I > 3$ are considered as sufficient to solve the cold flow-LES field.

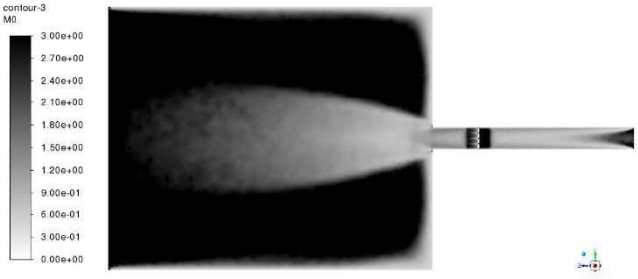


Fig. 6. M_I ratio calculated for 6.5M mesh.

In most parts of the domain, the ratio is smaller than 3. But, especially near the burner exit section, the meshing should be refined more to improve the resolution.

In the experiments for $\phi = 0.6$, the expected flame height is around 75 mm [6]. Therefore, the computational region of interest is around that location. It should be noted that, the first combustion chamber module height is 600 mm, therefore the refinement is restricted to the first 200 mm from the burner.

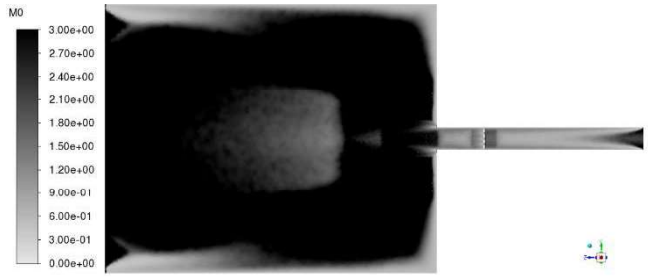


Fig. 7. M_I ratio calculated for 19.1M mesh.

The 19.1M mesh is found to be sufficient to respect the Ml criterion to resolve the integral length scale, therefore it is a good candidate for the LES computations. RANS computations are carried out for both meshes of 2.1M and 19.1M meshes to investigate the differences in capturing the turbulent field.

Table 1. Mesh statistics

	Mesh #1	Mesh #2	Mesh #3
Total number of cells	2.1 million	6.5 million	19.1 million
Max. Cell Volume [m^3]	1.0e-07	5.8e-08	2.5e-08
Min. Cell Volume [m^3]	1.7e-12	1.7e-12	1.7e-12

Boundary Conditions

The inlet boundary condition is arranged from the previous experiments as 1.97 m/s for air [REF]. The pilot flame has a co-flow velocity inlet of 0.71 m/s velocity. The pressure outlet condition simulates the exhaust at the top part of the chamber, and all the walls are modelled as isothermal at 300K temperature with no-slip velocity condition. The cooling of the outside walls is simulated. Gravitational forces are also modelled.

In the non-reacting simulations, the reaction terms are not active and only the flow is calculated without chemical species and without reactions for estimating the mesh quality.

2. RESULTS

2.1. RANS OF NON-REACTING FIELD

The non-reacting field is compared to the previous experimental data by Lachaux [7].

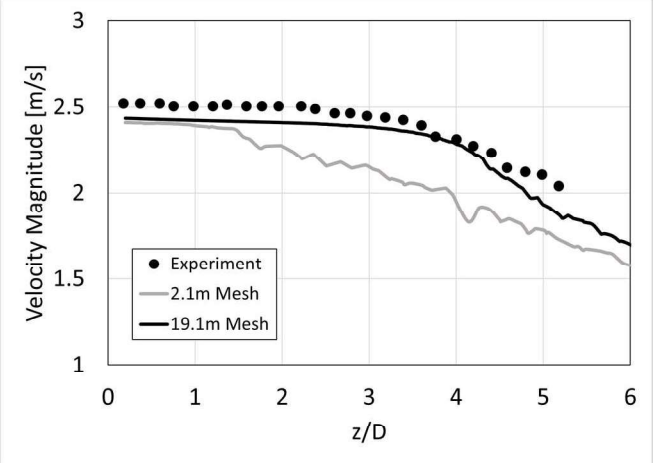


Fig. 8. Mean axial along the normalized vertical axis.

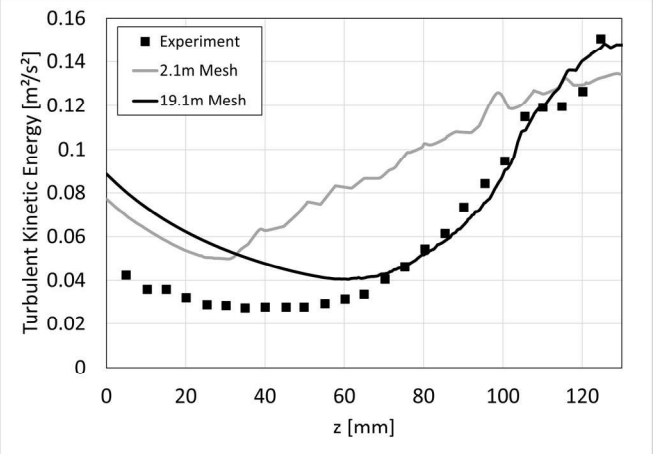


Fig. 9. Turbulent kinetic energy along the normalized vertical axis.

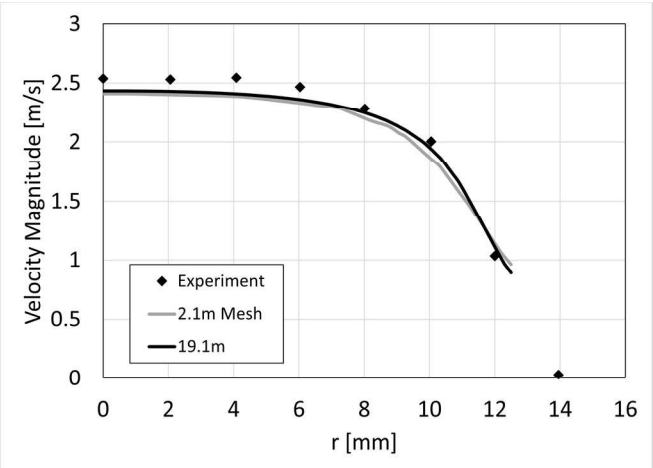


Fig. 10. Mean velocity variation in the radial direction, at 5 mm upstream of the burner exit.

Comparing with the previous experiments, the RANS results of 2.1m is inaccurate in terms of velocity magnitude and turbulent kinetic energy (TKE). The higher error in TKE may be also a defect caused by the k-ε turbulence model. The 19.1m mesh on the other hand represents the TKE and velocity magnitude satisfactorily in a steady simulation. This is a further validation of the effect of a well-designed mesh.

3. CONCLUSION

The finest mesh is found to be eligible for reacting flow calculations in the further numerical studies. Cold flow RANS calculations are completed for LES meshing steps and the meshes are validated with previous experimental data. Upcoming studies will include first the RANS calculations of the reacting field, then the reacting flow will be investigated by Ansys Fluent and the open-source CFD software OpenFOAM. The high-pressure turbulent flame experiments are being conducted using the Rayleigh scattering setup. The first experiments cover methane-air premixtures at various high-pressure conditions at different turbulence intensities. The results will help to understand the effect of pressure on turbulent premixed burners.

4. REFERENCES

[1] A. Boukhalfa, S. Sarh, and I. Gökalp, “The use of Rayleigh Scattering to measure instantaneous temperatures in turbulent flames”.

[2] C. Ghenai and I. Gökalp, “Correlation coefficients of the fluctuating density in turbulent premixed flames,” Springer-Verlag, 1998.

[3] S. B. Pope, “Ten questions concerning the large-eddy simulation of turbulent flows,” *New J Phys*, vol. 6, Mar. 2004, doi: 10.1088/1367-2630/6/1/035.

[4] B. Yilmaz, P. Supervisor and Z. Sibel Özdoğan, “Pure and Applied Sciences, Computational Analysis and Experimental Verification of Premixed Combustion of Hydrogen Methane/Air Mixtures, Thesis For The Degree Of Doctor Of Philosophy in Mechanical Engineering.”

[5] D. Laurence, S. Parpais, H. Touil, J. Bertoglio, and M. Michard, “Engineering Turbulence Modelling and Experiments-4 W A spectral closure for inhomogeneous turbulence applied to the computation of an engine related flow.”

[6] T. Lachaux, “Etude des effets de la haute pression sur la structure et la dynamique des flammes turbulentes de prémélange pauvre de méthane-air.” [Online]. Available: https://tel.archives-ouvertes.fr/tel-00010401

[7] F. Halter, “Caractérisation des effets de l’ajout d’hydrogène et de la haute pression dans les flammes turbulentes de prémélange méthane/air.” [Online]. Available: https://tel.archives-ouvertes.fr/tel-00591421

ELEKTRİK KAYNAKLI YANGINLAR

Cemil ÖZKALAY[1], Onur MAMMACIOĞLU[2], Hakan Serhad SOYHAN[3], Gökhan COŞKUN[4]

1. Sakarya Üniversitesi Fen Bilimleri Enstitüsü Yangın ve Yangın Güvenliği ABD/Sakarya email: cemilozkalay@gmail.com
2. Sakarya Üniversitesi Fen Bilimleri Enstitüsü Yangın ve Yangın Güvenliği ABD/Sakarya email: mammacioglu@gmail.com
3. Sakarya Üniversitesi Fen Bilimleri Enstitüsü Yangın ve Yangın Güvenliği ABD/Sakarya email: hsoyhan@sakarya.edu.tr
4. Sakarya Üniversitesi Fen Bilimleri Enstitüsü Yangın ve Yangın Güvenliği ABD/Sakarya email: gcoskun@sakarya.edu.tr

Öz

Bu çalışmada, elektrik kaynaklı yangınların ne kadar fazla hayatımızda yer aldığı, vermiş olduğu hasarlar istatistiki bilgiler ışığında ortaya konulmuştur. Yangın hakkında genel tanımlar yapılmış olup, yangın sınıfları anlatılmış, elektriğin bir yangın sınıfı olmadığı fakat yangının temel nedenlerinden biri olduğu açıklanmaya çalışılmıştır. Elektrik kaynaklı yangınların sebeplerine bakıldığında çoğunlukla; ark hataları, zayıf veya gevşek bağlantı, aşırı yüklenme ve kısa devre ile statik elektrik nedenli olarak sıralanmaktadır. Ülkemizde meydana gelen yangın olaylarına ait istatistiki verilere bakıldığında ise elektrikli ev aletlerinden kaynaklı yangınlar karşımıza sıklıkla çıkmaktadır. Türkiye'de meydana gelen elektrik kaynaklı yangınların aylara göre dağılımına bakıldığında ise yaz aylarının büyük bir kısmını kapladığı ifade edilebilir. Çalışmanın son bölümlerinde elektrik kaynaklı bir yangınla karşılaşıldığında hareket tarzlarını gösteren bir poster hazırlanmış olup, elektrik panosu gibi sıklıkla yangın çıkması muhtemel yerlere asılmasının bilinçlendirme ve müdahale yönünden faydalı olacağı değerlendirilmektedir. Sonuç olarak, yanmayı ve yangını hayatımızdan tamamen çıkartmak mümkün olmasa da daha bilinçli bir toplum sayesinde azaltmamızın mümkün olduğunu kesinlikle unutmamalıyız.

Anahtar Kelimeler: Elektrik, yangın, ark, kısa devre

FIRES CAUSED BY ELECTRICITY

Abstract

In this study, how much electrical fires take place in our lives and the damages they cause are revealed in the light of statistical information. General definitions about fire have been made, fire classes have been explained, and it has been tried to explain that electricity is not a fire class but is one of the main causes of fire. Considering the causes of electrical fires mostly; arc faults, poor or loose connection, overload and short circuit, and static electricity. When we look at the statistical data of fire events in our country, fires originating from electrical household appliances are frequently encountered. Considering the distribution of electricity-related fires in Turkey by months, it can be stated that they cover a large part of the summer months. In the last part of the study, a poster was prepared showing the ways of action when faced with an electrical fire, and it is considered that hanging it in places where fire is likely to occur frequently, such as electrical panels, will be beneficial in terms of awareness and intervention. As a result, we should definitely not forget that although it is not possible to completely eliminate burning and fire from our lives, it is possible to reduce it thanks to a more conscious society.

Keywords: Electricity, fire, arc, short circuit

1 GİRİŞ

Elektrik enerjisi iletilirken, dağıtılırken ve tüketilirken farklı sebeplerden dolayı arklar, patlamalar, hatta yangınlar meydana gelmektedir. Bu yangınlar ise, maddi hasarların yanı sıra yaralanmalar ve can kayıpları olarak sonuçlanmaktadır.

İnsanlık var olduğu günden beri barınma, giyinme, beslenme, ulaşım vb. ihtiyaçlarını karşılamak için yanma neticesinde ortaya çıkan enerjiden yararlanmıştır. Madde, oksijen ve ısı üçlüsü "kontrollü" bir yanma meydana getirmişse canlılar ve çevre için bir sorun oluşturmaz ama kontrol edilemez olduğunda "yangın" adını alır ve hem canlılar hem de çevre için çok ciddi sorunlara yol açan bir durum hâline gelir.

Yangına, havanın (O_2) ve yanıcı maddenin bulunduğu ortamda tahmin edilemeyen ya da beklenmeyen bir şekilde oluşan ısı kaynakları neden olmaktadır. Elektriğin yangının meydana gelmesinin nedenlerinden biri olduğu bilinen bir gerçektir. Elektrik ısınmış alan yakınlarındaki her türlü yanıcı maddeyi yakabilecek derecede yüksek ısılar üretme kabiliyetine sahiptir. Ulusal basınımızda "elektrik kaynaklı" olarak haberi yapılan önemli yangınlardan bazıları, aşağıda sıralanmıştır.

31 Temmuz 2008'de Manavgat'ta "Türkiye'nin en büyük ikinci orman yangını" olarak nitelendirilen orman yangını rüzgâr nedeniyle havai enerji nakil hatlarında kısa devreler oluşan arkların tarladaki anızları yakmasıyla başlamıştır. Kıvılcımlar rüzgâr aracılığıyla ormana taşınmış; 16 bin hektar orman alanı, çok miktarda köy evi ve hayvan ağılı yanmış; sayısız küçük ve büyükbaş hayvanla yaban hayvanı telef olmuştur.

22 Ocak 2013'te İstanbul'da, Galatasaray Üniversitesinin tarihî binasının çatısındaki yangın asansörün aşırı ısınan elektrik kablolarından kaynaklanmıştır.

11 Nisan 2014'te İzmir'de bir huzurevinde elektrik arkı nedeniyle meydana geldiği düşünülen yangında 2 vatandaşımız hayatını kaybederken 2 itfaiye eriyle 25 sivil, dumandan etkilenmiştir.

29 Kasım 2016'da Adana'nın Aladağ ilçesinde, 10 yurt öğrencisi, 1 eğitmen ve bir yurt yetkilisinin çocuğu hayatını kaybetmiştir. Yangının yurdun elektrik panosundan kaynaklandığı açıklanmıştır.

14 Ağustos 2022 tarihinde, Mısır'da Gize şehrindeki bir kilisede çıkan yangında en az 41 kişi hayatını kaybetti. Elektrik kaynaklı çıktığı düşünülen yangında, yaşları 3 ila 16 arasında değişen 18 çocuğunda hayatını kaybettiği açıklandı.

İstanbul Büyükşehir Belediyesi İtfaiye Daire Başkanlığı verilerine göre 2022 yılının ilk yarısında kentte çıkan yangınların yüzde 25'ini oluşturan 2 bin 717 olay elektrik kaynaklı yaşandı. Geçen yılın aynı döneminde 2 bin 352 yangının elektrik kaynaklı meydana geldiği belirtildi.

Bunlar gibi daha birçok örnekten de anlaşılacağı üzere elektrik kaynaklı yangınların meydana geldiği yerler; her tür yaşam alanı, okullar, camiler, hastaneler, fabrikalar, köyler hatta ormanlar olabilmekte; elektrik nedenli yangınlarda da farklı sebeplerden oluşan yangınlardaki gibi önemli oranda maddi hasar, yaralanma ve can kayıpları yaşanabilmektedir (Şengöz ve Merdan, 2015).

2 GENEL BİLGİLER

2.1. Yangın *Nedir?*

Yanma, hidrojen ve karbon gibi yakıtların oksijen ile birleşerek ısı enerjisini serbest bırakması ve gazların sıcaklık artışına neden olan kimyasal bir tepkimedir. Yangın ise, yanma olayının kontrol altına alınamamasının bir neticesidir.

2.1.1. Yanma üçgeni

Yanma olayının meydana gelebilmesi için 3 temel unsurun bir araya gelme şartı vardır. Bunlar; yanıcı madde, ısı ve oksijen şeklindedir.

2.1.2. Yangın sınıfları

Yangınların, sıklıkla karşımıza çıkması ve yangın nedenlerinin daha iyi araştırabilmesi adına yanıcı maddelerin türleri esas alınarak yangınları sınıflandırma yoluna gidilmiştir. Yangın sınıfları, Avrupa Birliği (AB) standartlarını kabul edip kullanan ülkemizde bu kodların önüne Türk Standartları (TS) eklenerek literatüre girmiştir. Yangın sınıfları; TS EN 2 ve TS EN 2/A1 Türk standartlarına göre aşağıdaki şekilde tarif edilmiştir:

A sınıfı yangınlar : Yanmanın, normal olarak parlak korların oluşumuyla yürüdüğü, genellikle organik esaslı katı madde yangınları,

B sınıfı yangınlar : Sıvılar veya sıvılaşabilir katılar ile ilgili yangınlar,

C sınıfı yangınlar : Gaz yangınları,

D sınıfı yangınlar : Metal yangınları,
F sınıfı yangınlar : Pişirme gereçlerindeki pişirme ortamı (bitkisel veya hayvansal sıvı ve katı yağlar) yangınları şeklindedir.

AB standartlarında elektrik yangınları ile ilgili bir sınıf tanımlanmamıştır. Elektrik bir yangın türü değil, yangın nedeni olarak ele alınmaktadır. Ancak elektrik kaynaklı yangınların çok olması sebebiyle, Amerikan yangın sınıflandırması ise elektrik yangınlarını C, Asya ülkeleri de E sınıfı yangın olarak tanımlama ihtiyacı hissetmiştir. Hatta elektrik yangınları ve alınması gereken önlemler ile ilgili ilk makale de 1747 yılında ABD başkanı Benjamin Franklin tarafından yazılmıştır.

2.2. Elektriğin Tehlikeleri ve Yangın ile İlişkisi

Risk açısından elektriğin enerjisi genel olarak çarpma ve yakma riski olarak karşımıza çıkmaktadır. Bu riskler, doğrudan yangına neden olabileceği gibi, dolaylı olarak da yangına yol açabilir. Başka bir sebepten başlamış olan yangının, elektrik hattına temas etmesi neticesinde elektrik enerjisinin de yangın üçgenine dâhil olması söz konusudur. Elektrik, hata ve arızaların bir sonucu olarak yangına yol açmaktadır. Elektrik başlı başına bir yangın nedeni olmayıp, yangının başlamasına yol açan bir etmendir. Elektrikten kaynaklanan bu hata ve arızalar birçok can ve mal kaybına neden olmaktadır. Örneğin, ABD'de sırf elektrik hata ve arızalarından dolayı yalnızca 2006 yılında 340 kişi ölmüş, 1400 kişi yaralanmış ve doğrudan 1.45 milyon dolarlık maddi zarar yaşanmıştır (Hall ve John, 2009). Aynı şekilde, İngiltere yangın ve kurtarma servisi (Fire Rescue Service) 2005 yılı boyunca 47 000'in üzerinde yangının yüzde 43'ünün elektrik probleminden kaynaklandığını raporlamıştır (Electrical Safety Council, vd.). Ülkemizde de bu durum farklı değildir. Örneğin, İstanbul Büyükşehir Belediyesi (İBB) İtfaiye Daire Başkanlığı tarafından yayınlanan Tablo-1'deki istatistiki sonuçlara göre, elektrik yangınları her yıl ikinci sırada yer almıştır. Ayrıca bu yangınlara elektrikli ev aletlerinden kaynaklı yangınları da dâhil edecek olursak, elektrik yangınlarının oranı daha ciddi seviyelere çıkmaktadır.

Tablo 1: İstanbul'da 2015-2020 yılları arası meydana gelen yangın sayıları (İBB 26.04.2020)

Kaynak	Yıl											
	2015		2016		2017		2018		2019		2020 Ocak-Mart	
	Sayı	Yüzde	Sayı	Yüzde	Sayı	Yüzde	Sayı	Yüzde	Sayı	Yüzde	Sayı	Yüzde
Sigara	10.532	39,0%	11.341	39,7%	8.420	33,6%	7.153	35,0%	9.201	40,8%	1.805	32,2
Elektrik	6.564	24,3%	6.155	21,5%	6.259	25,0%	5.442	26,7%	4.780	21,2%	1.323	27,1
Kasıt	2.058	7,6%	2.729	9,5%	1.981	7,9%	1.486	7,3%	1.749	7,8%	354	6,2
Baca	1.185	4,4%	1.093	3,8%	1.100	4,4%	858	4,2%	840	3,7%	328	6,6
Kıvılcım Sıçraması	1.021	3,8%	1.122	3,9%	1.178	4,7%	1.208	5,9%	1.214	5,4%	323	6,3
Tespit Edilemedi	956	3,5%	1.060	3,7%	1.824	7,3%	647	3,2%	1.129	5,0%	300	5,0
Elektrikli Ev Aletleri	1.245	4,6%	1.272	4,4%	1.206	4,8%	1.138	5,6%	1.238	5,5%	259	5,2
Kızışma (yüksek ısı ile)	1.107	4.1%	842	2.9%	943	3.8%	862	4.2%	924	4.1%	250	5.0
Diğer	823	3,1%	1.276	4,5%	1.014	4,0%	785	3,8%	575	2,6%	163	3,2
Çocukların Ateşle Oynaması	1.159	4,3%	1.374	4,8%	867	3,5%	553	2,7%	614	2,7%	98	1,9
Parlama (yanıcı sıvı (yemek parlaması vb.)	328	1,2%	322	1,1%	281	1,1%	284	1,4%	282	1,3%	76	1,4
Toplam	26.978	100%	28.986	100%	25.073	100%	20.416	100%	22.546	100%	5.279	100%

2.3. Elektrik Yangınlarının Sebepleri

Türkiye'de elektrik enerjisi, ilk kez 1902 yılında Tarsus'ta kurulan bir hidroelektrik santral ile üretilmeye ve kullanılmaya başlanmıştır. 1900'lerden günümüze kadar teknolojinin sürekli gelişmesi, yeni ve daha güçlü cihazların yapılması, elektrikli ev aletlerine duyulan ihtiyacın her geçen gün artması, elektrik enerjisini yaşamımızın olmazsa olmaz bir parçası haline getirmiştir. Günümüz ve gelecek teknolojisi akıllı ev modellemeleri ve hatta elektrikli araçların konutlardan şarj edilmesi dâhil yüksek enerji ihtiyacını ön plana çıkartacaktır. Fakat kurulan elektrik sistemlerinin 1900'lü yıllardaki yapısı, günümüzde talep edilen enerji miktarını karşılayamadığından elektrik sistemleri arıza vermektedir. Hatta hepimizin yakinen tanık olduğu 31 Mart 2015 tarihinde Türkiye geneli yaşanan elektrik kesintisi için Avrupa Elektrik İletim Ağı (ENTSO-E) Türkiye Proje Grubu ve Türkiye Elektrik İletim A.Ş. (TEİAŞ) tarafından ortaklaşa olarak hazırlanan 31 Mart Sistem Çökmesi Raporu'ndan yapılan derlemeye göre, söz konusu elektrik hatlarının aşırı yükten dolayı servis dışı kaldığı yönünde açıklama yapılmıştır (enerji enstitüsü, 25.06.2018).

Hem ülkemizde hem de dünyada incelenen yangınların büyük bir bölümünün eski binalarda yaşandığı görülmektedir. Hatta Amerikan Yangından Korunma Kurumu (NFPA) tarafından 1990'lı yıllarda geliştirilmeye başlanan Konutlar İçin Elektrik Kontrol Kodu (NFPA 73) bu duruma en güzel örnektir. Bu standart kodu geliştirilirken komite tarafından istatistiki veriler incelenmiş ve bu veriler ışığında bina yangınlarının yalnızca yüzde 5'lik kısmının 10 yaşından küçük binalarda meydana geldiği görülmüştür (Walker, 2009). Yani yangınların %95'lik kısmı 10 yıldan daha eski binalarda meydana gelmektedir. Bu durum, eski sistemlerin yenilenmemesi yada

günümüzdeki şartlara uygun olmayan ekipmanların kullanılmasının bir neticesidir. Yine aynı şekilde Enerji ve Tabii Kaynaklar Bakanlığı tarafından yayınlanan Elektrik İç Tesisatları Yönetmeliği'ne aykırı uygulamalarda elektrik yangınlarını tetiklemektedir.

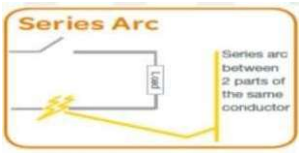
2.3.1. Ark hataları

Ark, elektriğin iletken bir boşlukta atlamaya çalışırken, yüksek sıcaklık ve ışıkla deşarjı şeklinde meydana gelen olaydır. Ark esnasında ortaya çıkan sıcaklık, bir kaç bin dereceye ulaşabilir. Bu sıcaklık değeri gerilim, akım ve iletken tipine bağlı olarak değişiklik gösterir (Clark ve ark., 2016). Babrauskas, arkların en az 6000K sıcaklık gösterdiğini bunun da bakır alüminyum gibi metalleri dahi eriterek yangın başlatabileceğini belirtmiştir (Babrauskas, 2003).

Nem ve çeşitli dış nedenler sebebiyle elektrik akımı izole bir yüzeyden yürüyerek bir karbon katmanı boyunca akabilir. Bu akım akarken arkın izlediği bu yol daha fazla akım iletir. Bu durum tespit edilemediği takdirde, bu akım çevresindeki yapı malzemelerini tutuşturana kadar devam eder. (Babrauskas, 2001).

2.3.1.1 Seri ark

Bir elektrik sisteminde aynı iletim kolu üzerinde meydana gelen arklardır (Şekil-1). Elektrik bağlantılarının gevşemesi, eskimesi, dışarıdan darbe alması ya da kemirgenler tarafından zarar verilmesi neticesinde oluşurlar.

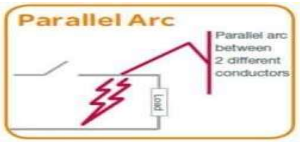


Şekil 1 Seri ark

Bu tür hataların önlenmesine yönelik geliştirilmiş ark hatası önleme cihazları mevcuttur. Ancak bu cihazların kullanımından kaçınılması, bağlantılarının uygun yapılmaması ya da cihaz seçiminde gerekli kriterlerin göz önüne alınmaması neticesinde ark hatası yüzünden birçok yangın meydana gelmektedir.

2.3.1.2 Paralel ark

Paralel ark, Şekil-2'dte görüldüğü gibi, bir hattın başka bir hatta değmesi ya da elektrik hattının toprak ile teması sonucu meydana gelen ark türleridir ve tehlikeli olan ark sınıfı da bunlardır. Artık akım cihazları ya da devre kesici sigortalar vasıtasıyla tespiti mümkündür. Ancak tespit edilememesi durumunda direkt olarak yangın nedenidir.



Şekil 2 Paralel ark

2.3.1.3 Ark yolu ve yalıtımın karbonlaşması

Kablolarda, gerilimin başka bir nokta ile temasını engellemek için kullanılan ve genellikle plastik menşeili olan yalıtım malzemeleri zamanla yıpranır. Yıpranan yalıtım malzemenin hasara, neme, tuzlara ya da aşırı ısıya maruz kalmaları durumunda iki iletken arasında sızıntı (küçük kaçak akımlar) akımları oluşmaya başlar (NFPA 921, 2011). Bu kaçak akımlar nedeniyle meydana çıkan ısı, iki iletken arasındaki izolasyonu karbonlaştırır. Bu duruma Resim-1'de görülen ark yolu denir (Benfer ve Gottuk, 2013). Ark yolunun elektrik yangınları ile olan ilişkisi hakkında birçok düşünce vardır. Yearence, elektrik yangınları analizi üzerine hazırladığı kitabında çoğu yangının ark yolundan meydana gelen küçük kıvılcımlar ile başladığını iddia etmiştir (Yereance, 1995).

Beyler ve Gratkowski, hasar görmüş olan düşük gerilimli devrelerin bile (12 Volt) ark yolu oluşturarak yangın çıkartabileceğini gözlemlemişlerdir (Beyler ve Gratkowski, 2006).

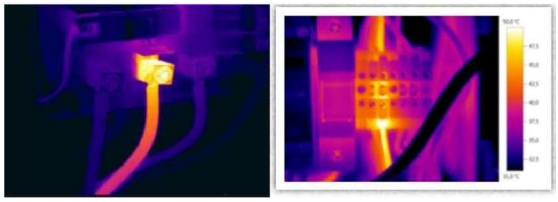


Resim 1 Ark yolu (wha-international, 16.07.2022)

2.3.2. Zayıf veya gevşek bağlantı

Elektrik enerjisinin iletilmesini zorlaştırıcı bir direnç sebebi ise kötü bir devre bağlantısıdır. Bu direnç zamanla kontakların ısınmasına neden olur ve oksit oluşumuna neden olur. Oksit, her ne kadar akımı ve devreyi işlevsel kılsa da, gösterdiği aşırı direnç sebebiyle oksit zamanla ısınır ve etrafındaki yanıcı maddeleri yakmaya başlar (NFPA 921, 2011). Elektrik sistemlerinin zamanla yıpranması ya da yetkisiz kişilerce ve bilinçsizce yapılan bakım onarım işlemleri nedeniyle tesisatta yer alan elemanların bağlantısı gevşek bırakılabilir. Resim-2'de görüldüğü gibi tüm kabloların ısınması normal derece iken ortada yer alan kablo bağlantısının gevşek kalması nedeniyle ısısı diğerlerinden daha fazla olacaktır. Bu ve benzeri

durumlarda kablodaki ısı etrafındaki malzemeleri de ısıtarak yangın tetikleyicisi olmaktadır.



Resim 2: Zayıf bağlantı (infrared imaging services, 16.07.2022)

Belki de çoğumuzun evlerinde bulunan ama önemsemediğimiz hatalı bağlanmış veya gevşek bir prizin neden olduğu yangının aşamaları farkındalık yaratmak için Şekil-3'te anlatılmıştır.



1. Yanlış veya gevşek yapılmış bir priz bağlantısı,

2. Bağlantılar yavaş yavaş ayrılır ve aşırı ısınır,

3. Kablo yalıtımı ve soketi ısıdan özelliğini kaybeder, yalıtım malzemesini iletken olarak işlev gören karbona dönüştürür,

4. Akımın bir kısmını tellerden geçirir ve elektrik arkları oluşturur,

5. Kablo yalıtımı ve soketi alev alır,

6. Yangın daha sonra odaya kolaylıkla yayılmaya başlar, (yakınındaki bir perdeye, duvar kaplamasına vb).

Şekil 3 Elektrik kaynaklı bir yangının (priz) aşamaları örnek çalışması

2.3.3. Aşırı yüklenme ve kısa devre

Aşırı yüklenme, bir elektrik kablosu ya da kablolama sistemi içerisinden kapasitesinin üzerinde bir akım geçirilmesi ile gerçekleşir (Wong, 2011). Bu durumda, aşırı yüklenmenin gerçekleştiği noktada sıcaklık artacak ve aşırı ısınmaya yol açacaktır. Kabloların yalıtım malzemesinin bu sıcaklığa dayanamaması neticesinde kablo içerisindeki iletkenler birbiri ile temas edecek ya da ark sebebi ile yangına neden olacaktır. Eğer çevrede eriyebilen malzemeler varsa, bu malzemelerinde ısıdan etkilenmesi sonucu alev alarak yangını başlatması söz konusudur. Ayrıca, telin erime sıcaklığı çok yüksek olduğundan dolayı noktasal olarak değil, hat boyunca bir ısınma meydana gelir. Yanlış kablo seçimi ya da maliyet azaltmak için daha dar kesitli kabloların kullanımı bu duruma yol açan ve sıklıkla rastlanan bir sonuçtur. Ülkemizde özellikle 30 yaş ve üzeri binaların elektrik projeleri hazırlanırken o günün şartları referans alınarak elektrik tesisatları kurulmuştur. O dönemin şartlarına bakıldığında elektrik, genellikle aydınlanma amacı ile kullanılmakta idi. Daha sonradan elektrikli ev aletlerinin gelişmesi, çoğalması ve kullanımının artması tesisatları yetersiz hale getirmiştir. Kablo kesitleri, kullanılan sigortalar, elektrik panoları hala o gün talep edilen güç değerinde kalmıştır. Birçok binada ya da yakın çevremizde "sigorta atması'' terimini duyuyor olmamız boşuna değildir. Uzatma kablolarının bilinçsiz şekilde kullanımı elektrik priz yangınlarının temelini oluşturduğu gibi aşırı yüklenmeden kaynaklı elektrik yangınlarının da en önemli sebebi konumundadır (Resim-3).



Resim 3 Aşırı yüklenme (ficoh, 11.06.2022)

Bir elektrik devresinde küçük dirençli ancak yüksek akımlı bir arıza kısa devre olarak adlandırılır. Bu durum, elektrik kablolarının birbirine temas etmesi ile meydana gelebileceği gibi, iki iletkenin birbirine teması ile de ortaya

çıkar. Devre kesici sigortalar bu tür durumlara karşı koruma sağlayacak şekilde tasarlanmıştır. Ancak yanlış ve bilinçsiz uygulamalar ya da bahsi geçen bu koruyucu sigortanın hiç bulunmaması elektrik kablolarından yangın çıkma riskini arttırmaktadır. Avrupa İstatistikleri ve Olası Yangın Güvenliği önlemlerine göre, bu tür kısa devre hataları, elektrik kablolamasından kaynaklanan yangınların en yaygın nedenidir (Kobes ve ark., 2009). Modern çoklu prizler, kapasitesinin üzerinde güç talep edildiğinde, aşırı yüklenmeyi önleyen bir aşırı akım koruyucusu ile donatılmıştır. Eski modeller ise aşırı akım koruyucuları içermez ve bu nedenle aşırı yüklemeye karşı koruma sağlayamazlar. Çoklu prizler taşınabilirliği nedeniyle, sabit prizlerden daha fazla hasar ve yıpranma eğilimi gösterirler (Gardner, 2005).

2.3.4. Statik elektrik

Maddenin yüzeyleri üzerinde sürtünme sonucu üretilen elektriksel yükten dolayı oluşur (Resim-4). Aşırı yüklenen maddelerin üzerindeki elektriksel yükün herhangi bir sebeple deşarjı esnasında oluşan kıvılcım yanmayı başlatabilir. Tutuşabilir sıvılar kaptan kaba aktarılırken meydana gelen yangının nedeni olarak genelde statik elektrik gösterilir. Bu nedenle tutuşabilir sıvı kapları, birbirleri arasında yakıt nakli yapılmadan önce mutlaka topraklanmalıdır.



Resim 4 Statik elektrik (fizik.net.tr/ 11.06.2022)

2.4. Ülkemizde Meydana Gelen Yangın Olaylarına ait İstatistiki Veriler

Tablo-2 Ülkemizde meydana gelen elektrik kaynaklı yangınların başlama yerleri ve miktarları gösterimektedir. Bu veriler ihbarı yapılan ve İtfaiye Daire Başkanlıkları tarafından rapor düzenlenen yangın olaylarından oluşmaktadır. Yani bildirilmeyen ve olay yerindekiler tarafından söndürülen elektrik kaynaklı yangınlar hakkında bilgi içermemektedir.

Tablo-2 Ülkemizde meydana gelen elektrik kaynaklı yangınların başlama yerleri ve miktarları

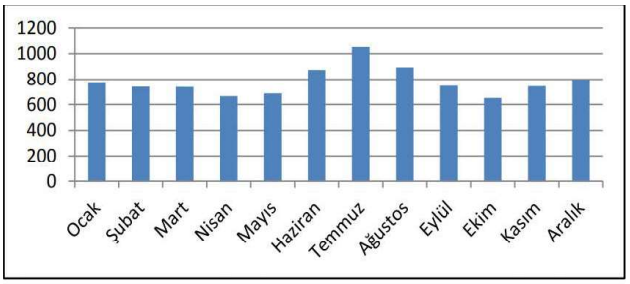
Elektrik Kaynaklı Yangınların Başlama Yerleri	Miktar
Pano yangını	1182
Bina ya da direk tipi trafo kaynaklı yangınlar	607
Havai hatların fırtına/sıcak nedeniyle sehim yaparak, koparak ya da ağaçlara temas ederek başlattıkları yangınlar	547
Elektrik tesisatının dış etkenlerden hasar görmesiyle açığa çıkan iletkenlerdeki arklardan meydana gelen yangınlar	516
Buzdolabı, mini buzdolabı, endüstriyel derin dondurucu yangını	466
Banyo şofben yangını	391
Aspiratör yangını	390
Elektrikli ısıtıcı yangını	369
Direklerde izolatör, sigorta ya da kabloların aşırı ısınmasından; direk lambalarından ya da direklerde meydana gelen arklardan kaynaklanan yangınlar	355
Çoklu priz yangını	306
Klima yangını	278
Elektrik nedenli olduğu düşünülen yangınlar	268
TV, müzik seti, DVD player vb. yangını	235
Çamaşır makinesi yangını	219
Yapı bağlantı hattı kablo yangını	217
Aydınlatma ve aydınlatma tesisatları kaynaklı yangınlar	210
Sigorta kutusu yangını	209
Sıva üstü tesisat kaynaklı yangınlar	199
Priz ve anahtar kaynaklı yangınlar	191
Şarj cihazı, dizüstü bilgisayar kaynaklı yangınlar	191
Küçük mutfak aletleri (fırın, su ısıtıcısı, tost/kahve mak. vb.) yangınları	184
Seyyar kablo kaynaklı yangınlar	179
Bulaşık makinesi yangını	159
Sayaç yangını	158
Elektrikle çalışan cihazların kablolarının hasar görmesi neticesinde meydana gelen arklardan kaynaklanan yangınlar	115
Çeşitli üretim makinelerinden kaynaklanan yangınlar	115
Tavan/duvar tipi havalandırma fanları, hava perdesi, vantilatör yangınları	113
Elektrikli battaniye yangını	111
Havai hatlarda kuşlardan kaynaklanan yangınlar	108
Çeşitli motorlardan kaynaklanan yangınlar	96

Tablo-2 Ülkemizde meydana gelen elektrik kaynaklı yangınların başlama yerleri ve miktarları (devamı)

Elektrikli kişisel aletlerden (saç kurutma mak., ütü vb.) kaynaklanan yangınlar	94
Tali pano yangını	86
Aşırı akım nedeniyle eriyen kablolarda meydana gelen arkların etraftaki yanıcı nesneleri tutuşturmasından kaynaklanan yangınlar	71
Güç kaynağı, jeneratör kaynaklı yangınlar	68
Aşırı akımda oluşan izolasyon eriyiklerinin çeşitli malzemeleri tutuşturması nedeniyle çıkan yangınlar	60
Doğal afetler neticesinde tesisatların zarar görmesiyle oluşan yangınlar	57
Kombilerden kaynaklanan yangınlar	50
Çeşitli büro makinelerinden kaynaklanan yangınlar	49
Bilgisayarlardan kaynaklanan yangınlar	45
Çay/kahve makinesi, su sebili yangınları	35
Exproof ve dustproof ekipman kullanılmamasından kaynaklanan yangınlar	16
Hatalı arıza ve bakım sonrasında gevşek bırakıldığı ya da çok sıkıldığı için kırılan bağlantı noktalarından kaynaklanan arkların neden olduğu yangınlar	15
Statik elektrik yüklerinin neden olduğu yangınlar	15
Topraklama hatasından dolayı su, doğalgaz tesisatına şase yangını	11
Elektrikli süpürge yangını	9
El tipi iş aletleri yangınları	3

Tablo-3'den anlaşıldığı üzere haziran, temmuz ve ağustos aylarında elektrik kaynaklı yangınların miktarında gözle görülür bir artış vardır. Bu aylardaki elektrik kaynaklı yangınların başlama yerlerinin belirlenmesi, İSG uzmanlarının ve konuyla ilgili birçok yöneticinin ilgi alanına girmektedir. Bu aylarda toplam 2822 elektrik kaynaklı yangın meydana gelmiştir.

Tablo-3 Türkiye'de meydana gelen elektrik kaynaklı yangınların aylara göre dağılımı



Yaz aylarında en sık görülen elektrik kaynaklı yangın sebepleri ve başlama yerleri açısından ilk 15 elektrik kaynaklı yangın, Tablo-4'te yer almıştır. Elektrik kaynaklı yangınların başlama yerleri ve miktarları özellikle mücadele konusunda yöneticilere, İSG uzmanlarına, iş yeri sahiplerine ve ikamet sahiplerine önemli bir uyarı oluşturacağı düşünülerek örneklendirilmiştir. Bunlar, Elektrik kaynaklı yangınların frekans bilgilerini vermektedir ve birçok risk değerlendirme yönteminde kullanılabilir durumdadır.

Kuşlardan kaynaklanan 108 elektrik kaynaklı yangınların 83'ü yaz aylarında meydana gelmiştir. Bu durumda kuşlardan yazın kaynaklanan elektrik kaynaklı yangınların kuşlardan kaynaklanan tüm elektrik kaynaklı yangınlara oranı %76.85 olmaktadır. Bu durum, pek çok bölgemizde, özellikle ormanlık ve tabi örtü alanları ile tarlalarda, önemli hasarlara yol açmıştır. Bu nedenle ormanlık ve tabi örtü ile tarım alanlarının olduğu yerlerdeki havai hatlarda, kuşlar için özel önlemler alınması gerektiği anlaşılmaktadır. Yazın kullanımı artan soğutma ihtiyaçlarının da yaz aylarındaki yangın olaylarında ana etken olduğu da görülmektedir.

Tablo-4 Yaz aylarında en sık görülen elektrik kaynaklı yangın sebepleri ve başlama yerleri

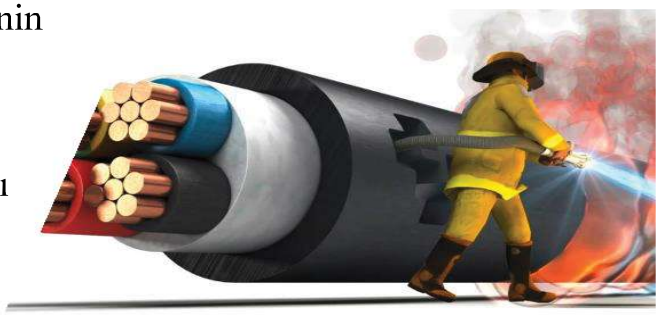
Elektrik kaynaklı yangın başlama yeri	Miktar	Oran
Havai hatların fırtına/sıcak nedeniyle sehim yaparak, koparak ya da ağaçlara temas ederek oluşturduğu yangınlar	337	%11.94
Pano yangını	328	%11.62
Bina ya da direk tipi trafo kaynaklı yangınlar	227	%8.04
Direklerdeki izolatör, sigorta ya da kabloların aşırı ısınmasından, direk lambalarından ya da direklerde meydana gelen arklardan kaynaklanan yangınlar	187	%6.62
Buzdolabı, mini buzdolabı, endüstriyel derin dondurucu yangını	183	%6.48
Elektrik tesisatının dış etkenlerden hasar görmesiyle açığa çıkan iletkenlerdeki arklardan oluşan yangınlar	137	%4.85
Banyo şofben yangını	99	%3.50
Elektrik nedenli olduğu düşünülen yangınlar	88	%3.11
Havai hatlarda kuşlardan kaynaklanan yangınlar	83	%2.94
Klima yangını	81	%2.87
Aspiratör yangını	79	%2.79
Çoklu priz yangını	64	%2.26
Yapı bağlantı hattı kablo yangını	63	%2.23
Sıva üstü tesisat kaynaklı yangınlar	61	%2.16
TV, müzik seti, DVD player vb. yangını	54	%1.91

ELEKTRİK KAYNAKLI BİR YANGIN DURUMUNDA YAPILMASI GEREKENLER

Öncelikle elektrik kaynaklı bir yangın durumuyla karşılaştığımızda ortamda elektrik yükünün devam ediyor olma ihtimalini aklımızdan çıkarmamalıyız. Aşağıda belirtilen yönergeler doğrultusunda müdahale işlemlerini yapmalıyız.



- Duman, yanık kokusu, alev gibi durumlarla karşılaşan kişiler soğukkanlı olmalı ve panik yapmadan çevresindeki kişileri uyarmalı,
- Elektrik yangınında mümkünse ilk olarak elektriği keserek yangının büyümesi engellenmeli,
- Yangın müdahale edebileceğiniz boyutlardaysa iletken olmayan yangın söndürme cihazlarıyla (kuru kimyevi tozlu, karbondioksitli veya halojen) yangına müdahale edilmeli, **(Kesinlikle Su ve Su İhtiva Eden Söndürücüler ile Müdahale Etmeyin!!!)**
- Varsa hemen yangın butonuna basarak alarm sistemini devreye sokmalı,
- Olay yerini hızla terk etmeli ve mümkünse kapı ve pencere kapatılmalı,
- **110** veya **112** aranarak yangın ekiplerinin gelmesi sağlanmalı,



- Yangın her yeri sarmış ve kaçış yolları kapalı ise, muhafazalı bir yere sığınmalı ve kapıyı kilitlemeden kapatarak yangın ekipleri durumdan haberdar edilmeli,
- Binadan çıktıktan sonra yangın kontrol altına alınmadan asla binaya tekrar geri dönülmemeli,
- Yangının sönmesine müteakip uzman bir elektrikçi çağırarak tesisat kontrol ettirmelidir.



Özkalay C. 2022

3 ELEKTRİK KAYNAKLI BAZI YANGINLARIN DEĞERLENDİRİLMESİ

Yangın sonrası incelemeleri yapılan Elektrik kaynaklı yangınların değerlendirilmelerine yönelik çalışmada;

Çeyiz Mağazası Yangını:

İnceleme ve değerlendirmeler sonucunda;

Yoğun yanma emaresini olduğu bölge belirlenerek başlangıç noktası olduğu değerlendirilen yerdeki elektrik kabloları incelendiğinde, vişne çürüğü renginin ortaya çıktığı ve boncuklanma olduğu gözlenmektedir. Bu noktada "Klimanın iç ünitesine elektrik panosundan gelen kabloların ark yapması sonucunda ortaya çıkan kıvılcımların malzemeler üzerinde bulunan naylonları tutuşturması" nın sebep olduğu değerlendirilmiştir.



Resim 5 Çeyiz Mağazasının Yangından Sonraki Görüntüsü (Girişe Göre Sağ Duvar Üzerindeki Klima)

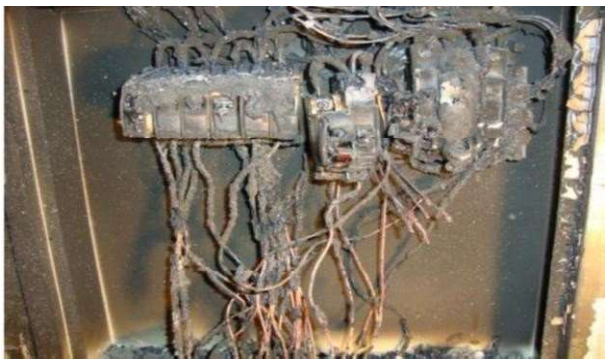


Resim 6 Çeyiz Mağazasının Yangından Sonraki Görüntüsü (Girişe Göre Sağ Duvar Üzerindeki Sigorta Panosundaki Bazı Kablolarda Tomurcuklanma ve Renk Değişimi)

Mobilya Mağazası Yangını:

İnceleme ve değerlendirmeler sonucunda;

Yoğun yanma emaresi nedeniyle yangının başlangıç yeri olarak bulunan noktadaki elektrik panoları ve elektrik kabloları incelendiğinde, boncuklanma ve renk olarakta vişne çürüğü rengini almış olduğu görülmüş, yapılan incelemelerde, işyerinin ana enerji panosu üzerinde, işletmenin teşhir salonunda spotlu gizli aydınlatmalar için kendileri tarafından özel olarak yaptırılmış farklı bir pano daha bulunduğu ve söz konusu spot lambalardan kaynaklı elektrik hatlarında meydana gelen akım yükselmesine bağlı olarak enerji kablolarının ısınarak ark yapması sonucunda çıkan kıvılcımların kablo izoleleri ile pano altında bulunan kâğıtları tutuşturması neticesinde söz konusu hadisenin meydana geldiği değerlendirilmiştir.



Resim 7 Mobilya Mağazası Sigorta Panosunda Kısa devre Sonucu Boncuklaşma ve Vişne Çürüğü Rengi

Lokanta Yangını:

İnceleme ve değerlendirmeler sonucunda;

Yangının başlangıç yerindeki elektrik prizi ve elektrik kabloları incelendiğinde, kablolarda boncuklanma ve vişne çürüğü rengi görülmüş olup yapılan incelemelerde, uzun süre prizde takılı elektrikli cihaz kablolarının, ısınarak izolelerinin eridiği, izoleleri eriyen kabloların şase yapması sonucunda çıkan kıvılcımların halı ve perdeleri tutuşturarak söz konusu hadiseye sebebiyet verdiği görüşüne varılmıştır.



Resim 8 Lokanta Yangınına Muhtemelen Sebep Olduğu Düşünülen Ark Kablo Telleri

Ayakkabı Mağazası Yangını:

İnceleme ve değerlendirmeler sonucunda;

Elektrik tesisatı ve prizler incelendiğinde, kablolarda boncuklanma ve vişne çürüğü rengi görülmüş olup, vitrinde bulunan spot lambaların aşırı ısınarak ark yapması sonucunda çıkan kıvılcımların vitrindeki ayakkabıları tutuşturması neticesinde söz konusu yangının meydana geldiği gözlemlenmiştir.



Resim 9 Ayakkabı Mağazası Yangınına Sebep Olan Aksesuar içindeki Elektrik Tesisatından Bir Görüntü

Oyuncak Deposu Yangını:
İnceleme ve değerlendirmeler sonucunda;

Başlangıç yerine yakın elektrik panosu ve elektrik tesisatı incelendiğinde, kablolarda boncuklanma ve vişne çürüğü rengi görülmüş olup işyeri yetkilileri ile yapılan görüşmelerde; yangın hadisesinin meydana geldiği günün öğlen saatlerinde üst kattaki otel tesisatlarından su sızıntısı olduğu alt kattaki oyuncak deposununelektrik panolarının tam üzerine gelecek şekilde su sızıntıları bulunduğu, personelin ifadesine göre elektrik sayacı üzerindeki duvarda nemlenmenin görüldüğü tespit edildiğinden yangının tavandan damlayan suyun elektrik panosuna sirayeti sonucunda kısa devre yaptırması ve bina elektrik tesisat kablolarının ısınmasına bağlı olarak üzerlerindeki izolelerin eridiği ve çıplak elektrik kablolarının birbirleri ile temas etmeleri sonucunda çıkan kıvılcımların, yanması kolay emtiaları tutuşturması neticesinde söz konusu hadisenin meydana geldiği görüşüne varılmıştır.



Resim 10 Oyuncak Deposu Yangını ile ilgili Borumda Muhtemelen Yangına Sebep Olan Sigorta Panosundan Bir Görüntü

Trafo Fabrikası Yangını:
İnceleme ve değerlendirmeler sonucunda;

İşyerinde bulunan yağ tesviye cihazı içerisinde ısınan yağın taşmasına bağlı olarak elektrik tesisatı ile temas ettiği ve kabloların şase yaptığı, dökülen yağların meydana gelen şase sonucu tutuşması sonucunda yangın hadisesinin gerçekleştiği görüşüne varılmıştır.



Resim 11 Trafo Fabrikası Yangını Muhtemelen Yangın Çıkış Noktasından Bir Görüntü

Elektrik Kaynaklı Orman Yangınları:

Bir enerji nakil hattı genellikle yüksek hızlı rüzgar, ağaç dalları başta olmak üzere bitki örtüsüyle temas, ekipman/iletim arızası veya insan/hayvan teması nedeniyle yangına neden olmaktadır. Bazen bu faktörlerden biri veya birden fazlası aynı anda etkili olabilmektedir (rüzgarın etkisiyle ağaç dallarının yüksek enerji hatlarına teması gibi).

Ayrıca elektrikli ekipmanlarınyere düşmesi ve düştüğü yerde özellikle ince ve kuru yakıtlar ile temas etmesi sonucu yangının başlaması karşılaşılan durumlardandır. İletkenler veya transformatörlerden gelen kıvılcım veya erimiş metal de yere düşüp yangına neden olabilir. Yerleşim yerlerine uzak ve enerji nakil hattının bakımsız olduğu durumlarda tespit ve ulaşımdaki kısıtlar nedeniyle müdahalede gecikmeler maalesef büyük orman yangınlarıyla karşılaşmamız sonucunu ortaya çıkarmaktadır.

Dağıtım hatları genelde zemine yakındır ve bakımları yapılmadığında çoğu zaman ağaç dallarıyla temas halindedirler. Elektrik hatlarında çıkan yangınlar iletken arızasından, yalıtkan arızasından, donanım arızasından, kuşlardan, sincap, fare benzeri küçük hayvanlardan veya uçan balon, uçurtma benzeri eğlence araçlarından kaynaklanmaktadır. Ayrıca ekipmanın bakımsız olması da ekipman arızasına yol açabilmektedir.



Resim 12 Hayvansal etkenler



Resim 13 Enerji Nakil Hatları ve Orman Yangınları

Elektrikli ve Hibrit Araçlarda Meydana Gelen Elektrik Kaynaklı Yangınlar:

Teknolojinin gelişmesiyle elektrik ve elektronik hayatımızda daha fazla yer almaya başlamıştır. Bunlardan biri de ulaşımda elektrik enerjisinin kullanımının artması ve populer olmaya başlamasıdır. Elektriğin ulaşımda kullanımının artmasıyla birlikte yangın riskleride artmaya başlamıştır.

Araç tipine göre araba yangınlarının oranını bulmak için, Amerika Birleşik Devletleri Ulusal Ulaşım Güvenliği Kurulu (NTSB), Ulaşım İstatistikleri Bürosu (BTS) ve Recalls.gov verilerinden oluşturulan yangın istatistiklerine bakıldığında; 100.000 satış başına en fazla yangın olayında birinci sırada Hibrit araçlar gelmektedir.



Şekil 4 Tiplerine göre araç yangınları

Yangın sonrasında olay yeri inceleme faaliyetlerinin eğitimli kişilerce bilime dayalı, doğru analizlerinin yapılarak raporlanmaları ve istatistiklerin gerçekci olarak tutulmaları gereklidir. Bu çalışmalar muhtemel yangın nedenlerinin bilincine varılarak ortadan kaldırılması, can ve mal kayıplarının en aza indirilmesi açısından önemli bir veridir. Örneklerden de görüldüğü gibi bir yangına neden olan faktörler yangın çıkmadan önce yapılacak kontrol ve alınacak tedbirlerle ortadan kaldırılabilir.

4 SONUÇ

İstatistiklere bakıldığında elektrik kaynaklı yangınların azımsanamayacak bir seviyede olduğu söylenebilir. Elektrik kaynaklı yangınlar özellikle ülkemizde sıkça meydana gelen ve kamuoyu tarafından nedenleri çok iyi bilinmeyen, alınabilecek önlemler konusunda gerekli bilincin oluşmadığı son derece tehlikeli ve sinsi bir tehdittir. Standartlara uyulmadığı, kontrollerinin sağlanmadığı tasarımlarının doğru ve uygun bir şekilde yapılmadığı sürece yangın riski çok yüksek olmaya devam edecektir. Elektrik yangınlarına doğru müdahale yönteminin uygulanması da son derece önemlidir. Bu anlamda yangın başlamasına müteakip elektriğin kesilmesiyle birlikte yanan maddenin cinsine göre sınıflandırma yapılarak müdahale edilmesi gerekliliği unutulmamalıdır.

Elektrik kaynaklı yangınları önleme ve korunma sürekli ve sürdürülebilir bir disiplin olarak ele alınmalıdır. Temel yangın disiplinleri çerçevesinde elektrik bilimine özel olarak üretilecek olan çözümler, teknikler her safhada bilimsel olarak değerlendirilmeli ve işletilmelidir.

- Yaşam alanlarında meydana gelen elektrik nedenli yangınların tanımlanarak bir kontrol listesi oluşturulmalıdır.
- Yangın tehlikesinin her zaman olabileceği bilinci ile hareket edilerek oluşabilecek yangın riskleri minimize edilmelidir.
- Yangın önleme ve yangından korunumun her aşamasında bilgi, tecrübe, eğitim, kalifikasyon ve Ulusal/Uluslararası standartlara uygunluk, ciddiyetle dikkat edilmesi gereken hususlardır.
- Yangın güvenlik ve önleme felsefesinde her zaman zorunluluklar ile beraber gereklilikleri değerlendirmek doğru bir yaklaşım olacaktır.
- Yanma ve yangın yok edebileceğimiz bir durum değildir; kontrol altına alıp birlikte yaşamayı öğrenebileceğimiz bilimsel bir disiplindir. Can kayıplarına ve maddi hasarlara yol açan elektrik nedenli yangınların önlenmesi tamamen mümkün olmasa da alınacak tedbirlerle azaltılmaları mümkündür.

REFERANSLAR

[1] 6331 Sayılı İş Sağlığı ve Güvenliği Kanunu.

[2] BYKHY, 2015. Binaların Yangından Korunması Hakkında Yönetmelik.

[3] Elektrik İç Tesisleri Yönetmeliği.

[4] ŞENGÖZ, M., (2018) Elektrik Nedenli Yangınların Araştırılması ve Fmea Yöntemi İle Risk Analizi, Doktora Tezi, Isparta.

[5] ŞENGÖZ M. C. (2011), Meskenlerdeki Elektrik Tesisatlarından Kaynaklanan Yangınların İncelenmesi ve Yangın Risk Analizlerinin Yapılması, Süleyman Demirel Üniversitesi, Fen Bilimleri Enstitüsü, Yüksek Lisans Tezi, Isparta.

[6] KUŞ E. (2019), Elektrik Panolarında Yangınlara Karşı Fine Kinney Yöntemi İle Risk Analizi Yapılması, Üsküdar Üniversitesi, Sağlık Bilimleri Enstitüsü, Yüksek Lisans Tezi, İstanbul.

[7] NFPA 921, (2011) "Guide for Fire and Explosion Investigations," National Fire Protection Association, Quincy, MA.

[8] NFPA 921, (2017) "Guide for Fire and Explosion Investigations," National Fire Protection Association, Quincy, MA.

[9] TÜYAK 2011 Yangın ve Güvenlik Sempozyumu Bildiriler Kitabı, (2011).

[10] Soyhan H., Özkalay C., Can K., Mammacıoğlu O., Yangın ve Yaşam Kitabı 1. Baskı, Cenevre Fikir ve Sanat Kitapevi, İstanbul, 2018.

[11] http://itfaiye.ibb.gov.tr/img/91719932020. pdf, (Erişim tarihi: 16.07.2022).

[12] https://www.ankaradanhaber.com/, (Erişim tarihi: 26.07.2022).

[13] http://www.hurriyet.com.tr/gundem, (Erişim tarihi: 10.04.2017).

[14] https://www-autoinsuranceez-com. (Erişim Tarihi: 24.02.2022).

ONE-POT HYDRODEOXYGENATION ROUTE OF MICROALGAE OIL TO BIO-JET FUEL OVER NI/DOLOMITE CATALYST

B. ER, A. CAKAN, B. KIREN and N. AYAS*

Faculty of Engineering, Department of Chemical Engineering, Eskişehir Technical University, Eskişehir; email: nazcan@eskisehir.edu.tr

Abstract

Energy is considered as one of the main drivers for economic and social development. However, depletion of primary energy sources as a result of overconsumption and its damage to the environment in forms of greenhouse gases and pollution prompted countries to move towards new permanent alternatives to solve issues. Specifically, global airline industry is incredibly energy-intensive and highly relied on conventional petroleum-based fuels. For these reasons, the aviation sector becomes a significant source of anthropogenic greenhouse gas (GHG) emissions, as it sends out 918 Mt CO_2 emissions from both commercial passenger flights and freight businesses. Therefore, the depleting reserves of fossil fuels along with increased environmental consciousness contributed to a strong driving force towards developing efficient bio-jet fuel technologies. To this aim, the catalytic activity and product selectivity of dolomite supported Ni probed through one-pot synthesis of bio-jet range fuels in the catalytic hydrodeoxygenation of microalgae oil (*Chlorella protothecoides*). The product mixture obtained as a result of the reaction of microalgae oil in the catalytic environment was subjected to distillation and the liquid product was separated. The liquid product composition was then determined by Gas chromatography-Mass spectrophotometer (GC-MS) analysis. Based on the results, the deoxygenation of microalgae oil over 10Ni/Dolomite attained the highest yield of liquid product (e.g., n-paraffins, isoparaffins, olefins, naphthenes, aromatic and intermediates) and jet paraffins selectivity (C_8–C_{16}) under 50 bar initial H_2 pressure, 1% catalyst to oil ratio, 350 °C for 2 h.

Keywords: Microalgae oil, Catalyst, Ni/Dolomite, Hydrodeoxygenation, Bio-jet fuel, Biokerosene

1 INTRODUCTION

The role of air transport in bringing regions much closer together and its substantial contribution to international economic growth has made this sector grow continuously. According to the International Air Transport Association (IATA), the number of worldwide air travelers in 2018 rose to more than 4.3 billion, while the commercial air industry transported 64 million tonnes of freight, creating economic activity with the value of $6.7 trillion and supporting 65 million jobs. The continuation of such immense industry activities is entirely dependent on the uninterrupted supply of fuel, thus augmenting aviation fuel market potential. Global fuel consumption by commercial airplanes was 340 million m^3 per annum in 2018, rising by nearly 30% from 2005. It seems not to lose its steam in the foreseeable future, and this trend is expected to increase continually by annually 5% until 2050 [1].

Therefore, the global airline industry is incredibly energy-intensive and highly relied on conventional petroleum-based fuels. For these reasons, the aviation sector becomes a significant source of anthropogenic greenhouse gas (GHG) emissions, as it sends out 918 Mt CO_2 emissions from both commercial passenger flights and freight businesses. This amount corresponds to 2.5% of world energy-related carbon dioxide emissions, increasing by 32% over the previous five years [2]. When the impact of non-CO_2 civil aircraft emissions taking into consideration, this amounts currently up to 5% of total emissions. Besides, it is forecasted that this impact might climb to an unprecedented rate of 22% by 2050 unless technological investment is introduced and sustained and coordinated action is generated to implement new regulations and infrastructural arrangements [3].

Therefore, biomass-derived jet fuel has become a primary element in the aviation sector for sizeable investments, operating costs and environmental impact. One of the particular ways to process fatty acids for bio-jet fuel production is deoxygenation which is based on

two individual mechanisms, namely decarboxylation/ decarbonylation and hydrodeoxygenation reactions. The former mechanism is related to the removal of oxygen atoms in the fatty acid in the form of CO and CO_2, respectively, to produce alkanes with one carbon lesser than the original fatty acid. The latter mechanism facilitates the scission of the C-O bond and thereby saturating double bonds of triglycerides (TG) by the possibility of removing oxygen (in the form of water). Therefore, the extent to which these processes take place relies on the nature of the catalyst and reaction conditions [4]. This study aimed to evaluate the catalytic activity of dolomite supported Ni catalysts in the deoxygenation of microalgae oil (*Chlorella protothecoides*) for the production of bio-jet fuel. Additionally, extensive characterization of synthesized catalysts was carried out to scrutinize the role of support materials and Ni comparatively in the deoxygenation process.

2 MATERIALS AND METHODS

Among the analytical grade chemicals used in this study, nickel (II) nitrate hexahydrate (99%, Chempur), microalgae oil was used as received. Dolomite was supplied as a raw material from a local company. Dolomite was grounded as below 50 µ powder form and, it was calcined in dry air atmosphere at 950 °C for 6 hours prior to use.

2.1 Catalyst Preparation

Ni/Dolomite catalysts were synthesized by using the conventional wet impregnation method. In order to synthesis 10 wt% Ni/Dolomite, an appointed amount of nickel nitrate hexahydrate salt was added in a 100 g of distilled water. After that, nickel nitrate hexahydrate solution was mixed with calcined dolomite in a beaker. The impregnation was performed at 80 °C for 6 hours. The slurry was dried in the oven at 105 °C for 24 hours. Hereafter, it was grinded in a mortar and, calcined at 500 °C for 3 hours.

2.2 Catalyst Characterization

The Scanning Electron Microscope (SEM) images of synthesized catalysts were operated using with scanning electron microscope by high-resolution method in 20 kV (ZEISS-SUPRA 50 VP) in order to specify morphological properties. The catalysts were sputter-coated with thin layers of Au/Pd in few seconds before analyzing. Fourier Transform Infrared Spectra (FTIR) using with the ATR crystal method (Thermo Fisher Scientific-Nicolet iS10) were examined to find out the chemical functional groups of the catalyst surface in the range of 4000–600 cm^{-1}. X-ray Fluorescence (XRF) was used to investigate the chemical element compositions of the catalysts (Rigaku ZSX100e). During the analysis, the device voltage and current were treated as 50 kV and 50 mA, respectively. Thermogravimetric analysis (TGA) was operated to determine the weight loss changes, of the catalysts against temperature (Perkin Elmer STA 6000). Thermogravimetric thermal analysis measurements were studied in the temperature range of 30-850 °C and the heating rate was 10 °C/min. Results were recorded in nitrogen medium at a flow rate of 50 mL. X-Ray Diffraction patterns (XRD) were defined using the Rigaku Rint 2200 for the determination of crystal structures. Analyzes were made while the device was operating at 40 kV and 40 mA conditions. XRD patterns were recorded in the range of 5-80°. The specific surface area and pore volume of the catalysts was calculated using Brunauer-Emmett-Teller methods (Micromeritics, ASAP 2020). Catalysts were degassed under vacuum at 150 °C for overnight before the analysis.

3 BIO-JET FUEL FROM MICROALGAE

The experiments were carried out using a high temperature and pressure Parr autoclave reactor (Parr Instruments Co., Inc. USA, model 4575). For each experiment, microalgae oil and the 10Ni/Dolomite catalyst (1 wt%) was placed in the reactor vessel. Initial hydrogen pressure was 50 bar. After the reaction, the obtained liquid products were analyzed by GC-MS. The reactor system is given in Figure 1.

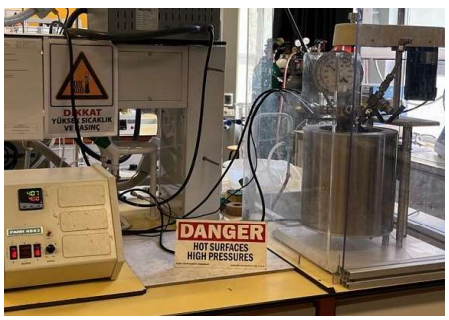


Figure 1. Reactor system

The obtained products subsequently were fractionated by using batch distillation system equipped with a Vigreux distillation column to separate jet fuel-range liquid hydrocarbon fuels. To implement that, the above-mentioned same procedure for GC-MS analysis was followed to differentiate and characterize the distilled bio-jet fuels.

Before the analysis, products were diluted with the dichloromethane. The capillary column HP-5 (30 m × 0.25 mm × 0.25 μm film thickness) was operated for compound identification in the GC/MS. The analysis method includes as 320 °C the injection port temperature, as initial temperature of 30 to 80 °C at a rate of 2 °C/min the GC program. After that, the column was hold for 20 min at 300 °C (heating ramp at 10 °C/min). The Wiley library was preferred for the identification of chromatogram peaks using with %90 similarity.

4 RESULTS AND DISCUSSIONS

Results of Catalyst Characterization

Dolomite and synthesized catalysts were characterized by XRD, XRF, TGA, FTIR, BET and SEM analyses. As a result, similar results were obtained when compared with the literature.

The impact of reaction conditions

Effect of the reaction time on the catalytic hydrodeoxygenation of microalgae oil

The reaction time has a major role in influencing the catalyst performance on conversion rate and product selectivity for deoxygenation reaction. The effect of the time interval within 2 to 6 h on the catalytic deoxygenation of microalgae oil at 350 °C and 50 bar H_2 initial pressure was examined over Ni/Dolomite.

The conversion of microalgae oil to different hydrocarbons fractions (gasoline, jet and diesel) through the deoxygenation reaction gradually proceeded over the course of reaction time. Based on the results, shorter reaction times exhibited considerable changes in selectivity, and the maximal bio-jet of 76.71% was attained at a reaction time of 2 h. However, there is no lighter hydrocarbon (C_4-C_7) in all samples. The results showed that the catalytic activity of Ni/Dolomite toward diesel production was improved from 1.70 to 9.60% when reaction time increased from 2 to 4 h, then decreased to 2.97% when reaction time was extended to 6 h.

5 CONCLUSIONS

The ever-increasing demand for jet fuel is growing at an unprecedented rate due to the growing aviation market. Contemporaneously to this, the depleting fossil-based fuels and their pernicious consequences of global warming and environmental degradation shifted the focus on the future aviation fuel to renewable energy sources. Catalytic upgrading of seed oil to bio-jet fuel via deoxygenation has recently become the main focus of the aviation industry. To this, the performance of Ni/Dolomite was tested to evaluate their catalytic activity and product selectivity in deoxygenation microalgae oil. With the increase in reaction duration from 2 to 6 h, the highest amount of jet fuel with value of 76.71%, it was attained at reaction duration of 2 h, whereas the maximum selectivity for diesel was achieved at reaction time of 4 h with value of 9.6%.

ACKNOWLEDGEMENTS

This research was financially supported by Eskisehir Technical University Scientific Research Project Fund through project no 22LÖP230 and, TUBITAK (Scientific and Technological Research Council of Turkey) 2209-A Undergraduate Thesis Programme under the grant number 1919B012112139. Authors would like to thank Özlem Karpuz for giving support at catalyst synthesises.

REFERENCES

[1] M. Ji and J. Wang, Review and comparison of various hydrogen production methods based on costs and life cycle impact assessment indicators, *International Journal of Hydrogen Energy*, Vol. 46, pp. 38612-38635, 2021.

[2] IEA, *Tracking Transport*. 2019.

[3] J. Larsson, A. Kamb, J. Nässén, and J. Åkerman, Measuring greenhouse gas emissions from international air travel of a country's residents methodological development and

application for Sweden, *Environmental Impact Assessment Review*, Vol. 72, pp. 137-144, 2018.

[4] S. Janampelli and S. Darbha, Metal Oxide-Promoted Hydrodeoxygenation Activity of Platinum in Pt-MO_x /Al_2O_3 Catalysts for Green Diesel Production, *Energy Fuels*, Vol. 32, pp. 12630-12643, 2018.

[5] T. Xu, F. Xu, G. G. Moyo, Y. Sun, Z. Chen, B. Xiao, X. Wang, Z. Hu, Comparative study of MxOy (M = Cu, Fe and Ni) supported on dolomite for syngas production via chemical looping reforming with toluene *Energy Conversion and Management*, Vol. 199, p. 111937, 2019.

Hidrojen Yangınlarının Önlenmesi ve Söndürme Metodları

Muhammet Mert Canca[1], Aliye Kaşarcı Hakan[2], Hakan Serhad Soyhan[1,3]

1 Sakarya Üniversitesi, Yangın ve Yanma Araştırma Merkezi, Serdivan, 54187 Sakarya
2 İstanbul Yeni Yüzyıl Üniversitesi, Sağlık Bilimleri Fakültesi, İş Sağlığı ve Güvenliği Bölümü 34010 İstanbul
3 Team-SAN Ltd. Sti., Esentepe Kampüsü, Sakarya Üniversitesi, 54050 Sakarya

Yeryüzünde en bol bulunan elementlerden olan hidrojen, fosil yakıtların yerini almaya başlayarak yeni bir enerji kaynağı olarak kabul edilebilmektedir ve son yıllarda yaygınlaşmakta öncelemektedir. Temiz olması ve taşınmasının kolay olması tercih sebepleri arasında yer almaktadır. Ancak hidrojen renksiz, kokusuz, tatsız ve zehirsiz olduğu için insan duyularıyla algılanamaması nedeniyle tehdit durumunun değerlendirilmesi zordur. Bunun yanı sıra hidrojen yakıt hücreli araçlar, geleceğin ulaşım sektörü için sıfır emisyonlu bir seçenek olarak görülmektedir. Ayrıca hidrojen, birim kütle başına daha yüksek enerji içeriğine rağmen diğer yakıtlara kıyasla düşük hacimsel enerji yoğunluğuna sahiptir. Ancak, kısıtlı ortamlardaki hidrojen yakıt hücreli araçlarla ilgili bazı güvenlik endişeleri de mevcuttur. Olası yangın senaryolarının risk analizi, hidrojen yangını kazalarından kaynaklanan risklerin belirlenmesi, değerlendirilmesi ve azaltılması için etkili bir yaklaşım olacaktır. Yalnız araçlarda kullanılmayan hidrojen yakıt tankları çeşitli sektörlerde yakıt olarak da tercih edilmektedir. Hidrojen, %4 ile %75 arasında değişen geniş bir yanıcılık aralığına sahiptir. Bu nedenle, hidrojenin kapalı bir alanda birikmesi, gecikmeli bir ateşleme olması durumunda patlamaya neden olabilmektedir. Ani tutuşma durumunda ise hidrojen yangını meydana gelebilir. Hidrojen yangını, yüksek yanma hızı göz önüne alındığında özellikle kapalı alanlarda ciddi bir güvenlik sorunudur.

Avantajları, hidrojen yenilenebilir enerji kaynakları da dahil olmak üzere herhangi bir enerji kaynağı kullanılarak üretilebilir. Son kullanımda hidrojen kullanılacak enerji şekline dönüşürken en yüksek verime sahiptir. Hidrojen fosil yakıtlardan %39 daha verimlidir. Kısaca hidrojen birincil enerji kaynaklarını korur. Hidrojen gaz şeklinde (büyük depolamada), sıvı şeklinde (hava ve uzay ulaşımında) veya metal hibrit şeklinde (araçlar ve diğer küçük depolamada) depolanabilir. Hidrojen elektrikten veya güneş enerjisinden üretilirken, taşınırken veya depolanırken son kullanımda herhangi bir kirletici üretmez ve çevreye zararlı herhangi bir etkisi yoktur. Hidrojenin yanması sonucu ürün olarak sadece su üretilir.

Dezavantajları, doğada son derece bol olmasına karşın enerji üretiminde kullanılan hidrojen gazının son derece saf olması gerekir. Saflaştırma işlemi maliyeti artıran en önemli süreçtir. Bu nedenle saf hidrojen üretiminin maliyeti petrol ve doğalgaza göre yaklaşık 4 kat daha yüksektir. Hidrojen ile çalışan yakıt hücreleri içten yanmalı motorlardan 10 kat daha pahalıdır. Hidrojen enerjisinden yararlanılırken uygulamada birkaç zorlukla karşılaşılmaktadır. Örneğin enerjinin üretildiği yakıt hücreleri ve hidrojenin depolandığı tankların hacmi geniş yer kaplamaktadır ve bu tankların kalınlıkları hidrojenin depolanmasında ve sızdırmazlığında önem arz etmektedir. Hidrojen petrole göre 4 kat fazla hacim kaplar; hidrojenin kapladığı hacmi küçültmek için hidrojeni sıvı halde depolamak

gereklidir. Bunun içinde yüksek basınç (350 – 700 bar) ve soğutma işlemine gerek vardır. Yüksek basınçta gaz haldeki hidrojenin sıvılaştırılması maliyeti arttırmasının yanı sıra risk arz etmektedir.

Kullanım alanı gittikçe yaygınlaşan hidrojen için, farklı ısı salım oranlarına (HRR) sahip çoklu hidrojen yangınlarının etkisini analiz etmek önem arz etmektedir. Bu çalışma ile hidrojenin kullanım alanlarına özgü yangın nedenleri belirlenerek, yangının çıkmasını engellemek için önlemlere değinilecek ve olası yangınlar için söndürme metodları hakkında bilgiler verilecektir.

Anahtar kelimeler: yangın, hidrojen, temiz enerji, güvenlik.

Salehi, F., Baalisampang, T., & Abbassi, R. (2022). Numerical modeling towards the safety assessment of multiple hydrogen fires in confined areas. *Process Safety and Environmental Protection*, *160*, 594-609.

Proust, C., Jamois, D., & Studer, E. (2011). High pressure hydrogen fires. *International journal of hydrogen energy*, *36*(3), 2367-2373.

Mousavi, J., & Parvini, M. (2016). *Analyzing effective factors on leakage-induced hydrogen fires. Journal of Loss Prevention in the Process Industries, 40, 29–42.*

In-situ fluid dynamic characterization of a gas turbine combustor for operation with low-btu gas from biomass

Sagar Ranjan Panda[a,1], Anand M Shivapuji[a], Dasappa Srinivasaiah[a,b]
[a]Centre for Sustainable Technologies, Indian Institute of Science, Bangalore
[b]Interdisciplinary Centre for Energy Research, Indian Institute of Science, Bangalore

Abstract

The need for bio-derived fuels to offset carbon-based emissions is well established and fuels like Hydrogen-rich syngas play a crucial role in offsetting fossil- fuels. Extensive research has led to technology development in the reciprocating engine sector, and limited work is reported on the gas turbine operation. Bio-derived combustible gas is typically a low calorific value fuel with an energy content of around 5 MJ/kg, stoichiometric Air-Fuel ratio of around 1.35 and an adiabatic flame temperature of 1800 K. When such low calorific value fuels with very low air to fuel ratio (as compared to conventional fuels) are to be used in energy conversion systems like gas turbine which are operated at overall lean operating stoichiometry to meet the turbine inlet temperature, a detailed fluid dynamic analysis is required. The analysis is required to establish the fluid dynamic profiles in the multiple zones and interventions as necessary introduced to ensure the desired thermal conditions, basically, the turbine inlet enthalpy is realized at the exit of the combustor. With this specific requirement, this article experimentally addresses the flow in the fluid domain of an externally mounted gas turbine combustor rated at 32 kWe for Jet fuel. The three-dimensional fluid-dynamic profile is established using pitot tube measurements mounted on a traverse mechanism with 1micron traverse resolution. Simultaneously the combustor is profiled for flow based on multi-dimensional numerical analysis. Having compared and validated the fluid flow profile, the numerical analysis is extended by initiating combustion and profiling the temperature. The k-ε Realizable turbulence model with non-premixed diffusion flamelet model coupled with detailed GRI Mech 3.0 kinetic mechanism was used for CFD analysis. The CFD model is used to estimate the flow distribution in the different regions of the combustor to arrive at the desired combustor exit enthalpy.

Keywords: Gas Turbine, Combustor, CFD, Producer gas/Syngas

[1] Corresponding author, email: sagarpanda@iisc.ac.in

1 INTRODUCTION

A wide variety of heat and power generations come from the combustion processes with adverse effect on the environment. In particular, emissions such as carbon dioxide (CO_2), oxides of sulphur (SO_x), unburned hydrocarbons (UHC), and oxides of nitrogen (NO_x) from the combustion process have detrimental impacts on the environment and human health. In order to lower these emissions, lean and clean combustion technology and alternative fuel should be considered [1].

Biomass energy, which is generated from organic materials, constitutes one of the renewable and sustainable sources of the alternative fuel productions [2]. Via thermochemical process biomass can be converted into useful gaseous fuels known as Producer gas/Syngas [3]. Combustion of such gaseous fuel has more advantages in carbon dioxide (CO_2) production per unit of the power generation less than solid and liquid fuels with controlled emissions [4]. The bio-derived Producer gas/Syngas mainly contains of combustible species like, CO, H_2, CH_4, and non-combustible species CO_2 and N_2. As compared to commercially used high-hydrocarbon fuels (Jet-A, Diesel, Natural gas, Gasoline etc.), the calorific value of bio-derived Producer gas/Syngas are 7-10 times lower. In these days, most of the power generating sectors are vastly depends upon high-hydrocarbon content fossilized fuels for power generation, transportation, aviation or in heating applications. Due to the enormous usage of such fuels leads to an abundant amount of CO2 emission and other harmful compounds to the atmosphere and depletion of fossil fuels from earth crust. So, to survive in such a difficulty situation and to fulfil the basic energy demands, attention has to be made to production and use of bio-derived green fuels and subsequently development, optimization of power producing units like, gas turbines, IC engines etc. Literature survey reports that well-known research has been done to run the IC engine with Producer gas/Syngas [5-6]. But, very limited work has been done to fuel the gas turbine with such exotic fuels. In the present article, a preliminary experimental and numerical investigations are carried out in a 32 kWe reverse flow gas turbine combustion chamber without any modification. The combustor was originally designed to operate with conventional fossil fuels (Jet-A). In this study attempt has been made to operate the combustor by fuelling with Producer gas/Syngas outside the gas turbine. To understand the fluid flow and combustion behaviour inside the combustor, both numerical and experimental study has been carried out. Finally, important suggestions have been made whether the further modification of the combustion chamber is required for the adaptation of alternative fuels.

2 MATERIALS AND METHODS

For the analysis of Producer gas-air combustion behaviour inside a realistic reverse flow gas turbine combustion chamber, an experimental setup has been designed as shown in Figure 1. The core component of the experimental setup includes, a reverse flow combustor designed for conventional fossil fuels (Jet-A). The rating of the combustor is 32 kWe. To perform the in-situ analysis, a double tangential entry casing has been designed and fabricated for the supply of air inside the combustor. A two-axis high precision traverse mechanism of 0.1µm traversal speed is used for mounting of thermocouple or pitot tube. The Producer gas/Syngas was supplied from 100 kg/hr down draft gasifier with maximum gas generation rate of 190 kg/hr. The compressed air was supplied from a Ingersoll-Rand vertical compressor of maximum air flow rate of 830 kg/hr. For the experiment, five different equivalence ratios were set and the same is presented in Table 1.

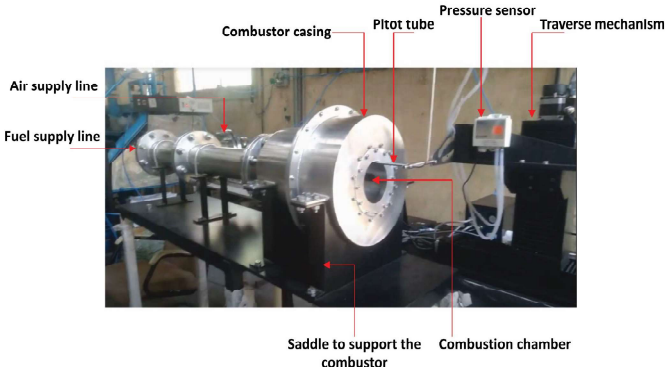


Figure 1: Experimental setup

Table 1: Mass flow rate of fuel and air for Producer gas combustion at different equivalence ratio

$\dot{m}_{air}$ (kg/hr)	$\dot{m}_{fuel}$ (kg/hr)	Φ_{Global}
140.30	15.25	0.200
147.32	15.25	0.190
154.33	15.25	0.182

161.35	15.25	0.174
168.36	15.25	0.167

2.1 Numerical methods and Boundary conditions

In the current work, RANS k-ε Realizable turbulence model was used for prediction of pressure, velocity, turbulence flow field inside the combustor. To understand the combustion behaviour, non-premixed combustion with a non-adiabatic, steady diffusion flamelet model with probability density function is used for Producer gas-air combustion by incorporating detailed GRI Mech 3.0 [7] chemistry. The mechanism consists of 53 species and 325 elementary reactions. To understand the reacting flow physics inside the gas turbine combustion chamber, numerical simulation has been carried out. A semi-implicit method for pressure-linked equations (SIMPLE) scheme was used for pressure-velocity coupling.

In the numerical analysis, the following assumptions were considered:

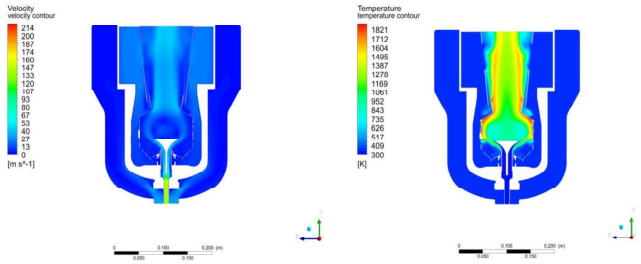
1. The mixture flow inside the combustion chamber is incompressible.
2. All the flow and mixture properties do not change with respect to time (steady-state).
3. The effect of gravity on the mixture inside the combustion chamber is neglected.
4. The heat transfer from the wall of the combustor is neglected.

Table 2: Boundary conditions imposed on the computational fluid domain

Combustor inlet and outlet	Boundary condition	Mean mixture fraction	Temperature	Turbulent intensity	Viscosity ratio
Air inlet	Mass flow inlet (0.04 kg/s)	Z=0	T_{air} =350 K	5%	10
Fuel inlet	Mass flow inlet (0.004 kg/s)	Z=1	T_{fuel} = 300 K	5%	10
outlet	Pressure outlet (Zero gauge)	-	$T_{Back\ flow}$ = 300 K	-	-
Combustor casing and walls	Adiabatic, no-slip with standard wall function	-	T_{wall} = 300 K	-	-

2.2 Results and discussions

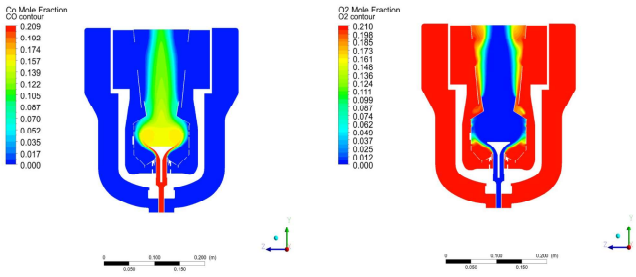
In the current investigation, the flow and combustion characteristics of a low calorific value fuel (producer gas) inside a reverse flow gas turbine combustion chamber has been analyzed. Before the experiments with Producer gas, a hot flow numerical analysis was performed. From the numerical results it has been observed that, due to the bluff body a strong recirculation zone was formed in the primary zone of the combustor. The size and intensity of recirculation zone helps to mix the fuel-air in primary zone. In this location the velocity of the fluid mixture was very low, which helps the flame to stabilize on the top of the bluff body. However, due to the high mass flow rate, it is observed that the mixing of fuel-air was not sufficient. Which leads to the incomplete combustion in the primary and secondary zone of the combustor as shown in Figure 2. Also, it has been observed that near to the wall of the combustor the temperature is higher because of appropriate air presence. Similarly, in the dilution zone temperature of the combustion is higher due to the higher air flow rate.



Velocity and Temperature flow field for Producer gas combustion

Figure 2: Velocity and temperature contour profile during Producer gas combustion

Figure 3 represents the CO and O_2 mole fraction contour during the Producer gas combustion. From the CO contour it is observed that the consumption of CO in primary zone is lower as compared in dilution zone. From O_2 contour profile it is found that in the primary zone the amount of air is less as compared to dilution zone which leads to an incomplete combustion.



CO and O_2 mole fractionduring Producer gas combustion

Figure 3: CO and O2 contour profile inside the combustor

Figure 4 presents the combustion of Producer gas inside the gas turbine combustor. From the experiments it is visualized that during Producer gas combustion, the flame was stretched near to the exit of the combustor which shows that the incomplete combustion of Producer gas inside the combustor, as the combustor was not designed to operate on such lower heating value fuels.

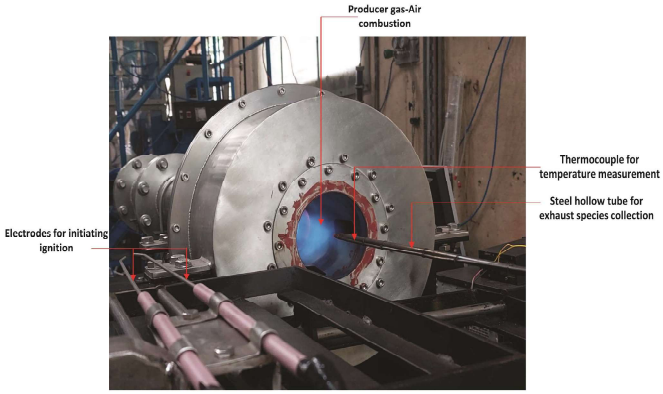


Figure 4: Producer gas combustion in a reverse flow gas turbine combustion chamber

In Figure 4, the numerically and experimentally obtained temperature along the central axis of the combustor are compared to validate the numerical CFD model with experimental results. From the result it is observed that the well-used k-ε Realizable turbulence model can accurately predict temperature variation inside the combustor for Producer gas combustion. The deviation between the numerical against the experimental data is observed to be within 3-5%.

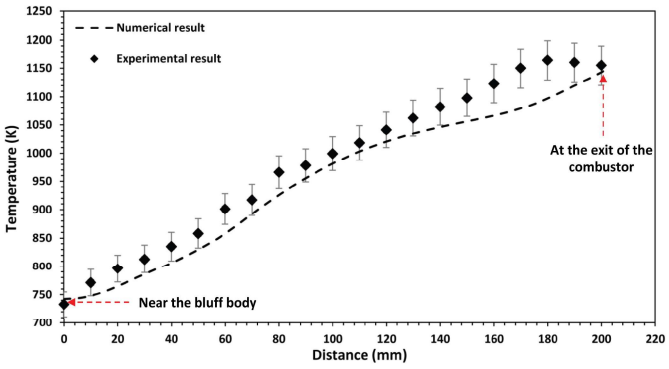


Figure 5: Numerical and experimental comparison of temperature variation along the axis of the combustor

The results indicate in Figure 4 that, at the exit of the combustor the temperature is nearly 1150 K and at the primary zone (near the bluff body) the temperature is 745 K. This shows the incomplete combustion of Producer gas inside the combustor when the modification of the combustor not carried out. In actual practise, the dilution zone is only meant to supply the air to reduce the temperature of the combustion to the required turbine inlet temperature. Similarly, in the primary zone the combustion needs to happen in a rich condition and in the secondary zone, the complete combustion will occur.

2.3 Conclusion and future work

In the current investigation, an attempt has been made to run the gas turbine with Producer gas without any modification of the combustion chamber. With the current flow rate of fuel and air the combustor was operated at 6% of the rated condition.

However, from the numerical and experimental analysis, it has been found that, for the adaptation of such exotic fuels in a conventional gas turbine combustor, modification of Primary, Secondary and dilution zone needs to be done. Also, to attain the proper air-fuel mixture in the primary zone and to carry out complete combustion before the secondary zone, the size of the primary and secondary holes needs to be increased and optimized. To attain the required turbine inlet temperature the dilution holes need to be optimized and is currently being attempted.

ACKNOWLEDGEMENTS

The authors are grateful to Department of Science and Technology, Government of India, DST/Coal/CST DSTO-19-0014 and DST/Coal/ICER DSTO-18-1995, for the contribution of resources to complete the analysis successfully.

REFERENCES

[1] Tamang,S.,et al.(2022). Numerical investigation of combustion characteristics for hydrogen mixed fuel in a gas turbine combustor. *International Journal of Hydrogen Energy*.

[2] Mukunda, H. S., et al.(1994). Gasifiers and combustors for biomass–technology and field studies. *Energy for Sustainable Development*.

[3] Mukunda, H. S., et al.(1993). Open-top wood gasifiers.

[4] Sridhar, H. V., et al.(2007, May). On the operation of a high-pressure biomass gasifier with gas turbine. 15th EUBCE Berlin, Germany.

[5] Shivapuji,A. M.,et al.(2014). In-cylinder investigations and analysis of a SI gas engine fuelled with H2 and CO rich syngas fuel.*international journal of hydrogen energy*.

[6] Shivapuji, A. M., et al.(2017). Quasi dimensional numerical investigation of syngas fuelled engine operation: *Applied Thermal Engineering*.

[7] Smith, G. P. (1999). GRI-Mech 3.0. *http://www. me. Berkley. edu/gri_mech/*.

INVESTIGATION OF CARBON DIOXIDE ABSORPTION CAPACITY AND DISSOLUTION RATE WITH GLYCEROL AND GLYCEROL + SODIUM HYDROXIDE HYBRID SOLUTION FOR POST-COMBUSTION SYSTEMS

İ. Koçyiğit Çapoğlu[1], H. Öztan[2], D. Uysal[3], Ö. M. Doğan[4]

1. Faculty of Engineering, Chemical Engineering Department, Gazi University, Maltepe, Ankara, 06570, Turkey, e-mail: iremkocyigit@gazi.edu.tr
2. Faculty of Engineering, Chemical Engineering Department, Gazi University, Maltepe, Ankara, 06570, Turkey, e-mail: hazaloztan@gazi.edu.tr
3. Faculty of Engineering, Chemical Engineering Department and Clean Energy Research Center (CERAC-TEMENAR), Gazi University, Maltepe, Ankara, 06570, Turkey, e-mail: duysal@gazi.edu.tr
4. Faculty of Engineering, Chemical Engineering Department, Gazi University, Maltepe, Ankara, 06570, Turkey, e-mail: mdogan@gazi.edu.tr

Abstract

The major effect of global warming is accepted as carbon dioxide (CO_2) emissions. At the highest rate, CO_2 occurs by burning fossil fuels for power and heat generation. CO_2 can be captured directly from the atmosphere, or from the point emission sources. Generally, the most used system to remove CO_2 at the point sources is post-combustion systems. The absorption process is widely used to reduce CO_2 emission and capture it at the source. In this study, glycerol, a biodiesel waste by-product, was investigated for CO_2 absorption from flue gases. Glycerol is a colorless chemical that has a high boiling point and is very soluble in water. Also, it is a suitable solvent for CO_2 absorption due to its low vapor pressure, low volatility, ease of access, and low solvent loss. The studies were performed using a stirred cell reactor and experiments were carried out at ambient temperature (20^oC) and atmospheric pressure (91 kPa). In experiments, glycerol has been used as 5-20 wt% solution and also by adding them to 0.5 M aqueous solution of sodium hydroxide (NaOH). In addition, the glycerol-based solvents examined in this study were compared with both distilled water and 0.5 M aqueous NaOH solutions in terms of total CO_2 absorption capacity and CO_2 dissolution rate. As a result of the experiments, the 20 wt% glycerol+0.5 M NaOH hybrid solution gave better results than the 0.5 M NaOH solution which means the addition of glycerol to the NaOH solution had a positive effect on the results.

Keywords: Global warming, Carbon dioxide, Absorption, Glycerol

1 INTRODUCTION

Global warming, one of the world's biggest concerns, is caused by greenhouse gases (GHGs) released into the atmosphere. Among all GHGs, carbon dioxide (CO_2) has the highest critical impact and should be captured. The CO_2 concentration in the atmosphere has increased by more than 100 ppm since pre-industrial times [1]. Currently, according to the latest measurements at the Mauna Loa Observatory, in Hawaii, the concentration of CO_2 in the atmosphere reached 419 ppm in July 2022 and the CO_2 emission trend is increasing [2]. To reduce these emissions, either CO_2 is captured directly from the atmosphere, or the point emission sources [3, 4]. For this, Carbon Dioxide Capture and Storage (CCS) or Carbon Dioxide Capture and Utilization (CCU) technologies are carried out to control CO_2 emissions in the atmosphere [5]. There are three types of CO_2 captured systems mainly: pre-combustion, post-combustion, and oxy-combustion. The gas streams' pressure and CO_2 concentration and the fuel type (gas or solid) are important factors in choosing the capture system [6].

In pre-combustion systems, the fuel is reacted with oxygen, air, or in some cases steam, and syngas (mixture of CO-carbon monoxide and H_2-hydrogen) are obtained. This process is known as gasification, partial oxidation, or reforming. Carbon monoxide reacts with steam to form carbon dioxide with additional hydrogen in a second reactor (a water-gas shift reactor-$CO+H_2O \leftrightarrow CO_2+H_2$). From this mixture of

hydrogen and carbon dioxide, carbon dioxide and hydrogen can then be separated. The resulting hydrogen gas is burned in integrated gasification combined cycle (IGCC) systems [7].

In oxy-combustion, the fuel is burned nearly pure oxygen (95-99%) instead of air. As a result of using oxygen, the flue gas contains a high concentration of carbon dioxide. While this system provides the advantage of easily separating CO_2 from the gas stream, the most important disadvantage of the system is that it needs a high amount of pure oxygen and consumes a lot of energy. Oxy-combustion systems are also being studied in gas turbine systems, but conceptual designs for such applications are still in the research phase [8].

The capture of CO_2 from the flue gases produced because of the combustion of fuels with high carbon sources such as fossil fuels and biomass is considered post-combustion capture. Instead of being emitted directly into the atmosphere, CO_2 is separated from the flue gases produced by combustion. Post-combustion systems generally use a liquid solvent to capture the small fraction of CO_2 (typically 3–15% by volume) present in a flue gas stream [9]. Post-combustion carbon capture has important potential because it can be retrofitted to existing units in the power sector. Currently, modern pulverized coal (PC) power plants or natural gas combined cycle (NGCC) power plants use post-combustion capture systems that employ an organic solvent such as monoethanolamine (MEA) [10].

There are many methods for capturing CO_2. Common methods for CO_2 capture are absorption, adsorption, separation with a membrane, cryogenic separation, etc. [11]. Among all these systems and methods, the most used system post-combustion/absorption mechanism.

There are several CO_2 capture solvents available including, alkanolamine solvents, ionic liquids (ILs), liquid ammonia, polyethylene glycol, methanol, potassium carbonate, and others [12]. Alkanolamine solvents such as monoethanolamine (MEA), diethanolamine (DEA), di-isopropanol amine (DIPA), and methyl diethanolamine (MDEA) are mostly used as an absorbent in commercial applications [13]. However, these solvents have several drawbacks related to limited cyclic carbon dioxide loading capacity and the operating cost is fairly high due to the high energy requirement for regeneration of the solution [14-16]. There is also a lot of work being done on ionic liquids. However, these liquids are not economically viable because they are too expensive [17]. Therefore, studies on CO_2 absorption have focused on finding efficient alternative solutions that may eliminate the disadvantages of the current systems.

Recently, glycerol has been introduced, which has a great potential for CO_2 capture [18]. It is overproduced as a by-product of the biodiesel industry [19]. Glycerol, a physical solvent used for CO_2 capture, is non-toxic, green and a stable solvent with low vapor pressure and is relatively inexpensive [20]. It also has a high solubility of CO_2 and is very soluble in water [21]. Glycerol utilization can lower costs and reduce the usage of toxic and hazardous solvents in capturing CO_2 [22].

Based on the mentioned above, glycerol which is a potential carbon capture solvent was investigated in this study. In the first stage of the study, 5, 10, 15 and 20 wt% glycerol solutions were prepared, and the total CO_2 absorption capacity and dissolution rate experiments were carried out in the stirred cell reactor. Then, the experiments were repeated by adding glycerol at the same weight ratios (5, 10, 15, 20 wt%) to the 0.5 M NaOH solution. Experimental results were also compared with distilled water and 0.5 M NaOH experimental data.

2 MATERIALS AND METHODS

Stirred cell reactors are known equipment used for conducting reaction and mass transfer studies in gas-liquid systems [23].

In this study, experiments on absorption capacity and dissolution rate were carried out in a stirred cell reactor. Absorption capacity can be defined as the amount of gas absorbed per unit volume of the absorption liquid. The dissolution rate expresses the rate of the absorption process relative to the total liquid volume.

2.1 Theoretical Investigation of the Absorption Capacity of Carbon Dioxide in Glycerol / Glycerol+NaOH

In the experimental setup, the gas pressure decreased due to the absorption of the gas trapped in the gas chamber from the interface to the liquid. This pressure drop was instantly recorded on the computer via the pressure transmitter and then these data were plotted against time. Calculations are made with the ideal gas equation shown in Equation (1).

$$PV_g = ZnRT \quad (1)$$

In this equation, P is the gas pressure [Pa] in the stirred cell reactor gas chamber; V_g is the gas volume [m^3], Z is the compressibility factor [0.995], n is the mole of carbon dioxide gas [mol], R is the gas constant [8.314 Pa-m^3-mol^{-1}-K^{-1}], T is the temperature [K].

The pressure measurement in the gas chamber of the stirred cell reactor is the difference between the atmospheric pressure and the pressure drop measured from the transmitter and is shown in Equation (2).

$$P = P_{atm} - \Delta P \quad (2)$$

Figure 1 shows an example of the graph of the pressure drop versus time in the stirred cell reactor. ΔP on the ordinate axis of the graph represents the pressure drop difference measured from the transmitter in Pa units, and the abscissa axis represents the time in seconds.

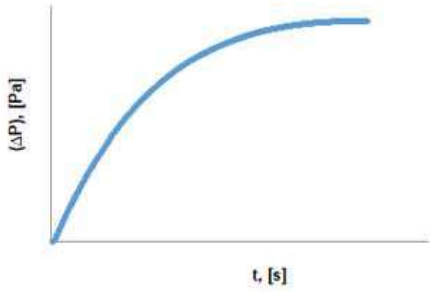


Figure 1. Decrease the pressure in the gas chamber of the stirred cell reactor with time

In the initial conditions, moles of CO_2 gas in the gas chamber and at the end of the experiment, the moles of CO_2 gas remaining in the gas chamber in the final state obtained by using the pressure drop data were calculated. Finally, by taking the difference between gas moles in the initial and final state, the amount of CO_2 absorbed into the unit volume of absorption liquid was calculated [24].

2.2 Theoretical Investigation of the Dissolution Rate of Carbon Dioxide in Glycerol / Glycerol+NaOH

Although the dissolution rate experiments were performed in the same procedure as the absorption capacity experiments, they differ in terms of theoretical calculation.

Equation (3) is obtained by taking and arranging the differential of the ideal gas equation represented by Equation (1) [25].

$$dn = \frac{V_g}{ZRT} dP \quad (3)$$

Since the experiments are performed as a function of time, the variation of the expression obtained by Equation (3) with time is shown in Equation (4) [25].

$$w = \frac{dn}{dt} = \frac{V_g}{zRT}\frac{dP}{dt} \quad (4)$$

Here w is the dissolution rate [mol-s^{-1}] of carbon dioxide in absorption liquids. The part on the right side of the equation expresses the change in moles of carbon dioxide due to the absorption of carbon dioxide in the gas chamber into the absorption liquids over time.

The pressure drop data recorded for each experiment are plotted in Figure 2. In order to determine the pressure change (dP/dt) over time, the slope of the first part of the graph, in which it proceeds linearly, was calculated.

Since the absorption process takes place in the liquid volume (V_L) in the liquid reservoir, the dissolution rate of carbon dioxide in liquids can be shown by Equation (5) [25].

$$r = \frac{w}{V_L} = -\frac{1}{V_L}\frac{V_g}{zRT}\frac{dP}{dt} \quad (5)$$

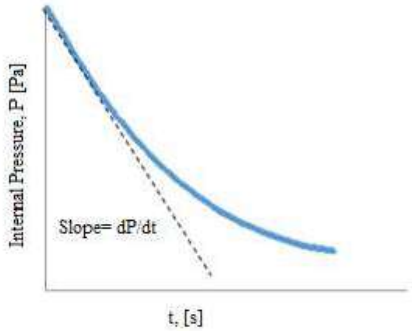
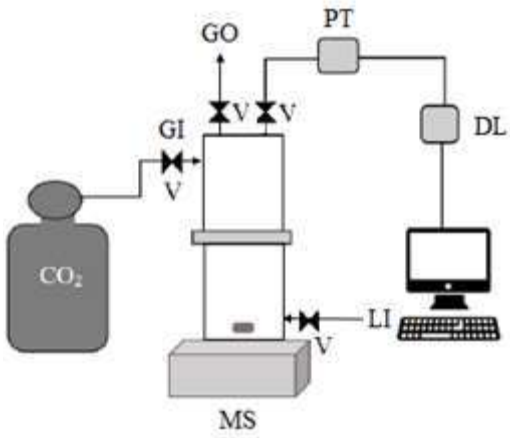


Figure 2. The change in the internal pressure of the carbon dioxide in the gas chamber overtime during the absorption of the gas from the interface into the liquid.

In Equation (5), the rate of the absorption process relative to the total liquid volume from the unit r, [mol-m^{-3}-s^{-1}], the slope read from the graph from the unit of dP/dt [Pa-s^{-1}] on the right side of the equation, V_L, liquid volume [m^3], V_g, gas volume [m^3], T is the gas constant in [K], temperature, R [8.314 Pa-m^3-mol^{-1}-K^{-1}].

3 EXPERIMENTAL

Stirred cell reactor experiments are based on the principle that the gas in the gas chamber is absorbed into the liquid. By observing the pressure drop in the gas chamber along with the amount of gas absorbed into the liquid, it is possible to calculate how much gas is absorbed. The stirred cell reactor system is shown in Figure 3.



(GI: Gas inlet; GO: Gas outlet; V: Valve; LI: Liquid inlet; PT: Pressure transmitter; DL: Data logger; MS: Magnetic stirrer)

Figure 3. The stirred cell reactor system

The experiments were carried out at an ambient temperature of 20°C and 91 kPa, which is the atmospheric pressure of Ankara. For this purpose, firstly solutions were prepared. In the first part of the experiment, 5, 10, 15, and 20 wt% glycerol solutions were prepared, respectively, and the experiments were carried out in the stirred cell reactor. In the second part of the experiment, the experiments were carried out with 5-20 wt% glycerol added to aqueous 0.5 M NaOH solutions. Finally, the experiments were completed with a 0.5 M NaOH solution and distilled water.

The stirred cell reactor consists of two parts, a 0.5 L gas chamber and a 0.4 L liquid reservoir and it is made of pyrex glass. The gas chamber has valves to which the gas inlet and outlet are connected. A CO_2 tube is attached to this experimental system. Pure CO_2 flow was provided to the gas chamber of the experimental system from the gas inlet and the air inside the system was swept. Afterward, all valves were closed simultaneously, and CO_2 gas was trapped in the system. It was stirred with a magnetic stirrer regarding no vibration/vortex formation at the interface of the liquid phase. Thus, with the mass transfer occurring at the liquid and gas interface, the CO_2 gas is absorbed by the solvent. The main purpose of mixing is to achieve homogeneity in the liquid by preventing the mass transfer resistances that may occur on the surface of the liquid and in the areas close to the surface as the gas is absorbed into the liquid. In the experimental system, the pressure drop occurring in the gas phase was instantly recorded on the computer with a data logger (ORDEL UDL100) using a pressure transmitter (HK Instruments DPT-R8). The pressure drop value occurring in the stirred cell reactor over time was fixed after a while, and the amount of CO_2 absorbed into the absorption liquids and the dissolution rates were calculated using the recorded values.

4 RESULTS AND DISCUSSION

In the investigation of CO_2 absorption in the stirred cell reactor, experiments were carried out with 5-20 wt% glycerol solution first. Subsequently, the experiments were repeated by adding 5-20 wt% glycerol solution to 0.5 M aqueous NaOH solution. Finally, experiments were completed with a 0.5 M NaOH solution and distilled water. For each solution, dissolution rate and total CO_2 absorption capacity calculations are made and presented in Table 1.

Table 1. Experimental results of total CO_2 absorption capacity and dissolution rate for each solution

Solution	w* (mol/s)	r** (mol/m^3-s)	Total CO_2 absorption capacity (g/L)
Distilled Water	$1.086x10^{-6}$	0.0027	0.0100
%5 wt Gly	$1.179x10^{-6}$	0.0029	0.0110
%10 wt Gly	$1.123x10^{-6}$	0.0028	0.0094
%15 wt Gly	$0.968x10^{-6}$	0.0024	0.0080
%20 wt Gly	$1.038x10^{-6}$	0.0026	0.0083
%5 wt Gly +0.5 M NaOH	$0.923x10^{-5}$	0.0231	0.1312
%10 wt Gly +0.5 M NaOH	$0.962x10^{-5}$	0.0240	0.1380
%15 wt Gly +0.5 M NaOH	$1.004x10^{-5}$	0.0251	0.1400
%20 wt Gly +0.5 M NaOH	$1.182x10^{-5}$	0.0295	0.1562
0.5 M NaOH	$1.130x10^{-5}$	0.0280	0.1410
w*: Dissolution rate			
r**: The rate of the absorption process relative to the total liquid volume			

Also, 5-20 wt% glycerol solution and glycerol+0.5 M NaOH hybrid solution were compared. Results are shown in Figure 4, Figure 5, and Figure 6.

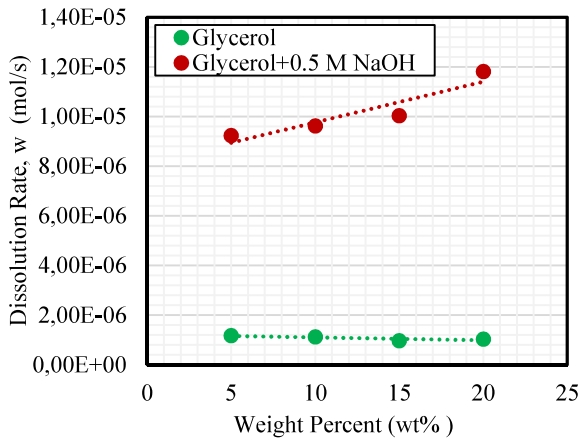


Figure 4. The dissolution rate of CO_2 in absorption solvents for comparison of glycerol and glycerol+0.5 M NaOH

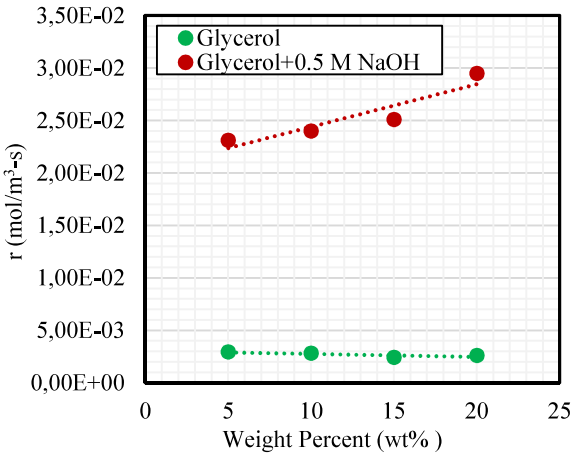


Figure 5. Rate of the absorption process relative to the total liquid volume for comparison of glycerol and glycerol+0.5 M NaOH

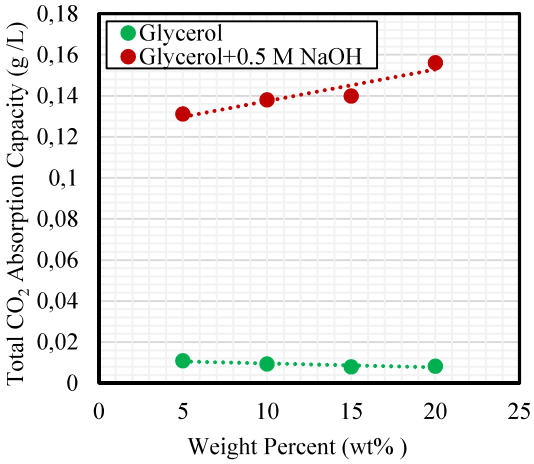


Figure 6. Total CO_2 absorption capacity for comparison of glycerol and glycerol+0.5 M NaOH

When the results were evaluated, 5-20 wt% glycerol solutions gave similar results to distilled water. On the other hand, adding glycerol to 0.5 M aqueous NaOH solution had a very positive effect on the dissolution rate and total CO_2 absorption capacity. When the results were compared, the glycerol+0.5 M NaOH hybrid solution showed better results, as expected from 5-20 wt% glycerol solution. Because NaOH solution is known to be good at capturing acidic gases such as CO_2 and SO_2.

It has been observed that 20 wt% glycerol+0.5 M NaOH hybrid solution gives better results than 0.5 M NaOH solution in terms of absorption capacity and dissolution rate.

5 CONCLUSION

Glycerol is a remarkable solvent to absorb carbon dioxide. Using glycerol for a CO_2 capture system can provide great potential for biodiesel waste management. Also, it is a green solvent for CO_2 capture systems so it can reduce the usage of hazardous and toxic solvents. It can also be used by adding it to commercially used amine or alkaline solvents. In this study, the total CO_2 capacity and dissolution rate of 5-20 wt% glycerol solution was almost similar to distilled water. On the other hand, the addition of glycerol to 0.5 M aqueous NaOH solution had a positive effect on the results. Moreover, the 20 wt% glycerol+0.5 M NaOH hybrid solution gave better results than the 0.5 M NaOH solution.

ACKNOWLEDGEMENTS

We would like to express our sincere gratitude to Prof. Dr. Bekir Zühtü UYSAL for guiding us on this path with his valuable knowledge and constructive suggestions. We also thank the graduation student Sonay YILDIRIM for her help in performing some of the experiments.

REFERENCES

[1] IPCC (Intergovernmental Panel on Climate Change), Fifth Assessment Report: Climate Change 2014: Synthesis Report. 2014, p. 151, Geneva, Switzerland. https://www.ipcc.ch/site/assets/uploads/2018/05/SYR_AR5_FINAL_full_wcover.pdf (accessed 2022-03-10).

[2] National Aeronautics and Space Administration (NASA), Climate Change Carbon Dioxide Latest Measurements, United States https://climate.nasa.gov/vital-signs/carbon-dioxide/ (accessed 2022-08-16).

[3] C. Li, H. Shi, Y. Cao, Y. Kuang, Y. Zhang, D. Gao, L. Sun, Modeling and optimal operation of carbon capture from the air driven by intermittent and volatile wind power. *Energy*, 87, 201-211, 2015.

[4] D. W. Keith, G. Holmes, D. St. Angelo, K. Heidel, A process for capturing CO2 from the atmosphere. *Joule*, 2 (8), 1573-1594, 2018.

[5] Z. Zhang, D. Huisingh, Carbon dioxide storage schemes: technology, assessment and deployment. *J. Clean. Prod.*, 142 (2), 1055-1064, 2017.

[6] A. A. Olajire, CO_2 capture and separation technologies for end-of-pipe applications–A review. *Energy*, 35 (6), 2610-2628, 2010.

[7] K. P. Resnik, W. Garber, D. C. Hreha, J. T. Yeh, H. W. Pennline, A parametric scan for regenerative ammonia-based scrubbing for the capture of CO_2. In Proceedings of the *23rd Annual International Pittsburgh Coal Conference*, Pittsburgh, PA, 2006.

[8] J. Godin, W. Liu, S Ren, C. C. Xu, Advances in recovery and utilization of carbon dioxide: A brief review, *J. Environ. Chem. Eng.*, 9 (4), 105644, 2021.

[9] J. D. Figueroa, T. Fout, S. Plasynski, H. McIlvried, R. D. Srivastava, Advances in CO_2 capture technology-The U.S. Department of Energy's Carbon Sequestration Program. *Int. J. Greenh. Gas Control*, 2(1), 9–20, 2008.

[10] IPCC. (2005). Carbon Dioxide Capture and Storage. Prepared by Working Group III of the Intergovernmental Panel on Climate Change, [Metz, B., O. Davidson, H. C. de Coninck, M. Loos, and L. A. Meyer (eds.)]. Cambridge University Press, Cambridge, United Kingdom and New York, NY, USA.

[11] G. Hu, N. J. Nicholas, K. H. Smith, K. A. Mumford, S. E. Kentish, G. W. Stevens, Carbon dioxide absorption into promoted potassium carbonate solutions: A review, *Int. J. Greenh. Gas Control*, 53, 28-40, 2016.

[12] İ. Koçyiğit Çapoğlu, *Absorption of Carbon Dioxide with Carbitol Acetate*, Master's Thesis, Gazi University, Ankara 2020.

[13] Y. Wu, J. Xu, K. Mumford, G. W. Stevens, W. Fei, Y. Wang, Recent advances in carbon dioxide capture and utilization with amines and ionic liquids. *Green Chem. Eng.*, 1 (1), 16-32, 2020.

[14] P. Luis, Use of monoethanolamine (MEA) for CO_2 capture in a global scenario: Consequences and alternatives, *Desalination.*, 380, 93-99, 2016.

[15] M. Wang, A. Lawal, P. Stephenson, J. Sidders, C. Ramshaw, Post-combustion CO_2 capture with chemical absorption: A state-of-the-art review, *Chem. Eng. Res. Des.,* 89 (9), 1609-1624, 2011.

[16] S. Ahn, H. J. Song, J. W. Park, J. H. Lee, I. Y. Lee, K. R. Jang, Characterization of metal

corrosion by aqueous amino acid salts for the capture of CO_2. *Korean J. Chem. Eng*., 27, 1576-1580, 2010.
[17] S. Babamohammadi, A. Shamiri, M. K. Aroua, A review of CO_2 capture by absorption in ionic liquid-based solvents. *Reviews in Chemical Engineering*, 31(4), 383-412, 2015.
[18] O. Aschenbrenner, P. Styring, Comparative study of solvent properties for carbon dioxide absorption, *Energy Environ. Sci*., 3, 1106-1113, 2010.
[19] C-Y. Chiang, D-W. Lee, H-S. Liu, Carbon dioxide capture by sodium hydroxide-glycerol aqueous solution in a rotating packed bed, *J Taiwan Inst Chem Eng*, 72, 29-36,2017.
[20] S. Mirzaei, A. Shamiri, M. K. Aroua, Simulation of Aqueous Blend of Monoethanolamine and Glycerol for Carbon Dioxide Capture from Flue Gas, *Energy&Fuels*, 30, 9540-9553, 2016.
[21] Y. Gu, F. Jerome, Glycerol as a sustainable solvent for green chemistry. *Green Chem*., 12, 1127-1138, 2010.
[22] A. Shamiri, M. S. Shafeeyan, H. C. Tee, C. Y. Leo, M. K. Aroua, N. Aghamohammadi, Absorption of CO_2 into aqueous mixtures of glycerol and monoethanolamine, *J Nat Gas Sci Eng*, 35, 605-613, 2016.
[23] L. Kucka, J. Richter, E. Y. Kenig, A. Górak, Determination of gas–liquid reaction kinetics with a stirred cell reactor. *Sep. Purif. Technol.*, 31(2), 163-175, 2003.
[24] G. Genç Çelikçi, *Carbon Dioxide Capture in Structured Packing Column with n-Butanol and Ethyl Acetate*, Ph.D. Thesis, Gazi University, Ankara 2020.
[25] D. Uysal, *Absorption of Carbon Dioxide into Calcium Acetate Solution*, Ph.D. Thesis, Gazi University, Ankara 2016.

CARBONIZATION OF WASTE ELASTOMER (ETHYLENE PROPYLENE DIENE MONOMER-EPDM) TO PRODUCE CARBONACEOUS MATERIALS

Muhammet Ramazan Eren[1], Işıl Güneş[2] and Esin Apaydın Varol[3]

1. Eskisehir Technical University, Faculty of Engineering, Dept. of Chemical Eng., Eskişehir, 26555, Turkey; email: mreren41@gmail.com
2. Eskisehir Technical University, Faculty of Engineering, Dept. of Chemical Eng., Eskişehir, 26555, Turkey; email; isilgunes004@gmail.com
3. Eskisehir Technical University, Faculty of Engineering, Dept. of Chemical Eng., Eskişehir, 26555, Turkey; email: eapaydin@eskisehir.edu.tr

Abstract

With the increasing industrialization in the world and our country, the conversion of elastomers into valuable and useful products has been one of the remarkable issues in recent years. In this study, the elastomer wastes, which have no application other than direct combustion or use in carbon black production and pose a problem as waste, and are difficult to dispose of in industrial areas, are converted to carbonaceous materials. Fourier Transform Infrared Spectroscopy (FTIR) was used to determine the functional groups of waste elastomer (Ethylene Propylene Diene Monomer-EPDM) to be used as a raw material in the production of carbonaceous material, and X-Ray Fluorescence Spectroscopy (XRF) was used for the analysis of the inorganic components. Using ASTM methods, moisture, ash, volatile matter, and fixed carbon contents were determined. After characterization, the thermal degradation behavior was investigated by thermogravimetric analysis. The carbonization process was applied at different temperatures ranging between 400 and 600 ^{o}C under an inert atmosphere. The most suitable temperature to obtain a solid product with a 54% yield was determined to be the carbonization temperature of 500 ^{o}C. According to the characterization of the solid products obtained at all temperatures, it was determined that the thermochemical conversion of EPDM to carbonaceous materials seems to be a promising method for the disposal of waste elastomers.

Keywords: Activation, Elastomers, EPDM, Carbonization, Carbon Material

1 INTRODUCTION

Waste rubbers (elastic polymers-elastomers) are becoming an important environmental problem in our country as well as in the world. In Turkey, an average of 30 million tires consume their life every year [1]. Waste elastomers are highly resistant to physical, chemical, and biological degradation. For this reason, they are not classified as environmentally friendly materials and can remain intact for a long time [2]. The complex nature of elastomers and tires makes their recovery difficult. Waste elastomers generate toxic gases when disposed of at the landfill site. These gases threaten the environment as they carry the risk of explosion under a certain pressure. In addition, scrap tire collection areas provide an ideal environment for the breeding of disease-carrying insects [3]. Since they do not deteriorate in nature for many years, they mix with different ecosystems and harm the lives of many living things and the environment they live in. Recycling processes gain importance to minimize these negative effects of waste and reduce costs. In our country, waste tires and elastomers are used in cement factories to obtain energy inefficiently, or they are used on the floors of playgrounds by reducing the particle size and compressing [4, 5, 6]. As an alternative to these uses, the utilization of waste elastomers in the production of carbon materials with high-added value has the potential to be a useful conversion technology for both our country and the world. Thus, with another approach, the damage to the environment will be prevented by recycling or upcycling.

Ethylene propylene diene (EPDM) is a saturated non-polar rubber. This synthetic rubber exhibits excellent heat, ozone, oxidation, weather, and aging resistance. EPDM rubber is used in many sectors such as the automotive sector, door-glass production, the production of radiator and heating hoses, and the white goods sector.

According to the literature research on EPDM rubber, it was seen that studies were carried out on the pyrolysis kinetics of ethylene propylene

diene monomer, where the relationship between EPDM and activation energy is discussed [7]. In another study, EPDM rubber recovery from devulcanized EPDM was investigated [8]. As a result of the literature search, no study was found on the production of carbonaceous material with improved surface properties from waste EPDM rubber.

In this study, the pyrolytic behavior of waste EPDM was studied in a fixed bed reactor at the temperature range from 400 to 600 °C under nitrogen (N_2) flow of 100 cm^3/min at a heating rate of 10 ºC/min. The objectives of this study are: (i) to determine the effect of carbonization temperature on product yields, (ii) to obtain the carbonaceous materials from waste EPDM, and (iii) to characterize carbonaceous materials, for their possible use

2 MATERIALS AND METHODS

2.1 Materials

In this study, waste EPDM rubber sample provided by ICarbon (Bursa) company was used as the raw material.

Using ASTM methods, moisture, ash, volatile matter, and fixed carbon contents were calculated.

Analysis of the inorganic components of EPDM was carried out using X-Ray Fluorescence Spectroscopy (Rigaku ZSX Primus II).

The bulk density of the raw material and carbonaceous material were calculated to determine the mass of the unit volume.

Thermal degradation behavior and thermal stability were determined by applying thermogravimetric analysis to the raw material. Thermogravimetric analysis was carried out using Setaram Labsys EVO Thermogravimetric Analyser. The Simultaneous TG and DTA data were obtained by applying a temperature program from 25 up to 1000 °C to the sample under nitrogen gas flow.

2.2 Carbonization of EPDM

Carbonization experiments of EPDM were carried out at different temperatures in a fixed-bed reactor at the temperature range from 400 to 600 °C under nitrogen (N_2) flow of 100 cm^3/min at a heating rate of 10 ºC/min. A schematic diagram of the unit is represented in Figure 1. The reactor has a volume of 450 cm^3 and is externally heated by an electrical furnace in which the temperature is measured by a thermocouple inside the bed. At the end of the carbonization, the reactor was set to cool to room temperature. The liquid products were collected in traps covering salty ice. The traps and reactor were washed with dichloromethane (DCM) solvent to obtain the liquid products. The residuals in the reactor were weighed directly and the solid product yields were calculated.

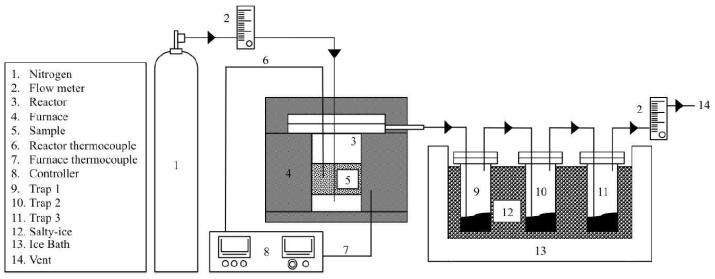


Figure 1. Schematic diagram of the fixed-bed reactor [9]

2.3 Characterization of Carbonaceous Materials

FT-IR spectra were recorded to determine the functional groups contained in the carbonaceous material and the raw material. The samples whose spectra will be recorded were first turned into pellets, and then the FT-IR spectra of the EPDM and carbonaceous materials were recorded in the transmission mode between 4000 and 500 cm^{-1} using a Thermo Nicolet IS10 Fourier Transform Infrared Spectrometer.

SEM images of raw material and carbonaceous materials were recorded by using Hitachi Regulus 8230 Scanning Electron Microscope. Samples were mounted on an aluminum stub using carbon bands and coated with a thin layer of gold-palladium in an argon atmosphere using Agar Sputter Coater.

3 RESULTS AND DISCUSSION

Moisture, Ash, Volatile Matter, and Fixed Carbon Contents

Moisture, ash, volatile matter, and fixed carbon contents were determined for the raw material and the carbonaceous material obtained at different temperatures, and the results are given in Figure 2. For the solid product obtained at 500 °C, it was determined that the amount of fixed carbon increased and the amount of volatile matter decreased significantly compared to the raw material.

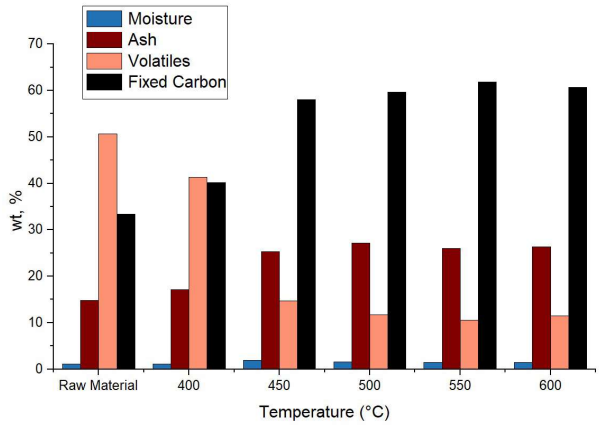


Figure 2. Moisture, ash, volatile matter, and fixed carbon content of raw material and carbonaceous material obtained at different temperatures

Thermogravimetric analysis

The thermal degradation curve of EPDM is given in Figure 3. It is seen that the thermal degradation of EPDM takes place in two main steps in an inert environment and is completed at about 500 °C.

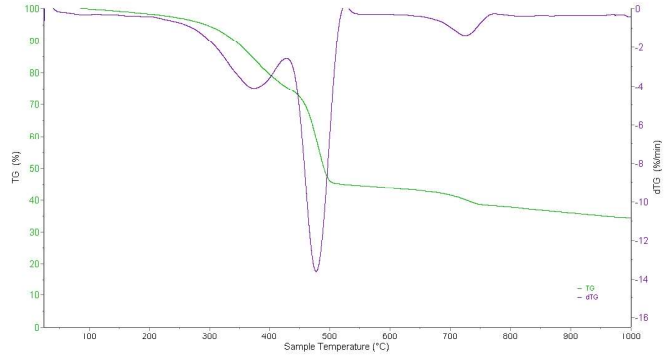


Figure 3. Weight loss curves (TG and dTG) of EPDM

X-Ray Fluorescence (XRF) Analysis

XRF analysis results of EPDM ash are given in Table 1. The inorganic components were determined to be predominantly Si and Ca.

Table 1. Inorganic content of EPDM

Component	(wt. %)
CaO	48.2
SiO_2	27.5
SO_3	9.62
Others	14.68

Carbonization Yields

The solid product yields obtained after the carbonization processes applied at different temperatures are given in Figure 4. After repeated experimental studies, it was determined that there was no significant change in the yield at temperatures of 500°C and higher. This is by the thermal degradation behavior of the raw material which confirmed that the pyrolysis reactions were completed at 500 °C. While the solid product yield was 80% at 400 °C, it was calculated to be 54% at 500 °C.

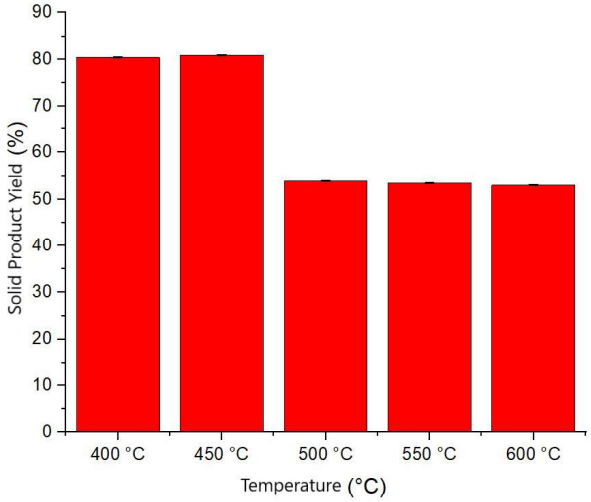


Figure 4. The solid product yields at different carbonization temperatures

Bulk Density

Bulk densities were determined for the characterization of raw material and carbonaceous materials and are shown in figure 5. It has been determined that the bulk density of the solid product is less than the raw material.

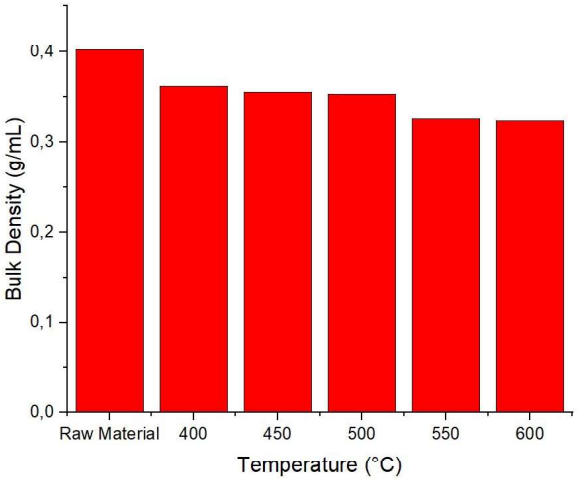


Figure 5. Bulk density of raw material and carbonaceous material obtained at different temperatures

FTIR Spectroscopy

FTIR analysis of the samples was carried out to determine the functional groups in carbonaceous materials and the spectra are given in Figure 6. The strong C-H stretching band in the wavelength range of 2950-2800 cm^{-1} disappeared as the carbonization temperature increased, and as a result, the solid product with

a carbonaceous structure remained behind. The vibration band between 1465 and 1450 cm^{-1} shows the C-H bending vibration indicating the presence of alkanes. The band between 1100 and 1000 cm^{-1} shows the C-O stretching vibration bands of the carbonyl groups originating from ester and ether and it was observed that they remained in the structure after carbonization. The same band also includes the vibrations arising from the S-O indicating the presence of sulfoxides.

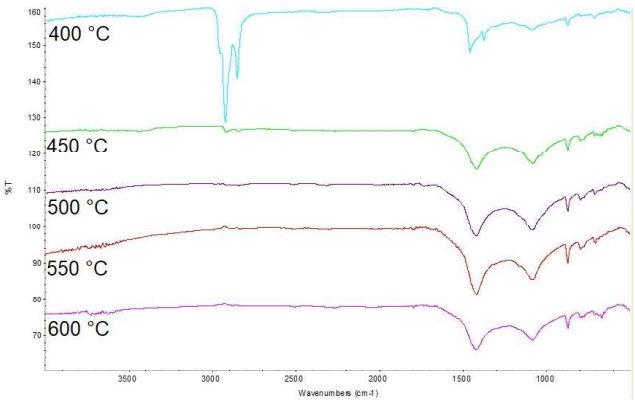


Figure 6. FT-IR spectra of the carbonaceous material obtained at different carbonization temperatures

SEM

The SEM images of raw material and carbonaceous material obtained at 500°C are given in Figure 7. The difference in the surface morphology of the raw materials and carbonaceous material can be observed in the figure. It is seen that after the carbonization process porosity of the material increases and the particle size decreases. The volatile components escaped from the structure during the carbonization process. Therefore, the size of voids and porosity increase after the carbonization.

4 CONCLUSION

As a result of the characterization of the carbonaceous material obtained at all temperatures, it was determined that a solid product rich in carbon could be obtained via the EPDM carbonization process. According to the experimental studies, it was determined that there was no significant change in the solid product yield after 500°C temperature and the pyrolysis reactions were completed at this temperature. The yield was determined as 54% when the temperature was 500 °C. In addition, according to the results of the thermogravimetric analysis of EPDM, it was observed that the thermal degradation was completed at approximately 500 °C. According to the XRF results of EPDM inorganic compounds, Si and Ca were the predominant elements. It has been foreseen that the carbonaceous material obtained as a result of EPDM carbonization can be used as a carbon source in the production of sorbent or composite materials by improving its surface properties directly or after its activation.

ACKNOWLEDGEMENTS

This study was carried out within the scope of the Scientific and Technological Research Council of Turkey (TUBITAK) 2209-A project, numbered 1919B012108128.

The authors would like to thank Erdem Mutlu from ICARBON Chemistry R&D and Engineering for his support in carrying out this study.

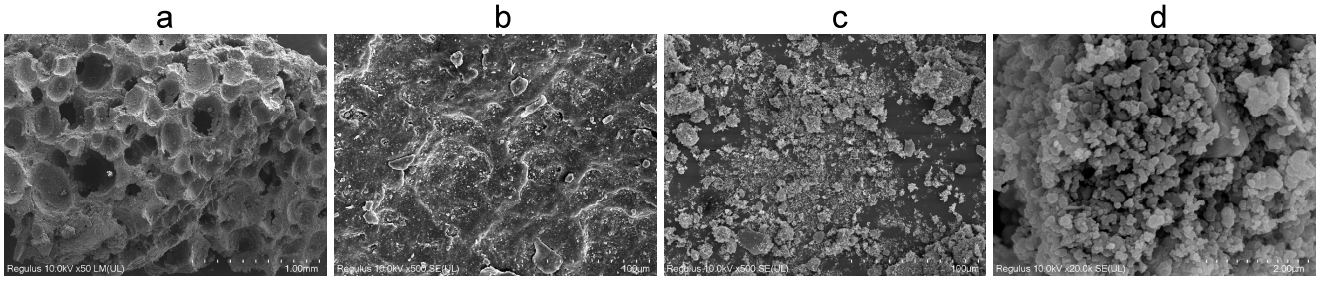


Figure 7. Sem images of EPDM sample a) 50X, b) 500X and carbonaceous material c) 500X, d) 20KX

REFERENCES

[1] Sugözü, İ., Mutlu İ., 2009. *"Atık Taşıt Lastikleri ve Değerlendirme Yöntemleri"*, Taşıt Teknolojileri Elektronik Dergisi, Cilt: 1, No: 1, 35-46.

[2] De D., Das A., De D., Dey B., Debnath S. C., Roy B. C., 2006. *"Reclaiming of ground rubber tire (GRT) by a novel reclaiming agent"*, European Polymer Journal, 42, 917–927.

[3] K. Sana et al., 2014. *"Managing the environmental hazards of waste tires,"* J. Eng. Des., vol. 20,

[4] Eryılmaz, H., Demirarslan, K. O., 2019. *"Ömrünü tamamlamış lastiklerin (ÖTL) sıvılaştırılarak geri dönüşümünün araştırılması"*, Sürdürülebilir Mühendislik Uygulamaları ve Teknolojik Gelişmeler Dergisi, 2 (1), 50-56.

[5] Karabörk F., Akdemir A., 2013. *"Atık taşıt lastiklerinin parçalanması ve lastik tozunun karakterizasyonu",* Erciyes Üniversitesi Fen Bilimleri Enstitüsü Fen Bilimleri Dergisi, c. 29, sayı. 1, ss. 29-40.

[6] Dwivedi, C., Manjare, S., Rajan, S. K., 2020. *"Recycling of waste tire by pyrolysis to recover carbon black: Alternative & environment-friendly reinforcing filler for natural rubber compounds"* Composites Part B: Engineering, 200, 108346.

[7] A. Perejón, P. E. Sánchez-Jiménez, E. Gil-González, L. A. Pérez-Maqueda, and J. M. Criado., 2013. *"Pyrolysis kinetics of ethylene-propylene (EPM) and ethylene-propylene-diene (EPDM)"*, Polym. Degrad. Stab., vol. 98, no. 9, pp. 1571–1577.

[8] P. Sutanto, F. Picchioni, L. P. B. M. Janssen, K. A. J. Dijkhuis, W. K. Dierkes, and J. W. M. Noordermeer, *"EPDM rubber reclaim from devulcanized EPDM,"* J. Appl. Polym. Sci., vol. 102, no. 6, pp. 5948–5957, 2006

[9] E. Apaydin-Varol, M. Kiliç, A. E. Pütün, G. Değirmen, and E. Pütün, *"Humulus lupulus as a raw material for bio-oil production via slow pyrolysis,"* Gazi Univ. J. Sci., vol. 30, no. 2, pp. 111–122, 2017

EXPERIMENTAL INVESTIGATION ON PERFORMANCE EVALUATION OF PEM ELECTROLYSIS CELL BY USING A TAGUCHI METHOD

Safiye Nur ÖZDEMİR[1], İmdat TAYMAZ[2], Emin OKUMUŞ[3], Fatmagül BOYACI SAN[4], Ece DEĞİRMENCİ[5], Ömer Bora ACAR[6],

1. Engineering Faculty, Mechanical Engineering Department, Sakarya University, Sakarya, TURKEY; email: safiyeozdemir@sakarya.edu.tr
2. Engineering Faculty, Mechanical Engineering Department, Sakarya University, Sakarya, TURKEY; email: taymaz@sakarya.edu.tr
3. Energy Institute, TÜBİTAK Marmara Research Center, Gebze, Kocaeli, TURKEY; email: emin.okumus@tubitak.gov.tr
4. Energy Institute, TÜBİTAK Marmara Research Center, Gebze, Kocaeli, TURKEY; email: fatmagul.boyaci@tubitak.gov.tr
5. Faculty of Chemical Metallurgical Engineering, Metallurgical and Materials Engineering, Istanbul Technical University, Istanbul, TURKEY; email: degirmenci.ece@outlook.com
6. Technology Faculty, Energy Systems Engineering, Kocaeli University, Kocaeli, TURKEY; email: o.boracar@gmail.com

Abstract

Proton exchange membrane (PEM) electrolysis cells play an essential role in hydrogen and oxygen production by utilizing renewable energy sources and can help reduce pollutant emissions. Operating parameters are one of the crucial factors required to provide high-performance PEM electrolysis cells (PEMEC); a careful balance between parasitic loads and performance must be considered to obtain the optimal output. In this study, a series of experiments were carried out to investigate the effects of the operating parameters (cell temperature, cell voltage, and pump value) on the performance of PEMEC. A PEM electrolysis cell with a 9 cm² active area and Nafion 115 membrane for the anode and cathode is employed as a membrane electrode assembly (MEA). Taguchi method was also implemented to optimize PEM electrolysis cell operating parameters. The ANOVA (analysis of variance) and signal-to-noise ratio (SNR) are also performed to compute the contributions of the control factors to the maximal current and hydrogen flow rate. Temperature, cell voltage, and pump value are the three main control factors that have been varied between 40-80°C, 1.6-2.4V, and 5-9, respectively. The results show that the optimal condition is ensured at maximum temperature, cell voltage, and pump value. The cell voltage has considerably affected the current and hydrogen flow rate with contributions of 91.91% and 90.81%, respectively. In comparison, the pump value has a minimal effect with contributions of 1.04% and 1.25%, respectively.

Keywords: PEM electrolysis cell, Operating parameters, Optimization, Taguchi method

1 INTRODUCTION

The rapid growth of the world population, urbanization, and industrialization caused a drastic increase in energy demand. Today, fossil fuels (coal, petroleum, and natural gas) widely meet the world's energy demand and are rapidly depleted. Also, their utilization adversely affects the ecology, causing global problems such as global warming, air pollution, acid rain, and ozone layer depletion. Renewable energy sources (RES) will play a crucial role in solving global problems and transitioning to a sustainable, zero-emission energy system [1-5]. To prevent air pollution and global warming, excessive use of fossil fuels should be decreased by efficiently utilizing renewable energies. In the 21 st century, hydrogen is the cleanest energy carrier capable of storing energy transformed from the energy sources such as fossil fuels, nuclear energy, and renewable energies. Also, hydrogen comprises a higher energy density per unit weight than conventional fuels [6-8]. Today, hydrogen is used in many fields, including chemical industries, transportation, gas grids, synthetic fuels, construction, etc. Hydrogen sources can be divided into three categories, namely gray hydrogen, blue hydrogen, and green hydrogen, due to the difference in hydrogen production methods. It is labeled gray if hydrogen is obtained through fossil fuels, such as natural gas, methane, etc. During the production of gray hydrogen,

carbon dioxide will be released into the environment. Blue hydrogen is generated from the producing hydrogen with a carbon capture and storage system (CCS) to eliminate carbon dioxide pollutants. Green hydrogen also called clean hydrogen, is produced by renewable energy sources, such as solar energy, wind energy, biomass energy, etc. Proton exchange membrane electrolysis cell (PEMEC) is widely considered a promising clean hydrogen production device via water electrolysis, owing to its several advantages, including high energy efficiency, fast system response, higher operating pressure levels, and high hydrogen purity [9-12]. Various methods are available to analyze a PEMEC such as numerical, analytical, and experimental approaches. In the literature, the multiphase flow phenomenon in the anode bipolar plate of the PEM electrolysis cell has been simulated by various CFD tools. However, it has been observed that the number of studies is relatively low because the simultaneous solution of electrochemical and governing equations is complex [13-15]. Besides, the experiments are costly and time-consuming, and the experimental study examining the electrolyzer performance is very few compared to PEM fuel cells. Therefore, the operating and design parameters that affect the PEM electrolysis cell performance should be optimized by a statistical method by reducing the number of experiments. Grigoriev et al. [16] performed numerical optimization of a high-pressure PEM electrolyzer. Their mathematical model includes gas cross-over phenomena, electrochemical reaction kinetics, and electro-osmotic drag of water molecules. The numerical results illustrate that low current densities are achieved due to gas cross-over phenomena. They also concluded that the gas content in the pores of the current collector plates and catalyst layers augmented with increasing water feed rate. Millet et al. [17] prepared different electrocatalysts for the electrolyzer electrodes. They tested them on a single cell PEM electrolyzer having a 7-23 cm^2 operating area, and then they combined multiple cells to form stacks with 250 cm^2 of the active area. Selamet et al. [18] conducted electrolysis experiments to create high-efficient PEM electrolysis cell/stacks. First, a single cell PEM electrolyzer having a 50 cm^2 active area was developed, and then its efficiency increased with some material and design improvements. Finally, their study generated a five and 10-cell stack and observed the effect of water flow rate and temperature on the polarization curve. They concluded that there was no significant change in electrolyzer efficiency when the number of cells was increased from 1 to 10. Han et al. [19] introduced a novel ohmic loss model for PEM water electrolysis. Different geometrical and operational factors, including operating pressure, temperature, membrane thickness, electrode thickness, interface resistance, and exchange current density, are discussed to evaluate and optimize the electrolyzer performance. They concluded that an increase in operating temperature positively affects the performance of the PEMEC. Still, an increase in electrode and membrane thicknesses adversely affects the performance of the PEM electrolyzer. Toghyani et al. [20] developed a steady state, three-dimensional CFD model using a finite volume method to investigate the effects of design and operating conditions on the PEM electrolyzer performance. Their results show that the hydrogen concentration decreases at lower temperatures due to electrochemical reaction kinetics slowing down. Also, they found that lower current densities are obtained by increasing the gas diffusion layer (GDL) and membrane thickness. The CFD simulation results also concluded that the GDL porosity had no significant effect on the PEM electrolyzer power density. Ma et al. [21] developed a PEM electrolysis cell having a 25 cm^2 active electrode area to simulate the performance of electrochemical reactions, species transport, and coupled thermal-fluid processes. This mathematical modeling can facilitate component optimization, laboratory testing, and material development. Su et al. [22] proposed a PEM electrolysis cell MATLAB/Simulink model to analyze the cell performance and bubble coverage by incorporating the dynamic behavior of bubbles. They found that parameters such as current density, temperature, pressure, water inlet velocity, and humidity affect the bubble coverage. Despite many numerical and experimental studies that have been carried out on electrolyzer systems, it is observed that there is no present study in the literature that realizes the effect of operating parameters on electrolyzer performance with an optimization algorithm. In this regard, the performance test results of the single-cell PEM electrolyzer cell and the optimization of the operating parameters that

significantly affect the cell performance will be gained in the literature. The layout of this study is as follows. First, the PEM electrolyzer test cell with a 9 cm² active area and experimental setup where performance tests are carried out is introduced. In the second stage, the effects of the cell potential, temperature, and pump value on cell performance were experimentally investigated with polarization curves. Since the experimental study is very time-consuming and costly, the Taguchi method, which optimizes the responses with a small number of performance tests, was also imposed on this paper. Interaction between each parameter is determined. Optimal input parameters are then calculated based on the cell's current and hydrogen flow rate. Finally, the contribution percentages of the operating parameters affecting the target parameter were calculated by ANOVA.

2 THERMODYNAMICS OF PEM ELECTROLYSIS CELL

A PEM electrolysis cell is a type of electrochemical device that uses DC power from renewable energy sources for example wind, solar, and biomass to decompose water into hydrogen and oxygen. The electrolyzer cell consists of an anode electrode and a cathode electrode. The anode electrode includes the port where the water enters and the port where the water/oxygen exits. Similarly, the cathode electrode consists of the port where the water enters and the port where the water/hydrogen exits. An electrolyte membrane is sandwiched between the anode electrode and the cathode electrode. Water is split into oxygen and hydrogen at their respective electrodes, such as oxygen at the anode and hydrogen at the cathode in the electrolysis cell. Water pumped to the anode electrode dissociates into electrons, hydrogen ions, and oxygen. The general view of a PEMEC is as in Figure 1. The electrochemical reaction at anode and cathode are as follows:

Anode: $H_2O \rightarrow 2H^+ + 2e^- + {}^1/_2\, O_2$ (1)

Cathode: $2H^+ + 2e^- \rightarrow H_2$ (2)

The overall reaction for the PEM water electrolyzer is expressed as;

Overall: $H_2O \rightarrow H_2 + {}^1/_2\, O_2$ (3)

Hydrogen ions are transported from the anode electrode to the cathode electrode through the polymer electrolyte membrane. Electrons pass from the anode side to the cathode side through the external power circuit, combine with hydrogen ions, and hydrogen gas is produced at the cathode electrode. Some energy is needed to decompose water into hydrogen and oxygen molecules.

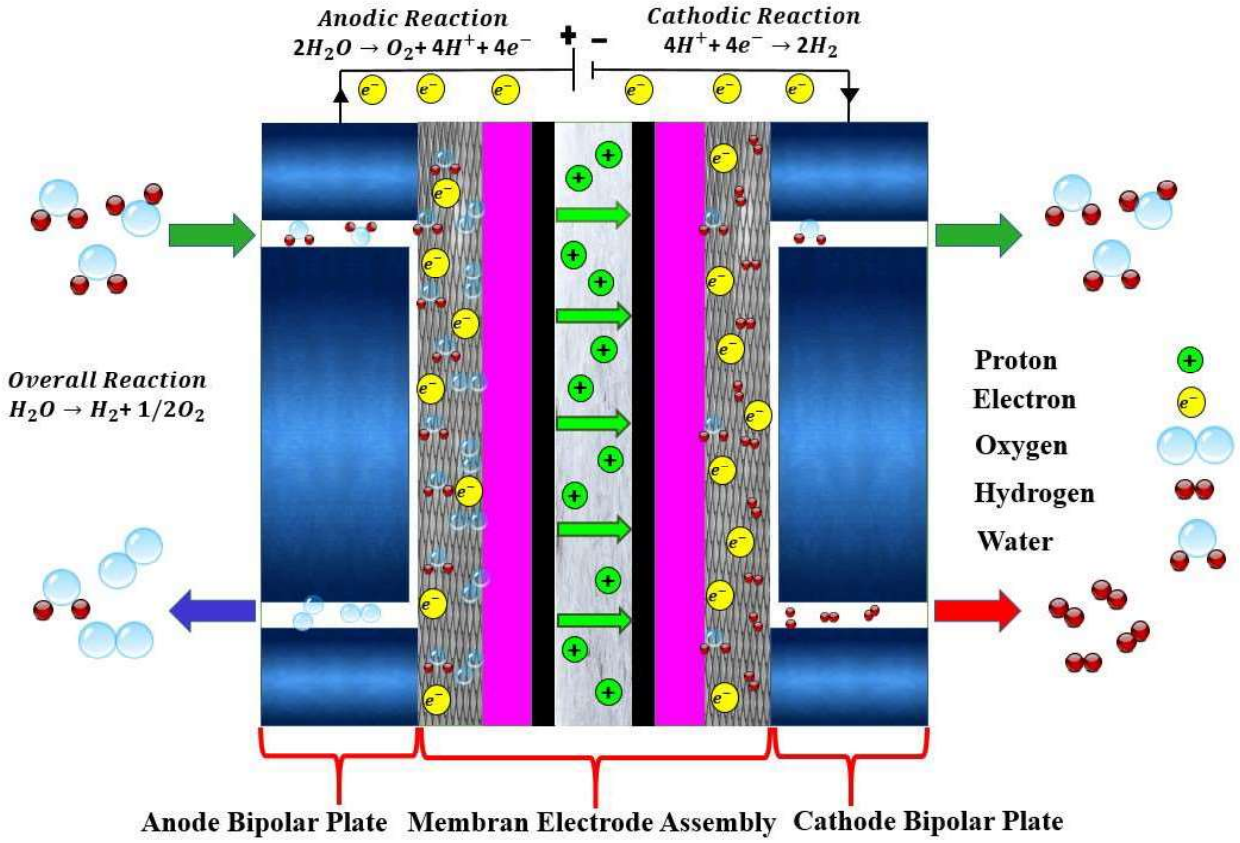


Figure 1. Schematic view of PEM electrolysis cell

In standard conditions, Gibbs free energy (ΔG) calculates the minimum energy required to split water as follows:

$$\Delta G = nFE_{rev} \quad (4)$$

where

n: Number of electrons (n=2)

F: Faraday's constant (F=96500)

E_{rev}: Reversible voltage

The following equation gives the reversible voltage;

$$E_{rev} = \frac{\Delta G}{nF} = 1.23 \text{ Volt} \quad (5)$$

Some entropy is produced during the electrolysis of water. Therefore, it would be more appropriate to use enthalpy (ΔH) instead of Gibbs free energy (ΔG) in calculating the thermo-neutral voltage (the minimum voltage required in the electrolysis of water). In standard conditions, Gibbs free energy change is $\Delta G = 237.22 \text{ kJ}mol^{-1}$ and the enthalpy change is $\Delta H = 285.84 \text{ kJ}mol^{-1}$. The thermo-neutral voltage can be calculated as follows;

$$V_{TN} = \frac{\Delta H}{nF} = \frac{\Delta G}{nF} + \frac{T\Delta S}{nF} = 1.48V \quad (6)$$

Where

T: Temperature

ΔS: Change in entropy

V_{TN}: Termo-neutral voltage

According to the first law of thermodynamics, the energy conservation law, water is broken down into oxygen and hydrogen by electrical energy. In other words, electrical energy is converted into chemical energy.

The water electrolyzer efficiency is calculated as follows;

$$\eta = \frac{V_{TN}}{V_{cell}} \quad (7)$$

Where

V_{cell}: Cell voltage

Electrolyzer efficiency will be higher because lower current densities are operated at lower voltages.

3 EXPERIMENTAL SETUP

The components of the PEM electrolysis cell with a 9 cm² membrane were brought together to fulfill performance tests in the TUBITAK MAM laboratory (see Figure 2). The experimental setup of a PEM electrolysis cell for the single-cell tests in the study is shown in Figure 3. The beaker supplied water, and an adjustable peristaltic pump (Masterflex model 77390-00) was used to feed the liquid water to the electrolysis cell single serpentine flow field plate. Before entering the cell, the water is heated to the desired temperature with the heater (Heidolph MR 3001 K). PEM electrolysis cell temperature was controlled by K-type thermocouples. A 0.76 kW (20V-38A) power supply system (TDK-Lambda) meets the energy needed for water electrolysis. A 100 mL soap film flowmeter was used to measure the volumetric flow rate of hydrogen gas produced in the electrolysis cell. All data were recorded on the computer through the data logger.

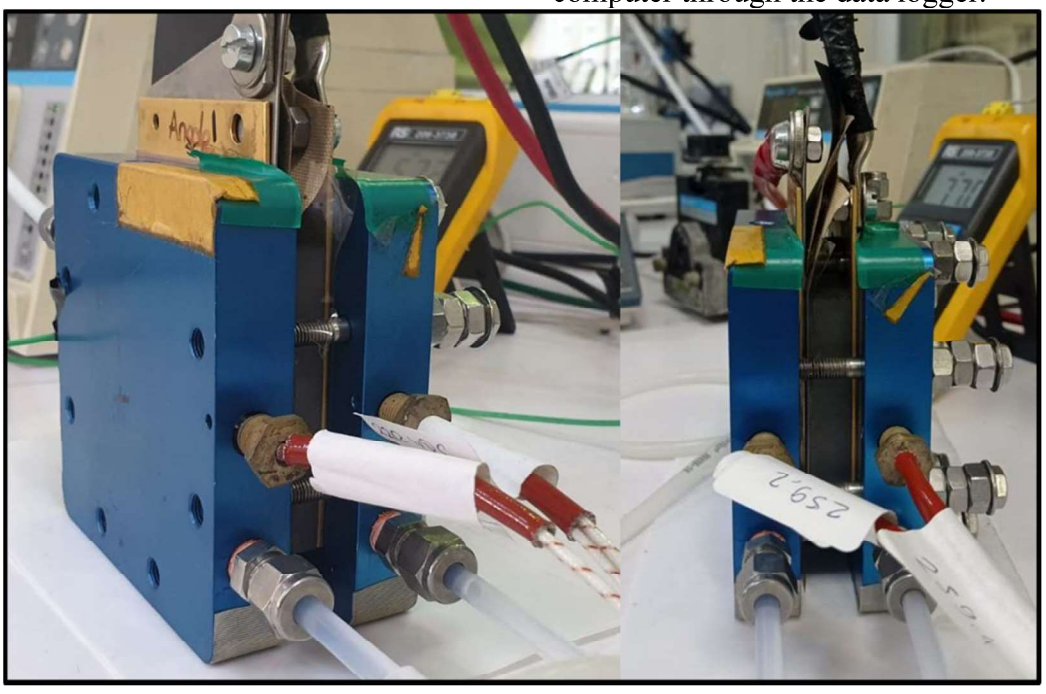


Figure 2. Experimental PEM electrolysis cell

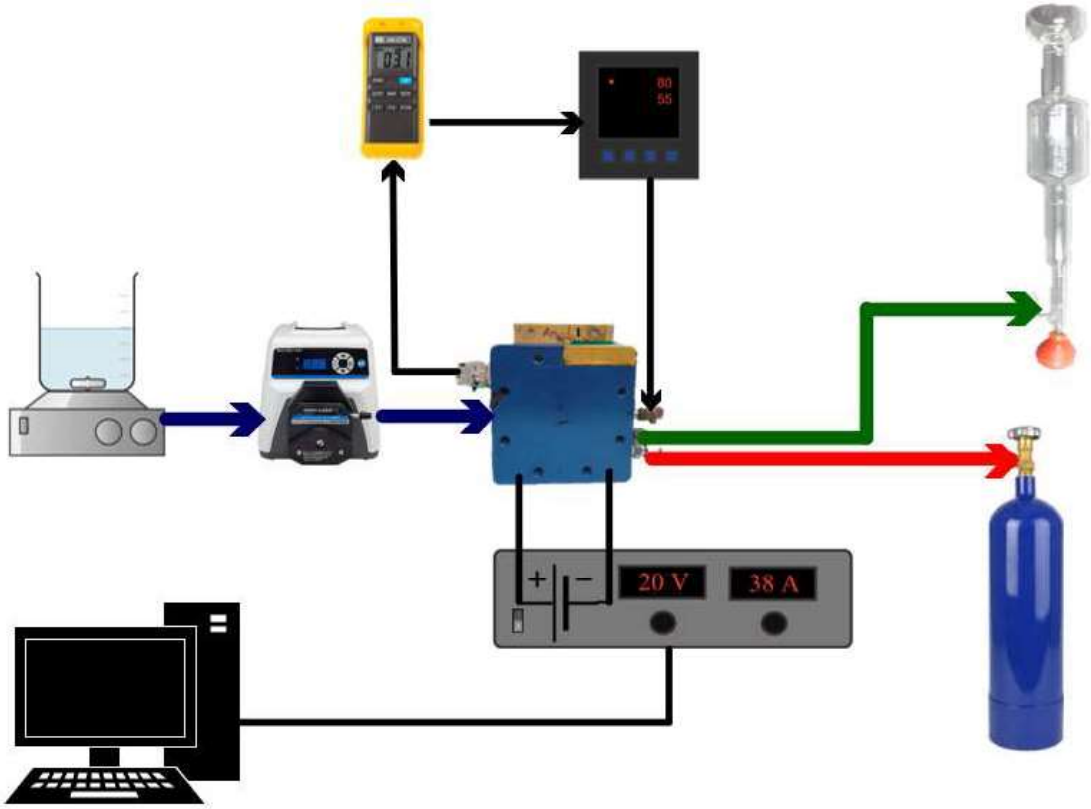


Figure 3. General view of the experimental layout for single cell testing

4 RESULTS AND DISCUSSION

4.1 Experimental results for the PEM electrolysis cell

In this study, a series of experiments are carried out to investigate the effect of cell temperature, pump value, and cell voltage on the current and hydrogen flow rates. The experiments are conducted with a single cell having a 9 cm² active area under atmospheric pressure. Figure 4 shows that the performance of the electrolysis cell improves with an increase of the operating temperature from 40°C to 80°C in 20°C increments for the water flow rates of 16.5 mL/min (pump value of 5), 23.0 mL/min (pump value of 7), and 30.6 mL/min (pump value of 9), respectively. An increase from 40 °C to 80 °C at a cell voltage of 2.4 V increases current density from 1.376 to 1.878 A/cm^2 for the water flow rate of 30.6 mL/min. The best performance was obtained at 80°C. From the experimental results, the current density improved with the increased kinetics of the charge transfer coefficient at the membrane-catalyst interface at high temperatures. Therefore, the activation over-potential decreased with increasing temperature. Also, proton conductivity increases, and the concentration over-potential decreases at higher temperatures caused by the acceleration of the kinetics of electrochemical reactions. However, cell temperature above 80 °C cause membrane dehydration, so Nafion membranes with high thermal resistance should be used. In Figure 5, the variation of the hydrogen flow rate is depicted at different water temperatures in the range of 40-80°C. As Figure 5 shows, all curves have the same trend; the operating temperature does not significantly affect the hydrogen flow rate. It was observed that the generating hydrogen flow rate was the maximum at a water temperature of 80°C. As a result of the studies, it was concluded that although the increased temperature accelerated the electrochemical reaction kinetics and improved the cell performance, there was no significant change in the hydrogen flow rate. Rising water temperature from 40 to 80°C at a cell voltage of 2.8V causes the hydrogen flow rate from 229 to 279.1 mL/min when the water flow rate is 16.5 mL/min, respectively.

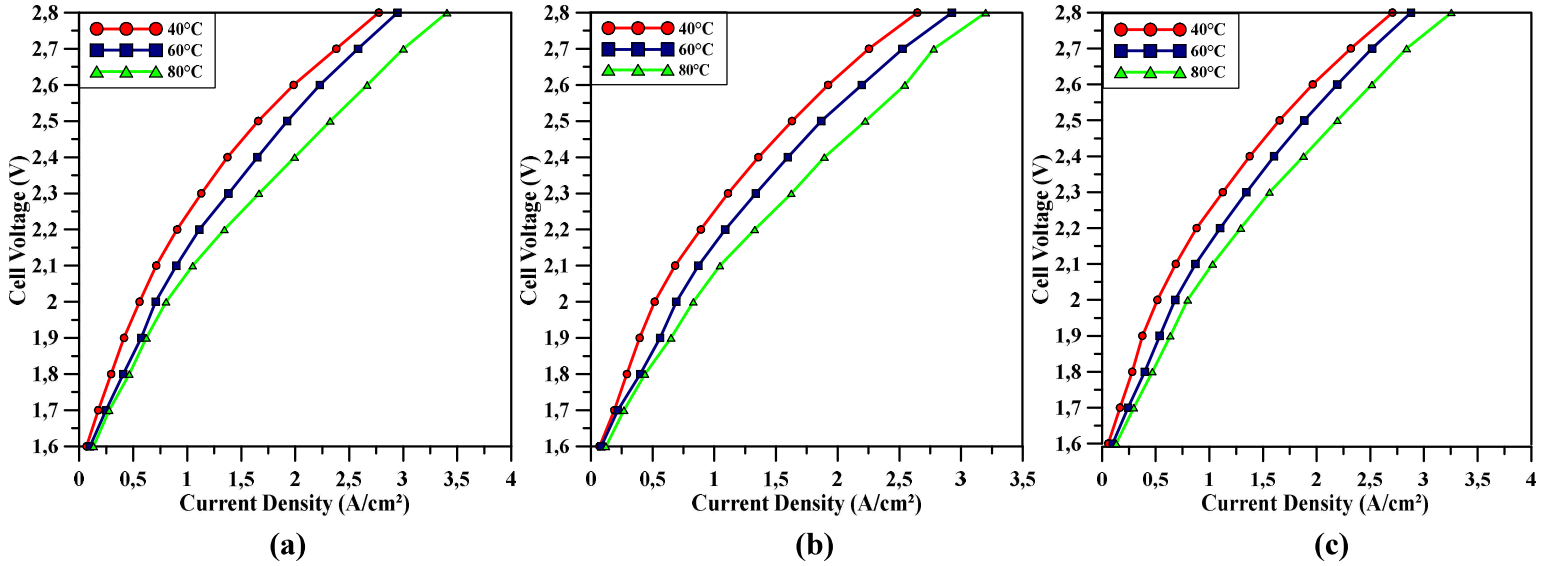


Figure 4. The effect of temperature on the polarization curve of the PEM electrolysis cell at a water flow rate of 16.5 mL/min (a), 23.0 mL/min (b), and 30.6 mL/min (c), respectively

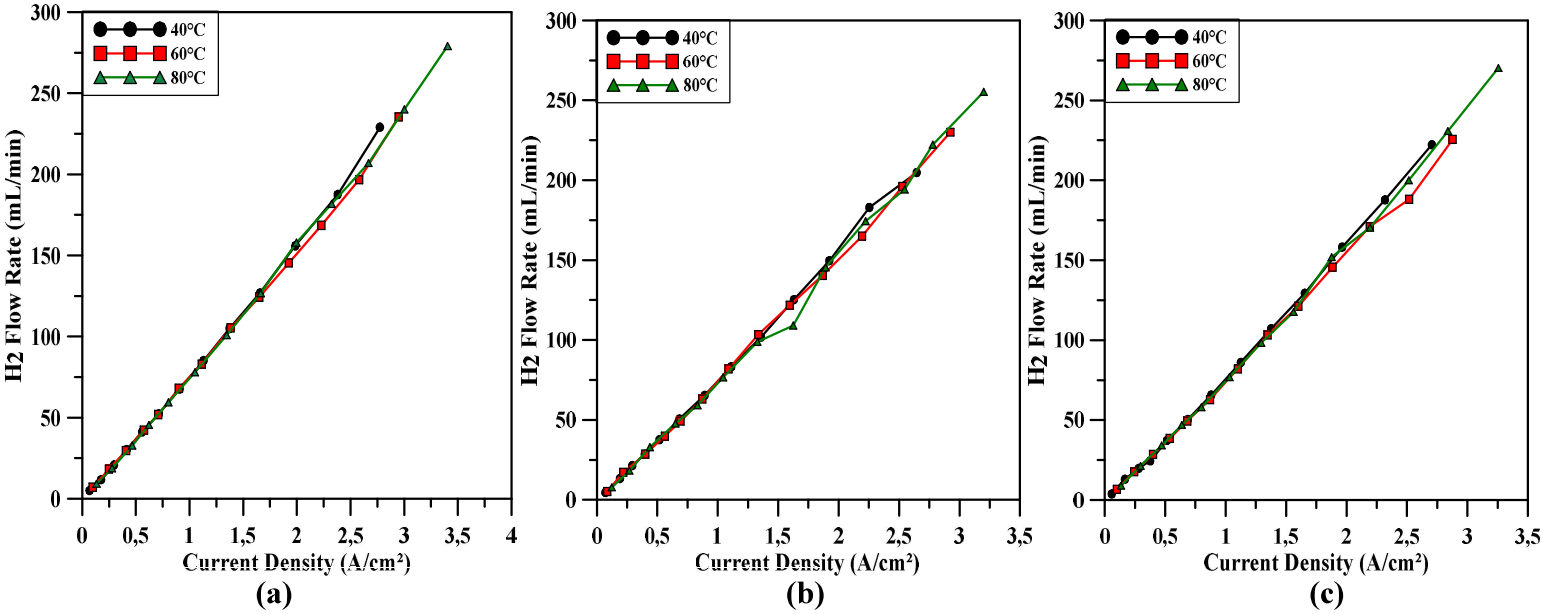


Figure 5. The effect of hydrogen flow rate on the polarization curve of the PEM electrolysis cell at a water flow rate of 16.5 mL/min (a), 23.0 mL/min (b), and 30.6 mL/min (c), respectively

4.2 Optimization results for the PEM electrolysis cell

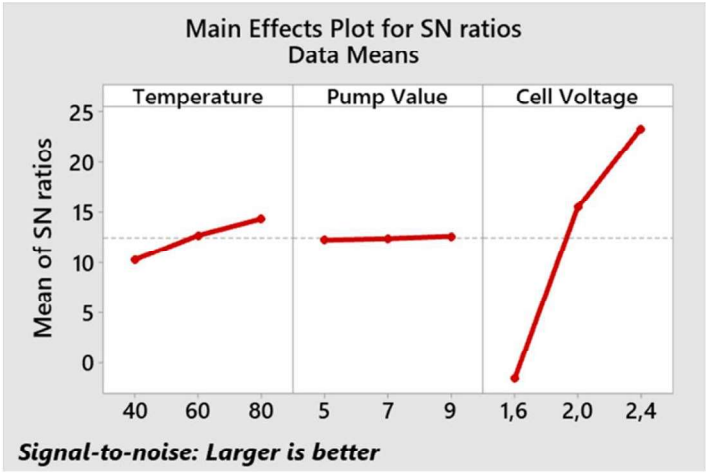
The Taguchi method is a powerful statistical method used for experimental optimization developed by Genichi Taguchi. It is a perfect engineering tool that generates the optimum combination of input factors for maximum PEM electrolyzer performance. This method helps to decrease the number of experiments. Here, the Taguchi method L9 standard orthogonal array (OA) with three operating parameters, e.g., cell temperature, pump value, cell voltage, and S/N ratios of experimental design, was used (see Table 1). The main aim of this optimization method using the L9 standard orthogonal array is to obtain the maximum current and hydrogen production yield. This optimization technique provides the required number of experiments with a signal-to-noise (S/N) ratio. The S/N ratio represents the amount of closeness to the target value. The signal indicates the average output, and the noise denotes the deviation of the average

output. The best electrolyzer performance is achieved with a high S/N ratio as the signal level is much higher than the random noise level. There are three different types of S/N ratio for statistical analysis (a) larger is better, (b) smaller is better, and (c) nominal is better. This study has applied the larger-the-better option to achieve higher current and hydrogen flow rates. The mean S/N ratio results and the effect of operating parameters on current and hydrogen flow rate are shown in Figure 6, respectively. As the S/N ratio increases, the electrolyzer cell works in better condition. In Table 1, the highest S/N ratio (43.9671) was obtained at a temperature of 80°C, pump value of 5, and 2.4V cell voltage. This means that the highest cell performance in the experimental design is achieved with these operating conditions. According to Figure 6, better cell performance was obtained at higher operating temperatures. It was concluded that the current and hydrogen flow rates increased when the temperature was increased from 40 °C to 80 °C. When the pump value was increased from 5 to 9, there was no significant change in hydrogen flow rate and current. Finally, the cell voltage considerably affects the two different responses.

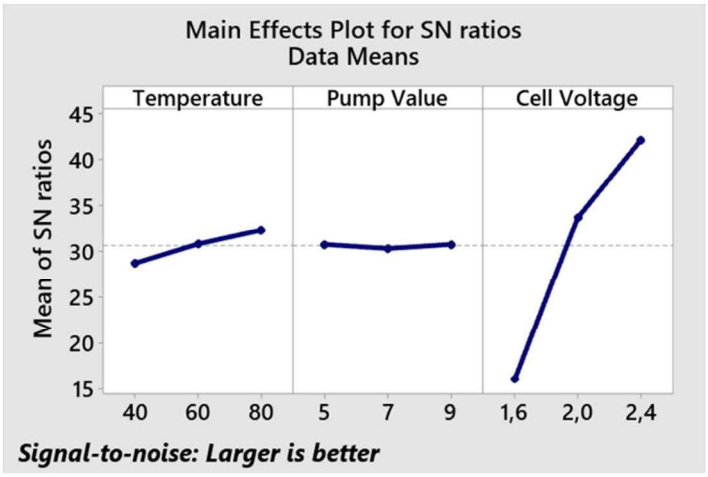
Table 1. L9 orthogonal array with three parameters and S/N ratios of experimental design

Run	Temp.(°C)	Pump Value	Cell Voltage (V)	S/N Ratio
1	40	5	1.6	14.0882
2	40	7	2	31.5061
3	40	9	2.4	40.5990
4	60	5	2	34.3033
5	60	7	2.4	41.7058
6	60	9	1.6	16.4955
7	80	5	2.4	43.9671
8	80	7	1.6	17.7860
9	80	9	2	35.2641

The controllable and uncontrollable noise sources affect the performance of the PEM electrolysis cell.



(a)



(b)

Figure 6. The effects of mean S/N ratio against temperature, pump value, and cell voltage on (a) current (A) and (b) hydrogen flow rate (mL/min)

Experiments were repeated three times to obtain consistent results and minimize the uncontrollable noise effect. In this study, we evaluate the response function of the optimal operating parameters based on the current and hydrogen flow rate; hence, we interpret the signal-to-noise (S/N) ratio based on larger is better.

$$\frac{S}{N} = -10log_{10}\left(\frac{1}{n_r}\sum_{i=1}^{n_r}\frac{1}{Y_i^2}\right) \quad (8)$$

Where,

n_r: Number of trials for the levels of the noise factors

Y_i: describes the value of the result data

The input parameters are then analyzed using the Taguchi method in Minitab 19 software for the Design of Experiments (DOE). The significance of three different independent parameters affecting the response function is measured with

a delta value. The operating parameter with the highest delta value indicates a higher significance factor. Conversely, rank indicates the order of influence of the key parameter on the response function. It was recorded that cell voltage was the predominant factor affecting the current of the PEMEC, followed by temperature and pump value. The response values of S/N ratios for each case are shown for three test levels in Table 2. The difference between maximum S/N and minimum S/N is defined in the table as Delta. A high delta value is the most influential parameter that affects cell performance positively or negatively. For example, Rank 1 demonstrates the most significant parameter, and Rank 3 indicates the most ineffective control factor. The highest level of control factors has been taken into account from the response table of the S/N ratio as the best value of the experimental system to obtain the maximum electrolyzer performance. The best control factors are cell voltage (CV) at level 1, temperature (T) at level 2, and pump value (PV) at level 3. The optimum level combination of three different control factors for maximum current and hydrogen flow rate can be summarized as CV1T2PV3. In this study, the analysis of variance (ANOVA) method was used as a statistical engineering tool to represent the relationship between operating parameters and optimization responses by showing the contribution rate of each parameter to optimization responses. The impact of the most critical operating parameter on the current and hydrogen flow rate can be determined using this technique. ANOVA is used to calculate the contribution rate of each parameter to optimization responses with different control factors such as a sum of squares (SS), mean of squares (MS), and degree of freedom (DF). The response results of the ANOVA analysis are shown in Table 3.

The F-value can be expressed as the ratio of model mean square to residual mean square. It can be deduced from the table that the cell voltage dramatically influences the current and hydrogen flow rate with its high F-value and corresponding low P-value. The ANOVA table shows the cell voltage's effect on the hydrogen flow rate with the highest contribution, around 90.81%, while the pump value shows a minor contribution, around 1.25%. The temperature contribution is also about 3.67%. Similarly, the effect of the cell voltage on the current with the highest contribution is around 91.91% while the pump value shows a minor contribution which is around 1.04%. The temperature contribution is also about 3.84%. The normal probability plot of the residuals described as the differences between the experimental and predicted values is shown in Figure 7. The position of experimental data as close to a straight line indicates that the data are in the normal range. As seen in Figure 7, there is a good agreement between the model and the actual experimental data. From this, it is concluded that the model has acceptable adequacy. Current and hydrogen flow rate as a function of cell voltage, pump value, and temperature on a three-dimensional polarization curve is shown in Figure 8(a-f). It is seen that the effect of cell voltage is more than the effect of temperature and pump value on the current and hydrogen flow rate. As shown in Figure 8, as the current drawn from the electrolysis cell increases, a high hydrogen flow rate is produced. At 80°C, a pump value of 5, a total current of 17.95 A was drawn, whereas hydrogen was produced at a flow rate of 157.89 mL/min. It is concluded that the pump value does not significantly affect the current and hydrogen flow rate.

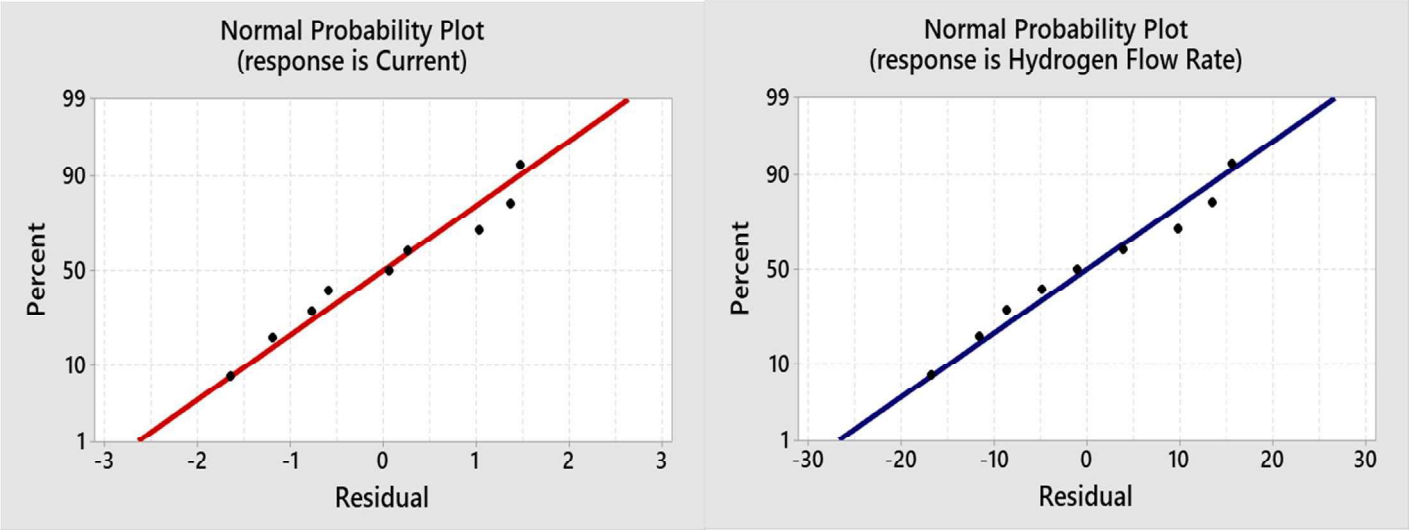
Table 2. Response table for S/N Ratios

	Hydrogen Flow Rate			**Current**		
Level	**Temperature**	**Pump Value**	**Cell Voltage**	**Temperature**	**Pump Value**	**Cell Voltage**
1	28.73	30.79	16.12	10.303	12.290	-1.493
2	30.83	30.33	33.69	12.738	12.440	15.522
3	32.34	30.79	42.09	14.348	12.659	23.360
Delta	3.61	0.45	25.97	4.045	0.369	24.852
Rank	2	3	1	2	3	1

For instance, at a temperature of 60°C, cell voltage of 2V, the current drawn from the electrolyzer cell at pump values of 5, 7, and 9 is 6.37, 6.23, and 6.14 A, respectively. Figure 8 shows that the current and hydrogen flow rate increase with increasing cell voltage.

Table 3. Results of analysis of variance (ANOVA)

	Hydrogen Flow Rate						Current				
Source	**DF**	**Contribution**	**Adj SS**	**Adj MS**	**F-Value**	**P-Value**	**Contribution**	**Adj SS**	**Adj MS**	**F-Value**	**P-Value**
Temperature	1	3.67%	907.7	907.7	4.29	0.093	3.84%	12.327	12.327	5.96	0.058
Pump Value	1	1.25%	309.1	309.1	1.46	0.281	1.04%	3.330	3.330	1.61	0.260
Cell Voltage	1	90.81%	22477.2	22477.2	106.13	0.000	91.91%	295.261	295.261	142.86	0.000
Error	5	4.28%	1059.0	211.8			3.22%	10.334	2.067		
Total	8	100.00%					100.00%				



(a) **(b)**

Figure 7. Normal probability plot of the residuals for (a) current and (b) hydrogen flow rate

5 CONCLUSIONS

This study shows how the cell voltage, pump value, and cell temperature affect the performance of the PEM electrolysis cell. In the literature, there is no present study in which the operating parameters affecting the PEM electrolyzer performance are optimized experimentally using optimization algorithms. To increase the hydrogen production rate and current, the operational parameters of the PEMEC system were optimized by the Taguchi method.

This paper determined the contribution percentages of operating parameters on the current and hydrogen flow rate with the Taguchi method so that the cost can be reduced by minimizing the number of experimental tests. The ANOVA is used to calculate the contribution percentages of the input parameters. In addition, three parameters (cell voltage, pump value, and current) with three levels for each of them and an L9 orthogonal array are regarded for analysis. The impact of these parameters on the polarization curve has been analyzed experimentally.

It is recorded that higher temperature, cell voltage, and pump value improved the performance of the PEMEC. Moreover, the cell voltage significantly affects the current and hydrogen flow rate with a contribution of about 91%, and the variation of the cell temperature and pump value slightly affects the output parameters with a contribution of about 3% and 1%, respectively.

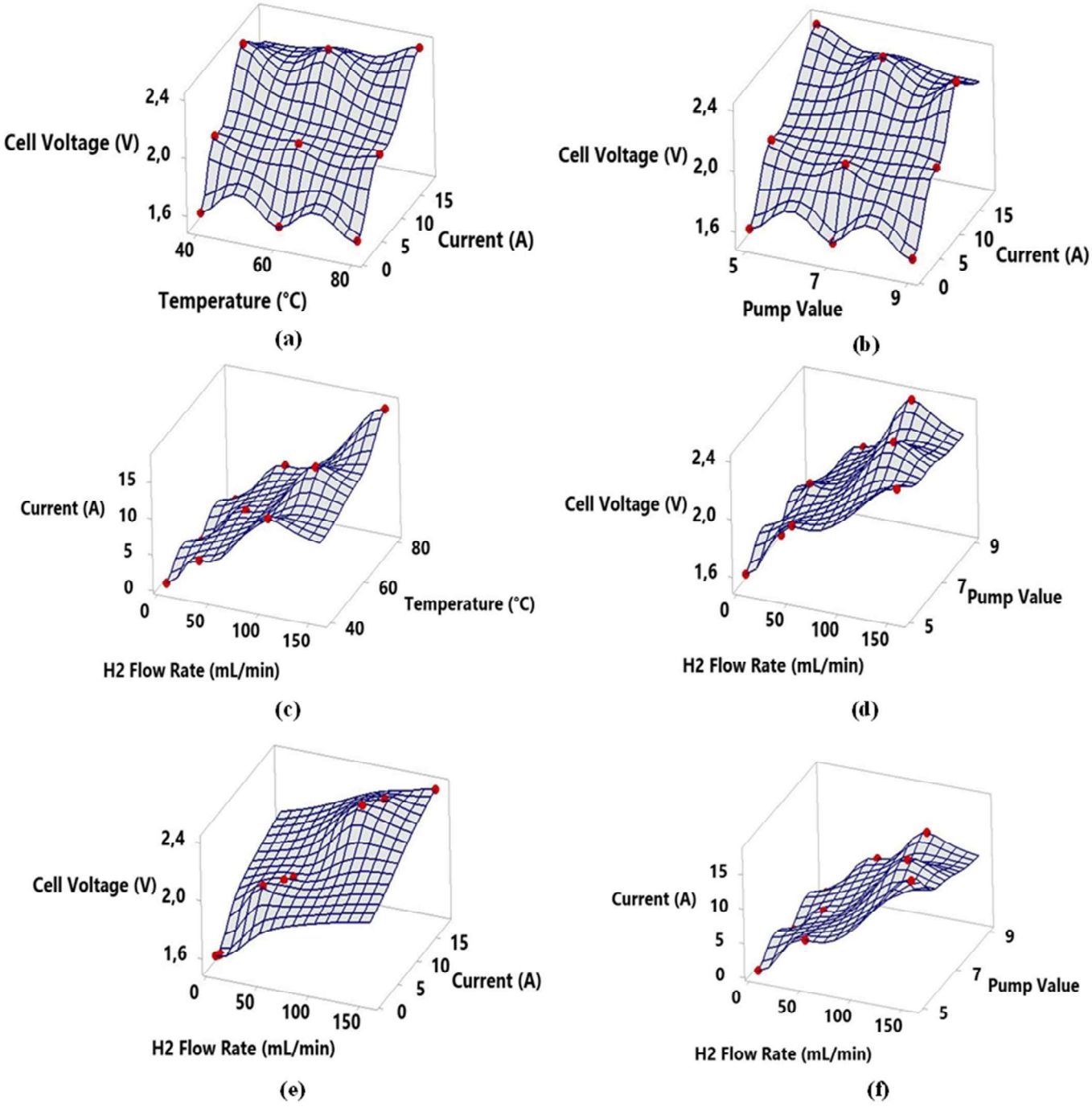


Figure 8. Surface plot of the effect of control factors on response

ACKNOWLEDGEMENTS

The study was supported by the Scientific and Technological Research Council of Turkey (TUBITAK, PN: 5212A01) and the Turkish Energy, Nuclear, and Mineral Research Agency (TENMAK).

REFERENCES

[1] D. Gielen, et al, The role of renewable energy in the global energy transformation, Energy Strategy Reviews, 24, 38–50, 2019.

[2] N. Z. Muradov and T. N. Veziroğlu, "Green" path from fossil-based to hydrogen economy: An overview of carbon-neutral technologies, International Journal of Hydrogen Energy, Vol. 33, Issue 23, pp. 6804–6839, 2008.

[3] A. Ursúa, et al, Hydrogen production from water electrolysis: Current status and future trends. Proceedings of the IEEE, 100(2), 410–426, 2012.

[4] B. D. Solomon, and A. Banerjee, A global survey of hydrogen energy research, development and policy, Energy Policy, 34(7), 781–792, 2006.

[5] S. Kumar and V. Himabindu, Hydrogen production by PEM water electrolysis – A review, In Materials Science for Energy Technologies, Vol. 2, Issue 3, pp. 442–454, 2019.

[6] F. Barbir, PEM electrolysis for production of hydrogen from renewable energy sources, Solar Energy, 78(5), 661–669, 2005.

[7] M. Momirlan, and T. N. Veziroglu, Current status of hydrogen energy, Renewable and Sustainable Energy Reviews, Vol. 6, 2002

[8] S. A. Grigoriev, et al, Pure hydrogen production by PEM electrolysis for hydrogen energy, International Journal of Hydrogen Energy, 31(2), 171–175, 2006

[9] J. Mo, et al, Discovery of true electrochemical reactions for ultrahigh catalyst mass activity in water splitting, Science advances, 2.11: e1600690, 2016.

[10] D. S Falcão, and A. M. F. R. Pinto, A review on PEM electrolyzer modelling: Guidelines for beginners, Journal of Cleaner Production, Vol. 261, 2020.

[11] A. Caravaca, et al, Electrochemical reforming of ethanol-water solutions for pure H 2 production in a PEM electrolysis cell, International Journal of Hydrogen Energy, 37(12), 9504–9513, 2012.

[12] A. T. Marshall, and R. G. Haverkamp, Production of hydrogen by the electrochemical reforming of glycerol-water solutions in a PEM electrolysis cell, International Journal of Hydrogen Energy, 33(17), 4649–4654, 2008.

[13] J. Nie, and Y. Chen, Numerical modeling of three-dimensional two-phase gas-liquid flow in the flow field plate of a PEM electrolysis cell, International Journal of Hydrogen Energy, 35(8), 3183–3197, 2010

[14] S. Toghyani, et al, Three-dimensional computational fluid dynamics modeling of proton exchange membrane electrolyzer with new flow field pattern, Journal of Thermal Analysis and Calorimetry, 135(3), 1911–1919, 2019.

[15] A. S. Tijani, et al, Computational Modelling of the Flow Field of An Electrolyzer System using CFD, Energy Procedia, 79, 195–203, 2015

[16] S. A. Grigoriev, et al, Mathematical modeling of high-pressure PEM water electrolysis, Journal of Applied Electrochemistry, 40(5), 921–932, 2010.

[17] P. Millet, et al, PEM water electrolyzers: From electrocatalysis to stack development, International Journal of Hydrogen Energy, 35(10), 5043–5052, 2010

[18] Ö. Selamet, et al, Development and testing of a highly efficient proton exchange membrane (PEM) electrolyzer stack, International Journal of Hydrogen Energy, 36(17), 11480–11487, 2011.

[19] B. Han, et al, Electrochemical performance modeling of a proton exchange membrane electrolyzer cell for hydrogen energy, International Journal of Hydrogen Energy, 40(22), 7006–7016, 2015.

[20] S. Toghyani, et al, Thermal and electrochemical performance assessment of a high temperature PEM electrolyzer, Energy, 152, 237–246, 2018.

[21] Z. Ma, et al, A comprehensive modeling method for proton exchange membrane electrolyzer development, International Journal of Hydrogen Energy, 46(34), 17627–17643, 2021

[22] X. Su, et al, Simulation of proton exchange membrane electrolyzer: Influence of bubble covering, International Journal of Hydrogen Energy, 47(46), 20027–20039, 2022.

EXPERIMENTAL STUDIES ON THE COMBUSTION BEHAVIOR OF DIFFERENT PLASTIC CONTENT REFUSE DERIVED FUEL UNDER DIFFERENT FURNACE CONDITIONS

Priyanka Tripathi[1] and Lakshminarayana Rao[2]

1. Centre for Sustainable Technologies, Indian Institute of Science, Bengaluru- 560012, India; email: priyankat@iisc.ac.in
2. Centre for Sustainable Technologies, Indian Institute of Science, Bengaluru- 560012, India; email: narayana@iisc.ac.in

Abstract

Three different RDF pellets having 5 %, 15 % and 35 % plastics were prepared and characterized for their combustion behaviour inside a cylindrical wire-mesh basket. The isothermal mass loss curves and conversion time were recorded for different plastic content RDF at different furnace temperature and air flow rate conditions. Under the same experimental condition, 5 %-RDF reported 70 % higher conversion time as compared to 35 %-RDF. This was because 5 %-RDF had 1.3 times higher density as compared to that of 35 %-RDF. The fuel reactivity was calculated as- 0.0028, 0.0035, 0.0039 s^{-1} for 5 %, 15 % and 35 %-RDF, respectively. However, for all RDF compositions, the calculated reactivities for bulk combustion inside the basket were 50 % lower as compared to single fuel particle reactivity. This indicates slower transport of products from the surface in the case of basket studies by the diffusion of oxygen. Also, an increase in temperature from 1048 K to 1173 K decreased the conversion time by 50 % and increased the fuel reactivity by 1.5 times. But as compared to furnace temperature variation, flow rate variation has a minimal impact on the conversion time of the fuel particles.

Keywords: Refuse derived fuel, plastic, density, solid fuel combustion, fuel reactivity

1 INTRODUCTION

The abysmal condition of municipal solid waste management has become a matter of utter concern all over the world including in India [1]. The global per capita waste generation stands at 1.2 kg per person per day and by the year 2025, it is expected to increase by 1.42 kg per person per day [2]. In India, about 31.2 % of its population lives in urban areas, generating about 1,70,000 TPD of waste which amounts a to per capita waste generation of 450 g per day [3,4]. Only, 28 % of the generated waste in India is treated and the rest is disposed of unscientifically in open fields [5]. This burgeoning problem of waste generation along with its disposal problem has the urged development of sustainable waste management practices. One of the sustainable ways to address the issue of waste management is thermochemical treatment of waste [6]. Refuse derived fuel (RDF) represents the combustible fraction of municipal solid waste (MSW) and it could be utilized for energy production [5,7]. RDF gasification is regarded as promising technology for converting RDF to value-added products like gas, chemicals, liquid fuels or hydrogen [8]. For the international scenario, RDF has been potentially gasified in Japan and Europe [9]. Whereas in India, RDF gasification technology is not commercialized due to various issues such as improper segregation of waste, high ash (18-20 %) and plastic content (30-35 %) of Indian commercial RDF and most importantly due to lack of fundamental research on the fuel itself [10,11]. The effect of RDF's plastic fraction and external operating conditions on fuel performance is required for a better understanding of the combustion behaviour of the bed of particles [12,13]. These data are missing in the literature for RDF. This work aims to fill this gap.

The combustion of solid fuel can be categorized into two main phases- flaming combustion or devolatilization and glowing or char combustion [14]. These processes are also important processes of a gasifier. The solid fuel combustion studies for widely used fuels for gasification like wood and coal are well-established in literature [15–20]. However, for different plastic content RDF under different operation conditions, no such study exists. Of the multiple components present in RDF, the plastic fraction of RDF plays an important role to influence the physio-chemical, combustion behaviour and reactivity of the bed of particles [10,12,21,22]. Also, the

conversion time scales as a function of different furnace temperature and flow rate conditions are required for the improved design of the various zones of a gasifier as well as for the sizing of the gasifier [13]. Hence, in the present work, an attempt was made to investigate the combustion characteristics of RDF as a function of plastic content and operating conditions.

In this work, simulated RDF pellets having different plastic content were prepared and then characterized for their combustion behaviour inside a cylindrical wire-mesh basket. The isothermal mass loss curves, conversion time and fuel reactivity were determined for different plastic content RDF at different furnace temperature and air flow rate conditions like that of a gasifier.

2 MATERIALS AND METHODS

2.1 Materials used

The materials used for simulated RDF pellet preparation were sawdust, paper (A4 sheets), food waste (refined wheat flour), textiles (rags, cotton thread) and plastic (mixture of HDPE, LDPE, and PP in the ratio of 44:44:12).

Table 1 provides information on the individual percentage contribution of the raw materials used for simulated pellet preparation. The RDF pellets were prepared based on the Indian commercial RDF composition having 35-40 % yard waste, 10 % food waste, 10-15 % paper waste and 30-35 % plastic[10]. The simulated RDF pellets were prepared by varying the plastic content from 5 % to 35 %. The variation in plastic content was compensated by variation in food waste content. Again, the selected raw materials were shredded to ensure uniformity in particle size and the fine mixing of the required blend.

Table 1. Individual percentage contribution of the raw materials

Fuel	Wood	Food	Textiles	Paper	Plastic
5 %-RDF	35	40	5	15	5
15 %-RDF	45	15	5	20	15
35 %-RDF	35	10	5	15	35

2.2 Equipment and method used

The pellets were prepared by a manual pelletizer, consisting of plunger-die assembly, as shown in Fig.1. The plunger was mounted on the threaded shaft which is connected to a rotating wheel on the other end. A hollow cylindrical chamber served as the die. The die was wrapped with heating tape to ensure pellet making at a higher temperature. A maximum temperature of only 373 K was allowed inside the die while heating to avoid softening of plastics. The diameter of the plunger-die assembly used was 15 mm.

The powdered mixture of the raw material was poured into the die and then plunger compressed the mixture. The compression provided by the plunger was controlled by rotating the wheel. For all cases, the same degree of compression was provided by lowering the plunger to the same level.

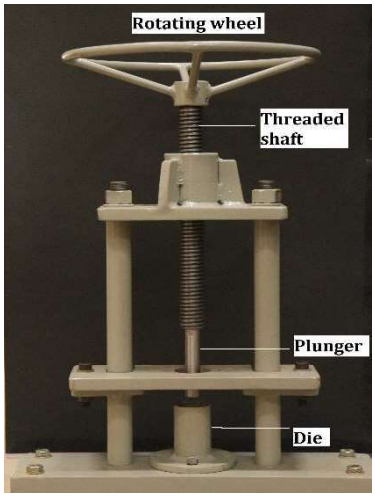


Fig.1 Pelletizer used

2.3 Characterization of prepared pellets

The prepared pellets were characterized for their physical, chemical and combustion properties. Physical properties include determining the proximate analysis and density of the fuel. In proximate analysis, moisture, volatile and ash content were measured as per ASTM standards-E871 – 82, E872 – 82, and E1755 – 01, respectively. The chemical properties include determining carbon (C), hydrogen (H), and nitrogen (N) of RDF and was conducted on Truspec CHN elemental analyzer from LECO Corporation. The oxygen content was determined by difference method. The Calorific value (CV) of the fuel was measured by Parr 6100 bomb calorimeter. The combustion properties of different plastic content RDF were determined by basket studies under different temperature and air flow rate conditions. During experiments, the temperature varied from 1048 K to 1173 K and the flow rate varied from particle Reynolds number (Re_p) = 3.5 to Re_p = 14. Also, the particle size of the cylindrical pellets used was expressed

in the equivalent diameter of the sphere. The basket experiments were conducted for a particle size of 16.2 mm equivalent diameter of the sphere.

2.4 Basket studies

The details and schematic of the experimental setup used for basket studies are provided in [23]. The setup consisted of a ceramic cylindrical reactor of 100 mm diameter, placed inside a high-temperature furnace. The heating of the reactor is conducted by the high-temperature furnace. The air flow into the reactor was sent through compressed air cylinders via rotameters. A self-made cylindrical wire-mesh basket having a length-to-diameter ratio of five was suspended by placing it in a basket-holding jig. About 50 g of RDF was fed into the basket. The isothermal mass loss data was recorded by a weighing balance and the data was continuously logged into the computer at every 1 s. The entire conversion process was viewed from an optical window present in the system.

The reactivity of the different plastic content RDF under isothermal conditions is defined as [24]-

$$R = \frac{1}{1-\alpha}\frac{d\alpha}{dt} \qquad (1)$$

And,

$$\alpha = \frac{m_0 - m_t}{m_0 - m_f}$$

Here, m_0, m_t, and m_f represent the initial, instantaneous, and final mass of the sample, respectively.

3 RESULTS AND DISCUSSIONS

3.1 Physio-chemical properties

Fig.2 (a-c) presents physio-chemical properties of the prepared pellets. As shown in Fig.2, with an increase in plastic content, the volatile fraction, C, H, and energy content of the fuel increases. However, the fixed carbon content reduced by half and oxygen content was reduced by 1.5 times by increasing the plastic content from 5 % to 35 %. Plastic being a polymer and high energy content fuel consists of complex hydrocarbon structures (C-83-84 %, H-10-11 %) [25]. Also, the fixed carbon (~ 0.1 %) and oxygen content (~ 5 %) available in plastic is almost negligible [26]. This leads to an increase in C, H, and CV content and a decrease in fixed carbon and oxygen content on increasing the plastic percentage in RDF.

Also, as can be seen from Fig.2c, pellet density of 5 %-RDF was 1.3 times higher than that of 35 %-RDF. This is due to the higher food waste content (~40 %) of 5 %-RDF as compared to 35 %-RDF (~10%). Food waste has a high starch content (~64 %) and has a high bulk density of 780 kg m^{-3}. These factors help in better binding and thus increased density in the case of 5 %-RDF.

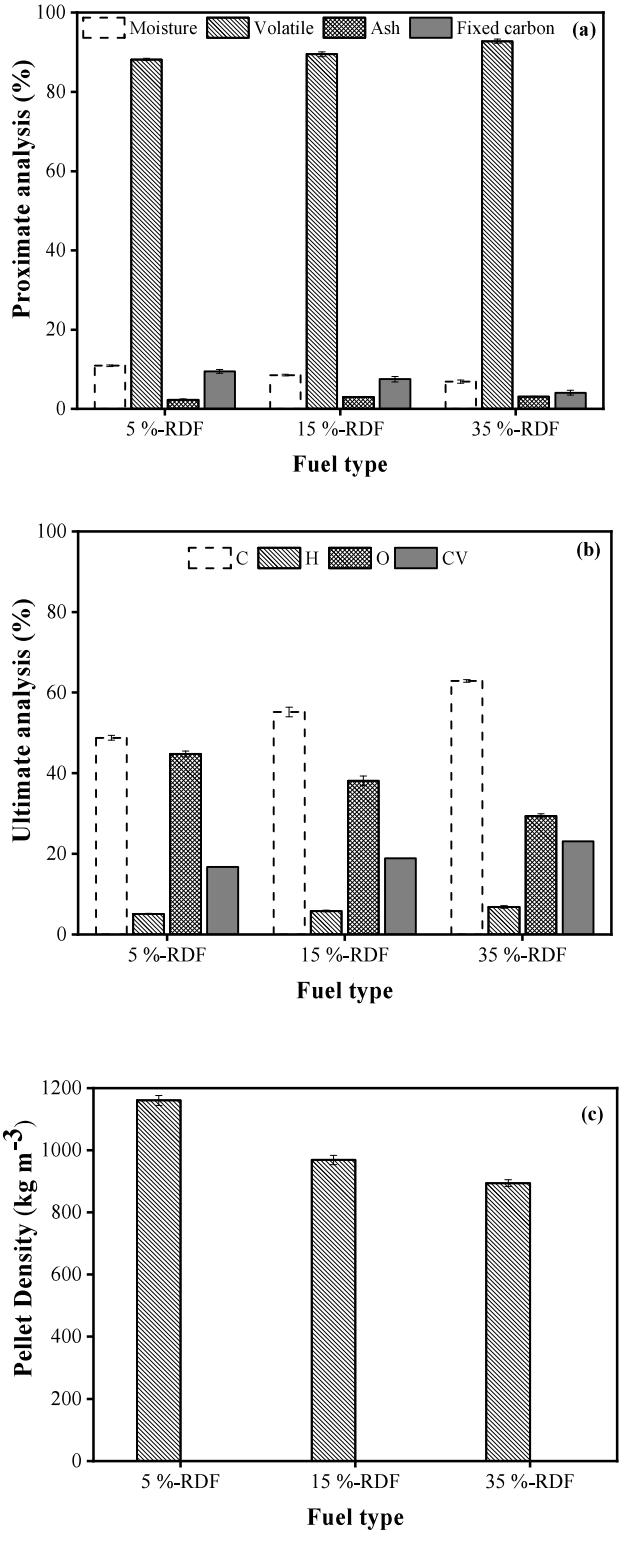


Fig.2 Physio-chemical properties of different plastic content RDF

3.2 Effect of fuel properties

This section explains the effect of the fuel physical-chemical properties of RDF on its combustion behaviour. Fig.3 shows the mass loss profile for different plastic content RDF for an equivalent diameter of 16.2 mm particle size at 1048 K and Re_p= 14. As can be seen from Fig.3, the major mass loss of the fuel bed has occurred in two distinct stages- an initial steep decrease between 0-300 sec, followed by a gradual decrease in the later part of the curve. This corresponded to two notable events of solid fuel combustion-flaming, char combustion/glowing. Flaming combustion refers to rapid mass loss which occurred in the initial 300 s due to the quick release of volatiles. Whereas glowing represented the gradual mass loss in the later part of the curve due to the slow heterogeneous reactions of the char with the incoming oxidizer.

As shown in Fig.3, 5 %-RDF has a 70 % higher conversion time as compared to 35 %-RDF. In fact, though 5 %-RDF has low volatile content, it still resulted in high devolatilization time. This is due to high moisture and pellet density of 5 %-RDF. As shown in Fig.2, due to the high food waste content in 5 %-RDF, its moisture is high which requires a high vaporization heat load. Again, the high pellet density is responsible for having higher internal thermal resistance to heat transfer inside the particle. So, the burning time in the case of 5 %-RDF is the highest.

However, the effect of density variation was more prominent in the glowing/char oxidation phase as the normalized burning rate increased by 47 % on increasing the plastic content from 5 % to 35 %.

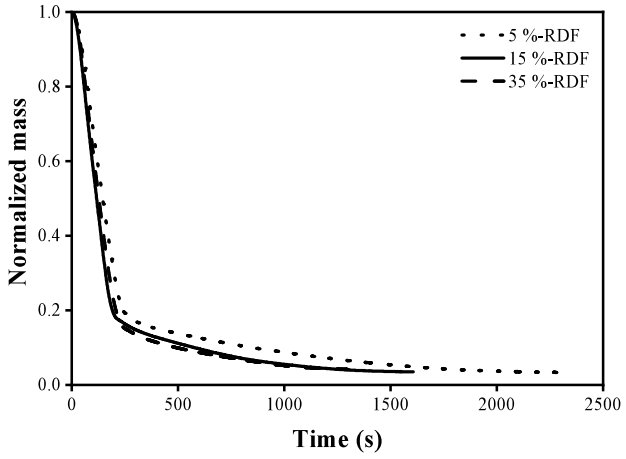


Fig. 3 Normalized mass loss curve for different plastic content RDF

The fuel reactivity was calculated at 1048 K as per equation (1) and is reported in Table 2. Table 2 shows that the reactivity of RDF increases with the increase in plastic content in the fuel. The reactivity for 35 %-RDF was 1.4 times higher than that of 5 %-RDF. This is due to higher volatile content and lower pellet density of 35 %-RDF. Lower density favours quick release of volatiles or quick penetration of heat inside the particle.

Table 2. Reactivities for different plastic content RDF under isothermal conditions

Fuel sample	Reactivities (S^{-1})
5 %-RDF	0.0028
15 %-RDF	0.0035
35 %-RDF	0.0039

Under same experimental condition, reactivities calculated for a single fuel particle of 5 %-RDF, 15 %-RDF, and 35 %-RDF were 0.0047 s^{-1}, 0.0075 and 0.01 s^{-1}, respectively. The calculated reactivities for a single fuel particle were 50 % higher as compared to a group of particles. This indicated slower transport of products from the surface by the diffusion of oxygen in the case of basket studies. This could be due to the non-uniform access of oxygen throughout the length of the basket.

3.3 Effect of furnace temperature variation

Fig.4 shows the effect of furnace temperature variation for 35 %-RDF (as representation case) for an equivalent diameter of 16.2 mm particle size at Re_p= 14. As shown in Fig.4, overall conversion time reduced on increasing furnace temperature from 1048 to 1173 K. The overall conversion time reduces by 56 %, 41 % and 49.8 % for 5 %, 15 %, and 35 %-RDF, respectively.

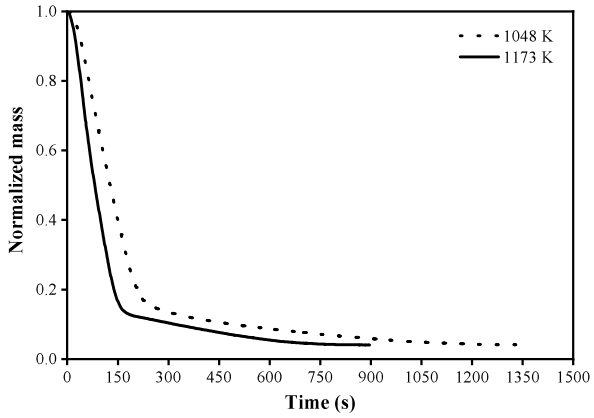


Fig.4 Effect of furnace temperature variation on conversion time of 35 %-RDF

Reduced conversion time indicated a higher burning rate. This in turn indicated higher heat flux to the particle which again is controlled by

free stream temperature. For a combusting particle, while the volatile-fed flame is a heat source, the heat loss from flame both to the particle and its surrounding is a heat sink. So, on increasing free stream temperature, the component of heat loss from the flame to the free stream reduces and heat flux to the particle increases, resulting in a higher burning rate.

3.4 Effect of flow rate variation

Fig.5 shows the effect of flow rate variation for 35 %-RDF for an equivalent diameter of 16.2 mm particle size at 1173 K. As shown in Fig.5, overall conversion time reduced on increasing Re_p from 3.5 to 14. On average, the overall conversion time was reduced by 16.9 % for all RDF. As combustion of pellets is limited by diffusion of oxygen to the surface, increased availability of oxygen to the surface at higher Re_p resulted in lower overall conversion time. However, as compared to furnace temperature, the effect of flow rate variation has a minimal impact.

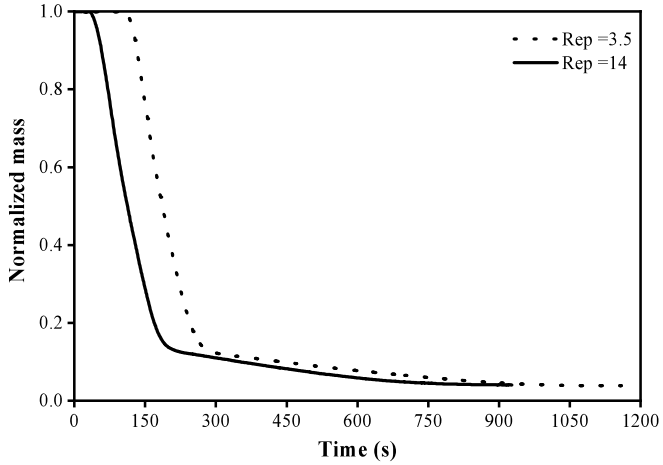


Fig.5 Effect of flow rate variation on conversion time of 35 %-RDF

4 CONCLUSIONS

Physio-chemical characterization of different plastic content RDF confirms that a higher plastic percentage leads to an increase in volatile matter content, carbon, hydrogen values and calorific values of the fuel and it decreased the oxygen and fixed carbon content of the fuel. Again, among different RDF compositions, 5 % plastic reported the highest particle density due to its high food waste content which improved the binding process.

The effect of physio-chemical properties was also reflected in the combustion properties of simulated RDF pellets. 5 %-RDF despite having low volatile content, has the highest flaming time due to its higher density. Also, the reactivity for 35 %-RDF was 1.4 times higher than that of 5 %-RDF. The effect of external conditions shows that free stream temperature had a strong effect on the burning rate relative to Re_p variation.

ACKNOWLEDGEMENTS

The authors duly acknowledge the financial support received from the Indian Institute of Science, Bangalore, India. The authors also thank Prof. S. Dasappa and Dr. Anand M Shivapuji of IISc Bangalore for providing the facilities at CGPL, IISc.

REFERENCES

[1] Sharholy M, Ahmad K, Mahmood G, Trivedi RC. Municipal solid waste management in Indian cities - A review. Waste Manag 2008;28:459–67. https://doi.org/10.1016/j.wasman.2007.02.008.

[2] Schiffer H-W. World Energy Resources 2016. World Energy Counc 2016 2016:6–46.

[3] Annepu RK. Sustainable Solid Waste Management in India. 2012. https://doi.org/10.1007/978-981-4451-73-4.

[4] Joshi R, Ahmed S. Status and challenges of municipal solid waste management in India: A review. Cogent Environ Sci 2016;2. https://doi.org/10.1080/23311843.2016.1139434.

[5] Report of the Task Force on Waste to Energy: In the context of Integrated MSW Management. vol. I. 2014.

[6] Kalyani KA, Pandey KK. Waste to energy status in India: A short review. Renew Sustain Energy Rev 2014;31:113–20. https://doi.org/10.1016/j.rser.2013.11.020.

[7] S. Psomopoulos C. Residue Derived Fuels as an Alternative Fuel for the Hellenic Power Generation Sector and their Potential for Emissions ReductionConstantinos S. Psomopoulos. AIMS Energy 2014;2:321–41. https://doi.org/10.3934/energy.2014.3.321.

[8] Sheth PN, Babu B V. Production of hydrogen energy through biomass (waste wood) gasification. Int J Hydrogen Energy 2010;35:10803–10. https://doi.org/10.1016/j.ijhydene.2010.03.009.

[9] Gendebien A, Leavens A, Blackmore K, Godley A, Lewin K, Whiting KJ, et al. Refuse Derived Fuel, Current Practice and Perspectives. 2003.

[10] Tripathi P, Rao L. Single particle and packed bed combustion characteristics of high ash and high plastic content refuse derived fuel. Fuel 2022;308:121983. https://doi.org/10.1016/j.fuel.2021.121983.

[11] Standing committee on energy report. Power generation from Municipal Solid Waste, MNRE, 20th report,. vol. 1932. 2016.

[12] Rezaei H, Panah FY, Lim CJ, Sokhansanj S. Pelletization of refuse-derived fuel with varying compositions of plastic, paper, organic and wood. Sustain 2020;12:1–11. https://doi.org/10.3390/su12114645.

[13] Simmons, Wayne W. and Ragland KW. Burning Rate of Millimeter Sized Wood Particles in a Furnace Burning Rate of Millimeter Sized Wood Particles. Combust Sci Technol 1986;46:1–15. https://doi.org/10.1080/00102208608959788.

[14] Das S, Sarkar PK, Mahapatra S. Single particle combustion studies of coal/biomass fuel mixtures. Energy 2021;217:119329. https://doi.org/10.1016/j.energy.2020.119329.

[15] Mason PE, Darvell LI, Jones JM, Pourkashanian M, Williams A. Single particle flame-combustion studies on solid biomass fuels. Fuel 2015;151:21–30. https://doi.org/10.1016/j.fuel.2014.11.088.

[16] Riaza J, Gibbins J, Chalmers H. Ignition and combustion of single particles of coal and biomass. Fuel 2017;202:650–5. https://doi.org/10.1016/j.fuel.2017.04.011.

[17] Das S, Kumar Sarkar P, Mahapatra S. Thermodynamic optimization of coal-biomass co-gasification process by using non-stoichiometric equilibrium modeling. Mater Today Proc 2018;5:23089–98. https://doi.org/10.1016/j.matpr.2018.11.039.

[18] Gort R. On the propagation of a reaction front in a packed bed. Thermal conversion of municipal waste and biomass. 1995.

[19] Mahapatra S, Dasappa S. Influence of surface area to volume ratio of fuel particles on gasification process in a fixed bed. Energy Sustain Dev 2014;19:122–9. https://doi.org/10.1016/j.esd.2013.12.013.

[20] Sharma M, Attanoor S, Dasappa S. Investigation into co-gasifying Indian coal and biomass in a down draft gasifier - Experiments and analysis. Fuel Process Technol 2015;138:435–44. https://doi.org/10.1016/j.fuproc.2015.06.015.

[21] Auprakul U, Promwungkwa A, Tippayawong N, Chaiklangmuang S. Factors affecting properties of fuel pellets from compaction of mixed biomass and waste plastics. Agric Eng Int CIGR J 2019;21:123–9.

[22] Madadian E, Crowe C, Lefsrud M. Evaluation of composite fiber-plastics biomass clinkering under the gasification conditions. J Clean Prod 2017;164:137–45. https://doi.org/10.1016/j.jclepro.2017.06.070.

[23] Asheruddin M, Shivapuji AM, Dasappa S. Thermochemical Conversion of Biomass Char under Carbon Dioxide Flux in a Thermally Supported Environment: Experimental and One-Dimensional Numerical Investigations. Energy and Fuels 2022;36:1574–91. https://doi.org/10.1021/acs.energyfuels.1c03550.

[24] Seo MW, Kim SD, Lee SH, Lee JG. Pyrolysis characteristics of coal and

RDF blends in non-isothermal and isothermal conditions. J Anal Appl Pyrolysis 2010;88:160–7. https://doi.org/10.1016/j.jaap.2010.03.010.

[25] Kuspangaliyeva B, Suleimenova B, Shah D, Sarbassov Y. Thermogravimetric study of refuse derived fuel produced from municipal solid waste of Kazakhstan. Appl Sci 2021;11:1–13. https://doi.org/10.3390/app11031219.

[26] Cozzani V, Nicolella C, Petarca L, Rovatti M, Tognotti L. A Fundamental Study on Conventional Pyrolysis of a Refuse-Derived Fuel. Ind Eng Chem Res 1995;34:2006–20. https://doi.org/10.1021/ie00045a010.

GLOBAL WARMING IMPACT ASSESSMENT DUE TO CARBON CAPTURE AND STORAGE TECHNOLOGIES IN ELECTRICITY GENERATING POWER PLANTS

Okan Kon[1] and İsmail Caner[2]

1. Departmant of Machine Engineering, Faculty of Engineering, Balikesir University, Balikesir; email: okan@balikesir.edu.tr
2. Departmant of Machine Engineering, Faculty of Engineering, Balikesir University, Balikesir; email: ismail@balikesir.edu.tr

Abstract

Power plants produce electricity by using high amounts of fossil fuels such as coal and natural gas. Using these fossil fuels releases a very high amount of emissions into the atmosphere. In order to reduce these emissions, carbon capture and storage (CCS) applications have been developed as new technologies. Thus, by capturing 96% of the CO_2 formed as a result of the burning of fuels in power plants, the global warming potentials (GWP) emitted by conventional electricity generation can be reduced by up to 80%. In the study, applications of carbon capture and storage (CCS) options to reduce emissions during electricity generation; CO_2 emissions, which are pre-combustion, post-combustion, oxy-fuel coupled global warming potentials (GWP), were investigated. ReCiPe midpoint method has been taken into account for CO_2 emission. The reduction in global warming potential is calculated with applications of carbon capture and storage (CCS) options. In the study, it is accepted that hard and brown coal is used as fuel in power plants that produce electricity. As a conclusion, the CO_2 emission as GWP in conventional electricity generation power plants is calculated as 152818306 kg in the power plants burning brown coal with the highest and the lowest as 21909420 kg in the power plants using Oxy-fuel CCS and burning hard coal.

Keywords: Carbon capture and storage, power plants, electricity generation, ReCiPe, coals

1 INTRODUCTION

With the rapid progress in the global population, there has been a significant increase in the consumption of electrical energy. Thus, high levels of pollutant emissions and environmental impacts show the necessity of reducing environmental impact and establishing appropriate pollution control systems for more sustainable electricity production. The Paris Climate Agreement recommends that only the increase in global average surface temperature should be limited to 1.5 °C by 2050. This shows that global greenhouse gas emissions should be reduced as soon as possible [1,2].

Among the techniques for eliminating global carbon emissions, carbon capture and storage CCS technologies are one of the most common. Carbon capture (CC), followed by storage or use (CCS) is one of the solutions explored to achieve the goal of combating climate change. In fact, the carbon capture and carbon storage CCS technology used in capturing the carbon dioxide emitted by fossil fuel-based thermal power plants is important. Carbon capture and storage (CCS) technologies enable the underground storage and disposal of global carbon dioxide emissions released in fossil fuel-burning thermal power plants, plants and factories [2,3].

With the increasing demand for electrical energy, electric energy with low carbon emissions is very important for electricity generation with CCS, considering the term of fifty years, a hundred years or more [4,5].

The International Energy Agency (IEA) predicts that global carbon dioxide emissions can be reduced by 20% in the most economical way through CCS technologies. In order to reach this level, the IEA advocates that at least 100 carbon capture facilities should be installed by 2020 and at least 3000 by 2050. However, currently only 10 carbon dioxide treatment plants are in operation in the world, and 28 carbon capture and storage facilities, mostly in North America, are under construction or planning [3].

Recently, technological advances designed to capture direct emissions of CO_2 produced from

power plants have shown reductions in CO2 emissions. These technological advances include carbon capture and storage (CCS) technologies, which can be categorized as pre-combustion, post-combustion and oxy-fuel CO_2 capture using chemical or physical solvents. The processes of CCS technologies often involve the separation and capture of CO_2 and storage on land or offshore to prevent release of CO_2 into the atmosphere [1].

The two methods used by a lifecycle environmental impact approach, such as ReCiPe, are midpoint and endpoint. The midpoint approach adopts categories that establish a certain level of cause and effect to calculate harms on the human health system. The endpoint approach takes further scrutiny by changing the midpoint impact categories to more specific damage categories on humans and ecosystems [6].

The aim of the study is to investigate applications of carbon capture and storage (CCS), one of the methods of reducing CO_2 emissions, which are global warming potentials (GWP) emitted into the atmosphere from power plants that produce electricity by burning coal. For this, firstly, the CO_2 emissions generated during the electricity production by burning hard and brown coal were determined by conventional electricity generation. Then there are applications of carbon capture and storage (CCS) options to reduce CO_2 emissions; pre-combustion, post-combustion, oxy-fuel have been researched. With these applications techniques, the amount of CO_2 emission reduction was calculated using the ReCiPe midpoint method. Figure 1 shows Power Plant with Pre-combustion Carbon Capture Systems. Figure 2 shows Power Plant with Post-combustion Carbon Capture Systems. Figure 3 shows Power Plant with Oxyfuel Carbon Capture Systems.

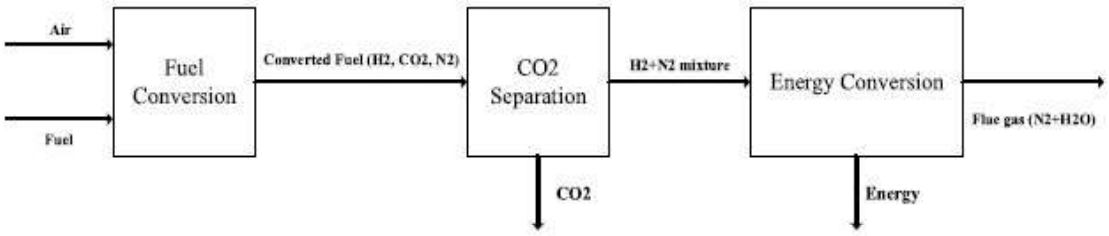


Figure 1. Power Plant with Pre-combustion Carbon Capture Systems [2,7]

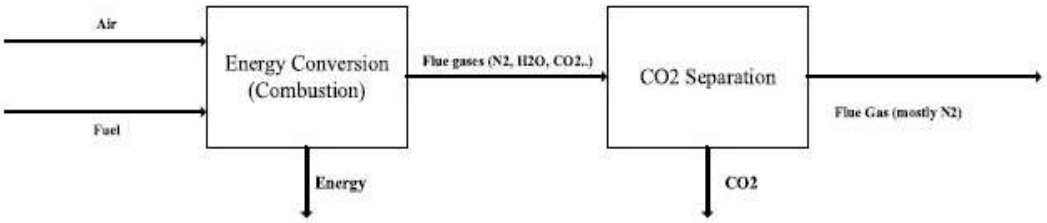


Figure 2. Power Plant with Post-combustion Carbon Capture Systems [2,7]

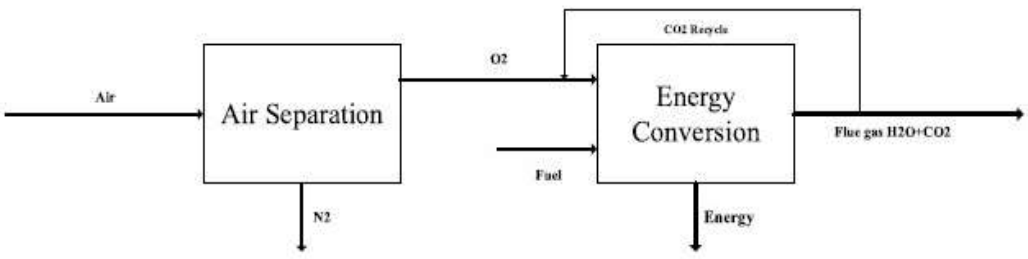


Figure 3. Power Plant with Oxyfuel Carbon Capture Systems [2,7]

The technologies used in the three main carbon capture systems associated with carbon capture and storage (CCS) differ due to the quality of CO_2 gas, noble gases, oxygen, sulfur and nitrogen gases, and other impure elements or compounds such as mercury. In addition, the CO_2 gas quality, gas cleaning cost, power plant and materials, transportation systems, as well as their storage are different [8-11].

2 MATERIAL AND METHOD

Turkey's electricity consumption is 329633995 MWh. The number of coal and lignite fired thermal power plants is 53. The registered installed power is 20215 MWe, the annual electricity production is 104202017 MWh, the ratio of the total installed power is 20.31%, the ratio of production to consumption is 31.61%. As of 2021, the electricity produced from power plants working with imported coal is 54888841 MWh and 49313176 MWh working with hard coal, lignite and asphaltite from domestic sources [12]. In Table 1, the distribution of electricity consumption in our country by sectors for the year 2021 is given. Table 2 shows the consumption amounts of electricity supplied from coal-fired thermal power plants for all cities of our country. In Table 3, global warming potential (GWP) values are given as CO_2 emissions according to the ReCiPe (midpoint) method for power plants that burn hard and borwn coal and use conventional systems. Table 4 shows the reduction in Global Warming Potential (GWP), CO_2 capture rate and Electricity efficiency in power plants that burn hard and borwn coal and use three different Carbon Capture and Storage (CCS) Options used in the calculations.

Table 1. Distribution of electricity consumption in 2021 by sectors [12]

Sector	Electricity Consumption (MWh)	Ratio (%)
Industry	111572994	33.9
Lost- Leakage	76600098	23.2
Business	61360984	18.6
Residences	61337915	18.6
Agricultural irrigation	13359193	4.1
Lighting	5402816	1.6
Total	329634000	100

Table 2. Consumption amounts of electricity supplied from coal-fired thermal power plants for all cities of Turkey [12]

City	Consumption (MWh)	City	Consumption (MWh)
İstanbul	19061614	Bolu	545876
İzmir	7565155	Kastamonu	528396
Ankara	6766160	Düzce	520147
Bursa	5896286	Van	507438
Kocaeli	5241807	Edirne	490187
Gaziantep	4058274	Isparta	485244
Antalya	3995253	Karaman	458193
Adana	3626778	Burdur	445073
Konya	3580983	Batman	443453
Tekirdağ	3452056	Erzurum	429548
Şanlıurfa	2941280	Çorum	418638
Hatay	2509059	Tokat	416966
Mersin	2440273	Bartın	408543
Manisa	2187313	Yalova	379515
Osmaniye	2058331	Nevşehir	374508
Sakarya	1932267	Yozgat	364735
Kahramanmaraş	1929190	Rize	360143
Kayseri	1926645	Giresun	339755
Balıkesir	1760538	Karabük	316962
Denizli	1749388	Erzincan	298705
Muğla	1693672	Şırnak	296253
Samsun	1629049	Amasya	294997
Eskişehir	1549907	Kırıkkale	288685
Diyarbakır	1450720	Çankırı	286346
Çanakkale	1407968	Kilis	275477
Aydın	1393286	Ağrı	225980
Kırklareli	1221579	Siirt	222246
Mardin	1102093	Kırşehir	204430
Bilecik	1085110	Artvin	203576
Afyonkarahisar	958763	Muş	196516
Uşak	943079	Gümüşhane	188176
Kütahya	869886	Bitlis	184060
Malatya	837310	Sinop	181502
Sivas	712670	Kars	150395
Trabzon	711680	Bingöl	149519
Ordu	640629	Hakkâri	132960
Elazığ	627949	Iğdır	101632
Niğde	624639	Tunceli	62380
Adıyaman	602291	Ardahan	61443
Zonguldak	573007	Bayburt	51051
Aksaray	570192		

Table 3. Global warming potential (GWP) values as CO_2 emission according to ReCiPe (midpoint) method in power plants burning hard and brown coal and using conventional system [1]

Impact	Hard Coal	Brown Coal
GWP (Global Warming Potential) (kg/MWh)	900	1300

Table 4. Reduction in Global Warming Potential (GWP), CO_2 capture rate and Electricity efficiency in power plants burning hard and brown coal and using three different Carbon Capture and Storage (CCS) alternative [1]

Carbon Capture and Storage (CCS) Options	GWP Reductions		Percentage reduction compared to conventional electricity generation options (%)	CO_2 capture rate (%)	Electricity efficiency (%)
	Hard Coal (kg/MWh)	Brown Coal (kg/MWh)			
Precombustion	189	273	79.0	85–90	32.5–48.1
Postcombustion	266.4	384.8	70.4	90–95	27.2–50.1
Oxy-fuel	185.4	267.8	79.4	90–96	33.4–49

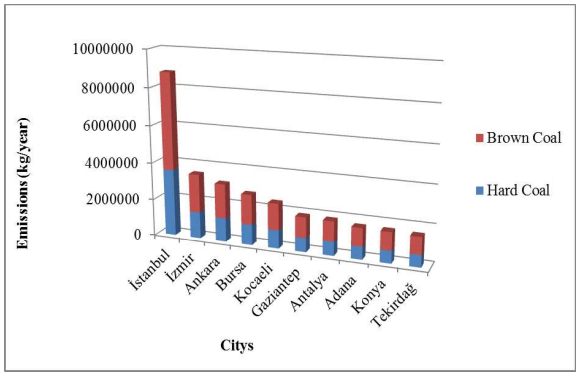
3 RESULTS AND DISCUSSIONS

CO_2 emission as GWP (Global Warming Potential) in conventional electricity generation power plants burning hard coal is calculated as 106310462 kg and 152818306 kg for those burning Brown coal. GWP emissions released to the atmosphere during electricity generation in power plants using pre-combustion CCS and burning hard coal were found to be 22261632 kg, and 32000028 kg in those burning brown coal. 31378301 kg was determined in power plants using post-combustion CCS and burning hard coal, and 45324212 kg in those burning Brown coal. It is 21909420 kg in power plants using oxy-fuel CCS and burning hard coal, and 31646940 kg in those burning brown coal.

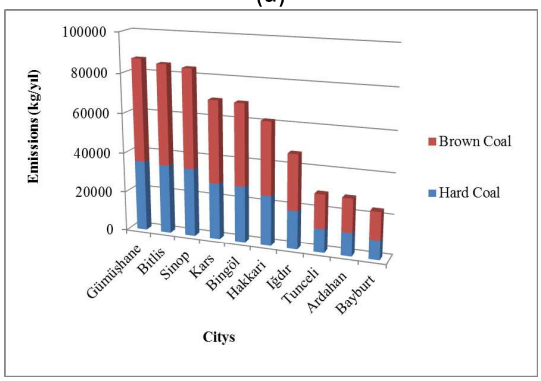
The ten cities with the highest electricity consumption in our country are; Istanbul, Izmir, Ankara, Bursa, Kocaeli, Gaziantep, Antalya, Adana, Konya, Tekirdag. The ten cities with the lowest electricity consumption are Gümüşhane, Bitlis, Sinop, Kars, Bingöl, Hakkari, Iğdır, Tunceli, Ardahan, Bayburt [12]. Considering the ten cities with the highest electricity consumption in Turkey, the GWP emission in conventional electricity generation power plants burning hard coal is calculated as 56919928 kg and 82217674 kg for those burning brown coal. GWP emissions released to the atmosphere during electricity production in power plants using Pre-combustion CCS and burning hard coal were found to be 11953185 kg, and 17265712 kg in those burning Brown coal. 16848299 kg was determined in power plants using Post-combustion CCS and burning hard coal, and 24336432 kg in those burning Brown coal. It was seen as 11725505 kg in power plants using oxy-fuel CCS and burning hard coal, and 16936841 kg in those burning brown coal.

Considering the ten cities with the lowest electricity consumption in Turkey, the GWP emission in conventional electricity generation power plants burning hard coal is calculated as 1136809 kg and 1642058 kg for those burning brown coal. The GWP emissions released to the atmosphere during electricity generation in power plants using pre-combustion CCS and burning hard coal were 238730 kg, and 344832 kg were found in those burning brown coal. It was determined that 336496 kg was found in power plants using post-combustion CCS and burning hard coal, and 486049 kg in those burning Brown coal. It is calculated as 234183 kg for power plants using oxy-fuel CCS and burning hard coal, and 338264 kg for those burning brown coal.

Figure 4 shows the cities with the highest GWP values a) cities with the highest b) cities with the lowest values for power plants burning Hard coal and Brown coal using Pre-combustion CCS. In Figure 5, the cities with the highest GWP emissions in Hard coal and Brown coal fired power plants using Post-combustion CCS are given. Figure 6 shows the cities with the highest GWP emissions in Hard coal and Brown coal fired power plants using Oxy-fuel CCS a) cities with the highest b) cities with the lowest.

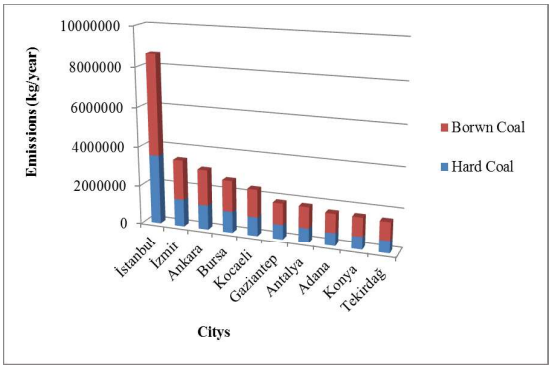


(a)

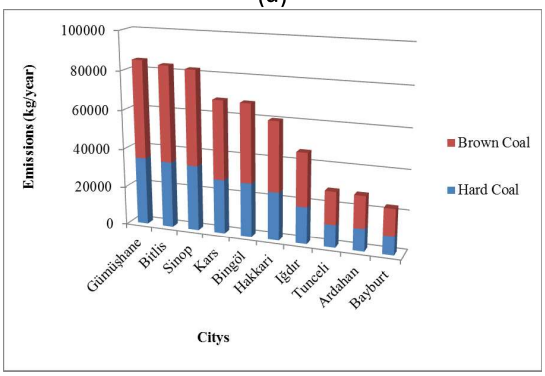


(b)

Figure 4. GWP emissions in hard coal and brown coal fired power plants using Pre Combustion CCS a) Cities with the highest b) Cities with the lowest

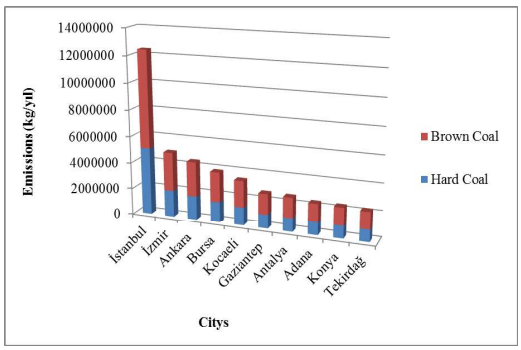


(a)

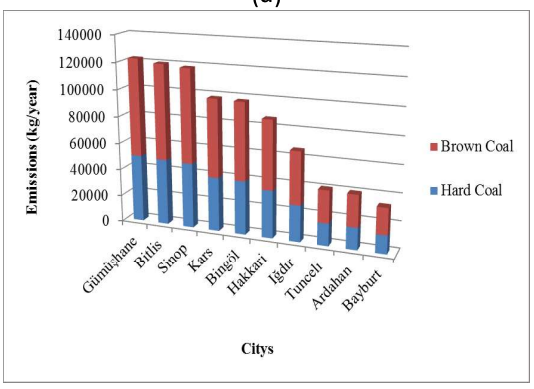


(b)

Figure 6. GWP emissions in Hard coal and Brown coal fired power plants using Oxy-Fuel CCS a) Cities with the highest b) Cities with the lowest



(a)



(b)

Figure 5. GWP emissions in Hard coal and Brown coal fired power plants using Post Combustion CCS a) Cities with the highest b) Cities with the lowest

4 CONCLUSIONS

In conventional electricity generation power plants, the CO_2 emission as GWP (Global Warming Potential) is calculated as 152818306 kg for the plants burning Brown coal with the highest and the lowest is calculated as 21909420 kg for the power plants using Oxy-fuel CCS and burning hard coal. Considering the ten cities with the highest electricity consumption in Turkey, the GWP emission in conventional electricity generation power plants burning hard coal is calculated as 82217674 kg for plants burning brown coal. It has been calculated as 11725505 kg in power plants using oxy-fuel CCS and burning hard coal. When the ten cities with the lowest electricity consumption are taken into account, the GWP emission in conventional electricity generation power plants burning hard coal is calculated as 1642058 kg for the plants burning Brown coal. It is calculated as 234183 kg in power plants using oxy-fuel CCS and burning hard coal.

Considering the ten cities with the highest electricity consumption in Turkey, it has a rate of 19.19% with 63244365 MWh in electricity consumption with coal and lignite fired thermal power plants. In the last ten cities, it has 3523351 MWh and 0.38%. For the city of Istanbul, it has a rate of 5.78% with 3523351 MWh.

Considering all the calculations made, the highest GWP emission was seen in power plants using Oxy-fuel CCS with 79.4% compared to conventional electricity generation power plants. The lowest was determined with 70.4% in power plants using Post-combustion CCS.

In electricity generating power plants, the use of hard coal produces 69.23% less GWP emissions than the use of brown coal. Therefore, it would be more appropriate to use hard coal in power plants that generate electricity.

In future studies, SO_2, PO_4, NO_x, PM, CFC, HCFC, etc. impacts from power plants that produce electricity by burning coal, natural gas, biomass and using CCS will be investigated.

REFERENCES

[1] Cho H. H., Strezov V., A Comparative Review on the Environmental Impacts of Combustion-Based Electricity Generation Technologies, *Energy Fuels* 2020, 34, 10486−10502.

[2] Olabi A.G., Obaideen K., Elsaid K., Wilberforce T., Sayed E. T., Maghrabie H. M., Abdelkareem M. A., Assessment of the pre-combustion carbon capture contribution into sustainable development goals SDGs using novel indicators, *Renewable and Sustainable Energy Reviews* 153, 2022, 111710.

[3] TMMOB Fizik Mühendisleri Odası, Faydalı Bilgiler https://www.fmo.org.tr/faydali-bilgiler/ (Date of access: 02.08.2022)

[4] Kon O., Caner İ., Investigation of electricity produced in power plants and used for cooling buildings with a life cycle approach of carbon capture and storage technology, *Journal of New Results in Science* 11, 2022, 1, 77-90.

[5] Rubin E. S., Davison J. E., Herzog H. J., The cost of CO_2 capture and storage, *International Journal of Greenhouse Gas Control* 40, 2015, 378–400.

[6] Alyaseri, I. and Zhou, J., Towards better environmental performance of waste water sludge treatment using endpoint approach in LCA methodology. *Heliyon* 3, 2017, 3, 00268.

[7] Singh B., Strømman A. H., Hertwich E. G., Comparative life cycle environmental assessment of CCS Technologies, *International Journal of Greenhouse Gas Control* 5, 2011, 911–921.

[8] Wall T., Stanger R., Liu Y., Gas cleaning challenges for coal-fired oxy-fuel technology with carbon capture and storage, Fuel, 108, 2013, 85-90.

[9] Pardemann, R. Meyer B., Pre-Combustion Carbon Capture, Mitigation Technologies, *Carbon Capture*, 2015.

[10] Kheirinik, M.; Ahmed, S.; Rahmanian, N. Comparative Techno-Economic Analysis of Carbon Capture Processes: Pre-Combustion, Post-Combustion, and Oxy-Fuel Combustion Operations. *Sustainability* 2021, 13, 13567.

[11] Theo W. L., Lim J. S., Hashim H., Mustaffa A. A., Ho W. S., Review of pre-combustion capture and ionic liquid in carbon capture and storage, *Applied Energy*, 183, 2016,1633-1663.

[12] Enerji Atlası https://www.enerjiatlasi.com (Date of access: 01.08.2022)

Elektrikli Araçların Lityum İyon Bataryalarında Termal Kaçak Mekanizması ve Isının Kontrol Altında Tutulması

Umit Senyurek [1], Hakan Serhad Soyhan [2], Cenk Celik [3]

1. Department of Mechanical Engineering, Kocaeli University, Kocaeli, Turkey, umitsenyurek@yahoo.com
2. Department of Mechanical Engineering, Sakarya University, Sakarya, Turkey, hsoyhan@sakarya.edu.tr
3. Department of Mechanical Engineering, Kocaeli University, Kocaeli, Turkey, cenkcelik@kocaeli.edu.tr

ÖZ

Elektrikli araçlara olan talebin ani artışı, beraberinde bu araçların ne kadar güvenli olduğu sorusunu da getirmiştir. Bu araçlarda karşılaşılan en yaygın acil durumlardan biri olarak yangın konusu öne çıkmaktadır. Elektrikli araçlarda en yaygın kullanılan batarya türlerinden olan lityum iyon bataryaların yangın mekanizmasını anlamamız, bu tür bataryaların kullanıldığı araçların daha güvenli nasıl üretilebileceğini ve kullanılabileceğini anlamamız için önem arz etmektedir. Bu çalışmada, elektrikli araçlardan lityum iyon türü enerji depolama birimi kullanılan araçların yangın sebebi olan termal kaçak oluşum mekanizması sebepleri ile birlikte irdelenecektir.

Anahtar Kelimeler: Elektrikli araç, lityum-iyon pil, termal kaçak, mekanik hasar, termal etki, aşırı şarj, kısa devre.

Thermal Runaway Mechanism at Lithium Ion Batteries of Electric Vehicles and Keeping the Heat Under Control.

ABSTRACT

The sudden increase in the demand for electric vehicles has brought with it the question of how safe these vehicles are. Fire is one of the most common emergencies in these vehicles. Understanding the firing mechanism of lithium-ion batteries, one of the most widely used battery types in electric vehicles, is essential to understanding how vehicles can be produced and used more safely. In this study, the causes of the thermal runaway mechanism, which is the cause of fire in vehicles using lithium-ion type energy storage units, will be studied together with the reasons.

Keywords: Electric vehicle, lithium-ion battery, thermal runaway, mechanical abuse, thermal affect, overcharge, short circuit.

1. INTRODUCTION

By the Paris Agreement in 2015, "Paris declaration on Electro-Mobility and Climate Change and Call to Action" [1] announced that; a global challenge is needed to put a limit to global warming, compared to the level before the industrialization period [13] as a long term goal. One hundred ninety-three parties (194 parties, including European Union) agreed to this agreement [19]. It is a big challenge to a significant technological change to adopt this agreement to reduce greenhouse gas emissions [13].

This challenge is only achievable if electric vehicles replace with internal combustion vehicles at a 35 % rate of the total number of vehicles sold by 2030 [9]. Because of this reason, after 2015, all kind of electric vehicle sales in increase trend worldwide. The increase in production volume and sales achievements is a proof that the electric vehicle age is already started [2]. Storing the energy for electric vehicles is one of the biggest concern. Because of that electric vehicle battery is the most critical part [2]. Today, various battery technologies with different rated voltages and energy densities are being developed. The comparison of the batteries is shown in Figure 1.

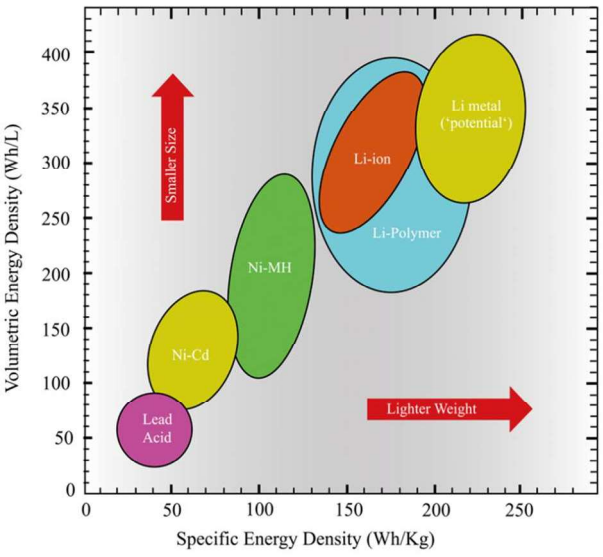


Figure 1. Battery types in different specific & volumetric energy density [20].

John B. Goodenough, M. Stanley Whittingham and Akira Yoshino indicated in their research that they were awarded the 2019 Nobel Prize [21]; Lithium is the third-smallest atom after hydrogen and helium, located in group 1A in the periodic table, which includes alkali metals. It is shown in Figure 2,

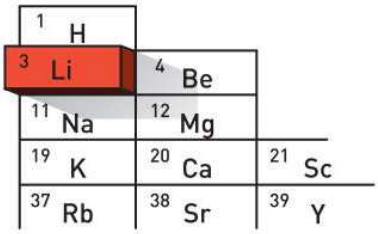


Figure 2. Periodical table, 1A metal category and place of lithium [21].

The characteristic of group 1A elements is their tendency to release their electrons and be positively charged, as shown in Figure 3 [21].

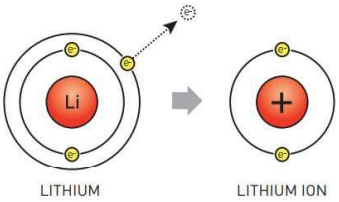


Figure 3. Lithium and lithium-ion [21].

Apart from these properties, lithium is the most suitable element for batteries. It has the most significant electrochemical potential among all metal elements and a higher energy density per weight.

As shown in Figure 1, the high energy density and power per mass of battery unit, high current (voltage), long cycle life, and does not have memory effect Lithium-ion (Li-Ion) type batteries are primarily preferred in electric vehicles [2]. Studies have recently developed to reduce their weights and smaller sizes at competitive prices [9]. The biggest market of Li-Ion battery is electric vehicles.

Their advantages and the reason they hold the most significant market are; moderate energy consumption (14.7 kWh/100 km), continuous cost improvement to decrease their prices, long cycle life, less weight, and higher energy storage features make Li-Ion batteries a reasonable choice in this field. But on the other hand, they bring some disadvantages, with high operating temperatures, which may adversely affect their energetic performances and lifecycle and also bring safety risks regarding fire and vehicle explosion [9].

The main risk is fire and explosion because of a stage when chemical reactions increase heat in a short-term. This situation is called a Thermal Runaway. The reason for a thermal runaway is

mainly decay of active materials, electrolye, it is resulting with a chain reaction and fire, and the explosion [3]. Because of the thermal instability of the battery, the extreme conditions triggering the risk of fire and explosion. The preliminary study to increase battery capacity and energy density may also increase this risk [3].

The energy density of Li-Io batteries is between 110-160 Wh/kg. In recent years many researchers have been working to improve the chemical structure to increase their energy density within their safety limits [5].

1.1. Li-Io Battery Types

There are mainly six types of batteries; the active materials define the kinds of Li-Io batteries. They may also write with the chemical symbols of active material; the name can be shortened by the first letter of the chemical characters [7].

(1) Lithium Iron Phosphate (LFP): Cathode material is phosphate, and anode material is graphite-carbon.This type has a high life cycle, and their thermal stability nad electrochemical performances are valuable.

They are proper where the high power required applications, durability and long life cycle, and safety concerns are the other benefits.

Their lifecycle is more than 2000 cycles, and discharging rate effect is low on their lifetime.

Because of the low resistance of the materials, they are stable and safe batteries. The thermal runaway start point is around 270 ^{0}C, and it is makes LFP batteries the most safest Li-Io battery type, as well when they are 100 % charge level.

The specific energy is smaller, in low temperatures may cause lithium plating and short circuits, these are the disadvantages [7].

(2) Lithium Cobalt Oxide (LCO): Because of the safety issues and high cost of material (cobalt), this type batteries will be replaced with other types in the future. They are widely using small portable electronics such as cameras, phones, computers. The most important advantage of these batteries is their high specific energy, which delivers this power over a long period but with a low load, which limits their usage in many applications. On the other hand, a shorter lifetime (500-1000 cycles), and small specific energy decreases its popularity. The thermal stability, which creates safety concerns, is another disadvantage of these batteries. [7].

(3) Lithium Manganese Oxide (LMO): The cathode material is lithium manganese oxide. Their internal structure improves the ion flow and reduces the internal resistance. That enhances the thermal stability and safety of the battery. LMO batteries widely using in portable power tools, medical equipment, andin electric vehicles. Advantages of LMO batteries; their charging speed is fast and they have a high specific power. Compared with LCO batteries, they can deliver more current, and the thermal stability is better. This means that their operation range can be higher than LCO batteries, making these batteries the proper type for high load applications. The disadvantage is its short lifetime. It is about 300-700 cycles, less than other Li-Io types [7].

(4) Lithium Nickel Manganese Cobalt Oxide (NMC): Mainly, three elements (nickel, mangenese, cobalt) are used as cathode material. The specific energy of nickel is high, but it is not stable, and manganese is stable, but its specific energy is low. It is a combination problem that finds the best mixture of the nickel-manganese to create stable and high specific energy requirements.
These batteries are generally used in power tools, some electric vehicles, electric bikes, and electric scooters. The advantages of these battery types; are high energy density, long lifecycle, low cost, and high thermal stability compared with LCO batteries. The major disadvantage is lower voltage than NMC batteries [7].

(5) Lithium Nickel Cobalt Aluminum Oxide (NCA): The specific energy and specific power of these batteries is high, because of that they have a long life cycle, these features makes them the most popular battery type for electric vehicles. Tesla company prefers NCA for its electric cars.

The disadvantage of these batteries is that they are; relatively expensive and are not safe compared to other batteries [7].

(6) Lithium Titanate (LTO): Instead of graphite, lithium titanate is used as the anode material, and LMO or NMC material is used as the cathode material. This makes these batteries safer. This battery has a longer lifetime and short charge time requirement compared with other Li-Io batteries.

Previous all these batteries were named with their cathode material. Still, the lithium titanate (LTO) battery type replaced the graphite in the anode and used in cathod one of these material; lithium

manganese oxide or lithium nickel manganese cobalt oxide.This type of battery is highly safe with a long lifetime, and the time that needs charge is shorter than other types.

The charging stations of electric vehicles, clean energy power storages, some applications in aerospace, and military applications are the most common usage areas.

Their advantages are the reason for using them widely; fast charge ability, wider operation temperatures, has a long lifetime. Because of their thermal stability, they are one of the safest batteries; however, they have some disadvantages, the most of the important is; low energy density, it is the reason that the battery store less energy than others and they are relatively expensive [7].

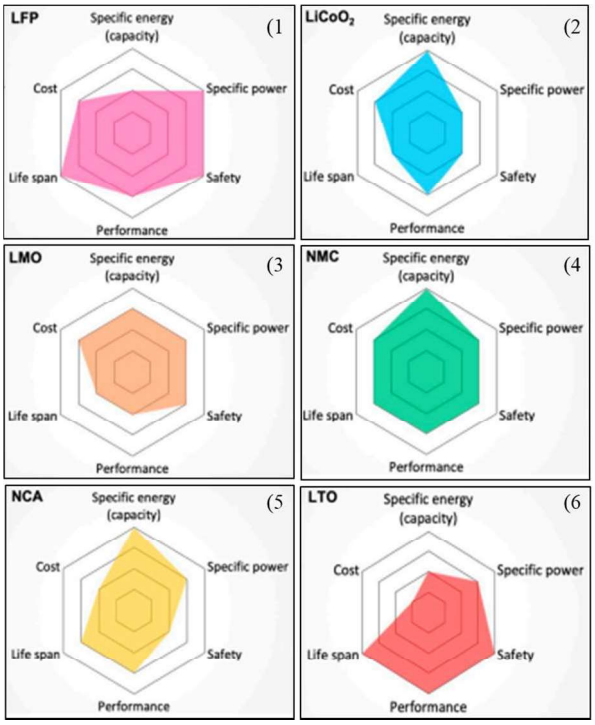


Figure 4. Li-Io Battery types comparison [18]

1.2. Li-Io Battery Working Principle

The negative electrode (anode) is mainly a carbon material with a microporous surface. The lithium compound is the positive electrode (cathode).

During discharge (usage of the battery and electric curent creation); lithium ions moves from anode (graphite) to cathode (lithium compound), this electron flows creates electric. At the time charge operation the opposite movement is obtain by the movement of lithium ions. The electron movement obtain via electrolyte. The working principle of a lithium ion battery is shown in Figure 5 [3].

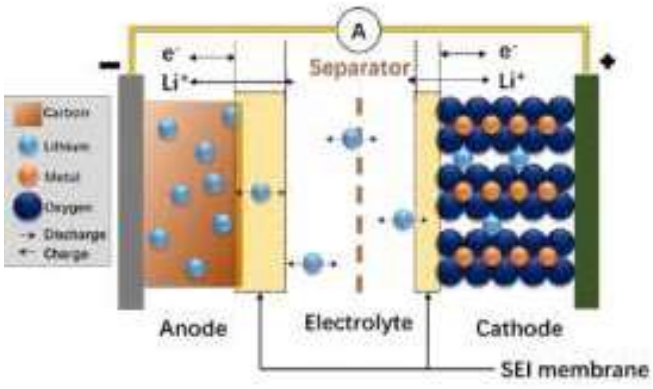


Figure 5. Li-Io battery working principle diagram [3]

1.3. Li-Io Battery Components and Structure

(A) Anode: The main material of anode is generally carbon-based; graphite and carbon are the most used materials.

The anode materials are under study to improve not only the battery's capacity but also its thermal stability. Lithium dendrites on the anode surface during the thermal runaway mechanism will create a considerable amount of heat, which will cause growing these dendrites on the anode and create unstable SEI (solid electrolyte layer) film [1].

(B) Cathode: The active materials mainly contain lithium compounds with high redox potential. Due to the increased battery capacity and high output voltage, the compound is the most important element [1].

The energy density of Li-Io batteries increased from 150Wh/kg to 300Wh/kg with the development of cathode materials in time [10].

(C) Electrolyte: Flame retardant (dimethyl phosphate, trimethyl phosphate) and anti-overcharging (diphenylamine, polytriphenylamine) additives are included in an electrolyte, phosphorous addition may decrease the electrochemical feature of Li-Io batteries, but the leakage risk still available when the thermal runaway happens [1].

(D) Separator: It is among cathode and anode to prevent contact of two poles, and let the ion transfer during charge and discharge operations. Because of the high level of ion conductivity ability, the most popular material is polyolefin as a separator material. Still, its low thermal stability is a disadvantage of this material and a significant safety problem. Another alternative material is ceramic, its thermal stability is good, but on the other hand, pure ceramic is not a good solution

because of the mechanical strength and cost effect [1].

(E) Binder: There are three criteria for selecting the appropriate binder material. Firstly, the volume change of anode material is essential; because of that, its mechanical properties should cover this volume change. Secondly, it should prevent the active substances from dissolving from the electrode materials to prevent severe capacity weakening and corrosion. Third, for a good life cycle, it should has the capacity to balance the intersection among electrode-electrolyte [1].

(F) Collector: Its primary role is being the electron path between cathode and anode; the collector must closely contact them.

Cooper foils, and aluminum foils are widely used as collector materials. Because of the low electron loss potential (oxidation) of cooper, they form of the anode side, and because of the high electron loss potential of aluminum they form of cathode side [1].

The main electrochemical reactions are given by the following equations [8].

- The cathode reaction:

$$LiFePO_4 \underset{\text{discharge}}{\overset{\text{charge}}{\rightleftharpoons}} Li_{1-x}FePO_4 + xLi^+ + xe^-$$

- The anode reaction:

$$xLi^+ + xe^- + 6C \underset{\text{discharge}}{\overset{\text{charge}}{\rightleftharpoons}} Li_xC_6$$

- Total reaction:

$$LiFePO_4 + 6C \underset{\text{discharge}}{\overset{\text{charge}}{\rightleftharpoons}} Li_{1-x}FePO_4 + Li_xC_6$$

According to shapes, Li-Io batteries can be categorized into four types;

(1) Cylindrical shape cells, The main advantages are; manufacturing simplicity and good mechanical stability. The cylinder form can resist a high internal pressure without deformation. Some of them have safety systems (the PTC switch and CID device)

PTC (Poistive Thermal Coefficient); while the battery reaches to maximum current, the conductivity of polymer, holds the current flow. It works like a short circuit relay.

CID (Charge Interrupt Device); when the internal pressure rise, it physically disconnects the cell.

The main usage areas of the cylindrical cells are power tools, medical instruments, laptops, and e-bikes. Tesla company uses this type for their electric vehicles. In the future battery, makers can face a material shortage because of the increasing electric vehicle demand. According to their volumes, cylindrical Li-Io batteries can be named 18650, 20700, 21700, and 22700.

When the cell volume and capacity are compared, 18650 battery cell has 16 ml, its capacity is 3000mAh, and 21700 battery cell has 24 ml with 6000mAh. It is shown that while the volume increases by 50 %, the cell capacity rises 100 %. [15] Because of the manufacturing simplicity and optimal capacity Tesla, Panasonic and Samsung companies produce 21700 type cells [16]. Illustrated in Figure 6,

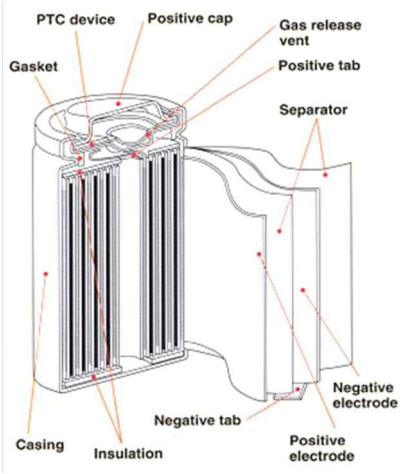


Figure 6. Cylindrical Type Lithium-ion Battery [6]

(2) Prismatic shape cells; Optimized size by using the layers stands out. They are mostly using in cell phones, portable computers, and their energy capacity change among 800mAh - 4,000mAh. They do not have a unique format; each manufacturer designs their own. They also have larger structures and their energy capacity is among 20–50Ah, and they are mostly using at electric vehicles [15]. BMW, Mercedes-Benz, and Volkswagen mainly use this type. They are more resistant to external impact but have relatively low energy density [16]. The battery type is illustrated in Figure 7.

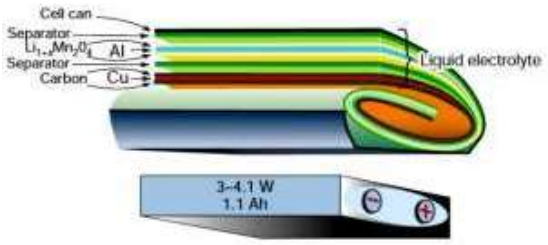


Figure 7, Prismatic Type Lithium-ion Battery [6]

(3) Button shape cells or coin cells; Their thin shape like a coin is mostly proper for portable hand devices. The crashing speed is vital for this battery type; if it is too fast cell can swell. They are non-rechargeable and also can be used in medical implants, watches, and vehicles' keys [15], they are illustrated in Figure 8.

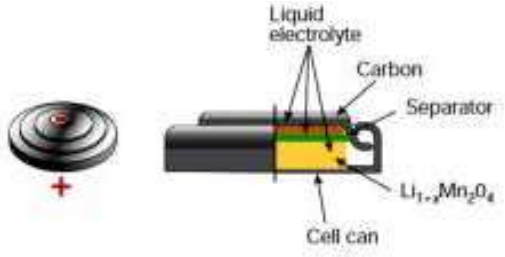


Figure 8, Button Type Lithium-ion Battery [6]

(4) Pouch shape cells are thin, have a high energy density, and are not rigid [16]. They provide flexibility and light battery design solutions. They have high load currents in light loading required conditions. Their packs are generally lithium-polymer format. They are primarily used in drones and other hobby equipment. Extreme swelling could be a safety concern [15]. They achieve 90-95 % packaging efficiency; GM and Hyundai companies use pouch batteries in their vehicle [16], illustrated in Figure 9.

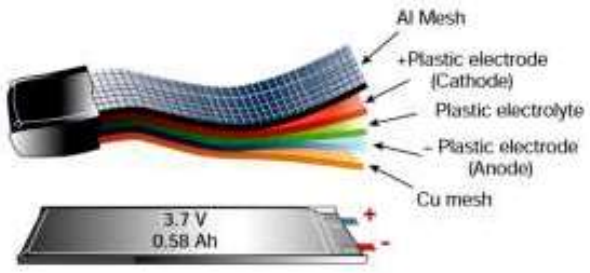


Figure 9, Ponch Type Lithium-ion Battery [6]

Different cell types are gathering together and generates modules. The modules are gathering together to generate the battery packs as it is illustrated in Figure 10.

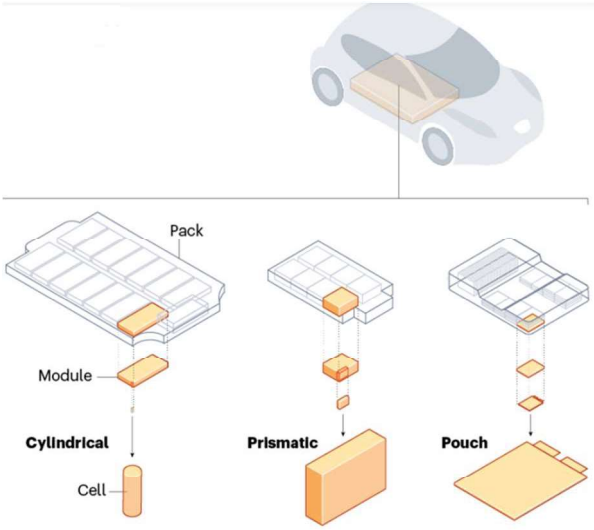


Figure 10, Cell to Battery Pack [6]

The connections from cell to battery packs and systems could be parallel or serial, as it is shown in Figure 11.

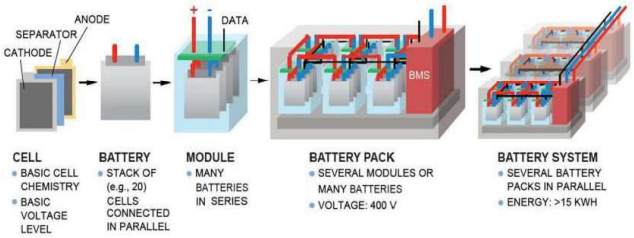


Figure 11, Packaging of typical battery systems [6]

2. WHAT IS THERMAL RUNAWAY

Thermal runaway is a condition in when the battery internal temperature uncontrollable raise by chemical reactions of battery fundamentals. These reactions are; corruption and the transformation of solid electron-insulating layer (SEI), reduction–oxidation reactions among; electrolyte - electrode, and reactions among; electrode - binder [1].

At the end of the thermal runaway, battery temperatures can reach 1000 ^{0}C and a huge amount of burnable and toxic gases can be released [4].

The common idea of the logic for a thermal runaway is; because of increasing the temperature inside the battery, the separator (polyolefin) melts

and then it will reason to an short circuit inside battery [1].

Uncontrolled internal heat increase can be because of chain reactions which are the basis of thermal runaway [1].

By the existence of oxygen, mainly electrolyte and separator include to the fire. The total weight of electrolyte and separator is low, but about 80% of the heat release during fire, because of burning of these [6].

2.1. Thermal Runaway Mechanism

The safety characteristics of a Li-ion battery depend on;

(a) The shape of cell type (geometry, materials),

(b) The previous conditions before any misuse (state of charge, aging effects),

(c) The type of misuse (over-temperature, over-charge, heating),

(d) Additional measures (built-in safety devices, cooling, confinement) [4].

The thermal runaway can be triggered by two reasons: it could by an ordinary failure, or a human related misuse condition under daily usage. The first possibility is fewer and it could be ignored. The second possibility can be categorized into three violence (abuse) situation [2]:

(1) mechanical,

(2) thermal,

(3) electrical,

If battery forces by external stress, and the surface deforms or penetrates, this can be cause of mechanical abuse.

Because of the characteristics of the electro-chemical reactions, batteries produce heat; additionally, an external heat source can exaggerate the heat accumulation and cause thermal abuse.

If the batteries are overcharged, it can cause a short circuit, and this causes electrical abuse.

These abuse conditions starts the chain reactions and internal heat can be increased sudenly.This can be lead to thermal runaway and results to fire, explosion, and toxic gas release. Because of these reasons, monitoring the batteries against thermal runaway is essential [1]. The stages of thermal runaway by the temperatures given in Table 1.

Table I Chain reaction in thermal runaway [1]

Temperature	Reaction
<90°C	▪Realizing one of the misuse condition,
90°C–120°C	▪The lithium salt $LiPF_6$ and SEI film to dissolve, ▪Dissolve of these cause heat increase to 120°C,
120°C–150°C	▪Extremely reactive LiC_6 starts an exothermal reaction, ▪Dissolving of electrolytes creates PF_5, ▪Activate the dissolving of organic solvents,
150°C–200°C	▪ Polyolefn separator melts, ▪A great area leads to short circuit, and accellerate heat release,
200°C–300°C	▪The cathode materials are dissolve and release oxygen, ▪Massive oxidation reaction with electrolytes, ▪Huge amount heat and hydrocarbon gases releases, ▪ The combustible gas mixture burns at 300°C,

The major chemical reactions is important to explain the mechanism and chain reactions of thermal runaway as shown in Table 2.

Table 2 Main reactions of thermal runaway [8]

Major Reactions	Equations
SEI decomposition	$(CH_2OCO_2Li)_2 \rightarrow Li_2CO_3 + C_2H_4 + CO_2 + 0.5O_2$
Anode reaction	$2Li + C_3H_4O_3\ (EC) \rightarrow Li_2CO_3 + C_2H_4$ $2Li + C_4H_6O_3\ (PC) \rightarrow Li_2CO_3 + C_3H_6$ $2Li + C_4H_6O_3\ (DMC) \rightarrow Li_2CO_3 + C_3H_6$
Melting of separator	-
$LiFePO_4$ cathode decomposition	$2Li_0FePO_4 \rightarrow Fe_2P_2O_7 + \frac{1}{2}O_2$
Electrolyte decomposition	$LiPF_6 \rightarrow LiF + PF_5$
Internal short circuit	-
Burning of electrolyte	$2.5O_2 + C_3H_4O_3(EC) \rightarrow 3CO_2 + 2H_2O$ $4O_2 + C_4H_6O_3(PC) \rightarrow 4CO_2 + 3H_2O$ $3O_2 + C_3H_6O_3(DMC) \rightarrow 3CO_2 + 3H_2O$

2.2. Thermal Runaway Causes

(1) Mechanical abuse can be caused by a destruction, confining, cutting, bending situations can cause structure damage and by these conditions it can basically cause short-circuits in the battery [2]. The cells in which state of charge (SOC) is more have a rapid internal temperature increase, reaching a peak in 5 seconds after a short circuit realization. It means that the heat

production of the battery directly depands the state of charge, its means if the charge amount increases the heat will be increased also [12].

(2) Electrical abuse conditions are mainly; holding in charge more than fully charged, deep discharging, and short circuits reasons which are the outer sourced reasons. These destroy the battery components, trigger exothermic reactions and start thermal runaway [2]. More charge over full charge (overcharge) situation may cause deterioration of cathode material by crossing metal fragmentation and phase change phenomena.

The chemical reaction (exothermic) beggining with lithium covering on the overcharged anode and quicken the heating of the battery. Damage to the battery package and the membrane melting by forcing the battey over fully charge condition are the most critical conditions that causation of the thermal runaway.

The experiments to understand the thermal runaway by continuous charge and discharge cycles, by increasing the amount of charge per unit time (it is calling by charging rate), the thermal runaway occurance time is reducing after battery overhcarged. Li-Io batteries are more prone to thermal runaway because of the dynamic environments.

Thermal runaway depends on battery capacity, ventilation, and design criteria.

According to the experiments on Li-Io batteries, while the voltage during overcharge reaches the critical breakpoint, if it could be stopped in 5 minutes, and the heat removed, the occurance of thermal runaway could be prevented [13]. And same experiments showed that faster-charging rates cause heat accumulation in a short time inside of the battery because loading more in a specific unit time [13].

(3) The local heat increase can occur because of bad contact and may start combustion in the vehicle and extract a lot of heat directly.

The hot weather and charging period may reach the battery temperatures. Over 55–65 ^{0}C and the thermal runaway may be more intensive than the average temperatures [10].

These abuses reason exothermic reactions, which generate heat, and this heat changes the composition of the battery; deterioration of the solid electrolyte intersection is a sample of these decompositions [2].

2.3. Controlling Thermal Runaway by Battery Management System

In order to hold the battery under stable condition, primaly the battery properties, design and material selection, secondary the battery management system (BMS) is important [2].

(a) Proper Design of Battery:

The cell size and its material is one of the most important element to affect on thermal stability of battery and prevent the adiabatic environment.

Inside temperature is directly related with the size of electrodes at the limit voltage when the battery is fully discharged (cut-off) to prevent battery harm. The thickness is important, and affect the battery temperature directly while the thickness increases the temperature increases.Because of these, at the production stage they have to be produced inline with safety standards [2]. Changing the cathode material by higher specific energy density one, required design and usage of thicker poles. For producing bigger cell, required usage of thin separator, and current collectors. These radical design requirement for creating higher energy density is limited by the safety of the Li-Io batteries' electro-chemical system.

Fire incidents realize when the abuse condition happens and breaks the boundary of the electro-chemical system [10].

(b) Battery Management System (BMS):

Li-Io batteries must be stayed in a safe operating area, the temperature and voltage of the battery operated and restricted in a defined range. Operating the battery out of these limits will reduce the battery performance and also a safety problem. The safe operating range is; for discharging at -20 to 55 ^{0}C and charging at 0-45 ^{0}C in some batteries (LTO); it could be extended up to -30 ^{0}C [17].

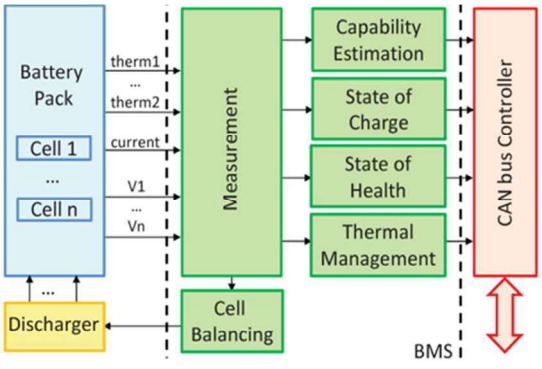


Figure 12, Battery management system operation parameters [22].

(1) Battery Thermal Management Systems (BTMS): At the time of charge and discharge processes, Li-Io battery cells generate heat, mainly by exothermic chemical reactions and losses due to activation energy, resistance to ion transfer, and chemical transportation. Most of this heat generation is realized at charge and discharge operations when SOC is between 20 and 80 percent [23]. The BTMS aims to keep the temperature between 15 °C - 35 °C; this is optimal for Li-Io batteries for electric vehicles to extend their lifetime and ensure operating safety [26]. The main problem is removing generated heat from the battery and keeping the heat in steady condition; this is a big challenge because of an increased volume of gravimetric energy in electric vehicles [26]. An air-cooling system has good results while the standard drive cycles, it is limits the temperature under 55 °C, and the temperature change limits less than 5 °C. At the other hand the maximum temperature range is more than the optimal range while the aggressive driving [26]. Working out of the operating temperature range will affect batteries' performance, lifetime, and safety. Severe conditions such as extreme temperature will trigger to the thermal runaway and abuse the safety, and short circuit cause overheating [24]; for these reasons, BTMS is essential for Li-Io batteries.

Song L and friends indicated that if the battery temperature increases 1°C, the total life of battery reduces two months. Because of that reason, continuous temperature monitoring and keeping in a range are essential for all batteries of electric vehicles. [1]. The cooling and heating systems keep the battery in the best temperature range for efficiency and safety. Practically there are two temperature controlling systems available, one is by air, and the other is by liquid. The designs could be active or passive; the most effective systems are liquid and active cooling types [5].

There are three types of battery thermal management systems; active systems, passive systems, and hybrid systems.

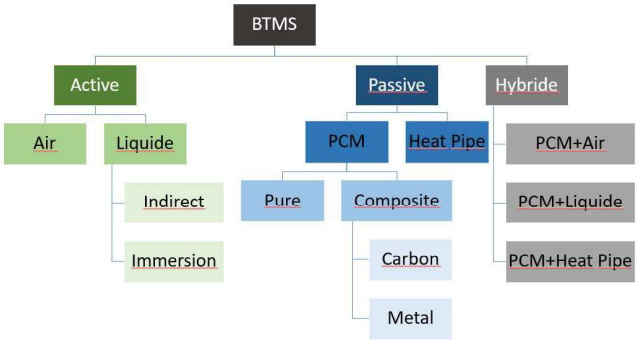


Figure 13, Battery management types [22].

(a) Active BTMS: For these cooling systems, external energy is required for its fans and pumps. The coolant materials could be air or liquid [24].

The liquid coolants can be in direct contact with the cells (immersed in the fluid) or circulate inside pipes and act as indirect cooling [25].

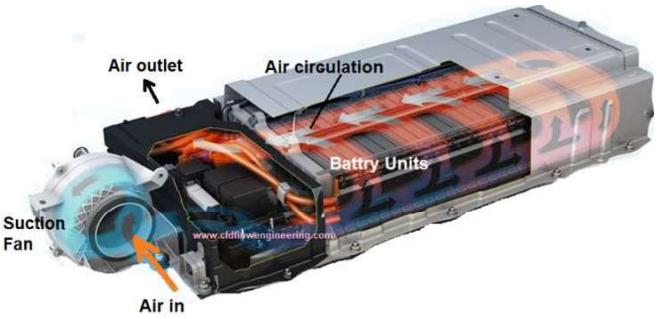


Figure 14, Battery air cooling system [22].

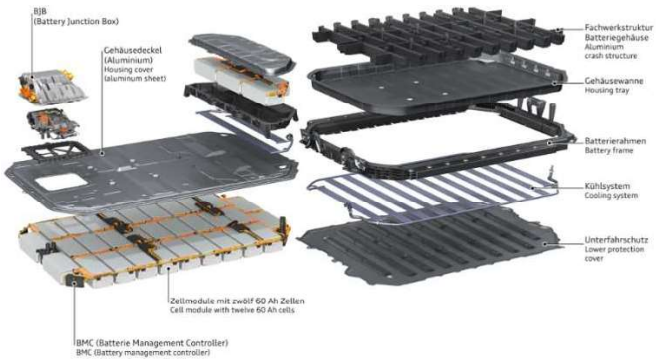


Figure 15, Battery liquid cooling system [22].

(b) Passive BTMS: The unique structures attached to surface for transfer heat as much as possible from battery surface to outside; they are phasing change material (PCM) or heat pipe applications [24].

The aim of phase change material (PCM) controlling the temperature steady by absorbing or releasing heat in the phase change process. The material is appropriately limiting the temperature and temperature difference. The state change

feature of material heat can be removed from battery packs. (Figure 16).

The system is becoming from PCM material and porous carrier.

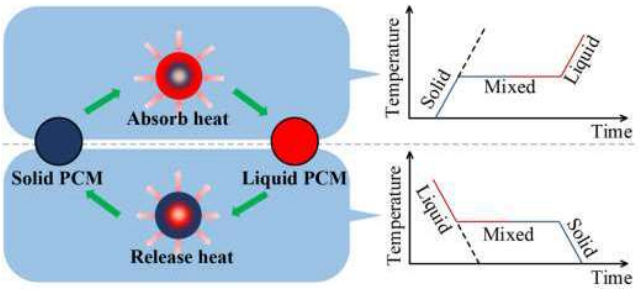


Figure 16, Working principle of PCMs [28].

The state change "phase change," could be observed in these forms: solid state to solid state, solid state to liquid state, solid state to gas state, and liquid state to gas state [28]. Because of the the chemical composition of materials, PCM materials could be organic or inorganic PCMs [28].

Some important organic materials are;

paraffin wax – petroleum wax (PW),

polyethylene glycol (PEG),

capric acid (CA),

lauric acid (LA),

palmitic acid (PA),

stearic acid (SA).

Among these material, PW is commonly using in Li-Io because of some these advantages:

(1) phase change temperature is more relevant,

(2) large heat of transformation – latent,

(3) relatively high ability conducting the heat,

(4) volume change ratio is low,

(5) no state separation,

(6) low undercooling,

(7) high chemical stability,

(8) non-toxic, non-corrosive,

(9) lower cost. [28].

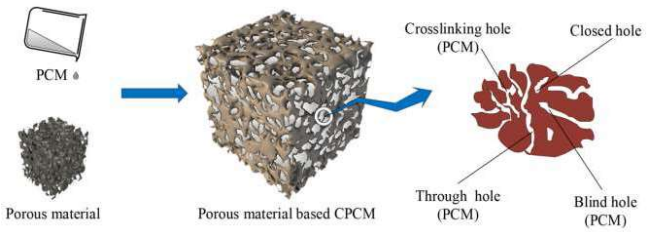


Figure 17, The structure of PCMs [28].

The porous material is the main holder material. The structure of the material is composed of attached or closed openings. Honeycomb and foam materials are two materials [28].

Porous material physical features; high durability, wide surface, proper pore size, and high thermal conductivity [28].

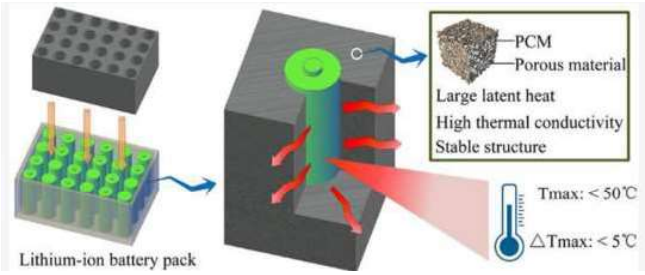


Figure 18, Li-Io Battery Pack, PCMs [28].

Hybrid BTMS: In many applications, active and passive cooling systems are combined to reach different cooling ranges. The trend shows that hybrid systems on applications are increasingly preferred [24].

The hybrid systems are the combinations of air, liquide, phase change material or heat pipe thermal management systems [2].

According to Chen D. and friends, the energy requirement of the air-cooling systems 2 -3 times more than other cooling applications at the same temperature average. The temperature increase rate is lowest value at the indirect liquid cooling systems. At the fin cooling method, Another cooling method is fin cooling system, the system brings 40% more load to the cell (in same volume) The application of indirect liquid cooling is more feasible than direct liquid cooling. Briefly the cooling performance is lower. [26].

All cooling systems have some advantages and disadvantages; the air cooling system is the most straight forward system, it is able to reduce temperature increase. At the other hand hard driving conditions creates high working

temperatures and it results a large irregular temperature distribution in the battery.

However, in parallel HEVs, air cooling is the more proper solution. The liquid cooling systems are more effective to remove heat, however they are more complex. For the reason of the cost effect and potential liquide leakage, manufacturers are hesitate to use it. PCM application could increase mass and volume, which manufacturers do not want. Heat must be exhausted during continuous cycling, which is identified as the maximum temperature situation. Heat pipe systems are limited by gravity, weight, and lack of control mechanism. Three systems are popular cooling methods in EVs: air cooling, liquid cooling, and fin cooling [26].

(2) State of Charge (SOC) monitoring: Electric abuse is mainly caused by deep discharge or overcharge. The battery SOC system mainly identifies the charge level of the battery, preventing overcharging or deep discharging and by thus preventing thermal runaway occurrence [2].

According to the studies by Chen M. and friends, it is understood that the SOC is very important to Li-Io batteries start of a fire, and higher SOC is more dangerous; 100% SOC shows the most significant mass loss and peak the heat release rate (HRR) [11].

(3) Detection of Short Circuit and Health State (SOH) Monitoring: The system mainly detects the internal short circuit and proactively warns. The temperature and current values are essential to creating this early warning system [2].

CONCLUSION

Increasing demand on clean energy because of international effort to limit the global warming triggered the global producers using li-io batteries instead of gasoline and diesel fuels in vehicles. The fire safety concern of Li-Io batteries becoming more important by increasing of their usage in our daily lifes and this is only possible by development in specific & volumetric energy density. According to the anode and cathode material diversity there are 6 main battery types, and these can be in 4 phsical shapes. All producers just combine these in their products. One of the most critical issue in Li-Io batteries is fire safety, and the phenomena named thermal runaway. It limit manufacturers for their design and battery combination. The thermal stability of elements in battery is one of the most important structural feature. The thermal runaway chain reaction starts by misuse conditions such as mechanical abuse, electrical abuse or thermal abuse. When the reaction starts, the temperature may get over 1000 ^{0}C and huge amount of fatal toxic gases (such as hydrogen flouride, carbon monoxide, carbon dioxide) releases can be observed. Breaking of the chain reaction is almost imposible. Because of that reason, holding the battery in safe working range is essential for electric vehicle producers. The battery management systems (BMS) is a main controlling unit of a electric vehicle that protect the battery against thermal runaway. It controlls the main parameters of thermal stability, charge balance, health of the battery which may affects the thermal runaway directly. The thermal stability is one of the most important issue that need to be kept battery between 15 °C - 35 °C as the optimal working range. There are mainly 3 thermal management systems and all producers choose one of them which is more suitable for their vehicle's work parameters. The hybrid electric vehicles generally use the simple cooling methods such as active air cooling systems, and fully electric vehicles may use more complex systems such as active liquide, or PCM cooling systems. The state of charge (SOC) monitoring and controlling is also important to protect battery against thermal runaway abuse conditions. It is holding the battery between 20 % -80 % charge level, to protect against deep discharge and over charge conditions. The state of health (SOH) monitoring is another important preventive issue Even by those preventive measures, fire still happens in electric vehicles. More complex detection systems which may detect thermal runaway before it happening will be essential for electric vehicles in future.

REFERENCES

[1] Song L., ZhengY., Xiao Z., Wang C., Review on Thermal Runaway of Lithium-Ion Batteries for Electric Vehicles, Journal of Electronic Materials (2022) 51:30–46, November 2021.

[2] Zhang X., Li L., Zhang W., Review of Research about Thermal Runaway and Management of Li-ion Battery Energy Storage Systems, IEEE 9th International Power Electronics and Motion Control

Conference (IPEMC2020-ECCE Asia), 2020.

[3] Guo D., Sun L., Zhang X., Xiao P., Liu Y., Tao F., The Causes of Fire and Explosion of Lithium Ion Battery for Energy Storage, 978-1-5386-8549-5/18/$31.00 ©2018 IEEE, 2018.

[4] Golubkov A. W., Scheikl S., Planteu R., Voitic G, Wiltsche H.,Stangl C., Fauler G, Thaler A., Hacker V., Thermal runaway of commercial 18650 Li-ion batteries with LFP and NCA cathodes – impact of state of charge and overcharge, The Royal Society of Chemistry 2015, 22 June 2015.

[5] Kocakulak T., Solmaz H., Determination of Lithium Ion Battery Characteristics for Hybrid Vehicle Models, International Journal of Automotive Science and Technology 4 (4): 264-271, 2020.

[6] Ghiji M. ,Novozhilov V. ,Moinuddin K., Joseph P., Burch I., Suendermann B., Gamble G., A Review of Lithium-Ion Battery Fire Suppression, Energies 2020, 13, 5117; doi:10.3390/en13195117, 1 October 2020.

[7] Dragonfly Energy, A Guide To The 6 Main Types Of Lithium Batteries, Access date: 28.07.2022, https://dragonflyenergy.com/types-of-lithium-batteries-guide/?msclkid=0fba649dc07a11ec8aea2c921e996134, September 27, 2021

[8] Peng Y., Zhou X., Hu Y., Ju X., Liao B., Yang L., A new exploration of the fire behaviors of large format lithium-ion battery, Journal of Thermal Analysis and Calorimetry (2020) 139:1243–1254, 19 July 2019.

[9] Iclodean C., Varga B., Burnette N., Cimerdean D., Jurchiş B., Comparison of Different Battery Types for Electric Vehicles, IOP Conf. Series: Materials Science and Engineering 252 (2017) 012058 doi:10.1088/1757-899X/252/1/012058, 2017.

[10] Jin C. ,Sun Y., Wang H., Zheng Y., Wang S., Rui X., Xu C., Feng X., Wang H., Ouyang M., Heating power and heating energy effect on the thermal runaway propagation characteristics of lithium-ion battery module: Experiments and modeling, Applied Energy 312 (2022) 118760, 2022.

[11] Chen M., Dongxu O., Cao S., Liu J., Wang Z., Wang J., Effects of heat treatment and SOC on fire behaviors of lithium-ion batteries pack, Journal of Thermal Analysis and Calorimetry (2019) 136:2429–2437, 2019.

[12] Xu Y., Liu F., Guo J., Li M., Han B., Mechanical properties and thermal runaway study of automotive lithium-ion power batteries, 2021

[13] Chen W., Jiang J., Wen J., Thermal runaway induced by dynamic overcharge of lithium-ion batteries under different environmental conditions, Journal of Thermal Analysis and Calorimetry (2021) 146:855–863, 2020.

[14] The Paris Agreement, Access date:10.08.2022, https://unfccc.int/process-and-meetings/the-paris-agreement/the-paris-agreement#:~:text=The%20Paris%20Agreement%20is%20a,compared%20to%20pre%2Dindustrial%20levels

[15] BU-301a: Types of Battery Cells, Access date:10.08.2022, https://batteryuniversity.com/article/bu-301a-types-of-battery-cells

[16] LG Energy Solution mulls adding prismatic type to EV cell lineup, Access date: 10.08.2022, https://m.pulsenews.co.kr/view.php?year=2022&no=20482

[17] Lu L., Han X., Li J., Hua J., Ouyang M., A review on the key issues for lithium-ion battery management in electric vehicles, Journal of Power Sources, 26 November 2012

[18] Miao Y., Hynan P., Jouanne A., Yokochi A.,Current Li-Ion Battery Technologies in Electric Vehicles and Opportunities for Advancements, Energies 2019, 12, 1074;, 20 March 2019

[19] The Paris Agreement, Access date: 10.08.2022, https://www.un.org/en/climatechange/paris-agreement#:~:text=Today%2C%20193%20Parties%20(192%20countries,have%20joined%20the%20Paris%20Agreement.

[20] Arksand E., Parametrization of a lithium-ion battery, Degree project in chemical science and engineering, Stockholm, Sweden 2021

[21] Press release: The Nobel Prize in Chemistry 2019, Access date: 28.07.2022, https://www.nobelprize.org/prizes/chemistry/2019/press-release/

[22] Buccolini L., A. Ricci, Scavongelli C., DeMaso-Gentile G., S. Orcioni, M. Conti, Battery Management System (BMS) simulation environment for electric vehicles, Published in 2016 IEEE 16th International Conference on Environment and Electrical Engineering (EEEIC) 2016

[23] Immersion Cooling – Potential Alternative to Traditional Battery Cooling, Access date: 28.07.2022, https://www.futurebridge.com/industry/perspectives-mobility/immersion-cooling-potential-alternative-to-traditional-battery-cooling/

[24] Zhao C., Zhang B., Zheng Y., Huang S., Yan T., and Liu X., Hybrid Battery Thermal Management System in Electrical Vehicles: A Review, 27 November 2020.

[25] CIC energiGUNE, ‘’Battery Thermal Management Systems (Btms) For Mobility Applications’’, Access date: 28.07.2022, https://cicenergigune.com/en/blog/battery-thermal-management-system-btms-electric-vehicle

[26] Chen D., Jiang J. , Kim G., Yang C., Pesaran A., Comparison of different cooling methods for lithium-ion battery cells, 2015.

[27] Moghaddam H., Mazyar S., Designing battery thermal management systems (BTMS) for cylindrical Lithium-ion battery modules using CFD, 2018.

[28] Fang M., Zhou J., Fei H., Yang K., He R., Porous-Material-Based Composite Phase Change Materials for a Lithium-Ion Battery Thermal Management System, Energy Fuels, 2022.

NUMERICAL INVESTIGATIONS ON THERMAL PERFORMANCE AND FLAME STABILITY OF HYDROGEN DILUTED AMMONIA FUELED SWIRL BURNER AND FURNACE

Ozan KEKUL[1], Mustafa ILBAS[2], Serhat KARYEYEN[3]

1. Graduate School of Natural and Applied Science, Gazi University, Ankara; email: ozan.kekul@gazi.edu.tr
2. Faculty of Technology, Gazi University, Ankara; email: ilbas@gazi.edu.tr
3. Faculty of Technology, Gazi University, Ankara; email: serhatkaryeyen@gazi.edu.tr

Abstract

Ammonia (NH_3) has a substantial potential for being a good alternative fuel since its' high hydrogen storage capacity. However, in order to use NH_3 in the combustion systems as a fuel, there are some difficulties should be negotiated. Compared to the traditional fossil fuels, the main drawbacks of NH_3/air mixture are lower burning velocity and flame temperature, requirement of high ignition energy and limited flammability range. In this study, it is aimed to improve the combustion performance of NH_3/air flame. Within this scope, effects of adding of hydrogen (H_2) into NH_3/air mixture were investigated numerically by using an existing non-premixed burner. Thus, resultant temperature and NO emission profiles in the combustor for NH_3/air and NH_3/H_2/air mixture were compared and the results were discussed. Besides, the mixing ratio of NH_3 and H_2 was determined as 70% NH_3 and 30% H_2 by mass. In the numerical modelling, the PDF/Mixture Fraction combustion model with a reduced reaction mechanism which was generated for NH_3/H_2 fuel mixtures' combustion was used. According to the predicted results, it was observed that H_2 addition into NH_3/air mixture provided higher temperature profiles throughout the combustor. Moreover, according to the axial temperature profiles predicted, mixing of H_2 with NH_3 enhanced the burning velocity of NH_3/air mixture. On the other hand, increasing flame temperature induced comparatively higher NO emissions owing to thermal NO mechanism.

Keywords: NH_3/H_2/air flames, Combustion, CFD Analysis, NO, PDF/Mixture Fraction

1 INTRODUCTION

In order to fulfill increasing energy requirement without CO_2 emissions, using of carbon-free fuels in the combustion systems should be generalized. Within this scope, NH_3 and H_2 are remarkable energy carriers to reduce CO_2 emissions [1]. Although H_2 is the most abundant element in the earth, it has a low density and due to this physical property, storage of H_2 with a fulfilling energy capacity can be a challenge [2].

NH_3 has a substantial hydrogen storage capability (17.8% by mass) and liquefaction of NH_3 can be achieved by compressing it to 9.9 atm at the atmospheric temperature or reducing its' temperature to -33.8 °C at the atmospheric pressure. Hence, it can be concluded that NH_3 is a promising energy carrier for the combustion systems [3]. However, NH_3/air flame has some drawbacks such as low burning speed and flame temperature, high NO_x emissions and narrow flammability limit. In order to use NH_3 as a fuel, these difficulties should be eliminated [4].

Studies in the literature about improving the combustion and emission performance of NH_3 become widespread day after day. Some combustion strategies such as mixing NH_3 with H_2 or traditional fossil fuels, oxygen enrichment and two stage combustion are used in these studies. Han et al. performed a study to better understanding the combustion features of NH_3/air, NH_3/H_2/air, NH_3/CO/air and NH_3/CH_4/air premixed flames. Within this scope, burning velocities of the mixtures were experimentally investigated at various equivalence ratios and molar concentrations of the ingredients. They reported that blending NH_3 with H_2 is the most effective way to improve the burning velocity of NH_3/air mixture. In addition to this, adding CO into NH_3/air mixture provided better burning velocity performance than adding CH_4 [5]. Wang et al. aimed to improve laminar burning velocity of NH_3 via oxy-combustion

method. In their study, it was concluded that increasing oxygen concertation in the oxidizer promoted the laminar burning velocity of NH_3. The highest laminar burning velocity value (125.05 m/s) was achived when the pure oxygen is used as oxidizer [6]. Okafor et al. burnt NH_3 in a swirling micro gas turbine combustor chamber and asserted some combustion methods and combustion chamber design for obtaining sufficient burning performance and lower NO_x emissions in case NH_3 combustion. In this experimental and numerical study, they focused on the effects of fuel inlet angle, inlet temperature of the combustor, equivalence ratio, and ambient pressure on combustion and emissions distributions of the NH_3 flame. According to the obtained results of their study, two-stage rich-lean combustion method provides an efficient NH_3 combustion with low NO emissions. Furthermore, there is a relationship between NO_x emissions and OH radicals' formation. Accordingly, the control of the OH radical distributions in the combustor is crucial for optimizing the NO_x emissions. Increasing the ambient pressure decreases the NO_x emissions, especially under the premixed combustion conditions [7].

When the studies in the literature examined, it can be concluded that investigations on the combustion and emission characteristics of NH_3/H_2 fuel mixtures under the non-premixed combustion conditions are scarce. Hence, this study concentrates on the combustion of NH_3-air and NH_3-H_2-air mixtures by using an existing non-premixed burner. On the other hand, it was aimed to improve the combustion performance of NH_3-air mixture by mixing it with H_2 and to investigate the combustion and emission behaviors of these mixtures in a model combustor. In this way, temperature and NO emission profiles emerged in the combustor were predicted by using CFD code and the results were compared and scrutinized for NH_3/air and NH_3/H_2/air mixtures.

2 CFD MODELLING

Ansys Fluent code was used for the numerical simulations and all combustion cases were planned for a thermal power of 10 kW and an equivalence ratio of 0.83. Thus, fuel and air inlet mass flow rates were calculated for the combustion conditions aforementioned and were given in Table 1.

The mixture fraction/PDF combustion model with steady laminar flamelet approach was selected in the modelling. On the other hand, a reduced reaction mechanism [8], which has been generated for NH_3 and NH_3/H_2 fuel mixtures, was integrated to the modelling. This reaction mechanism comprises of 21 species and 67 elementary reactions. Moreover, the non-premixed burner used in the present study has a low swirl number because the vane angle is 15°. Therefore, Standard k-epsilon turbulence model was utilized as this turbulence model provides satisfactory results in case of low swirl numbers. In Figure 1 and Figure 2, 3D model and the engineering drawing of the burner are shown, respectively. More information about the burner can be reached in one of the authors' studies [9] .

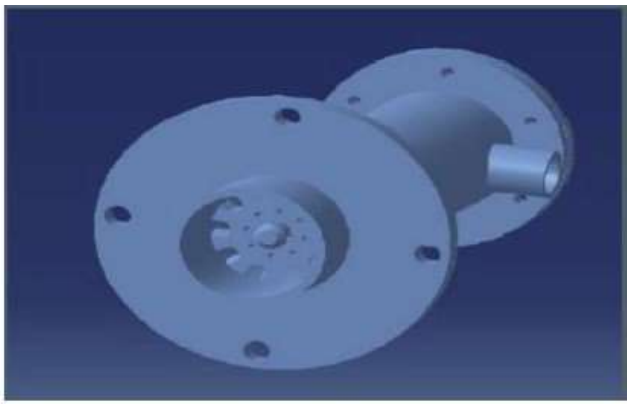


Figure 1. 3D model of the Burner

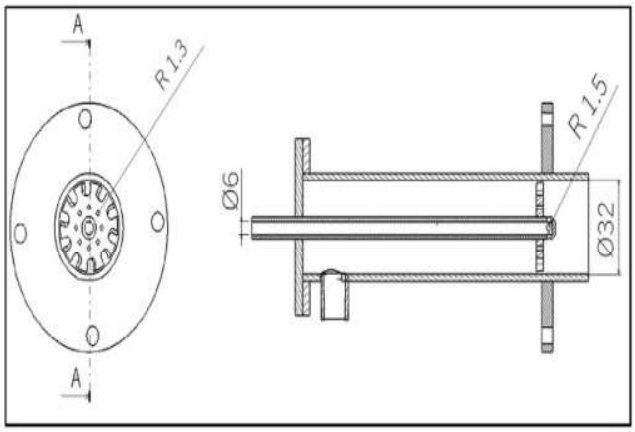


Figure 2. Engineering Drawing of the Burner

Table 1. Inlet Mass Flow Rates

Fuel Composition	Fuel Mass Flow Rate (kg/s)	Air Mass Flow Rate (kg/s)
NH_3/air	0,0005376	0,0039290
NH_3/H_2/air	0,0002033	0,0035659

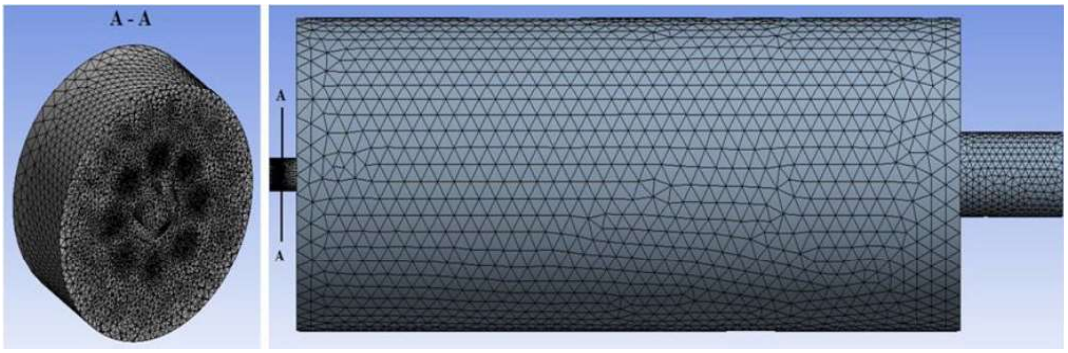


Figure 3. Mesh Structure

When the flame temperature is higher than 1000 K, a radiation model should be included to the modelling to obtain accurate temperature predictions within the combustor. Therefore, P-1 radiation model was used in the present study. There are some advantages of using P-1 radiation model. The equations are easily solved with little CPU demand, thus, this model provides lower computational cost. In addition, the P-1 model can easily be applied to complicated geometries with curvilinear coordinates [10].

In Figure 3, the mesh structure created is illustrated. As it can be seen in Figure 3, the mesh structure was elaborated in the mixing region of the burner since the mixing process of the reactants and combustion reactions begin in this area. This mesh structure has 613947 tetrahedron cells and 112719 node points. The highest skewness value is 0.833, the average skewness value is 0.232, and the lowest orthogonal quality value is 0.167.

3 RESULTS AND DISCUSSIONS

In this section of the study, predicted temperature and NO emission profiles throughout the combustor are presented for 70% NH_3-30% H_2 and 100% NH_3 fuels. Thus, effects of hydrogen addition on combustion and emissions characteristics of NH_3-air mixture are investigated under the non-premixed combustion conditions.

In Figure 4, the axial temperature profiles predicted in the combustor are presented for each fuel composition. When Figure 4 examined, axial temperature profiles in the flame region attracts attention firstly. The axial temperatures values in the flame region increased considerably by adding H_2 into NH_3-air mixture. The maximum temperature values in the flame region for 100% NH_3 and 70% NH_3-30% H_2 fuels are 1296.82 K and 1594.46 K, respectively. From this viewpoint, it can be said that H_2 addition improved the reactivity of NH_3-air mixture substantially and consequently, higher flame temperature obtained. On the other hand, temperature profiles approached each other towards to the combustor outlet because of the heat transfer from the combustor. However, when the temperature values at the combustor outlet evaluated, again, higher temperature value was achieved by the fuel containing hydrogen. These temperature values at the combustor outlet are 786.813 K for 70%NH_3-30%H_2 fuel mixture and 718.255 K for 100% NH_3 fuel.

The axial temperature profiles can give an idea about the burning velocity of the fuels. As it can be seen in Figure 4, the axial temperature profile of 70%NH_3-30%H_2 fuel mixture is closer to the combustor inlet in the flame region. Accordingly, it can be concluded that H_2 addition enhanced the burning velocity of NH_3-air mixture. This result is also consistent with the findings in the literature.

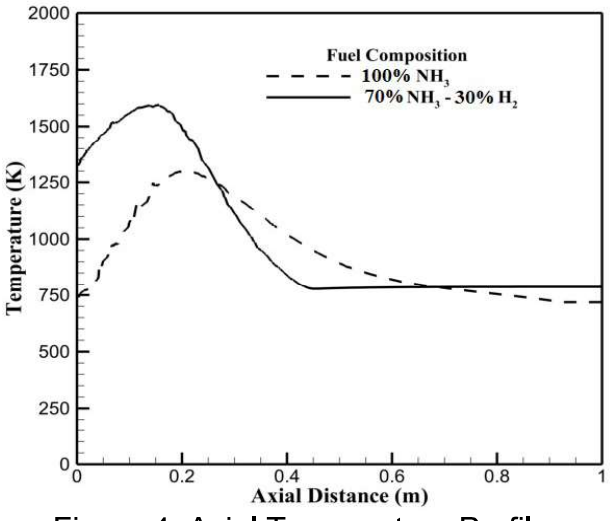


Figure 4. Axial Temperature Profiles

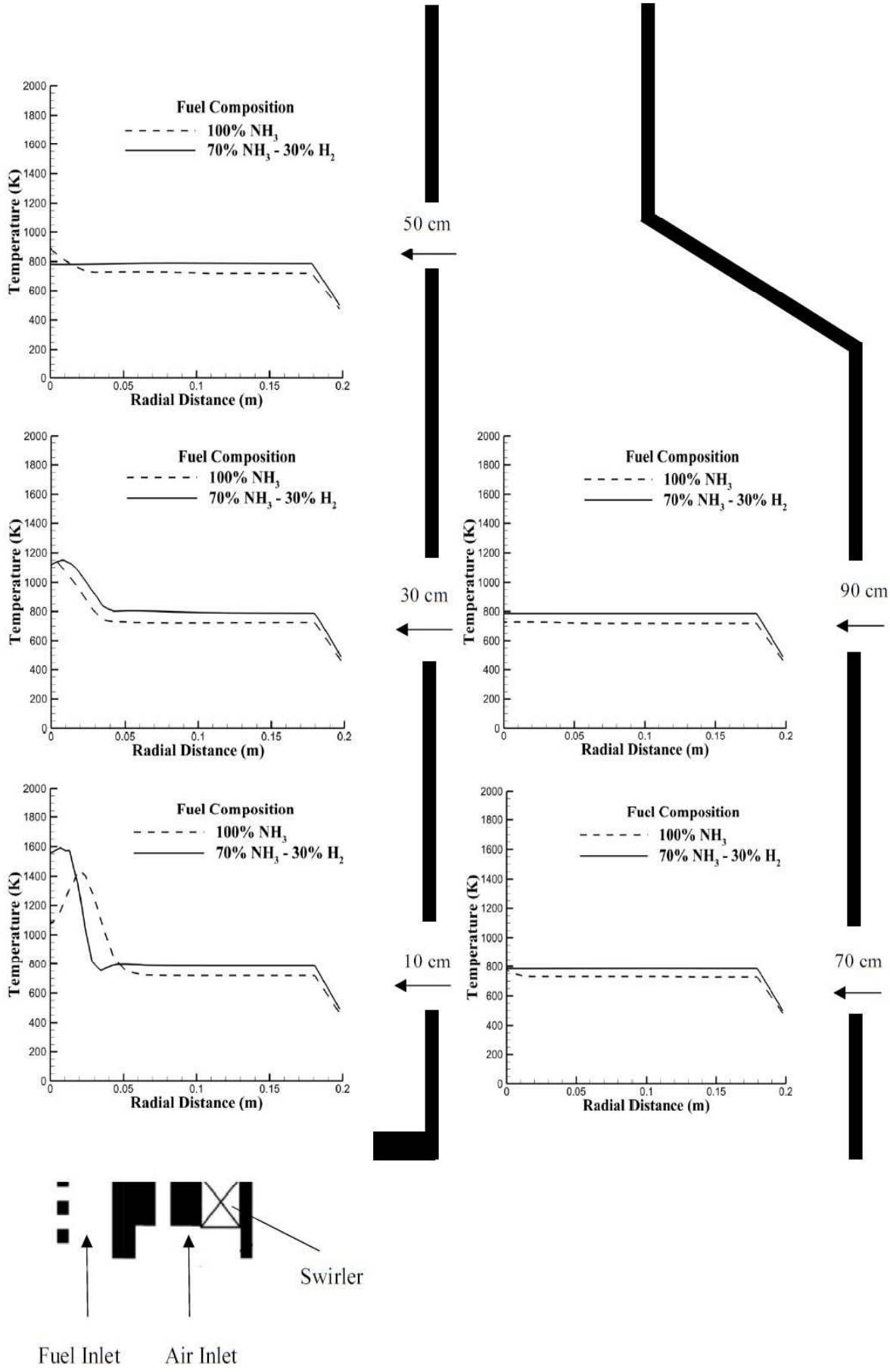


Figure 5. Radial Temperature Profiles

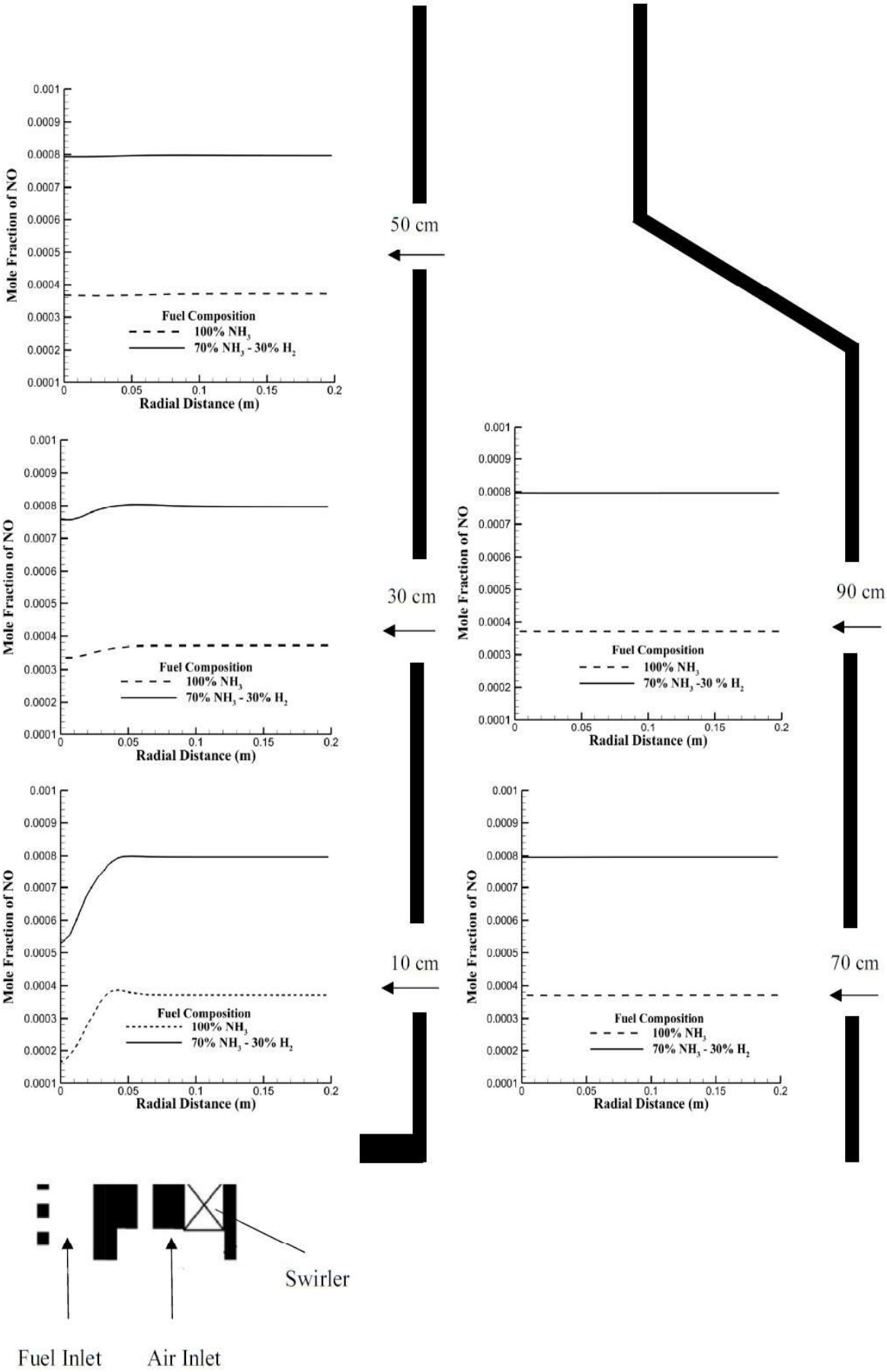


Figure 6. NO emission profiles

In Figure 5, effects of hydrogen addition into the NH_3-air on the radial temperature distribution throughout the combustor are shown. When the combustion performance of each fuel evaluated generally, it is seen that 70% NH_3-30% H_2 fuel mixture exhibited a better performance in terms of radial temperature values. There are two main reasons to be obtained higher temperature values in the combustor when the hydrogen containing fuel mixture is burnt. The first one is, the flame temperature of 70% NH_3-30% H_2 is higher than that of NH_3-air. Hence, the higher flame temperature provided a higher temperature values within the combustor. The latter is, LHV of the hydrogen containing fuel is higher. This feature of the 70% NH_3-30% H_2 fuel mixture contributed for obtaining better combustion performance. On the other hand, the temperature profiles of the fuels exhibited a rapid decrease in the flame region. The reason of this phenomenon is that the combustor used in the present study has a sudden expansion. Furthermore, from the flame region towards to the combustor outlet, the difference of the temperature values between the combustor center and combustor walls decreased. Especially after the 30 cm of the axial distance, temperature distribution was largely homogeneous for the each fuels' combustion. This can be explained by the uniform distributions of the flue gases in these regions.

In Figure 6, NO emission distributions in the combustor are illustrated. Interestingly, NO emissions was promoted by H_2 addition in the fuel mixture although 70% NH_3-30% H_2 fuel mixture contains lesser NH_3 concentration. Hence, the hydrogen containing fuel exhibited higher NO emission distributions throughout the combustor. Accordingly, one can say that fuel-NO mechanism is not dominant for the combustion of NH_3-H_2 fuel mixtures. Therefore, it can be concluded that because of the effects of thermal-NO mechanism, 70% NH_3-30% H_2 fuel mixture generated much more NO emissions. In order to validate this finding, temperature profiles in the flame region should be examined. According to the temperature profiles in Figure 4 and Figure 5, flame temperature of 70% NH_3-30% H_2 fuel mixture is higher than that of the fuel containing 100% NH_3. Consequently, since the hydrogen addition enhanced the flame temperature, NO emissions increased in case of the combustion of 70% NH_3-30% H_2 fuel mixture. When the NO formation throughout the combustor evaluated generally, it can be said that the formation of NO emissions increased rapidly in the reaction zone and after 30 cm of axial distance of the combustor, these NO emissions reached to the chemical equilibrium. On the other hand, it can be observed that distribution of NO emissions became more uniform towards to combustor outlet.

4 CONCLUSIONS

In this study, the effects of hydrogen addition into NH_3-air mixture was investigated via a non-premixed burner. To this aim, temperature and NO emission distributions in a model combustor were predicted. After the numerical modelling performed, following conclusions have been obtained;

- Hydrogen blending strategy improves the reactivity of NH_3-air mixture. Thus, flame temperature of NH_3-air mixture enhances with the hydrogen addition.

- According to the axial temperature profiles in the flame region, it was observed that the flame of the hydrogen containing fuel is closer to the combustor inlet. From this viewpoint, it can be said that hydrogen addition enhanced the burning velocity of NH_3-air mixture.

- The hydrogen containing fuel has provided higher temperature distributions in the combustor, generally. The main reason of this phenomenon is the flame temperature and LHV of hydrogen containing fuel is higher.

- Although hydrogen addition generates some positive effects on the combustion performance of NH_3-air mixture, NO emissions increase when hydrogen exists in the fuel mixture. The main reason for increasing NO emissions is the thermal-NO mechanism is more effective than fuel-NO mechanisms for the NH_3-H_2 fuel mixtures' combustion. Thus, it can be conclude that higher flame temperature induced higher NO emissions in the combustor owing to

thermal-NO mechanism. On the other hand, NO emissions increased rapidly in the reaction zone and after the 30 cm of axial distance of the combustor, these emissions reached chemical equilibrium for each fuel composition.

REFERENCES

[1] M. Cheng, H. Wang, H. Xiao, K. Luo, and J. Fan, "Emission characteristics and heat release rate surrogates for ammonia premixed laminar flames," *Int. J. Hydrogen Energy*, vol. 46, no. 24, pp. 13461–13470, Apr. 2021, doi: 10.1016/j.ijhydene.2021.01.154.

[2] M. Hirscher, *Handbook of Hydrogen Storage: New Materials for Future Energy Storage*. Wiley, 2010.

[3] P. Dimitriou and R. Javaid, "A review of ammonia as a compression ignition engine fuel," *Int. J. Hydrogen Energy*, vol. 45, no. 11, pp. 7098–7118, Feb. 2020, doi: 10.1016/j.ijhydene.2019.12.209.

[4] H. Kobayashi, A. Hayakawa, K. D. K. A. Somarathne, and E. C. Okafor, "Science and technology of ammonia combustion," *Proc. Combust. Inst.*, vol. 37, no. 1, pp. 109–133, 2019, doi: 10.1016/j.proci.2018.09.029.

[5] X. Han, Z. Wang, M. Costa, Z. Sun, Y. He, and K. Cen, "Experimental and kinetic modeling study of laminar burning velocities of NH3/air, NH3/H2/air, NH3/CO/air and NH3/CH4/air premixed flames," *Combust. Flame*, vol. 206, pp. 214–226, 2019, doi: 10.1016/j.combustflame.2019.05.003.

[6] D. Wang, C. Ji, Z. Wang, S. Wang, T. Zhang, and J. Yang, "Measurement of oxy-ammonia laminar burning velocity at normal and elevated temperatures," *Fuel*, vol. 279, no. June, p. 118425, Nov. 2020, doi: 10.1016/j.fuel.2020.118425.

[7] E. C. Okafor *et al.*, "Towards the development of an efficient low-NOx ammonia combustor for a micro gas turbine," *Proc. Combust. Inst.*, vol. 37, no. 4, pp. 4597–4606, 2019, doi: 10.1016/j.proci.2018.07.083.

[8] E. C. Okafor *et al.*, "Measurement and modelling of the laminar burning velocity of methane-ammonia-air flames at high pressures using a reduced reaction mechanism," *Combust. Flame*, vol. 204, pp. 162–175, Jun. 2019, doi: 10.1016/j.combustflame.2019.03.008.

[9] M. Ilbas, O. Kekul, A. Bektas, and S. Karyeyen, "Oxidizer effects on ammonia combustion using a generated non-premixed burner," *Int. J. Hydrogen Energy*, vol. 47, no. 24, pp. 12317–12337, 2022, doi: 10.1016/j.ijhydene.2021.05.105.

[10] I. ANSYS, "ANSYS Fluent Theory Guide." ANSYS, Inc., 2014.

Carbonization, Activation and Investigation of Different Uses of Wastewater Treatment Sludge

Serhat Bilgin[*,1], S. Orhan Akansu[1], M. İlhan İlhak[2]

[*]: srhtblgn@gmail.com, ORCID: 0000-0002-6812-6641
[1]: *Department of Mechanical Engineering, Faculty of Engineering, Erciyes University, Kayseri*
[2]: *Department of Mechanical Engineering, Faculty of Engineering, Omer Halis Demir University, Nigde*

ABSTRACT

Due to the limited clean water resources in the world, the wastewater from the wastewater networks of the cities is subjected to treatment processes in the wastewater treatment plants (WWTP). The water treated after the wastewater treatment process; While it is discharged to the relevant areas within acceptable limits, a waste called sewage sludge (SS) comes out from the facility. These wastes are disposed of in different ways. In this study, studies were carried out on different usage areas of WWW, which is WWTP waste. SS was first dried, then subjected to physical and chemical activation processes and turned into activated carbon. Activated carbon from SS was obtained at different temperature ranges. FT-IR, XRD, ICP-MS, TG-DTA, CHNS, SEM-EDX analyzes were performed on the obtained activated carbons. This study examines the performance, combustion and emission characteristics of the mixtures made with diesel fuel at 50 ppm and 100 ppm ratios of selected samples in line with the analysis results. Engine performance and exhaust emission measurements were made in a 12-cylinder diesel engine at a constant speed of 600 rpm and under five different loads (0, 50, 100, 150 and 200 Nm). Maximum efficiency values were measured in the experiments. CO, HC, CO_2, O_2 and NO_x measurements and comparative evaluations were made in emission characteristics. As a result of the study, the test data were compared with fossil fuel diesel fuel and no-load conditions at constant speed as a reference. In this study, it was investigated whether the activated carbons originating from SS could be used as a diesel fuel additive.

Keywords— *Carbonization, Activation, Activated Carbon, Pyrolysis, Diesel Engine, Emission, Wastewater Treatment, Sewage Sludge*

ROKETLERDE TAHRİK İLKESİ VE NÜKLEER ROKETLERİN KAVRAMSAL DEĞERLENDİRİLMESİ

Hayri YAMAN[1] ve Murat Kadir YESILYURT[2]

1. Kırıkkale Üniversitesi Kırıkkale Meslek Yüksekokulu Otomotiv Teknolojisi Programı, Kırıkkale; email: hayriyaman@kku.edu.tr
2. Yozgat Bozok Üniversitesi Mühendislik-Mimarlık Fakültesi Makine Mühendisliği Bölümü, Yozgat; email: kadir.yesilyurt@bozok.edu.tr

Özet

Günümüzde insanlığın en çok ilgisini çeken konuların başında uzayın keşfedilmesi konusu gelmektedir. Bu konuda günümüzün en önemli ulaşım araçları sürekli geliştirilmekte olan roketlerdir. Roketler savunma alanında kullanıldığı gibi daha çok haberleşme ve ticari uyduların dünya yörüngesine yerleştirmede kullanılan tek araçlardır. Ayrıca Güneşin gezegenlerinin ve gezegenlerin uydularının keşfi, dünyadan farklı gezegenlerde yaşam alanlarının olup olmadığının araştırılmaları çalışmalarında kullanılabilecek önemli araçlardan biri olarak değerlendirilmektedir. Bu kapsamda uzaya ulaşımın sağlanması ancak çok yüksek enerji kullanımı ile sanabileceği bilinen bir gerçektir. Uzayın daha derinliklerine doğru diğer yıldızların gezegenlerinde yaşam olup olmadığının keşfi için mevcut kullanımda olan kimyasal enerjili roketler ile gidilip gelinmesi günümüz şartlarında imkansız olacağı bilinmektedir. Bu nedenle son dönemlerde nükleer enerjili roketlerin geliştirilmesi ve devreye alınması için kapsamlı Ar-Ge çalışmaları yoğun olarak sürdürülmektedir. Roketler temelde Newton'un 3.hareket yasası kapsamında etkiye tepki prensibine göre çalışan araçlar olarak tanımlanmaktadır. Roketlerde etkiye tepki mantığında birçok itki oluşturma yöntemi kullanılmaktadır. Bu kapsamda en çok tercih edilen roketlerde itki üretimi; roket içerisinde kimyasal yakıtın yanması neticesinde oluşan gazın kütle akışı ve roket içerisinde herhangi bir akışkanın ısıtılarak yüksek hızda roket içerisinden akışının sağlanması neticesinde itki oluşturulmaktadır. Roketlerde oluşturulacak itki kuvvetin büyüklüğü kullanılacak yakıtın enerji kabiliyetine ve roketin çalışma prensibine doğrudan bağlıdır. Mevcut şartlarda en çok kimyasal enerjili roketlerin yüksek yakıt yüklenebilmesi nedeniyle tercih edilmektedir. Ancak geliştirme aşamasının devam ettirildiği nükleer roketlerin yakın gelecekte bazı tehlike oluşturabilecek yönlerinin çözümlenmesi ile uzun uçuşlarda kimyasal yakıtlı roketlerin yerine tercih edileceği görülmektedir. Nükleer roketler kimyasal yakıtlı roketlere göre en az 2 kat daha fazla itki ve daha verimli çalışabilecek yapıda olmaları önemli avantaj oluşturmaktadır. Nükleer roketlerin en güvenli yapısal tasarımı içerisinde ise nükleer reaktörün olduğu ve hidrojen itki yakıtının 3000 °C'ye kadar ısıtılarak itkisinin sağlandığı Nükleer Termal Roket (NTP) sistemlerdir. Roketleri genel yapısı ile bu konularda değerlendirildiğinde nükleer roketler için umut verici gelişmelerin olacağı görülmektedir.

Anahtar Kelimeler: Roketler, İtki, Roket Yakıtları, Nükleer Roketler, Hidrojen, Yanma

PRINCIPLE OF PROPULSION IN ROCKETS AND CONCEPTUAL EVALUATION OF NUCLEAR ROCKETS

Abstract

One of the most interesting subjects of humanity today is the exploration of space. In this regard, today's most important means of transportation are rockets, which are constantly being developed. Rockets are used in the field of defense as well as the only vehicles used to place communication and commercial satellites in earth orbit. In addition, the discovery of the planets of the sun and the satellites of the planets is considered one of the important tools that can be used in the studies of researching whether there are living spaces on planets other than Earth. In this context, it is a known fact that access to space can only be achieved with very high energy use. It is known that it will be impossible in today's conditions to go to the depths of space with the chemical energy rockets currently in use to discover whether there is life on the planets of other

stars. For this reason, extensive R&D studies have been carried out recently for the development and commissioning of nuclear-powered rockets. Rockets are basically defined as vehicles that work according to the principle of reaction to impact within the scope of Newton's 3rd law of motion. Many thrust generation methods are used in the impulse response logic in rockets. In this context, the most preferred rockets are thrust production; the thrust is created as a result of the mass flow of the gas formed as a result of the combustion of the chemical fuel in the rocket and the heating of any fluid in the rocket and the flow of it through the rocket at high speed. The magnitude of the thrust to be created in rockets is directly dependent on the energy capability of the fuel to be used and the working principle of the rocket. In current conditions, chemical energy rockets are mostly preferred because of their high fuel loading. However, it is seen that nuclear rockets, which are still in development, will be preferred instead of chemical-fueled rockets for long flights, with the analysis of the aspects that may pose some danger in the near future. Nuclear-powered rockets have an important advantage in that they have at least 2 times more thrust and can operate more efficiently than chemical fuel rockets. The safest structural design of nuclear rockets is the Nuclear Thermal Propulsion Rocket (NTP) system, in which the nuclear reactor is located and the hydrogen propellant is heated up to 3000 °C and its thrust is provided. When the rockets are evaluated on these issues with their general structure, it is seen that there will be promising developments for nuclear-propelled rockets.

Keywords: Rockets, Propulsion, Rocket Propellants, Nuclear Rockets, Hydrogen, Combustion

CHARACTERIZATION OF HYDROCHAR PRODUCTION FROM ORANGE PEEL AND SEWAGE SLUDGE BY HYDROTHERMAL PROCESSES

R. N. Mutlu[1], İ. Gökalp[1], H. Ece[2*], G. Çelik[2], A. T. Koçer[3] and D. Özçimen[3]

1. Department of Mechanical Engineering, Middle East Technical University, Ankara;
2. Department of Chemical Engineering, Middle East Technical University, Ankara;
3. Deparment of Bioenergy Engineering, Yıldız Technical University, İstanbul
Email[*]: eceh@metu.edu.tr

Abstract

This paper presents our recent results on the hydrothermal carbonization process of orange peel and sewage sludge. Biomass energy, as a renewable and sustainable energy source, is considered as the fourth largest energy source in the world. Recently, hydrothermal carbonization (HTC) has received great attention as a bio-waste treatment technique, avoiding of pre-drying procedures for wet raw organic waste materials. HTC is a thermo-chemical process in an aqueous medium at relatively mild temperatures (180–250°C) and autogenous pressures. As a result of HTC process, valuable carbonaceous residue called hydrochar is obtained. Orange peel is a typical bio-waste in the food industry, derived from the massive global production of orange juices. Similarly, sewage sludge is an organic waste generated every day in huge quantities globally. Such organic waste streams are difficult to dispose of because of their original humidity and the cost of re-drying processes. HTC appears therefore as a suitable waste management process for such materials. In this study, hydrothermal treatment was applied to orange peels and sewage sludge grated in small pieces at different temperatures (180-220 °C), for different treatment times and for different solid to water ratios (1:6, 1:12). After the hydrothermal process, % weight of the solid product compared to the initial dried material weight is calculated. Proximate analysis, FTIR analysis, determination of elemental composition and higher heating value tests were applied to hydrochar samples. Chemical oxygen demand, total organic carbon, pH, conductivity, salinity and total dissolved solid tests were also applied to the process water. The main differences of the HTC pretreatment process results for the two organic waste stream samples are discussed.

Keywords: Hydrothermal carbonization, bio-waste, hydrochar, sludge

THE ACTIVITY OF ZEOLITE-SUPPORTED NICKEL CATALYST IN CO_2 HYDROGENATION TO PRODUCE CH_4

Tuğba Yarbaş[1] and Nezihe Ayas[2,*]

1. Chemical Engineering Department, Engineering Faculty, Bilecik Seyh Edebali University, Bilecik; email: tugba.yarbas@bilecik.edu.tr
2. Chemical Engineering Department, Engineering Faculty, Eskisehir Technical University, Eskisehir; email: nazcan@eskisehir.edu.tr

Abstract

The utilization of CO_2 by converting it into different products is a very important and remerkable research area because of CO_2s harmful environmental effects. In this study, the natural zeolite was impregnated with nickel, which is known for its effectiveness in catalytic hydrogenation reactions. The prepared 15%Ni/Zeo catalyst was characterized by XRF, XRD, FT-IR, SEM and TGA techniques. The activity of catalyst was investigated in the CO_2 methanation. Catalytic activity studies were performed by a Microactivity Effi reactor system. The catalyst was reduced in-situ with H_2 for 1 hour at 400°C before the reaction. The H_2/CO_2 molar ratio was set to 4. The experimental studies were carried out at atmospheric pressure and the temperatures of 300, 400, 500 and 600°C. 15%Ni/Zeo is the most effective in CO_2 methanation at 400°C with 66.36% CO_2 conversion and 99.33% CH_4 selectivity. Characterization studies and catalytic activity results showed that zeolite is a suitable support for CO_2 methanation.

Keywords: CO_2, Nickel-zeolite, Hydrogenation, CH_4

1 INTRODUCTION

CO_2 is one of the most important greenhouse gases with its increasing rate in the atmosphere in recent years. The usage, storage or evaluation of carbon dioxide by converting it into different products has been a remarkable research topic in recent years. CH_4 is the largest component of natural gas and is an important fuel. Therefore, the conversion of CO_2 to CH_4 is significant research [1].

The Fischer-Tropsch (FT) process is used to convert syngas to high C-number products and consists of a series of complex catalytic reactions [2]. The conversion of CO_2 to CH_4 takes place by hydrogenation of CO_2 and is part of the FT process. The catalysts used in the FT process vary according to the demanded product [3]. In general, high yield Ni catalysts are preferred in hydrogenation reactions to obtain CH_4 from CO_2 [4].

Zeolites have chemically active nanostructures [5] and are often preferred as support materials due to their properties such as porosity, crystal structure and thermal resistance. In addition, metal contents in natural zeolites can increase the efficiency of the catalyst.

There are a few studies in the literature in which Ni-containing catalysts prepared using commercial zeolites are used in CO_2 methanation [6–8]. However, no study was found in which the Ni catalyst prepared with the untreated natural zeolite support was used in the same reaction.

In this study, the untreated natural clinoptilolite zeolite supported catalyst with 15% Ni content was prepared, characterized and used in the production of CH_4 from CO_2.

2 EXPERIMENTAL

2.1 Synthesis of Catalyst

Natural zeolite with clinoptilolite properties was obtained from Balıkesir, Turkey. The impregnation method was used in the preparation of the catalyst. Calculated amount of nickel nitrate ($Ni(NO_3)_2.6H_2O$) was dissolved in water and added onto the natural zeolite. The solution was stirred, dried and the remaining solid powder was calcined with a stream of dry air at 500°C for 4 hours [9]. The final material was named as 15% Ni/Zeo.

2.2 Characterization

A Rigaku ZSX100 Primus X-Ray Fluorescence (XRF) device was used to determine bulk composition of catalyst.

The X-Ray Diffraction (XRD) patterns of fresh and used catalysts were recorded by using a Rigaku MiniFlex600 X Ray diffractometer in the 2θ range of 5° - 80° (Cu Kα radiation at 40Kv, step size: 0.04°).

Fourier Ttransform Infrared Spectroscopy (FT-IR) was performed with a Thermo Science Nicolet IS10 by using ATR technique. Spectra was recorded between 4000 cm^{-1} and 650 cm^{-1} wavenumbers.

The Scanning Electron Microscopy (SEM) of sample were recorded by a ZEISS-SUPRA 50 VP scanning electron microscope at 20 kV.

The Thermogravimetric (TG) analysis of the catalyst used was recorded with the Perkin Elmer STA6000 device in the temperature range of 30-900°C.

2.3 Methanation of CO_2

Possible reactions that can occur in the hydrogenation of CO and CO_2 have been shared in the literature [4,10]. The reaction of CO_2 methanation (R1) is as follows:

$$CO_2 + 4H_2 \leftrightarrow CH_4 + 2H_2O \quad \Delta H_{298K} = -165 \text{ kJ/mol (R1)}$$

The efficiency of the 15%Ni/Zeo catalyst in the methanation of CO_2 was determined using the MicroActivity Effi reactor. The reduction and reaction were carried out in-situ consecutively. The catalyst was placed in a stainless steel reactor and reduced for 1 hour under H_2 flow rate of 30 mL/min. Experimental studies were carried out at the temperatures of 300, 400, 500 and 600°C and atmospheric pressure. The H_2/CO_2 molar feed ratio was used as 4 and the gas hourly space velocity (GHSV) was maintained at 3600 mL/h.gcat. The composition of the gaseous products was determined online by the μGC device. A very small amount of liquid product was ignored.

2.4 Equations

The CO_2 conversion (X_{CO2}) and CH_4 selectivity (S_{CH4}) equations used in this study are as follows:

$$X_{CO2} = ((F_{CO2,in} - F_{CO2,out})/F_{CO2,in})*100 \quad (1)$$

$$S_{CH4} = (F_{CH4,out}/(F_{CH4,out}+F_{CO,out}+F_{C2H4,out}+ F_{C2H6,out}+ F_{C3H6,out}+ F_{C3H8,out}))*100 \quad (2)$$

Where $F_{X,in}$ and $F_{X,out}$ (mL/min) symbolize the amount of X in inlet and outlet, respectively.

3 RESULTS

3.1 Characterization Results

The XRF results of fresh catalyst are shown in the Table 1.

Table 1. The chemical composition of 15%Ni/Zeo

Component	wt. %
SiO_2	54.89
NiO	18.72
Al_2O_3	9.14
CaO	3.01
K_2O	2.76
Fe_2O_3	1.15
Others	0.81
LOI[a]	9.52

[a] Loss on ignition.

As it is seen from Table 1, the three main components of the catalyst are SiO_2, NiO and Al_2O_3 respectively. The NiO component was determined as 18.72%. According to the XRF results, it was clarified that the desired 15%Ni/Zeo catalyst was successfully synthesized.

The XRD diffraction patterns of fresh and used catalyst are shown in the Figure 1.

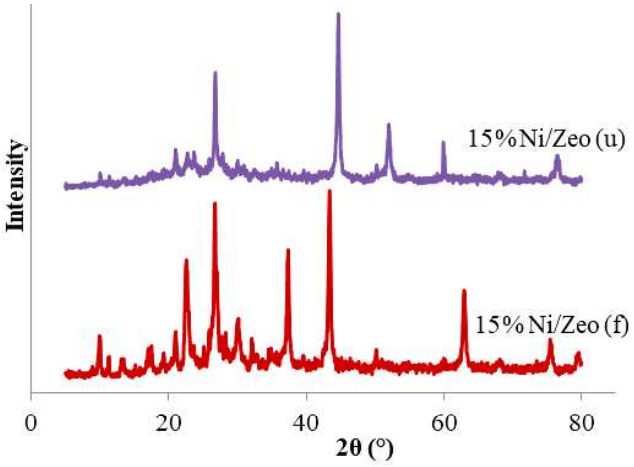


Figure 1. XRD patterns of fresh and used 15%Ni/Zeo

The clinoptilolite phases are observed at 2θ = 11, 14, 16, 20, 30, 33, 35 and 37,5° values in the Figure 1 [11]. The peak seen at 2θ = 26° corresponds to quartz SiO_2 phase [12] and it is also consistent with XRF results. Almost all of these peaks were detected in the fresh catalyst. It is understood that the natural zeolite used contains clinoptilolite. The peaks at 2θ = 37, 43 and 63° indicate the NiO phase in the fresh catalyst [6–8,13–15]. On the other hand, the metallic Ni peaks were observed at 44.5, 52 and 76.6° in the used catalyst [15,16].

The FT-IR spectra of the 15%Ni/Zeo is given in the Figure 2.

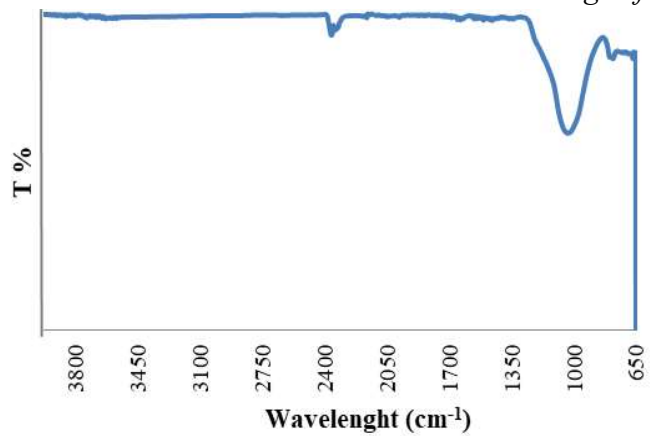


Figure 2. FT-IR spectra of 15%Ni/Zeo

The 791 cm^{-1} band is due to Si-O-Si vibrations indicating the presence of the quartz phase [17,18]. The 1004 cm^{-1} band is an indicator of the T-O bonds in the structure of the material (T = Al, Si) [19]. The bending vibration of water are observed at 1635 cm^{-1} [19]. And finally, the 3620 cm^{-1} band indicates the presence of structural OH groups.

The SEM micrograph of the 15%Ni/Zeo is given in the Figure 3.

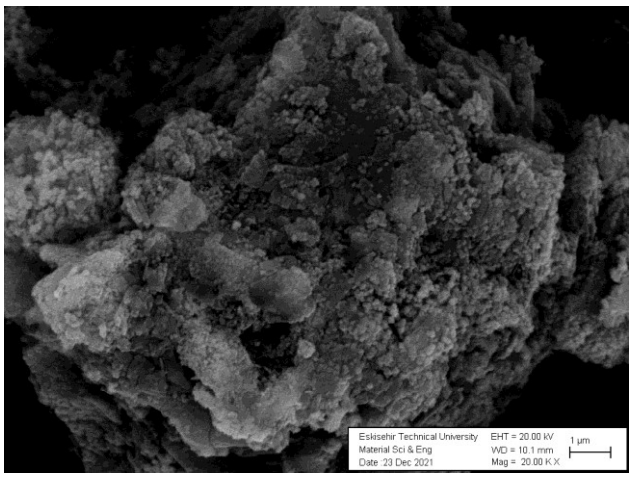


Figure 3. SEM micrograph of fresh 15%Ni/Zeo

The NiO particles was uniformly dispersed on the zeolite surface in the Figure 3. The different stone-like structures are observed in the SEM image of 15%Ni/Zeo catalyst that can be associated with the use of the support material as received. Hence, it is determined that the SEM image of the catalyst is compatible with the literature [11,20].

The TG curves of fresh and used 15%Ni/Zeo catalyst were given in the Figure 4.

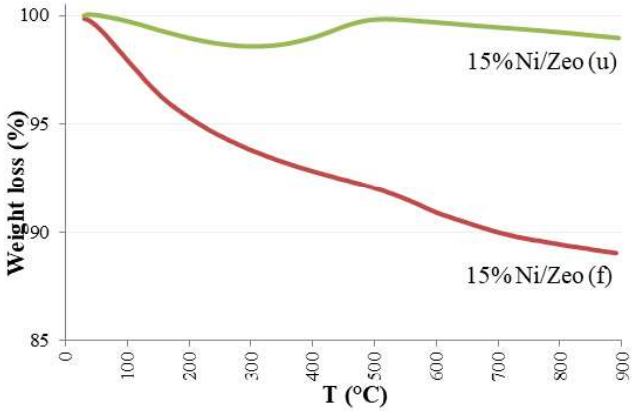


Figure 4. TG curves of 15%Ni/Zeo

The fresh catalyst lost about 11% of its mass at 900°C. The high mass loss can be attributed as normal as the natural zeolite without pretreatment. The mosture in the catalyst structure is removed below at 400°C and the OH group at 400-700°C [11,19]. The mass losses in the used catalyst up to 300°C are due to the removal of moisture and volatile components absorbed on the catalyst. The C species begin to leave above 300°C. The significant weight gain observed in the range of 300-500°C is due to metallic Ni oxidation, which suppresses the combustion of carbon species [21,22]. The amorphous carbon is oxidized at lower temperature in the range of 250-350°C. The mass losses at temperatures higher than 550°C are due to the oxidation of inert carbon (graphitic carbon) [23]. The used catalyst lost only 1.04% of its mass at 900°C. Therefore, it can be said that the accumulation of C on the catalyst is ignorable.

3.2 The Catalytic Activity Results

The catalytic activity results of 15%Ni/Zeo in terms of X_{CO2} (Equation 1) and S_{CH4} (Equation 2) are shown in Figures 5 and 6, respectively.

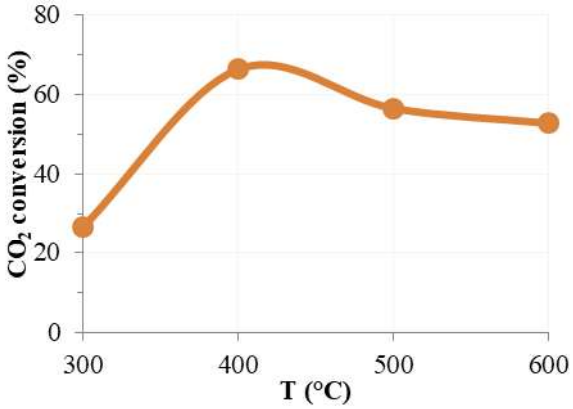


Figure 5. CO_2 conversion of 15%Ni/Zeo

15%Ni/Zeo reached the highest X_{CO2} at 400°C (66.36%). The commercial zeolite supported Ni catalysts was achieved 71% X_{CO2} at 400°C [6] and 65.5% at 450°C [7] in the literature. Because of the exothermic character of CO_2 methanation, X_{CO2} is reduced at 500 and 600°C. It was determined that the optimum temperature for 15%Ni/Zeo was 400°C in terms of X_{CO2} in the temperature range of 300-600°C.

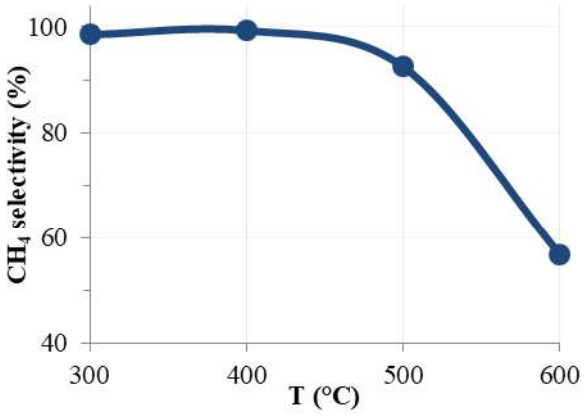


Figure 6. CH_4 selectivity of 15%Ni/Zeo

According to Figure 6, the S_{CH4} is almost 100% at 300 and 400°C. But the S_{CH4} gradually decreases as different endothermic reaction products appear above 400°C. The Ni-commercial zeolite catalysts was exhibited 95% S_{CH4} at 400°C [6] and 94.2% at 450°C [7] in the literature. In this study, the S_{CH4} is higher than the literature at 400°C. In terms of S_{CH4} for 15%Ni/Zeo in the temperature range of 300-600°C, the most suitable temperature was determined to be 400°C.

4 CONCLUSIONS

The untreated natural zeolite supported 15% Ni catalyst showed similar efficiency with the commercial zeolite supported Ni catalysts in the literature in terms of X_{CO2} in CO_2 methanation. It also provided about 100% S_{CH4} at 300 and 400°C. According to the XRD diffraction pattern, it was observed that the addition of Ni has no effect on the structure of the natural zeolite. The negligible mass loss was observed in the TG analysis of the used catalyst. This means that very small amount of C is deposited on the catalyst. The highest X_{CO2} and S_{CH4} values were achieved in the CO_2 methanation reaction carried out at 400°C. The positive structural properties and activity results show that the 15%Ni/Zeo is a suitable and potential catalyst for CO_2 methanation.

REFERENCES

[1] W. Li, X. Nie, X. Jiang, A. Zhang, F. Ding, M. Liu, Z. Liu, X. Guo, C. Song, ZrO_2 support imparts superior activity and stability of Co catalysts for CO_2 methanation, *Applied Catalysis B: Environmental*, Vol. 220, pp. 397–408, 2018.

[2] C.G. Okoye-Chine, M. Moyo, X. Liu, D. Hildebrandt, A critical review of the impact of water on cobalt-based catalysts in Fischer-Tropsch synthesis, *Fuel Processing Technology*, Vol. 192, pp. 105–129, 2019.

[3] A. Jayan, K. Anand, J. Stephen, An Overview of Ferrous and Cobalt Catalysts Used in the Conversion of Synthetic Gas to Fuels, *International Journal of ChemTech Research*, Vol. 10, pp. 494–505, 2017.

[4] A. Kakoee, A. Gharehghani, Carbon oxides methanation in equilibrium; a thermodynamic approach, *International Journal of Hydrogen Energy*, Vol. 45, pp. 29993–30008, 2020. https://doi.org/10.1016/j.ijhydene.2020.08.073.

[5] X. Su, J. Xu, B. Liang, H. Duan, B. Hou, Y. Huang, Catalytic carbon dioxide hydrogenation to methane: A review of recent studies, *Journal of Energy Chemistry*, Vol. 25, pp. 553–565, 2016.

[6] M.C. Bacariza, I. Graça, J.M. Lopes, C. Henriques, Enhanced activity of CO_2 hydrogenation to CH_4 over Ni based zeolites through the optimization of the Si/Al ratio, *Microporous and Mesoporous Materials*, Vol. 267, pp. 9–19, 2018.

[7] I. Graça, L.V. González, M.C. Bacariza, A. Fernandes, C. Henriques, J.M. Lopes, M.F. Ribeiro, CO_2 hydrogenation into CH_4 on NiHNaUSY zeolites, *Applied Catalysis B: Environmental*, Vol. 147, pp. 101–110, 2014.

[8] A. Quindimil, U. De-La-Torre, B. Pereda-Ayo, J.A. González-Marcos, J.R. González-Velasco, Ni catalysts with La as promoter supported over Y- and BETA-zeolites for CO_2 methanation, *Applied Catalysis B: Environmental*, Vol. 238, pp. 393–403, 2018.

[9] T. Xie, J. Wang, F. Ding, A. Zhang, W. Li, X. Guo, C. Song, CO_2 hydrogenation to hydrocarbons over alumina-supported iron catalyst: Effect of support pore size, *Journal of CO_2 Utilization*, Vol. 19, pp. 202–208, 2017.

[10] J. Gao, Y. Wang, Y. Ping, D. Hu, G. Xu, F. Gu, F. Su, A thermodynamic analysis of methanation reactions of carbon oxides for the production of synthetic natural gas, *RSC Advances*, Vol. 2, pp. 2358–2368, 2012.

[11] N. Mansouri, N. Rikhtegar, H. Ahmad Panahi, F. Atabi, B.K. Shahraki, Porosity, characterization and structural properties of natural zeolite - Clinoptilolite - As a sorbent, *Environment Protection Engineering*, Vol. 39, pp. 139–152, 2013.

[12] S.F. Kurtoğlu, S. Sarp, C. Yılmaz Akkaya, B. Yağcı, A. Motallebzadeh, S. Soyer-Uzun, A. Uzun, COx-free hydrogen production from ammonia decomposition over sepiolite-supported nickel catalysts, *International Journal of Hydrogen Energy, Vol*. 43, pp. 9954–9968, 2018.

[13] B. Daroughegi Mofrad, M. Rezaei, M. Hayati-Ashtiani, Preparation and characterization of Ni catalysts supported on pillared nanoporous bentonite powders for dry reforming reaction, *International Journal of Hydrogen Energy*, Vol. 44, pp. 27429–27444, 2019.

[14] N. Dong, Q. Ye, M. Chen, S. Cheng, T. Kang, H. Dai, Sodium-treated sepiolite-supported transition metal (Cu, Fe, Ni, Mn, or Co) catalysts for HCHO oxidation, *Chinese Journal of Catalysis*, Vol. 41, pp. 1734–1744, 2020.

[15] Y. Jiang, T. Huang, L. Dong, Z. Qin, H. Ji, Ni/bentonite catalysts prepared by solution combustion method for CO_2 methanation, *Chinese Journal of Chemical Engineering*, Vol. 26, pp. 2361–2367, 2018.

[16] D. Li, L. Zeng, X. Li, X. Wang, H. Ma, S. Assabumrungrat, J. Gong, Ceria-promoted Ni/SBA-15 catalysts for ethanol steam reforming with enhanced activity and resistance to deactivation, *Applied Catalysis B: Environmental*, Vol. 176–177, pp. 532–541, 2015.

[17] R. Chihi, I. Blidi, M. Trabelsi-Ayadi, F. Ayari, Elaboration and characterization of a low-cost porous ceramic support from natural Tunisian bentonite clay, *Comptes Rendus Chimie*, Vol. 22, pp. 188–197, 2019.

[18] L.F. Cótica, V.F. Freitas, I.A. Santos, M. Barabach, F.J. Anaissi, R.Y. Miyahara, P.W.C. Sarvezuk, Cobalt-modified Brazilian bentonites: Preparation, characterisation, and thermal stability, *Applied Clay Science*, Vol. 51, pp. 187–191, 2011.

[19] T. Perraki, A. Orfanoudaki, Mineralogical study of zeolites from Pentalofos area, Thrace, Greece, *Applied Clay Science*, Vol. 25, pp. 9–16, 2004.

[20] J. Kabuba, M. Banza, Ion-exchange process for the removal of Ni (II) and Co (II) from wastewater using modified clinoptilolite: Modeling by response surface methodology and artificial neural network, *Results in Engineering*, Vol. 8, pp. 100189, 2020.

[21] G. Wang, S. Xu, L. Jiang, C. Wang, Nickel supported on iron-bearing olivine for CO_2 methanation, *International Journal of Hydrogen Energy*, Vol. 41, pp. 12910–12919, 2016.

[22] L. Yao, J. Zhu, X. Peng, D. Tong, C. Hu, Comparative study on the promotion effect of Mn and Zr on the stability of Ni/SiO_2 catalyst for CO_2 reforming of methane, *International Journal of Hydrogen Energy,* Vol. 38, pp. 7268–7279, 2013.

[23] N. Wang, W. Chu, T. Zhang, X.S. Zhao, Synthesis, characterization and catalytic performances of Ce-SBA-15 supported nickel catalysts for methane dry reforming to hydrogen and syngas, *International Journal of Hydrogen Energy*, Vol. 37, pp. 19–30, 2012.

NUMERICAL INVESTIGATION OF A RCCI ENGINE PERFORMANCE USING NATURAL GAS (NG) / DIESEL FUEL UNDER LOW LOAD CONDITIONS

Müjdat Fırat[1], Mutlu Okcu[2], Şehmus Altun[3] and Yasin Varol[4]

1. Department of Automotive Engineering, Fırat University, Elazığ, Türkiye; email: mujdatfirat@gmail.com
2. Department of Electrical-Electronic Engineering, Ardahan University, Ardahan, Türkiye; email: mutluokcu@gmail.com
3. Department of Mechanical Engineering, Batman University, Batman, Türkiye; email: altun.sehmus@gmail.com
4. Department of Automotive Engineering, Fırat University, Elazığ, Türkiye; email: yvarol@gmail.com

Abstract

In this study, ANSYS-Forte Software was used to simulate the use of natural gas (NG) in diesel engines with reactivity controlled compression ignition (RCCI) and to examine the impact of premixed ratio (Rp). The engine model was built by using a 3D Scan view of a real single-cylinder diesel research engine and the results were obtained for different premixed fuel ratios at 20% engine load. The results showed that by increasing the premixed ratio at 20% load, the in-cylinder pressure and heat release rate decreased while the ignition delay (ID) period increased. Moreover, NOx and HC emissions were observed to be increased whereas CO and C_2H_2 emissions tended to be declined as Rp increased. However, engine efficiency started to decrease as Rp increased.

Keywords: Natural Gas (NG), CH_4, RCCI mode, numerical analysis, emissions

1 INTRODUCTION

In recent years, there have been many studies that investigate combustion concepts with the aim of emissions reduction from diesel engines. In these researches, the low-temperature concept (LTC) is widely suggested to reduce these emissions. In the LTC concept, it is tried to control the formation of air, exhaust gases and fuel mixture to obtain a low and homogeneously distributed local equivalence ratio in the cylinder. As a result, lowering local cylinder temperatures during combustion development reduces NOx and particulate matter at the same time [1]. According to the literature, the RCCI mode, which has been recently introduced, can minimize NOx and soot emissions in diesel engines while maintaining engine thermal efficiency [2, 3]. RCCI mode is an LTC concept that allows two different fuels with different reactivity to be injected into the same cylinder by different injection systems [4, 5]. In RCCI mode, low reactivity fuel is injected into the manifold by a port fuel injection (PFI) while high reactivity fuel is injected directly into the cylinder. According to recent studies on the RCCI concept, by adjusting the ratios of both low and high-reactivity fuels the combustion might be controlled [6, 7]. In the studies, it has been seen that different fuels are used as low reactivity fuel (LRF) in RCCI mode. Okcu et al. conducted an experimental investigation with a single-cylinder CRDI engine run on RCCI mode using heptanol and octanol as LRF while commercial diesel fuel as high reactivity fuel (HRF) and increased the CO and UHC emissions were reported with increasing LRF premixed ratio [4]. Thomas et al. investigated the effects of hexanol and diesel as LRF and HRF in an RCCI engine. It was reported a simultaneous decrease in smoke and NOx but an increase in HC and CO emissions [8]. Harari et al. used the mixtures of diesel fuel and biodiesel whereas gasoline was premixed fuel. In the study, NOx and smoke opacity were reported to be reduced while HC and CO emissions were increased [9]. As seen in the literature review, with conventional fuels, RCCI combustion leads to an increase in CO/HC emissions at a great level. therefore, alternative premixed fuels such

as gaseous fuels may be a solution for increasing incomplete combustion during RCCI operation in diesel engines. For example, compressed natural gas (CNG) was reported to have lower unburned HC and CO emissions due to its low carbon/hydrogen ratio [10]. Kakaee et al. studied numerically the use of CH_4 in RCCI engine and reported that NOx emissions increased while a reduction in UHC and CO emissions were obtained [11]. In a study by Li et al., natural gas (low cetane fuel) was mixed with air in the intake port before entering the cylinder while diesel fuel is injected directly into the cylinder. The use of premixed natural gas lowered CO, NO, and soot emissions [12]. Paykani et al. investigated the effect of the amount of premixed natural gas, the first and second diesel fuel injection timings and the division of the injected diesel mass between the two injections on RCCI combustion. The results showed that with the parameters used, engine efficiency can be increased, soot and NOx emissions can be reduced. On the other hand, it has shown that there are deteriorations in HC and CO emission values [13].

In RCCI engines, although reduction in NOx and PM emissions, the increase in unburned HC and CO emissions is still a problem to be solved. It is evaluated that natural gas can reduce unburned HC and CO emissions in RCCI engines when used as a low reactivity fuel due to its low carbon content. Therefore, the purpose of this study was to numerically examine the NG/diesel RCCI combustion in terms of its ability to reduce unburned HC and CO emissions. Despite the subject being widely studied before, the effect of the premixed ratio of NG was rarely reported, and thus, the effects of the NG premixed ratio on the combustion and emission characteristics of an RCCI engine fueled with natural gas/diesel fuel were investigated numerically.

2 MATERIAL AND METHOD

In previous studies, it was shown that methane (90%-96%) is the most abundant of the NG components and therefore it is exclusively employed in numerical calculations instead of NG [14, 15]. So, methane was used instead of NG in this study. A numerical study was carried out using the ANSYS-Forte package program. This software uses CHEMKIN combined with ANSYS to account for extensive chemical kinetics and various fuel chemistries. In numerical simulations, a fuel mechanism comprising 178 species was used. In this mechanism, methane (CH_4) was used as LRF and n-heptane (C_7H_{16}) as HRF. Table 1 shows the technical characteristics of the engine and Table 2 shows the characteristics of the fuels used in numerical analysis.

Table 1. Technical features of the test engine.

Power output @3000 rpm	7.4kW
Number of cylinder	1
Max. torque @ 2400 rpm	25.7Nm
Injection pressure	300 bar
Displacement	0.406 L
Bore x Stroke	86x70 mm
Compression ratio	18.1:1
Exhaust valve open	145°CA aTDC
Exhaust valve close	2°CA aTDC
Inlet valve open	9°CA bTDC
Inlet valve close	93°CA bTDC

Table 2. The study used methane and diesel fuel properties.

Parameters	**Diesel**	**NG**
Density (kg/m³)	829.4	657[17]
Boiling point (°C)	180-350	-162[17]
Flashpoint (°C)	67	-
Viscosity (mm²/s)	2.889	-
Low calorific value (MJ/kg)	43.14	50[17]
Latent heat of evaporation (kJ/kg)	358	-
Self-ignition temperature (°C)	210-250	-
Carbon content (%)	80.13	-
Hydrogen Content (%)	12.86	-
Oxygen content (%)	6.35	-
Octane number	-	120[17]
Cetane number	56	-

Combustion analysis in numerical studies is highly dependent on the accuracy of the geometry of the engine model used. The numerical analysis used a complete engine model, including intake and exhaust ports. To use in numerical studies, parts of a single-cylinder diesel engine were scanned by a 3D scanner and 3D geometric data were obtained. At the end of the scanning process, 3-dimensional solid engine parts that are very similar to reality were created. Figure 1 shows photographs of the scanning process for engine parts. In addition, images of the full engine model generated at the end of the scan may be found in Figure 2.

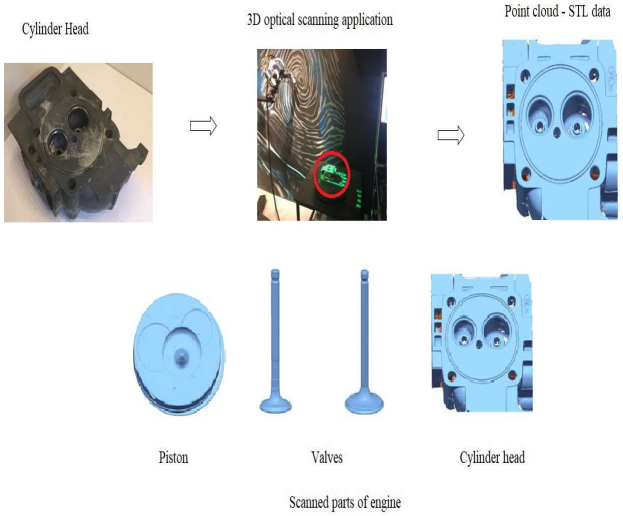


Figure 1 A solid model of the engine parts scanned by a 3D scanner

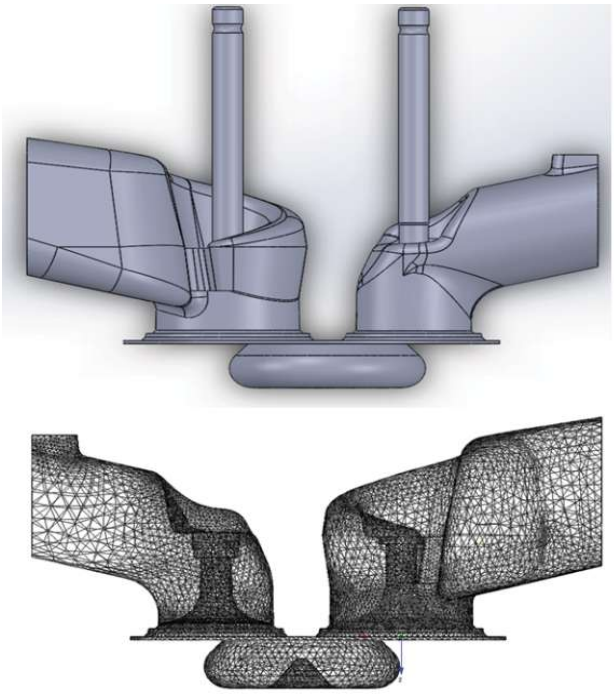


Figure 2 Full engine model for CFD simulation

In the study, the effects of using methane as LRF and diesel as HRF on engine performance and emissions were investigated. The investigations were carried out at 2400 rpm, which is the maximum torque speed, and at 20% engine load. RCCI was applied in all experiments as 15%, 30% and 45% of this amount of energy to keep the total energy of the fuel provided to the engine in conventional diesel combustion per cycle constant. Table 3 shows the study boundary conditions used in the experimental investigation.

Table 3. Boundary conditions of the numerical study.

Parameters	RCCI	CDM
Load (% of max. torque)	20	20
Engine speed (rpm)	2400	2400
E_{total} (J/cycle) @ % load	310@20%	310@20%
CRDI pressure (bar)	300	300
PFI pressure (bar)	5	-
DI timing (^oCA bTDC)	21^oCA	21^oCA
PFI timing (^oCA aTDC)	15	--
Rp (LRF premixed ratio)	0, 15, 30, 45	--
HRF used in study	Diesel	Diesel
LRF used in study	Methane (CH_4)	-

To determine Rp used in the analysis, the E_{total} given in Table 3 was used. For example, in the experiments, it was determined that when diesel is used at 20% load in an engine with RCCI mode, 310 J/cycle total energy is supplied to the engine. At this load, it is desired to apply a mixture ratio of 15%. Therefore, 15% of the total energy (310 J/cycle) given to the engine at 20% load was given with the use of LRF and the remaining 85% as HRF. Thus, the experiment has been made that LRF premixed ratio was 15% at 20% engine load. To determine other LRF premixed ratios, this approach was used. In addition, Equation 1 was used to determine LRF premixed ratio.

$$R_p = \frac{M_L \text{ x } Hu_L}{M_L x Hu_L + M_H x Hu_H} \quad (1)$$

In this equation, it is expressed as Rp. In addition, M and Hu represent the mass and lower thermal value of the fuels, respectively. Subscript L denotes to low reactivity fuel and subscript H denotes to high reactivity fuel.

3 RESULTS AND DISCUSSIONS

Fig. 3 shows the effects of different Rp at 20% load on in-cylinder pressure and rate of heat release rate. As shown in Fig. 3, the RCCI mode was found to be effective in maintaining and increasing pressure and heat release rate at 15% Rp, but it caused pressure drop at 30% and 45% Rp. The pressure peak value decreased with the use of NG, and this reduction occurred at 30% and 45% Rp, about 3% and 5.2%, respectively. When NG was utilized, the heat release rate increased about 22% and 3%, respectively, for 15% and 30% Rp. However, at 45% Rp, it was not changed. It is thought that the reason for the partial prolongation of the ignition delay in the operation is the higher octane number and auto-

ignition temperature of NG compared to diesel. In previous studies, it was stated that the high octane number and auto-ignition temperature of the fuels prolonged the ignition delay [13, 16]. In the presented study, as Rp increased, the ignition delay increased for similar reasons.

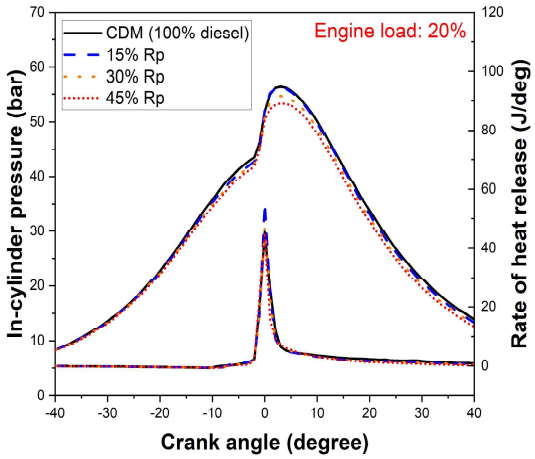


Figure 3. The changes in the in-cylinder pressure and heat release rate with the use of NG at different ratios.

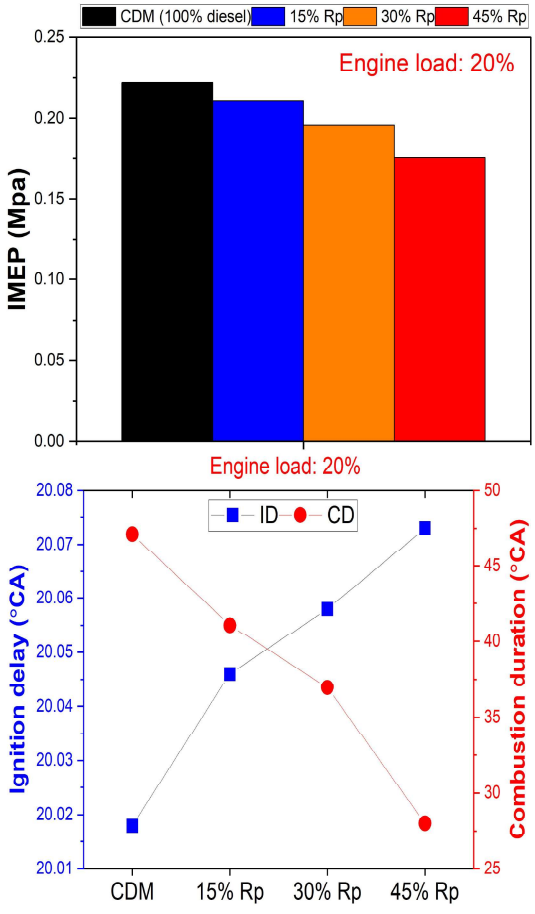


Figure 4. The changes in the IMEP, ignition delay and combustion duration with the use of NG at different ratios.

Figure 4 shows the effects of different Rp at 20% load on IMEP and ignition delay/combustion duration. As shown in Fig. 4, when Rp was increased, the ignition delay increased, IMEP and combustion duration decreased. IMEP decreased with increasing Rp (from 15% to 45%) about 5%, 12%, and 21%, respectively. Although there was a partial reduction in the ignition delay, the combustion duration gradually decreased greatly with the increase of Rp. Combustion duration decreased with increasing Rp (from 15% to 45%) about 13%, 21%, and 40%, respectively It has been found that the use of NG increases the ignition delay and decreases the combustion duration because of the high octane number, especially at high Rp. As known, IMEP varies depending on the amount of work completed and the volume of the cylinder [17]. The amount of work completed is a function of the highest pressure and the crank angle at which this pressure occurs to TDC. A similar change was also expressed Pan et al. [18]. So, in the presented study, as Rp increased, pressure decreased and therefore IMEP decreased.

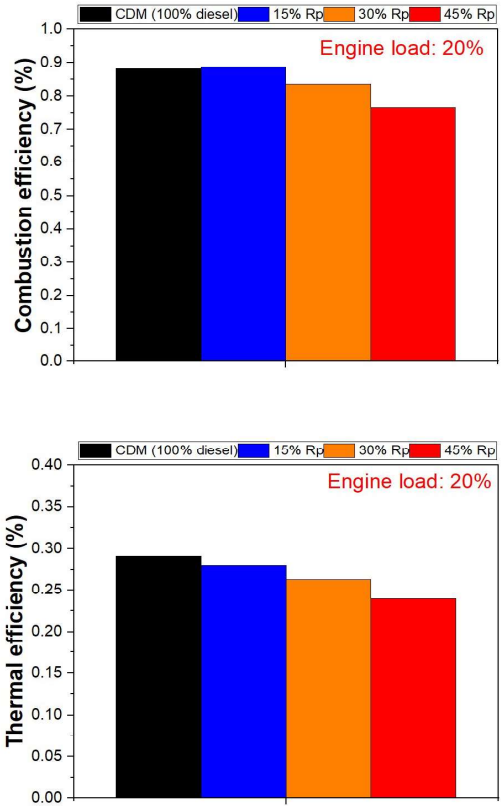


Figure 5. The changes in the combustion and thermal efficiency with the use of NG at different ratios.

Figure 5 shows the impact of increasing the NG premixed ratio on combustion and thermal efficiency. As shown in Fig. 5, RCCI mode decreased thermal efficiency for all Rp. Also, the combustion efficiency decreased at 30 and 45% Rp, although there was no increased or decreased at 15% Rp. The highest decrease in combustion efficiency was 13% at 60% Rp. On the other hand, a gradual decline in thermal efficiency was observed with an increase in Rp. Also, as Rp increased, the decrease of thermal efficiency increased, and the decrease rate was determined to be about 3.5%, 9%, and 17.5%, respectively. The high auto-ignition temperature and octane number of NG made it difficult for the charge to begin burning, and thus both combustion and thermal efficiency were reduced. Paykani et al. also obtained similar results in their study [13]. As a consequence, it was determined that increasing the premixed ratio gradually decreased both combustion and thermal efficiency in the present investigation at low engine load by using RCCI mode.

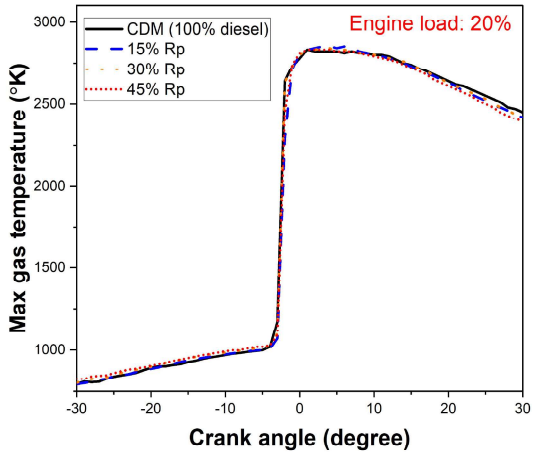


Figure 6. The changes in maximum gas temperature (MGT) with the use of NG at different ratios.

Figure 6 shows the effects of different Rp at 20% load on the maximum in-cylinder gas temperature. As sown in Fig. 6, the temperature increased using RCCI and CDM at the start of the combustion processes (3°CA bTDC) in all simulations. Use of RCCI mode, MGT decreased slightly in comparison to CDM as the premixed ratio increased. The main decrease in temperature happened as the crank angle improved, and it was observed that this decrease was more distinct at 20°CA (aTDC), and the decrease rate improved as Rp increased. The temperature peak value increased slightly (0.8%) when LRF was used at 15% and 30% Rp compared to diesel but stayed constant at 45% Rp (5°CA bTDC). With the use of LRF, the temperature started to decrease between 20 and 30 °CA (aTDC), and there was a decrease of about 3% at 45% Rp compared to diesel at 40 °CA (aTDC). The partial decrease in temperature is thought to be caused by the high auto-ignition temperature of NG and octane number, especially at high premixed ratios.

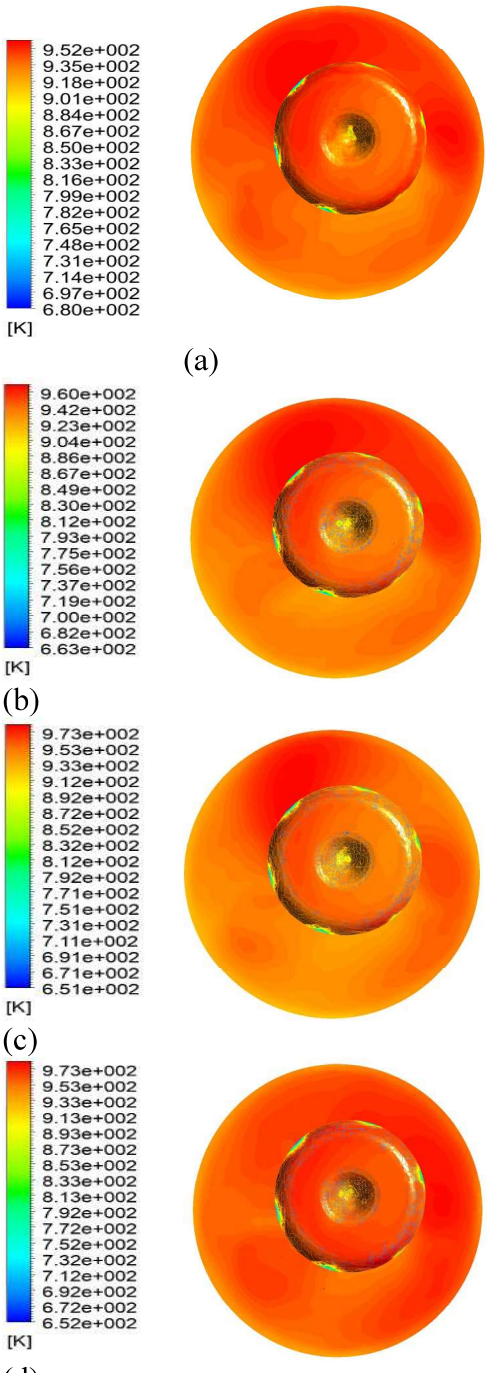


Figure 7. The change in the in-cylinder temperature contour formation in the use of NG

at different ratios at 10 °CA bTDC. (a) Diesel, (b) 15% Rp, (c) 30% Rp and (d) 45% Rp

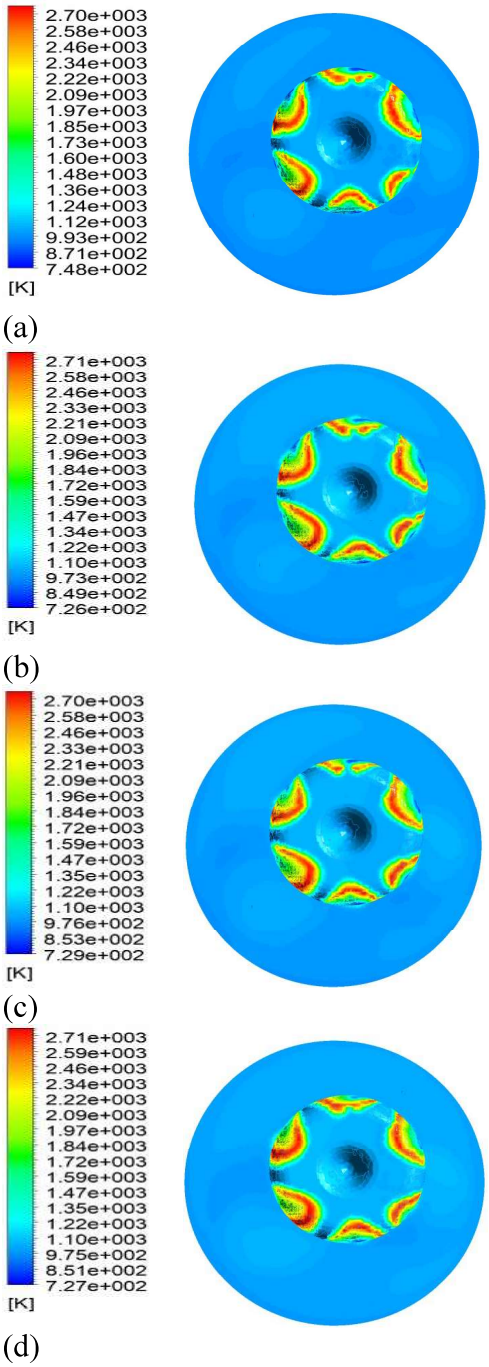
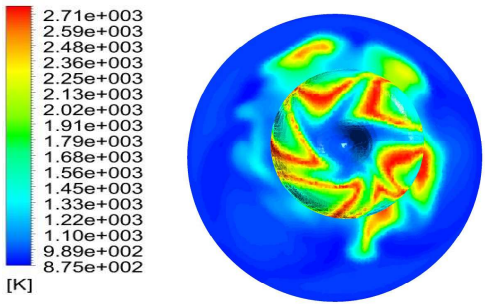


Figure 8. The change in the in-cylinder temperature contour formation in the use of NG at different ratios at TDC. (a) Diesel, (b) 15% Rp, (c) 30% Rp and (d) 45% Rp.



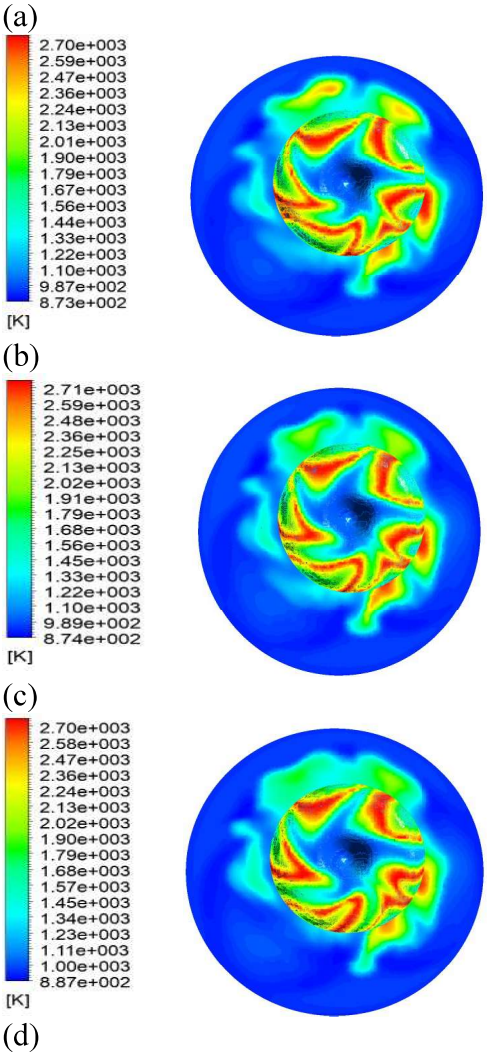


Figure 9. The change in the in-cylinder temperature contour formation in the use of NG at different ratios at 10 °CA aTDC. (a) Diesel, (b) 15% Rp, (c) 30% Rp and (d) 45% Rp.

Figure 7-9 shows the effects of different Rp on the temperature contours at the combustion chamber at 20% load. The combustion reaction temperature and the hot areas in the combustion chamber increased as LRF premixed ratio increased when the piston was at TDC. Similar changes occurred when the piston was at 10 °CA before and after TDC. The NG injected during the intake stroke is thought to create a homogenous mixture with the air, thus increasing the hot zones in the combustion chamber and cylinder. Paykani et al. obtained similar results in their investigation [13]. It is thought that the temperature change in these crank angles gives important information about engine emissions.

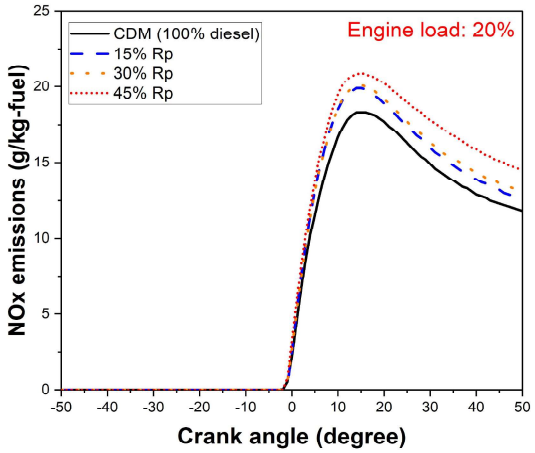


Figure 10. The changes in NOx emissions with the use of NG at different ratios.

Figure 10 shows the effects of different Rp on NOx emissions at 20% load. As shown in Fig. 10, NOx emissions increased with the use of RCCI mode. Also, when LRF premixed ratio was increased from 15% to 45%, NOx emissions increased by about 8.7%, 9.8%, and 14%, respectively. As stated in previous studies, NOx emissions are a combustion product that is influenced by a variety of parameters including in-cylinder temperature, oxygen content in the charge, rate of heat release rate and combustion duration [19, 20]. As shown in Fig. 10, as the ratio of NG increased, the combustion reactions began slightly faster than the diesel, and the cylinder temperature reached its maximum value in a shorter time. So, NOx emissions increased with increasing temperature. In conclusion, when the RCCI mode was employed, NOx emissions increased, and the increase rate improved as the NG ratio increased.

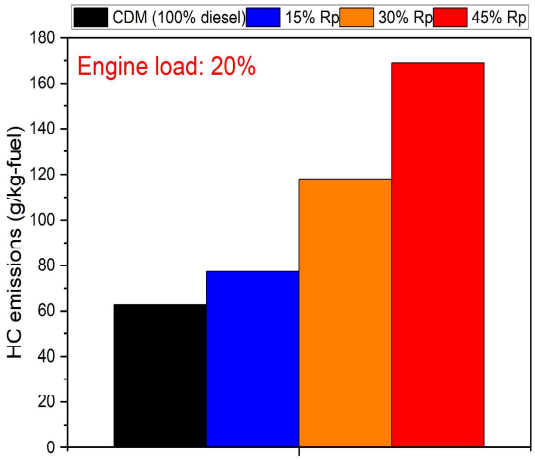


Figure 11. The changes in HC emissions with the use of NG at different ratios.

Figure 11 shows the impact of increasing the NG premixed ratio on HC emissions at 20% load. As shown in Fig. 11, HC emissions increased with the use of RCCI mode. When LRF premixed ratio was increased from 15% to 45%, HC emissions increased about 23%, 88%, and 169%, respectively, compared to CDM. For RCCI mode, the inability of the fuel accumulated on the cylinder wall to fully participate in the combustion reactions is known to be the principal cause of HC emissions [21, 22]. Although the carbon/hydrogen ratio decreased as LRF premixed ratio increased, it is thought that HC emission increased due to the accumulation of NG injected at the intake stroke on the cylinder walls. As a result, although increasing the NG ratio increased HC emissions, the small rise rate with the use of LRF at 15% Rp is accepted to be important for RCCI mode.

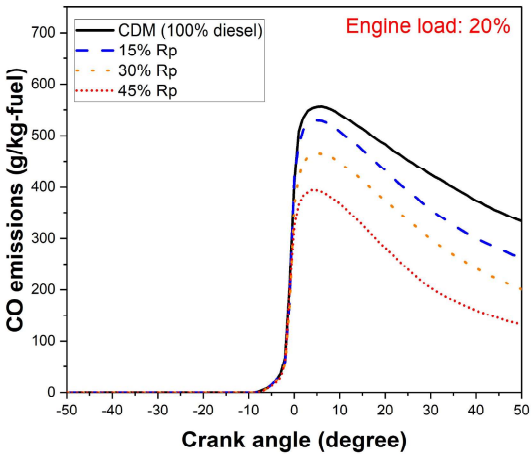


Figure 12. The changes in CO emissions with the use of NG at different ratios.

Figure 12 shows the effects of different Rp on CO emissions at 20% load. As shown in Fig. 12, CO emissions decreased as LRF premixed ratios. Also, when LRF premixed ratio was increased from 15% to 45%, CO emissions decreased about 4.8%, 16%, and 29%, respectively, compared to diesel. Similar changes occurred in the study by Singh and Maji [23]. CO emissions are known to be influenced by the amount of unburned gas fuel, incomplete combustion of the fuel, oxygen content and the temperature of the mixture [24]. Some of these parameters were valid in presented study. Firstly, as the ratio of NG increased due to the lower calorific value of NG, the carbon ratio in the charge decreased and thus CO emissions decreased. Secondly, also as Rp increased, the cylinder temperature increased and therefore CO emission decreased. As a result, thanks to the present study, it has been shown that employing

NG as LRF can reduce CO emissions, which is one of the most serious issues in engines with RCCI mode.

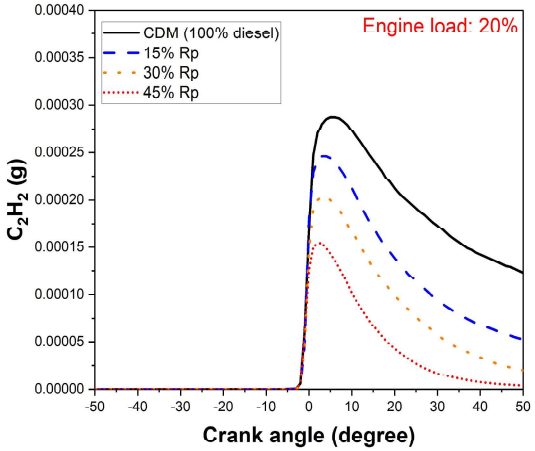


Figure 13. The changes in C_2H_2 emissions with the use of NG at different ratios.

In previous studies, acetylene (C_2H_2) was expressed as a hydrocarbon type that gives information about the formation of soot emissions [25, 26]. In light of this, the change in C_2H_2 was studied and presented in Figure 13 to provide information about the change in soot emission. As shown, C_2H_2 decreased as LRF premixed ratio increased. When the highest C_2H_2 levels were compared, the most significant reduction occurred at about 46.5% at 45% Rp. Furthermore, when 45% Rp is used, C_2H_2 emissions are reduced by 97% compared to diesel at 50 °CA aTDC. As earlier mentioned, HC emission increased with the use of Rp. This increase in HC emissions is predicted to lower soot emissions. In the study of Zehni et al., the change between these two emission types was also expressed [25]. As a result, when the RCCI mode is used, great progress has been made in lowering C_2H_2, which is known as a precursor to soot emissions.

4 CONCLUSIONS

In this study, the use of NG in diesel engines operated with RCCI mode was simulated by ANSYS-Forte Software and the effect of Rp was investigate at 20% load. RCCI engine were investigated at the maximum toque speed of 2400 rpm. The following conclusions can be drawn from the experimental findings:

- There were no changes in pressure and heat release rate when NG was utilized at %15 Rp. There was, however, decrease in pressure and an increase in heat release rate as Rp increased.
- As Rp increased, IMEP decreased. Increasing Rp from 15% to 45% decreased IMEP by 5%, 12%, and 21%, respectively.
- It has been determined that when 15% Rp is used, the combustion efficiency did not decrease, but the thermal efficiency decreased slightly. However, when other Rps were used, both thermal and combustion efficiency were reduced.
- The increase in LRF premixed ratio increased the temperature, and thus increasing the NOx and HC emission while decreasing the CO and C_2H_2 emissions.

ACKNOWLEDGEMENTS

The Scientific and Technological Research Council of Turkey (TUBITAK) is great acknowledgment for financial support with project numbered 118M650.

REFERENCES

[1] A.P. Carlucci, D. Laforgia, S. Motz, R. Saracino, and S. P. Wenzel, Advanced closed loop combustion control of a LTC diesel engine based on in-cylinder pressure signals, *Energy Conversion and Management,* vol. 77, pp. 193-207, 2014.

[2] A. K. Agarwal, A. P. Singh, and R. K. Maurya, Evolution, challenges and path forward for low temperature combustion engines, *Progress in Energy and Combustion Science*, vol. 61, pp. 1-56, 2017.

[3] M. A. Said, I. B. Dalha, Z. A. A. Karim, and M. El-Adawy, Influence of biogas mixing parameters on the combustion and emission characteristics of diesel RCCI engine, *Alexandria Engineering Journal*, vol. 61(2), pp. 1479-1497, 2022.

[4] M. Okcu, M. Fırat, Y. Varol, Ş. Altun, F. Kamışlı, and O. Atila, Combustion of high carbon (C7-C8) alcohol fuels in a reactivity controlled compression ignition (RCCI) engine as low reactivity fuels and ANN approach to predict RCCI emissions, *Fuel*, vol. 319, p. 123735, 2022.

[5] R. K. Maurya, Characteristics and control of low temperature combustion engines, Cham, Switzerland: Springer pp. 31-133, 2018.

[6] D. Z. Zhou, W. M. Yang, H. An, J. Li, and C. Shu, A numerical study on RCCI engine fueled by biyodiesel/methanol, *Energy Conversion and Management*, vol. 89, pp. 798-907, 2015.

[7] Y. Zhong, W. Han, C. Jin, X. Tian, H. Liu, Study on effects of the hydroxyl group position and carbon chain length on combustion and emission characteristics of Reactivity Controlled Compression Ignition (RCCI) engine fueled with low-carbon straight chain alcohols, *Energy*, vol. 239, p. 122259, 2022.

[8] J. J. Thomas, V. R. Sabu, G. Basrin, and G. Nagarajan, Hexanol: A renewable low reactivity fuel for RCCI combustion, *Fuel*, vol. 286, p. 119294, 2021.

[9] P. A. Harari, N. R. Banapurmath, V. S. Yaliwal, T. Y. Khan, M. E. M. Soudagar, and A. M. Sajjan, Experimental studies on performance and emission characteristics of reactivity controlled compression ignition (RCCI) engine operated with gasoline and Thevetia Peruviana biodiesel, *Renewable Energy*, vol. 160, pp. 865-875, 2020

[10] E. Ansari, K. Poorghasemi, B. K. Irdmousa, M. Shahbakhti, and J. Naber, Efficiency and emissions mapping of a light duty diesel-natural gas engine operating in conventional diesel and RCCI modes, *SAE Technical Paper,* (2016-01), 2309.

[11] A. H. Kakaee, P. Rahnama, and A. Paykani, Influence of fuel composition on combustion and emissions characteristics of natural gas/diesel RCCI engine. *Journal of Natural Gas Science and Engineering*, vol. 25, pp. 58-65, 2015.

[12] J. Li, W. M. Yang, T. N. Goh, H. An, and A. Maghbouli, Study on RCCI (reactivity controlled compression ignition) engine by means of statistical experimental design, *Energy*, vol. 78, pp. 777-787, 2014.

[13] A. Paykani, A. H. Kakaee, P. Rahnama, and R. D. Reitz, Effects of diesel injection strategy on natural gas/diesel reactivity controlled compression ignition combustion, *Energy*, vol. 90, pp. 814-826, 2015

[14] A. Yousefi, H. Guo, and M. Birouk, An experimental and numerical study on diesel injection split of a natural gas/diesel dual-fuel engine at a low engine load, *Fuel*, vol. 212, pp. 332-346, 2018.

[15] M. M. Salahi, V. Esfahanian, A. Gharehghani, and M. Mirsalim, Investigating the reactivity controlled compression ignition (RCCI) combustion strategy in a natural gas/diesel fueled engine with a pre-chamber. *Energy Conversion and Management*, vol. 132, pp. 40-53, 2017.

[16] S. Bari, and S. N. Hossain, Performance of a diesel engine run on diesel and natural gas in dual-fuel mode of operation, *Energy Procedia*, vol. 160, pp. 215-222, 2019.

[17] ANSYS Forte 17.0, ANSYS: San Diego, 2015.

[18] S. Pan, X. Liu, K. Cai, X. Li, W. Han, and B. Li, Experimental study on combustion and emission characteristics of iso-butanol/diesel and gasoline/diesel RCCI in a heavy-duty engine under low loads, *Fuel*, vol. 261, p. 116434, 2020.

[19] A. Gharehghani, R. Hosseini, M. Mirsalim, S. A. Jazayeri, and T. Yusaf, An experimental study on reactivity controlled compression ignition engine fueled with biodiesel/natural gas, *Energy*, vol. 89, pp. 558-567, 2015.

[20] A. P. Carlucci,., A. de Risi, D. Laforgia, and F. Naccarato, Experimental investigation and combustion analysis of a direct injection dual-fuel diesel–natural gas engine. *Energy*, vol. 33(2), pp. 256-263, 2008.

[21] M. Yao, Z. Chen, Z. Zheng, B. Zhang, and Y. Xing, Study on the controlling strategies of homogeneous charge compression ignition combustion with fuel of dimethyl ether and methanol, *Fuel*, vol. 85(14-15), pp. 2046-2056, 2006.

[22] O. K. Demirci, and C. Çınar, The Investigation of the Effects of Using Natural Gas on the Performance and Exhaust Emissions in an HCCI-DI Engine, *Gazi University Journal of Science Part C: Design and Technology*, vol. 7(2) pp. 317-330, 2019.

[23] R. Singh, and S. Maji, Performance and exhaust gas emissions analysis of direct injection cng-diesel dual fuel engine, *International Journal of Engineering Science and Technology*, vol. 4(3), pp. 833-846, 2012.

[24] S. A. Ahmed, Z. H. O. U. Song, and Z. H. U. Yuangqing, Performance and emission characteristics analysis of dual fuel compression ignition engine using natural gas and diesel. *International Journal of Thermodynamics*, vol. 21(1), pp. 16-25, 2018.

[25] A. Zehni, R. K. Saray, and K. Poorghasemi, Numerical comparison of PCCI

combustion and emission of diesel and biodiesel fuels at low load conditions using 3D-CFD models coupled with chemical kinetics, *Applied Thermal Engineering*, vol. 110, pp. 1483-1499, 2017.

[26] S. Liu, L. Shen, Y. Bi, and J. Lei, Effects of altitude and fuel oxygen content on the performance of a high pressure common rail diesel engine, *Fuel,* vol. 118, pp. 243-249, 2014.

Numerical Comparison of premixed turbulent combustion models for ethylene/air mixtures up to 1 MPa

Siva PR Muppala
The Faculty of Engineering, Computing and the Environment
Kingston University London, UK
email: s.muppala@kingston.ac.uk

Abstract
This numerical study involves the evaluation of four popular premixed turbulent combustion models for ethylene/air mixtures of different Lewis numbers at high operating pressures. The mean reaction rates are based on algebraic closures, the Bray-Moss-Libby and Lindstedt–Váos models, and flame surface density (Cant-Pope-Bray and Coherent Flame Model) models.

The RANS simulated turbulent burning velocity is compared with Kobayashi experimental data and analysed for the workability of each model separately. These comparative studies show that these combustion models were originally developed for methane/air mixtures at atmospheric pressure and may require the tuning of pre-constants or the addition of external terms for quantitative adjustments for the Lewis number effects and influence of high pressures.
Keywords: Premixed turbulent combustion, lean mixtures, high pressure, reaction models, RANS

1 INTRODUCTION

In turbulent premixed combustion, premixed flame fronts exist and propagate into turbulent fluid flow. If the turbulent intensity is not too high, highly convoluted, stretched and wrinkled laminar premixed flame fronts are formed [1]. This has the advantage over the laminar flame in that, for the same volume of flame, significant increase in the flame area is created, thus increasing the reaction-rate-per-unit volume by several folds – a desired condition for many industrial applications [2]. If physically interpreted, this twisted turbulent flame can be viewed as an ensemble of many premixed laminar flames. Such a flame is designated as a flamelet. Figure 1a illustrates (single shot) instantaneous turbulent premixed flame [3]. For Fig. 1b, lean premixed fuel and oxidizer (air) flows upwards with mean velocity U, and the flame produced is stabilised on a Bunsen burner. The full flame cone angle θ is measured in the paper of the mean averaged flame and the turbulent flame speed S_T is obtained from the half cone flame angle, $S_T/U = \sin(\theta/2)$ [4,5]

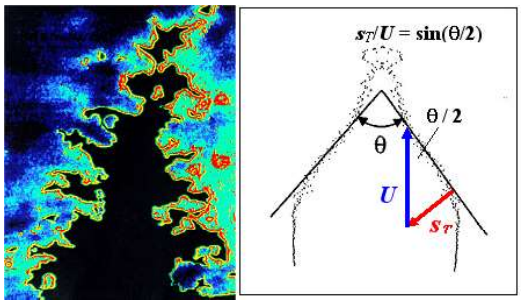


Fig. 1 a) Instantaneous turbulent 80mm Bunsen flame structure obtained using light-sheet LIF measurement, Re_t =750, Ka = 0.48 [3]; b) a typical mean flame contour depicts the relationship between the flame cone angle (θ), inflow velocity (U) and turbulent flame speed S_T [6].

High-pressure combustion is a plausible way to achieve high laden in combustors. However, measurements in

such an environment and characterisation of high-pressure combustion are limited, mainly because of difficulties in conducting experiments at these pressures. Therefore, numerical simulations partly fill this gap. With its definite use in spark-ignition engines and gas turbine combustors, where the pressure loads reach up to 4.0 MPa, refined treatments to turbulent premixed flames continue to drag the attention of application engineers.

The primary goal of this study is to determine the turbulent flame speed numerically from four premixed turbulent models, with an emphasis on investigating the influence of pressures above 1 bar, for a broad range of different turbulent intensities and mixture compositions. The numerical results in terms of the normalised turbulent flame speed are compared with the corresponding Kobayashi data and discuss the limited applicability of the models.

1 Theory of flamelets

Premixed turbulent flames are often seen as turbulent flamelets. With thin flame elements, the inner structure is similar to a laminar case, but is wrinkled by turbulence motions. This allows a flamelet concept applied to premixed flames. Such a flame falls in the regime $Ka < 1$ and $Da > 1$. Following [7], the average reaction rate is given as $\overline{w}_c = \rho_u s_L I_0 \Sigma$.

Concerning the average reaction rate approach (Eq. 1), ρ_u and s_L are known quantities, while I_0 and Σ require modelling. Modelling of I_0 is a special scenario such as in the BML model where it is modelled separately. In other cases, its value is taken as unity. Modelling Σ is an essential aspect of turbulent premixed flamelet models. Of many approaches to modelling this term available in the literature, two model classes are handled here, namely algebraic and flame surface density models.

2 Experimental Details

In this numerical study, ethylene data used from a large set of experimental data on turbulent premixed stationary flames in a high-pressure chamber up to 30 bar were presented in three papers [6,8,9], which are used for validation purposes. These measurements were performed on a 20mm Bunsen burner with grid-induced turbulence was used to determine the average flame shape. Measured data show a distinct bimodal structure between the unburned and burned parts of an instantaneous flame, which is typical of a flamelet regime. These flames are distributed into regimes of wrinkled flamelets, corrugated flamelets and thin reaction zones.

These data were obtained on a wide range of velocity fluctuation intensities for ethylene-air mixtures for turbulence velocity normalised with unstretched laminar flame speed up to $u'/s_L < 24$, mean flow velocity U = 1.5 to 8.8 m/s and lateral integral length scale l_x ~ 1.8mm and turbulent Reynolds number Re_t up to 1220.

3 General computational details, Numerical Implementation and Combustion models

The finite volume method commercial solver Fluent is used in the validation calculations. All the progress variable

based combustion closures are handled externally with subroutines. The convective fluxes are interpolated using a second-order scheme.

The grid dependency was investigated for a typical flame and settled with a grid resolution of 25 cells/cm, which corresponds to a total number of grid points slightly above 15,000 cells. Pressure-velocity coupling is based on the SIMPLE scheme, while for turbulence modelling, the standard formulation of the $k-\varepsilon$ model is used.

3.1. Favre-averaged algebraic flame closures

The Favre-averaged conservation equation for the reaction progress variable, assuming a gradient approach is

$$\frac{\partial}{\partial x_i}\left(\rho\widetilde{u}_i\widetilde{c}\right)=\frac{\partial}{\partial x_i}\left(\rho\frac{\nu_t}{Sc}\frac{\partial\widetilde{c}}{\partial x_i}\right)+\overline{w}_c \quad \text{Eq.1}$$

where ρ is variable gas density, ν_t is turbulent viscosity, $\tilde{c}$ is the Favre-averaged reaction progress variable, a normalised temperature for the reaction source term $\overline{w}_c=\rho_u s_L I_0\Sigma$. In this, ρ_u is the unburned gas density, s_L is unstretched laminar flame speed, I_0 is stretch factor and for all the simulations, is taken as equal to unity, and Σ is the turbulent flame area to the averaged flame area that requires modelling.

3.1.1. The Bray-Moss-Libby model

Following the modelling of the characteristic wrinkling flame length and flame stretch factor from [7], it leads to the reaction rate, $\overline{w}_c=\rho_u s_L I_0\Sigma$ known as the BML model

$$\overline{w}_c=\rho_u s_L\left(\left(\frac{u'}{s_L}\right)^{-0.568}\left(\mathrm{Re}_t\right)^{0.392}\left(\frac{1}{(1+\tau\cdot\widetilde{c})^2}\frac{\widetilde{c}(1-\widetilde{c})}{l_x}\right)\right) \quad \text{Eq.2}$$

3.1.2. The Lindstedt and Váos model

Lindstedt and Váos proposed an algebraic closure expression (Eq.3) for the flame surface density; its measurement is obtained using an algebraic expression, derived on the presumption that the flamelet geometry is fractal [10] i.e., based on the length scale cut-off limits. The closure of the mean reaction rate expression becomes

$$\overline{w}_c=C_R\rho_u\frac{s_L}{V_K}\frac{\widetilde{\varepsilon}}{\widetilde{k}}\widetilde{c}(1-\widetilde{c}) \quad \text{Eq.3}$$

where V_K is the Kolmogorov time scale, given as $(\varepsilon\nu)^{\frac{1}{4}}$, ε is turbulent dissipation rat, ν is molecular kinematic viscosity and C_R is the reaction rate parameter, equal to 2.6.

3.2. Flame surface density models

The second approach, based on the concept of flame surface density (FSD), i.e. flame surface area per unit volume of flame, requires a transport equation for Σ, in addition to that of $\tilde{c}$. Here, both the scalar transport equations are solved simultaneously (as shown schematically below) until a stable flame is obtained (Eq.4).

$$\frac{\partial}{\partial x_i}\left(\rho\widetilde{u}_i\widetilde{c}\right)=\frac{\partial}{\partial x_i}\left(\rho\frac{\nu_t}{Sc}\frac{\partial\widetilde{c}}{\partial x_i}\right)+\rho_u s_L I_0\Sigma$$

$$\frac{\partial}{\partial x_i}\left(\widetilde{u}_i\Sigma\right)=\underbrace{\frac{\partial}{\partial x_i}\left(\frac{\nu_t}{Sc}\frac{\partial\Sigma}{\partial x_i}\right)}_{=S_1}+\underbrace{k_m\Sigma}_{=S_2}+\underbrace{k_t\Sigma-D}_{=D} \quad \text{Eq.4}$$

The left side are the transient and the mean convective term and the right

side are turbulent diffusive transport and reaction rate. The model S_2 terms is proportional to $(\varepsilon/\nu)^{1/2}\Sigma$, $(\varepsilon/k)\Sigma$ and $\mathrm{Re}_t^{1/2}(\varepsilon/k)\Sigma$, respectively, also bear the same units with (time)$^{-1}$; unit of Σ is (length)$^{-1}$. The turbulent transport term $\nabla.\left(\left\langle u'' \right\rangle_s \Sigma\right)$ is connected directly to the corresponding term in the transport of the mean progress variable $\widetilde{c}$. Along the flame front, flame surface density and the mean reaction rate are almost proportional.

The stretch rate k_m is directly related to the deformation tensor, $k_m = A_{ik}\left(\partial \overline{U}_k / \partial x_i\right)$. Its relevance is seen in flames with shear flows or in stagnant point flows. As S_1 term has no influence on the flame angle determination, for all simulations it is ignored. The S_2 term is the strain rate induced by turbulent fluctuations. Modelling S_2 is one of the central difficulties in flamelet modelling. In [11], the authors claim that simple estimates like the small-scale strain $\sqrt{\varepsilon/\nu}$ (of the CPB model) or the large-scale strain (ε/k) fail to produce effects of chemistry or of turbulence length scales on the turbulent flame speed s_T.

All user-defined subroutines and the scalar transport equations for progress variable and flame surface density are externally linked to the solver. In case of the FSD models (CPB and CFM), the transport equations for flame surface density and the progress variable are solved exclusively, along with the governing equations for fluid flow.

5 Results and Discussion

All four models are calculated for c-contours, from which the turbulent flame speed is evaluated and compared with the experimental data. A detailed validation of these models is based on turbulent lean premixed sixty-four ethylene flames from three stoichiometric ratios (0.5, 0.7, and 0.9) of different Lewis numbers for three pressures (1, 5 and 10 bar) and varied flow and turbulence conditions with u'/s_L reaching as high as 24.

This enormous data holds scientific relevance in the view that it features a wide range of turbulence and flame conditions, a conditional sufficiency for combustion model validation. The reactant fluid flow conditions are determined at the cold boundary of the flame zone. All the calculations are based on a two-dimensional symmetry grid of 15,000 cells, optimised for grid independency.

5.1. Algebraic models

5.1.1 The BML model

The classical BML model given in Eq. 2 belongs to the class of algebraic models. Of its many forms (because of modifications made according to the required application) of algebraic models in literature, we chose to investigate model [7].

In the low range of $u'/s_L < 4.0$, especially for higher equivalence ratios at atmospheric pressure, the BML model works quite well. Overall, it captures a full *distributed-trend* of the experiments, as shown in Fig. 2a & 2b.

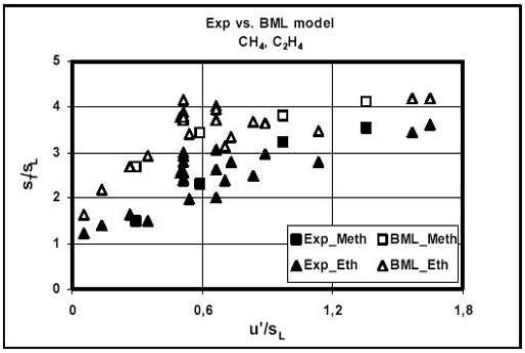
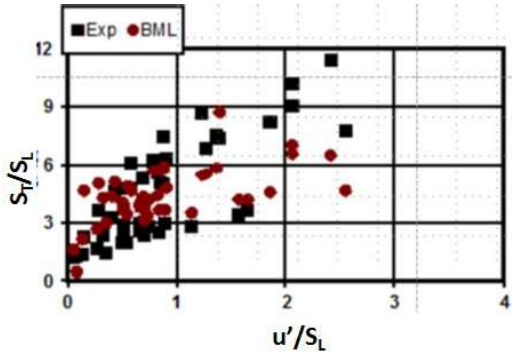


Fig. 2. Plot comparing measured and calculated flame angle as s_T/s_L (BML) for a) left – lean (ϕ = 0.7, 0.9) CH_4/air flames at 1, 5, and 10 bar for $u'/s_L < 4.0$. Methane data is also included. The model works unity Lewis number but



b) right – for lean (ϕ = 0.5, 0.7) C_2H_4-air flames at 5 and 10 bar for $u'/s_L > 4.0$

For high turbulence and high pressures, i.e. $u'/s_L > 4.0$, the BML model is not applicable because it was devised for atmospheric pressure. Interestingly, the overall exponent of u' is negative with the I_0 relation. This leads to a reduction in the reaction rate for higher turbulence velocity, as can be seen in Fig. 2b.

5.1.2. The Lindstedt and Váos model

This algebraic model in Eq.5. was proposed by Lindstedt and Váos (LV) [12]. This model has been formulated for the flamelet regime of combustion. It is one of the simplest and easily adoptive models available in the literature. The closure of the mean reaction rate from this model is

$$\overline{w}_c = C_R \rho_u \frac{s_L^0}{V_K} \frac{\tilde{\varepsilon}}{\tilde{k}} \tilde{c}(1-\tilde{c}) \qquad \text{Eq.5}$$

where $\tilde{k}$ and $\tilde{\varepsilon}$, respectively, are turbulent kinetic energy and turbulent dissipation rate. The pre-constant is $C_R = 2.6$ for *flames stabilised in a counterflow* [11].

Fig. 3 shows a large set of experimental data accounting for two equivalence ratios, 0.7 and 0.9, three different pressures, and varied flow and flame conditions.

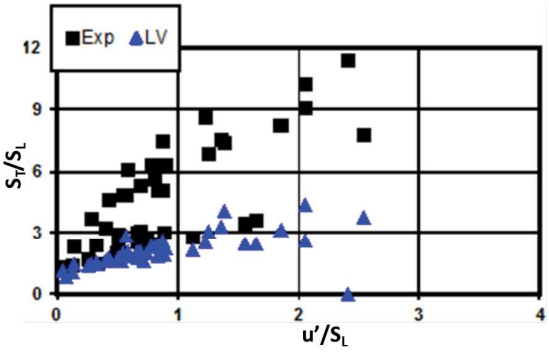


Fig. 3 Plot comparing measured and calculated (LV) for lean (ϕ = 0.7, 0.9) ethylene-air flames at 1,5, and 10 bar for $u'/s_L < 4.0$

Similar to the BML model, the LV model also captures the quantitative trends at very low turbulence. Here, the low turbulence data is broadly split into two categories, with some closer agreement with experiments reached in the low-pressure range $u'/s_L < 1.0$. The deviation is higher to cover most parts of the high-pressure data, and represents 1-bar flame data at 1 bar. The model shows strong deviation for higher turbulence at higher operating pressures. The latter results are not shown here because the gap is too high to fit them in the same

scale. It is not so evident whether the Lewis number effects and influence of pressure are captured in this single broad data (Fig. 3).

A proper formulation, for example, with a tuned pre-constant, may supposedly improve the results.

5.1. Flame surface density models

5.1.1. The CPB model

Plot of s_T / s_L vs. u'/s_L for $u'/s_L < 4.0$ in Fig. 4 shows the model only responds reasonably well to a small number of cases in the data-mist of C_2H_4 flames for 1 bar and 5 bar, and it deviates strongly for 10-bar cases, compared to the experiments.

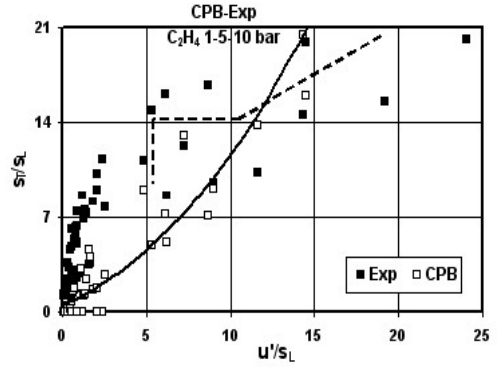


Fig. 4. The CPB model: Plot comparing measured and calculated s_T/s_L for lean (ϕ = 0.5, 0.7, 0.9) for ethylene-air flames at 1, 5 and 10 bar

Interestingly, the CPB model yields proper quantification in the broken flamelet regime, $4 < u'/s_L < 19$.

5.1.2. The CFM Model

Fig. 5 shows that for the ethylene flames for u'/s_L<4.0, the quantitative predictions are not satisfactory and, for most of the cases, yielding zero values of s_T/s_L.

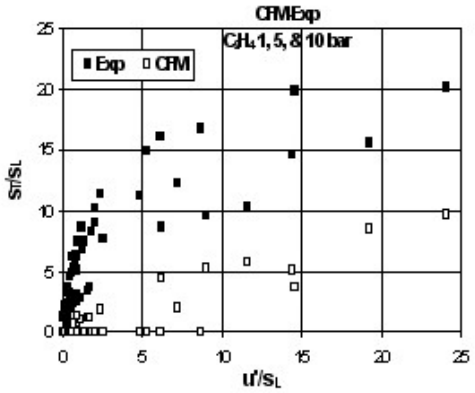


Fig. 5. The CFM model: Plot comparing measured and calculated s_T/s_L for ethylene–air flames. for lean i) (ϕ = 0.7, 0.9) at 1,5, & 10 bar for $u'/s_L < 4.0$. ii) for lean (ϕ = 0.5, 0.7) ethylene-air flames at 5 & 10 bar for $u'/s_L > 4.0$.

We found that several flame are not describable in this range of data as the flame are too long and therefore could not estimate the cone angles. Overall, it is clear that for most of the data the model significantly under predicts, although it promising for ϕ = 0.9 at atmospheric pressure.

Conclusions

All four turbulent premixed combustion models; two algebraic models – the BML and the Lindstedt and Váos models, and the two flame surface density models – CPB and CFM models, were numerically studied and compared with Kobayashi experimental data of ethylene–air mixtures, for three lean equivalence ratios, 0.5, 0.7, 0.9, for a wide range of turbulence and flow conditions $0 < u'/s_L < 24$, and $1.5 < U <$ 8.8m/s) and operating pressures up to 10 bar.

The CPB model was suitable in the range $0 < u'/s_L < 24$ and drawn well for u'/s,<4, with a very distant

qualitative trend. In most other cases, this model either under predicted or produced no flame. The LV model under predicts for most of the data. The BML equation was shown to yield partly satisfactory results.

References

[1] Alqallaf, A., Klein, M., and Chakraborthy, N (2019). Effects of Lewis number on the evolution of curvature in spherically expanding turbulent premixed flames. Fluid 4(1):12.

[2] Ghanta, M, Fhey, D, and Subramaniam, B(2014). Environmental impacts of ethylene production from diverse feedstocks and energy sources. Applied Petrochemical Research 4. pp. 167–179.

[3] Buschmann, A. Dinkelacker, F., Schäfer, T., Schäfer, M., Wolfrum, J. (1996). Measurement of the instantaneous detailed flame structure in turbulent premixed combustion. Symposium (International) on Combustion, Vol. 26, Issue 1, pp. 437–445.

[4] Muppala, S.P.R., Aluri, N.K. Dinkelacker, F., Leipertz, A. (2005). Development of an algebraic reaction rate closure for the numerical calculation of turbulent premixed methane, ethylene, and propane/air flames for pressures up to 1.0 MPa, Combustion and Flame, Volume 140, Issue 4, pp. 257–266.

[5] Keppeler, R., Tanermann, E., Allaudin, U., and Pfitzner, M. (2014). LES of Low to High turbulent combustion in an elevated pressure environment. Flow Turbulence and Combustion. 92. pp. 767–802.

[6] Kobayashi, H., Nakashima, T., Tamura, T., Maruta, K. and Niioka, T. (1997) 'Turbulence measurements and observations of turbulent premixed flames at elevated pressures up to 3.0 MPa', Comb. Flame, Vol. 108, pp. 104–117.

[7] Bray, K.N.C. (1990). Studies of the turbulent burning velocity. Proc. R. Soc. Lond. A 431, pp. 315–335.

[8] Kobayashi, H., Tamura, T., Maruta, K. and Niioka, T. (1996) 'Burning velocity of turbulent premixed flames in a high pressure environment', Proc. Combust. Inst., Vol. 26, pp. 389–396.

[9] Kobayashi, H., Kawabata, Y. and Maruta, K. (1998) 'Experimental study on general correlation of turbulent burning velocity at high pressure', Proc. Combust. Inst., Vol. 27, p. 941.

[11] Vaos, E.M.(1998). Second Moment Methods for turbulent flaws with reacting scalars. PhD thesis. Imperial college, University of London.

[12] Lindstedt, P. and Vaos, E.M., Modelling of premixed turbulent flames with second moment methods. Combust. Flame 116 (1999) 461–485.

[13] Duclos, J.M., Veynante, D. and Poinsot, T. (1993). A comparison of flamelet models for premixed turbulent combustion. Combustion and Flame, Volume 95, Pages 101–117.

3D SIMULATION OF AMMONIA/HYDROGEN FUEL BLENDS COMBUSTION UNDER HIGH SWIRL GAS TURBINE CONDITIONS

O. Kumuk[1,2] and M. Ilbas[3]

1. Graduate School Natural and Applied Science, Gazi University, Ankara; email: osman.kumuk@iste.edu.tr
2. Unmanned Aerial Vehicle Technology and Operatorship Program, Iskenderun Vocational School of Higher Education, Iskenderun Technical University, Hatay; email: osman.kumuk@iste.edu.tr
3. Department of Energy Systems Engineering, Faculty of Technology, Gazi University, Ankara; email: ilbas@gazi.edu.tr

Abstract

Ammonia can be a sustainable and preferred fuel for internal combustion engines and gas turbines in as much as it does not contain carbon and carries hydrogen. In this study, combustion conditions, temperature analysis, emission analysis, velocity and turbulence analysis of ammonia supported hydrogen fuels in a turbulent eddy model gas turbine combustion chamber will be examined. For this purpose, numerical models were generated using an ANSYS Fluent commercial computational fluid Dynamics code. In the modeling, P-1 radiation model and, standard k-Ɛ turbulence model have been used for simulation. For the inlet parameters, hydrogen from the central surface of the burner and ammonia from 12 different symmetrical surfaces around the burner were provided. The ammonia compound was decided until 50% hydrogen-50% ammonia mixture in an intermission of 10% by heat fraction. It has been observed that the maximum temperature levels in the combustion chamber decrease with the addition of ammonia and the flame moves towards the exhaust of the combustion chamber because of the lower burning rate of ammonia in the regions where the flame occurs. Although the addition of ammonia in the combustor increases the NOx levels in the flame zone rapidly because of the bound nitrogen in the ammonia, the predicted levels of NOx at the combustion chamber's exit of the seem to converge for all cases. As a result, it can be thought that ammonia supported hydrogen fuels have a significant possible as an alternative and sustainable fuel in terms of combustion performance. Also, considering NOx levels with the addition of ammonia, ammonia can be seen as a new and helpful fuel for the gas turbine combustion chamber due to its high energy content from hydrogen in it.

Keywords: Ammonia, Hydrogen, Gas Turbine Combustion, CFD.

1 INTRODUCTION

Global warming is a very serious global problem faced by human life. Most NOx and other contaminants are caused by burning fossil fuels. Transportation in air vehicles is provided by gas turbine engines and many countries are investigating clean alternative energy sources to limit NOx and other pollutant emissions. Ammonia and hydrogen are alternative renewable energy sources and are non-carbon flammable fuels. [1] Xin et al. have experimentally worked on 61kPa absolute pressures and different ammonia volume fractions in an internal combustion engine running on hydrogen. With ammonia addition, the flame build-up time and flame propagation time are extended and have little effect on NOx emissions. [2] Yang et al. have researched different equivalent ratio values such as 0.9, 1.0, and 1.1 in a model engine and for the turbulent premixed flame configuration of ammonia-hydrogen fuel mixtures with 10% and 15% hydrogen capacity according to volume. By adding hydrogen to the ammonia, the flame's reactivity has increased and the combustion process has improved. It has also been seen that the ammonia addition, which shows the highest value for the combustion rate, is 10% hydrogen. [3] Changwei et al. analyzed the difference between absolute pressure 61 kPa, engine speed 1300 rpm, and Ammonia and 2.2% volume fraction of pure hydrogen fuel in their experimental studies. The addition of ammonia has augmented ignition postpone and flame improvement times, as well as reduced pressure rise rate in the cylinder. The result is that ammonia can be used as a combustion inhibitor so that it can be a new reference for the development of hydrogen-fueled engines. [4] In their experimental work, Goldman et al.

investigated the boundary layer recoil (BLF) for various H2/NH3/N2/O2/air mixtures in vortexes premixed burner at atmospheric pressure and partially high temperature. They found that the rebound tendency decreased with increasing nitrogen content and increased with increasing ammonia content. In the current paper, the gas turbine model burner has been choosen as a combustor in which ammonia and hydrogen-assisted ammonia fuels are consumed non-premixed to investigate the combustion performance and the introduction of the burner with hydrogen for the NOx emission level. Above, various studies on NOx, emissions, velocity, hydrogen and ammonia are included. In addition, studies are known for burning ammonia, hydrogen and carbon-based fuels [5–9].

2 MATHEMATICAL MODELING

The model of combustor has been created and designed using a solid modeling program. The annular-circular gas türbine burner has 18 pieces (20 degrees) equally circular. It is made for one piece from all parts symmetrically to simplify the gas turbine. The H2 zone, NH3 zone, swirl air zone, dome zone, primary air zone, secondary air zone, and dilution air zone inlet for the combustor under consideration are shown in Figure 1.

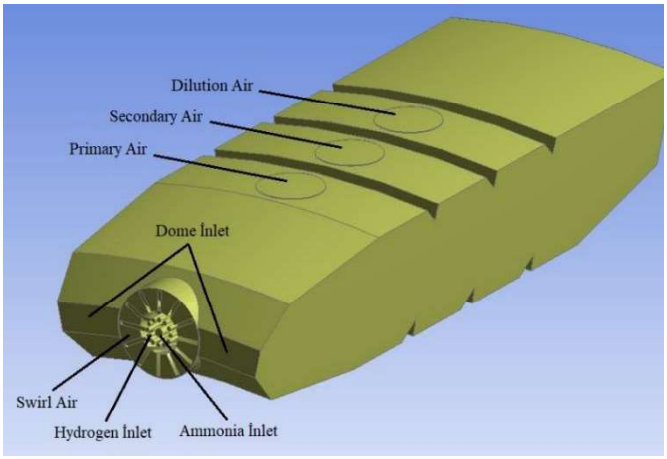


Figure 1. The Model Combustor

The ANSYS Fluent is used for all numerical reagent analysis. Axial temperature profiles from ammonia combustion have been validated with reference profiles for more modelings. For this aim, the design parameters are given in Table 1. The 11.17 MW gas turbine is used to study ammonia and hydrogen-assisted ammonia fuels for its burner. This causes the effect of hydrogen crops on the gas turbine's combustion performance. For this aim, burner hydrogen is used with a heat fraction of 10% in the 50% hydrogen to 50% ammonia range without changing the total heat load in the burner.

Table 1. Design Parameters

Parameter	Value
Air flow rate	1.553 kg/s
Fuel inlet temperature	743.352 K
Air pressure	2083450 Pa
Fuel flow rate	0.03316 kg/s

3 RESULT AND DISCUSSION

The kerosene axial temperature profiles forecasted in this study and acquired from the literature [10,11] have been approved as shown in Figure 2. According to Figure 2, the projected axial temperature profiles are satisfactory levels. It is in good harmony with the results obtained from the literature.

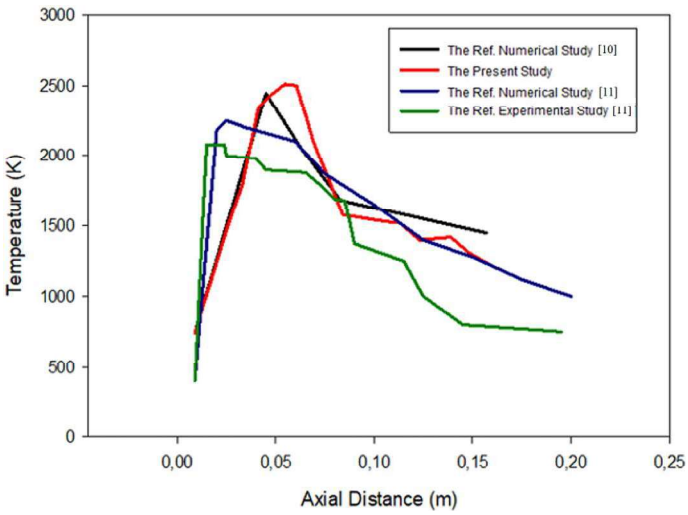


Figure 2. The validation of axial temperature profiles [10,11]

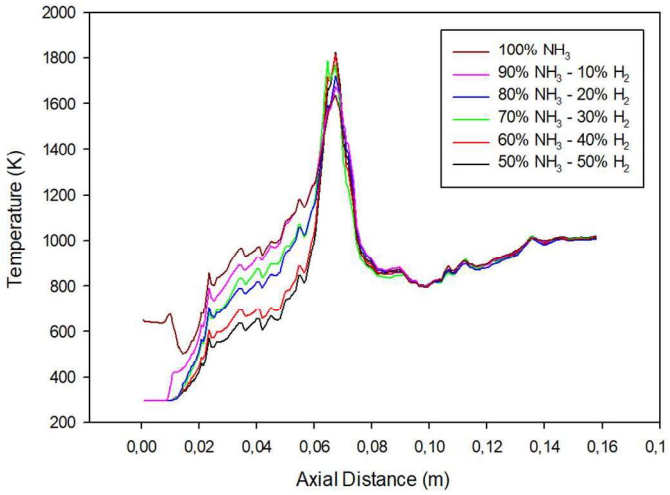


Figure 3. The axial temperature profiles at different ammonia-hydrogen mixtures

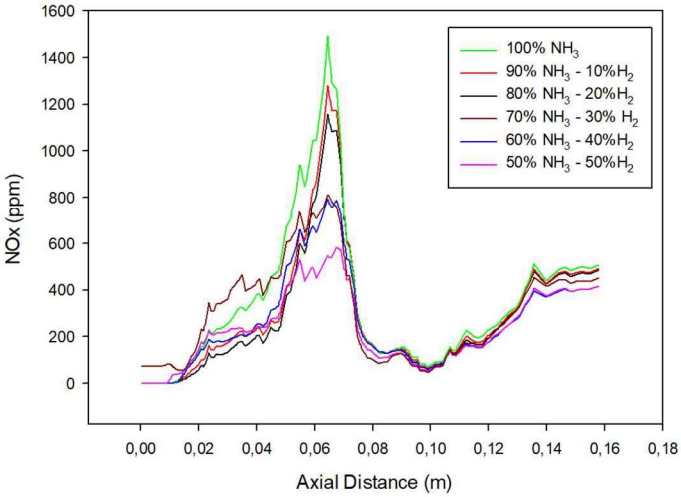


Figure 4. The axial NOX profiles at different ammonia-hydrogen mixtures

Figure 3 shows the axial temperature profiles at different ammonia-hydrogen mixtures. As shown in Figure 3, the temperature levels of all states in the primary region have increased rapidly because of flame formation. Then, the temperature levels of all states in the secondary region are significantly reduced. However, temperature levels are almost the same due to the outputs of the secondary area used to ensure the temperature balance within the combustion chamber in gas turbines and the diluted air zone. It has been observed that the temperature of the ammonia flame does not change as hydrogen enters the burner. However, the primary region shows that the flame is reaching the combustion chamber's exit with an addition of hydrogen. This relies on the higher combustion speed of the hydrogen compared to the combustion speed of the ammonia. Put differently, the total velocity of the mixture is more excessive than the combustion velocity. The maximum temperature values for ammonia and hydrogen-assisted ammonia fuels are 1639 K, 1677 K, 1724 K, 1770 K, 1816 K and 1824 K with 100% ammonia, 90% ammonia - 10% hydrogen, 80% ammonia - 20% hydrogen, 70% ammonia - 30% hydrogen, 60% ammonia - 40% hydrogen, 50% ammonia - 50% hydrogen.

100% ammonia, 90% ammonia-10% hydrogen, 80% ammonia-20% hydrogen, 70% ammonia-30% hydrogen, 50% ammonia-50% hydrogen, 60% ammonia-40% hydrogen, 50% ammonia-50% hydrogen fuels are available as flammable distributions. In Figure 5 and Figure 6, the temperature and NOx contours of all states are shown as axial sections respectively. As previously stated, when the values are examined, the ammonia maximum temperature level does not change with the addition of hydrogen into the burner, and the flame position moves more because of the higher combustion rate. After the end of the secondary zone where the secondary and dilution air is mixed in the combustion to suppress the high NOx levels in the gas turbine burner, the temperature distribution of all consumed states can be said to be almost identical.

NOx emission is the other important combustion parameter and is examined due to thermal, fast, and fuel NOX mechanism. Figure 4 shows the axial NOx profiles at different ammonia-hydrogen mixtures. The fuel NOx mechanism, especially in the primary region, has significantly increased the estimated NOx levels using ammonia. NOX levels are estimated at more than 1450 ppm, 1250 ppm, 1100 ppm, 800 ppm, 750 ppm and 550 ppm for 100% ammonia, 90% ammonia - 10% hydrogen, 80% ammonia - 20% hydrogen, 70% ammonia - 30% hydrogen, 60% ammonia - 40% hydrogen and 50% ammonia - 50% hydrogen fuels, respectively. The same results as adding hydrogen can be seen as contours in Figure 5 and Figure 6.

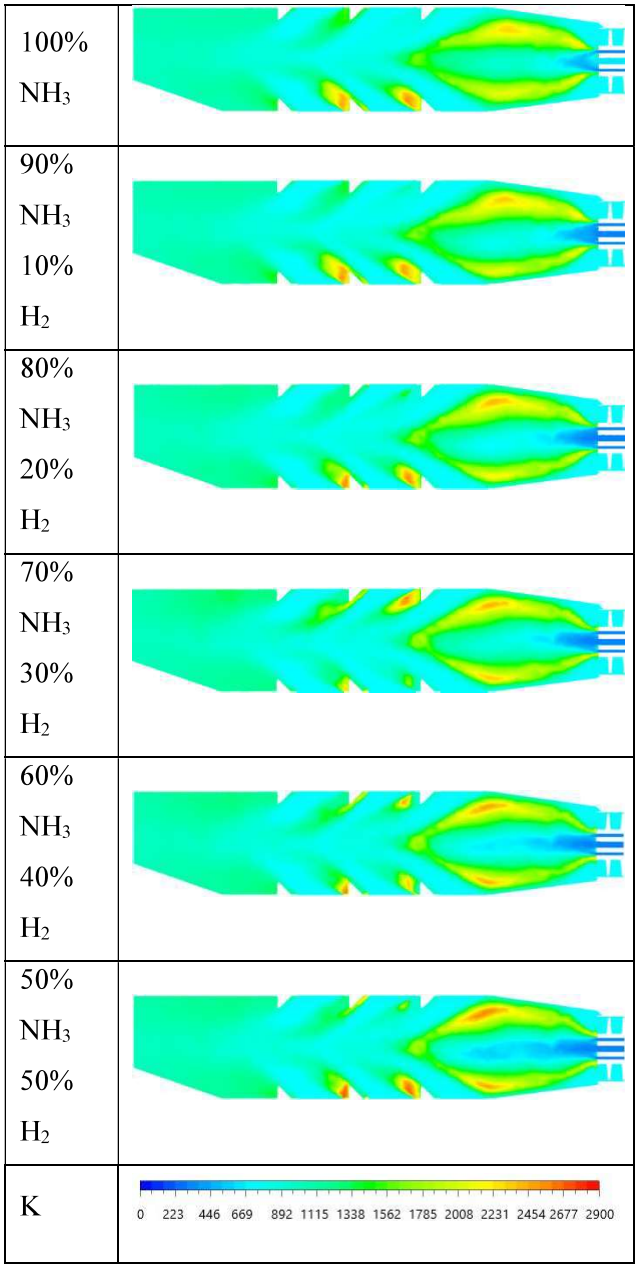
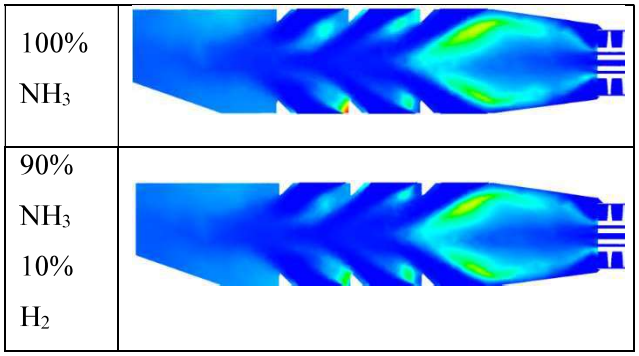


Figure 5. The temperature contours for all cases of hydrogen mixture fuel as cross-sectional



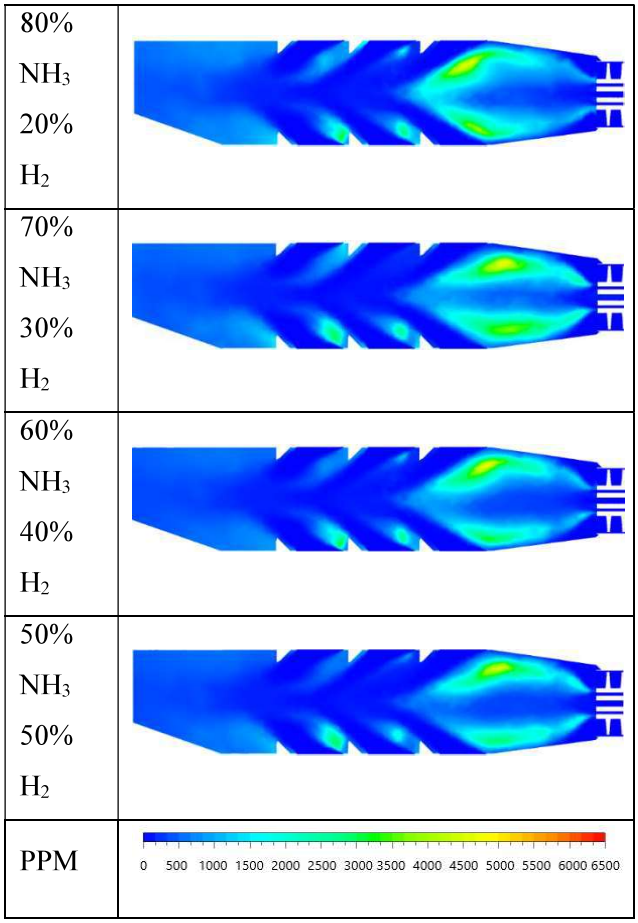


Figure 6. The NOx contours for all cases of hydrogen mixture fuel as cross-sectional

4 CONCLUSIONS

The turbulent turbulence of ammonia and hydrogen-assisted ammonia fuels has been studied about temperature and NOx pollutant distributions in the gas turbine flammable model. The ANSYS Fluent CFD program was used to model different ammonia-hydrogen mixtures examined and so the axial temperature and NOx profiles and contours were shown and conversed about in detail in this study. The primary result was that the maximum temperature level of ammonia did not change much more when hydrogen was inside the burner. Another result in the flammable temperature distribution is that the ammonia flame was moved further by adding hydrogen because of a higher combustion rate compared to hydrogen. Although the decrease in ammonia in the burner significantly reduces NOx levels in the flame zone due to ammonia attached nitrogen contributing to the NOx, it has been shown that the estimated NOx levels are not too extreme at the output of the combustion chamber.

ACKNOWLEDGEMENT

We would like to thank Gazi University for the use of Ansys Fluent academic computer code.

REFERENCES

[1] Ji C, Xin G, Wang S, Cong X, Meng H, Chang K, vd. Effect of ammonia addition on combustion and emissions performance of a hydrogen engine at part load and stoichiometric conditions. *International Journal of Hydrogen Energy* 2021;46:40143–53.

[2] Yang W, Ranga Dinesh KKJ, Luo KH, Thevenin D. Direct numerical simulation of turbulent premixed ammonia and ammonia-hydrogen combustion under engine-relevant conditions. *International Journal of Hydrogen Energy* 2022;47:11083–100.

[3] Xin G, Ji C, Wang S, Meng H, Chang K, Yang J. Effect of different volume fractions of ammonia on the combustion and emission characteristics of the hydrogen-fueled engine. *International Journal of Hydrogen Energy* 2022.

[4] Goldmann A, Dinkelacker F. Investigation of boundary layer flashback for non-swirling premixed hydrogen/ammonia/nitrogen/oxygen/air flames. *Combustion and Flame* 2022;238:111927.

[5] Ilbas M, Kumuk O, Karyeyen S. Numerical study of a swirl gas turbine combustor for turbulent air and oxy-combustion of ammonia/kerosene fuels. *Fuel* 2021;304:121359.

[6] Ilbas M, Kekul O, Karyeyen S. Investigation into Thermal-Fluid interaction of ammonia turbulent swirling flames under various Non-Premixed burner conditions. *Fuel* 2022;312:122967.

[7] Pacheco alo P, Rocha RC, Franco MC, A Mendes MA, Fernandes EC, Coelho PJ, vd. Experimental and Kinetic Investigation of Stoichiometric to Rich NH 3 /H 2 /Air Flames in a Swirl and Bluff-Body Stabilized Burner 2021.

[8] Franco MC, Rocha RC, Costa M, Yehia M. Characteristics of NH3/H2/air flames in a combustor fired by a swirl and bluff-body stabilized burner. *Proceedings of the Combustion Institute* 2021;38:5129–38.

[9] Elbaz AM, Wang S, Guiberti TF, Roberts WL. Review on the recent advances on ammonia combustion from the fundamentals to the applications. *Fuel Communications* 2022;10:100053.

[10] Mark CP, Selwyn A. Design and analysis of annular combustion chamber of a low bypass turbofan engine in a jet trainer aircraft. *Propulsion and Power Research* 2016;5:97–107.

[11] Yan Y, Liu Y, Fang W, Liu Y, Li J. A simplified chemical reaction mechanism for two-component RP-3 kerosene surrogate fuel and its verification. *Fuel* 2018;227:127–34.

RANS SIMULATION OF BLUFF-BODY TURBULENT SWIRLING FLAME

Orhan Veli Kazancı[1] and Yakup Erhan Böke[2]

1. PhD Student, Mechanical Engineering Faculty, Istanbul Technical University, Istanbul; email: kazancio@itu.edu.tr
2. Professor, Mechanical Engineering Faculty, Istanbul Technical University, Istanbul; email: boke@itu.edu.tr

Abstract

Swirling flows have complex flow features and these features make them an essential part of many engineering applications. Due to the complex features, swirling flows can be simulated correctly by DNS or LES methods, which are highly expensive techniques. This condition made the RANS approach a popular method for the industrial arena because of lower resource requirements than LES. Nevertheless, a large amount of existing RANS simulations on swirl stabilized turbulent flow are 2D and these simulations are not sufficient for predicting the significant flow features of swirling flows.
In the present study, 3D RANS simulation of swirling reacting flow was investigated. Numerical analysis is executed by using ANSYS Fluent CFD code and results are compared with the high-quality experimental database of SM1 flame which was performed by Sandia National Laboratories, the University of Sydney. Turbulence is modeled with the k-ω SST type model and the analysis showed good agreements between numerical results and experimental data.

Keywords: Turbulent flow, Swirling flame, RANS, Non-Premixed Combustion

1 INTRODUCTION

Energy consumption is essential for today's world, and a high amount of energy is produced from fossil fuels. On the other hand, production efficiency is a really important issue, because of the emissions of fossil fuels. So combustion methods are really important factors to achieve efficient use of fuels. One of these methods is swirl stabilized turbulent flames and they are relevant for many industrial applications, e.g. gas turbines, furnaces, because of their specific advantages compared to non-swirling turbulent flames [1]. The evident features of swirl stabilized turbulent flames are mixing improvement, flame stability, blow-off characteristics, and pollution reduction [2].

Numerous experimental studies, including those conducted at the TNF (Turbulent Non-premixed Flames) workshop, have examined swirl-stabilized flows and flames [3]. The TNF workshop has a well-established experimental database of turbulent non-premixed flame configurations consisting of; simple jet, bluff-body stabilized flames, and swirl-stabilized flames. Due to the presence of two recirculation zones in a particular combination of low swirl number and higher primary axial velocity as compared to the bluff-body stabilized flows, which has only one recirculation zone [4]–[9], the swirl-stabilized flame configuration is the most difficult test case to evaluate the validity of various turbulence and combustion models [10].

In the TNF workshop project, there is a Sydney swirl project sub-category. This project includes two non-reacting and eight reacting swirling flow cases for three different types of fuels. All cases' experimental results have been described in depth in several papers [4, 5, 9, 11–13].

Numerous research teams have conducted numerical examinations on isothermal swirling flow and swirling flame cases of the Sydney swirl project and the majority of these numerical analyses were performed using homegrown codes, although certain instances of using commercial CFD packages [14, 15] have also been documented in the published literature [16].

A comparative numerical study in the 2D axisymmetric domain was employed by Kashir et al. [2] using k-ω SST and modified k-ε turbulence models. Both models produce satisfactory findings for the flow field, mixture fraction, temperature, and carbon monoxide mass fraction when compared to experimental data, according to that comparison. Another study in 2D domains was performed by Radwan et al. [14] using standard and realizable k-ε, standard k-ω, and Reynolds stress model. The investigation was largely concerned with comparing experimental data to predictions of

generic flow patterns. In their study of the prediction of mean and fluctuating velocity components, West et al. [17] compared the performance of an SST-based DES model with that of LES and 2D unsteady RANS models. The swirl-type regeneration burner was investigated by Fu et al. [18] using four different 2-equation RANS models. They concluded that the SST k-ω and realizable k-ε models can more accurately replicate the flow field.

Safavi and Amani [10] have done one of the most recent research on swirl flow and flame cases. They conducted a comparison of various steady and unsteady turbulence models, including 2D RANS models (RNG k-ε, SST k-ω, Transition-SST, and Reynolds stress model), LES (Germano's dynamic SGS), 3D Hybrid models (SST k-ω based Scale-adaptive simulation (SAS), Realizable k-ε based Detached eddy simulation (DES) and SST k-ω based DES). The findings were concentrated on the flow field as a whole and flow features such as the vortex breakdown (VB) bubble.

Rahman et al. [16] largely focused on how well 3D RANS schemes can capture the key flow features of the swirl-stabilized isothermal turbulent flow. Researchers examined the impact of numerical concerns such as mesh refinement in critical zones, mesh structure, discretization schemes, and various turbulence models on the precise prediction of notable flow features.

Out of RANS simulations, various LES investigations have also been conducted by Malalasekera et al. [8, 19], El-Asrag and Menon [20], Hu et al. [21], Yang and Kaer [15], Dinesh et al. [7]. LES works have demonstrated good agreement with the experimental results of the Sydney swirl burner, however, because LES requires a lot of time and is costly computationally, it is not favored in industry-based activities. The RANS approach, which is computationally more affordable and time-efficient than the LES approach, has been the dominant technique in industrial CFD applications over the past few decades [22].

The literature review done for this study has shown that the primary flow characteristics of the swirl-stabilized turbulent flow inside a burner cannot be well captured by 2D axisymmetric RANS simulations. The vortex breakdown (VB) bubble and upper recirculation zone are 3D in nature, and a 2D method is unlikely to adequately reflect their flow physics. Therefore, a 3D method is preferable and requires a thorough RANS framework investigation. Nevertheless, the limited 3D RANS investigations that have been described in the literature have mostly focused on forecasting velocity patterns in the various flow regime zones.

In the present study, 3D RANS simulation of swirling reacting flow was investigated. Utilizing the ANSYS Fluent 2020 R1 CFD code, numerical analysis is carried out, and the findings are compared with the very accurate experimental record of the SM1 flame produced by Sandia National Laboratories and the University of Sydney. Turbulence is modeled with the k-ω SST type model and the analysis showed good agreements between numerical results and experimental data.

2 EXPERIMENTAL SETUP

The Sydney swirl burner which is selected for simulation has a 50 mm diameter ceramic bluff-body face with a 3.6 mm diameter central jet tube. Swirling flow is provided through a 5 mm wide annulus that surrounds the bluff body. The burner induces swirl aerodynamically by air entering through three tangential ports. The burner is placed in a secondary co-flow wind tunnel with a cross-section of 130x130 mm, for providing well-defined boundary conditions. The detailed schematics of the burner can be seen in Figure 1. This burner has four important velocities that affect and form the flow field. These are the axial velocity of the central jet (U_j), the axial and tangential velocity of the swirling air annulus (U_s and W_s), and the axial velocity of the co-flow air of the wind tunnel (U_e). S_g is a geometric swirl number and it is used to quantify the swirl strength, which is linearly proportional to the momentum swirl number S ($S=0.9S_g$). In this study, SM1 swirl flame is validated. The fuel of the SM1 case is pure CH_4. Flow parameters of the SM1 case are summarized in Table 1.

Table 1. Physical properties of SM1 flame

Flame	U_s	W_s	U_j	U_e	S_g
SM1	38.2	19.1	32.7	20	0.54

More details of the Sydney swirl burner and experimental results can be found in the literature [4, 9, 11, 23].

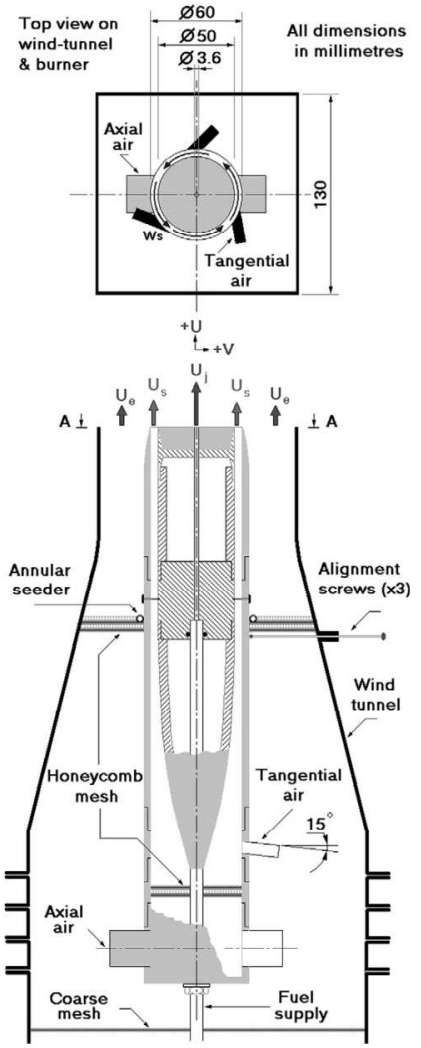


Figure 1. Schematics of Sydney Swirl Burner

3 NUMERICAL ANALYSIS

3.1 Computational Domain

The 3D domain dimensions used in this study can be seen in Figure 2. Cylinder's outer diameter is 146 mm and the length of the domain is 300 mm downstream. Considering the small angle of the secondary co-flow wind tunnel, the secondary co-flow inlet starts 35mm before the air and fuel inlet plane. The spatial discretization of the 3D domain is done in ANSYS Fluent mesher, using a structured grid



Figure 2. Schematic diagram of the computational geometry

with 3.1 Million cells.

The meshed domain can be seen isometric and frontal view in Figure 3 and in Figure 4, respectively. Near the inlet plane, the grid resolution is finer (about 0.2 mm), and it becomes coarser further downstream.

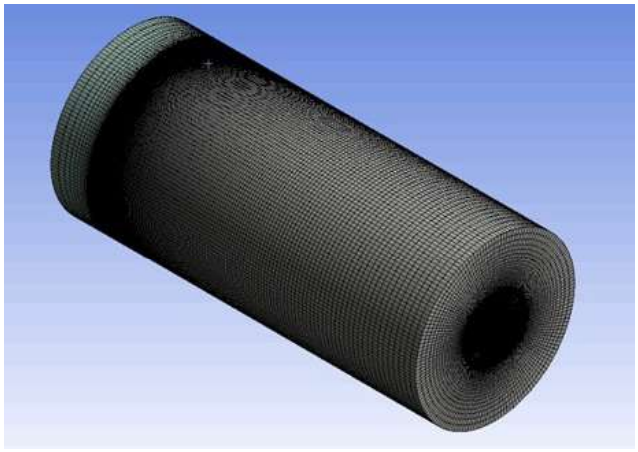


Figure 3. Isometric view of computational grid

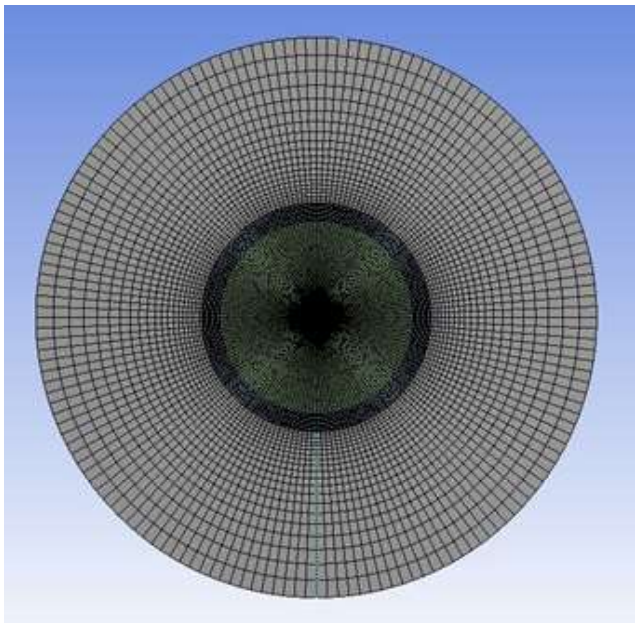


Figure 4. Frontal view of computational grid

3.2 Numerical Analysis Setup

The computational platform for the current study has used the ANSYS FLUENT 2020 R1 code, which is based on the finite volume method. For calculations, k-ω SST, P1, and Steady Diffusion Flamelet model which is in Non-Premixed Combustion is chosen for turbulence model, radiation, and combustion, respectively. Detailed information about k-ω SST [24-26], P1 [27], and Steady Diffusion Flamelet model [28] can be found in literature.

For the pressure-velocity coupling, the Semi-Implicit Method for Pressure Linked Equations (SIMPLE) is used. For pressure the PRESTO!

scheme and for momentum, the QUICK scheme is used. The second-order upwind approach is applied to other governing equations as well. For all equations, the convergence criteria are 10^{-6}.

4 RESULTS AND DISCUSSION

The k-ω SST turbulence model with radiation is used to simulate the SM1 flame in the current study. The measured temperature and mixture fraction are contrasted with the projected findings.

According to the measurements, the SM1 flame has an upstream recirculation zone (RZ) that stagnates 43 mm downstream of the bluff body and a secondary RZ that runs from 65 to 110 mm downstream [11]. The recirculation zone is an important characteristic of the swirl flames and this structure makes up the complex flow field. Consequently, the primary standard for the numerical approaches is the accurate simulation of a recirculation zone [29]. Recirculation zones of SM1 can be seen in the temperature contour in Figure 5.

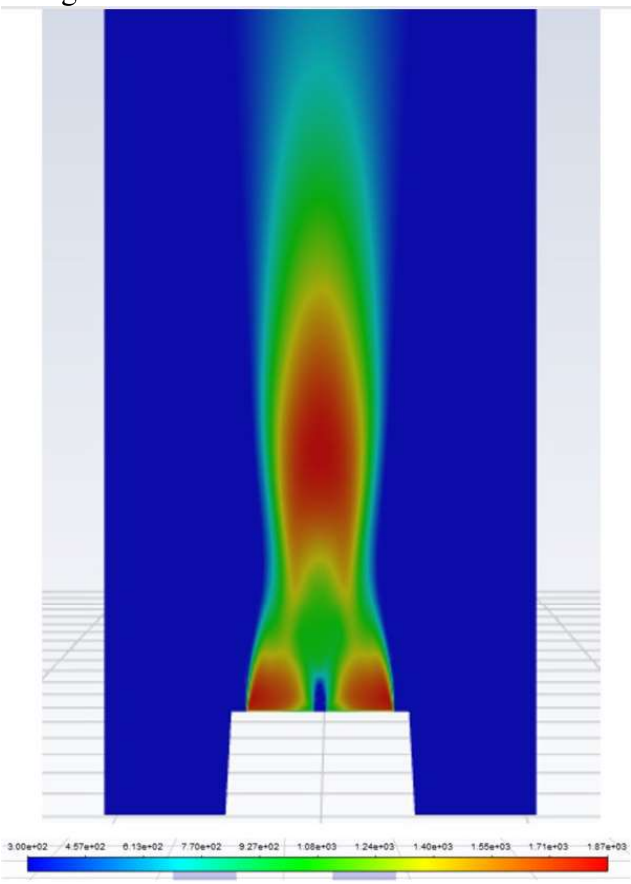


Figure 5. Temperature contour of the SM1 flame

Figure 6 shows the radial changes of the mean mixture fraction (f) at different axial locations. Between r/R=0.4-0.8 at Figure 6A and Figure 6B, the radial spread of the mean mixture fraction is significantly under anticipated. This is because the turbulence model does not account for the center jet's precession and exhibits a straight flow movement, which causes fuel to be redistributed from the jet to the upstream recirculation zone [28]. The LES simulation of SM1 swirling flame has also shown this trend as well [8, 19]. Despite these two locations, at other downstream axial positions, the trend between calculations and measurements is good.

Figure 7 shows the radial profiles of the temperature at different axial locations. Because of the complexity of the flow field and combustion, experimental and numerical temperature field contrast is quite acceptable at most axial locations. The temperature appears to be over-predicted in response to minor underprediction of the radial distribution of the mean mixture fraction, as can be seen at positions A and B in Figure 7. The results are similar to the LES findings reported by Malalasekera et al. [8] in other axial regions.

Ultimately, the RANS simulation of SM1 that was performed in this study, provides some quantitative differences but high qualitative agreement with experimental observations.

5 CONCLUSION

In this paper, a turbulent swirling reacting flow test case from the Sydney swirl burner experimental series studied by Masri and coworkers [13, 23] was taken into consideration using RANS (k-ω SST) and Non-premixed Combustion models by using ANSYS Fluent CFD 2020 R1 code. The numerical method is applied to the SM1 flame, a swirling flame from the SM group with a swirl number of 0.5.

Several complex recirculation zones, including a vortex breakdown zone, have been seen in the experiments. According to the calculations, the k-ω SST turbulence model has done a good job of capturing both the downstream vortex breakdown (VB) region and the upstream recirculation zone maintained by the bluff body. The collar-like flow features, downstream of the bluff body stabilized recirculation zone captured as well. The agreement between RANS predictions and experimental data is good for mean mixture fraction profiles, and temperature, according to a thorough comparison.

This accomplishment confirms the capability of a good RANS setup to forecast turbulence chemistry interactions in complicated combusting flows, which is good given the complexity of the flow.

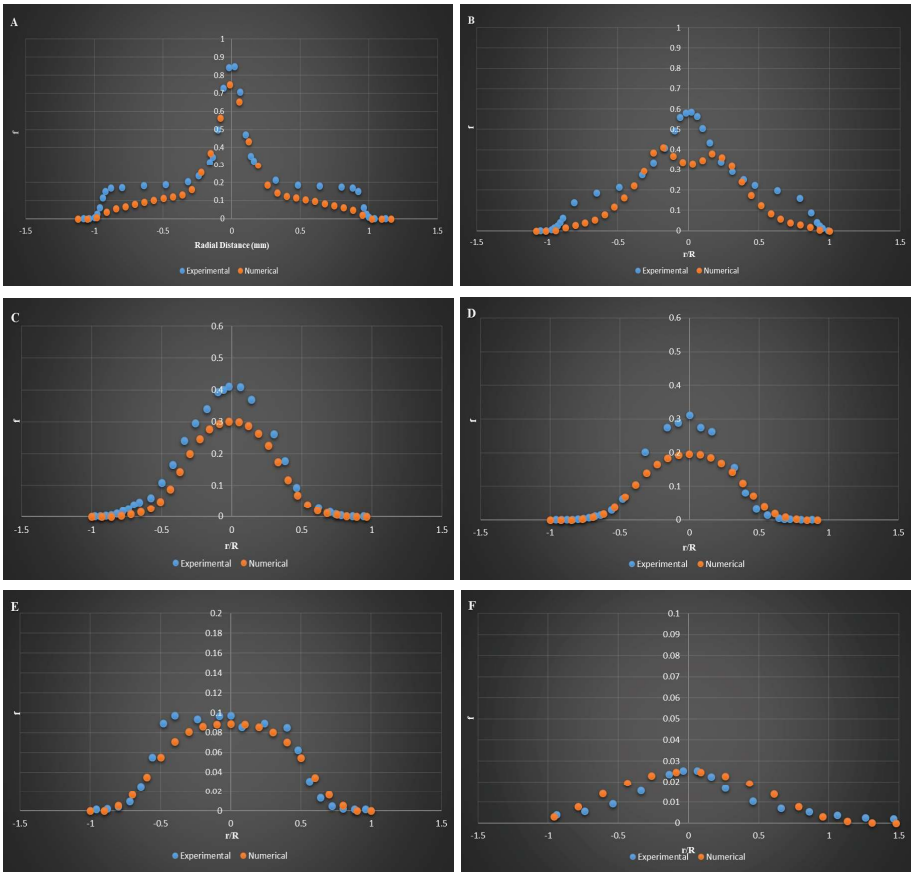


Figure 6. Mean mixture fraction (f) comparison at different locations (A=10mm, B=20mm, C=40mm, D=55mm, E=75mm, F=150mm)

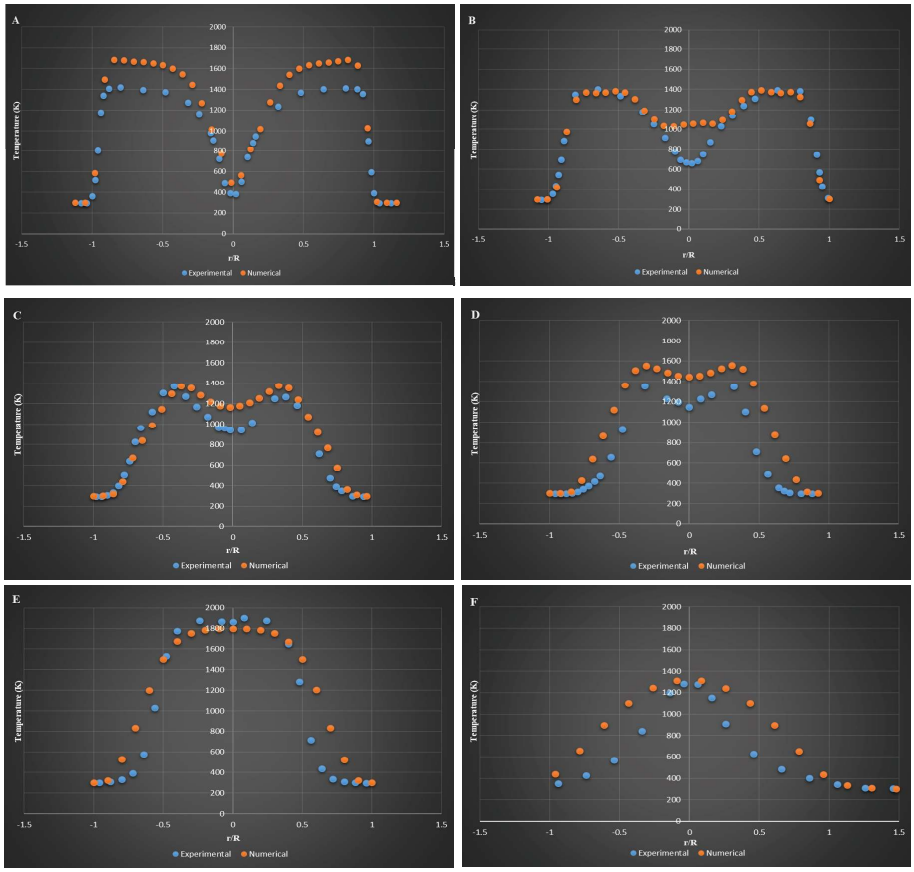


Figure 7. Temperature comparison at different locations (A=10mm, B=20mm, C=40mm, D=55mm, E=75mm, F=150mm)

In some areas of swirling flames, some differences between experimental data and predictions imply that the steady diffusion flamelet model may not be accurate enough and the temperature and mixture predictions will benefit from further development of the combustion models.

REFERENCES

[1] B. M. R. De Meester, B. Naud, U. Maas, "Hybrid RANS/PDF Calculations of a Swirling Bluff Body Flame ('SM1'): Influence of the Mixing Model," in *MCS 7*, 2011, vol. 13, no. 1, pp. 43–50.

[2] B. Kashir, S. Tabejamaat, and N. Jalalatian, "A numerical study on combustion characteristics of blended methane-hydrogen bluff-body stabilized swirl diffusion flames," *Int. J. Hydrogen Energy*, vol. 40, no. 18, pp. 6243–6258.

[3] "TNF Workshop." https://tnfworkshop.org/

[4] Y. M. Al-Abdeli and A. R. Masri, "Recirculation and flowfield regimes of unconfined non-reacting swirling flows," *Exp. Therm. Fluid Sci.*, vol. 27, no. 5, pp. 655–665, 2003.

[5] Y. M. Al-Abdeli, A. R. Masri, G. R. Marquez, and S. H. Starner, "Time-varying behaviour of turbulent swirling nonpremixed flames," *Combust. Flame*, vol. 146, no. 1–2, pp. 200–214, 2006.

[6] W. Malalasekera, K. K. J. R. Dinesh, S. S. Ibrahim, and M. P. Kirkpatrick, "Large eddy simulation of isothermal turbulent swirling jets," *Combustion Science and Technology,* vol. 179, no. 8. 2007.

[7] K. K. J. Ranga Dinesh, K. W. Jenkins, A. M. Savill, and M. P. Kirkpatrick, "Swirl effects on external intermittency in turbulent jets," *Int. J. Heat Fluid Flow*, vol. 33, no. 1, pp. 193–206, 2012.

[8] W. Malalasekera, K. K. J. Ranga-Dinesh, S. S. Ibrahim, and A. R. Masri, "LES of recirculation and vortex breakdown in swirling flames," *Combust. Sci. Technol.*, vol. 180, no. 5, pp. 809–832, 2008.

[9] Y. M. Al-Abdeli and A. R. Masri, "Precession and recirculation in turbulent swirling isothermal jets," *Combust. Sci. Technol.*, vol. 176, no. 5–6, pp. 645–665, 2004.

[10] M. Safavi and E. Amani, "A comparative study of turbulence models for non-premixed swirl-stabilized flames," *J. Turbul.*, vol. 19, no. 11, pp. 1017–1050, 2019.

[11] P. A. M. Kalt, Y. M. Al-Abdeli, A. R. Masri, and R. S. Barlow, "Swirling turbulent non-premixed flames of methane: Flow field and compositional structure," *Proc. Combust. Inst.*, vol. 29, no. 2, pp. 1913–1919, 2002.

[12] A. R. Masri, P. A. M. Kalt, Y. M. Al-Abdeli, and R. S. Barlow, "Turbulence-chemistry interactions in non-premixed swirling flames," *Combust. Theory Model.*, vol. 11, no. 5, pp. 653–673, 2007.

[13] A. R. Masri, P. A. M. Kalt, and R. S. Barlow, "The compositional structure of swirl-stabilised turbulent nonpremixed flames," *Combust. Flame*, vol. 137, no. 1–2, pp. 1–37, 2004.

[14] A. Radwan, K. A. Ibrahim, A. Hanafy, and K. M. Saqr, "On rans modeling of unconfined swirl flow," *CFD Lett.*, vol. 6, no. 4, pp. 159–174, 2014.

[15] Y. Yang and S. K. Kær, "Large-eddy simulations of the non-reactive flow in the Sydney swirl burner," *Int. J. Heat Fluid Flow*, vol. 36, pp. 47–57, 2012.

[16] T. M. R. Rahman, W. Asrar, and S. A. Khan, "An investigation of RANS simulations for swirl-stabilized isothermal turbulent flow in a gas turbine burner," *CFD Lett.*, vol. 11, no. 9, pp. 14–31, 2019.

[17] J. P. West, C. P. T. Groth, and J. T. C. Hu, "Assessment of hybrid RANS/LES methods for gas-turbine combustor-relevant turbulent flows," *22nd AIAA Comput. Fluid Dyn. Conf.*, no. June, pp. 1–20, 2015.

[18] J. Fu, Y. Tang, J. Li, Y. Ma, W. Chen, and H. Li, "Four kinds of the two-equation turbulence model's research on flow field simulation performance of DPF's porous media and swirl-type regeneration burner," *Appl. Therm. Eng.*, vol. 93, pp. 397–404, 2016.

[19] A. Kempf, W. Malalasekera, K. K. J. Ranga-Dinesh, and O. Stein, "Large eddy simulations of swirling non-premixed flames with flamelet models: A comparison of umerical methods," *Flow, Turbul. Combust.*, vol. 81, no. 4, pp. 523–561, 2008.

[20] H. El-Asrag and S. Menon, "Large eddy simulation of bluff-body stabilized swirling non-premixed flames," *Proc. Combust. Inst.*, vol. 31 II, no. 2, pp. 1747–1754, 2007.

[21] L. Y. Hu, L. X. Zhou, and Y. H. Luo, "Large-eddy simulation of the Sydney swirling NonPremixed flame and validation of several

subgrid-scale models," *Numer. Heat Transf. Part B Fundam.*, vol. 53, no. 1, pp. 39–58, 2008.
[22] Y. Zhiyin, "Large-eddy simulation: Past, present and the future," *Chinese J. Aeronaut.*, vol. 28, no. 1, pp. 11–24, 2015.
[23] Y. M. Al-Abdeli and A. R. Masri, "Stability characteristics and flowfields of turbulent non-premixed swirling flames," *Combust. Theory Model.*, vol. 7, no. 4, pp. 731–766, 2003.
[24] A. Dewan, *Tackling Turbulent Flows in Engineering*, vol. 15, no. 2. Berlin, Heidelberg: Springer Berlin Heidelberg, 2011.
[25] K. M. Saqr and M. A. Wahid, "Comparison of Four Eddy-Viscosity Turbulence Models in the Eddy Dissipation Modeling of Turbulent Diffusion Flames," *Int. J. Appl. Math Mech*, vol. 7, no. 19, pp. 1–18, 2011.
[26] F. R. Menter, M. Kuntz, and R. Langtry, "Ten Years of Industrial Experience with the SST Turbulence Model Turbulence heat and mass transfer," *Cfd.Spbstu.Ru*, vol. 4, no. July 2014, pp. 625–632, 2003.
[27] "P1." https://www.afs.enea.it/project/neptunius/docs/fluent/html/th/node112.htm.
[28] S. Vakilipour, Y. Tohidi, J. Al-Zaili, and R. Riazi, "A numerical investigation of CO2 dilution on the thermochemical characteristics of a swirl stabilized diffusion flame," *Appl. Math. Mech. (English Ed.*, vol. 41, no. 2, pp. 327–348, 2020.
[29] X. Yang, Z. He, S. Dong, and H. Tan, "Combustion Characteristics of Bluff-Body Turbulent Swirling Flames with Coaxial Air Microjet," *Energy and Fuels*, vol. 31, no. 12, pp. 14306–14319, 2017.

EFFECTS OF EXCESS AIR AND OXYGEN ENRICHMENT ON SOOTING FLAMES OF BIOGAS

M. S. Cellek*,1, U. Demir2

1. Department of Mechanical Engineering, Bingol University, Bingol, Turkey; email: mscellek@bingol.edu.tr
2. Department of Mechanical Engineering, Bilecik Şeyh Edebali University, Bilecik, Turkey; email: usame.demir@bilecik.edu.tr

Abstract

In this study, turbulent and non-premix combustion characteristics and pollutant emissions such as CO, CO_2, NO_x, and soot of biogas fuels have been investigated under different excess air coefficients (1.4, 1.8, 2.5, and 4), and oxygen enrichment (21, 23, 25, and 27%) at a thermal capacity of 8.6 kW. The results obtained from this study show that with the increase in the excess air coefficient from 1.4 to 4.0, there is a decrease in the flame temperature, soot volume fraction, CO, CO_2, and NO_x emissions. Furthermore, flame length tends to shorten with the increment in the excess air coefficient. On the other hand, due to oxygen enrichment in the combustion of biogas from 21% to 27%, flame temperature, soot volume fraction, as well as CO_2 and NOx pollutants tend to increase. Furthermore, despite the peak level of CO emission increasing with oxygen enrichment in the combustion chamber, the amount of emission measured towards the outlet decreases.

Keywords: Oxygen-enrichment, excess air, soot, biogas flame, calorific value

1 INTRODUCTION

The fact that energy has become an essential need in our lives brings the concern of the current energy resources being exhausted over time. Therefore, evaluating renewable or alternative energy sources and investing in technologies will gain importance today and in the future. Biogas fuels as a biomass energy source can be shown among the prominent alternative fuels such as ammonia, synthetic gas, shale gas, and hydrogen gaseous. The combustion behavior of biogas fuels has been considered in different combustion systems. Charest et al. [1] studied the soot formation of biogas fuels under elevated pressures ranging from 1 to 20 atm in a laminar diffusion flame. It stated that dilution with CO_2 suppressed soot formation at all pressure. Fischer and Jiang [2] studied the chemical kinetic aspects of the flame of biogas. They declared that for stoichiometric and lean mixtures, an increment in the initial CO_2 concentration lowers NO production and raises CO at higher temperatures. NO is far smaller for rich conditions and does not follow this way. Hoerlle et al. [3] compared the superposition WSGG radiation pattern with LBL spectral integration for a series of laminar unmixed counter flow flames of ethylene burning with an oxygen-rich oxidizer. They combined soot generation with numerical and chemical solutions for thermal radiation approaches. The role of thermal radiation and the importance of radiation absorption on soot formation were explored by systematically replacing N_2 with CO_2 in the fuel or oxidizer. As a result, they observed that a low strain rate occurs due to some non-negligible differences. Evaluation of the soot spectral radiation coefficient (Ck,s) revealed a significant effect on the soot fraction for low CO_2 addition levels. Liu et al.[4] experimentally and numerically investigated the soot formation and exchange properties in premixed methane/ethylene-oxygen-argon flames. The numerical simulation results obtained with the validated SWOSMC method showed excellent agreement with the experimental results. The results showed that while the coagulation rate increased in ethylene flame, condensation and nucleation rates increased in methane flame. Wei et al. [5] calculated the emission indexes (EI) of laminar mixed biogas-hydrogen flames undergoing flame-wall interaction (FWI) by experimentally measuring the total CO, NOx, and NO_2/NOx ratios. The results showed that with the addition of H_2, the EICO of the BG75-hydrogen flame steadily increased with the high reactivity of H_2, efficiently suppressing CO oxidation for the OH radical. Hosseini and Vahid [6] experimentally observed the performance of the flameless combustion chamber using biogas in a flameless combustion furnace under laboratory conditions. As a result, they showed that

flameless combustion is one of the most suitable strategies and techniques for biogas. Zhen et al. [7] experimentally studied the stability of a biogas diffusion flame and the effect of hydrogen addition on impingement heat transfer. By volume, they kept the hydrogen content between 5% and 10% of the biogas. They revealed changes in the flame's appearance, stability, and heat transfer properties upon the addition of hydrogen to the biogas flame. The addition of hydrogen significantly increased the stability of the biogas flame. The initial 5% hydrogen addition was more efficient at improving stability than the other 5% hydrogen addition. Amar et al. [8] studied the effects of diluting a mixture of biogas BG75 (75% CH_4 and 25% CO_2) and hydrogen with a volume of water vapor ranging from 10% to 50%. As a result, it was shown that the combustion structure was susceptible and variable to the water vapor and hydrogen mixture parameters. Nourbakhsh et al. [9] performed a thermodynamic analysis of syngas production by partial oxidation of biogas (POX) and performed chemical equilibrium calculations for the partial oxidation of (CH_4+CO_2) mixtures based on the Gibbs free energy minimization method, which emphasizes soot formation. They revealed that process temperature plays a crucial role in increasing syngas production and soot reduction. Also, the pressure had an impractical effect on the syngas production efficiency. It was determined that both hydrogen and carbon monoxide caused a decrease in soot formation. Sabnis and Aggarwal [10] conducted a simulation study to investigate NOx and soot emissions in n-heptane/methane triple flames in a counter-jet configuration. As a result of the simulation, it was observed that the benzene emission index and the soot emission decreased as the methane in the mixture increased. Kruczek et al. [11] investigated the emission levels of methane and biogas from anaerobic decomposition and its effect under engine operating conditions. As a result, NO_x emissions for biogas were significantly low due to the relatively low-temperature in-cylinder. Fischer and Jiang [12] conducted a simulation study of un-premixed jet flames of methane (CH_4) and biogas with the LES (Large Vortex Simulation) turbulence model to examine the effect of CO_2 addition on carbon monoxide formation. In the simulation data, a significant increase in the mass fractions of CO was revealed in the presence of CO_2. The kinetic model of methane and biogas showed a strong increase in CO_2. Although many studies have focused on biogas flame and emissions, it is understood that there are still deficiencies in the literature regarding combustion emissions and soot pollutants. This study has been prepared to contribute to this section of the literature.

2 NUMERICAL MODEL

For modeling chemical reactions of biogas, non-premix combustion with a Steady Diffusion Flamelet technique has been used in ANSYS Fluent 18.2 [13]. Gri-mech 3.0 has been utilized for the chemical kinetic mechanism of the simulated fuels [14].

The DO radiation model has been used for the heat transfer of radiation energy. For the modeling of turbulent flow, the Realizable k-ε turbulence model has been utilized [15]. Due to using boundary layer mesh, the Enhanced Wall Treatment near-wall model has been utilized [16]. Coupled and PRESTO! have been adapted for the pressure-velocity coupling scheme and pressure spatial discretization, respectively. Second-Order Upwind is chosen for governing equations [17],[18]. Moss and Brookes soot model is used for the soot formation prediction [19]. The 2-D view and mesh structure of the combustion chamber with a length of 1.25 m and a diameter of 0.155 m are shown in Figure 1.

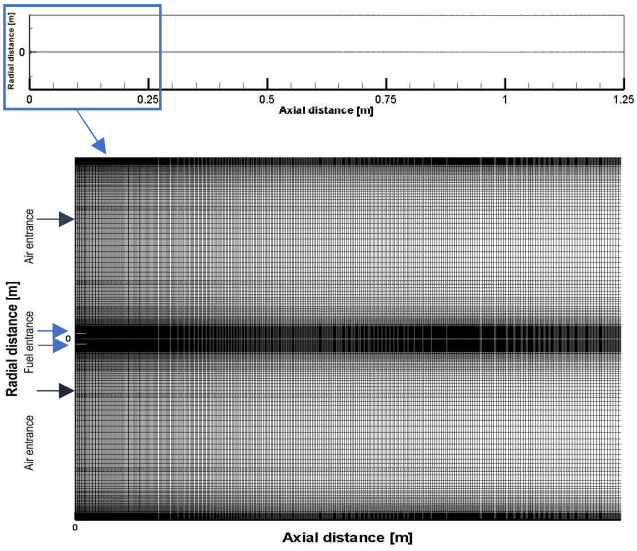


Figure 1. Geometrical model and boundary layer mesh generation for the computational zone

Although synthetic gases draw the attention of researchers due to the increment in energy demand [20–23], methane is more easily accessible and has cleaner combustion nature

with a lower carbon/hydrogen ratio causing less CO_2 and HC emissions [24]. On the other hand, biogas fuels contain high amounts of carbon dioxide by volume. Hence, the calorific energy value of biogas fuels is lower than other conventional gaseous fuels such as pure methane, natural gas, propane, and hydrogen. The basic disadvantage of biogas fuels is their weak flame due to their low heating values (calorific value) [25]. Therefore, their calorific value can be enhanced by fuel H_2-blending fuels [26]. Component and volumetric percentages of biogas have been obtained from the study published by Ilbas et al. [27]. The numerical simulations of biogas fuel have been carried out at the same thermal capacity of 8.6 kW under lean conditions. The utilize of the lean combustion leads to a low formation of polluting species with an unstable flame that is crucial to industrial applications [8].

3 RESULTS AND DISCUSSION

3.1 Verification and Validation of the Numerical Model

In this study, the numerical combustion of methane gas has been validated with experimental data published by Brookes and Moss[28]. Predicted data of soot volume fraction obtained at two different pressure values (1-3 atm) have been compared with experimental data as shown in Figure 2. The obtained results show that soot volume fraction prediction of the numerical results on the radial lines at two locations are close to experimental results under both pressures. Therefore, it is considered that validation is approximately provided.

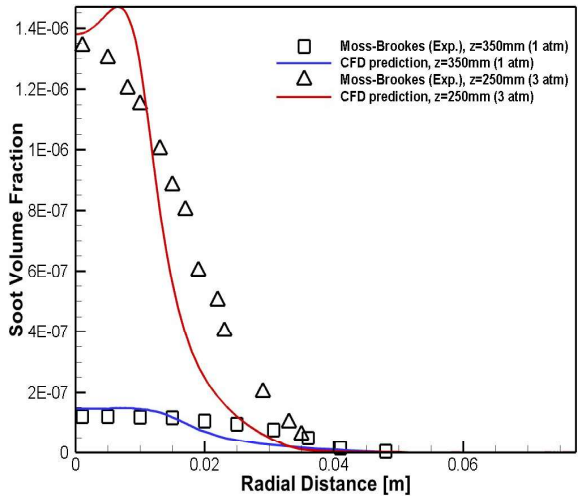


Figure 2. Comparison of numerical and experimental results for CH_4 fuel

3.2 Effects of excess air and oxygen enrichment on combustion and emission

In this section, the excess air coefficient was changed to 1.4, 1.8, 2.5, and 4, respectively, to examine the combustion and emissions of biogas fuel. Thus, the effect of excess air on emission and soot formation was investigated. Besides, for the case where the excess air coefficient is 4, the oxygen enrichment percentage is gradually increased from 21% to 27% to reveal the effect of oxygen enrichment on biogas combustion. The effect of the excess air coefficient on the flame temperature of biogas fuel is shown in Figure 3a. It is observed that the maximum flame temperature decreases with increasing air excess coefficient. Similarly, the combustion chamber outlet temperature decreases with increasing air excess coefficient. When the effects of oxygen-enriched combustion are examined in Figure 3b, it is seen that the flame peak temperature, as well as flue gas temperature, increase with the increasing oxygen percentage. Increasing the oxygen percentage from 21% to 27% has increased the maximum flame temperature and flue gas temperature by approximately 200 K and 120 K, respectively.

When the soot formation graph (Figure 3c) is examined along the combustion chamber axis, the increasing air excess coefficient decreases the amount of soot formed. It is seen that the formation of soot is completed when the air excess coefficient is 4. However, it continues to increase towards the exit for other excess air coefficients. It appears that the soot formation starts to increase significantly when the flame temperature is in the range of 1400-1600K. In oxygen-enriched combustion, it has been observed that the increased amount of oxygen encourages the formation of soot and increases it gradually as shown in Figure 3d.

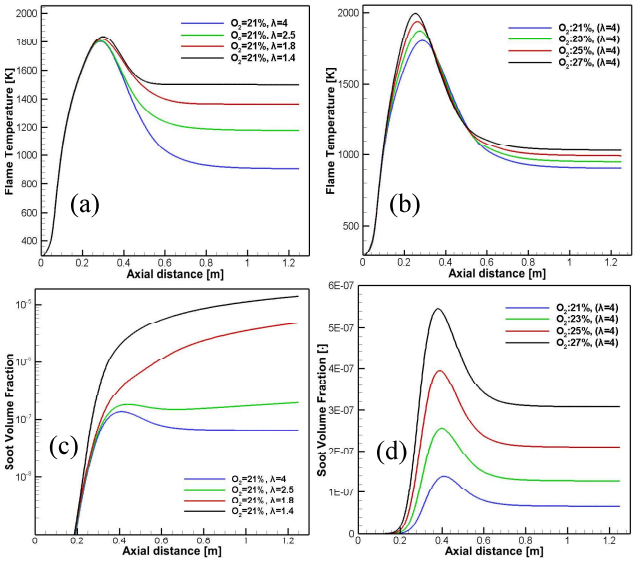


Figure 3. Variation of flame temperatures and soot formation of biogas under various excess air and oxygen enrichment conditions

It has been observed that the increase in the excess air coefficient reduces the amount of carbon dioxide in the combustion chamber axis towards the combustion chamber outlet, as shown in Figure 4a. This situation can be explained by the fact that a high mass fraction of CO_2 species in the fuel drops slowly towards the flame due to other species such as N_2, H_2O, O_2, and others appearing in the flue gas after combustion occurs. CO_2 formation has been encouraged with lower excess air coefficients. In oxygen-enriched combustion, the formation of CO_2 increases with the increasing oxygen percentage, as presented in Figure 4b. However, the amount of increase in CO_2 formation is relatively lower than in the cases with excess air coefficient.

As for CO emissions, as shown in Figure 4c-d, the effect of increasing excess air coefficient on CO emissions is minimal. On the other hand, although the CO level formed in the combustion chamber increases significantly with increasing oxygen percentage, CO is depleted by participating in the reaction chain after a short distance to form CO_2.

Figure 4e-f shows the effect of excess air and oxygen enrichment variation on NO_x emissions. NO_x formations have decreased with the high effect of flame temperatures decreasing, as shown in Figure 4e. The maximum point of NO_x formation occurred in the range of axial distance 0.30-0.55 m. The maximum level of NO_x is about 600 ppm for λ=1.4, while it is 293 ppm for λ=4. Since the reduction of the excess air coefficient increases the flame temperatures towards the combustion chamber exit, this results in an increase in NO_x in the combustion chamber exit region. When the effect of oxygen-enriched air on NO_x emission is examined by keeping λ constant in Figure 4f., the maximum NOx formation occurred at 0.35 m axial distance for all cases. It has also been observed that the amount of NO_x released on the axial line increases gradually with increasing oxygen enrichment. Although NO_x emission levels in the outlet region decrease, the amount of emissions emitted at the outlet also increases slightly with oxygen enrichment. In the flame enriched with oxygen, the maximum levels of NO_x measured in the combustion chamber are 2400, 1400, 680, and 293 ppm for 27%, 25%, 23%, and 21% cases, respectively.

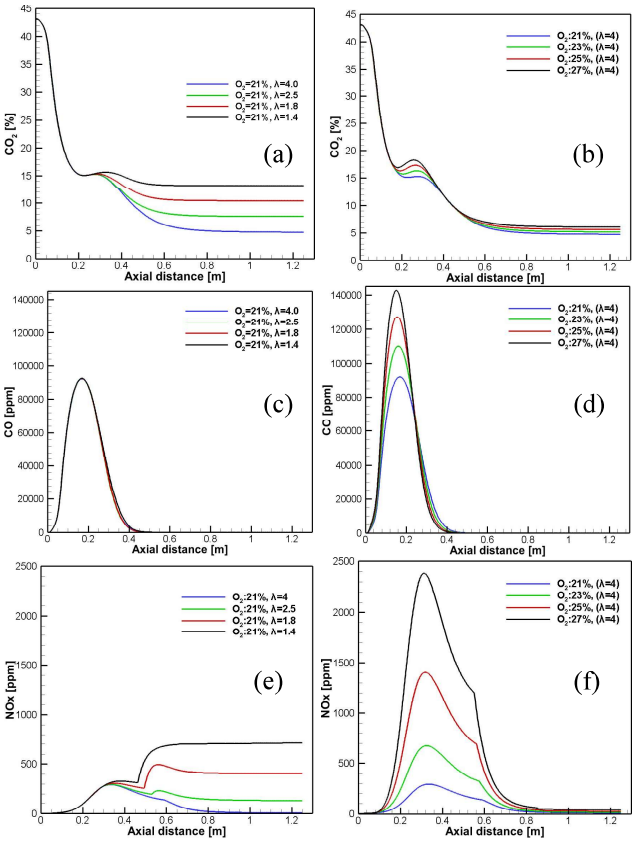


Figure 4. Variation of pollutant emission under excess air and oxygen enrichment

The effect of changing air excess ratio (λ) on mean flame temperature, soot volume fraction, and NO_x can be seen in Figure 5. The effect of decreasing the λ value on mean flame temperature distribution can be seen in Figure 5a. Decreasing λ value increases mean flame temperatures. The peak flame temperatures measured on the center plane are 1804, 1808, 1820, and 1840 K for λ=4, 2.5, 1.8, and 1.4, respectively. The combustion

chamber temperature has reached its maximum value around 1823 K at 0.5 m axial distance for λ =1.4, and it is around 1223 K for λ=4.

The effect of decreasing λ value on soot volume fraction distribution can be seen in Figure 5.b. Since the color scale is in the range of 10^{-6}-1.7× 10^{-5}, it has been observed that it is almost completely blue (minimum level) for λ =4 and λ=2.5. On the other hand, due to the color scale opposite effect is seen completely red in λ =1.8 and λ =1.4. In other words, the amount of soot increases significantly with the decreasing λ. The reason for this may be the increase in the amount of unburned carbon at a low λ value. The effect of decreasing λ value can some effects on the NOx formation. The amount of NO_x released gradually increases with the decrease in λ, as shown in Figure 5.c. These results also show the advantage of lean combustion conditions obtained with a high excess air coefficient. Low NO_x is emitted in the reaction zone in the inlet parts, while a high amount of NO_x is emitted in the high-temperature zone. The amount of NO_x to be thrown into the environment is the values read at the exit of the combustion chamber.

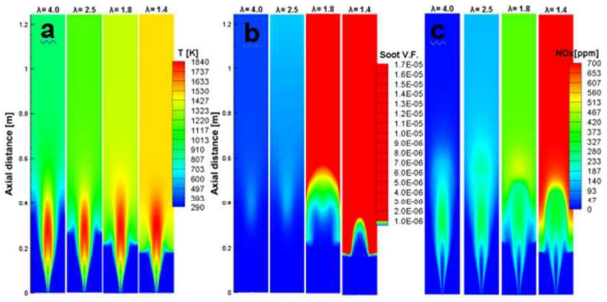


Figure 5. Temperature, Soot Volume Fraction and NO_x with changing excess air coefficients image

The effects of oxygen concentration on mean flame temperature, soot volume fraction, and NOx can be seen in Figure 6. Mean flame temperature increased with increasing content of oxygen, as shown in Figure 6.a. Mean flame temperature reached its maximum value of 2000 K in the range of 0.3-0.35 m axial distance. The effect of increasing oxygen amount in the air on soot volume fraction is seen in Figure 6.b. Soot volume fraction increased with increasing oxygen amount. Regardless of the amount of oxygen, the soot volume fraction reached its maximum value in four cases at 0.4 m axial distance, slightly beyond the maximum value of mean flame temperature. As a result of oxygen enrichment, the nitrogen in the air reacts with more oxygen to form more NOx, especially around the reaction zone, as shown in Figure 6c. The highest NOx amount comes out as a result of the highest oxygen enrichment. Outside the reaction zone, NOx has gradually reduced for all cases due to the reaction of 2NO and N_2 to $2N_2O$ species.

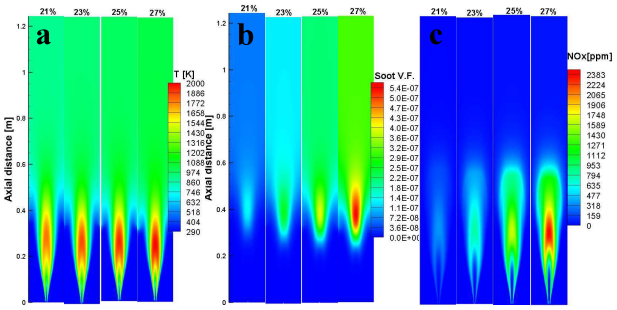


Figure 6. Temperature, Soot Volume Fraction

4 CONCLUSION

In this study, after validation of the numerical model with soot volume fraction data published by Moss and Brookes for methane combustion, the combustion, and emissions of biogas fuels under excess air and oxygen-enriched combustion conditions have been investigated. As a result of the numerical analysis, increasing excess air coefficient shorten the flame length and decrease flue gas temperatures. Furthermore, CO_2, NO_x, and soot emission in the combustion chamber tend to decrease. On the other hand, increment the oxygen percentage from 21% to %27 gradually extends the flame lenght and rises flue gas temperatures, CO_2, NO_x, and soot emissions. On the other hand, there is a slight decrease in CO emission levels with an increase in excess air coefficient. With an increase in the oxygen percentage, the CO level through the flame in the combustion chamber has increased and turned into CO_2 emission earlier in the reaction chain.

ACKNOWLEDGEMENTS

The author is grateful for the use of the computing resources provided by the National Center for High Performance Computing of Turkey (UHEM, UYBHM) under grant number 1010322021.

REFERENCES

[1] Charest MRJ, Gülder ÖL, Groth CPT. Numerical and experimental study of soot formation in laminar diffusion flames burning simulated biogas fuels at elevated pressures. Combust Flame 2014;161:2678–91. https://doi.org/10.1016/J.COMBUSTFLAME.2014.04.012.

[2] Fischer M, Jiang X. An investigation of the chemical kinetics of biogas combustion. Fuel 2015;150:711–20. https://doi.org/10.1016/J.FUEL.2015.01.085.

[3] Hoerlle CA, França FHR, Pagot PR, Pereira FM. Effects of radiation modeling on non-premixed sooting flames simulations under oxyfuel conditions. Combust Flame 2020;217:294–305. https://doi.org/10.1016/J.COMBUSTFLAME.2020.04.012.

[4] Liu S, Chan TL, He Z, Lu Y, Jiang X, Wei F. Soot formation and evolution characteristics in premixed methane/ethylene-oxygen-argon burner-stabilized stagnation flames. Fuel 2019;242:871–82. https://doi.org/10.1016/J.FUEL.2018.12.051.

[5] Wei Z, Zhen H, Leung C, Cheung C, Huang Z. Effects of H2 addition on the formation and emissions of CO/NO2/NOx in the laminar premixed biogas-hydrogen flame undergoing the flame-wall interaction. Fuel 2020;259:116257. https://doi.org/10.1016/J.FUEL.2019.116257.

[6] Sarvestani NS, Abbaspour-Fard MH, Tabasizadeh M, Nayebzadeh H, Van TC, Jafari M, et al. Synthesize of magnetite Mg-Fe mixed metal oxide nanocatalyst by urea-nitrate combustion method with optimal fuel ratio for reduction of emissions in diesel engines. J Alloys Compd 2020;838:155627. https://doi.org/10.1016/J.JALLCOM.2020.155627.

[7] Zhen HS, Leung CW, Cheung CS. Effects of hydrogen addition on the characteristics of a biogas diffusion flame. Int J Hydrogen Energy 2013;38:6874–81. https://doi.org/10.1016/J.IJHYDENE.2013.02.046.

[8] Amar H, Abdelbaki M, Fouzi T, Zeroual A. Effect of the addition of H2 and H2O on the polluting species in a counter-flow diffusion flame of biogas in flameless regime. Int J Hydrogen Energy 2018;43:3475–81. https://doi.org/10.1016/J.IJHYDENE.2017.11.159.

[9] Nourbakhsh H, Rahbar Shahrouzi J, Zamaniyan A, Ebrahimi H, Jafari Nasr MR. A thermodynamic analysis of biogas partial oxidation to synthesis gas with emphasis on soot formation. Int J Hydrogen Energy 2018;43:15703–19. https://doi.org/10.1016/J.IJHYDENE.2018.06.134.

[10] Sabnis P, Aggarwal SK. A numerical study of NOx and soot emissions in methane/n-heptane triple flames. Renew Energy 2018;126:844–54. https://doi.org/10.1016/J.RENENE.2018.04.007.

[11] Kruczek G, Przybyła G, Ziółkowski Ł, Adamczyk WP. Comparative assessment of the application of methane and biogas in energy production: An experimental and numerical investigation. Renew Energy 2019;143:1519–30. https://doi.org/10.1016/J.RENENE.2019.05.087.

[12] Fischer M, Jiang X. Numerical studies of CO formation during biogas combustion. Energy Procedia 2017;142:426–31. https://doi.org/10.1016/J.EGYPRO.2017.12.067.

[13] Moussa O, Driss Z. Numerical Investigation of the Turbulence Models Effect on the Combustion Characteristics in a Non-Premixed Turbulent Flame Methane-Air. Am J Energy Res Vol 5, 2017, Pages 85-93 2017;5:85–93. https://doi.org/10.12691/AJER-5-3-3.

[14] Gregory P. Smith, David M. Golden, Michael Frenklach, Nigel W. Moriarty, Boris Eiteneer, Mikhail Goldenberg, C. Thomas Bowman, Ronald K. Hanson, Soonho Song, William C. Gardiner, Jr., Vitali V. Lissianski and ZQ. Gri-mech 3.0. n.d.

[15] Salih Cellek M. Flameless combustion modeling of CH4/H2 in the laboratory-scaled pilot furnace. n.d.

[16] Cellek MS. Turbulent flames investigation of methane and syngas fuels with the perspective of near-wall treatment models. Int J Hydrogen Energy 2020;45:35223–34. https://doi.org/10.1016/J.IJHYDENE.2020.05.039.

[17] Kekec KB, Karyeyen S. H2 – CH4 blending fuels combustion using a cyclonic burner on colorless distributed combustion. Int J Hydrogen Energy 2021. https://doi.org/10.1016/j.ijhydene.2021.08.118.

[18] Kenan Bilgin Kekeca SK. Combustion Characteristics on Colorless Distributed Combustion (CDC) in a Cyclonic Burner. Int J ENERGY Stud 2020;5:43–55.

[19] CELLEK MS. Combustion Characteristics and Soot Formation of Shale Gases. Eur J Sci Technol 2020:49–59. https://doi.org/10.31590/ejosat.839848.

[20] Alabaş B, Tunç G, Taştan M, Yılmaz İ. Examination of combustion characteristics of oxygen enriched synthetic gases mixtures at various acoustic frequencies. Int J Hydrogen Energy 2021. https://doi.org/10.1016/j.ijhydene.2021.07.035.

[21] Yilmaz I, Ilbas M. An experimental study on hydrogen-methane mixtured fuels. Int Commun Heat Mass Transf 2008. https://doi.org/10.1016/j.icheatmasstransfer.2007.06.004.

[22] Yilmaz İ, Alabaş B, Taştan M, Tunç G. Effect of oxygen enrichment on the flame stability and emissions during biogas combustion: An experimental study. Fuel 2020;280. https://doi.org/10.1016/j.fuel.2020.118703.

[23] Yilmaz H, Cam O, Tangoz S, Yilmaz I. Effect of different turbulence models on combustion and emission characteristics of hydrogen/air flames. Int J Hydrogen Energy 2017;42:25744–55. https://doi.org/10.1016/j.ijhydene.2017.04.080.

[24] Şanlı A, Yılmaz İT, Gümüş M. Investigation of combustion and emission characteristics in a TBC diesel engine fuelled with CH4–CO2–H2 mixtures. Int J Hydrogen Energy 2021;46:24395–409. https://doi.org/10.1016/j.ijhydene.2021.05.014.

[25] Zouagri R, Mameri A, Tabet F, Hadef A. Characterization of the combustion of the mixtures biogas-syngas at high strain rates. Fuel 2020;271:117580. https://doi.org/10.1016/j.fuel.2020.117580.

[26] Mameri A, Tabet F. Numerical investigation of counter-flow diffusion flame of biogas-hydrogen blends: Effects of biogas composition, hydrogen enrichment and scalar dissipation rate on flame structure and emissions. Int J Hydrogen Energy 2016;41:2011–22. https://doi.org/10.1016/j.ijhydene.2015.11.035.

[27] İlbaş M, Şahin M, Karyeyen S. 3D numerical modelling of turbulent biogas combustion in a newly generated 10 KW burner. J Energy Inst 2018;91:87–99. https://doi.org/10.1016/j.joei.2016.10.004.

[28] Brookes SJ, Moss JB. Measurements of soot production and thermal radiation from confined turbulent jet diffusion flames of methane. Combust Flame 1999;116:49–61. https://doi.org/10.1016/S0010-2180(98)00027-3.

A STUDY ON THE NANOPARTICLE CONTRIBUTION IN A DUAL FUEL DIESEL ENGINE

Esenay Arslan[1], M. Raşit Atelge[2], Nafiz Kahraman[3], Sebahattin Ünalan[4], Bilge A. Çeper[5]

1. Department of Electricity and Energy, Kayseri University, Kayseri; email: esenayarslan@kayseri.edu.tr
2. Department of Mechanical Engineering, Siirt University, Siirt; email: rasitatelge@siirt.edu.tr
3. Department of Aerospace Engineering, Erciyes University, Kayseri; email: nafiz@erciyes.edu.tr
4. Department of Mechanical Engineering, Erciyes University, Kayseri; email: s-unalan@erciyes.edu.tr
5. Department of Aerospace Engineering, Erciyes University, Kayseri; email: balbayrak@erciyes.edu.tr

Abstract

In this experimental study, the effects of nanoparticle additive on engine performance and emissions in a compression ignition engine operating in dual fuel mode were investigated. Tests were carried out under five different load conditions, including the no-load condition, on a dual fuel diesel engine with natural gas (NG) added to the combustion air. Then, carbon nanotubes (CNT) were added to diesel fuel as nanoparticle additive and a homogeneous mixture was obtained by using an ultrasonic mixer. The test engine was tested at a constant operating speed of 1500 rpm. The amount of nanoparticle added to the diesel fuel was determined as 50ppm (CNT), and the tests were carried out under the same conditions for all fuel conditions with and without CNT additives. The test results obtained were compared in terms of basic engine performance parameters for diesel, diesel/NG, diesel/CNT and diesel/CNT/NG fuel conditions. When the in-cylinder pressures were compared in terms of full load, the maximum pressure was obtained for D/CNT. The maximum pressure difference compared to diesel was 3% with D/CNT. On the other hand, the contribution of NG and CNT to diesel fuel increased in-cylinder pressure only compared to diesel fuel (except diesel/CNT). With the addition of natural gas to the D/CNT mixture, brake specific fuel consumption increased slightly at 50%, 75% and full load. In terms of emissions, when NG is added to the D/CNT fuel mixtures, there is an increase in CO and HC emissions and a slightly decrease in CO_2 and NO_x emissions.

Keywords: carbon nanotube additive, natural gas, combustion, diesel engine, nanoparticle

EXPLOSIONS OCCURED IN A URBAN TERRAIN ACCORDING TO EXPLOSIVE TYPE

M. Sahin[1], S. Tulumcu[2] and M. Yıldız[3]

1. MSÜ, Ankara, Türkiye, E-posta: msahin@kho.msu.edu.tr
2. MSÜ, Ankara, Türkiye, E-posta: stulumcu@kho.msu.edu.tr
3. MSÜ, Ankara, Türkiye, E-posta: melihyildiz@kho.msu.edu.tr

Abstract

Specially designed structural elements are available for military installations containing potentially explosives and civilian structures requiring explosion protection measures. Traditional designs are made and manufactured from heavy materials to withstand bursting or high pressure impacts. These designs not only increase product and construction costs, but also reduce the operational performance of these protective products. To solve these problems, many researchers have tried to use high-strength materials and different structural forms in structural design to resist burst and impact loads. In this study, firstly, the deformation of the steel plates was validated through an experimental study and then the numerical analyzes of the panels in various formations were evaluated. By using the finite element method Ls-Dyna, the burst loading resistance capacity and energy absorption capacity were numerically investigated. Numerical analysis method is used to understand the dynamic response of the blast gate and their displacement patterns with different types of explosives. The calibrated numerical model is used to simulate the dynamic responses of panels exposed to different types of explosives. The peak and permanent displacements of the center point of the front surface at the internal energy absorption and the boundary reaction force of the different panels were calculated and compared. The most effective explosive type was determined by comparing the effect of explosive types according to the displacement amounts in the panel forms in the same amount of explosive types evaluated.

Keywords: Blast Proof Door, Explosion, Dynamic Simulation, Safety and Hazard.

1 INTRODUCTION

Explosion is a very rapid combustion reaction situation. There are many factors, situations and environments that cause an explosion. The common point of all of them is the explosive substance and the necessary conditions for its triggering [1]. These conditions are sometimes provided consciously. Examples of these are explosives used in wars as well as explosives used in terrorist attacks [2]. At the same time, explosives are actively used in excavation works such as tunnels and pipelines and in the demolition of unused buildings. In addition to these uses, explosions sometimes occur as a result of accident. Explosive production facilities, warehouses where explosives are stored, industrial facilities where chemicals are used intensively, gas stations and vehicles containing fuel and many environments can be counted as examples of accidental explosions [3]. There are various situations that occur as a result of the explosion. Burst pressure, toxic release, fire are some of them. These effects vary according to the severity, location and environment of the explosion and the degree of danger is different. The effectiveness of these results changes as you move away from the center of the explosion.[4]

The main factor in the formation of the effects of explosives is their chemical structure. These chemical properties determine how strong explosives are and how they affect the environment when they explode. There are many types of explosives used for different purposes. There are many parameters that are measured and compared in research to understand the nature of the explosive. Examples of these are parameters such as detonation rate, density, CJ (Chapman-Jouguet) pressure [5]. It is aimed to examine the effects of the changes in these parameters on the combustion event and the differences in the effects of the explosive spread to the environment within the scope of this paper.

For the verification of the numerical analysis made within the scope of the study, the experimental and numerical analysis data and results made in another publication were used.

This verification is described in the next section. These numerical modeling studies were carried out using the widely used LS-DYNA.

2 NUMERICAL ANALYSIS VALIDATION

Finite element simulation is performed using LS-DYNA. It is a general purpose finite element program that can simulate complex real-world problems. Ls-Dyna, the Implicit and Explicit Finite Element Method software, is one of the most advanced simulation tools for nonlinear structural analysis. It is widely used to analyze problems related to structure response to high-speed impact, large deformation, and burst load and strain rate behavior of materials. It has been proven to provide reliable numerical estimates of damage as a result of the structural response to blast loads. The stiffener proposed in this study is used to simulate the response given by the displacement of the plates.

To verify the reliability of the numerical model in LS-DYNA, a tested and numerically modeled steel panel was used to calibrate the model [4]. A series of burst tests were performed to investigate the response of a 12.7 mm thick steel faceplate subjected to burst loads from a 1 kg explosive on top of the panel. In the tests, the distance of the charge is 280 mm. The 610 x 610 mm faceplate steel plate is bolted to two I-beams to a 19 mm thick steel plate. The 610 x 610 mm steel frame is supported as shown in Figure 1. The test data obtained here were used to calibrate the numerical model developed in Ls-Dyna in this study.

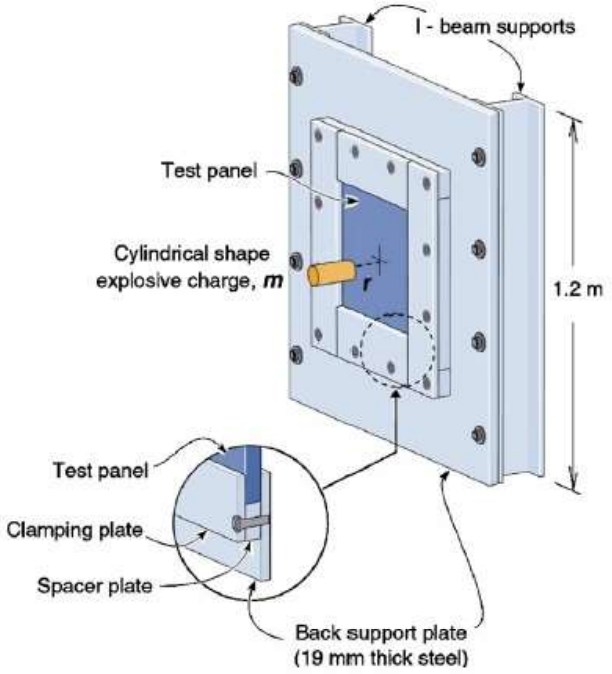


Figure 1 - Schematic Experiment Illustration [4]

3 MATERIALS AND METHODS

Comprehensive nonlinear three-dimensional numerical analysis using the Lagrange-Eulerian (ALE) method in LS-DYNA was used to numerically model the near-burst experimental setup. The purpose of numerical simulations is to develop validated models based on experimental findings used for parametric studies. This chapter includes sections on developing critical models and defining material models for accurate generation of numerical models.

3.1 Model

The model consists of an air zone, plate and blast rig. Air is modeled as an Euler field. solid element is modeled exactly as Lagrange (air is modeled as a 610 mm cube). Air is considered as Linear Polynomial equation of state in explosion simulations via *EOS_LINEAR_POLYNOMIAL in LS-DYNA. The equation is given below:

$$P = C_0 + C_1\mu + C_2\mu^2 + C_3\mu^3 + (C_4 + C_5\mu + C_6\mu^2)E$$

The tested plate thickness is 12.7 mm and has dimensions of 610X610 mm. *CONSTRAINED_LAGRANGE _IN _SOLID board is used to enable interaction between Eulerian air region and plate. The explosion charge was modeled using the *INITIAL_VOLUME_ FRACTION_GEOMETRY keyword and the explosion was initiated with the *INITIAL_DETONATION card. Shock wave propagation after the explosion is described by the Jones-Wilkins-Lee (JWL) equation:

$$p = A\left[1-\frac{w}{R_1V}\right]e^{-R_1V} + B\left[1-\frac{w}{R_2V}\right]e^{-R_2V} + \frac{wE}{V}$$

The modeling of the air zone is limited by the dimensions of the plate. *BOUNDARY_NON_REFLECTING card is defined for air surfaces to simulate under real conditions the release of air to pass outside this zone. In this case, under the defined flow conditions, when the pressure wave reaches the air limit, it will be excluded from the analysis calculations. With this method, it will not be affected by the limit reflection value that may occur.

As can be seen in Figure ……, when the explosive reaches the plate, it interacts and deforms. In addition, the issue that the explosive pressure does not pass through the plate and spread to another area shows an important issue in evaluating the accuracy of the ALE model. It can be determined that there is no leakage from the Lagrangian element.

When a shock wave encounters a target surface at an oblique angle of incidence the effective pressure is given by

$$P_{eff} = P_{ref}\cos^2\theta + P_{inc}\left(1+\cos\theta-2\cos^2\theta\right)$$

3.2 Materials

Modeling the strain rate dependent behavior of steel is crucial to accurately simulating deformation. Near burst loads can create stresses that exceed the yield strength of the material. The steel material model was created with the *MAT_PIECEWISE_LINEAR_PLASTICIT Y material card. It is a structural material model to represent stress-strain behavior for metal materials. Table ……. shows the typical mechanical properties of the steel grade used in the numerical analysis.

*MAT_PIECEWISE_LINEAR_PLASTICITY material model was used to show the stress-strain behavior of STEEL 304L steel realized in this study.

4 RESULTS AND DISCUSSION

Finite element analysis was carried out using LS-DYNA to examine the dynamic response of three different explosives under certain ambient conditions. The properties of the explosives used in the analyzes are given in Table 1. There are many factors that cause the effects to occur during the explosion, but in this study, these three parameters were evaluated in themselves. During this explosion, explosives of the same weight were used and the same experimental environment was modeled.

Table 1. Parameters of Explosives

	C-J Detonation Velocity (m/s)	C-J Pressure (Pa)	Density (kg/m^3)
TNT	6930	3681000	1630
C4	8193	5621000	1601
ANFO	4160	2668000	931

In order to minimize the effects of the environmental factor on the results of the simulations, a simple steel plate was used and attention was paid to the symmetry of the load effects on the plate. The effect of the installation is shared in Figure-2.

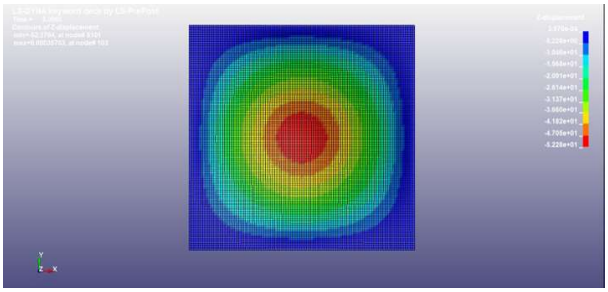
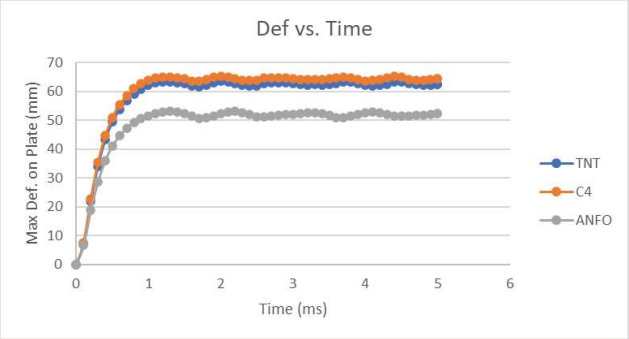


Figure 2 - Example of Deformed Steel Plate on Sımulation

The deformation results obtained from the study showed similarities with each other in some aspects, as expected for all three explosives, but also revealed differences within themselves. When we compare the values in Table-1 to understand the reasons for the differences, the deformation caused by the ANFO explosive, whose all features are obviously smaller than the others, is clearly lower as seen in Graph 1. TNT and C4 explosives, which are similar in some aspects and differ in others, are similar in terms of the deformation they create. Although the density of TNT explosive is higher than C4 explosive, this parameter did not prevent C4 from forming higher deformation. It is seen that the difference in both the detonation rate and C-J Pressure values of the C4 explosive against TNT also affects the amount of deformation.



Graph 1– Deformation vs. Time Results for Different Explosives

This topic seems to be a very suitable topic for in-depth study. The effects of the parameters observed in this study on other explosives and their common effects with different parameters can be examined by those who are interested.

REFERENCES

[1] RATHBUN VE DIG., "Performance of metallic honeycomb-core sandwich beams under shock loading", International Journal of Solids and Structures 43 , 2006.

[2] ZHENYU XUE, "Preliminary assessment of sandwich plates subject to blast loads", International Journal of Mechanical Sciences 45, 2003.

[3] LS DYNA Keywords User's Manual, "Livermore Software Technology Corporation (LSTC)", May 2007.

[4] KUMAR P. DHARMASENA, "Mechanical response of metallic honeycomb sandwich panel structures to high-intensity dynamic loading", International Journal of Impact Engineering 35, 2008.

[5] YANG YI; HE XUEQIU; LUO GENG; WANG HUIA. Effect of meshy obstacle on methane gas explosion. 2011

NUMERICAL INVESTIGATION OF HCCI COMBUSTION FOR TWO DIFFERENT COMBUSTION CHAMBER GEOMETRIES

Oğuz BOSTANCIOĞLU [1] and Nureddin DİNLER [2]

1. Department of Mechanical Engineering, Faculty of Engineering, Gazi University 06570, Maltepe, Ankara, Turkiye; email: oguz.bostancioglu@gmail.com
2. Department of Mechanical Engineering, Faculty of Engineering, Gazi University 06570, Maltepe, Ankara, Turkiye; email: ndinler@gazi.edu.tr

Abstract

Internal combustion engines are evolving in time depending on the requirements of people, governments and technology. For fuel economy optimal performance and reduced emissions different cycles, operating modes of the engines have been studying. One of these studies are HCCI engines. In this paper, design of the combustion chamber for compression ignition internal combustion in diesel engine is studied to decrease the emissions. Two combustion chamber geometries were taken into account. Effects of the geometry combustion chambers on HCCI operation performance of the engine. The combustion chamber has a remarkable influence on the emission rate of the engine because it is the place where the combustion occurs. The combustion efficiency is related with the geometry of the combustion chamber. In addition, three different compression ratios were investigated in this study. Numerical simulations were performed using AVL FIRE software. The in-cylinder pressure, temperature, heat release, NOx mass fraction and soot fraction graphics were given and compared.

Keywords: Internal combustion engine, homogeneous charge compression ignition (HCCI), computational fluid dynamics, piston geometry.

1 INTRODUCTION

It is known that one of the reasons for urban air pollution is exhaust gasses. Nowadays, the increase of the exhaust gasses in the atmosphere leads to health problems and it is harmful for all creatures in the world. One of the most widespread pollutants is vehicle engines.

The emission of the exhaust gasses of that vehicles has a high percentage effect on the environmental pollution. Awareness of increased pollution around the world leads researcher to improve the emission and the efficiency of the pollutants. One of the researching topics according to that problem is designing a more efficient combustion chamber of internal combustion engines which is the most widespread engine for all kinds of vehicles.

The first practical engine was invented by Lenoir in 1860. Rudolpf Diesel developed his compression ignition engine in 1892, which is known as Diesel engine [1].

The combustion chamber geometry has a remarkable influence on the emission rate of the engine. The combustion efficiency is directly based on the geometry of the combustion chamber. The proper geometry of the combustion chamber leads the efficiency of the combustion to increase. That means less unburnt gasses occur and less greenhouse gasses are exhausted to the atmosphere.

One of the first studies of combustion chamber is carried out by Whatmough [2]. The study is about the concept of combustion, properties of different types of combustion chambers, compression of the effects of different layouts on the cycle in theory and practice. Another early study of Newhall is about the design process of the combustion chamber to provide high specific power output with low fuel consumption [3]. Also, Matsumoto et al. [4] investigated the effects of the combustion chamber design and the compression ratio are evaluated under a variety of engine operating conditions. Combustion chamber studies are not a new subject, it has been studied for many years and still goes on.

Lotfi and Ghassemi studied on the effect of combustion chamber design on performance, ignition, and emission. In the study, different layouts of combustion chambers were designed and solved by using numerical methods. The paper is used for compression of the combustion chamber layouts and investigating the numerical methods for the design process [5]. Yousefi et al. [6] investigated combustion characteristics and

emissions of a homogeneous charge compression ignition (HCCI) engine with and without pre-combustion chamber. They used experimental and computational methods. AVL FIRE software was adopted to compare combustion phasing, engine performance and emissions in term of equivalence ratio for both HCCI combustion engines with and without pre-combustion chamber. So that, the effects of pre-combustion chamber on HCCI combustion engine were studied.

In addition to design considerations, there are different studies on HCCI engines. For example, Cerit and Soyhan [7] studied on the thermal behaviour of an HCCI engine piston for clean and deposited conditions numerically. Feroskhan et al. [8] studied on operating parameters of an HCCI engine effecting the combustion, emissions and engine performance. Pham et al. [9] conducted the research on the combustion and emission characteristics of a four-stroke dual-fuel (natural gas–diesel) marine engine at full load. Three-dimensional simulations of the combustion process and emission formations inside the engine cylinder in both diesel and dual-fuel mode to analyse the in-cylinder pressure, temperature, and emission characteristics by using AVL FIRE. Kannan et al. [10] studied on combustion of LPG in a diesel engine using HCCI mode operation. Polat [11] conducted engine tests for ethanol blends usage for a low compression ratio early direct injection HCCI engine. Çelebi et al. [12] investigated the naphta as fuel on an HCCI engine. Also, controlling strategies are important. The review of control strategies are given in [13]. Nowadays, the companies which produce passenger cars, started to produce the vehicles with electric motors instead of internal combustion engines to decrease the rate of emission. The power of the electric motors can prove enough thrust for passenger cars; however, it is not proper for heavy duty vehicles. The reason why, one of the ways to decrease emission of heavy-duty vehicles is designing combustion chambers with high efficiency. In this paper, design of the combustion chamber for compression ignition internal combustion is studied to decrease the emission rates with respect to a modified combustion chamber geometry. Commercial computational fluid dynamics software, AVL FIRE, is used for simulation of the processes in combustion chambers with different layouts, geometries and dimensions and combustion modes.

2 PROBLEM STATEMENT

Awareness of increased pollution around the world leads to improved emission and efficiency of internal combustion engines. Structural improvements of the charge motion inside the cylinder can improve combustion. Better combustion means higher combustion efficiency and lower emissions. The main target of combustion chamber geometry is holding higher performance while the emission rates are decreasing. Combustion chamber is surrounded by the cylinder head, cylinder wall, piston and the valves. The distance between the cylinder head and the piston, location and slope of the valves are parts of the design process of the combustion chamber.

In this study, a compression ignition (CI) internal combustion engine is aimed to turn into homogeneous charge compression ignition (HCCI) mode and a modified combustion chamber design. In the analyses firstly, HCCI combustion is compared with CI combustion on one-cylinder experimental engine for the same combustion chamber geometry. Moreover, impact of different compression ratios and combustion geometries of HCCI engine on engine performance and emission are investigated. Compression ratio and combustion chamber geometry were considered to improve the efficiency together with combustion chamber geometry. AVL FIRE software was used for design and simulation processes.

3 SOLUTION METHODS

The design process of the combustion chamber can be done by using theoretical, experimental and computational methods. Real operating condition results can be obtained by using experimental methods. However, initial costs such as preparing setup, manufacturing of each product with different properties, preparation of setup for the experimental purposes, and operational costs such as laboratory expenses are extremely high and insufficient with respect to budget and time. For this reason, numerical methods are preferred to design the conceptional and preliminary model of the product. Rather than whole models, only the final model is evaluated by using experimental methods to decrease money and time consumption [14].

Recent decades, the development of computer technology provided numerical methods for design processes with high accuracy in relatively short time durations. Computational fluid

dynamics (CFD) tools are computational tools specialized on fluid dynamics by using finite volume methods [9]. A reasonable prediction of the parameters which can be obtained by experimental methods, with the utilization of appropriate approaches is offered by CFD simulations. CFD preference instead of experimental studies reduces the costs of the design process [15]. In addition to developments in computer technologies, the challenge in a competitive market between the companies working on CFD tools increases the speed of development of the tools for engineering.

3.1 Engine Geometry and Parameters

A one-cylinder engine was used for the investigation of engine performance and emission difference of CI combustion and HCCI combustion modes. Also, effects of different compression ratios and combustion chamber geometries were examined by using the engine. The engine with the specifications in Table 1 was determined to use in the calculations. The combustion chamber geometry, which is used in this study, is given in the Figure 1.

Table 1. Engine Specifications

Cylinder Diameter (mm)	76.2
Stroke (mm)	111.1
Stroke Volume (m^3)	5.07e-04
Engine Speed (rpm)	1500
Maximum Power (kW)	9.4

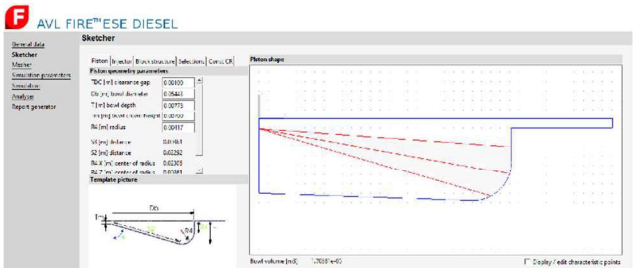


Figure 1. Combustion Chamber Geometry

3.2 Governing Equations

Continuity equation (conversation of mass), Navier-Stokes (momentum) equations, turbulence equations, energy equation and concentration (species) equation are used on computational fluid dynamics tools with finite volume method. These equations cannot solve analytically without simplifying, due to the coupled nature of momentum equation numerical methods must be used. The computations could be done by a code developed by the users, or a software. AVL-FIRE, which uses finite volume method, solves the equations such as continuity, momentum, conservation of energy and turbulence. The equations are given below [16].

Continuity Equation (Conservation of Mass)

Continuity or conservation of mass means the mass balance in the control volume of the flow region.

$$\frac{\partial \rho}{\partial t}+\frac{\partial\left(\rho U_j\right)}{\partial x_j}=0 \tag{1}$$

Momentum Equation

The fluid motion is described by a dynamic equation can be obtained by applying Newton's second law of motion [15].

$$\rho \frac{DU_i}{Dt}=\rho g_i-\frac{\partial p}{\partial x_i}+\frac{\partial}{\partial x_j}\left[\mu\left(\frac{\partial U_i}{\partial x_j}+\frac{\partial U_j}{\partial x_i}-\frac{2}{3}\frac{\partial U_k}{\partial x_k}\delta_{ij}\right)\right] \tag{2}$$

where $\frac{D}{Dt}$ is the material (substantial) derivative.

Energy Equation

Conservation of energy is a physics law that the rate of energy change in a control volume equals to transported energy by heat and/or work to the fluid particles.

$$\rho \frac{DH}{Dt}=\rho \dot{q}_g+\frac{\partial p}{\partial t}+\frac{\partial\left(\tau_{ij}U_j\right)}{\partial x_i}+\frac{\partial}{\partial x_j}\left(\lambda \frac{\partial T}{\partial x_j}\right) \tag{3}$$

where $H=h+\frac{U^2}{2}$

Concentration equation

Concentration of species are evaluated usinf the concentration equation.

$$\rho \frac{DC}{Dt}=\rho \dot{r}+\frac{\partial}{\partial x_j}\left(D\frac{\partial C}{\partial x_j}\right) \tag{4}$$

3.3 Boundary Conditions

The solutions were obtained from the inlet boundary conditions by using instantaneous mass flow rate. This can be done assuming the incompressible fluid flow. Also, no-slip boundary conditions were applied for all velocities at walls. The two-dimensional Navier-Stokes equations are solved on a moving mesh and turbulent fluxes are modelled by using k-ε model. Boundary conditions for the considered physical model are given in the Table 2.

Table 2. Boundary Conditions

Inlet Temperature (K)	400
Side Temperature of Combustion Chamber (K)	575
Temperature of Piston Head (K)	575
Velocities on Cylinder Wall	u = 0, v = 0
Velocities on Piston Surface	u = 0, v=v_{piston}

3.4 Numerical Procedure

AVL FIRE ESE Diesel is used to obtain the numerical solutions. The module is a simulation environment for Diesel engines with enhanced pre- and post-processing. It is developed under the assumption that Diesel-spray and Diesel-combustion happen under axial symmetric conditions from intake valve closing to exhaust valve opening. Therefore, only a slice of the cylinder, generated from a 2D sketch, can be used for modelling the phenomena. This assumption reduces complexity of the meshing requirements without any significant influence on the reliability of the results. However, this assumption reduces meshing complexity from a 3D problem down to the 2D for which the reliable meshing techniques are already available.

The preparing procedure of the analysis in the module is designed to lead the user through the workflow consisting of a few steps. Firstly, 2D sketch which contains the cylinder bowl, squish volume and the injector is provided by the user. In order to simplify the work at this initial stage, many pre-defined geometries are on disposal to the user. The geometry can be loaded by using Sketcher, which allow the user adjusting the template to the actual geometry under consideration. The piston movement is also specified at this stage.

Once the geometry sketch is finished, the procedure proceeds to the meshing step, which is performed by using paving and transfinite interpolation as the backbone algorithms. After the mesh is finished, boundary conditions and solver parameters are set up. When the necessary data of boundary conditions and solver parameter are input, the CFD solver can be run.

4 NUMERICAL RESULTS

Results of engine performance and emission were obtained. During the computation, 'Section Analysis' method was used in order to lower the calculation time due to multiple solutions for different conditions. The method reduces complexity of the meshing requirements without any significant influence on the reliability of the results. In this method, a 2D sketch which represents a slice of the cylinder, is used for modelling.

After the modelling of the combustion chamber, mesh generation was done with respect to the geometry. Meshes are necessary to solve the governing partial differential equations in the allocated cell. The mesh model of the combustion chamber geometry, which is used in this study, is given in the Figure 2.

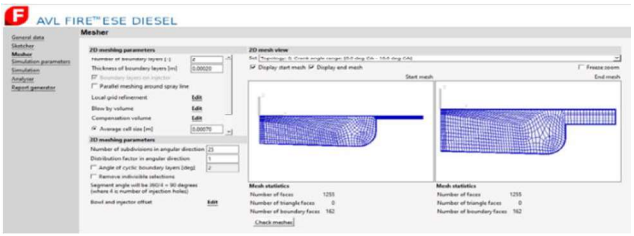


Figure 2. Mesh Model of Combustion Chamber

In this study, ECFM-3Z model was used for combustion modelling, shell model was used for ignition modelling for CI combustion modelling. For HCCI combustion modelling, Eddy Breakup model was used for combustion modelling, HCCI model was used for ignition modelling. For both cases, Extended Zeldovich model was used for NO modelling and kinetic model was used for soot modelling where momentum, continuity, energy and k-ε turbulence equations were used.

4.1 CI Combustion

CI combustion was analysed between 540 and 850 crank angle degrees. In the analysis, ECFM-3Z combustion model was used with Shell ignition model. The aim of the analysis was obtaining the engine performance and emission data for CI combustion mode of the engine.

Engine specific outputs of the analysis are given in the Table 3 in terms of brake mean effective pressure, brake specific fuel consumption, friction mean effective pressure, indicated mean effective pressure, indicated power, and indicated torque.

Table 1. Engine Specific Outputs

Brake Mean Effective Pressure (bar)	8.14
Brake Specific Fuel Consumption (kg/kWh)	0.3493
Friction Mean Effective Pressure (bar)	1.58
Indicated Mean Effective Pressure (bar)	9.72
Indicated Power (kW)	6.15
Indicated Torque (Nm)	39.17

4.2 HCCI Combustion

HCCI combustion was analysed between 540 and 850 crank angle degrees same as CI combustion. In this part of analyses, eddy breakup model combustion model was used with HCCI ignition model. The aim of the analysis was obtaining the engine performance and emission data for HCCI combustion mode of the engine.

Engine specific outputs of the analysis are given in the Table 4 in terms of brake mean effective pressure, brake specific fuel consumption, friction mean effective pressure, indicated mean effective pressure, indicated power, indicated torque.

Table 2. Engine Specific Outputs

Brake Mean Effective Pressure (bar)	7.99
Brake Specific Fuel Consumption (kg/kWh)	0.3559
Friction Mean Effective Pressure (bar)	1.58
Indicated Mean Effective Pressure (bar)	9.56
Indicated Power (kW)	6.06
Indicated Torque (Nm)	38.56

4.3 Comparison Between CI Combustion and HCCI Combustion

Both the cycle analysis of CI combustion and HCCI combustion were done under the same conditions except combustion and ignition mode to observe the effect of the combustion mode in the means of engine performance and emission. ECFM-3Z combustion model with Shell ignition model was used for CI combustion and eddy breakup combustion model with HCCI ignition model was used for HCCI combustion.

As a result of the analyses, it is seen that diesel engines reached higher maximum pressure than HCCI engines during the combustion stroke for the same compression ratio (Figure 3). However, HCCI engines reached higher maximum temperature than HCCI engines under the same conditions. In means of pressure, the maximum value of HCCI engine was 97.6 percent of the maximum value of diesel engine. In terms of temperature, the maximum value of diesel engine was 99.4 percent of the maximum value of HCCI engine (Figure 4). That case leaded the diesel engine to reach higher power and torque values than HCCI engine because of the higher difference between the pressure values than temperature values. The analysis showed that better engine performance is obtained by diesel engine.

One of the other results of the analyses, a rapid heat release was observed in HCCI engine rather than diesel engine as seen in Figure 5. The heat

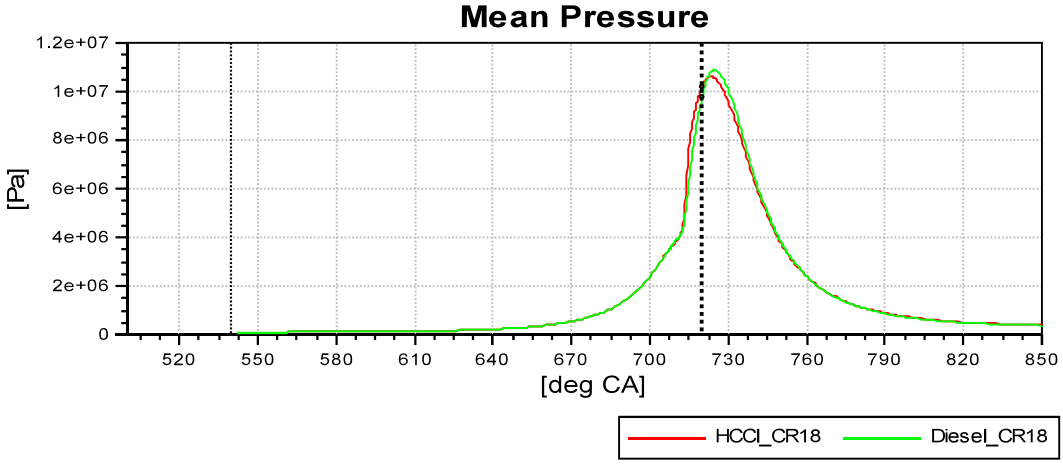


Figure 3. Mean Pressure Comparison for HCCI and CI Combustion

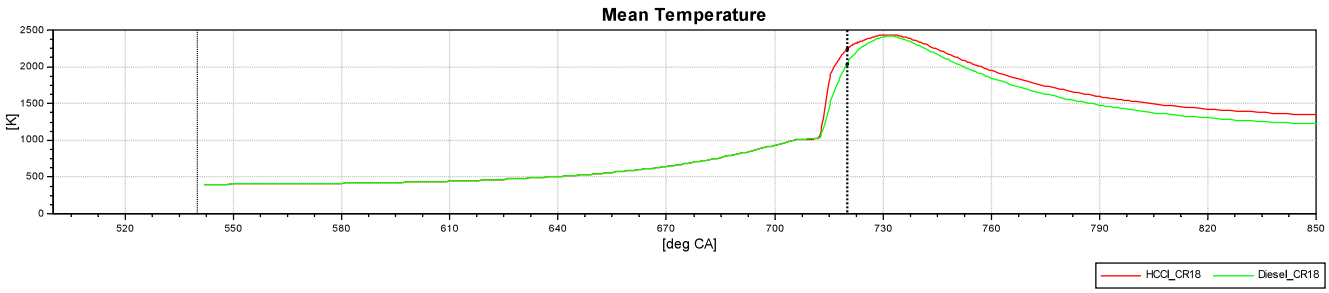


Figure 4. Mean Temperature Comparison for HCCI and CI Combustion

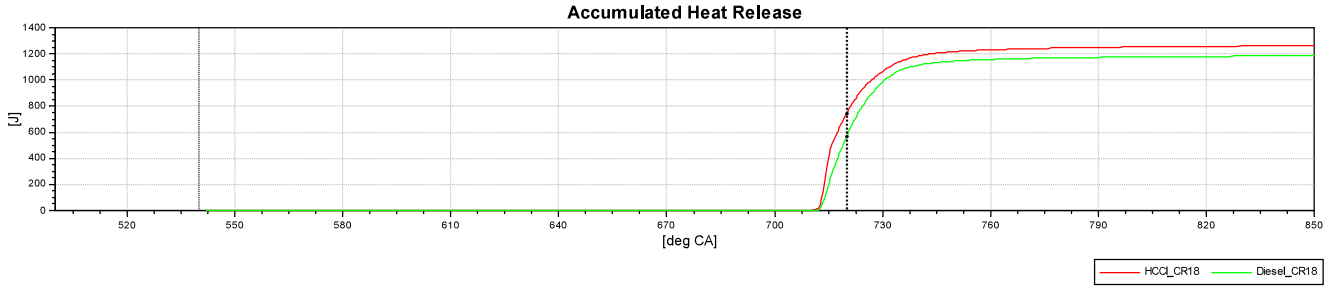


Figure 5. Accumulated Heat Release Comparison for HCCI and CI Combustion

release started with the ignition of the fuel. It was seen that the heat release of the HCCI engine started earlier than the diesel engine and it reached the maximum point within 20 crank angle degrees. On the other hand, the heat release of diesel engine increased slower than HCCI engines. It continued during combustion and expansion strokes and reached the maximum point in longer term. The main reason for that characteristic is the lean combustion in HCCI combustion. It led the combustion to start earlier in the HCCI engine. Homogeneous charge of HCCI engine led to ignition of the fuel in different regions of the combustion chamber at the same time. As a result of that, the maximum heat release value reached earlier in the HCCI engine.

The other results of the analyses are about emission characteristics of the combustion modes. The overall NO and soot mass fractions of diesel and HCCI combustion were compared. Both of them started to occur earlier in HCCI combustion rather than CI combustion. They started to occur whereupon 715 crank angle degrees and the maximum point of the NO mass fraction and soot mass fraction were observed whereupon 730 crank angle degrees as 0.0037 and 0.0148, respectively (Figure 6-7).

On the other hand, the maximum values of overall NO mass fraction and overall soot mass fraction were observed whereupon 720 and 740 crank angle degrees as 0.0023 and 0.0084, respectively. The results show that NO emission rates of HCCI engines is 1.6 times higher than diesel combustion. On the other hand, it is seen that soot emission rates of HCCI engine reaches higher values during lean combustion period, the soot rates decrease lower values than diesel engine in rich combustion period. The soot rate of HCCI engine is 82.4 percent of the diesel engine at 750 crank angle degrees.

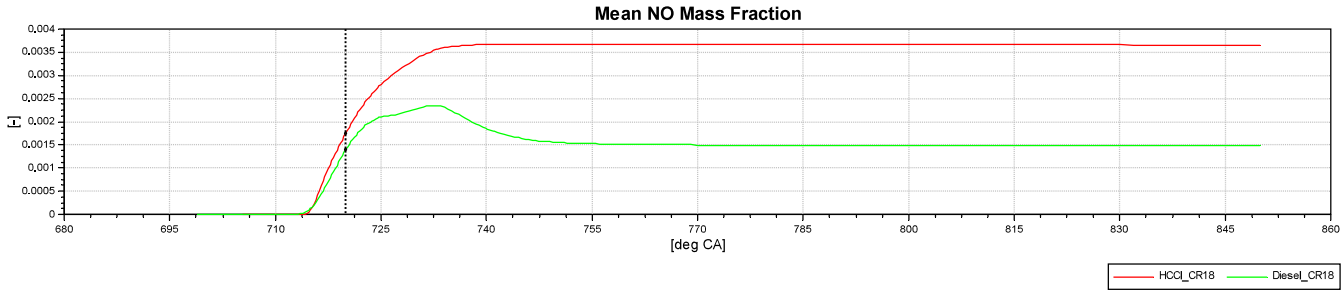


Figure 6. Mean NO Mass Fraction Comparison for HCCI and CI Combustion

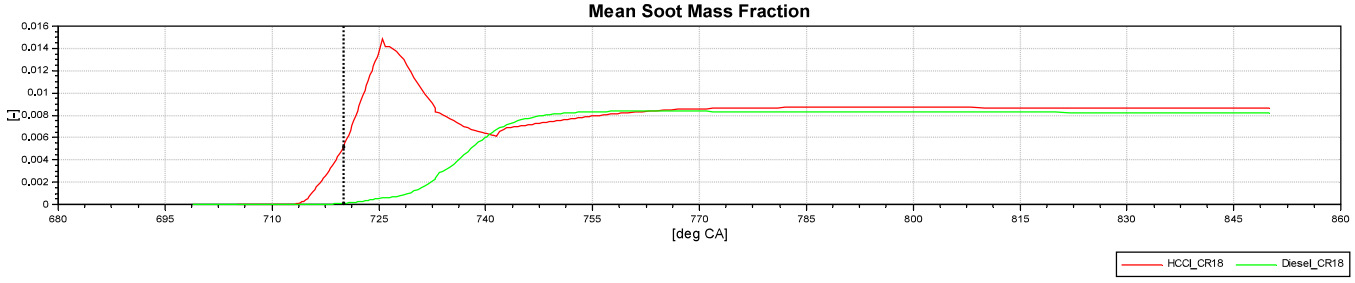


Figure 7. Mean Soot Mass Fraction Comparison for HCCI and CI Combustion

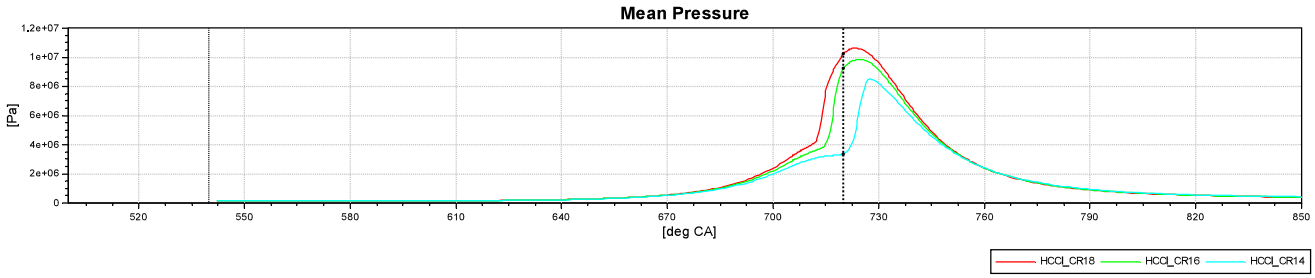


Figure 8. Mean Pressure Comparison of HCCI Combustion Under Different Compression Ratios

4.4 Comparison of HCCI Combustion under Different Compression Ratios

All the cycle analysis of HCCI combustion were done under the same conditions except compression ratio to observe the effect of the combustion mode in the means of engine performance and emission. Compression ratios of 14, 16 and 18 were compared with each other for the same combustion chamber geometry.

From Figure 8, it is seen that higher compression ratio modification reached higher pressure and temperature than the lower compression ratio modification during the combustion stroke for the same combustion chamber geometry. In the means of pressure, the maximum value of HCCI engine with compression ratio of 18 was 1.0787 and 1.2495 times of the maximum value of HCCI engine with compression ratio of 16 and 14, respectively. On the other hand, the maximum temperature value of HCCI engine with compression ratio of 14 was 1.0103 and 1.0509 times of the maximum value of HCCI engine with compression ratio of 16 and 18. The analysis showed that despite of higher maximum pressure of the higher compression ratio, higher temperature can be achieved by lower compression ratio due to its higher air-fuel ratio (Figure 9).

The accumulated heat release for different compression ratios of HCCI combustion for 14, 16, 18, respectively can be seen in Figure 10. The maximum accumulated heat release value of HCCI engine with compression ratio of 14 was 1.0117 and 1.0262 times of the maximum value of HCCI engine with compression ratio of 16 and 18. The analysis showed that higher air-fuel ratio of the lower compression ratio leaded to higher accumulated heat ratio.

The other result of the analysis is about emission characteristics of the combustion modes. The

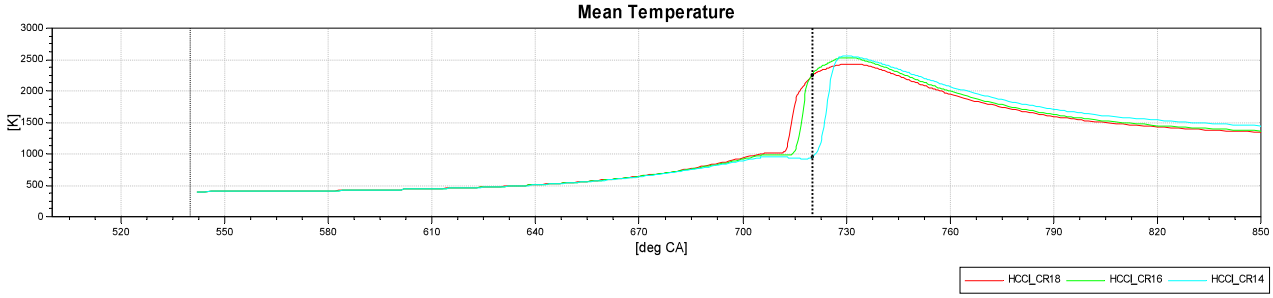


Figure 9. Mean Temperature Comparison of HCCI Combustion Under Different Compression Ratios

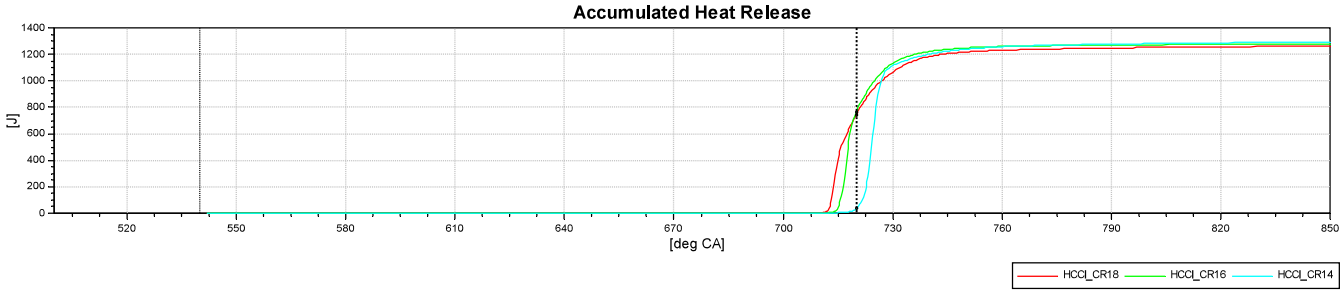


Figure 10. Accumulated Heat Release Comparison of HCCI Combustion Under Different Compression Ratios

overall NO and soot mass fractions HCCI combustion under different compression ratios (14, 16, 18) were compared in Figures 11 and 12. These emissions were started to occur whereupon 712 crank angle degrees and the maximum point of the overall NO mass fraction and overall soot mass fraction were observed whereupon 728 and 725 crank angle degrees respectively for the compression ratio of 18 which is the most rapid one for both cases. The results show that, emission rates of HCCI engine with compression ratio of 18 was 0.90 and 1.73 times of the value of HCCI engine with compression ratio of 14 and 16 at 750 crank degrees. Higher accumulated heat release due to better combustion and earlier combustion leaded to lower emissions.

4.5 Comparison of HCCI Combustion under Different Combustion Chamber Geometries

All the cycle analysis of HCCI combustion were done under the same conditions except combustion chamber geometry to observe the effect of the combustion mode in the means of engine performance and emission. A geometry with higher bowl volume was created and the same pre-processing procedure was done for same initial conditions with same mathematical models. The prepared geometry and mesh data is given in the Figure 13.

Engine specific outputs of the analysis are given in the Table 5 in terms of brake mean effective pressure, brake specific fuel consumption, friction mean effective pressure, indicated mean effective pressure, indicated power, and indicated torque.

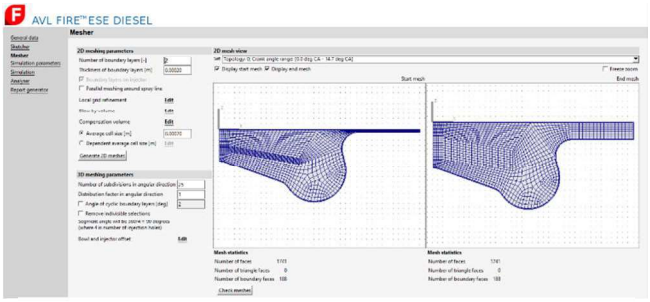


Figure 13. Mesh Model of Combustion Chamber Geometry with Higher Bowl Volume

Table 3. Engine Specific Outputs

Brake Mean Effective Pressure (bar)	8.00
Brake Specific Fuel Consumption (kg/kWh)	0.3554
Friction Mean Effective Pressure (bar)	1.58
Indicated Mean Effective Pressure (bar)	9.58
Indicated Power (kW)	6.06
Indicated Torque (Nm)	38.61

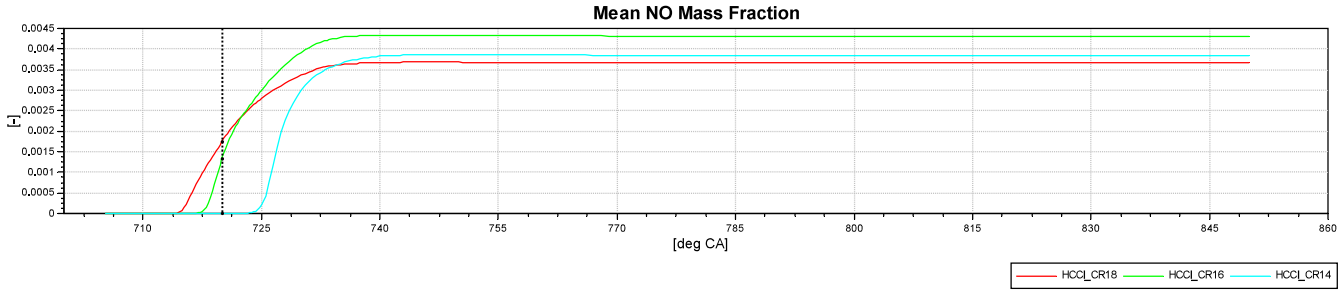


Figure 11. Mean NO Mass Fraction Comparison of HCCI Combustion Under Different Compression Ratios

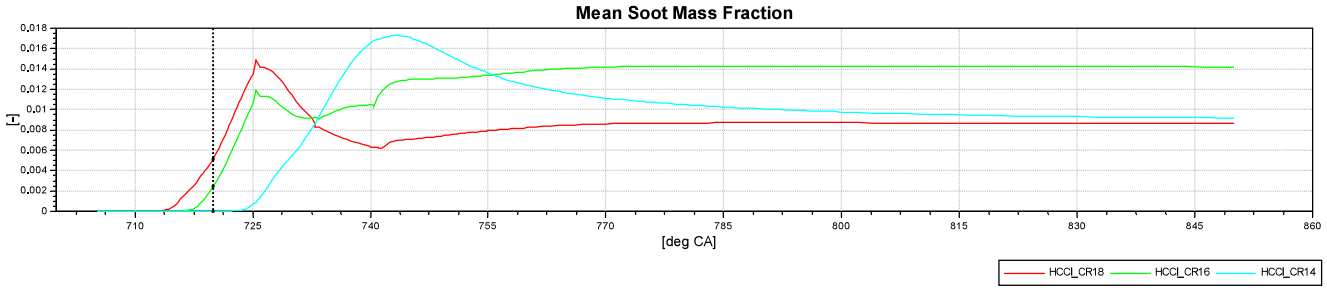


Figure 12. Mean Soot Mass Fraction Comparison of HCCI Combustion Under Different Compression Ratios

Both cycle analysis of HCCI combustion were done under the same conditions except combustion chamber geometry to observe the effect of the combustion mode in the means of engine performance and emission. HCCI ignition model was used for HCCI combustion with Eddy Breakup combustion model in both cases.

It is seen from the Figures 14 and 15 the combustion chamber geometry with higher bowl volume reached higher maximum pressure and maximum temperature values during the combustion stroke for the same compression ratio. In the terms of pressure, the maximum value of initial geometry was 94.3 percent of the initial geometry. In the terms of temperature, the maximum value of initial geometry was 98.2 percent of the maximum value of geometry with higher bowl volume. The analysis showed that higher maximum pressure and higher temperature can be achieved by geometry with higher bowl volume due to its higher air-fuel ratio.

One of the other results of the analysis is the accumulated heat release of HCCI combustion for different combustion chamber geometries (Figure 16). The maximum accumulated heat release value of HCCI engine with geometry with higher bowl volume was 1.0178 times of the maximum value of initial geometry. The analysis showed that higher air-fuel ratio of the geometry with higher bowl volume led to higher accumulated heat ratio.

The other result of the analysis is about emission characteristics of the combustion modes. The overall NO and soot mass fractions HCCI combustion under different combustion chamber geometries were compared (Figures 17 and 18). Both two masses were started to occur whereupon 715 crank degrees and the maximum point of the overall NO mass fraction and overall soot mass

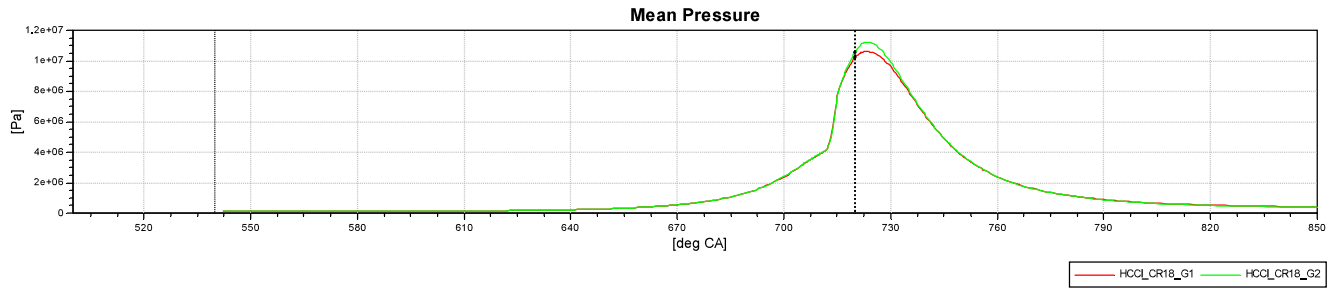


Figure 14. Mean Pressure Comparison of HCCI Combustion Under Different Combustion Chamber Geometries

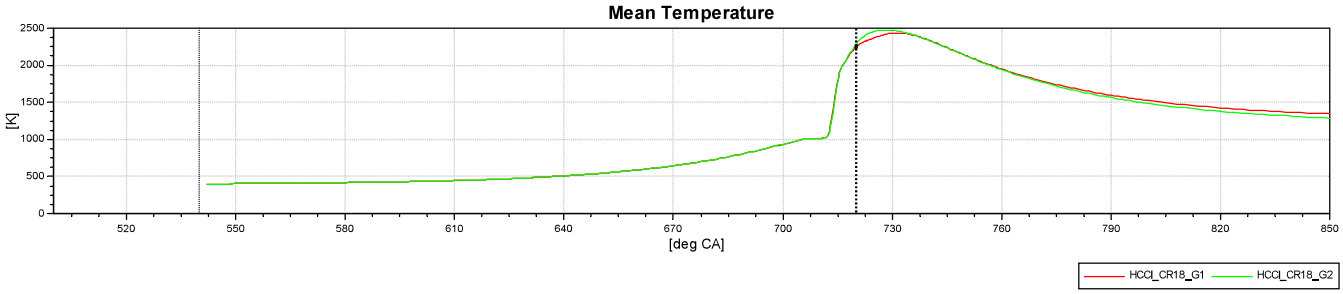


Figure 15. Mean Temperature Comparison of HCCI Combustion Under Different Combustion Chamber Geometries

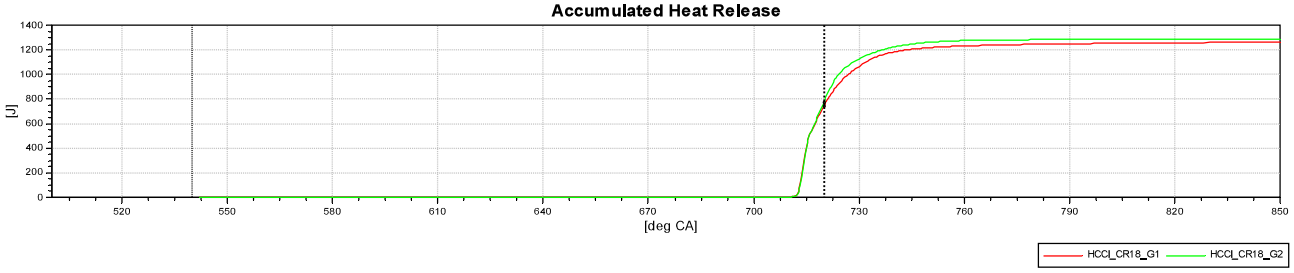


Figure 16. Accumulated Heat Release Comparison of HCCI Combustion Under Different Combustion Chamber Geometries

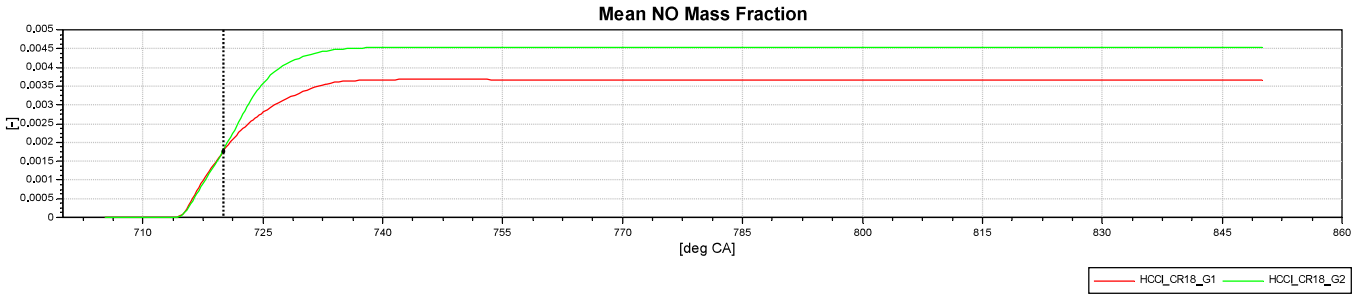


Figure 17. Mean NO Mass Fraction Comparison of HCCI Combustion Under Different Combustion Chamber Geometries

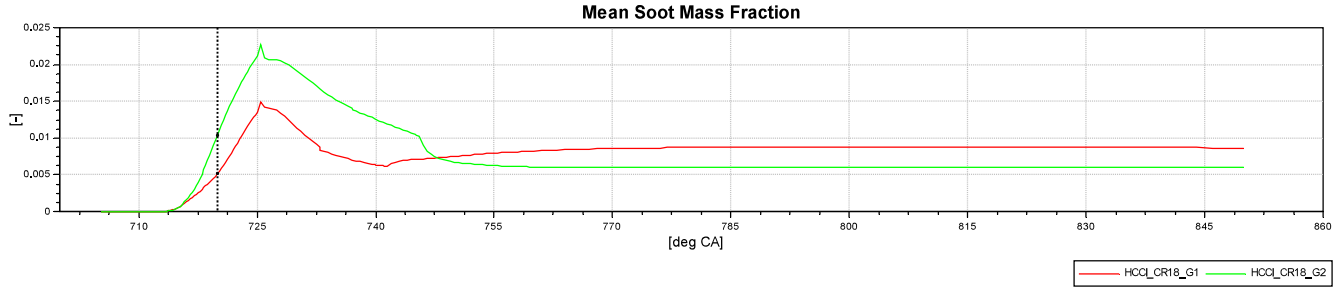


Figure 18. Mean Soot Mass Fraction Comparison of HCCI Combustion Under Different Combustion Chamber Geometries

fraction were observed whereupon 730 crank degrees. The results show that, NO emission rates of HCCI engine with geometry with higher bowl volume was 1.216 times of the initial geometry. Higher temperature values in the combustion chamber leaded to higher NO emissions. Moreover, soot emission rates of HCCI engine with geometry with higher bowl volume was 0.813 times of the initial geometry at 750 crank degrees. Higher equivalence ratio leaded to higher soot emissions.

5 CONCLUSION

In this study, HCCI combustion was investigated numerically. Design concept of different layouts of combustion chamber were investigated. Combustion modes of compression ignition and homogeneous charge compression ignition were researched.

The combustion modes of compression ignition and homogeneous charge compression ignition were analysed by using numerical methods. The results were validated with the numerical and experimental results of Yousefi et al. [6] which were examined for similar engine specifications with HCCI combustion. Firstly, compression ignition and homogeneous charge compression ignition were compared in each other for the same combustion chamber geometry. In that part of the study, it was seen that HCCI mode can be used to decrease emissions of high amount without highly performance changes.

The HCCI combustion is studied under different compression ratios and combustion chamber geometries. That study showed that higher compression ratio modification reached higher pressure and temperature than the lower compression ratio modification during the combustion stroke for the same combustion chamber geometry. The HCCI engine with higher compression ratio led to lower soot emissions. Also, higher bowl volume led to higher maximum pressure with higher NO emission.

In consequence of the study, a combustion chamber for a diesel engine can be modified to obtain lower emissions without high performance loss by using the results of the study.

ACKNOWLEDGEMENTS

Authors would like to thank Gazi University and AVL List GmbH for software support.

REFERENCES

[1] W. W. Pulkrabek, W. W. *Engineering Fundamentals of the Internal Combustion Engine*. 2nd Ed., Pearson Prentice Hall, 2004.

[2] W. A. Whatmough, Combustion-Chamber Design in Theory and Practice, *SAE Transactions*, pp. 115-138, 1929.

[3] H. K. Newhall, Combustion process fundamentals and combustion chamber design for low emissions, *SAE Transactions*, pp. 2805-2818, 1975.

[4] K. Matsumoto, T. Inoue, K. Nakanishi, T. Okumura, The effects of combustion chamber design and compression ratio on emissions, fuel economy and octane number requirement, *SAE Transactions*, pp. 886-898, 1977.

[5] A. Lotfi, H. Ghassemi, A review on the different geometries of combustion chamber in CI engines on performance, ignition and emission, *Journal of Atmospheric Pollution*, vol. 5, 2, pp. 40-46, 2017. doi: 10.12691/jap-5-2-1.

[6] A. Yousefi, A. Gharehghani, M. Birouk, Comparison study on combustion characteristics and emissions of a homogeneous charge compression ignition (HCCI) engine with and without pre-combustion chamber', *Energy Conversion and Management*, vol. 100, pp. 232-241, 2015.

[7] M. Cerit, H. S. Soyhan, Thermal analysis of a combustion chamber surrounded by deposits in an HCCI engine, *Applied Thermal Engineering*, vol. 50, 1, pp. 81-88, 2013. https://doi.org/10.1016/j.applthermaleng.2012.06.004.

[8] M. Feroskhan, T. Thangavel, B., Subramanian, R. K. Sankaralingam, S. Ismail, A. Chaudhary, Effects of operating parameters on the performance, emission and combustion indices of a biogas fuelled HCCI engine, *Fuel*, vol. 298, 120799, 2021. https://doi.org/10.1016/j.fuel.2021.120799.

[9] V.C. Pham, J.-H. Choi, B.-S. Rho, J.-S. Kim, K. Park, S.-K. Park, V. V. Le, W.-J. Lee, A numerical study on the combustion process and emission characteristics of a natural gas-diesel dual-fuel marine engine at full load, *Energies,* 14, 5, 1342, 2021. https://doi.org/10.3390/en14051342.

[10] S. Kannan, S. Mahalingam, S. Srinath, M. Sivasankaran, S. Kannan, An experimental study in HCCI combustion of LPG in diesel engine, *Materials Today: Proceedings*, vol. 37, pp. 3625-3629, 2021. https://doi.org/10.1016/j.matpr.2020.09.774.

[11] S. Polat, An experimental investigation on combustion, performance and ringing operation characteristics of a low compression ratio early direct injection HCCI engine with ethanol fuel blends, *Fuel*, vol. 277, 2020, 118092, 2020. https://doi.org/10.1016/j.fuel.2020.118092.

[12] S. Çelebi, C. Haşimoğlu, A. Uyumaz, S. Halis, A. Calam, H. Solmaz, E. Yılmaz, Operating range, combustion, performance and emissions of an HCCI engine fueled with naphtha, *Fuel*, vol. 283, 118828, 2021. https://doi.org/10.1016/j.fuel.2020.118828.

[13] X. Duan, M.-C. Lai, M. Jansons, G. Guo, J. Liu, A review of controlling strategies of the ignition timing and combustion phase in homogeneous charge compression ignition (HCCI) engine, *Fuel*, Volume 285, 2021,119142, https://doi.org/10.1016/j.fuel.2020.119142.

[14] H. Yu, W. Wang, D Sheng, H. Li, S. Duan, Performance of combustion process on marine low speed two-stroke dual fuel engine at different fuel conditions: Full diesel/diesel ignited natural gas. *Fuel*, vol. 310, 122370, 2022. https://doi.org/10.1016/j.fuel.2021.122370.

[15] V. Novozhilov, Computational fluid dynamics modeling of compartment fires, *Progress in Energy and Combustion Science*, vol. 27, 6, pp. 611-666, 2001.

[16] AVL FIRE User Manuel version 2021, AVL LIST GmbH, Graz, Austria.

YAŞLI BAKIM TESİSLERİNDE YANGIN SIRASINDA BAKIMA MUHTAÇ KİŞİLERİN TAHLİYE OLANAKLARININ BİLGİSAYAR DESTEKLİ SİMÜLASYON PROGRAMI İLE İNCELENMESİ

Kerem İlbay, Gökhan Coşkun[2] ve Ekrem Büyükkaya[3]

1. Yangın ve Yangın Güvenliği Yüksek Lisans Öğrencisi, Sakarya Üniversitesi, kerem.ilbay1@ogr.sakarya.edu.tr
2. Doç Dr, Makine Mühendisliği Bölümü, Sakarya Üniversitesi, gcoskun@sakarya.edu.tr
3. Prof Dr, Makine Mühendisliği Bölümü, Sakarya Üniversitesi, ebkaya@sakarya.edu.tr

Özet

Bu çalışmada bedensel olarak bakıma muhtaç ve hareket kabiliyetleri sınırlı ya da kendi başlarına hareket edemeyen insanların yangın durumunda bulunduğu binadan korunaklı olarak tahliyesinin, farklı senaryolar üzerinden incelenerek tahliye anında yangın sonucu çıkan gazlardan, sıcaklık ve görüş mesafesi gibi etkilerin incelenmesi ve bunun sonucunda yaşamsal durumunun analizinin yapılması incelenecektir. Mimari modelde kat koridrolarında duman kontrol sisteminin yapıldığı ve yapılmadığı, yağmurlama söndürme sisteminin bulunup bulunmadığı tahliye senaryoları oluşturulacak ve bu sonuçlar birbirleri ile karşılaştırıştırılacaktır. Tahliye olacak kişiler ise sedye ile tekerlekli sandalye ve kendi kendine tahliye olabilecek şekilde çeşitlendirilecektir.

Anahtar kelimeler: Tahliye, Yangın, Huzur evi, Can güvenliği, Acil durum

1 GİRİŞ

Huzur evleri ve yaşlı bakım evleri gibi sağlık yapıları, acil durum anlarında bina içinde bulunan insanların hareket kabiliyeti sınırlı olduğundan binanın tahliyesi, diğer yapılara göre daha yavaş olacaktır. Bu nedenle binada tahliye yolları mümkün olduğu kadar sık yapılmalı, yangından korunumlu tahliye koridorlarına mümkün olduğunca hızlı ulaşılabilmelidir. Otoriteler tarafından oluşturulmuş yönetmeliklerde tahliye ve diğer mimari durumlar için koşullar belirtilmiş olsada bazı durumlarda saha koşulları, mimari ya da mekanik etmenler neticesinde yapılan uygulama çok sağlıklı olamamaktadır. Örneğin refakatçi ile yapılması gereken bir tahliye ile ilgili detaylı açıklamalar bulunmamakta ya da sedye ile taşınması gerekli insanlar için acil durum asansörü kullanılcak ise asansör kapasitesinin ne olması gerektiği ile ilgili bir standart Binaların Yangından Korunması Hakkındaki Yönetmelik (BYKHY) içerisinde bulunmamaktadır.

Bu çalışmada yönetmeliksel olarak bir binada tahliye sisteminin mimari, mekanik ve elektriksel açıdan yönetmeliklerce nasıl olması gerektiği anlatılacak olup (Temel gereklilikler ilgili maddeler refere edilerek belirtilecektir. Her binanın, kullanım sınıfı, yapı yüksekliği, kullanılan cephe elemanı gibi çeşitli etkilere göre farklı ihtiyaçları bulunabilir.) daha sonrasında bilgisayar destekli tasarım programı ile yönetmeliklere mimari olarak uygun bir yaşlı bakım evinin çeşitli seneryolar ile tahliye simulasyonu incelenerek bakım evinde bulunan kişilerin yangın ve duman etkisi altında kalmaları incelenecek ve seneryolar birbirleri ile karşılaştırılıp yorumlanacaktır. Yapmış olduğum bu çalışmada yangın sırasında sıcaklıktan etkinlenme durumları da görüş mesafeleri incelenecektir.

Ülkemizde binaların yangından korunması ile ilgili geçerli tek tasarım metodu yönergesel tasarım olup bilgisayar temelli tasarım, bilgi ve tecrübe arttıkça ülkemizde de geçerlilik kazanacağı öngörülmektedir. Hem dünyada hem de ülkemizde yönetmeliksel olarak mimari uygunluk bulunmayan ya da maliyet azaltmak adına yapılarda alternatif olarak kullanılmaya zamanla başlanması beklenmektedir.

2 YÖNETMELİKTE BELİRTİLEN GEREKLİLİKLER

Bir binada tahliye mesafesi, çıkışa ulaşım, çıkış ve çıkıştan tahliye için kat edilen mesafelerin toplamıdır. Bu mesafeler için BYKHY ve (Ülkemizde ilk uygulanması gereken standartlar BYKHY de belirtilen kurallardır.) gerekli olması durumunda NFPA veya diğer uluslararası

standartlara başvurulabilinir. Aşağıda tüm binalar için gerekli ortak gereklilikler açıklanmıştır. Bunun yanısıra BYKHY ve NFPA 101' de yaşlı bakım evleri ile ilgili ayrıca gereklilikler de belirtilmiştir. Bir insanın binadan tahliyesi çıkışa ulaşım, çıkış ve çıkıştan tahliye olarak üç temel başlık altında açıklanabilir. Bunlar; çıkışa ulaşım, çıkış ve çıkıştan tahliye olarak açıklanabilir.

BYKHY'e göre yağmurlama sistemi (Sprinkler sistemi) bulunmayan bir huzurevinde tek yönde kaçış mesafesi 15 metre, iki yönde kaçış mesafesi ise en fazla 30 metre olabilir. Yağmurlama sistemi bulunan bir bir huzurevinde tek yönde kaçış mesafesi 25 metre çift yönde kaçış mesafesi ise en fazla 45 metre olabilmektedir. [1].

NFPA yaşlı bakım evlerini gün içinde bakım yapılan yapılar ile tam zamanlı bakım yapılan ve gerektiğinde tedavi de yapılabilen binalar olarak ayırmaktadır. Her iki bina tipi için de tek yönde tahliye mesafesi yağmurlama sistemi bulunmayan binalarda 23 metre, yağmurlama sistemi bulunan binalarda 30 metredir. İki yönlü tahliye mesafesi ise yağmurlama sistemi bulunmayan binalarda 46 metre, yağmurlama sistemi bulunan binalarda 61 metredir. Tedavi merkezleri ve ram zamanalı bakım yapılan hastane gibi merkezlerde yağmurlama sistemi bulunması zorunludur.

Çıkış başlığı altında yangın holleri ve kaçış merdiveni özellikleri ve merdiven kapı, basamak, sahanlık gibi etmenler incelenmektedir. Çıkışların birbirine alternatif oluşturabilmesi, çıkış lokasyonlarının belirlenmesinde başlıca dikkat edilecek noktadır. 2 veya daha fazla çıkış olan odalarda ve bina yangın merdiveni kapılarında iki çıkış arasındaki mesafe, kat veya oda diyagonal mesafesinin minimum üçte biri kadar olmak zorundadır.Yağmurlama sistemi bulunmayan mekanlarda iki kaçış arasındaki mesafe, kat veya oda diyagonalmesafesinin yarısı kadar olmalıdır. [1]. [2].

3 BİLGİSAYAR DESTEKLİ TASARIMDA DİKKAT EDİLMESİ GEREKEN KAVRAMLAR

Bilgisayar destekli yangın ve tahliye simülasyon programları ile tasarım yaparken kontrol edilmesi gereken kriterler; ortam sıcaklığı ve ortamdaki görüş mesafesidir. İstatistiksel çalışmalarda; ölümlerin % 90'ından fazlasına zehirli dumanın neden olduğu görülmüştür. Yanma ürünleri genellikle partiküller, yanmamış ürünler, su buharı, karbondioksit ve karbonmonoksit ile diğer zehirleyici ve korozif gazları içerir. Bir birey, yangında mahsur kaldığında veya aciz kaldığında, koşullar birkaç saniye ila birkaç dakika içinde ölümcül hale gelebilir. Yangınların ürettiği ısı, duman ve zehirli gazlar gibi etmenler katlanarak artabilir. Bir yangında hayatta kalmanın temel belirleyicisi, insan kabiliyetlerini yapamadığı duruma gelme süresidir.

Isıya maruz kalmanın yetersizliğe ve ölüme yol açabileceği üç temel yol vardır. Bunlar; sıcak çarpması, vücut yüzey yanıkları ve solunum yolu yanıklarıdır. Cilde ısı temasından kaynaklanan ağrı, 0.1 mm derinlikteki cilt sıcaklığı 44.8˚ C'ye ulaştığında ortaya çıkar. Bu, Lawrence ve Bull'un, sıcak bir tutamaç ile elin derisi arasındaki ara yüz 43 ˚C'ye ulaştığında rahatsızlığın yaşandığını tespit eden araştırmasıyla ortaya çıkmıştır.

Bir yangın olayı sırasında esas olarak radyant ısıya (örneğin sıcak bir duman tabakasının altında yürürken veya bir alevi geçerken), konveksiyonlu ısıya (örneğin aşırı ısınmış bir odada) veya radyant ve konveksiyonlu ısı kombinasyonuna maruz kalınır. Babrauskas 2,5 kW / m2'lik bir dayanıklılık sınırı öngörmektedir. 2.5 kW / m2 seviyesinde, Buettner, Simms ve Hinkley ağrının yaklaşık 30-60 saniye maruziyette meydana geldiğini bulmuşlardır. Radyant akış azaldıkça tolerans süreleri üssel olarak artar; Mudan ve Croce, maruziyet süresine bakılmaksızın, altında hiçbir ağrı yaşanmayan 1.7 kW / m2'lik kritik bir ısı akışı belirtmiştir. 2,5 kW / m2 üzerindeki radyant ısı, ciltte ağrıya ve ardından birkaç saniye içinde yanmalara neden olur [5].

Tablo 1. Isı mazuriyetine karşı insan toleransı [6].

Isı transferi türü	Yoğunluk	Tolerans
Işınım	<2,5 kW · m^{-2}	>5 dak
	2,5 kW · m^{-2}	30 sn
	10 kW · m^{-2}	4 sn

Taşınım	<60 ºC %100	
	100 ºC < %10 H_2O[a]	>30 dak
	120 ºC < %10 H_2O	8 dak
	140 ºC < %10 H_2O	4 dak
	160 ºC < %10 H_2O	3 dak
	180 ºC < %10 H_2O	2 dak 1 dak

[a] %10 H2O' nun bir hacim fraksiyonu (v/v)

Bir çıkış yolu boyunca görünürlüğün azalması, kendi başına bireyleri etkisiz hale getirmeyecek veya ölüme neden olmayacaktır. Bir yangının ürettiği aşırı ısıya maruz kalma ve yüksek dozda zehirli gazlar, iş göremezlik ve ölümle sonuçlanabilir. Görünürlük eksikliği (kısa vadeli) fizyolojik bir etkiye neden olmaz, bu da insanların karanlık odalarda seyahat edebilecekleri anlamına gelir. Seyahatin karanlık tarafından yavaşlatılması beklenebilir, ancak doğrudan yaralanma tek başına karanlığa (kısa vadede) atfedilemez. Benzer şekilde, insanların deneylerde ve bazı yangın olaylarında yoğun dumanın içinde değişen hızlarda hareket ettikleri gösterilmiştir. Azaltılmış görüş, hareket hızının düşmesine, ısıya ve zehirli gazlara daha uzun süre maruz kalmasına neden olur. Yeterli ve sürekli olarak ısıya ve / veya toksik gazlara maruz kalındığında, hareket hızı insanların hareketini yavaşlatmaya devam edebilir ve zihinsel yeteneklerini azaltabilir. Azalan görüş mesafesi, yol bulmayı da etkiler ve çıkışları bulmak için geçen süreyi uzatabilir.

4 SİMULASYON SENARYOLARI VE METADOLOJİ

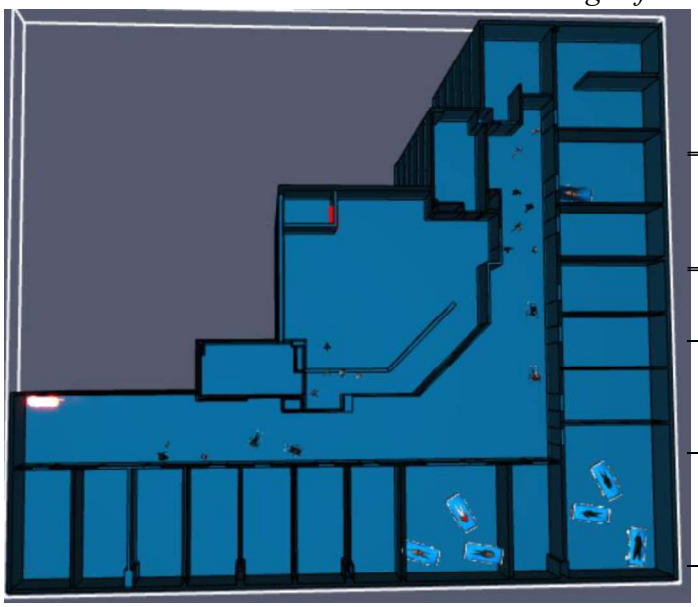
Modelleme sırasında ilk adım, mimari yapı Autocad programına aktarılması ve BYKHY'ede belirtilen mimari gerekliliklere (Kaçış mesafeleri, merdiven ve kapı genişliği, gerekli minimum çıkış sayısı gibi) göre iki boyutlu olarak oluşturulmasıdır. Daha sonra iki boyutlu çizim Sketchup programında üç boyutlu olarak modellenmiştir. 3 boyutlu olarak medellenen çizim Pyrosim (Yangın simulayon programı) ve Pathfinder (Acil Durum Tahliye Programı) simulasyon hesap programlarına aktarılmıştır. Kullanılan yangın simulasyon programları ve temel girdiler aşağıdaki gibi tanımlanabilir.

PyroSim, Yangın Dinamikleri Simülatörü (FDS) için bir grafik kullanıcı arayüzüdür. FDS modelleri yangın sırasında oluşan duman, sıcaklık, karbon monoksit ve diğer maddeleri tahmin edebilir. Bu simülasyonların sonuçları, binaların henüz tasarım aşamasındayken güvenliğini sağlamak, mevcut binaların güvenlik seçeneklerini değerlendirmek, kaza sonrası inceleme için yangınları yeniden inşa etmek ve itfaiyecilerin eğitimine yardımcı olmak için kullanılabilir.

HAD, Ulusal Standartlar ve Teknoloji Enstitüsü'nde (NIST) geliştirilmiş güçlü bir yangın simülatörüdür. FDS, düşük hızlı, termal olarak yönlendirilen akış için optimize edilmiş hesaplamalı akışkanlar dinamiğini (HAD) kullanarak yangın senaryolarını simüle eder. Bu yaklaşım çok esnektir ve çok çeşitli yangınlara uygulanabilir. Binalarda havalandırma gibi yangın içermeyen durumları da modelleyebilir

PyroSim metrik veya İngiliz birimlerinde çalışabilir ve ikisi arasında istediğiniz zaman geçiş yapabilirsiniz. PyroSim ayrıca diyagonal duvarlar, eskiz için arka plan görüntüleri, nesne gruplama, esnek görüntüleme seçenekleri ve engellerin kopyalanması gibi üst düzey 2D ve 3D geometri oluşturma özellikleri sunar.

Pathfinder Ulusal Standartlar ve Teknoloji Enstitüsü'nde (NIST) geliştirilmiş güçlü bir yangın tahliye simülatörüdür. Hastanelerden stadyumlara kadar çok çeşitli mimari yapılarda simülasyon imkanı sunmaktadır. DXF, DWG ve Pyrosim modelleri içe aktarılabilir. Bu sayade pyrosim tarafından oluşturulan bir yangın pathfinder programına aktarılarak, tahliye sırasında yangın dumanının vermiş olacağı zararlar da belirlenebilir. Bunun yanında tahliye olacak kişilerin sedye ya da refakatçi eşliğinde taşınması da simüle edilebilir.



Şekil 1. Pathfinder programında yangının çıktığı katın gösterimi

Simülasyon hesaplamalarında ısı salınım oranı, tahliye hızı gibi etmenler belirlenmelidir. Bu değerler simülasyon analizinin temelini oluşturmaktadır.

Tahliye hızı cinsiyet durumu, yaş ve fiziksel etmenlere bağlı olmakla birlikte yangın anında solunan duman ve görülebilirlikte etkili olmaktadır. Pathfinder ile duman yoğunluğunun hareket hızına etkisi hesaplanabilmektedir.

Yürüme hızı= min(1, maks(0,2*(1-324*(3/görülebilirlik mesafesi) (2.1)

Burada yürüme hızı en fazla 1 m/s en az 0,2 m/s arasında duman yoğunluğuna göre değişim göstermektedir [7].

Isı salınım oranı (ISO) performansa dayalı tasarımda, tasarımın başlangıç değişkenlerinden biridir. Binalardaki yangın davranışının hesaplanması, yangının ısı yayma oranı bilinmedikçe mümkün değildir. Birçok nesne ve ürün için yayınlanmış ISO mevcut değildir, bu nedenle, bir yanıt gerekirse laboratuvar testlerinin yapılması gereklidir. Bununla birlikte, bazı malzemeler için, örnek veriler bulunmaktadır. Tasarım için yangın yükü poliüretan koltuğu yanması üzerine belirlenmiştir.

Tablo 2. Çeşitli mazlemelerin en yüksek ısı salınımları [4].

Yanıcı yük	Kütle	En Yüksek Isı Seviyeleri
Koton yatak	12-13 kg	40-70 kW
Plastik çöp kutusu	1,2 kg	120-350 kW
Poliüretan yatak	3-14 kg	810-2630 kW
Poliüretan sofa	51 kg	3120 kW
Yılbaşı ağacı	6-20 kg	3000-5000 kW
Ahşap mobilya	70-121 kg	1900-6400 kW

Simulasyon hesaplamarı dört farklı senaryo üzerinde yapılıp sonuçları karşılaştırılmıştır. Senarolar aşağıdaki gibi açıklanabilir.

Senaryo1; Senaryoda koridor üzerinde bulunan bir koltuğun yanması ile yağmurlama sistemi bulunmadan huzurevi sakinlerinin tahliyesi incelenecektir.

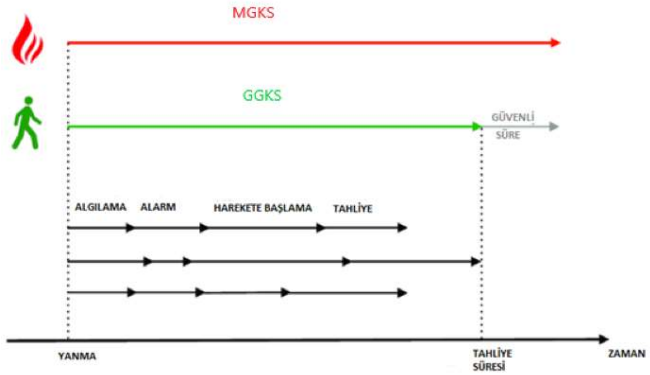
Senaryo2; Senaryoda koridor üzerinde bulunan bir koltuğun yanması ile yağmurlama sistemi bulunan huzurevi sakinlerinin tahliyesi incelenecektir.

Senaryo3; Senaryoda koridor üzerinde bulunan bir koltuğun yanması ile yağmurlama sistemi bulunmayan ancak duman tahliye sistemi bulunan bir mekanda huzurevi sakinlerinin tahliyesi incelenecektir.

Senaryo4; Senaryoda koridor üzerinde bulunan bir koltuğun yanması ile yağmurlama sistemi ve duman tahliye sistemi bulunan bir mekanda huzurevi sakinlerinin tahliyesi incelenecektir.

5 SİMULASYON SONUÇLARININ DEĞERLENDİRİLMESİ

MGKS> GGKS durumu güvenli tahliye için gerekli kriterdir. MGKS değerine ulaşabilmek için binada tahliye tatbikatı yapılması gerekir. Ancak tedavi gören bireylerin bulunabileceği durumlarda huzur evlerinde tatbikat yapmak mümkün olmayabilir. Simulsayon sonucunda RSET değerine ulaşılabilir.

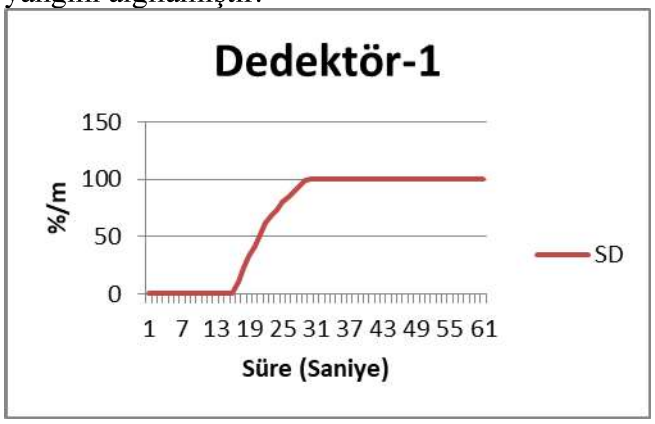


Şekil2. Mevcut güvenli kaçış süresine (MGKS) dahil olan süreçlerin basitleştirilmiş şeması

GGKS= $t_d + t_n + t_{p-e} + t_e$

T_d = Yangının tutuşmasından algılamaya kadar geçen süre, algılama aşaması

Simulasyonda 0.saniyede tutuşma başlamaktadır. Birinci dedektör ilk algılamayı 16 saniye sonra yapmıştır. İkinci dedektör dedektör ise yangın başladıktan 33 saniye sonra yangını algılamıştır.



Şekil3. Birinci dedektör algılama süresi

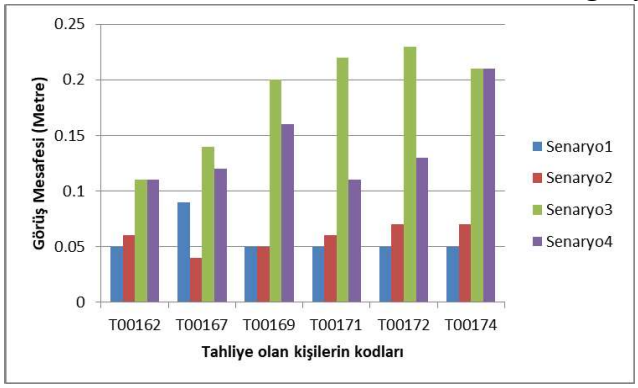
Senaryolar böümünde daha önce belirtildiği gibi NFPA72 de belirtilen pozitif alarm senaryosu uygulandığından başka bir dedektör 180 saniye içerisinde algılama yapmaz ise bu süre geçene kadar binada alarm durumuna geçilmeyecektir. Ancak otuzuncu saniyelerde başka bir dedektörde duman algıladığı için artık bina alarm durumuna geçecektir. Simulasyonda T_d süresi yaklaşık 30 saniyedir.



Şekil4. İkinci dedektör algılama süresi

T_n = Tespitten yangın acil durumunun bina sakinlerine bildirilmesine kadar geçen süre, bildirim aşaması;
Binada otomatik yangın alarm sistemi olduğu düşünülmüş ve ikinci dedektöründe duman algılayınca bekleme yapmadan alarm durumuna geçildiği düşünülmüştür. Bu nedenle bu değer 0 olarak düşünülmüştür.
t_{p-e} = Bildirimden tahliyenin başlamasına kadar geçen süre, ön tahliye aşaması;
Bu süre içinde kesin bir bilgi tatbikat yapılmadan anlaşılamayacaktır. Aynı zamanda yangının uyku durumunda ya da gün içinde çıkması bu süreyi etkileyecektir. Simulasyonda bu değer 15 saniye olarak tasarlanmıştır.
t_e = Tahliye hareketinin başlamasından güvenli alana ulaşılana kadar geçen süre, tahliye aşaması;
Tahliye 45. saniyede başlamış olup, t_e süresi 150 saniye sürmektedir. Güvenli alana en son geçen kişi 195.saniyede ulaşmaktadır. Yani GGKS süresi 195 saniye olarak kabul edilebilir.
Yangın çıkan katta güvenli alana ulaşım üç dakika altında gerçekleşmektedir. Güvenli alana geçtikten sonra dumana maruz kalınmayacaktır.

Görüş mesafesi için kat zemininden 1,8 metre yükseklik referans alınarak yorumlamlar yapılmıştır. Görüş mesafeleri kişilerin tahliye zamanı ve tahliye olduğu bölgelerdeki duman yoğunluğuna göre değişiklik göstermektedir. Aşağıdaki tabloda kişilerin en az görüş mesafesinin bulunduğu mesafe, parantez içinde bu mesafenin hangi sürede olduğu saniye cinsinden belirtilmiştir.



Şekil5. Simulasyonların sonuçlarına göre görüş mesafelerini karşılaştırılması

Tüm senaryolarda 70. saniyeden itibaren koridorun büyük bir bölümünde görüş mesafesi sıfırlanmaktadır. Refakatçi eşliğinde tahliye olan insanlar 70.saniyede odalarını boşaltmaya başlayıp hepsinin güvenli alana geçmeleri 175.saniyeye kadar devam etmektedir. Bu zaman içerisinde görüş mesafesi neredeyse sıfıra yakın olduğundan görüş mesafesi baz alındığında tahliye uygun olmayacaktır. BYKHY'de koridrolarda olması gereken duman egzoz fanı tasarım kriteri net olarak belirtilmemiştir. Ülkemizdeki genel anlayış koridor hacminin saatte 10 katı kadar hava çevremi sağlayacak şekilde havalandırma yapılmasıdır. Kimi görüşlerde yangın çıkan katın alt ve üst katındaki kat koridorlarını da bu hacme eklemesi gerektiğidir. Bu şekilde yorumlandığında bina mimarisine göre koridor için BYKHY gerekliliklerine göre yaklaşık 17900m^3 /saat (4,9 m^3/s) kapasiteli egzoz fanı ihtiyacı oluşmaktadır. Simülasyon sonuçları üç kat için 5 m^3/s kapasiteli bir fan kullanılarak incelenmiş ve görüş mesafesinin bir süre sonra kat zemininden 1,8 metre yükseklik için yeterli olmadığı Şekil 5.'de belirtilen değerler baz alındığında görülmüştür.

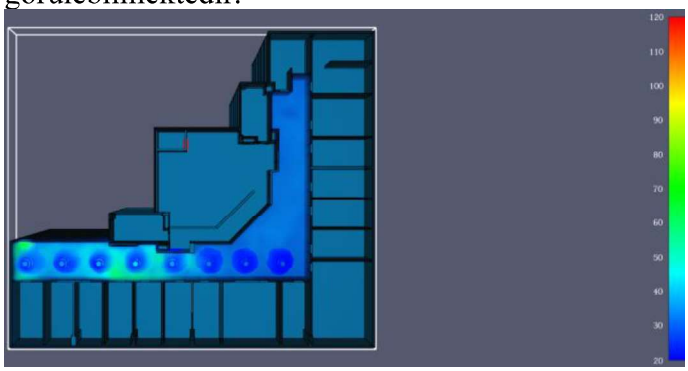
Yapılan simülasyonda koltuk yangının tasarlanması, kullanılan mazlemenin poliüretan olması nedeni ile yoğun duman oluşturması ve yangın yükünün yüksek olması da görüş mesafesinin bu derece düşük olmasında etkili olabilir. Bununla beraber, bu tip yapılarda ana koridorlarda zemin seviyesinde de yönlendirme işaretlerinin bulunmasının, dumanın tavandan başlayıp zemine doğru birikeceği düşünüldüğünde iyileştirici bir durum yaratacaktır. Ana koriorlarda görüş mesafesinin iyileştirilmesi için kullanılan mobilya tekstil malzemelerinin yoğun duman çıkarmayan ürünlerden seçilmesi uygun olacaktır.

Aşağıdaki şekillerde koridorda oluşan sıcaklık dağılımı belirtilmektedir. Yağmurlama başlığı ve duman egzoz sitemi olmayan birinci senaryoda sıcaklık 220°C ye ulaşmaktadır. Tüm senaryolar içerisinde ulaşılan en yüksek sıcaklık olarak görülmektedir.



Şekil 6. Senayo1'e göre 270.saniyede koridorda oluşan sıcaklık değerleri

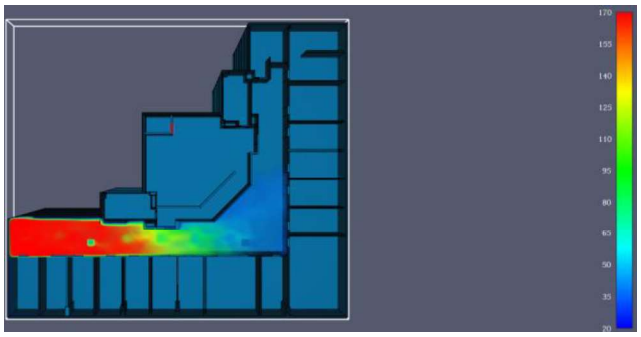
Sadece sprinkler sistemi bulunan ikinci senaryoda sıcaklık en fazla 120°C ye çıkmaktadır. İlk yağmurlama başlığı 33.saniyede aktif olmuştur. 102.saniyeye kadar koridorun yarısında sıcaklık 120°C ye ulaşmıştır. 102. saniyeden sonra yağmurlama başlıklarının sekiz tanesinin aktif olması ile birlikte ortam soğumaya başlayarak 270.saniyede ortamda sıcaklık 70°C ve daha altında kaldığı görülmektedir. Buradan yağmurlama başlıklarının ortamnın soğutulmasında ne derece etkili olduğu anlaşılmaktadır. Toplamda 8 adet yağmurlama başlığını ile yangın kontrol altına alınmıştır. Bu durum Şekil 7.' de görülebilmektedir.



Şekil 7. Senayo2'ye göre 270.saniyede koridorda oluşan sıcaklık değerleri

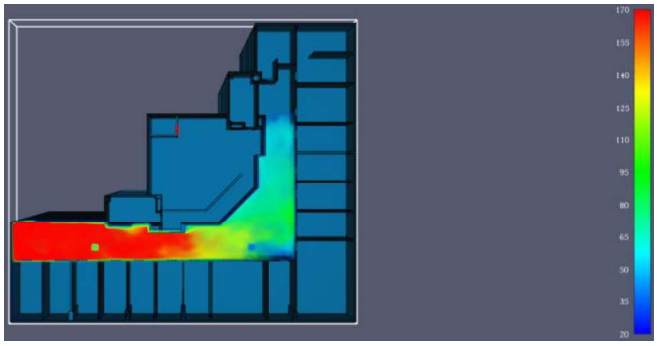
Hem yağmurlama sistemi hem de duman egzoz sisteminin bulunduğu üçüncü senaryoda ulaşılan en yüksek sıcalık 170 °C dir. Bu senaryoda da ilk yağmurlama başlığı 33.saniyede aktif olmuştur. Daha sonra 7 adet yağmurlama başlığı

aktif olmuş ve 200.saniyede yangına yakın tahliye kapısında da sıcaklık 90 °C a kadar düşmüştür. Duman egzoz fanının bulunması daha az yağmurlama başlığının açılması ile yangının kontrol altına alınmasını sağlamıştır.



Şekil 8. Senayo3'e göre 270.saniyede koridorda oluşan sıcaklık değerleri

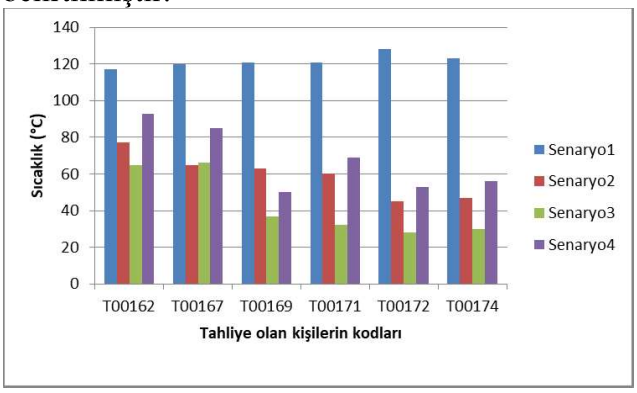
Sadece duman egzoz menfezlerinin bulunduğu dördüncü senaryoda görülen en yüksek sıcaklık 170 °C dir.



Şekil 9. Senayo4'e göre 270.saniyede koridorda oluşan sıcaklık değerleri

Senaryolar sonucunda ortaya çıkan simulasyon sonuçlarına göre, sadece yağmurlama sistemi bulunan ortamda ortam sıcaklığı en düşük seviyededir. Sadece duman egzoz sistemi buluna ve yağmurlama başlığı ile duman egzoz sistemi bulunan senaryolarda ise en yüksek sıcaklık aynı değerlere çıkmaktadır. Sadece yağmurlama sistemi ile hem duman egzoz sistemi hem de yağmurlama sisteminin bir arada olduğu senaryolarda ulaşılan en yüksek sıcaklığın farklı olmasının nedeni, duman egzoz sisteminde ortama dış ortamdan oksijenin ilave edilmesiyle açıklnabilir. Egzoz sistemi olmayan senaryoda oksijen oranı daha hızlı azaldığı için yanma şiddeti daha düşüktür. Bu nedenle sıcaklık en fazla 120°C olmaktadır. Senaryo3 ve senaryo4 de ulaşılan en yüksek sıcaklık aynıdır fakat ortamın soğuması için yağmurlama sisteminin gerekliliği, iki senaryo incelendiğinde görülmektedir.

Aşağıda bulunan tabloda ise tahliye olan kişilerin tahliye sırasında koridordan geçiş süreleri ile geçiş anındaki sıcaklık aralıkları belirtilmiştir.



Şekil 10 Yangın çıkan koridorda insana tesir eden en yüksek sıcaklık değerlerinin grafik ile karşılaştırılması (°C)

Bir kişinin cildinde sıcaklık nedeni ile ağrı cilt sıcaklığı 44.8˚ C'ye ulaştığında ortaya çıkmaktadır. Bu nedenle tüm senaryolarda yangının yaydığı ısı kaynaklı cilt ağrısı olma ihitimali bulunmaktadır. Yapılan araştırmalar sonucunda Şekil 10. da görüldüğü üzere, ısı mazuriyetine karşı insan toleransı 140˚ C sıcaklığın altında 3 dakikadır. Yukarıdaki grafikte (Şekil10.) bu sınırdaki toplam temas süresi en fazla 15 saniye olduğundan mevcut senaryoların tümünde sıcaklık açısından tolere edilebilir sınırlar içerisinde kalınmıştır. Sıcaklık bazında incelendiğinde simulayon can güvenliği bakımından uygundur.

REFERANSLAR

[[1]. Binaların Yangından Korunması Hakkında Yönetmelik -(09/07/2015)-29411, 2015.
[2]. NFPA 101 Life Safety Code. 2018 Edition
[3]. Fire Protection Handbook 20 th Edition
[4]. SFPE Handbook of Fire Protection Engineering-5th Edition-Morgan J_2015-2016
[5]. BS 7899-2:1999 Assessment of hazard to life and health from fire - Part 2: Guidance on methods for the quantification of hazards to life and health and estimation of time to incapacitation and death in fires
[6]. SFPE Guide to Human Behavior in Fire 2nd Edition
[7]. Walking Speed in Smoke: Representation in Life Safety Verifications- Karl Fridof, Daniel Nilsson, Hakan Frantzich, Enrico Ronchi (2018)